

Carbon Materials: Chemistry and Physics 7

Series Editors: Franco Cataldo · Paolo Milani

Ali Reza Ashrafi

Franco Cataldo

Ali Iranmanesh

Ottorino Ori *Editors*

# Topological Modelling of Nanostructures and Extended Systems

 Springer

# Topological Modelling of Nanostructures and Extended Systems

## **CARBON MATERIALS: CHEMISTRY AND PHYSICS**

A comprehensive book series which encompasses the complete coverage of carbon materials and carbon-rich molecules from elemental carbon dust in the interstellar medium, to the most specialized industrial applications of the elemental carbon and derivatives. A great emphasis is placed on the most advanced and promising applications ranging from electronics to medicinal chemistry. The aim is to offer the reader a book series which not only consists of self-sufficient reference works, but one which stimulates further research and enthusiasm.

### *Series Editors*

Dr. Prof. Franco Cataldo  
Via Casilina 1626/A,  
00133 Rome, Italy

Professor Paolo Milani  
Department of Physics  
University of Milan  
Via Celoria, 26  
20133, Milan, Italy

---

### **VOLUME 7: TOPOLOGICAL MODELLING OF NANOSTRUCTURES AND EXTENDED SYSTEMS**

### *Volume Editors*

Prof. Dr. Ali Reza Ashrafi  
Department of Mathematics  
University of Kashan  
87317-5116, Kashan, Iran

Prof. Dr. Franco Cataldo  
Department of Materials Science  
Tor Vergata University  
Rome, Italy

Prof. Dr. Ali Iranmanesh  
Department of Mathematics  
Tarbiat Modares University  
Tehran, Iran

Prof. Dr. Ottorino Ori  
Actinium Chemical Research  
Rome, Italy

For further volumes:

<http://www.springer.com/series/7825>

Ali Reza Ashrafi • Franco Cataldo • Ali Iranmanesh  
Ottorino Ori  
Editors

# Topological Modelling of Nanostructures and Extended Systems

 Springer

*Editors*

Ali Reza Ashrafi  
Department of Mathematics  
University of Kashan  
Kashan, Iran

Franco Cataldo  
Department of Materials Science  
Tor Vergata University  
Rome, Italy

Ali Iranmanesh  
Department of Mathematics  
Tarbiat Modares University  
Tehran, Iran

Ottorino Ori  
Actinium Chemical Research  
Rome, Italy

ISSN 1875-0745

ISBN 978-94-007-6412-5

DOI 10.1007/978-94-007-6413-2

Springer Dordrecht Heidelberg New York London

ISSN 1875-0737 (electronic)

ISBN 978-94-007-6413-2 (eBook)

Library of Congress Control Number: 2013939601

© Springer Science+Business Media Dordrecht 2013

This work is subject to copyright. All rights are reserved by the Publisher, whether the whole or part of the material is concerned, specifically the rights of translation, reprinting, reuse of illustrations, recitation, broadcasting, reproduction on microfilms or in any other physical way, and transmission or information storage and retrieval, electronic adaptation, computer software, or by similar or dissimilar methodology now known or hereafter developed. Exempted from this legal reservation are brief excerpts in connection with reviews or scholarly analysis or material supplied specifically for the purpose of being entered and executed on a computer system, for exclusive use by the purchaser of the work. Duplication of this publication or parts thereof is permitted only under the provisions of the Copyright Law of the Publisher's location, in its current version, and permission for use must always be obtained from Springer. Permissions for use may be obtained through RightsLink at the Copyright Clearance Center. Violations are liable to prosecution under the respective Copyright Law.

The use of general descriptive names, registered names, trademarks, service marks, etc. in this publication does not imply, even in the absence of a specific statement, that such names are exempt from the relevant protective laws and regulations and therefore free for general use.

While the advice and information in this book are believed to be true and accurate at the date of publication, neither the authors nor the editors nor the publisher can accept any legal responsibility for any errors or omissions that may be made. The publisher makes no warranty, express or implied, with respect to the material contained herein.

Printed on acid-free paper

Springer is part of Springer Science+Business Media ([www.springer.com](http://www.springer.com))

*Dedicato al Prof. Ante Graovac,  
amico e maestro per molti di noi.  
Ciao TONKO !*

*Dedicated to Prof. Ante Graovac,  
a teacher and a friend.  
Bye TONKO!*



# Foreword

Among the chemical elements that populate the periodic table, carbon has arguably had the most dramatic impact in human civilization. Carbon appears naturally in two different crystalline forms known as diamond and graphite. The main difference among these two allotropes is given by the way in which carbon atoms are *connected* to each other. In graphite, carbon atoms form regular hexagonal lattices in which every atom is *connected* to three others. In diamond, however, carbon atoms are arranged into a variation of the face-centred cubic shape in which every atom is connected to the other four. This mere *connectivity* of the atoms defines a series of properties which remain invariant after any deformation of the molecule that does not involve breaking (or creating) any bond. When these topological arrangements of atoms are embedded into the three-dimensional (3D) space, other characteristic properties of the allotropes emerge. The cubic network of diamond, for instance, results in a very rigid structure which is characteristic of its hardness, while graphite forms the typical planar sheets that can displace one over the other. The first group of properties is referred to as *topological*, while the second group is referred to as *geometric*.

The mathematical differences between the topological and the geometric views of the molecular structure can be even more appreciated in another carbon allotrope: fullerenes.

The topology of fullerenes consists of carbon atoms which are connected to other three atoms; however, whereas graphite has only hexagons in their structure, fullerenes have also pentagons. Topologically speaking, fullerenes are planar like graphite, i.e. they can be embedded into a plane without their bonds being crossed. However, when fullerenes are embedded into the 3D space, their typical spherical shape emerges. This is a consequence of other physical and chemical properties of carbon atoms, such as hybridization. In fullerenes, carbon has  $sp_2$  hybridization which, together with the appropriate location of the pentagonal rings, makes the spherical shape emerging.

From a chemist viewpoint, *topology* implies a series of physical and chemical properties such as hybridization and inter-atomic repulsion, which allow a better understanding of the properties of materials. For instance, in carbon nanotubes, the



different topological arrangements, i.e. armchair, zigzag or chiral, largely influence the electronic band structure of these molecules and their physical properties like the metallic or semiconducting character.

Carbon is so rich in its molecular arrangements that we can study topology and geometry by using it as an example. For instance, graphene can be used to study Euclidean geometry due to its zero Gaussian curvature. Fullerenes, on the other hand, can be used to illustrate spherical or elliptical geometry where the Gaussian curvature is positive and the sum of angles of a triangle is larger than  $180^\circ$ . Even more, it has been proved that carbon nanomaterials in which the surface bends with negative curvature, like in hyperbolic spaces, are also possible. The 'schwarzites' belong to this category of compounds.

The topologies of many of carbon nanomaterials are also nontrivial. Apart from the fullerenes with *genus* equal to zero, like the sphere, toroidal graphite has also been found to be stable, matching the topology with *genus* equal to one, like a torus. More exotic structures have also been proposed which correspond to topologies with *genus* larger than 20 and even to spheres with more than 20 handles. This volume presents some of these exciting carbon geometries and topologies. Interesting properties of fullerenes, nanotubes, graphene, schwarzites and other nanomaterials are inferred here from the analysis of the connectivity patterns of these topological arrangements. More sophisticated techniques are also explored, although the authors have mainly focused on the connectivity patterns defining the nature of these molecules.

This book will appeal to mathematicians as well as chemists, physicists and material scientists. The former, particularly the ones interested in exploring carbon allotropes and the nanomaterials deriving from them, will find the book of great interest as it exemplifies some of the concepts they use in their everyday work and it challenges them with some of the problems of this area. The latter, particularly the ones studying carbon materials, will be attracted by the basic concepts of topology and geometry examined in the book. Not only they will develop a better understanding of molecular, physical and chemical properties of these nanomaterials, but they will also get introduced to new topological and geometrical worlds still unexplored.

*Carbon will surely surprise us all.*

Glasgow  
18/04/2012

Ernesto Estrada

# Preface

*Topological Modelling of Nanostructures and Extended Systems* gathers the contributions of renowned leading experts in this new branch of science that we could also name ‘Mathematical Nanoscience’ and that were presented at the MATH/CHEM/COMP Meeting held in Dubrovnik, Croatia, in 2010.

This volume completes and expands upon the previously published title *The Mathematics and Topology of Fullerenes* (Carbon Materials: Chemistry and Physics series, Vol. 4, Springer 2011) by gathering the latest research and advances in materials science at nanoscale. It introduces a new speculative area and novel concepts like *topochemical reactions* and *coloured reactive topological indices* which allow the reader to gain a better understanding of the physical–chemical behaviours of extended systems. Moreover, a charming new family of *space-filling fullerene crystals* is here analysed for the first time.

Mathematical chemistry is an interdisciplinary area with not only numerous theoretical developments but also countless applications to practical problems. The basal influence exercised on chemical and physical properties by *long-range topological mechanisms* links the various topics covered in the book. Carbon nanostructures, made by three-linked nodes variously connected, appear in fact quite sensitive to topological effects.

Nanonetworks have a spanning dimensionality. In fact, they can assume every possible dimensionality, from 0D (finite fullerenes) to 1D (nanotubes or nanoribbons), 2D (graphenic layers), 3D (diamond or schwarzites) and even to fractal dimensionality (fractal schwarzites). Such a characteristic makes them the optimal subjects for topological investigations. Moreover, topological modelling methods can be relied on to support the accuracy of large-scale first principles calculations, as it is largely documented in the original theoretically and experimentally results examined in this book.

In a way, we would like to think that this volume confirms what Prof. Harold Kroto, 1996 Nobel Prize for Chemistry, wrote in the Foreword of our previous title: ‘Beauty Is Inherently Part of the Human Being Actions’.

And this could not be more true when thinking of Prof. Ante Graovac, the mind behind this volume, who prematurely passed away leaving us all with an immense sense of void. Words fail us to express our gratitude for this great academic, both a mentor and a friend.

We are grateful to Springer for giving us the opportunity to publish this book and for their top-quality professional support.

Dubrovnik, Croatia

Ali Iranmanesh  
Ali Reza Ashrafi  
Franco Cataldo  
Ottorino Ori

# Contents

<b>1</b>	<b>Helical Wrapping of Graphene Sheets and Their Self-Assembly into Core-Shelled Composite Nanostructures with Metallic Particles</b> .....	1
	Hui Li, Yunfang Li, Yezeng He, and Yanyan Jiang	
<b>2</b>	<b>First-Principles Study of the Electronic and Magnetic Properties of Defects in Carbon Nanostructures</b> .....	41
	Elton J.G. Santos, Andrés Ayuela, and Daniel Sánchez-Portal	
<b>3</b>	<b>Structural Defects on the Electronic Transport Properties of Carbon-Based Nanostructures</b> .....	77
	Hui Zeng, Jun Zhao, Jianwei Wei, and Jean-Pierre Leburton	
<b>4</b>	<b>Topological Versus Physical and Chemical Properties of Negatively Curved Carbon Surfaces</b> .....	105
	Marzio De Corato, Marco Bernasconi, Luca D'Alessio, Ottorino Ori, Mihai V. Putz, and Giorgio Benedek	
<b>5</b>	<b>Topochemistry of Spatially Extended <math>sp^2</math> Nanocarbons: Fullerenes, Nanotubes, and Graphene</b> .....	137
	Elena F. Sheka	
<b>6</b>	<b>A Pariser–Parr–Pople Model Hamiltonian-Based Approach to the Electronic Structure and Optical Properties of Graphene Nanostructures</b> .....	199
	Kondayya Gundra and Alok Shukla	
<b>7</b>	<b>Topological Invariants of Möbius-Like Graphenic Nanostructures</b> ..	229
	Mihai V. Putz, Marzio De Corato, Giorgio Benedek, Jelena Sedlar, Ante Graovac, and Ottorino Ori	
<b>8</b>	<b>Spanning Fullerenes as Units in Crystal Networks</b> .....	245
	Mircea V. Diudea and Beata Szeffler	

<b>9</b>	<b>Introducing “Colored” Molecular Topology by Reactivity Indices of Electronegativity and Chemical Hardness</b> .....	265
	Mihai V. Putz, Ottorino Ori, Marzio De Corato, Ana-Maria Putz, Giorgio Benedek, Franco Cataldo, and Ante Graovac	
<b>10</b>	<b>Nanostructures and Eigenvectors of Matrices</b> .....	287
	István László, Ante Graovac, and Tomaž Pisanski	
<b>11</b>	<b>Theoretical Analysis of the Reactivity of Carbon Nanotubes: Local Versus Topological Effects</b> .....	303
	Massimo Fusaro, Vincenzo Barone, Mauro Causa, Maddalena D’Amore, and Carmine Garzillo	
<b>12</b>	<b>Computation of the Szeged Index of Some Nanotubes and Dendrimers</b> .....	325
	Ali Iranmanesh	
<b>13</b>	<b>The Edge-Wiener Index and Its Computation for Some Nanostructures</b> .....	425
	Ali Iranmanesh	
<b>14</b>	<b>Study of Fullerenes by Some New Topological Index</b> .....	473
	Ali Reza Ashrafi, Mohammad Ali Iranmanesh, and Zahra Yarahmadi	
<b>15</b>	<b>Topological Study of (3,6) – and (4,6) –Fullerenes</b> .....	487
	Ali Reza Ashrafi and Zeinab Mehranian	
<b>16</b>	<b>Enumeration of Hetero-molecules by Using Pólya Theorem</b> .....	511
	Modjtaba Ghorbani	
	<b>Index</b> .....	561

# Contributors

**Andrés Ayuela** Centro de Física de Materiales (CFM-MPC) CSIC-UPV/EHU, San Sebastián, Spain

**Ali Reza Ashrafi** Department of Mathematics, Faculty of Mathematics, Statistics and Computer Science, University of Kashan, Kashan, Islamic Republic of Iran

**Vincenzo Barone** Scuola Normale Superiore, Pisa, Italy

**Giorgio Benedek** Dipartimento di Scienza dei Materiali, Università di Milano-Bicocca, Milan, Italy

Donostia International Physics Center (DIPC), Donostia/San Sebastián, Spain

**Marco Bernasconi** Dipartimento di Scienza dei Materiali, Università di Milano-Bicocca, Milan, Italy

Donostia International Physics Center (DIPC), Donostia/San Sebastián, Spain

**Franco Cataldo** Actinium Chemical Research, Rome, Italy

**Mauro Causa** Department of Chemical Sciences, University “Federico II”, Napoli, Italy

**Marzio De Corato** Dipartimento di Scienza dei Materiali, Università di Milano-Bicocca, Milan, Italy

Centro S3, CNR-Istituto Nanoscienze, Modena, Italy

Dipartimento di Fisica, Università di Modena e Reggio Emilia, Modena, Italy

**Luca D’Alessio** Department of Physics, Boston University, Boston, MA, USA

**Maddalena D’Amore** Department of Chemical Sciences, University “Federico II”, Napoli, Italy

**Mircea V. Diudea** Faculty of Chemistry and Chemical Engineering, Babes-Bolyai University, Cluj, Romania

**Massimo Fusaro** Department of Chemical Sciences, University “Federico II”, Napoli, Italy

**Carmine Garzillo** Department of Preventive Medical Sciences, University “Federico II”, Napoli, Italy

**Modjtaba Ghorbani** Department of Mathematics, Faculty of Science, Shahid Rajaei Teacher Training University, Tehran, Islamic Republic of Iran

**Ante Graovac** (Deceased)

**Kondayya Gundra** Theoretical Physics Division, Bhabha Atomic Research Centre, Mumbai, India

Department of Physics, Indian Institute of Technology, Mumbai, India

**Yezeng He** Key Laboratory for Liquid-Solid Structural Evolution and Processing of Materials, Ministry of Education, Shandong University, Jinan, People’s Republic of China

**Ali Iranmanesh** Department of Mathematics, Tarbiat Modares University, Tehran, Iran

**Mohammad Ali Iranmanesh** Department of Mathematics, Yazd University, Yazd, Islamic Republic of Iran

**Yanyan Jiang** Key Laboratory for Liquid-Solid Structural Evolution and Processing of Materials, Ministry of Education, Shandong University, Jinan, People’s Republic of China

**István László** Department of Theoretical Physics, Institute of Physics, Budapest University of Technology and Economics, Budapest, Hungary

**Jean-Pierre Leburton** Beckman Institute, University of Illinois at Urbana-Champaign, Urbana, IL, USA

**Hui Li** Key Laboratory for Liquid-Solid Structural Evolution and Processing of Materials, Ministry of Education, Shandong University, Jinan, People’s Republic of China

**Yunfang Li** Key Laboratory for Liquid-Solid Structural Evolution and Processing of Materials, Ministry of Education, Shandong University, Jinan, People’s Republic of China

**Zeinab Mehranian** Department of Nanocomputing, Institute for Nanoscience and Nanotechnology, University of Kashan, Kashan, Islamic Republic of Iran

**Ottorino Ori** Actinium Chemical Research, Rome, Italy

**Tomaž Pisanski** Department of Mathematics, Faculty of Mathematics and Physics, University of Ljubljana, Ljubljana, Slovenia

**Ana-Maria Putz** Institute of Chemistry Timișoara of the Romanian Academy, Timișoara, Romania

**Mihai V. Putz** Laboratory of Computational and Structural Physical Chemistry, Biology-Chemistry Department, West University of Timișoara, Timișoara, Romania

Research Center for Einstein Physics, Institute of Theoretical Physics, Free University Berlin, Berlin, Germany

**Daniel Sánchez-Portal** Centro de Física de Materiales (CFM-MPC) CSIC-UPV/EHU, San Sebastián, Spain

Donostia International Physics Center (DIPC), San Sebastián, Spain

**Elton J. G. Santos** Centro de Física de Materiales (CFM-MPC) CSIC-UPV/EHU, San Sebastián, Spain

Donostia International Physics Center (DIPC), San Sebastián, Spain

Harvard School of Engineering and Applied Sciences, Harvard University, Cambridge, MA, USA

Cruft Laboratory, Cambridge, USA

**Jelena Sedlar** Faculty of Civil Engineering, Architecture and Geodesy, University of Split, Split, Croatia

**Elena F. Sheka** Peoples Friendship University of Russia, Moscow, Russia

**Alok Shukla** Department of Physics, Indian Institute of Technology, Bombay, Powai, Mumbai, India

**Beata Szeffler** Department of Physical Chemistry, Collegium Medicum, Nicolaus Copernicus University, Bydgoszcz, Poland

**Jianwei Wei** College of Optoelectronic Information, Chongqing Institute of Technology, Chongqing, China

**Zahra Yarahmadi** Department of Mathematics, Faculty of Science, Khorramabad Branch, Islamic Azad University, Khorramabad, Islamic Republic of Iran

**Hui Zeng** College of Physical Science and Technology, Yangtze University, Jingzhou, Hubei, China

**Jun Zhao** College of Physical Science and Technology, Yangtze University, Jingzhou, Hubei, China



# Chapter 1

## Helical Wrapping of Graphene Sheets and Their Self-Assembly into Core-Shelled Composite Nanostructures with Metallic Particles

Hui Li, Yunfang Li, Yezeng He, and Yanyan Jiang

**Abstract** A series of atomistic molecular dynamics (MD) simulations have been conducted to explore how the carbon nanotube (CNT), metal nanowire (NW), and C60 affect the stability of the graphene. The graphene nanoribbons (GNRs) can helically wrap and insert the single-walled CNT spontaneously to form helical configurations, which are quite close to the helices found in nature. The graphene nanosheets (GNSs) can spontaneously self-scroll onto the Fe NWs irreversibly, which results in the structural transition of the GNS from two-dimensional to three-dimensional phase and the formation of the stable metal/carbon core-shell nanostructure. MD simulation results also show that impact of C60 molecule would induce nanoscale dynamic ripples on the graphene no matter whether the graphene is plane or corrugated. This study provides possible applications for the GNS and GNR to serve as conveyor belt for molecule delivery. And also, the discoveries of this study are of great significance for the deeper understanding of the instability and properties of graphene at an atomic level.

### 1.1 Introduction

Graphene nanosheet (GNS), a monatomic layer of carbon atoms arranged in a honeycomb lattice with  $sp^2$ -bonding, has attracted ever-increasing research interest since it was first isolated by mechanical exfoliation from graphite crystals (Novoselov et al. 2004). Recent experimental approaches involving mechanical cleavage (Meyer et al. 2007a), top-down lithography, cutting (Fujii and Enoki 2010) and peeling (Sen et al. 2010), chemical vapor deposition (Juang et al. 2010),

---

H. Li (✉) • Y. Li • Y. He • Y. Jiang

Key Laboratory for Liquid-Solid Structural Evolution and Processing of Materials, Ministry of Education, Shandong University, Jinan 250061, People's Republic of China  
e-mail: [lihuilmy@hotmail.com](mailto:lihuilmy@hotmail.com); [liyf308@hotmail.com](mailto:liyf308@hotmail.com); [hyz0217@hotmail.com](mailto:hyz0217@hotmail.com); [happy Lucy2006@yahoo.com.cn](mailto:happy Lucy2006@yahoo.com.cn)

and epitaxial growth (Prakash et al. 2010) have been applied to fabricate GNSs with desired sizes and shapes. Such synthesized two-dimensional (2-D) GNS may very well be the promising candidate material from electronic building blocks to reinforced composites due to its outstanding properties such as quantum electronic transport (Novoselov et al. 2005a, b), controllable electronic structure (Kim et al. 2009), large thermal conductivity (Seol et al. 2010), and extremely high elasticity (Savini et al. 2011). Recently, a number of researchers have also paid their attention to the applications of GNSs in biochemical and medical realms (Yang et al. 2008; Kalbacova et al. 2010).

The isolation of planar GNS seems to contradict the common viewpoint about the existence of 2D crystals (Mermin 1968; Ledoussal and Radzihovsky 1992). Experimental and theoretical studies have suggested that nanometer-scale ripples through the free GNS membrane might be responsible for stabilizing its 2D structure (Meyer et al. 2007b; Fasolino et al. 2007). Compared with the stable and stiff carbon nanotube (CNT), the GNS is very instable and flexible that tends to transform into a 3D structure in order to minimize its surface energy. Buehler et al. demonstrated that the geometrical conformation of the GNS is determined by its aspect ratio. When the aspect ratio is large enough, the narrow graphene nanoribbon (GNR) would self-fold from planar 2D phase to multifold or even scroll 3D phase spontaneously (Xu and Buehler 2010). Other research work also revealed the intrinsic instability and spontaneous twist of pristine GNRs (Bets and Yakobson 2009). Recent theoretical study clearly showed that the water nanodroplet had great effect on the conformation of the GNS (Patra et al. 2009), which arouses one to imagine whether other material would affect the stability of the GNS as well.

In this chapter, systematic theoretical investigations have been carried out to present the detailed analysis and explanation of how the carbon nanotube (CNT) (Jiang et al. 2011; Li et al. 2011b), metal nanowire (NW) (Li et al. 2011c, 2012), and C60 (He et al. 2011) affect the stability of the graphene.

## 1.2 Helical Wrapping and Insertion of Graphene Nanoribbon to Single-Walled Carbon Nanotube

In the carbon family, nanotube and graphene with a perfect honeycomb lattice tightly bounded by  $sp^2$  hybridization are two of the most promising nanomaterials, which have attracted tremendous attention to the theoretical research and the potential applications in many realms because of their ideal 1D and 2D structures and unique properties. The cylindrical single-walled carbon nanotube (SWNT) possesses a large specific surface area and hollow interior that provide an excellent opportunity to integrate with other materials to fabricate composite nanostructures. The integration of SWNTs into other materials can impact their toughness (Zhang et al. 2003a), mechanical strength, crystalline morphology (Li et al. 2009a), and other properties like electrical conductivity. The noncovalent “wrapping” of

polymer chains around an SWNT is an interesting phenomenon (Numata et al. 2005; Naito et al. 2008) which can be utilized to solubilize and disperse SWNTs (Tasis et al. 2006; Zorbas et al. 2004), drive assembled mechanisms (Baskaran et al. 2005; Nish et al. 2007), and alter the fictionalization of the tubes (Chen et al. 2001). Moreover, previous experimental and theoretical results have shown that open nanotubes could act as “molecular straws” capable of absorbing dipolar molecules by capillary action (Pederson and Broughton 1992). On the one hand, the insertion of “foreign” materials, such as metals, liquids, fullerenes (Warner and Wilson 2010), or even proteins (Sorin and Pande 2006) and DNAs (Gao et al. 2003), into SWNTs can alter the properties of the tube and fillers, leading to nanostructures with exciting new applications. On the other hand, the carbon shell is considered as a natural protective layer of the fillers against oxidation and shape fragmentation (Choi et al. 2003). Therefore, the “SWNT composite” has great potential in heterogeneous catalysis, nanodevices, electromagnetic wave absorption, magnetic data storage, and even drug and gene delivery in biological field (Svensson et al. 2004; Gao et al. 2004).

In this section, convincing systematic theoretical results are presented to reveal how the GNR interacts with the SWNT and what is the shape of the GNR adhering onto the sidewall of the SWNT. In particular, the possible interacting mechanism is examined to establish the nature of the interaction of 1D GNR and SWNT. This study is not only helpful for the better understanding of the thermal instability and properties of GNRs at an atomistic level but also essential to help guide exploring new theories and fabricating functional nanoscale devices.

### ***1.2.1 Simulation Method***

In the present study, all calculations are carried out using molecular dynamics (MD) simulation, which is an effective tool for studying material behavior on the nanometer scale and provides detailed information at the atomic level. The force field of condensed-phase optimized molecular potentials for atomistic simulation studies (COMPASS) (Sun 1998) is applied to model the atomic interaction. The COMPASS is an ab initio force field that is parametrized and validated using condensed-phase properties in addition to various ab initio and empirical data. It aims to achieve high accuracy in prediction of the properties of very complex mixtures (Bunte and Sun 2000; Li et al. 2011a), and it has been proven to be applicable in describing the mechanical properties of graphene sheets (Zheng et al. 2010). MD simulations are performed under an NVT ensemble (i.e., the canonical ensemble, the number of particles  $N$ , the volume  $V$ , and the temperature  $T$  were constant) at temperature 300 K. The Andersen method in the thermostat is applied to control the temperature and generate the correct statistical ensemble. The thermodynamic temperature is kept constant by allowing the simulated system to exchange energy with a “heating bath.” The initial velocities of carbon atoms follow a temperature-dependent Maxwell-Boltzmann distribution, and the Verlet algorithm

is adopted to integrate the motion of equations of the whole system. The time step is set to be 1.0 fs, and data were collected every 5.0 ps to record the full-precision trajectory for further analysis. Each of the GNR-SWNT systems was simulated long enough to achieve an equilibrium state. The SWNTs were fixed as rigid tube structures. The GNRs can be cut from the parallel layers in graphite bulk, and so some of GNRs have open edges with dangling  $\sigma$ -orbitals on carbon atoms, whereas the others are not due to the  $\pi$ - $\pi$  stacking interaction between adjacent layers. Initially, all GNR crystals were placed at the entrances of the SWNTs along the axial direction and overlapped 15 Å with the SWNTs to overcome the deformation force from the GNRs themselves and ensure that the distances between them are in the range of the cutoff distance of vdW interaction. To illustrate the interaction process more clearly, the long sinuous GNR tails were not shown.

## 1.2.2 Results and Discussion

### 1.2.2.1 Helical Wrapping and Insertion

Direct simulations in Figs. 1.1 and 1.2 provide the representative snapshots of a GNR helically wrapping onto the SWNT (16, 16) and inserting into the SWNT (20, 20), respectively. Two SWNTs have the same lengths of 66.41 Å. The size of GNR is 500.61 Å in length and 7.81 Å in width. When one end of the GNR is captured by the SWNT (outer or inner surface) and the deformation force from the GNR itself is overcome, the GNR adheres onto the tube wall parallel owing to the vdW coupling and moves toward the tube. When the simulation begins, the GNR is so thin that it tends to be thermodynamically unstable, becoming discontinuous wrinkles or corrugations at thicknesses of several nanometers, which accords well with Yakobson et al.'s result (Bets and Yakobson 2009). It is believed that the planar GNR is easily twisted or bent in a free space because of edge stress. As a result, the GNR assumes polymer-like chain conformation. Although the corrugations and ripples are intrinsic to graphene membranes and stabilize their 2D structures (Fasolino et al. 2007), the 1D wavy fluctuation in narrow GNR is rather than the 2D ripples in graphene membrane. It is mainly because when an out-of-plane bending deformation along one direction is formed, the resistance to bending along another direction will be significantly enhanced.

As the simulations progress, the GNRs start to move forward along the sidewalls of SWNTs gradually in a straight or helical mode after an initial correlation time, in which the GNRs are held tightly against the sidewalls of SWNTs and the wrinkles vanish because of the interaction between them. When the simulation time is up to  $t = 8$  and 4.5 ns, the GNRs display clear helical conformations on the surface and in the hollow interior of the SWNTs with large pitch, respectively, trying to occupy the entire tubes. Then, spirals become denser because of the vdW binding. The GNR heads are pushed to move forward circumferentially owing to the curvature of the tube wall, and the ribbon tails just continue to wrap or encapsulate the tubes in

**Fig. 1.1** Representative snapshots of a GNR helically wrapping onto the SWNT (16, 16). The long sinuous GNR tails are removed for better visualization. The *inset* is the top view of the snapshot at  $t = 28$  ns

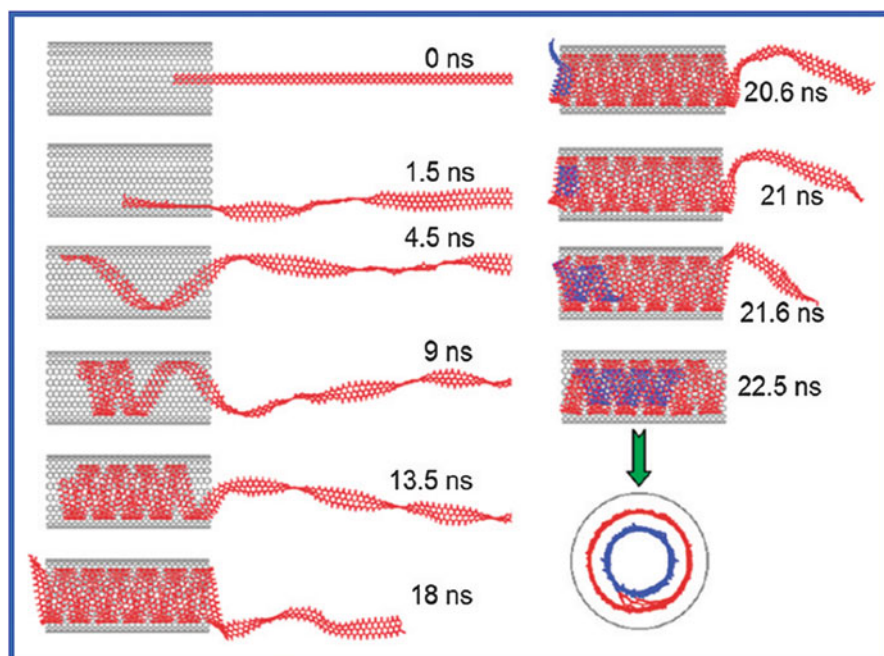
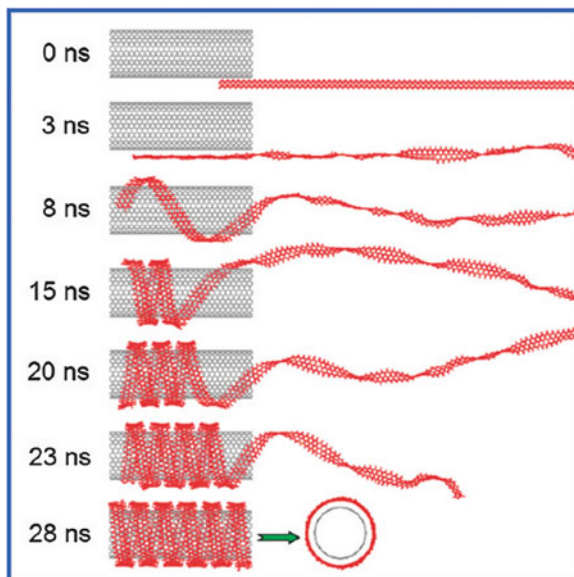


**Fig. 1.2** Representative snapshots of a GNR helically inserting into the SWNT (20, 20). The new helix in the former one is marked *blue*. The long sinuous GNR tails are removed for better visualization. The *inset* is the top view of the snapshot at  $t = 22.5$  ns

a helical way. Eventually, perfect circular GNR helices, with remarkably constant pitches and constant value  $3.5 \text{ \AA}$  of the gap between neighboring spiral, wrap around and fill up the SWNTs at  $t = 28$  and  $18 \text{ ns}$ , respectively. The self-assembled GNR-SWNT systems achieve their dynamic equilibrium through spontaneous wrapping and encapsulation. These two helix-forming processes are irreversible no matter whether the final GNR-SWNT composite nanostructures are cooled or heated to any point of temperature. The handedness of the GNR helix is determined by the initial deflection of the captured end, which can be right- or left-handed with equal probability. It can be controlled by a small initial angle between the GNR and the tube axis.

These helical GNR structures are quite close to the helices found in nature. The GNR helix wrapping around the SWNT is quite similar to the soft stem of the scammony (such as morning glory) helically climbing around the trunk to make itself strong and grow upward, whereas the GNR helix encapsulating in the SWNT is just like a spirogyra cell in which the chloroplast ribbon grows helically over its whole length to make the photosynthesis and the starch storage more efficient (Ohiwa 1976). Perhaps these coincidences with the natural phenomenon can bring some enlightenment on a broad new class of potential applications of these helical carbon nanostructures. Moreover, helicity is one of the essential features of life and integral to various biological functions. In biological systems, various important substances such as polypeptides and DNA in confining cells are found to present helical structures. It is believed that helicity is intimately associated with the living processes even though their origin remains unclear.

It is worth noting the subsequent evolution of the inserting process in Fig. 1.2 when the interior of the SWNT is fully filled. As the simulation goes on, the GNR tail is not stopping but continues to enter the SWNT helically. The head of the helix in the SWNT is pushed out a bit by the tail, but it is not possibly completed because the vdW attractive force from the tube is strong enough to trap the GNR helix. It is very interesting that the pushed out GNR head is captured by the inner hollow space of the GNR helix (marked blue at snapshot of  $t = 21 \text{ ns}$ ) instead of forming new segment of the helix due to the attractive force from the inner space of GNR helix, whereas the ribbon tail just keeps on encapsulating into the SWNT helically. The captured GNR head inserted into the hollow space of the former helix also follows the helical manner and finally produces a new helix with opposite handedness (marked blue), becoming a double-shelled helix at the other entrance of the SWNT at  $t = 22.5 \text{ ns}$ . (The inset is the top view.) The result suggests that the attraction between the GNR helix and the SWNT is stronger than that between GNR helices.

### 1.2.2.2 Interaction Mechanism

What we are concerned with is why the GNR moves toward the SWNT and develops a helical manner. Generally speaking, for a single GNR, as in the polymer chains, there is a persistence length  $l_p = DW/k_B T$  for the width  $W$ , where  $D$  is the bending rigidity of the GNR,  $k_B$  is the Boltzmann constant, and  $T$  is the temperature.

Therefore, the critical aspect ratio for a GNR is  $n = l_p/W = D/k_B T$ . When the aspect ratio is smaller than  $n$ , the GNR will exhibit a worm-like chain conformation, whereas if the aspect ratio is beyond this value of  $n$ , then the GNR will tend to fold into 3D labyrinthic wedge, loop, or scroll nanostructures spontaneously, driven by thermal fluctuation and the loss of orientational order. From our theoretical estimate, the critical aspect ratio is not accessible  $n = 34$  for GNR with width 7.81 Å at room temperature and that of the GNR we chose ( $n = 64$ ) is greatly in excess of this value. However, when the GNR is introduced to SWNT, the GNR helix is formed on the inner or outer surface of the SWNT.

There should be three main interaction effects that exist between the GNR and the SWNT during the helical wrapping and insertion processes. The first effect results from the vdW interaction between the GNR and the SWNT that drives the GNR continuously moving toward the tube, and the well-known vdW potential well of the SWNT traps the GNR. To reveal the energy evolution and the role of the vdW interaction quantitatively, we give in Fig. 1.3 the evolution of the potential energies ( $E_p$ ) of the above-mentioned two GNR-SWNT systems and the vdW interaction energies ( $E_{vdW}$ ) between GNRs and SWNTs against time. During the whole helix-forming courses, the potential energy of these two GNR-SWNT systems appears to be in steady decline with the simulation times, indicating that the helical wrapping and insertion of GNR to SWNT are spontaneous and the systems gradually reach more stable states. Increase in the contact area between the GNR and SWNT reduces the systematic potential energy and enhances the stability of the GNR-SWNT system. Then, the two systems reach the lowest energy states; thereafter, the systemic potential energies remain unchanged, suggesting that the whole systems are in their equilibrium states. It is worth mentioning that in the potential energy curve of inserting process (Fig. 1.3b), there is a “platform” after the tube is fully filled owing to the fact that the contact area between GNR and SWNT is virtually unchanged; then, a “rapid drop” after the ribbon head is captured by the inner space of the former GNR helix because of the increase in the contact area between two GNR helices, which also enhances the stability of the GNR-SWNT system.

From Fig. 1.3, the vdW interactions are negative, suggesting that the vdW interactions between the GNRs and SWNTs are attractive. The vdW attraction energy increases nearly linearly with the increase in the contact areas until the GNRs fully wrap onto or insert into the SWNTs, which endows the GNRs with kinetic energy and sustain the continuous wrapping and insertion. Moreover, the variations of vdW attraction energies are nearly synchronous with that of potential energies, respectively. Therefore, we suggest that the vdW interaction between the GNR and the SWNT offers the main driving force to drive the GNR continuously moving toward the SWNT. The vdW attraction energy reaches up to  $-1.70$  and  $-2.25$  Mcal/mol, respectively, indicating that the adhesion is so strong that it is hard to strip the GNRs off the SWNTs to recover their planar structures again.

The second effect should be the offset face-to-face  $\pi$ - $\pi$  stacking interaction between GNR and SWNT (Głóbwka et al. 1999; Hunter and Sanders 2009), which is an intermolecular interaction in the paralleled six-membered rings, which causes the GNRs to be held tightly against the sidewalls of the tubes and take a helical shape. In the GNR-SWNT system, the offset face-to-face  $\pi$ - $\pi$  stacking interaction

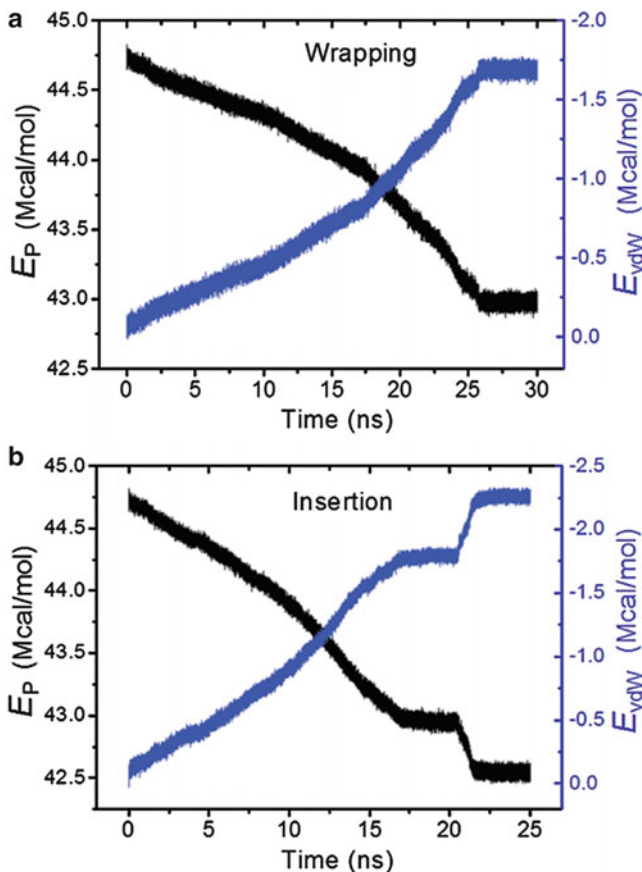


**Fig. 1.3** Potential energy ( $E_p$ ) of GNR-SWNT system and the vdW interaction energy ( $E_{vdW}$ ) between the GNR and SWNT as a function of simulation time: (a) helical wrapping and (b) helical insertion

contains two kinds of interactions: the  $\pi$ - $\pi$  electron interaction and the  $\pi$ - $\sigma$  interaction. The  $\pi$ - $\pi$  electron interaction is an important repulsive force, which is roughly proportional to the area of  $\pi$ -overlap of the two six-membered rings. Certainly, displacement of the interaction system diminishes the repulsion. The  $\pi$ - $\sigma$  interaction is an attractive force between  $\pi$  electrons of one ring and the  $\sigma$ -framework around the inner edge of the cavity of the other one. Different from  $\pi$ - $\pi$  electron interaction, this attractive interaction can be maximized in displaced stacking. Furthermore, in a stacking system, stacked structures should be exactly parallel to reduce the repulsion and increase the attraction of the  $\pi$ -system. It must be pointed out that the  $\pi$ - $\pi$  stacking interaction along the radial direction, of course, does not affect the GNR to move freely along the axial and circumferential directions of SWNT. Therefore, the best way to keep the displaced stacking,



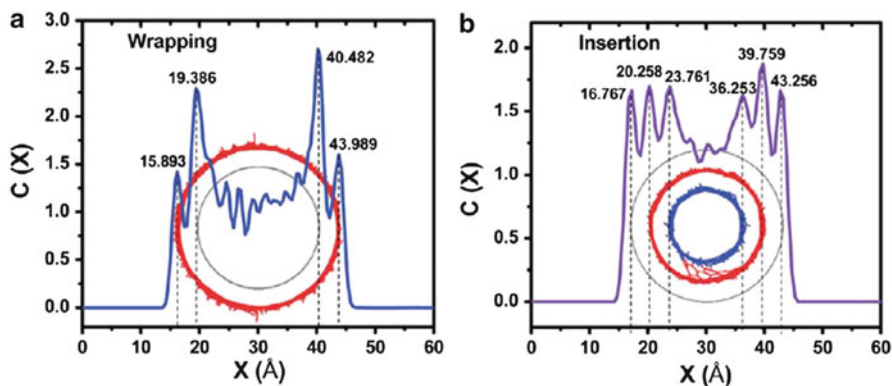


**Fig. 1.4** Concentration distribution profiles of the final GNR-SWNT configurations in the  $X$  direction. Inserts are peak values: (a) helical wrapping and (b) helical insertion

perfect parallel, and the most contact area in the GNR-SWNT system is that the arrangement of the GNR follows a helical mode adhering onto the sidewall of the SWNT when increasingly longer GNR is trapped on the surface and inside the tube. Moreover, the displacement of the carbon rings favors to minimize the repulsive  $\pi$ - $\pi$  interaction and maximize the attractive  $\pi$ - $\sigma$  interaction with the sidewall of tube in GNR helix with paralleled arrangements of six members with SWNT. To testify the effect of the  $\pi$ - $\pi$  stacking interaction further, we characterize the geometric parameters of the final GNR-SWNT configurations by the concentration distribution profiles in the  $X$  direction, as shown in Fig. 1.4. From the peak details marked in the insets, the distances between the helices and the SWNTs as well as those between two GNR helices inside the tube are close to  $3.5 \text{ \AA}$ , which accords well with the parallel stacking distance of the offset face-to-face  $\pi$ - $\pi$  stacking interaction (Głóbwka et al. 1999; Hunter and Sanders 2009), proving that the  $\pi$ - $\pi$  stacking interaction plays a dominant role in the helical wrapping and insertion processes.

The third most important effect is the dangling  $\sigma$ -orbitals on carbon atoms at the open edges of GNR, which reinforces the  $\pi$ - $\pi$  stacking interaction in GNR-SWNT system through the extra attraction with the  $\pi$  electrons in the sidewall of the SWNT (Głóbwka et al. 1999) that ensure that the arrangement of the GNRs follows a helical mode. In a planar  $sp^2$  graphene system, the electronic states split into in-plane ( $\sigma$ ) and out-of-plane ( $\pi$ ) states that are decoupled by symmetry. At unsaturated zigzag edges, the hexagonal carbon network is interrupted, and both the  $\sigma$  and the  $\pi$  systems form edge states. The edge states of the  $\sigma$  system are unpaired electrons in  $sp^2$  orbital, which are dangling  $\sigma$  bonds. To reveal the effect of the dangling  $\sigma$ -orbitals, we also studied the interactions between the SWNTs and GNRs with no dangling  $\sigma$ -orbitals (NGNRs). After the NGNR head attaches onto the tube (inner or outer wall), although the vdW attraction and the  $\pi$ - $\pi$  stacking interaction still work, the NGNR tends to ignore the existence of the SWNT and

form labyrinthic stacks, just like the self-folding of a free GNR (Xu and Buehler 2010). The interaction process is uncontrollable, and the final structure is very random. We also simulate the interactions between SWNT and NGNR when the dangling  $\sigma$ -orbitals on carbon atoms are substituted or saturated by hydrogen atoms, but there is still no helix forming. We think it is mainly due to the fact that the drive force is the vdW interaction between the NGNR layers rather than that between the SWNT and NGNR because the  $\pi$ - $\pi$  stacking interaction between the SWNT and the NGNR is so weak that it cannot overcome that from the NGNR itself.

However, under the guidance of the GNR with dangling  $\sigma$ -orbitals on carbon atoms at the open edges, the NGNR can also form a helix, as shown in Fig. 1.5. The lengths of the zigzag SWNTs (28, 0) and (35, 0) are 73.13 Å, and two GNRs are both with 260.76 Å in length. In the wrapping process (Fig. 1.5a), two GNRs are placed at one entrance of SWNT and 6 Å away from the tube wall. Two GNRs move forward; then, the GNR with open edges starts to fold helically at  $t = 3.5$  ns first and guides the other one to wind. The possible cause should be that open edges reinforce the  $\pi$ - $\pi$  stacking interaction with the SWNT through the extra attraction between dangling  $\sigma$ -orbitals on carbon atoms of the open edges and the  $\pi$  electrons in the sidewall of the SWNT. Up to  $t = 7$  ns, helices arise to both the ribbons, and the two tail layers contact each other because of the  $\pi$ - $\pi$  interaction. As the MD simulation goes on, the GNR with open edges is gradually separated from the other one because of the extra attraction with tube wall. Finally, two GNRs form a double-helix structure on the tube surface, which closely resembles the double-stranded DNA. In the inserting process (Fig. 1.5b), two GNRs are separated from each other 15 Å away at one entrance of SWNT. As the simulation begins, the GNRs adhere onto the tube wall rapidly, whereas the parts outside the tube contact each other because of the  $\pi$ - $\pi$  interaction between two layers. We suggest that the  $\pi$ - $\pi$  stacking interaction in the GNR-SWNT system should be stronger than that between two GNR layers. As time goes on, the GNR with open edges is gradually separated from the other one mainly because of the extra attraction between dangling  $\sigma$ -orbitals on carbon atoms of the open edges and the  $\pi$  electrons in the sidewall and forms the helical configuration earlier. Consequently, a DNA-like double helix is also constructed inside the SWNT at  $t = 7.5$  ns. When time progresses, two GNR tails also enter the inner space of the double helix to produce new helices, becoming a double-shelled helix in the tube, which accords well with the encapsulation of one GNR into the tube (as shown in Fig. 1.2). From our calculations, two equilibrated GNRs in double helix always have the same handedness. The results indicate that the driving force of the formation of double helix should be the vdW interaction between the SWNT and GNRs. Therefore, the dangling  $\sigma$ -orbitals on carbon atoms at the open edges play an important role in the helix forming of the GNRs during the interaction with SWNTs.

The cylindrical structure of the SWNT is also very important in the helix-forming process, which provides uniform curvature to make the GNR move along the circumferential direction of SWNT. Furthermore, the high flexibility dependent on the perfect hexagonal honeycomb architectures and the intrinsic instability (Xu and Buehler 2010; Bets and Yakobson 2009) of the GNR has also contributed to the formation of the GNR helix. The rigid MoS<sub>2</sub> inorganic nanoribbon encapsulated

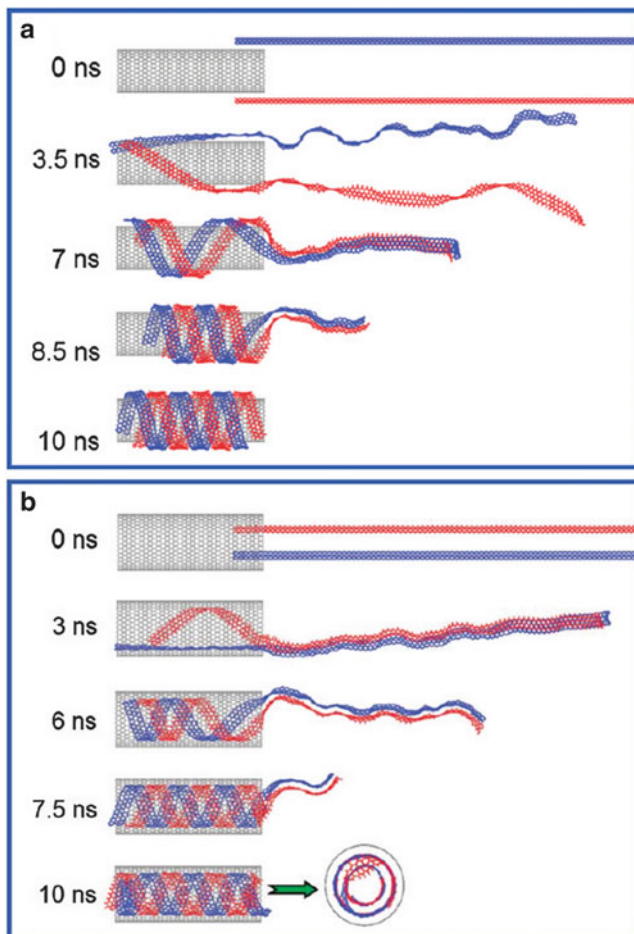


**Fig. 1.5** Evolution snapshots of two GNRs interacting with SWNT. (a) Helical wrapping of GNRs onto the SWNT (28, 0) and (b) helical insertion of GNRs into the SWNT (35, 0). The *inset* in part **b** is the top view of configuration at  $t = 10$  ns

in single- and double-walled carbon nanotube can only display planar conformation (Wang et al. 2010). Experimental results of Snir and Kamien (2005) are very helpful for better understanding this unique phenomenon. Snir and Kamien constructed the system as a flexible, unbreakable solid tube immersed in a solution of the mixture of hard spheres, and they found that the best shape of the short flexible tube that takes the least amount of energy and takes up the least space is a helix with a geometry that is close to that of the helices found in nature. Other theoretical result also revealed that the heterogeneous nucleation of silicon occurred on carbon nanocones preferred to follow a spiral mechanism (Li et al. 2009b). Therefore, we suggest that the helical wrapping and encapsulation of GNR to the SWNT perhaps are because the GNR helix takes the least amount of energy and is a natural space saver.

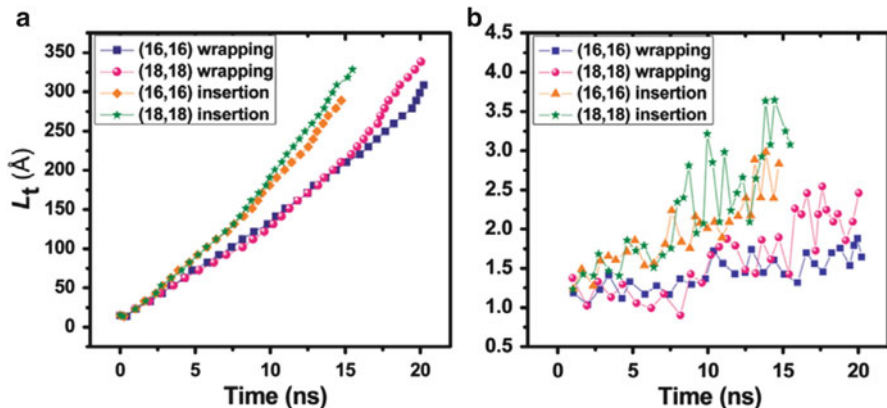


**Fig. 1.6** Variations of the ribbon length adhered onto the SWNTs  $L_t$  and the instantaneous velocities  $V_t$  against time during the GNR wrapping and inserting the SWNTs (16,16) and (18,18), respectively. (a) Ribbon length versus time and (b) instantaneous velocity versus time

### 1.2.2.3 Dependence of Size, Chirality, and Integrality

To exploit the effect of SWNT diameters on the interaction character between GNR and SWNT deeper, we give in Fig. 1.6 the variations of the ribbon length  $L_t$  adhered onto the SWNT and the instantaneous velocity  $V_t$  relative to the tube entrance versus time  $t$  during the GNR helically wrapping and inserting SWNTs (16, 16) and (18, 18) with lengths 73.79 Å. The GNRs are all placed 6.0 Å away from the sidewalls of SWNTs and overlapped 15.0 Å with the SWNTs. The speed is determined by the strength of vdW forces acting on the GNR and the rate of its momentum dissipation due to friction with the sidewall of SWNT. As shown in Fig. 1.6a, the changes of  $L_t$  display nonlinear dependence on time  $t$ , indicating that the helical wrapping and insertion are not uniform motions. It should be pointed out that because of the deformation force, the GNR pulls out a bit from the SWNT but bounces back very soon owing to the attraction from the tube. Then, the velocity of GNR reaches its intrinsic speed. From Fig. 1.6b, it is seen that the velocities of the GNRs inserting into the SWNTs are obviously higher than that of those wrapping onto the SWNTs owing to stronger vdW attraction from the interior confining space of the tube, which accelerates GNRs to encapsulate into tubes. However, the velocity of the GNR in wrapping or inserting the SWNT with larger diameter is only slightly higher than that in the SWNT with smaller diameter. It is worth noting that all velocities show an increase in their tendency with time except for some fluctuations. In fact, the motion of GNRs is a variable accelerated motion because the attractive force from the tubes remains virtually unchanged, while the mass of the unattached GNR tails keeps decreasing, which can also be reflected from the change rate of the  $E_p$  and  $E_{vdW}$ .

To realize the control to GNR helix, a key issue crucial to know is that of the dependence of the diameter and chirality of SWNT as well as the width of GNR in the helix-forming process. In the helical wrapping, the GNR can wind onto any kind of SWNTs spontaneously and form GNR helix, even the ultrathin SWNT (4, 4) with the diameter only 5.42 Å. As shown in Fig. 1.7a, the helical wrapping of the GNR is slightly dependent on the diameter and the chirality of SWNT. Figure 1.7b illustrates the effect of the width of GNR on the helical wrapping. The width of the narrowest GNR with open edges is 5.681 Å in which it contains only one string of carbon six-membered rings. The GNRs with different widths can helically wrap onto the SWNT (15, 15) because the exterior of the SWNT is free and the motion of GNR is not confined.

However, the situation of the helical insertion is much more complex because of the confinement of tube wall. The encapsulation of GNR into SWNTs with different diameters and chiralities is simulated to deeper clarify, just as shown in Fig. 1.7c. If the SWNT with diameter is not larger than 10.85 Å (for instance, the armchair SWNT (8, 8)), then the GNR cannot encapsulate into the tube, even the narrowest GNR with width of 5.681 Å. With a slight increase in the diameter of the SWNT, although it can fill the tube, the narrowest GNR just keeps planar or twisted because the inside space is so confined that the helix cannot form, as seen by the GNR in the armchair SWNT (9, 9). From our calculations, if the diameter of the SWNT is in the range from 13.31 to 14.92 Å, then the narrowest GNR with 5.681 Å in width can form a helix with a large pitch in the tube to take up as much as space and keep the whole system stable, as shown by the GNR in the zigzag SWNT (17, 0). Only when the diameter reaches 14.92 Å (the armchair SWNT (11, 11)) can the GNR produce a perfect helix inside the nanotube. Just as seen in Fig. 1.7c, the perfect GNR helix can be formed in the SWNTs with different chiralities when the diameter of SWNT is  $\geq 14.92$  Å. Our calculations indicate that the helical encapsulation of the GNR into the SWNT is strongly dependent on the tube diameter but slightly dependent on the tube chirality. To investigate the effect of the GNR width, as shown in Fig. 1.7d, we found that the width of GNR  $W$  that ensures the helical insertion of the GNR into a given SWNT should be narrower than the threshold value  $W_{\text{into}} = D - 2 \times 3.5$  Å, where  $D$  is the diameter of the tube and 3.5 Å is the optimized distance of the interaction between carbon atoms. If the GNR is a bit wider than the maximum  $W_{\text{into}}$  and a little narrower than  $D$ , then the helical structure will still be formed during the encapsulation process when the GNR can self-adjust well through slight bend or twist, but it is much more difficult and uncertain. Therefore, for a given SWNT with the diameter larger than 14.92 Å, to ensure a perfect GNR helical structure to be formed in the encapsulation process, it should satisfy the fact that the width of the GNR is in the range of 5.681 Å and the threshold value  $W_{\text{into}}$ . In all GNR helices, the gap between neighboring spirals is a constant value of 3.5 Å, so the pitch of the GNR helix  $P$  is only determined by the width of the GNR that  $P = W + 3.5$  Å. Therefore, we can control the GNR helix by the SWNT diameter and the GNR width.

To clarify quantitatively the influence of the chirality and diameter of SWNT on the adhesion of GNR-SWNT system, we have further determined the saturation interaction energies per unit area  $\Delta E$  between a GNR and the SWNTs with different

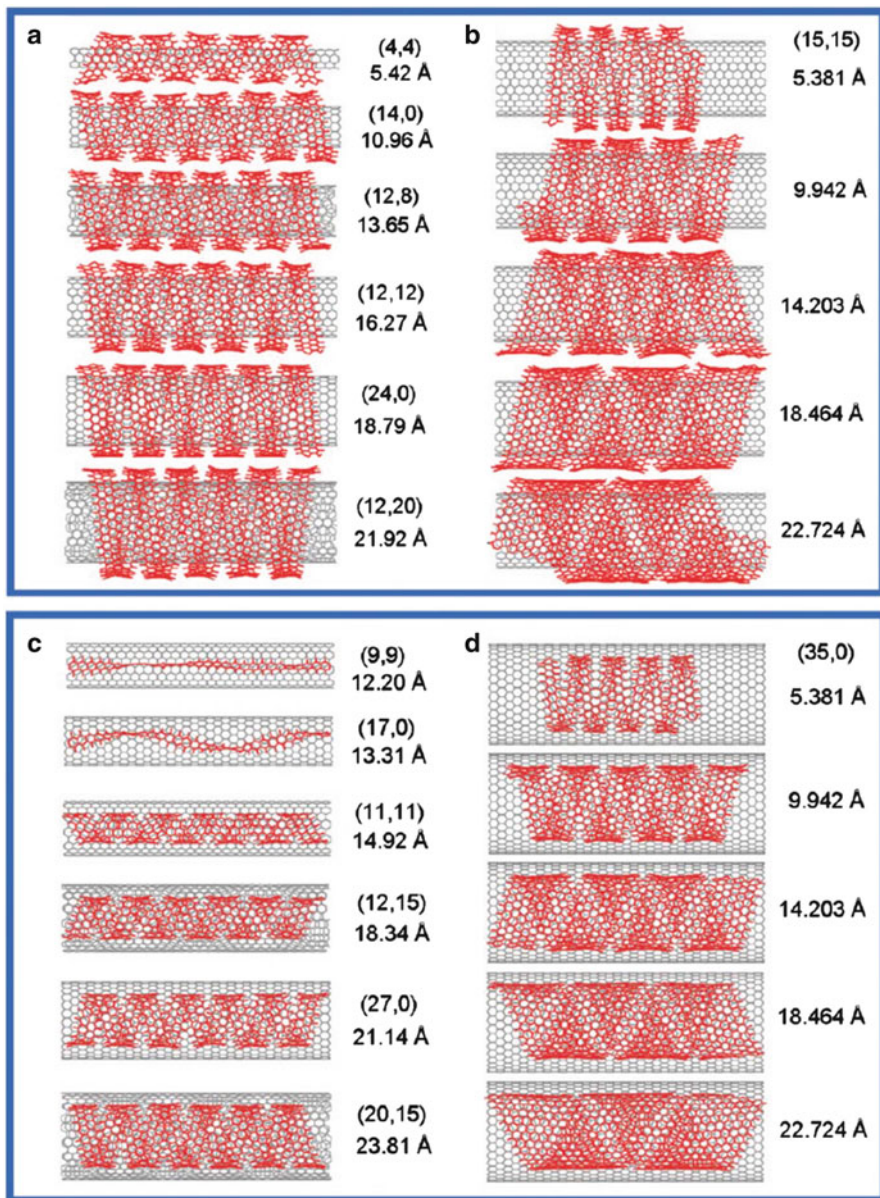


**Fig. 1.7** Dependence of the diameter and chirality of SWNT and the width of GNR in the helix-forming process. (a) Helical wrapping of GNR onto the SWNT with different diameters and chiralities, (b) helical wrapping of GNR with different widths onto the SWNT (15, 15), (c) helical encapsulation of GNR into the SWNT with different diameters and chiralities, and (d) helical encapsulation of GNR with different widths into the SWNT (35, 0)

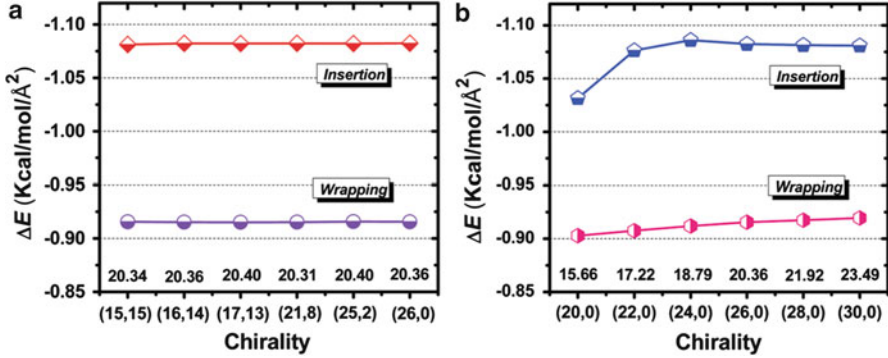


**Fig. 1.8** (a) Saturation interaction energies per unit area between the GNRs and the SWNTs with different chiralities. (b) Saturation interaction energies per unit area between the GNRs and zigzag SWNTs with different diameters

chiralities and diameters showing in Fig. 1.8.  $\Delta E$  reflects the adhesion intensity between the GNR and SWNT that can be calculated from the following equation:

$$\Delta E = \frac{E_{\text{total}} - (E_{\text{GNR}} + E_{\text{SWNT}})}{A_{\text{GNR-SWNT}}} \quad (1.1)$$

where  $E_{\text{total}}$  is the total potential energy of the optimized GNR-SWNT system,  $E_{\text{GNR}}$  is the intrinsic energy of the single GNR without SWNT,  $E_{\text{SWNT}}$  is the minimum energy of the isolated SWNT without GNR, and  $A_{\text{GNR-SWNT}}$  is the contact area between the GNR and SWNT. From Fig. 1.8a, we can observe that the  $\Delta E$  between the GNR and SWNTs with different chiralities remains almost constant, indicating that the SWNT chirality has a negligible influence on the adhesion. It further verifies the fact that the helical wrapping and insertion depend slightly on the tube chirality. The insets are the diameters of SWNTs. However, when the GNR helix is in the hollow interior, the  $\Delta E$  is obviously higher than that of the GNR helix on the exterior of the SWNTs, suggesting that the GNR helix in the hollow interior is more stable than that on the outer surface of the SWNT. It is mainly because the vdW potential well inside the SWNT is deeper, therefore, providing more vdW attraction than that from the exterior of the tube. Figure 1.8b shows that the diameter of SWNT has a great effect on the adhesion. When the GNR wraps onto the SWNT, the  $\Delta E$  is increased with the increase in the tube diameter linearly, proving the fact that the more flat the SWNT wall (lower curvature), the stronger the adhesion intensity between GNR and SWNT. However, in the case of insertion, the  $\Delta E$  increases firstly and then reaches to an equilibrium value with no effect of the tube curvature.

We have further simulated the dependence of the integrality of SWNT on the helical wrapping and insertion. We make the gap on SWNT by deleting the carbon atom chains along the axial direction to destroy the continuity of the tube wall. The edges of gaps are marked blue. The GNRs are all 300.12 Å in length and placed

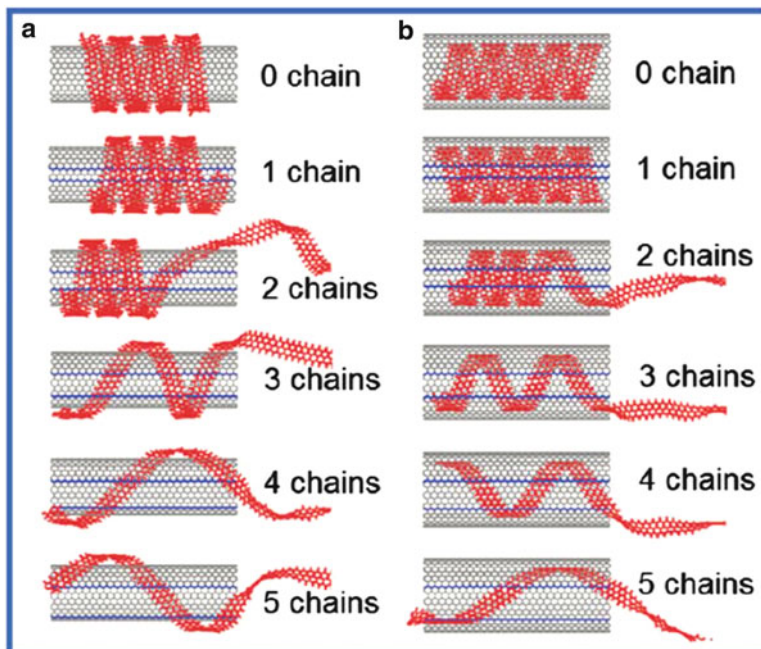


**Fig. 1.9** Effect of the gap of SWNT on the helix-forming process. The edges of gaps are marked *blue*. **(a)** Helical wrapping of GNR onto the SWNTs (15, 15) with gaps. **(b)** Helical encapsulation of GNR into the SWNT (20, 20) with gaps. *Insets* are the number of carbon atom chains that the gap contains

in the same location in all initial configurations. Figure 1.9 shows configurations of the GNR wrapping onto the SWNTs (15, 15) and inserting into the SWNTs (20, 20) with gaps at  $t = 13.5$  and 10 ns, respectively. The insets are the number of carbon atom chains that the gap contains. Figure 1.9 demonstrates that the small gaps (containing 1 chain) have no obvious effect, whereas the larger gaps on the tube walls slow or impede the helical wrapping and insertion. It could be seen that the gap that contains four chains stops the helical wrapping, whereas the gap that contains five chains stops the helical insertion. It is mainly because the motion of GNR along the circumferential direction depending on the curvature of the tube wall is destroyed. So the integrality of SWNT is also very important for the helical wrapping and insertion of the GNR.

#### 1.2.2.4 Possible Application

The unique phenomenon that the GNR can helically wraps onto and encapsulates into the SWNT spontaneously inspires our interests to utilize the GNR as nanoscale vehicle to deliver molecules onto the surface or into the confining nanospace of tube,



respectively. On one respect, the surface of SWNTs is often chemically modified to reach proper dispersion and compatibility (Khan et al. 2007). However, chemical modifications will create defects in the external wall of the SWNTs and affect their properties (Sulong et al. 2009). The spontaneous wrapping of GNR may be the more gentle approach to modify the SWNT, and attached molecules on the outer surface may guide the tube to a specific target. On the other respect, the larger inner confined volume of the SWNT can be used as the drug container and targeted delivery capsule (Hilder and Hill 2009). The spontaneous insertion of the GNR can carry the molecules into the confining nanospaces of tubes without any other external force. In this simulation, we chemically attach some norepinephrine molecules to the GNRs with length of 300.12 Å uniformly. The norepinephrine is an important drug in biology and medicine that has a key neurotransmitter function in the human organism to regulate motor coordination, behavior, learning and memory, sleep-wake cycle, and stress response (Zhu et al. 2010; Nagy et al. 2003; Zhou et al. 2007). Just as shown in Fig. 1.10, the norepinephrine-modified GNRs gradually wrap (Fig. 1.10a) and insert (Fig. 1.10b) the SWNTs to form the helical configurations. The attached molecules have a comparatively small impact on the helix-forming process and the interval between the neighboring segments. Besides norepinephrine, other drugs, catalysts, enzymes, and functional groups can also be attached to the GNR and easily carried to the exterior or interior of SWNTs. We can easily manage the amount of the modified and encapsulated molecules and locate them at the specified positions for a given SWNT because it is easy to know the pitch of GNR helix and the distance between the tube and the helix and that of the neighboring spirals. Then, we can distribute the required molecules according to the individual requirement and make full use of the spontaneous and helical properties of the GNR when GNRs interact with SWNTs. Therefore, the GNR can be a promising nanoscale vehicle to deliver substances, and the GNR-SWNT system is expected to explore numerous prospective chemical and biological applications.

### 1.3 A Graphene Sheet Spontaneously Scrolling Round an Iron Nanowire

The structures and properties of NWs are quite different from those of bulk materials owing to the strong impact of the surface. Because of magnetic performance, iron (Fe) NWs are studied intensively, and various techniques have been developed for the production of long and regular Fe NWs. Highly ordered Fe NWs with diameters of several nanometers have been fabricated by the decomposition of a suitably chosen perovskite (Mohaddes-Ardabili et al. 2004), electrodeposition using porous alumina templates (Zhang et al. 2003b; Borissov et al. 2009), and iron deposition on suspended CNT substrates (Zhang and Dai 2000). Moreover, Fe NWs of atomic size can be generated using CNTs (Demoncy et al. 1998) or polymer (Thurn-Albrecht et al. 2000; Hong et al. 2001) and biological templates like DNA (Seidel et al. 2002).

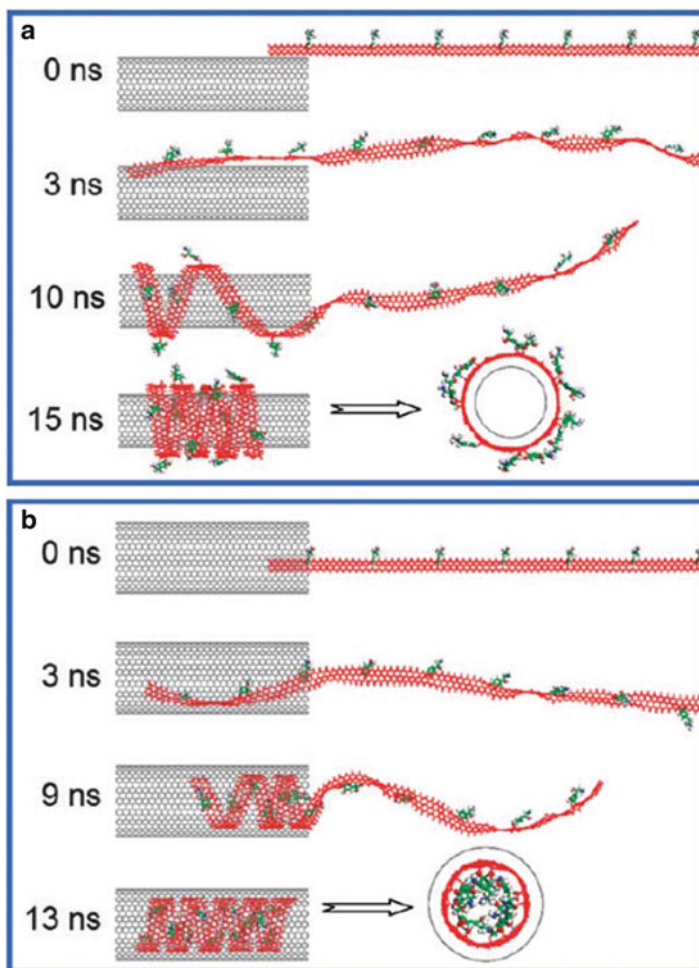


**Fig. 1.10** Evolution snapshots of the GNR modified with norepinephrine molecules interacting with the SWNT. **(a)** Helical wrapping of modified GNR onto the SWNT (15, 15); **(b)** helical encapsulation of modified GNR into the SWNT (20, 20). The *insets* are the top views of final configurations

Although there have been a large number of important research studies on the stability and properties of GNS, the study of the interaction between the GNS and a metallic NW is still limited. Understanding their interacting mechanism is of great importance in exploring the practical applications of GNSs and fabricating new composite functional materials (Potts et al. 2011; Goswami et al. 2011).

In this section, theoretical results are presented to reveal that GNSs can fully self-scroll onto Fe NWs to produce magnetic core-shell nanostructures, which can be potential candidates for use in nanodevices, in wave-absorption materials, and

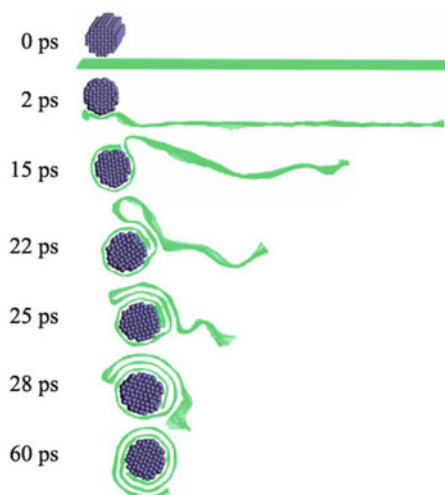
in the magnetic storage industry. In particular, the interacting mechanism and the thermodynamic model are examined to establish the nature of the spontaneous scrolling of GNS. This study is not only helpful for the better understanding the thermal instability and properties of GNS at an atomic level but essential to expand the practical application of GNS and explore new theories and functional devices.

### 1.3.1 *Simulation Method*

In this work, all calculations are also carried out by MD simulation, and the atomic interaction is described by the force field of COMPASS. The MD simulations are performed under an NVT ensemble at room temperature of 300 K. The Nose method is employed in the thermostat to control the temperature and generate the correct statistical ensemble. The thermodynamic temperature is kept constant by allowing the simulated system to exchange energy with a “heating bath.” The Verlet algorithm is adopted to integrate the equations of motion for the whole system. The time step is set to be 1.0 fs, and data were collected every 0.1 ps to record the full-precision trajectory for further analysis. The cylindrical Fe NWs are prepared in body-centered cubic crystal structure of Fe (Sandoval and Urbassek 2009; Yan et al. 2009; Opitz et al. 2002) and the wire axes oriented in the (001) direction with radius range from 5 to 10 Å in order to maintain their small size effect and structural stability. It has also shown that a wire radius favors for larger than a critical radius with cross section of about two to seven atoms, in dependence on the used metallic element (Kondo and Takayanagi 1997; Wang et al. 2001; Gulseren et al. 1998). Below this critical radius, the wire structure is helical (Kondo and Takayanagi 1997; Wang et al. 2001; Gulseren et al. 1998; Kondo and Takayanagi 2000). Initially, the width of a GNS aligns parallel to the Fe NW and with a separation distance of 8.0 Å. Each system is simulated long enough to achieve an equilibrium state.

Because Fe is a transition metal, the spin-unrestricted density function theory (DFT) is performed to study the interaction between Fe and carbon on the GNS. The DFT computations are carried out through an all-electron method with a generalized gradient approximation (GGA) for the exchange-correlation term. The double numerical basis set including the d-polarization functions (DND) basis set and PW91 (Perdew and Wang 1992) functional is adopted. A convergence criterion of  $10^{-6}$  au on the total energy and electron density is adopted for the self-consistent field (SCF) calculations. The real-space global orbital cutoff radius is chosen as 4.6 Å. The Brillouin zone is sampled with  $3 \times 3 \times 1$   $k$ -points. The transition state is located through the synchronous method with conjugated gradient refinements (Govind et al. 2003). This method involves linear synchronous transit (LST) maximization, followed by repeated conjugated gradient (CG) minimizations, and then quadratic synchronous transit (QST) maximizations and repeated CG minimizations until a transition state was located.

**Fig. 1.11** Snapshots of the spontaneous self-scrolling of a GNS onto a Fe NW



## 1.3.2 Results and Discussion

### 1.3.2.1 The Spontaneous Scrolling of GNS

Direct simulation in Fig. 1.11 provides snapshots of the spontaneous scrolling of an armchair GNS with size of  $207.36 \text{ \AA}$  (armchair direction)  $\times$   $63.96 \text{ \AA}$  (zigzag direction) (contains 5,194 carbon atoms) onto an Fe NW with radius of  $8.6 \text{ \AA}$ . The GNS is placed vertically to the axis of Fe NW and the attractive force between them makes the GNS approach to the Fe NW rapidly. The GNS displays discontinuous wrinkles or corrugations in several nanometers thick, showing its thermodynamic instability. According to the so-called Mermin-Wagner theorem (Mermin 1968), long-wavelength fluctuations destroy the long-range order of 2D crystals, and these fluctuations can be suppressed by anharmonic coupling between bending and stretching modes, which presents that a 2D GNS can exist but exhibit strong fluctuations with some ripples and corrugations (Fasolino et al. 2007). After the GNS attaching onto the Fe NW, the GNS begins to curl and quickly wrap around the Fe NW to form a coiling with a tail just like a tadpole (at  $t = 15 \text{ ps}$ ). When it totally wraps the Fe NW, the GNS begins to scroll spontaneously. At  $t = 25 \text{ ps}$ , it is found that the tadpole-like part starts to fold and slide with a lower speed. Eventually, the self-scrolling completes and the configuration of GNS transforms from a planar membrane to a tubular scroll. During the self-scrolling, the speed is determined by the rate of releasing potential energy into the kinetic energy. Our simulation result indicates that the average self-scrolling speed of the GNS reaches up to  $3.16 \text{ \AA/ps}$  ( $316 \text{ m/s}$ ). Interestingly, the Fe NW is also found to be deformed owing to the strong interaction between GNS and Fe NW during the self-scrolling process.

The spontaneous self-scrolling of a GNS onto an Fe NW leads to the structural transition of the GNS from a 2D to a 3D phase, and this process is irreversible no

matter whether the core-shell structure is cooled or heated to any temperature. The irreversibility of the structural transition clearly shows that the 2D structure of GNS is not the lowest energy configuration but is a metastable state like a supercooled liquid. We would expect a similar behavior of a GNS using metallic NWs of other elements and hope this distinctive property of metastable 2D GNS can bring more applications. Moreover, the multilayered scroll formed is very similar to multi-walled CNTs encapsulating with an Fe NW. Our results also demonstrate that such self-scrolling is a common phenomenon when the GNS adheres to other metallic NWs such as Cu, Au, Ag, Ge, and Sn. On the one hand, it would be a lot better to trigger the self-scrolling of a GNS onto a metallic NW in a controlled manner to produce metal/carbon core-shell nanostructures instead of the insertion of metallic particles into CNTs because it is extremely difficult to insert metals into the CNTs, which requires the conditions of the high temperature, catalyst, or other external energy (Li et al. 2007, 2006; Blank et al. 2010) due to the wetting and small size effect. This would provide a new method to prepare future nanoscale structures with a higher level of sophistication. The self-scrolling of GNS onto the metallic NW is also helpful for preventing the NW from oxidation when exposed to air.

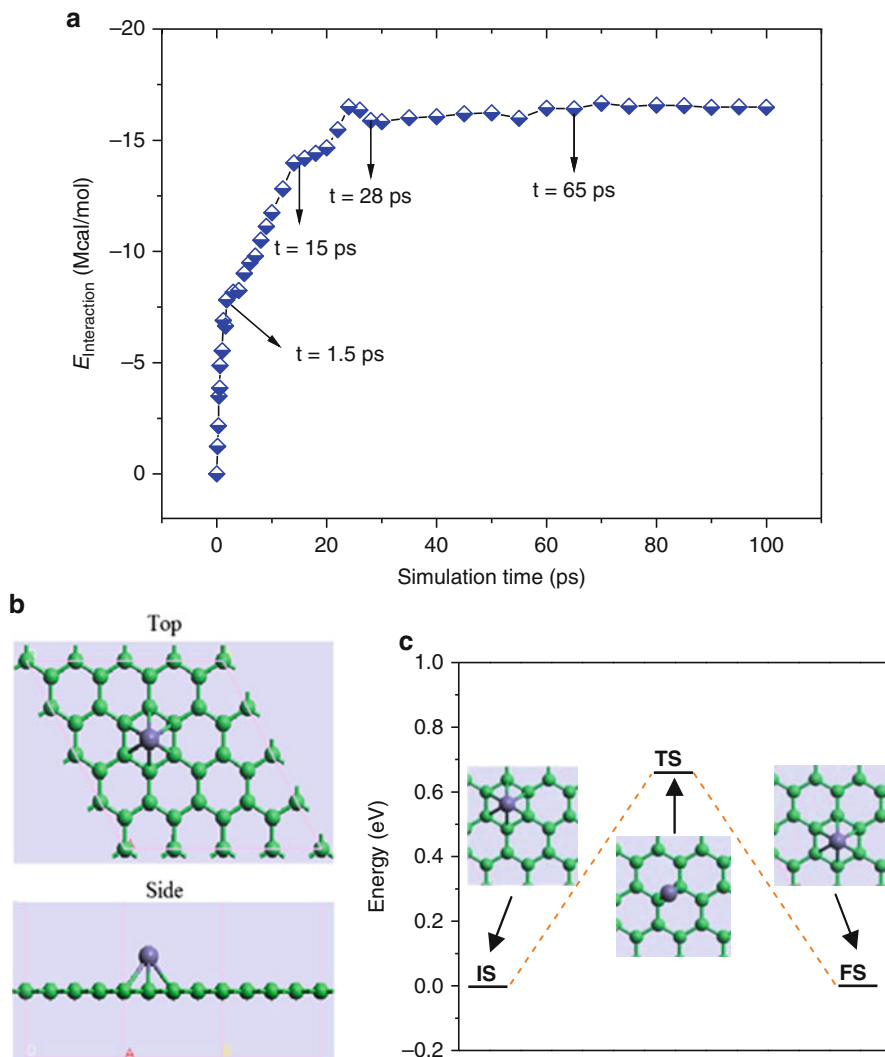
### 1.3.2.2 Interface Characteristics

The interaction energy reflects the adhesion intensity between the GNS and the Fe NW which can be calculated from the following equation:

$$E_{\text{interaction}} = E_{\text{total}} - (E_{\text{GNS}} + E_{\text{NW}}), \quad (1.2)$$

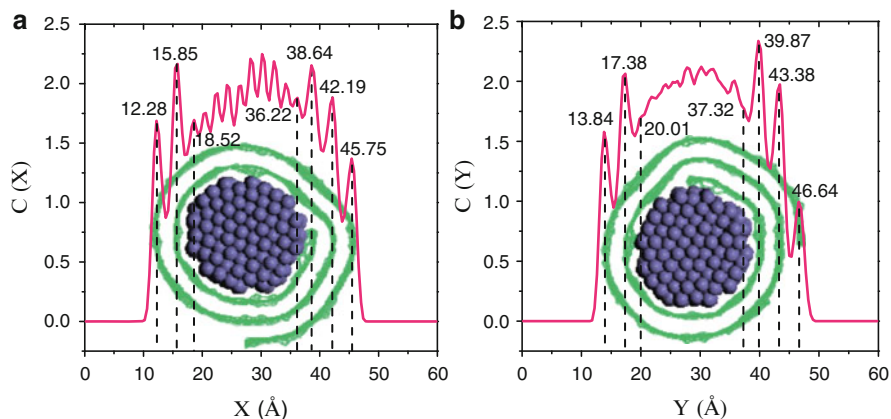
where  $E_{\text{total}}$  is the potential energy of the system,  $E_{\text{GNS}}$  is the intrinsic energy of the single GNS without Fe NW, and  $E_{\text{NW}}$  is the energy of the single Fe NW without GNS.

Figure 1.12a shows the interaction energy between the GNS and the Fe NW during the self-scrolling. As the simulation continues, the interaction energy shows a rapid increase during the attaching process from  $t = 0$  to 1.5 ps. From  $t = 1.5$  to 15 ps, the interaction energy increases linearly with the increase of the contact area until the GNS just coils around the Fe NW. In order to further study the interaction between transitional Fe and  $sp^2$  carbon on the GNS, DFT calculation has been performed. Figure 1.12b shows that the Fe atom is located above the center of the carbon hexagon on GNS with hollow H-site to form six covalent-like bonds with small adsorption energy of 0.96 eV. The bond length between Fe and the neighboring carbon is 2.14 Å, and the distance between Fe and GNS is 1.58 Å. We also computed the energy barrier for Fe migration in GNS from one H-site to its neighboring one. Figure 1.12c shows that some bonds break and Fe atom locates at the bridge B-site during the migration. The rather small migration energy barrier (0.66 eV) indicates that the H-site Fe atom can easily migrate on pristine GNS. Because the chemical energy between GNS and Fe NW is very weak, the covalent-like bonds do not affect the spontaneous scrolling of GNS onto Fe NW.



**Fig. 1.12** (a) The interaction energy between GNS and Fe NW with time. (b) *Top* and *side* views of the geometric structures of Fe adsorbed on GNS calculated by DFT. (c) Energy profile for Fe diffusion on GNS from one H-site to its neighboring one; the *insets* are the initial state (IS), transition state (TS), and final state (FS)

From  $t = 15$  ps, the increasing rate of interaction energy is much lower because the distance between the unwrapped GNS and the Fe NW increases with the increase of the scroll layer. It suggests that the interaction energy should be mainly determined by the contact area between the GNS layer and the Fe NW. From  $t = 28$  ps (the sliding process), the interaction energy becomes almost unchanged until  $t = 65$  ps



**Fig. 1.13** Concentration profiles of the final structure in the  $X$  direction (a) and the  $Y$  direction (b). The insets are the snapshots of the core-shell structures and peak values

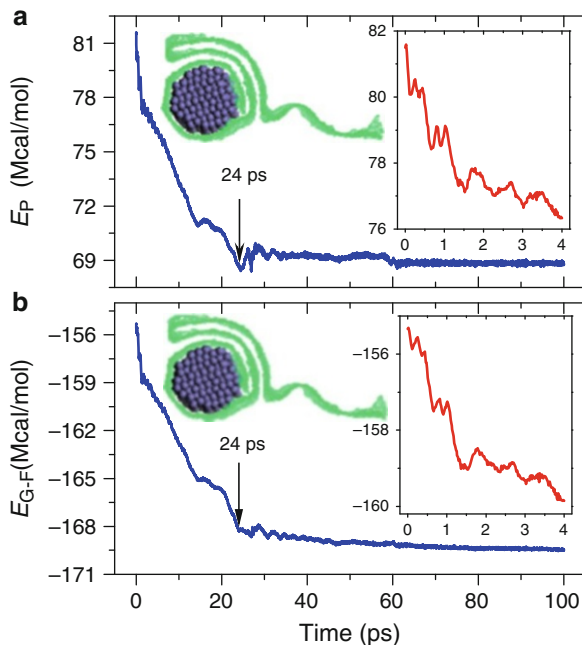
which indicates that the structural transition of the GNS has completed and the system reaches the equilibrium state. Therefore, we suggest that the structural transition of the GNS is maintained not only by the interaction between the GNS and the Fe NW but also by the interaction between the scrolled and unwrapped GNS layer.

The final structure can be further characterized by the concentration profile. Figure 1.13 shows the concentration profiles of the final structure consisting of the Fe NW and the GNS scroll in the  $X$  and  $Y$  directions. The separation of the adjacent layers can be obtained from the distance between two neighboring peaks in the concentration profiles. From the peak details marked in the inserts, on the one hand, the average separation distance between the innermost layer of the scroll and the Fe NW is 2.61 Å, bigger than that of DFT data. This difference may be due to distinct exchange and correlation functions used. However, this value is very close to the scale of the chemical bonding, still indicating that the interaction between them is very strong. On the other hand, the distance between the scrolled layers is about 3.52 Å, which is very close to the wall thickness of the multi-walled CNTs (3.4 Å), meaning this distance is in the strong-adhesive-binding region. In addition, the interaction energy between the GNS and the Fe NW reaches up to  $-16.5$  Mcal/mol, suggesting that the adhesion is so strong that it is hard to strip the GNS off the Fe NW to recover its planar structure again.

### 1.3.2.3 The Mechanism

What we are concerned with is what causes the structural transition of the GNS from 2D to 3D phase. In principle, an isolated GNS can only lower its energy by bending to form corrugation to keep its 2D flat structure. The transition of an isolated, flat

**Fig. 1.14** The evolutions of total potential energy  $E_P$  (a) and vdW energy  $E_{vdW}$  (b) versus time. The *insets* are the enlarge images of these two energies from  $t = 0$  to 4 ps and snapshots at  $t = 24$  ps



GNS membrane into a smaller, folded package is problematic because the intrinsic elastic energy of the GNS always tends to keep the GNS flat and generates energy barrier for the structural transition. When the Fe NW is introduced, the transition of GNS from a 2D planar membrane to a 3D scroll happens. It must be pointed out that there are two interaction effects responsible for this unique phenomenon. One interaction is the vdW interaction between GNS and Fe NW, which helps the GNS overcome the energy barrier and provides attractive force to drive the GNS to curl; the other one is the offset face-to-face  $\pi$ - $\pi$  stacking interaction (Zhu et al. 2010) between GNS layers that causes the GNS continuously to hold tightly against the rolled surface to form scroll.

To reveal the effect of the vdW interaction between GNS and Fe NW on the structural transition of GNS, the evolutions of total potential energy  $E_P$  (a) and vdW energy  $\Delta E_{vdW}$  (b) of the whole system versus time were tracked, as shown in Fig. 1.14. The inserts are enlarged images of two energies from  $t = 0$  to 4 ps. The decrease of total potential energy of the system indicates that the spontaneous self-scrolling of GNS is a process of energy decreasing in which the system gradually reaches to a more stable state. During the structural transition, the evolutions of the vdW energy and the potential energy are nearly synchronous. The vdW energy is converted into kinetic energy partially, which sustains the structural transition. So we suggest that the interaction between GNS and Fe NW offers the main driving force to drive the structural transition, which keeps the GNS continuously moving toward and scrolling onto the Fe NW. It is worthy of note that, only from  $t = 0$  to 24 ps



(the insets are the snapshots at  $t = 24$  ps), both the potential energy and vdW energy have a rapid decrease. Thereafter, the potential energy reaches a minimum and remains almost unchanged, which indicates that the system has reached the most stable state from the suggestion of thermodynamics. Moreover, at 24 ps later, the release of the vdW energy becomes very slow, but the structural transition of the GNS still continues, suggesting that the vdW interaction between GNS and Fe NW only controls the former stage rather than the later one. The subsequent structural transition of the GNS is mainly determined by another interaction: the offset face-to-face  $\pi$ - $\pi$  stacking interaction between GNS layers (Zhu et al. 2010; Nagy et al. 2003), resulted from an intermolecular interaction in the paralleled six-membered rings, which sustains the structural transition to form a multi-walled scroll in the end.

The offset face-to-face  $\pi$ - $\pi$  stacking interaction has two sub-interactions, one is the  $\pi$ - $\pi$  electron interaction and the other one is the  $\pi$ - $\sigma$  interaction. The  $\pi$ - $\pi$  electron interaction is an important repulsive force, which is roughly proportional to the area of  $\pi$ -overlap of the two six-membered rings. The  $\pi$ - $\sigma$  interaction is an attractive force between  $\pi$  electrons of one ring and the  $\sigma$ -framework around the inner edge of the cavity of the other one. Different from  $\pi$ - $\pi$  electron interaction,  $\pi$ - $\sigma$  interaction can be maximized in displaced stacking. Furthermore, in a stacking system, stacked molecules should be exactly parallel with a vdW distance of about 3.5 Å (for the carbon skeleton) and overlapping at least partially to minimize repulsive interaction and maximize the attractive interaction of the  $\pi$ -system. Therefore, the best way to keep the displaced stacking and perfect parallel in GNS is that the arrangement of the GNS follows a scroll mode around the Fe NW when the GNS is self-scrolling onto the Fe NW. In the scroll, the paralleled six-membered system, displacement of the carbon rings favors minimization of repulsive  $\pi$ - $\pi$  interaction and maximization of attractive  $\pi$ - $\sigma$  interaction. To some extent, the high flexibility dependent on the perfect hexagonal honeycomb architectures and the intrinsic instability of the GNS has also contributed to the formation of the GNS scroll during the structural transition. Our simulation result just illustrates that the distances between the scrolled layers are exactly close to 3.5 Å, which accords well with the stacking distance of the offset face-to-face  $\pi$ - $\pi$  stacking interaction (Głóbwka et al. 1999; Hunter and Sanders 2009; Yang et al. 2008). It indicates that the  $\pi$ - $\pi$  stacking interaction plays a dominant role in the latter “scroll-forming” stage of the structural transition.

#### 1.3.2.4 The Thermodynamic Model

To develop a thermodynamic model to further illustrate the nature of the structural transition of the GNS, we consider a GNS with length  $L$  and width  $W$  rolled onto a Fe NW with radius  $r_0$ . Thermodynamically, the occurrence of the structural transition of GNS is determined by the competition between the GNS-Fe binding energy,  $E_{G-F} = -\sigma_{G-F}A_{G-F}$ , and the GNS intrinsic elastic bending energy,  $E_G = \sigma_G A_G$ , where  $\sigma$  is the density of the binding energy and  $A$  is the binding area. The GNS-Fe (GNS-GNS) binding energies  $E_{G-F}$  ( $E_G$ ) are easily obtained from the difference of the total

vdW energy of the system at two different states: One state is the distance between GNS and Fe NW is in their normal binding length, and the other one is the Fe NW is separated from the GNS by a very long distance. Scrolling of the GNS onto Fe NW is driven by the decrease of the GNS-Fe binding energy,  $E_{G-F} = -\sigma_{G-F}A_{G-F}$ . In the case as shown in Fig. 1.11, the GNS-Fe density of the binding energy is estimated as  $\sigma_{G-F} \approx 2.388 \text{ kcal}/(\text{mol} \cdot \text{\AA}^2)$ . When the GNS scrolls into a single-layered cylinder (at  $t = 15 \text{ ps}$ ), the initial and final GNS-Fe binding areas are  $A_{G-F}^{\text{ini}} \rightarrow 0$  and  $A_{G-F}^{\text{end}} = 2\pi(8.6 + 2.6) \times 63.96 \text{ \AA}^2$ , respectively. The elastic binding energy of this GNS cylinder is  $E_G = \sigma_G A_G$ , where  $A_G \approx A_{G-F}^{\text{end}}$  is the binding area. In order to obtain the strain energy density  $\sigma_G$  of the GNS cylinder, the flexural rigidity  $D$  of the pristine GNS is calculated firstly avoiding the effect of the Fe NW. To obtain the value of the parameter  $D$ , a pristine GNS with the size of  $a \times b = 51.84 \times 31.98 \text{ \AA}^2$  is simulated, which is rolled into a cylinder with the radius of  $R_0 = a/2\pi$ . The  $\sigma_e$  is obtained by calculating the energy difference between the flat GNS and the cylinder. We obtain the value of  $D = 25.6 \text{ kcal/mol}$  using  $\sigma_e = (1/2)D\kappa^2$ , where  $\kappa = 1/R_0$  is valid in the linear elastic regime, which is in good agreement with ab initio result (Kudin and Scuseria 2001) and other model studies (Patra et al. 2009; Arroyo and Belytschko 2004), indicating that our study should be reasonable. Because  $R_G \approx R_{\text{NW}} + 2.6 = 11.2 \text{ \AA}$  and  $\kappa = 1/R_G$ , the obtained  $\sigma_G \approx 0.102 \text{ kcal}/(\text{mol} \cdot \text{\AA}^2)$  is far less than the calculated  $\sigma_{G-F} \approx 2.388 \text{ kcal}/(\text{mol} \cdot \text{\AA}^2)$ , meaning  $\sigma_{G-F} > \sigma_G$ . Because  $A_{G-F} \approx A_G$  during the wrapping process of the GNS onto the Fe NW before  $t = 15 \text{ ps}$ , we obtain the energy condition of the structural transition of the GNS activated by the Fe NW:

$$E_{G-F} + E_G < 0 \quad (1.3)$$

During the wrapping process, the structure would become more and more stable since  $E_{G-F}$  decreases rapidly due to the increase of the  $A_{G-F}$ .

During the structural transition, the self-scrolling of GNS has the outer radius  $R$ , the interlayer spacing  $h$ , and the fixed inner core radius  $r_0$ . The scrolled part of the GNS can be described by the polar equation  $r = r_0 + (h/2\pi)\theta$ , and parameters  $L$ ,  $R$ ,  $r_0$  and  $h$  meet the relation  $\pi(R^2 - r_0^2) = xh$  approximately, where  $x$  denotes the length of the rolled GNS and  $x \leq L$ . The elastic energy per unit area of the scroll is taken to be  $dQ(r)/dA = (1/2)D \times (1/r^2)$ . Because of that  $dA \approx Wr d\theta$  and  $\theta = (r - r_0)2\pi/h$ , the total elastic energy in the scroll can be obtained as  $Q = \pi DW/h \ln(R/r_0)$ . When an infinitesimal length  $\delta x$  of the GNS is rolled, the outer radius  $R$  of the scroll would increase by  $2\pi R \delta R = h \delta x$ . Then the change of the strain energy is  $\delta Q = (\pi DW/h) (\delta R/R) = DW \delta x / [2(xh/\pi + r_0^2)]$ . The total surface energy of the scroll is altered by  $\delta S = W(\gamma_{\text{CC}} + \gamma_{\text{CF}})\delta x$ , where  $\gamma_{\text{CC}}$  is the interlayer interaction energy per unit area of the GNS scroll and  $\gamma_{\text{CF}}$  is the interaction energy per unit area between the rolled GNS layer and Fe NW. Sum of the elastic energy and the surface energy is the total potential energy. Therefore, when displacement  $\delta x$  of GNS is rolled, the change of the total potential energy is  $\delta V/\delta x = \delta Q/\delta x + \delta S/\delta x$ . The releasing rate of the potential energy per unit area  $f$  is written as

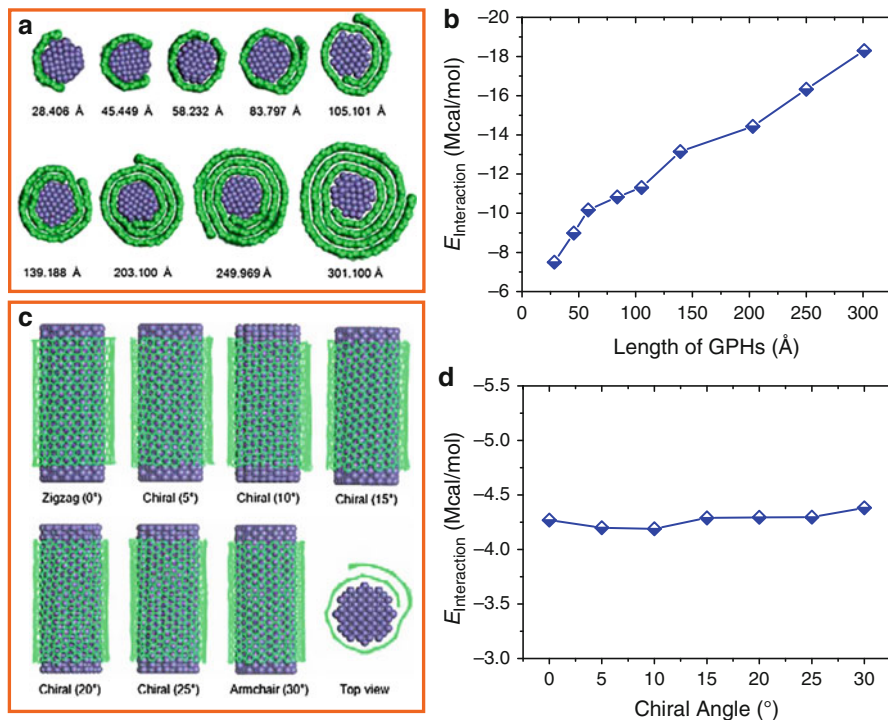


**Fig. 1.15** (a) The self-scrolling of GNSs with different lengths onto the Fe NW with same radius 6.4 Å and (b) the saturation interaction energies. (c) Different chirality GNSs wrapping onto Fe NW exhibit different chiralities and (d) the saturation interaction energies

$$f = \frac{\delta V}{\delta x} \frac{1}{W} = \gamma_{\text{CC}} + \gamma_{\text{CF}} + \frac{D}{2(xh/\pi + r_0^2)} \quad (1.4)$$

which is the net driving energy of the continuous structural transition of the GNS. Given the initial condition and corresponding net driving energy, Eqs. (1.3) and (1.4) can be integrated to predict the structural transition of GNS activated by the Fe NW.

### 1.3.2.5 The Effect of Size, Chirality, and Position

We further studied the self-scrolling of nine GNSs with same width of 66.420 Å (zigzag direction) but different lengths of 28.406, 45.449, 58.232, 83.797, 105.101, 139.188, 203.100, 249.969, and 301.100 Å (armchair direction), respectively. Figure 1.15a illustrates that all GNSs are activated to completely self-scroll onto Fe NWs, forming arcs and single-layered or multi-shell structures with the Fe NW cores. Figure 1.15b shows the saturated interaction energy between the Fe NW and the GNS with different lengths. It can be seen that the interaction energy between the

GNS and the Fe NW rapidly increases until the length of the GNS reaches  $58.232 \text{ \AA}$ , which corresponds to the length of the GNS that just completely wraps the NW with one circle. The final core-shell structure can be controlled by the radius of the Fe NW and the length of the GNS. If the length of the GNS  $L$  fit the equation

$$L = 2\pi (R_{\text{NW}} + d), \quad (1.5)$$

a perfect core-shell structure with single layer will be formed, where  $R_{\text{NW}}$  is the radius of the Fe NW and  $d$  is the average distance between the Fe NW and the GNS layer. When  $L > 2\pi (R_{\text{NW}} + d)$ , the GNS would overlap to form the multilayered scroll. If  $L < 2\pi (R_{\text{NW}} + d)$ , the GNS would paste onto the Fe NW to form an arc.

It is well known that the chirality has a significant effect on properties of GNSs, which can change their type from quasi-metallic to semiconducting (Jia et al. 2009). So it is essential to investigate the effect of the chirality on the structural transition. Figure 1.15c indicates that there are no obvious differences in their self-scrollings. Different kinds of scrolls exhibit different chiralities like CNT structures. To further clarify the effect of the chirality on the adhesion, Fig. 1.15d gives the saturation interaction energy between the Fe NW and the GNS with different chiralities. It shows that the chirality has a slight influence on the adhesion between the GNS and the Fe NW. Because the physical properties of the GNSs with different chiralities are different, we can produce different types of metal/GNS heterogeneous materials through this simple spontaneous scrolling, which are promising candidates for various applications including nanomechanical devices or nanocircuits.

The position of the Fe NW on GNS has a great effect on the self-scrolling. When the GNS length  $L$  and Fe NW radius  $R_{\text{NW}}$  meet the equation  $L \leq 2\pi (R_{\text{NW}} + d)$ , the GNS will paste to the NW no matter where the Fe NW is located as illustrated in Fig. 1.16a. However, when  $L > 2\pi (R_{\text{NW}} + d)$ , the self-scrolling of GNS would be greatly affected by the position of the Fe NW. In order to explore the position effect of the Fe NW, We study the self-scrolling of an armchair GNS with length  $207.361 \text{ \AA}$  onto a Fe NW with radius  $6.41 \text{ \AA}$ . Figure 1.16b illustrates the snapshots of the Fe NW located in different positions i, ii, iii, and iv. For the Fe NW with the radius of  $6.41 \text{ \AA}$ , only the distance  $D$  between the Fe NW and one end of the GNS meets  $D \leq 37.9 \text{ \AA}$ ; the GNS can wrap onto the Fe NW to form multilayered scroll. When  $D > 37.9 \text{ \AA}$ , though the structural transition is also activated, the GNS does not self-scroll onto the Fe NW to form multilayered scroll but a knot structure, as illustrated at positions iii and iv, respectively. Figure 1.16c shows snapshots of the typical structural transition activated by the Fe NW located at the middle. At  $t = 1.5 \text{ ps}$ , the GNS starts to wrap onto the NW. After two sides of the GNS meet, they contact each other to create more contact area and then fold tightly in opposite directions, respectively. Two ends oscillate up and down and finally a knot structure with double shells forms.

Next, we will further clarify how the initial angle ( $\varphi$ ) between the GNS and the Fe NW affects the self-scrolling. In Fig. 1.17a, the tip of a narrow GNR with size of  $22.85 \times 277.67 \text{ \AA}^2$  is initially positioned on the Fe NW at the angle of  $\varphi = 60^\circ$  with

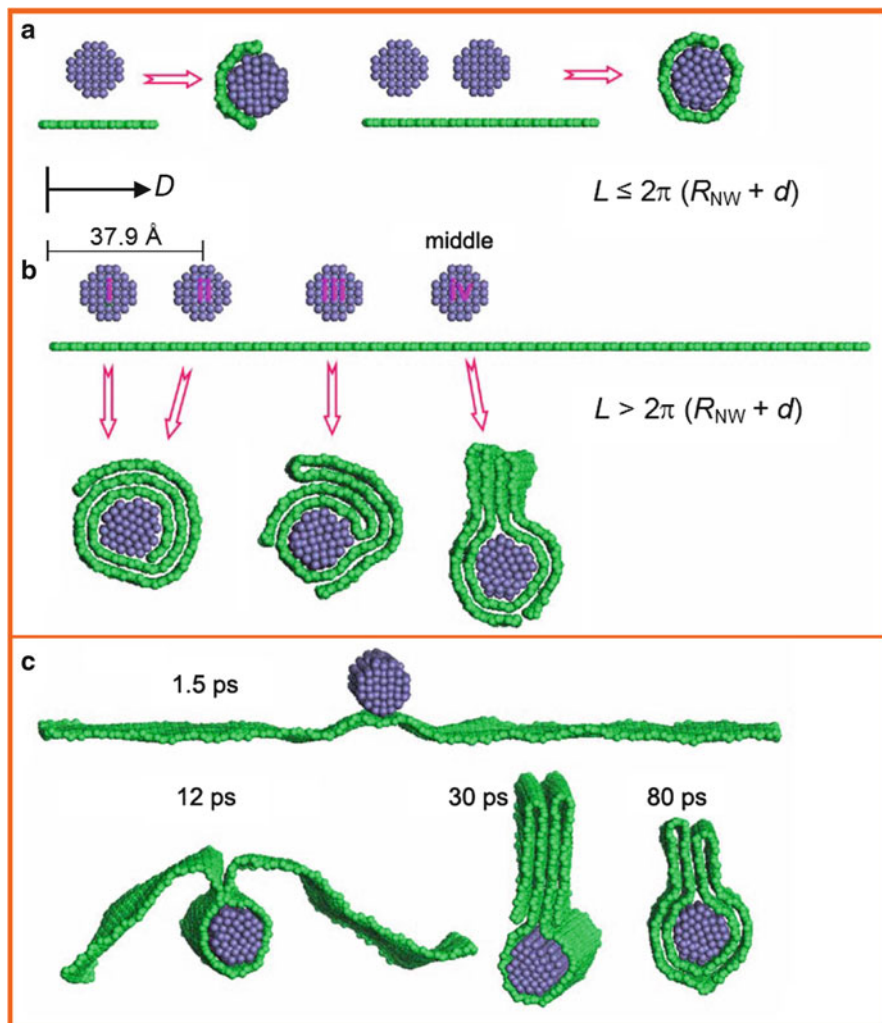


**Fig. 1.16** (a, b) Illustration of the position effect of the Fe NW on the self-scrolling of the GNS with different lengths and the final nanostructures. (c) A typical self-scrolling of the GNS onto the Fe NW located at the *middle*

respect to the axis of the Fe NW. The tip is attracted to the Fe NW fast and then move forward along the axial direction until the tip reaches another end of Fe NW. At  $t = 30$  ps, the GNR starts to scroll around the Fe NW spirally with large pitch. Then the pitch becomes small, and GNR eventually forms a stable helix with the distance between the neighboring edges  $3.5 \text{ \AA}$ . In this process, the GNS and Fe NW also satisfy the above-mentioned energy condition:  $E_{G-F} + E_G < 0$ , and the increase

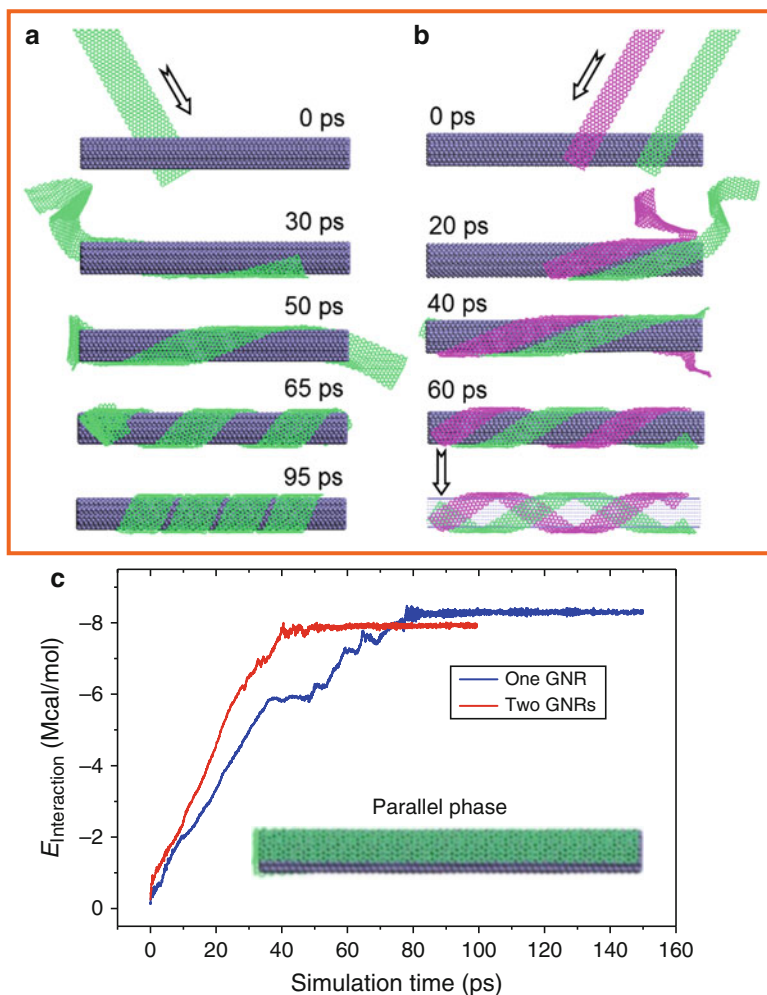


**Fig. 1.17** Snapshots of the helical rolling of one (a) and two GNRs (b) when placed at the angle of  $\varphi = 60^\circ$  with respect to the axis of the Fe NW. (c) The interaction energies between GNS and Fe NW during these two structural transition processes. The *inset* in (c) is the parallel phase of GNR on Fe NW

of the contact area enhances the stability of the whole system. We further study the spontaneous wrapping of two GNRs ( $183.93 \times 14.76 \text{ \AA}^2$ ) with initial angle  $\varphi = 60^\circ$  on the Fe NW, as shown in Fig. 1.17b. As simulation begins, two GNRs start to move forward side by side on the Fe NW. At  $t = 20$  ps, they start to fold helically in the same direction. Finally, they form a loose double helix with large pitch, which

closely resembles to the double-stranded DNA. The interaction energy between the Fe NW and GNR during the scrolling is shown in Fig. 1.17c. In two cases, the interaction energy between them increases linearly with the increase of the contact area until the GNRs fully wrap the Fe NWs. It verifies the fact that the interaction energy is mainly determined by the contact area between the GNS and Fe NW. Our simulations further reveal that if the initial angle is small, the thin GNR does not wrap spirally but adhere on the Fe NW parallel (parallel phase), as seen the inset in Fig. 1.17c. The above results indicate that the self-scrolling and final configuration of GNS can be controlled by the position, initial angle, and GNS width.

In the above discussion, we mainly focused on the self-scrolling of the GNS onto the NW that is long enough to form the core-shell structure. In order to determine whether there exists a critical length of NW, below which the perfect self-scrolling (as shown in Fig. 1.11) of GNS will not operable, the interaction between a GNS ( $83.80 \times 83.797 \text{ \AA}^2$ ) and a series of Fe NWs with different lengths and same radius ( $8.6 \text{ \AA}$ ) is further studied. From our calculations, the length of Fe NW ( $L_{\text{NW}}$ ), ensuring the perfect self-scrolling of GNS, should be longer than the critical value  $W_{\text{GNS}}/2$  ( $L_{\text{NW}} \geq W_{\text{GNS}}/2$ ), where  $W_{\text{GNS}}$  is the width of GNS parallel aligned with the NW. Otherwise, the GNS will fold onto Fe NW to form knot or dumpling-like structures. However, when the Fe NW is a bit shorter than the critical value, the perfect core-shell structure will still be formed if the GNR can well self-adjust, but it is much more difficult and uncertain.

### 1.3.2.6 Possible Applications

The unique self-scrolling properties of the GNS arouse our interest to utilize it as nanoscale conveyor belt to deliver substances to the surface of Fe NW for modification. Recent experiment showed that the NW modified by the aminothioliol molecule can be used to deliver plasmid DNA into different cells (Kuo et al. 2008). To explore the possible application, some butyl aminothioliol molecules are chemically attached to the GNS uniformly. Just as shown in Fig. 1.18, the GNSs modified by aminothioliol molecules can spontaneously wrap the Fe NWs and form the scroll and helix. The attached molecules have a little influence on the structural transition and the final structure. Besides the aminothioliol, other molecules such as drugs, catalysts, and enzymes can also be attached to the GNS and easily carried onto the Fe NW. The amount of the modified molecules can be easily managed and located at the specified position on a given Fe NW, since the distance between the NW and the GNS and that of the neighboring segments in GNS helix is easily known. Then the functional molecules can be distributed according to the individual requirement. Hence, the GNS can be a promising nanoscale conveyor belt to deliver molecules to modify the metallic NWs to develop their probing to the biological and medical systems.

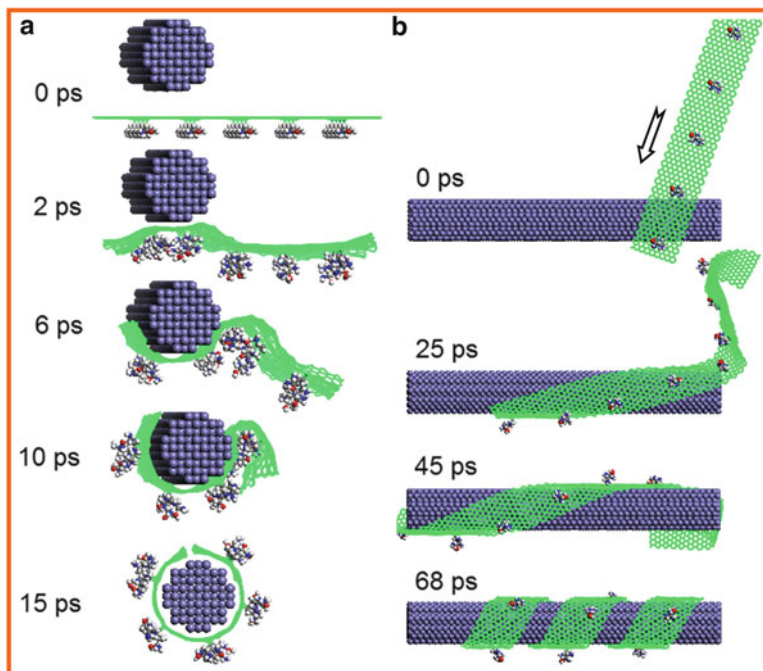


**Fig. 1.18** Snapshots of the aminothiols-modified GNS (a) and GNR (b) gradually wrapping onto Fe NWs

#### 1.4 Dynamic Ripples Reduced by the Impact of a C60 Molecule in Single-Layer Graphene

Recently, it has been found that a freestanding isolated graphene layer can be intrinsically corrugated to produce ripples, which are expected to affect its conductivity (Meyer et al. 2007b). Another approach to create periodic ripples into graphene has been reported by Bao and colleagues by utilizing the negative expansion coefficient of graphene sheet (Bao et al. 2009). The formation of ripple, which is related to the periodic variation of electronic properties of graphene, is expected to be used for synthesizing graphene-based electronic devices (Miranda and Vázquez de Parga 2009).

Here, we report an MD simulation of ripple formation and propagation in a single-layer graphene (SLG), induced by the impact of a C60 molecule. To mimic the classical single- or double-slit experiments, we also demonstrate the diffraction and interference of ripples in graphene.



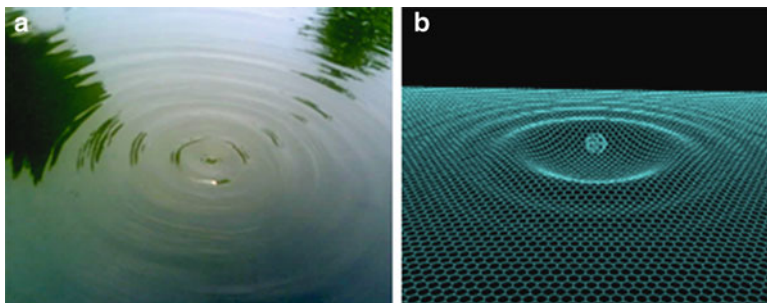


**Fig. 1.19** Snapshots of water wave and graphene ripple. (a) Water waves are generated by means of throwing a pebble to the static water pond (Nikon coolpix L22). (b) Graphene ripples are generated on the graphene which is stroked by an energetic C60 molecule

### 1.4.1 Simulation Method

In this MD simulation, the second-generation reactive empirical bond order (REBO) potential is used to describe the C–C interaction (Brenner et al. 2002; Li et al. 2009c), and the Lennard-Jones 12-6 potential is used to calculate the long-range van der Waals interaction. It is important to note that the ultrathin 2D graphene sheet is the medium of ripple propagation. Graphenes of two different sizes are studied. One graphene sheet has a size of  $197 \text{ \AA}$  (zigzag direction)  $\times$   $169 \text{ \AA}$  (armchair direction) (containing 12,880 atoms). The size of another is  $254 \text{ \AA}$  (armchair direction)  $\times$   $153 \text{ \AA}$  (zigzag direction) (containing 14,040 atoms). In order to observe the wave diffraction and interference, two symmetrical slits with a width of  $3 \text{ \AA}$  are created along a centerline of the latter graphene (all C atoms on the centerline, except those that belong to the slits, are fixed during the simulation). Initially, a C60 molecule is placed  $6.5 \text{ \AA}$  above the graphene. At time zero, the C60 starts to impact the SLG with an initial vertical velocity of  $15 \text{ \AA/ps}$ . The time step of the MD simulation is 1 fs and each trajectory runs for 10 ps.

### 1.4.2 Results and Discussion

A snapshot of circular ripples propagating in the SLG during the simulation is shown in Fig. 1.19b. It is interesting that these circular ripples are very similar to the water waves stirred by dropping a pebble into a pond (Fig. 1.19a). Different from the water wave in a pond, the ripple in SLG is arisen by distortion of C–C bonds. As vibration energy is passing through the graphene from the impacting center to another place, the ripples are formed. The ripple propagation in the SLG actually means that the “strong” impact energy is transformed into the “soft” wave energy, illustrating that the graphene can be used as an energy buffer to withstand shocks.

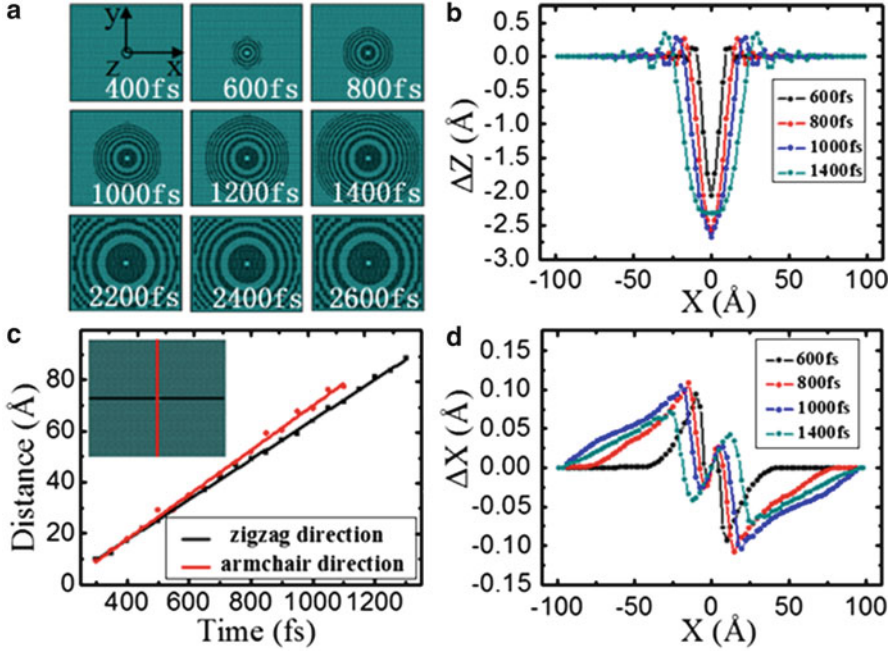


**Fig. 1.20** (a) The onset of the graphene ripple generated by striking with C60 molecule and its propagation on the surface of the graphene. The original ripples and the reflective ripples arouse interference pattern in the last three snapshots. (b) and (d) show the Z direction displacements ( $\Delta z$ ) and X direction displacements ( $\Delta x$ ) of atoms along the centerline [colored black in (c)], respectively. (c) The travelling distance of the ripples along different directions

The onset of the graphene ripple and its propagation in the SLG are demonstrated in Fig. 1.20a. The Z direction displacements ( $\Delta z$ ) of atoms on the centerline versus time curves Fig. 1.20b are used to illustrate the transverse waves. At 800 fs, the displacement of the atoms at the impacting point is about 2.6 Å. The amplitude of the nearest wave crest of the impacting point is 0.26 Å. The amplitude of the wave decays as the following exponential function:

$$A(x) = 2.59943 \exp(-|x|/7.33993) - 0.01351, \quad (1.6)$$

where  $x$  (in angstrom) is the horizontal position and  $A(x)$  (in angstrom) is the corresponding amplitude. The distances of ripple propagation at different times are shown in Fig. 1.20c. The average propagating speed of ripples along the zigzag direction is 78.32 Å/ps, while the propagating speed of ripples along the armchair direction is 87.02 Å/ps. The small difference between the two displacement lines results in a hexagonal symmetry of the ripples rather than complete circles (as shown in Fig. 1.20a). Meyer et al. mentioned that, under the condition of thermal equilibrium, ripples in freestanding graphene are intrinsic, random, and

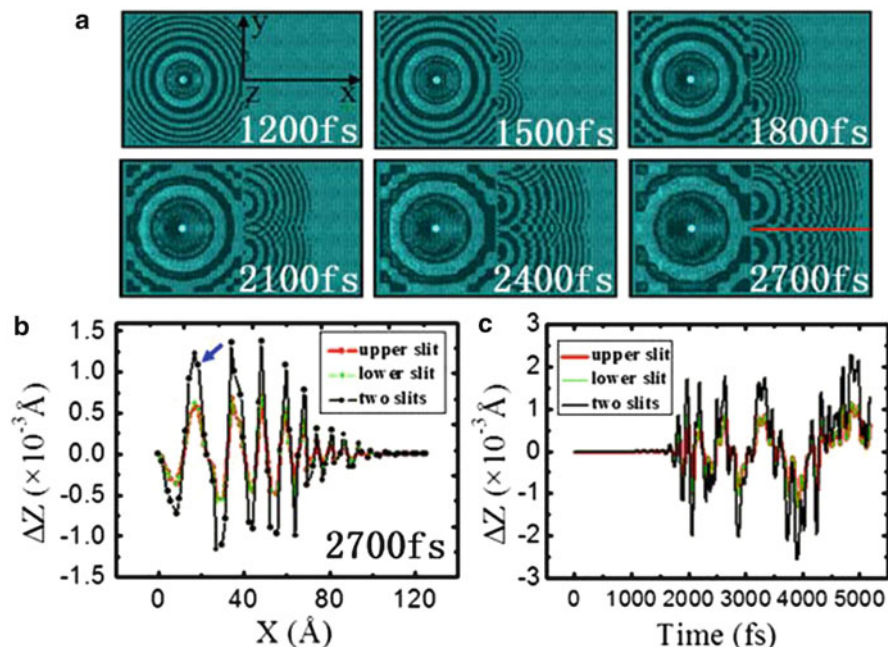


**Fig. 1.21** (a) Snapshots of interference of ripples coming from two slits. (b) The Z direction displacements ( $\Delta z$ ) of atoms on the centerline [colored red in (a)]. (c) The Z direction displacements of the atom pointed by a blue arrow in (b) at different times. The red line and green line indicate the displacement caused by the diffraction wave when the two slits are closed, respectively, while the black line indicates the displacement caused by the diffraction wave when the two slits are both open

uncontrollable (Meyer et al. 2007a, b). However, this study shows that, by C60 striking, the ripple forming on the surface of SLG is reproducible and controllable. For example, the amplitude of ripple can be easily tuned by varying the impacting speed of the C60.

The X direction displacements ( $\Delta x$ ) of atoms along the centerline are shown in Fig. 1.20d. The atoms near the zero point do not move along the X direction. With the increase of distance from the impacting point,  $\Delta x$  fluctuates between positive and negative. By comparing  $\Delta x$  with  $\Delta z$ , it is found that the Z direction displacement of atoms is much larger than the X direction displacement. Graphene shrinks as any other 2D membranes due to transverse bending vibrations. Muñoz et al. (2010) discussed the ballistic heat conductivity of graphene and showed that the soft bending mode dominated the graphene thermal conductivity at low temperature. This is in agreement with our simulation that propagation of the transverse wave is free in the graphene, which means that the free path of bending mode phonons is very large.

When the ripples reach a narrow slit, the atoms in the slit vibrate like a point source. Noticeable diffraction is shown in Fig. 1.21a. The diffraction wave

resembles a circular ripple with the slit as its center. Our results indicate that this mechanical ripple can spread out along the narrow slit (one atom distance), which would provide a possible technique to detect defects in graphene. For example, if there is a vacancy defect in the graphene, the shape of ripple would be different due to the wave diffraction at the vacancy defect. When the ripple arrives at the vacancy point, the smooth circle ripple at the defect point would form a small crater or even be separated into two parts, which is dependent on the size and shape of the vacancy. If lots of vacancy defects exist, the circle ripple would become quite unsmooth with some concaves. Therefore, we can determine the existence of vacancy defect by observing the shape of ripple.

When the two diffraction waves encounter in the double-slit interference experiment, interference is generated (shown in Fig. 1.21a). Figure 1.21b shows the displacements of a string of atoms along the centerline at 2,700 fs. The two point sources of the diffraction waves are also bilaterally symmetrical due to two localized bilaterally symmetrical slits. When the two slits are closed, respectively, it is found that the two displacement curves would almost fully overlap. However, once the two slits are both open, the resultant displacement is equal to the sum of the above two displacements, which accords with the principle of superposition of waves. In this way, the vibrations of all the atoms along the centerline are strengthened. Then, a single atom is picked from the central row of atoms in order to study the change of displacement as a function of time (shown in Fig. 1.21c). It is found that the displacement-time curves of the single atom are also corresponded to the above superposition principle. The above phenomena indicate that ripples propagating in a 2D single-atom-thick media can produce interference. We can use this concept of “superposition of waves” to design a “lens” that focuses wave energy on the SLG sheet, which would open an exciting possibility of the fabrication of nanodevices (e.g., signal transducer).

The above-mentioned graphenes are perfect 2D crystals which are not stable according to both theory and experiment (Mermin 1968; Meyer et al. 2007a, b; Novoselov et al. 2005a, b). There should be intrinsic ripples at finite temperatures due to its thermodynamic stability. When a graphene with intrinsic ripples is stroked by a C60 molecule, ripples also exist at the impacting point and propagate outside as shown in Fig. 1.22. It is found that impacting ripples on the plane graphene are different from those on the corrugated graphene. On one hand, the intrinsic ripples would inevitably affect the impacting ripples. The bending and stretching of the graphene layer result in the intrinsic ripples which are distributed randomly and uncontrollably. Therefore, the graphene surface is no longer plane and symmetric. During the propagating process, the impacting ripples vary with the different directions. On the other hand, the impacting ripples would affect the intrinsic ripples in turn. The propagation of impacting ripples breaks the original stability of graphene and thus changes the intrinsic ripples. As shown in Fig. 1.22, there are many cloudlike shades outside the impacting ripples, which mean that the amplitudes of intrinsic ripples in these areas have decreased. When the impacting ripples arrive at a slit, diffraction still occurs and brings cloudlike shades. However, interference of diffraction ripples coming from the two slits is

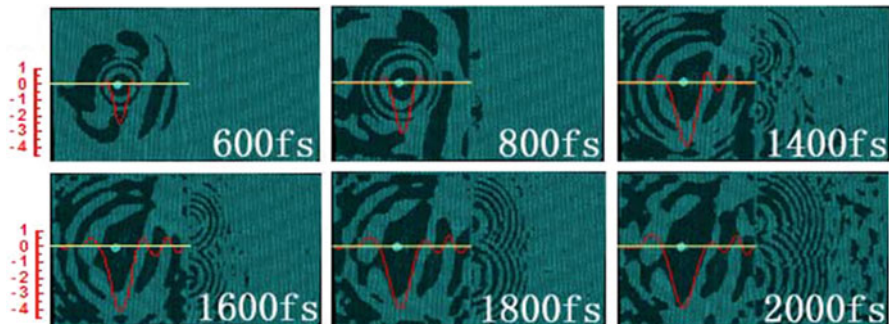


**Fig. 1.22** The propagation, diffraction, and interference of impacting ripples in the corrugated graphene. The inset *red line* of each graph is the *Z* direction displacements of atoms on the *yellow line*. Tick labels on the *left* are in unit of angstrom

not as clear as that of plane graphene. Although the intrinsic ripples disturb the impacting ripples, the signal carried by the impacting ripples does not fade away but still propagates forward. Intrinsic ripples in graphene are expected to strongly influence its electronic properties by introducing spatially varying potentials or effective magnetic fields (Park et al. 2008; Castro Neto et al. 2009). Different from intrinsic ripples, the impacting ripples made from C60 will disappear after the system is fully relaxed. However, the impacting ripple has its own excellent feature such as reducing local excessive deformation, transferring signals caused by striking, and detecting cracks or defects.

## 1.5 Conclusion

A series of atomistic MD simulations has been conducted to explore the interaction and the structural properties of GNR-SWNT and GNS-NW systems. The GNRs can helically wrap and insert the SWNT spontaneously to form helical configurations, which are quite close to the helices found in nature. The steady decline of the potential energy in the GNR-SWNT system suggests that the helical wrapping and insertion are spontaneous phenomena and systems are increasingly stable during these two processes. The vdW attraction drives the GNR continuously moving toward the tube and traps the GNR to adhere on the sidewalls of tubes, whereas the formation of the GNR helix is attributed to the  $\pi$ - $\pi$  stacking interaction between GNR and SWNT as well as the dangling  $\sigma$ -orbitals on carbon atoms at the open edges of GNR. A DNA-like double helix with same handedness would be formed with the wrapping and insertion of two GNRs. The velocity of GNR in helical wrapping is obviously lower than that in helical insertion. The diameter and chirality of tube have a neglect influence on the wrapping, whereas the encapsulation is limited by the diameter greatly.

Moreover, the GNSs can spontaneously self-scroll onto the Fe NWs irreversibly, which results in the structural transition of the GNS from 2D to 3D phase and the formation of the stable metal/carbon core-shell nanostructure. The planar GNS is in metastable state, just like the supercooled liquid. The interaction between the GNS and Fe NW as well as the  $\pi$ - $\pi$  stacking interaction between GNS layers may be responsible for this unique phenomenon. The decline of the potential energy of the whole system suggests that the self-scrolling of the GNS onto Fe NW is spontaneous, and the system is increasingly stable during this process. A thermodynamic model has been proposed to explain and predict the structural transition of GNS. The final core-shell nanostructure can be controlled by the positions of GNS and Fe NW.

MD simulation results also show that impact of C60 molecule would induce nanoscale dynamic ripples on the graphene no matter whether the graphene is plane or corrugated, although there are lots of differences between them. A GNS may be a well-promising material to be served as an energy buffer to withstand shocks. The propagation orientation and amplitude of ripples can be controlled via changing the locally insert slits and the speed of C60. The graphene ripple is a kind of surface wave which carries a lot of surface information, and the wave energy could also be focused due to the interference of ripples. The controlled ripples and their diffraction and interference in graphene are of great significance to detect the cracks and defects in the graphene sheet by receiving the wave signals.

This study provides possible applications for the GNS and GNR to serve as conveyor belt for molecule delivery. And also, the discoveries of this study are of great significance for the deeper understanding of the instability and properties of graphene at an atomic level and the further exploration of the properties of the GNR-SWNT and GNS-NW systems.

**Acknowledgments** The authors would like to acknowledge the support provided by the National Basic Research Program of China (Grant No. 2012CB825702). This work is also supported by the National Natural Science Foundation of China (Grant Nos. 51271100). The authors would also thank the support provided by promotive research fund for excellent young and middle-aged scientists of Shandong Province (Grant Nos. BS2010CL027).

## References

- Arroyo M, Belytschko T (2004) *Phys Rev B* 69:115411
- Bao W, Miao F, Chen Z, Zhang H, Jang W, Dames C, Lau CN (2009) *Nat Nanotechnol* 4:562
- Baskaran D, Mays JW, Bratcher MS (2005) *Chem Mater* 17:3389
- Bets KV, Yakobson BI (2009) *Nano Res* 2:161
- Blank VD, Kulnitskiy BA, Perezhogin IA, Polyakov EV, Batov DV (2010) *Acta Mater* 58:1293
- Borissov D, Isik-Uppenkamp S, Rohwerder M (2009) *J Phys Chem C* 113:3133
- Brenner DW, Shenderova OA, Harrison JA, Stuart SJ, Ni B, Sinnott SB (2002) *J Phys Condens Matter* 14:783
- Bunte SW, Sun HJ (2000) *Phys Chem B* 104:2477
- Castro Neto AH, Guinea F, Peres NMR, Novoselvo KS, Geim AK (2009) *Rev Mod Phys* 81:109

- Chen RJ, Zhang Y, Wang D, Dai H (2001) *J Am Chem Soc* 123:3838
- Choi WY, Kang JW, Hwang HJ (2003) *Phys Rev B* 68:193405
- Demoncey N, Stephan O, Brun B, Collix C, Loiseau A, Pascard H (1998) *Eur Phys J B* 4:147
- Fasolino A, Los JH, Katsnelson MI (2007) *Nat Mater* 6:858
- Fujii S, Enoki T (2010) *J Am Chem Soc* 132:10034
- Gao H, Kong Y, Cui D, Ozkan CS (2003) *Nano Lett* 3:471
- Gao XP, Zhang Y, Chen X, Pan GL, Yan J, Wu F, Yuan HT, Song DY (2004) *Carbon* 42:47
- Głóbwka ML, Martynowski D, Kozłowska K (1999) *J Mol Struct* 474:81
- Goswami S, Maiti UN, Maiti S, Nandy S, Mitra MK, Chattopadhyay KK (2011) *Carbon* 49:2245
- Govind N, Petersen M, Gitzgerald G, King-Smith D, Andzelm J (2003) *J Comput Mater Sci* 28:250
- Gulseren O, Ercolessi F, Tosatti E (1998) *Phys Rev Lett* 80:3775
- He YZ, Li H, Si PC, Li YF, Yu HQ, Zhang XQ, Ding F, Liew KM, Liu XF (2011) *Appl Phys Lett* 98:063101
- Hilder TA, Hill JM (2009) *Small* 5:300
- Hong B, Bae S, Lee CW, Jeong S, Kim K (2001) *Science* 294:348
- Hunter CA, Sanders JKM (2009) *J Am Chem Soc* 112:5525
- Jia XT, Hofmann M, Meunier V, Sumpter BG, Campos-Delgado J, Romo-Herrera JM, Son H, Hsieh Y, Reina A, Kong J, Terrones M, Dresselhaus MS (2009) *Science* 323:1701
- Jiang YY, Li H, Li YF, Yu HQ, Liew KM, He YZ, Liu XF (2011) *ACS Nano* 5:2126
- Juang ZY, Wu CY, Lu AY, Su CY, Leou KC, Chen FR, Tsai CH (2010) *Carbon* 48:3169
- Kalbacova M, Broz A, Kong J, Kalbac M (2010) *Carbon* 48:4323
- Khan U, Ryan K, Blau WJ, Coleman JN (2007) *Compos Sci Technol* 67:3158
- Kim KS, Zhao Y, Jang H, Lee SY, Kim JM, Kim KS, Ahn J-H, Kim P, Choi JC, Hong BH (2009) *Nature* 457:706
- Kondo Y, Takayanagi K (1997) *Phys Rev Lett* 79:3455
- Kondo Y, Takayanagi K (2000) *Science* 289:606
- Kudin KN, Scuseria EG (2001) *Phys Rev B* 64:235406
- Kuo CW, Lai JJ, Wei KH, Chen PL (2008) *Nanotechnology* 19:025103
- Ledoussal P, Radzihovsky L (1992) *Phys Rev Lett* 69:1209
- Li YF, Hatakeyama R, Kaneko T, Izumida T, Okada T, Kato T (2006) *Appl Phys Lett* 89:093110
- Li YF, Hatakeyama R, Shishido J, Kato T, Kaneko T (2007) *Appl Phys Lett* 90:173123
- Li H, Li YF, Liew KM, Zhang JX, Liu XF, Fan RH (2009a) *Appl Phys Lett* 95:063106
- Li H, Li YF, Liew KM, Zhang JX, Liu XF (2009b) *Appl Phys Lett* 95:183101
- Li H, Sun FW, Liew KM, Liu XF (2009c) *Scr Mater* 60:129
- Li H, Knaup JM, Kaxiras E, Vlassak JJ (2011a) *Acta Mater* 59:44
- Li YF, Sun FW, Li H (2011b) *J Phys Chem C* 115:18459
- Li YF, Yu HQ, Li H, An CG, Zhang K, Liew KM, Liu XF (2011c) *J Phys Chem C* 115:6229
- Li YF, Li H, Zhang K, Liew KM (2012) *Carbon* 50:566
- Mermin ND (1968) *Phys Rev* 176:250
- Meyer JC, Geim AK, Katsnelson MI, Novoselov KS, Obergfell D, Roth S, Girit C, Zettl A (2007a) *Solid State Commun* 143:101
- Meyer JC, Geim AK, Katsnelson MI, Novoselov KS, Booth TJ, Roth S (2007b) *Nature* 446:60
- Miranda R, Vázquez de Parga AL (2009) *Nat Nanotechnol* 4:549
- Mohaddes-Ardabili L, Zheng H, Ogale SB, Hannover B, Tian W, Wang J, Lofland SE, Shinde SR, Zhao T, Jia Y, Salamanca-Riba L, Schlom DG, Wuttig M, Ramesh R (2004) *Nat Mater* 3:533
- Muñoz E, Lu J, Yakobson BI (2010) *Nano Lett* 10:1652
- Nagy PI, Alagona G, Ghio C, Takács-Novák K (2003) *J Am Chem Soc* 125:2770
- Naito M, Nobusawa K, Onouchi H, Nakamura M, Yasui K, Ikeda A, Fujiki M (2008) *J Am Chem Soc* 130:16697
- Nish A, Hwang JY, Doig J, Nicholas RJ (2007) *Nat Nanotechnol* 2:640
- Novoselov KS, Geim AK, Morozov SV, Jiang D, Zhang Y, Dubonos SV, Grigorieva IV, Firsov AA (2004) *Science* 306:666
- Novoselov KS, Geim AK, Morozov SV, Jiang D, Katsnelson MI, Grigorieva IV, Dubonos SV, Firsov AA (2005a) *Nature* 438:197

- Novoselov KS, Jiang D, Schedin F, Booth TJ, Khotkevich VV, Morozov SV, Geim AK (2005b) *Proc Natl Acad Sci USA* 102:10451
- Numata M, Asai M, Kaneko K, Bae AH, Hasegawa T, Sakurai K, Shinkai S (2005) *J Am Chem Soc* 127:5875
- Ohiwa T (1976) *Bot Mag* 89:259
- Opitz J, Zahn P, Mertig I (2002) *Phys Rev B* 66:245417
- Park CH, Yang L, Son Y-W, Cohen ML, Louie SG (2008) *Nat Phys* 4:213
- Patra N, Wang BY, Kral P (2009) *Nano Lett* 9:3766
- Pederson MR, Broughton JQ (1992) *Phys Rev Lett* 69:2689
- Perdew JP, Wang Y (1992) *Phys Rev B* 45:13244
- Potts JR, Lee SH, Alam TM, An J, Stoller MD, Piner RD, Ruoff RS (2011) *Carbon* 49:2615
- Prakash G, Capano MA, Bolen ML, Zemlyanov D, Reifengerger RG (2010) *Carbon* 48:2383
- Sandoval L, Urbassek HM (2009) *Nano Lett* 9:2290
- Savini G, Dappe YJ, Öberg S, Charlier JC, Katsnelson MI, Fasolino A (2011) *Carbon* 49:62
- Seidel R, Mertig M, Pompe W (2002) *Surf Interface Anal* 33:151
- Sen D, Novoselov KS, Reis PM, Buehler MJ (2010) *Small* 6:1108
- Seol JH, Jo I, Moore AL, Lindsay L, Aitken ZH, Pettes MT, Li X, Yao Z, Huang R, Broido D, Mingo N, Ruoff RS, Shi L (2010) *Science* 328:213
- Snir Y, Kamien RD (2005) *Science* 307:1067
- Sorin EJ, Pande VS (2006) *J Am Chem Soc* 128:6316
- Sulong AB, Muhamad M, Sahari J, Ramli R, Deros BM, Park J (2009) *Eur J Sci Res* 29:13
- Sun H (1998) *J Phys Chem B* 102:7338
- Svensson K, Olin H, Olsson E (2004) *Phys Rev Lett* 93:145901
- Tasis D, Tagmatarchis N, Bianco A, Prato M (2006) *Chem Rev* 106:1105
- Thurn-Albrecht T, Schotter J, Kstle G, Emley N, Shibuachi T, Krusin-Elbaum L, Guarini K, Black CT, Tuominen MT, Russell TP (2000) *Science* 290:2126
- Wang B, Yin S, Wang G, Buldum A, Zhao J (2001) *Phys Rev Lett* 86:2046
- Wang ZY, Li H, Liu Z, Shi ZJ, Lu J, Suenaga K, Joung SJ, Okazaki T, Gu ZN, Zhou J, Gao ZX, Li GP, Sanvito S, Wang E, Iijima S (2010) *J Am Chem Soc* 132:13840
- Warner JH, Wilson M (2010) *ACS Nano* 4:4011
- Xu ZP, Buehler MJ (2010) *ACS Nano* 4:3869
- Yan KY, Xue QZ, Xia D, Chen HJ, Xie J, Dong MD (2009) *ACS Nano* 3:2235
- Yang XY, Zhang ZY, Liu ZF, Ma YF, Huang Y, Chen YS (2008) *J Phys Chem C* 112:17554
- Zhang Y, Dai HJ (2000) *Appl Phys Lett* 77:3015
- Zhang GD, Kuntz JD, Wan J, Mukherjee AK (2003a) *Nat Mater* 2:38
- Zhang XY, Wen GH, Chan YF, Zheng RK, Zhang XX, Wanga N (2003b) *Appl Phys Lett* 83:3341
- Zheng QB, Geng Y, Wang SJ, Li ZG, Kim JK (2010) *Carbon* 48:4315
- Zhou Z, Zhen J, Karpowich NK, Goetz RM, Law CJ, Reith MEA, Wang DN (2007) *Science* 317:1390
- Zhu CZ, Guo SJ, Fang YX, Dong SJ (2010) *ACS Nano* 4:2429
- Zorbas V, Ortiz-Acevedo A, Dalton AB, Yoshida MM, Dieckmann GR, Draper RK, Baughman RH, Jose-Yacamán M, Musselman IH (2004) *J Am Chem Soc* 126:7222



# Chapter 2

## First-Principles Study of the Electronic and Magnetic Properties of Defects in Carbon Nanostructures

Elton J.G. Santos, Andrés Ayuela, and Daniel Sánchez-Portal

**Abstract** Understanding the magnetic properties of graphenic nanostructures is instrumental in future spintronics applications. These magnetic properties are known to depend crucially on the presence of defects. Here we review our recent theoretical studies using density functional calculations on two types of defects in carbon nanostructures: substitutional doping with transition metals, and  $sp^3$ -type defects created by covalent functionalization with organic and inorganic molecules. We focus on such defects because they can be used to create and control magnetism in graphene-based materials. Our main results are summarized as follows:

1. Substitutional metal impurities are fully understood using a model based on the hybridization between the  $d$  states of the metal atom and the defect levels associated with an unreconstructed  $D_{3h}$  carbon vacancy. We identify three different regimes, associated with the occupation of distinct hybridization levels, which determine the magnetic properties obtained with this type of doping.

---

E.J.G. Santos (✉)

Centro de Física de Materiales (CFM-MPC) CSIC-UPV/EHU, Paseo Manuel de Lardizabal 5, San Sebastián 20018, Spain

Donostia International Physics Center (DIPC), Paseo Manuel de Lardizabal 4, San Sebastián 20018, Spain

Present address: Harvard School of Engineering and Applied Sciences, Harvard University, Cambridge, MA 02138, USA

Cruft Laboratory, Office Number: 406, 4th Floor, Oxford Street, Cambridge, MA 02138, USA  
e-mail: [esantos@seas.harvard.edu](mailto:esantos@seas.harvard.edu)

A. Ayuela • D. Sánchez-Portal

Centro de Física de Materiales (CFM-MPC) CSIC-UPV/EHU, Paseo Manuel de Lardizabal 5, San Sebastián 20018, Spain

Donostia International Physics Center (DIPC), Paseo Manuel de Lardizabal 4, San Sebastián 20018, Spain

e-mail: [swxayfea@ehu.es](mailto:swxayfea@ehu.es); [sqbsapod@ehu.es](mailto:sqbsapod@ehu.es)

2. A spin moment of  $1.0\mu_B$  is *always* induced by chemical functionalization when a molecule chemisorbs on a graphene layer via a single C–C (or other weakly polar) covalent bond. The magnetic coupling between adsorbates shows a key dependence on the sublattice adsorption site. This effect is similar to that of H adsorption, however, with universal character.
3. The spin moment of substitutional metal impurities can be controlled using strain. In particular, we show that although Ni substitutionals are nonmagnetic in flat and unstrained graphene, the magnetism of these defects can be activated by applying either uniaxial strain or curvature to the graphene layer.

All these results provide key information about formation and control of defect-induced magnetism in graphene and related materials.

## 2.1 Introduction

The experimental discovery of graphene, a truly two-dimensional crystal, has led to the rapid development of a very active line of research. Graphene is not only a fundamental model to study other types of carbon materials, but exhibits many uncommon electronic properties governed by a Dirac-like wave equation (Novoselov et al. 2004, 2005). Graphene, which exhibits ballistic electron transport on the submicrometer scale, is considered a key material for the next generation of carbon-based electronic devices (Geim and Novoselov 2007; Castro Neto et al. 2009). In particular, carbon-based materials are quite promising for spintronics and related applications due to their long spin relaxation and decoherence times owing to the spin-orbit interaction and the hyperfine interaction of the electron spins with the carbon nuclei, both negligible (Hueso et al. 2008; Trauzettel et al. 2007; Tombros et al. 2007; Yazyev 2008a). In addition, the possibility to control the magnetism of edge states in nanoribbons and nanotubes by applying external electric fields introduces an additional degree of freedom to control the spin transport (Son et al. 2006; Mananes et al. 2008). Nevertheless, for the design of realistic devices, the effect of defects and impurities has to be taken into account. Indeed, a substantial amount of work has been devoted to the study of defects and different types of impurities in these materials. The magnetic properties of point defects, like vacancies, adatoms, or substitutionals, have been recognized by many authors (Lehtinen et al. 2003; Palacios et al. 2008; Kumazaki and Hirashima 2008; Santos et al. 2010a,b; Chen et al. 2010; Ugeda et al. 2010; Yazyev and Helm 2007). It has now become clear that the presence of defects can affect the operation of graphene-based devices and can be used to tune their response.

In this chapter, we provide a review of several recent computational studies on the role of some particular type of defects in determining the electronic and, in particular, the magnetic properties of graphene and carbon nanotubes (Santos et al. 2008, 2010a,b, 2011, 2012a,b,c). We will consider two types of defects: substitutional transition metals and covalently bonded adsorbates. For the substitutional transition metals, we first present some of the existing experimental evidence about the

presence of such impurities in graphene and carbon nanotubes. Then, we summarize our results for the structural, electronic, and magnetic properties of substitutional-transition metal impurities in graphene. We show that all these properties can be explained using a simple model based on hybridization between the  $d$  shell of the metal atoms and the defects states of an unrelaxed carbon vacancy. We also show that it is possible to change the local spin moment of the substitutional impurities by applying mechanical deformations to the carbon layer. This effect is studied in detail in the case of Ni substitutionals. Although these impurities are nonmagnetic at a zero strain, we demonstrate that it is possible to switch on the magnetism of Ni-doped graphene either by applying uniaxial strain or curvature to the carbon layer. Subsequently, we explore the magnetic properties induced by covalent functionalization of graphene and carbon nanotubes. We find that the magnetic properties in this case are universal, in the sense that they are largely independent of the particular adsorbate: As far as the adsorbate is attached to the carbon layer through a single C–C covalent bond (or other weakly-polar covalent bond), there is always a spin moment of  $1 \mu_B$  associated with each adsorbate. We show that this result can be understood in terms of a simple model based on the so-called  $\pi$ -vacancy, that is, one  $p_z$  orbital removed from a  $\pi$ -tight-binding description of graphene. This model captures the main features induced by the covalent functionalization and the physics behind. In particular, using this model, we can easily predict the total spin moment of the system when there are several molecules attached to the carbon layer simultaneously. Finally, we have also studied in detail the magnetic couplings between Co substitutional impurities in graphene. Surprisingly, the Co substitutional impurity is also well described in terms of a simple  $\pi$ -vacancy model.

## 2.2 Substitutional Transition-Metal Impurities in Graphene

### 2.2.1 *Experimental Evidences*

Direct experimental evidence of the existence of substitutional impurities in graphene, in which a single metal atom substitutes one or several carbon atoms in the layer, has been recently provided by Gan and coworkers (2008). Using high-resolution transmission electron microscopy (HRTEM), these authors could visualize individual Au and Pt atoms incorporated into a very thin graphitic layer probably consisting of one or two graphene layers. From the real-time evolution and temperature dependence of the dynamics, they obtained information about the diffusion of these atoms. Substantial diffusion barriers ( $\sim 2.5$  eV) were observed for in-plane migration, which indicates the large stability of these defects and the presence of strong carbon–metal bonds. These observations indicate that the atoms occupy substitutional positions.

In another experiment using double-walled carbon nanotubes (DWCNT) (Rodriguez-Manzo et al. 2010), Fe atoms were trapped at vacancies likewise the previous observations for graphene layers. In these experiments, the electron beam was directed onto a predefined position and kept stationary for few seconds in order to create a lattice defect. Fe atoms had been previously deposited on the nanotube surface before the defect formation. After irradiation, a bright spot in the dark-field image was observed. A quantitative analysis of the intensity profile showed an increase of the scattered intensity at the irradiated position relative to the center of the pristine DWCNT. This demonstrates that at the defect position, on the top or bottom side of the DWCNT, an Fe atom was trapped.

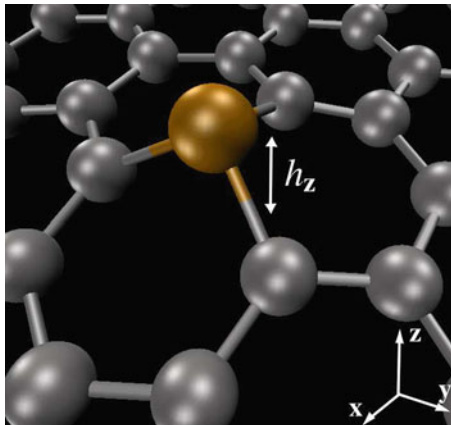
Recent evidence was also reported for substitutional Ni impurities in single-walled carbon nanotubes (SWCNT) (Ushiro et al. 2006) and graphitic particles (Banhart et al. 2000). Ushiro and coauthors (2006) showed that Ni substitutional defects were present in SWCNT samples synthesized using Ni-containing catalysts even after careful purification. According to their analysis of X-ray absorption data (XANES), the most likely configuration for these defects has a Ni atom replacing a carbon atom.

The presence of substitutional defects in the samples can have important implications for the interpretation of some experiments. For example, substitutional atoms of transition metals are expected to strongly influence the magnetic properties of graphenic nanostructures. Interestingly, transition metals like Fe, Ni, or Co are among the most common catalysts used for the production of SWCNTs (Dresselhaus et al. 2001). Furthermore, the experiments by Banhart and coworkers (Rodriguez-Manzo and Banhart 2009) have demonstrated that it is possible to create individual vacancies at desired locations in carbon nanotubes using electron beams. This experiment, combined with the observed stability of substitutional impurities, opens a route to fabricate new devices incorporating substitutional impurities at predefined locations. These devices would allow for the experimental verification of the unusual magnetic interactions mediated by the graphenic carbon network that have been predicted recently (Brey et al. 2007; Kirwan et al. 2008; Santos et al. 2010b). This becomes particularly interesting in the light of the recent finding that the spin moment of those impurities could be easily tuned by applying uniaxial strain and/or mechanical deformations to the carbon layer (Santos et al. 2008; Huang et al. 2011; Santos et al. 2012a). In spite of this, the magnetic properties of substitutional transition-metal impurities in graphenic systems were not studied in detail until very recently. Few calculations have considered the effect of this kind of doping on the magnetic properties of the graphenic materials, and this will be the main topic of the following sections.

### ***2.2.2 Structure and Binding***

In Fig. 2.1 we show the typical geometry found in our calculations for a graphene layer where one carbon atom has been substituted by a metal impurity. The metal atom appears always displaced from the carbon layer. The height over the plane

**Fig. 2.1** Typical geometry of transition and noble substitutional metal atoms in graphene. The metal atom moves upwards from the layer and occupies, in most cases, an almost perfectly symmetric threefold position with  $C_{3v}$  symmetry

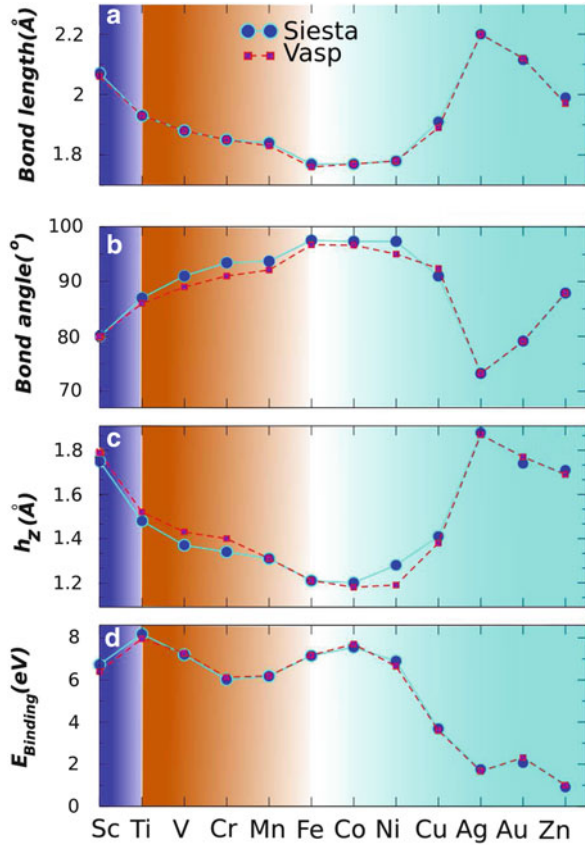


defined by its three nearest carbon neighbors is in the range 1.7–0.9 Å. These three carbon atoms are also displaced over the average position of the graphene layer by 0.3–0.5 Å. The total height ( $h_z$ ) of the metal atom over the graphene plane is the sum of these two contributions and ranges between 1.2 and 1.8 Å, as shown in panel (c) of Fig. 2.2.

In most cases the metal atom occupies an almost perfectly symmetric configuration with  $C_{3v}$  symmetry. Exceptions are the studied noble metals that are slightly displaced from the central position and Zn that suffers a Jahn-Teller distortion in its most stable configuration. However, we have found that it is also possible to stabilize a symmetric configuration for Zn with a binding energy only  $\sim 150$  meV smaller. This configuration will be referred to as  $Zn_{C_{3v}}$  throughout this chapter.

Figure 2.2a–c presents a summary of the structural parameters of substitutional  $3d$  transition metals, noble metals and Zn in graphene. Our calculations are in very good agreement with the results of a similar study performed by Krasheninnikov et al. (2009), although they overlooked the existence of the high-spin  $Zn_{C_{3v}}$  configuration. Solid circles correspond to calculations using the SIESTA code (Soler et al. 2002) with pseudopotentials (Troullier and Martins 1991) and a basis set of atomic orbitals (LCAO), while open squares stand for VASP (Kresse and Hafner 1993; Kresse and Furthmüller 1996) calculations using plane-waves and PAW potentials (Blöchl 1994). As we can see, the agreement between both sets of calculations is excellent. Data in these figures correspond to calculations using a  $4\times 4$  supercell of graphene. For several metals we have also performed calculations using a larger  $8\times 8$  supercell and find almost identical results. This is particularly true for the total spin moments, which are less dependent on the size of the supercell but require a sufficiently dense k-point sampling to converge. The behavior of the metal–carbon bond length and  $h_z$  reflects approximately the size of the metal atom. For transition metals these distances decrease as we increase the atomic number, with a small discontinuity when going from Mn to Fe. The carbon–metal bond length reaches its minimum for Fe ( $d_{C-Fe}=1.76$  Å), keeping a very similar value for Co and Ni. For Cu and Zn, the distances increase reflecting the fully occupied  $3d$  shell and the large size of the  $4s$  orbitals. Among the noble metals, we find

**Fig. 2.2** Structural parameters and binding energies of substitutional transition and noble metals in graphene. Bond lengths and angles have been averaged for the noble metals. The data presented for Zn correspond to the high-spin solution with  $C_{3v}$  symmetry and are very close to the averaged results for the most stable distorted solution (Adapted from Santos et al. 2010a)



that, as expected, the bond length largely increases for Ag with respect to Cu, but slightly decreases when going from Ag to Au. The latter behavior is understood from the compression of the  $6s$  shell due to scalar relativistic effects.

As already mentioned, noble metals and Zn present a distorted configuration. In Table 2.1 we find the corresponding structural parameters. For Cu and Ag, one of the metal–carbon bond lengths is slightly larger than the other two, whereas for Au one is shorter than the others. However, the distortions are rather small with variations of the bond lengths below 2%. The significant scalar relativistic effects in Au give rise to slightly smaller metal–carbon bond lengths for this metal as compared to Ag. In the case of Zn atoms, the distorted configuration presents one larger Zn–C bond (by  $\sim 3.5\%$ ) and two shorter bonds ( $\sim 5\%$ ) compared with the bond length ( $1.99 \text{ \AA}$ ) of the undistorted geometry. The distorted configuration is more stable by 160 meV (with SIESTA, this energy difference is reduced to 120 meV using VASP). This rather small energy difference between the two configurations might point to the appearance of non-adiabatic electronic effects at room temperature.

**Table 2.1** Structural parameters for substitutional noble metals and Zn in graphene

	$d_{C-M}$ (Å)	$h_z$ (Å)	$\theta$ (°)
Cu	1.93, 1.90, 1.90	1.40	88.9, 88.9, 95.2
Ag	2.23, 2.19, 2.19	1.84	71.7, 71.7, 76.7
Au	2.09, 2.12, 2.12	1.71	78.0, 78.0, 81.6
Zn	2.06, 1.89, 1.89	1.54	88.3, 88.3, 103.9
Zn <sub>C<sub>3v</sub></sub>	1.99	1.67	87.9

$d_{C-M}$  indicates the bond distances between the metal atom and its three carbon neighbors, and  $h_z$  is the height of the impurity over the carbon layer (see the text). The bond angles are also given

The binding energies of the studied substitutional metal atoms in graphene are shown in Fig. 2.2d. In general, these energies correlate with the carbon–metal bond length, although the former exhibits a somewhat more complicated behavior. The binding energies for transition metals are in the range of 8–6 eV. Substitutional Ti presents the maximum binding energy, which can be easily understood since for this element all the metal–carbon bonding states (Santos et al. 2010a) are fully occupied. One could expect a continuous decrease of the binding energy as we move away from Ti along the transition metal series, and the nonbonding  $3d$  and the metal–carbon antibonding levels become progressively populated. However, the behavior is non-monotonic, and the smaller binding energies among the  $3d$  transition metals are found for Cr and Mn, and a local maximum is observed for Co. This complex behavior is explained by the simultaneous energy downshift and compression of the  $3d$  shell of the metal impurity as we increase the atomic number (Santos et al. 2010a). In summary, the binding energies of the substitutional  $3d$  transition metals are determined by two competing effects: (a) as the  $3d$  shell becomes occupied and moves to lower energies, the hybridization with the carbon vacancy states near the Fermi energy ( $E_F$ ) is reduced, which decreases the binding energy; (b) the transition from Mn to late transition metals is accompanied by a reduction of the metal–carbon bond length by  $\sim 0.1$  Å, which increases the carbon–metal interaction and, correspondingly, the binding energy.

The binding energies for noble metals are considerably smaller than for transition metals and mirror the reverse behavior of the bond lengths: 3.69, 1.76, and 2.07 eV, respectively, for Cu, Ag, and Au. The smallest binding energy ( $\sim 1$  eV) among the metals studied here is found for Zn, with both  $s$  and  $d$  electronic shells filled.

### 2.2.3 Spin-Moment Formation: Hybridization Between Carbon Vacancy and $3d$ Transition-Metal Levels

Our results for the spin moments of substitutional transition and noble metals in graphene are shown in Fig. 2.3 (Santos et al. 2010a). Similar results have been found by several authors (Krasheninnikov et al. 2009; Huang et al. 2011).

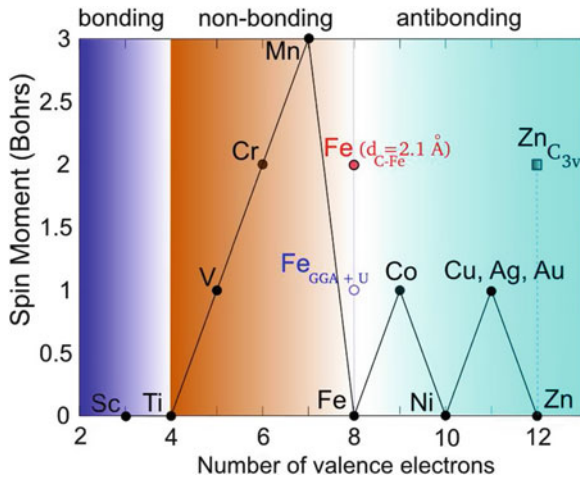


**Fig. 2.3** Spin moment of substitutional transition and noble metals in graphene as a function of the number of valence electrons (Slater-Pauling-type plot). *Black symbols* correspond to the most stable configurations using GGA. Results are almost identical using SIESTA and VASP codes. Three main regimes are found as explained in detail in the text: (1) filling of the metal–carbon bonding states gives rise to the nonmagnetic behavior of Ti and Sc; (2) nonbonding  $d$  states are filled for V, Cr, and Mn giving rise to high-spin moments; and (3) for Fe all nonbonding levels are occupied and metal–carbon antibonding states start to be filled giving rise to the observed oscillatory behavior for Co, Ni, Cu, and Zn. *Open and red symbols* correspond, respectively, to calculations of Fe using GGA+U and artificially increasing the height of the metal atom over the graphene layer (see the text). Symbol marked as  $Zn_{C_{3v}}$  corresponds to a Zn impurity in a high-spin symmetric  $C_{3v}$  configuration (Adapted from Santos et al. 2010a)

We have developed a simple model that allows to understand the behavior of the spin moment, as well as the main features of the electronic structure, of these impurities (Santos et al. 2010a). Our model is based on the hybridization of the  $3d$ -states of the metal atom with the defect levels of a carbon vacancy in graphene. In brief, we can distinguish three different regimes according to the filling of electronic levels:

- *Bonding regime*: all the carbon–metal bonding levels are filled for Sc and Ti and, correspondingly, their spin moments are zero.
- *Nonbonding regime*: nonbonding  $3d$  levels become populated for V and Cr giving rise to a spin moment of, respectively, 1 and  $2\mu_B$  with a strong localized  $d$  character. For Mn one additional electron is added to the antibonding  $d_{z^2}$  level and the spin moment increases to  $3\mu_B$ .
- *Antibonding regime*: finally, for Fe and heavier atoms, all the nonbonding  $3d$  levels are occupied and the spin moment oscillates between 0 and  $1\mu_B$  as the antibonding metal–carbon levels become occupied.

The sudden decrease of the spin moment from  $3\mu_B$  for Mn to  $0\mu_B$  for Fe is characterized by a transition from a complete spin polarization of the nonbonding



**Table 2.2** Mulliken population analysis of the spin moment for different substitutional impurities in graphene

	$S_M(\mu_B)$	$S_C(\mu_B)$	$S_{\text{tot}}(\mu_B)$
V	1.21	-0.09	1.0
Cr	2.53	-0.20	2.0
Mn	2.91	-0.10	3.0
Co	0.44	0.06	1.0
Cu	0.24	-0.03, 0.31, 0.31	1.0
Ag	0.06	-0.31, 0.54, 0.54	1.0
Au	0.16	-0.28, 0.50, 0.50	1.0
Zn <sub>C<sub>3v</sub></sub>	0.23	0.37	2.0

$S_{\text{tot}}$  is the total spin moment in the supercell,  $S_M$  is the spin moment in the central metal impurity and  $S_C$  is the spin moment in the carbon nearest neighbors

$3d$  levels to a full occupation of those bands. However, this effect depends on the ratio between the effective electron–electron interaction within the  $3d$  shell and the metal–carbon interaction (Santos et al. 2010a). If the hybridization with the neighboring atoms is artificially reduced, for example, by increasing the Fe–C distance, Fe impurities develop a spin moment of  $2\mu_B$  (see the red symbol in Fig. 2.3). Our results also show that it is possible to switch on the spin moment of Fe by changing the effective electron–electron interaction within the  $3d$  shell. These calculations were performed using the so-called GGA+U method. For a large enough value of  $U$  (in the range 2–3 eV), Fe impurities develop a spin moment of  $1\mu_B$ . It is noteworthy that this behavior is unique to Fe: using similar values of  $U$  for other impurities does not modify their spin moments.

At the level of the GGA calculations, Fe constitutes the border between two different trends of the spin moment associated with the substitutional metal impurities in graphene. For V, Cr, and Mn, the spin moment is mainly due to the polarization of the  $3d$  shell of the transition-metal atoms. The strongly localized character of the spin moment for those impurities, particularly for V and Cr, is corroborated by the Mulliken population analysis shown in Table 2.2. For Co, Ni, the noble metals, and Zn, the electronic levels close to the  $E_F$  have a much stronger contribution from the carbon neighbors. Thus, for those impurities we can talk about a “defective graphene”-like magnetism. Indeed, it is possible to draw an analogy between the electronic structure of the late transition, noble metals and Zn substitutional impurities and that of the isolated unreconstructed ( $D_{3h}$ ) carbon vacancy (Santos et al. 2008, 2010a,b). The stronger carbon contribution and delocalization in the distribution of the spin moment for Co, the noble metals, and Zn impurities is evident in Table 2.2.

In the following we present the “hybridization” model that allows to distinguish the three regimes of the spin-moment evolution described before, corresponding to the filling of levels of different character. We have found that the electronic structure of the substitutional impurities can be easily understood as a result of the interaction of two entities: (a) the localized defect levels associated with a symmetric  $D_{3h}$  carbon vacancy and (b) the  $3d$  states of the metal atom, taking also into account the

down shift of the  $3d$  shell as the atomic number increases. We considered explicitly the  $3d$  states of the metal atom since our calculations show that, at least for transition metals, the main contribution from  $4s$  orbitals appears well above  $E_F$ .

To illustrate the main features of our model, in Fig. 2.4a we present a schematic representation of the hybridization of the  $3d$  levels of Ti with those of an unreconstructed  $D_{3h}$  carbon vacancy in graphene. The interested reader can see (Santos et al. 2010a) for an extension of the model for the other metals and technical details. The defect levels of the unreconstructed  $D_{3h}$  vacancy can be easily classified according to their  $sp$  or  $p_z$  character and whether they transform according to A- or E-type representations. A scheme of the different level can be found in Fig. 2.4, while the results of a DFT calculation are depicted in Fig. 2.5b (see also Santos et al. 2010a and Amara et al. 2007). Close to the  $E_F$ , we can find a fully symmetric A  $p_z$  level (thus belonging to the  $A_2''$  irreducible representation of the  $D_{3h}$  point group) and two degenerate defect levels with E symmetry and  $sp$  character ( $E'$  representation). Approximately 4 eV below  $E_F$ , we find another defect level with A  $sp$  character ( $A_1'$  representation). Due to the symmetric position of the metal atom over the vacancy, the system has a  $C_{3v}$  symmetry, and the electronic levels of the substitutional defect can still be classified according to the A or E irreducible representations of this point group. Of course, metal and carbon vacancy states couple only when they belong to the same irreducible representation. Thus, occupied A  $p_z$  and A  $sp$  vacancy levels can only hybridize with the  $3d_{z^2}$  orbitals ( $A_1$  representation), while all the other  $3d$  metal orbitals can only couple to the unoccupied E  $sp$  vacancy levels.

With these simple rules in mind and taking into account the relative energy position of carbon and metal levels that changes as we move along the transition-metal series, we can understand the electronic structure of substitutional transition metals in graphene as represented in Fig. 2.4a, b. Some parameters in the model can be obtained from simple calculations. For example, a rough estimate of the position of the  $3d$  shell of the metal atom respect to the graphene  $E_F$  is obtained from the positions of the atomic levels. The relative strengths of the different carbon–metal hoppings can be estimated from those of the corresponding overlaps. With this information, it is already possible to obtain most of the features of the model in Fig. 2.4. However, some uncertainties remain, particularly concerning the relative position of levels with different symmetry. To solve these uncertainties, the simplest approach is to compare with first-principles calculations. The details of the model presented in Fig. 2.4 have been obtained from a thorough analysis of our calculated band structures (Santos et al. 2010a). In particular, we have used the projection of the electronic states into orbitals of different symmetry as an instrumental tool to classify the levels and to obtain the rationale that finally guided us to the proposed model. In contrast, it is interesting to note that some features that derive from our way to understand the electronic structure of these defects are very robust and could actually be guessed without direct comparison with the calculated band structures. For example, the fact that for V we start to fill the nonbonding  $3d$  states and this impurity, as well as Cr and Mn, develops a spin moment can be argued from simple symmetry and electron-counting arguments.

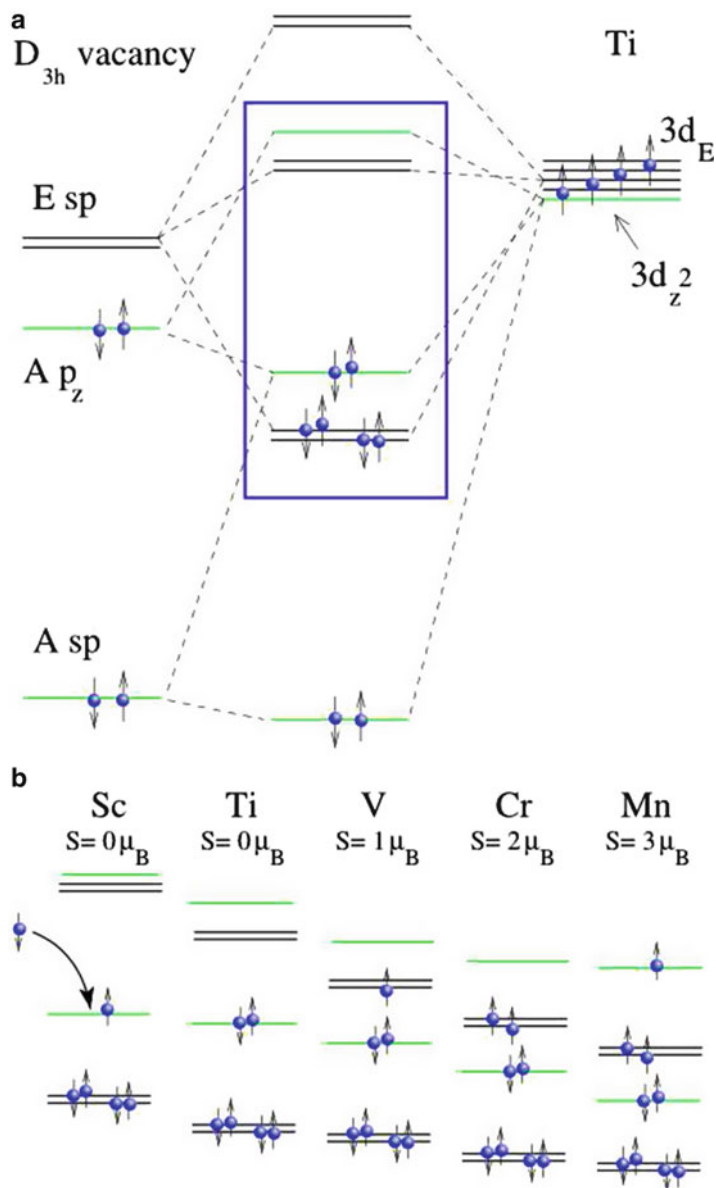


**Fig. 2.4** (a) Scheme of the hybridization between the  $3d$  levels of Ti and the localized impurity levels of the  $D_{3h}$  carbon vacancy. Only  $d$  levels of Ti are represented since our calculations show that, at least for transition metals, the main contribution from  $s$  levels appears well above  $E_F$ . Levels with A symmetry are represented by *gray (green) lines*, while those with E symmetry are marked with *black lines*. The region close to  $E_F$  is highlighted by a *square*. (b) Schematic representation of the evolution of the electronic structure near  $E_F$  for several substitutional transition metals in graphene. The spin moment ( $S$ ) is also indicated. Substitutional Sc impurities act as electron acceptors, causing the p-doping of the graphene layer (Adapted from Santos et al. 2010a)

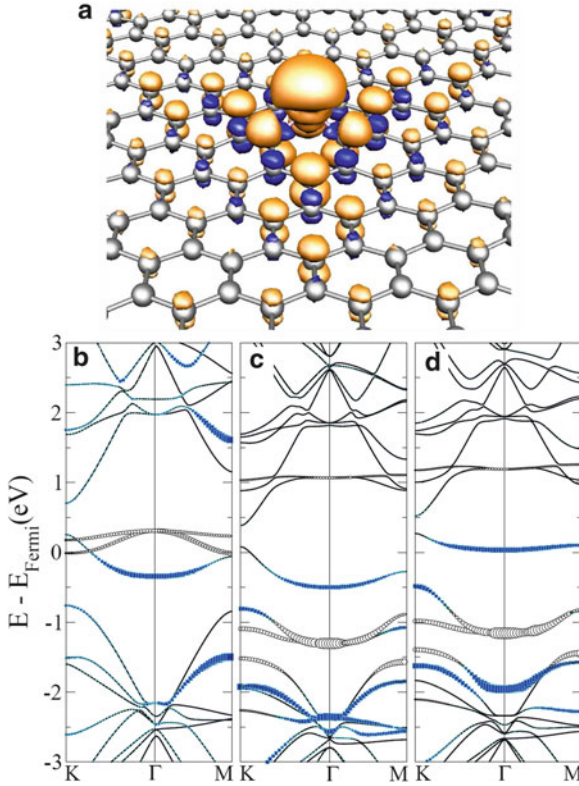


**Fig. 2.5** (a) Isosurface of the spin density induced by a  $\text{Co}_{\text{sub}}$  defect. Positive and negative spin densities correspond to light and dark surfaces with isovalues of  $\pm 0.008 \text{ e}^-/\text{Bohr}^3$ , respectively. Panel (b) presents the spin-unpolarized band structure of an unreconstructed  $D_{3h}$  carbon vacancy. Panels (c, d) show, respectively, the band structure of majority and minority spins for a  $\text{Co}_{\text{sub}}$  defect in a similar cell. The size of *filled symbols* in panel (b) indicates the contribution of the  $p_z$  orbitals of the C atoms surrounding the vacancy, whereas empty symbols correspond to the  $sp^2$  character. In panels (c, d), the *filled* and *empty circles* denote the contribution of hybridized Co  $3d_{z^2}$ -C  $2p_z$  and Co  $3d$ -C  $2sp^2$  characters, respectively.  $E_F$  is set to zero (Adapted from Santos et al. 2010b)

According to our model for the substitutional metals, there are three localized defect levels with  $A_1$  character and three twofold-degenerate levels with  $E$  character. Two of these  $E$  levels correspond to bonding-antibonding  $sp$ - $d$  pairs, while the third one corresponds to  $3d$  nonbonding states. For Sc–Mn the three  $A_1$  levels can be pictured as a low-lying bonding level with  $A$   $sp$ - $d_{z^2}$  character and a bonding-antibonding pair with  $A$   $p_z$ - $d_{z^2}$  character. As shown in Fig. 2.4, we have four metal-vacancy bonding levels (two  $A$  and one doubly degenerate  $E$  levels) that can host up to eight electrons. For instance, Ti contributes with four valence electrons, and there are four electrons associated with the localized carbon-vacancy levels. Ti has the bonding states completely occupied. Consequently, Ti presents the highest binding energy among all  $3d$  transition metals and has a zero spin

moment. Figure 2.4b shows the situation for other impurities in the series Sc–Mn. Substitutional Sc impurities have zero spin moment because they act as electron acceptors. Note that all the bonding levels are also filled for Sc, causing a p-doping of the graphene layer. As already mentioned V, Cr, and Mn present an increasing spin moment due to the filling of the nonbonding levels, while for Fe the nonbonding shell is completely filled.

Late transition, noble metals and Zn substitutional impurities have the filled levels coming from an antibonding interaction between the carbon vacancy and the metal states. The character and spatial localization of those levels are very similar to those of the levels of the  $D_{3h}$  vacancy close to  $E_F$ .

Co substitutionals present a singly degenerate half-occupied defect level at  $E_F$ . As we will discuss in more detail in the next section, this level is reminiscent of the state that appears at  $E_F$  associated with a single carbon vacancy in a  $\pi$ -tight-binding description of graphene (Palacios et al. 2008). A second electron occupies this level for Ni impurities, and the spin polarization is lost (Santos et al. 2008).

An additional electron is added for noble metal impurities. This electron populates a doubly degenerate level coming from the antibonding interaction of the  $2sp^2$  lobes in the nearest carbon neighbors, with the orbitals of  $d_{xz}$  and  $d_{yz}$  symmetries in the metal impurity. This state is reminiscent of E  $sp$  level of the  $D_{3h}$  carbon vacancy. The occupation of this twofold-degenerate state with only one electron explains both, the observed  $1 \mu_B$  spin moment and the structural distortion of the noble metal impurities (Santos et al. 2010a). As we will see in Sect. 2.3.1, the E  $sp$  impurity levels also play a crucial role to explain the switching on of the magnetism of Ni impurities under mechanical deformations and uniaxial strain.

For Zn two electrons occupy the twofold-degenerate E  $sp$  level. As a consequence, the system suffers a Jahn–Teller distortion and has a zero spin moment. However, it is possible to stabilize a symmetric configuration ( $Zn_{C_{3v}}$ ) with a moment of  $2 \mu_B$  and only slightly higher in energy (Santos et al. 2010a).

### 2.2.4 Co Substitutionals in Graphene as a Realization of Single $\pi$ -Vacancies

In this section we examine in detail the analogy that can be established between substitutional Co atoms in graphene ( $Co_{sub}$ ) and the simplest theoretical model trying to account for the properties of a carbon vacancy in graphene. The electronic structure and magnetic properties of a  $Co_{sub}$  impurity are analogous to those of a vacancy in a simple  $\pi$ -tight-binding description of graphene. This toy model system, the  $\pi$ -vacancy, has been extensively studied in the graphene literature due to its very interesting magnetic properties directly related to the bipartite character of the graphene network (Castro Neto et al. 2009; Palacios et al. 2008).

We begin by looking at the spin density of the  $Co_{sub}$  impurity as shown in Fig. 2.5a. The spin polarization induced in the carbon atoms has a  $p_z$ -like shape and decays slowly as we move away from the impurity. The sign of the spin

polarization follows the bipartite character of graphene: the polarization aligns parallel (antiparallel) to the spin moment located in the Co impurity for carbon atoms in the opposite (same) sublattice. The value of the total spin moment is  $1.0 \mu_B$  per defect. Using Mulliken population analysis, the moment on the Co atom has a value of  $0.44 \mu_B$ , the three first carbon neighbors have  $0.18 \mu_B$ , and there are  $0.38 \mu_B$  delocalized in the rest of the layer. Therefore, the total spin moment has contribution from both Co and carbon orbitals.

To understand the origin of this spin polarization, we now analyze in detail the band structure. Figure 2.5c, d presents the results for a  $\text{Co}_{\text{sub}}$  defect in a  $4 \times 4$  graphene supercell. Similar results are obtained using a  $8 \times 8$  cell. For comparison, panel (b) shows the spin-compensated band structure of a single unreconstructed  $D_{3h}$  carbon vacancy. For the  $D_{3h}$  vacancy, there are three defect states in a range of  $\sim 0.7$  eV around  $E_F$ . Two states appear above  $E_F$  at 0.3 eV at  $\Gamma$  and have a large contribution from the  $sp^2$  lobes of the C atoms surrounding the vacancy. These levels correspond to the two degenerate  $E$   $sp$  states appearing in Fig. 2.4. Another state at 0.35 eV below  $E_F$  shows a predominant  $p_z$  contribution and corresponds to the A  $p_z$  level in Fig. 2.4. This last level represents the defect state that appears at  $E_F$  for a vacancy using a  $\pi$ -tight-binding description. For a  $\text{Co}_{\text{sub}}$ , the defect states of the vacancy described above hybridize with the Co  $3d$  states. The two  $2sp^2$  defect bands, now an antibonding combination of Co  $3d$  and the original C  $2sp^2$  vacancy levels, are pushed at higher energies,  $\sim 1.0$  eV above  $E_F$  (see Fig. 2.5c, d). The singly occupied  $p_z$  state, now hybridized mainly with the Co  $3d_{z^2}$  orbital, remains at  $E_F$  and becomes almost fully spin-polarized. The  $\text{Co}_{\text{sub}}$  impurity becomes thus analogous to a vacancy in the  $\pi$ -tight-binding model of graphene.

This analogy is a powerful one, since it brings our results for the magnetism of  $\text{Co}_{\text{sub}}$  impurities into contact with Lieb's theorem for a half-filled Hubbard model (Lieb 1989), where the spin polarization is an intrinsic property of the defective bipartite lattice. Applying this theorem and our analogy, we can expect that the total spin of an array of  $\text{Co}_{\text{sub}}$  impurities can be described according to the simple rule  $S = |N_A - N_B|$ , where  $N_A$  and  $N_B$  indicate the number of Co substitutions in A and B sublattices, respectively. In Sect. 2.4.1 we will show results from first-principles calculations that confirm this behavior. However, Lieb's theorem is global, in the sense that it refers to the total spin moment of the system and does not enter into the local description of the magnetic interactions. This will be described in more detail in Sect. 2.4.1, where we will compute the exchange couplings between  $\text{Co}_{\text{sub}}$  defects.

Other realistic defects, besides  $\text{Co}_{\text{sub}}$  impurities, can also be mapped onto the simple  $\pi$ -vacancy model. In Sect. 2.4.2 we will see that complex adsorbates chemisorbed on carbon nanotubes and graphene generate a spin polarization. The magnetism due to such covalent functionalization displays a behavior similar to that of the  $\pi$ -vacancies. Some concepts already used here will be again invoked to explain the main features of the magnetism associated with these defects, leading to a universal magnetic behavior independent of the particular adsorbate.

### 2.3 Tuning the Magnetism of Substitutional Metals in Graphene with Strain

In the previous section, we have considered in detail the formation of local spin moments induced by a particular class of defects in graphene, substitutional transition metals. Although this is an important subject, other aspects are also crucial to understand and control the magnetism associated with this kind of doping. For example, one needs to explore the characteristics of the couplings between local moments, as well as the possibility to control such couplings, and the size of the local moments, using external parameters. This kind of knowledge is instrumental in possible applications in spintronics and quantum information devices. The subject of the magnetic couplings will be postponed until Sect. 2.4. In this section we analyze how the structural, electronic, and magnetic properties of substitutional defects in carbon nanostructures can be controlled using strain. We focus on Ni substitutionals and conclude that externally applied strain can provide a unique tool to tune the magnetism of Ni-doped graphene.

Strain provides a frequently used strategy to modify the properties of materials. For example, strain is intentionally applied to improve mobility in modern micro-electronic devices. This so-called strain engineering has taken a key position over years. Recently, strain effects have also been proposed as a route to control the electronic properties of pristine graphene, which had a deep impact on the physics of this material (Guinea et al. 2010; Pereira and Castro Neto 2009).

Here, we show that the application of uniaxial strain can be used to switch on the magnetism of graphene doped with Ni substitutional impurities ( $\text{Ni}_{\text{sub}}$ ) (Santos et al. 2012a). Whereas  $\text{Ni}_{\text{sub}}$  defects are nonmagnetic in flat graphene, we find that their spin moment changes from zero when no strain is applied, up to  $1.9 \mu_B$  at  $\sim 7.0\%$  strain. This strong variation stems from the modifications of the local structure of the defect, which cause changes in the electronic structure of the defect that can be related to those of the unreconstructed carbon vacancy in graphene under strain. The similarities between the electronic structure of the  $\text{D}_{3h}$  vacancy and that of  $\text{Ni}_{\text{sub}}$  were already stressed in the previous section.

We also show that substitutional metallic impurities in carbon nanotubes display a different magnetic behavior from that observed in flat graphene. Using  $\text{Ni}_{\text{sub}}$  dopants as an example, we demonstrate that the intrinsic curvature of the carbon layer in the SWCNTs can be used to switch on the magnetism of Ni substitutionals (Santos et al. 2008). The defect electronic structure is modified by curvature in a similar way as by uniaxial strain. In addition, we find a strong dependence of the spin moment on the impurity distribution, tube metallicity, and diameter of the nanotube.

### 2.3.1 Switching on the Magnetism of Ni-Doped Graphene with Uniaxial Strain

In this subsection, we study the electronic structure of  $\text{Ni}_{\text{sub}}$  defects in graphene under uniaxial strain. According to the analysis presented in Sect. 2.2.3, at a zero strain,  $\text{Ni}_{\text{sub}}$  defects are nonmagnetic in flat graphene (Santos et al. 2008, 2010a). However, we find that under moderate uniaxial strain, these impurities develop a nonzero spin moment, whose size increases with that of the applied strain. This magnetoelastic effect might be utilized to design a strain-tunable spin device based on defective graphene.

Figure 2.6a, b shows the spin moment of a  $\text{Ni}_{\text{sub}}$  defect as a function of the applied strain along the  $(n, n)$  and  $(n, 0)$  directions, respectively. The curves with filled squares show simulations using geometries from a non-spin-polarized calculation with a DZ basis set (see references Soler et al. 2002 and Artacho et al. 1999 for a description of the different basis sets). The spin moment and electronic structure are always calculated using a more complete DZP basis. The open squares indicate systems that were calculated using the previous procedure, that is, a DZ basis, but the geometries have been obtained from spin-polarized calculations. The triangles display calculations with DZP basis set for both geometry and spin moment. At zero strain the  $\text{Ni}_{\text{sub}}$  defect is nonmagnetic. As the uniaxial tension is applied, the system starts to deform. At  $\sim 3.5\%$  strain, the system becomes magnetic with a spin moment that evolves nearly linearly with the uniaxial strain up to values of  $\sim 0.30\text{--}0.40 \mu_B$  at  $\sim 6.0\%$ . The magnetism of the system using different basis set is very similar. At  $\sim 6.8\%$  the spin moment increases sharply from  $\sim 0.40 \mu_B$  to  $\sim 1.9 \mu_B$ . This transition takes place for both directions, although it is somewhat more abrupt along the  $(n, n)$  direction (Fig. 2.6a) where no intermediate steps are observed. Thus, the magnetic properties depend on the local defect geometry and, to a much lesser extent, on the defect orientation relative to the applied strain. Panels (c) and (d) in Fig. 2.6 present the local defect geometry. When the strain is applied, the triangle formed by the three C neighboring atoms to the Ni impurity deforms. The C–C distances along the strain direction increase, whereas distances along the perpendicular direction decrease in response to such elongation. The distance of the Ni atom to the first carbon neighbors also increases, but this bond length changes for the studied strains are less than  $\sim 5.0\%$  (averaged over both strain directions) in comparison with  $\sim 20.0\%$  for the C–C distances. The analysis of distances suggests that the carbon neighbors and the central Ni impurity interact strongly, which is also reflected in the high stability of the defect with a binding energy  $\sim 7.9$  eV to the carbon vacancy.

In order to understand the magnetic moment in  $\text{Ni}_{\text{sub}}$  defects, the density of states (DOS) around  $E_F$  under strains of 0.0, 2.2, 5.3, and 7.2% are shown in Fig. 2.7. The strain is along the  $(n, n)$  direction although the qualitative behavior is similar to other directions. Several defect levels around  $E_F$  have Ni and C mixed character. As pointed out before (Sect. 2.2), the metal atom over the vacancy has a  $C_{3v}$  symmetry at a zero strain, and the electronic levels are classified according to the  $A$  or  $E$



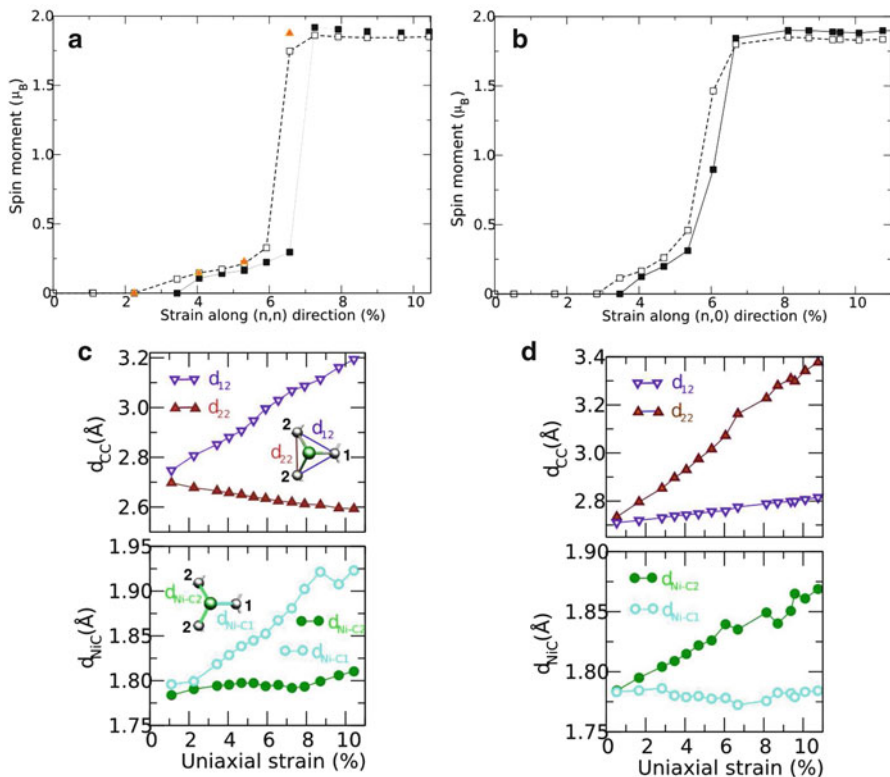
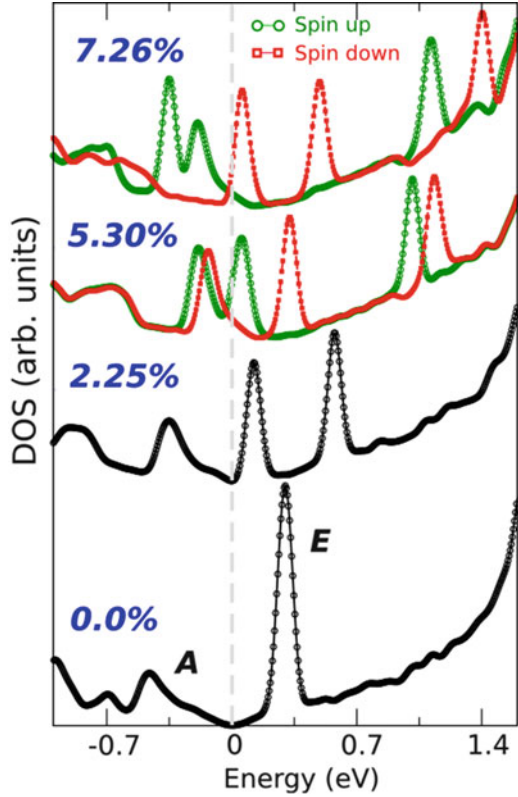


**Fig. 2.6** Spin moment as a function of the applied strain along (a) the (n, n) and (b) the (n, 0) directions. In panels (a) and (b), *filled squares* indicate results obtained using geometries from a non-spin-polarized calculation using a DZ basis. The spin moment and electronic structure are calculated using a DZP basis using such geometry. *Open squares* indicate a similar calculation, but the geometries have been obtained from a spin-polarized calculation. The *triangles* represent full calculations (geometry and spin moment) with DZP basis set. Panels (c) and (d) show the results for the structural parameters as a function of the applied strain along (n, n) and (n, 0), respectively. Bond lengths between the different C atoms are denoted  $d_{12}$  and  $d_{22}$ , while the bond lengths between Ni and C atoms are  $d_{Ni-C1}$  and  $d_{Ni-C2}$ . The structural information was calculated using a DZ basis (Adapted from Santos et al. 2012a)

irreducible representations of this point group. Essentially, these three defect states and their evolution as a function of the applied strain determine all the observed physics.

One of them with *A* character is occupied and appears around  $\sim 0.50$  eV below  $E_F$  at zero strain. This level comes from a fully symmetric linear combination of the  $2p_z$  orbitals ( $z$ -axis normal to the layer) of the nearest C neighbors interacting with the  $3d_{z^2}$  orbital of Ni. The other twofold-degenerate levels with *E* character, coming from the hybridization of the in-plane  $sp^2$  lobes of the carbon neighbors with the Ni  $3d_{xz}$  and  $3d_{yz}$  orbitals, appear at 0.50 eV above  $E_F$  at a zero strain. Because this

**Fig. 2.7** Density of states (DOS) of the  $\text{Ni}_{\text{sub}}$  defect under 0.0, 2.25, 5.30, and 7.26 % strain applied along the  $(n, n)$  direction. Symbols  $A$  and  $E$  indicate the character and symmetries of the defect states, with large weight of Ni hybridized with C states.  $A$  corresponds to  $\text{Ni } 3d_{z^2}-\text{C } 2p_z$ , and  $E$  represents  $\text{Ni } 3d_{x^2}, 3d_{yz}-\text{C } 2sp$ . At 5.30 and 7.26 % strains, the *open squares* (green curve) represent the spin-up channel and *filled squares* (red curve) the spin down. For clarity, the curves have been shifted. The Fermi energy is marked by the dashed (gray) line and is set to zero (Adapted from Santos et al. 2012a)

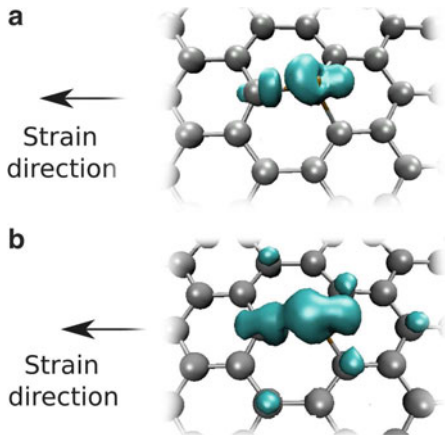


electronic structure has the Ni  $3d$  states far from  $E_F$  and no flat bands crossing  $E_F$ , the spin moment of the  $\text{Ni}_{\text{sub}}$  impurity in graphene is zero. Interestingly, these three levels that appear close to  $E_F$  in Fig. 2.7 are reminiscent of those found for the unreconstructed carbon vacancy in graphene as we have already seen in Sect. 2.2.

The energy position of the three levels shifts as a function of the applied strain. When the strain is applied, the degeneracy between  $\text{Ni } 3d_{xz}-\text{C } 2sp$  and  $\text{Ni } 3d_{yz}-\text{C } 2sp$  states is removed, and a gradual shift towards  $E_F$  of one of them is observed. This level becomes partially populated, and the system starts to develop a spin moment. The  $\text{Ni } 3d_{z^2}-\text{C } 2p_z$  state also changes its position approaching  $E_F$ , although for small values of the strain, this level does not contribute to the observed magnetization. However, around a 7 % strain, both the  $\text{Ni } 3d_{z^2}-\text{C } 2p_z$  and the  $\text{Ni } 3d_{xz,yz}-\text{C } 2sp$  levels become fully polarized and the system develops a moment close to  $2.00 \mu_B$ .

Figure 2.7 also shows the resulting spin-polarized DOS at 5.3 and 7.2 % strain (upper part of the panel). The exchange splittings of the  $3d_{xz}$  and  $3d_{yz}$  levels are, respectively,  $\sim 0.29$  and  $\sim 0.13$  eV at 5.3 %, increasing with the applied strain and the associated spin moment. The energy gain with respect to the spin-compensated solutions develops from 13.9 meV at 5.3 % to 184.1 meV at 7.26 %. Thus,

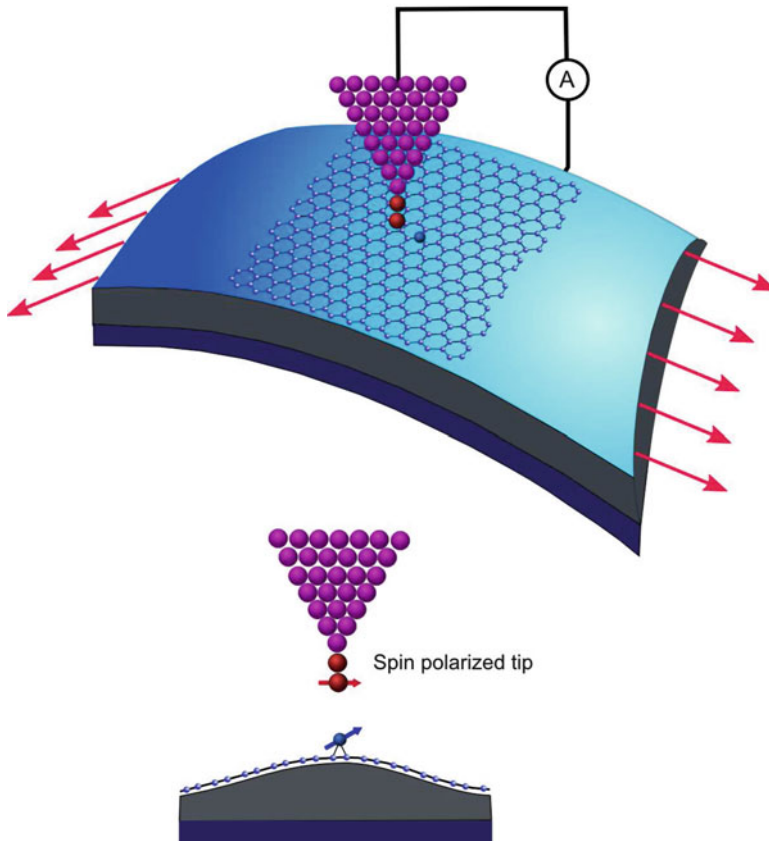
**Fig. 2.8** (a, b) Spin densities for  $\text{Ni}_{\text{sub}}$  defects at strains of 5.30 and 7.26 % along the  $(n, n)$  direction. The strain direction is marked by the arrows in both panels. The isovalue cutoff at (a, b) panels is  $\pm 0.035$  and  $\pm 0.060$   $e^-/\text{Bohr}^3$  (Adapted from Santos et al. 2012a)



a moderate variation of the strain applied to the graphene layer changes the spin state and enhances the stability of the defect-induced moment. According to these results, if it is possible to control the strain applied to the graphene layer, as shown in recent experiments (Mohiuddin et al. 2009; Kim et al. 2009), the magnetism of Ni-doped graphene could be turned *on* and *off* at will, like switches used in *magnetoelastic devices*, however, with no applied magnetic field. This suggests a sensitive and effective way to control the magnetic properties of graphene, which is interesting for its possible applications in nanoscale devices (Santos et al. 2012a).

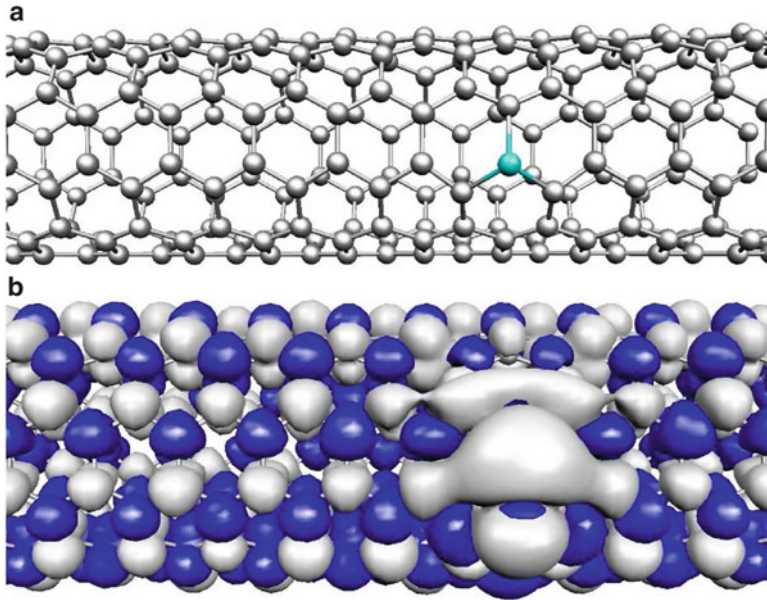
Figure 2.8a, b shows the spin magnetization patterns induced by the presence of a  $\text{Ni}_{\text{sub}}$  defect under two different magnitudes of uniaxial strain applied along the  $(n, n)$  direction. The spin polarization induced in the neighboring carbon atoms has shape and orbital contributions that depend sensitively on strain. At 5.30 % the spin density is mainly localized at the Ni impurity and at the C atom bonded to Ni along the strain direction. The antibonding character of the  $E$  defect state that originates the magnetization is clear (see the node in the bond direction). The spin density at this C atom shows a  $2sp$ -like shape to be contrasted with that at 7.26 % strain, in which apart from the  $2sp$ -like shape, a  $2p_z$  component is clearly observed. At this larger strain, farther neighboring-carbon atoms also contribute to the spin density with mainly  $2p_z$  character. This additional contribution to the spin polarization pattern corresponds to the Ni  $3d_{z^2}$ -C  $2p_z$ -defect state at  $E_F$  for strains above  $\sim 7\%$ , as explained in the previous section using the DOS.

Figure 2.9 shows a possible experimental setup that could be used to test our predictions. This is similar to a mechanically controlled break junction setup with an elastic substrate (Mohiuddin et al. 2009; Kim et al. 2009). Graphene is deposited in the center of such a substrate in order to obtain a uniform strain. Bending or stretching the substrate causes an expansion of the surface, and the deposited graphene will follow this deformation. In principle, the modifications on the electronic structure can be detected using a scanning tunneling microscope (STM) since the involved defect levels are localized around the Fermi energy. For example, Ugeda et al. were able to measure using STM the energy position and



**Fig. 2.9** Experimental setup that could be utilized to measure the effect of strain on the magnetic properties of Ni-doped graphene. The layer is deposited on a stretchable substrate which keeps a large length-to-width ratio in order to obtain a uniform tensile strain in the graphene film. Spectroscopy measurements using scanning tunneling microscope (STM) would allow to identify the shift of the different defect levels. If the magnetic anisotropy is large enough or there is an external magnetic field, it could be also possible to measure the presence and orientation of a magnetic moment at the defect site using a spin-polarized tip

spatial localization of the defect levels associated with a carbon vacancy in the surface of graphite (Ugeda et al. 2010). If the magnetic anisotropy of the defect is high enough, at sufficiently low temperatures, a preferential orientation of the moment would be stabilized, and in principle, an STM with a spin-polarized tip (spin-STM) could allow to monitor the evolution of the magnetic properties of the Ni-doped graphene with strain. Instead, an external magnetic field may be used to align the magnetic moments of the defects and define the hard/easy axis of the system. It is noteworthy that the break junction-like setup has already been successfully used (Standley et al. 2008).



**Fig. 2.10** (a) Relaxed geometry of a substitutional Ni ( $\text{Ni}_{\text{sub}}$ ) impurity in a (5, 5) SWCNT and (b) isosurface ( $\pm 0.002 e^-/\text{Bohr}^3$ ) of the magnetization density with light (gray) and dark (blue) surfaces corresponding, respectively, to majority and minority spin (Adapted from Santos et al. 2008)

### 2.3.2 *Ni Substitutionals in Carbon Nanotubes: Curvature-Induced Magnetism*

Although  $\text{Ni}_{\text{sub}}$  impurities are nonmagnetic in flat graphene, their magnetic moment can be switched on by applying curvature to the structure. To understand why, we will begin looking at the equilibrium structure of  $\text{Ni}_{\text{sub}}$  for a (5,5) SWCNT. The Ni atom is displaced  $\sim 0.9 \text{ \AA}$  from the carbon plane. Although both outward and inward displacements can be stabilized, the outward configuration is always more stable. The calculated Ni–C distances ( $d_{\text{Ni}-\text{C}}$ ) are in the range  $1.77\text{--}1.85 \text{ \AA}$  in good agreement with experiment (Ushiro et al. 2006; Banhart et al. 2000). Armchair tubes exhibit two slightly shorter and one larger values of  $d_{\text{Ni}-\text{C}}$ ; the opposite happens for zigzag tubes, whereas for graphene we obtain a threefold symmetric structure with  $d_{\text{Ni}-\text{C}}=1.78 \text{ \AA}$ . Ni adsorption inhibits the reconstruction (Amara et al. 2007) of the carbon vacancy. Furthermore, we have checked that for a vacancy in graphene, a symmetric structure is obtained after Ni addition even when starting from a relaxed vacancy.

Figure 2.10b shows the magnetization density profile for a  $\text{Ni}_{\text{sub}}$  defect in a (5, 5) metallic nanotube at large dilution (0.3 % Ni concentration). The total spin moment is  $0.5 \mu_B$ . The magnetization is on the Ni atom and its C neighbors. However, it also

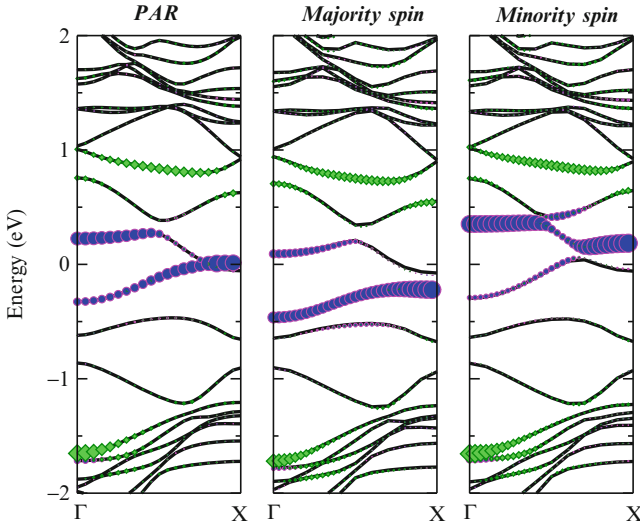


**Fig. 2.11** Band structure of a (5, 5) nanotube containing a  $\text{Ni}_{\text{sub}}$  impurity in four unit cells for (left panel) a paramagnetic calculation (PAR) and for (middle panel) majority and (right panel) minority spins. Circles and diamonds correspond respectively to the amount of Ni  $3d_{yz}$  and  $3d_{xz}$  character. X-axis is parallel to the tube axis and y-axis is tangential (Adapted from Santos et al. 2008)

extends considerably along the tube, particularly in the direction perpendicular to the tube axis. This profile indicates that the spin polarization follows some of the delocalized electronic states in the metallic nanotube. Indeed, as we clarify below, the magnetism in substitutionally Ni-doped SWCNTs only appears associated with the curvature and the metallicity of the host structure.

The basic picture described in Sect. 2.2 is still valid for the electronic structure of the  $\text{Ni}_{\text{sub}}$  impurity in SWCNTs. However, the modifications that appear due to the curvature of the carbon layer are responsible for the appearance of a magnetic moment. Figure 2.11a shows the band structure of a paramagnetic calculation of a (5, 5) SWCNT with a  $\text{Ni}_{\text{sub}}$  impurity every four unit cells. Comparing the band structure in Fig. 2.11a with the electronic structure of the  $\text{Ni}_{\text{sub}}$  impurity in flat graphene (lower curve in Fig. 2.7), we appreciate the effects of curvature. The degeneracy between  $d_{xz}$  and  $d_{yz}$  states is removed (x-axis taken along the tube axis and y-axis along the tangential direction at the Ni site).

The  $d_{yz}$  contribution is stabilized by several tenths of eV, and a quite flat band with strong  $d_{yz}$  character is found *pinned* at  $E_F$  close to the Brillouin-zone boundary. Under these conditions, the spin-compensated solution becomes unstable and a magnetic moment of  $0.48 \mu_B$  is developed. Figure 2.11b, c shows, respectively, the band structure for majority and minority spins. The exchange splitting of the  $d_{yz}$  level is  $\sim 0.4 \text{ eV}$  and the energy gain with respect to the paramagnetic solution is 32 meV.

In general, whenever a flat band with appreciable Ni  $3d$  character becomes partially filled, we can expect the appearance of a spin moment. The population of such an impurity level will take place at the expense of the simultaneous depopulation of some of the delocalized carbon  $2p_z$  levels within the host structure. For this reason, the development of a spin moment is more likely for  $\text{Ni}_{\text{sub}}$  impurities in metallic structures like the armchair tubes. The crucial role of the host states also explains the delocalized character of the magnetization density depicted in Fig. 2.10b. However, it is important to stress that the spin moment associated with a  $\text{Ni}_{\text{sub}}$  impurity in SWCNTs forms driven by the local curvature of the carbon layer, because the energy position of one of the impurity levels shifts downwards until it crosses  $E_F$ . A schematic representation of this phenomenon is shown in Fig. 2.12 where we also emphasize the similarities between the levels of the  $\text{Ni}_{\text{sub}}$  defect and those of the unreconstructed carbon vacancy. Notice the similarities with the effects of uniaxial strain described in the previous section. At large tube diameters, the limit of flat graphene with zero spin moment (see Sect. 2.2) is recovered.

For semiconducting tubes, the situation is somewhat different. The  $d_{xz}$ - and  $d_{yz}$ -like levels remain unoccupied unless their energies are shifted by a larger amount that pushes one of them below the top of the valence band. If the tube has a large enough gap, the spin moment is zero irrespective of the tube diameter. We have explicitly checked that a zero spin moment is obtained for (8, 0) and (10, 0) semiconducting tubes for Ni concentrations ranging from 1.5 to 0.5%. The different magnetic behavior of  $\text{Ni}_{\text{sub}}$  impurities depending on the metallic and semiconducting character of the host structure provides a route to experimentally identify metallic armchair tubes.

## 2.4 Magnetic Coupling Between Impurities

In previous sections, we have considered the formation of local moments associated with defects in carbon nanostructures, as well as the use of mechanical deformations to tune the sizes of such local moments. Here, we present calculations of the exchange couplings between the local moments in neighboring defects. This is a necessary step to elucidate whether it is possible to induce magnetic order in these materials, which is crucial in the application of carbon-based nanostructures in spintronics. We focus on defects that can be mapped onto the simple model provided by the fictitious  $\pi$ -vacancy. According to the results presented in Sect. 2.2.4, Co substitutional impurities belong to this class of defects. In this section we present another type of impurities that behave according to the same analogy: molecules attached to graphene and carbon nanotubes through weakly polar covalent bonds.

A  $\pi$ -vacancy corresponds to a missing  $p_z$  orbital in a graphene plane described using a  $\pi$ -tight-binding model. The magnetic properties of the  $\pi$ -vacancies have been extensively studied (Castro Neto et al. 2009; Palacios et al. 2008). Among other interesting properties, the magnetism of the  $\pi$ -vacancy model reflects faithfully the bipartite character of the graphene lattice. For example, the total spin of the system

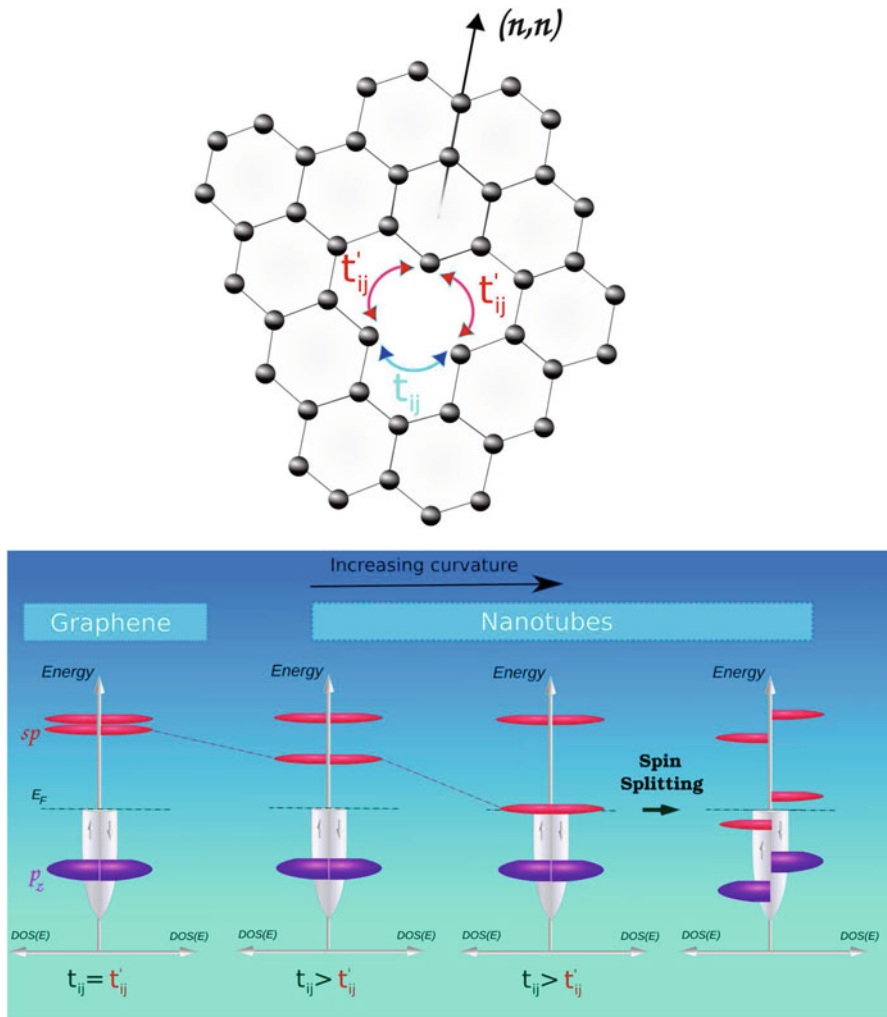


**Fig. 2.12** Effect of curvature (anisotropic strain) on Ni<sub>sub</sub> in  $(n,n)$  tubes. *Upper panel:* illustration of the dominant hoppings at the defect site in graphene. The equivalence between the electronic structure of a Ni<sub>sub</sub> impurity and a carbon vacancy is stressed here. The carbon sheet is rolled around the  $(n, 0)$  direction in order to form the armchair tubes. *Lower panel:* scheme of the main Ni<sub>sub</sub> impurity energy levels as a function of curvature. One of the impurity levels with antibonding C  $2sp$ -Ni  $3d$  character is shifted downwards and, for large enough curvatures, becomes partially populated and spin-polarized (Adapted from Santos et al. 2008)

is  $S = |N_A - N_B|$ , where  $N_A$  and  $N_B$  are the number of  $\pi$ -vacancies in each of the graphene sublattices. This behavior can be traced back to Lieb's theorem for a half-filled Hubbard model in a bipartite lattice (Lieb 1989). In the following, we will see that the calculated data for Co substitutionals and covalently chemisorbed molecules indeed follow the predictions of Lieb's theorem. In addition, we analyze in detail the spatial decay of the exchange couplings.



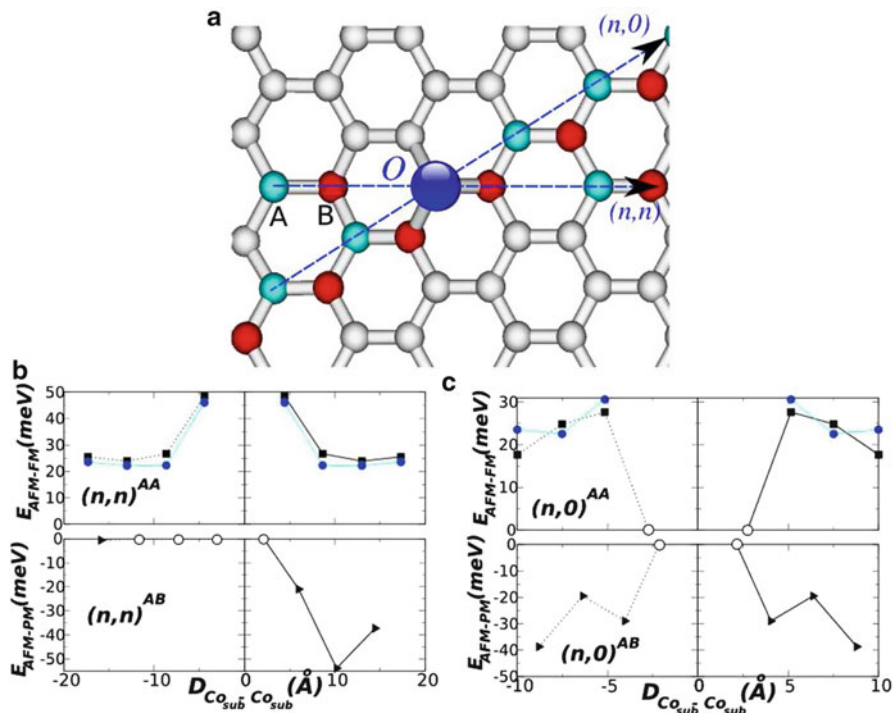


**Fig. 2.13** (a) Schematic representation of the geometry used to calculate the relative stability of ferromagnetic (*FM*), antiferromagnetic (*AFM*), and spin-compensated (*PAR*) solutions as a function of the positions of two  $Co_{sub}$  impurities. Sublattices *A* and *B* are indicated by *blue* and *red* circles, respectively. One of the impurities is fixed at a central *A*-type site, whereas the other is moved along the  $(n, n)$  and  $(n, 0)$  directions. Panels (b, c) show the results of the energy differences for  $(n, n)$  and  $(n, 0)$  configurations, respectively. *Solid squares* at positive values indicate *FM* spin alignments, while *solid triangles* at negative values correspond to *AFM* ones. The *empty circles* represent spin-compensated solutions and the *full circles* for *AA* substitutions correspond to a fit of a Heisenberg model (see text for details) (Adapted from Santos et al. 2010b)

### 2.4.1 Magnetic Couplings Between Co Substitutional Impurities in Graphene

Here, we consider the magnetic couplings between  $Co_{sub}$  defects. For this purpose we perform calculations using a large  $8 \times 8$  supercell with two  $Co_{sub}$  impurities. We calculate the energy difference between spin alignments as a function of the relative position of the defects. Figure 2.13 shows the results along with a schematic representation of our notation. Positive values indicate ferromagnetic (*FM*) spin alignment, while negative values are antiferromagnetic (*AFM*) ones. Several observations from spin couplings in Fig. 2.13 can be made: (a) when the impurities are located in the same sublattice (*AA* systems), the *FM* configuration is more stable than the *AFM* one; (b) if the *Co* atoms are in opposite sublattices

( $AB$  systems), it is very difficult to reach a FM solution,<sup>1</sup> instead the system finds either a spin-compensated (PAR) or an AFM solution; and (c) at short distances ( $<3.0 \text{ \AA}$ ), the systems always converge to spin-compensated solutions.

The FM cases of Fig. 2.13 always have total spin magnetization about  $2.00 \mu_B$ . The spin population on every Co atom remains almost constant  $\sim 0.50 \mu_B$ , and it is  $\sim 0.30 \mu_B$  on the three C nearest-neighbors. In other cases the total spin is zero. Thus, the total spin moment of the system follows the equation  $S = |N_{\text{sub}}^A - N_{\text{sub}}^B|$ , where  $N_{\text{sub}}^{A(B)}$  is the number of  $\text{Co}_{\text{sub}}$  defects in the  $A(B)$  sublattices. Our total moment is consistent with Lieb's theorem for bipartite lattices (Lieb 1989). This finding supports the analogy, presented in Sect. 2.2.4, between the electronic structure of  $\text{Co}_{\text{sub}}$  defects and single vacancies in a simplified  $\pi$ -tight-binding description of graphene.

Some selected configurations have their spin magnetization densities plotted in Fig. 2.14. Although the spin is quite localized on the Co atom and the neighboring C atoms, part of the magnetization density is delocalized with alternated signs in both graphene sublattices. The triangular spin patterns reflect the threefold symmetry of the layer with different orientations for  $A$  and  $B$  substitutions. This explains the anisotropic  $AB$  interaction along the  $(n, n)$  direction seen in Fig. 2.13b: the energy difference between AFM and PAR solutions for  $(n, n)^{AB}$  configurations strongly depends on the relative position of the impurities, showing such a directionality. Similar patterns have already been observed experimentally (Kelly and Halas 1998; Mizes and Foster 1989; Rutter et al. 2007; Ruffieux et al. 2000) for point defects in graphene using STM techniques and theoretically discussed for  $\pi$ -vacancies (Yazyev 2008b; Palacios et al. 2008; Pereira et al. 2008). For  $\text{Co}_{\text{sub}}$ , similar STM experiments should display the topology of the spin densities given in Fig. 2.14.

We can also investigate the magnetic interactions within the framework of a classical Heisenberg model:

$$H = \sum_{i < j} J_{AA/AB}(\mathbf{r}_{ij}) \mathbf{S}_i \mathbf{S}_j \quad (2.1)$$

where  $\mathbf{S}_i$  is the local moment for a  $\text{Co}_{\text{sub}}$  impurity at site  $i$ . The angular dependence of the exchange  $J(\mathbf{r}_{ij})$  is taken from an analytical RKKY coupling as given in Saremi (2008). We fit the exponent for the distance decay to our *ab initio* results. The exchange interaction for  $AA$  systems can be fitted with a  $|r_{ij}|^{-2.43}$  distance dependence (see the full circles in Fig. 2.13b, c). This distance dependence is in reasonable agreement with the  $|r_{ij}|^{-3}$  behavior obtained with analytical models for substitutional defects and voids (Saremi 2008; Vozmediano et al. 2005). In the

---

<sup>1</sup>When we could stabilize a FM solution, it lies at higher energy, around 0.2 eV above the PAR one.

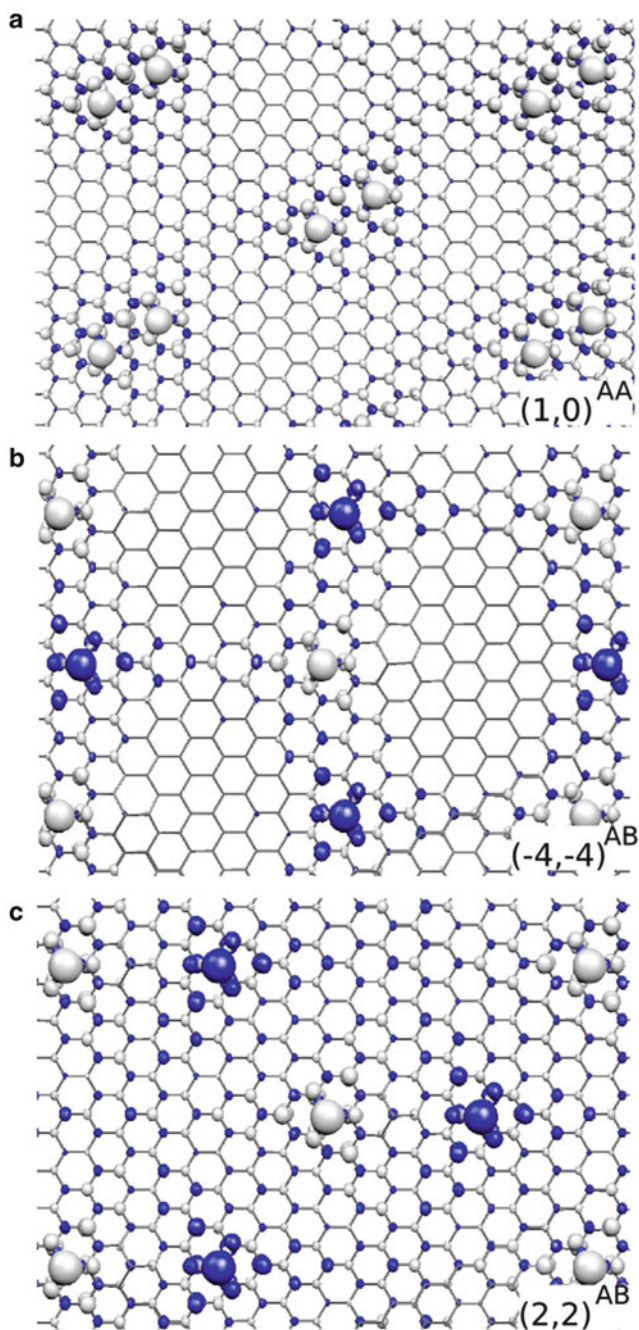


**Fig. 2.14** (a) Spin densities for configurations (a)  $(1,0)^{AA}$ , (b)  $(-4,-4)^{AB}$ , and (c)  $(2,2)^{AB}$  (see Fig. 2.13a for the nomenclature). Positive and negative spin densities are indicated by light (*gray*) and dark (*blue*) isosurfaces corresponding to  $\pm 0.001 e^-/\text{Bohr}^3$ , respectively (Adapted from Santos et al. 2010b)

case of  $AB$  systems, a simple RKKY-like treatment fails to describe accurately the interactions, at least for the short distances between defects considered in our calculations.

We next explain how PAR solutions appear in Fig. 2.13. The PAR solutions are stable because defect states in neighboring impurities interact strongly for  $AB$  systems. This interaction opens an appreciable *bonding–antibonding* gap in the  $p_z$  defect band.<sup>2</sup> For  $AA$  systems, however, the bipartite character of the graphene lattice makes the interaction between the defects much smaller. This explains why  $AA$  configurations show a local spin polarization. Even for  $AA$  configurations, when the impurities are very close, nonmagnetic solutions are stabilized because a larger defect–defect interaction opens a large gap. It is interesting to point out that similar behaviors have been observed for vacancies described within a  $\pi$ -tight-binding model (see Sect. 1.6.1) (Yazyev 2008b; Kumazaki and Hirashima 2007; Palacios et al. 2008).

#### 2.4.2 Covalent Functionalization Induces Magnetism: Universal Properties

In this section we show that, apart from playing an increasingly important role in technological applications, chemical functionalization can be also used to induce spin moments in carbon nanostructures. Here, we focus on SWCNT and demonstrate that, when a single C–C bond is established on the carbon surface by covalent functionalization, a spin moment is induced into the system. This moment has a universal value of  $1.0 \mu_B$  and is independent of the particular adsorbate. In our recent work (Santos et al. 2011), we showed that this effect occurs for a wide class of organic and inorganic molecules of different biological and chemical activity (e.g., alkanes, polymers, diazonium salts, aryl and alkyl radicals, nucleobases, amido and amino groups, acids). Furthermore, we have recently found that a similar universal behavior is obtained for covalent functionalization of graphene (Santos et al. 2012b). We have also found that, either for metallic and semiconducting SWCNTs or for graphene, only when neighboring adsorbates are located at the same sublattice, a spin moment is developed. For metallic tubes, and graphene, the local moments align ferromagnetically, while for semiconducting tubes we have almost degenerate FM and AFM spin solutions (Santos et al. 2011, 2012b).

To understand the origin of the spin moment induced when a covalent bond is formed in the tube wall, we analyze the total spin-polarized density of states (t-DOS) when different adsorbates are attached to metallic and semiconducting

---

<sup>2</sup>For the  $AB$  systems, we find bonding–antibonding gaps in the impurity bands ranging from 0.3 to 0.9 eV for the  $(1, 1)^{AB}$  and the  $(-1, -1)^{AB}$  configuration, respectively. These values are similar to the  $\sim 0.5$  eV spin splitting of the  $\text{Co}_{\text{sub}}$  defect. In fact, all those  $AB$  systems with gaps larger than 0.4 eV converge to PAR solutions.

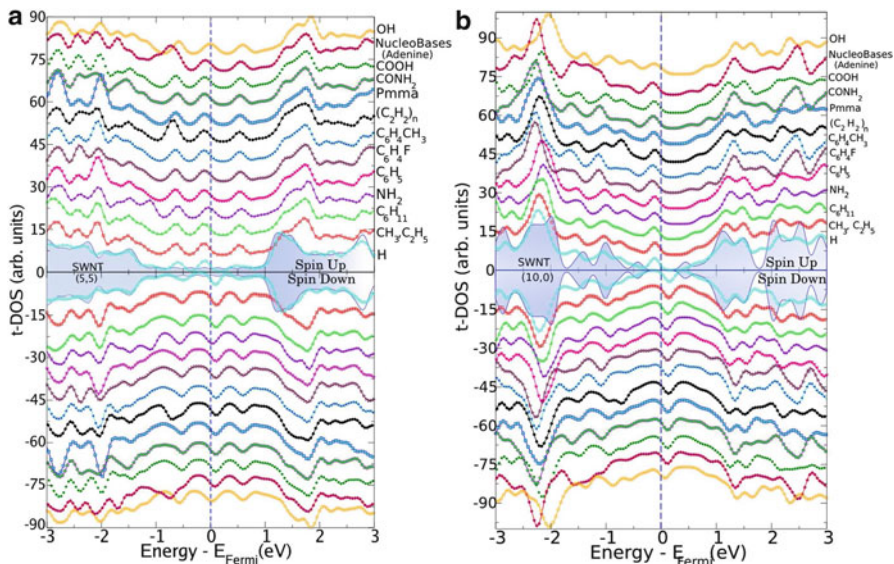


**Fig. 2.15** Total spin-polarized density of states (t-DOS) for (a) (5, 5) and (b) (10, 0) SWCNTs with a single adsorbate of different types chemisorbed on top of one carbon atom in the supercell. Positive and negative t-DOS correspond to spin up and spin down, respectively. The t-DOS for pristine (5, 5) and (10, 0) SWCNTs is also shown for comparison. For clarity, the curves in panel (a, b) have been shifted and smoothed with a Lorentzian broadening of 0.12 eV. Fermi energy is marked by the dashed lines and is set to zero in both panels

tubes (see Fig. 2.16 for the structure of some of these systems). Figure 2.15 presents results for (a) (5, 5) and (b) (10, 0) SWCNTs. We consider first the well-known case of the adsorption of atomic hydrogen. In both cases, when a single H atom chemisorbs on top of a C atom, a defect state appears pinned at  $E_F$  with full-spin polarization. This state is mainly composed of the  $p_z$  orbitals at the nearest C neighbors of the defect site, with almost no contribution from the adsorbate. A detailed Mulliken analysis of this  $p_z$ -defect state assigns a contribution of the adsorbate of about  $\sim 1\%$ . Thus, the adsorbate has a primary role in creating the bond with the nanotube and the associated defect level, but it does not appreciably contribute to the spin moment. More complex adsorbates, notwithstanding their biological and chemical activity (e.g., alkanes, polymers, diazonium salts, aryl and alkyl radicals, nucleobases, amido and amino groups, acids), show a similar behavior. This is observed in the t-DOS curves corresponding to other adsorbates in metallic (5, 5) and semiconducting (10, 0) SWCNTs as shown in Fig. 2.15a, b, respectively. Several common points are worth mentioning: (a) all molecules induce a spin moment of  $1.0\mu_B$  localized at the carbon surface; (b) the origin of the spin polarization corresponds to a  $p_z$ -defect state with a character and a spatial distribution similar to those of the state appearing at  $E_F$  for a  $\pi$ -vacancy defect; and (c) the t-DOS around  $E_F$  follows the same pattern in all cases. This match

demonstrates that the spin moment induced by covalent functionalization is largely independent of the particular type of adsorbate. These results also demonstrate the complete analogy between a single C–H bond and more complex adsorbates linked to graphene through a single C–C bond (or other weakly polar covalent bonds) (Santos et al. 2011, 2012b). Such similarity is not obvious and could not be easily anticipated.

Next, we study the spin polarization texture induced by the adsorbates on the carbon nanotube wall. The analysis of local spin moments for all the adsorbates assigns general trends to both types, metallic and semiconducting, of SWCNTs. The C atoms that participate directly in the bond formation, at either the molecule or the surface, show a local spin moment smaller than  $\sim 0.10 \mu_B$ . However, the wall carbon atoms contribute with  $0.40 \mu_B$  in the three first C nearest-neighbors,  $-0.10 \mu_B$  in the next nearest-neighbors, and  $0.20 \mu_B$  in the third neighbors. The adsorbate removes a  $p_z$  electron from the adsorption site and leaves the  $p_z$  states of the nearest carbon neighbors uncoordinated. This gives rise to a defect state localized in the carbon layer, reminiscent of that of a vacancy in a  $\pi$ -tight-binding model of graphenic nanostructures. The carbon spins polarize parallel (antiparallel) with respect to the C atom that binds to the surface when sitting in the opposite (same) sublattice. Figure 2.16 shows the magnetization density in semiconducting (10, 0) and metallic (5, 5) SWCNTs for several molecules: (a) Pmma polymer chain (Haggenmueller et al. 2000), (b) adenine group nucleobase (Singh et al. 2009), (c)  $C_6H_4F$  salt (Bahr et al. 2001), and (d)  $CH_3$  molecule (Saini et al. 2002). The spin density in the metallic (5, 5) (Fig. 2.16c, d) is more spread over the whole surface than in the semiconducting (10, 0) (Fig. 2.16a, b). Thus, the electronic character of the nanotube wall plays a role in determining the localization of the defect states and, as will be seen below, in mediating the interaction between adsorbates.

Now we deal with the relative stability of the different magnetic solutions when two molecules are simultaneously adsorbed on the walls of CNTs. Due to the universal character of the magnetism associated with covalent functionalization of SWCNTs and in order to alleviate the computational effort, we have considered here hydrogen atoms. However, we have explicitly checked for some configurations for the case of SWCNTs, and for flat graphene (Santos et al. 2012b), that identical results are obtained when using  $CH_3$  instead of H. For the metallic (5, 5) and semiconducting (7, 0) single-walled CNTs, we calculate the variation of the total energy for several spin alignments as a function of the distance between the adsorbates. The relative positions of the adatoms along the tube are schematically shown in Fig. 2.17a, c. One H is sited at the origin and the other sites in different positions along the tube axis. Several observations can be first made on the stability when two adsorbates are located at the same sublattice (AA configurations). In the metallic (5, 5), the FM configuration is most stable than the nonmagnetic one (PAR). The energy difference between these two spin solutions along the tube axis oscillates, and no AFM solution could be stabilized at all. In the semiconducting (7, 0), the FM and AFM solutions are almost degenerate, with a small energy difference (exchange coupling).

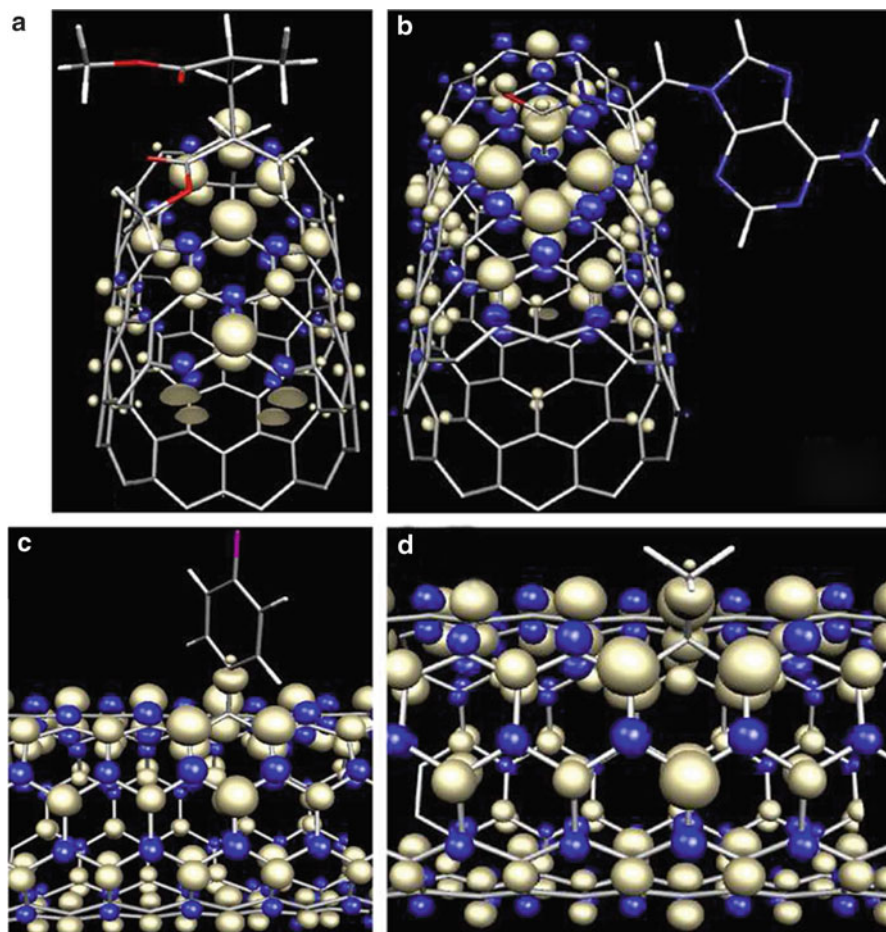


**Fig. 2.16** Isosurface of the magnetization density induced by some adsorbates at the SWCNT surface: (a) Pmma and (b) adenine derivative in a (10, 0) tube and (c)  $C_6H_4F$  and (d)  $CH_3$  in a (5, 5) tube. Majority and minority spin densities correspond respectively to light and dark surfaces, which alternate on the honeycomb lattice with a long decaying order in all cases. The cutoff is at  $\pm 0.013 e^- / bohr^3$  (Adapted from Santos et al. 2011)

If the two molecules are now located at different sublattices ( $AB$  configurations), we were not able to stabilize any magnetic solution for both nanotubes. Instead the systems are more stable without magnetic polarization. This behavior for adsorbates at opposite sublattices is related to the interaction between the defect levels. As already pointed out for Co substitutionals, while for  $AA$  configurations the interaction is negligible, for  $AB$  ones this interaction opens a bonding–antibonding gap around  $E_F$  in the  $p_z$  defect band and, thus, contributes to the stabilization

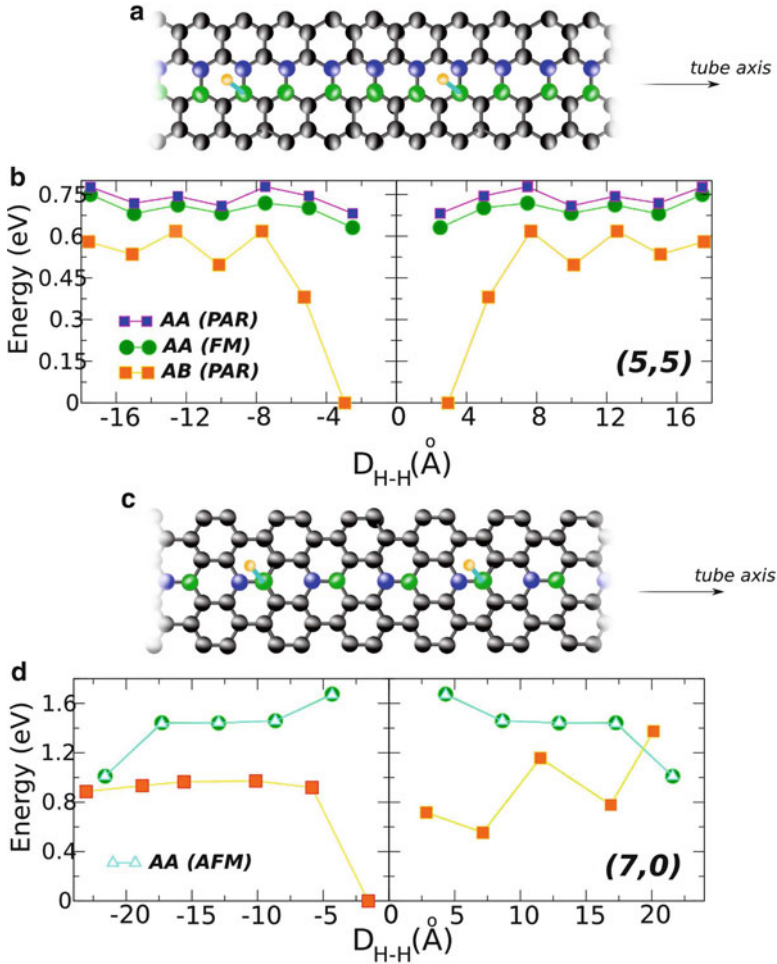


**Fig. 2.17** Variation of total energy as a function of the relative adsorption positions of two H atoms on (a) a (5, 5) and (c) a (7, 0) SWCNT. for different magnetic solutions. One of the adsorbates moves parallel to the axis of the tube, while the other remains at the origin. In (b, d), the light (yellow) and dark (blue) squares correspond to PAR spin solutions at AB and AA sublattices, respectively; the circles and triangles indicate the FM and AFM solutions, respectively, at the same sublattice (Adapted from Santos et al. 2011)

of PAR solutions. If the gap is larger than the spin splitting of the majority and minority spin defect bands, the system will be nonmagnetic (see Sect. 2.4.1). In fact, our detailed analysis of the band structure fully confirmed such an explanation. However, it is worth noting that AB adsorption seems to be always more stable in our calculations. This indicates that if the adsorption takes place at random sites, the magnetic solutions will only be stable for low-density functionalization.



## 2.5 Conclusions

In this chapter, we have reviewed the structural, electronic, and magnetic properties of two types of defects, substitutional metal impurities and  $sp^3$ -type covalent functionalization, in carbon nanostructures. We have focused on their role to induce and control magnetism in graphene and carbon nanotubes. Density functional theory was the main tool used to compute the properties of the studied systems. We also developed simple models to understand the observed trends. For instance, substitutional dopants in graphene were understood in terms of the hybridization of the  $d$  states of the metal atoms with those of an unreconstructed carbon vacancy. The main ingredients of the model are the assumption of a threefold symmetric bonding configuration and the approximate knowledge of the relative energy positions of the levels of the carbon monovacancy and the  $d$  shell of the metal impurity as we move along the transition series. With this model, we understood the variations of the electronic structure, the size and localization of the spin moment, and the binding energy of transition, noble metals and Zn substitutional impurities in graphene (Santos et al. 2010a). Our model also allowed us to draw an analogy between substitutionals of the late transition metals and the symmetric  $D_{3h}$  carbon vacancy.

As a result of our analysis, a particularly powerful analogy was established between the substitutional Co impurity and the fictitious  $\pi$ -vacancy in graphene (Santos et al. 2010b). The  $\pi$ -vacancy corresponds to a missing  $p_z$  orbital in a simple description of graphene using a  $\pi$ -tight-binding model. The magnetic properties of the  $\pi$ -vacancies have been extensively studied. This analogy brings our results for the magnetism of  $\text{Co}_{\text{sub}}$  defects into contact with the predictions of Lieb's theorem for a half-filled Hubbard model in a bipartite lattice. We found that, according to Lieb's theorem, the total spin of the system is  $S=|N_A - N_B|$ , where  $N_A$  and  $N_B$  are the number of substitutions performed in each of the graphene sublattices. Thus, the couplings between local moments for  $AA$  substitutions are ferromagnetic and predominantly antiferromagnetic for  $AB$  substitutions. We have also used a simple RKKY model to extract the distance decay of the couplings.

Adsorbates attached to graphene or SWCNTs through covalent bonds, particularly if the bonds are weakly polar, constitute another example of defects whose magnetism is analogous to that of the  $\pi$ -vacancy. We have analyzed the magnetic properties induced by such a covalent functionalization using many types of adsorbates: polymers, diazonium salts, aryl and alkyl radicals, nucleobases, amide and amine groups, sugar, and organic acids, for SWCNTs (Santos et al. 2011) and graphene (Santos et al. 2012b). A universal spin moment of  $1.00 \mu_B$  is induced on the carbon surface when a single C-C bond is formed between an adsorbate and the graphenic layer. In metallic carbon nanotubes and graphene, molecules chemisorbed at the same sublattice ( $AA$  adsorption) have their local moments aligned ferromagnetically. In semiconducting nanotubes, FM and AFM solutions are almost degenerate even for  $AA$  adsorption. For two molecules in

different sublattices ( $AB$  adsorption), we could not stabilize any magnetic solution, and the system is more stable without a local spin moment.

We have also explored the possibility to control the magnetism induced by substitutional impurities using mechanical deformations. We have found that the spin moment of substitutionally Ni-doped graphene can be controlled by applying mechanical deformations that break the hexagonal symmetry of the layer, like curvature or uniaxial strain. Although  $\text{Ni}_{\text{sub}}$  impurities are nonmagnetic in flat graphene, we have observed that stretching the layer by a few percents along different crystalline directions is enough to turn the nonmagnetic ground state of Ni atoms embedded in graphene to a magnetic state (Santos et al. 2012a). The spin moment slowly increases as a function of the applied strain. However, at a critical strain value of 6.8 %, a sharp transition to high-spin ( $\sim 2 \mu_B$ ) state is observed. This transition is independent of the orientation of the applied strain. A detailed analysis indicates that this strain-tunable spin moment is the result of changes of the positions of three defect levels around Fermi energy which are antibonding combinations of the Ni  $3d$  states and the  $2p_z$  and  $2sp^2$  orbitals of the neighboring C atoms. This tunable magnetism observed in  $\text{Ni}_{\text{sub}}$  defects via strain control may play an interesting role in flexible spintronics devices.

Our calculations show that  $\text{Ni}_{\text{sub}}$  magnetism can also be switched on by applying curvature (Santos et al. 2008). For metallic carbon nanotubes, the curvature of the carbon layer around the defect can drive the transition of the  $\text{Ni}_{\text{sub}}$  impurities to a magnetic state. For semiconducting tubes, the  $\text{Ni}_{\text{sub}}$  impurities remain nonmagnetic irrespective of the tube diameter. We have analyzed in detail the origin and distribution of the magnetic moment. We found that the spin moment associated with  $\text{Ni}_{\text{sub}}$  impurities forms accompanied by the simultaneous polarization of delocalized electronic states in the carbon layer. Furthermore, the spin moment of  $\text{Ni}_{\text{sub}}$  is a signature of the metallicity of the structure: only metallic tubes develop a moment that depends on the tube diameter and Ni concentration.

Our work predicts a complex magnetic behavior for transition-metal impurities in carbon nanotubes and graphene. This investigation is highly relevant in the interpretation of experimental results since it has been proposed that appreciable amounts of metal atoms could be incorporated into the carbon network, forming this type of substitutional defects in the course of synthesis, and are very difficult to eliminate afterwards. Our results also indicate that covalent functionalization provides a powerful route to tune the magnetism of graphene and carbon nanostructures. This is particularly attractive due to the recent successful synthesis of different graphene derivatives using surface chemical routes (Cai et al. 2010; Treier et al. 2010). Thus, the synthesis of carbon nanostructures with functional groups at predefined positions, for example, starting from previously functionalized monomers, seems plausible nowadays. According to our results, this could be applied to synthesize magnetic derivatives of graphene that behave according to well-studied theoretical models like the  $\pi$ -vacancy.

**Acknowledgments** This work has been partially supported by the Spanish MINECO under Grant No. FIS2010-19609-C02-02, the Basque Departamento de Educación and the UPV/EHU (Grant No. IT-366-07), and the Nanoiker project (Grant No. IE11-304) under the ETORTEK program funded by the Basque Research Department of Industry and the Diputación Foral de Gipuzkoa.

## References

- Amara H, Latil S, Meunier V, Lambin PH, Charlier JC (2007) *Phys Rev B* 76:115423
- Artacho E, Sánchez-Portal D, Ordejón P, García A, Soler JM (1999) *Phys Status Solidi B* 215: 809–817
- Bahr JL, Yang J, Kosynkin DV, Bronikowski MJ, Smalley RE, Tour JM (2001) *J Am Chem Soc* 123:6536
- Banhart F, Charlier JC, Ajayan PM (2000) *Phys Rev Lett* 84:686
- Blöchl PE (1994) *Phys Rev B* 50:17953
- Brey L, Fertig HA, Das Sarma S (2007) *Phys Rev B* 99:116802
- Cai J, Ruffieux P, Jaafar R, Bieri M, Braun T, Blakenburg S, Muoth M, Seitsonen AP, Saleh M, Feng X, Müllen K, Fasel R (2010) *Nature* 466:470
- Castro Neto AH, Guinea F, Peres NMR, Novoselov KS, Geim AK (2009) *Rev Mod Phys* 1:109
- Chen JH, Li L, Cullen WG, Williams ED, Fuhrer MS (2010) *Nat Phys* 7:535
- Dresselhaus MS, Dresselhaus G, Avouris P (2001) *Carbon nanotubes: synthesis, structure, properties, and applications*. Springer, Berlin
- Gan Y, Sun L, Banhart F (2008) *Small* 4:587
- Geim AK, Novoselov KS (2007) *Nat Mater* 6:183
- Guinea F, Katsnelson MI, Geim AK (2010) *Nat Phys* 6:30
- Haggenmueller R, Gommans HH, Rinzler AG, Fischer JE (2000) *Chem Phys Lett* 330:219
- Huang B, Yu JJ, Wei SH (2011) *Phys Rev B* 84:075415
- Hueso LE, Pruneda JM, Ferrari V, Burnell G, Valdes-Herrera JP, Simons BD, Littlewood PB, Artacho E, Fert A, Mathur ND (2008) *Nature* 445:410
- Kelly KF, Halas NJ (1998) *Surf Sci* 416:L1085
- Kim KS, Zhao Y, Jang H, Lee SY, Kim JM, Kim KS, Ahn JH, Kim P, Choi JY, Hong BH (2009) *Nature* 457:706
- Kirwan DF, Rocha CG, Costa AT, Ferreira MS (2008) *Phys Rev B* 77:085432
- Krasheninnikov AV, Lehtinen PO, Foster AS, Pyykkö P, Nieminen RM (2009) *Phys Rev Lett* 102:126807
- Kresse G, Furthmüller J (1996) *Phys Rev B* 54:11169
- Kresse G, Hafner J (1993) *Phys Rev B* 47:558
- Kumazaki H, Hirashima DS (2007) *J Phys Soc Jpn* 76:064713
- Kumazaki H, Hirashima DS (2008) *Low Temp Phys* 34:805
- Lehtinen PO, Foster AS, Ayuela A, Krasheninnikov A, Nordlund K, Nieminen RM (2003) *Phys Rev Lett* 91:017202
- Lieb EH (1989) *Phys Rev Lett* 62:1201
- Mananes A, Duque F, Ayuela A, Lopez MJ, Alonso JA (2008) *Phys Rev B* 78:035432
- Mizes HA, Foster JS (1989) *Science* 244:559
- Mohiuddin TMG, Lombardo A, Nair RR, Bonetti A, Savini G, Jalil R, Bonini N, Basko DM, Galiotis C, Marzari N, Novoselov KS, Geim AK, Ferrari AC (2009) *Phys Rev B* 79:205433
- Novoselov KS, Geim AK, Morozov SV, Jiang D, Zhang Y, Dubonos SV, Grigorieva IV, Firsov AA (2004) *Science* 306:666

- Novoselov KS, Geim AK, Morozov SV, Jiang D, Katsnelson MI, Grigorieva IV, Dubonos SV, Firsov AA (2005) *Nature* 438:197
- Palacios JJ, Fernandez-Rossier J, Brey L (2008) *Phys Rev B* 77:195428
- Pereira VM, Castro Neto AH (2009) *Phys Rev Lett* 103:046801
- Pereira VM, Lopes Santos JMB, Castro Neto AH (2008) *Phys Rev B* 77:115109
- Rodriguez-Manzo JA, Banhart F (2009) *Nano Lett* 9:2285
- Rodriguez-Manzo JA, Cretu O, Banhart F (2010) *ACS Nano* 4:3422
- Ruffieux P, Groning O, Schwaller P, Schlapbach L, Groning P (2000) *Phys Rev Lett* 84:4910
- Rutter GM, Crain JN, Guisinger NP, Li T, First PN, Stroscio JA (2007) *Science* 317:219
- Saini RK, Chiang IW, Peng H, Smalley RE, Billups WE, Hauge RH, Margrave JL (2002) *J Am Chem Soc* 125:3617
- Santos EJG, Ayuela A, Fagan SB, Filho JM, Azevedo DL, Filho AGS, Sánchez-Portal D (2008) *Phys Rev B* 78:195420
- Santos EJG, Ayuela A, Sánchez-Portal D (2010a) *New J Phys* 12:053012
- Santos EJG, Sánchez-Portal D, Ayuela A (2010b) *Phys Rev B* 81:125433
- Santos EJG, Sánchez-Portal D, Ayuela A (2011) *Appl Phys Lett* 99:062503
- Santos EJG, Ayuela A, Sánchez-Portal D (2012a) *J Phys Chem C* 116:1174
- Santos EJG, Ayuela A, Sánchez-Portal D (2012b) *New J Phys* 14:043022
- Santos EJG, Riikonen S, Sánchez-Portal D, Ayuela A (2012c) *J Phys Chem C* 116:7602
- Saremi S (2008) *Phys Rev B* 76:184430
- Singh P, Kumar J, Toma FM, Raya J, Prato M, Fabre B, Verma S, Bianco A (2009) *J Am Chem Soc* 131:13555
- Soler JM, Artacho E, Gale JD, Garcia A, Junquera J, Ordejón P, Sánchez-Portal D (2002) *J Phys Condens Matter* 14:2745
- Son Y-W, Cohen ML, Louie SG (2006) *Nature* 444:347
- Standley B, Bao W, Zhang H, Bruck J, Lau CN, Bockrath M (2008) *Nano Lett* 8:3345
- Tombros N, Jozsa C, Popinciuc M, Jonkman HT, van Wees BJ (2007) *Nature* 448:571
- Trauzettel B, Bulaev DV, Loss D, Burkard G (2007) *Nat Phys* 3:192
- Treier M, Pignedoli CA, Laino T, Rieger R, Müllen K, Passerone D, Fasel R (2010) *Nat Chem* 3:61
- Troullier N, Martins JL (1991) *Phys Rev B* 43:1993
- Ugeda MM, Brihuega I, Guinea F, Gomez-Rodriguez JM (2010) *Phys Rev Lett* 104:096804
- Ushiro M, Uno K, Fujikawa T, Sato Y, Tohji K, Watari F, Chun WJ, Koike Y, Asakura K (2006) *Phys Rev B* 73:144103
- Vozmediano MAH, Lopez-Sancho MP, Stauber T, Guinea F (2005) *Phys Rev B* 72:155121
- Yazyev OV (2008a) *Nano Lett* 8:1011
- Yazyev OV (2008b) *Phys Rev Lett* 101:037203
- Yazyev OV, Helm LH (2007) *Phys Rev B* 75:125408

# Chapter 3

## Structural Defects on the Electronic Transport Properties of Carbon-Based Nanostructures

Hui Zeng, Jun Zhao, Jianwei Wei, and Jean-Pierre Leburton

**Abstract** Carbon-based materials are expected to be used as the components of nanodevices in the future. The fabrication and characterization of carbon-based materials with unique electronic and transport properties in terms of atomic engineering at nanoscale have been experimentally realized. However, the occurrence of various defects is widely regarded to be inevitable during the chemically synthesized and lithographically patterned approaches. Moreover, scientist can now make use of electron or ion beams to tailor the atomic structure of low-dimensional material with high precision to obtain particular characteristics. Enormous experimental and theoretical works are dedicated to the understanding of the role of defects on nanomaterials, with special emphasis on carbon-based nanosystems. In this chapter, we report recent advances in the area and present multiscale modeling to investigate the influences of structural defects, including vacancy, substitutional doping, topological defects, Stone–Wales defects, as well as composite defects, on the electronic transport properties of carbon-based low-dimensional materials.

---

H. Zeng • J. Zhao (✉)

College of Physical Science and Technology, Yangtze University, Jingzhou,  
Hubei 434023, China

e-mail: [zenghui@yangtzeu.edu.cn](mailto:zenghui@yangtzeu.edu.cn); [zhaojun@yangtzeu.edu.cn](mailto:zhaojun@yangtzeu.edu.cn)

J. Wei

College of Optoelectronic Information, Chongqing Institute of Technology,  
Chongqing 400054, China

J.-P. Leburton

Beckman Institute, University of Illinois at Urbana-Champaign, Urbana,  
IL 61801, USA

e-mail: [jleburto@illinois.edu](mailto:jleburto@illinois.edu)

### 3.1 Introduction

We have made great achievements in silicon-based electronic devices that have been widely used in computing, communications, automation, and other applications, and the miniaturization of electronic devices is the remarkable characteristic to a large extent. However, the approach of conventional routes realized in the silicon-based devices will soon encounter challenges in fundamental scientific and technological limitations (Purewal et al. 2006). It is urgent for us to make an effort to develop alternative device technologies. Owing to the excellent electrical properties, carbon-based nanomaterials, such as one-dimensional (1-D) carbon nanotubes (CNT) (Iijima 1991) and two-dimensional (2-D) graphene layers (Novoselov et al. 2004), are viewed as the most promising materials to make next-generation electronic devices. Tremendous theoretical (Charlier et al. 2007; Castro Neto et al. 2009) and experimental investigations (Geim and Novoselov 2007) are devoted to explore the electronic structure, transport, as well as optoelectronic properties (Avouris 2010; Geim 2009; Ando 2005; Dresselhaus et al. 2010) and, even more important, to develop and design the carbon-based electronic functionalized as a key component of nanodevices in the future (Baughman et al. 2002; Avouris et al. 2007).

Carbon is the basis of life, and the carbon-based structures are shown to have a large number of different structures with large variety of physical properties owing to the flexibility of its bonding (Fig. 3.1). Moreover, the physical properties of the carbon-based system are dependent on the dimensionality of the structures to a great extent. With the development of the nanotechnology, carbon-based materials, in particular for the low-dimensional nanomaterials (Krasheninnikov and Banhart 2007), have attracted fundamental and technological interests. As for the zero-dimensional carbon material, fullerenes are molecules where carbon atoms are arranged spherically (Kroto et al. 1985), which are recognized by the Nobel Prize in chemistry in 1996. In 1991, Iijima has experimentally synthesized the carbon nanotube (CNT) and characterized its structure, symbolizing the formidable success in the synthesis and characterization of one-dimensional (1D) systems (Iijima 1991). Further, the single-walled carbon nanotubes (SWNTs) have been artificially fabricated in 1993 (Iijima and Ichihashi 1993), and their outstanding physical properties make them promising candidates for the ultimate miniaturization of electronic functions at the molecular level. Carbon nanotube can be geometrically viewed as the rolling of honeycomb lattice into a hollow cylinder along a given direction (Iijima and Ichihashi 1993). Interestingly, CNTs can be metallic or semiconducting, which are determined on the chirality of their electronic structure (Charlier et al. 2007). The novel electronic structures provide this 1-D nanomaterial great applications to build logic devices at the nanometer scale, as illustrated in many laboratories (Ouyang et al. 2002; Nicholas et al. 2008). Depending on the purposes and interests, and potential applications, CNTs can be regarded as either single molecules or quasi-one-dimensional crystals with translational periodicity along the tube axis. On the other hand, graphene, appearing as the thinnest known material in the universe, is the truly artificial two-dimensional nanomaterial, first time

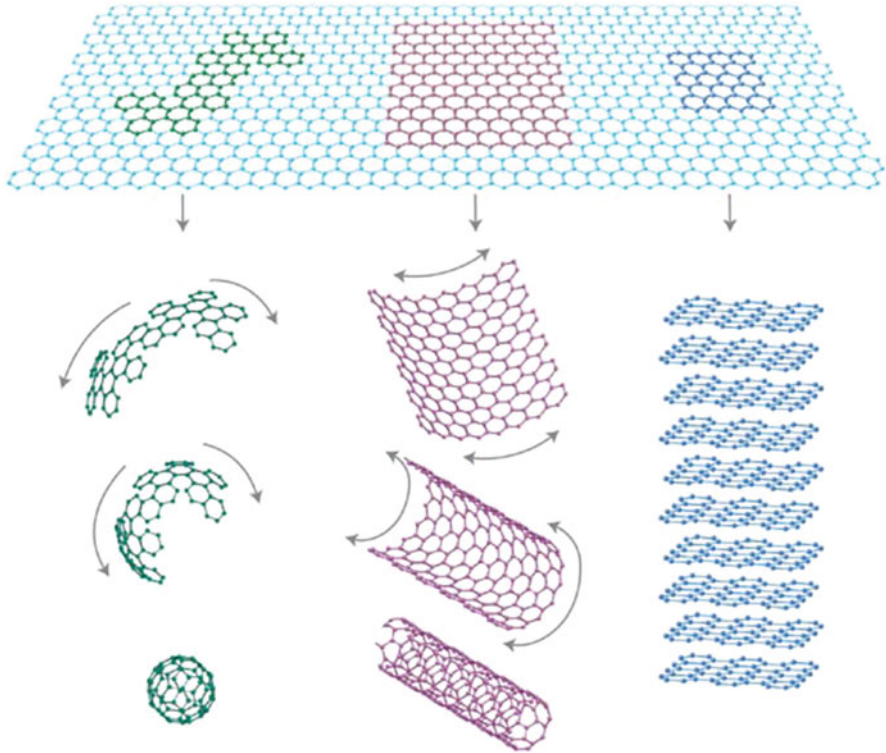


**Fig. 3.1** Structures of the different allotropes of carbon materials. Graphene (*top*) is the building blocks for carbon materials of all other dimensionalities. It can be wrapped up into 0-D buckyballs, rolled into 1-D nanotubes, or stacked into 3-D graphite (Reprinted by permission from Geim and Novoselov 2007. Copyright (2007) by Macmillan Publishers Ltd)

fabricated by means of mechanical exfoliation from graphite in 2004 (Novoselov et al. 2004), and therefore has attracted rapidly increasing amount of literatures on the fundamental research of various sort of applications (Geim 2009). Graphene is composed of a hexagonal monolayer network of  $sp^2$ -hybridized carbon atoms (Geim and Novoselov 2007). Owing to the unique electronic structure, graphene is considered as the most promising carbon-based nanomaterial on the designing and applications of nanodevice in the future (Geim 2009; Katsnelson 2007). Moreover, the available massive graphene body by means of large-scale synthesis routes, such as chemical vapor deposition (CVD) (Reina et al. 2009), epitaxial growth, bottom-up growth (Cai et al. 2010), and unzipping carbon nanotube (Kosynkin et al. 2009), allows us to synthesize large-scale counterpart for industrial manufacture and applications.

The electronic and transport properties of carbon-based low-dimensional samples with perfect atomic lattice are intriguing based on the theoretical predictions (Charlier et al. 2007; Castro Neto et al. 2009; Katsnelson 2007). Accordingly,

the presence of impurities and defects in crystals is normally considered as an undesirable phenomenon, and many routes are proposed to synthesize perfection sample (Cai et al. 2010; Terrones 2004; Jia et al. 2009; Li et al. 2009). As is known to all, the imperfections in lattices have great important influences on the mechanical, optical, electronic structure, and transport properties of the nanomaterial (Du and Smith 2011; Banhart 1999; Girit et al. 2009). Specifically, the structural defects, which are being widely recognized to be inevitable during material production processes, are usually thought to introduce disorder and deteriorate the performance of carbon-based devices (Avouris et al. 2007). However, experimental measurements on electron or ion irradiated carbon nanostructures explicitly demonstrate that the presence of various defects could have beneficial effects for some device applications (Banhart 1999), as this technology provides us the ability to tailor the atomic structure of nanomaterial with high precision to obtain dedicated properties (Banhart et al. 2011; Tapasztó et al. 2008; Gómez-Navarro et al. 2005).

Recently, considerable studies have confirmed the emergences of either native or physically introduced defects in the carbon-based nanomaterial. In addition, high-resolution transmission electron microscopy (HR-TEM) and scanning tunneling microscopy (STM) instruments allow us to obtain images of defective sample at atomic scale. The experimental results are presently incorporated with the computational simulations to simplify the predications on the properties of carbon nanomaterials, and this approach has already been convinced to achieve significant progress on the designing and fabrication of fullerene and carbon nanotubes. This article is concerned with the present theoretical advances in the rapidly carbon-related materials involving the impacts of different types of defects on the electronic transport properties (Stephan et al. 1994; Czerw et al. 2001; Wei et al. 2007a, b, 2008, 2009a; Biel et al. 2009a, b; Triozon et al. 2005; Choi et al. 2000; Zeng et al. 2010a, 2011a; Wang et al. 2010). In particular, the reconstruction around intrinsic defects can lead to outstanding properties and potential use for applications (Zeng et al. 2010b, 2011b, c; Rodriguez-Manzo and Banhart 2009; Kotakoski et al. 2006; Padilha et al. 2011). Meanwhile, the extrinsic defects, such as foreign atoms, can be artificially introduced in experiments by using irradiation of nanostructures (Wang et al. 2009; Guo et al. 2010; Bangert et al. 2010), are of particular importance for designing carbon-based devices with novel properties (Biel et al. 2009a; Wei et al. 2009b; Zeng et al. 2011d; Martins et al. 2007), and have also been discussed in this short chapter.

### 3.2 Types of Defects

In the absence of foreign atoms in three-dimensional crystal, the defects are referred to as intrinsic defects when the translational symmetry is broken. Conversely, the foreign atoms always referred to as impurity, are the extrinsic defects in the crystalline. In macroscopic crystalline materials, intrinsic defects have different dimensionalities. As a matter of fact, the honeycomb network of carbon-based



materials is not as perfect as usually assumed. Various structural defects, such as pentagons, heptagons, vacancies, substitutional impurities, and adatoms, have been theoretically proposed and indeed experimentally characterized in carbon-based materials, and furthermore, their existence can dramatically alter the electronic structure and properties of the host carbon materials. Defects can also be deliberately introduced into these low-dimensional materials for special purposes by means of irradiation (Banhart 1999), chemical treatments (Park and Ruoff 2009), and so on (Geim 2009). Point defects can occur in various forms, mainly including the vacancies and foreign impurity atoms, which are zero-dimensional defects. The atomic vacancies are intuitively understood as the absence of one or several carbon atoms in the hexagonal network of the nanomaterials. Removing the atoms normally results in the rearrangement of the perfect carbon network by saturation of highly reactive dangling bonds at undercoordinated carbon atoms because an atomic reconstruction around the vacancy is found to be more stable energetically as compared with the unreconstructed nanostructure. Extensive experimental efforts have been developed to investigate the kinetics of atomic-scale defect formation in the nanostructure, since defects play a decisive influence on their electronic, transport, and mechanical properties. High-resolution transmission electron microscopy (HR-TEM) combined with X-ray diffraction (XRD) studies has shown clear evidence of the presence of point defects such as monovacancy, interstitial vacancy defects, and pentagon–heptagon defects in carbon nanotubes (CNTs) and graphene. To date, various molecular dynamic theoretical methods, among which density functional theory (DFT) method is the most widely used, are developed to analyze and predict the most stable nanostructure of multiscale simulation. The presence of foreign impurity atoms will give rise to substitutional or interstitial defects in the nanostructure. These may be caused by thermal effects or may be artificially introduced by energetic particle radiation. Besides, foreign atoms can also be treated as zero-dimensional defects when they substitute individual atoms of the hexagonal network or are located on interstitial sites. Dopant atoms not only can dramatically modify the local electronic structure but also can inject charge into the electron system of carbon nanomaterials. It should be noted that modern logic devices are fundamentally based on p- or n-doped junctions. Therefore, the issue of chemical doping is of crucial importance to the utilization of carbon-related nanomaterial in electronic devices. A considerable number of research are dedicated to the comprehensive understanding of chemical doping mechanism on the electronic transport properties in order to exploit chemically functionalized devices. Although foreign atoms can extend to more dimensions in principle, the reduced dimensionality of the low-dimensional materials in turn effectively decreases the possibility of types of constructed defects. Vacancies, substitutional atoms, and interstitial atoms are all point defects. Generally, the presence of point defects has indistinctive impacts on the deformation of the carbon-related systems. In contrast, the dislocation is viewed as linear defects of one dimensionality. Moreover, the dislocation in CNTs could lead to the modification of their chirality, and such type of defects in graphene could induce remarkable reconstruction around the defects. The research on the influences of complex defects and the relationship

between the distribution and properties of nanomaterials are intriguing because the experimentally characterized defects are in common composed of more than one types. On the other hand, the structural defects in reality are not always located stationary, and furthermore, their migration can play an important role in the properties as well as the ultimate applications of the defective nanosystem. The migration processes of various defects in nanomaterials are now experimentally measured with high-resolution images by using scanning transmission electron microscope (STEM). The migration is basically determined by an activation barrier which is dependent on the defect types.

### **3.2.1 Stone–Wales Defects**

The Stone–Wales (SW) defects are one of the simplest defect types that occur in the carbon-related nanosystems, which do not relate to any vacancy or adatoms. The creation of SW defects can be theoretically understood by the  $90^\circ$  rotation of any C–C bond in the hexagonal network. The transformation occurs via an in-plane bond rotation by simultaneous movement of the two involved atoms. As a result, four hexagons are transformed into two pentagons and two heptagons, and no dangling bonds are introduced, as illustrated in Fig. 3.2. Such a topological defect can be introduced in terms of strain and its evidence is unambiguously identified in both the carbon nanotubes (Suenaga et al. 2007) and graphene (Hashimoto et al. 2004) nanomaterials recently. The transformation of SW defects in CNTs is approximately several eV, and this value is generally lower than that of the SW defects in graphene. When the transformation occurs via an in-plane bond rotation by simultaneous movement of the two involved atoms, the kinetic barrier is about 10 eV. The comparatively high transformation energy of the SW defect ensures a negligible concentration at equilibrium in nanosystems. However, SW defects are found to be stable at room temperature once the defects are induced under high temperature or under irradiation circumstance, which is attributed to incomplete annealing of the nanomaterial. The SW defect can be intentionally introduced along with heat treatment (Suenaga et al. 2007) or spatially created by electron and ion bombardment. Moreover, the theoretical works predict distribution as well as symmetry as an important even for the whole properties and behavior of nanosystems.

### **3.2.2 Monovacancy Defects**

Vacancy is the simplest and quite general defect in any material. The rise of missing lattice atom is always accompanied with the fabrication of nanomaterial sample. Vacancies in nanomaterial can be experimentally observed and visualized by using TEM and STM. Generally, the presence of large vacancy cluster in nanosystem

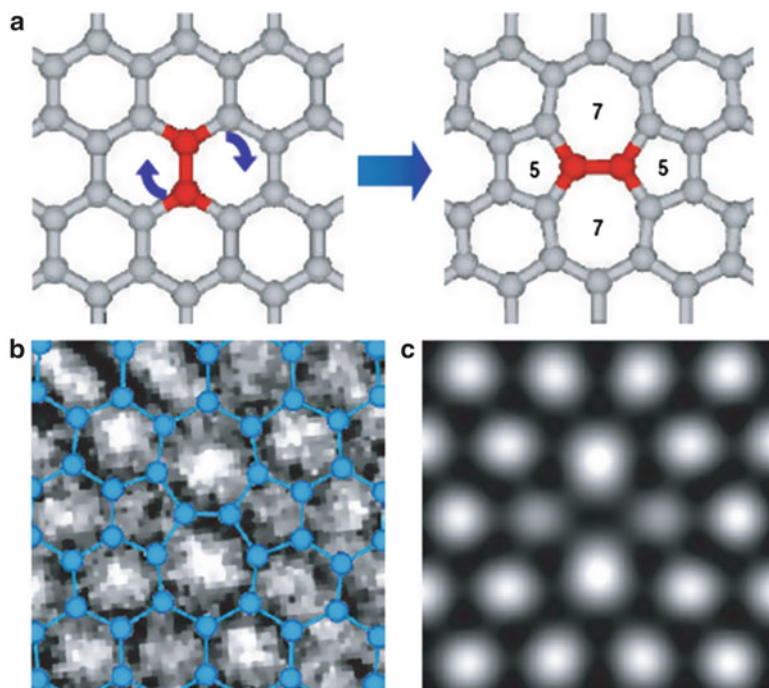


**Fig. 3.2** Formation and characterization of the Stone–Wales (SW) defects. (a) The SW transformation leading to the 5–7–7–5 defect, generated by  $90^\circ$  rotation of a C–C bond in a hexagonal network. (b) High-resolution transmission electron microscopy image (HR-TEM) obtained for the SW model. (c) Simulated HR-TEM image for the model shown in (b) (Reprinted with permission from Suenaga et al. 2007. Copyright (2007) by Macmillan Publishers Ltd)

often needs comparative higher energy impact engineering on the sample. To date, an immense amount of theoretical investigations has been concentrated on the influences of small vacancy clusters on the nanosystem. Of special interest is the study of monovacancy and divacancy defects. As for the monovacancy, removing one atom in the hexagonal lattices generally gives rise to a pentagon–enneagon pair as a result of the saturation of two of the three dangling bonds (DB) toward the missing atoms and leaves a so-called 5-1DB defects, as evidenced by the experimental image shown in Fig. 3.3. Eventually, one dangling bond (DB) always remains after the atomic reconstruction around the defects and due to the geometrical consideration. The DB could provide the chemically active site for adsorption, which can be used as catalysts for thermal dissociation of water. The orientations of the 5-1DB defect in CNTs can be different, which is determined not only by the location of removed atom but also by the chirality. In general, the defect orientation is defined as the angle made by the axis of defect with the horizontal direction. Moreover, the DB manifests as a protrusion under STM due to an increase in the local density of states (LDOS) at the Fermi energy. Obviously, the transformation energy is high owing to the presence of the undercoordinated carbon atom. Hence, the calculations

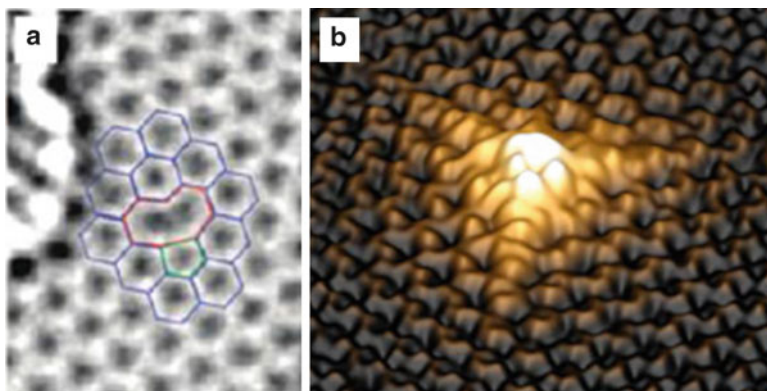


**Fig. 3.3** Single vacancy (5-1DB) defects (a) the image as shown in TEM (Meyer et al. 2008); (b) the experimental image of a single vacancy, exhibiting as a protrusion due to an increase in the local density of states at the dangling bond (Reprinted with permission from Ugeda et al. 2010. © 2010 The American Physical Society)

reveal that the transformation of monovacancy is larger than that in the divacancy. As for the migration of monovacancy in graphene, the calculated migration barrier is approximately 1.3 eV (El-Barbary et al. 2003). It was worth to mention that carbon-related nanostructures can reconstruct under electron irradiation above a temperature of about 200–300 °C. Electrons or ions irradiation at room temperature could intentionally induce a continuous formation, which leads to the creation of holes and amorphization in nanosystems. Furthermore, bond rotations can also derive from irradiation at room temperature, such as the presence of the SW defects in nanostructure.

### 3.2.3 Divacancy Defects

Divacancy defect is found to be one of the most stable vacancy defects in nanostructure, which can be introduced either by the coalescence of double monovacancy defects or directly by removing two neighboring atoms. In the latter case, four uncoordinated carbon nanotubes around the missing carbon atoms have bonded together, generating a pentagon–octagon–pentagon (so-called 5–8–5) defect, as shown in Fig. 3.4. It is noted that there is no DB in the completely reconstructed divacancy configuration. In the case of graphene, calculated results indicate that the transformation energy of a divacancy is of the same order as for a monovacancy, whereas the energy per missing atom is much lower than for a monovacancy. It is worth mentioning that the 5–8–5 defect is the most stable defect in CNTs because of its lowest transformation energy as a result of saturation of dangling bond. In contrast to the situation in CNTs, the 5–8–5 defect is not the only

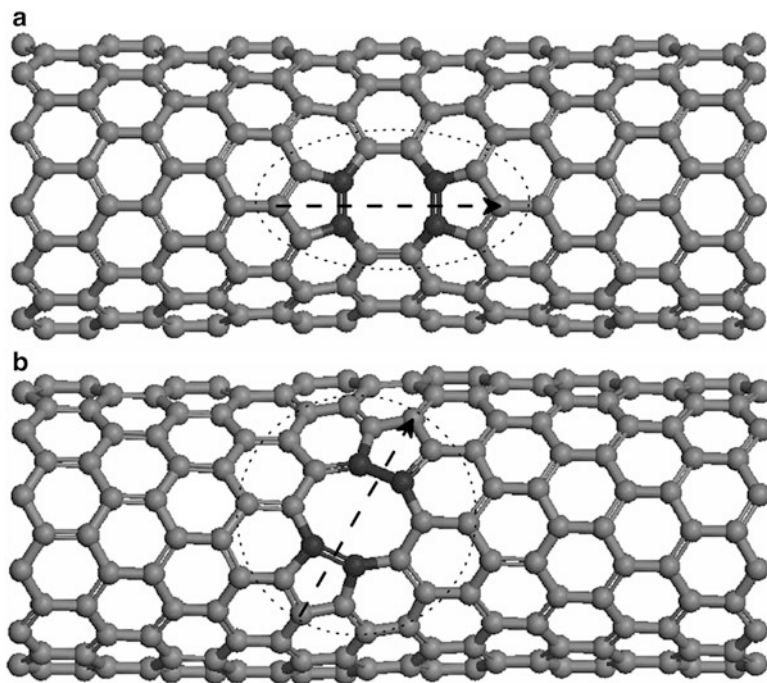


**Fig. 3.4** Ball-and-stick models of divacancy defects in SWNT. The newly formed C–C bonds during the reconstruction are *highlighted darker color*. The pentagon–octagon–pentagon (5–8–5) defects are formed in the defective area (marked by *dotted line*) after reconstruction. (a) Parallel 5–8–5 defects in (12,0) SWNT and (b) tilted 5–8–5 defects in the (12,0) SWNT (Reprinted with permission from Zeng et al. 2010b. Copyright (2010) American Chemical Society)

accessible configuration for the graphene lattice to accommodate divacancy defects. As a matter of fact, the three pentagons and three heptagons (555–777) defects are energetically favored divacancy configuration, and its formation is twisting one of the bonds in the octagon of the 5–8–5 defects. The 555–777 defects are also visualized by using electron microscopy, as illustrated in Fig. 3.5. Previous analysis reveals that the total formation energy of this defect is about 1 eV lower than that of 5–8–5 defects (Kotakoski et al. 2011). We could further transfer the 555–777 defects to 5555–6–7777 defects by twisting another C–C bond. The migration and dynamics of divacancy defects in nanostructure are an attracting issue. The migration of a divacancy approximately needs activation energy much higher than that for a monovacancy. This ensures that the divacancy defects are fairly stable even at very high temperatures. More recently, SW-type transformations are found to take responsibility for the migration and structural transformations of divacancy, and furthermore, the SW defects manifest as an intermediate structure in graphene.

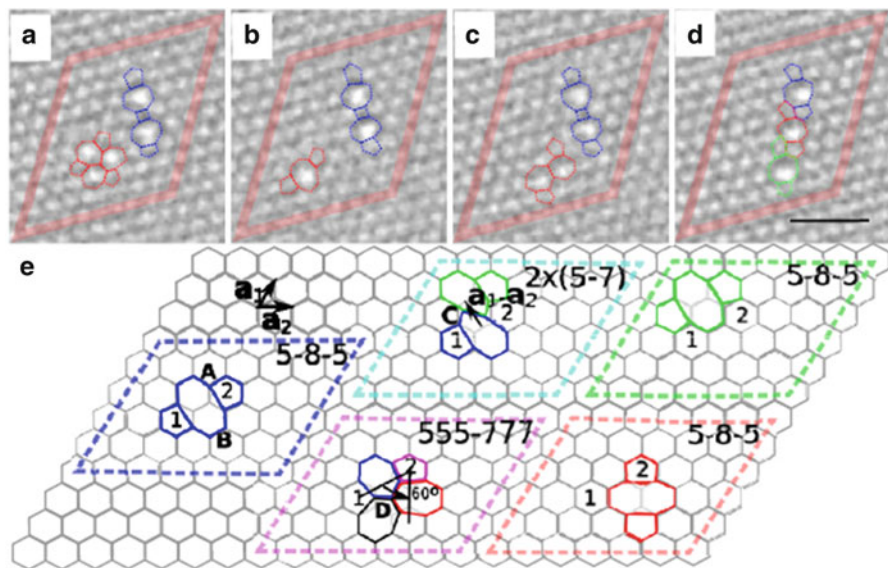


**Fig. 3.5** Divacancy migration in graphene observed in experiment (a–d). The changes in the bond configuration leading to the migration of a divacancy are illustrated by figure (e). Transformation of 5–8–5 defects to 5–7–7–5 defects is initiated by the rotation of bond A, and the 5–8–5 defects to 555–777 defects by the rotation of bond B. Rotating bonds C and D will lead to the final 5–8–5 defects (Reproduced from Kotakoski et al. 2011)

### 3.2.4 Vacancy Cluster

Energetic irradiation impact could be used to artificially create vacancy cluster in reconstructed atomic nanostructure. Recently, vacancy cluster defects and their migration in CNTs (Jin et al. 2008) and graphene nanoribbons (GNRs) (Girit et al. 2009) have been directly detected by in situ HR-TEM at elevated temperatures in experiments. The vacancy cluster is intuitively regarded as the result of missing more than two atoms in perfect hexagonal lattices. It is possible to a larger number of atoms instantly and even cut the nanostructure with nanometer precision in experiments. As a consequence, significant reconstructions deriving from the shrink of its surface area will lead to the reduced diameter for CNT and bending of the layer for graphene. In these cases, it becomes more likely to form hole-like vacancy with unsaturated bonds around its circumference in the nanostructure, as shown in Fig. 3.6. A large amount of simulations reveal that an even number of missing atoms allow complete saturation of dangling bonds, and such configuration is energetically more favorable, whereas dangling bonds always remain as an odd number of atoms removed (Kotakoski et al. 2006). Generally, the presence of the large vacancy cluster in nanostructure is not favorable, and such vacancy cluster tends to split into pentagon–heptagon pair (5–7) defects or separated pentagon and heptagon during atomic reconstruction. However, it does not preclude the presence of large vacancy

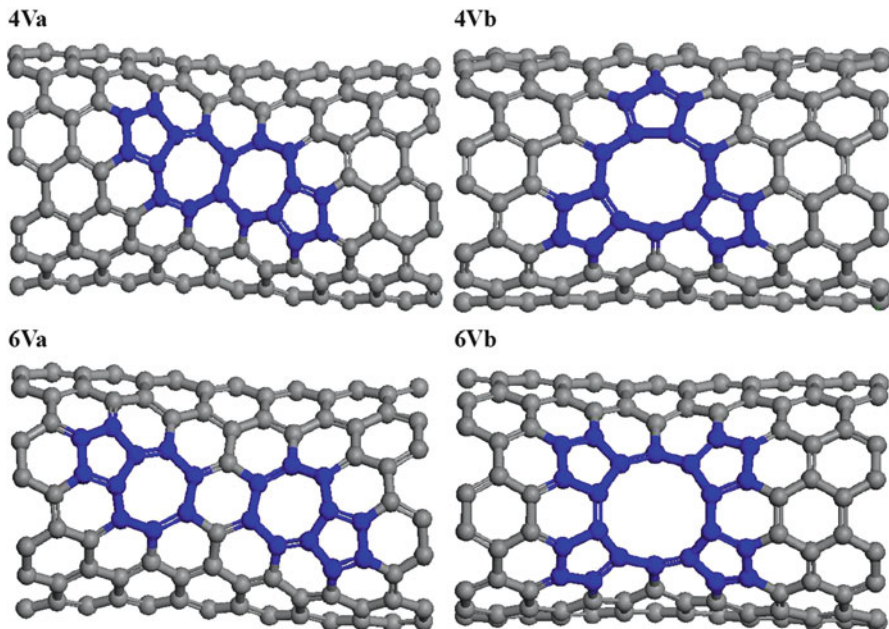


**Fig. 3.6** Schematic structures of defective (7,7) SWNT after the atomic reconstruction; the vacancy defects are *highlighted by blue atoms*. The Arabic number indicates the number of missing atoms in the nanostructure; tetravacancy configurations are shown in *top panel* and hexavacancy configurations are shown in *bottom panel*, respectively. The 4Va configuration consists of two 5–7 pairs connected by each other (*left panel*), while the 4Vb configuration consists of the 5–5–5–9 defects manifesting as a hole in the nanostructure (*right panel*). The 6Va configuration consists of two separate 5–7 pairs connected by the twisted hexagon, while the 6Vb configuration consists of four *pentagons* symmetrically connected with a *decagon* in the *center*, manifesting as a larger hole in the defective area of the tube (Reprinted from Zeng et al. 2011b. Copyright (2011), with permission from Elsevier)

cluster in the nanostructure by the nanoelectronic lithography technique (Jin et al. 2008; Aref et al. 2008). The vacancy cluster in the nanostructure could induce interesting electric transport properties, which can be understood from the electronic band structure analysis. As can be seen clearly in Fig. 3.7, in the band structure of the pristine nanotube, the highest occupied band  $\alpha$  and the lowest unoccupied band  $\alpha'$  cross at the Fermi level, away from the  $\Gamma$ -point. In the 4Va configuration, the 5–7–7–5 defect creates a defect state labeled  $\gamma$  that is located above the Fermi level. The  $\gamma$  band is the lowest unoccupied band at present, and it hybridizes with the  $\alpha$  and  $\alpha'$  bands to evolve into the  $\beta$  and  $\beta'$  bands that anticross at the Fermi level. As a result, the defect state opens a direct band gap of about 0.25 eV at the  $\Gamma$ -point, while the indirect gap of this configuration is about 0.22 eV. Correspondingly, the electronic structure is dominated by a large-scale deformation (5–7–7–5 defects). In the 4Vb configuration, the Fermi level is shifted downward in comparison with the pristine CNT. This downward shift of the Fermi level makes the conductance

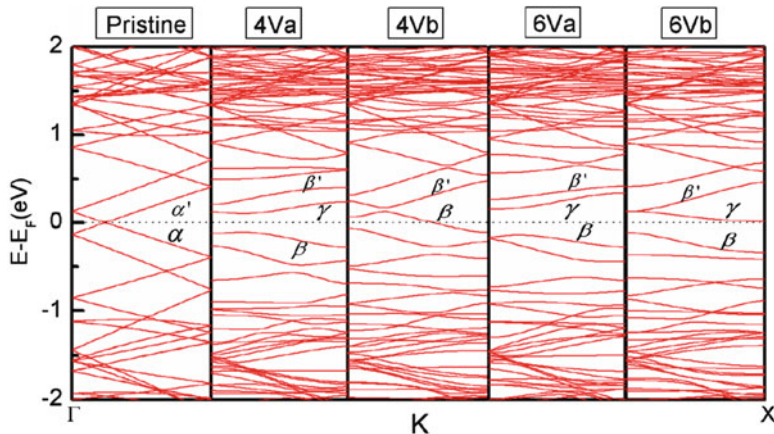


**Fig. 3.7** The corresponding electronic band structures of the defective (7,7) SWNT with various vacancy clusters. The result of the pristine is also shown for comparison (Reprinted from Zeng et al. 2011b. Copyright (2011), with permission from Elsevier)

of this configuration much larger than that in the 4Va case. The gap of the 6Va configuration is further increased to 0.33 eV due to the split  $\beta$ ,  $\beta'$ -bands, and the  $\gamma$ -bands move away from the Fermi level significantly. In the 6Vb configuration, the  $\gamma$ -state approaches the Fermi level with a long dispersionless tail, especially close to the X-point. This roll-off at large  $k$  vectors effectively reduces the direct band gap to about 0.246 eV and indirect gap to about 0.115 eV. Generally, electronic band structure results reveal that the vacancy cluster can effectively reduce the band gap in contrast to the comparable large band gap induced by small pieces of pentagon and heptagon (5–7) defects. As a consequence, the hole-like defects in the CNT lead to more prominent electronic transport compared to the situation in the defective CNT consisting of pentagon–heptagon pair defects. The anomalous conductance variation in the zigzag nanotubes has also shown that the transport in a defective CNT is not a direct function of the number of missing atoms but of the chirality and defect pattern in the nanostructure (Zeng et al. 2010b). The investigation on the defective zigzag CNT revealed that the variety of hexavacancy defect leads to the similar results (Zeng et al. 2011b, c). This phenomenon is attributed to the states linked to large vacancies hybridize with the extended states of the nanotubes to modify their band structure.

### 3.2.5 Substitutional Doping

Impurity atom can be incorporated into the perfect hexagonal lattices as substitutional doping. In such case, the substitutional impurity atom replaces one or two carbon atoms to form the doped configuration. Boron and nitrogen dopants



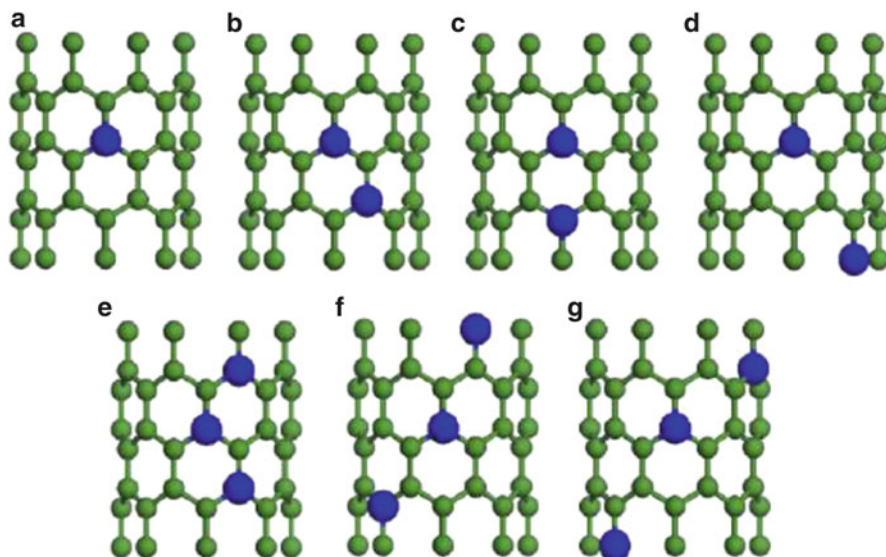


**Fig. 3.8** Model of nitrogen substitutional in the (8,0) carbon nanotube. (a) is the single substitutional doping; (b–d) are different configurations for two foreign atoms doping; (e–g) are different configurations for three foreign atoms doping. The *light-gray atoms* denote nitrogen atoms, and the *deep-gray atoms* denote carbon atoms (Reprinted from Wei et al. 2008. Copyright (2008), with permission from Elsevier)

in carbon nanostructures have been considerably investigated since both of them have roughly the same atomic radius. The substitutional dopants can be expected to be very stable due to strong covalent bonding. Replacing carbon by boron or nitrogen atoms is a subject of great interest to researchers because the substitutional doping not only shifts the Fermi level but also significantly alter the electronic structure of the nanomaterial, as evidenced by the DFT simulation shown in Fig. 3.8. As for instance, nitrogen substitutional doping has been shown to be an efficient route to functionalize these materials owing to the introduction of reactive sites in the nanostructures (Wei et al. 2008; Biel et al. 2009a; Wang et al. 2009; Aref et al. 2008; López-Bezanilla et al. 2009). Compared to the case of N-doping, the B-doped nanostructures exhibit acceptor features, which is also an issue attracting extensive investigations (Wei et al. 2007b; Martins et al. 2007; Yu et al. 2010). Considerable progress has been made with laser-ablation, arc-discharge, and ion irradiation and substitution reaction methods to synthesize high-quality sample. In addition, the Raman spectroscopy was used to monitor the process of irradiation and in characterizing the properties of nanostructure in experiments. In principle, the substitutional atoms in the hexagonal C lattice break the symmetry of perfect graphite and result in the defects reflected by an increase of the D-band intensity in Raman scattering. Further, the presence of dopant in the nanostructure can induce a strong backscattering of the propagating wave packets at specific region, which is similar to the case of vacancy effects. This reduction of conductance at the energy

of the quasi bound states associated with various defects can be ascribed to the remarkable resonant backscattering. Moreover, Son and coauthors have shown the possibility of the position in energy of these quasi bound states effectively tuned by the applied transverse field (Son et al. 2005). The case of a single impurity has been the most theoretically studied; the ab initio calculation performed by Chio et al. provides insight on the scattering potential generated by dopants or defects through the investigation of quasi bound state influenced by isolated defect (Choi et al. 2000). Meanwhile, some studies have been devoted to the effect of a random distribution of substitutional dopant (Lherbier et al. 2008a, b; Terrones et al. 2002) and the different concentrations of dopant (Pershoguba et al. 2009; Pereira et al. 2008). Such studies regarding the mesoscopic transport allow us to evaluate the realistic systems performed on various models and make a quantitative estimation with experimental measurement. It has been also shown previously that it is possible to tune the conductance of SWNTs by ion irradiation in the Anderson localization regime provided that the transport regime remains quantum mechanically coherent. The substitutional doping could provide the chemically active site for adsorption, as a result, the issue of doping by physisorption of gas molecules, and more generally, the modification of the electronic properties of nanostructures by molecular adsorption is fascinating to design commercial sensors (Kong et al. 2000; Schedin et al. 2007). Obviously, the key point for the potential use of chemical sensors based on carbon nanomaterial is whether we can distinguish measurable variation of the minimum concentration between the proto and adsorbed sample in order to ensure the selectivity and sensitivity of such devices for application. The sensing properties of 1-D CNT and 2-D graphene material can be further modified by covalent functionalization or tailored by energetic ion irradiation. Even though considerable experimental fabrications of functionalized nanomaterials have been reported, the systematical theoretical investigation on the modulated electronic transport is still lacking.

### **3.2.6 Impurity Adatom**

The impact of impurity adatom on the properties of nanomaterial is mainly determined on the bonding between the impurity and the host nanomaterial. Only physisorption due to van der Waals interaction is needed to take into account provided that the bond is weak. In contrast, covalent bonding between the foreign atom and the nearest carbon atoms in the atomic structure could lead to chemisorption when the interaction is stronger. The most stable bonding configurations normally correspond to high-symmetry position, including on top of a carbon atom, on top of the center of a hexagon, or the bridge position. Most importantly, some previous studies have demonstrated that the decoration of metal nanoparticle could substantially improve the sensitivity of nanomaterial, thereby the decorated nanomaterials is perspective to function as a component of gas sensor in industry and defense areas (Kauffman et al. 2010; Lin et al. 2009). The theoretical

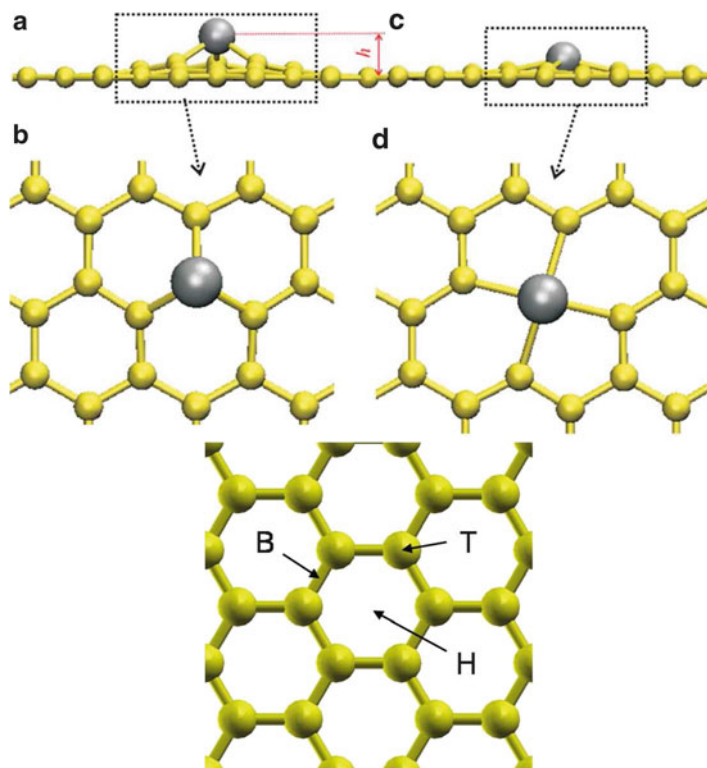


**Fig. 3.9** Atomic structures of TM atoms adsorbed on single and double vacancies in the graphene. Metal atom on a single vacancy: *side view* (a) and *top view* (b). Metal atom on divacancy: *side view* (c) and *top view* (d) (Krasheninnikov et al. 2009). The *bottom panel* illustrates the typical adsorption sites considered, hollow (H), bridge (B), and top (T) (Reproduced from Chan et al. 2008)

investigations of the bonding between interstitial adatom and the bare nanomaterial have been extensively performed and have confirmed the weak bonding between graphene and transition adatoms (Krasheninnikov et al. 2009; Chan et al. 2008) and the formation of chemisorption in defective CNTs (Kauffman et al. 2010). However, only a few experimental observations about the migration of foreign adatom have been reported. Specifically, the decoration of metal cluster in the defective nanomaterial consisting of structural defects is more intriguing as the topological defects normally provide the trapping sites for the interstitial adatoms (Krasheninnikov et al. 2009), as shown in Fig. 3.9. As for instance, the metal cluster can be pinned by the dangling bond and 555–777 defects by forming strong bonds with the defects (Lehtinen et al. 2004; Barinov et al. 2007; Cretu et al. 2010). Moreover, ion irradiation is found to be a suitable method to detrap the adatom at high temperature. It may be used to create the reactive site and therefore significantly modify the electronic properties of the carbon nanostructure.

### 3.3 Creation of Structural Defects

Generally, the following routes are widely adopted to deliberately introduce nonequilibrium defects in carbon nanosystems, including energetic particle irradiation, epitaxial growth, and chemical treat. The energetic particle irradiation is the most promising method owing to the advance of engineering controllable point defects in nanomaterial with high precision due to the ballistic ejection of carbon atoms. The threshold energy is directly transferred to the atomic structure to make carbon atoms leave its host site, and the migration of atoms can also be simultaneously observed. The irradiated material sample can be explicitly characterized by using electron microscopy at atomic resolution by means of in situ measurement, and the irradiation and imaging can be accomplished with the electron or ion energetic beam. Irradiation concentrating on preselected area of nanomaterial sample allows us to create large hole or vacancy cluster (Banhart 2006) and, even more, to physically cut the nanomaterial sample (Banhart et al. 2005). In comparison to the result of highly focused irradiation, uniform irradiation of larger areas generally produces randomly distributed vacancies in the carbon nanomaterials. However, remarkable reconstruction owing to the uncoordinated atoms in the defective will lead to an increased rate of defect formation. The reconstruction of vacancies transformation and its stability have been theoretically demonstrated (Zeng et al. 2010b, c; Kotakoski et al. 2006) and more recently convinced by aberration-corrected electron microscopy in experiments (Rodriguez-Manzo and Banhart 2009; Jin et al. 2008). In addition to the electron irradiation, the ion irradiation is also implemented in common to create the vacancy defects or pattern at highly focused areas. Similarly, the ion irradiation can be used to cut graphene with high precision (Lemme et al. 2009). Furthermore, the defective nanomaterial of the irradiated sample associated with structural defects can be recognized by monitoring the evolution of so-called D peak by means of Raman spectrum analysis. Apart from the particle irradiation, chemical treatment approach is conventionally utilized to eliminate carbon atoms through the reaction of foreign species with host atoms and therefore leads to the presence of various defects or complex defects in nanomaterial. It should be noted that such approach usually allows a very limited loss of atoms. This treatment has been incorporated with chemical functionalization to fabricate functionalized nanocomposites with advanced and powerful functions, which is essential to the development and application of nanomaterials. Chemical vapor deposition (CVD) is one of the fundamentally important synthesis approaches as it provides the controllable technique to the sample fabrication with high equality. Generally, line defects and coalescence of defects can be generated simultaneously at different locations on a substrate during the growth. Further, coalescence in the nanomaterial could result in considerable modification of electronic structure, which is particularly notable in the context of graphene because of the formation of pentagons and octagons along with edge reconstruction (Koskinen et al. 2008, 2009; Zeng et al. 2011e).

## 3.4 Properties of Defective Carbon Materials

### 3.4.1 Reconstruction of Defects

The Brillouin zone of CNTs is one dimensional owing to their one-dimensional structure. Because the CNTs are subject to the restriction of periodic boundary conditions (PBC) along the circumferential direction, the wave vectors along circumferential direction can only have discrete values, while the wave vectors along the axial direction remain continuous. Early theoretical calculations based on zone-folding approximation pointed out that the chirality vectors  $(n,m)$  of CNTs determine the length and orientation and electronic structure. One of the most fascinating aspects of CNTs is that their electronic properties are directly and sensitively related to their geometrical structure. It can manifest as metallic or semiconducting depending on whether or not  $n-m$  is a multiple of 3, respectively. Thus, it is not surprising that the resultant production of SWNTs contains approximately 2/3 semiconducting SWNTs and 1/3 metallic SWNTs. Taken the curvature effects into account, the planar symmetry is then broken, thereby its  $\pi$  and  $\sigma$  states can rehybrid and the mixture of  $\pi$  and  $\sigma$  orbitals have  $sp^2$  and  $sp^3$  characteristics. The zigzag metallic carbon nanotubes are known to develop a small band gap (Ouyang et al. 2002) (semimetallic) as a result of the deviation of the  $k_F$  away from the  $K$  point, whereas the armchair metallic carbon nanotubes remain gapless around the Fermi level. The separation of metallic and semiconducting is also of fundamental importance to the application of CNTs in the future.

The presence of vacancies generally deteriorates the genuine properties of nanotubes, and the electronic transport is related with the number of missing atoms in the CNTs. However, the electronic transport property of CNTs is not a monotonic function of the defect size and geometry but depends on the reconstruction around the defect and its spatial symmetry, as illustrated in Fig. 3.10. The electronic properties can be comprehensively evaluated from the electronic band calculation. The corresponding electronic band structure of the two types of nanotubes with various defect configurations and their pristine analogues are displayed in Fig. 3.11. It has been shown that defect states related to the vacancies hybridize with the extended states of the nanotubes to modify the band edge and change the energy gap. Paradoxically, tetravacancy and hexavacancy nanotubes have higher conductance than divacancy nanotubes, which is due to the presence of midgap states originating from the defect, thereby enhancing the electronic transport (Zeng et al. 2010b, 2011b, c).

Further, the intramolecular junctions of SWNTs are expected to function as basic component in nanoscale devices (Yao et al. 1999). In principle, the connection of two segments of SWNTs with different diameters and helicities by introducing the pentagon–heptagon or pentagon–hexagon–heptagon defect into the ideal hexagonal network accordingly creates the metal–semiconductor (M–S), semiconductor–semiconductor (S–S), or metal–metal (M–M) heterojunction

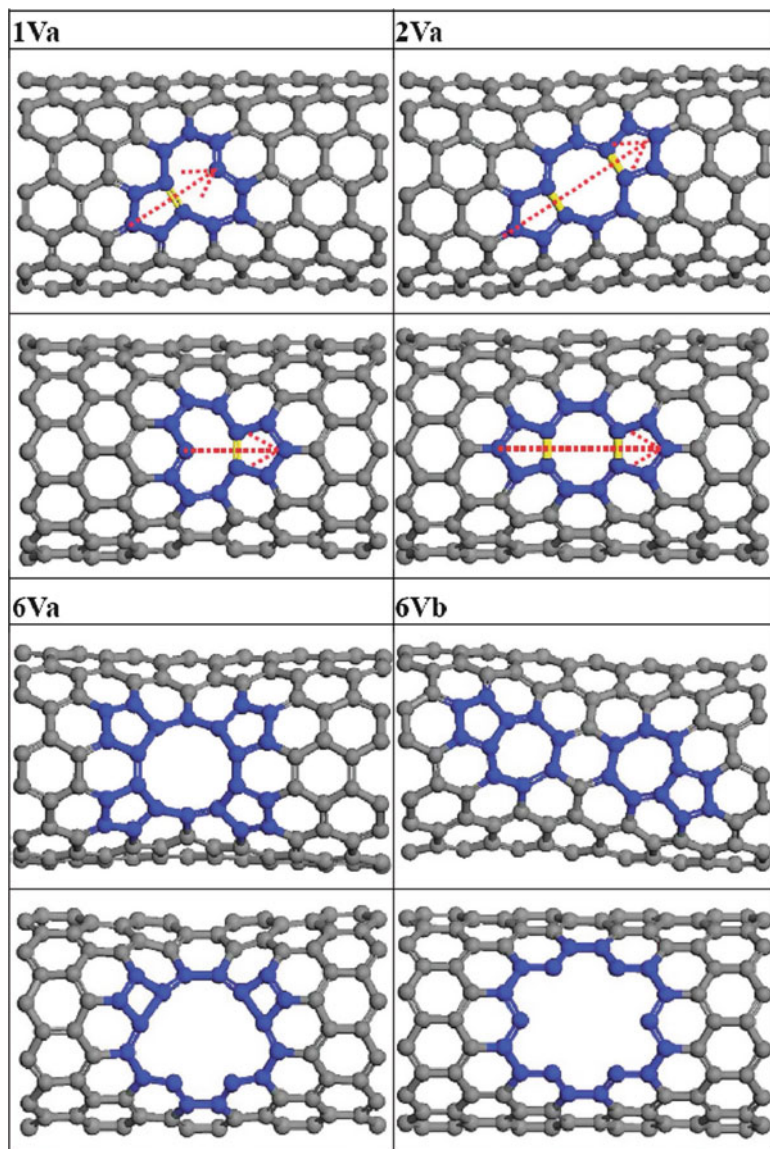


**Fig. 3.10** Vacancy configurations of all structural models. Ball-and-stick model for (7,7) (*upper panel*) and (12,0) (*lower panel*) SWNT with monovacancy, divacancy, and hexavacancy, respectively. The newly formed C–C bonds during the reconstruction are *highlighted* by yellow, and the atoms at the far side are omitted for clarity (Reprinted with permission from Zeng et al. 2010b. Copyright (2010) American Chemical Society)

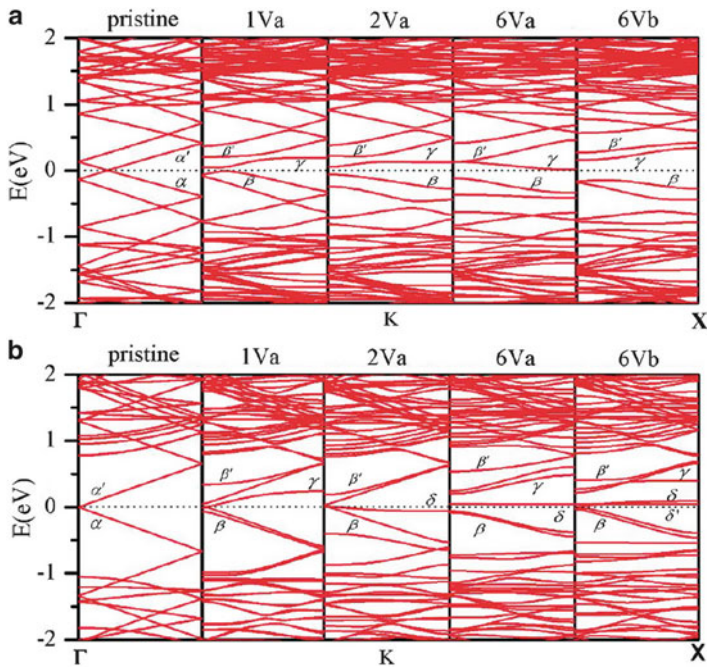


**Fig. 3.11** Band structure of (a) (7,7) and (b) (12,0) SWNT with various vacancies. The band structure of the pristine nanotube is also given for comparison (Reprinted with permission from Zeng et al. 2010b. Copyright (2010) American Chemical Society)

(Saito et al. 1996; Zeng et al. 2008). Experimental and theoretical studies indicated that intramolecular junction structures could perform as nanoscale electronic device that is made completely from carbon atoms (Ouyang et al. 2002; Charlier 2002; Meyer et al. 2011).

Furthermore, it is well known that the electron behavior in 2-D graphene material is described by the Dirac equation rather than the Schrödinger equation. Correspondingly, it will have significant effects on the electronic properties of the nanomaterial. The challenge for the broad-range applications in nanoelectronics for graphene is opening an energy gap between valence and conduction bands. Using lithographically patterned technology or patterned adsorption of atomic engineering at nanoscale, a tunable band gap opening has been experimentally realized in narrow graphene nanoribbon (GNR), turning this nanostructure into a promising material for circuit fabrication. Most importantly, GNR-based nanodevices are expected to behave as molecular devices with electronic properties similar to those of carbon nanotubes (CNTs). The electronic properties of nanoribbons are dependent on the width and atomic geometry of their edge, namely, zigzag or armchair. One of the most intriguing issues is the research of edge states in the electronic structure of zigzag GNR (ZGNR) because the nanosystems are expected to have great possibilities for novel spintronic devices. The presence of either native or physically

introduced structural defects in GNRs has been explicitly evidenced in several experimental studies. Recently, the investigation of the formation and annealing of SW defects in graphene membranes reveals that the existence of SW defects is energetically more favorable than in CNTs or fullerenes (Meyer et al. 2008). While both symmetric and asymmetric SW defects in GNRs give rise to complete electron backscattering region, the well-defined parity of the wave functions in symmetric SW defects configuration is preserved. Unexpectedly, calculations predict that the asymmetric SW defects are more favorable to electronic transport than the symmetric defects configuration, which is caused by the different couplings around the charge neutrality point (CNP) (Zeng et al. 2011a). The electronic structure is strongly dependent on the atomic arrangement of the GNR's edge, and the graphene layer terminated free and passivated with hydrogen atoms has been extensively investigated. The simplest atomic structures of the edge are the armchair and the zigzag. More recently, experimental evidence confirms the anomalous edge orientations other than pure zigzag or armchair edges by using the aberration-corrected TEM (Koskinen et al. 2008, 2009). The rise of defective edges is derived from local changes in the reconstruction type or sustained removal of carbon atoms from the edges. As for instance, removing one carbon atom from a zigzag-edged GNR will lead to one pentagon in the middle of a row of hexagons, as visualized in Fig. 3.12. The edge reconstructions in AGNR could lead to various combinations of pentagons and heptagons around the edge (Zeng et al. 2011e). The density functional calculations reveal that the unpassivated (57) ZZ edge is energetically more favorable. In contrast, the AC edge has the lowest transformation energy if all the dangling bonds are passivated with hydrogen atoms according to theoretical calculations. It is noted that in experimental measurement, other chemical groups that can saturate dangling bonds at the edge substantially increase the possibility of the emergence of anomalous edge defects.

### 3.4.2 *Effects of Substitutional Doping in Defects*

The doping of heteroatom has an important impact upon the electronic structure and the electronic transport of SWCNTs. The deliberate introduction of defects and impurities into CNT could offer a possible route to change and tune its electronic properties and thus have a significant bearing on a broad range of applications. It is well known that the CNTs with substitutional boron and nitrogen could be regarded as the P-type- and N-type-substituted carbon nanotubes, respectively. The defective nanomaterials with different concentration as well as distribution of substitutional doping manifest distinct electronic transport properties. The impurity leads to the presence of a dispersive acceptor or donor-like band in the band gap compared with the undoped tube. The electronic band modification can be attributed to the hybridization taking place between the impurity states of boron atoms and the existing occupied state for the boron doping and unoccupied state for nitrogen



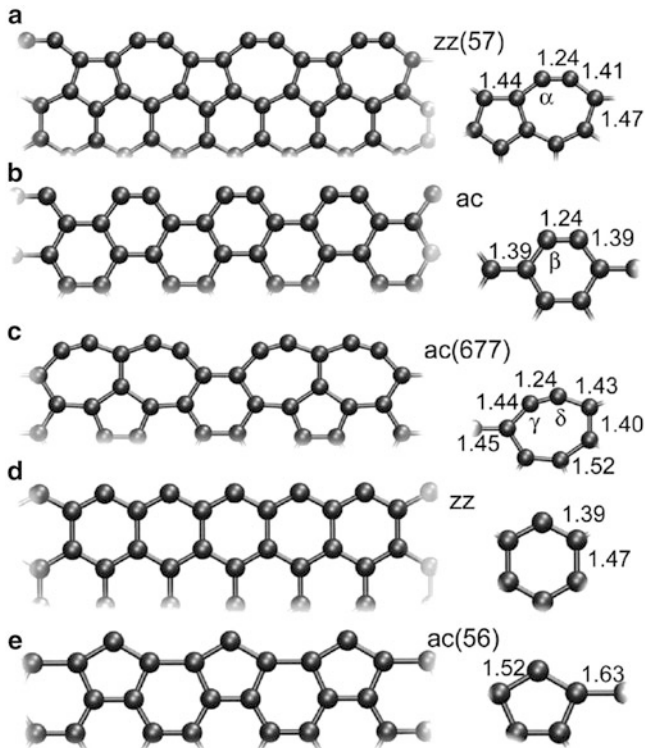


**Fig. 3.12** Different geometric reconstruction of the graphene edges: (a) reconstructed zigzag [zz(57)], (b) armchair (ac), (c) reconstructed armchair [ac(677)], (d) zigzag (zz), and (e) pentagonal armchair [ac(56)]. Some bond lengths (in Å) and bond angles are denoted on the right: The bond angles are  $\alpha = 143^\circ$ ,  $\beta = 126^\circ$ ,  $\gamma = 148^\circ$ , and  $\delta = 147^\circ$ . The edge can be passivated with hydrogen atoms (Reprinted with permission from Koskinen et al. 2008. © 2008 The American Physical Society)

doping, respectively. The dopant in the semiconducting SWNT can give rise to M–S transition with nonlinear current–voltage curve, and their structures strongly dominate their electrical properties. DFT calculations indicate that transport properties of the doped nanotubes are sensitive not only to the concentration of nitrogen atoms but also to their distribution (Wei et al. 2007b, 2008). The effects of substitutional doping in SW on electronic transport are shown to be different in the CNTs with different chirality. The impurity is found to be energetically favorable for the site of pentagon ring but not for the heptagon ring. It is found that the nitrogen in SW produces half-filled band near the Fermi level in which the electron effective mass varies with the changing of the position of doping, as shown in Fig. 3.13. The total transmission coefficients nearby the Fermi level increase and the others decrease after doping. The nitrogen doping and SW defect enhance the transport property in semiconducting zigzag SWNT and weaken in quasimetallic zigzag SWNT.

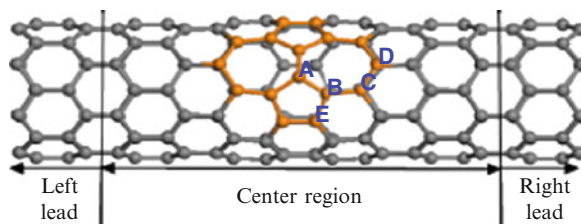


**Fig. 3.13** Schematic description of the nitrogen substitutional doping position and the structure of the two-probe system; two semi-infinite *left* and *right* electrodes are comprised by one unit cell; *A–E* denotes the different doping positions (Reprinted with permission from Wei et al. 2007a. Copyright (2007), American Institute of Physics)

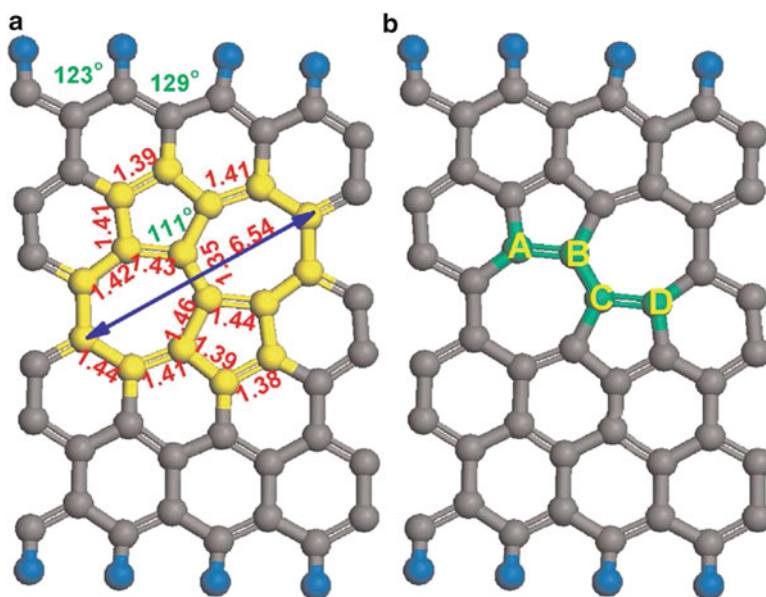


**Fig. 3.14** Schematics of the atomic structure after asymmetric SW defects introduced and different substitutional sites in the structural model of defective 6-ZGNR with asymmetric SW defects. (a) The asymmetric SW defects are highlighted by *yellow atoms*; some C–C bond lengths (in Å) and angles (in degree) are depicted by the *red numeral* and *green numeral*, respectively. (b) Different doping sites in the SW defects; the substitutional impurity is denoted by *A, B, C, and D* (Reprinted with permission from Zeng et al. 2012. Copyright (2012) John Wiley & Sons)

Meanwhile, the functionalization of GNRs can be achieved through substitutional doping. Boron substitutional doping in GNRs could induce metal to semiconductor (M–S) transition (Martins et al. 2007). Hence, the predicted extraordinary properties of nitrogen-doped nanomaterials have now been experimentally confirmed, and they exhibit the potential applications in electronic nanodevices (Meyer et al. 2011). The occurrence of many types of defects, especially for the N-doped composite in GNRs (see Fig. 3.14) and their influences, is found to

give rise to one or two resonance backscattering in the case of defective GNRs consisting of the asymmetric SW defects, and the location of which depends on the dopant distribution (Zeng et al. 2012). Moreover, the dopant in the asymmetry is energetically more favorable to locate near the edge. Thus, the doped nanostructures can be substantially modulated as a result of modifications on electronic bands induced by substitutional dopant.

As demonstrated previously, defects are shown to be able to effectively tailor the electronic properties of carbon-based materials. More recently, the possibility of artificially creating individual vacancies in carbon nanostructures by using an electron beam of 1 Å diameter has been reported. It was also shown that higher-order defects can be formed by removing a group of atoms with high-energy impacts or chemical etching. Structural defects related with vacancy, interstitial vacancy defects, and pentagon–heptagon defects and their influence on electronic structure on defective carbon nanotubes (CNTs) and graphene have been hitherto examined by an abundant amount of publications. On the contrary, the researches regarding the effects of composite defects on the electronic transport properties have just begun. There is still a demand for the knowledge of theoretical predictions to be further combined with vast amount of experimental results to enable new potential nanodevices and foster innovative applications. In addition, despite surface's physics and electronic properties of nanomaterial being currently at the center of the attention at this stage, the associated chemistry properties of the defective nanomaterials have remained largely veiled.

### 3.4.3 *Chemical Properties*

The dangling bonds in nanosystem provide the chemical reactive site, and many simulations indeed have revealed that hydroxyl, carboxyl, or other groups can easily be adsorbed by the vacancy defects. Specifically, it has been predicted that the chemical adsorption at the edge of graphene nanoribbons could lead to significant modification of electronic structure. Not only the edges of ZGNRs can provide chemical reactive site but also the reconstructed vacancies and SW defects without dangling bonds are shown to increase the local reactivity. Moreover, the evidence of trapping of metal atoms in reconstructed vacancies has been confirmed by experimental studies. Overall, it is possible to develop the functionalization of carbon-based sample and design electronic transport properties of materials in terms of various chemical treatments once the creation of defects with high selectivity can be controlled in high precision.

**Acknowledgements** The authors thank Prof. K.-L. Yao and Dr. Y. Xu for the fruitful discussion. We also acknowledge technical assistance from Dr. T. Markussen and M.A. Kuroda. Extensive calculations are performed in the MAC OS X Turing cluster. This work is supported by NSF of China Grant No. 11047176 and the Research Foundation of Education Bureau of Hubei Province of China under Grant Nos. Q20111305, B20101303, and T201204.

## References

- Ando T (2005) Theory of electronic states and transport in carbon nanotubes. *J Phys Soc Jpn* 74:777–817
- Aref T, Remeika M, Bezryadin A (2008) High-resolution nanofabrication using a highly focused electron beam. *J Appl Phys* 104:024312(1–6)
- Avouris P (2010) Graphene: electronic and photonic properties and devices. *Nano Lett* 10:4285–4294
- Avouris P, Chen Z, Perebeinos V (2007) Carbon-based electronics. *Nat Nanotechnol* 4:605–615
- Bangert U, Bleloch A, Gass M, Seepujak A, Berg JVD (2010) Doping of few-layered graphene and carbon nanotubes using ion implantation. *Phys Rev B* 81:245423(1–11)
- Banhart F (1999) Irradiation effects in carbon nanostructures. *Rep Prog Phys* 62:1181–1221
- Banhart F (2006) Irradiation of carbon nanotubes with a focused electron beam in the electron microscope. *J Mater Sci* 41:4505–4511
- Banhart F, Li J, Terrones M (2005) Cutting single-walled carbon nanotubes with an electron beam: evidence for atom migration inside nanotubes. *Small* 1:953–956
- Banhart F, Kotakoski J, Krasheninnikov AV (2011) Structural defects in graphene. *ACS Nano* 5:26–41
- Barinov A, Üstünel H, Fabris S, Gregoratti L, Aballe L, Dudin P, Baroni S, Kiskinova M (2007) Defect-controlled transport properties of metallic atoms along carbon nanotube surfaces. *Phys Rev Lett* 99:046803(1–4)
- Baughman RH, Zakhidov AA, Heer WA (2002) Carbon nanotubes – the route toward applications. *Science* 297:787–792
- Biel B, Triozon F, Blase X, Roche S (2009a) Chemically induced mobility gaps in graphene nanoribbons: a route for upscaling device performances. *Nano Lett* 9:2725–2729
- Biel B, Blase X, Triozon F, Roche S (2009b) Anomalous doping effects on charge transport in graphene nanoribbons. *Phys Rev Lett* 102:096803(1–4)
- Cai J, Ruffieux P, Jaafar R, Bieri M, Braun T, Blankenburg S, Muoth M, Seitsonen AP, Saleh M, Feng X, Müllen K, Fasel R (2010) Atomically precise bottom-up fabrication of graphene nanoribbons. *Nature* 466:470–473
- Castro Neto AH, Peres NMR, Novoselov KS, Geim AK (2009) The electronic properties of graphene. *Rev Mod Phys* 81:109–162
- Chan KT, Neaton JB, Cohen ML (2008) First-principles study of metal adatom adsorption on graphene. *Phys Rev B* 77:235430(1–12)
- Charlier JC (2002) Defects in carbon nanotubes. *Acc Chem Res* 35:1063–1069
- Charlier JC, Blasé X, Roche S (2007) Electronic and transport properties of nanotubes. *Rev Mod Phys* 79:677–732
- Choi H, Ihm J, Louie S, Cohen ML (2000) Defects, quasibound states, and quantum conductance in metallic carbon nanotubes. *Phys Rev Lett* 84:2917–2920
- Cretu O, Krasheninnikov AV, Rodríguez-Manzo JA, Sun L, Nieminen RM, Banhart F (2010) Migration and localization of metal atoms on strained graphene. *Phys Rev Lett* 105:196102(1–4)
- Czerw R, Terrones M, Charlier JC, Blase X, Foley B, Kamalakaran R, Grobert N, Terrones H, Tekleab D, Ajayan PM, Blau W, Rühle M, Carroll DL (2001) Identification of electron donor states in N-doped carbon nanotubes. *Nano Lett* 1:457–460
- Dresselhaus MS, Jorio A, Hofmann M, Dresselhaus G, Saito R (2010) Perspectives on carbon nanotubes and graphene Raman spectroscopy. *Nano Lett* 10:751–758
- Du A, Smith SC (2011) Electronic functionality in graphene-based nanoarchitectures: discovery and design via first-principles modeling. *J Phys Chem Lett* 2:73–80
- El-Barbary A, Telling R, Ewels C, Heggie M, Briddon PR (2003) Structure and energetics of the vacancy in graphite. *Phys Rev B* 68:144107(1–7)
- Geim AK (2009) Graphene: status and prospects. *Science* 324:1530–1534

- Geim AK, Novoselov KS (2007) The rise of graphene. *Nat Mater* 6:183–191. doi:10.1038/nmat1849/sj
- Girit CO, Meyer JC, Emi R, Rossell MD, Kisielowski C, Yang L, Park CH, Crommie MF, Cohen ML, Louie SG, Zettl A (2009) Graphene at the edge: stability and dynamics. *Science* 323:1705–1708
- Gómez-Navarro C, Pjé P, Gómez-Herrero J, Biel B, Garcia-Vidal FJ, Rubio A, Flores F (2005) Tuning the conductance of single-walled carbon nanotubes by ion irradiation in the Anderson localization regime. *Nat Mater* 4:534–539
- Guo B, Liu Q, Chen E, Zhu H, Fang L, Gong JR (2010) Controllable N-doping of graphene. *Nano Lett* 10:4975–4980
- Hashimoto A, Suenaga K, Gloter A, Urita K (2004) Direct evidence for atomic defects in graphene layers. *Nature* 430:17–20
- Iijima S (1991) Helical microtubules of graphitic carbon. *Nature* 354:56–58
- Iijima S, Ichihashi T (1993) Single-shell carbon nanotubes of 1-nm diameter. *Nature* 363:603–605
- Jia X, Hofmann M, Meunier V, Sumpter BG, Campos-Delgado J, Romo-Herrera JM, Son H, Hsieh YP, Reina A, Kong J, Terrones M, Dresselhaus MS (2009) Controlled formation of sharp zigzag and armchair edges in graphitic nanoribbons. *Science* 323:1701–1705
- Jin C, Suenaga K, Iijima S (2008) Vacancy migrations in carbon nanotubes. *Nano Lett* 8:1127–1130
- Katsnelson MI (2007) Graphene: carbon in two dimensions. *Mater Today* 10:20–27
- Kauffman DR, Sorescu DC, Schofield DP, Allen BL, Jordan KD, Star A (2010) Understanding the sensor response of metal-decorated carbon nanotubes. *Nano Lett* 10:958–963
- Kong J, Franklin NR, Zhou C, Chapline MG, Peng S, Cho K, Dai H (2000) Nanotube molecular wires as chemical sensors. *Science* 287:622–625
- Koskinen P, Malola S, Häkkinen H (2008) Self-passivating edge reconstructions of graphene. *Phys Rev Lett* 101:115502(1–4). <http://link.aps.org/doi/10.1103/PhysRevLett.101.115502>
- Koskinen P, Malola S, Häkkinen H (2009) Evidence for graphene edges beyond zigzag and armchair. *Phys Rev B* 80:073401(1–3)
- Kosynkin DV, Higginbotham AL, Sinitskii A, Lomeda JR, Dimiev A, Price BK, Tour JM (2009) Longitudinal unzipping of carbon nanotubes to form graphene nanoribbons. *Nature* 458:872–876
- Kotakoski J, Krasheninnikov A, Nordlund K (2006) Energetics, structure, and long-range interaction of vacancy-type defects in carbon nanotubes: atomistic simulations. *Phys Rev B* 74:245420(1–5)
- Kotakoski J, Krasheninnikov A, Kaiser U, Meyer J (2011) From point defects in graphene to two-dimensional amorphous carbon. *Phys Rev Lett* 106:105505(1–4)
- Krasheninnikov AV, Banhart F (2007) Engineering of nanostructured carbon materials with electron or ion beams. *Nat Mater* 6:723–733
- Krasheninnikov AV, Lehtinen PO, Foster AS, Pyykkö P, Nieminen RM (2009) Embedding transition-metal atoms in graphene: structure, bonding, and magnetism. *Phys Rev Lett* 102:126807(1–4)
- Kroto HW, Heath JR, O'Brien SC, Curl RF, Smalley RE (1985) C<sub>60</sub>: Buckminsterfullerene. *Nature* 318:162–163
- Lehtinen PO, Foster AS, Ma Y, Krasheninnikov AV, Nieminen RM (2004) Irradiation-induced magnetism in graphite: a density functional study. *Phys Rev Lett* 93:187202(1–4)
- Lemme MC, Bell DC, Williams JR, Stern LA, Baugher BWH, Jarillo-Herrero P, Marcus CM (2009) Etching of graphene devices with a helium ion beam. *ACS Nano* 3:2674–2676
- Lherbier A, Biel B, Niquet YM, Roche S (2008a) Transport length scales in disordered graphene-based materials: strong localization regimes and dimensionality effects. *Phys Rev Lett* 100:036803(1–4)
- Lherbier A, Blase X, Niquet YM, Triozon F, Roche S (2008b) Charge transport in chemically doped 2D graphene. *Phys Rev Lett* 101:036808(1–4)

- Li X, Cai W, An J, Kim S, Nah J, Yang D, Piner R, Velamakanni A, Jung I, Tutuc E, Banerjee SK, Colombo L, Ruoff RS (2009) Large-area synthesis of high-quality and uniform graphene films on copper foils. *Science* 324:1312–1314
- Lin Y, Watson KA, Fallbach MJ, Ghose S, Smith JG, Delozier DM, Cao W, Crooks RE, Connell JW (2009) Rapid, solventless, bulk preparation of metal nanoparticle-decorated carbon nanotubes. *ACS Nano* 3:871–884
- López-Bezanilla A, Triozon F, Roche S (2009) Chemical functionalization effects on armchair graphene nanoribbon transport. *Nano Lett* 9:2537–2541
- Martins T, Miwa R, Ada S, Fazzio A (2007) Electronic and transport properties of boron-doped graphene nanoribbons. *Phys Rev Lett* 98:196803(1–4)
- Meyer JC, Kisielowski C, Erni R, Rossell MD, Crommie MF, Zettl A (2008) Direct imaging of lattice atoms and topological defects in graphene membranes. *Nano Lett* 8:3582–3586
- Meyer JC, Kurasch S, Park HJ, Skakalova V, Künzel D, Gross A, Chuvilin A, Algara-Siller G, Roth S, Iwasaki T, Starke U, Smet JH, Kaiser U (2011) Experimental analysis of charge redistribution due to chemical bonding by high-resolution transmission electron microscopy. *Nat Mater* 10:209–215
- Nicholas RJ, Mainwood A, Eaves L (2008) Introduction. Carbon-based electronics: fundamentals and device applications. *Philos Trans A Math Phys Eng Sci* 366:189–193
- Novoselov KS, Geim AK, Morozov SV, Jiang D, Zhang Y, Dubonos SV, Grigorieva IV, Firsov AA (2004) Electric field effect in atomically thin carbon films. *Science* 306:666–669
- Ouyang M, Huang JL, Lieber CM (2002) Fundamental electronic properties and applications of single-walled carbon nanotubes. *Acc Chem Res* 35:1018–1025
- Padilha JE, Amorim RG, Rocha AR, Silva AJR, Fazzio A (2011) Energetics and stability of vacancies in carbon nanotubes. *Solid State Commun* 151:482–486
- Park S, Ruoff RS (2009) Chemical methods for the production of graphenes. *Nat Nanotechnol* 4:217–224
- Pereira VM, Lopes dos Santos JMB, Castro Neto AH (2008) Modeling disorder in graphene. *Phys Rev B* 77:115109(1–17)
- Pershoguba SS, Skrypnik YV, Loktev VM (2009) Numerical evidence of spectrum rearrangement in impure graphene. *Phys Rev B* 80:214201(1–9)
- Purewal MS, Zhang Y, Kim P (2006) Unusual transport properties in carbon based nanoscaled materials: nanotubes and graphene. *Phys Status Sol B* 243:3418–3422
- Reina A, Jia X, Ho J, Nezich D, Son H, Bulovic V, Dresselhaus MS, Kong J (2009) Large area, few-layer graphene films on arbitrary substrates by chemical vapor deposition. *Nano Lett* 9:30–35
- Rodríguez-Manzo JA, Banhart F (2009) Creation of individual vacancies in carbon nanotubes by using an electron beam of 1 Å diameter. *Nano Lett* 9:2285–2289
- Saito R, Dresselhaus G, Dresselhaus MS (1996) Tunneling conductance of connected carbon nanotubes. *Phys Rev B* 53:2044–2050
- Schedin F, Geim AK, Morozov SV, Hill EW, Blake P, Katsnelson MI, Novoselov KS (2007) Detection of individual gas molecules adsorbed on graphene. *Nat Mater* 6:652–655
- Son YW, Ihm J, Cohen ML, Louie SG, Choi H (2005) Electrical switching in metallic carbon nanotubes. *Phys Rev Lett* 95:216602(1–4)
- Stephan O, Ajayan PM, Colliex C, Redlich P, Lambert JM, Bernier P, Lefin P (1994) Doping graphitic and carbon nanotube structures with boron and nitrogen. *Science* 266:1683–1685
- Suenaga K, Wakabayashi H, Koshino M, Sato Y, Urita K, Iijima S (2007) Imaging active topological defects in carbon nanotubes. *Nat Nanotechnol* 2:358–360. doi:[10.1038/nnano.2007.141](https://doi.org/10.1038/nnano.2007.141)
- Tapasztó L, Dobrik G, Lambin P, Biró LP (2008) Tailoring the atomic structure of graphene nanoribbons by scanning tunnelling microscope lithography. *Nat Nanotechnol* 3:397–401
- Terrones M (2004) Carbon nanotubes: synthesis and properties, electronic devices and other emerging applications. *Int Mater Rev* 49:325–377

- Terrones M, Ajayan PM, Banhart F, Blase X, Carroll DL, Charlier JC, Czerw R, Foley B, Grobert N, Kamalakaran R, Kohler-Redlich P, Rühle M, Seeger T, Terrones H (2002) N-doping and coalescence of carbon nanotubes: synthesis and electronic properties. *Appl Phys A* 74:355–361
- Triozon F, Lambin P, Roche S (2005) Electronic transport properties of carbon nanotube based metal/semiconductor/metal intramolecular junctions. *Nanotechnology* 16:230–233
- Ugeda MM, Brihuega I, Guinea F, Gómez-Rodríguez JM (2010) Missing atom as a source of carbon magnetism. *Phys Rev Lett* 104:096804(1–4). <http://link.aps.org/doi/10.1103/PhysRevLett.104.096804>
- Wang X, Li X, Zhang L, Yoon Y, Weber PK, Wang H, Guo J, Dai H (2009) N-doping of graphene through electrothermal reactions with ammonia. *Science* 324:768–771
- Wang Z, Hu H, Zeng H (2010) The electronic properties of graphene nanoribbons with boron/nitrogen codoping. *Appl Phys Lett* 96:243110(1–3)
- Wei J, Hu H, Zeng H, Wang Z, Wang L, Peng P (2007a) Effects of nitrogen in Stone-Wales defect on the electronic transport of carbon nanotube. *Appl Phys Lett* 91:092121(1–3)
- Wei JW, Hu HF, Zeng H, Wang ZY, Wang L, Zhang LJ (2007b) Influence of boron distribution on the transport of single-walled carbon nanotube. *Appl Phys A* 89:789–792
- Wei J, Hu H, Zeng H, Zhou Z, Yang W, Peng P (2008) Effects of nitrogen substitutional doping on the electronic transport of carbon nanotube. *Physica E* 40:462–466
- Wei J, Hu H, Wang Z, Zeng H, Wei Y, Jia J (2009a) Effect of nitrogen-vacancy complex defects on the electronic transport of carbon nanotube. *Appl Phys Lett* 94:102108(1–3)
- Wei D, Liu Y, Wang Y, Zhang H, Huang L, Yu G (2009b) Synthesis of N-doped graphene by chemical vapor deposition and its electrical properties. *Nano Lett* 9:1752–1758
- Yao Z, Postma H, Balents L (1999) Carbon nanotube intramolecular junctions. *Nature* 402:273–276
- Yu S, Zheng W, Wang C, Jiang Q (2010) Nitrogen/boron doping position dependence of the electronic properties of a triangular graphene. *ACS Nano* 4:7619–7629
- Zeng H, Hu HF, Wei JW, Yang WW, Peng P (2008) Quantum transport properties of carbon nanotube with topologic defects. *Eur Phys J Appl Phys* 43:19–22
- Zeng H, Hu H, Wei J, Wang Z (2010a) Transport properties of single-walled carbon nanotube with intramolecular junctions. *Mod Phys Lett B* 24:2445–2455
- Zeng H, Hu H, Leburton JP (2010b) Chirality effects in atomic vacancy-limited transport in metallic carbon nanotubes. *ACS Nano* 4:292–296
- Zeng H, Leburton JP, Xu Y, Wei J (2011a) Defect symmetry influence on electronic transport of zigzag nanoribbons. *Nanoscale Res Lett* 6:254(1–6)
- Zeng H, Leburton JP, Hu H, Wei J (2011b) Vacancy cluster-limited electronic transport in metallic carbon nanotube. *Solid State Commun* 151:9–12
- Zeng H, Zhao J, Hu H, Leburton JP (2011c) Atomic vacancy defects in the electronic properties of semi-metallic carbon nanotubes. *J Appl Phys* 109:083716(1–6)
- Zeng H, Zhao J, Wei JW, Hu HF (2011d) Effect of N doping and Stone-Wales defects on the electronic properties of graphene nanoribbons. *Eur Phys J B* 79:335–340
- Zeng H, Zhao J, Wei JW (2011e) Electronic transport properties of graphene nanoribbons with anomalous edges. *Eur Phys J Appl Phys* 53:20602(1–5)
- Zeng H, Zhao J, Wei J, Xu D (2012) Role of nitrogen distribution in asymmetric Stone-Wales defects on electronic transport of graphene nanoribbons. *Phys Status Sol B* 249:128–133. doi:10.1002/pssb.201147371. <http://onlinelibrary.wiley.com/doi/10.1002/pssb.201147371/abstract>

# Chapter 4

## Topological Versus Physical and Chemical Properties of Negatively Curved Carbon Surfaces

Marzio De Corato, Marco Bernasconi, Luca D'Alessio, Ottorino Ori, Mihai V. Putz, and Giorgio Benedek

**Abstract** Some relevant physical and chemical properties of negatively curved carbon surfaces like  $sp^2$ -bonded schwarzites can be predicted or accounted for on the basis of purely topological arguments. The general features of the vibrational spectrum of complex  $sp^2$ -carbon structures depend primarily on the topology of the bond network and can be estimated, in a first approximation and for systems with only nearest-neighbor interactions, from the diagonalization of the adjacency

---

M. De Corato

Dipartimento di Scienza dei Materiali, Università di Milano-Bicocca, Via R. Cozzi 53, 20125 Milan, Italy

Centro S3, CNR-Istituto Nanoscienze, I-41125 Modena, Italy

Dipartimento di Fisica, Università di Modena e Reggio Emilia, I-41125 Modena, Italy

e-mail: [m.decorato@campus.unimib.it](mailto:m.decorato@campus.unimib.it); [marzio.decorato@unimore.it](mailto:marzio.decorato@unimore.it)

M. Bernasconi • G. Benedek

Dipartimento di Scienza dei Materiali, Università di Milano-Bicocca, Via R. Cozzi 53, 20125 Milan, Italy

Donostia International Physics Center (DIPC), Paseo M. de Lardizábal 4, 20018 Donostia/San Sebastián, Spain

e-mail: [marco.bernasconi@mater.unimib.it](mailto:marco.bernasconi@mater.unimib.it); [marco.bernasconi@unimib.it](mailto:marco.bernasconi@unimib.it); [giorgio.benedek@mater.unimib.it](mailto:giorgio.benedek@mater.unimib.it); [giorgio.benedek@unimib.it](mailto:giorgio.benedek@unimib.it)

L. D'Alessio

Department of Physics, Boston University, 590 Commonwealth Av., Boston, MA 02215, USA

e-mail: [dallessio@buphy.bu.edu](mailto:dallessio@buphy.bu.edu)

O. Ori

Actinium Chemical Research, Via Casilina 1626/A, 00133 Rome, Italy

e-mail: [ottorino.ori@gmail.com](mailto:ottorino.ori@gmail.com)

M.V. Putz

Laboratory of Computational and Structural Physical Chemistry, Biology-Chemistry Department, West University of Timișoara, Pestalozzi Street No.16, Timișoara RO-300115, Romania

e-mail: [mv\\_putz@yahoo.com](mailto:mv_putz@yahoo.com)



matrix. Examples are discussed for three- and two-periodic carbon schwarzites, where a direct comparison with ab initio calculations is possible. The spectral modifications produced by the insertion of defects can also be analyzed on pure topological grounds. Two-periodic (planar) schwarzites can be viewed as regular arrays of Y-shaped nanojunctions, which are basic ingredients of carbon-based nano-circuits. A special class of planar schwarzites is obtained from a modification of a graphene bilayer where the two sheets are linked by a periodic array of hyperboloid necks with a negative Gaussian curvature. Ab initio density functional calculations for some structures among the simplest planar schwarzites –  $(C_{18})_2$ ,  $(C_{26})_2$ , and  $(C_{38})_2$  – are presented and discussed in light of the structural stability predictions derived from a topological graph-theory analysis based on the Wiener index. A quantum-mechanical justification is provided for the effectiveness of the Wiener index in ranking the structural stability of different  $sp^2$ -conjugated structures.

*El universo (que otros llaman la Biblioteca)  
se compone de un número indefinido,  
y tal vez infinito, de galerías hexagonales . . .*<sup>1</sup>  
(Jorge Luis Borges, Ficciones, 1941)

## 4.1 Introduction

There are atomic surfaces which have no underlying bulk and are free-standing thanks to their covalent bonding architecture. Their vibrational structure reflects, in its general features, their topological constitution, thus playing a relevant role in the growth mechanisms and spectroscopic characterization. The recognition to the studies on graphene (Novoselov et al. 2004, 2005a, b; Geim and Novoselov 2007; Castro Neto et al. 2009) has, by extension, revived the interest in the vast zoo of curved surfaces of carbon which are made possible by  $sp^2$  hybridization. Besides the well-known forms like fullerenes (Kroto et al. 1985), single-walled and multi-walled nanotubes (Iijima 1991), worth mentioning are the three-dimensional forms of  $sp^2$  carbon, random schwarzites. Figure 4.1a, c shows a transmission electron microscope (TEM) image of a random carbon schwarzite obtained by supersonic cluster beam deposition with a deposition energy of 0.1 eV/atom (Barborini et al. 2002; Donadio et al. 1999; Benedek et al. 2003). Raman and near-edge x-ray absorption fine structure (NEXAFS) spectra indicate a pure  $sp^2$ -bonding structure, suggesting a single, highly connected graphene sheet with an average pore diameter in the range of 100 nm. Although carbon schwarzites have been first synthesized and characterized more than a decade ago (Barborini et al. 2002; Donadio et al. 1999;

---

<sup>1</sup>The universe (that others call the Library) is composed by an undefined, sometimes infinite number of hexagonal tunnels.

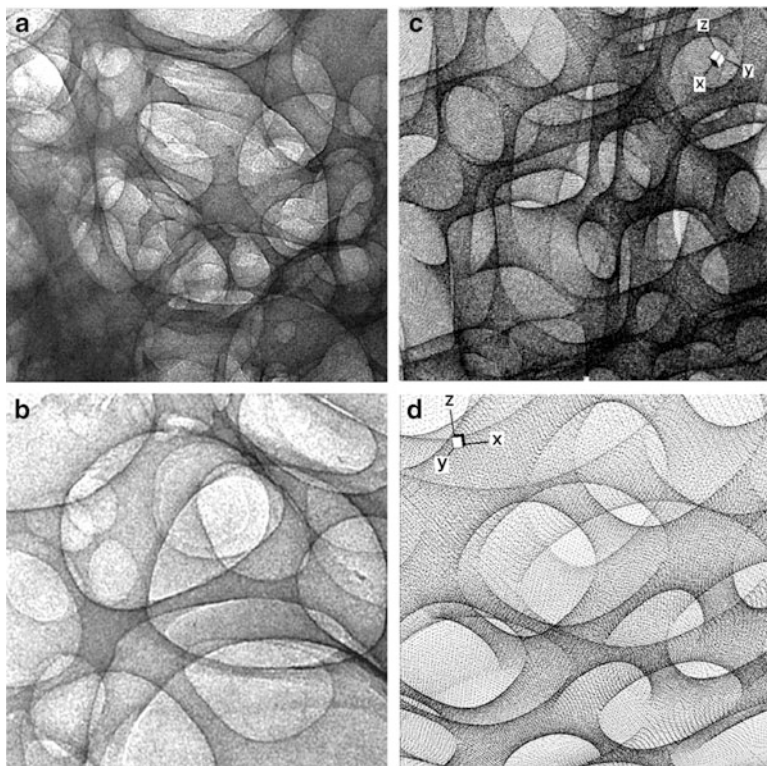


**Fig. 4.1** Two transmission electron microscope (TEM) pictures (a, b) of a random carbon schwarzite as grown by supersonic cluster beam deposition (Reprinted from Benedek et al. 2003, Copyright (2003), with permission from Elsevier) and two simulations (c, d, respectively) of the TEM images obtained from analytical approximations of three-periodic minimal surfaces (gyroids) with a self-affine distortion (Reprinted with permission from Barborini et al. 2002, Copyright (2002), American Institute of Physics)

Benedek et al. 2003), they did not meet the glamour of the ordered  $sp^2$  carbon forms. Nevertheless, random schwarzites, otherwise termed spongy carbon (Donadio et al. 1999), qualify for their unique properties, such as unconventional magnetism (Rode et al. 2004; Arçon et al. 2006), and applications in efficient super-capacitors (Diederich et al. 1999), field emitters (Boscolo et al. 2000; Benedek et al. 2001; Ferrari et al. 1999), and carbon-based composites (Bongiorno et al. 2005) up to the recent demonstration of interfacing live cells with nano-carbon substrates (Agarwal et al. 2010).

Triply periodic minimal surfaces as possible  $sp^2$  carbon structures have been theoretically suggested already in the mid-1980s (McKay 1985) then with more momentum in the early 1990s, following the nanotube vogue (McKay and Terrones 1991; Terrones and McKay 1993; O’Keeffe et al. 1992; Lenosky et al. 1992; Townsend et al. 1992; Vanderbilt and Tersoff 1992).

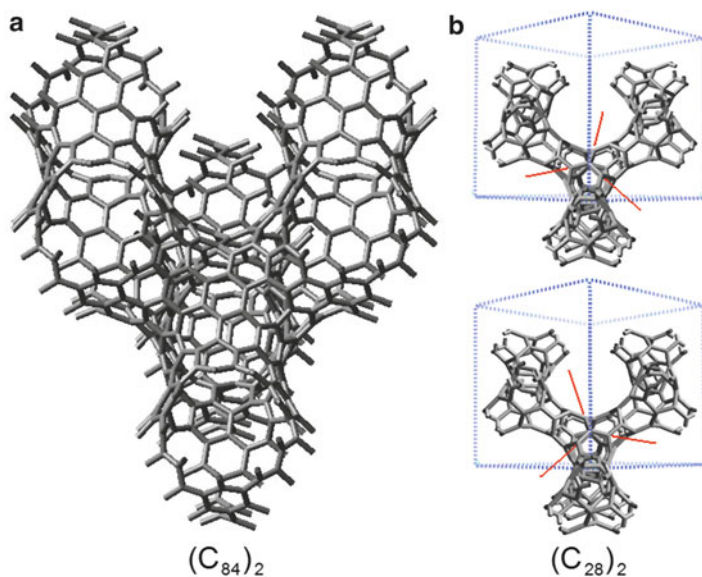


**Fig. 4.2** The tiling with 6 (*light gray*) and 7 (*dark gray*) rings of the unit cell of a P-type (a) and D-type (b) schwarzite, both having 216 atoms per unit cell. The 7 rings are 24 per unit cell in both cases. The unit cell of the D-type schwarzite is made of two identical but nonequivalent elements, containing twelve 7 rings each, joined in the staggered position as atoms are in the diamond lattice (Reprinted from Spagnolatti et al. 2003. Copyright (2003) with kind permission from Springer Science and Business Media)

They have since termed *schwarzites* after the name of the mathematician Hermann Schwarz (Schwarz 1990) who first investigated that class of surfaces. The synthesis of random schwarzites was obtained by means of supersonic cluster beam deposition (SCBD) (Barborini et al. 2002). SCBD experiments demonstrated that spongy carbon grows in the presence of finely dispersed Mo nano-catalysts, with porous size decreasing with increasing deposition energy and no tendency to form triply periodic structures. These aspects, as well as the growth in the form of a self-affine minimal random surface, have been theoretical elucidated on the basis of pure topological arguments (Benedek et al. 2003, 2005; Bogana et al. 2001). Many relevant properties of schwarzites can actually be derived in a first approximation from a topological analysis. For a thorough discussion of these aspects, the reader is referred to the previously published chapter (Benedek et al. 2011) in this series of book. In this chapter, it is shown that also the vibrational spectra of schwarzitic structures can be estimated from topology, more precisely from the adjacency matrices. After assessing the method on standard cases as the fullerene  $C_{60}$  and the simplest three-periodic schwarzite  $fcc-(C_{28})_2$ , for which the vibrational spectra are well established, the novel class of two-periodic schwarzites (Fig. 4.2) shall be introduced and their vibrational spectra as derived with the adjacency matrix method discussed. The interest for two-periodic schwarzites, here discussed for the first time, is related to the possibility of growing them by means of near-to-come

planar technologies through the direct joining of nanotubes. We will also present the main result of the first *ab initio* study about the most interesting planar schwarzite. This study gives us the opportunity to make a comparison between the stability of atoms obtained from *ab initio* calculation and topological arguments involving the Wiener index. Finally, a quantum-mechanical argument will be exposed and discussed which justifies the success and outlines the applicability range of the Wiener index in determining the stability scale of isomeric carbon structures.

## 4.2 Adjacency Matrix

For a mono-atomic network of  $N$  nodes labeled by an index  $i = 1, 2, \dots, N$ , the simplest topological characterization is provided by its adjacency matrix (AM)  $A$  whose elements are defined by

$$A_{ij} = \begin{cases} 1 & \text{if nodes } i, j \text{ are linked by a bond} \\ 0 & \text{otherwise, including } i = j \end{cases} \quad (4.1)$$

There are elementary structural and physical properties of atomic networks which can be qualitatively understood in terms of the AM. For example, the eigenvectors of  $A$  lead to the definition of topological coordinates of three-coordinated carbon structures like fullerenes (Manolopoulos and Fowler 1992) and nanotubes (László et al. 2001). The topological coordinates may be defined as the set of atomic positions having the highest point symmetry compatible with the adjacencies. The topological coordinates can be defined also for D-type schwarzites, either referring to a single element (genus 2) or to a unit cell (genus 3), and provide a straightforward method to construct a structure with all the same adjacency matrix and point symmetries of the real structure, which may serve as the starting configuration for a molecular dynamics minimization procedure.

As shown in more detail elsewhere (D'Alessio, Master thesis, 2007, Unpublished), isomers of a D-type schwarzite element can be enumerated with the spiraling procedure similar to that introduced for fullerenes (Manolopoulos and Fowler 1992). As an example, Tables 4.1, 4.2, 4.3, and 4.4 list the isomers of

**Table 4.1** Isomers of the D-type schwarzite  $(C_{32})_2$  element classified according the sequence of 7- and 6-membered rings determined with the spiraling procedure

$C_{32}$ isomer	Sequence	Sym	Ord	$N$	$M$	$W$	$\rho$
1	06777777077706770	$C_2$	2	8	8	3,915	1.20239558
2	707767767077707770	$D_{2d}$	8	3	8	3,884	1.16148325

The four 0s in each sequence represent the four terminations of the element. The other columns indicate the point group (Sym), the number of symmetry operations (Ord), the class sequence multiplicity ( $N$ ) (D'Alessio, Master thesis, 2007, Unpublished), the maximum topological distance of the element ( $M$ ), the Wiener index ( $W$ ), and the topological efficiency index ( $\rho$ ). Here and in the following tables, isomers are listed for increasing  $W$

**Table 4.2** Same as Table 4.1 for the isomers of the D-type schwarzite  $(C_{34})_2$  element

$C_{34}$ isomer	Sequence	Sym	Ord	$N$	$M$	$W$	$\rho$
1	7077777770667707760	$C_2$	2	5	8	4,370	1.19496855
2	7770777077770776660	$C_3$	3	2	8	4,404	1.20426579
3	7776076777707770670	$C_{2v}$	4	3	9	4,471	1.22258682

**Table 4.3** Same as Table 4.1 for the isomers of the D-type schwarzite  $(C_{36})_2$  element. Note that the spiraling procedure to enumerate isomers is unable to find the highest symmetry isomer of  $T_d$  symmetry

$C_{36}$ isomer	Sequence	Sym	Ord	$N$	$M$	$W$	$\rho$
1	0777676777707706760	$C_{2v}$	4	6	8	4,839	1.13912429
2	0776677777076607707	$C_2$	2	7	8	4,846	1.18079922
3	07777667670777707670	$D_2$	4	5	9	4,848	1.17441860
4	07766777667077707770	$C_S$	2	10	9	4,854	1.19674556
5	0776777767706760770	$D_{2d}$	8	2	8	4,856	1.14962121
6	07777767670676770770	$C_2$	2	3	9	4,875	1.20192308
7	0676777777760770760	$C_1$	1	7	8	4,887	1.21205357
8	07777677670677670770	$C_1$	1	9	9	4,891	1.20586785
9	0677777707670776670	$C_1$	1	11	9	4,897	1.20734714
10	7760777767706760770	$D_2$	4	1	9	4,906	1.21676587
11	07777677760767670770	$C_2$	2	5	9	4,918	1.20539216
12	6777760770677707706	$C_1$	1	7	9	4,954	1.23602794
13	6077777067767770670	$C_2$	2	6	9	4,966	1.22435897
14	6077777067767770760	$C_1$	1	12	9	4,993	1.23834325
15	6777767076077707706	$C_2$	2	6	9	5,020	1.24503968
16	6077776077777670670	$D_2$	4	6	9	5,046	1.25148810
17	6077776077777607606	$S_4$	4	6	9	5,046	1.24408284
18	6067777770777076670	$C_2$	2	5	10	5,049	1.26731928
19	6707707707677676770	$T_d$	24	—	9	5,214	1.17432430
20	076677707777707606	$C_2$	2	7	11	5,399	1.31554581
21	66707707777770660	$D_{2d}$	8	4	11	5,868	1.32162162

the smallest D-type elements  $C_{2h+28}$  with  $h = 0, 2-6$ . For  $h = 2-6$  only schwarzites within the restricted class with hexagonal necks joining adjacent elements are considered. In this class the isolated elements have therefore a 6-membered ring also at each of the four terminations. The spiral sequences of the 6- and 7-membered rings and the four terminations (0) are listed for each isomer in the second column of Tables 4.1, 4.2, 4.3, and 4.4. For each isomer the point group of the element is also indicated. The smallest D-type schwarzite with  $h = 0$  only contains 7-membered rings and exists in two isomers, one with hexagonal necks (Fig. 4.3) and one with dodecagonal necks. Both isomers are chiral and have their own enantiomer. Examples of topologically equivalent structures constructed by means of the topological coordinates are illustrated in Figs. 4.3 and 4.4 for the elements of the D-type schwarzite  $(C_{28})_2$  and of the three isomers of  $(C_{34})_2$ , respectively.

**Table 4.4** Same as Table 4.1 for the isomers of the D-type schwarzite ( $C_{38}$ )<sub>2</sub> element

$C_{38}$ isomer	Sequence	Sym	Ord	$N$	$M$	$W$	$\rho$
1	067677777677707706760	$C_s$	2	4	8	5,382	1.18285714
2	077776776707776607760	$C_2$	2	9	9	5,382	1.20268156
3	077677777766077607706	$C_2$	2	7	9	5,384	1.18983425
4	077667777670677077670	$C_1$	1	5	9	5,396	1.21258427
5	076677777670776607770	$C_1$	1	11	9	5,397	1.20603352
6	077667777760767077670	$C_1$	1	8	9	5,402	1.20044444
7	676076767677077707770	$C_s$	2	5	9	5,404	1.19425414
8	60776777776707660770	$C_2$	2	5	9	5,414	1.20983240
9	67607677776077760770	$C_1$	1	2	9	5,422	1.23227273
10	077776677706767077670	$C_s$	2	3	9	5,426	1.21251397
11	707777770676707676660	$C_1$	1	4	9	5,426	1.19911602
12	676067767767077707770	$C_s$	2	4	10	5,469	1.22212291
13	60777670767776770670	$C_2$	2	9	9	5,470	1.20883978
14	76607776770677076770	$C_1$	1	5	9	5,477	1.22391061
15	07677677067767770670	$C_1$	1	11	9	5,482	1.24590909
16	06777777077706776660	$C_1$	1	3	10	5,494	1.24863636
17	06666777777077706770	$C_1$	1	10	10	5,538	1.25152542
18	06777676707677770670	$C_1$	1	19	10	5,563	1.23622222
19	76607777760777076670	$C_1$	1	5	10	5,603	1.25910112
20	776067707777676670770	$C_2$	2	3	10	5,639	1.27435028
21	06677777076677770760	$C_1$	1	10	10	5,645	1.26145251
22	76706770777766670770	$C_1$	1	2	10	5,768	1.28893855
23	77706776067777707606	$C_1$	1	1	11	5,988	1.31604396
24	67707706677777707606	$C_1$	1	5	11	6,021	1.32329670

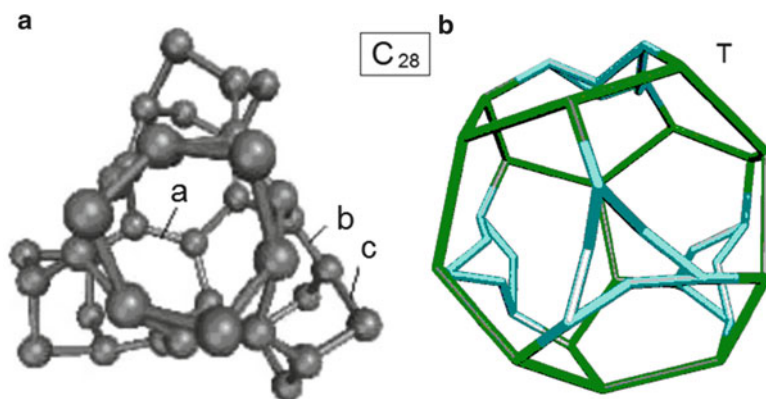
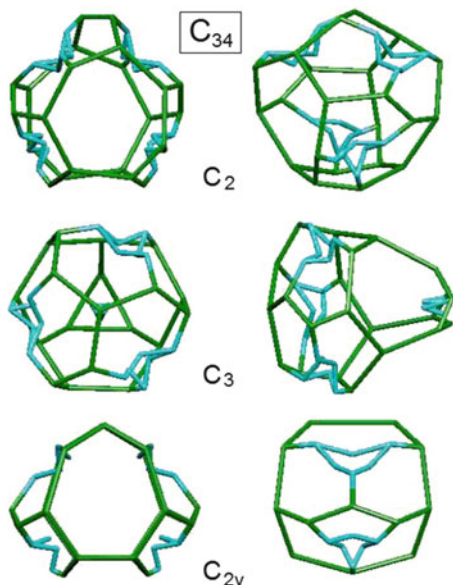


**Fig. 4.3** The element of the ( $C_{28}$ )<sub>2</sub> isomer with hexagonal necks (a) and its topological coordinate model (b). There are three inequivalent bond lengths labeled by  $a$ ,  $b$ , and  $c$  (D'Alessio, Master thesis, 2007, Unpublished)

**Fig. 4.4** *Front and side views of the three topological coordinate models of  $(C_{34})_2$  isomers classified according to their point symmetry groups (see Table 4.2) (D'Alessio, Master thesis, 2007, Unpublished)*

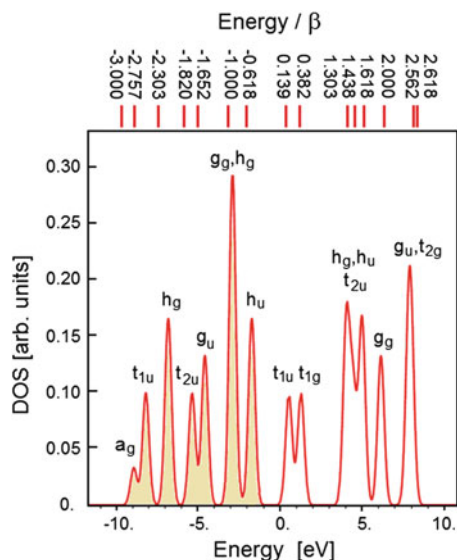


As seen in Table 4.3, the isomer of highest ( $T_d$ ) symmetry (#19) is not the most stable according to the ranking based on the Wiener index  $W$  and topological efficiency index  $\rho$ . In any case the stability ranking based on the global topological indices, accounting for the conjugation long-range effects, is in clear conflict with the ranking based on the transferability of fixed bonding energies assigned to the three geometrically inequivalent bonds (D'Alessio, Master thesis, 2007, Unpublished). The former proved to account quite well for the theoretical isomer ranking of some fullerenes (Vukicevic et al. 2011), and it is suggested that it should work equally well for schwarzites. However, both approaches agree in explaining why more compact, though less symmetric isomers are more stable, which favors the growth of random rather than periodic schwarzites in SCBD experiments (Barborini et al. 2002).

### 4.3 Topological Electronic States

A straightforward application of the AM is the calculation of the electronic energies of a mono-atomic network in the tight-binding (TB) approximation for a band originated from a single atomic state, for example, the  $p_z$  band in an  $sp^2$  carbon network. By assuming the same diagonal matrix element  $\alpha$  of the Hamiltonian for all atomic orbitals, the same overlap integral  $s$ , and the same Hamiltonian matrix element (resonance integral)  $\beta$  between the atomic orbitals for all nearest-neighbor

**Fig. 4.5** The topological energy levels (in eV) of icosahedral  $C_{60}$  from the diagonalization of the adjacency matrix ( $\alpha = -2.60$  eV,  $\beta = 3.01$  eV,  $s = 0$ ) compared with Hückel energy levels (in units of  $\beta$ ) (Reprinted with permission from Bühl and Hirsch 2001. Copyright (2001) the American Chemical Society). *Shadowed peaks* correspond to occupied states



pairs, the energy eigenvalues  $E = E_j$  and the eigenvectors  $\mathbf{c} = \mathbf{c}_j$  providing the coefficients of atomic orbital combinations are obtained by solving the TB equation:

$$(\mathbf{I} - s\mathbf{A})^{-1}(\beta\mathbf{A} + \alpha\mathbf{I})\mathbf{c} = E\mathbf{I}\mathbf{c} \quad (4.2)$$

where  $\mathbf{I}$  is the unitary matrix. The extension of this equation to the periodic schwarzite lattice would provide the valence band structure. In this way a qualitative information about the size of the gap between the highest occupied (HOMO) and the lowest unoccupied (LUMO) molecular orbitals can be obtained as a function of the topology, here represented by the adjacency matrix, and to infer whether the periodic schwarzite will be an insulator or a metal.

As previously shown for tetrahedral D-type schwarzites with 6-membered necks (Gaito et al. 1998; Benedek et al. 2011), the smallest members of the series are alternatively metallic and insulating. The link of the HOMO and LUMO states to basic chemical properties such as site reactivity, electronegativity, and chemical hardness in polyaromatic hydrocarbons (PAH's) is exploited in the formulation of the so-called colored molecular topology (Putz et al., Chap. 9). In this way these properties, though intrinsically dependent on the electronic structure, may receive a first estimation on purely topological grounds. Figure 4.5 displays a simple application to the icosahedral  $C_{60}$  molecule, where the energy levels of the 60  $\pi$ -electrons calculated by solving Eq. (4.2) with  $\alpha = -2.60$  eV,  $\beta = 3.01$  eV,  $s = 0$  are compared with the Hückel energy levels reported by Bühl and Hirsch in units of  $\beta$  (Bühl and Hirsch 2001). In the approximation where  $\beta$  is the same for all bonds, the Hückel energy levels scale exactly as the topological eigenvalues.



## 4.4 Topological Phonon Structure

With the same formalism, though slightly complicated by the vector nature of the atomic displacements, one can investigate the vibrational spectra at zero wavevector of these periodic structures, at least for the part which depends on topology. It is indeed expected that in systems where atoms are all alike and approximately bonded in the same way the gross features of the vibrational spectrum are first of all determined by topology.

It is noted that the vibrational spectra extracted from the adjacency matrix of a P-type element or a D-type schwarzite unit cell, with each of their six terminations closed on the opposite one so as to form a three-handle torus, are topologically equivalent to the spectra at zero wavevector ( $\mathbf{q} = 0$ ) of the corresponding three-periodic solid with periodic boundary conditions. For a flat surface (graphene), the vector nature of the phonon displacement field at  $\mathbf{q} = 0$  is factorized into a transverse out-of-plane component, corresponding to a transverse optical mode normal to the surface ( $\text{TO}_\perp$  mode) having a frequency  $\omega_\perp = 16.3$  rad/s, and two orthogonal in-plane components corresponding to the parallel optical ( $\text{TO}_\parallel$ ) and longitudinal optical (LO) modes, having the same frequency of  $\omega_\parallel = 29.8$  rad/s. The degeneracy of  $\text{TO}_\parallel$  and LO modes at  $\mathbf{q} = 0$  is intrinsically due to the symmetry of the three  $sp^2$  bonds forming three angles in plane of  $120^\circ$  and is only approximately fulfilled for a heterocyclic nonplanar structure. In general, on curved surfaces the three angles are distorted and no longer in plane, a fact which is however irrelevant at the topological level. This level of approximation may be referred to as *topological dynamics* and the eigensolutions as *topological phonons*.

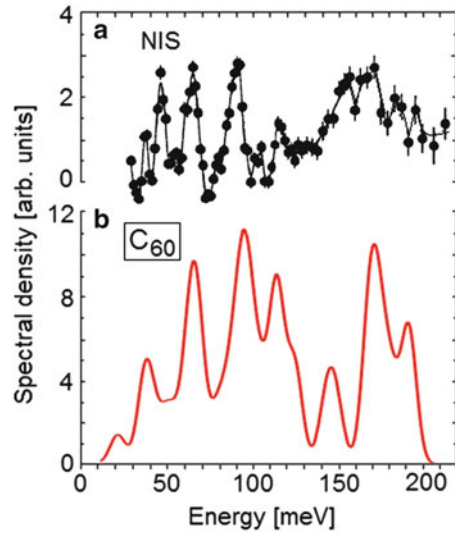
The assumption that each of the orthogonal components of each atomic displacement only couples with the same component of the three adjacent atoms reduces the dynamical problem to the diagonalization of three independent combinations of the adjacent matrix. In a simplified nearest-neighbor interaction picture, only two nearest-neighbor force constants  $f_\perp$  and  $f_\parallel$  are needed. The eigenvalue equation providing the angular frequencies  $\omega = \omega_{\alpha\nu}$  and the components  $u_i = u_{i\alpha,\nu}$  of the atomic displacements for each phonon  $\nu$  and each polarization  $\alpha = \perp, \parallel$  can be expressed in terms of the adjacency matrix as

$$-M\omega^2 u_i = f_\alpha \sum_j (A_{ij} - 3\delta_{ij}) u_j, \quad \alpha = \perp, \parallel \quad (4.3)$$

where  $M$  is the carbon atom mass, and the term with the Kronecker delta is implied by the translational invariance of the system Hamiltonian. The force constants  $f_\alpha$  are fitted to the respective angular frequencies  $\omega_\perp$  and  $\omega_\parallel$  for graphene given above and considered to be transferable to other  $sp^2$  carbon structures. The angular frequencies are directly obtained from the eigenvalues  $\lambda_{\alpha\nu}$  of the adjacency matrix and are given by

$$\omega_{\alpha\nu} = \left[ \frac{f_\alpha}{M} (3 - \lambda_{\alpha\nu}) \right]^{1/2}. \quad (4.4)$$

**Fig. 4.6** Comparison between the vibrational spectrum of the icosahedral fullerene C<sub>60</sub> measured with neutron inelastic scattering (NIS) (Cappelletti et al. 1991) (a) and the topological phonon spectrum calculated from the adjacency matrix (b). In the latter spectrum, a finite line width is attributed to each phonon peak in order to obtain a smooth spectrum with a resolution comparable to that of experiment (Image reproduced from De Corato and Benedek 2012. Copyright © 2012 World Scientific, New York)



#### 4.4.1 Topological Phonons of Fullerenes and Schwarzites

An example of topological phonon spectrum derived from Eq. (4.3) is shown in Fig. 4.6 for the icosahedral isomer of the fullerene C<sub>60</sub>. There is a good correspondence between the calculated topological phonon spectrum and the experimental spectrum derived by inelastic neutron scattering (NIS) (Cappelletti et al. 1991; Pintschovius 1996). This indicates that the gross features of the C<sub>60</sub> vibrational spectrum are accounted for by its topology, that is, by its bonding network.

A similar calculation has been done for the D-type schwarzite (C<sub>28</sub>)<sub>2</sub> for which a comparison is possible between ab initio and topological phonon spectra (De Corato et al. 2012) (Fig. 4.7). While the ab-initio spectrum in Fig. 4.7c carries the information about the detailed equilibrium structure of the schwarzite element as depicted in Fig. 4.7a, the topological spectrum only depends on the structure of the graph shown in Fig. 4.7b. Nevertheless, the comparison of the ab initio eigenvectors to those of topological phonons permits to associate four spectral regions of the ab initio spectrum (Fig. 4.7c) to corresponding regions (marked by segments in Fig. 4.7d) of the topological spectrum.

The topological phonon spectrum may be conveniently used in the calculation of integral properties such as the vibrational part of thermodynamic functions. As an example, it is perfectly sufficient to use the topological phonon frequencies for the calculation of the mean-square atomic displacement relative to the interatomic distance  $d$ , given with the equation

$$f_c \equiv \frac{1}{d} \langle u^2 \rangle_T^{1/2} = \frac{1}{d} \left[ \sum_{\lambda} \frac{\hbar}{2NM\omega_{\lambda}} \left( \frac{1}{e^{\hbar\omega_{\lambda}/kT} - 1} + \frac{1}{2} \right) \right]^{1/2} \quad (4.5)$$

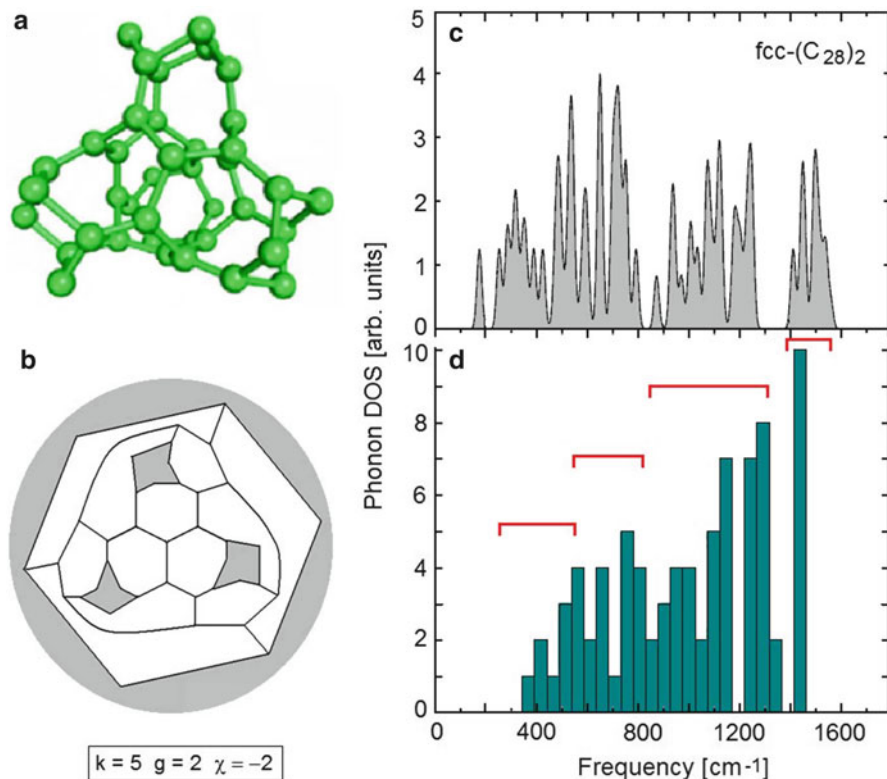


**Fig. 4.7** The element  $C_{28}$  of the smallest D-type schwarzite with 6-membered necks (a), the corresponding planar graph (b) with its topological constants (*gray regions* represent the four necks), and the zero-wavevector ab initio vibrational spectrum of its fcc lattice  $(C_{28})_2$  (c) (Reprinted from Spagnolatti et al. 2003. Copyright (2003) with kind permission from Springer Science and Business Media). The topological phonon spectrum is shown in (d) for comparison. The analysis of the eigenvectors allows to associate four spectral regions of the ab initio spectrum (c) to the marked topological spectral regions in (d). The three modes of zero frequency corresponding to the free translations are not shown

where  $T$  is the absolute temperature. It is possible to estimate the temperature at which the bonds start breaking, leading to melting by means of the Lindemann criterion: For carbon materials, this occurs at  $f_c = 0.084$  (Gersten and Smith 2001). A semi-empirical tight-binding molecular dynamics simulation of the topological connectivity as a function of temperature for the D-type schwarzite  $(C_{36})_2$  (Fig. 4.8a) (Rosato et al. 1999) shows that a graphitization transition, consequent to a rapid break of prevalently single bonds, is predicted to occur around 4,000 K. At this temperature, the ratio  $f_c$  derived from Eq. (4.5), with the topological phonon spectrum (Fig. 4.8b) and the graphite interatomic distance  $d = 1.42 \text{ \AA}$ , is equal to 0.077. Raising the temperature beyond graphitization, melting of graphite sheets

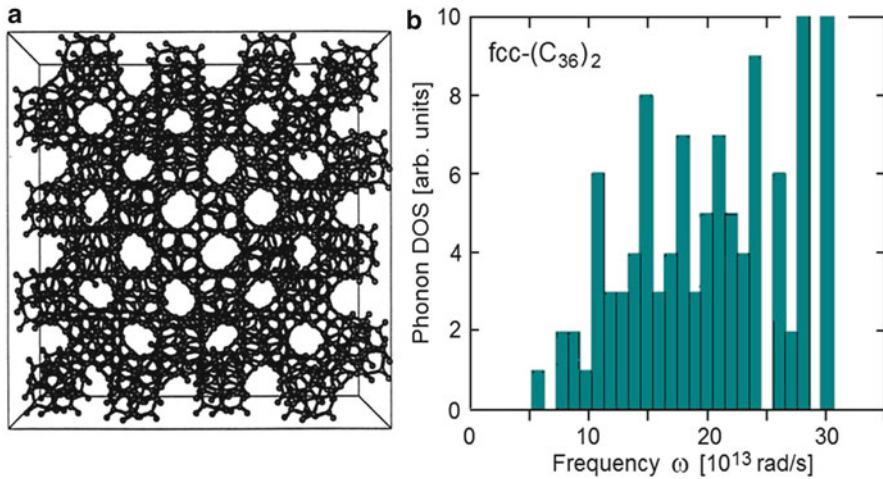


**Fig. 4.8** (a) The three-dimensional fcc lattice generated by the schwarzite  $(C_{36})_2$  (Image reproduced from Rosato et al. 1999, Copyright (1999) by the American Physical Society). (b) The predicted topological phonon distribution at zero wavevector for a single element of the schwarzite  $(C_{36})_2$  using adjacency matrix diagonalization

occurs. A simulation for graphene by Zakharchenko et al. (2011) gives a melting temperature of 4,900 K, which would correspond, on the basis of Eq. (4.5), to  $f_c = 0.085$ , in good agreement with the Lindemann criterion for carbon materials. In view of such a good correspondence for melting, this analysis provides therefore a criterion for the graphitization transition of schwarzite structures, which can be confidently fixed at  $f_c = 0.077$ .

#### 4.4.2 Topological Phonon Spectrum Versus Genus

It is interesting to compare the topological phonon spectrum for three isomeric structures mapped on closed surfaces of different genus  $g$ , for example, a sphere ( $g = 0$ ), a one-handle torus ( $g = 1$ ), and a two-handle torus ( $g = 2$ ). A very simple structure is a hypothetical fourfold coordinated molecule  $X_{20}$  with a single nearest-neighbor force constant (Fig. 4.9). The topological phonon spectra for shear displacements normal to the surface are shown in Fig. 4.10 for the three surfaces. The observed trend is a *compactification* of the spectrum towards the higher frequencies with increasing genus. Note that the three surfaces represent, in the case of threefold coordination, the topology of fullerene, nanotubes, and the unit cell of a squared planar schwarzite, respectively, the latter two with cyclic boundary conditions.

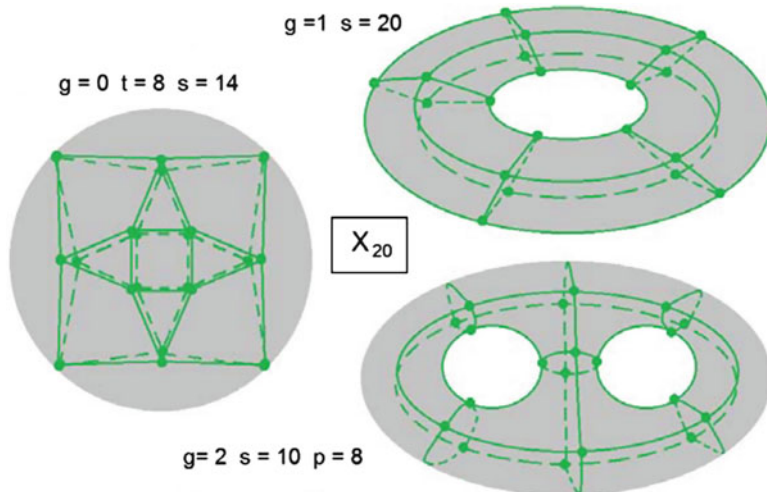


**Fig. 4.9** Isomeric structures of a hypothetical fourfold coordinated molecule  $X_{20}$  mapped on closed surfaces of different genus  $g$ : a sphere ( $g=0$ ), a one-handle torus ( $g=1$ ), and a two-handle torus ( $g=2$ )

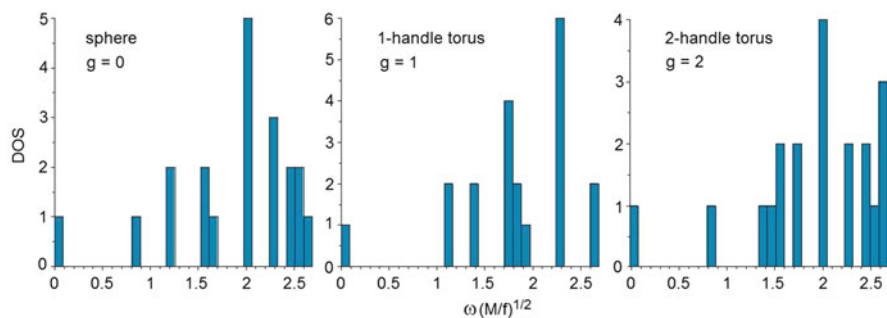


**Fig. 4.10** The topological phonon spectra for shear displacements normal to the surface for the fourfold coordinated isomers shown in Fig. 4.9. The increasing genus of the tessellated surface leads to a compactification of the spectrum towards higher frequencies with increasing genus

## 4.5 Planar Schwarzites

After the discovery of nanotubes (Iijima 1991), the prediction (Fig. 4.11, Spadoni et al. 1997) and the experimental realization of X- and Y-shaped nanotube junctions (Fig. 4.12b, Barborini et al. 2002; Fig. 4.12c, Satishkumar et al. 2000; Deepak et al. 2001) have been the object of an extensive investigation over a decade, with the aim of fabricating electronic devices on the nanoscale (Bandaru et al. 2005).

A more ambitious goal is the construction of complex structures of potential interest in nanoelectronics in one (*linear schwarzites*) and two dimensions (*planar*

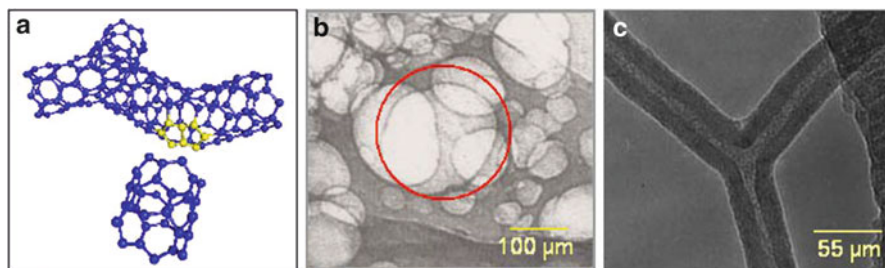


**Fig. 4.11** (a) Illustration of formation of Y-shaped nanojunctions through the welding of a nanotube at the knee of another nanotube and the replacement of two 5-membered rings (yellow) with four (two per corner) 7-membered rings (Reproduced by Spadoni et al. 1997 doi:10.1209/epl/i1997-00346-7. Copyright (1997) by IOP Publishing). Y-shaped nanotubes have been observed in both experiments (b) SCBD (Adapted with permission from Barborini et al. 2002. Copyright (2002), American Institute of Physics) and (c) pyrolysis; see also Satishkumar et al. (2000) and Deepak et al. (2001)

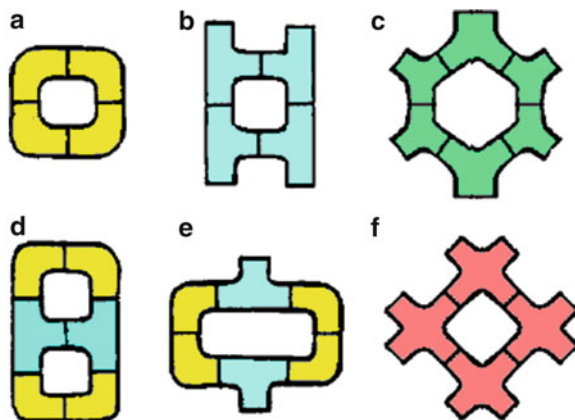


**Fig. 4.12** The plumber art of connecting elbow-shaped nanotubes (a) and T- (b) and Y-shaped (c) nanotube junctions allows for the fabrication of complex 0-D (d), 1-D (b, e), and 2-D networks (c) of potential use in nanoelectronics; 4-branched schwarzite elements (f) may be used for the construction of either planar or D-type 3-D networks (Adapted from Chernozatonskii 1993. Copyright (1993), with permission from Elsevier)

*schwarzites*) through the connection of nanotube segments, as envisaged in the early works by Chernozatonskii (1993) and Spadoni et al. (1997) and following experimental achievements by Terrones et al. (2002) and Romo-Herrera et al. (2007) (Fig. 4.13).

On pure geometrical grounds, these architectures could in principle be obtained also through a transformation of a graphene bilayer, where covalent bonds between the two graphene sheets are formed so as to join them through a periodic array of throats, in the manner illustrated in Fig. 4.14. The toll to be paid to topology

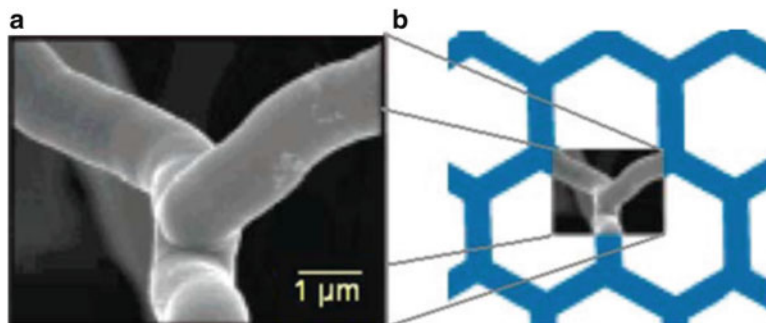


**Fig. 4.13** The welding of nanotubes (a) (Adapted with permission from Romo-Herrera et al. 2007. Copyright (2007) American Chemical Society) (From Terrones et al. 2002. © 2002 The American Physical Society) allows in principle to engineer periodic 2-D schwarzitic networks (b) suitable for nanoelectronics

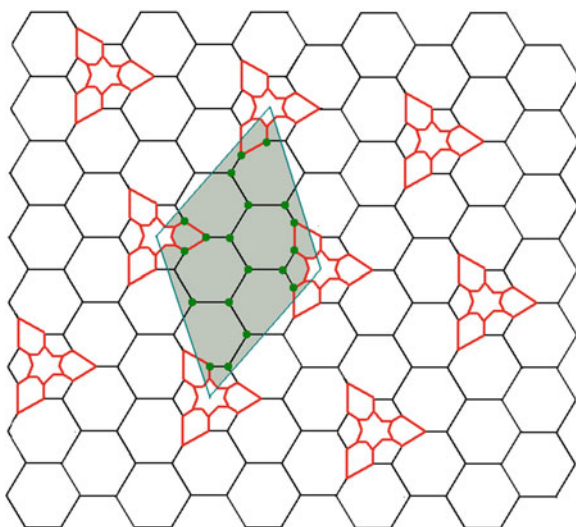


**Fig. 4.14** The transformation of a graphene bilayer into a planar schwarzite  $(C_{38})_2$ : A ring of six hexagons in the lower graphene sheet is transformed into a ring of six heptagons by inserting six new (red) bonds. In this way a throat is formed with six new (red) hexagons and dangling bonds to be saturated by the equivalent bonds of the specular upper portion. The smallest hexagonal array of such connections has a unit cell (gray area) made of  $19 \times 2$  atoms (green dots) (Reproduced from De Corato et al. 2012, ([https://www.novapublishers.com/catalog/product\\_info.php?products\\_id=33851](https://www.novapublishers.com/catalog/product_info.php?products_id=33851)). Copyright (2012) by Nova Science Publishers)

is the formation of a suitable number of 7-membered rings – 12 per throat. The smallest unit cell of this kind of planar graphite-like (G-type) schwarzites contains just 12 heptagons with no hexagonal ring and has the formula  $(C_{14})_2$  (Fig. 4.15).

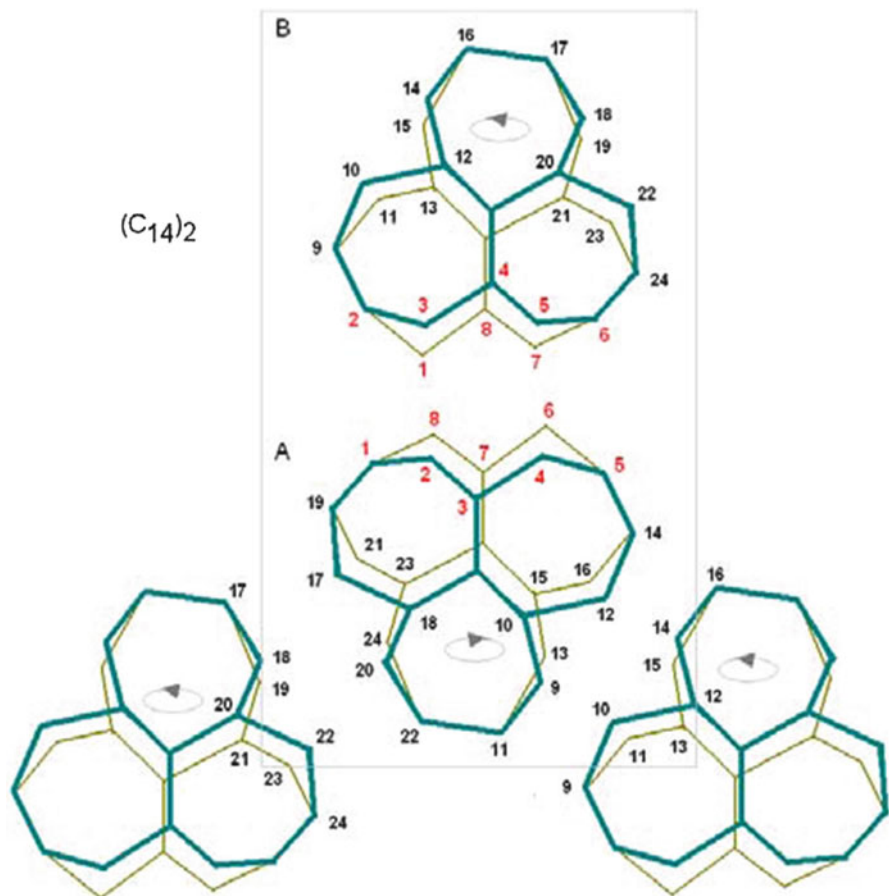


**Fig. 4.15** Elements of the smallest G-type planar schwarzite  $(C_{14})_2$  exclusively made of 7-membered rings. Two elements (A + B) form the unit cell of the periodic graphite-like lattice (Reproduced from De Corato and Benedek 2012. Copyright @ 2012 World Scientific, New York)

The threefold symmetric  $C_{14}$  elements can be connected in various ways by nanotubular throats as, for example, in the planar schwarzites  $(C_{18})_2$  and  $(C_{26})_2$  depicted in Fig. 4.16.

It should be noted that planar G-type schwarzites are all topologically equivalent, independently of the length of the nanotube connectors, with the same number (12) of 7-membered rings per unit cell. Due to the potential interest of planar schwarzites in devices, the characterization of possible defective structures by means of vibrational spectroscopies is rather important. The defect-induced modification of the vibrational spectrum represents another convenient example of the application of the topological phonon concept.



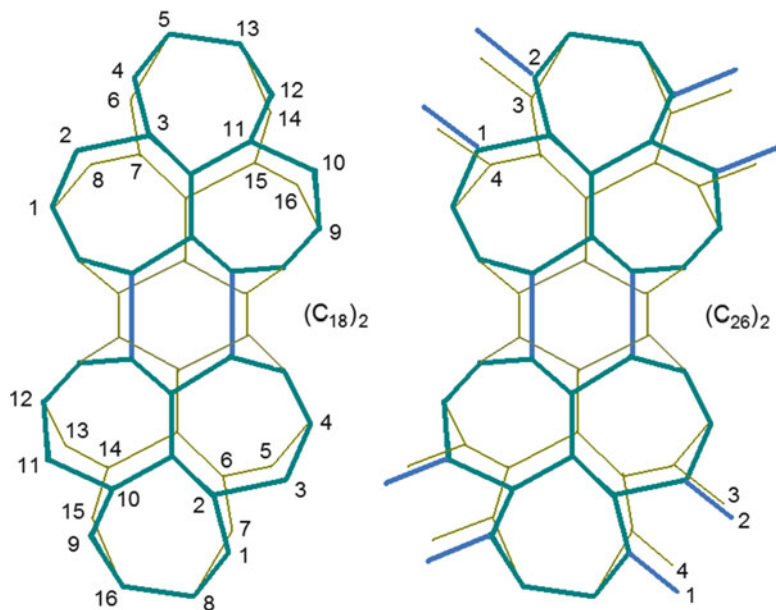


**Fig. 4.16** Graphs representing the planar schwarzites  $(C_{18})_2$  with one tubular neck per element and  $(C_{26})_2$  with three necks per element. A similar planar schwarzite with two such necks per element (not shown) has the formula  $(C_{22})_2$  (Reproduced from De Corato and Benedek 2012. Copyright © 2012 World Scientific, New York)

#### 4.5.1 *Vibrational Characterization of Perfect and Defective Planar Schwarzites*

Since infrared absorption and Raman vibrational spectroscopies only involve long-wave phonons, the calculation of the zero-wavevector ( $\mathbf{Q} = 0$ ) topological phonons for ideal and defective planar schwarzites should be sufficient for the characterization of their general features. As regards the defects, the following configurations have been considered: (a) the ideal planar schwarzite, (b) a single bond broken, (c) a single bond stiffened, (c) the stiffening of all the three bonds of an atom, (d) a mass defect, and (e) a vacancy. The calculated topological phonon spectra are shown in Figs. 4.17, 4.18, and 4.19 for  $(C_{14})_2$ ,  $(C_{18})_2$ , and  $(C_{26})_2$  and the five above defect configurations.

The main vibrational spectral features of schwarzite surfaces depend on the topological structure more than on their two-dimensional nature. In this respect the calculation of the defect perturbation of the phonon density of states (DOS) based on adjacency matrix approximation is sufficiently reliable as long as the general features are concerned. A reason for this prevalence of the topological effects is that the spectral perturbation mostly depends on the Hilbert transform of the bulk densities projected onto the defect sites, that is, on the real parts of the projected

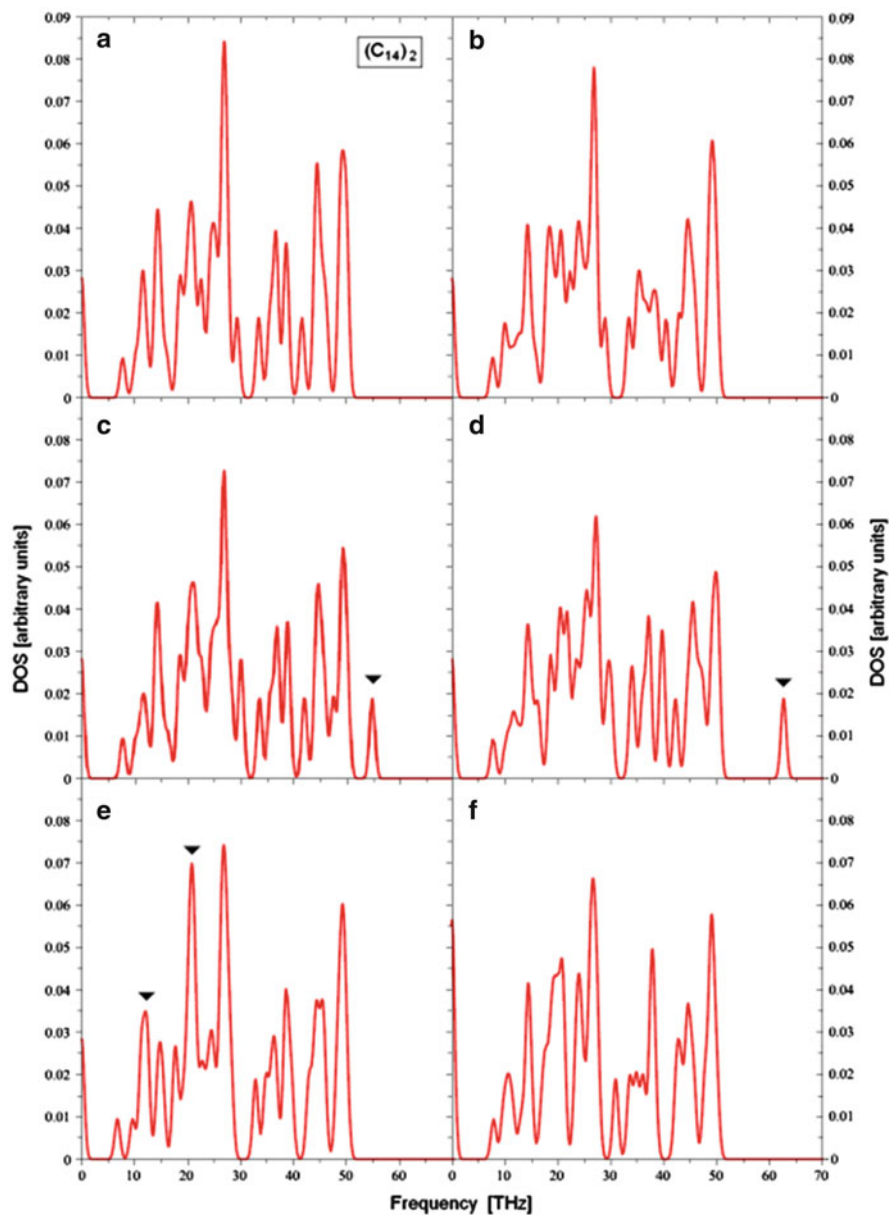


**Fig. 4.17** The topological vibrational spectra at zero wavevector of the smallest G-type planar schwarzite  $(C_{14})_2$ : (a) pure lattice, (b) one bond broken at a central atom, (c) one of the three force constants connecting a central atom is doubled, (d) all three force constants of a central atom are doubled, (e) the mass of a central atom is multiplied by 4, and (f) a vacancy at a central atom site (Reproduced from De Corato and Benedek 2012. Copyright © 2012 World Scientific, New York)

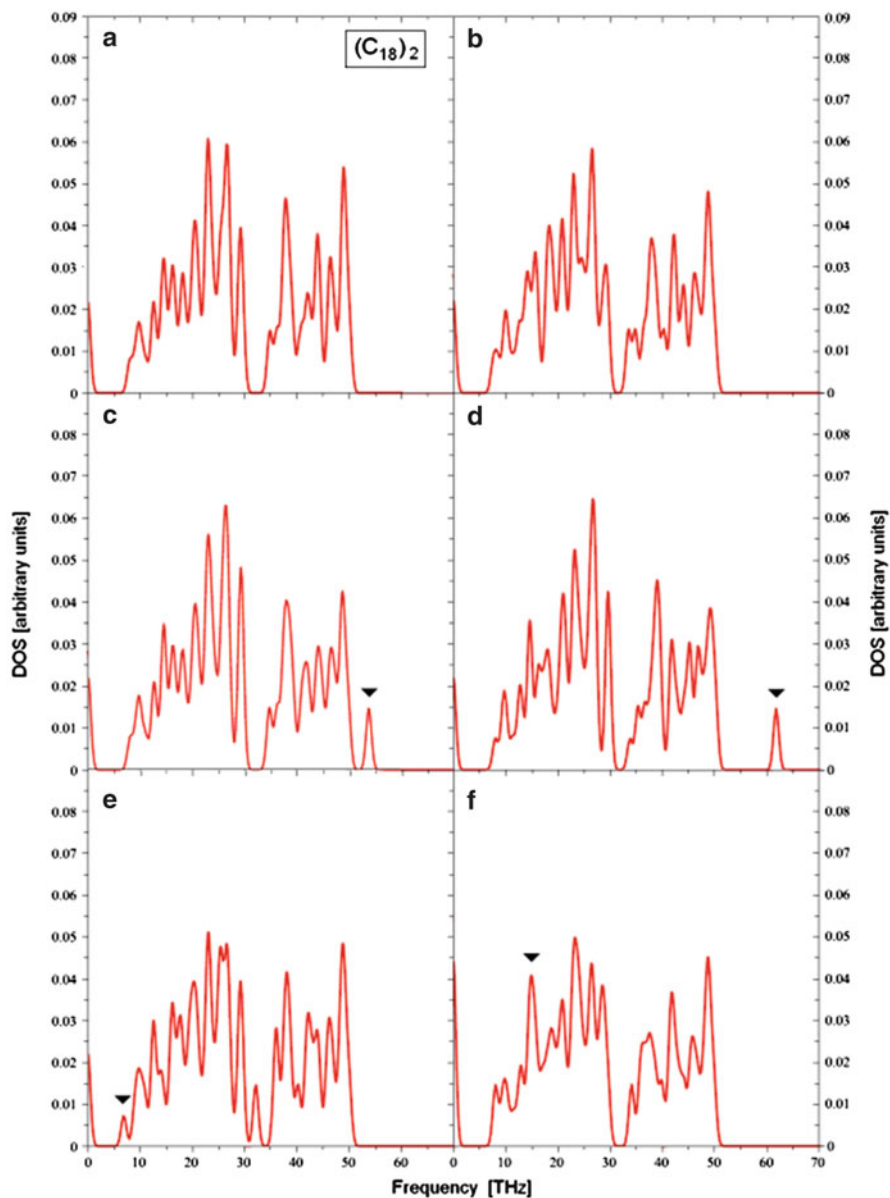


**Fig. 4.18** Same as in Fig. 4.17 for  $(C_{18})_2$  (Reproduced from De Corato and Benedek 2012. Copyright © 2012 World Scientific, New York)

Green's functions: They are integral functions and essentially depend on the gross features of the unperturbed spectra. In detail it appears that the stiffening of the force constants leads to localized modes above the maximum frequency of the

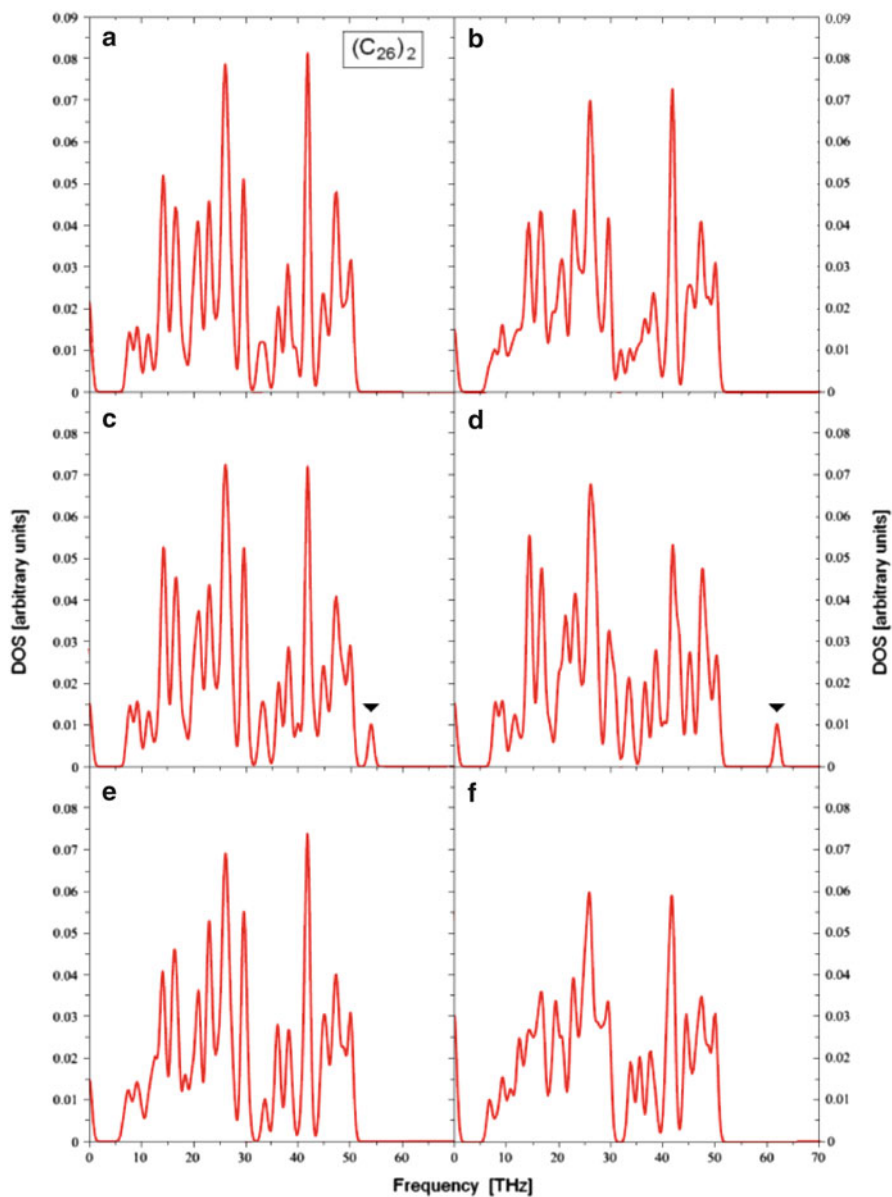


**Fig. 4.19** Same as in Fig. 4.17 for  $(C_{26})_2$  (Reproduced from De Corato and Benedek 2012. Copyright © 2012 World Scientific, New York)

unperturbed spectrum (black triangles in Figs. 4.17, 4.18, and 4.19c, d), whereas the break of bonds and the mass increase produce a general phonon softening, with the emergence of resonances in the lower part of the spectrum (black triangles in

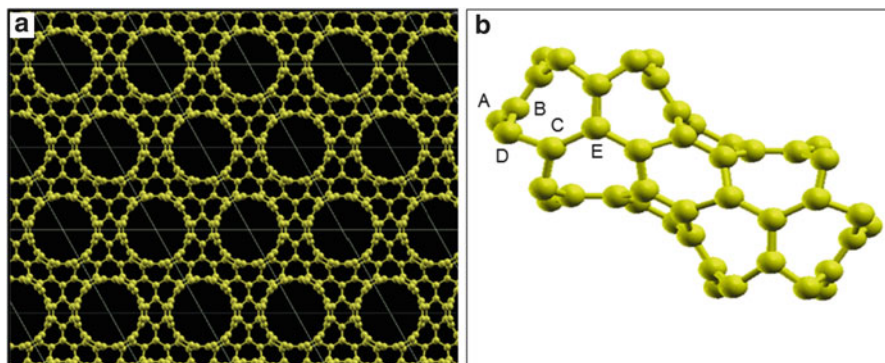


**Fig. 4.20**  $(C_{38})_2$  planar schwarzite: a top view of the lattice (a) and unit cell (b) (Reproduced from De Corato et al. 2012, (<https://www.novapublishers.com/catalog/productinfo.php?productsid=33851>). Copyright (2012) by Nova Science Publishers))

Figs. 4.17, 4.18e). In all structures there is a narrow gap around 32 THz, separating the lower phonon band of shear vertical (ZO) modes from the upper longitudinal (LO) and shear horizontal (SH) phonon bands. In some cases the local perturbation causes the appearance of a gap mode, as, for example, for a vacancy in  $(C_{14})_2$  (Fig. 4.17f) or a mass increase perturbation in  $(C_{18})_2$  (Fig. 4.18e).

These few examples illustrate the optical vibrational spectra expected for this class of graphene-like carbon nanostructures and the spectral modifications induced by defects, or in general by any local structure which may occur, for example, in functionalized  $sp^2$  carbon samples.

### 4.5.2 The Planar Schwarzite $(C_{38})_2$

In addition to the proposed structure, we have fully investigated another type of planar carbon schwarzite which has the standard nanotube connection and so is the best candidate for experimental growth. Ab initio calculations have been performed for this particular junction in order to investigate the geometry, the electronic structure, and its phonon frequency distribution at gamma. The carbon planar schwarzite like  $(C_{38})_2$  contains 12 hexagons and the canonical 12 heptagons per element. As argued from the top view of the structure obtained from ab initio calculations and of its unit cell (Fig. 4.20), there are short nanotubes made of six hexagons connected by islands made of six heptagons each. These features reflect in the band structure. The 2-D lattice is hexagonal within the layer group  $P6/mmm$  (80); only five atoms are found to be independent by symmetry.

The calculations are based on Quantum ESPRESSO codes (Giannozzi et al. 2009) within the density functional theory, with a Perdew-Burke-Ernzerhof exchange-correlation functional (Perdew et al. 1996), a ultrasoft pseudopotential

**Table 4.5** Ab initio cohesive energy per atom of the planar schwarzite  $(C_{38})_2$  with respect to other three-dimensional D-type schwarzites and diamond

Structure	Cohesive energy (eV/atom)	Conduction properties
Planar $(C_{38})_2$	7.91	Metal
D-type $(C_{28})_2$	7.66	Metal
D-type $(C_{36})_2$	7.71	Insulator
D-type $(C_{40})_2$	7.92	Metal
D-type $(C_{64})_2$	7.94	Metal
Diamond	8.36	Insulator

Gaito et al. (1998) and Spagnolatti et al. (2003)

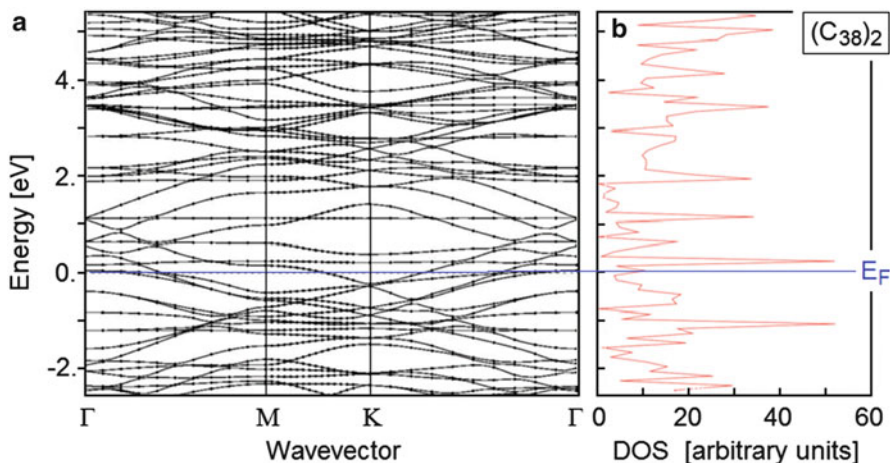


**Fig. 4.21** Electronic band structure (a) and density of states (DOS) (b) of the planar schwarzite  $(C_{38})_2$ . The zero energy corresponds to the Fermi level ( $E_F$ )

(Vanderbilt 1990), a plane-wave expansion of Kohn-Sham orbitals up to the kinetic cutoff of 30 Ry, and a charge-density cutoff up to 240 Ry. The integration over the Brillouin Zone (BZ) has been performed over a  $2 \times 2 \times 1$  Monkhorst-Pack mesh (Monkhorst and Pack 1976) corresponding to 2  $k$ -points in the irreducible two-dimensional wedge. The structure has been optimized by computing its equation of state at zero temperature (energy per unit area) keeping a vacuum distance of 15 Å within the replicas in order to avoid their interaction. The optimized lattice parameter turns out to be  $a = 10.82$  Å. The calculated cohesive energy with respect to that of diamond (Table 4.5) is consistent with previous calculations for three-dimensional schwarzites (Gaito et al. 1998; Spagnolatti et al. 2003).

The planar schwarzite  $(C_{38})_2$ , as appears from the calculated band structure along high symmetry directions (Fig. 4.21a), is metallic. The band structure shows a large number of flat bands due to the presence of heptagonal rings which break conjugation. This peculiarity, similar to that of 3-D schwarzites (Spagnolatti et al. 2003), yields sharp peaks in the electronic density of states (Fig. 4.21b).

**Table 4.6** The five local (first-order) Wiener indices  $w_i^{(1)}$  of  $(C_{38})_2$  compared with the respective bond lengths from an ab initio calculation

Atom	$w_i^{(1)}$	Average bond length (Å)			
		$d_1$ (Å)	$d_2$ (Å)	$d_3$ (Å)	
A	345	1.408	1.37	1.42	1.42
B	346	1.415	1.46	1.36	1.42
C	348	1.494	1.52	1.48	1.48
D	349	1.455	1.46	1.48	1.42
E	352	1.522	1.52	1.52	1.52

Topology, in particular graph theory, also allows predicting the relative stability of isomers and single atoms. As explained in the next section, for  $sp^2$ -bonded structures, this goal can be achieved by using the Wiener index (Wiener 1947). This topological index provides a stability hierarchy of various isomers in the sense that, to a good approximation, the minimum value of the Wiener indices for various isomeric structures indicates the most stable one. This topological approach has been proven successful in the prediction, for example, of the most stable isomers of the fullerene  $C_{66}$  (Vukicevic et al. 2011).

Also the stability hierarchy of single atoms can be established by the ordering of local Wiener indices. Each independent atom has its particular local Wiener index according to its topological position in the graph, and the best connected atom is shown to give the minimum local Wiener index. On the contrary, the least connected atom will provide the maximum local Wiener index. Due to symmetry, only a limited number of independent atoms have different local Wiener indices. In the case of  $(C_{38})_2$ , there are only five independent atoms in the unit cell, indicated by the letters A to E in Fig. 4.20b. The corresponding local Wiener indices are reported in Table 4.6 and compared with the medium bond length obtained from DFT calculations.

It appears from Table 4.6 that the most stable atom (A), having the shortest average bond length, also has the minimum local Wiener index. Similarly the least stable (E) atom with the longest bond lengths has the maximum local Wiener index. The correspondence is however not so precise for the intermediate values. As seen in the next section, the Wiener index is the simplest among various topological indices. Better performances with respect to stability can be obtained with other indices like higher-order Wiener and efficiency. In practice, the stability of single atoms is also related to their chemical reactivity.

## 4.6 A Physical Basis for the Wiener Index

The physical meaning of the Wiener index for a conjugated  $sp^2$  carbon network and its role in providing a stability hierarchy of isomers can be derived from a tight-binding model for the  $\pi$  electron band structure. Although in the tight-binding picture only nearest-neighbor (nn) matrix elements of the Hamiltonian and overlap integrals between  $p_z$  atomic orbitals are considered, conjugation effects are felt at

large topological distances and contribute a long-range potential energy term which depends on the isomer topology. The wavefunctions of the  $\pi$  electronic band are written as linear combination of atomic orbitals:

$$\psi_k(\mathbf{r}) = \mathcal{N}_k^{-1/2} \sum_m e_{km} \varphi(\mathbf{r} - \mathbf{r}_m), \quad (4.6)$$

where  $k$  labels the electronic states,  $m$  the atoms of the network at positions  $\mathbf{r}_m$ , and  $e_{km}$  are the projections of the wavefunctions  $\psi_k$  on the atomic orbitals  $\varphi(\mathbf{r} - \mathbf{r}_m)$ . Normalization requires that

$$\mathcal{N}_k \equiv \sum_{l'l'} e_{kl'}^* e_{kl} s_{l'l'} = 1 + \sum_{ln_l} \left( e_{kl}^* e_{kn_l} s_{ln_l} + e_{kn_l}^* e_{kl} s_{n_l l} \right), \quad (4.7)$$

where

$$s_{mm'} \equiv \int d^3r \varphi^*(\mathbf{r} - \mathbf{r}_m) \varphi(\mathbf{r} - \mathbf{r}_{m'}) = \begin{cases} 1 & m' = m \\ s_{mn} & m' = n \text{ of } m \equiv n_m; \\ 0 & m' \neq m, n_m \end{cases} \quad (4.8)$$

index  $n_m$  labels the three closest atoms of atom  $m$ . The contribution of the electron in the state  $k$  to the expectation value of the energy  $U_m(\mathbf{r})$  of an atom at a conventional origin ( $m = 0$ ) is written as

$$\langle U_0 \rangle_k = \mathcal{N}_k^{-1} \sum_{mm'} e_{km}^* e_{km'} \int d^3r \varphi^*(\mathbf{r} - \mathbf{r}_m) U_0(\mathbf{r}) \varphi(\mathbf{r} - \mathbf{r}_{m'}). \quad (4.9)$$

Although the matrix element in Eq. (4.9) is nonvanishing only for  $m', m = 0, n_0$ , the above expression is a function of the atom positions at any distance  $\mathbf{r}_m$  from the origin via the normalization factor. Its derivative with respect to  $\mathbf{r}_m$  for  $m \neq 0, n_0$ , after some algebraic manipulation, is found to be

$$\begin{aligned} \frac{\partial \langle U_0 \rangle_k}{\partial \mathbf{r}_m} &= -\mathcal{N}_k^{-1} \langle U_0 \rangle_k \sum_{l'l'} e_{kl'}^* e_{kl} (\delta_{l'm} - \delta_{lm}) \boldsymbol{\gamma}_{l'l'} \\ &\quad + 2\mathcal{N}_k^{-1} \text{Re} \sum_l e_{km}^* e_{kl} \int d^3r U_0(\mathbf{r}) \phi(\mathbf{r} - \mathbf{r}_l) \frac{\partial}{\partial \mathbf{r}} \phi^*(\mathbf{r} - \mathbf{r}_m) \\ &\equiv \mathbf{F}_{k,m0}. \end{aligned} \quad (4.10)$$

where

$$\boldsymbol{\gamma}_{l'l'} = -\boldsymbol{\gamma}_{l'l}^* = \begin{cases} \int d^3r \frac{\partial \varphi^*(\mathbf{r} - \mathbf{r}_l)}{\partial \mathbf{r}} \varphi(\mathbf{r} - \mathbf{r}_{l'}), & l' = n_l, \\ 0, & l' \neq n_l, \end{cases} \quad (4.11)$$



The vectors  $\boldsymbol{\gamma}_{l'l}$  are nonvanishing only when  $l$  and  $l'$  are nearest neighbor and are directed along the  $ll'$  bond. Consistently with the tight-binding approximation, the integral term in Eq. (4.10) is hereafter neglected, since  $m \neq 0, n_0$ . Equation (4.10) defines a nonvanishing long-range force  $\mathbf{F}_{k,m0}$  between atoms 0 and  $m$  acting due to an electron in the  $k$ -th state of the  $\pi$ -band. The sum over all band states,  $\sum_k \mathbf{F}_{k,m0}$ , is null due to the completeness of coefficients  $e_{kl}$ , but the sum restricted to the occupied states of an unfilled band, like that required by conjugation, generally yields a nonvanishing force, which we call *conjugation force*. On the other hand, it is easily seen that the sum over the conjugation forces exerted by all atoms  $m$  on atom 0 vanishes,  $\sum_m \mathbf{F}_{k,m0} = 0$ , as required by equilibrium.

We now search a potential for the conjugation forces. After neglecting the integral term in Eq. (4.10), the latter can be rewritten as

$$\begin{aligned} \frac{\partial}{\partial \mathbf{r}_m} \ln \langle U_0 \rangle_k &= -2\mathcal{N}_k^{-1} \operatorname{Re} \sum_l e_{kl}^* e_{km} \boldsymbol{\gamma}_{lm} \\ &= -2\mathcal{N}_k^{-1} \operatorname{Re} \left[ e_{km}^* \sum_{n_m} e_{kn_m} \boldsymbol{\gamma}_{mn_m} \right] \equiv -\boldsymbol{\alpha}_{k;m}. \end{aligned} \quad (4.12)$$

For  $\langle U_0 \rangle_k$  a central potential, vector  $\boldsymbol{\alpha}_{k;m}$ , expressing the inverse of the conjugation potential range, points in the same direction as  $\mathbf{r}_m$ , as one can argue from a careful inspection of Eqs. (4.10) and (4.11) when the wavefunctions  $\varphi(\mathbf{r})$  refer to  $p_z$  states. However, it does not depend explicitly on the position of the atom  $m$  but on the phase changes of the  $k$ -th wavefunction, associated to the products  $e_{km}^* e_{kn_m}$ , between atom site  $m$  and its nearest neighbors  $n_m$ . For a double bond between  $m$  and one of its neighbors,  $e_{km}^* e_{kn_m}$  is positive, whereas the other two single bonds starting from  $m$  give a negative  $e_{km}^* e_{kn_m}$ . Thus, the inverse-range vector  $\boldsymbol{\alpha}_{k;m}$  is in general nonvanishing; it is however of order  $N^{-1}$ , with  $N$  the number of atoms, due to the normalization to unity of the coefficients  $e_{km}$ . It should be noted, however, that these arguments are valid for threefold coordination and could fail, for example, for atoms on the contour of the network. We assume that the contour effects are either removed by periodic boundary conditions or neglected by considering a large number  $N$  of atoms.

It is now convenient to consider the network of  $N$  atoms as made of  $s$  atomic shells, each shell including the  $s_j$  atoms which have the same topological distance  $j$  from the origin atom ( $j=0$ ). Since the maximum topological distance normally depends on the choice of the origin atom,  $s$  is defined as the maximum topological distance in the given network. With these definitions, a sum over the atom index  $m$  from 0 to  $N-1$  is replaced by a sum over the  $s_j$  atoms belonging to the  $j$ -th shell times the sum over the  $s+1$  shells (including the origin,  $j=0$ ,  $s_0=1$ ), that is, by a sum over the indices  $(i,j)$ :

$$\sum_{l=0}^{N-1} \rightarrow \sum_{j=0}^s \sum_{i=1}^{s_j}. \quad (4.13)$$

With the prescription of a constant  $\mathcal{N}_k$  referred to the equilibrium configuration, the conjugation force  $\mathbf{F}_{k,m0}$  can be derived from the potential energy:

$$\begin{aligned} U_k^{(c)}(r_{i,j}) &= U_k \exp[-\alpha_{k;i,j} \cdot (\mathbf{r}_{i,j} - \mathbf{r}_{i,j-1}) - (j-1)\beta_{k;i,j}a] \\ &= U_k \exp(-j\beta_{k;i,j}a), \end{aligned} \quad (4.14)$$

where index  $i$  has been conventionally used for the atom on each shell belonging to the shortest topological path from atom 0 to atom  $m = (i,j)$ . We have defined  $a$  as the average interatomic distance and

$$\beta_{k;i,j} \equiv \alpha_{k;i,j} \cdot \frac{\mathbf{r}_{i,j} - \mathbf{r}_{i,j-1}}{a} \quad (4.15)$$

as the projections of the inverse-range vectors onto the bonds connecting atom  $(i,j-1)$  to atom  $(i,j)$ .  $U_k$  is an integration constant which eventually needs to be derived from ad hoc ab initio calculations and is expected to be negative (attractive), similarly to tight-binding resonance integrals between nearest neighbors. A dimensional argument requires  $U_k = o(N^{-2})$ .

The total conjugation potential energy  $U_{0,N}$  of atom 0 in an  $sp^2$  network of  $N$  atoms is calculated by summing over all occupied electron states of the  $\pi$ -band and all atoms  $m = (i,j)$ :

$$\begin{aligned} U_{0,N} &= \sum_k^{(\text{occ})} \sum_{j=0}^s \sum_{i=1}^{s_j} U_k \exp(-j\beta_{k;i,j}a) \\ &= \sum_k^{(\text{occ})} \sum_{j=0}^s \sum_{i=1}^{s_j} U_k \left[ 1 - j\beta_{k;i,j}a + o(\beta_{k;i,j}^2) \right] \\ &\equiv \sum_k^{(\text{occ})} U_k \sum_{j=0}^s s_j \left[ 1 - j\bar{\beta}_k a + o(\bar{\beta}_k^2) \right] \\ &= U_\infty - w_0^{(1)} \left( a \sum_k^{(\text{occ})} U_k \bar{\beta}_k \right) + w_0^{(2)} \left( a^2 \sum_k^{(\text{occ})} U_k \bar{\beta}_k^2 \right) - \dots, \end{aligned} \quad (4.16)$$

where in the third row of Eq. (4.16), the inverse-range constants have been substituted by their average  $\bar{\beta}_k$ . It is this important approximation which allows expressing the conjugation potential energy in terms of the *local Wiener index of order 1 for site 0*

$$w_0^{(1)} \equiv \sum_{j=0}^s j s_j, \quad (4.17)$$

of the *local Wiener index of order 2 for site 0*,

$$w_0^{(2)} \equiv \frac{1}{2} \sum_{j=0}^s j^2 s_j, \quad (4.18)$$

etc. Actually, the expansion to all orders of the exponent in Eq. (4.10) involves the *local Wiener index of order n for site 0*

$$w_0^{(n)} \equiv \frac{1}{n!} \sum_{j=0}^s j^n s_j. \quad (4.19)$$

One may also consider the *exponential local Wiener index for site 0*

$$w_0^{(\text{exp})} \equiv \sum_n (-1)^n w_0^{(n)} = \sum_{j=0}^s s_j e^{-j}. \quad (4.20)$$

As regards the dependence on the network size, that is, on atom number  $N$ , the sum  $\sum_k^{(\text{occ})} U_k$  over the occupied states  $k$  is of order  $N^{-1}$  and the first term in Eq. (4.16) tends to a constant  $U_\infty$  for  $N \rightarrow \infty$  which is independent of the site. The Wiener index  $w_0^{(1)}$  for a single site grows with the number of atoms as  $N^{\beta/2}$ , so that the term in Eq. (4.10) proportional to  $w_0^{(1)}$  is of order  $N^{-1/2}$ . Similarly  $w_0^{(n)} \sim o(N^{1+n/2}/n!)$  and therefore the corresponding term in the expansion of Eq. (4.16) is of order  $N^{-n/2}/n!$

Since  $U_k < 0$  and  $\bar{\beta}_k > 0$ , Eq. (4.10) tells that, for a sufficiently large  $N$  so that only the Wiener index of order 1 is retained in the expansion, the network site 0 which gives a *minimum of the conjugation potential energy corresponds to a minimum in the local Wiener index*  $w_0^{(1)}$ . For small atom numbers  $N$  the local higher-order Wiener indices may not be negligible and deviations from the minimum- $w_0^{(1)}$  rule may occur. The sum over all sites gives the total conjugation potential energy:

$$U_N^{\text{tot}} = NU_\infty - W^{(1)} \left( a \sum_k^{(\text{occ})} U_k \bar{\beta}_k \right) + W^{(2)} \left( a^2 \sum_k^{(\text{occ})} U_k \bar{\beta}_k^2 \right) - \dots \quad (4.21)$$

where

$$W^{(1)} = \frac{1}{2} \sum_{h=0}^{N-1} w_h^{(1)}, \quad W^{(2)} = \frac{1}{2} \sum_{h=0}^{N-1} w_h^{(2)}, \dots \quad (4.22)$$

are the Wiener indices of order 1, 2, ... of the network. The factor  $\frac{1}{2}$  is needed to avoid double counting of the interaction terms. In the first-order approximation, the minimum of the Wiener index of order 1 indicates the most stable isomer.

Moreover, it is convenient to define the *topological efficiency index*  $\rho$  as follows (Ori et al. 2009):

$$\rho = \frac{W^{(1)}}{N w_{\min}^{(1)}}, \quad (4.23)$$

where  $w_{\min}^{(1)}$  is the minimum of the local Wiener indices  $w_h^{(1)}$ . In case all sites are equivalent (as, e.g., for the icosahedral isomer of  $C_{60}$ ) so as to give the same local Wiener index, it is  $\rho = 1$ . In any other isomer with inequivalent sites, that is, with a lower symmetry, it is  $\rho > 1$ , its departure from unity being a measure of a lower topological efficiency.

Within this approach also physical properties directly related to the energy  $U_{0,N}$  can in principle be expanded with the respect to the Wiener indices of increasing order, similarly to Eq. (4.16). Among these properties of fundamental importance are the electronegativity  $\chi$  and chemical hardness  $\eta$ , which are its first- and second-order functional derivatives of the total energy with respect to the electron density, respectively (see Chap. 9). Actually the present approach leads with a novel way in re-defining the so called intrinsic framework electronegativity (Genechten et al. 1987) and chemical hardness, which can be written as

$$\chi^W = \sum_k X_k W^{(k)}, \quad (4.24)$$

$$\eta^W = \sum_k H_k W^{(k)}, \quad (4.25)$$

where  $X_k$  and  $H_k$  are suitable coefficients to be determined from the functional derivation of the conjugation energy expressed by Eq. (4.16). Similar expressions can be obtained for the respective local quantities in terms of the local Wiener indices of increasing order, thus providing an analytical route to the coloring procedure (see Chap. 9). The minimal properties, illustrated for the Wiener indices and topological indicators like the topological efficiency index  $\rho$ , reflect also on the derived properties, providing fruitful routes for assessing stability (e.g., minimum topological electronegativity  $\chi^W$  and maximum topological chemical hardness  $\eta^W$ ) or reactivity ( $\max \chi^W$ ,  $\min \eta^W$ ). They work as abstract chemical reactivity principles (Putz 2010, 2011) among various nano-isomers based on topo-chemical reactivity.

## 4.7 Conclusions

It has been shown that  $sp^2$ -bonded extended systems host an infinite-range interaction associated with conjugation. This global property dominates in many respects over local features so as to make the general topological characteristics of the structure, such as the genus of the supporting surface, the eigenvalues and eigenvectors

of the adjacency matrix, the total and local Wiener indices, and the topological efficiency of the corresponding graph, sufficient to estimate many general physical properties such as global and local stability. It is shown elsewhere in this book (Putz et al., Chap. 9) that also local chemical properties such as the chemical potential, chemical hardness, and reactivity can be referred to local topological properties. Topological intrinsic defects in  $sp^2$ -carbon structures can as well be characterized by topological indices as far as their stability and thermodynamic probability are concerned. Besides establishing a stability hierarchy of isomers, which is relevant to the configurational entropy of the structure, the topological approach also allows to approximately determine the vibrational contribution to the thermodynamic functions through the diagonalization of the adjacency matrix. The discussion presented in Sect. 4.5 on physical meaning of the stability criteria based on topological indices also warns about the limitations of these indices when applied to small systems. Higher-order Wiener indices may be necessary for a more precise and predictive analysis of isomer stability. Neither this convergence issue nor the effectiveness of the local exponential Wiener index has been so far investigated in comparison with first-principle calculation of the electronic structure. In view of the enormous potential of the topological approach and its numerical applications in disentangling relevant physical properties of complex structures, it is hoped that this chapter will stimulate further studies in this direction.

**Acknowledgements** We thank Prof. Antonio Papagni and Dr. Gabriele Cesare Sosso (University of Milano-Bicocca), and Dr. Fabio Petrucci (EPFL, Lausanne) for many stimulating discussions. One of us (GB) acknowledges Ikerbasque (ABSIDES project) and the Donostia International Physics Center (DIPC) for support. MVP thanks Romanian Ministry of Education and Research for support through the CNCS-UEFISCDI project Code TE-16/2010-2013.

## References

- Agarwal S, Zhou X, Ye F, He Q, Chen GCK, Soo J, Boey F, Zhang H, Chen P (2010) *Langmuir Lett* 26:2244
- Arcon D, Jaglicic Z, Zorko A, Rode AV, Christy AG, Madsen NR, Gamaly EG, Luther-Davies B (2006) *Phys Rev B* 74:014438
- Bandaru PR, Daraio C, Jin S, Rao AM (2005) *Nat Mater* 4:663
- Barborini E, Piseri P, Milani P, Benedek G, Ducati C, Robertson J (2002) *Appl Phys Lett* 81:3359; highlighted by E Gerstner, *Nature, Materials Update*, 7 Nov 2002. <http://www.nature.com/materials/news/news/021107/portal/m021107-1.html>
- Benedek G, Milani P, and Ralchenko VG (eds) (2001) *Nanostructured carbon for advance applications*. Kluwer, Dordrecht and papers therein
- Benedek G, Vahedi-Tafreshi H, Barborini E, Piseri P, Milani P, Ducati C, Robertson J (2003) *Diamond Relat Mater* 12:768
- Benedek G, Vahedi-Tafreshi H, Milani P, Podestà A (2005) *Fractal growth of carbon schwarzites*. In: Beck C et al (eds) *Complexity, metastability and non-extensivity*. World Scientific, Singapore, pp 146–155
- Benedek G, Bernasconi M, Cinquanta E, D'Alessio L, De Corato M (2011) The topological background of schwarzite physics. In: Cataldo F, Graovac A, Ottorino O (eds) *Mathematics*

- and topology of fullerenes, Springer series on carbon materials chemistry and physics. Springer, Heidelberg/Berlin, Chap 12
- Bogana M, Donadio D, Benedek G, Colombo L (2001) *Europhys Lett* 54:72
- Bongiorno G, Lenardi C, Ducati C, Agostino RG, Caruso T, Amati M, Blomqvist M, Barborini E, Piseri P, La Rosa S, Colavita E, Milani P (2005) *J Nanosci Nanotechnol* 10:1
- Boscolo I, Milani P, Parisotto M, Benedek G, Tazzioli F (2000) *J Appl Phys* 87:4005
- Bühl M, Hirsch A (2001) *Chem Rev* 101:1153
- Cappelletti RL, Copley JRD, Kamitakahara WA, Li F, Lannin JS, Ramage D (1991) *Phys Rev Lett* 66:3261
- Castro Neto AH, Guinea F, Peres NMR, Novoselov KS, Geim AK (2009) *Rev Mod Phys* 81:109
- Chernozatonskii LA (1993) *Phys Lett A* 172:173
- De Corato M, Benedek G (2012) Dynamics and spectral properties of free-standing negatively curved carbon surfaces. In: Proceedings of the 49th course of the international school of solid state physics. Edited by: Antonio Cricenti (Istituto di Struttura della Materia, Italy). World Scientific, New York
- De Corato M, Benedek G, Ori O, Putz MV (2012) *Int J Chem Model* 4:105–114
- Deepak FL, Govindaraj A, Rao CNR (2001) *Chem Phys Lett* 345:5
- Diederich L, Barborini E, Piseri P, Podestà A, Milani P, Scheuwli A, Gallay R (1999) *Appl Phys Lett* 75:2662
- Donadio D, Colombo L, Milani P, Benedek G (1999) *Phys Rev Lett* 84:776
- Ferrari AC, Satyanarayana BS, Robertson J, Milne WI, Barborini E, Piseri P, Milani P (1999) *Europhys Lett* 46:245
- Gaito S, Colombo L, Benedek G (1998) *Europhys Lett* 44:525
- Geim AK, Novoselov KS (2007) *Nat Mater* 6:183
- Genechten KA van, Mortier WJ, Geerlings P (1987) *J Chem Phys* 86:5063
- Gersten JI, Smith FW (2001) *The physics and chemistry of materials*. Wiley, New York, 176
- Giannozzi P, Baroni S, Bonini N, Calandra M, Car R, Cavazzoni C, Ceresoli D, Chiarotti GL, Cococcioni M, Dabo I, Dal Corso A, Fabris S, Fratesi G, de Gironcoli S, Gebauer R, Gerstmann U, Gougoussis C, Kokalj A, Lazzeri M, Martin-Samos L, Marzari N, Mauri F, Mazzarello R, Paolini S, Pasquarello A, Paulatto L, Sbraccia C, Scandolo S, Sclauzero G, Seitsonen AP, Smogunov A, Umari P, Wentzcovitch RM (2009) QUANTUM ESPRESSO: a modular and open-source software project for quantum simulations of materials. *J Phys Condens Matter* 21:395502
- Iijima S (1991) *Nature* 324:56
- Kroto HW, Heath JR, O'Brien SC, Curl RF, Smalley RE (1985) *Nature* 318:162
- László I, Rassat A, Fowler PW, Graovac A (2001) *Chem Phys Lett* 342:369
- Lenosky T, Gonze X, Teter M, Elser V (1992) *Nature* 355:333
- Manolopoulos DE, Fowler PW (1992) *J Chem Phys* 96:7603
- McKay AL (1985) *Nature* 314:604
- McKay AL, Terrones H (1991) *Nature* 352:762
- Monkhorst HJ, Pack JD (1976) *Phys Rev B* 13:5188
- Novoselov KS, Geim AK, Morozov SV, Jiang D, Zhang Y, Dubonos SV, Grigorieva IV, Firsov AA (2004) *Science* 306:666
- Novoselov KS, Geim AK, Morozov SV, Jiang D, Katsnelson MI, Grigorieva IV, Dubonos SV, Firsov A (2005a) *Nature* 438:197
- Novoselov KS, Jiang D, Booth T, Khotkevich VV, Morozov SM, Geim AK (2005b) *Proc Natl Acad Sci USA* 102:10451
- O'Keeffe M, Adams GB, Sankey OF (1992) *Phys Rev Lett* 68:2325
- Ori O, Cataldo F, Graovac A (2009) *Fuller Nanotub Carbon Nanostruct* 17(3):308–323
- Perdew JP, Burke K, Ernzerhof M (1996) *Phys Rev Lett* 77:3865
- Pintschovius L (1996) *Rep Prog Phys* 59:473, and references therein
- Putz MV (2010) *MATCH Commun Math Comput Chem* 64:391–418
- Putz MV (2011) In: Putz MV (ed) *Carbon bonding and structures: advances in physics and chemistry*. Series of carbon materials: chemistry and physics. Springer, London, pp 1–32

- Rode V, Gamaly EG, Christy AG, Fitz Gerald JG, Hyde ST, Elliman RG, Luther-Davies B, Veinger AI, Androulakis J, Giapintzakis J (2004) *Phys Rev B* 70:054407, highlighted by R F Service (2004) *Science* 304:42
- Romo-Herrera JM, Terrones M, Terrones H, Dag S, Meunier V (2007) *Nano Lett* 7:570
- Rosato V, Celino M, Gaito S, Benedek G (1999) *Phys Rev B* 60:16928
- Satishkumar BC, John Thomas P, Govindaraj A, Rao CNR (2000) *Appl Phys Lett* 77:2530
- Schwarz HA (1990) *Gesammelte Mathematische Abhandlungen*, 11. Springer, Berlin
- Spadoni S, Colombo L, Milani P, Benedek G (1997) *Europhys Lett* 39:269
- Spagnolatti I, Bernasconi M, Benedek G (2003) *Eur Phys J B* 32(2):181–187
- Terrones H, McKay AL (1993) In: Kroto HW, Fisher JE, Cox DE (eds) *The fullerenes*. Pergamon Press, Oxford, p 113
- Terrones M, Banhart F, Grobert N, Charlier JC, Terrones H, Ajayan PM (2002) *Phys Rev Lett* 89:075505
- Townsend SJ, Lenosky T, Muller DA, Nichols CS, Elser V (1992) *Phys Rev Lett* 69:921
- Vanderbilt D (1990) *Phys Rev B* 41:7892
- Vanderbilt D, Tersoff J (1992) *Phys Rev Lett* 68:511
- Vukicevic D, Cataldo F, Ori O, Graovac A (2011) *Chem Phys Lett* 501(4–6):442
- Wiener H (1947) *J Am Chem Soc* 1(69):17
- Zakharchenko KV, Fasolino A, Los JH, Katsnelson MI (2011) *J Phys Condens Matter* 23:202202

# Chapter 5

## Topochemistry of Spatially Extended $sp^2$ Nanocarbons: Fullerenes, Nanotubes, and Graphene

Elena F. Sheka

**Abstract** This chapter presents  $sp^2$  nanocarbons as a new class of topochemical species from the insight of the computational study of peculiar properties that accompany the formation of different composite, at least, one member of that is a  $sp^2$  nanocarbon. The composites, which are resulted from either the “double-(C–C)-bond” reactions between two  $sp^2$  nanocarbons or the “atom-(C–C)-bond” reactions, concerned with a monatomic species deposition on the nanocarbons, manifest clearly seen properties that can be addressed to the action of either internal or external topology. The internal topology is attributed to the inherited properties of each nanocarbon while the external topology is related to external factors that drastically influence the chemical reactions involving nanocarbons.

### 5.1 Introduction

The modern topology in chemistry covers two large valleys, namely, formal, mathematical and empirical, chemical. The former is concerned with the description of molecular structures on the basis of finite topological spaces. The space shows itself as a mathematical image or instrument of theoretical study. A large collection of comprehensive reviews, related to a topological description of fullerenes from this viewpoint, has recently been published (Cataldo et al. 2011). The second field covers vastly studied topochemical reactions. The space in this case is a physical reality defining the real place where the reactions occur. If the appearance of mathematical topology in chemistry can be counted off the publication of the Merrifield and Simmons monograph in 1989 (Merrifield and Simmons 1989), topochemical reactions have been studying from the nineteenth century (see Schmidt 1971 and

---

E.F. Sheka (✉)  
Peoples Friendship University of Russia, 117198 Moscow, Russia  
e-mail: [sheka@icp.ac.ru](mailto:sheka@icp.ac.ru)



references therein). The first stage of the study was completed in the late 1920s (de Jong 1923) and then obtained a new pulse after appearing the Woodward and Hoffmann monograph, devoted to the conservation of orbital symmetry, in 1970 (Woodward and Hoffmann 1970). Since then, topochemical reactions have become an inherent part of not only organic but inorganic chemistry, as well. The readers, who are interested in this topic, are referred to a set of comprehensive reviews (Schmidt 1971; Enkelmann 1984; Hasegawa 1986; Boldyrev 1990; MacGillivray and Papaefstathiou 2004), but a few. The current situation in this field can be seen by the example of a direct structural understanding of a topochemical solid-state photopolymerization reaction (Guo et al. 2008).

Nowadays, we are witnessing the next pulse, stimulating investigations in the field, that should be attributed to the appearance of a new class of spatially extended molecular materials, such as  $sp^2$  nanocarbons. Obviously, the main members of the class such as fullerenes, nanotubes, and numerous graphene-based species are absolutely different from the formal topology viewpoint. Thus, fullerenes exist in the form of a hollow sphere, ellipsoid, or tube consisting of differently packed benzenoid units. Carbon nanotubes present predominantly cylindrical packing of the units. In graphene, the benzenoid units form one-atom-thick planar honeycomb structure. If we address the common terms of the formal topology, namely, the connectivity and adjacency, we have to intuitively accept their different amount in the above three species. In its turn, the connectivity and adjacency determine the “quality” of the C–C bond structure of the species, thus, differentiating them by this mark. Since non-saturated C–C bonds are the main target for chemical reactions of any type, one must assume that identical reactions, involving the bonds, will occur differently for different members of the  $sp^2$  nanocarbon family. Therefore, one may conclude that the spatially extended  $sp^2$  nanocarbons present not only peculiarly structural chemicals but the class of species for which the formal and empirical topology overlap. The results presented in this chapter are aimed at revealing this tight interconnection in terms of molecular quantum theory. Not only fullerenes but carbon nanotubes and graphene (their fragments) are considered at the molecular level. The obtained results are related to the computational study of the intermolecular interaction (IMI) between one of the above  $sp^2$  nanocarbon molecules and one of the other addends, among which there are both  $sp^2$  nanocarbons and monatomic species. The intermolecular interaction lays the foundation of any reaction, so that its topological peculiarities may evidence a topochemical character of the reaction under study.

This chapter is organized as follows. Section 5.2 presents main concepts that form the grounds of the IMI consideration as well as introduces terms and quantities in use. Section 5.3 is devoted to the IMI investigation in the  $(C_{60})_n$  composites related to the dimerization and oligomerization of fullerene  $C_{60}$ . The IMI peculiarities, characteristic for composites fullerene-carbon nanotube ( $C_{60} + CNT$ ) and fullerene-nanographene (NGr) ( $C_{60} + NGr$ ), are considered in Sects. 5.4 and 5.5, respectively. Section 5.6 summarizes conclusive remarks about  $[2 + 2]$  cycloadditions that present a typical contact zone for the three types of the studied composites. Section 5.7 is devoted to carbon nanotube-nanographene ( $CNT + NGr$ ) composites.

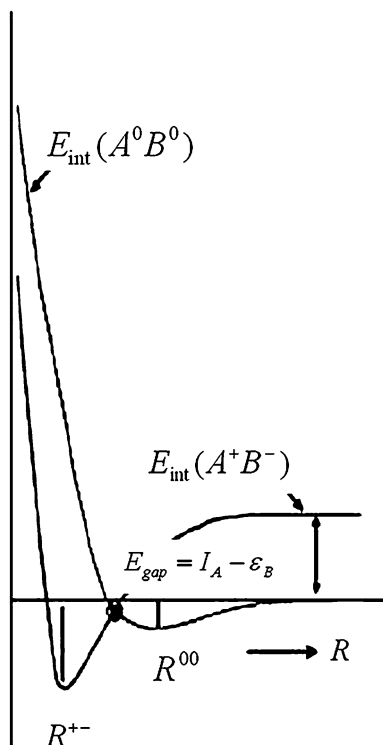
Section 5.8 presents a comparative study of the topochemical behavior of the hydrogenation of fullerene  $C_{60}$  and nanographene. Topological view on the graphene deformation is discussed in Sect. 5.9. General conclusion is presented in Sect. 5.10.

## 5.2 Odd Electrons and Donor–Acceptor Ability as Leitmotifs of Intermolecular Interaction in $sp^2$ Nanocarbons

Two cornerstones lay the foundation of the electronic properties of  $sp^2$  nanocarbon molecules. The first concerns odd-electron nature of their atomic system, aggravated with the correlation of these electrons and is intramolecular by nature. The second is provided with extremely high donor and acceptor characteristics of these molecules and is intimately connected with intermolecular interaction that is smoothly transformed into peculiar intramolecular properties of the species derivatives and composites. While, on the subject of covalent bonding, which involves any of  $sp^2$  nanocarbons, we should always proceed from the molecule partial radicalization due to exceeding C–C bond length the critical value  $R_{cov}^{crit}$  1.395 Å under which the odd electrons are non-correlated and fully covalently bound-forming classical  $\pi$  electron pairs and over which those become correlated and effectively unpaired (Sheka 2011a, 2012). Thus, appeared effectively unpaired electrons form a pool of molecular chemical susceptibility determined by the total number of the unpaired electrons  $N_D$ . Distributed over the molecule atoms by partial number  $N_{DA}$ , the electrons highlight the map of its chemical activity in terms of atomic chemical susceptibility (ACS)  $N_{DA}$ . The atom with the highest ACS first enters the reaction.

The second fundamental property concerns IMI. In all cases, the IMI is greatly contributed with the donor–acceptor (DA) interaction since all the  $sp^2$  nanocarbons are simultaneously good donors and acceptors of electron (Sheka 2004, 2007a, 2011a). Within the framework of general characteristics of the DA interaction, the IMI term configuration in the ground state depends on the difference of the asymptotes,  $E_{gap} = I_A - \varepsilon_B$ , of the  $E_{int}(A^+B^-)$  and  $E_{int}(A^0B^0)$  terms that describe the interaction between molecular ions and neutral molecule, respectively. Here,  $I_A$  and  $\varepsilon_B$  present ionization potential and electron affinity of components  $A$  and  $B$ . When  $E_{gap}$  is as big as in the case of  $C_{60}$  dimers, the IMI term of the ground state has a typical two-well shape (Sheka 2007a) shown in Fig. 5.1. The formation of a stationary product  $AB$  at the point  $R^{+-}$  is accompanied by the creation of “intermolecular” chemical bonds between  $A$  and  $B$  partners. Oppositely, quite widely spaced neutral moieties form a charge transfer complex  $A + B$  in the vicinity of  $R^{00}$  (Sheka 2004, 2007a, 2011a). In spite of the formation of  $AB$  product is energetically profitable, the yield of the relevant reaction, which starts from  $A + B$  mixture at all time, is determined by a barrier that separates  $A + B$  and  $AB$  products. This chapter in its main part is focused on the determination (1) how similar are the IMI profiles for three types of composites, namely,  $C_{60} + C_{60}$ ,  $C_{60} + CNT$ , and  $C_{60} + NGr$ , that include  $C_{60}$  as a permanent component while the other component

**Fig. 5.1** Scheme of terms of an IMI potential of type 1 (Sheka 2011a). ( $A^0B^0$ ) and ( $A^+B^-$ ) match the term branches related to the IMI between neutral molecules and their ions, respectively



is either  $C_{60}$  or CNT and NGr and (2) how big is the barrier of the  $AB$  product formation in each case. In the abbreviated form, the problem will be discussed as regards CNT + NGr composites, as well.

It should be noted that the above-mentioned composites are similar to those that are formed by non-saturated organic moieties, whose topochemical [2 + 2] photocyclo-dimerization-polymerization in solid state has been the main subject of a quite exhausted studying for many years (see Schmidt 1971; Enkelmann 1984; Hasegawa 1986; Guo et al. 2008), but a few. However, until now these topochemical reactions have not been considered from the position of the IMI complication caused by the donor–acceptor interaction. Starting from the monograph of Woodward and Hoffmann (1970), all the explanations have been concentrated on the consideration of the formation of chemically bound  $AB$  products. As will be shown in what follows, the consideration of the composite properties at the platform of the DA-complicated IMI opens much larger perspectives to enter the depth of the considered phenomenon.

This chapter presents the view of the touched problems from the insight of quantum-chemical calculations. The main part of the results was obtained by computations carried out by the author team when using the AM1 semiempirical version of unrestricted broken symmetry Hartree-Fock (UBS HF) approach (Sheka 2011a, 2012).

## 5.3 Fullerene + Fullerene Composites

### 5.3.1 Ground State Term of the $C_{60} + C_{60}$ Dyad. Equilibrium Structure and Mechanism of Dimerization

According to the scheme in Fig. 5.1, the reaction of the  $(C_{60})_2$  dimer formation can be considered as moving the two molecules towards each other, once spaced initially at large intermolecular distance  $R$ , then equilibrated and coupled as  $A + B$  complex in the  $R^{00}$  minimum and afterwards achieved the minimum at  $R^{+-}$  to form tightly bound adduct  $AB$ . The last stage implies overcoming a barrier, which is followed by the transition from  $(A^0 B^0)$  to  $(A^+ B^-)$  branch of terms after which the Coulomb interaction between molecular ions completes the formation of the final  $AB$  adduct at the  $R^{+-}$  minimum.

Concerning covalent bonding, which involves fullerene  $C_{60}$ , we should usually begin from the map of chemical activity of  $C_{60}$  in terms of atomic chemical susceptibility (ACS)  $N_{DA}$  (Sheka and Zayetz 2005; Sheka 2007b). Plottings of the ACS distribution over atoms of the  $C_{60}$  molecule are shown in Fig. 5.2 and are emphasized by different colors in the insert that distinguish atoms with different ACS. Among the latter, the most active atoms are shown by light gray. Those are the first targets involved into initial stages of any addition reaction. Following this indication, the initial composition of a pair of the  $C_{60}$  molecules shown in Fig. 5.3a becomes quite evident. The starting configuration corresponds to  $R_{CC}^{st}$  1.7 Å that corresponds to the distances between 1–1' and 2–2' target atoms. A bound dumbbell-like dimer is formed (Fig. 5.3b) after the structure optimization aimed at the total energy minimization is completed. It turns out that two monomers within the dimer are contacted via a typical [2 + 2] cycloaddition of “66” bonds that form a cyclobutane ring (Sheka 2007a). Main electronic characteristics of the  $(C_{60})_2$  adduct are presented in Table 5.1. A detailed comparison with the available computational data is given elsewhere (Sheka 2007a). A large negative  $E_{cpl}^{tot}$  value undoubtedly evidences that  $(C_{60})_2$  dimer is a typical  $AB$  adduct attributed to the  $R^{+-}$  minimum on the IMI ground state term in Fig. 5.1.

When  $R_{CC}^{st} = 3.07$  Å, optimization of the initial structure leads to the formation of a weakly bound pair of molecules spaced by  $R_{CC}^{in} = 4.48$  Å. Monomer molecules preserve their initial configurations and, as seen from Table 5.1, form a classical charge transfer complex. The fragment composition of the HOMO and LUMO is cross-partitioned; the former should be attributed to Mol 2 while the latter to Mol 1, just showing that a charge transfer from Mol 2 to Mol 1 occurs when the complex is photoexcited.

The obtained results allow for highlighting mechanisms of  $C_{60}$  dimerization. Since the IMI interaction in the  $C_{60}$  pair is described by two-well terms shown in Fig. 5.1, at ambient conditions, the dimerization does not occur spontaneously which points to the reaction barrier. According to experimental findings, the barrier (activation energy) is 1.25 eV (Wang et al. 1994) in the case of photostimulated dimerization and 1.40 eV (Davydov et al. 2001) when high pressure is applied.

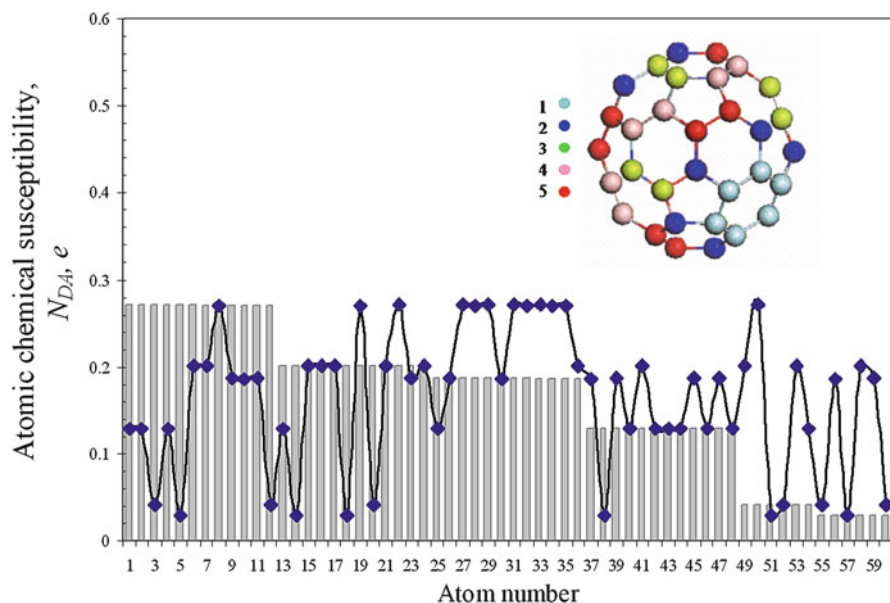


**Fig. 5.2** Atomic chemical susceptibility of fullerene  $C_{60}$  (Sheka 2011a), distributed over the molecule atoms according to either their numeration in the output file (*curve with rhombs*) or in the  $Z \rightarrow A$  manner (*histogram*). Different colors in the insert distinguish five atomic groups shown by the histogram

**Fig. 5.3** (a) Starting composition of the  $C_{60} + C_{60}$  dyad. (b) Equilibrium structure of the  $(C_{60})_2$  dimer;  $R_{CC}^{st} = 1.7 \text{ \AA}$ ,  $R_{CC}^{fn} = 1.55 \text{ \AA}$ . Both distances correspond to spacings between 1-1' and 2-2' atoms

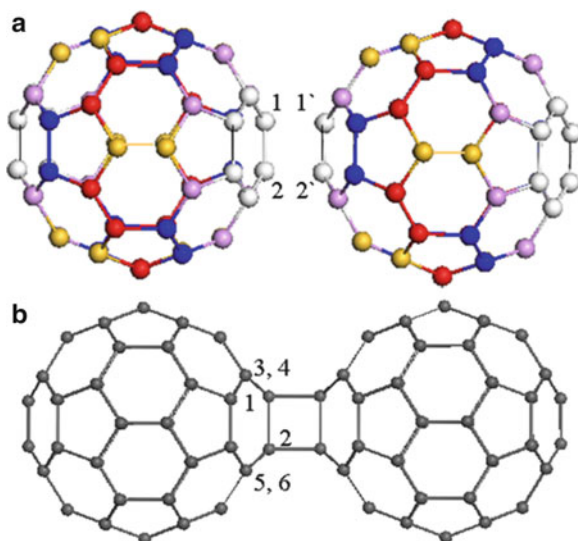


**Table 5.1** Electronic characteristics of the  $C_{60} + C_{60}$  dyad

Computed quantities, UBS HF AM1 singlet state	Monomer $C_{60}$	$R_{CC}^{st}$	
		1.71 Å	3.07 Å
Heat of formation <sup>1</sup> , $\Delta H$ , kcal/mol	955.56	1,868.49	1,910.60
Coupling energy <sup>2</sup> , $E_{cpl}^{tot}$ , kcal/mol	–	–42.63	–0.52
Ionization potential <sup>3</sup> , $I$ , eV	9.86 (8.74 <sup>a</sup> )	9.87	9.87
Electron affinity <sup>3</sup> , $\varepsilon$ , eV	2.66 (2.69 <sup>b</sup> )	2.62	2.66
Dipole moment, $Db$	0.01	0.001	0.001
Squared spin, ( $S^{*2}$ )	4.92	10.96	9.87
Total number of effectively unpaired electrons, $N_D$ <sup>4</sup>	9.84	21.93	19.75
Gained charge to Mol 1	–	0.0	0.0
Transferred charge from Mol 2	–	0.0	0.0
Symmetry	$C_i$	$C_{2h}$	$C_i$
HOMO, fragment compositions, $\eta$	–	$\eta_{Mol1} = 61.8 \%$ $\eta_{Mol2} = 38.1 \%$	$\eta_{Mol1} = 0 \%$ $\eta_{Mol2} = 100 \%$
LUMO, fragment compositions, $\eta$	–	$\eta_{Mol1} = 83.9 \%$ $\eta_{Mol2} = 15.8 \%$	$\eta_{Mol1} = 100 \%$ $\eta_{Mol2} = 0 \%$

Reprinted from Sheka (2007a). Copyright (2007) with permission from Elsevier

<sup>1</sup>Molecular energies are heats of formation  $\Delta H$  determined as  $\Delta H = E_{tot} - \sum_A (E_{elec}^A + E_{HEAT}^A)$ . Here  $E_{tot} = E_{elec} + E_{nuc}$ , while  $E_{elec}$  and  $E_{nuc}$  are the electron and core energies.  $E_{elec}^A$  and  $E_{HEAT}^A$  are electron energy and heat of formation of an isolated atom, respectively

<sup>2</sup>Coupling energy is determined by Eq. (5.1)

<sup>3</sup>Here  $I$  and  $\varepsilon$  correspond to the energies of HOMO and LUMO, respectively, just inverted by sign. Experimental data for the relevant orbitals are taken from Weaver et al. (1991)<sup>a</sup> and Wang et al. (1999)<sup>b</sup>

<sup>4</sup>The total number of effectively unpaired electrons,  $N_D$ , displays the molecular chemical susceptibility of the species (Sheka and Zayetz 2005; Sheka 2007b)

The barrier can be overcome by different ways, which describes a large variety of the technological schemes in use. Among the latter, there are thermal and high pressure technologies (Yamawaki et al. 1993; Pekker et al. 1994; Iwasa et al. 1994), field-stimulated dimer formation and decomposition (Zhao et al. 1994; Nakaya et al. 2008), but the first place is taken by the photoexcitation technology (Ecklund et al. 1995).

A triplet state photochemical mechanism is usually accepted, according to which one monomer in the excited triplet state  $^3M^*$  reacts with the other monomer in the ground state  $M$  to yield the dimer  $D$ , that is,  $^3M^* + M \rightarrow D$ . This view on the mechanism of the photopolymerization has come from those topochemical reactions that were discussed earlier. However, another mechanism seems to be more efficient. As shown above, two  $C_{60}$  molecules separated by  $\sim 4.5$  Å form a charge transfer complex at the point  $R^{00}$  (Sheka et al. 2007). In solid  $C_{60}$ , photostimulated charge transfer between adjacent molecules causes the appearance of charge transfer excitons (Pac et al. 1998; Kazaoui et al. 1998). The related absorption bands, both in molecular solutions and solids, are provided by phototransitions out of minimum  $R^{00}$  belonging to the term  $E_{int}(A^0B^0)$  to the branch of the term  $E_{int}(A^+B^-)$

(see Fig. 5.1) in due course of which the ground state of weakly interacting neutral molecules is transformed into the charge transfer state of molecular ions. By this means, photoexcitation of a van der Waals  $C_{60}$  pair by visible-UV light is followed by the formation of the ion pair located above the barrier. Coulomb's interaction between the ions provides their passing towards the  $R^{+-}$  minimum where the dimer is formed.

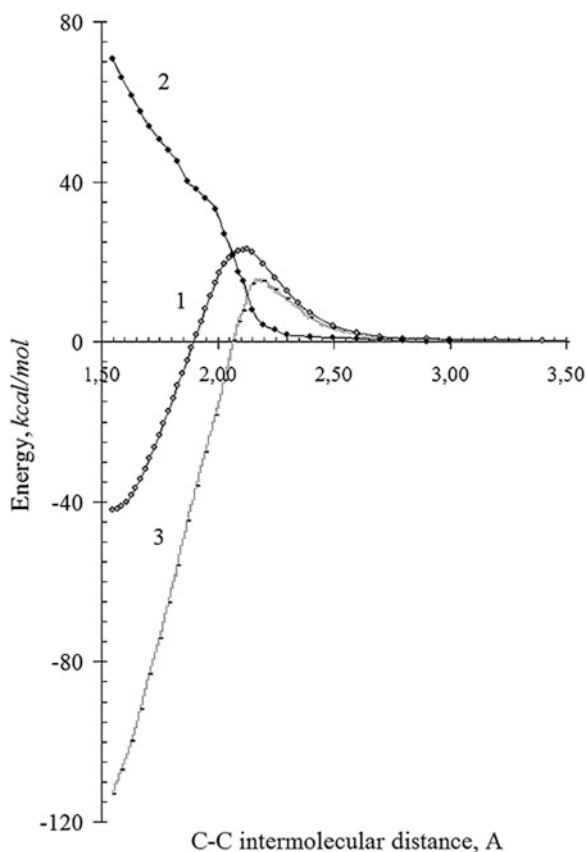
This mechanism may explain a severe requirement, known for more than a century, for solid-state photostimulated reactions: the molecular moieties should be spaced not more than 4.2–4.7 Å for the topochemical photodimerization-oligomerization to occur (Schmidt 1971; Enkelmann 1984; Friscic and MacGillivray 2005). The distance is characteristic for  $R^{00}$  that determines the equilibrium spacing in charge transfer complexes. If the formation of the charge transfer complex provides this photoreaction, the encountered molecules should be simultaneously donors and acceptors of electrons. During the preparation of this chapter, the author has proven the “4.2–4.7” rule for such typical representatives of the discussed topochemical reactants as  $\alpha$ -cinnamic acid and *n*-diethynilbenzene. As turned out, they both are good donors and acceptors of electrons, indeed.

### 5.3.2 *The Barrier for the Formation and/or Decomposition of $(C_{60})_2$ Dimer*

To get the barrier profile of the reaction under consideration, it is necessary not only to determine equilibrium configurations  $A + B$  and  $AB$  but to trace a continuous transition from one state to the other. Computationally, it is no difference to study the profile by either shifting monomer molecules of the  $A + B$  complex towards each other, thus contracting the corresponding intermolecular C–C distances and determining the barrier of the  $C_{60}$  dimerization or separating the molecules of the  $AB$  product by elongation of the relevant intermolecular C–C bonds and thus getting the barrier of the dimer decomposition. In contrast to the equilibrium configuration  $A + B$ , which does not critically depend on mutual orientation of the partners, a particular combination of the partners' atoms constructs the contact zone of the  $AB$  product (see Fig. 5.3a). Since that, the determination of the decomposition barrier is more structurally substantiated. The procedure involves a regular elongation of the relevant intermolecular bonds of the equilibrium  $AB$  structure. These bonds are kept fixed at each elongation step while  $C_{60}$  molecules relax in looking for the total energy minimum. According to this, two intermolecular C–C distances, namely, 1–1' and 2–2' separations of the [2 + 2] cycloaddition in Fig. 5.3b, are gradually elongated with a constant increment of 0.05 Å during the first stage of elongation from 1.57 to 2.22 Å and then of 0.1 Å during the second stage. Figure 5.4 presents a profile of thus obtained barrier for the dimer  $(C_{60})_2$  decomposition presented by the total coupling energy  $E_{\text{cpl}}^{\text{tot}}$  determined as

$$E_{\text{cpl}}^{\text{tot}}(R_{\text{CC}}) = \Delta H_{\text{dim}}(R_{\text{CC}}) - 2\Delta H_{\text{mon}}^{\text{eq}}, \quad (5.1)$$

**Fig. 5.4** Profile of the barrier of the dimer ( $C_{60}$ )<sub>2</sub> decomposition (Reproduced from Sheka and Shaymardanova (2011b), with permission from the Royal Society of Chemistry).  
 1.  $E_{cpl}^{tot}(R_{CC})$ ; 2.  $E_{def}^{tot}(R_{CC})$ ;  
 3.  $E_{chem}^{tot}(R_{CC})$  (see text)



where  $\Delta H_{dim}(R_{CC})$  and  $\Delta H_{mon}^{eq}$  are heats of formation of dimer at the current intermolecular distance  $R_{CC}$  and of monomer in equilibrium, respectively. This energy is evidently complex by nature since, at least, two components contribute into its value, namely, the energy of both monomers deformation  $E_{def}^{tot}$  and the energy of the covalent coupling  $E_{cov}^{tot}$  between the monomers. The former component can be determined as

$$E_{def}^{tot}(R_{CC}) = \Delta H_{mon1}^{op}(R_{CC}) + \Delta H_{mon2}^{op}(R_{CC}) - 2\Delta H_{mon}^{eq}. \quad (5.2)$$

Here,  $\Delta H_{mon1}^{op}(R_{CC})$  and  $\Delta H_{mon2}^{op}(R_{CC})$  present the one-point-geometry heats of formation of the skeletons of both monomer molecules of the  $C_{60} + C_{60}$  dyad at a given intermolecular distance  $R_{CC}$ . The second component  $E_{cov}^{tot}$  is determined as

$$E_{cov}^{tot}(R_{CC}) = E_{cpl}^{tot}(R_{CC}) - E_{def}^{tot}(R_{CC}). \quad (5.3)$$



The discussed distance-dependent energies are shown in Fig. 5.4. As seen in the figure, the deformation energy is the largest in equilibrium dimer and then steadily decreases when  $R_{CC}$  grows, once positive, until approaching zero when monomers are spaced by more than 3 Å. Similarly, the energy of the covalent coupling is the largest in equilibrium dimer then steadily decreases by the absolute value being negative and showing a clearly vivid maximum that coincides with that of  $E_{\text{cpl}}^{\text{tot}}(R_{CC})$ . Proceeding with further spacing, the energy falls by the absolute value, changes sign in the vicinity of  $R^{00} \sim 4.4$  Å, once being small by the absolute value, and then approaches zero for largely spaced monomers. Referring to schemes of electronic terms in Fig. 5.1, one should accept that this is the energy  $E_{\text{cov}}^{\text{tot}}$  that should be attributed to the *netto* barrier profile. However, the energy  $E_{\text{cpl}}^{\text{tot}}(R_{CC})$  as a *brutto* barrier profile will obviously govern the formation of fullerene dimers in practice. Obviously, the obtained barrier is identical to the dimerization barrier that corresponds to the energy-distance dependence when going from initially large spacing between the monomers regularly contracting the latter.

### 5.3.3 $C_{60}$ Oligomers

The detailed study of the IMI term's profiles, which governs  $C_{60}$  dimerization discussed above, opens the way to throw light on peculiarities of the  $C_{60}$  oligomerization. Reasonably, the oligomerization can be computationally considered as a stepwise reaction  $(C_{60})_n = (C_{60})_{n-1} + C_{60}$  for which the IMI term of the  $[(C_{60})_{n-1} + C_{60}]$  dyad controls the formation of the final product  $(C_{60})_n$ . One cannot exclude more complex scheme, such as  $(C_{60})_n = (C_{60})_m + (C_{60})_k$  where  $m + k = n$ ,  $(C_{60})_n = (C_{60})_m + (C_{60})_k + (C_{60})_l$  where  $m + k + l = n$ , and so forth. However, all the schemes are subordinated to common regularities whose main characteristics can be considered for the  $(C_{60})_{n-1} + C_{60}$  dyad as an example.

If accepting that the type of IMI terms is mainly determined by  $E_{\text{gap}} = I_A - \varepsilon_B$  as discussed in Sect. 5.3.1, passing to oligomers one faces a peculiar situation characteristic for fullerenes. The matter is that both ionization potential and electronic affinity of  $(C_{60})_n$  oligomer only slightly depend on  $n$  and practically coincide with those related to monomer molecule. This can be seen in Table 5.1 for dimer and has been computationally justified for oligomers of complex structure characterized by  $n$  varying up to 10 (Sheka et al 2006). Consequently, the IMI term of the  $C_{60} + C_{60}$  dyad determines the general behavior of both  $(C_{60})_{n-1} + C_{60}$  and  $(C_{60})_m + (C_{60})_k$  dyads at each successive step of oligomerization. As in the case of dimers, two products, namely, either  $(C_{60})_{n-1} + C_{60}$  or  $(C_{60})_m + (C_{60})_k$ , charge transfer complexes, and  $(C_{60})_n$  oligomer will correspond to equilibrium positions at  $R^{00}$  and  $R^{+-}$  minima of the IMI term, respectively. Following this suggestion and taking into account the main concepts of computational chemistry of fullerenes, one can suggest a definite scheme of the expected successive oligomerization of  $C_{60}$  molecules when going, say, from dimer to tetramer within the  $(C_{60})_n = (C_{60})_{n-1} + C_{60}$  oligomerization scheme, as shown in Fig. 5.5.

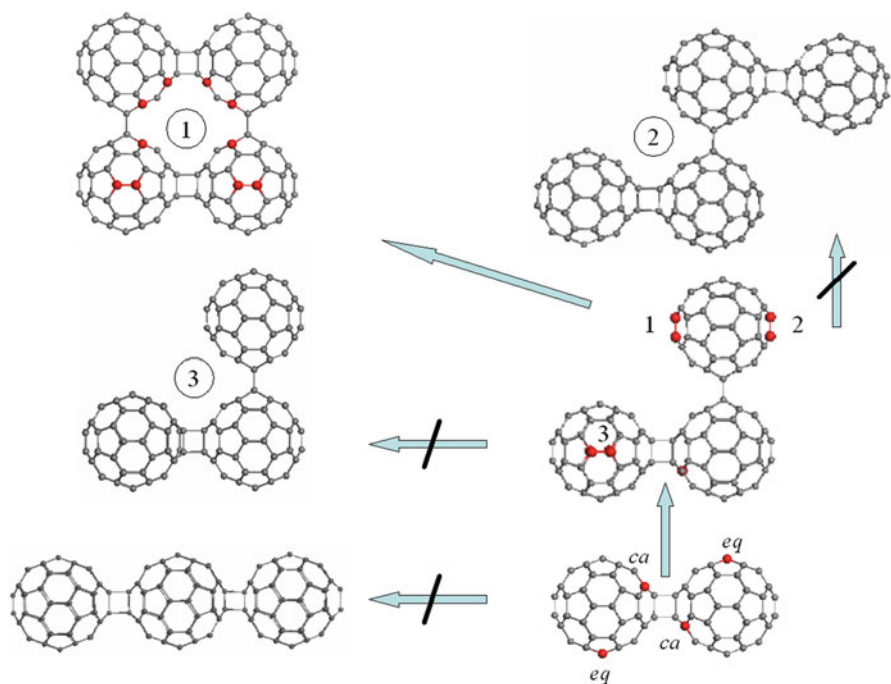


**Fig. 5.5** Stepwise oligomerization of  $C_{60}$  from dimer to tetramer. Equilibrium structures. *Crossed arrows* indicate unfavorable continuations. Coupling energies constitute  $-42.23$  kcal/mol (dimer);  $-74.73$  kcal/mol (trimer);  $-164.63$  kcal/mol (tetramer 1);  $-13.84$  kcal/mol (tetramer 2);  $-117.66$  kcal/mol (tetramer 3) (Reproduced from Sheka and Shaymardanova (2011b), with permission from the Royal Society of Chemistry)

According to the ACS map of dimer ( $C_{60}$ )<sub>2</sub>, there are four pairs of high-rank  $N_{DA}$  atoms that are marked by red balls in the right low corner of Fig. 5.5. The first two pairs combine the most reactive atoms adjacent to the cycloaddition (below, contact-adjacent or *ca* atoms) (see atoms 3, 4, 5, and 6 in Fig. 5.3). Next by reactivity four atoms are located in equatorial planes of both monomers (below, equatorial or *eq* atoms). In spite of high chemical reactivity of *ca* atoms, those are not accessible in due course of the further oligomerization so that *eq* atoms of both monomers are actual targets. Following these ACS indication, a right-angle trimer (90°-trimer) must be produced. Therefore, not the “pearl necklace” configuration, intuitively suggested as the most expected for  $C_{60}$  oligomerization (Fischer 1994), but more complicated 2D one is favorable for trimerization.

Similarly, the high-rank  $N_{DA}$  atoms of trimer as seen in Fig. 5.5 form an incomplete *ca* pair of the highest activity and three pairs of *eq* atoms of comparable activity. Three tetramer compositions, which follow from the high-rank ACS indication related to trimer, are shown in Fig. 5.5. None of them is among the “pearl necklace” family thus presenting 2D tetramers 1 and 2 and 3D tetramer 3.

Among the latter, tetramer 1 possesses the least energy and is expected to continue the oligomerization offering its high-rank  $N_{DA}$  atoms, marked by red balls, as targets for the next  $C_{60}$  addition. Those form six pairs of the most active *ca* atoms and four pairs of *eq* atoms, position of which dictates the continuation of oligomerization as the formation of 3D configurations of pentamers.

Before passing to comparison with experimental data, it should be noted that the considered oligomerization is related to the addition reaction that occurs between partners in a vacuum without any constraints on their orientation. Empirical reality turns out to be much more complicated since the performed experiments differ quite drastically when going from the study of  $C_{60}$  clusters in the gas phase (see Hedén et al. 2005; Enders et al. 2006 and references therein) to that one in solutions (Sun et al. 1995), solid films and powders (Ecklund et al. 1995; Pusztai et al. 1999; Nakayama et al. 1999; Kunitake et al. 2002; Nakaya et al. 2008), and solids (Núñez-Regueiro et al. 1995; Soldatov et al. 2001; Zhang et al. 2010). All the studies clearly evidence the formation of  $(C_{60})_n$  clusters with  $n = 2, 3, 4$ , and more while the information concerning the cluster's structure is rather scarce. The best situation concerns dimers whose dumbbell-like structure was proven by many ways (see Sheka 2007a and references therein). Applying to trimers, there are two sources of information related to different ways of their production that conditionally can be denoted as "chemical" (Kunitake et al. 2002) and "physical" (Nakayama et al. 1999; Nakaya et al. 2008). "Chemical" experiments deal with  $C_{180}$  species produced in due course of solid-state mechanochemical reaction under high-speed vibration milling conditions. The final product exhibits two fractions (A and B in the ratio of  $\sim 5:4$ ), the former predominantly ( $\sim 60\%$ ) consisting of  $90^\circ$ -trimers while 100% of the latter is presented by cyclic 60-trimers. "Physical" experiments deal with trimers produced under photoillumination of either  $C_{60}$  films preliminarily deposited on some substrates (Ecklund et al. 1995; Nakayama et al. 1999; Nakaya et al. 2008) or pristine  $C_{60}$  crystal (Núñez-Regueiro et al. 1995). Linear three-ball chains were observed in these studies only.

Evidently, all the above experimental procedures put additional restriction on the space where the reactions occur. Here, we are facing a quite unique situation, once a consequence of the simultaneous action of two topologies, one of which is inherent to fullerene molecule while the other is provided by external conditions. From this viewpoint, even a predominant presence of  $90^\circ$ -trimers within fraction A of the "chemical" experiment cannot be considered as a doubtless proof of compositions predicted by the ACS-guided covalent chemistry of  $C_{60}$  since three other  $108^\circ$ -,  $120^\circ$ -, and  $144^\circ$ -trimers, observed within fraction A, as well as  $60^\circ$ -trimers of fraction B (Kunitake et al. 2002) seriously contradict the scheme shown in Fig. 5.5. Even more stronger contradiction is revealed by comparison with the "physical" experiments that exhibit only linear "pearl necklace" trimers, the less probable in accordance with the ACS-based analysis. At the same time, compositionally simple "physical" findings evidently connect the trimerization events with a predetermined molecular packing. As known, the latter is evidently the main factor for any topochemical reaction, firstly attributed to fullerenes when explaining both the linear trimerization and linear polymerization of  $C_{70}$  in solid state (Soldatov et al. 2001).

From this viewpoint, the production of linear orthorhombic crystalline modification of polymerized  $C_{60}$  (Núñez-Regueiro et al. 1995) should be considered as a result of the relevant topochemical reaction. On the other hand, the mechanochemical reaction, responsible for triangle trimers, evidently has a topological odor as well thus providing formation of differently configured trimers due to obvious anisotropy of the stress application to the pristine  $C_{60}$  crystal under milling.

The situation with tetramers is not simple, as well. The first suggestion concerning a closed structure of  $(C_{60})_4$  clusters analogous to tetramer 1 in Fig. 5.5 was issued for clusters in solutions (Sun et al. 1995). Later on, the suggestion was supported by the analysis of Raman spectra of photoilluminated  $C_{60}$  powders (Pusztai et al. 1999) as well as direct STM observation of deposited  $(C_{60})_n$  clusters on the (111) surface of gold (Zhang et al. 2010). In spite of a seemingly favorable fitting of the experimental data to the predicted ones, one has to take into account that both experiments are performed under evident conditions that favor topochemical reactions. Thus, not only  $(C_{60})_4$  clusters deposited on the gold surface have 2D tetragonal shape similar to tetramer 1 but all other  $(C_{60})_n$  clusters with  $n > 4$  clearly exhibit 2D configurations in contrast to the predicted 3D ones for pentamers and higher oligomers, which follows from the high-rank  $N_{DA}$  ACS indication concerning the tetramer 1 structure shown in Fig. 5.5. The tendency of  $(C_{60})_n$  clusters to be inclined to topochemical reaction is uppermost realized in 1D orthorhombic as well as in 2D tetragonal and rhombohedral configurations of polymerized  $C_{60}$  crystals, whose production is controlled by varying one-direction contraction of the pristine  $C_{60}$  crystal structure at high pressures and temperatures (Núñez-Regueiro et al. 1995).

## 5.4 Fullerene $C_{60}$ + Carbon Nanotube Composites

### 5.4.1 Barrier Profile for $C_{60}$ -CNT Nanobuds

There have been known a few attempts to synthesize  $C_{60}$  + CNT complexes that present a single structure in which the fullerenes are covalently bonded to the tube body. A few techniques have been suggested to obtain  $C_{60}$  + CNT composites in which fullerene is located either inside (see Giacalone and Martín 2010 and references therein) or outside (Li et al. 2003, 2007; Nasibulin et al. 2007a, b) the CNT wall. The terms *peapod* (Giacalone and Martín 2010) and *carbon nanobud* (CNB) (Nasibulin et al. 2007a) were suggested to distinguish the two configurations. For the first time, the  $C_{60}$  nanobud based on a single-wall CNT (SWCNT) was obtained by means of solid-phase mechanochemical reactions (Lee et al. 2000). The next time, the  $C_{60}$  + SWCNT nanobud was synthesized via a microwave-induced functionalization approach (Li et al. 2003). The findings have led the foundation for a further large investigation aimed at producing fullerene-functionalized SWNTs (Li et al. 2007; Nasibulin et al. 2007b; Tian et al. 2008).

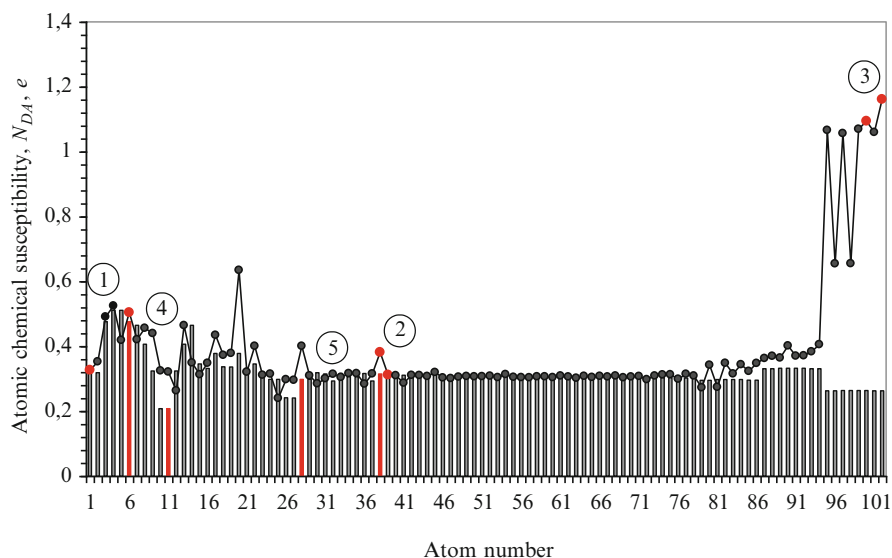
Computational consideration of CNBs has been restricted so far to three publications (Li et al. 2007; Wu and Zeng 2008; Sheka and Shaymardanova 2011b). Two former computations were performed in the framework of the density functional theory (DFT) using periodic boundary conditions (PBCs) in the restricted closed-shell approximation. A few different compositions of intermolecular C–C bonds forming the contact zone on the sidewall of the tubes have been considered among which [2 + 2] cycloaddition turned out to be the most efficient. An alternative approach, which considers the formation of CNB in terms of molecular theory as a result of a DA reaction whose general energetic scheme is presented in Fig. 5.1, is given in the third publication. Broken symmetry approach, based on unrestricted open-shell Hartree-Fock approximation, forms the computations ground. The approach is more suitable for partially radicalized both fullerene C<sub>60</sub> and CNTs (Sheka and Chernozatonskii 2010b; Sheka 2011a) than above-mentioned restricted DFT one and suggests much more picturesque vision of the CNBs formation and properties.

#### 5.4.2 UBS HF Computational Synthesis of Carbon Nanobuds

Partial radicalization of CNTs is due to a rather strong correlation of their odd electrons (Sheka 2012). The appearance of effectively unpaired electrons is resulted from the exceeding of C–C bond lengths the critical value  $R_{\text{cov}}^{\text{crit}}$  (Sheka and Chernozatonskii 2010b), similarly to the situation with fullerenes discussed in Sect. 5.3.1. Distributed over the tube atoms by fractional number of  $N_{\text{DA}}$ , the effectively unpaired electrons highlight the map of the tube chemical activity in terms of atomic chemical susceptibility (ACS)  $N_{\text{DA}}$ . Figure 5.6 presents the ACS distribution over atoms of two (4, 4) SWCNTs shown in Fig. 5.7. The tubes differ by the end atom termination only.

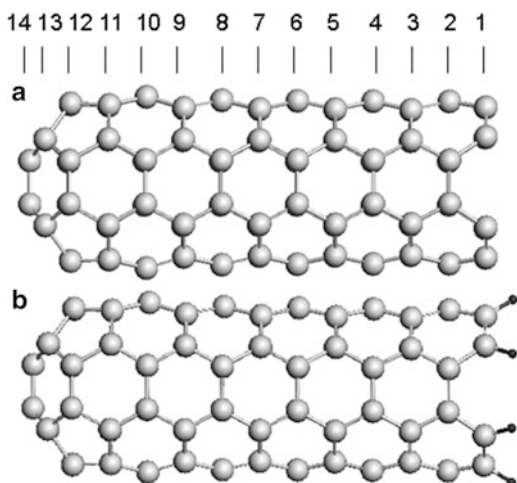
As seen in Fig. 5.6, there are three zones in the ACS distribution related to the tube caps, sidewalls, and ends, respectively. Accordingly, one can choose three pairs of target atoms on tube 1 (1, 2, and 3), which are shown by red dots on the curve, and two pairs on tube 2 (4 and 5) shown by red bars. As was discussed in Sect. 5.3.1, the most active atoms of fullerene C<sub>60</sub> form particularly oriented two hexagons, each atom of which is the target that first meets any addend. The two features, related to chemical portraits of CNTs and fullerene molecule, make it possible to construct five starting configurations of possible [C<sub>60</sub> + (4,4)] CNBs that alongside with equilibrium structures are presented in Fig. 5.8. The starting intermolecular C–C distances were taken 1.7 Å.

Figure 5.9a, b present changing in the ACS maps of both (4, 4) SWCNT and fullerene C<sub>60</sub> related to CNB 5. As seen in the figure, the attachment of the fullerene molecule to the sidewall of the tube causes only local changing that concerns atoms participating in the formation of the [2 + 2] cycloaddition. The other part of the atomic activity distribution of the tube retains non-perturbed. This finding evidently favors a multiple attachment of fullerenes to the tube sidewall in a superposition



**Fig. 5.6** Distribution of the atomic chemical susceptibility  $N_{DA}$  over atoms of (4, 4) single-walled carbon nanotubes with empty (*curve with dots*) and hydrogen-terminated (*histogram*) ends (Reproduced with permission from *International Journal of Quantum Chemistry*, Sheka and Chernozatonskii 2010c. Copyright (2010) by John Wiley & Sons, Inc.). The atom numbering corresponds to that one over the tubes from the tube caps to their ends. *Ringed numbers* denote atom pairs subjected to further  $C_{60}$  addition (see text)

**Fig. 5.7** Equilibrium structures of (4, 4) single-walled carbon nanotube with empty (tube 1) (a) and hydrogen-terminated (tube 2) (b) ends



manner. Oppositely, the fullerene ACS map changes considerably indicating a significant redistribution of the atomic chemical activity over the molecule atoms after attachment. Red dots on plotted curve in Fig. 5.9b highlight new the most active atoms prepared for the next reaction events.

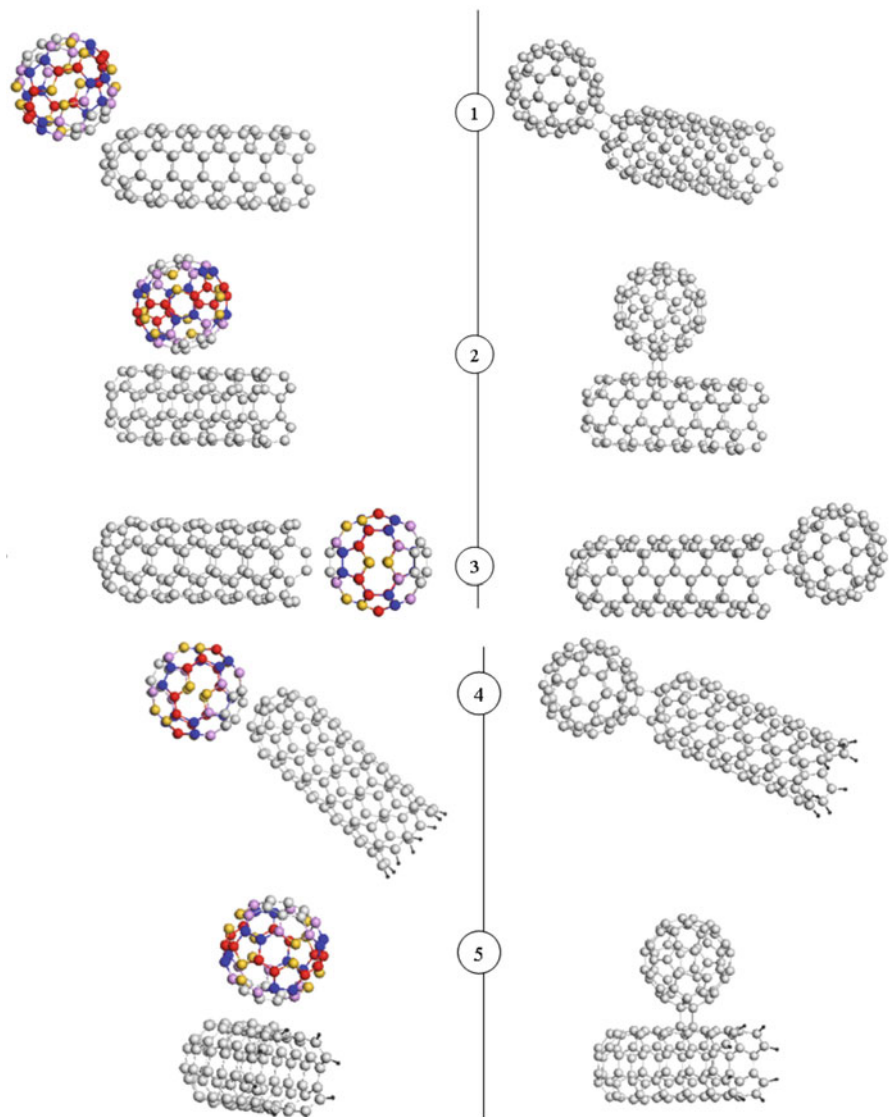


**Fig. 5.8** Starting (*left*) and equilibrium (*right*) structures of carbon nanobuds formed by attaching  $C_{60}$  to (4, 4) single-walled carbon nanotube with empty (1–3) and hydrogen-terminated (4, 5) ends. Figures number the nanobuds (Reproduced from Sheka and Shaymardanova 2011b, with permission from the Royal Society of Chemistry)

To check a high tolerance of the tube body to a multiple attachment of the fullerene molecules, two and three  $C_{60}$  molecules were attached to an elongated (4, 4) SWCNT (tube 3) forming CNB 6 and CNB 7 (see Fig. 5.10). As shown (Sheka and Chernozatonskii 2010b), the tube elongation causes the elongation of

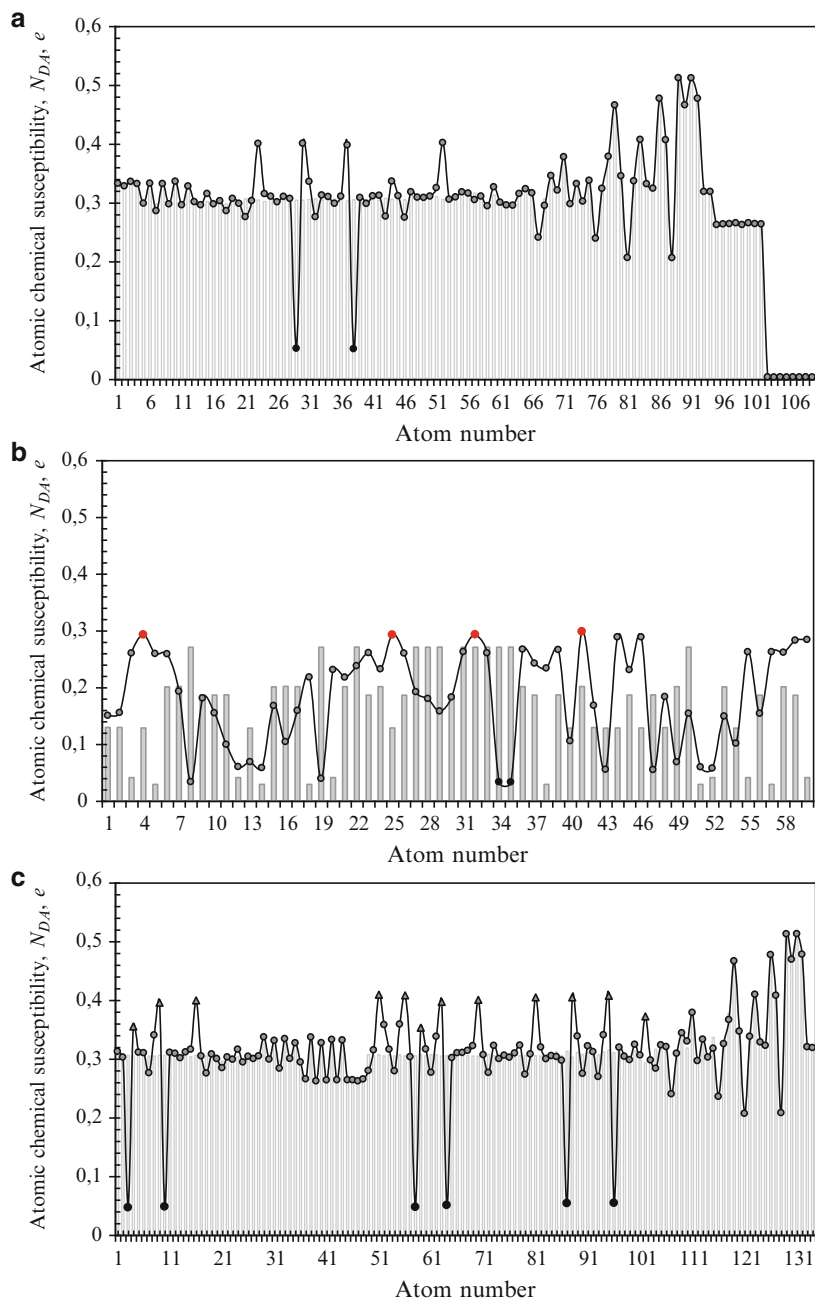


**Fig. 5.9** Evolution of the atomic chemical susceptibility distribution caused by carbon nanobuds formation. (a) Tube 2 (CNB 5); (b) fullerene  $C_{60}$  (CNB 5); (c) tube 3 (CNB 7) (see text). Histograms present data for the pristine species (Reproduced from Sheka and Shaymardanova 2011b, with permission from the Royal Society of Chemistry). Curve with dots plot data related to the formed CNBs



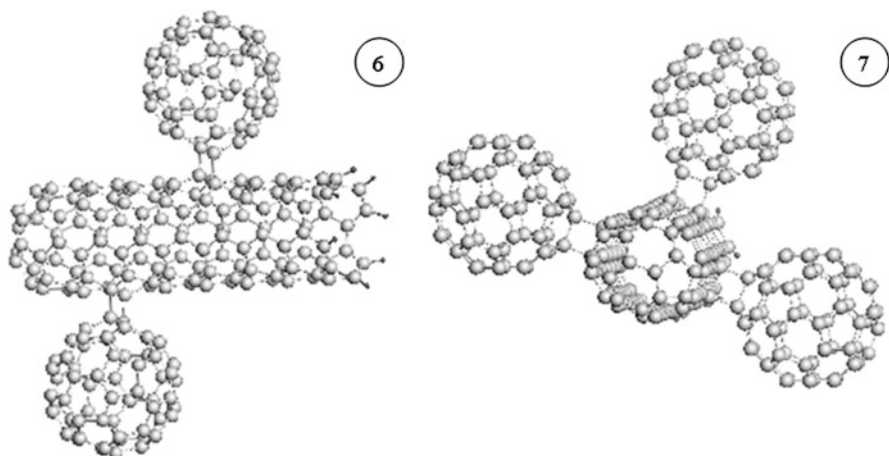


**Fig. 5.10** Equilibrium structures of  $[C_{60} + (4, 4)]$  CNBs related to double (CNB 6) and triple (CNB 7) attachments of  $C_{60}$  to the sidewall of (4, 4) single-walled carbon nanotube with hydrogen-terminated ends (Reproduced from Sheka and Shaymardanova (2011b), with permission from the Royal Society of Chemistry)

the sidewall zone in the ACS map only and does not touch either cap or end atom regions. That is why the conditions for the formation of CNBs 5, 6, and 7 are practically identical. All the attached  $C_{60}$  molecules are joined with the tube sidewall via  $[2 + 2]$  cycloadditions. Changing in the ACS distribution related to tube 3 is shown in Fig. 5.9c. A clearly seen superposition of the three attachments is perfectly exhibited by the map, indicating that practically countless number of fullerene molecules can be attached to SWCNTs long enough.

Figure 5.11 presents a collection of typical  $[C_{60} + (4,4)]$  CNBs whose detail analysis shows that the intermolecular junctions as  $[2 + 2]$  cycloadditions are formed only in the case when fullerene is covalently coupled with the tube sidewalls. This concerns CNBs 2, 6, and 7 while the junctions in CNBs 1 and 3 are not  $[2 + 2]$  cycloaddition in spite of four-atom membership. Coloring most active fullerene atoms highlights targets on the  $C_{60}$  body that may stimulate a further chemical modification of the CNBs. As seen in the figure, in all the cases of  $[2 + 2]$  cycloadducts, the evolution of chemical activity of fullerene in CNBs is the same and practically identical to that one typical for the  $C_{60}$  oligomerization (ca. Fig. 5.5). As previously, the most active atoms form pairs of contact-adjacent *ca* atoms that are followed by slightly less active equatorial *eq* atoms. Obviously, *ca* atoms are accessible only for small addends while *eq* atoms take the responsibility on themselves when continuing the CNBs chemical modification via subsequent expanded attachments to the fullerene that intend to be the best suitable for a particular application. As for CNBs 1 and 3, the situation is somewhat different. However, a predetermined position of *ca* and *eq* atoms makes a further modification of CNBs via attached  $C_{60}$  predictable and controlled in all the cases.

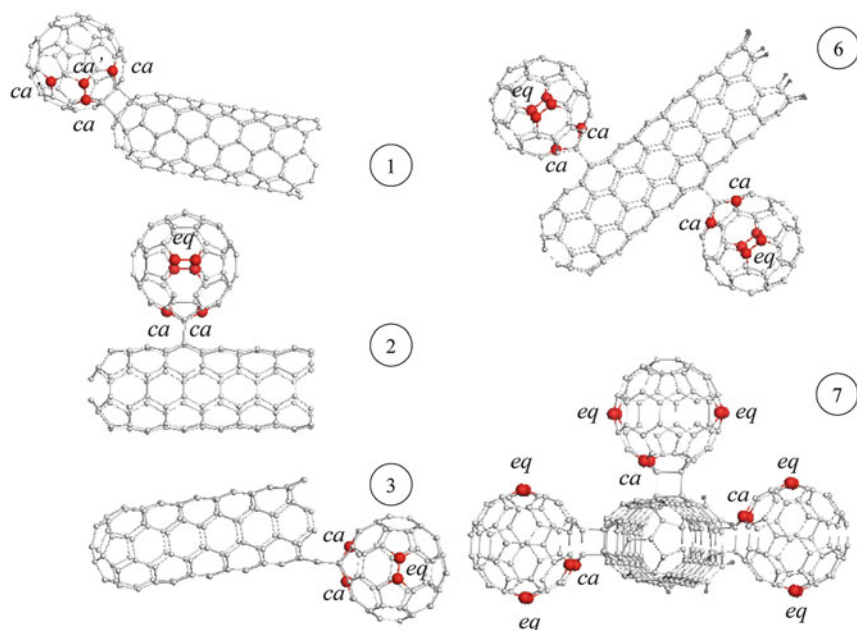


**Fig. 5.11** Equilibrium structures of  $[C_{60} + (4,4)]$  CNBs (Reproduced from Sheka and Shaymardanova (2011b), with permission from the Royal Society of Chemistry). *Red balls* indicate atoms of fullerene  $C_{60}$  with the high-rank  $N_{DA}$  values

**Table 5.2** Energetic characteristics of equilibrium  $[C_{60} + (4,4)]$  CNT nanobuds, kcal/mol

Nanobuds <sup>a</sup>	$E_{cpl}^{tot}$	$E_{def}^{tot}$	$E_{defCNT}$	$E_{defC_{60}}$	$E_{cov}^{tot}$
1. (cap)	-36,33	51,16	10,62	40,53	-87,48
2. (wall)	-3,38	59,64	24,64	35	-63,02
3. (end)	-86,65	47,65	8,25	39,4	-134,31
4. (cap)	3,09	114,38	62,76	51,62	-111,29
5. (wall)	-4,26	74,33	39,26	35,07	-78,59
6. (wall)	-8,21 (-4,10) <sup>b</sup>	155,62	85,33 (42,66) <sup>b</sup>	70,29 (35,15) <sup>b</sup>	-163,83 (-81,92) <sup>b</sup>
7. (wall)	-11,02 (-3,67) <sup>b</sup>	221,64	116,59 (38,86) <sup>b</sup>	105,05 (35,02) <sup>b</sup>	-232,66 (-79,55) <sup>b</sup>

Reproduced from Sheka and Shaymardanova (2011b), with permission from the Royal Society of Chemistry

<sup>a</sup>Figures number CNBs as in Figs. 5.8 and 5.10

<sup>b</sup>Data per one attached  $C_{60}$  molecule

### 5.4.3 Energetic Parameters and Reaction Barrier of Carbon Nanobuds

Energetic characteristics related to a set of  $[C_{60} + (4,4)]$  CNBs are presented in Table 5.2. The coupling energy  $E_{cpl}^{tot}$  is determined as

$$E_{cpl}^{tot} = \Delta H_{CNB} - \Delta H_{CNT} - \Delta H_{C_{60}}. \quad (5.4)$$

Here,  $\Delta H_{\text{CNB}}$ ,  $\Delta H_{\text{CNT}}$ , and  $\Delta H_{\text{C}_{60}}$  present heats of formation of the equilibrium structures of CNB, (4,4) SWCNT, and  $\text{C}_{60}$ , respectively.

As discussed in Sect. 5.3.2, the total coupling energy reflects two processes that accompany the fullerene attachment to the tube, namely, the deformation of both CNB components and their covalent coupling. The energy caused by deformation is determined as

$$E_{\text{def}}^{\text{tot}} = E_{\text{def CNT}} + E_{\text{def C}_{60}}, \quad (5.5)$$

where

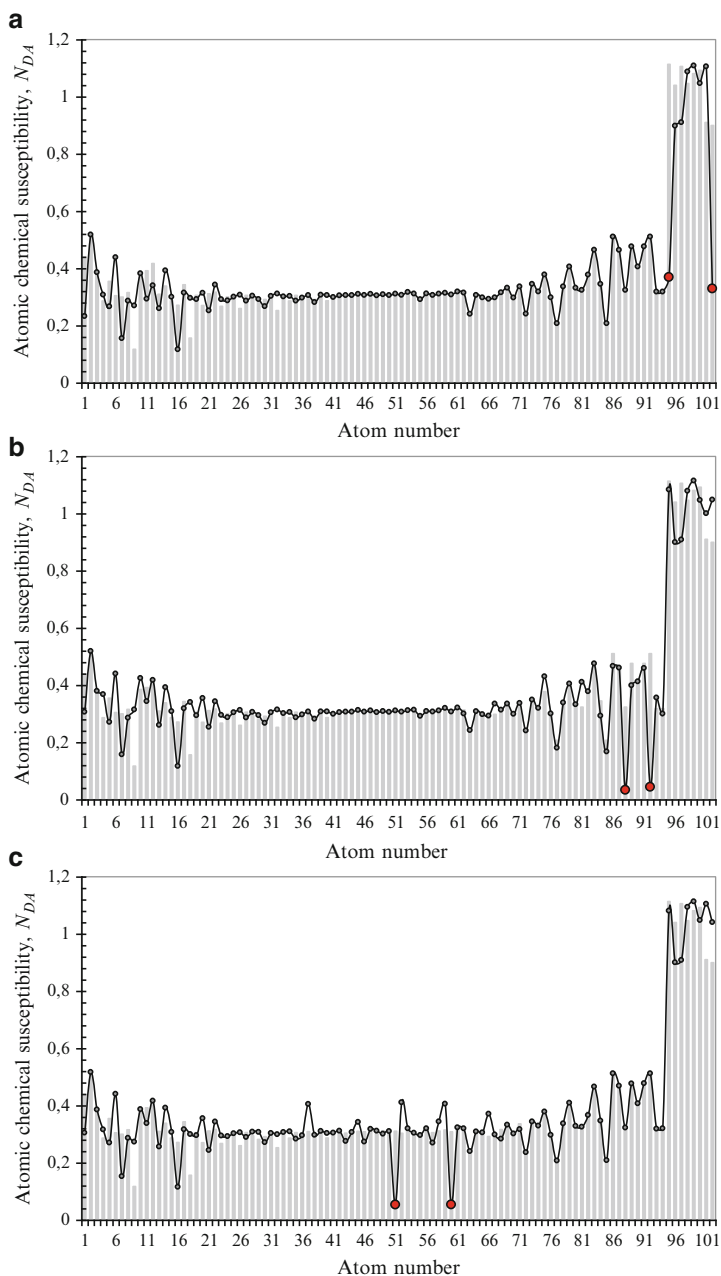
$$E_{\text{def CNT}} = \Delta H_{\text{CNT/CNB}}^{\text{op}}(R_{\text{CC}}) - \Delta H_{\text{CNT}}^{\text{eq}} \quad \text{and} \quad E_{\text{def C}_{60}} = \Delta H_{\text{C}_{60}/\text{CNB}}^{\text{op}}(R_{\text{CC}}) - \Delta H_{\text{C}_{60}}^{\text{eq}}. \quad (5.6)$$

Here,  $\Delta H_{\text{CNT/CNB}}^{\text{op}}(R_{\text{CC}})$  and  $\Delta H_{\text{C}_{60}/\text{CNB}}^{\text{op}}(R_{\text{CC}})$  present heats of formation of the one-point-geometry configurations of the SWCNT and fullerene components of the CNBs equilibrium configurations corresponding to the intermolecular distance  $R_{\text{CC}}$ . Accordingly, the chemical contribution into the coupling energy is determined as

$$E_{\text{cov}}^{\text{tot}} = E_{\text{cpl}}^{\text{tot}} - E_{\text{def}}^{\text{tot}}. \quad (5.7)$$

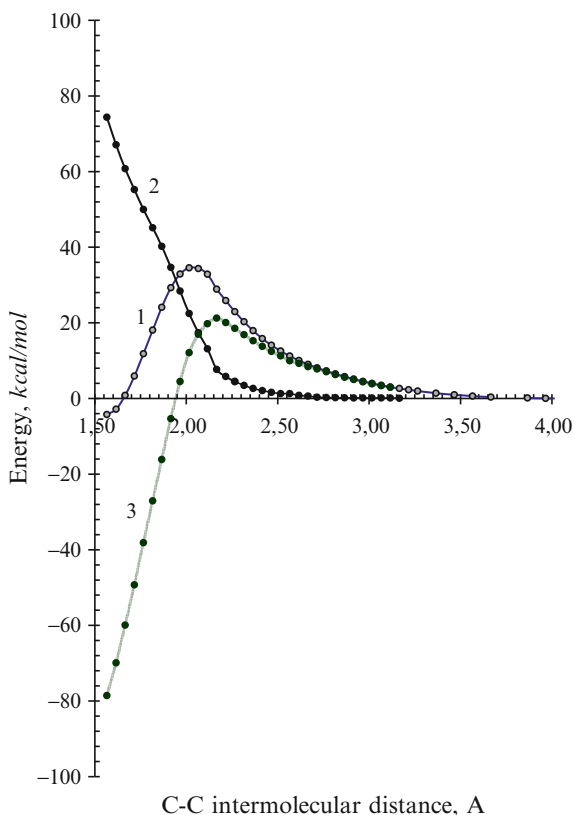
The data listed in Table 5.2 show two distinct features. The first concerns the difference in the energetic characteristics of CNBs, fullerene component of which is attached to either the cap or end atoms of the tube. The second is related to a close similarity of the latter for CNBs with fullerene attached to the tube sidewall. As seen in the table, the empty end of the tube, once the most active according to the ACS map in Fig. 5.6, provides the fullerene attachment with the biggest coupling energy and the smallest deformation energy related to the tube. It means that, at any contact of such tube with fullerene (as well as with any other addend), the first attachment occurs at the tube end. The next events will take place at the tube cap. The coupling energy decreases by 2.4 times while the deformation energy slightly increases. After these two events, there comes a turn of the tube sidewall, but the coupling energy decreases by  $\sim 26$  times when the deformation energy increases three times. The three events are quite superpositional as can be seen in Fig. 5.12. Each addition concerns a strictly local area so that highly active attachments to the end and cap region should not prevent from covering the main tube body by multiple attached fullerenes.

Figure 5.13 presents the dependence of the basic energetic characteristics of the CNBs on the C–C intermolecular distance  $R_{\text{CC}}$  by the example of CNB 5. As in the case of fullerene dimers discussed in Sect. 5.3.2, the barrier energy computation follows a stepwise elongation of two C–C bonds, which provide intermolecular contact via [2 + 2] cycloaddition, starting from the equilibrium configuration of the bud. The first minimum of the coupling energy  $E_{\text{cpl}}^{\text{tot}}$  is located at  $R_{\text{CC}} = 1.57 \text{ \AA}$  and constitutes  $-4.26 \text{ kcal/mol}$ . The maximum position at  $2.05 \text{ \AA}$  shows that at starting



**Fig. 5.12** Evolution of the atomic chemical susceptibility distribution over tube 1 under CNB formation when  $C_{60}$  is attached to the tube empty end (a), cap (b), and sidewall (c) (Reproduced from Sheka and Shaymardanova (2011b), with permission from the Royal Society of Chemistry). Histograms present data for the pristine tube. Curves with dots plot the data related to the formed CNBs 1, 2, and 3, respectively. Circled dots mark atoms, to which fullerene is attached. Atom numbering corresponds to that one in the output files

**Fig. 5.13** Profile of the barrier of the  $[C_{60} + (4, 4)]$  CNB decomposition (CNB 5) (Reproduced from Sheka and Shaymardanova (2011b), with permission from the Royal Society of Chemistry).  
 1.  $E_{\text{cpl}}^{\text{tot}}(R_{\text{CC}})$ ; 2.  $E_{\text{def}}^{\text{tot}}(R_{\text{CC}})$ ;  
 3.  $E_{\text{chem}}^{\text{tot}}(R_{\text{CC}})$  (see text)



distances exceeding this value, CNT and  $C_{60}$  form a weakly coupled complex with equilibrium spacing between components of  $4.47 \text{ \AA}$  and coupling energy of  $-0.06 \text{ kcal/mol}$ . The complex possesses all the characteristics of the charge transfer one, where CNT donates while  $C_{60}$  accepts electron under photoexcitation. Here we meet again the confirmation of the “ $4.2\text{--}4.7 \text{ \AA}$ ” rule that governs photodimerization and/or oligomerization of  $C_{60}$  molecules discussed in Sect. 5.3.1. A deep parallelism in the behavior of fullerene molecules, either singly bound to the tube body or in a company with other molecules in the case of multiple attachments, provides a good reason to expect the same parallelism between the energy dependences for these molecules, as well.

Since the contact zone between components of  $(C_{60})_2$  dimer and the considered CNB is presented by  $[2 + 2]$  cycloaddition, one could expect a deep similarity in the barrier profiles in the two cases. However, a comparison of plottings presented in Figs. 5.4 and 5.13 has revealed that this expectation has been realized only partially. Actually, one can see a similarity of the profile shape related to both the total coupling energy  $E_{\text{cpl}}^{\text{tot}}$  and  $E_{\text{def}}^{\text{tot}}$ ,  $E_{\text{cov}}^{\text{tot}}$  components in both cases. At the same time, the difference in numerical values of all the energies is so pronounced that

starting at much shallower minimum of  $E_{\text{cpl}}^{\text{tot}}$  in the case of CNB, much lesser barrier for the CNB formation and/or decomposition is achieved. So far no explanation of the difference other than the revealing of topochemistry of the addition reactions  $C_{60} + C_{60}$  and  $C_{60} + \text{CNT}$  can be suggested. A deep analysis of similar reactions for  $C_{60} + \text{NGr}$  dyads, given in the next section, convincingly supports the suggestion and exempts it from the last doubts.

## 5.5 Fullerene $C_{60}$ + Graphene Composites

### 5.5.1 Barrier Profile for $C_{60} + \text{NGr}$ Nanobuds

In contrast to fullerene oligomers and carbon nanobuds, the latter known now not only for  $C_{60}$  but for  $C_{70}$  as well (Nasibulin et al. 2007b; Tian et al. 2008), no indication of the existence of chemically bound fullerene-NGr compositions has been so far obtained. In contrast, it is worthwhile to remind a curious observation of intercalation of a graphite monolayer (authors' term) on iridium substrate by  $C_{60}$  molecules from a thick film made of fullerene deposited over graphene at  $T \sim 800$  K (Rut'kov et al. 1995), which speaks about a quite particular binding of the fullerene molecule with graphene.

Computations performed by Wu and Zeng (2009) were first to lift the veil above the feature. They have shown that the reaction of covalent addition of  $C_{60}$  to graphene basal plane is endothermic and requires a considerable amount of energy in contrast to  $(C_{60})_2$  dimer and  $[C_{60} + (4,4)]$  CNBs discussed in Sects. 5.3 and 5.4. However, the mentioned computations have been carried out in a standard configuration of the spin-restricted close-shell PBC DFT approach in spite of the fact pointed by the authors themselves that local and semilocal functionals in DFT generally give poor description of weak interaction. Similarly, insufficient is the response of the technique to the correlated odd electrons of graphene that is why test calculations of the authors within a spin-unrestricted DFT could not show any difference from the spin-restricted one due to overpressing the configurational part of the functionals. Similar test performed within the framework of the UBS HF approach (Sheka and Shaymardanova 2011b) results in 23 % (or 641.6 kcal/mol by the absolute value) lowering of the total energy of the (9, 9) NGr (the nomenclature follows the suggested in Gao et al. (2008)), which was chosen as supercell in the PCB DFT computations (Wu and Zeng 2009), when going from RHF to UBS HF approach.

Besides what has been said above, describing possibility to arrange periodic graphene nanobuds (GNBs), Wu and Zeng concentrated their attention on the basal plane of (9, 9) NGr as a substrate for a single  $C_{60}$  leaving the sheet edges aside as well as supposing homogeneous chemical activity of carbon atoms through over the sheet. It is actually not the case since a high non-homogeneity in the ACS distribution over NGr atoms divides its space into three regions, namely, zigzag

and armchair edges and the basal plane (Sheka and Chernozatonskii 2010c, d) similarly to cap, end, and sidewall of SWNT discussed in the previous section. This circumstance forms the grounds for the dependence of the formed nanobuds from the place of location of  $C_{60}$  and the state-of-the-art termination of both end and edge atoms. Empirically, the extreme chemical activity of the graphene edge atoms has been observed for various addends (Yan et al. 2012). Computationally, it has been predicted for such addends as carbon nanotubes (Sheka and Chernozatonskii 2010a) and  $C_{60}$  (Sheka and Shaymardanova 2011a). Obviously, the feature is of a particular importance for elaborating technology of producing graphene-based nanocarbon composites.

As was shown by the example of fullerene  $C_{60}$  (Sheka 2011a), the best way to eliminate features related to spatial inhomogeneity of the chemical activity of the molecule is to perform a computational stepwise synthesis of the derivatives in an algorithmic manner following the high-rank ACS value at each addition step. However, when the molecule is spatially extended such as CNTs and graphene sheets, different parts of the molecules may enter the reaction simultaneously, which drastically complicates the computational analysis, particularly when these parts are characterized by different chemical activity as is the case of CNT and graphene and when their electronic systems are interconnected. This circumstance faces one the problem of the substitution of a single-reaction approach usually used at simulations with a multi-reaction one. So far there has not been any multiple-reaction approach that could consider a simultaneously occurring community of reactions under so complicated conditions. A conventional single-reaction approach, applied to either solitary or stepwise reaction, can describe a multiple reaction only if the latter presents a set of events, nondependent on each other. As shown in the preceding section, such an approach was quite accessible for the description of CNBs. A similar superpositional approach was applied in Sheka and Shaymardanova (2011b) to the  $[C_{60} + (5, 5)]$  GNB to trace the dependence of the reaction product on the place of contact of the  $C_{60}$  molecule with (5, 5) NGr. As previously with dimer  $(C_{60})_2$  and CNBs, each of the reaction related to the formation of  $[C_{60} + (5, 5)]$  GNB is considered in terms of the scheme shown in Fig. 5.1.

### 5.5.2 *Computational Single-Reaction Synthesis of Graphene Nanobuds*

Similarly to fullerenes and CNTs, the length of C–C bonds in graphene noticeably exceeds the critical value  $R_{cov}^{crit}$  at which a complete covalent bonding of the relevant odd electrons is terminated, so that odd electrons of graphene are quite strongly correlated (Sheka 2011a, 2012) and effectively unpaired, thus providing quite valuable molecular chemical susceptibility  $N_D$  of the NGr molecule as a whole and noticeable atomic chemical susceptibility (ACS)  $N_{DA}$  related to each atom. Distributed over the NGr atoms,  $N_{DA}$  maps the chemical activity of the molecule atoms. Figure 5.14 presents the ACS distributions over atoms of (5, 5) NGr under

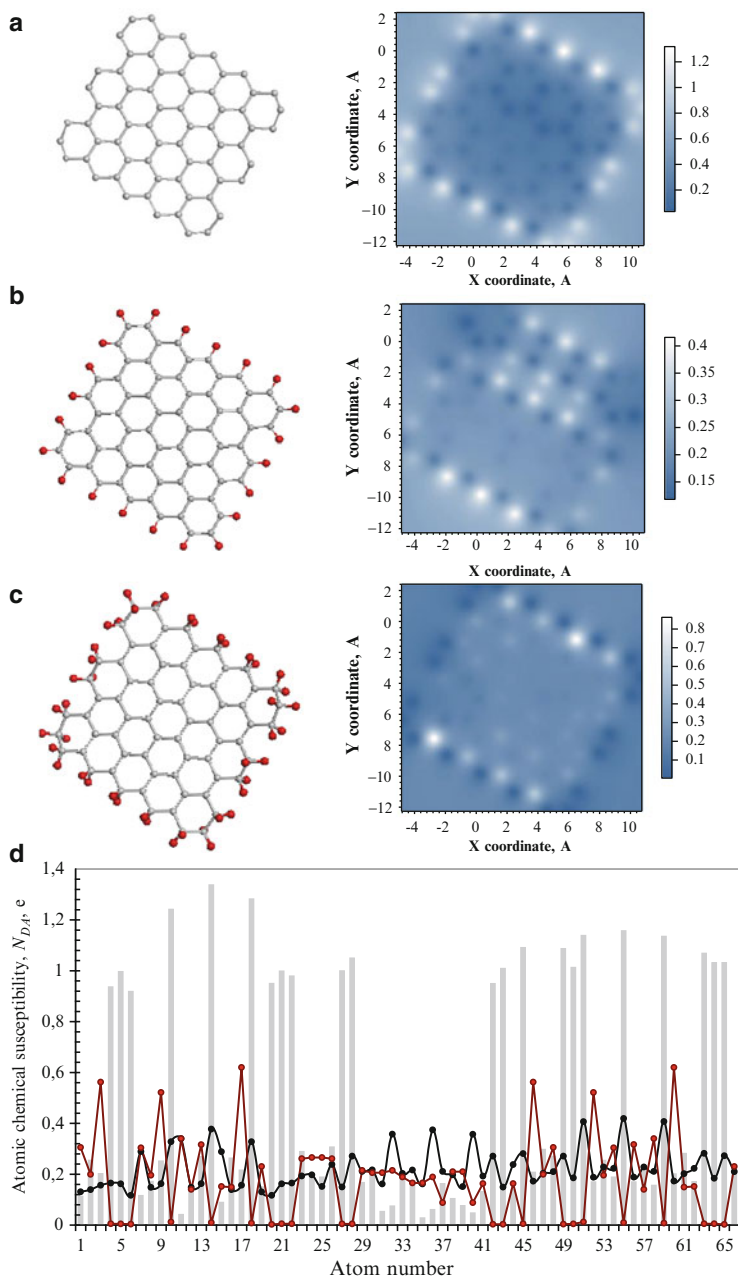


**Fig. 5.14** Equilibrium structures (*left*) and chemical portraits (*right*) of (5, 5) nanographene with empty (a) and hydrogen-terminated edge atoms by one (b) and two (c) terminators per carbon atom. Vertical scales determine the  $N_{DA}$  values amplitude. Distribution of the chemical susceptibility over nanographene atoms (d) light gray histogram (a), black curve with dots (b), and dark red curve with dots (c) (Reproduced from Sheka and Shaymardanova (2011b), with permission from the Royal Society of Chemistry)



conditions when the sheet edges are either non-terminated (empty) (a) or hydrogen-terminated by one (single-H) (b) and two (double-H) (c) atoms per one carbon. The color pictures present “chemical portraits” of the three molecules while plotting in Fig. 5.14d discloses the ACS distributions by the absolute values.

As seen in the figure, the portraits diverge considerably exhibiting the difference in both molecular and atomic chemical activity making the three molecules absolutely different with respect to the same chemical reactions. Non-terminated sheet is the most reactive. Then follow single-H- and double-H-terminated ones, the latter is the least active with respect to the total molecular susceptibility. In the case of  $C_{60}$ , its addition to the graphene sheet will obviously occur quite differently depending on particular-edge sample and the place of contact to the latter. Since zigzag and armchair edges as well as basal plane are the main space marks of graphene, let us consider possible situations concerning the  $C_{60}$  attachment to the (5, 5) NGr in view of the variation of both contact places and chemical termination of edge atoms. Each place-located reaction will be analyzed basing on the ACS distribution over the atoms related to the chosen place configuration.

As turned out, in all the cases, the chemically bound products are formed when the starting intermolecular C–C distances are less than 2.0 Å. At longer distances, each pair of  $C_{60}$  and (5, 5) NGr forms a classical charge transfer complex where graphene’s atoms contribute into the HOMO while  $C_{60}$ ’s atoms govern the LUMO, which causes the charge transfer from NGr to fullerene under photoexcitation.

### 5.5.2.1 Deposition of $C_{60}$ on (5, 5) Nanographene with Non-terminated Edges

According to the ACS map in Fig. 5.14a, atoms of zigzag empty edges are characterized by the highest ACS values. Approaching the edge, fullerene molecule will orient itself in such a way to provide the closeness between its most reactive atoms with two zigzag carbon atoms thus providing the formation of GNB 1 (see Fig. 5.15). Equilibrium structure of the formed GNB is shown next to the start configuration alongside with the ACS maps related to the graphene constituent of the GNB formed. Energetic parameters are presented in Table 5.3. We shall refer so far to the total coupling energy  $E_{\text{cpl}}^{\text{tot}}$  only, leaving the discussion of other quantities to the next section. The coupling energy is determined as

$$E_{\text{cpl}}^{\text{tot}}(R_{\text{CC}}) = \Delta H_{\text{GNB}}(R_{\text{CC}}) - \Delta H_{\text{NGr}}^{\text{eq}} - \Delta H_{\text{C}_{60}}^{\text{eq}}, \quad (5.8)$$

where  $\Delta H_{\text{GNB}}(R_{\text{CC}})$ ,  $\Delta H_{\text{NGr}}^{\text{eq}}$ , and  $\Delta H_{\text{C}_{60}}^{\text{eq}}$  determine heats of formation of the considered equilibrium GNB, characterized by intermolecular distance  $R_{\text{CC}}$  as well as equilibrated NGr and fullerene  $C_{60}$ , respectively. As seen in the table, GNB 1 formation is accompanied by high coupling energy whose negative sign points to the energetically favorable process.

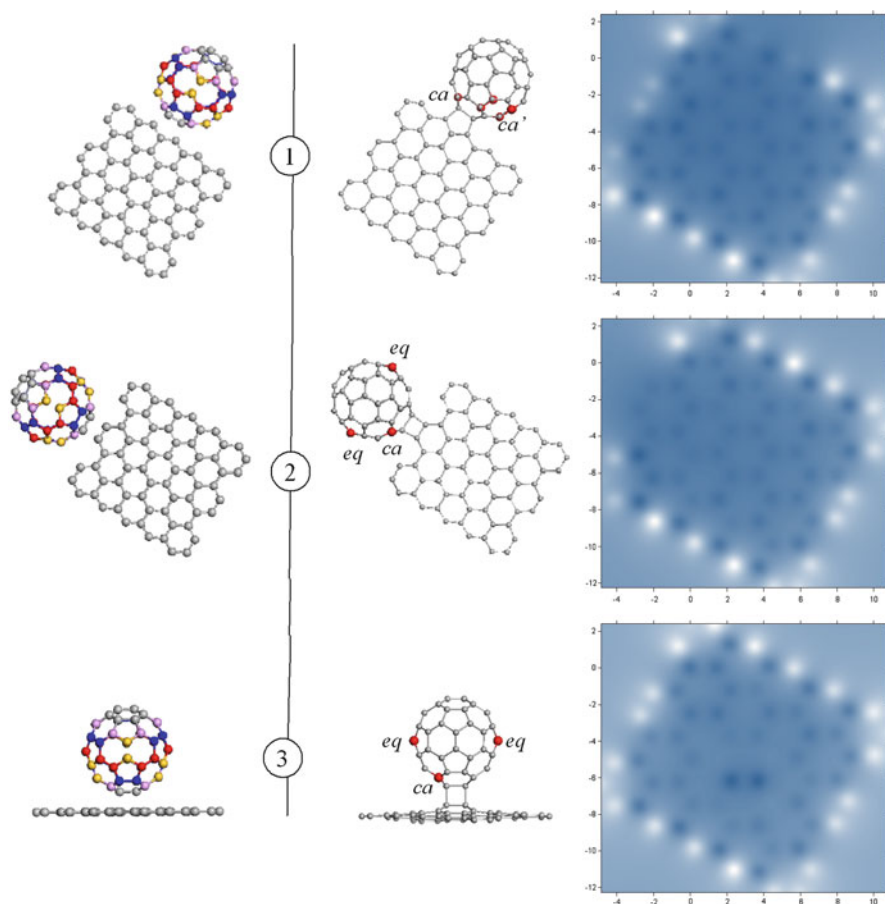


**Fig. 5.15**  $[C_{60} + (5, 5)]$  graphene nanobuds formed by attaching  $C_{60}$  fullerene to zigzag (1) and armchair (2) edge atoms as well as to the basal plane (3) of (5, 5) nanographene. Starting (left) and equilibrium (right) configurations with ACS maps of the latter. Red balls on equilibrium structures point fullerene atoms with the high-rank ACS values (Reproduced from Sheka and Shaymardanova (2011b), with permission from the Royal Society of Chemistry)

Looking at the ACS map of GNB 1 in Fig. 5.15, one can easily trace the effect of  $C_{60}$  attachment to the graphene substrate. Thus, two brightly shining zigzag atoms in the left, upper corner of the map in Fig. 5.14a are substituted with two dark spots in Fig. 5.15 while ACS of the remainder atoms is less altered. The quantified change in the ACS is presented by plottings in Fig. 5.16. The behavior of the attached fullerene seems to be quite similar to that considered in the previous sections. The molecule remains still chemically active. Its ACS map considerably changes after addition revealing new target atoms shown by red balls on equilibrium structures. The fullerene activity zone is quite similar to that one related to CNB 1 in Fig. 5.11 that should be expected due to zigzag structure of the (4, 4) SWCNT open end.

**Table 5.3** Energetic characteristics of equilibrium  $[C_{60} + (5,5)]$  graphene nanobuds, kcal/mol

Composite <sup>a</sup>	$E_{\text{cpl}}^{\text{tot}}$	$E_{\text{def}}^{\text{tot}}$	$E_{\text{defgr}}$	$E_{\text{def}C_{60}}$	$E_{\text{chem}}^{\text{tot}}$
1. zg	-128,45	70,56	20,7	49,86	-199,01
2. ach	-123	52,67	13,37	39,3	-175,67
3. bs	-12,11	86,8	53,76	33,04	-98,91
4. zgH1	-52,74	109,89	69,08	40,81	-162,63
5. achH1	-70,17	91,53	58,10	33,44	-161,71
6. bsH1	-27,38	96,63	63,48	33,25	-124,11
7. bsH2	1,82	62,24	28,97	33,27	-60,42
8. bsH1 <sup>b</sup>	32	88,98	55,75	33,23	-56,98

Reproduced from Sheka and Shaymardanova (2011b), with permission from the Royal Society of Chemistry

<sup>a</sup>Figures correspond to GNB's numbers in Figs. 5.15, 5.18, and 5.19

<sup>b</sup>Data for  $[C_{60} + (9, 8)]$  GNB

Graphene nanobuds 2 and 3 in Fig. 5.15 are formed by attaching fullerene  $C_{60}$  to either armchair edge of the graphene sheet or its basal plane. The intermolecular junctions look like characteristic  $[2 + 2]$  cycloadditions in both cases. However, a typical  $[2 + 2]$  junction, identical to that one for  $C_{60}$  oligomers and CNBs, takes place in GNB 3 only. In the case of GNB 2, the four-atom contact zone is supported by carbon atoms with two neighbors from the graphene side while the support atoms of fullerene have three neighbors. In spite of the difference, the junctions provide a high similarity in the construction of the fullerene active zones in the two cases. The latter consists of pairs of contact-adjacent *ac* and equatorial *eq* atoms and is fully identical to those discussed earlier for  $[2 + 2]$  cycloadducts related to both  $C_{60}$  oligomers and CNBs. Any further chemical modification of the GNBs via fullerene will depend on the addend size and will be favorable by targeting *ca* atoms by small addends while becoming preferable when targeting *eq* atoms by bulky addends. In contrast to structural similarity, energetic parameters of the two GNBs are quite different. If those for GNB 2 are similar by value to those of GNB 1, the coupling energy  $E_{\text{cpl}}^{\text{tot}}$  of GNB 3 is more than ten times fewer by the absolute value.

At first glance, the relevant ACS maps in Fig. 5.15 and their plottings in Fig. 5.16 evidence a quite local character of the  $C_{60}$  attachment to the graphene sheet. This might allow for suggesting a superpositional multiple attachment of the molecule forming multiple  $[(C_{60})_n + (5, 5)]$  GNBs looking like one of numerous possible examples presented in Fig. 5.17a. In its turn, attached fullerenes might serve as centers for further chemical modification of the GBDs by the formation of branched chains of different configurations (see Fig. 5.17b). However, in contrast to the above-considered CNBs, the fullerene attachment to the graphene sheet causes rather noticeable perturbations in the odd electronic state of the graphene, different in the considered three cases, as seen in Fig. 5.16. This feature may indicate a non-locality of the contact zones and puts a serious question concerning a superpositional character of multiple  $C_{60}$  attachments similar to those shown in Fig. 5.17a.

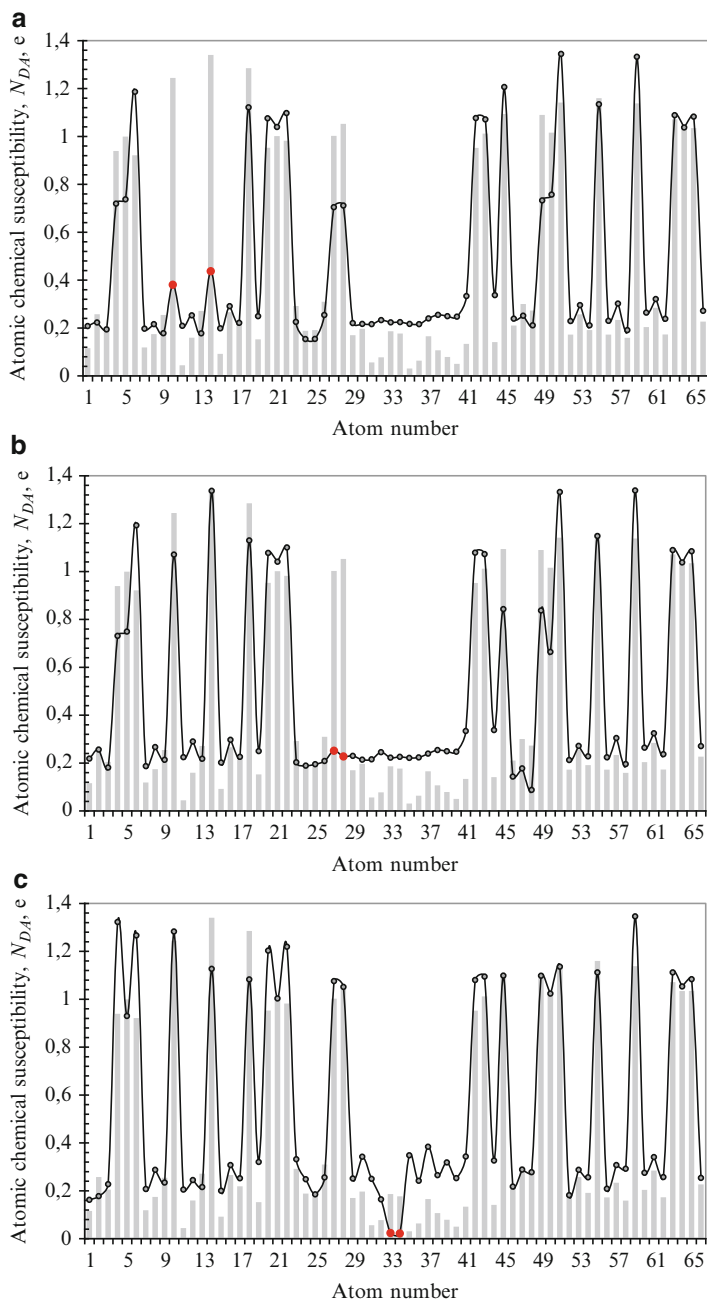


**Fig. 5.16** Atomic chemical susceptibility distribution over graphene atoms (*curves with dots*) in  $[C_{60} + (5, 5)]$  graphene nanobuds: GNB 1 (**a**), GNB 2 (**b**), and GNB 3 (**c**). *Red balls* mark graphene atoms to which  $C_{60}$  is covalently attached. *Light gray histograms* present ACS distribution for the pristine empty-edge (5, 5) nanographene (Reproduced from Sheka and Shaymardanova (2011b), with permission from the Royal Society of Chemistry)

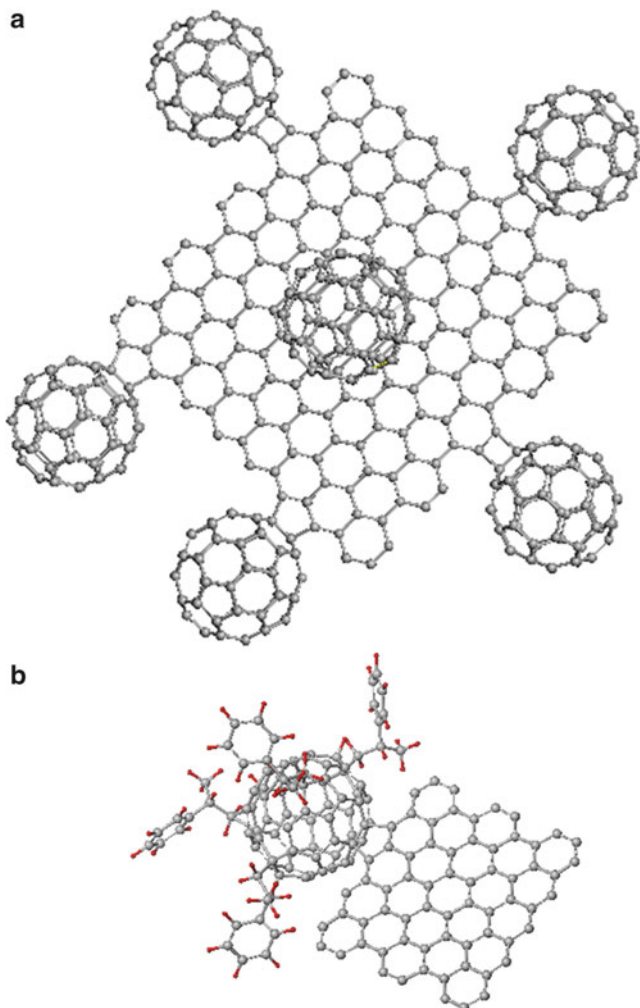


**Fig. 5.17** (a) A multiple  $[(C_{60})_6 + (5,5)]$  graphene nanobud. (b).  $[\{C_{60}Styr_4\} + (5,5)]$  graphene nanobud with  $C_{60}$ -tetrastylene

### 5.5.2.2 Deposition of $C_{60}$ on (5, 5) Nanographene with Hydrogen-Terminated Edges

Figure 5.18 presents single-reaction GNBs that can be formed in this case. As seen in the figure, the  $[C_{60} + (5,5)]$  GNBs' behavior is similar to that described in the previous section concerning the character of the graphene perturbation, the dependence on the place of contact, and the contact zone configurations. In the case of double-H-terminated graphene, the activity of zigzag and armchair edges is fully suppressed so that only contacts on the basal plane take place in the GNB

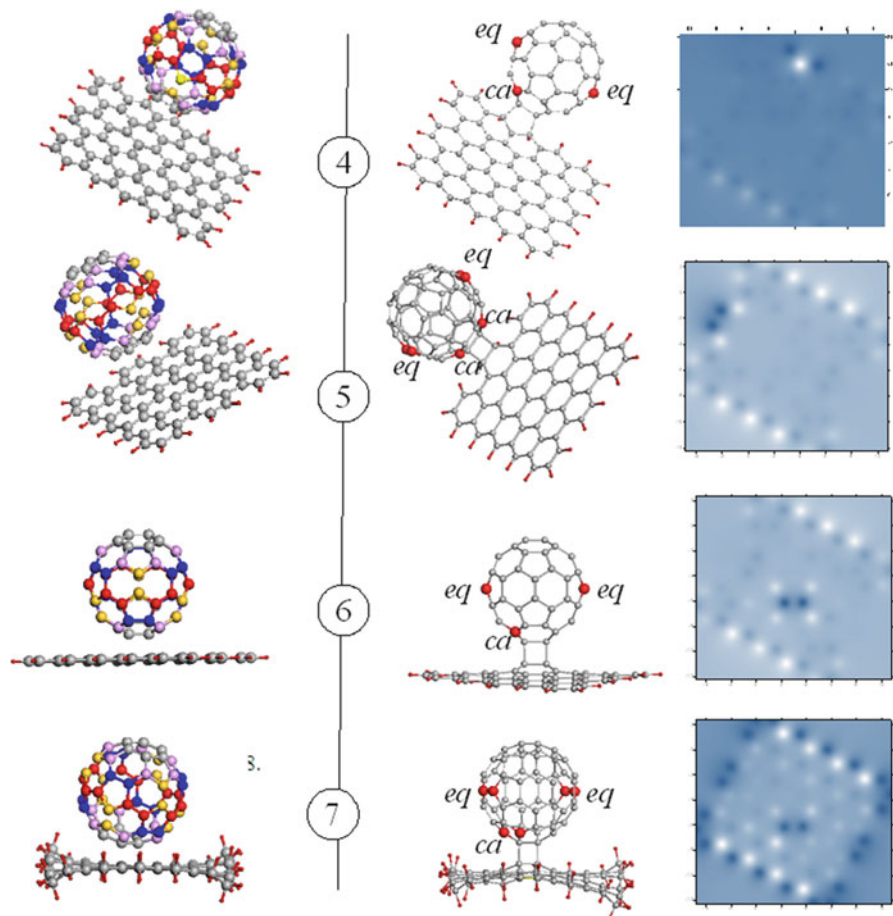
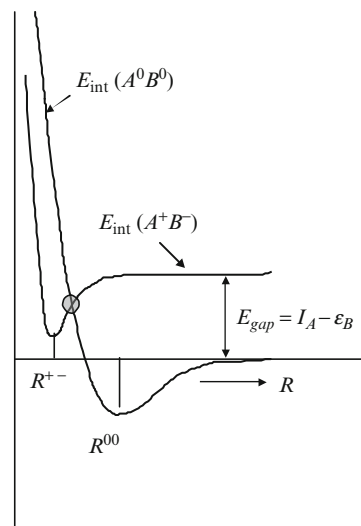


**Fig. 5.18**  $[C_{60} + (5, 5)]$  graphene nanobuds formed by attaching  $C_{60}$  fullerene to zigzag (4) and armchair (5) edge atoms as well as to the basal plane (6) and (7) in the case of single-H (4–6)- and double-H (7)-terminated (5, 5) nanographene. Starting (left) and equilibrium (right) configurations with ACS maps of the latter. Red balls on equilibrium structures point to fullerene atoms with the high-rank ACS values (Reproduced from Sheka and Shaymardanova (2011b), with permission from the Royal Society of Chemistry)

formation. As previously, the contact zones of GNBs 4 and 5 are not explicitly  $[2 + 2]$  cycloaddition junctions while those of GNBs 6 and 7 belong to the latter.

Changes in the chemical activity of the edge atoms greatly influence energetic parameters of the covalent bonding as seen in Table 5.3. The coupling energies  $E_{\text{cpl}}^{\text{tot}}$  related to the addition to zigzag and armchair edges of single-H-terminated graphene decrease more than twice by value. At the same time, addition to the basal plane is accompanied by more than twice increase in the value. The double termination of the graphene edge atoms causes the transformation of the

**Fig. 5.19** Scheme of terms of an IMI potential of type 3 (Sheka 2011a).  $(A^0B^0)$  and  $(A^+B^-)$  match the term branches related to the IMI between neutral molecules and their ions, respectively



endothermic reaction for GNB 6 into the exothermic one for GNB 7 that needs for its completion  $\sim 2$  kcal/mol thus showing that the IMI is not described more by the potential of type 1, presented in Fig. 5.1, but the potential of type 3 shown in Fig. 5.19 should enter the action.

Not only the change in the edge atom single-H-double-H termination causes that one in the IMI potential type, but a similar effect may be provided by increasing the size of the graphene single-H-terminated sheet. This is the case of GNB 8 formed by  $C_{60}$  covalently coupled with atoms on the basal plane of single-H-terminated (9, 8) nanographene (Fig. 5.20). A typical [2 + 2] cycloaddition forms the contact zone and the relevant coupling energy is high by value but positive. This means that in contrast to  $[C_{60} + (5, 5)]$  GNB, the creation of  $[C_{60} + (9, 8)]$  GNB requires energy while its stability depends on the high of the relevant barrier energy, which will be considered in the next section.

### 5.5.3 Energetic Parameters and Single-Reaction Barrier of Graphene Nanobuds

Looking for the reasons of so high changeability of GNBs forces to perform a comparative analysis of  $C_{60}$ -based composites, including  $(C_{60})_2$ , CNBs, and GNBs, at the level of energetic barriers. As was discussed in Sects. 5.3.2 and 5.4.3, it is quite reasonable to present the total coupling energy  $E_{cpl}^{tot}$  related to GNBs consisting of two components, namely,  $E_{def}^{tot}$  and  $E_{chem}^{tot}$  that take the form

$$E_{def}^{tot} = E_{defgr} + E_{defC_{60}}, \quad (5.9)$$

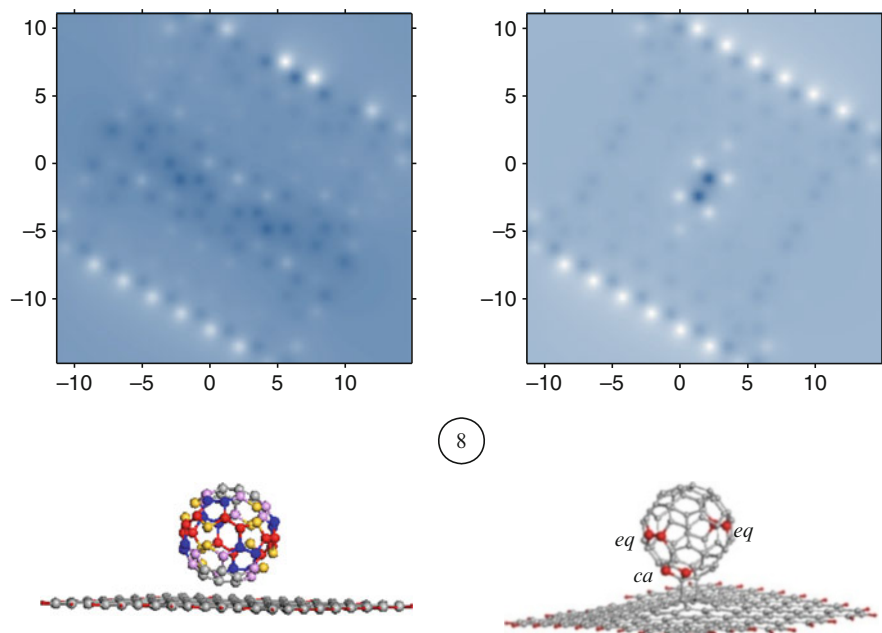


**Fig. 5.20**  $[C_{60} + (9, 8)]$  graphene nanobud formed by attaching  $C_{60}$  fullerene to the basal plane of  $(9, 8)$  nanographene. Starting (*left*) and equilibrium (*right*) configurations with ACS maps (*above*) related to initial and perturbed graphene. *Red balls* on equilibrium structures point to fullerene atoms with the high-rank ACS values (Reproduced from Sheka and Shaymardanova (2011b), with permission from the Royal Society of Chemistry)

where

$$E_{\text{defgr}}(R_{CC}) = \Delta H_{\text{NGr/GNB}}^{\text{op}}(R_{CC}) - \Delta H_{\text{NGr}}^{\text{eq}} \quad (5.10a)$$

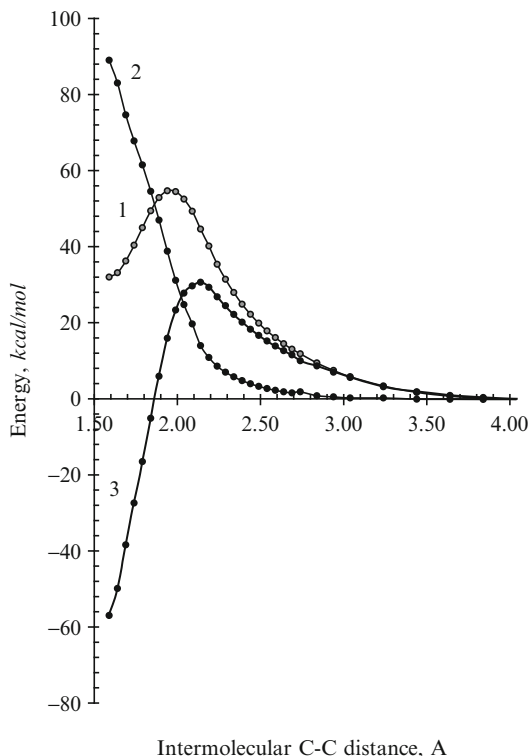
and

$$E_{\text{def}C_{60}}(R_{CC}) = \Delta H_{C_{60}/\text{GNB}}^{\text{op}}(R_{CC}) - \Delta H_{C_{60}}^{\text{eq}}. \quad (5.10b)$$

Here,  $\Delta H_{\text{NGr/GNB}}^{\text{op}}(R_{CC})$  and  $\Delta H_{C_{60}/\text{GNB}}^{\text{op}}(R_{CC})$  present heats of formation of the one-point-geometry configurations of the NGr and fullerene components of the equilibrium configurations of the studied GNB characterized by the intermolecular distance  $R_{CC}$ . Accordingly, the chemical contribution into the coupling energy can be determined following (5.7). Figure 5.21 presents the dependence of  $E_{\text{cpl}}^{\text{tot}}(R_{CC})$ ,  $E_{\text{def}}^{\text{tot}}(R_{CC})$ , and  $E_{\text{chem}}^{\text{tot}}(R_{CC})$  on the intermolecular 1–1' and 2–2' C–C distances (see Fig. 5.3a) for GNB 8. The three plottings in the figure are generally similar to those presented in Fig. 5.4 and Fig. 5.13 related to the  $(C_{60})_2$  dimer and  $[C_{60} + (4, 4)]$  CNB. This is obviously resulted from the similarity of atomic structure of the contact zones formed in all the considered cases by  $[2 + 2]$  cycloadditions. The coupling



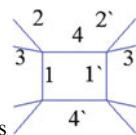
**Fig. 5.21** Profile of the barrier of the  $[C_{60} + (9, 8)]$  GNB decomposition (GNB 8) (Reproduced from Sheka and Shaymardanova (2011b), with permission from the Royal Society of Chemistry).  
 1.  $E_{\text{cpl}}^{\text{tot}}(R_{\text{CC}})$ ; 2.  $E_{\text{def}}^{\text{tot}}(R_{\text{CC}})$ ;  
 3.  $E_{\text{chem}}^{\text{tot}}(R_{\text{CC}})$  (see text)



energy  $E_{\text{cpl}}^{\text{tot}}$  can be evidently divided into  $E_{\text{def}}^{\text{tot}}$  and  $E_{\text{cov}}^{\text{tot}}$  components of the same type as those related to the previous two cases. However, the difference in numerical values of the two components at starting point results in a remarkable lifting of the  $E_{\text{cpl}}^{\text{tot}}(R_{\text{CC}})$  minimum for GNB 8 moving it into positive energy region. Consequently the barrier energy  $E_{\text{barr}}^{\text{GNB}}$  lowers up to 22.7 kcal/mol. Here again we are facing a peculiar feature that cannot be explained by other things than the topochemistry involved in the addition reaction  $C_{60} + \text{NGr}$ .

## 5.6 The Identity of [2 + 2] Cycloadditions and Topochemistry of Addition Reactions

The discussed nanobuds, including  $C_{60}$  oligomers, CNBs, and GNBs, are resulted from a single-reaction covalent pair-pair bonding between the components, where each of the latter delegates a pair of the most chemically active atoms to form intermolecular junctions. The formed nanobuds present a rather complicated set of covalently bound composites that differ by both coupling energies and the structure of intermolecular junctions. Thus, only  $(C_{60})_2$  dimer, sidewall CNBs,

**Table 5.4** Joint characteristics of the nanobud [2 + 2] cycloadditions

Nanobuds	C–C bonds, Å <sup>a</sup>				$N_{DA}^{b, e}$	$E_{chem}^{tot}$ , kcal/mol	$E_{barr}^{NB}$ , kcal/mol
	1	2	3	4			
$C_{60} + C_{60}^c$	1.548	1.515	1.515	1.596	0.271, 0.271	−112.97	65.24
	1.548	1.516	1.516	1.596			
CNB 3 <sup>d</sup>	1.567	1.483	1.486	1.652	0.308, 0.307	−134,31	–
	1.567	1.520	1.518	1.590			
CNB 5 <sup>d</sup>	1.566	1.484	1.486	1.652	0.305, 0.304	−78,59	36.07
	1.566	1.520	1.518	1.590			
GNB 3 <sup>e</sup>	1.591	1.496	1.496	1.581	0.183, 0.173	−98,91	–
	1.591	1.519	1.518	1.579			
GNB 6 <sup>e</sup>	1.589	1.493	1.494	1.578	0.216, 0.201	−124,11	–
	1.589	1.519	1.517	1.580			
GNB 7 <sup>e</sup>	1.590	1.492	1.492	1.578	0.189, 0.165	−60,42	–
	1.589	1.517	1.519	1.580			
GNB 8 <sup>f</sup>	1.591	1.494	1.494	1.576	0.227, 0.174	−56.98	22.70
	1.592	1.519	1.518	1.580			

Reproduced from Sheka and Shaymardanova (2011b), with permission from the Royal Society of Chemistry

<sup>a</sup>The bond numeration corresponds to the insert. Two-row presentation distinguishes the primed bonds (the second rows) related to  $C_{60}$  in all cases from unprimed ones (the first rows) related to the  $C_{60}$  partner

<sup>b</sup>The data are related to the pair of atoms of  $C_{60}$  partners in the nanobuds. The data for fullerene partner are presented in the first cell

<sup>c</sup> $C_{60}$  dimer

<sup>d</sup>[ $C_{60} + (4,4)$ ] CNB. CNB' numbering corresponds to that in Figs. 5.7 and 5.9

<sup>e</sup>[ $C_{60} + (5,5)$ ] GNB. GNB' numbering corresponds to that in Figs. 5.14 and 5.17

<sup>f</sup>[ $C_{60} + (9,8)$ ] GNB (see Fig. 5.18)

and basal plane GNBs can be characterized by the [2 + 2] cycloaddition as alike intermolecular junction. Table 5.4 summarizes data covering these three cases.

As seen in the table, structural characteristics concerning the [2 + 2] cycloadditions are practically identical within CNB and GNB groups while the coupling energies differ therewith quite considerably. Obviously, the observed feature is a convincing manifestation of the topological nature of the reaction considered. However, nowadays there is a lack of appropriate concepts and terms that could interconnect methodologies of quantum chemistry and chemical topology at a quantitative level so that we have to stay among habitual chemical ideas as well to try to find among them those points that may indicate the difference in topology. Thus, within the framework of single-reaction approach, one of the first attempts to interpret topological peculiarities in the terms of usual application was made by Haddon (1993) who suggests the dependence of chemical activity of  $sp^2$  nanocarbons on the curvature of the carbon skeleton. However, as thoroughly shown later (Sheka and

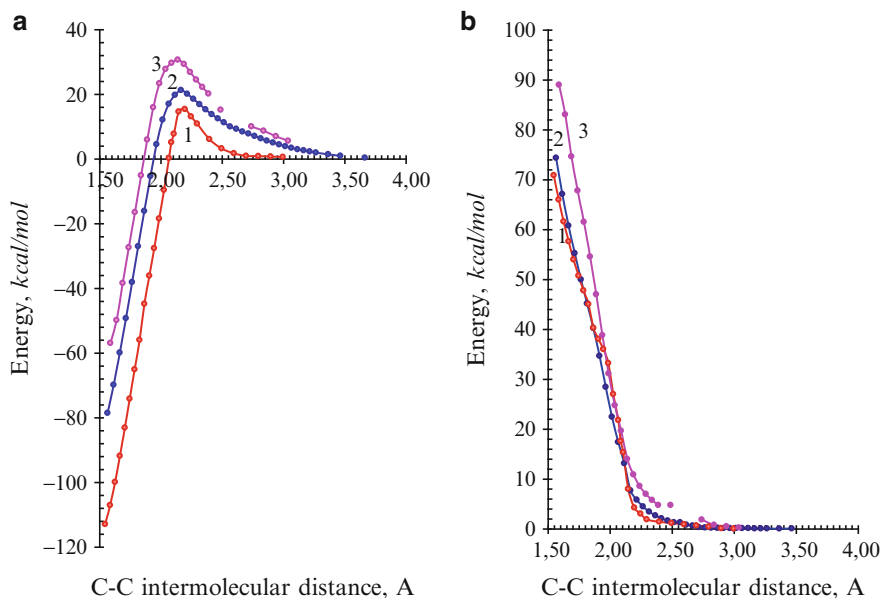


**Fig. 5.22**  $E_{cov}^{tot}(R)$  (a) and  $E_{def}^{tot}(R)$  (b) plottings for  $(C_{60})_2$  dimer (1),  $[C_{60} + (4, 4)]$  CNB 5 (2), and  $[C_{60} + (9, 8)]$  GNB 8 (3) (Reproduced from Sheka and Shaymardanova (2011b), with permission from the Royal Society of Chemistry)

Chernozatonskii 2007), the Haddon approach is quantitatively supported in rare cases only, that is why the approach based on simultaneous consideration of covalent coupling and deformation suggested later (Sheka and Shaymardanova 2011b) seems to open up much larger possibilities in describing chemical modification of  $sp^2$  nanocarbons. According to the latter, the discussed inconsistency of changeable energetic characteristics with the identity of the intermolecular [2 + 2] cycloaddition junctions may be addressed to a specificity of the intermolecular interaction between the components of the nanobuds.

The specificity concerns two facets related to covalent bonding in the contact area and to the deformation of carbon skeletons. Characterized by  $E_{cov}^{tot}(R_{CC})$  and  $E_{def}^{tot}(R_{CC})$ , respectively, a comparative presentation of the considered composites is shown in Fig. 5.22. As mentioned earlier,  $E_{cov}^{tot}(R_{CC})$  curves present barrier profiles in terms of DA-assisted intermolecular interaction schematically shown in Figs. 5.1 and 5.19. The energy gap  $E_{gap} = I_A - \varepsilon_B$  is of key importance for the case, so that changing in either ionization potential or electron affinity of partners may influence both the depth of the energy minimum at  $R^{+-}$  and the barrier high. Table 5.5 summarizes the relevant data for the studied nanobuds. The energy  $E_{gap}$  is different due to decreasing ionization potential when going from  $C_{60}$  fullerene to graphene (9.87, 9.19, and 8.2 eV for  $C_{60}$ , (4, 4) SWCNT, and (9, 8) NGr, respectively). In the latter case, the ionization potential depends on both the graphene sheet size and the edge saturation and constitutes  $\sim 8.5 \pm 0.2$  eV in the case of non-saturated edges. Energies  $E_{cov}^{tot}$  and  $E_{barr}$  synchronously follow the  $E_{gap}$  changes, decreasing by the

**Table 5.5** Parameters of donor–acceptor interaction in  $C_{60}$ -based nanobuds

Nanobud	$E_{\text{gap}}$ , eV	$E_{\text{cov}}^{\text{tot}}$ , kcal/mol	$E_{\text{barr}}$ , kcal/mol	Charge, $e$	
				$C_{60}$	Partner 2
$(C_{60})_2$	7.21	−112.97	15.36	0	0
CNB 5	6.53	−78.59	21.22	−0.028	0.028
GNB 8	5.54	−56.99	30.62	−0.092	0.092

Reproduced from Sheka and Shaymardanova (2011b), with permission from the Royal Society of Chemistry

absolute value in the former case thus lowering the barrier. The gap decreasing promotes a significant charge transfer between the nanobud components in the ground state as well. Therefore, data presented in Fig. 5.22a and Table 5.5 reveal changes in the DA interaction in the studied nanobuds that significantly influence the covalent bonding in the relevant [2 + 2] cycloadditions.

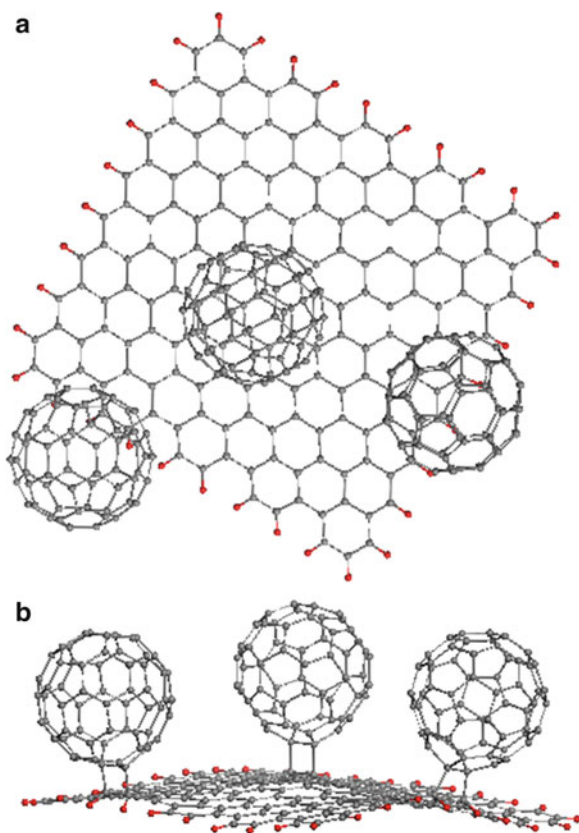
As for deformation energies, those presented in Fig. 5.22b show quite similar dependence on the spacing between nanobuds components, differing only in the near vicinity of the relevant cycloadditions. For the latter, the energies constitute 70.83, 74.33, and 88.98 kcal/mol related to  $(C_{60})_2$ , CNB 5, and GNB 8, respectively, thus highlighting the growth of the difficulty to adopt the structure of the carbon skeleton to the  $sp^2$ – $sp^3$  transformation caused by the formation of [2 + 2] cycloaddition when going from fullerene to CNT and graphene.

Still open there has been a question concerning topological effects on odd-electron system of graphene. An obvious consequence concerns a suspected non-locality of the contact zone of GNBs. Last examinations have revealed a clearly seen non-superpositional character of multiple additions to a single graphene sheet (Sheka 2012, unpublished). A triple [ $(C_{60})_3 + (9, 8)$ ] GNB with single-H-terminated edge atoms is shown in Fig. 5.23 in two projections. The molecules are attached to the basal plane of the sheet as well as to the armchair and zigzag edges. As turned out, the coupling energy of this bud deviates drastically from a sum of the coupling energies related to three single GNBs that correspond to the attachments mentioned above. Moreover, it was shown that after decomposition of both the triple GNB as well as of the three different single GNBs, the graphene sheet is characterized by lower energy in comparison with that of pristine one. Therefore, the addition of fullerene provokes a structural transition in the substrate thus revealing a nonstability of the pristine structure. The structural nonstability seems to be a characteristic feature of a large graphene sheet that greatly complicates the consideration of topology effects, if not only these effects manifestation.

## 5.7 Graphene + Carbon Nanotube Composites

All the above-considered composites can be attributed to the composites with a single contact that was provided by the peculiarities of the  $C_{60}$  fullerene. In the case of CNT + graphene composites, we are facing the situation with multiple

**Fig. 5.23** Equilibrium structure of a triple  $[(C_{60})_3 + (9, 8)]$  GNB in *top* (a) and *side* (b) views (Sheka 2012, unpublished)



contacts in each case due to extreme specificity of both components (Sheka and Chernozatonskii 2010a). Therefore, the composites form the platform for elucidation the topochemical character of the interaction between spatially extended species.

As previously, both components are good donors and acceptors of electrons (Sheka and Chernozatonskii 2010b, c, d), so that the IMI between them is subordinated to two-well shape of the ground state energy term shown in Figs. 5.1 and 5.19. This provides the formation of two modes of composites, one of which consists of weakly interacting components  $A + B$  located at comparatively large distance while the second  $AB$  is formed in the range of short interatomic distances and corresponds to strongly coupled composition.

The next point concerns the obvious difference in the structure of contact zones of the composites, in contrast to  $C_{60}$ -carbon and  $C_{60}$ -graphene nanobuds, where the contact zones were limited to  $[2 + 2]$  cycloadditions. In view of a considerable electron correlation in both species, the formation of contact zones between them is subordinated to not only point high-rank ACS, as previously, but the ACS high-rank profiles over sets of atoms from both sides.

The third complication concerns a great variety of multi-derivative structures, which can be formed, when both tubes and graphene serve either as main bodies or present attached additives. The first attempt to consider properties of these complicated structures has been undertaken in Sheka and Chernozatonskii (2010a). Computed profiles of the atomic chemical susceptibility (ACS) along the tube and across their body as well as over NGr sheets served as quantified pointers that allowed localizing the most active contact zones of interacting partners.

To make the presented below more clear, let us remind peculiarities of the ACS distributions of both partners that allow for predicting addition reactions to be expected. While, on the subject of carbon nanotubes, we must take into account the following (Sheka and Chernozatonskii 2010b):

- The space of chemical reactivity of SWCNTs coincides with the coordinate space of their structures while different for the particular structure elements. This both complicates and facilitates chemical reactions involving the tubes depending on a particular reaction goal.
- Local additions of short-length addends (involving individual atoms, simple radical, and so forth) to any SWCNT are the most favorable at open empty ends, both armchair and zigzag ones, the latter more effective. Following these places in activity are cap ends, defects in the tube sidewall, and sidewall itself. The reactivity of the latter is comparable with the highest reactivity of fullerene atoms.
- Chemical contacts of SWCNTs with spatially extended reagents (graphene sheets) can occur in three ways: namely, when the tube is oriented either normally or parallel to the surface and when graphene acts as a “cutting-blade” to the tube sidewall.
- Addition reactions with the participation of multi-walled CNTs will proceed depending on the target atoms involved. If empty open ends of the tubes are main targets, the reaction will occur as if one deals with an ensemble of individual SWCNTs. If sidewall becomes the main target of the reaction, output will depend on the accessibility of inner tubes additionally to the outer one.

A concentrated view on the reactivity of atoms of a rectangular NGr presented in Fig. 5.14 allows for stating that (Sheka and Chernozatonskii 2010c):

- Any chemical addend will be firstly attached to the NGr zigzag edges, both hydrogen-terminated and empty.
- Slightly different by activity non-terminated armchair edges compete with zigzag ones.
- Chemical reactivity of basal atoms only slightly depends on the edge termination and is comparable with that of SWCNT sidewall and fullerenes, thus providing a range of addition reactions at the NGr surface.
- The disclosed chemical reactivity of both edges and the main body of NGr causes a particular two-mode pattern of the NGr attaching to any spatially extended molecular object such as either CNT or substrate surface, namely, a normal mode and a tangent or parallel one.

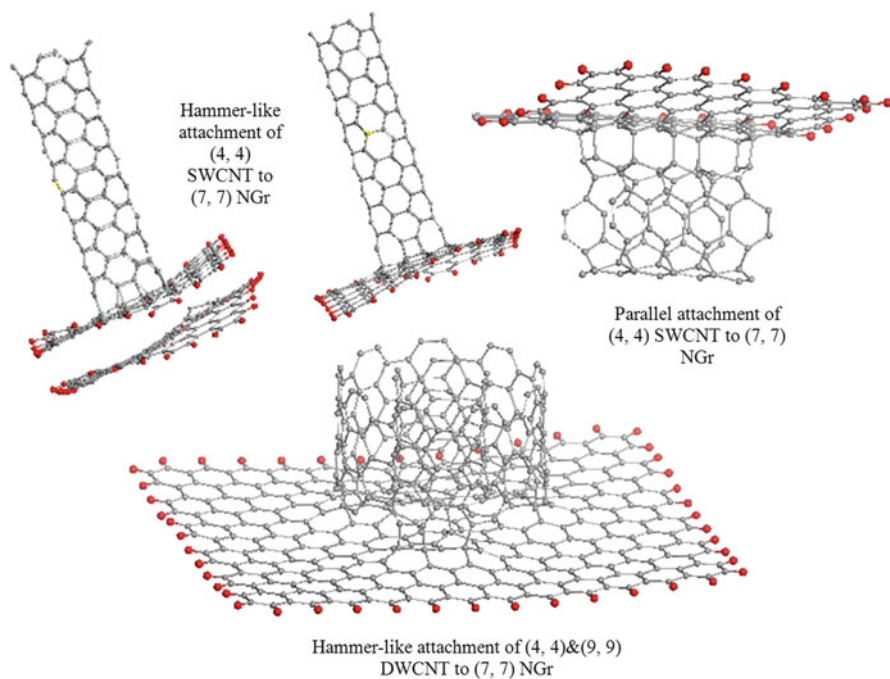


**Fig. 5.24** Equilibrium structures of CNT + NGr composites

Two SWCNT fragments presenting  $(n, n)$  and  $(m, 0)$  families, namely,  $(4, 4)$  and  $(8, 0)$  and a set of NGr of different size are chosen to reveal general tendencies of the composite formation (Sheka and Chernozatonskii 2010a). Due to the fact that the space of chemical reactivity of both CNTs and graphene coincides with the coordinate space of their structures, even single addition reactions, which lead to the composite formation, are not local but are largely extended in the space. This greatly complicates the construction of starting dyads, triads, and more complex configurations of components making their number practically endless. However, a thorough analysis of the ACS profiles of both components made it possible selecting two main groups of the composites, conditionally called “hammer” and “cutting-blade” structures. The former follows from the fact that empty ends of SWCNTs are the most chemically active so that the tubes might be willingly attached to any NGr forming a hammer handle. The latter is a consequence of exclusive chemical reactivity of both zigzag and armchair edges of non-terminated NGr, so that NGr can touch a SWCNT sidewall tangentially as a blade.

Figure 5.24 briefly sums up the main features that accompany the attachment of CNT to the basal plane of graphene in the hammer-like manner. The formation of composites significantly disturbs the NGr plane due to  $sp^2$ – $sp^3$  transformation of its carbon atoms involved in the contact zone, and this transformation is transferred even to the second layer of graphene. When the tube is oriented parallel to the

plane, the equilibrium structure occurs to depend on whether the tube open ends are either empty or terminated (say, by hydrogens). In the first case, the tube and the NGr attract each other willingly and seven newly formed intermolecular C–C bonds provide the tight connection between the partners. When tracing subsequent steps of the joining (optimization) (Sheka and Chernozatonskii 2010a), one can see that the coupling starts at the tube ends by the formation of single bonds at first and then a pair of the C–C bonds at each end. Afterwards, these bonds play the role of the strops of gymnastic rings that pull the tube body to the sheet. However, when the tube ends are hydrogen-terminated, no intermolecular C–C bonds are formed, and the total energy coupling energy becomes repulsive.

The fragment of a double-wall CNT (DWCNT) in Fig. 5.24 consists of fragments of (4, 4) and (9, 9) SWCNTs with the same number of benzoid units along the vertical axis and open empty ends on both sides. Owing to the slightly different periodicity of the Kekule-incomplete Clar-complete Clar networks (Matsuo et al. 2003) in the two tubes, the fragment lengths do not coincide exactly. In due course of the optimization, the attachment of the joint fragment to the graphene sheet starts from the formation of intermolecular C–C bonds with either inner or outer tube depending on which is closer to the sheet. When opposite free ends of the tube are not fixed, the remaining fragment slides outwards, transforming the composition into a peculiar “telescope” system. When the free ends are fixed, both inner and outer fragments are joined to the sheet as shown in the figure. The coupling energy is large enough to provide a strong coupling between the graphene sheet and the DWCNT that explains a high stability of recently synthesized MWCNTs-graphene composite under conditions when one end of each MWCNT was fixed (Kondo et al. 2008).

Analyzing the presented data, it makes possible to conclude the following (Sheka and Chernozatonskii 2010a):

1. The normal attachment of an empty-end SWCNT to graphene sheet is energetically favorable.
2. The horizontal attachment of the tube is also possible while much weaker.
3. H termination of the tube ends renders the horizontal attachment impossible and severely weakens the normal one.
4. Both multiple normal attaching of SWCNTs and a single and multiple attaching of a DWCNT are energetically favorable, and graphene sheets can be easily fixed over tubes in case their open ends are empty.
5. Graphene sheets are extremely structure flexible and even a weak intermolecular interaction causes a loss of the sheet flatness.

Cutting-blade composites are shown in Fig. 5.25. Two SWCNT fragments, namely, (8, 0) and (4, 4), as well as (7, 7) NGr were chosen to demonstrate typical compositions to be formed in this case (Sheka and Chernozatonskii 2010a). At start each time, the NGr edge was oriented parallel to the cylinder axis in the vicinity of SWCNT along a line of sidewall atoms in such a way to maximize the number of intermolecular C–C contacts. Since ACS distribution over the cross-sectional atoms of both tubes is well homogeneous (Sheka and Chernozatonskii 2010b), there is no azimuthal selectivity of the line position in this case. As for NGr,



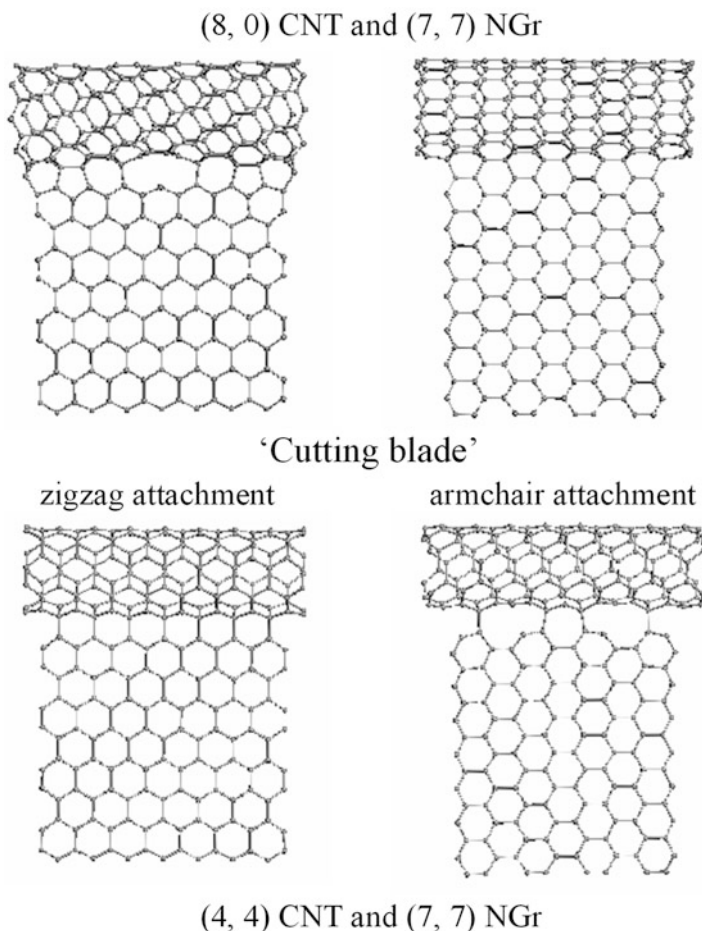


**Fig. 5.25** Equilibrium structures of cutting-blade CNT + NGr composites

zigzag and armchair edges of NGr with empty edges are comparable (see Fig. 5.14) while somewhat different. Due to this, two NGr orientations with respect to the tube sidewall were examined. Basing on the coupling energy, the preference in the cutting-blade structures should be given to armchair attachment in the case on (8, 0) SWCNT while the zigzag attachment is preferential for (4, 4) SWNT.

Since the cutting-blade attachment disturbs the ACS distribution along the line of atoms involved in the contact only, a multiple addition of the graphene sheets is possible, whose number is governed by sterical constrains mainly. Figure 5.26 presents a set of such dicomposites. Obviously, for large-diameter tubes, a sequential addition of a number of NGr will result in the formation of a multi-tooth gear. A particular attention should be drawn to a cradle-like composite shown in the figure. It may be considered as the illustration of a possible fixation of an individual

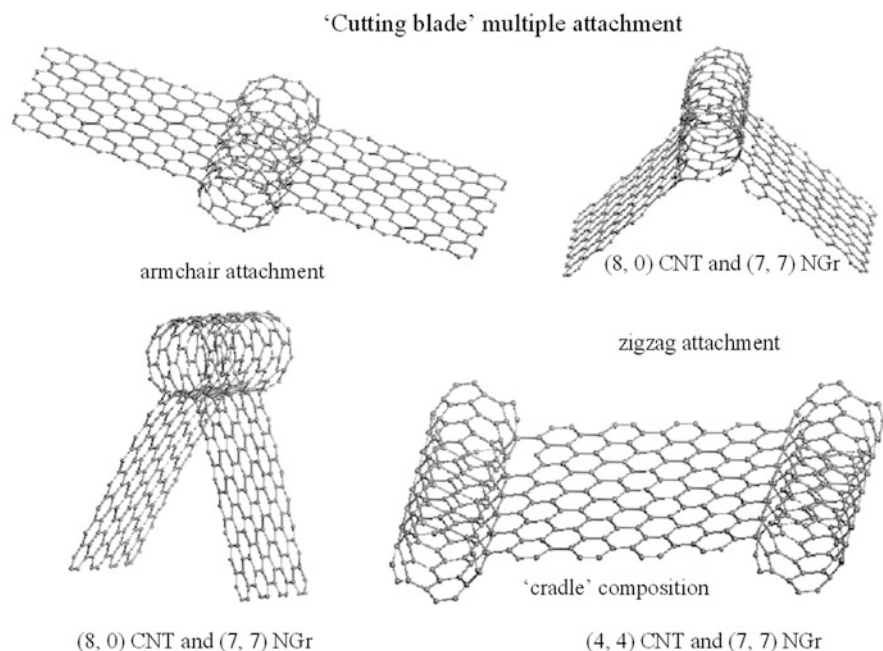


**Fig. 5.26** Equilibrium structures of CNT + NGr dicomposites

graphene sheet under conditions of the least perturbation of the sheet. Obviously, not (4, 4) SWCNT but much larger tubes should be taken as supporters. Since ACS of SWCNTs depends on the tube diameter only slightly (Sheka and Chernozatonskii 2010b), the cradle composite formation can be provided by any tubes, even different in diameter within the pair.

In spite of the doubtless exemplary of studied composites (Sheka and Chernozatonskii 2010a), the performed investigations allowed making the following general conclusions:

1. The formation of the hammer and cutting-blade composites is energetically favorable not only as mono-addition of NGr to the tube body and vice versa but a multi-addend attachment, as well.
2. A strong contact between the tube and NGr is provided by the formation of an extended set of the intermolecular C–C bonds, number of which is comparable with the number of either tube end or NGr edge atoms.
3. The contact strength is determined by both the energy of the newly formed C–C bonds and their number. Optimization of the latter dictates a clear preference towards zigzag or armchair edges of the attaching NGr depending on the tube configuration. Thus, (8, 0) SWCNT (as all other members of the (m, 0) family) prefers armchair contacts that maximize the number of point contacts. In its turn, (4, 4) SWCNT (as well as other members of the (n, n) family) favors zigzag contacts due to the same reason.

4. The total coupling energy between the NGr addend and tube involves both the energy of the C–C bond formed and the energy of deformation caused by the reconstruction of  $sp^2$  configuration for the carbon atom valence electrons into  $sp^3$  one. It can be thought that the latter depends on the tube diameter. However, the data are so far rather scarce, and an extended investigation of the problem is needed.
5. In general, the coupling energy of cutting-blade composites is much more than that of hammer ones, which is important for practical realization of the composites production
6. The final product will depend on whether both components of the composition are freely accessible or one of them is rigidly fixed. Thus, in diluted solutions where the first requirement is met, one can expect the formation of cutting-blade composites due to significant preference in the coupling energy. Oppositely, in gas reactors where often either CNTs or graphene sheets are fixed on some substrates, the hammer composites will be formed as it has been shown just recently (Kondo et al. 2008; Chen et al. 2011).
7. All the mentioned peculiarities provide an extremely large field for a detailed study of different topological effects.

## 5.8 Topochemical Character of the Graphene Hydrogenation

### 5.8.1 General Design of the Graphene Hydrogenation

As has been revealed just recently, a significant correlation of odd electrons of graphene strongly influences its chemical modification, the hydrogenation, in particular (Sheka and Popova 2012a, b). The hydrogenation has been considered in a manner of consequent single reactions subordinated to a stepwise addition of hydrogen atoms to a double-H-terminated (5, 5) NGr membrane shown in Fig. 5.14c, alongside with the corresponding ACS map. Two initial states of the membrane are considered related to either fixed (fixed membrane) or unrestricted motion (free-standing membrane) of the carbon atoms situated over the membrane perimeter. The perimeter atom fixation implies that the relevant atoms are excluded from the optimization procedure at further steps of a consequent hydrogenation. The stepwise addition of hydrogen to membranes is subordinated to a particular algorithm described in details in Sheka (2011a) that is governed by the highest ACS of the carbon atoms, calculated at every step of the reaction.

Both the hydrogenation of graphene itself and the final hydrides formed depend on several external factors, namely, (1) the state of the fixation of the membrane, (2) the accessibility of the substrate sides to hydrogen, and (3) molecular or atomic composition of the hydrogen vapor. These circumstances make both computational consideration and technology of the graphene hydrogenation multimode with the number of variants not fewer than eight if only molecular and atomic adsorption

does not occur simultaneously. The study (Sheka and Popova 2012a, b) has involved all the hydrogenation modes related to atomic adsorption and to two modes of the molecular adsorption. Taking together, the results allow for suggesting a rather integral picture of the events that accompany hydrogenation of graphene. It is summed up in Table 5.6. Additionally to the general picture, the following answers to crucial questions related to the hydrogenation of graphene were suggested.

1. *Which kind of the hydrogen adsorption, namely, molecular or atomic, is the most probable?*

Following from Table 5.6, the study has convincingly shown that only atomic adsorption is effective and energetically favorable, which is consistent with a widely known fact of a practical absence of molecular hydrogen adsorption on graphite. It is important to note that the reason has a direct relation to the main topic of this chapter.

As for atomic adsorption, the formation of hydrides with practically total covering of the basal plane occurs quite possibly. When both sides of the membrane are accessible to hydrogen atoms, the hydrogenation of NGr is completed by the formation of the 100 % covered regularly structured provided with chair-like cyclohexanoid units (Fig. 5.27a). If the membrane is accessible from one side only, the consequent attachment of hydrogen atoms to the substrate causes arching of its carbon skeleton that takes the shape of a canopy at the final stage (Fig. 5.27b). In both cases, C–C bonds lengthen taking 1.51–1.53 Å. However, under fixation of the membrane edges, not all the bonds are able to meet the requirement so that a part of them should stay quite short. Under this condition, a pair of hydrogen atoms, which had to be attached to two carbon atoms forming the bonds, is not allowed to perform the job thus stimulating atoms to associate and to form a hydrogen molecule outside of the basal plane. As seen in Fig. 5.27b, the last atoms 43 and 44 had such a fate, which resulted in desorption of one hydrogen molecule and lowering the plane covering up to 96 %.

At first glance, the final stage of the two-side adsorption of hydrogen atoms on the free-standing membrane (Fig. 5.27c) seems to be similar to that presented in Fig. 5.27a. However, attentive consideration reveals that the chair-like configuration of cyclohexanoids, regularly composed in the upper side of the sample, is violated when approaching the sample bottom so that we have to speak about the mixing of the cyclohexanoid conformers, which causes the distortion of the regular structure of the carbon skeleton. This circumstance does not prevent from achieving 100 % filling of the basal plane; nevertheless, the sample itself presents a mixture of a regular area neighboring with some elements of amorphous structure. Obviously, the partial contribution of each component depends on the graphene sample size.

In contrast to what has been said above, the one-side adsorption of the free-standing membrane has resulted in the formation of a peculiar basket that is formed when two ends of a rectangular figure situated over its diagonal are closely approached each other (Fig. 5.27d). The formation of the 100 % hydride of so peculiar shape is accompanied by the energy gain of  $\sim 1$  kcal/mol per each carbon atom.

**Table 5.6** Final products of the hydrogen adsorption on (5,5) nanographene

<i>Atomic adsorption</i>	Two-side access	One-side access	<i>Molecular adsorption</i>	Two-side access	One-side access
Fixed membrane	100 %-covered hydride of crystalline graphane structure (Fig. 5.27a)	96 %-covered hydride of canopy structure (Fig. 5.27b)	Fixed membrane	~5 %-covered hydride of nonplanar sheet structure	No results
Free-standing membrane	100 %-covered hydride of crystalline graphane structure accompanied by fragments of amorphous structure (Fig. 5.27c)	100 %-covered hydride of a basket structure (see text) (Fig. 5.27d)	Free-standing membrane	10–15 %-covered hydride of irregular structure of bent sheet	No results

Reproduced from Sheka and Popova (2012b) with kind permission from Springer Science and Business Media

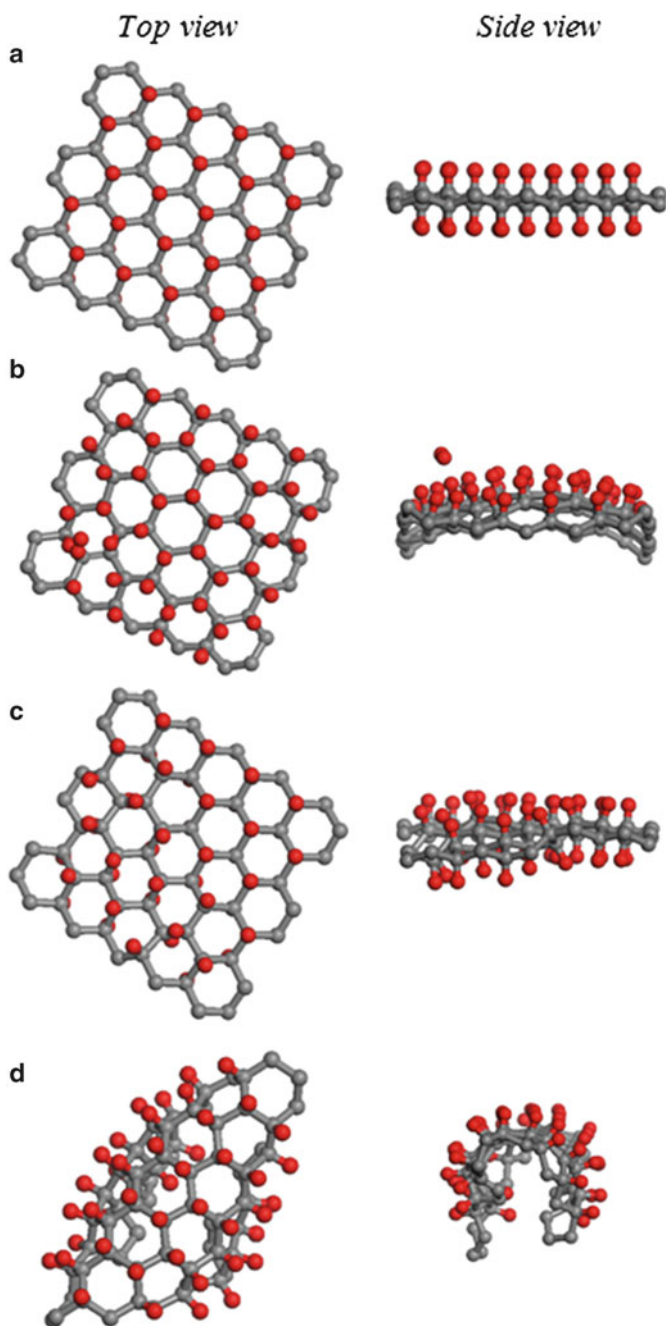


**Fig. 5.27** Top and side views of the equilibrium structures of hydrides formed at the atomic adsorption of hydrogen on the fixed (**a, b**) and free-standing (**c, d**) (5,5) nanographene membrane, accessible to the adsorbate from both (**a, c**) and one (**b, d**) sides (Reproduced from Sheka and Popova (2012b), with kind permission from Springer Science and Business Media)

The reason for so dramatic difference between atomic and molecular adsorption has an evident topochemical nature and is a consequence of the tendency of the graphene substrate to conserve the hexagon pattern. But obviously, the pattern conservation can be achieved if only the substrate hydrogenation provides the creation of the cyclohexanoid structure that corresponds to either one of the conformers of the latter or their mixture. If non-coordinated deposition of individual atoms can meet the requirement, a coordinated deposition of two atoms on neighboring carbons of substrate evidently makes the formation of a cyclohexanoid-conformer pattern much less probable thus making molecular adsorption unfavorable.

*2. What is characteristic image of the hydrogen atom attachment to the substrate?*

The hydrogen atom is deposited on top of the carbon ones in both up and down configurations. In contrast to a vast number of organic molecules, the length of C–H bonds formed under adsorption exceeds 1.10 Å, therewith differently for different adsorption events. Thus, C–H bonds are quite constant by value of 1.122 Å in average for framing hydrogens that saturate edge carbon atoms of the substrate. Deposition on the basal plane causes enlarging the value up to maximum 1.152 Å (Sheka and Popova 2012a, b). However, the formation of a regular chair-like cyclohexanoid structure like graphane (Sofa et al. 2007; Elias et al. 2009) leads to equalizing and shortening the bonds to 1.126 Å. The above picture, which is characteristic for the fixed membrane, is significantly violated when going to one-side deposited fixed membrane or two-side deposited free-standing membrane that exhibits the difference in the strength of the hydrogen atoms coupling with the related substrates.

*1. Which carbon atom is the first target subjected to the hydrogen attachment?*

And

*2. How are carbon atoms selected for the next steps of the adsorption?*

Similarly to fullerenes and carbon nanotubes (Sheka 2011a), the formation of graphene polyhydrides (CH)<sub>n</sub> has been considered in the framework of single-reaction algorithmic stepwise computational synthesis, each subsequent step of which is controlled by the distribution of atomic chemical susceptibility in terms of fractional numbers of effectively unpaired electrons on atom,  $N_{DA}$ , of the preceding derivative over the substrate atoms. The quantity is a direct consequence of the odd-electron correlation. The high-rank  $N_{DA}$  values definitely distinguish the atoms that should serve as targets for a forthcoming chemical attack. Additionally, the lowest total energy criterion has provided the choice of the most energetically stable hydride. The successful generation of the polyderivative families of fluorides (Sheka 2010) and hydrides (Sheka 2011b) as well as other polyderivatives of fullerene C<sub>60</sub> (Sheka 2011a), of 100 % polyhydride (CH)<sub>n</sub> related to chair-like graphane described above as well as ~96 % of table-like cyclohexanoid hydride (CH)<sub>n</sub> of the canopy shape, has shown a high efficacy of the approach in viewing process of the polyderivatives formation which makes it possible to proceed with a deep insight into the mechanism of the chemical modification.

### 3. *Is there any connection between the sequential adsorption pattern and cyclohexanoid conformers formed in due course of hydrogenation?*

The performed investigations have shown that there is a direct connection between the state of the NGr substrate and the conformer pattern of the polyhydride formed. The pattern is governed by the cyclohexanoid conformer whose formation under ambient conditions is the most profitable. Thus, a regular chair-like cyclohexanoid-conformed graphene with 100 % hydrogen covering, known as graphane (Sofa et al. 2007; Elias et al. 2009), is formed in the case when the NGr substrate is a perimeter-fixed membrane, both sides of which are accessible for hydrogen atoms. When the membrane is two-side accessible, but its edges are not fixed, the formation of a mixture of chair-like and boat-like cyclohexanoid patterns has turned out more profitable. As shown, the polyhydride total energy involves deformational and covalent components. That is why the difference in the conformer energy in favor of chair-like conformer formed in free-standing membrane is compensated by the gain in the deformation energy of the carbon carcass caused by the formation of boat-like conformer, which simulates a significant corrugation of the initial graphene plane. The mixture of the two conformers transforms therewith a regular crystalline behavior of graphane into a partially amorphous-like behavior in the latter case.

When the fixed membrane is one-side accessible, the configuration produced is rather regular and looks like an infinite array of *trans*-linked table-like cyclohexanoid conformers. The coupling of hydrogen atoms with the carbon skeleton is the weakest among all the considered configurations, which is particularly characterized by the longest C–H bonds of 1.18–1.21 Å in the length. The carbon skeleton takes a shape of a canopy exterior.

## 5.8.2 *Energetic Characteristics Accompanying the Nanographene Hydrogenation*

Total coupling energy that may characterize the molecule hydrogenation can be presented as

$$E_{\text{cpl}}^{\text{tot}}(n) = \Delta H_{n \text{ Hgr}} - \Delta H_{\text{NGr}} - n\Delta H_{\text{at}}. \quad (5.11)$$

Here  $\Delta H_{n \text{ Hgr}}$ ,  $\Delta H_{\text{NGr}}$ , and  $\Delta H_{\text{at}}$  are heats of formation of graphene hydride with  $n$  hydrogen atoms, a pristine nanographene, and hydrogen atom, respectively. When one is mainly interested in the adsorption on basal plane, it is worthwhile to refer the coupling energy related to the basal adsorption to the energy of the framed membrane in the form

$$E_{\text{cpl}}^{\text{tot bs}}(k) = E_{\text{cpl}}^{\text{tot}}(k + 44) - E_{\text{cpl}}^{\text{tot fr}}(44), \quad (5.12)$$



where  $k = n - 44$  numbers hydrogen atoms deposited on the basal plane and  $E_{\text{cpl}}^{\text{tot bs}}(k)$  presents the coupling energy counted off the energy of the framed membrane  $E_{\text{cpl}}^{\text{tot fr}}(44)$ .

The tempo of hydrogenation may be characterized by the coupling energy needed for the addition of each next hydrogen atom. Attributing the energy to the adsorption on the basal plane, the per step energy can be determined as

$$E_{\text{cpl}}^{\text{step bs}}(k) = E_{\text{cpl}}^{\text{tot}}(k + 44) - E_{\text{cpl}}^{\text{tot}}[(k + 44) - 1]. \quad (5.13)$$

Evidently, two main contributions, namely, the deformation of the fragment carbon skeleton (def) and the covalent coupling of hydrogen atoms with the substrate resulted in the formation of C–H bonds (cov), determine both total and per step coupling energies. Supposing that the relevant contributions can be summed up, one may evaluate them separately. Thus, the total deformation energy can be determined as the difference

$$E_{\text{def}}^{\text{tot}}(n) = \Delta H_{n\text{Hgr}}^{\text{sk}} - \Delta H_{\text{NGr}}. \quad (5.14)$$

Here,  $\Delta H_{n\text{Hgr}}^{\text{sk}}$  presents the heat of formation of the carbon skeleton of the hydride at the  $n$ th step of hydrogenation, and  $\Delta H_{\text{NGr}}$  presents the heat of formation of the initial graphene fragment. The value  $\Delta H_{n\text{Hgr}}^{\text{sk}}$  can be obtained as a result of one-point-structure determination applied to the  $n$ th equilibrium hydride after removing all hydrogen atoms. Attributed to the basal plane,  $E_{\text{def}}^{\text{tot}}(n)$  has the form

$$E_{\text{def}}^{\text{tot bs}}(k) = E_{\text{def}}^{\text{tot}}(k + 44) - E_{\text{def}}^{\text{tot fr}}(44). \quad (5.15)$$

Here,  $E_{\text{def}}^{\text{tot fr}}(44)$  presents the deformation energy of the framed membrane.

The deformation energy, which accompanies each step of the hydrogenation, can be determined as

$$E_{\text{def}}^{\text{step bs}}(k) = \Delta H_{(k+44)\text{Hgr}}^{\text{sk}} - \Delta H_{[(k+44)-1]\text{Hgr}}^{\text{sk}}, \quad (5.16)$$

where  $\Delta H_{(k+44)\text{Hgr}}^{\text{sk}}$  and  $\Delta H_{[(k+44)-1]\text{Hgr}}^{\text{sk}}$  match heats of formation of the carbon skeletons of the relevant hydrides at two subsequent steps of hydrogenation.

Similarly, the total and per step chemical contributions caused by the formation of C–H bonds on the basal plane can be determined as

$$E_{\text{cov}}^{\text{tot bs}}(k) = E_{\text{cpl}}^{\text{tot bs}}(k) - E_{\text{def}}^{\text{tot bs}}(k) \quad (5.17)$$

and

$$E_{\text{cov}}^{\text{step bs}}(k) = E_{\text{cov}}^{\text{tot}}(k + 44) - E_{\text{cov}}^{\text{tot}}(k + 44 - 1). \quad (5.18)$$

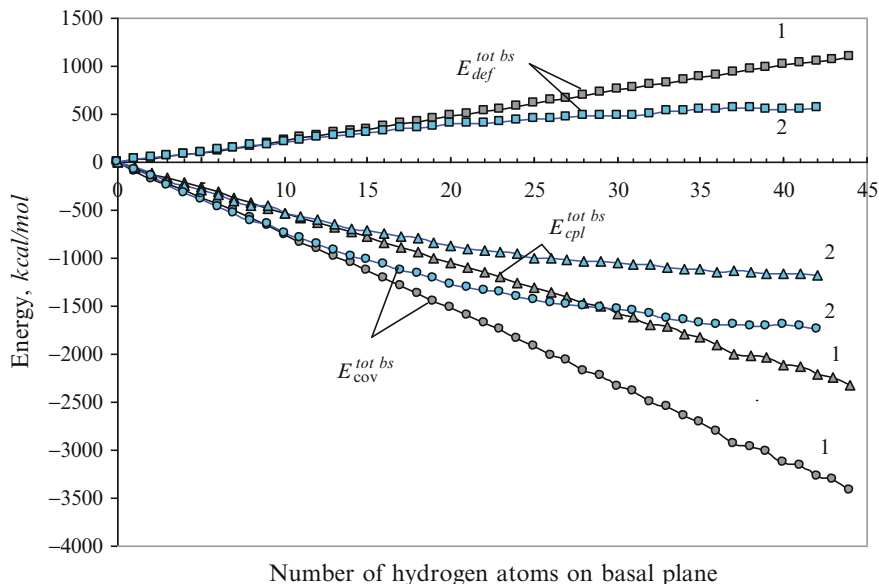


**Fig. 5.28** Total energies of coupling  $E_{cpl}^{tot\ bs}$  (triangles), deformation  $E_{def}^{tot\ bs}$  (squares), and covalent bonding  $E_{cov}^{tot\ bs}$  (circles) via the number of hydrogen atoms deposited on the basal plane for hydrides 1 (dark gray) and 2 (light blue) according to (5.13), (5.16), and (5.18), respectively

Figure 5.28 displays the calculated total energies for hydrides related to the fixed (1) and free-standing (2) membranes. The relevant per step energies are shown in Fig. 5.29. As seen in Fig. 5.28, the total energies  $E_{cpl}^{tot\ bs}$  of both hydrides are negative by sign and gradually increase by the absolute value when the number of adsorbed atoms increases. Besides, the absolute value growth related to hydrides 2 is evidently slowing down starting at step 11 in contrast to the continuing growth for hydrides 1. This retardation is characteristic for other two energies presented in Fig. 5.28 thus quantitatively distinguishing hydrides 2 from hydrides 1. The growth retardation of both  $E_{cpl}^{tot\ bs}$  and  $E_{cov}^{tot\ bs}$  energies obviously shows that the addition of hydrogen to the fixed membrane of hydrides 2 at coverage higher than 30 % is more difficult than in the case of hydrides 1. This conclusion is supported by the behavior of per step energies  $E_{cpl}^{step\ bs}$  and  $E_{cov}^{step\ bs}$  plotted in Fig. 5.29a, c. If, in the case of hydrides 1, the energy values oscillate around steady average values of  $-52$  and  $-72$  kcal/mol for  $E_{cpl}^{step\ bs}$  and  $E_{cov}^{step\ bs}$ , respectively, in the case of hydrides 2,  $E_{cpl}^{step\ bs}$  oscillates around average values that grow from  $-64$  to  $-8$  kcal/mol. Similar  $E_{cov}^{step\ bs}$  oscillations occur around a general level that starts at  $-88$  kcal/mol and terminates at  $-8$  kcal/mol (see Fig. 5.29c). Therefore, the reaction of the chemical attachment of hydrogen atoms to hydrides 1 is thermodynamically profitable through over the covering that reaches 100 % limit. In contrast, the large coverage for hydrides 2 becomes less and less profitable so that at final steps adsorption and desorption

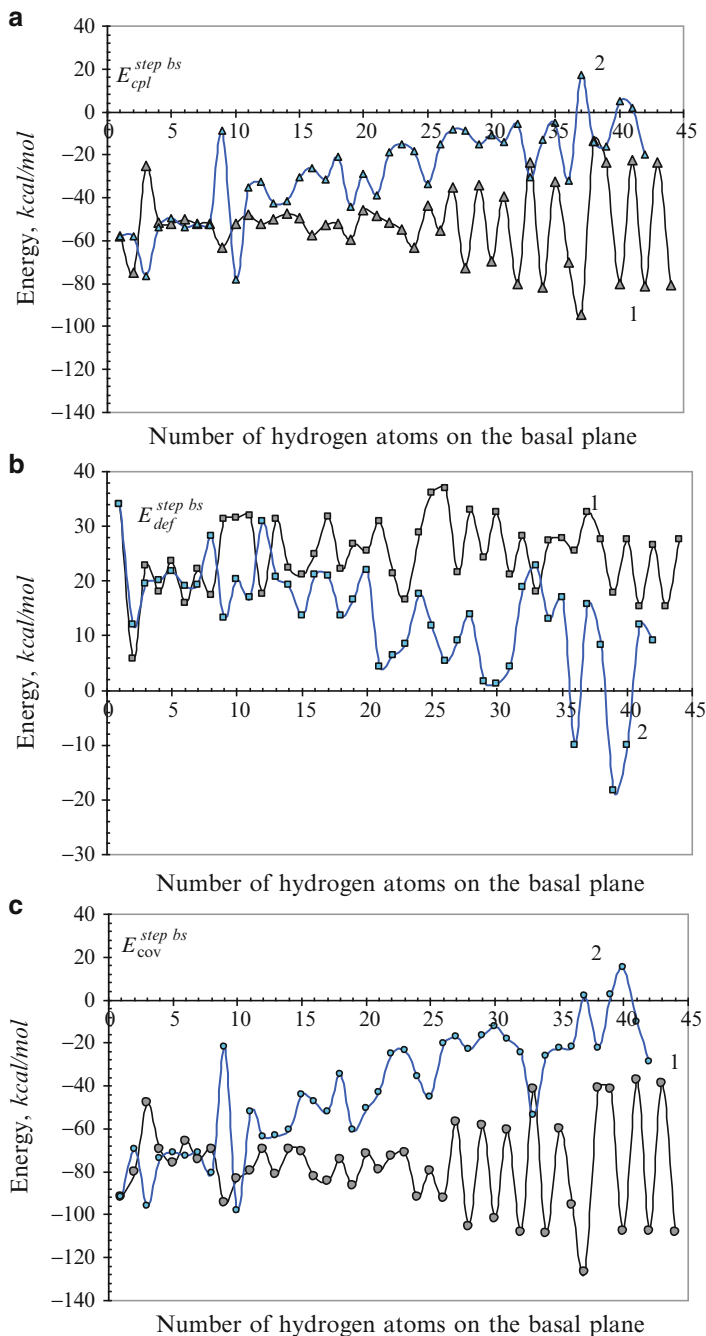


**Fig. 5.29** Per step energies of coupling  $E_{cpl}^{step\ bs}$  (a), deformation  $E_{def}^{step\ bs}$  (b), and covalent bonding  $E_{cov}^{step\ bs}$  (c) via the number of hydrogen atoms deposited on the basal plane for hydrides 1 (dark gray) and 2 (light blue) according to (5.13), (5.16), and (5.18), respectively

become competitive thus resulting in desorption of hydrogen molecules, which was described in the previous section.

An attention should be given to changing the deformation of the carbon skeleton caused by  $sp^2 \rightarrow sp^3$  transformation of the carbon atom electron configuration. Gradually increased by value for both hydride families, the energy  $E_{\text{def}}^{\text{tot bs}}$  shown in Fig. 5.28 describes strengthening the deformation in due course of growing coverage of the basal plane. Irregular dependence of  $E_{\text{def}}^{\text{step bs}}$  on covering presented in Fig. 5.29b allows for speaking about obvious topochemical character of a multistep attachment of hydrogen atoms to the membrane basal plane.

### 5.8.3 Comparative View on the Hydrogenation of Fullerene $C_{60}$ and Graphene

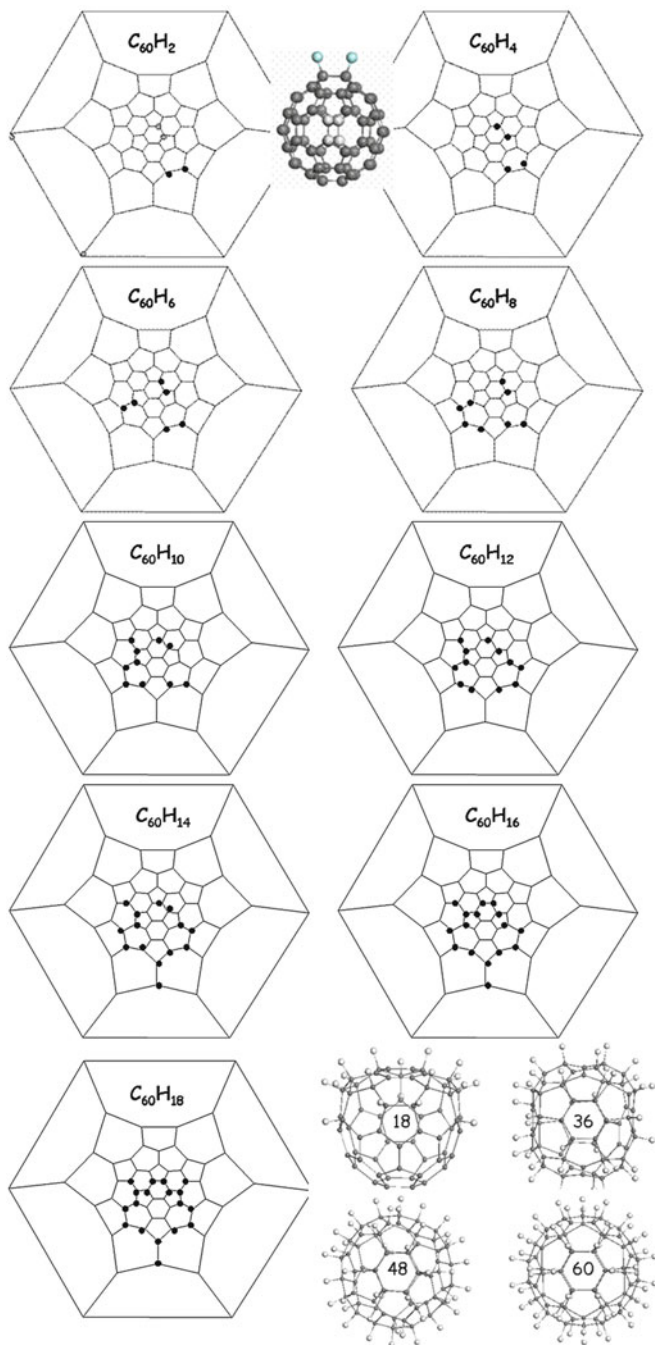
The topochemistry revealed above might imply, on the first glance, chemical reactions occurred in a space subordinated to restricting conditions like reactions on the solid surfaces (Schmidt 1971). However, one has to take into account the inherent topology of the graphene substrate that was mentioned in Sect. 5.1. If so and if the topology of graphene and fullerene is different, the hydrogenation seems to be the straight way to exhibit the difference.

Figure 5.30 present a summarized view on the consequent steps of the fullerene  $C_{60}$  stepwise hydrogenation, governed by the ACS algorithm, in due course of which a complete family of the  $C_{60}$  hydrides has been obtained (Sheka 2011b). When comparing the fullerene hydrides with those of graphene, one has to give the obvious preference to the graphene hydrides 2 obtained under the one-side adsorption on the basal plane of the fixed membrane. Energetic characteristics, which accompany the hydrogenation of fullerene  $C_{60}$  and (5, 5) NGr, are shown in Fig. 5.31. As seen in the figure, seemingly identical reactions are drastically different from the energy viewpoint. One may think that the final irregular hydrogen covering of hydrides 2 might be the reason for the difference. However, a comparison with the data related to hydrides 1, presented in Fig. 5.31, as well, not only does not improve the situation but significantly worsens it. It should be concluded that the hydrogenation has turned out a very indicative chemical procedure that has made the inherent difference in the topology of fullerenes and graphene the most impressive.

## 5.9 Inherited Topology and Deformation of Graphene

In this section we will consider a particular topological effect caused by the influence of the graphene edge termination on the inherited topology of the sheet. As turned out, the graphene deformation under external mechanical loading is extremely sensitive to the state of the sheet edge atoms and makes it possible to disclose a topological nature of this sensitivity.

Within the framework of the molecular theory, the response of nanographene sheet to external stresses is considered in terms of a mechanochemical reaction



**Fig. 5.30** Schlegel diagrams of successive steps of the C<sub>60</sub> hydrogenation from C<sub>60</sub>H<sub>2</sub> to C<sub>60</sub>H<sub>18</sub> and atomic structures of C<sub>60</sub>H<sub>18</sub>, C<sub>60</sub>H<sub>36</sub>, C<sub>60</sub>H<sub>48</sub>, and C<sub>60</sub>H<sub>60</sub> molecules (Reproduced from Sheka 2011b, with kind permission from Springer Science and Business Media)

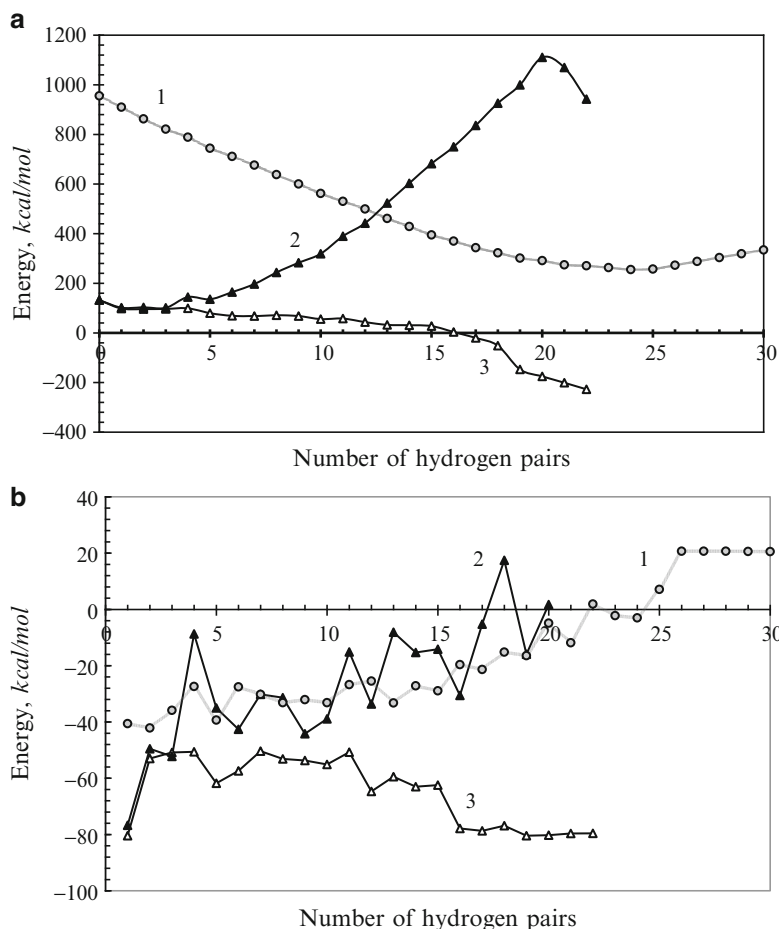


**Fig. 5.31** Total energy (a) and per step coupling energy (b) for the families of  $C_{60}$ -fullerene hydrides (curves with balls), (5, 5) nanographene hydrides 1 (curves with filled triangles), and hydrides 2 (curves with open triangles)

(Sheka et al. 2011a, b). The quantum-chemical realization of the approach is based on the coordinate-of-reaction concept for the purpose of introducing a mechanochemical internal coordinate (MIC) that specifies a deformational mode (Nikitina et al. 1999). In the case of tensile deformation, the benzenoid pattern of graphene sheets and a regular packing of the units predetermined the choice of either parallel or normal MICs orientation with respect to the chain of C–C bonds. In the rectangular nanographene sheets and nanoribbons, the former orientation corresponds to tensile deformation applied to the zigzag edges (*zg* mode) while the latter should be attributed to the armchair edges (*ach* mode). The MIC configurations of the *ach* and *zg* tensile modes of the (5,5) NGr sheet are presented in Fig. 5.32. The deformation proceeds as a stepwise elongation of the MICs with

the increment  $\delta L = 0.1 \text{ \AA}$  at each step so that the current MIC length constitutes  $L = L_0 + n\delta L$ , where  $L_0$  is the initial length of the MIC and  $n$  counts the number of the deformation steps. Right ends of all the MICs are fixed so that these blue-colored atoms are immobilized while atoms on the left ends of MICs move along the arrows providing the MIC successive elongation, once excluded from the optimization as well. The relevant force of response is calculated as the energy gradient along the MIC, while the atomic configuration is optimized over all of the other coordinates under the MIC constant-pitch elongation.

Thus arranged computations revealed that a high stiffness of the graphene body is provided by the stiffness of benzenoid units. The anisotropy of the unit mechanical behavior in combination with different packing of the units either normally or parallel to the body C–C bond chains lays the ground for the structure-sensitive mechanism of the mechanical behavior of the object that drastically depends on the deformation modes. The mechanical behavior of (5, 5) NGr with empty edges under *zg* and *ach* deformation modes is similar to that of a tricotage when either the sheet rupture has both commenced and completed by the rupture of a single stitch row (*ach* mode) or the rupture of one stitch is “tugging at thread” the other stitches that are replaced by still elongated one-atom chain of carbon atoms (*zg* mode). The final equilibrium structures corresponding to the complete rupture are shown in Fig. 5.33a. To achieve the rupture, 18 and 250 steps of successive tension were needed for *ach* and *zg* modes, respectively (Sheka et al. 2011a, b).

Quite unexpectedly, the character of the deformation has occurred to be strongly dependent on chemical situation at the sheet edges (Sheka et al. 2012). As seen in Fig. 5.33b, single-H termination slightly elongates the rupture related to the *ach* mode up to the 20th step while considerably shortens the regime of the *zg* deformation mode up to the 125th step. The tricotage-like behavior of the deformation is still preserved while noticeably changes the pattern. Even more drastic changes for this mode occur when the edge atoms are double-H-terminated (Fig. 5.33c). Still, the *ach* mode is quite conservative while *zg* mode becomes practically identical to the former. The tricotage-like character of the deformation is completely lost and the rupture occurs at the 33rd step.

The observed phenomenon can be understood if suggested that (1) the deformation and rupture of the sheet is a collective event that involves the electron system of the sheet as a whole, (2) the electron system of the graphene sheet is highly delocalized and thus topologically sensitive, and (3) chemical termination of edge atoms so strongly influences the topological change of the whole sheet due to extreme correlation.

## 5.10 Conclusion

Discussion in this chapter has been aimed at convincing readers that  $sp^2$  nanocarbons present a new class of topochemical objects. The novelty lies in the fact that these species demonstrate a complicated topological behavior as regards chemical reactions with their participation that manifests a combination of the inherent

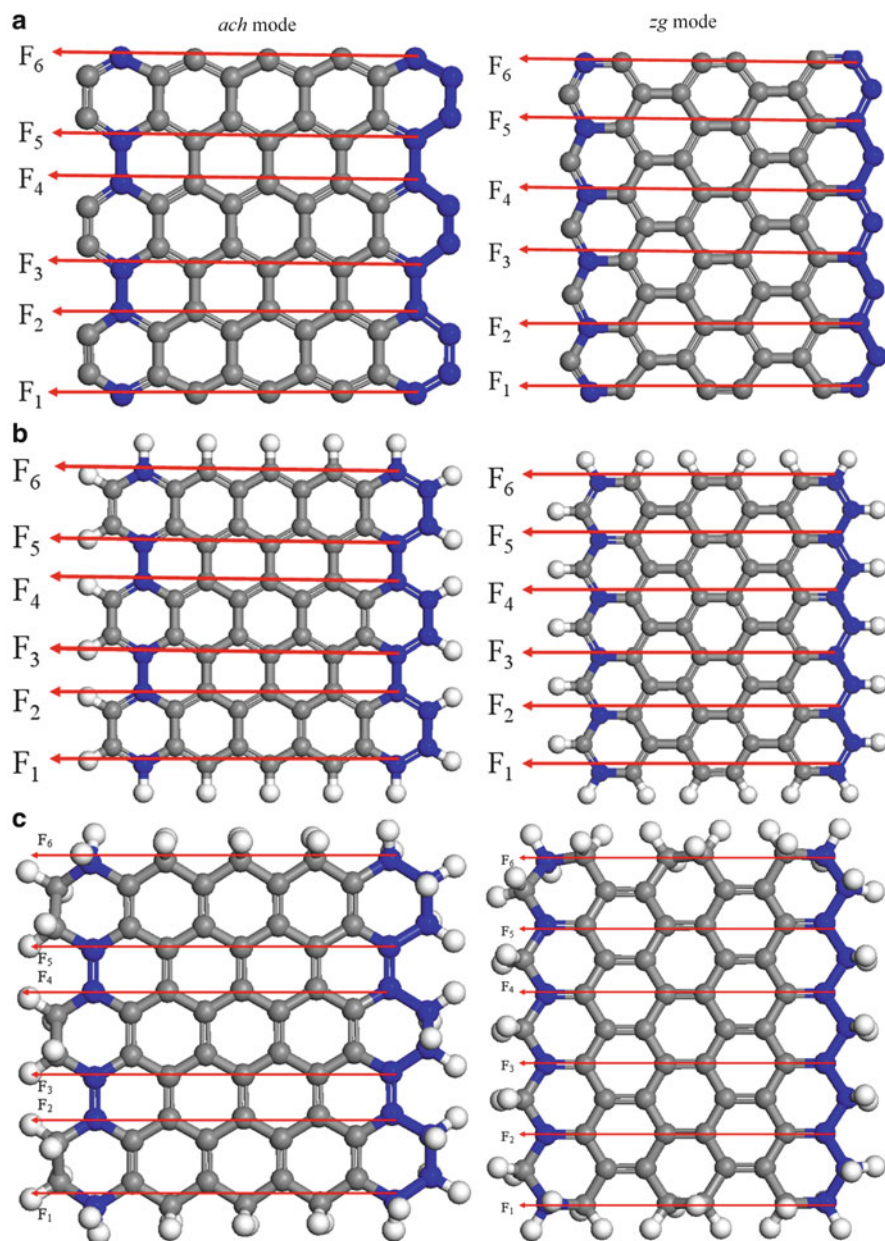


**Fig. 5.32** Configurations of six mechanochemical internal coordinates related to two deformation modes of (5, 5) nanographene sheet with empty (a), single-H-terminated (b), and double-H-terminated (c) edge atoms. Atoms marked in blue are excluded from the optimization procedure (Sheka et al. 2012)



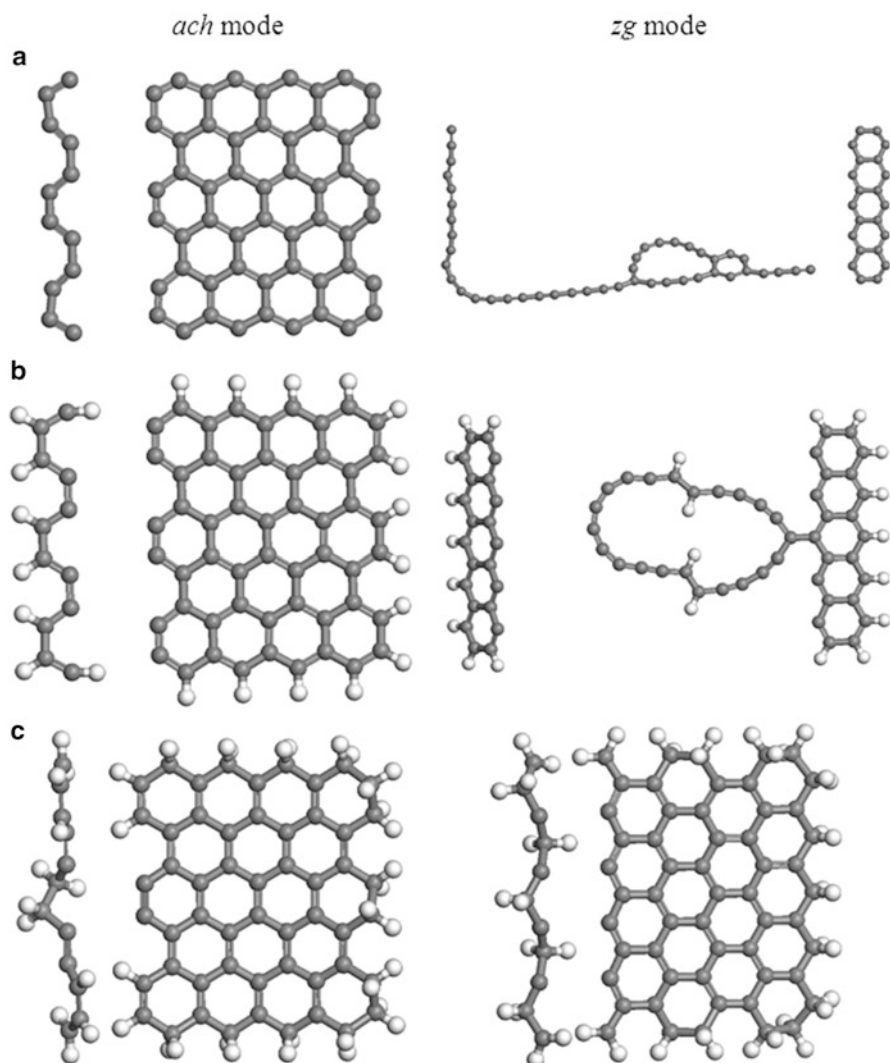


**Fig. 5.33** The rupture-point final structures of (5, 5) nanographene sheet with empty (a), single-H-terminated (b), and double-H-terminated (c) edge atoms at two deformation modes (Sheka et al. 2012)

topology of the species, or the internal topology, with that provided by the action of external factors. The internal topology is manifested through identical reactions that involve different members of the class. Two types of such reactions have been considered, namely, the “double-(C–C)-bond” reactions between two  $sp^2$  class members and “atom-(C–C)-bond” reactions that concern a monatomic species deposition on the  $sp^2$  nanocarbons. The former reaction is mainly addressed to a

number of composites that are formed by fullerene  $C_{60}$  attachment to either itself or carbon nanotube and nanographene. As turned out, in spite of structural similarity of the “double-(C–C)-bond” contact zones, which are mainly presented by  $[2 + 2]$  cycloaddition junctions, the energetic parameters of the composites have revealed a deep discrepancy that manifest the different inherent topology of the species. This conclusion finds support in case of composites formed by carbon nanotubes and graphene, as well. But the brightest proof of the difference in the inherent topology of fullerenes and graphene has been obtained by comparing the hydrogenation of fullerene  $C_{60}$  and (5, 5) nanographene.

The external topological events have been demonstrated computationally by differing both structural image and energetic characteristics of (5, 5) nanographene hydrides under conditions when the pristine graphene membrane was subjected to the action of different external factors, such as immobilization of the perimeter carbon atoms, restrictions of the accessibility of both sides of the membrane, and exploring either atomic or molecular hydrogen. This finding seems to be of particular importance since it should be addressed to the chemical modification of graphene as a methodology aimed at a controllable changing of the graphene electronic properties. It is quite obvious that chemical behavior of graphene in the form of free-standing and fixed membranes, deposited layers on different substrates, in solutions and gaseous surroundings will be different. The analysis of the available experimental data gave a large support of the conclusion demonstrating, say, a sharp difference in the  $C_{60}$  fullerene oligomerization in crystalline phase, due to mechanochemical reaction in solutions, and once deposited on different substrates.

It might be thought that the revealed peculiarities of the topological behavior of  $sp^2$  nanocarbons do not manifest its complexity in the full extent. This conclusion highlights the importance of the species consideration at the level of formal mathematical topology. It might be expected that some new faces of the phenomenon could be visualized and explained in terms of the connectivity and adjacency characteristic for the studied objects.

Meeting reproach, which might be caused by a restricted referring to studies performed by other people, it should be noted that this chapter presents the author view on the processes described. Each of the touched topics covers a large field so that the exhausted referring to what happening in the field would unavoidably make the manuscript too cumbersome. In case if some compensation may be suggested, the author publications considered in the chapter covers the situation concerning the study of each particular question quite thoroughly.

## References

- Boldyrev VV (1990) *React Solid* 8:231  
Cataldo F, Graovac A, Ori O (eds) (2011) *The mathematics and topology of fullerenes*. Springer, New York  
Chen S, Chen P, Wang Y (2011) *Nanoscale* 3:4323

- Davydov VA, Kashevarova LS, Rakhmanina AV, Senyavin VM, Pronina OP, Oleynikov NN, Agafonov V, Céolin R, Allouchi H, Szwarc H (2001) *Chem Phys Lett* 333:224
- de Jong AWK (1923) *Ber Dtsch Chem Ges* 56:818
- Ecklund PC, Rao AM, Zhou P, Wang Y, Holden JM (1995) *Thin Solid Film* 257:185
- Elias DC, Nair RR, Mohiuddin TMG, Morozov SV, Blake P, Halsall MP, Ferrari AC, Boukhvalov DW, Katsnelson MI, Geim AK, Novoselov KS (2009) *Science* 323:610
- Enders A, Malinowski N, Ievlev D, Zurek E (2006) *J Chem Phys* 125:191102
- Enkelmann V (1984) *Adv Polym Sci* 63:91
- Fischer JE (1994) *Science* 264:1548
- Friscier T, MacGillivray LR (2005) *Z Kristallogr* 220:351
- Gao X, Zhou Z, Zhao Y, Nagase S, Zhang SB, Chen Z (2008) *J Phys Chem C* 112:12677
- Giacalone F, Martín N (2010) *Adv Mater* 22:4220
- Guo F, Marti-Rujas J, Pan Z, Hughes CE, Harris KDM (2008) *Phys Chem C* 112:19793
- Haddon RC (1993) *Science* 261:1545
- Hasegawa M (1986) *Pure Appl Chem* 58:1179
- Hedén M, Hansen K, Campbell EEB (2005) *Phys Rev A* 71:055201
- Iwasa Y, Arima T, Fleming RM, Siegrist T, Zhou O, Haddon RC, Rothberg LI, Lyons KB, Carter HL Jr, Hebard AF, Tycko R, Dabbagh G, Kraewski JJ, Thomas JA, Yagi T (1994) *Science* 264:1570
- Kazaoui S, Minami N, Tanabe Y, Byrne HJ, Eilmes A, Petelenz P (1998) *Phys Rev B* 58:7689
- Kondo D, Sato S, Awano Y (2008) *Appl Phys Express* 1:074003
- Kunitake M, Uemura S, Ito O, Fujiwara K, Murata Y, Komatsu K (2002) *Angew Chem Int Ed* 41:969
- Lee KH, Eun HM, Park SS, Suh YS, Jung K-W, Lee SM, Lee YH, Osawa E (2000) *J Phys Chem B* 104:7038
- Li X, Liu L, Qin Y, Wu W, Guo Z-C, Dai L, Zhu D (2003) *Chem Phys Lett* 377:32
- Li C, Chen Y, Wang Y, Iqbal Z, Chhowallab M, Mitra S (2007) *J Mater Chem* 17:2406
- MacGillivray LR, Papaefstathiou GS (2004) *Encyclopedia of supramolecular chemistry*. Marcel Dekker, New York, p 1316. doi:[10.1081/E-ESMC-120012761](https://doi.org/10.1081/E-ESMC-120012761)
- Matsuo Y, Tahara K, Nakamura E (2003) *Org Lett* 5:3181
- Merrifield RE, Simmons HE (1989) *Topological methods in chemistry*. Wiley, New York
- Nakaya M, Kuwahara Y, Aono M, Nakayama T (2008) *Small* 4:538
- Nakayama T, Onoe J, Nakatsuji K, Nakamura J, Takeuchi T, Aono M (1999) *Surf Rev Lett* 6:1073
- Nasibulin AG, Anisimov AS, Pikhitsa PV, Jiang H, Brown DP, Choi M, Kauppinen EI (2007a) *Chem Phys Lett* 446:109
- Nasibulin AG, Pikhitsa PV, Jiang H, Brown DP, Krasheninnikov AV, Anisimov AS, Queipo P, Moisala A, Gonzalez D, Lientschnig G, Hassanien A, Shandakov SD, Lolli D, Resasco DE, Choi M, Tománek D, Kauppinen EI (2007b) *Nat Nanotechnol* 2:156
- Nikitina EA, Khavryuchenko VD, Sheka EF, Barthel H, Weis J (1999) *J Phys Chem A* 103:11355
- Núñez-Regueiro M, Marques L, Hodeau J-L, Béthoux O, Perroux M (1995) *Phys Rev Lett* 74:278
- Pac B, Petelenz P, Slawik M, Munn RW (1998) *J Chem Phys* 109:7932
- Pekker S, Janossy A, Mihali L, Chauvet O, Forro L (1994) *Science* 265:1077
- Pusztai T, Oszlányi G, Faigel G, Kamaras K, Granasy L, Pekker S (1999) *Solid State Commun* 111:595
- Rut'kov EV, Tontegode AY, Usufov MM (1995) *Phys Rev Lett* 74:758
- Schmidt GMJ (1971) *Pure Appl Chem* 27:647
- Sheka EF (2004) *Int J Quantum Chem* 100:388
- Sheka EF (2007a) *Chem Phys Lett* 438:119
- Sheka EF (2007b) *Int J Quantum Chem* 107:2803
- Sheka EF (2010) *J Exp Theor Phys* 111:395
- Sheka EF (2011a) *Fullerene nanoscience: nanochemistry, nanomedicine, nanophotonics, nanomagnetism*. Taylor & Francis, Boca Raton
- Sheka EF (2011b) *J Mol Mod* 17:1973
- Sheka EF (2012) *Int J Quantum Chem* 112:3076

- Sheka EF, Chernozatonskii LA (2007) *J Phys Chem C* 111:10771
- Sheka EF, Chernozatonskii LA (2010a) *J Comput Theor Nanosci* 7:1814
- Sheka EF, Chernozatonskii LA (2010b) *Int J Quantum Chem* 110:1466
- Sheka EF, Chernozatonskii LA (2010c) *Int J Quantum Chem* 110:1938
- Sheka EF, Chernozatonskii LA (2010d) *J Exp Theor Phys* 110:121
- Sheka EF, Popova NA (2012a) arXiv:1201.1618v1 [cond-mat.mtrl-sci]
- Sheka EF, Popova NA (2012b) *J Mol Mod* 18:3751
- Sheka EF, Shaymardanova LKh (2011a) arXiv:1101.4893 [cond-mat.mes-hall]
- Sheka EF, Shaymardanova LK (2011b) *J Mater Chem* 21:17128
- Sheka EF, Zayetz VA (2005) *Russ J Phys Chem* 79:2009
- Sheka EF, Zayetz VA, Ginzburg IY (2006) *J Exp Theor Phys* 103:728
- Sheka EF, Razbirin BS, Starukhin AN, Nelson KD (2007) *Opt Spectrosc* 102:432
- Sheka EF, Popova NA, Popova VA, Nikitina EA, Shaymardanova LK (2011a) *J Exp Theor Phys* 112:602
- Sheka EF, Popova NA, Popova VA, Nikitina EA, Shaymardanova LK (2011b) *J Mol Mod* 17:1121
- Sheka EF, Popova NA, Popova VA (2012) arXiv:1301.1895v1 [cond-mat.mtrl-sci]
- Sofo JO, Chaudhari AS, Barber GD (2007) *Phys Rev B* 75:153401
- Soldatov AV, Roth G, Dzyabchenko AV, Johnels D, Lebedkin S, Meingast C, Sundqvist B, Haluska M, Kuzmany H (2001) *Science* 293:680
- Sun Y-P, Ma B, Bunker CE, Liu B (1995) *J Am Chem Soc* 117:12705
- Tian Y, Chassaing D, Nasibulin AG, Ayala P, Jiang H, Anisimov AS, Kauppinen EI (2008) *J Am Chem Soc* 130:7188
- Wang Y, Holden JM, Bi X-X, Eklund PC (1994) *Chem Phys Lett* 217:413
- Wang X-B, Ding C-F, Wang L-S (1999) *J Chem Phys* 110:8217
- Weaver JH, Martins JL, Komeda T, Chen Y, Ohno TR, Kroll GH, Troullier N, Haufler R, Smalley RE (1991) *Phys Rev Lett* 66:1741
- Woodward RB, Hoffmann R (1970) *The conservation of orbital symmetry*. Verlag Chemie, Weinheim/Bergstr
- Wu X, Zeng XC (2008) *ACS Nano* 2:1459
- Wu X, Zeng XC (2009) *Nano Lett* 9:250
- Yamawaki H, Yoshida M, Kakudate Y, Usuba S, Yokoi H, Fujiwara S, Aoki K, Ruoff R, Malhotra R, Lorentz D (1993) *J Phys Chem* 97:11161
- Yan L, Zheng UB, Zhao F, Li S, Gao X, Xu B, Weiss PS, Zhao Y (2012) *Chem Soc Rev* 41:97
- Zhang X, Tang L, Guo Q (2010) *J Phys Chem C* 114:6433
- Zhao IB, Poirier DM, Pechman RJ, Weaver JH (1994) *Appl Phys Lett* 64:577

# Chapter 6

## A Pariser–Parr–Pople Model Hamiltonian-Based Approach to the Electronic Structure and Optical Properties of Graphene Nanostructures

Kondayya Gundra and Alok Shukla

**Abstract** The electronic structure of graphene and related nanostructures such as graphene nanoribbons and quantum dots is frequently described within the  $\pi$ -electron approaches such as the tight-binding model, which completely ignores the electron–electron interactions, or the Hubbard model which takes into account only the on-site part. In theoretical chemistry, Pariser–Parr–Pople (PPP) model Hamiltonian, which takes into account the long-range part of the inter-electron Coulomb interaction, has been employed extensively, and with considerable success, to study the electronic structure and optical properties of  $\pi$ -conjugated molecules and polymers. Therefore, with the aim of exploring the influence of long-range Coulomb interactions on the electronic structure and optical properties of graphene nanostructures, we have recently developed a numerical approach based upon the PPP model Hamiltonian and used it to study their band structure, magnetic order, and the linear optical absorption spectra. In this chapter, we describe our approach in detail and present its numerous applications ranging from finite systems such as fullerene C<sub>60</sub> and graphene quantum dots to infinitely long quasi-one-dimensional graphene nanoribbons. Our approach is computationally inexpensive and yields results in good agreement with the large-scale first-principles calculations reported by other authors. Furthermore, some of the novel predictions resulting from our approach are also discussed.

---

K. Gundra

Theoretical Physics Division, Bhabha Atomic Research Centre, Mumbai 400085, India

Department of Physics, Indian Institute of Technology, Bombay, Powai, Mumbai 400076, India

e-mail: [naiduk@barc.gov.in](mailto:naiduk@barc.gov.in)

A. Shukla (✉)

Department of Physics, Indian Institute of Technology, Bombay, Powai, Mumbai 400076, India

e-mail: [shukla@phy.iitb.ac.in](mailto:shukla@phy.iitb.ac.in)

## 6.1 Introduction

The electronic structure and optical properties of  $\pi$ -conjugated molecules have attracted both physicists and chemists alike for a long time (Barford 2005; Barieswyl et al. 1992; Salem 1966), because of their potential applications in optoelectronic devices such as light-emitting diodes, field-effect transistors, lasers, and solar cells etc. (Malliaras and Friend 2005). This field received a further boost with the synthesis of molecules like  $C_{60}$  (Kroto et al. 1985) and other fullerenes (Andreoni 2000), as also carbon nanotubes (Dresselhaus et al. 2001; Iijima 1991), all of which have tremendous potential for device applications. However, ever since the synthesis of graphene (Novoselov et al. 2004) and its nanostructures such as graphene nanoribbons, and nanodisks, etc. (Geim and Novoselov 2007), interest in the physics of  $\pi$ -electron systems has grown many folds (Neto et al. 2009). These systems exhibit exotic transport and electronic properties, leading to the possibility that in future electronic devices, graphene will be able to replace silicon as the material of first choice (Geim and Novoselov 2007; Neto et al. 2009; Palacios et al. 2010).

For a theoretician, several possible approaches are available which can describe the electronic structure of graphene and related nanostructures, as well as other  $\pi$ -conjugated systems: (a) fully first-principles approaches based upon the mean-field methods such as the density-functional theory (DFT) (Barone et al. 2006; Prezzi et al. 2008; Son et al. 2006a; Yang et al. 2007a,b, 2008) or the Hartree-Fock (HF) method (Kertesz 1982; Pisani and Dovesi 1980; Shukla et al. 1996, 1999, 1998), (b) methods based upon effective  $\pi$ -electron models such as the one-particle tight-binding (TB) theory (Ezawa 2006; Fujita et al. 1996; Nakada et al. 1996) and its electron-correlated extensions such as the Hubbard (Jung and MacDonald 2009; Voronov 2007; Yazyev 2008) or the extended Hubbard model (Yamashiro et al. 2003), and (c) Dirac-equation-based massless Fermion approach (Neto et al. 2009). The first-principles methods are normally computationally quite expensive because they treat all electrons (except the core electrons) explicitly and therefore require the use of large basis sets to provide a reasonable description of the electronic structure of such systems. In case of graphene nanoribbons (GNRs) of large widths, large graphene nanoflakes, and also polymers with big unit cells, the number of degrees of freedom involved in the problem may impose severe computational constraints on the problems which can be tackled.

The Dirac-equation-based massless Fermion approach to the graphene and its nanostructures is quite popular among theoreticians at present (Neto et al. 2009). It is derived from the TB model for graphene under the effective mass approximation and is based upon the linearity of the band structure with respect to the  $\mathbf{k}$  vector in the vicinity of the so-called Dirac points (Neto et al. 2009). Therefore, its validity is restricted to a small region of the Brillouin zone (BZ) near the Dirac points, and it is far less justified to use it for the reduced-dimensional graphene structures such as the nanoflakes and the nanoribbons.

Compared to the first-principles approaches, effective  $\pi$ -electron models offer an attractive alternative in that they explicitly deal only with the  $\pi$  electrons, thereby reducing the number of electrons to be taken into account significantly, and, thus allowing one to simulate systems of much larger sizes. In such models, the effect of  $\sigma$ -electrons is included in an implicit manner in terms of various parameters of the Hamiltonian such as the hopping matrix elements. Furthermore, they can be used both for finite and infinite systems. In particular, for infinite periodic systems, their range of validity extends over the entire BZ, unlike the Dirac-equation-based approaches, which are applicable only in the neighborhood of the Dirac points. The disadvantage of such approaches is their semiempirical nature, implying the presence of parameters in the model which are determined by means other than the first principles. However, when materials with a large number of atoms need to be studied, first-principles approaches are computationally often not feasible. For such systems model Hamiltonians are sometimes the only possible options. The fact that such models are extremely popular in physics even for smaller systems, testifies to the insights they offer into the electronic structure of such materials, irrespective of their size.

Among the semiempirical methods employed most commonly in the studies of  $\pi$ -conjugated systems, the TB model (called the Hückel model in the chemistry literature) is conceptually the simplest, but it does not include the effects of electron–electron (e–e) interactions. One can correct that deficiency by employing the Hubbard model or its extended versions which include the on-site and the nearest-neighbor Coulomb interactions, respectively. However, it is well known in the chemistry literature that in  $\pi$ -electron systems such as aromatic molecules and conjugated polymers, the long-range part of the e–e interactions plays a very important role in determining their electronic structure (Barford 2005; Barieswyl et al. 1992; Salem 1966). In the 1950s, Pariser, Parr, and Pople proposed a conceptually simple model which incorporates the essential physics of interacting  $\pi$ -electron systems in an elegant manner (Pariser and Parr 1953) and has come to be known as the PPP model since then. This model can also be seen as an extension of the Hubbard model in that, in addition to the on-site repulsion (Hubbard  $U$ ), long range e–e interactions are taken into account by means of suitable Coulomb parameters. Unlike the extended Hubbard models the PPP model imposes no restrictions on the range of Coulomb interactions, thereby leading to the inclusion of interactions between all the sites, irrespective of the distance between them. Because the PPP model is also a  $\pi$ -electron model, the number of degrees of freedom remains the same as in the Hubbard model and leads to no significant increase in the computational effort in spite of inclusion of the long-range Coulomb interactions. Because of the lack of large-scale computational facilities during the 1950s, such an approach was unavoidable even for relatively small molecules such as benzene. However, the remarkable fact is that in spite of so many approximations involved, PPP-model-based calculations were extremely successful in describing the electronic structure, in general, and the optical properties of  $\pi$ -conjugated systems, in particular (Salem 1966).

During last several years, we, along with collaborators elsewhere, have extensively used a PPP-model-based approach, to study the electronic structure and optical properties of conjugated molecules and oligomers (Ghosh et al. 2000; Shukla 2002, 2004a,b; Shukla et al. 2001, 2003, 2004; Shukla and Mazumdar 1999; Sony and Shukla 2005a,b,c, 2007, 2009). The underlying theory, along with the computational approach and the associated computer program developed in our group for dealing with the finite  $\pi$ -conjugated systems, has been published recently (Sony and Shukla 2010). The approach developed therein can also be applied to study graphene fragments, in addition to the aromatic hydrocarbons and conjugated polymers (Sony and Shukla 2010). We note that numerous other groups (Barford 2005; Barieswyl et al. 1992; Bursill and Barford 2009; Jug 1990; Psiachos and Mazumdar 2009; Raghu et al. 2002; Salem 1966; Soos et al. 1993; Ye et al. 2003) have also used the PPP model to study such systems. Furthermore, very recently we extended the PPP model approach also to study infinitely long one-dimensional (1D) periodic  $\pi$ -conjugated systems, with the aim of studying the electronic structure and the optical properties of GNRs (Gundra and Shukla 2011a,b). The Fortran 90 computer program which we developed for the purpose, along with the associated theory, has also been published recently (Gundra and Shukla 2012).

In this work, we review our PPP-model-based electronic-structure methodology applied to both finite and infinite  $\pi$ -electron systems, with particular emphasis on systems such as  $C_{60}$ , graphene nanodisks, and GNRs. For the finite systems, we apply the methodology both at the mean-field HF level and at the configuration-interaction (CI) level, including the influence of electron correlation effects, to study the electronic structure and optical properties of buckminster fullerene and graphene nanodisks. As far as infinite 1D systems are concerned, we study the band structure and optical properties of various GNRs and carbon nanotubes using our mean-field restricted HF (RHF) and the unrestricted HF (UHF) methodology. In particular, we probe the edge magnetism, electric-field-driven half-metallicity, linear optical absorption, and electro-absorption of various GNRs.

The remainder of this chapter is organized as follows. In Sect. 6.2 we briefly review the theory associated with the PPP model Hamiltonian and present the RHF equations for both the finite and 1D periodic systems. We present and discuss the results of various calculations on various finite and infinite systems in Sect. 6.3. Finally, in Sect. 6.4, we present our conclusions, as well as discuss possible future directions.

## 6.2 Theory

In this section, we briefly discuss the PPP model Hamiltonian and its HF implementations for both the finite and the periodic systems.



### 6.2.1 Pariser–Parr–Pople Hamiltonian

The underlying assumption in the PPP model (Pariser and Parr 1953) is that the electronic structure and optical properties of  $\pi$ -conjugated systems such as planar hydrocarbons can, to a very good approximation, be described strictly in terms of the dynamics of its  $\pi$  electrons. In other words, the  $\sigma$  (and the core) electrons can be assumed to be inert as far as the low-lying excitations of such systems are concerned. The reason behind the success of the  $\sigma$ – $\pi$  separation implicit in the PPP model is that the energies of the  $\sigma$  electrons are so far away from the Fermi level that they are unaffected when these systems are exposed to external perturbations such as light. Of course, the influence of the core and  $\sigma$  electrons is incorporated implicitly in the parameters of the effective Hamiltonian. It is further assumed that (a) each carbon atom of the system contributes one  $\pi$  electron, represented by a  $p_z$  orbital localized on that atom (assuming that the system lies in the  $xy$  plane), and (b) the  $p_z$  orbitals form an orthonormal basis set consistent with the zero-differential overlap (ZDO) approximation developed by Parr (1952). Thus, the PPP model Hamiltonian can be expressed in the second-quantized form as

$$H_{PPP} = \sum_{i,\sigma} \epsilon_i c_{i\sigma}^\dagger c_{i\sigma} - \sum_{i,j,\sigma} t_{ij} (c_{i\sigma}^\dagger c_{j\sigma} + c_{j\sigma}^\dagger c_{i\sigma}) + U \sum_i n_{i\uparrow} n_{i\downarrow} + \sum_{i<j} V_{ij} (n_i - 1)(n_j - 1) \quad (6.1)$$

where  $\epsilon_i$  represents the site energy associated with the  $i$ th carbon atom,  $c_{i\sigma}^\dagger$  creates an electron of spin  $\sigma$  on the  $p_z$  orbital of atom  $i$ ,  $n_{i\sigma} = c_{i\sigma}^\dagger c_{i\sigma}$  is the number of electrons with the spin  $\sigma$ , and  $n_i = \sum_\sigma n_{i\sigma}$  is the total number of electrons on atom  $i$ . The parameters  $U$  and  $V_{ij}$  are the on-site and long-range Coulomb interactions, respectively, while  $t_{ij}$  is the one-electron hopping matrix element. On setting  $V_{ij} = 0$  (with  $U \neq 0$ ), the Hamiltonian reduces to the Hubbard model, while on setting both  $U = 0$  and  $V_{ij} = 0$ , the TB model is obtained. Choosing for the long-range  $V_{ij}$ , the form

$$V_{ij} = \frac{U}{\left[1 + \left(\frac{R_{ij}}{r_0}\right)^2\right]^{1/2}} \quad (6.2)$$

gives the Ohno variant (Ohno 1964) of the PPP model, whereas taking

$$V_{ij} = \frac{U}{\left[1 + \left(\frac{R_{ij}}{r_0}\right)\right]} \quad (6.3)$$

gives the Mataga–Nishimoto parametrization (Mataga and Nishimoto 1957). In the exponential version (Schulten et al. 1975),  $V_{ij}$  takes the form

$$V_{ij} = U \exp\left(-\frac{R_{ij}}{r_0}\right) \quad (6.4)$$

In Eqs. (6.2), (6.3), and (6.4),  $R_{ij} = |\mathbf{r}_i - \mathbf{r}_j|$  is the distance between sites  $i$  and  $j$  in Å, while  $r_0$  is another parameter in the same units.

In this work, we report calculations based upon the Ohno parametrization of the PPP model mentioned above (cf. Eq. 6.2). Moreover, to account for the interchain screening effects, we use a slightly modified form introduced by Chandross and Mazumdar (1997),

$$V_{ij} = U/\kappa_{ij}(1 + 0.6117R_{ij}^2)^{1/2}, \quad (6.5)$$

where  $\kappa_{ij}$  depicts the dielectric constant of the system which can simulate the effects of screening and  $R_{ij}$  is defined above. In various calculations performed on phenylene-based conjugated polymers including PDPAs (Ghosh et al. 2000; Shukla 2004a,b; Shukla et al. 2001, 2003, 2004; Shukla and Mazumdar 1999; Sony and Shukla 2005a), it was noticed that “screened parameters” with  $U = 8.0$  eV and  $\kappa_{ii} = 1.0$ , and  $\kappa_{ij} = 2.0$ , otherwise, proposed by Chandross and Mazumdar (1997), lead to much better agreement with the experiments, as compared to the “standard parameters” with  $U = 11.13$  eV and  $\kappa_{i,j} = 1.0$ , proposed originally by Ohno (1964). Most of the calculations in this work will be based upon these two sets of parameters, unless otherwise specified. In our computer programs implementing the PPP model at the HF level for the finite (Sony and Shukla 2010) and 1D periodic systems (Gundra and Shukla 2012), we have provided the users with the freedom to choose these “standard,” “screened” or any other user-defined parameters for the Coulomb interactions.

In order to calculate static dielectric polarizabilities for finite systems, or the electronic structure of 1D periodic systems such as the GNRs under the gated configurations, one can solve the HF equations in the presence of an external static electric field. Thus, to deal with those situations, we simply modify Eq. (6.1) under the electric dipole approximation by introducing the corresponding term containing the uniform electric field  $\mathbf{E}$ . The overall Hamiltonian of the system is then given by

$$H_{\text{PPP}}^{\text{efield}} = H_{\text{PPP}} - \boldsymbol{\mu} \cdot \mathbf{E} = H_{\text{PPP}} + |e|\mathbf{E} \cdot \mathbf{r}, \quad (6.6)$$

where  $H_{\text{PPP}}$  is the unperturbed Hamiltonian (cf. Eq. 6.1) which describes the system in the absence of the external electric field,  $e$  represents the electronic charge,  $\boldsymbol{\mu} = -e\mathbf{r}$ , is the dipole operator, and  $\mathbf{r}$  is the position operator.

For finite systems, we can easily go beyond the mean-field approach and perform CI on the systems concerned. For the purpose, using the Hartree-Fock molecular orbitals (MOs), one first transforms the PPP model Hamiltonian from the site representation of Eq. (6.1) to the MO representation, and subsequently CI calculations of various levels are carried out by performing virtual excitations from the occupied HF MOs to the unoccupied (virtual) MOs. If a single electron is excited from the occupied to the unoccupied orbitals, the method is called singles-CI (SCI) method; if two electrons are excited in this way, it is called the singles-doubles-CI

(SDCI) method; and so forth. When up to two electrons are virtually excited with respect to multiple reference configurations, the approach is called the multi-reference SDCI (MRSDCI) method. The MRSDCI approach is quite powerful when it comes to dealing with systems with strong electron correlations, as well as in obtaining accurate representation of the excited states. In our PPP-model-based calculations of the electronic structure and optical properties of conjugated polymers, we have made extensive use of the MRSDCI approach (Ghosh et al. 2000; Shukla 2002, 2004a; Shukla et al. 2001, 2003, 2004; Shukla and Mazumdar 1999; Sony and Shukla 2005a,b,c, 2007, 2009).

Going beyond the HF approach for periodic infinite systems is more complicated, and in future, we plan to implement the approaches aimed at achieving that goal.

## 6.2.2 Hartree-Fock Equations

For the sake of completeness, we present the RHF equations corresponding to the PPP model, first for the finite systems and then for infinite periodic systems. Details for the corresponding UHF equations can be found in our earlier publications (Gundra and Shukla 2012; Sony and Shukla 2010).

### 6.2.2.1 Finite Systems

The RHF approach is applicable when the system is a closed-shell one, with an even number of  $\pi$  electrons, so that each molecular orbital (MO) is doubly occupied with an up- and a down-spin electron. We solve the RHF equations using the linear combination of atomic orbitals (LCAO) approach, in which each MO is expressed as a linear combination of a finite-basis set

$$\psi_{\mu} = \sum_i C_{i\mu} \phi_i, \quad (6.7)$$

where  $\psi_{\mu}$  represents the  $\mu$ th MO of the system,  $\phi_i$ 's represent the  $p_z$ -orbitals localized on various carbon atoms, and the determination of the unknown linear coefficients  $C_{i\mu}$  amounts to the solution of the RHF equations. As per the ZDO approximation (Parr 1952), atomic orbitals,  $\phi_i$ 's, are assumed to form an orthonormal basis set. Using the conjecture of Eq. (6.7) in conjunction with the Hamiltonian above, one obtains the RHF equations in the matrix form

$$\sum_j (F_{ij} - \varepsilon_{\mu}) C_{j\mu} = 0, \quad (6.8)$$

where  $\varepsilon_{\mu}$  is the RHF eigenvalue of the  $\mu$ th MO;  $F_{ij}$  is the Fock matrix defined by the equations

$$F_{ij} = t_{ij} - \frac{1}{2} P_{ij} V_{ij}, \quad (i \neq j) \quad (6.9)$$

$$F_{ii} = \epsilon_i - \sum_{j \neq i} V_{ij} + \sum_j P_{jj} V_{ij} - \frac{1}{2} P_{ii} V_{ii}, \quad (i = j) \quad (6.10)$$

where  $\epsilon_i$ ,  $t_{ij}$  and  $V_{ij}$  are defined above (cf. Eq. 6.1); and  $P_{ij}$  is the density matrix element, defined as

$$P_{ij} = 2 \sum_{\mu=1}^{n_{\text{occ}}} C_{i\mu}^* C_{j\mu}, \quad (6.11)$$

where  $n_{\text{occ}} = N_{\text{el}}/2$  denotes the number of occupied orbitals for a system in which the number of  $\pi$  electrons is  $N_{\text{el}}$ . Once the Fock matrix is constructed, one diagonalizes it to obtain a new set of orbitals and density matrix, and the process is repeated until self-consistency is achieved.

### 6.2.2.2 Periodic Systems

The RHF method is applicable to periodic systems with an even number of electrons per unit cell, so that each band is doubly occupied. In principle, the RHF theory for periodic systems is identical to that for finite systems, except for the additional complications due to the Bloch nature of the orbitals. Next, we briefly review the RHF theory for 1D periodic systems when the PPP model is utilized. The  $\mu$ th doubly occupied Bloch orbital of the system, corresponding to the crystal momentum  $k$ , is expressed as a linear combination of  $m$  basis functions per unit cell,

$$\psi_{\mu}(k) = \sum_{i=1}^m C_{i\mu}(k) \phi_i(k), \quad (6.12)$$

where  $C_{i\mu}(k)$ 's represent the linear expansion coefficients, to be determined at a set of  $k$ -points in the 1D BZ, and the  $i$ th Bloch function  $\phi_i(k)$  is given by

$$\phi_i(k) = \frac{1}{\sqrt{N}} \sum_l e^{ikR_l} \phi_i(r - R_l), \quad (6.13)$$

where  $N \rightarrow \infty$  is the total number of unit cells in the system and  $\phi_i(r - R_l)$  is the  $i$ th atomic orbital (AO) ( $p_z$  orbital mentioned in Sect. 6.2.1) located in the  $l$ th unit cell defined by the lattice vector  $R_l$ . It is easy to verify that the Bloch basis functions  $\phi_i(k)$  will form an orthonormal set owing to the orthonormality of the  $p_z$  basis functions  $\phi_i(r - R_l)$ , leading to the simplified RHF equations in the matrix form

$$F(k)C_{\mu}(k) = \epsilon_{\mu}(k)C_{\mu}(k), \quad (6.14)$$

where, for a given  $k$  value,  $F(k)$  represents the Fock matrix,  $C_\mu(k)$  represents the corresponding  $C_{i\mu}(k)$  coefficients, arranged in the form of a column vector, and  $\varepsilon_\mu(k)$  denotes the band eigenvalue. The Fock operator is given by

$$F(k) = h(k) + (J(k) - \frac{1}{2}K(k)) \quad (6.15)$$

above  $h(k)$ ,  $J(k)$ , and  $K(k)$  are obtained by Fourier transforming the one-electron, direct, and exchange integrals corresponding to the PPP Hamiltonian (cf. Eq. 6.1), using the general formula

$$O_{ij}(k) = \sum_{l=-\infty}^{\infty} e^{ikR_l} O_{ij}(R_l), \quad (6.16)$$

where  $O_{ij}(R_l)$  denotes the matrix elements of a general real-space one-electron operator  $O$ . In particular, the real-space versions of the Coulomb and the exchange integrals  $J_{ij}(R_l)$  and  $K_{ij}(R_l)$  for the PPP model are given by

$$J_{ij}(R_l) = \sum_{p=1}^m V_{i(o)k(R_l)} D_{pp}(o) \delta_{ij}, \quad (6.17)$$

and

$$K_{ij}(R_l) = V_{i(o)j(R_l)} D_{ij}(R_l), \quad (6.18)$$

where  $V_{i(o)j(R_l)}$  denotes the long-range part of the Coulomb interaction of the PPP Hamiltonian assuming that the basis function  $i$  is located in the reference unit cell, while  $j$  is located in the unit cell labeled by  $R_l$ . Therefore,  $V_{i(o)j(R_l)}$  can be computed using any of the Coulomb parametrization described in Sect. 6.2.1, and the density matrix elements  $D_{ij}(R_l)$  are given by

$$D_{ij}(R_l) = \frac{2}{\Delta} \int \sum_{\mu=1}^{n_{\text{occ}}} C_{i\mu}^*(k) C_{j\mu}(k) e^{ikR_l} dk, \quad (6.19)$$

where the integral over  $k$  is performed over the 1D BZ of length  $\Delta$  and  $n_{\text{occ}}$  denotes the number of occupied Bloch orbitals per unit cell. The total energy per unit cell of a given system is computed using the real-space expression

$$E_{\text{cell}} = \sum_l \sum_{i,j} D_{ij}(R_l) \left\{ h_{ij}(R_l) + J_{ij}(R_l) - \frac{1}{2} K_{ij}(R_l) \right\}. \quad (6.20)$$

The RHF equations of the system, leading to the band structure ( $\varepsilon_\mu(k)$ ) and the corresponding Bloch orbitals, can be solved by iterative diagonalization technique applied to Eq. (6.14) at a set of  $k$ -points, until the total energy per cell of the system (cf. Eq. 6.20) converges. We have recently numerically implemented the approach

outlined here to solve both the RHF and the UHF equations for 1D periodic systems, within the PPP model (Gundra and Shukla 2012). In our program (Gundra and Shukla 2012), during the self-consistent HF iterations, the integration over the BZ is performed using the Gauss-Legendre quadrature technique as suggested by André et al. (1984), with the additional flexibility that the number of points used for the quadrature can be chosen by the user.

## 6.3 Applications

In this section, we demonstrate our approach by applying it first to the finite systems and next to 1D periodic infinite systems.

### 6.3.1 Finite Systems

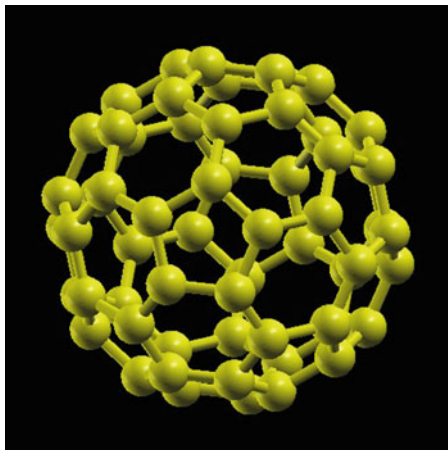
As far as finite systems are concerned, in our previous papers, we have applied our PPP-model-based approach to study the electronic structure and the optical properties of the oligomers of a number of conjugated polymers such as poly(di)phenyl-polyacetylene (PDPA) (Ghosh et al. 2000; Shukla 2004b; Shukla et al. 2001; Shukla and Mazumdar 1999; Sony and Shukla 2005a,b), poly-phenylene-vinylene (PPV) (Shukla 2002; Shukla et al. 2003, 2004), and polyacenes (Sony and Shukla 2005c, 2007, 2009). In what follows, we demonstrate our approach by applying it to study the optical properties of two systems: (a) fullerene  $C_{60}$  and (b) graphene nanodisks.

#### 6.3.1.1 Optical Properties of Fullerene $C_{60}$

Because of its curved geometry, strictly speaking, fullerene  $C_{60}$  is not a  $\pi$ -electron system. Nevertheless, we can treat it as an approximate  $\pi$ -electron system given that each carbon atom possesses an electron which can be called a  $\pi$  electron in a local sense, described by a  $p$  orbital directed perpendicular to the fullerene surface at that atom. Because of that reason, several authors have used the PPP model, and the related Hubbard and the extended Hubbard models, to study the electronic structure, dielectric response, and optical properties of  $C_{60}$ , both at the SCF and the CI levels (Harigaya and Abe 1994; Kim and Su 1994; László and Udvardi 1987, 1989; Ruiz et al. 2001, 1998). Next, we perform SCI calculations, within the PPP model, to calculate the linear optical absorption spectrum of  $C_{60}$ . We also calculate the energy of the lowest triplet excited state using the same approach and compare our results to the experiments wherever possible.

As illustrated in Fig. 6.1, we consider the soccer ball configuration of  $C_{60}$ , corresponding to the point group  $I_h$ , with hexagons and pentagons on its surface.

**Fig. 6.1** Soccer ball structure of  $C_{60}$  considered in these calculations



The nearest-neighbor C–C distances in  $C_{60}$  can be classified as “single bonds” and “double bonds,” with the single bonds being the sides shared between a pentagon and a hexagon, while the double bonds are those shared between two hexagons. In these calculations we took the double bond length to be 1.39 Å, and the single bond length as 1.45 Å, as obtained by Greer using an ab initio density-functional theory-based approach (Greer 2000). In these calculations, we included only the nearest-neighbor hoppings, computed using the relation  $t_{ij} = t_0 \exp[-\beta(\frac{r_{ij}}{a} - 1)]$  (Kim and Su 1994), with  $t_0 = -2.4$  eV,  $\beta = 3.6$ ,  $a = 1.40$  Å, and  $r_{ij}$  being the distance between sites  $i$  and  $j$ . This yields the values of the hopping matrix elements  $t_D = -2.462$  eV and  $t_S = -2.111$  eV, for the double bond and the single bond, respectively. Using these hopping matrix elements and bond lengths, coupled with the Ohno parametrization of the Coulomb matrix elements using both the standard and the screened parameters, we first performed the RHF calculations on  $C_{60}$  to obtain its MOs, which were subsequently used to perform the correlated SCI calculations on the system, which provides us with a representation of not just the ground state but also its various excited states. These SCI level excited states for the spin-singlet states were used to compute the linear optical absorption spectrum of  $C_{60}$ , employing the electric-dipole approximation, and the Lorentzian line shapes.

Before discussing the optical absorption spectrum of  $C_{60}$ , we briefly discuss its electronic structure. The highest occupied molecular orbital (HOMO) of  $C_{60}$  is five-fold degenerate and belongs to the irreducible representation (irrep)  $h_u$  of the point group  $I_h$ . The lowest unoccupied molecular orbital (LUMO), on the other hand, is threefold degenerate and belongs to the irrep  $t_{1u}$ . Because the HOMO and LUMO have the same symmetry under the inversion operator, electric dipole transitions are forbidden between them, and no absorption takes place at the HOMO-LUMO gap. We present our PPP-model-based SCI optical absorption spectrum in Fig. 6.2, computed using both the standard and the screened Coulomb parameters discussed earlier in Sect. 6.2.1. From the plots, it is obvious that quantitatively speaking the

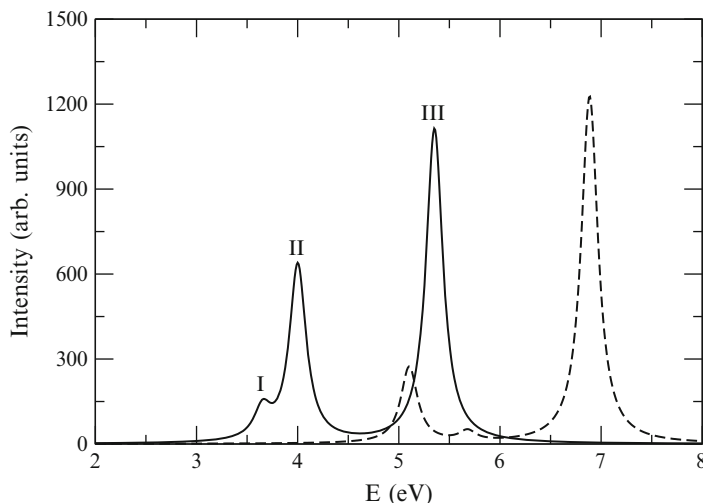


**Fig. 6.2** Optical absorption spectra of  $C_{60}$ , computed using the SCI approach, within the PPP model employing the screened parameters (*solid line*) and the standard parameters (*dashed line*). A Lorentzian line shape, along with a line width of 0.1 eV, was used to plot the spectra

standard-parameter-based spectrum is substantially blue-shifted compared to the screened parameter spectrum. Furthermore, there are some qualitative difference also between the two calculations in that the relative intensities of the first two peaks are just reverse of each other. When compared to the optical absorption experiments on  $C_{60}$  (Ajje et al. 1990; Gasyna et al. 1991; Leach et al. 1992; Lee et al. 1992; Ren et al. 1991), our screened parameter-based results are in much better agreement with it, as compared to the standard parameter ones. Therefore, henceforth, we restrict our discussion only to our screened parameter spectrum which exhibits three prominent absorption peaks labeled I, II, and III in Fig. 6.2. In its ground state,  $C_{60}$  is a closed-shell system in the  ${}^1A_g$  state; therefore, as per selection rules, it can make an electric-dipole transition only to excited states belonging to  ${}^1T_{1u}$  irrep. Indeed, all the three labeled peaks in the plotted spectrum correspond to threefold degenerate excited states, consistent with the dimension of the  $T_1$  irrep. In Fig. 6.2, peaks I, II, and III are located at 3.67, 4.00, and 5.35 eV, respectively. Relative intensities and general features of our screened parameter-based spectrum agree quite well with the measured spectrum of  $C_{60}$  reported by Gasyna et al. (1991), who also reported three major absorption bands of increasing intensities located at 3.81, 4.91, and 5.97 eV. Given that our calculations have been performed using the SCI method, which does not include the electron-correlation effects in a sophisticated manner, the agreement between the theory and experiments is quite reasonable. At present a large-scale MRSDCI calculation of the electric-dipole optical transitions in  $C_{60}$ , employing the PPP model, is under way in our group, and the results will be published in future.

Next, we discuss the lowest triplet excited state of  $C_{60}$ , the  ${}^1{}^3T_{2g}$  state. The wave function of this state is dominated by the configuration with singly occupied HOMO and LUMO orbitals, along with triplet spin multiplicity. Our PPP-model-based SCI



value of 2.42 eV for the excitation energy of this state is in excellent agreement the value 2.46 eV reported by [László and Udvardi \(1987\)](#), also based upon the PPP-SCI approach, although using a different set of Coulomb parameters. Experimentally speaking, the exact value of the excitation energy of this state appears not to be very certain, although [Leach et al. \(1992\)](#) have reported the onset of triplet absorption near 1.78 eV.

### 6.3.1.2 Optical Absorption Spectrum of Graphene Nanodisks

Because of the gapless nature of 2D graphene, its device applications are extremely limited. That is one of the reasons behind the considerable amount of research effort in the field of reduced dimensional nanostructures of graphene such as quasi-1D GNRs ([Barone et al. 2006](#); [Palacios et al. 2010](#); [Prezzi et al. 2008](#); [Son et al. 2006a](#); [Yang et al. 2007a,b, 2008](#)) and 0D graphene nanodisks ([Ezawa 2008](#); [Fernández-Rossier and Palacios 2007](#); [Güçlü et al. 2009](#); [Hod et al. 2008](#); [Kinza et al. 2010](#); [Ridder and Lyding 2009](#); [Schumacher 2011](#); [Wang et al. 2008, 2009](#); [Yazyev 2010](#)), which are also called graphene quantum dots or graphene nanoflakes. Graphene nanodisks, which are nothing but finite-sized graphene fragments, can, in general, be of any shape, regular or irregular. Regular-shaped nanodisks are characterized by their shapes as well as by the nature of their edges, which can be of the zigzag type or the armchair type. Some of the regular-shaped graphene nanodisks which have been studied in the literature are shown in [Fig. 6.3](#). For example, triangular graphene nanodisks with zigzag edges shown in [Fig. 6.3a](#) have been theoretically predicted to have magnetic ground states ([Fernández-Rossier and Palacios 2007](#); [Güçlü et al. 2009](#); [Kinza et al. 2010](#); [Wang et al. 2008, 2009](#); [Yazyev 2010](#)). Optical properties of graphene nanodisks were recently studied theoretically by [Schumacher \(2011\)](#) using a time-dependent density functional theory-based approach. Because of their interesting optical and magnetic properties, graphene nanodisks have potential applications in the field of optoelectronics and spintronics ([Yazyev 2010](#)).

In this work, we present the calculations of the linear optical absorption spectrum of the nanodisks shown in [Fig. 6.3](#), using our PPP-model-based approach, employing the screened Coulomb parameters and the SCI method. The aim of this work is to understand the optical properties of graphene nanodisks and, particularly, to probe the influence of the shape of the nanodisks on their absorption spectra. We note that except for the zigzag triangular nanodisk (cf. [Fig. 6.3a](#)), which has an odd number of  $\pi$  electrons, and hence an open shell doublet ground state, the rest of the nanodisks have an even number of  $\pi$  electrons, and a closed-shell singlet ground state. Results of our calculations for various nanodisks are presented in [Fig. 6.4](#). On comparing the absorption spectra of various nanodisks, the following trends emerge: (a) for the triangular zigzag nanodisk, the absorption starts with a very weak feature near 4 eV, while the most intense absorption occurs at energies higher than 7 eV; (b) for the triangular armchair nanodisk, the most intense absorption occurs for

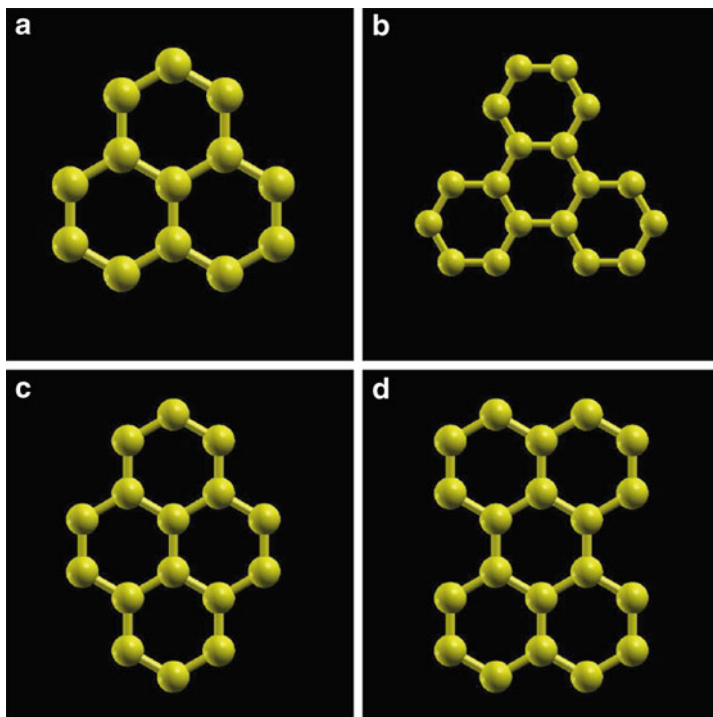


**Fig. 6.3** Structures of a few symmetric graphene nanodisks. (a) Zigzag triangular. (b) Armchair triangular. (c) Diamond shaped. (d) Bowtie shaped

the first peak of the spectrum located at 4.4 eV, with somewhat weaker features at higher energies; (c) for the diamond-shaped disk, the first peak which is reasonably strong occurs at even lower energy close 3.2 eV, with several intense peaks at higher energies; and (d) in the bowtie-shaped disk, the optical absorption starts at the lowest energy ( $\approx 2.6$  eV) of all the nanodisks described considered here, with stronger peaks at higher energies as well. Thus, we see an obvious correlation between the shapes of the nanodisks, and their absorption spectra. Furthermore, for the triangular nanodisks, the nature of edges (armchair vs. zigzag) also influences the optical absorption both qualitatively and quantitatively. Therefore, it is conceivable that one can determine the shapes and edge structures of graphene nanodisks through optical absorption spectroscopy.

As far as the nature of excited states contributing to the optical absorption in various nanodisks is concerned, a common feature emerges. In all the nanodisks, the first absorption peak is characterized by an excited state which mainly consists of the configuration obtained by a single-electron excitation from the HOMO to the LUMO orbital. A more detailed study of the optical absorption in graphene nanodisks, including higher-level CI treatments and the influence of disorder, will be published elsewhere in future.

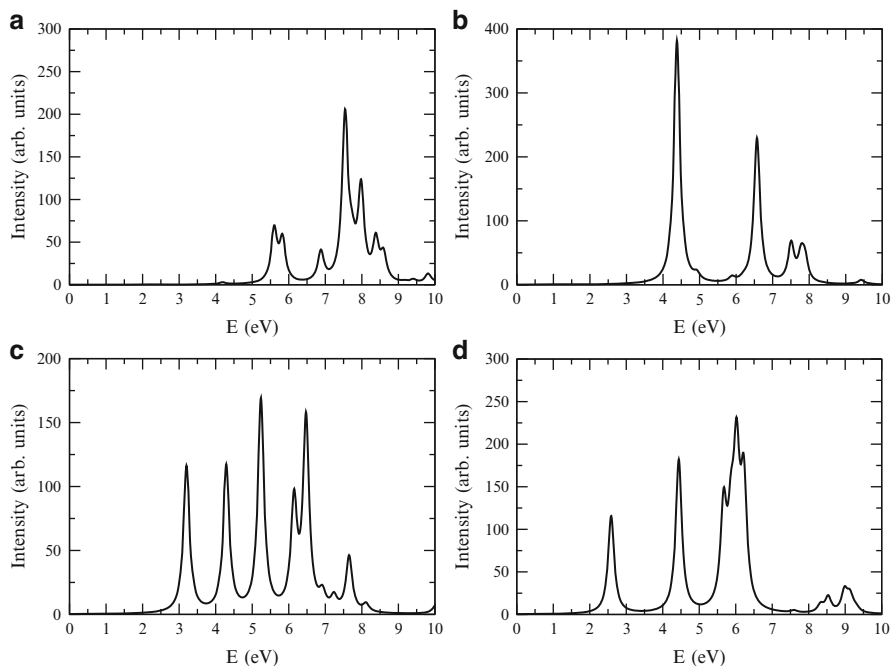


**Fig. 6.4** Linear optical absorption spectra of various graphene nanodisks computed using the PPP-SCI approach and screened Coulomb parameters. A uniform line width of 0.1 eV was used to plot all the spectra. (a) Zigzag triangular. (b) Armchair triangular. (c) Diamond shaped. (d) Bowtie shaped

### 6.3.2 Infinite 1D Periodic Systems

As far as infinite 1D periodic systems are concerned, we apply our approach to study the band structure and optical properties of mono- and multilayer-GNRs, and single-walled carbon nanotubes.

#### 6.3.2.1 Band Structure of Graphene Nanoribbons

GNRs are quasi 1D structures which can be obtained by patterning graphene using various techniques (Han et al. 2007). Unlike monolayer graphene, GNRs exhibit energy band gaps (Son et al. 2006a) much needed for device applications. Theoretical works on GNRs mainly focus on ribbons with armchair edge termination known as armchair GNRs (AGNRs) and zigzag edge termination known as zigzag GNRs (ZGNRs). The structures of an AGNR, and a ZGNR, are shown in Figs. 6.5a and b

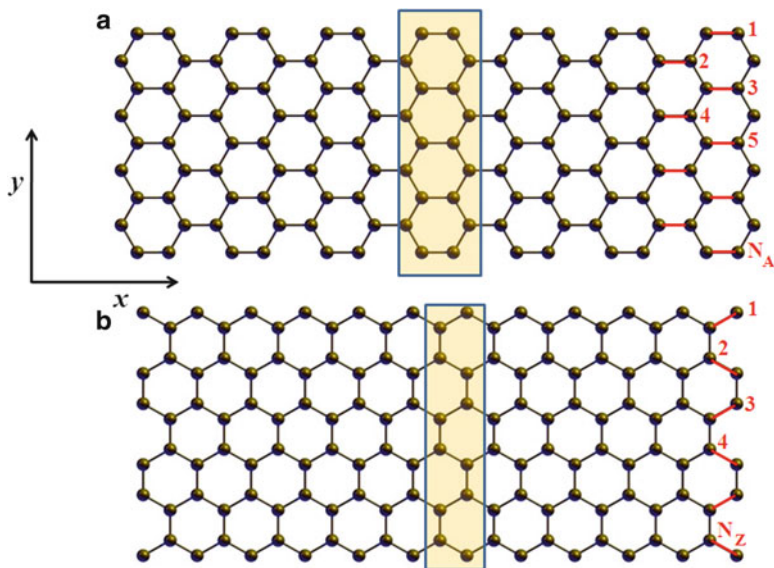
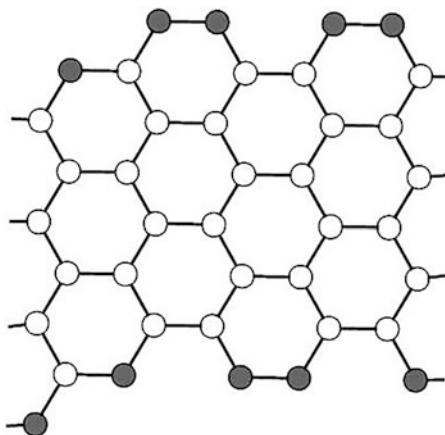


**Fig. 6.5** The schematic representation of (a) armchair graphene nanoribbon with  $N_A = 9$  and (b) zigzag graphene nanoribbon with  $N_Z = 6$ . The ribbons are assumed to lie in the  $xy$  plane, with the periodicity in the  $x$ -direction. The unit cells of these ribbon are enclosed in the *shaded rectangles*

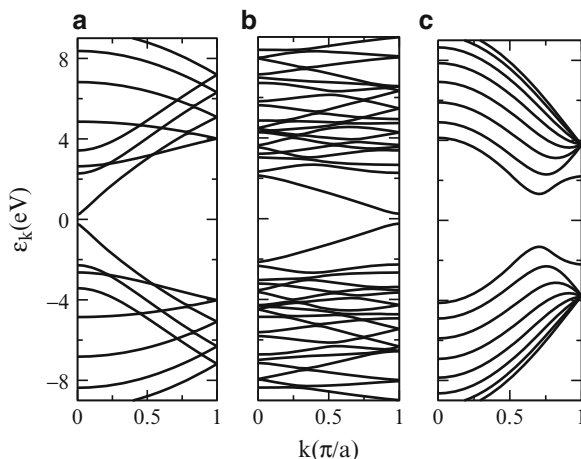
**Fig. 6.6** The unit cell of a general GNR with eight dimer lines across the width



respectively. In the case of AGNRs,  $N_A$  denotes the number of carbon-carbon dimer lines across the width (cf. Fig. 6.5a), while in the case of ZGNRs, width  $N_Z$  denotes the number of zigzag lines (cf. Fig. 6.5b) across the width.

In addition to the GNRs with well-defined edge terminations such as the AGNRs and the ZGNRs, we also present calculations on general GNRs, which possess mixed type of edge terminations, including both the armchair and zigzag edges. The schematic structure of such a general GNR is presented in Fig. 6.6, in which

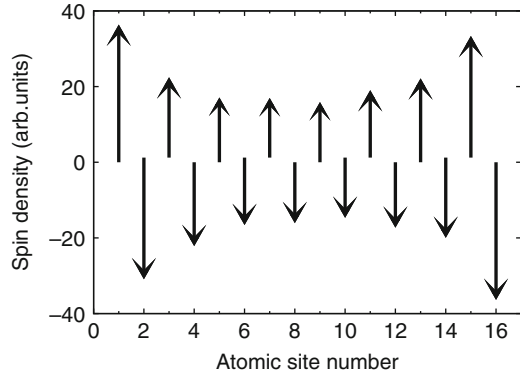
**Fig. 6.7** Band structure of (a) AGNR-8 obtained using PPP-RHF method, (b) general GNR (cf. Fig. 6.6) obtained using PPP-RHF method, and (c) ZGNR-8 obtained using PPP-UHF method



the atoms at the edges are represented by solid circles. An armchair edge can be identified by a dimer line connecting two edge atoms, whereas a zigzag edge can be identified by an edge atom which is connected only with the atoms in the bulk of the ribbon.

In all the calculations performed on GNRs of any type, the carbon-carbon nearest-neighbor distance was taken to be  $1.42 \text{ \AA}$ , and all the bond angles were assumed to be  $120^\circ$ . In case of multilayer GNRs, the distance between the adjacent layers was taken to be  $3.35 \text{ \AA}$ . The hopping is restricted only to the nearest neighbors within each layer, and between the adjacent layers, with the values  $t = 2.7 \text{ eV}$  (intraplane), and  $t_\perp = 0.4 \text{ eV}$  (inter-plane) respectively. As far as the Coulomb parameters are concerned, we have used the screened parameters of Chandross and Mazumdar (Chandross and Mazumdar 1997), with  $U = 8.0 \text{ eV}$  and  $\kappa_{i,j} = 2.0$  ( $i \neq j$ ) and  $\kappa_{i,i} = 1$ . The band structures of AGNR-8 (AGNR- $N_A$  denotes an AGNR with width  $N_A$ ), and the general GNR, obtained using the PPP-RHF method are presented in Figs. 6.7a and b, respectively. It is evident from Fig. 6.7 that all the GNRs exhibit finite band gaps, and their band structures depend crucially on their geometry. A band gap of  $0.5 \text{ eV}$  was observed at  $k = 0$  for AGNR-8 (cf. Fig. 6.7a). It is worth mentioning that AGNR-8 is metallic at the TB level. In fact depending on the value of  $N_A$ , AGNRs are classified into three categories with  $N_A = 3p$ ,  $3p + 1$ , and  $3p + 2$ ,  $p$  being an integer. At the TB level, all the AGNRs with  $N_A = 3p + 2$  are predicted to be gapless (Nakada et al. 1996). However, ab initio DFT calculations predict all types of AGNRs to be gapped (Son et al. 2006a). As far as the PPP-model-based calculations are concerned, the long-range electron–electron interactions which it incorporates play a crucial role in opening the band gaps in  $3p + 2$  class AGNRs (Gundra and Shukla 2011a). In case of the general GNR, the band gap is direct in nature, with the value  $0.49 \text{ eV}$ , located at  $k = \pi$ . Furthermore, as is obvious from Fig. 6.7, band structure of the general GNR is significantly different from those of both the AGNR and the ZGNR.

**Fig. 6.8** The spin density distribution of ZGNR-8 obtained using PPP-UHF method, plotted at various atomic sites in the unit cell across the width



In the case of ZGNRs, the ground state is predicted to be magnetic with oppositely oriented spins localized on the zigzag edges located on the opposite sides of the ribbons (Son et al. 2006a). The ZGNRs are gapless at the TB level, characterized by flat bands near the Fermi energy ( $E_F$ ), leading to a van Hove singularity at  $E_F$ , suggesting an instability. And indeed, a symmetry broken state with magnetic ordering mediated by Coulomb interactions (Son et al. 2006b) stabilizes the system. We obtain this broken-symmetry ground state exhibiting edge magnetism on performing the PPP-UHF calculations (Gundra and Shukla 2011a), which are based upon separate mean-fields for the up- and the down-spin electrons. On the other hand, the PPP-RHF method, by its very nature, predicts a nonmagnetic ground state for ZGNRs which has a higher energy per unit cell as compared to that obtained for the spin-polarized state using the PPP-UHF method. The band structure of ZGNR-8 (ZGNR- $N_Z$  denotes a ZGNR with width  $N_Z$ ) obtained using PPP-UHF approach is presented in Fig. 6.7c. A significant band gap of 2.64 eV is opened up at  $k = \frac{2\pi}{3}$  because of the magnetic ordering. The spin density distribution for ZGNR-8, plotted for the sites across its width, presented in Fig. 6.8 clearly exhibits edge magnetism. The electrons of different spins are localized at adjacent sites along the width, indicating an antiferromagnetic order. However, a ferromagnetic order is observed on a given edge, along its length (Gundra and Shukla 2012).

### 6.3.2.2 Band Structure of Gated Graphene Nanoribbons

GNRs display interesting electronic properties in the presence of an external gate bias. For example, ZGNRs exhibit half-metallic behavior in the presence of a lateral electric field ( $E_y$ ), i.e., ZGNRs are conducting for the electrons of one spin and insulating for those of the other spin (Son et al. 2006b). Therefore, gated ZGNRs have potential device applications in the field of spintronics.

This is illustrated in Fig. 6.9 in which the band structure of ZGNR-12 in the presence of a lateral electric field of strength 0.2 V/Å is presented. While the bands of the up ( $\alpha$ ) and down ( $\beta$ ) spin electrons are degenerate in the absence of the

**Fig. 6.9** Band structure of ZGNR-12 in the presence of lateral electric field of strength  $0.2 \text{ V/\AA}$ . The *solid lines* represent the bands corresponding to electrons of spin- $\alpha$ , and the *broken lines* represent the bands corresponding to electrons of spin- $\beta$

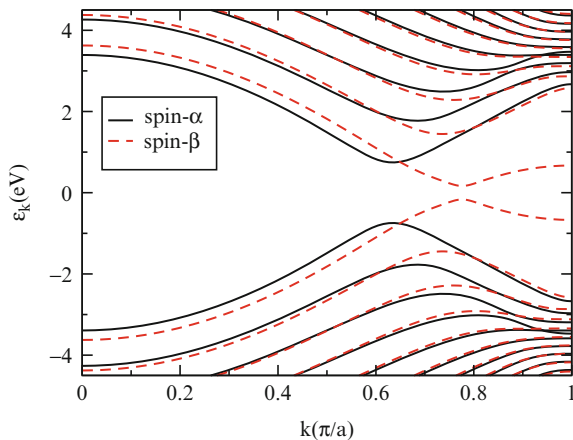
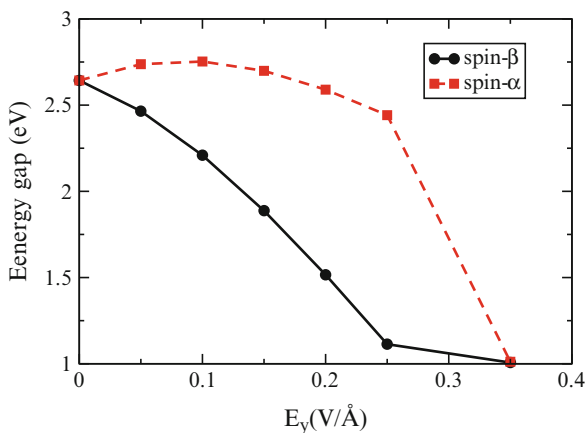


**Fig. 6.10** Variation of energy band gaps with electric field applied along  $y$ -axis of ZGNR-8, obtained using the PPP-UHF method. The *solid black line* represents energy gaps for spin-down electrons, and the *red broken line* represents energy gaps for spin-up electrons



field with a band gap of 2.1 eV, the degeneracy is lifted in the presence of external electric field ( $E_y$ ) along  $y$ -axis, and the band gap for electrons of spin- $\alpha$  changes to 1.5 eV, while that for electrons of spin- $\beta$  reduces drastically to 0.3 eV, indicating the tendency towards the half-metallic nature. The half-metallic nature of ZGNRs can be understood from the fact that in the absence of external electric field, oppositely oriented spin states are localized on the opposite edges of the ribbon. In the presence of a nonzero  $E_y$ , the ZGNR develops a potential difference across its width, thereby energies of the localized edge states are increased on one edge and decreased on the other one, leading to different band gaps for the electrons of different spin orientations (Son et al. 2006b). With the increasing field strength  $E_y$ , the band gaps of spin- $\beta$  electrons tend to decrease, while those of  $\alpha$  electrons exhibit a slight increase up to a certain field strength, beyond which they also decrease monotonically. After a critical field strength, the energy gaps for electrons of both spins attain the same value, and the half-metallic behavior exhibited by the ZGNRs disappears. To illustrate this point, in Fig. 6.10 we present the variation of band gaps

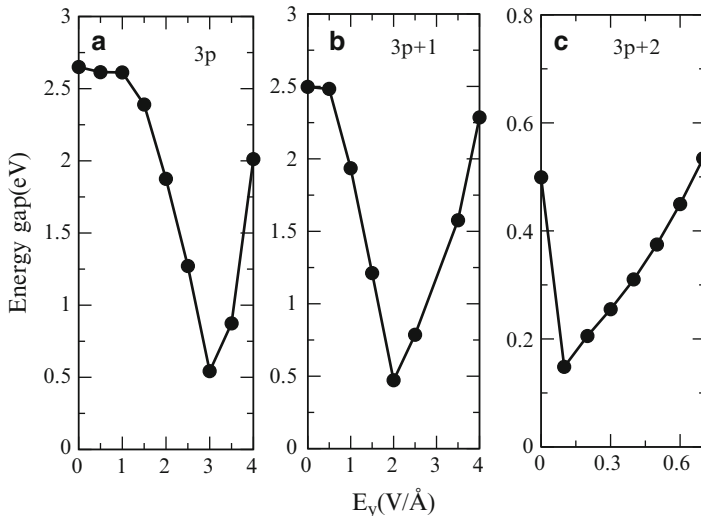


**Fig. 6.11** Variation of the band gaps of the AGNRs with respect to the electric field applied along the  $y$ -axis, for (a)  $N_A = 3p$ , (b)  $N_A = 3p + 1$ , and (c)  $N_A = 3p + 2$ , with  $p = 2$

of spin- $\alpha$  and spin- $\beta$  electrons with  $E_y$  for ZGNR-8, calculated using the PPP-UHF method. The half-metallic nature is observed when  $0 \leq E_y \leq 0.35$  V/Å, with band gaps for electron of spin- $\alpha$  and spin- $\beta$  being well separated, and for  $E_y > 0.35$  V/Å, the energy gaps for electrons of both the spins are again identical, with the value of the band gap being lower than the corresponding value in the absence of  $E_y$ . Thus, the half-metallic behavior disappears for  $E_y > 0.35$  V/Å. The first-principles DFT-based calculations by Kan et al. (2007) also predicted a similar behavior in ZGNRs.

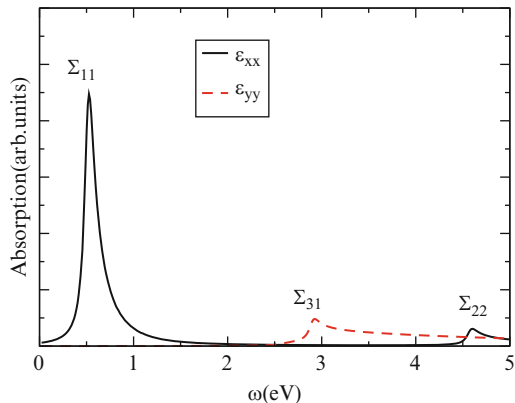
The external electric field has profound effect on the band gaps of AGNRs as well. We illustrate the variation of band gaps with  $E_y$  for AGNRs of width  $N_A = 3p$ ,  $3p + 1$  and  $3p + 2$ , for  $p = 2$  in Fig. 6.11. In all the ribbons the gap decreases initially with increase in the strength of  $E_y$ . But beyond a critical field strength ( $E_y^c$ ), a reverse trend is observed, where the gap increases with further increase in the field strength. Even though we have presented the results corresponding to  $p = 2$ , a similar behavior is observed for  $p > 2$  as well. We observe that in each category of AGNRs, the value of  $E_y^c$  decreases with the increase in their width, e.g., we have obtained  $E_y^c = 3$  V/Å for AGNR-6, whereas the corresponding value for AGNR-9 is 2 V/Å.

### 6.3.2.3 Optical Properties of Graphene Nanoribbons

As discussed earlier, the geometry of GNRs plays a crucial role in determining their electronic structure. Therefore, the optical properties of the ribbons will also be quite sensitive to their geometry, thereby allowing the possibility of determining



**Fig. 6.12** Optical absorption spectrum of AGNR-8 calculated by the PPP-RHF method. The *solid black line* represents  $\epsilon_{xx}(\omega)$ , while the *dotted red line* represents  $\epsilon_{yy}(\omega)$ . A line width of 0.05 eV was assumed

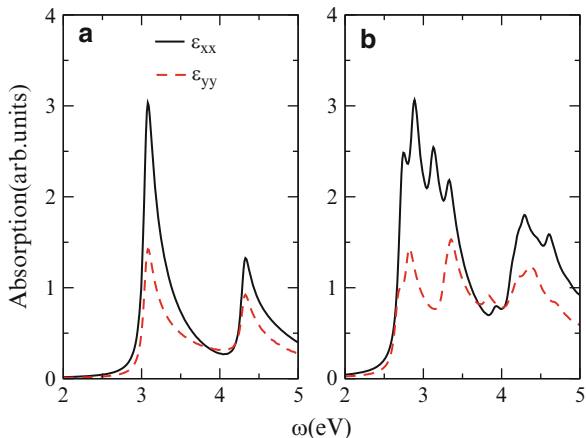


the geometry of GNRs by means of optical measurements. Next, we present results of our calculations of the optical absorption spectra of various GNRs and CNTs, for the incident radiation polarized in  $x$  (or longitudinal) or  $y$  (or transverse) directions, computed in the form of  $\epsilon_{xx}(\omega)$  and  $\epsilon_{yy}(\omega)$ , respectively, where  $\epsilon_{ii}(\omega)$  denotes the imaginary part of the dielectric constant tensor for the  $i$ th Cartesian component and  $\omega$  denotes the frequency of incident photons. The calculations of various components of the  $\epsilon_{ii}(\omega)$  were performed using the standard approach outlined in our previous publications (Gundra and Shukla 2011a,b, 2012). The optical absorption spectrum of AGNR-8, obtained using the PPP-RHF method, is displayed in Fig. 6.12. If  $\Sigma_{mn}$  denotes a peak in the spectrum due to a transition from  $m$ th valence band (counted from top) to the  $n$ th conduction band (counted from bottom), the peak of  $\epsilon_{xx}(\omega)$  at 0.54 eV is  $\Sigma_{11}$ , and the peak at 4.60 eV is  $\Sigma_{22}$ . Whereas, the peak in  $\epsilon_{yy}(\omega)$  at 2.93 eV corresponds to  $\Sigma_{31}$ . The individual peaks in the absorption spectrum of AGNR-8 are well separated in energy and correspond to either  $x$ - or  $y$ -polarized photons, consistent with the dipole selection rules of  $D_{2h}$  point group symmetry of AGNRs.

In Fig. 6.13a we present the optical absorption spectrum of ZGNR-6 computed using the PPP-UHF method. Even though the point group of ZGNRs is also  $D_{2h}$ , in contrast to AGNRs, most of the prominent peaks of ZGNR-6 exhibit mixed polarization characteristics. This is due to the fact that the edge-polarized magnetic ground state of ZGNRs no longer exhibits  $D_{2h}$  symmetry, because the reflection symmetry about the  $xz$ -plane is broken, thereby leading to mixed polarizations in the optical absorption. Thus, by using optical probes, one can predict whether a given ribbon is an AGNR or a ZGNR by analyzing the polarization characteristics of the absorption peaks.

Apart from determining the geometry of GNRs, optical absorption spectra can also be used to differentiate the monolayer GNRs from the bilayer and the multilayer GNRs. We illustrate this by comparing the optical absorption spectrum of monolayer ZGNR-6 with that of its bilayer counterpart. Similar to the case of monolayer ZGNR-6, most of the prominent peaks of bilayer ZGNR-6 also exhibit

**Fig. 6.13** Optical absorption spectrum of (a) ZGNR-6 and (b) bilayer-ZGNR-6, obtained by the PPP-UHF method. The solid black line represents  $\epsilon_{xx}(\omega)$ , while the dotted red line represents  $\epsilon_{yy}(\omega)$ . A line width of 0.05 eV was assumed



mixed polarization characteristics (cf. Fig. 6.13b) due to edge magnetism (Castro et al. 2007). However, it is interesting to note that in the case of monolayer ZGNRs, the shape of the spectra corresponding to  $\epsilon_{xx}(\omega)$  and  $\epsilon_{yy}(\omega)$  remains similar, though the magnitude of peaks of  $\epsilon_{yy}(\omega)$  is smaller when compared to those of  $\epsilon_{xx}(\omega)$ . This scenario is completely changed in the case of bilayer ZGNR-8, in which due to the presence of second layer, many additional peaks are observed in  $\epsilon_{xx}(\omega)$  as compared to  $\epsilon_{yy}(\omega)$ . Therefore, the optical response of monolayer ZGNRs is quite different from that of the bilayer ZGNRs and can, in principle, be used to distinguish between them through optical measurements.

### 6.3.2.4 Band Structure and Optical Properties of Bilayer AGNRs

Bilayer and multilayer AGNRs exhibit interesting electronic and optical properties which we have investigated in an earlier publication (Gundra and Shukla 2011b). For example, the intensity of the linear optical absorption in multilayer AGNRs increases rapidly with the increasing number of layers and depends crucially on the relative orientation of adjacent layers (Gundra and Shukla 2011b). In this section, we discuss the band structure and optical properties of bilayer AGNR-8 obtained using the PPP-RHF method. We assume Bernal stacking for bilayer AGNRs and consider two types of edge alignments, namely,  $\alpha$  alignment and  $\beta$  alignment, shown schematically in Fig. 6.14 (Gundra and Shukla 2011b). To illustrate the influence of edge alignment on the electronic structure of bilayer AGNRs, we present the band structure of bilayer AGNR-8 in  $\alpha$  and  $\beta$  alignments in Figs. 6.15a and b, respectively. The individual energy bands near Fermi energy are separated by larger energy in  $\alpha$  alignment when compared to  $\beta$  alignment (Gundra and Shukla 2011b). This has important implications on the optical absorption spectra which is presented in Figs. 6.15c and d, for the two alignments. It is obvious that the optical absorption spectra for the two alignments are substantially different from each

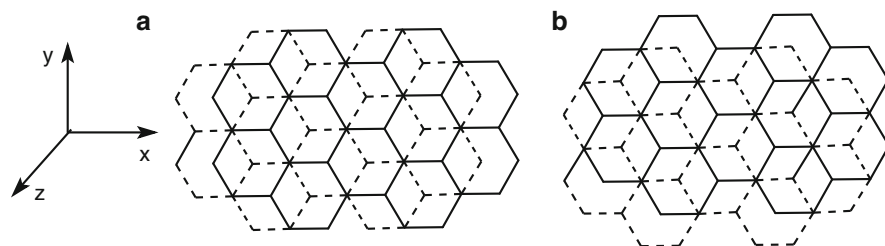


**Fig. 6.14** Schematic structure of a bilayer AGNR in (a)  $\alpha$  alignment and (b)  $\beta$  alignment

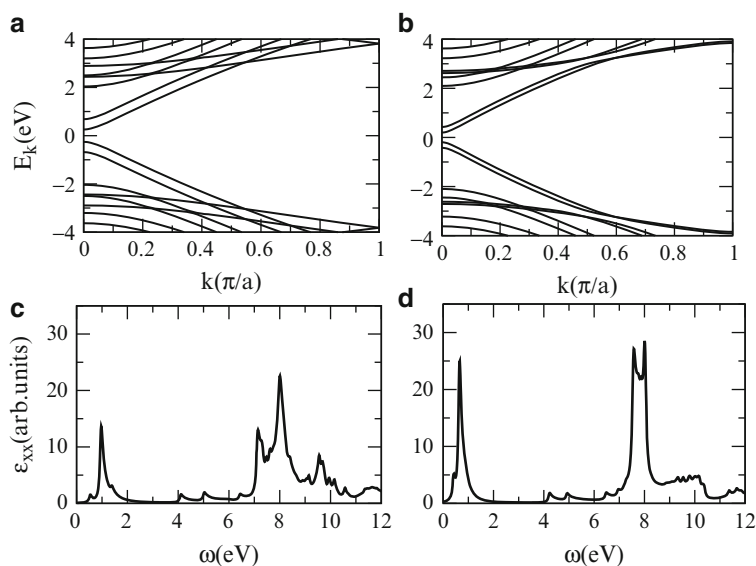


**Fig. 6.15** Band structure of bilayer ANGR-8, obtained using the PPP-RHF method in (a)  $\alpha$  alignment and (b)  $\beta$  alignment. Optical absorption spectra of the same ribbon in (c)  $\alpha$  alignment and (d)  $\beta$  alignment

other so that their experimental measurement, coupled with our theoretical results, can possibly be used to determine the nature of alignment in multilayer ribbons. For a comprehensive discussion of the influence of edge alignment on the optical properties of multilayer AGNRs, we refer the reader to our recent work ([Gundra and Shukla 2011b](#)).

### 6.3.2.5 Electro-Absorption in Zigzag Graphene Nanoribbons

Electro-absorption (EA), which is nothing but the optical absorption in the presence of a static external electric field, is a commonly used probe of optical properties of materials and has been used extensively in the field of  $\pi$ -conjugated polymers ([Lies](#)

**Fig. 6.16** Linear absorption spectrum (solid black line) and the electro-absorption spectrum (dotted red line) of ZGNR-10 in the presence of lateral electric field ( $E_y$ ) of strength  $0.2 \text{ V/\AA}$ , calculated by the PPP-UHF method

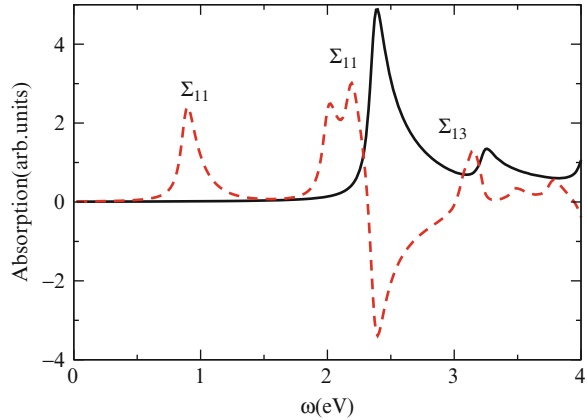
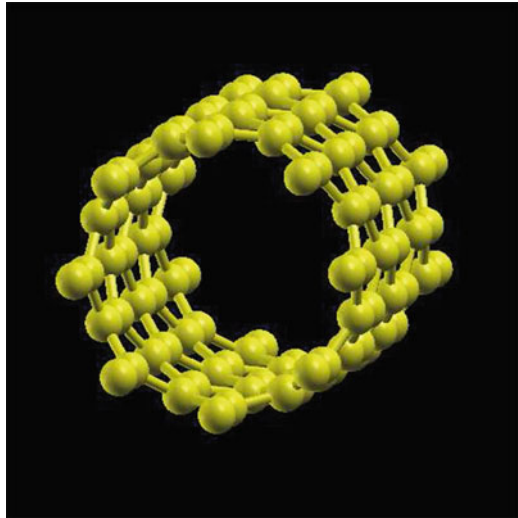
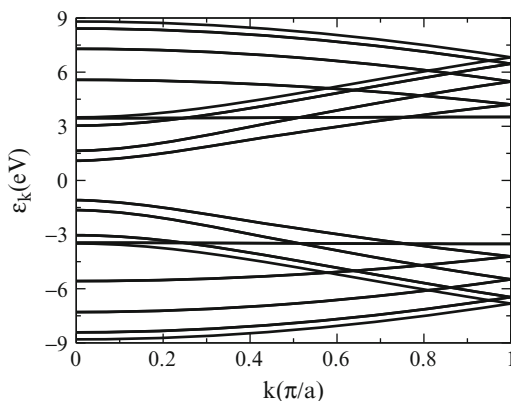


**Fig. 6.17** The schematic structure of SWCNT (8,0). For brevity, carbon atoms belonging to the first three unit cells are displayed



et al. 1997). Quantitatively, it is defined as the difference of the optical absorption spectrum with, and without, an external static electric field. In a recent work (Gundra and Shukla 2011a), we argued that the EA spectroscopy provides a natural way of probing the electric-field-driven half-metallicity of ZGNRs. To illustrate this, we present the EA spectrum of ZGNR-10 in Fig. 6.16, calculated in the presence of a lateral external electric field of strength  $0.2 \text{ V/\AA}$ , using our PPP-UHF approach. The linear absorption spectrum of the ribbon without the external field, for its spin-polarized ground state, is also presented in the same figure. The electric-field-driven half-metallic nature of ZGNR-10 is clearly evident with the presence of two energetically split peaks, corresponding to two different  $\Sigma_{11}$  transitions, among the spin-up and spin-down electrons. Therefore, EA spectroscopy can serve as a useful optical probe to probe both the edge magnetism and related half-metallic nature of ZGNRs.

**Fig. 6.18** Band structure of SWCNT (8,0), obtained using the PPP-RHF method

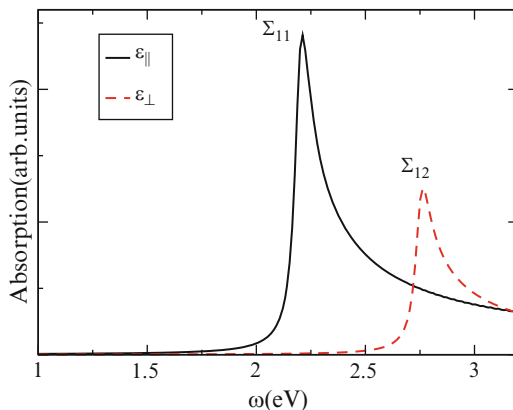


### 6.3.2.6 Band Structure and Optical Absorption Spectrum of Carbon Nanotubes

Single-walled carbon nanotubes (SWCNTs) exhibit excellent electronic properties and have been studied extensively over the last few decades (Dresselhaus et al. 2001). In this work, we present the band structure and optical properties of insulating SWCNT (8,0) obtained using PPP-RHF method. Even though the PPP model has been used by other authors to explore the electronic and optical properties of carbon nanotubes (Wang et al. 2006, 2007; Zhao and Mazumdar 2004, 2007; Zhao et al. 2006), the calculations are restricted to nanotubes of finite length, and periodic boundary conditions were not imposed. The schematic structure of SWCNT (8,0) is presented in Fig. 6.17. In these calculations, carbon-carbon nearest-neighbor distance was taken to be  $1.42 \text{ \AA}$ , and hopping was restricted to the nearest neighbors, with the hopping term  $t = 2.4 \text{ eV}$ . Similar to the case of GNRs, we have used the screened Coulomb parameters of Chandross and Mazumdar (1997), with  $U = 8.0 \text{ eV}$  and  $\kappa_{i,j} = 2.0$  ( $i \neq j$ ) and  $\kappa_{i,i} = 1$ . Figure 6.18 displays the band structure of SWCNT (8,0) obtained using our approach. We note that the band structure of this SWCNT is similar to that of AGNRs, with a direct band gap of  $2.18 \text{ eV}$  at  $k = 0$ .

The optical absorption spectrum of SWCNT (8,0), computed using the PPP-RHF approach, is presented in Fig. 6.19. Due to the cylindrical symmetry of CNTs, their electric-dipole optical transitions are either through longitudinally polarized photons with polarization direction along the axis of the tube ( $x$ -direction), or the transversely polarized photons, with the polarization in the radial direction, in the  $yz$  plane. In Fig. 6.19, we denote the longitudinally polarized absorption spectrum as  $\epsilon_{\parallel}(\omega)$  ( $= \epsilon_{xx}(\omega)$ ), and the transverse one as  $\epsilon_{\perp}(\omega)$  ( $= \sqrt{\epsilon_{yy}(\omega)^2 + \epsilon_{zz}(\omega)^2}$ , with  $\epsilon_{yy}(\omega) = \epsilon_{zz}(\omega)$ ). While a detailed investigation of the optical absorption of SWCNTs will be published elsewhere, we note that the peaks corresponding to two types of polarizations are well separated in energy, and, therefore, can be identified in absorption experiments. The peak in  $\epsilon_{\parallel}(\omega)$  corresponds to the  $\Sigma_{11}$  transition,

**Fig. 6.19** Optical absorption spectrum of SWCNT (8,0), obtained by PPP-RHF method. The *solid black line* represents  $\epsilon_{\parallel}(\omega)$ , while the *dotted red line* denotes  $\epsilon_{\perp}(\omega)$ . A line width of 0.05 eV was assumed



located at the direct band gap (2.18 eV), while the peak in  $\epsilon_{\perp}(\omega)$  at 2.77 eV denotes  $\Sigma_{12}$  transition. These results of ours on SWCNT (8,0) in the infinite length limit are in good quantitative agreement with the corresponding PPP-HF results reported by [Zhao and Mazumdar \(2004\)](#), based upon finite fragment calculations.

## 6.4 Conclusions and Future Directions

In this chapter, we have applied a PPP model Hamiltonian-based approach to study the electronic structure and optical properties of finite, as well as 1D periodic, graphene nanostructures such as fullerene  $C_{60}$ , graphene nanodisks, graphene nanoribbons, and single-wall carbon nanotubes. In case of periodic systems, calculations were performed at the mean-field Hartree-Fock level, whereas for the finite systems, we went beyond the mean field and included the electron-correlation effects at the SCI level. We computed the linear optical absorption spectrum of fullerene  $C_{60}$ , and the results obtained with screened Coulomb parameters were found to be in good agreement with the experiments. We also probed the optical absorption in graphene nanodisks using our approach and found that their shape, and the edge structure, influences their absorption spectrum considerably.

For 1D periodic systems, we computed the band structure and optical absorption spectra of monolayer GNRs of different geometries, and bilayer GNRs in Bernal stacking, but with different edge alignments. We found that the band structure and optical absorption spectra of GNRs depend crucially on their geometrical parameters, thereby allowing the possibility of an all-optical determination of the nature of their edge termination, as well as number and alignment of different layers for multilayer GNRs. We also demonstrated the sensitivity of the optical absorption spectrum of the ZGNRs to the nature of their edge-magnetized ground state and argued that their EA spectrum provides an efficient way of probing their electric-field-driven half-metallicity. Furthermore, for the first time, we applied our

PPP-model-based approach to compute the band structure and optical absorption spectrum of an insulating SWCNT in the infinite periodic limit.

It is quite remarkable that the PPP model, which was originally developed to describe the electronic structure of  $\pi$ -conjugated molecules and polymers, also can be applied successfully to describe the physics of other  $\pi$ -electron systems such as graphene nanostructures, as also the curved systems such as fullerenes and carbon nanotubes, for which the  $\sigma$ – $\pi$  separation is no longer valid. In the future we aim to extend our PPP model-based preliminary calculations on fullerene C<sub>60</sub>, and graphene nanodisks, by performing higher-level CI calculations employing approaches such as the MRSDCI method to study their optical properties and low-lying excited states. For the case of 1D periodic systems such as GNRs and CNTs, we intend to include the influence of electron correlation effects on their band structure. Furthermore, we also plan to incorporate the excitonic effects in the optical absorption spectra of these systems. It will also be of interest to extend this PPP-model-based approach to study multi-wall CNTs, as well as higher-dimensional systems such as graphene, and graphite. The work along these directions is currently under way in our group, and the results will be presented in future publications.

**Acknowledgements** We thank the Department of Science and Technology (DST), Government of India, for providing financial support for this work under Grant No. SR/S2/CMP-13/2006. K. G. is grateful to Dr. S. V. G. Menon for his continued support of this work.

## References

- Ajje H, Alvarez MM, Anz SJ, Beck RD, Diedrich F, Fostiropoulos K, Huffman DR, Krätschmer W, Rubin Y, Shriver KE, Sensharma D, Whetten RL (1990) *J Phys Chem* 94:8630
- André JM, Vercauteren DP, Bodart VP, Fripiat JG (1984) *J Comp Chem* 5:535
- Barford W (2005) *Electronic and optical properties of conjugated polymers*. Clarendon Press, Oxford
- Barieswyl D, Campbell DK, Mazumdar S (1992) In: Keiss H (ed) *Conjugated conducting polymers*. Springer-Verlag, Berlin
- Barone V, Hod O, Scuseria GE (2006). *Nano Letts* 6:2748
- Bursill RJ, Barford W (2009) *J Chem Phys* 130:234302
- Castro EV, Novoselov KS, Morozov SV, Peres NMR, dos Santos JMBL, Nilsson J, Guinea F, Castro AH (2007) *Phys Rev Lett* 99:216802
- Chandross M, Mazumdar S (1997) *Phys Rev B* 55:1497
- Dresselhaus MS, Dresselhaus G, Avouris P (2001) *Carbon nanotubes: synthesis, structure, properties, and applications*, Vol 80. Topics in applied physics. Springer, Berlin
- Ezawa M (2006) *Phys Rev B* 73:045432
- Ezawa M (2008) *Physica E* 40:1421
- Fernández-Rossier J, Palacios JJ (2007) *Phys Rev Lett* 99:177204
- Gasyňa Z, Schatz PN, Hare JP, Dennis TJ, Kroto HW, Taylor R, Walton DRM (1991) *Chem Phys Lett* 183:283
- Güçlü AD, Potasz P, Voznyy O, Korkusinski M, Hawrylak P (2009) *Phys Rev Lett* 103:246805
- Geim AK, Novoselov KS (2007) *Nat Mat* 6:183
- Ghosh H, Shukla A, Mazumdar S (2000) *Phys Rev B* 62:12763

- Greer JC (2000) *Chem Phys Lett* 326:1567
- Gundra K, Shukla A (2011a) *Phys Rev B* 83:075413
- Gundra K, Shukla A (2011b) *Phys Rev B* 84:075442
- Gundra K, Shukla A (2012) *Comp Phys Comm* 183:677
- Han MY, Ozyilmaz B, Zhang YB, Kim P (2007) *Phys Rev Lett* 98:206805
- Harigaya K, Abe S (1994) *Phys Rev B* 49:16746
- Hod O, Barone V, Scuseria GE (2008) *Phys Rev B* 77:035411
- Iijima S (1991) *Nature* 354:56
- Jug K (1990) *Int J Quant Chem* 37:403
- Jung J, MacDonald AH (2009) *Phys Rev B* 79:235433
- Kan EJ, Li Z, Yang J, Hou JG (2007) *Appl Phys Lett* 91:243116
- Kertesz M (1982) *Adv Quant Chem* 15:161
- Kim J, Su WP (1994) *Phys Rev B* 50:8832
- Kinza M, Orloff J, Honerkamp C (2010) *Phys Rev B* 82:155430
- Kroto HW, Heath JR, O'Brien SC, Curl RF, Smalley RE (1985) *Nature* 318:162
- László L, Udvardi L (1987) *Chem Phys Lett* 136:418
- László L, Udvardi L (1989) *J Mol Struct (Theochem)* 183:271
- Leach S, Vervloet M, Després A, Bréheret E, Hare JP, Dennis TJ, Kroto HW, Taylor R, Walton DRM (1992) *Chem Phys* 160:451
- Lee M, Song OK, Seo JC, Kim D, Suh YD, Jin SM, Kim SK (1992) *Chem Phys Lett* 196:325
- Lies M, Jeglinski S, Vardeny ZV, Ozaki M, Yoshino K, Ding Y, Barton T (1997) *Phys Rev B* 56:15712
- Fujita M, Wakabayashi K, Nakada K, Kusakabe K (1996) *J Phys Soc Jpn* 65:1920
- Malliaras G, Friend R (2005) *Phys Today* 58:53
- Mataga N, Nishimoto K (1957) *Z Physik Chemie* 12:140
- Nakada K, Fujita M, Dresselhaus G, Dresselhaus MS (1996) *Phys Rev B* 54:17954
- Neto AHC, Guinea F, Peres NMR, Novoselov K, Geim AK (2009) *Rev Mod Phys* 81:109
- Novoselov KS, Geim AK, Morozov SV, Jiang D, Zhang Y, Dubonos SV, Grigorieva IV, Firsov AA (2004) *Science* 306:666
- Ohno K (1964) *Theor Chim Acta* 2:219
- Palacios JJ, Rossier JF, Brey L, Fertig HA (2010) *Semicond Sci Tech* 25:033003
- Pariser R, Parr RG (1953) *Trans Faraday Soc* 49:1275
- Parr RG (1952) *J Chem Phys* 20:239
- Pisani C, Dovesi R (1980) *Int J Quant Chem* 17:501
- Prezzi D, Varsano D, Ruini A, Marini A, Molinari E (2008) *Phys Rev B* 77:041404
- Psiachos D, Mazumdar S (2009) *Phys Rev B* 79:155106
- Raghu C, Pati YA, Ramasesha S (2002) *Phys Rev B* 66:035116
- Ren SL, Wang Y, Rao AM, McRae E, Holden JM, Hager T, Wang K, Lee WT, Ni HF, Selegue J, Eklund P (1991) *Appl Phys Lett* 59:2678
- Ridder KA, Lyding JW (2009) *Nat Mat* 8:235
- Ruiz A, Bretón J, Liorente JMG (2001) *J Chem Phys* 114:1272
- Ruiz A, Hernández-Rojas J, Bretón J, Liorente JMG (1998) *J Chem Phys* 109:3573
- Salem L (1966) *The molecular orbital theory of conjugated systems*. W. A. Benjamin, Inc., New York
- Schulten K, Ohmine I, Karplus M (1975) *J Chem Phys* 64:4422
- Schumacher S (2011) *Phys Rev B* 83:081417(R)
- Shukla A (2002) *Phys Rev B* 65:125204
- Shukla A (2004a) *Chem Phys* 300:177
- Shukla A (2004b) *Phys Rev B* 69:165218
- Shukla A, Dolg M, Stoll H (1998) *Phys Rev B* 58:4325
- Shukla A, Dolg M, Stoll H, Fulde P (1996) *Chem Phys Lett* 262:213
- Shukla A, Dolg M, Stoll H, Fulde P (1999) *Phys Rev B* 60:5211
- Shukla A, Ghosh H, Mazumdar S (2001) *Synth Met* 116:87
- Shukla A, Ghosh H, Mazumdar S (2003) *Phys Rev B* 67:245203



- Shukla A, Ghosh H, Mazumdar S (2004) Synth Met 141:59  
Shukla A, Mazumdar S (1999) Phys Rev Lett 83:3944  
Son YW, Cohen ML, Louie SG (2006a) Phys Rev Lett 97:216803  
Son YW, Cohen ML, Louie SG (2006b) Nature 444:347  
Sony P, Shukla A (2005a) Phys Rev B 71:165204  
Sony P, Shukla A (2005b) Synth Met 155:368  
Sony P, Shukla A (2005c) Synth Met 155:316  
Sony P, Shukla A (2007) Phys Rev B 75:155208  
Sony P, Shukla A (2009) J Chem Phys 131:014302  
Sony P, Shukla A (2010) Comp Phys Comm 181:821  
Soos ZG, Ramasesha S, Galvao DS (1993) Phys Rev Lett 71:1609  
Voronov GS (2007) Phys Rev Lett 99:177204  
Andreoni W (2000) Physics of fullerene-based and fullerene-related materials. Kluwer Academic, Dordrecht  
Wang WL, Meng S, Kaxiras E (2008) Nano Lett 8:241  
Wang WL, Yazyev OV, Meng S, Kaxiras E (2009) Phys Rev Lett 101:157201  
Wang Z, Zhao H, Mazumdar S (2006) Phys Rev B 74:195406  
Wang Z, Zhao H, Mazumdar S (2007) Phys Rev B 76:115431  
Yamashiro A, Shimoi Y, Harigaya K, Wakabayashi K (2003) Phys Rev B 68:193410  
Yang L, Cohen ML, Louie SG (2007a) Nano Lett 7:3112  
Yang L, Cohen ML, Louie SG (2008) Phys Rev Lett 101:186401  
Yang L, Park CH, Son YW, Cohen ML, Louie SG (2007b) Phys Rev Lett 99:86801  
Yazyev O (2010) Rep Prog Phys 73:056501  
Yazyev OV (2008) Phys Rev Lett 101:037203  
Ye A, Shuai Z, Bredas JL (2003) Phys Rev B 65:045208  
Zhao H, Mazumdar S (2004) Phys Rev Lett 93:157402  
Zhao H, Mazumdar S (2007) Phys Rev Lett 98:166805  
Zhao H, Mazumdar S, Sheng CX, Tong M, Vardeny ZV (2006) Phys Rev B 73:075403

# Chapter 7

## Topological Invariants of Möbius-Like Graphenic Nanostructures

Mihai V. Putz, Marzio De Corato, Giorgio Benedek, Jelena Sedlar, Ante Graovac<sup>†</sup>, and Ottorino Ori

**Abstract** Topological invariants are computed for some carbon zigzag nanoribbons in the limit of infinite carbon atoms  $N$  by applying standard and Möbius-like periodicity. Topological modeling considerations allow then to assign to the half-twisted molecules a certain grade of chemical stability based on the actions of

---

<sup>†</sup>Dedicated to Professor Ante Graovac, coauthor of this chapter, who prematurely passed away soon after the manuscript was completed.

M.V. Putz (✉)

Laboratory of Computational and Structural Physical Chemistry, Biology-Chemistry Department, West University of Timișoara, Pestalozzi Street No.16, Timișoara RO-300115, Romania  
e-mail: [mv\\_putz@yahoo.com](mailto:mv_putz@yahoo.com)

M. De Corato

Dipartimento di Scienza dei Materiali, Università di Milano-Bicocca, Via R. Cozzi 53, 20125 Milan, Italy

Centro S3, CNR-Istituto Nanoscienze, I-41125 Modena, Italy

Dipartimento di Fisica, Università di Modena e Reggio Emilia, I-41125 Modena, Italy  
e-mail: [m.decorato@campus.unimib.it](mailto:m.decorato@campus.unimib.it); [marzio.decorato@unimore.it](mailto:marzio.decorato@unimore.it)

G. Benedek

Dipartimento di Scienza dei Materiali, Università di Milano-Bicocca, Via R. Cozzi 53, 20125 Milan, Italy

Donostia International Physics Center (DIPC), Paseo M. de Lardizábal 4, 20018 Donostia/San Sebastián, Spain

e-mail: [giorgio.benedek@mater.unimib.it](mailto:giorgio.benedek@mater.unimib.it); [giorgio.benedek@unimib.it](mailto:giorgio.benedek@unimib.it)

J. Sedlar

Faculty of Civil Engineering, Architecture and Geodesy, University of Split, Matice hrvatske 15, HR-21000 Split, Croatia

e-mail: [jsedlar@gradst.hr](mailto:jsedlar@gradst.hr)

O. Ori (✉)

Actinium Chemical Research, Via Casilina 1626/A, 00133 Rome, Italy  
e-mail: [ottorino.ori@gmail.com](mailto:ottorino.ori@gmail.com)

two basic topological properties, compactness and efficiency, which represent the influence that long-range connectivity has on lattice stability. Conclusions about Möbius-nanoribbon topological dimensionality are also presented.

## 7.1 Introduction

Since its discovery made in 1858 by August Ferdinand Möbius (1858) and, almost simultaneously, by Johann Listing, the *chiral* structure of the Möbius strip attracts the continuous attentions of mathematicians, scientists, architects, and artists (Gardner 1978; Pickover 2006). To produce this fascinating object, one just needs to half twist a paper rectangle before gluing the opposite edges. The resulting form, a sort of twisted belt represented in Fig. 7.1, reveals intriguing topological properties, including chirality, never encountered before. Being the number of rotations of the paper ribbon practically endless, this note deals with the normal Möbius strip produced by just one half twist. The first aspect worth of notice concerns the *edge* of the Möbius strip which, surprisingly, now consists of a single line that one follows until the tour around the structure is completed. Unlike the cylinder produced by gluing the same paper rectangle *without* making the twist, the Möbius strip has a *single edge* and also presents a *single surface*. At every lap, the landscape along this surface varies dramatically, exchanging top with bottom, clockwise with counter clockwise. The length of each lap  $L$  coincides with the length of the initial open rectangle. Because of this property, the Möbius strip is defined mathematically *non-orientable*. More information about this influential shape are provided in literature by a parade of scientific articles. In particular Möbius strip surface topology can be characterized by Hilbert *connectivity*  $k = 2$ , half-integer genus  $g = 1/2$ , or by its *Euler–Poincaré characteristic*  $\chi = 1$ . The tiling properties of a closed (contourless) Möbius ring with saturated threefold carbon atoms (e.g., the coordination implied by  $sp^2$  hybridization) require a tessellation

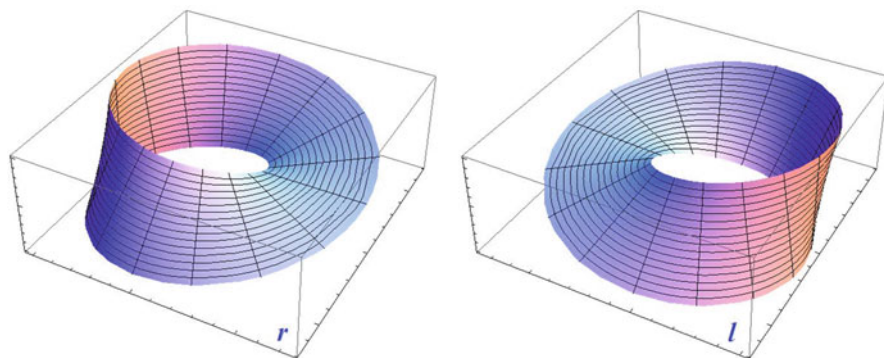


**Fig. 7.1** The Möbius one-sided surface with a single twist in its two right- ( $r$ ) and left-handed ( $l$ ) chiral forms (Reproduced from Weisstein 2012)

with only hexagons ( $f_6$ ), pentagons ( $f_5$ ), and heptagons ( $f_7$ ), where  $f_5 - f_7 = 6$  following Poincaré's formula. The reader will find a systematic description of surface polygonal tiling fundamental topological features in the extended study (Benedek et al. 2011).

Aromatic hydrocarbons with the Möbius ring topology have been predicted long ago (Heilbronner 1964) and synthesized more recently by Ajami and coworkers (2003). Further examples of Möbius rings have been assembled at the micrometric scale from ribbon-shaped NbSe<sub>3</sub> crystals (Tanda et al. 2002, 2005) under specific growth conditions. Moreover, this canonical one-sided surface has been recently reproduced (Han et al. 2010; Yang et al. 2012) by joining up DNA filaments to create Möbius structures of about 50 nm, with the final goal of developing useful biochemical devices and drug delivery mechanisms exploiting the peculiarities of such twisted nano-architecture.

In mechanical engineering the presence of a single surface makes the Möbius shape the best candidate for realizing long-lasting mechanical transmission belts.

The physical properties of the Möbius structures have been subject of intense investigations (Starostin and van der Heijden 2007) boosted by the theoretical evidence given in (Hayashi and Ebisawa 2001) that topological effects force the existence of new states in superconducting Möbius strip in a magnetic field. Important qualitative changes in the behavior of a quantum particle confined on the Möbius surface derive from the curvature of the ribbon (Gravesen and Willatzen 2005); among other effects, the twice-encircling properties of the surface produce a peculiar split of the degenerate electronic ground state of the reference cylindrical system.

On the Möbius strip, a  $4\pi$  rotation is required to guarantee the invariance of the eigenfunctions, offering a theoretical pathway for new discoveries in chemistry, physics, as well as for the design of new materials and electronic devices. Quantum properties inherently depend on geometrical and topological characteristics of the global system. Yakubo et al. (2003) evidenced measurable differences of the electronic behavior by comparing flux periodicity of persistent electronic currents in a cylinder and in a Möbius strip; in their model the presence of a moderate disorder makes experimentally observable the differences between these two systems of noninteracting electrons. Theoretical simulations of graphene-based nanoribbons *with a variable number of twists* have been intensively undertaken in the past decade. Semiempirical calculations, based on molecular geometries optimized with classical force field methods, feature common results like (1) lower symmetry than the original graphenic ribbon and (2) larger HOMO–LUMO energy due to electronic localization effects created by the twisting (Caetano et al. 2008, 2009); worth noting is that this last property directly connects with the celebrated *maximum chemical hardness  $\eta$  principle* (Parr and Chattaraj 1991; Chattaraj et al. 1995; Putz 2008) required by molecular structures stabilization, due to the conceptual density functional definition rewritten in the frozen core approximation (Koopmans 1934),  $\eta = (\varepsilon_{\text{LUMO}} - \varepsilon_{\text{HOMO}})/2$ ; see, for instance, Chap. 9 of the present monograph as well as earlier and recent references (Parr and Pearson 1983; Parr and Yang 1989; Putz 2012a, b). Twisted nanoribbons present distinct UV/visible spectra, with the

first absorption peaks in the orange–violet wavelengths domain while strong absorption is forecasted in the ultraviolet region. Authors suggest moreover the possibility that twisted nanoribbons could form stable crystals. Although molecules with Möbius geometry are not found in nature, the original theoretical prediction, made by Heilbronner in 1964, about the existence of Möbius aromaticity in  $[4n]$ annulenes in twisted conformations having the p orbitals on the surface of a Möbius strip, has stimulated so far the search for twisted aromatic (or antiaromatic) systems with  $[4n]$  (or  $[4n + 2]$ )  $\pi$ -electrons. Möbius-aromatic molecules are quite difficult to synthesize and detect; see the recent extensive summary (Yoon et al. 2009) reporting the generation of Möbius topologies in porphyrinic systems as the first example of molecules with distinct Möbius aromaticity. Knot-shaped molecules have been also synthesized, producing fantastic chiral molecules having the topology of *trefoil* and *pentafoil knot* – see the recent paper from Ayme et al. (2012) and related literature.

At a molecular level, remarkable improvements in the theoretical description of belt-shaped carbon allotropes have been recently provided in Estrada and Simón-Manso (2012). Authors start from octadehydro[12]annulene building blocks to produce belt structure of both types, for example, Hückel-like (or cylindrical) and Möbius-like molecules, and they baptize *Escherynes* this new class of *all-carbon* molecules in homage to the influential Dutchman artist. The stability of Möbius-like Escherynes prevails when the size of the system reaches the threshold of 60 carbon atoms or more according with the results of ab initio DFT calculations reported in Estrada and Simón-Manso (2012). Those studies moreover predict for Möbius belts an important optical activity, a topic for future experimental works.

Theoretical investigations about electronic and magnetic properties of graphenic ribbons with *zigzag edges* (see, for instance, Figs. 7.2 and 7.4) under the periodic or Möbius boundary conditions evidence that the application of the twist induces the formation of magnetic subdomains replacing the ferrimagnetic states of the original nanoribbons, whose extension depends on the Coulomb interaction and spin coupling (Wakabayashi and Harigaya 2003). The growth of magnetic regions in the lattice is a “somewhat intuitive” consequence of Möbius boundary condition that, by connecting the similar sublattices on both sides of the cylindrical carbon nanoribbons, induces magnetic frustration in the ferrimagnetic alignments. The unusual topological features of graphene Möbius strip have been enriched by the theoretical study of Guo et al. (2009) who have predicted that such a carbon nanostructure, again in the zigzag edge configuration, behaves like topological insulator, whereas that is not the case for armchair nanoribbons. A *topological insulator* is an electronic system characterized by an insulating bulk and a metallic surface, and its conductive edge states are stable under perturbations. Due to its nontrivial topology, the zigzag Möbius strip possesses such a robust metallic surface.

In this work we investigate some details of the topological character of zigzag Möbius carbon nanoribbons, considered in the following like pure *chemical graphs* with a carbon skeleton, by computing distance-based topological invariants in the limit of infinite lattices, for example, with the number of carbon atoms  $N \rightarrow \infty$ . An introduction to the formalisms is provided in the next paragraph.

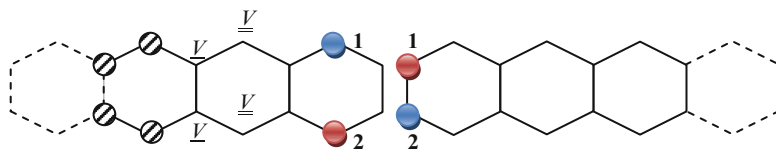


**Fig. 7.2** Cyclacene zigzag belts are obtained by closing the molecule connecting the atoms with the same labels (Hückel-type) or with the same colors (Möbius-type). In both cases, the minimal vertices  $\underline{V}$  correspond to the 3-connected ones.  $\underline{V}$  nodes produce the maximum contribution  $w_i$  to  $W$ . Translational unit cell is made by four shaded atoms. The two opposite dotted hexagons coincide; thus the represented molecules include seven unit cells,  $N = 28$  atoms and  $B = 35$  bonds

## 7.2 Graph Invariants

According with the topological modeling formalism, the *distance*  $d_{ij}$  between two nodes  $i$  and  $j$  is in effect *the chemical distance* corresponding to the number of bonds connecting the two atoms following the *shortest path* in the graph; clearly when  $d_{ij} = k$ , atom  $j$  lies in the  $k$ th coordination shell of atom  $i$  and vice versa. Indicating with  $M$  the length of the longest path of the graph (integer  $M$  corresponds to the graph *diameter*) and with  $b_{ik}$  the number of  $k$ -neighbors of atom  $i$ , the effect of lattice long-range topology on node  $i$  is summarized by the topological invariant  $w_i$ :

$$w_i = \frac{1}{2} \sum_k k b_{ik} \quad k = 1, 2, \dots, M-1, M \quad (7.1)$$

where  $N-1 = \sum_k b_{ik}$  and  $b_{i1} = 3$  for any fullerene or infinite graphene node  $i$ . Symbol  $\underline{w}$  indicates the smallest among  $w_i$ . Nodes featuring  $w_i = \underline{w}$  are the so-called minimal vertices  $\underline{V}$  of the graph. Set  $\{b_{ik}\}$  identifies the Wiener-weights (WW) of vertex  $i$ . Wiener index  $W$ , the oldest among the molecular invariants (Todeschini and Consonni 2000), is the semisum of the chemical distances  $d_{ij}$  of the graph with  $N$  nodes:

$$W(N) = \frac{1}{2} \sum_{ij} d_{ij} = \sum_i w_i \quad i, j = 1, 2, \dots, N-1, N \quad (7.2)$$

It measures the overall compactness of the chemical structure.

The first basic approximation of *topological modeling* methods is (Ori et al. 2009):

*Higher chemical stability is assigned to atoms with lower  $w_i$ .*

The averaged *topological efficiency index*

$$\rho = \frac{W}{N\underline{w}} \quad \text{being } \rho \geq 1 \quad (7.3)$$

measures the efficiency of the lattice to self-arrange around the minimal nodes, the most efficient nodes in preserving graph compactness. Index (7.3) works quite well in selecting chemical stable fullerene isomers (Vukicevic et al. 2011) and plays a role in the graphenic nanocone growth (Cataldo et al. 2010). It also ranks *topological sphericity* of a given chemical structures, examples of *topologically spherical graphs* with  $\rho = 1$  being  $C_{60}(I_h)$  fullerene, infinite lattices of graphene, cubic lattices, and sodalite, a type of zeolite.

The second basic approximation of the topological modeling is then:

*Higher chemical stability is assigned to structures with low  $\rho$ .*

Both approximations hold when similar structures are compared. However, much caution has to be paid with index (7.3), since, usually sphericity reaches its maximum for more stable and favorite structures when the minimum potential condition is realized; this should be the case with definition (7.3) through involving inverse of  $\min\{w\}$ ; yet the competition between  $w^{-1}$  and  $W$  minimum optimization will lead to a  $\{\max\} \times \{\min\}$  pairs that should arrange the favorite structures in local optimal configurations (Ori and Putz 2013).

Following the recent study of Xing et al. (2011) on the influence of molecular symmetry on [18]-cyclacene molecular orbitals, the first application of our computational methods considers infinite cyclacene molecules with Hückel-type and Möbius-type closure. Figure 7.2 shows the translational building unit of such a cyclacene system consisting in the four shaded nodes and the two possible ways of imposing periodic conditions, Hückel (by connecting the atoms with the same label) and Möbius (by connecting the atoms with identical color red and blue). Opposite dotted hexagons coincide; thus, for example, the circular molecule represented in Fig. 7.2 is made by 7 building units, for a grand total of  $N = 28$  carbon atoms and  $B = 35$  chemical bonds.

The topological indices for Hückel-type cyclacenes are given in Table 7.1. The minimal vertices  $\underline{V}$  of this set of molecules, for example, the nodes embedded in the graph in the most compact way, coincide with the internal 3-connected (triangular) nodes; their  $w_i$  values are listed in column  $\underline{w}$ . As expected (Cataldo et al. 2010), also in this case the topological distance-based invariants respect typical polynomial laws *depending from the dimensionality  $d$  of the system*. The growth of the Wiener index, for example, follows in fact the  $W \approx N^s$  power law where the leading exponent  $s$  only depends from system dimensionality being  $s = 2 + 1/d$ . This formula for  $s$  unveils the presence of deep, mutual influence between the long-range connectivity properties of a system and its dimensionality presented in paper (Ori et al. 2010) with some more details.

Present simulations are performed on molecular systems with dimensionality  $d = 1$ , and therefore these elegant relationships for Hückel-type cyclacenes are easily computable:

$$W(N) = N^3/16 + N^2/4 + N/2 \quad (7.4a)$$

$$\underline{w} = N^2/16 + N/4 \quad (7.4b)$$

**Table 7.1** Graph invariants for cyclacene zigzag belts with  $N$  atoms and  $B$  bonds

Cyclacene		Hückel-type				Möbius-type			
$N$	$B$	$M$	$W$	$\underline{w}$	$\rho$	$M$	$W$	$\underline{w}$	$\rho$
8	10	3	52	6	1.08333	3	48	5.5	1.09091
12	15	4	150	12	1.04167	3	144	11.5	1.04348
16	20	5	328	20	1.025	4	320	19.5	1.02564
20	25	6	610	30	1.01667	5	600	29.5	1.01695
24	30	7	1,020	42	1.01190	6	1,008	41.5	1.01205
28	35	8	1,582	56	1.00893	7	1,568	55.5	1.00901
32	40	9	2,320	72	1.00694	8	2,304	71.5	1.00699
72	90	19	24,660	342	1.00146	18	24,624	341.5	1.00146
1,000	1,250	251	62,750,500	62,750	1.00000797	251	62,750,000	62,749.5	1.00000797

$M, W, \underline{w}, \rho$  are, respectively, the graph diameter, the Wiener index, the lowest  $w_i$  values, the topological efficiency index and are separately listed for Hückel-type and Möbius-type systems

The limit condition on  $\rho$  immediately comes from definition (7.3) and formulae (7.1, 7.2):

$$\rho \rightarrow 1 \quad \text{for } N \rightarrow \infty \tag{7.4c}$$

Other polynomial laws for Hückel-type cyclacene are  $M(N) = N/4 + 1$  and  $B(N) = 5N/4$  or  $B(N) = 5(M - 1)$ . Previous indices (7.4) slowly converge to their asymptotic values, as shown by the data computed for the closed molecule made by 250 unit cells and  $N = 1,000$  atoms; see the last row of Table 7.1. For completeness, cyclacene *open* molecules have the  $W^O \approx N^3/12$  leading term instead of the corresponding term  $W^C \approx N^3/16$  given in Eq. (7.4a) for the *closed* structure. This result confirms the Wiener polynomial form early introduced by Bonchev and Mekenyan (1980); it also allows to verify, once more, the general rule for the *compression factor*  $\alpha = W^C/W^O$  which, for any monodimensional lattice, assumes the *universal* value  $\alpha = 3/4$  (Cataldo et al. 2010). More features about this intriguing topological quantity may be found in the recent investigation by Sedlar et al. (2013).

For Hückel-type cyclacenes, the WW strings divide the nodes in two classes, the central minimal vertices  $\underline{V}$  and the maximal ones  $\overline{V}$  placed on the edge (Fig. 7.2). The firsts show WW strings with a specific composition depending from  $M$ :  $b_1 = 3; b_k = 4$  for  $k = 2, 3, \dots, M - 3, M - 2; b_{M-1} = 3; b_M = 1$ . The remaining edge-nodes  $\overline{V}$  of the molecule have  $b_1 = 2; b_2 = 4; b_3 = 5; b_k = 4$  for  $k = 4, 5, \dots, M - 3, M - 2; b_{M-1} = 3; b_M = 1$ . For example, for  $N = 72, M = 19$  and we have therefore

$$\{b_{\underline{V}_k}\} = \{3 \ 4 \ 4 \ 4 \ 4 \ 4 \ 4 \ 4 \ 4 \ 4 \ 4 \ 4 \ 4 \ 4 \ 4 \ 4 \ 4 \ 3 \ 1\} \quad \text{and}$$

$$\{b_{\overline{V}_k}\} = \{2 \ 4 \ 5 \ 4 \ 4 \ 4 \ 4 \ 4 \ 4 \ 4 \ 4 \ 4 \ 4 \ 4 \ 4 \ 4 \ 4 \ 3 \ 1\}$$

for  $\underline{V}$  and  $\overline{V}$ , respectively. In Hückel-type cyclacenes, the general identity  $\overline{w} = \underline{w} + 1$ , valid for each molecular size  $N$ , connects the contribution to the Wiener index arising from minimal and maximal atoms.



Table 7.1 also lists the topological indices for the Möbius belts pictured in Fig. 7.2 which one realizes by joining the boundary nodes with the same colors. Our calculations points out that the topological invariants that characterize Möbius-type cyclacenes have polynomial rules very close to the forms (7.4), previously derived for the untwisted cases:

$$W(N) = N^3/16 + N^2/4 \quad (7.5a)$$

$$\underline{w} = N^2/16 + N/4 - 1/2 \quad (7.5b)$$

Again, for  $N \rightarrow \infty$  we have  $\rho \rightarrow 1$ . Exponent 3 in the leading term of Wiener index (7.5a) evidences first of all that also Möbius-type cyclacenes have, from the topological point of view, *the same dimensionality  $d = 1$  of the Hückel-type ones*.

On the other hand, Table 7.1 introduces also significant differences between the two types of cyclacenes belts. For a fixed number  $N$  of carbon atoms, Table 7.1 shows that the graph diameter  $M$  of the Möbius-type cyclacenes *is shorter* (for  $N \geq 12$ ), being  $M(N) = N/4$ . Möbius structures are therefore topologically *more compact* than their isomeric Hückel counterparts. The higher compactness of Möbius-type cyclacenes is confirmed by the calculated trends of  $W$  and  $\underline{w}$  invariants.

The topological characterization of cyclacenes systems allows concluding that:

*The tendency to produce compact structures confers to Möbius-type cyclacenes a certain theoretical stability and possibility to be synthesized.*

Further insights about cyclacenes stability derive from the study of the evolution of the topological efficiency  $\rho$  computed, in both cases, by expanding the molecular size  $N$ . Figure 7.3 illustrates such a competition between  $\rho^H$  and  $\rho^M$  as a function of the number of atoms  $N$ , and it is interesting noticing that Möbius-type cyclacenes reach the same topological efficiency typical of the Hückel structures after a certain threshold size  $n_0$  is reached. Our approximated topological simulations fix that threshold in the region  $n_0 \approx 16$  atoms, corresponding to a Möbius-cyclacenes made of four cells, as reported in Fig. 7.3.

On the basis of these results we also predict that:

*The topological stability of the Möbius-type cyclacenes increases with the size of the molecule.*

We end this introductive topological characterization of cyclacenes by analyzing the structure of the atomic coordination shells in the infinite limit. Like in the Hückel-type cyclacenes, atoms of a Möbius-cyclacenes are split again in two classes, namely, the minimal  $\underline{V}$  and maximal  $\overline{V}$  vertices placed as shown in Fig. 7.2 with  $\underline{w} = \overline{w} + 1$  for both lattices. Depending on  $M$ , minimal nodes present WW strings with a peculiar composition:  $b_1 = 3$ ;  $b_k = 4$  for  $k = 2, 3, \dots, M - 1, M$ . Molecular edge-nodes  $\underline{V}$  have instead  $b_1 = 2$ ;  $b_2 = 4$ ;  $b_3 = 5$ ;  $b_k = 4$  for  $k = 4, 5, \dots, M - 1, M$ . We already know that  $M$  goes in the infinite lattice limit as  $N/4$ , thus Möbius-cyclacenes with  $N = 72$  nodes have, for example,  $M = 18$  and

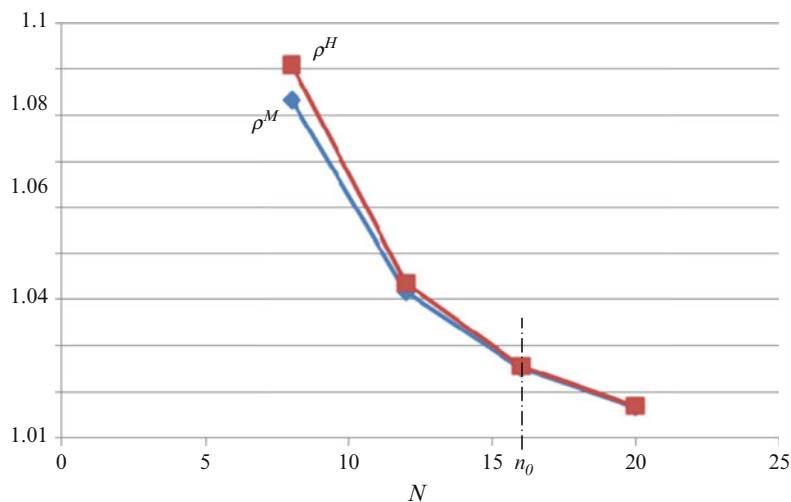


**Fig. 7.3** Cyclacene zigzag belts compete in terms of topological efficiency:  $\rho^H$  and  $\rho^M$  are plotted in function of the number of atoms  $N$  showing that Hückel-type molecules are better organized till a certain threshold size of  $n_0 \approx 16$  atoms is reached. Möbius-like and Hückel-like cyclacenes with a number of  $N$  atoms larger than  $n_0$  have a comparable topological stability

$$\{b_{\underline{V}_k}\} = \{3\ 4\ 4\ 4\ 4\ 4\ 4\ 4\ 4\ 4\ 4\ 4\ 4\ 4\ 4\ 4\ 4\ 4\} \quad \text{and}$$

$$\{b_{\underline{\underline{V}}_k}\} = \{2\ 4\ 5\ 4\ 4\ 4\ 4\ 4\ 4\ 4\ 4\ 4\ 4\ 4\ 4\ 4\ 4\ 4\}$$

for  $\underline{V}$  and  $\underline{\underline{V}}$  nodes, respectively.

After the above introduction to the topological modeling algorithms and to the topological representation of chemical structures with Möbius-like periodic conditions, the next section will deal with the topological characterization of some carbon nanoribbons.

### 7.3 Topological Invariants in Möbius-Like Carbon Nanoribbons

The variety of carbon nanostructures studied in literature is very large. Here we adopt the carbon structure with zigzag edges described by Wakabayashi and Harigaya (2003) and Guo et al. (2009) having infinite length  $L$  and finite width  $Y$ . Figure 7.4 represents the considered system having  $Y = 12$  atoms in the translational unit cell (represented by shaded circles). These graphenic belts may be closed in the standard circular way to produce a cylinder  $Z^0$  or, after a half twist, to produce

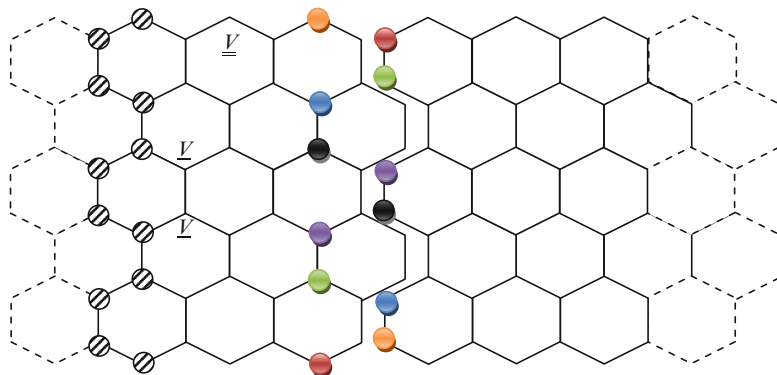


**Fig. 7.4** Closed graphenic zigzag nanoribbons are obtained by imposing cylindrical standard periodic conditions or by connecting the atoms with the same colors (Möbius-type). Translational unit cell is made by  $Y = 12$  shaded atoms. The opposite dotted hexagons coincide; thus, the represented molecules include 7 unit cells,  $N = 84$  atoms and  $B = 119$  bonds

a Möbius-like nanoribbons  $Z^Y$  with  $N$  atoms. The application of the half twist is algorithmically achieved by connecting “upside-down” the three pairs of bridging atoms represented in Fig. 7.4 with the same colors.

The results of our computations are summarized in Table 7.2. The number of chemical bonds in both structures is equal to  $B = 17N/12$ , and also for this carbon nanostructure, Möbius boundary conditions minimize the lattice diameter, being in fact  $M(Z^Y) = M(Z^0) - 3$  for  $N \geq 108$ . The graphenic nanoribbons in Fig. 7.4 keeps, for constant  $Y$ , a *monodimensional structure* which forces therefore the topological invariants obeying the  $N^3$  polynomial relationships previously introduced for the Wiener index of cyclacenes in Eqs. (7.4) and (7.5). Present conclusions about  $d = 1$  *topological dimensionality* of Möbius-nanoribbons contradicts somehow other observations in literature stating that the two-dimensional nature of the Möbius graphene strip plays a key role in ab initio simulations of the electronic properties of this “nontrivial topological structure”; see Guo et al. (2009).

We therefore consider the monodimensional character of the Möbius-nanoribbons within the topological modeling scope, and it has to be compared with similar findings. For example, tubular fullerenes with  $N$  carbon atoms, consisting in two 6-pentagon poles connected by hexagonal nanotubes, show a similar dependence  $d = 1$  and  $s = 3$  with  $W(N) = N^3/30 + 235N^2/6 - 670$  when  $N \geq 50$ , a polynomial form which partially improves previously reported results by Graovac et al. (2011), representing an exception with respect to the larger family of fullerene  $d = 2$  hollow molecules having normally  $W \approx N^{2.5}$ .

For both nanoribbons in Fig. 7.4, the periodic infinite lattices  $Z^0$  and  $Z^Y$  present these invariants:

$$W(Z^0) = N^3/48 + 35N^2/36 + 35N/2 \quad (7.6a)$$

**Table 7.2** Graph invariants for nanoribbons  $Z^0$  and  $Z^1$  with  $Y = 12$  belts with  $N$  atoms and  $B$  bonds

Nanoribbon		$Y = 12$ Cylindrical $Z^0$				$Y = 12$ Möbius-type $Z^1$			
$N$	$B$	$M$	$W$	$\underline{w}$	$\rho$	$M$	$W$	$\underline{w}$	$\rho$
24	34	11 <sup>a</sup>	1,188 <sup>a</sup>	38	1.30263	6 <sup>a</sup>	844 <sup>a</sup>	31.5	1.11640
36	51	11 <sup>a</sup>	2,826 <sup>a</sup>	62	1.26613	7 <sup>a</sup>	2,349 <sup>a</sup>	60.5	1.07851
48	68	11 <sup>a</sup>	5,376 <sup>a</sup>	92	1.21739	8 <sup>a</sup>	4,872 <sup>a</sup>	90.5	1.12155
60	85	11 <sup>a</sup>	9,050	128	1.17839	10 <sup>a</sup>	8,575 <sup>a</sup>	126.5	1.12978
72	102	11	14,076	170	1.15000	11 <sup>a</sup>	13,620 <sup>a</sup>	168.5	1.12265
84	119	12	20,678	218	1.12920	11 <sup>a</sup>	20,202 <sup>a</sup>	216.5	1.11085
96	136	13	29,072	272	1.11336	11 <sup>a</sup>	28,544	270.5	1.09920
108	153	14	39,474	332	1.10090	11	38,880	330.5	1.08926
120	170	15	52,100	398	1.09087	12	51,440	396.5	1.08113
132	187	16	67,166	470	1.08262	13	66,440	468.5	1.07435
144	204	17	84,888	548	1.07573	14	84,096	546.5	1.06862
156	221	18	105,482	632	1.06988	15	104,624	630.5	1.06371
168	238	19	129,164	722	1.06487	16	128,240	720.5	1.05945
180	255	20	156,150	818	1.06051	17	155,160	816.5	1.05573

$M, W, \underline{w}, \rho$  are, respectively, the graph diameter, the Wiener index, the lowest  $w_i$  values, the topological efficiency index and are separately listed for cylindrical and Möbius-type systems

<sup>a</sup>Values outside the convergence range of Eqs. (7.6) and (7.7)

$$\underline{w}(Z^0) = N^2/48 + 3N/4 + 8 \tag{7.6b}$$

$$M(Z^0) = N/12 + 5 \tag{7.6c}$$

and

$$W(Z^1) = N^3/48 + 35N^2/36 + 12N \tag{7.7a}$$

$$\underline{w}(Z^1) = N^2/48 + 3N/4 + 13/2 \tag{7.7b}$$

$$M(Z^1) = N/12 + 2 \tag{7.7c}$$

From Eqs. (7.6) and (7.7) and  $\rho$  definition (Eq. 7.3), the asymptotic value  $\rho \rightarrow 1$  for  $N \rightarrow \infty$  also holds for both graphenic systems of Fig. 7.4.

Equations (7.6) and (7.7) show that also in this case, the presence of the half twist reduces the graph diameter  $M$  and the values of indices  $W$  and  $\underline{w}$ , increasing the compactness of the graphenic nanoribbons with periodic Möbius conditions.

The half twist moreover induces in the  $Z^1$  hexagonal mesh the remarkable effect of equalizing atomic eccentricities. With eccentricity of an atom  $i$ , one defines the maximum of the distances involving  $i$ , for example,  $e_i = \max\{d_{ij}\}$ . Clearly,

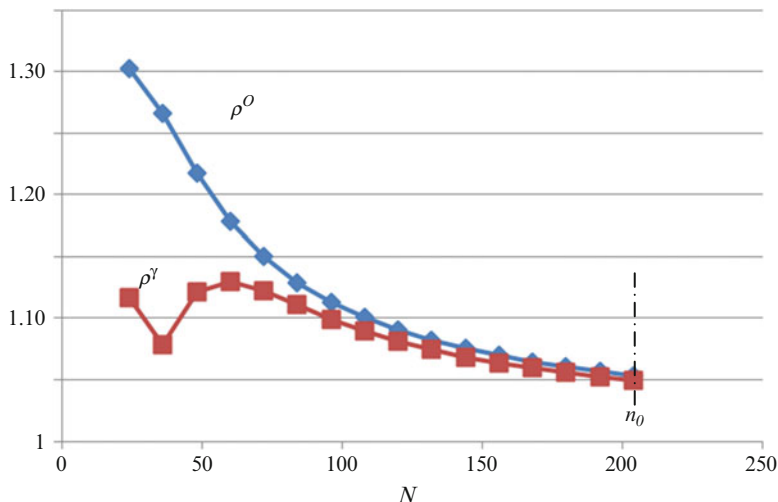


**Fig. 7.5**  $Z^O$  and  $Z^Y$  belts topological competition: topological efficiency indices  $\rho^O$  and  $\rho^Y$  vary in function of the number of atoms  $N$  privileging the Möbius-like molecules which exhibit a larger topological efficiency and sphericity. After the  $n_0 \approx 200$  limit, Möbius-like and Hückel-like nanoribbons possess a comparable topological stability

we have  $M = \max\{e_i\}$ . To understand the importance of this topological effect, we consider first the cylindrical nanoribbons  $Z^O$  which presents a nonuniform distribution of  $e_i$  values as one may easily compute. With  $N = 120$ , for example, topological eccentricity assumes  $\{e_i\} = \{13, 14, 15\}$  values, but it promptly recovers a lower and *constant* value  $e_i = 12$  when Möbius periodic conditions are in place. Thus, Möbius-twist practically induces a sort of *topological sphericalization* of the graphenic nanoribbons structure, a condition that, according to topological modeling approach, favors the stability of the  $Z^Y$  system.

The topological competition between these two types of boundary condition of the  $Y = 12$  nanostructure is illustrated in Fig. 7.5 by plotting the  $\rho$  values which, for  $N \leq n_0$ , show the prevalence of the Möbius ring  $Z^Y$  over the cylindrical nanoribbons  $Z^O$ . The threshold varies with  $Y$ , and for  $Y = 12$ , it stays in the region  $n_0 \approx 200$ .

Based on above topological simulations, the following conclusion is derived:

*Möbius-type nanoribbons stay topologically efficient at any size  $N$  of the molecule. In particular for  $N \leq n_0 \approx 200$  atoms, the Möbius ring  $Z^Y$  is topologically favored.*

Topological modeling quickly indicates therefore the critical scale  $n_0$  which characterizes the growth of the nanostructures in Fig. 7.4. This is an indubitable merit of the present approximation which arises from the polynomial nature generally shown by the distance-based topological invariants.

In the cylindrical structure  $Z^0$ , the two symmetric central nodes  $\underline{V}$  of the  $Y = 12$  unit cell, see Fig. 7.4, play the role of graph minimal vertices with the following WW string:  $b_1 = 3$ ;  $b_k = 3k$  for  $k = 2, 3, 4, 5$ ;  $b_6 = 14$ ;  $b_k = 13$  for  $k = 7, 8, \dots, M - 6$ ;  $b_{M-5} = 11$ ;  $b_{M-4} = 8$ ;  $b_{M-3} = 4$ ;  $b_{M-2} = 1$ . Also the Möbius-nanoribbons  $Z'$  admit the same minimal vertices  $\underline{V}$  and the related WW set is  $b_1 = 3$ ;  $b_k = 3k$  for  $k = 2, 3, 4, 5$ ;  $b_6 = 14$ ;  $b_k = 12$  for  $k = 7, 8, \dots, M - 2$ ;  $b_{M-1} = 8$ ;  $b_M = 4$ . The difference in the contributions to the molecular Wiener index coming from the minimal vertices of the two lattices assumes the constant value  $w(Z^0) - w(Z') = 3/2$  for  $N \geq 36$ ; see Table 7.2. In both cases, edge-nodes  $\underline{V}$  behave again as maximal nodes; see Fig. 7.4.

## 7.4 Conclusions and Perspectives

Topological modeling methods applied in this work on topologically nontrivial structures maintain its ability to describe suitable growing mechanism for graphenic nanostructure made by a network of hexagons. In particular some topological invariants have been computed for the first time for a certain class of graphenic nanoribbons  $Z^0$  and  $Z'$  with normal and Möbius-like closing conditions, respectively. The polynomial behavior of the Wiener index in the limit of large  $N$  is consistent with the  $d = 1$  topological dimensionality of such a class of chemical structures.

The Wiener index evidences the tendency of the nanostructure to form compact structures when Möbius-type periodicity is imposed, providing in such a way a certain grade of chemical stability to the Möbius-nanoribbons, especially for lattices having the size  $N$  under the typical scale  $n_0$ , a parameter which topologically drives the system growth. Moreover, a nontrivial *sphericalization* effect derives from the long-range connectivity properties of the twisted molecules, and it appears able to influence the formation mechanisms of these structures. Future investigations are needed in order to correlate the *sphericalization* mechanism with the chemical-physical properties of the Möbius-like nanostructures.

Present findings may be further extended by a quantum mechanical perspective. This can be done, for instance, while noticing that, under Slater–Clementi valence atomic density (Slater 1930; Clementi and Raimondi 1963; Clementi et al. 1967), the valence atomic radii follow the Parr–Bartolotti–Putz relationship (Parr and Bartolotti 1982; Putz 2012c):

$$\frac{r}{n} = \frac{16}{21 - 5N_{\text{bonding}}} \quad (7.8)$$

which would lead to *negative radii over the  $N_{\text{bonding}} \geq 21/5$  threshold*, fixing in fact the  $N_{\text{bonding}} = 4$  limit that is consistent with the maximum bond order met in Nature, being this threshold connected with golden ratio by the golden-spiral optimization of bond order (Boeyens and Levendis 2012).

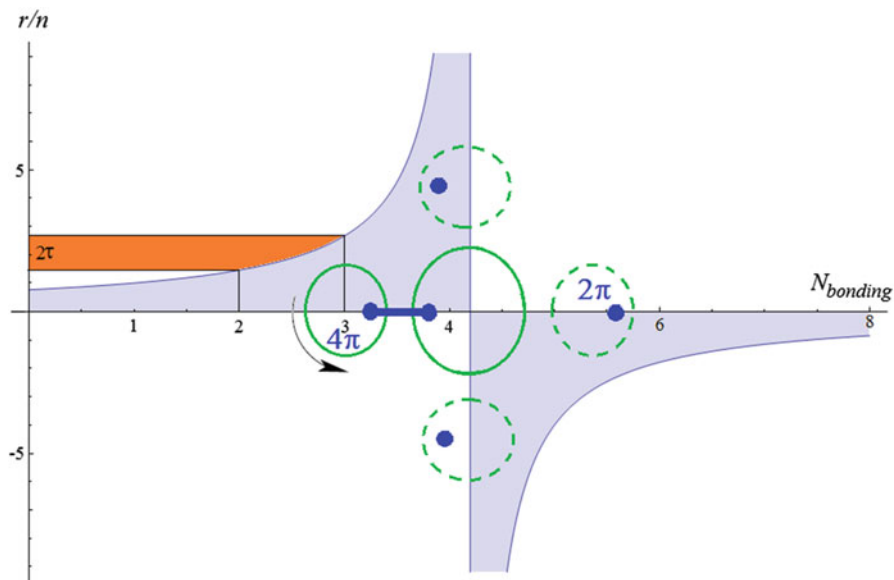


**Fig. 7.6** The  $4\pi$  folded symmetry of chemical bonding superimposed on the valence normalized atomic radii involved in covalent binding dependency by the bonding electrons. The  $4\pi$  folded symmetry of chemical bonding superimposed on the valence normalized atomic radii involved in covalent binding dependency by the bonding electrons (Reproduced from Putz (2012c). Copyright (2012) Putz; licensee Chemistry Central Ltd.)

The Möbius  $4\pi$  symmetry, connected to the concave-to-convex radius variation through the twist, may relate with golden ratio ( $\tau$ ) found to drive the Pauli principle in chemical bonding through the second to the third binding electron involved in the chemical bond,  $(r/n)_{N_{\text{bonding}}=3} - (r/n)_{N_{\text{bonding}}=2} \cong 2\tau$  (see Fig. 7.6 inset (Putz 2012c) and Chap. 4 of the present monograph).

Nevertheless, such a “spinning” also reminds the graviton symmetry (Hawking 2001) – the highest spherical symmetry in Nature, with spin equals 2 – and justifies the recent treatments of chemical bonding by means of the quasi-particles known as bondons (Putz 2010; Putz and Ori 2012) and may lead to important implications about the electronic behavior in extended systems like the present carbon nanoribbons.

**Acknowledgement** MVP thanks the Romanian Ministry of Education and Research for support through the CNCS-UEFISCDI project Code TE-16/2010-2013.

## References

- Ajami D, Oeckler O, Simon A, Herges R (2003) Nature 426:819  
 Ayme J-F, Beves JE, Leigh DA, McBurney RT, Rissanen K, Schultz D (2012) Nat Chem 4:15.  
 doi:10.1038/nchem.1193

- Benedek G, Bernasconi M, Cinquanta E, D'Alessio L, De Corato M (2011) In: Cataldo F, Graovac A, Ori O (eds) *The mathematics and topology of fullerenes. Carbon materials: chemistry and physics 4*. Springer, Dordrecht, p 217. doi:[10.1007/978-94-007-0221-9\\_12](https://doi.org/10.1007/978-94-007-0221-9_12)
- Boeyens JC, Levendis DC (2012) *Int J Mol Sci* 13:9081
- Bonchev D, Mekenyan O (1980) *Z Naturforsch* 35a:739
- Caetano EWS, Freire VN, dos Santos SG, Galvao DS, Sato F (2008) *J Chem Phys* 128:164719
- Caetano EWS, Freire VN, dos Santos SG, Albuquerque EL, Galvao DS, Sato F (2009) *Langmuir* 25(8):4751
- Cataldo F, Ori O, Iglesias-Groth S (2010) *Mol Simul* 36(5):341
- Chattaraj PK, Liu GH, Parr RG (1995) *Chem Phys Lett* 237:171
- Clementi E, Raimondi DL (1963) *J Chem Phys* 38:2686
- Clementi E, Raimondi DL, Reinhardt WP (1967) *J Chem Phys* 47:1300
- Estrada E, Simón-Manso Y (2012) *Chem Phys Lett* 548:80
- Gardner M (1978) Möbius Bands. In: *Mathematical magic show: more puzzles, games, diversions, illusions and other mathematical sleight-of-mind from Scientific American*. Vintage, New York, pp 123–136, Ch. 9
- Graovac A, Ori O, Faghani M, Ashrafi AR (2011) *Iran J Math Chem* 2(1):99
- Gravesen J, Willatzen M (2005) *Phys Rev A* 72:032108
- Guo ZL, Gong ZR, Dong H, Sun CP (2009) *Phys Rev B* 80:195310
- Han D, Pal S, Liu Y, Yan H (2010) *Nat Nanotechnol* 5:712
- Hawking S (2001) *The universe in a nutshell*. Bantam Books, New York
- Hayashi M, Ebisawa H (2001) *J Phys Soc Jpn* 70:3495
- Heilbronner E (1964) *Tetrahedron Lett* 29:1923
- Koopmans T (1934) *Physica* 1:104
- Möbius AF (1858) *Werke* 2:519
- Ori O, Putz MV (2013) *Fuller Nanotub Carbon Nanostruct* 21:000
- Ori O, Cataldo F, Graovac A (2009) *Fuller Nanotub Carbon Nanostruct* 17:308
- Ori O, Cataldo F, Vukicevic D, Graovac A (2010) *Iran J Math Chem* 1(2):5
- Parr RG, Bartolotti LJ (1982) *J Am Chem Soc* 104:3801
- Parr RG, Chattaraj PK (1991) *J Am Chem Soc* 113:1854
- Parr RG, Pearson RG (1983) *J Am Chem Soc* 105:7512
- Parr RG, Yang W (1989) *Density functional theory of atoms and molecules*. Oxford University Press, New York
- Pickover CA (2006) *The Möbius strip: Dr. August Möbius's marvelous band in mathematics, games, literature, art, technology, and cosmology*. Thunder's Mouth Press, New York
- Putz MV (2008) *MATCH Commun Math Comput Chem* 60:845
- Putz MV (2010) *Int J Mol Sci* 11:4227
- Putz MV (2012a) *Quantum theory: density, condensation, and bonding*. Apple Academics/CRC Press, Toronto/Newark
- Putz MV (2012b) *Chemical orthogonal spaces. Mathematical chemical monographs, vol 14*. Faculty of Sciences, University of Kragujevac, Kragujevac
- Putz MV (2012c) *Valence atom with bohmian quantum potential: the golden ratio approach. Chem Cent J* 6:135. doi:[10.1186/1752-153X-6-135](https://doi.org/10.1186/1752-153X-6-135)
- Putz MV, Ori O (2012) *Chem Phys Lett* 548:95
- Sedlar J, Vukicevic D, Cataldo F, Ori O, Graovac A (2013) available on-line at <http://amc.imfm.si> (printed edn. 2014) *ARS MATHEMATICA CONTEMPORANEA* 7:1, ISSN 1855-3966 (printed edn.), ISSN 1855-3974 (electronic edn.)
- Slater JC (1930) *Phys Rev* 36:57
- Starostin EL, van der Heijden GHM (2007) *Nat Mater* 6:563
- Tanda S, Tsuneta T, Okajima Y, Inagaki K, Yamaya K, Hatakenaka N (2002) *Nature* 417:397
- Tanda S, Tsuneta T, Toshima T, Matsuura T, Tsubota M (2005) *J Phys IV (France)* 131:289
- Todeschini R, Consonni V (2000) *Handbook of molecular descriptors*. Wiley-VCH, Weinheim
- Vukicevic D, Cataldo F, Ori O, Graovac A (2011) *Chem Phys Lett* 501:442
- Wakabayashi K, Harigaya K (2003) *J Phys Soc Jpn* 72:998



- Weisstein EW (2012) Moebius Strip. From MathWorld-A Wolfram Web Resource. <http://mathworld.wolfram.com/MoebiusStrip.html>
- Xing SK, Li Y, Zhao XZ, Cai ZS, Shang ZF, Wang GC (2011) Acta Phys Chim Sin 27(5):1000
- Yakubo K, Avishai Y, Cohen D (2003) Phys Rev B 67:125319
- Yang Y, Han D, Nangreave J, Liu Y, Yan H (2012) ACS Nano 6(9):8209
- Yoon ZS, Osuka A, Kim D (2009) Nat Chem 1:113

# Chapter 8

## Spanning Fullerenes as Units in Crystal Networks

Mircea V. Diudea and Beata Szeffler

**Abstract** Fullerenes are molecules consisting of tri-connected polyhedral cages of various covering. Spanning fullerenes can be obtained by deleting some atoms or bonds, thus resulting in open structures with di-connected atoms which can further join to atoms of the same or different repeating units in construction of crystal- or quasicrystal-like networks. In this chapter, a variety of spanning fullerenes, designed either by opening cages or by sequences of map operations, are used to build more complex nanostructures. Energetics of some spanning fullerenes has been calculated on optimized structures at Hartree-Fock and/or DFT level of theory. The topology of crystal networks is described in terms of Omega polynomial.

### 8.1 Introduction

*Fullerenes* are molecules consisting of tri-connected polyhedral cages of various coverings or tessellations. When there is a single type of polygonal faces, the covering is called Platonic; when there are two types of faces, the covering is called Archimedean (Diudea 2010a). A molecule can be represented by a molecular graph. A graph  $G(V, E)$  is an ordered pair of two sets,  $V$  and  $E$ ,  $V = V(G)$  being a finite nonempty set and  $E = E(G)$  a binary relation defined on  $V$  (Harary 1969; Diudea et al. 2002). A graph can be visualized by representing the elements of  $V$  by points (i.e., vertices) and joining pairs of vertices  $(i, j)$  by a bond (i.e., edge) if and only if  $(i, j) \in E(G)$ . The number of vertices in  $G$  equals the cardinality  $\nu = |V|$  of this set.

---

M.V. Diudea (✉)

Faculty of Chemistry and Chemical Engineering, Babes-Bolyai University, 400028 Cluj, Romania  
e-mail: [diudea@gmail.com](mailto:diudea@gmail.com)

B. Szeffler

Department of Physical Chemistry, Collegium Medicum, Nicolaus Copernicus University,  
Kurpińskiego 5, 85-950 Bydgoszcz, Poland  
e-mail: [beatas@cm.umk.pl](mailto:beatas@cm.umk.pl)

A graph is said connected if any two vertices,  $i$  and  $j$ , are the endpoints of a path; otherwise, it is disconnected. The molecular graphs are in general connected graphs.

Spanning fullerenes can be designed by deleting, from their molecular graph, some vertices/atoms or edges/bonds, thus resulting in open structures with disconnected atoms which can further be joined with atoms of the same or different repeating units in designing *periodic nanostructures*, as those encountered in nanodendrimers, in crystals or quasicrystals. Note that spanning of fullerenes can be obtained in laboratory by irradiating the closed cages by electron or ion beams, while many of the molecular constructions to be presented in the following can be seen as potentially real structures. Since fullerenes can be designed from the Platonic polyhedra, tetrahedron T, cube C, octahedron Oct, dodecahedron Do, and icosahedron Ico, by applying some operations on maps, the spanning fullerenes can be designed by such sequences of operations, the “opening” Op operation included.

A map is a discretized (closed) surface. Among the most important map operations we mention are the following: dual  $Du$ , medial  $Med$ ,  $P_k$ -mapping,  $k = 3-5$ , *Leapfrog Le*, *Chamfering Q*, and *Capra Ca*. These operations are implemented in the CVNET software package (Stefu and Diudea 2005). More about map operation the reader can find in Diudea (2010a) and Stefu et al. (2005).

*Dendrimers* are hyper-branched structures with a well-tailored architecture. Their endgroups can be functionalized, thus modifying their initial properties. Dendrimers have gained a wide range of applications in supramolecular chemistry, particularly in host-guest reactions and self-assembly processes. Promising applications come from polyamidoamine dendrimers as gene transfer vectors and peptide dendrimers as anti-peptide antibodies and synthetic vaccines (Diudea 2010a, p. 80).

The number of edges emerging from each branching point is called the *progressive degree* (Diudea and Katona 1999),  $p$  (i.e., the edges increasing the number of points of a newly added generation). It equals the classical vertex degree  $d$  minus 1:  $p = d - 1$ .

The stepwise growth of a dendrimer follows a mathematical progression. A first problem in studying the topology of dendrimers is that of enumerating its constitutive parts: vertices, edges, or fragments.

The number of vertices in the  $i$ th orbit (i.e., that located at distance  $i$  from the center) of a regular dendrimer can be expressed as a function vertex degree  $d$ :

$$v_i = (2 - z)(d + z - 1)(d - 1)^{(i-1)}; \quad i > 0 \quad (8.1)$$

where  $z = 1$  for a monocentric dendrimer and  $z = 0$  for a dicentric one. By using the progressive degree  $p$ , relation (8.1) becomes

$$v_i = (2 - z)(p + z)p^{(i-1)}; \quad i > 0 \quad (8.2)$$

For the core, the number of vertices is  $v_0 = 2 - z$ , while the number of external vertices (i.e., the endpoints) is obtained by

$$v_r = (2 - z)(p + z)p^{(r-1)} \quad (8.3)$$

where  $r$  is the radius of the dendrimer and equals the number of its orbits/generations.

The total number of vertices  $v(D)$ , in dendrimer, is obtained by summing the populations on all orbits:

$$v(D) = (2 - z) + (2 - z)(p + z) \sum_{i=1}^r p^{(i-1)} \quad (8.4)$$

By developing the sum in (8.4), one obtains

$$v(D) = (2 - z) + (2 - z)(p + z) \left( \frac{p^r - 1}{p - 1} \right) = \frac{2(p^{r+1} - 1)}{p - 1} - zp^r \quad (8.5)$$

A useful recurrence enables one to calculate  $v(D)$  from the number of vertices of the precedent term of a dendrimer family (i.e., a homologous series of dendrimers, having the same progressive degree,  $p$ )  $v(D_{r+1}) = pv(D_r) + 2$ , irrespective of monocentric or dicentric the dendrimer is.

The term nano-dendrimer refers here to hyper-branched structures of which branching nodes represent nanotube junctions (i.e., spanned fullerenes), while the bonds joining them are nanotubes of various length.

Crystals are (MacKay 1981; Hargittai and Hargittai 2010) periodic structures, of which (one-type) unit cells, consisting of one or more atoms or other identical components, repeat a large number of times by three noncoplanar translations. Corresponding atoms in each unit cell have almost identical surrounding, while the fraction of atoms near the surface is small and the effects of the surface can be neglected.

Quasicrystals are quasiperiodic structures (Levine and Steinhardt 1984), showing more than one type of repeating unit, or the same unit repeating quasi-regularly. Quasicrystals can have the topology of multi-tori, particularly of those with icosahedral symmetry. These kinds of periodic structures will be exemplified in the following.

Multi-tori are structures of high genera, consisting of more than one tubular ring (Diudea and Petitjean 2008). They are supposed to result by self-assembly of some repeat units or monomers; their geometry is eventually superimposed on surfaces of negative curvature, like FRD or P-surface, and shows a high porosity. Multi-tori can be designed starting from small cages, for example, the Platonic solids. Modeling of porous structures has been previously reported by Mackay and Terrones (1991), Lenosky et al. (1992) and Terrones and Mackay (1993), etc. Such structures appear in spongy carbon (already synthesized, Benedek et al. 2003), in schwarzites (named in honor of mathematician Schwarz 1865, 1890), or in zeolites (natural aluminosilicates).

## 8.2 Design of Spanning Fullerenes

There are at least two ways to design a tubular nano-junction: (1) by sequences of map operations and (2) by spanning appropriate fullerenes.

### 8.2.1 Junctions by Map Operations

Three basic map operations Leapfrog  $Le$ , Chamfering (Quadrupling)  $Q$ , and Capra  $Ca$  (the reader is invited to consult: Diudea 2004, 2005; Diudea et al. 2003, 2006a; Stefu et al. 2005), associated with the opening  $Op$  operation, are most often used to transform small polyhedral objects (basically, the Platonic solids) into tubular junctions (Diudea and Nagy 2007). These transforms preserve the symmetry of the parent map. Figure 8.1 presents a realization by Leapfrog  $Le$  operation (Nagy et al. 2011).

### 8.2.2 Junctions by Spanning Fullerenes

Spanning a fullerene graph can be done by deleting/braking some edges (and vertices), thus getting a particular patch (eventually identical to a circulene molecule). Figure 8.2 illustrates the case of coronene-preserving opening (left) and sumanene-preserving opening (right) of fullerene  $C_{84}-20-T_d$  (Diudea 2010b). Figure 8.3 presents three octahedral nano-junctions derived from the hypothetical fullerene  $C_{168}$  that consists of eight (disjoint) sumanene patches (Szeffler et al. 2012a), lying in the corners of cube, while on cube faces having octagons, Sum\_CZ\_192 and Sum\_CA\_216 are obtained by opening operations  $Op(1a)$  and  $Op(2a)$ , respectively; the third one, Sum\_OctS<sub>2</sub>LeX\_168, results by simply deleting the alternating edges of octagon,  $Op(-a)$ . Observe that the last numbers in the name of structures represent the number of carbon atoms. Other particular monomeric units will be presented below.

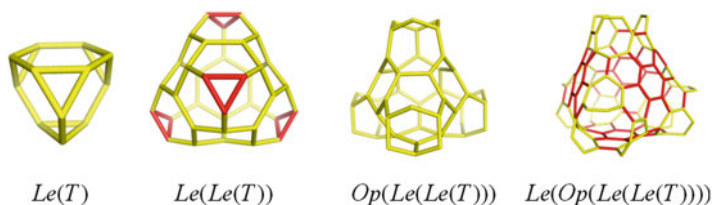


**Fig. 8.1** Design of a tetrapodal junction by Leapfrog  $Le$  map operation

**Fig. 8.2** Opening  $C_{84\_20-T_d}$ : as coronene,  $4[6:6_6]$ ,  $v = 84$ ,  $e = 114$ ,  $f_6 = 28$ ,  $g = 2$  (left – also designed by the sequence of map operations – see Fig. 8.1) and sumanene,  $4[6:(5,6)_3]$ ,  $v = 84$ ,  $e = 114$ ,  $f_5 = 12$ ,  $f_6 = 16$ ,  $g = 2$  (right) patches, respectively; optimized structures are shown in the *bottom row*

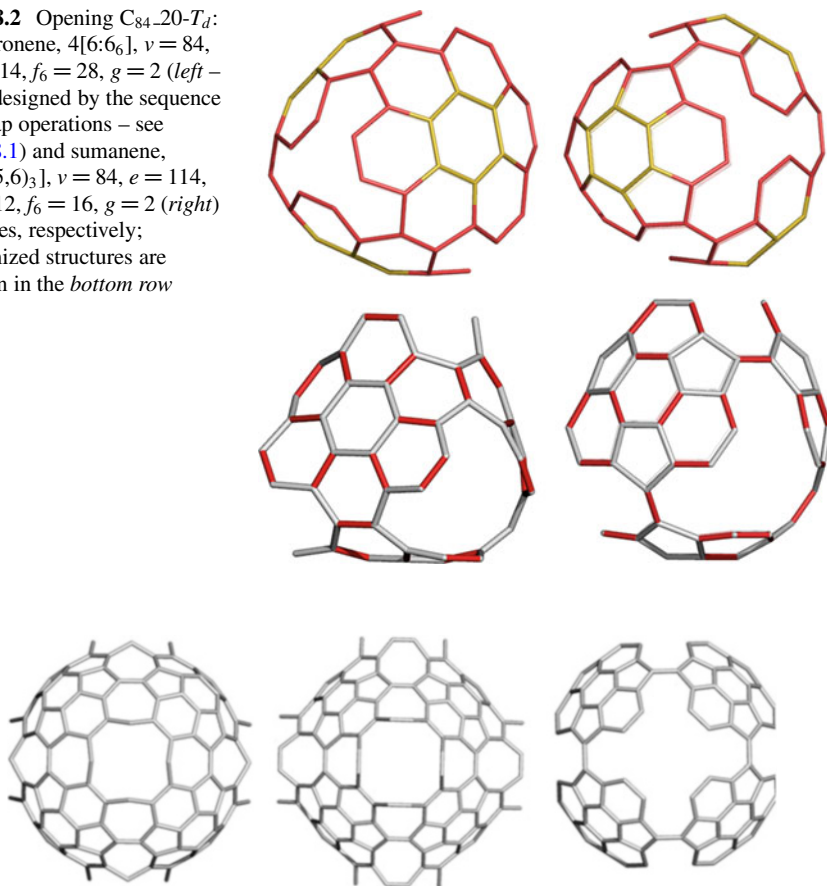


**Fig. 8.3** Sumanene motif decorating octahedral nano-junctions: Sum\_CZ\_192 (left), Sum\_CA\_216 (middle), and Sum\_OctS<sub>2</sub>LeX\_168 (right)

The spanned cages can be used to build dendrimers or other periodic nanostructures by joining with other units (the same or not) or by identifying common substructures (see below).

Table 8.1 lists the energetics of these hypothetical nano-junctions, optimized at the Hartree-Fock level of theory, as hydrogen-ended molecules. When compared to the values for  $C_{60}$ , the reference structure in nanoscience, one can see the spanned fullerenes show at least (or higher) the stability of the reference. The extent of strain, as given by POAV theory (Haddon 1987, 1990), is favorable for the opened fullerenes (Table 8.1, last column) in comparison to that of  $C_{60}$ , the structures included in this table being real candidates to the status of real molecules.

**Table 8.1** Total energy  $E_{\text{tot}}$  and HOMO-LUMO gap, at Hartree-Fock HF (HF/6-31 G(d,p)) level of theory, for some hypothetical nano-junctions and  $C_{60}$  reference nanostructure

Structure	$E_{\text{tot}}$ (au)	$E_{\text{tot}}/C$ (au/mol)	HF_gap (eV)	POAV/C (kcal/mol)
1 Cor_T_84	-3,194.767	-38.033	7.347	1.477
2 Sum_T_84	-3,155.466	-38.028	7.562	1.685
3 Sum_CZ_192	-7,298.367	-38.012	6.044	1.049
4 Sum_CA_216	-8,206.401	-37.993	6.442	0.550
5 Sum_OctS <sub>2</sub> LeX_168	-6,389.018	-38.030	6.637	0.821
6 C <sub>60</sub>	-2,271.830	-37.864	7.418	8.256

### 8.3 Dendrimers

Dendrimers (Fig. 8.4) can be designed from monomers with tetrahedral symmetry, either by joining the two-connected terminal vertices or by identification of appropriate (open) faces (Diudea 2010b). Dendrimers at 2nd generation are illustrated in Fig. 8.5 (Diudea 2010c).

The corresponding dimers (Fig. 8.6, top) are “intercalated” ones. A possible linear evolution of the above monomers is presented in Fig. 8.6, bottom (Diudea 2010b).

Other examples come from polybenzenes (Fig. 8.7), which are nanostructures consisting of benzene ring as the main motif (O’Keeffe et al. 1992) of tessellation.

### 8.4 Crystal-Like Networks

When monomers have octahedral symmetry, they can embed in the P-type surface in getting crystal-like networks which belong to the space group  $P_n3m$ . Figure 8.8 illustrates nets showing the sumanene 6:(5,6)<sub>3</sub> motif (Szeffler et al. 2012a).

Other examples of crystal-like networks are given in Fig. 8.9 (Szeffler and Diudea 2013): their covering consists of motifs of hexagon triples (unit C\_3HexZ\_104) and heptagon triples (unit C\_3HepA\_104), respectively, for which the energetic data are given in Table 8.2.

Again the open structures (i.e., nano-junctions) appear less strained than the reference  $C_{60}$  fullerene and, according to the total energy (calculated on the optimized structures at Hartree-Fock HF and DFT levels of theory) and HOMO-LUMO gap, are at least as stable as the reference molecule. The strain of heptagon triple motif is one order of magnitude lower than that of hexagon triple one and two orders of magnitude lower than that of the reference fullerene, also reflected in the values of TE/C. In view of a possible identification among nano-materials, IR and RAMAN spectra have been simulated (Szeffler and Diudea 2013). Polybenzenes can also be embedded in the P-type surface (Fig. 8.10).

**Fig. 8.4** Dendrimers by monomers with coronene (*left*) and sumanene (*right*) motifs, at 1st generation

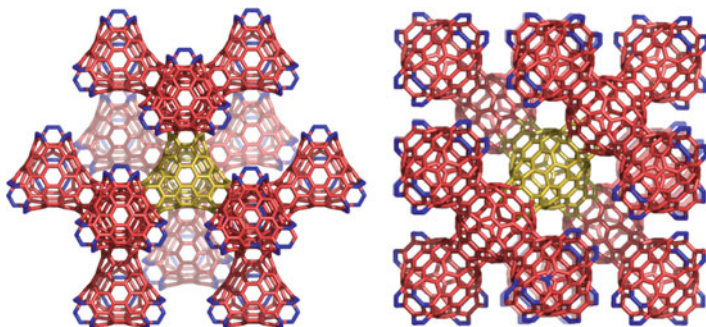
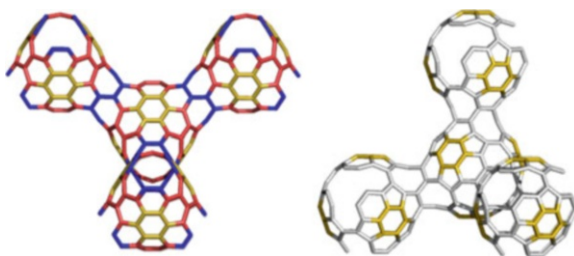


**Fig. 8.5** Dendrimer with coronene motif at 2nd generation (two different views)

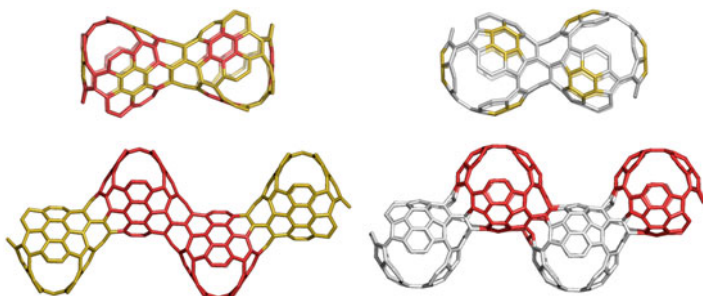


**Fig. 8.6** Linear evolution of the monomers with coronene (*left column*) and sumanene (*right column*) motifs

D-type surface can also embed a polybenzene structure (Fig. 8.11). This last net shows the topology of  $D_6$ -diamond: a face-centered cube  $f_{cc}$ -structure, belonging to the space group  $Pn3m$  (Szeffler and Diudea 2012).

Calculations have been performed at HF/6-31 G(d, p) and B3LYP/6-311 + G(d, p) level of theory, respectively, on Gaussian 09 software package (2009).

Stability of the monomers and the corresponding dimmers with respect to the reference  $C_{60}$  fullerene can be compared from data in Table 8.3. Note the three types of dimers originating in BTA\_48, function of the identified face/ring and



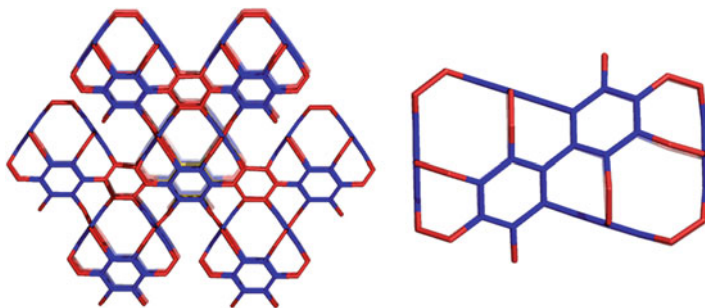


**Fig. 8.7** Polybenzene dendrimer (*left*) and its “intercalated” dimer (*right*)

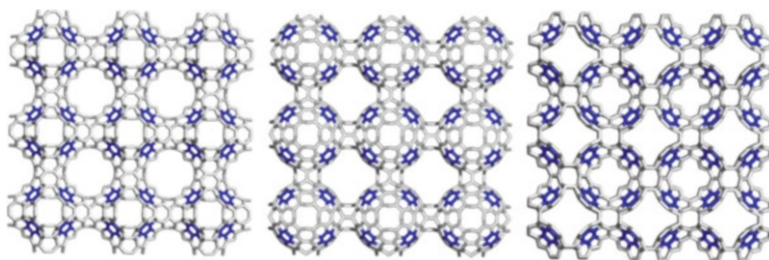


**Fig. 8.8** P-type surface embedding of monomers in Fig. 8.3: Sum\_CA\_216 (*left*), Sum\_CZ\_192 (*middle*), and Sum\_OctS<sub>2</sub>LeX\_168 (*right*)

**Fig. 8.9** *Top row:* C\_3HexZ\_104 ( $v = 104$ ;  $e = 144$ ;  $f_6 = 36$ ;  $g = 3$ ) and its p-type crystal-like net ( $v(3,3,3) = 2,808$ ); *bottom row:* C\_3HepA\_104 ( $v = 104$ ;  $e = 132$ ;  $f_7 = 24$ ;  $g = 3$ ) and its p-type crystal-like net (junctions designed by map operation sequences  $Op_{2a}(S_2(C))$  and  $Op(S_1(C))$ , respectively)

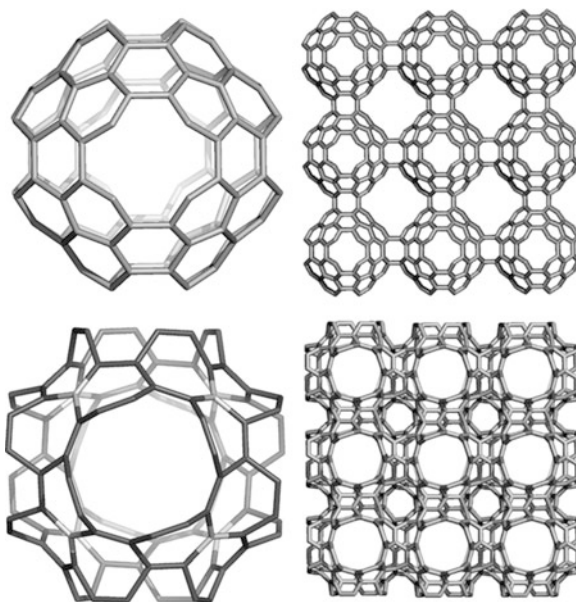
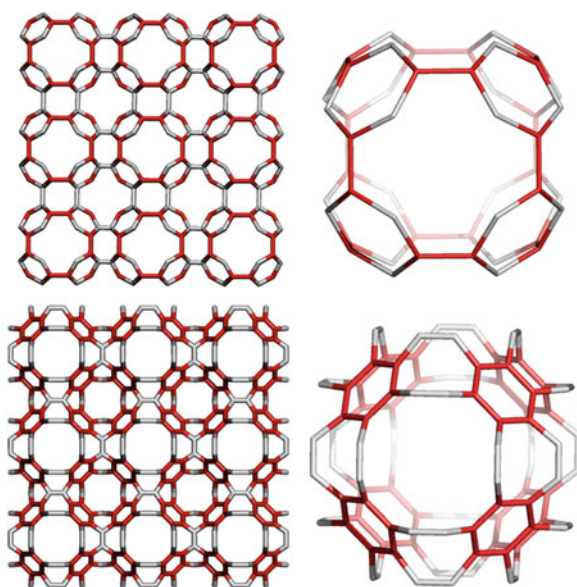


**Table 8.2** Energies (total energy per carbon atom TE/C, in Hartree H; HOMO-LUMO gap, HL gap, in electron volts; POAV strain energy per carbon atom S/C, kcal/mol) of the optimized structures at HF and DFT level of theory

	Molecule	Carbon atoms	TE/C (H)	HL gap (eV)	POAV/C (kcal/mol)
HF					
1	C_3HexZ_104	104	-37.999	5.342	2.329
2	C_3HepA_104	104	-38.127	6.942	0.240
3	C <sub>60</sub>	60	-37.864	7.418	8.256
DFT					
4	C_3HexZ_104	104	-38.244	1.658	2.352
5	C_3HepA_104	104	-38.376	1.354	0.192
6	C <sub>60</sub>	60	-38.110	2.724	8.256

**Fig. 8.10** Polybenzenes embedded in the P-type surface: *p*-BCZ\_48 (*top*) and *p*-BCA\_96 (*bottom*) and the corresponding units (*right column*)



conformation: (BTA\_48)2.84\_dendrim ( $R_{12}$ , intercalate, Table 8.3, entry 2, and Fig. 8.7, right), (BTA\_48)2.88\_  $f_{cc}$  ( $R_8$ , Table 8.3, entry 3, and Fig. 8.11, right), and (BTA\_48)2.90\_MT ( $R_{12}$ , eclipsed, Table 8.3, entry 4, and Fig. 8.12, bottom, left) (Szefer et al. 2012b).

One can see that the strain in polybenzenes, as calculated by POAV theory, is far less than that in C<sub>60</sub>, and the overall stability is at least as that of the reference fullerene. Infrared and Raman spectra have been simulated (Szefer et al. 2012b) in view of possible use in laboratory identifying such structures, tessellated with the simplest benzene ring motif. The high values of HOMA index of aromaticity (Krygowski and Ciesielski 1995, 1996), in the last column of Table 8.3, suggest that the benzene ring geometry is not too much modified in comparison to the

**Fig. 8.11** Polybenzene embedded in the D-type surface:  $f_{cc}$ -BTA\_48 and its  $f_{cc}$ -dimer (right)

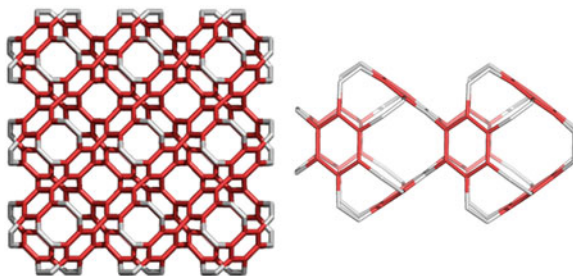


**Table 8.3** Total energy  $E_{tot}$  per atom (kcal/mol) and HOMO-LUMO gap, at Hartree-Fock HF level of theory, strain by POAV theory and HOMA index in benzene-patched units and their dimers and  $C_{60}$  reference structure, as well

Structure	No. units	$E_{tot}/(\text{au})$	$E_{tot}/\text{atom}$ (au)	HL gap (eV)	POAV/C (kcal/mol)	HOMA (R[6])
1 BTA_48	1	-1,831.484	-38.156	11.285	0.083	0.951
2 (BTA_48)2_84_dendrim	2	-3,201.679	-38.115	10.895	0.061	0.975
3 (BTA_48)2_88_ $f_{cc}$	2	-3,355.431	-38.130	10.970	0.074	0.972
4 (BTA_48)2_90_MT	2	-3,428.847	-38.098	10.085	0.220	0.957
5 BCZ_48	1	-1,831.097	-38.148	8.134	3.395	0.989
6 (BCZ_48)2_96	2	-3,657.417	-38.098	7.043	2.842	0.114
7 BCA_96	1	-3,662.991	-38.156	10.253	0.124	0.939
8 (BCA_96)2_184	2	-7,013.828	-38.119	9.805	0.180	0.936
9 $C_{60}$	1	-2,271.830	-37.864	7.418	8.256	0.493

free benzene molecule (HOMA value = 1), while the hexagonal rings in  $C_{60}$  are much more affected (HOMA = 0.493) by the presence of pentagons (see also Cysewski and Szeffler 2010). The HOMA value is even dropped in case of dimer (BCZ\_48)2\_96 (Table 8.3, entry 6) because the units bound directly at the benzene ring. The loss in pi-electron resonance is partly compensated by the loss in strain energy, visible when compared with the BCZ\_48 unit (Table 8.3, entry 5). However, in an infinite network, the strain will drop even more (Szeffler et al. 2012b), and the geometry approaches to that of the unit-free molecule.

## 8.5 Quasicrystal Nanostructures

Multi-tori are designed by using “eclipsed” dimers (Diudea and Nagy 2007), as shown in Fig. 8.12, bottom row. The dimer BMTA2\_90 was included in Table 8.3 (as (BTA\_48)2\_90\_MT, entry 4). The unit BTZ\_24, due to its simplicity, can form only the dimer BMTZ2\_48, leading to multi-tori. The multi-tori bearing the benzene patch will have B as a prefix in their name. Next, because the opening faces show

**Fig. 8.12** *Left column:* BTA\_48 (*top*) formed by spanning the cage Le(P<sub>4</sub>(T))\_48 (by deleting the *blue bonds – middle*) and its multi-torus BMTA2\_90 dimer ((BTA\_48)<sub>2</sub>\_90\_MT in Table 8.3, entry 4). *Right column:* BTZ\_24 (*top*) originating in S<sub>2</sub>(T)\_28 = C<sub>28</sub> (the four *blue* points located at the center of pentagon triples to be deleted – *middle*) and its multi-torus BMTZ2\_48 dimer

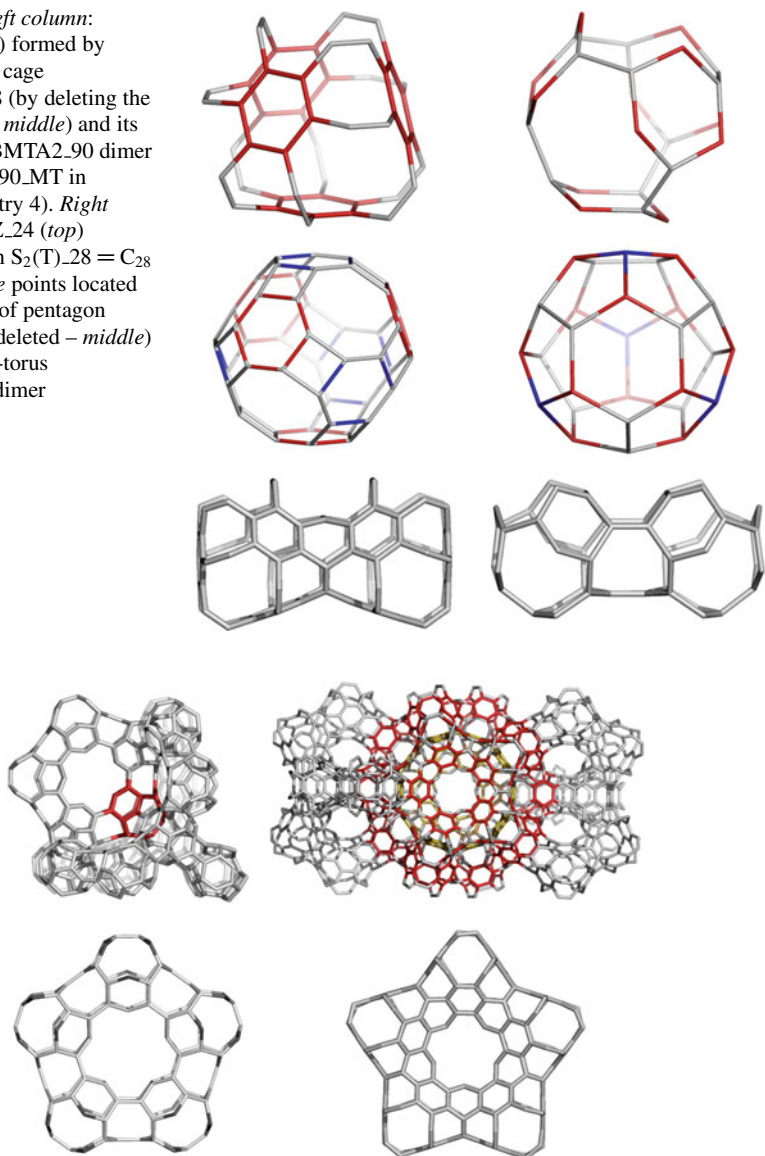
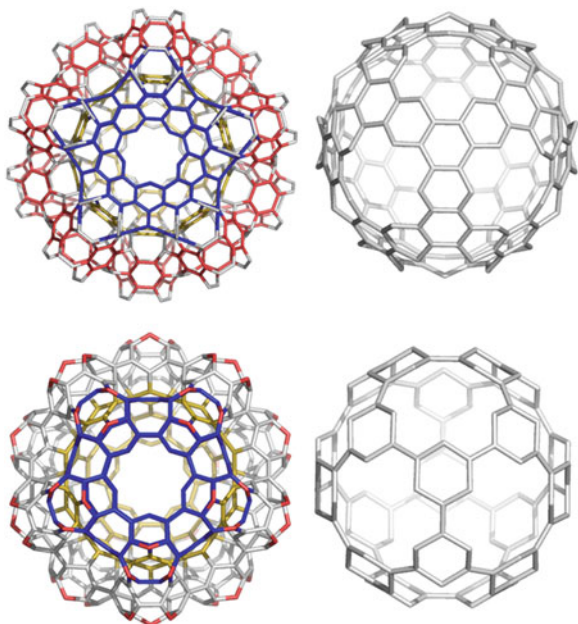


**Fig. 8.13** *Left column:* BMTZ17\_408 and its hyper-pentagon MMTZCy5\_120. *Right column:* BMTA34\_1332 and its hyper-pentagon BMTACy5\_210

either “zigzag” or “armchair” endings, “Z” or “A” will be added as a suffix to their name. The number of repeating units and/or number of atoms will be added after the letters.

The BMTX<sub>2</sub> dimers, because of their “eclipsed” conformation, will form pentagonal hyper-rings BMTX<sub>2</sub>Cy<sub>5</sub> (Fig. 8.13, bottom) in a self-assembly process.

**Fig. 8.14** *Top row:* multi-torus BMTA20\_1\_780 (*left*) and its core ( $-f_5(Le_{2,2}(Do))$ , *right*); *bottom row:* multi-torus BMTZ20\_1\_480 (*left*) and its core ( $-d_5(S_2(Ico))$ , *right*)



These can further evolve to the multi-torus BMTX17 ( $X = Z$ , Fig. 8.3, left), of which reduced graph is just  $C_{17}$ , the structure proposed by Diudea (2010d) as the seed for the diamond  $D_5$ . By analogy to  $D_5$ , a hyper-dimer BMTX34 can be designed ( $X = A$ , Fig. 8.3, right). We mention that its reduced graph is  $C_{34}$ , the repeating unit of the triple periodic structure of  $D_5$ . Recall that  $D_5$  is an *mtn* triple periodic 3-nodal net, named ZSM-39 (a structure found in clathrates of type II), of point symbol net:  $\{5^5.6\}12\{5^6\}5$  and  $2[5^{12}] + [5^{12}.6^4]$  tiling. It is also known as the *fcc-C<sub>34</sub>* structure (Blase et al. 2010; Diudea et al. 2011), because of its face-centered cubic lattice that belongs to the space group  $Fd\bar{3}m$ . Thus, we can expect a 3D network derived from these benzene-patched units, similar to  $D_5$ .

A spherical multi-torus BMTX20 (Fig. 8.14, left column) can be constructed and is a  $g = 21$  multi-torus, with a well-defined core:  $\text{Core(BMTA20)}_{180} = -f_5(Le_{2,2}(Do))$  while  $\text{Core(BMTZ20)}_{120} = -d_5(S_2(Ico))$ . In the above,  $-f_5$  means deletion of all pentagonal faces in the Leapfrog (2,2) transform of the dodecahedron  $Do$ , and  $-d_5$  is deletion of vertices of degree  $d = 5$ , in the transform of Icosahedron =  $Ico$  by the septupling  $S_2$  operation. Also,  $-d_5(S_2(Ico)) = Op(Le(Ico))$ . Recall that  $g$  is the genus of the surface that embeds a structural graph and accounts for the number of simple tori of which consists that graph (Diudea and Szeffler 2012).

A linear array BMTX20 $_k$ ,  $k = 1, 2, \dots$  with the repeating unit formed by two units superimposing one pentagonal hyper-face (i.e., BMTXCy5), rotated to each other by an angle of  $\pi/5$  as in the “dimer” BMTA20\_2 (Fig. 8.15, top, left). Next, the structure can evolve with a one-dimensional periodicity, as shown in BMTA20\_4 (Fig. 8.15, top, right) or in the hyper-cycle BMTZCy20\_5 (Fig. 8.15, bottom, left).

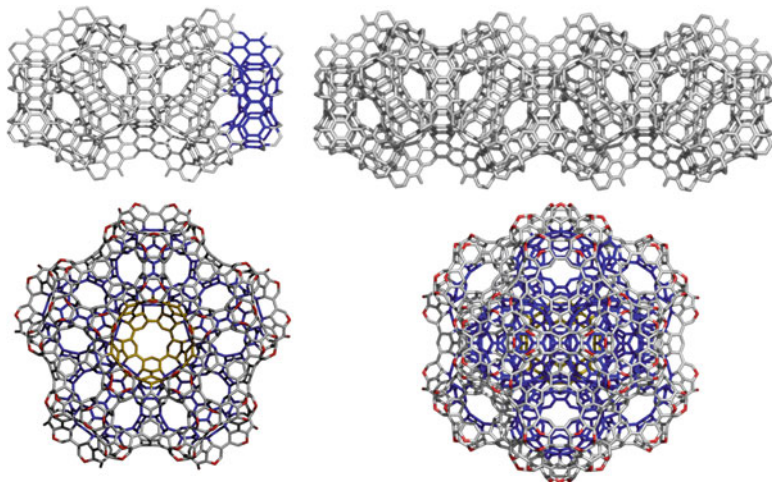


**Fig. 8.15** Top row: the repeat unit BMTA20.2\_1350 (left) and a rodlike BMTA20.4\_2490 (right); bottom row: multi-tori BMTZCy20\_5\_1800 (left) and BMTZSp20\_12\_3120 (twofold symmetry)

Twelve units of BMTX20 can form a spherical array (of icosahedral symmetry), as in case of BMTZSp20\_12 (Fig. 8.15, bottom, right), of which core is just BMTZ20 (a 13th unit).

**Theorem 8.1** *In multi-tori built up from open tetrahedral units, the genus of structure equals the number of its units plus one, irrespective of the unit tessellation.*

*Demonstration* comes out from construction and is illustrated on the multi-tori BMTXCy5 (Fig. 8.13, bottom row): there are five units open to be inserted in exactly five simple tori and one more torus that join all the above five units, thus demonstrating the first part of the theorem (Diudea and Szeffler 2012).

For the second part, we apply the Euler's theorem (1758):

$$v - e + f = \chi = 2(1 - g) \quad (8.6)$$

where  $v = |V(G)|$  is the number of vertices/atoms,  $e = |E(G)|$  is the number of edges/bonds, and  $f$  is the number of faces of the graph/molecule. In the above,  $g$  is the *genus* of the (orientable) surface  $S$  on which a molecular graph is embedded. The genus is related to the Gaussian curvature of the surface  $S$  by means of Euler's characteristic  $\chi$  of  $S$  (Gauss-Bonnet 1853) theorem as for  $g = 0$  (case of sphere)  $\chi > 0$  (positive curvature); for  $g = 1$  (case of torus)  $\chi = 0$ , while for  $g > 1$  (surfaces of high genera),  $\chi < 0$ ,  $S$  will show a negative curvature. More about surfaces of negative curvature the reader can find in Diudea and Nagy (2007).

To complete the demonstration, we will use the data in Table 8.4 providing the values of  $g$  in several BMTX multi-tori, tessellation differing as  $X = A$  or  $Z$ .

The number of tetrahedral units BMTX1 in the linear array of BMTX20 $_k$  (Table 8.4, entries 3–6) is  $u = 20k - 5(k - 1) = 15k + 5$ , according to the construction mode. The term  $-5(k - 1)$  accounts for the superimposed hyper-

**Table 8.4** Euler formula calculation in multi-tori BMTX

BMTX	$v$	$e$	$f_6$	$f_8$	$f_{\text{tot}}$	$2(1-g)$	$g$	$u$	$u$ -formula
1 BMTACy5	210	285	35	30	65	-10	6	5	$f_8/6$
2 BMTZCy5	120	165	20	15	35	-10	6	5	$f_6/4$
3 BMTA20_1	780	1,110	170	120	290	-40	21	20	$f_8/6$
4 BMTZ20_1	480	690	80	90	170	-40	21	20	$f_6/4$
5 BMTA20_5	3,060	4,410	710	480	1,190	-160	81	80	$f_8/6$
6 BMTZ20_5	1,920	2,790	320	390	710	-160	81	80	$f_6/4$
7 BMTZCy20_5	1,800	2,625	300	375	675	-150	76	75	$f_6/4$
8 BMTZ20_12	4,440	6,465	740	915	1,655	-370	186	185	$f_6/4$
9 BMTZSp20_12	3,120	4,590	520	690	1,210	-260	131	130	$f_6/4$

rings, BMTZCy5. In case of BMTZCy20\_5 (Table 8.4, entry 7), the formula is  $u = 20k - 5k = 15k$ ,  $k = 5$ , the last hyper-ring unit being omitted because of the cyclic structure. Thus, the drop in  $g$  is of 5 units for each fivefold hyper-cycle (compare Table 8.4, entries 6 and 7).

In case of the spherical array BMTZSp20\_12 (Table 8.4, entry 9),  $u = 20k - 2[5(k - 1)]$ ,  $k = 12$ . Remark the twice subtraction of the term  $5(k - 1)$ , in case of the spherical array, which accounts for the difference in  $g$  to the linear array of  $k = 12$  (Table 8.4, entries 8 and 9):  $186 - 131 = 55 = 5(12 - 1)$ . This drop in  $g$ , in case of the spherical array, seems to parallel the well-known result that sphere is the minimal surface among all known solid objects. The number  $u$  is also related to the number of simple faces/rings as follows:  $u = f_8/6$  in case BMTA and  $u = f_6/4$  in case BMTZ.

On the ground of Theorem 8.1, the spherical array BMTZSp20\_12 seems to be the *minimum*  $g$  (lower bound) while BMTZ20\_ $k$  the *maximum*  $g$  (upper bound) among all the studied structures (Diudea and Szeffler 2012). We just demonstrated the following:

**Theorem 8.2** *The genus in multi-tori shows the lower-bound value in structures of icosahedral symmetry, while the upper-bound value is shown in linear structures provided the same number of (open) tetrahedral units.*

Note these icosahedral multi-tori represent quasicrystal nanostructures; quasicrystals have been Nobel prized in 2011.

Carbon atom *orbit analysis* in BMTZSp20\_12 revealed a  $6.8^2$  massive class (2,580 atoms, about 83 %), located inside, of the same signature as in polybenzene, and two smaller classes, of signature 6.8 (360 atoms), and 6 (180 atoms), disposed outside of the spherical structure. Compare with % of  $6.8^2$  in the linear array BMTZ20\_ $k$  (about 74 % at  $k = 12$ ) and in BMTA20\_ $k$  (about 26 %, at  $k = 9$ ). Knowing the (calculated by O’Keeffe et al. 1992) stability of polybenzene, consisting of only  $6.8^2$  atoms (in the infinite triple periodic net), the orbit analysis provides a “topological” proof of stability of the spherical array BMTZSp20\_12 (Diudea and Szeffler 2012).

## 8.6 Omega Polynomial in Polybenzenes

In a connected graph  $G(V, E)$ , with the vertex set  $V(G)$  and edge set  $E(G)$ , two edges  $e = uv$  and  $f = xy$  of  $G$  are called *codistant e cof* if they obey the relation (John et al. 2007)

$$d(v, x) = d(v, y) + 1 = d(u, x) + 1 = d(u, y) \quad (8.7)$$

which is reflexive, that is,  $e \text{ cof } e$  holds for any edge  $e$  of  $G$ , and symmetric, if  $e \text{ cof } f$ , then  $f \text{ cof } e$ . In general, relation  $\text{co}$  is not transitive; if “ $\text{co}$ ” is also transitive, thus it is an equivalence relation, then  $G$  is called a *co-graph*, and the set of edges  $C(e) := \{f \in E(G); f \text{ cof } e\}$  is called an *orthogonal cut oc* of  $G$ ,  $E(G)$  being the union of disjoint orthogonal cuts:  $E(G) = C_1 \cup C_2 \cup \dots \cup C_k$ ,  $C_i \cap C_j = \emptyset, i \neq j$ . Klavžar (2008) has shown that relation  $\text{co}$  is a theta Djoković (1973)–Winkler (1984) relation.

We say that edges  $e$  and  $f$  of a plane graph  $G$  are in relation *opposite, e opf*, if they are opposite edges of an inner face of  $G$ . Note that the relation  $\text{co}$  is defined in the whole graph while  $\text{op}$  is defined only in faces. Using the relation  $\text{op}$ , we can partition the edge set of  $G$  into *opposite edge strips, ops*. An *ops* is a quasi-orthogonal cut *qoc*, since *ops* is not transitive.

Let  $G$  be a connected graph and  $S_1, S_2, \dots, S_k$  be the *ops* strips of  $G$ . Then, the *ops* strips form a partition of  $E(G)$ . The length of *ops* is taken as maximum. It depends on the size of the maximum-fold face/ring  $F_{\max}/R_{\max}$  considered so that any result on Omega polynomial will have this specification.

Denote by  $m(G, s)$  the number of *ops* of length  $s$  and define the Omega polynomial as (Diudea 2006; Diudea et al. 2006b, 2008, 2009; Ashrafi et al. 2008; Diudea and Klavžar 2010; Vizitiu et al. 2007)

$$\Omega(G, x) = \sum_s m(G, s) \cdot x^s \quad (8.8)$$

Its first derivative (in  $x = 1$ ) equals the number of edges in the graph:

$$\Omega'(G, 1) = \sum_s m(G, s) \cdot s = e = |E(G)| \quad (8.9)$$

On Omega polynomial, the Cluj-Ilmenau index (John et al. 2007),  $\text{CI} = \text{CI}(G)$  was defined:

$$\text{CI}(G) = \{[\Omega'(G, 1)]^2 - [\Omega'(G, 1) + \Omega''(G, 1)]\} \quad (8.10)$$

Formulas to calculate Omega polynomial and CI index in three infinite networks,  $f_{\text{cc}}$ -BTA\_48 (Fig. 8.11),  $p$ -BCZ\_48 (Fig. 8.10, top), and  $p$ -BCA\_96 (Fig. 8.10, bottom), are listed in Table 8.5. Formulas were derived from the numerical data



**Table 8.5** Omega polynomial and net parameters in polybenzene networks

Net	Omega polynomial
BTA_48	$R_{\max}(8)$ $\Omega(\text{BTA}_{48}) = 18k^2X^2 + 6k(k-1)X^{2k} + 6kX^{4k} + \sum_{s=1}^{k-1} 12kX^{4s}$ $\Omega'(1) = 12k^2(3k+2) =  E(G)  = \text{edges}$ $\text{CI}(G) = 8k^2(162k^4 + 216k^3 + 61k^2 + 3k - 13)$ $\text{atoms} = 24k^2(k+1) =  V(G)$ $R_6 = 4k^3; R_8 = 6k^3 - 3k^2 + 3k$
	$R_{\max}(12)$ $\Omega(\text{BTA}_{48}) = 6X^{2k(2k+1)} + 3X^{4k^2(k+1)} + \sum_{s=1}^{k-1} 12X^{2s(2k+1)}$ $\Omega'(1) = 12k^2(3k+2) =  E(G)  = \text{edges}$ $\text{CI}(G) = 8k(6k^2 + 2k - 1)(26k^3 + 24k^2 + 6k + 1)$ $R_{12} = 4k^3$
Examples	$R_{\max}(8)$ $k = 5; \Omega(G) = 450X^2 + 60X^4 + 60X^8 + 120X^{10} + 60X^{12} + 60X^{16} + 30X^{20};$ $\text{CI} = 25,955,400; \text{atoms} = 3,600; \text{edges} = 5,100; R_6 = 500; R_8 = 690$ $k = 6; \Omega(G) = 648X^2 + 72X^4 + 72X^8 + 252X^{12} + 72X^{16} + 72X^{20} + 36X^{24};$ $\text{CI} = 74,536,992; \text{atoms} = 6,048; \text{edges} = 8,640; R_6 = 864; R_8 = 1,206$
	$R_{\max}(12)$ $k = 5; 12X^{22} + 12X^{44} + 12X^{66} + 12X^{88} + 6X^{110} + 3X^{600};$ $\text{CI} = 246,831,60; R_{12} = 500$ $k = 6; 12X^{26} + 12X^{52} + 12X^{78} + 12X^{104} + 12X^{130} + 6X^{156} + 3X^{1008};$ $\text{CI} = 71,009,232; R_{12} = 864$
BCZ_48	$R_{\max}(8)$ $\Omega(\text{BCZ}_{48}) = 12kX + 12k(k+1)X^2 + 3k(k-1)(2k-1)X^4 + \sum_{s=1}^{k-1} 24kX^{(2+4s)}$ $\Omega'(1) = 12k^2(6k-1) =  E(G)  = \text{edges}$ $\text{CI}(G) = 4k(1,296k^5 - 432k^4 + 4k^3 - 24k^2 + 32k - 3)$ $\text{atoms} = 48k^3 =  V(G) $ $R_6 = (2k)^3; R_8 = 12k^2(k-1)$
	$R_{\max}(12)$ $\Omega(\text{BCZ}_{48}) = (6k-3)X^{(2k)^2} + 6X^{(2k)^3}$ $\Omega'(1) = 12k^2(6k-1) =  E(G)  = \text{edges}$ $\text{CI}(G) = 96k^4(50k^2 - 19k + 2)$ $R_{12} = 6k(2k^2 - 2k + 1)$
Examples	$R_{\max}(8)$ $k = 5; 60X + 360X^2 + 540X^4 + 120X^6 + 120X^{10} + 120X^{14} + 120X^{18}$ $\text{CI} = 75,601,140; \text{atoms} = 6,000; \text{edges} = 8,700; R_6 = 1,000; R_8 = 1,200.$ $k = 6; 72X + 504X^2 + 990X^4 + 144X^6 + 144X^{10} + 144X^{14} + 144X^{18} + 144X^{22}$ $\text{CI} = 228,432,312; \text{atoms} = 10,368; \text{edges} = 15,120; R_6 = 1,728; R_8 = 2,160.$
	$R_{\max}(12)$ $k = 5; 27X^{100} + 6X^{1000}; \text{CI} = 69,420,000; R_{12} = 1,230.$ $k = 6; 33X^{144} + 6X^{1728}; \text{CI} = 210,014,208; R_{12} = 2,196.$

(continued)

**Table 8.5** (continued)

Net	Omega polynomial
BCA_96	$R_{\max}(8)$ $\Omega(\text{BCA}_96) = 36kX^2 + 12k(k-1)X^3 + 3(k-1)(k^2 - k + 8)X^4$ $+ 24(k-1)X^8 + 12k^2X^{4k} + \sum_{s=0}^{k-3} 24(k-s-2)(X^{10+6s} + X^{14+6s})$ $\Omega'(1) = 12k^2(9k+1) =  E(G)  = \text{edges}$ $\text{CI}(G) = 12k(972k^5 + 216k^4 - 16k^3 - 4k^2 + 3k + 1)$ $\text{atoms} = 24k^2(3k+1) =  V(G) $ $R_6 = 4k(5k-3); R_8 = 12k^3; R_{12} = 6k(k-1)^2$
Examples	$R_{\max}(8)$ $k=5; \Omega(G) = 180X^2 + 240X^3 + 336X^4 + 96X^8 + 72X^{10} + 72X^{14} + 48X^{16}$ $+ 348X^{20} + 24X^{22} + 24X^{26}$ $\text{CI} = 190,224,960; \text{atoms} = 9,600; \text{edges} = 13,800; R_6 = 2,200; R_8 = 1,500.$ $k=6; \Omega(G) = 216X^2 + 360X^3 + 570X^4 + 120X^8 + 96X^{10} + 96X^{14} + 72X^{16}$ $+ 72X^{20} + 48X^{22} + 432X^{24} + 48X^{26} + 24X^{28} + 24X^{32}$ $\text{CI} = 564,093,144; \text{atoms} = 16,416; \text{edges} = 23,760; R_6 = 3,888; R_8 = 2,592$

calculated on cuboids of  $(k, k, k)$  dimensions by the Nano Studio software (Nagy and Diudea 2009). Omega polynomial was calculated at  $R_{\max}(8)$  and  $R_{\max}(12)$ , respectively; examples are given in view of an easy verification of the general formulas. Also, formulas for the number of atoms, edges, and rings ( $R_6$ ,  $R_8$  and  $R_{12}$ ) are included in this table (Szeffler and Diudea 2012).

Formulas to calculate Omega polynomial and CI index in the two infinite networks BMTA20k and BMTZ20k, designed on the ground of BMTA1\_48 and BMTZ1\_24 units, are presented in Tables 8.6 and 8.7. Formulas were derived from the numerical data calculated on rods consisting of  $k$  units BMTX20. Omega polynomial was calculated at  $R_{\max} = R_8$ . Formulas for the number of atoms, edges, and rings ( $R_6$ ,  $R_8$ , and  $R_{15}$ , the last one being the simple ring of the hyper-ring BMTACy5) are included in Tables 8.6 and 8.7. Numerical examples are also given (Diudea and Szeffler 2012).

Omega polynomial description can be looked as an alternative to the crystallographic description, helping in understanding the topology of these networks.

## 8.7 Conclusions

Spanning fullerenes can be obtained by deleting some atoms or bonds from the graph of closed fullerenes, thus resulting in open structures which can further join to atoms of the same or different repeating units in construction of crystal- or quasicrystal-like networks. A variety of spanning fullerenes, designed either by cage opening or by sequences of map operations, has been used to build nano-dendrimers

**Table 8.6** Formulas for Omega polynomial and net parameters in linear periodic BMTA20.*k* network

BMTA20. <i>k</i>	$R_{\max}(8)$ $\Omega(\text{BMTA20.}k\text{-}R_8) = 10(k+2)X^3 + 5(k-1)X^4 + (11k+1)X^5 + 20(k+3)X^8$ $+ 10(k-1)X^{10} + 15(k-1)X^{12} + (11k+1)X^{20} + 10X^{2(3k+1)}$ $\Omega'(1) = 825k + 285 =  E(G)  = \text{edges};$ $\text{CI}(G) = 15(45, 351k^2 + 30, 715k + 5, 332);$ $\text{atoms} = 10(57k + 21) =  V(G) ;$ $R_6 = 5(27k + 7); \quad R_8 = 30(3k + 1); \quad R_{15} = 11k + 1$ $u_{48} = 20k - 5(k - 1) = 5(3k + 1) = R_8/6;$ $g = 1 + u_{48}$
Examples	$k = 5;$ $\text{CI} = 19,390,230; \text{atoms} = 3,060; \text{edges} = 4,410; R_6 = 710; R_8 = 480; R_{15} = 56;$ $u_{48} = 80; g = 81.$ $k = 6;$ $\text{CI} = 27,333,870; \text{atoms} = 3,630; \text{edges} = 5,235; R_6 = 845; R_8 = 570; R_{15} = 67;$ $u_{48} = 95; g = 96.$

**Table 8.7** Formulas for Omega polynomial and net parameters in linear periodic BMTZ20.*k* network

BMTZ20. <i>k</i>	$R_{\max}(8)$ $\Omega(\text{BMTZ20.}k\text{-}R_8) = 10(k+2)X^2 + 30kX^3 + (11k+1)X^5 + 10(k+5)X^6$ $+ 10(k-1)X^8 + 10(k-1)X^{10} + 6kX^{20}$ $\Omega'(1) = 525k + 165 =  E(G)  = \text{edges}$ $\text{CI}(G) = 5(55, 125k^2 + 33, 653k + 5, 392)$ $\text{atoms} = 120(3k + 1) =  V(G)  = 24u_{24} = 6R_6$ $R_6 = 20(3k + 1) =  V(G) /6; \quad R_8 = 15(5k + 1); \quad R_{15} = 11k + 1$ $u_{24} = 20k - 5(k - 1) = 5(3k + 1) = R_6/4;$ $g = 1 + u_{24}$
Examples	$k = 5; 70X^2 + 150X^3 + 56X^5 + 100X^6 + 40X^8 + 40X^{10} + 30X^{20}$ $\text{CI} = 7,758,910; \text{atoms} = 1,920; \text{edges} = 2,790; R_6 = 320; R_8 = 390; R_{15} = 56;$ $u_{24} = 80; g = 81$ $k = 6; 80X^2 + 180X^3 + 67X^5 + 110X^6 + 50X^8 + 50X^{10} + 36X^{20}$ $\text{CI} = 10,959,050; \text{atoms} = 2,280; \text{edges} = 3,315; R_6 = 380; R_8 = 465; R_{15} = 67;$ $u_{24} = 95; g = 96$

and crystal- and quasicrystal-like structures. Energetics of some open fullerenes has been calculated on optimized structures at Hartree-Fock and/or DFT level of theory. All of the discussed open fullerenes have shown less strained structures in comparison to C<sub>60</sub> reference fullerene, while the overall stability, as suggested by the total energy and HOMO-LUMO gap, is comparable or even better to the reference fullerene, thus being candidates to the status of real molecules. Omega polynomial was used to describe the topology of some periodic networks, designed by using benzene as the simplest patch.

**Acknowledgments** The work was supported in part by the Romanian CNCSIS-UEFISCSU project PN-II-ID-PCE-2011-3-0346 and in part by the computational grant no. 133 of PCSS (Poznań, Poland).

## References

- Ashrafi AR, Jalali M, Ghorbani M, Diudea MV (2008) *MATCH Commun Math Comput Chem* 60:905
- Benedek G, Vahedi-Tafreshi H, Barborini E, Piseri P, Milani P, Ducati C, Robertson J (2003) *Diamond Relat Mater* 12:768
- Blase X, Benedek G, Bernasconi M (2010) In: Colombo L, Fasolino A (eds) *Computer-based modeling of novel carbon systems and their properties. Beyond nanotubes*. Springer, Dordrecht, p 171
- Bonnet O (1853) *CR Acad Sci Paris* 37:529
- Cysewski P, Szeffler B (2010) *J Mol Model* 16:1709
- Diudea MV (2004) *Forma (Tokyo)* 19:131
- Diudea MV (2005) *J Chem Inf Model* 45:1002
- Diudea MV (2006) *Carpath J Math* 22:43
- Diudea MV (2010a) *Nanomolecules and nanostructures – polynomials and indices*, vol 10. University of Kragujevac, Serbia
- Diudea MV (2010b) *Int J Chem Model* 2:155
- Diudea MV (2010c) *MATCH Commun Math Comput Chem* 63:247
- Diudea MV (2010d) *Studia Univ Babeş Bolyai Chemia* 55(4):11
- Diudea MV, Katona G (1999) In: Newkome GA (ed) *Advances in dendritic macromolecules*. JAI Press Inc. Stamford, Connecticut, vol 4, p 135
- Diudea MV, Klavžar S (2010) *Acta Chim Slov* 57:565
- Diudea MV, Nagy CL (2007) *Periodic nanostructures*. Springer, Dordrecht
- Diudea MV, Petitjean M (2008) *Symmetry Cult Sci* 19(4):285
- Diudea MV, Gutman I, Jäntschl L (2002) *Molecular topology*. NOVA, New York
- Diudea MV, John PE, Graovac A, Primorac M, Pisanski T (2003) *Croat Chem Acta* 76:153
- Diudea MV, Cigher S, Vizitiu AE, Ursu O, John PE (2006a) *Croat Chem Acta* 79:445
- Diudea MV, Stefu M, John PE, Graovac A (2006b) *Croat Chem Acta* 79:355
- Diudea MV, Cigher S, John PE (2008) *MATCH Commun Math Comput Chem* 60:237
- Diudea MV, Cigher S, Vizitiu AE, Florescu MS, John PE (2009) *J Math Chem* 45:316
- Diudea MV, CsL N, Ilić A (2011) In: Putz MV (ed) *Carbon bonding and structures*. Springer, Dordrecht/Heidelberg/London/New York, p 273
- Diudea MV, Szeffler B (2012) *Nanotube junctions and the genus of multi-tori*. *Phys Chem Chem Phys* 14:8111–8115
- Djoković DŽ (1973) *J Comb Theor Ser B* 14:263
- Euler L (1758) *Novi Commun Acad Sci Imp Petrop* 4:109
- Gaussian 09, (2009) Revision A.1, Frisch MJ, Trucks GW, Schlegel HB, Scuseria GE, Robb MA, Cheeseman JR, Scalmani G, Barone V, Mennucci B, Petersson GA, Nakatsuji H, Caricato M, Li X, Hratchian HP, Izmaylov AF, Bloino J, Zheng G, Sonnenberg JL, Hada M, Ehara M, Toyota K, Fukuda R, Hasegawa J, Ishida M, Nakajima T, Honda Y, Kitao O, Nakai H, Vreven T, Montgomery JA, Peralta JE, Ogliaro F, Bearpark M, Heyd JJ, Brothers E, Kudin KN, Staroverov VN, Kobayashi R, Normand J, Raghavachari K, Rendell A, Burant JC, Iyengar SS, Tomasi J, Cossi M, Rega N, Millam NJ, Klene M, Knox JE, Cross JB, Bakken V, Adamo C, Jaramillo J, Gomperts R, Stratmann RE, Yazyev O, Austin AJ, Cammi R, Pomelli C,

- Ochterski JW, Martin RL, Morokuma K, Zakrzewski VG, Voth GA, Salvador P, Dannenberg JJ, Dapprich S, Daniels AD, Farkas Ö, Foresman JB, Ortiz JV, Cioslowski J, Fox DJ, Gaussian Inc, Wallingford
- Haddon RC (1987) *J Am Chem Soc* 109:1676
- Haddon RC (1990) *J Am Chem Soc* 112:3385
- Harary F (1969) *Graph theory*. Addison – Wesley, Reading
- Hargittai M, Hargittai I (2010) *Symmetry through the eyes of a chemist*. Springer, Dordrecht/London/New York/Heidelberg, p 488
- John PE, Vizitiu AE, Cigher S, Diudea MV (2007) *MATCH Commun Math Comput Chem* 57:479
- Klavžar S (2008) *MATCH Commun Math Comput Chem* 59:217
- Krygowski TM, Ciesielski A (1995) *J Chem Inf Comput Sci* 35:203
- Krygowski TM, Cyranski M (1996) *Tetrahedron* 52:1025564
- Lenosky T, Gonze X, Teter M, Elser V (1992) *Nature* 355:333
- Levine D, Steinhardt PJ (1984) *Phys Rev Lett* 53:2477
- Mackay AL (1981) *Kristallografiya (Sov Phys Chrystallogr)* 26:910 (517)
- Mackay AL, Terrones H (1991) *Nature* 352:762
- Nagy CL, Diudea MV (2009) *Nano studio software*. Babes-Bolyai University, Cluj
- Nagy K, Nagy CL, Diudea MV (2011) *MATCH Commun Math Comput Chem* 65:163
- O’Keeffe M, Adams GB, Sankey OF (1992) *Phys Rev Lett* 68:2325
- Schwarz HA (1865) *Über Minimalflächen*, Monatsber. Berlin Akad
- Schwarz HA (1890) *Gesammelte Matematische Abhandlungen*. Springer, Berlin
- Stefu M, Diudea MV (2005) *CVNET software*. Babes-Bolyai University, Cluj
- Stefu M, Diudea MV, John PE (2005) *Studia Univ Babes Bolyai Chemia* 50(2):165
- Szeffler B, Diudea MV (2012) *Polybenzene revisited*. *Acta Chim Slov* 59:795–802
- Szeffler B, Saheli M, Diudea MV (2012a) *Sumanene units in P-type surface networks*. *Acta Chim Slov* 59:177–182
- Szeffler B, Ponta O, Diudea MV (2012b) *Energetics of polybenzene multi tori*. *J Molec Struct* 1022:89–93
- Szeffler B, Diudea MV (2013) *Strain in Platonic fullerenes*. *Struct Chem*. doi:[10.1007/s11224-013-0244-y](https://doi.org/10.1007/s11224-013-0244-y)
- Terrones H, Mackay AL (1993) *Chem Phys Lett* 207:45
- Vizitiu AE, Cigher S, Diudea MV, Florescu MS (2007) *MATCH Commun Math Comput Chem* 57:457
- Winkler PM (1984) *Discrete Appl Math* 8:209

# Chapter 9

## Introducing “Colored” Molecular Topology by Reactivity Indices of Electronegativity and Chemical Hardness

Mihai V. Putz, Ottorino Ori, Marzio De Corato, Ana-Maria Putz, Giorgio Benedek, Franco Cataldo, and Ante Graovac<sup>†</sup>

**Abstract** Within the context of conceptual density functional theory chemical reactivity definitions of electronegativity (EN) and chemical hardness (HD), nine forms of their finite difference are expressed in order to consider the global “coloring” of the molecular topology with respect to their symmetry centers (atomic centers or bonding centers), according to the so-called Timișoara–Parma rule. The resulting parabolic-reactive energy in terms of EN and HD is compared with the

---

<sup>†</sup>Dedicated to Professor Ante Graovac, coauthor of this chapter, who prematurely passed away soon after the manuscript was completed.

M.V. Putz (✉)

Laboratory of Computational and Structural Physical Chemistry, Biology-Chemistry Department, West University of Timișoara, Pestalozzi Street No.16, Timișoara RO-300115, Romania

Research Center for Einstein Physics, Institute of Theoretical Physics, Free University Berlin, Arnimallee 14, 14195 Berlin, Germany

e-mail: [mvputz@cbg.uvt.ro](mailto:mvputz@cbg.uvt.ro); [mv\\_putz@yahoo.com](mailto:mv_putz@yahoo.com)

O. Ori (✉) • F. Cataldo

Research and Development Division, Actinium Chemical Research, Via Casilina 1626/A, 00133 Rome, Italy

e-mail: [ottorino.ori@alice.it](mailto:ottorino.ori@alice.it); [franco.cataldo@fastwebnet.it](mailto:franco.cataldo@fastwebnet.it)

M. De Corato

Dipartimento di Scienza dei Materiali, Università di Milano-Bicocca, Via R. Cozzi 53, 20125 Milan, Italy

Centro S3, CNR-Istituto Nanoscienze, I-41125 Modena, Italy

Dipartimento di Fisica, Università di Modena e Reggio Emilia, I-41125 Modena, Italy

e-mail: [m.decorato@campus.unimib.it](mailto:m.decorato@campus.unimib.it); [marzio.decorato@unimore.it](mailto:marzio.decorato@unimore.it)

A.-M. Putz

Laboratory of Inorganic Chemistry, Institute of Chemistry Timișoara of the Romanian Academy, 24 Mihai Viteazul Bld, Timișoara RO-300223, Romania

e-mail: [putzanamaria@yahoo.com](mailto:putzanamaria@yahoo.com)

bond topological Wiener index for short list of PAH (poly-aromatic hydrocarbons) selected as paradigmatic structures for validating the new reactivity descriptors based on topological quantities.

## 9.1 Introduction

Nowadays, many topological indices have been proposed and accepted in the chemical literature for representing relevant chemical features of an organic molecule by means of a number derivable from its structural formula or, in the modern interpretations, from its molecular graph, the available number of possible descriptors exceeding 1,000 and still increasing (see the updated atlas by Todeschini and Consonni 2000). To avoid the documented risk of dealing with elegant but purposeless graph-based formalism (Hollas et al. 2005), many molecular descriptors deal with Hückel  $\pi$ -electron energies and, in particular, with  $\pi$ -electron energies of the lowest unoccupied molecular orbitals (LUMOs), revealing the importance of the LUMO energy in quantitative structure–property relationships (QSPR) and quantitative structure activity relationship (QSAR) studies to predict various properties of *polycyclic aromatic hydrocarbons* (PAHs) (Nikolic et al. 2006; Bultinck et al. 2006; Mallion 2008). Descriptors related to the shape of momentum-space electron density (Al-Fahemi et al. 2009) or to the count of Kekulé structures (Vukicevic et al. 2006) are also successfully used, but probably the largest number of topological investigations are *based on graph connectivity* and *graph distance matrices*, as documented by the recent survey articles (Zhou and Trinajstić 2008, 2010), where an extensive use of the predictive properties of a number of molecular invariants is made, including the celebrated Wiener and Balaban indices. This approach is followed in this chapter, where we shall exploit the measures of the *topological molecular compactness*, conveyed by the Wiener index  $W(N)$ , combined with chemical information as the *atoms-in-molecules'* electronegativity and chemical hardness emerging from semiempirical quantum computation. By combining connectivity properties and  $\pi$ -electron energies, this enriched model generates new *colored* forms of the *reactive Wiener index*, returning the topological determinations of *molecular* electronegativity, chemical hardness, and  $\pi$ -parabolic energy described in the following paragraph. The introduction to this original formalism and the results of its application to a representative set of PAHs are given in the next sections.

---

G. Benedek

Dipartimento di Scienza dei Materiali, Università di Milano-Bicocca, Via R. Cozzi 53,  
20125 Milan, Italy

Donostia International Physics Center (DIPC), Paseo M. de Lardizábal 4,  
20018 Donostia/San Sebastián, Spain

e-mail: [giorgio.benedek@mater.unimib.it](mailto:giorgio.benedek@mater.unimib.it); [giorgio.benedek@unimib.it](mailto:giorgio.benedek@unimib.it)

## 9.2 Method of Reactivity-Colored Topological Indices

### 9.2.1 Electronegativity and Chemical Hardness Reactivity Indices (Putz 2011a)

Density functional theory (DFT) (Hohenberg and Kohn 1964) finds its application to open chemical systems, where the number  $N$  of electrons is subject to variations  $\Delta N$ , via the Fukui function (Yang et al. 1984; Parr and Yang 1989),

$$f(\mathbf{r}) \equiv \left( \frac{\partial \rho(\mathbf{r})}{\partial N} \right)_{V(\mathbf{r})} \quad (9.1)$$

representing the change of electron density  $\rho(\mathbf{r})$  due to the addition of one electron while keeping the potential  $V(\mathbf{r})$  constant and the normalization  $\int \rho(\mathbf{r}) d\mathbf{r} = N$ .

Electronegativity  $\chi$  and chemical hardness  $\eta$  acquire a central place in chemical reactivity through their conceptual reformulation in terms of the energy functional of the system  $E[\rho]$  (Gázquez et al. 1987; Putz 2011b):

$$\chi = \int \chi(\mathbf{r}) f(\mathbf{r}) d\mathbf{r}, \quad \chi(\mathbf{r}) \equiv - \left( \frac{\delta E[\rho]}{\delta \rho(\mathbf{r})} \right)_{V(\mathbf{r})}, \quad (9.2)$$

$$\eta = \int \eta(\mathbf{r}) f(\mathbf{r}) d\mathbf{r}, \quad \eta(\mathbf{r}) \equiv \int \eta(\mathbf{r}, \mathbf{r}') f(\mathbf{r}') d\mathbf{r}',$$

$$\eta(\mathbf{r}, \mathbf{r}') \equiv \frac{1}{2} \left( \frac{\delta^2 E[\rho]}{\delta \rho(\mathbf{r}) \delta \rho(\mathbf{r}')} \right)_{V(\mathbf{r})}, \quad (9.3)$$

where  $\chi(\mathbf{r})$  and  $\eta(\mathbf{r})$  are the *local* electronegativity and chemical hardness functions, respectively (Chattaraj et al. 1995; Fuentealba 1995; Torrent-Sucarrat et al. 2007, 2008, 2010), and  $\eta(\mathbf{r}, \mathbf{r}')$  is the chemical hardness kernel (Fuentealba 1995). Replacement of Eq. (9.1) into Eqs. (9.2) and (9.3) and integrations over the system volume yield, respectively (Parr et al. 1978; Parr and Pearson 1983),

$$\chi = - \left( \frac{\partial E}{\partial N} \right)_{V(\mathbf{r})} = -\mu, \quad \eta = \frac{1}{2} \left( \frac{\partial^2 E}{\partial N^2} \right)_{V(\mathbf{r})} = \frac{1}{2} \left( \frac{\partial \mu}{\partial N} \right)_{V(\mathbf{r})}, \quad (9.4)$$

where  $\mu$  is the chemical potential. Thus, within DFT, electronegativity is identified with the opposite of the electron chemical potential and the chemical hardness as one half of its derivative with respect to the electron number.

The total energy change in a chemical reaction implying a change in the electron density can then be approximately expressed as a *parabolic* function of the finite charge transfer  $\Delta N$  with coefficients  $\chi$  and  $\eta$ :

$$E[\rho + \Delta \rho] \cong E[\rho] - \chi \Delta N + \eta (\Delta N)^2 \quad (9.5)$$



**Table 9.1** Numerical parameters for the compact finite second (2C)-, fourth (4C)-, and sixth (6C)-order central differences; standard Padé (SP) schemes; sixth (6T)- and eight (8T)-order tridiagonal schemes; and eighth (8P)- and tenth (10P)-order pentadiagonal schemes up to spectral-like resolution (SLR) schemes for the electronegativity

Scheme	Electronegativity							
	$a_1$	$b_1$	$c_1$	$\alpha_1$	$\beta_1$	$e_1$	$e_2$	$e_3$
2C	1	0	0	0	0	1	0	0
4C	4/3	-1/3	0	0	0	1.167	-0.167	0
6C	3/2	-3/5	1/10	0	0	1.233	-0.267	0.033
SP	5/3	1/3	0	1/2	0	1	-0.667	0
6T	14/9	1/9	0	1/3	0	1.039	-0.463	0
8T	19/12	1/6	0	3/8	0	1.072	-0.510	0
8P	40/27	25/54	0	4/9	1/36	1.053	-0.530	-0.041
10P	17/12	101/150	1/100	1/2	1/20	1.048	-0.392	-0.068
SRL	1.303	0.994	0.038	0.577	0.090	1.061	-0.267	-0.105

Reproduced from Putz et al. (2004). Copyright (2004) by John Wiley and Sons; Putz (2010, b), Copyright (2011) by Bentham Science Publisher; Putz (2011c) – Copyright (2011) by NOVA Science Publishers, Inc.)

At this level of approximation, the Kohn–Sham equation can be cast into a compact finite difference (CFD) expression (Putz et al. 2004; Putz 2010, 2011b, c) and the coefficients  $\chi$  and  $\eta$  of the total energy expansion, Eq. (9.5), expressed in terms of the electron eigenstates near the Fermi level. As shown by Putz et al. (2004, Putz 2010, 2011b, c) in PAH molecular systems, the energies of the first three LUMO and HOMO (highest occupied molecular orbital) eigenstates,  $\varepsilon_{\text{LUMO}(k)}$ ,  $\varepsilon_{\text{HOMO}(k)}$  ( $k = 1, 2, 3$ ), respectively, allow to express  $\chi$  and  $\eta$  to a very good approximation, the convergence by addition of further LUMO and HOMO pairs being quite fast.

Ordinary topological descriptors of carbon networks are based on binary (0,1) adjacency matrices and topological distances as sums on binary elements. Colored molecular topology corrects binary topology for the configurational differences locally affecting electronegativity and chemical hardness, depending on the topological environment. As shown in Refs. Putz et al. (2004), and Putz (2010, 2011b, c), nine topological classes of increasing complexity can be defined, including the compact finite second (2C)-, fourth (4C)-, and sixth (6C)-order central differences, the standard Padé (SP), the sixth (6T)- and eight (8T)-order tridiagonal schemes, and the eighth (8P)- and tenth (10P)-order pentadiagonal schemes, up to spectral-like resolution (SLR) schemes. As shown in Appendix 9.A, for each of these topological classes, the CFD solution of Kohn–Sham equation, expressed through the parameters  $a_i$ ,  $b_i$ ,  $c_i$ ,  $\alpha_i$ ,  $\beta_i$ , where  $i = 1$  for  $\chi$  (Table 9.1) and  $i = 2$  for  $\eta$  (Table 9.2), allows to derive the corresponding CFD values  $\chi_{\text{CFD}}$  and  $\eta_{\text{CFD}}$  in terms of the 1st, 2nd, and 3rd HOMO and LUMO energies:

**Table 9.2** Same as Table 9.1 for the chemical hardness

Scheme	Chemical hardness							
	$a_2$	$b_2$	$c_2$	$\alpha_2$	$\beta_2$	$h_1$	$h_2$	$h_3$
2C	1	0	0	0	0	1	0	0
4C	4/3	-1/3	0	0	0	1.250	-0.083	0
6C	12/11	3/11	0	2/11	0	0.961	-0.130	0
SP	6/5	0	0	1/10	0	1.080	-0.120	0
6T	3/2	-3/5	1/5	0	0	1.372	-0.128	0.022
8T	147/152	51/95	-23/760	9/38	0	0.869	-0.098	-0.003
8P	320/393	310/393	0	344/1,179	23/2,358	0.790	-0.032	-0.008
10P	1,065/1,798	1,038/899	79/1,798	334/899	43/1,798	0.694	0.088	-0.009
SRL	0.216	1.723	0.177	0.502	0.056	0.582	0.354	0.008

$$\begin{aligned} \chi_{\text{CFD}} = & - \left[ a_1 (1 - \alpha_1) + \frac{1}{2} b_1 + \frac{1}{3} c_1 \right] \frac{\varepsilon_{\text{HOMO}(1)} + \varepsilon_{\text{LUMO}(1)}}{2} \\ & - \left[ b_1 + \frac{2}{3} c_1 - 2a_1 (\alpha_1 + \beta_1) \right] \frac{\varepsilon_{\text{HOMO}(2)} + \varepsilon_{\text{LUMO}(2)}}{4} \\ & - (c_1 - 3a_1 \beta_1) \frac{\varepsilon_{\text{HOMO}(3)} + \varepsilon_{\text{LUMO}(3)}}{6} \end{aligned} \quad (9.6)$$

$$\begin{aligned} \eta_{\text{CFD}} = & \left[ a_2 (1 - \alpha_2 + 2\beta_2) + \frac{1}{4} b_2 + \frac{1}{9} c_2 \right] \frac{\varepsilon_{\text{LUMO}(1)} - \varepsilon_{\text{HOMO}(1)}}{2} \\ & + \left[ \frac{1}{2} b_2 + \frac{2}{9} c_2 + 2a_2 (\beta_2 - \alpha_2) \right] \frac{\varepsilon_{\text{LUMO}(2)} - \varepsilon_{\text{HOMO}(2)}}{4} \\ & + \left[ \frac{1}{3} c_2 - 3a_2 \beta_2 \right] \frac{\varepsilon_{\text{LUMO}(3)} - \varepsilon_{\text{HOMO}(3)}}{6} \end{aligned} \quad (9.7)$$

When Eqs. (9.6) and (9.7) are written in the condensed form

$$\begin{aligned} \chi_{\text{CFD}} = & - \sum_{k=1}^3 e_k (\varepsilon_{\text{LUMO}(k)} + \varepsilon_{\text{HOMO}(k)}) / 2 \\ \eta_{\text{CFD}} = & \sum_{k=1}^3 h_k (\varepsilon_{\text{LUMO}(k)} - \varepsilon_{\text{HOMO}(k)}) / 2, \end{aligned} \quad (9.8)$$

it appears that the coefficients  $e_k$  and  $h_k$ , also listed in Table 9.1, are close to 1 for  $k = 1$  and  $\ll 1$  for  $k > 1$ . This confirms a dominant role of the first HOMO–LUMO pair, some contribution from the second pair, and a negligible role of the third pair, i.e., a good convergence of the CFD method.

Then, once the electronegativity and chemical hardness are computed up to the third HOMOs and LUMOs, the parabolic energy Eq. (9.5) can be eventually specialized for aromatic or  $\pi$ -systems under the working form

$$E_{\pi}(\chi, \eta) \cong -\chi N_{\pi} + \eta N_{\pi}^2 \quad (9.9)$$

Remarkably, it was recently shown to resemble the so-called  $\pi$ -reactive (generalized Huckel) energy (Putz 2011d),

$$E_{\pi}(\text{molecule}) \cong E_{\text{Bind}}(\text{molecule}) + E_{\text{Heat}}(\text{molecule}) - E_{\text{Total}}(\text{molecule}) \quad (9.10)$$

with a great accuracy also for complex aromatic compounds, making this approach most suitable for extended systems modeling; here  $E_{\text{Heat}}$  means the subtraction of the atomic heats of formation from the binding energy.

### 9.2.2 Coloring Topology by Reactivity via Timisoara–Parma Rule

One establishes the hierarchy of the above CFD methods by assessing the best correlation model between the two forms of energies, the  $\pi$ -parabolic and the  $\pi$ -reactive energies of Eqs. (9.9) and (9.10), respectively. The resulting correlation provides the hierarchy ranking of the CFD models according to their richness in electronic frontier orbitals' information.

The founding CFD hierarchy should be further respected when implemented to “color” the various parts of a molecule with electronegativity and chemical hardness information, according to the so-called *reactivity coloring (Timisoara–Parma) rule*: *The chemical descriptor ( $\chi$  or  $\eta$ ) values are distributed over all nodes of a molecule, grouped on sublattices, starting from the “central” most populated ones with bonding and nodes (frontier) electrons, while considering the equivalent/equidistant sublattice until all molecular atoms are colored, by decreasing the CFD values of such descriptors, assigning the last CFD value to the remaining atoms in the molecular space, if any.*

Figure 9.1 gives such an example for a PAH structure, the pentacene molecule, with the imposed CFD hierarchy (Putz et al. 2013).

From now on, any conventional topological index  $T$  is “translated” into its *topo-reactive* counterpart  $T(\chi)$  by coloring the nodes of the chemical graph with the molecular electronegativity values  $\chi$  to comply with the (Timisoara–Parma) rule. Then, by taking the square roots for any pair of atoms involved in a chemical bond, the bond itself is colored after this first computational step. Successive iterations allow the coloring of any paths connecting molecular nodes; by following the same process for chemical hardness values, the topological-reactivity energy assigned to invariants  $T(\chi)$  and  $T(\eta)$  arises from the parabolic form:

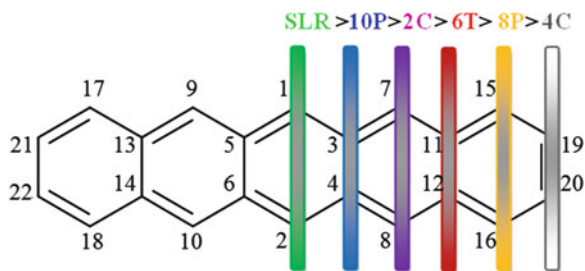


**Fig. 9.1** The chemical graph, with  $N = 22$  vertices, associated to hydrogen-depleted pentacene molecule. The coloring hierarchy of the CFD models is indicated by rectangles colored according to the distance of the vertices from the central atoms 1,2 characterized by SLR data. Rectangles respect the molecular plane of symmetry, e.g., 5,6 and 3,4 atom pairs feature 10P data, respectively (Tables 9.4 and 9.5), and so on

$$E_{(\chi,\eta)}^W = -T(\chi) N_\pi + T(\eta) N_\pi^2 \quad (9.11)$$

Note that the *topo-reactive* indices specifically adopted in this work do not need further normalization factors; this is because the colored invariants are directly generated on the basis of the coloring hierarchy of the CFD-like energy matrices, see Eqs. (9.19) and (9.20).

### 9.2.3 Topological Invariants of Molecular Graphs

On a chemical graph  $G(N)$  with  $N$  atoms,  $W(N)$  represents an invariant of the graph arising from the half summation of the minimum topological distances  $d_{ij}$  between all pairs of  $G(N)$  vertices (Wiener 1947; Cataldo et al. 2010, 2011a; Iranmanesh et al. 2012):

$$W(N) = 1/2 \sum_{ij} d_{ij}, \quad d_{ii} = 0, \quad i, j = 1, 2, \dots, N - 1, N. \quad (9.12)$$

Topological distances  $d_{ij}$  compose the  $N \times N$  symmetric distance matrix of the graph  $\widehat{D} = [d_{ij}]$ . In the present study,  $N$  corresponds not only to the number carbon atoms but also to the number  $N_\pi$  of available  $\pi$ -electrons in each PAH.

The Wiener index, Eq. (9.12), measures the average *topological compactness* of the molecular graphs and, when a minimum principle is imposed on it,  $W(N)$  promptly selects the stable systems among isomeric candidates, as demonstrated by recent studies on fullerene isomers or defective graphenic planes. Different applications of topological modeling (TM) methods are illustrated in Ori and D’Mello (1992, 1993), and in the recent extended report Iranmanesh et al. (2012), as well as in Chap. 6. Indicating with  $M(N)$  the graph *diameter* (e.g., the largest

distance in the graph) and with  $b_{ik}$  the number of  $k$ -neighbors of the  $i$ -atom, the contribution  $w_i$  to (9.12) is

$$w_i = 1/2 \sum_k k b_{ik}, \quad k = 1, 2, \dots, M-1, M \quad (9.13)$$

with  $W(N) = \sum_i w_i$  and  $1 - N = \sum_k b_{ik}$  for each graph vertex  $i$ .

Carbon  $sp^2$  networks such as fullerenes, nanotori and graphene, and schwarzites with periodic boundary conditions have coordination  $b_{i1} = 3$  at each node. In case of PAH molecules, atom coordination is either  $b_{i1} = 2$  or  $b_{i1} = 3$ , the lowest value occurring at the molecular boundary. From Eq. (9.13), both minimal  $\underline{w}$  and maximal  $\underline{\underline{w}}$  contributions to  $W(N)$

$$\underline{w} = \min \{w_i\} \quad i = 1, 2, \dots, N-1, N \quad (9.14)$$

$$\underline{\underline{w}} = \max \{w_i\} \quad i = 1, 2, \dots, N-1, N \quad (9.15)$$

originate two new important invariants, the *topological efficiency index*  $\rho$  and the *extreme topological efficiency index*  $\rho^E$ :

$$\rho = \frac{W}{N\underline{w}} \quad \rho \geq 1 \quad (9.16)$$

$$\rho^E = \frac{\underline{\underline{w}}}{\underline{w}} \quad \rho^E \geq 1 \quad (9.17)$$

Descriptor  $\rho$  has been firstly introduced in Ref. Cataldo et al. (2011b), on graphenic lattices, whereas  $\rho^E$  has been recently proposed by Vukicevic (2010, personal communication) and successfully applied to schwarzitic structures (De Corato et al. 2012) being also implemented in currently nano-structures' computational codes (Schwerdtfeger et al. 2012). By definition these invariants shall privilege, with some numerical differences, chemical structures growing in the most compact way around their minimal sites. For icosahedral  $C_{60}$  fullerene and benzene ring, both invariants reach the lower limits  $\rho = \rho^E = 1$  to signal that all atoms are equivalent by symmetry. This result inspires the TM guiding criterion for stable systems: *the smallest is the topological efficiency index, the highest is the stability of the chemical structure under examination*. For a given vertex  $i$  of  $G$ , its *eccentricity*  $\varepsilon_i$  is the largest distance between  $i$  and any other vertex of  $G$ , the maximum possible eccentricity corresponding to graph diameter  $M = \max\{\varepsilon_i\}$ . The *eccentric connectivity index*  $\xi(N)$  of a graph  $G$  is a molecular descriptor defined as (Sharma et al. 1997; Dureja and Madan 2007)

$$\xi(N) = 1/2 \sum_i b_{i1} \varepsilon_i \quad (9.18)$$

where  $b_{i1}$  gives the number of bonds of atom  $v_i$ . Clearly,  $b_{ik} = 0$  for  $\varepsilon_i < k < M$ . Recent papers (Kumar et al. 2004; Ashrafi et al. 2011; Došlić et al. 2010, 2011) present various applications of the topological invariant (9.18) to the study of chemical–physical properties of crystallographic materials.

The key passage of our method consists therefore in computing the colored or reactive version  $\widehat{W}_\chi$  and  $\widehat{W}_\eta$  of the distance matrix  $\widehat{D}$  as requested by the above computational scheme. These operators, also called Wiener electronegativity and Wiener chemical hardness matrices, properly carry the chemical information, leading to the reactive forms of the Wiener index for electronegativity  $W(\chi)$  and chemical hardness  $W(\eta)$ . The extraction of the  $W(\chi)$  and  $W(\eta)$  reactive indices from the newly defined operators  $\widehat{W}_\chi$  and  $\widehat{W}_\eta$  may follow several mathematical routes. Here, in order to evidence the rich chemical implications of our model, a basic formal choice for these new topological descriptors has been made:

$$W(\chi) = \det^{1/N_\pi} \left\| \widehat{W}_\chi \right\|, \quad (9.19)$$

$$W(\eta) = \det^{1/N_\pi} \left\| \widehat{W}_\eta \right\|. \quad (9.20)$$

Both matrices  $\widehat{W}_\chi$  and  $\widehat{W}_\eta$  are symmetric, preserving the symmetry of the  $\widehat{D}$  template. Clearly both Wiener-reactive invariants  $W(\chi)$  and  $W(\eta)$  given in Eqs. (9.19) and (9.20) are the simplest representatives of a wide class of topological invariants obtainable from the matrices  $\widehat{W}_\chi$  and  $\widehat{W}_\eta$  with more elaborate mathematical operations.

The final formulae for the elements of the Wiener-reactive matrices (also called reactive members or colored members or weights) consider, for obvious dimensional reasons, the geometric average of the  $1 + d_{ij}$  colors of the atoms present in the path  $i \rightarrow j$ :

$$w_{ij}(\chi) = [\widehat{W}_\chi]_{ij} = \left( \prod_{i \rightarrow j} \chi_\alpha \right)^{1/(1+d_{ij})} \quad (9.21)$$

$$w_{ij}(\eta) = [\widehat{W}_\eta]_{ij} = \left( \prod_{i \rightarrow j} \eta_\alpha \right)^{1/(1+d_{ij})} \quad (9.22)$$

In the above expressions, the index  $\alpha$  runs over the  $1 + d_{ij}$  atoms in the minimal path  $i \rightarrow j$  connecting  $i$  to  $j$ . The forms of the reactive members of Eqs. (9.21) and (9.22) evidence the essential role played by molecular topological information stored in the minimal path  $i \rightarrow j$  in predicting the chemical–physical properties of the molecule.

### 9.3 Working Example: Short List of PAHs

The colored algorithm is here illustrated for a short list of PAH structures: benzene, naphthalene, pentacene, and perylene; while for pentacene the colored recipe was illustrated in Fig. 9.1, the same rule is applicable to the other compounds, e.g., to perylene (Fig. 9.2).

The electro-topological coloring algorithm presented in Sect. 9.2 is unfolded for the working PAHs following the successive steps:

- Computing the first three HOMOs and LUMOs, reported in Table 9.3.
- Evaluating the compact finite differences of electronegativity and chemical hardness, employing the values of Table 9.3 in the Eq. (9.8) with coefficients of Tables 9.1 and 9.2, with the results in Tables 9.3 and 9.4, respectively.
- Considering the working PAHs upon the scheme of CFD hierarchy, as deduced by best fitting of the resulted parabolic energies with pi-energies, Eqs. (9.9) and (9.10), for a larger set of PAH molecules (Putz et al. 2013), with the coloring example showcased in Fig. 9.1.

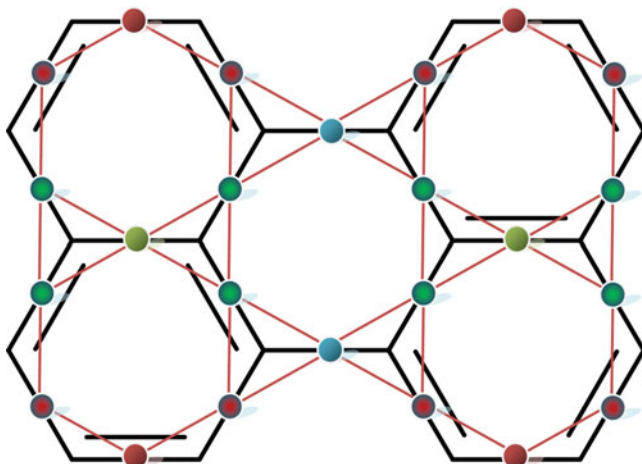


**Fig. 9.2** Illustration of the coloring of the perylene structure, respecting its most “dense” symmetrical (*horizontal-middle*) axis, following the Timisoara–Parma rule, as described in Fig. 9.1 and Sect. 9.2.2

**Table 9.3** Electronic frontier energetic (in electron volts) properties for benzene, naphthalene, pentacene, and perylene PAH molecules as computed from semiempirical PM3 method

No. crt.	Molecule	$N_\pi$	HOMO1	LUMO1	HOMO2	LUMO2	HOMO3	LUMO3
1.	Benzene	6	-9.751329	0.396204	-9.75139	0.396271	-12.3761	2.86574
2.	Naphthalene	10	-8.836945	-0.40645	-9.43547	0.064889	-10.678	1.081978
3.	Perylene	20	-7.98719	-1.27454	-9.49631	0.007553	-9.54391	0.055699
4.	Pentacene	22	-7.611723	-1.62693	-8.8098	-0.5153	-9.11749	-0.33304

**Table 9.4** Electronegativity values (in electron volts) for the molecules of Table 9.2 as computed upon Eq. (9.6) and the numerical schemes of Table 9.1

No.	$\chi_{2C}$	$\chi_{4C}$	$\chi_{6C}$	$\chi_{SP}$	$\chi_{6T}$	$\chi_{8T}$	$\chi_{8P}$	$\chi_{10P}$	$\chi_{SLR}$
1.	4.677563	4.677563	4.68015	1.559189	2.945133	2.63113	2.54733	2.528442	2.783443
2.	4.621695	4.611096	4.610614	1.498169	2.880514	2.567244	2.483035	2.463587	2.716915
3.	4.630863	4.611944	4.604367	1.467943	2.863175	2.54692	2.467261	2.450888	2.711043
4.	4.619324	4.61212	4.611329	1.510958	2.888452	2.576307	2.494174	2.476	2.730185

**Table 9.5** Chemical hardness values (in electron volts) for the molecules of Table 9.3 as computed upon Eq. (9.7) and the numerical schemes of Table 9.2

No.	$\eta_{2C}$	$\eta_{4C}$	$\eta_{6C}$	$\eta_{SP}$	$\eta_{6T}$	$\eta_{8T}$	$\eta_{8P}$	$\eta_{10P}$	$\eta_{SLR}$
1.	5.073767	5.919389	4.214153	4.870808	6.483366	3.884713	3.781969	3.895765	4.808069
2.	4.21525	4.873214	3.431467	3.982449	5.307959	3.176384	3.128272	3.287641	4.180482
3.	3.356327	3.799414	2.606034	3.054601	4.105097	2.433524	2.458452	2.701619	3.67288
4.	2.992399	3.394895	2.335101	2.734121	3.673915	2.178059	2.193885	2.399796	3.243817

**Table 9.6** Topological descriptors are detailed for short list of PAH's subject of the present investigation

No.	$N_{\pi}$	$W(N)$	W-EL	W-CH	W-E <sub>p</sub>	$\xi(N)$	$\rho$	$\rho^E$
1.	6	27	3.413	5.458	176.022	36	1	1
2.	10	109	3.504	4.745	439.457	90	1.282	1.471
3.	20	654	3.050	3.601	1,379.215	286	1.258	1.462
4.	22	1,011	3.328	3.207	1,478.855	448	1.259	1.658

Table reports the number of  $\pi$ -electrons and the Wiener index  $W(N)$ , along its colored reactive forms as such electronegativity (W-EL), chemical hardness (W-HD), and parabolic reactivity energy (W-E<sub>p</sub>); for comparison purposes also the eccentric connectivity  $\xi(N)$  and both topological efficiency indices  $\rho$  and  $\rho^E$  were added; all these invariants are computed properly considering Eqs. (9.12), (9.13), (9.14), (9.15), (9.16), (9.17), (9.18), (9.19), (9.20), (9.21) and (9.22)

- Coloring the topological descriptors with reactivity (frontier orbitals) contents: the conventional or newly proposed topological index is “translated” into a topo-reactive one by considering the topological matrix of that index and coloring it with molecular electronegativity values for nodes according to the Timisoara–Parma rule; then, take  $n$ -roots for any  $n$ -coupling reticules of whatever nodes within the molecule forming bonds and paths for given molecule or extended system.
- For a given scheme of coloring, Eqs. (9.12), (9.13), (9.14), (9.15), (9.16), (9.17), (9.18), (9.19), (9.20), (9.21) and (9.22) are applied with the computed electronegativity and chemical hardness values of Tables 9.4 and 9.5 to produce the parabolic-reactive counterpart – Eq. (9.11) – of the Wiener classical index, with the results listed in Table 9.6, along other topological indices of interest, e.g., eccentric connectivity  $\xi(N)$  and both topological efficiency indices  $\rho$  and  $\rho^E$  (erho).



**Table 9.7** Experimental octanol–water partition coefficients ( $\log K_{OW}$ ) and the (van Den Dool–Kratz) retention indices (RI) Van Den Dool and Kratz (1963) for the actual PAHs; the non-available data by literature (marked with “\*”) were interpolated through the correlations with the molecular weight (MW, Da) (Putz et al. 2013)

No.	Molecule	CAS	Formula	MW (D) <sup>a</sup>	$\log K_{OW}$ <sup>b</sup>	RI
1.	Benzene	71-43-2	C <sub>6</sub> H <sub>6</sub>	78.11	2.13	663 <sup>c</sup>
2.	Naphthalene	91-20-3	C <sub>10</sub> H <sub>8</sub>	128.17	3.33	1,208 <sup>c</sup>
3.	Perylene	198-55-0	C <sub>20</sub> H <sub>12</sub>	252.31	6.16*	2,795 <sup>d</sup>
4.	Pentacene	135-48-8	C <sub>22</sub> H <sub>14</sub>	278.35	7.19	3,125.02*

<sup>a</sup>Chemical Book (2011), <sup>b</sup>Duchowicz et al. (2007), <sup>c</sup>Engel and Ratel (2007) and <sup>d</sup>Beernaert (1979)

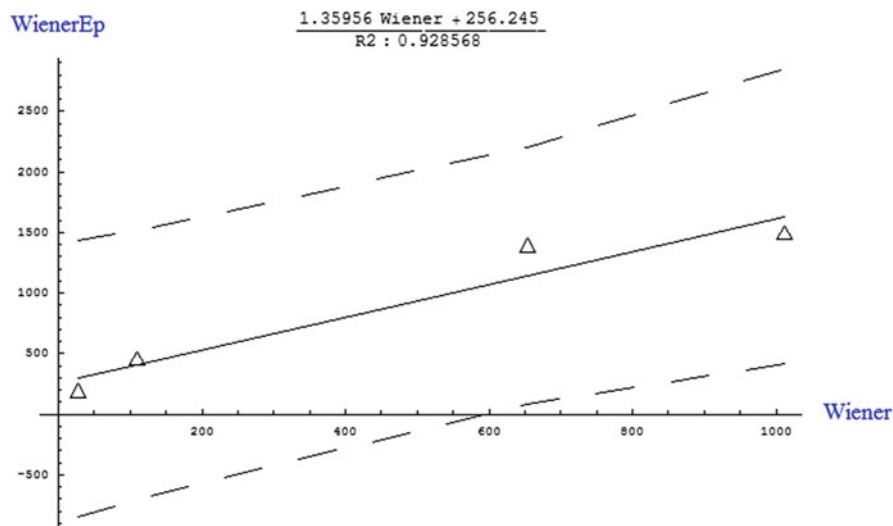


**Fig. 9.3** The linear correlation, with confidence interval emphasized, between colored parabolic Wiener index (WienerEp) and the classical one (Wiener) for the short list of PAH values of Table 9.6

- For further analysis purpose, the structural–experimental values of octanol–water partition coefficients ( $\log K_{OW}$ ), retention indices (RI), and molecular weight (MW) are also considered in Table 9.7.

The main results of Table 9.6 allow the following interesting analysis and remarks:

- The reactive-parabolic colored Wiener index (WEp) correlates satisfactory with the classical Wiener index ( $W$ ), as illustrated by Fig. 9.3.
- In general, the reactive-parabolic colored Wiener index (WEp) correlates below the performances of the classical Wiener ( $W$ ) index respecting the structural properties as eccentric connectivity  $\xi(N)$  and both topological efficiency indices  $\rho$  and  $\rho^E$  (erho) of Table 9.6, as reported in Table 9.8 and Fig. 9.4.

**Table 9.8** Synopsis of the correlations of the colored parabolic Wiener (W-Ep) and classical Wiener (W) indices respecting the topological–structural and experimental–structural indices of Tables 9.6 and 9.7, respectively

Index	Colored Wiener (W-Ep)		Wiener (W)	
	Correlation equation	$R^2$	Correlation equation	$R^2$
Topo				
$\xi$	$152.918 + 3.32776 \xi$	0.913574	$-79.3108 + 2.46307 \xi$	0.996269
$\rho$	$N_{\pi}^2 (9.17285 - 4.35587\rho)$	0.476645	$N_{\pi}^2 (-2.16655 + 2.96521\rho)$	0.449428
$\rho^E$	$N_{\pi}^2 (7.54575 - 2.574 \text{ etho})$	0.731919	$N_{\pi}^2 (-1.16315 + 1.82731 \text{ etho})$	0.7501
Exp				
MW	$-384.741 + 6.80179 \text{ MW}$	0.995143	$-412.854 + 4.6848 \text{ MW}$	0.939732
RI	$-199.444 + 0.548237 \text{ RI}$	0.996871	$-287.352 + 0.378693 \text{ RI}$	0.946806
$\log K_{ow}$	$N_{\pi}^2 (5.62047 - 0.35589 \log K_{ow})$	0.998674	$N_{\pi}^2 (0.229253 + 0.247041 \log K_{ow})$	0.97911

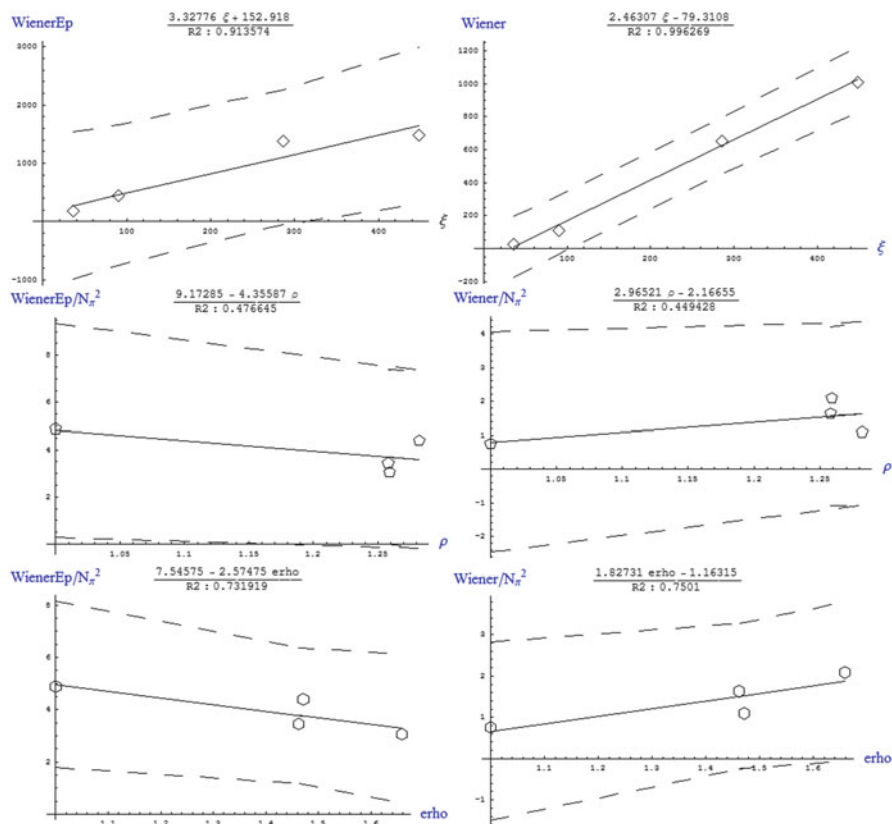


**Fig. 9.4** The linear correlations, with confidence intervals emphasized, between colored parabolic Wiener index (WienerEp) and the topo-structural PAHs' properties of Table 9.6 vis-à-vis with the same type of correlations for the classical one (Wiener). Parameter “erho” corresponds to  $\rho^E$

- Instead, the reactive-parabolic colored Wiener index (WEp) always correlates above the performances of the classical Wiener (W) index respecting the experimental properties as octanol–water partition coefficients ( $\log K_{OW}$ ), retention indices (RI), and molecular weight (MW) of Table 9.7, as reported in Table 9.8 and Fig. 9.5.

Overall, it appears that the present scheme of parabolically coloring the topological indices by chemical reactivity information of electronegativity and chemical hardness, Eqs. (9.18) and (9.19), (9.20), (9.21) and (9.22), provides a richer topo-reactive information whose reliability is proved by better correlation with experimentally recorded (or interpolated) structural observation. However, such promising finding has to be further tested for an enlarged set of PAH, on other paradigmatic working analogues, and implemented for other topological invariants.

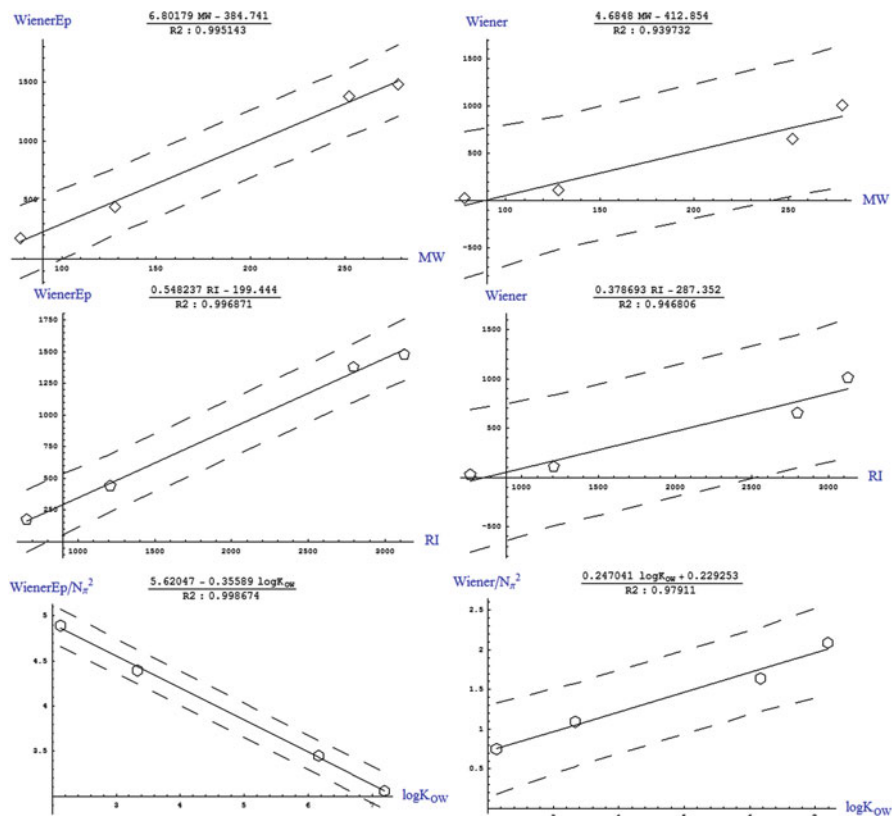


**Fig. 9.5** The linear correlations, with confidence intervals emphasized, between colored parabolic Wiener index (WienerEp) and the experimental–structural PAHs’ properties of Table 9.7 vis-à-vis with the same type of correlations for the classical one (Wiener) for the values of Table 9.6

## 9.4 Conclusion

In order to provide more significance to the topological indices, the present work advances the idea of “coloring” them by employing the parabolic energetic dependency of chemical reactivity by electronegativity and chemical hardness, as prescribed by the celebrated conceptual density functional theory applied to quantum chemistry. The result is an original method that makes use of the nine compact finite difference (CFD) forms of electronegativity and chemical hardness to be considered, *mutatis mutandis*, like a ninth-order expansion of a single-global reactivity index, respectively. The coloring procedure relies on the so-called Timisoara–Parma rule, according to which, given a molecular structure, the nine forms of electronegativity and chemical hardness are distributed on equivalent nodes/vertices on sublattices starting from the central axis where the most dense

population of electrons is located. The CFD hierarchy employed for coloring the molecular structure provides the best correlations, recorded in the parabolic energy, between chemical reactivity and the  $\pi$ -reactive energy. The coloring procedure as a whole appears therefore different in respect to a “simple” weighting of the molecular topology with *different atomic chemical reactivity indices* on different nodes, depending on the chemical nature of those nodes; instead, the adopted coloring scheme considers here *the same molecular chemical reactivity index* (electronegativity and chemical hardness) distributed over all nodes of the molecule up to the ninth CFD forms (or better, perturbation forms involving more and more complex combinations of HOMOs and LUMOs), according to the axial distribution of equivalent nodes in respect to the central most dense population. It is somehow equivalent to “light dispersion” in a medium, leading to unfolding of its spectra – from where originates the coloring name. The present application to the Wiener index on a short list of PAHs shows that the resulted parabolically colored counterparts give a good correlation with the experimental–structural properties in a greater measure than the classical topological index.

Grouping molecular graph nodes into shells of atoms having the same eccentricity represents another interesting ranking method based on topology that, starting from the shell of maximum eccentricity  $M$ , scales down to the central atoms having the minimum eccentricity  $M - m + 1$ , where  $m$  is the number of shells. Each shell is colored with different values  $\chi_j$  and  $\eta_j$  ( $j = M - m + 1, M - m + 2, \dots, M$ ) of the local electronegativity and chemical hardness. This alternative method relies on the assumption that  $\chi_j$  and  $\eta_j$  for increasing  $m$  converge to constant values  $\chi_{\text{SLR}}$  and  $\eta_{\text{SRL}}$  and that sufficiently good convergence is reached for  $m > 7$  so that eight colors are sufficient to characterize the chemical graph as in the Timisoara–Parma recipe. These considerations open therefore a promising way of combining the fruitful topological mathematical information extracted from chemical systems (that works better as the system is more extended) with the observability character of the chemical information encompassed in chemical reactivity modeled by parabolic paradigm of electronegativity and chemical hardness within the density functional theory.

Finally we want to stress that the paradigmatic choice of PAHs for illustrating the use of colored topological indices is related to the worldwide academic and industrial interest for PAH health impact and environmental protection. To summarize a few relevant aspects, it is known that:

1. Mixtures of PAHs can cause skin irritation and inflammation. Anthracene, benzo(*a*)pyrene, and naphthalene are direct skin irritants, while anthracene and benzo(*a*)pyrene are reported to be skin sensitizers, i.e., cause an allergic skin response in animals and humans (INCHEM 1998).
2. Benzo(*a*)pyrene is the most common PAH to cause **cancer** in animals, and this compound is notable for being the first chemical carcinogen to be discovered. Based on the available evidence, both the [International Agency for Research on Cancer \(2005\)](#) and [US EPA \(1994\)](#) classified a number of PAHs as carcinogenic to animals and some PAH-rich mixtures as carcinogenic

to humans. The EPA has classified seven PAH compounds as probable human carcinogens: benz(*a*)anthracene, benzo(*a*)pyrene, benzo(*b*)fluoranthene, benzo(*k*)fluoranthene, chrysene, dibenz(*ah*)anthracene, and indeno(1,2,3-*cd*)pyrene.

- Most of the PAHs are not genotoxic by themselves, and they need to be metabolized to the diol epoxides which react with DNA, thus inducing genotoxic damage. However, genotoxicity plays important role in the carcinogenicity process and maybe in some forms of developmental toxicity as well.

These few examples suggest that a large number of more complex and poorly known harmful PAHs may be formed in industrial as well as in natural processes, which require a rapid and viable assessment of their reactivity. The topological approach, besides providing an efficient tool to predict possible complex structures not yet identified or hard to isolate and directly test in the laboratory, also allows, in its colored upgraded version, to predict their reactivity and their potential hazardousness.

**Acknowledgments** MVP and AMP thank Romanian Ministry of Education and Research for supporting the present work through the CNCSIS–UEFISCDI project “Quantification of the Chemical Bond Within Orthogonal Spaces of Reactivity. Applications on Molecules of Bio-, Eco- and Pharmaco-Logical Interest,” Code TE-16/2010-2013. MVP thanks German Academic Exchange Service (Deutscher Akademischer Austausch Dienst) for the fellowship DAAD/A/11/05356/322, allowing this chapter to be initiated at Free University of Berlin; MVP and OO are grateful to Prof. Hagen Kleinert and Dr. Axel Pelster for the warm hospitality at Free University Berlin in the summer of 2011 where this chapter was initiated.

## Appendix 9. A Compact Finite Differences for Electronegativity and Chemical Hardness

Given the values of a function  $f(n)$  on a set of nodes  $\{\dots, n-3, n-2, n-1, n, n+1, n+2, n+3, \dots\}$ , the finite difference approximations of the first  $f'_n$  and second  $f''_n$  derivatives in the node  $n$  will spectrally depend on all the nodal values. However, the compact finite differences, or Padé, schemes that mimic this global dependence is written as (Lele 1992)

$$\begin{aligned} & \beta_1 f'_{n-2} + \alpha_1 f'_{n-1} + f'_n + \alpha_1 f'_{i+1} + \beta_1 f'_{n+2} \\ & = c_1 \frac{f_{n+3} - f_{n-3}}{6} + b_1 \frac{f_{n+2} - f_{n-2}}{4} + a_1 \frac{f_{n+1} - f_{n-1}}{2} \end{aligned} \quad (9.A.1)$$

$$\begin{aligned} & \beta_2 f''_{n-2} + \alpha_2 f''_{n-1} + f''_n + \alpha_2 f''_{i+1} + \beta_2 f''_{n+2} \\ & = c_2 \frac{f_{n+3} - 2f_n + f_{n-3}}{9} + b_2 \frac{f_{n+2} - 2f_n + f_{n-2}}{4} + a_2 (f_{n+1} - 2f_n + f_{n-1}). \end{aligned} \quad (9.A.2)$$

The involved sets of coefficients,  $\{a_1, b_1, c_1, \alpha_1, \beta_1\}$  and  $\{a_2, b_2, c_2, \alpha_2, \beta_2\}$ , are derived by matching Taylor series coefficients of various orders. In this way, their particularizations can be reached as the second (2C)-, fourth (4C)-, and sixth (6C)-order central differences; standard Pade (SP) schemes; sixth (6T)- and eight (8T)-order tridiagonal schemes; and eighth (8P)- and tenth (10P)-order pentadiagonal schemes up to spectral-like resolution (SLR) ones; see Table 9.1.

Assuming that the function  $f(n)$  is the total energy  $E(N)$  in the actual node that corresponds to the number of electrons and the compact finite difference, the derivatives of Eqs. (9.2) and (9.5) may be accurately evaluated through considering the states with  $N-3, N-2, N-1, N+1, N+2$ , and  $N+3$  electrons, whereas the derivatives in the neighbor states will be taken only as their most neighboring dependency. This way, the working formulas for electronegativity will be (Putz 2010)

$$\begin{aligned}
 -\chi &= \frac{\partial E}{\partial N} \Big|_{|N\rangle} \\
 &\cong a_1 \frac{E_{N+1} - E_{N-1}}{2} + b_1 \frac{E_{N+2} - E_{N-2}}{4} + c_1 \frac{E_{N+3} - E_{N-3}}{6} \\
 &\quad - \alpha_1 \left( \frac{\partial E}{\partial N} \Big|_{|N-1\rangle} + \frac{\partial E}{\partial N} \Big|_{|N+1\rangle} \right) - \beta_1 \left( \frac{\partial E}{\partial N} \Big|_{|N-2\rangle} + \frac{\partial E}{\partial N} \Big|_{|N+2\rangle} \right) \\
 &= a_1 \frac{E_{N+1} - E_{N-1}}{2} + b_1 \frac{E_{N+2} - E_{N-2}}{4} + c_1 \frac{E_{N+3} - E_{N-3}}{6} \\
 &\quad - \alpha_1 \left( a_1 \frac{E_N - E_{N-2}}{2} + a_1 \frac{E_{N+2} - E_N}{2} \right) \\
 &\quad - \beta_1 \left( a_1 \frac{E_{N-1} - E_{N-3}}{2} + a_1 \frac{E_{N+3} - E_{N+1}}{2} \right) \\
 &= a_1 (1 + \beta_1) \frac{E_{N+1} - E_{N-1}}{2} + (b_1 - 2a_1\alpha_1) \frac{E_{N+2} - E_{N-2}}{4} \\
 &\quad + (c_1 - 3a_1\beta_1) \frac{E_{N+3} - E_{N-3}}{6} \tag{9.A.3}
 \end{aligned}$$

and respectively for the chemical hardness as (Putz et al. 2004)

$$\begin{aligned}
 2\eta &= \frac{\partial^2 E}{\partial N^2} \Big|_{|N\rangle} \\
 &\cong 2a_2 \frac{E_{N+1} - 2E_N + E_{N-1}}{2} + b_2 \frac{E_{N+2} - 2E_N + E_{N-2}}{4} + c_2 \frac{E_{N+3} - 2E_N + E_{N-3}}{9} \\
 &\quad - \alpha_2 \left( \frac{\partial^2 E}{\partial N^2} \Big|_{|N-1\rangle} + \frac{\partial^2 E}{\partial N^2} \Big|_{|N+1\rangle} \right) - \beta_2 \left( \frac{\partial^2 E}{\partial N^2} \Big|_{|N-2\rangle} + \frac{\partial^2 E}{\partial N^2} \Big|_{|N+2\rangle} \right)
 \end{aligned}$$

$$\begin{aligned}
&= 2a_2 \frac{E_{N+1} - 2E_N + E_{N-1}}{2} + b_2 \frac{E_{N+2} - 2E_N + E_{N-2}}{4} + c_2 \frac{E_{N+3} - 2E_N + E_{N-3}}{9} \\
&\quad - \alpha_2 \left( 2a_2 \frac{E_N - 2E_{N-1} + E_{N-2}}{2} + 2a_2 \frac{E_{N+2} - 2E_{N+1} + E_N}{2} \right) \\
&\quad - \beta_2 \left( 2a_2 \frac{E_{N-1} - 2E_{N-2} + E_{N-3}}{2} + 2a_2 \frac{E_{N+3} - 2E_{N+2} + E_{N+1}}{2} \right) \\
&= 2a_2 (1 + 2\alpha_2 - \beta_2) \frac{E_{N+1} + E_{N-1}}{2} + (8a_2\beta_2 + b_2 - 4a_2\alpha_2) \frac{E_{N+2} + E_{N-2}}{4} \\
&\quad + (c_2 - 9a_2\beta_2) \frac{E_{N+3} + E_{N-3}}{9} - \left( 2a_2 + \frac{1}{2}b_2 + \frac{2}{9}c_2 + 2a_2\alpha_2 \right) E_N \quad (9.A.4)
\end{aligned}$$

where the involved parameters discriminate between various schemes of computations and the spectral-like resolution – SLR (Lele 1992).

Next, Eqs. (9.A.3) and (9.A.4) may be rewritten in terms of the observational quantities, as the ionization energy and electronic affinity are with the aid of their basic definitions from the involved eigen-energies of  $i$ th ( $i = 1, 2, 3$ ) order:

$$I_i = E_{N-i} - E_{N-i+1} \quad (9.A.5)$$

$$A_i = E_{N+i-1} - E_{N+i} \quad (9.A.6)$$

As such they allow the energetic equivalents for the differences (Putz 2010)

$$E_{N+1} - E_{N-1} = -(I_1 + A_1) \quad (9.A.7)$$

$$E_{N+2} - E_{N-2} = -(I_1 + A_1) - (I_2 + A_2) \quad (9.A.8)$$

$$E_{N+3} - E_{N-3} = -(I_1 + A_1) - (I_2 + A_2) - (I_3 + A_3) \quad (9.A.9)$$

and for the respective sums (Putz et al. 2004)

$$E_{N+1} + E_{N-1} = (I_1 - A_1) + 2E_N \quad (9.A.10)$$

$$E_{N+2} + E_{N-2} = (I_1 - A_1) + (I_2 - A_2) + 2E_N \quad (9.A.11)$$

$$E_{N+3} + E_{N-3} = (I_1 - A_1) + (I_2 - A_2) + (I_3 - A_3) + 2E_N \quad (9.A.12)$$



being then implemented to provide the associate “spectral” molecular analytical forms of electronegativity (Putz 2010)

$$\begin{aligned}\chi_{\text{CFD}} = & \left[ a_1 (1 - \alpha_1) + \frac{1}{2}b_1 + \frac{1}{3}c_1 \right] \frac{I_1 + A_1}{2} \\ & + \left[ b_1 + \frac{2}{3}c_1 - 2a_1 (\alpha_1 + \beta_1) \right] \frac{I_2 + A_2}{4} \\ & + (c_1 - 3a_1\beta_1) \frac{I_3 + A_3}{6}\end{aligned}\quad (9.A.13)$$

and for chemical hardness (Putz et al. 2004)

$$\begin{aligned}\eta_{\text{CFD}} = & \left[ a_2 (1 - \alpha_2 + 2\beta_2) + \frac{1}{4}b_2 + \frac{1}{9}c_2 \right] \frac{I_1 - A_1}{2} \\ & + \left[ \frac{1}{2}b_2 + \frac{2}{9}c_2 + 2a_2 (\beta_2 - \alpha_2) \right] \frac{I_2 - A_2}{4} \\ & + \left[ \frac{1}{3}c_2 - 3a_2\beta_2 \right] \frac{I_3 - A_3}{6}\end{aligned}\quad (9.A.14)$$

It is worth remarking that when particularizing these formulas for the fashioned two-point central finite difference, i.e., when having  $a_1 = 1, b_1 = c_1 = \alpha_1 = \beta_1 = 0$  and  $a_2 = 1, b_2 = c_2 = \alpha_2 = \beta_2 = 0$  of Table 9.1, one recovers the consecrated Mulliken (spectral) electronegativity (Mulliken 1934)

$$\chi_{2\text{C}} = \frac{I_1 + A_1}{2}\quad (9.A.15)$$

and the chemical hardness basic form relating with the celebrated Pearson nucleophilic–electrophilic reactivity gap (Pearson 1997; Parr and Yang 1989)

$$\eta_{2\text{C}} = \frac{I_1 - A_1}{2}\quad (9.A.16)$$

Finally, for computational purposes, formulas (9.A13) and (9.A14) may be once more reconsidered within the Koopmans’ frozen core approximation (Koopmans 1934), in which various orders of ionization potentials and electronic affinities are replaced by the corresponding frontier energies

$$I_i = -\varepsilon_{\text{HOMO}}(i)\quad (9.A.17)$$

$$A_i = -\varepsilon_{\text{LUMO}}(i)\quad (9.A.18)$$

so that the actual working compact finite difference (CFD) orbital molecular electronegativity and chemical hardness unfold as given in Eqs. (9.6) and (9.7), respectively.

Note that the actual CFD electronegativity and chemical hardness expressions do not distinguish for the atoms-in-molecule contributions, while providing post-bonding information and values, i.e., for characterizing the already stabilized/optimized molecular structure towards its further reactive encountering.

## References

- Al-Fahemi JHA, Cooper DL, Allan NL (2009) *Croat Chem Acta* 82(1):311–316
- Ashrafi AR, Došlić T, Saheli M (2011) *MATCH Commun Math Comput Chem* 65:221–230
- Beernaert H (1979) *J Chromatogr* 173:109–118
- Bultinck P, Ponec R, Gallegos A, Fias S, Van Damme S, Carbó-Dorca R (2006) *Croat Chem Acta* 79(3):363–371
- Cataldo F, Ori O, Iglesias-Groth S (2010) *Mol Simul* 36(5):341–353
- Cataldo F, Ori O, Graovac A (2011a) *Int J Chem Model* 3(1–2):45–63
- Cataldo F, Ori O, Vukicevic D, Graovac A (2011b) In: Cataldo F, Graovac A, Ori O (eds) *The mathematics and topology of fullerenes, Carbon materials: chemistry and physics*. Springer, Dordrecht, pp 205–216
- Chattaraj PK, Cedillo A, Parr RG (1995) *J Chem Phys* 103:7645–7646
- Chemical Book (2011) web: <http://www.chemicalbook.com>. Accessed 19 Aug 2011
- De Corato M, Benedek G, Ori O, Putz MV (2012) *Int J Chem Model* 4:105–114
- Došlić T, Saheli M, Vukičević D (2010) *Iranian J Math Chem* 1:45–55
- Došlić T, Graovac A, Ori O (2011) *MATCH Commun Math Comput Chem* 65:745–752
- Duchowicz PR, Bucknum MJ, Castro EA (2007) *J Math Chem* 41:193–208
- Dureja H, Madan AK (2007) *Med Chem Res* 16:331–341
- Engel E, Ratel J (2007) *J Chromatogr A* 1154:331–341
- Fuentealba P (1995) *J Chem Phys* 103:6571–6575
- Gázquez JL, Vela A, Galvan M (1987) *Struct Bond* 66:79–98
- Hohenberg P, Kohn W (1964) *Phys Rev* 136:864–871
- Hollas B, Gutman I, Trinajstić N (2005) *Croat Chem Acta* 78(4):489–492
- IARC (2005) *Some non-heterocyclic polycyclic aromatic hydrocarbons and some related exposures*, vol 92, *Monographs on the evaluation of carcinogenic risks to humans*. International Agency for Research on Cancer, Lyon
- INCHEM (1998) *International Programme on Chemical Safety. Polycyclic aromatic hydrocarbons, selected non-heterocyclic. Environmental health criteria 202*. World Health Organization, Geneva, web: <http://www.inchem.org/documents/ehc/ehc/ehc202.htm>
- Iranmanesh A, Ashrafi AR, Graovac A, Cataldo F, Ori O (2012) In: Gutman I, Furtula B (eds) *Distance in molecular graphs. Mathematical chemistry monographs*, vol 13. University of Kragujevac and Faculty of Science. Kragujevac, pp 135–155. See <http://match.pmf.kg.ac.rs/mcm13.html>
- Koopmans T (1934) *Physica* 1:104–113
- Kumar V, Sardana S, Madan AK (2004) *J Mol Model* 10:399–407
- Lele SK (1992) *J Comput Phys* 103:16–42
- Mallion RB (2008) *Croat Chem Acta* 81(2):227–246
- Mulliken RS (1934) *J Chem Phys* 2:782–793
- Nikolic S, Milicevic A, Trinajstić N (2006) *Croat Chem Acta* 79(1):155–159
- Ori O, D’Mello M (1992) *Chem Phys Lett* 197(1–2):49–54
- Ori O, D’Mello M (1993) *Appl Phys A Solids Surf* 56(1):35–39
- Parr RG, Pearson RG (1983) *J Am Chem Soc* 105:7512–7516
- Parr RG, Yang W (1989) *Density functional theory of atoms and molecules*. Oxford University Press, New York

- Parr RG, Donnelly RA, Levy M, Palke WE (1978) *J Chem Phys* 68:3801–3807
- Pearson RG (1997) *Chemical hardness: applications from molecules to solids*. Wiley, Weinheim
- Putz MV (2010) *MATCH Commun Math Comput Chem* 64:391–418
- Putz MV (2011a) *Int J Chem Model* 3(4):371–384
- Putz MV (2011b) *Curr Phys Chem* 1:111–139
- Putz MV (2011c) In: Putz MV (ed) *Quantum frontiers of atoms and molecules*. NOVA Science Publishers, Inc., New York, pp 251–270
- Putz MV (2011d) *Carbon bonding and structures: advances in physics and chemistry, Carbon materials: chemistry and physics*. Springer, London, pp 1–32
- Putz MV, Russo N, Sicilia E (2004) *J Comput Chem* 25:994–1003
- Putz MV, Ori O, Cataldo F, Putz AM (2013) *Curr Org Chem* (to be published in Hot Topic Special Issue Ref: HT-SBJ-COC-0050, Topic: Polycyclic Aromatic Hydrocarbons: From Structure to Chemical Reactivity to Biological Activity, Guest Editors: Mihai V. Putz)
- Schwerdtfeger P, Wirz L, Avery J (2012) Topological analysis of fullerenes – a fortran and C++ Program (Version 4.2). Massey University Albany, Auckland. Available from <http://ctcp.massey.ac.nz/index.php?group=&page=fullerenes&menu=fullerenes>. Accessed Dec 2012
- Sharma V, Goswami R, Madan AK (1997) *J Chem Inf Comput Sci* 37:273–282
- Todeschini R, Consonni V (2000) *Handbook of molecular descriptors*. Wiley, Weinheim
- Torrent-Sucarrat M, Salvador P, Solà M, Geerlings P (2007) *J Comput Chem* 29:1064–1074
- Torrent-Sucarrat M, De Proft F, Geerlings P, Ayers PW (2008) *Chem Eur J* 14:8652–8660
- Torrent-Sucarrat M, De Proft F, Ayers PW, Geerlings P (2010) *Phys Chem Chem Phys* 12:1072–1080
- US Environmental Protection Act (1994) (Current as at 14 March 2013); <http://www.legislation.qld.gov.au/legisltn/current/e/envprota94.pdf>
- Van Den Dool H, Kratz PD (1963) *J Chromatogr* 11:463–471
- Vukicevic D (2010) Preprint (personal communication with Ori O)
- Vukicevic D, Lukovits I, Trinajstić N (2006) *Croat Chem Acta* 79(3):509–512
- Wiener H (1947) *J Am Chem Soc* 69:17–20
- Yang W, Parr RG, Pucci R (1984) *J Chem Phys* 81:2862–2863
- Zhou B, Trinajstić N (2008) *Croat Chem Acta* 81(2):319–323
- Zhou B, Trinajstić N (2010) *Croat Chem Acta* 83(2):227–242

# Chapter 10

## Nanostructures and Eigenvectors of Matrices

István László, Ante Graovac<sup>†</sup>, and Tomaž Pisanski

**Abstract** Very often the basic information about a nanostructure is a topological one. Based on this topological information, we have to determine the Descartes coordinates of the atoms. For fullerenes, nanotubes, and nanotori, the topological coordinate method supplies the necessary information. With the help of the bi-lobal eigenvectors of the Laplacian matrix, the position of the atoms can be generated easily. This method fails, however, for nanotube junctions and coils and other nanostructures. We have found recently a matrix  $\mathbf{W}$  which could generate the Descartes coordinates not only of fullerenes, nanotubes, and nanotori but also of nanotube junctions and coils. Solving namely the eigenvalue problem of this matrix  $\mathbf{W}$ , its eigenvectors with zero eigenvalue give the Descartes coordinates. There are nanostructures, however, whose  $\mathbf{W}$  matrices have more eigenvectors with zero eigenvalues than it is needed for determining the positions of the atoms in 3D space. In such cases the geometry of nanostructure can be obtained with the help of a projection from a higher-dimensional space in a similar way as the quasicrystals are obtained.

In this chapter, we study the structure and geometrical properties of some selected graphs which bring us to higher-dimensional spaces. A simple harmonic potential is suggested for constructing the matrix  $\mathbf{W}$ .

---

<sup>†</sup>deceased

I. László (✉)

Department of Theoretical Physics, Institute of Physics, Budapest University of Technology and Economics, Budapest H-1521, Hungary

e-mail: [laszlo@eik.bme.hu](mailto:laszlo@eik.bme.hu)

T. Pisanski

Department of Mathematics, Faculty of Mathematics and Physics, University of Ljubljana, Jadranska 19, Ljubljana SI-1000, Slovenia

## 10.1 Introduction

Most of the physical and chemical properties of nanostructures depend on how the atoms are arranged in space. We need Descartes coordinates of atoms also for detailed visualization of the structures in question. In many cases we know only the topological arrangement of the atoms that gives only some loose information about their positions, that is, the neighboring atoms are near each other in the 3D Euclidean space  $R^3$ . Our aim is to generate the geometrical structure from the topological one. We describe the topological structure with the help of a graph, where its vertices represent the atoms and the edges of the pairs of neighboring atoms which are in most cases connected by chemical bonds. The recovering of geometry from topology corresponds to embedding the graph into the Euclidean space  $R^3$  or  $R^2$ . There are many methods for geometric representation and visualization of graphs (Di Battista et al. 1999; Godsil and Royle 2001; Kaufmann and Wagner 2001; Koren 2005; Lovász and Vesztegombi 1999; Pisanski et al. 1995; Tutte 1963). Here we study the possibility to generate Descartes coordinates of atoms in nanostructures by use of graph spectra and eigenvectors of selected graph matrices (Biyikoglu et al. 2007; Colin de Verdière 1998; Godsil and Royle 2001; van der Holst 1996; László 2005, 2008).

First basic notations and definitions are given, and then, algorithms for generating eigenvectors needed to draw graph are described. Then, we generate the matrix  $\mathbf{W}$  based on harmonic potentials. This method is applied then for clusters cut out from simple cubic, basis-centered cubic, face-centered cubic, and diamond lattices. In the graph-drawing algorithms those eigenvectors of  $\mathbf{W}$  will be used which have zero eigenvalues. If the degeneracy of the zero eigenvalue is four, the method is straightforward. The cases of higher degeneracy and accordingly of higher-dimensional spaces are studied and analyzed.

## 10.2 Basic Notions and Definitions

The topological structure of the atomic arrangement will be represented with a graph  $G(V, E)$ , where  $V$  is the set of vertices and  $E$  is the set of edges. Molecular graphs are chemical graphs which represent the constitution of molecules (Trinajstić 1992) or atomic arrangements, that is, each vertex  $v \in V$  represents an atom in the structure under study, and each edge  $(u, v) \in E$  means that the atoms  $u$  and  $v$  are in some way related to each other, that is, they are chemically bonded or they are some kind of neighboring atoms. The value  $n = |V|$  equals the number of vertices, that is, of atoms in the structure studied.

The matrix  $\mathbf{A} = \mathbf{A}(G) = (a_{uv})$  is the adjacency matrix of the graph  $G(V, E)$ , where  $a_{uv} = 1$  if  $(u, v) \in E$  and  $a_{uv} = 0$  if  $u$  is not adjacent to  $v$  or  $u = v$ . The identity matrix and the all-1 matrix (where  $J_{ij} = 1$  for all  $i$  and  $j$ ) will be denoted

by  $\mathbf{I}$  and  $\mathbf{J}$ , respectively. If the graph  $G$  is a weighted graph, the values  $a_{uv}$  equal the corresponding weights. The Laplacian matrix  $\mathbf{Q}$  of graph  $G$  is defined by  $\mathbf{Q} = \mathbf{Q}(G) = \mathbf{Q}(\mathbf{A}) = \mathbf{D} - \mathbf{A}$ , where  $\mathbf{D} = (d_{vv})$  is the diagonal matrix with  $d_{vv} = \sum_{u:(u,v) \in E} a_{uv}$ . The eigenvalues of the adjacency matrix  $\mathbf{A}$  and those of the Laplacian matrix  $\mathbf{Q}$  are numbered in descending and in ascending order, respectively. It can be proved easily that  $\mathbf{Q}\mathbf{c} = 0$  if the components of the eigenvector  $\mathbf{c}$  are the same, for example,  $c_i = (1/\sqrt{n})$ , that is,  $\mathbf{c}$  is the eigenvector with the eigenvalue equal to 0.

We now define lobality of eigenvectors. An eigenvector  $\mathbf{c}$  is  $m$ -lobal if in the graph  $G(V, E)$  after deleting the vertices  $i \in V$  if  $c_i = 0$  and the edges  $(i, j) \in E$  if the signs of  $c_i$  and  $c_j$  are different, a graph with  $m$  components is obtained. According to the corresponding sign, there are thus positive and negative components. In our graph-drawing procedures, the bi-lobal eigenvectors ( $m = 2$ ) will be the most important. For the nodal properties of graph Laplacians, see the reference Biyikoglu et al. (2004).

Under embedding a graph  $G(V, E)$  into  $R^k$ , we mean a mapping

$$\tau : V(G) \rightarrow R^k. \quad (10.1)$$

In Godsil and Royle (2001) and Pisanski and Žitnik (2009), such an embedding is called graph representation. We will denote by  $\tau_i$  the  $n$ -dimensional vector formed by taking the  $i$ th coordinate  $\tau(u)_i$  of  $\tau(u)$  for all  $u \in V$ . Thus,  $\tau_i$  is an  $n$ -dimensional vector indexed by the vertices of the graph  $G(V, E)$ .

As an example, let  $\mathbf{X} = \tau_1$ ,  $\mathbf{Y} = \tau_2$ , and  $\mathbf{Z} = \tau_3$ , then  $(x_u, y_u, z_u) = (\tau(u)_1, \tau(u)_2, \tau(u)_3)$ .

## 10.3 Algorithms for Generating Eigenvectors in Graph Drawing

### 10.3.1 Algorithms: Based on Analogy

#### 10.3.1.1 Spherical Clusters and Fullerenes

The idea of using eigenvectors (molecular orbitals) for drawing molecular graphs was used first in chemical setting by Fowler and Manolopoulos (Manolopoulos and Fowler 1992; Fowler and Manolopoulos 1995). Their idea is based on Stone's tensor surface harmonic theory (Stone 1981). Stone has found a good approximation for eigenvectors of spherical metallic clusters by calculating the values of spherical harmonics at the atomic positions. Fowler and Manolopoulos constructed the coordinates from eigenvectors attributed to spherical harmonics. They have found that the first few Hückel molecular orbitals of fullerenes invariably contain three

bi-lobal eigenvectors which are discrete version of the continuous  $p_x$ ,  $p_y$ , and  $p_z$  orbitals. Since the  $p_x$ ,  $p_y$ , and  $p_z$  orbitals on a sphere are proportional to the  $x$ ,  $y$ , and  $z$  coordinates, the three lowest bi-lobal eigenvectors  $c^{k_1}$ ,  $c^{k_2}$ , and  $c^{k_3}$  determine the  $(x_i, y_i, z_i)$  topological coordinates of the  $i$ th atom by the relations

$$x_i = S_1 c_i^{k_1}, \quad (10.2)$$

$$y_i = S_2 c_i^{k_2}, \quad (10.3)$$

$$z_i = S_3 c_i^{k_3}, \quad (10.4)$$

with the scaling factors  $S_\alpha = S_0$  or  $S_\alpha = \frac{S_0}{\sqrt{\lambda_1 - \lambda_{k_\alpha}}}$  (Manolopoulos and Fowler 1992; Fowler and Manolopoulos 1995). The most realistic picture of fullerenes (Dresselhaus et al. 1996) can be found by the scaling factor  $S_\alpha = \frac{S_0}{\sqrt{\lambda_1 - \lambda_{k_\alpha}}}$  (Manolopoulos and Fowler 1992; Fowler and Manolopoulos 1995; László 2004a, b; Pisanski and Shawe-Taylor 1993; Fowler et al. 1995; Rassat et al. 2003).

### 10.3.1.2 Nanotori

Graovac et al. (2000) generated the Descartes coordinates of nanotori using three eigenvectors  $\mathbf{c}^2$ ,  $\mathbf{c}^3$ , and  $\mathbf{c}^{\text{opt}}$  of the adjacency matrix  $\mathbf{A}$  describing a 3-valent toroidal structure. The second and third eigenvectors are  $\mathbf{c}^2$  and  $\mathbf{c}^3$ . The eigenvector  $\mathbf{c}^{\text{opt}}$  was selected in a way to obtain optimal drawing. The toroidal structures, however, obtained from three eigenvectors usually are distorted or flattened in some way (Graovac et al. 2000; László et al. 2001). This problem was solved using four eigenvectors of the adjacency matrix (László et al. 2001). In this method the position of a point on the surface of a torus is given as the sum of two vectors  $\mathbf{R}$  and  $\mathbf{r}$ , where the vector  $\mathbf{R}$  is in the  $xy$  plane and  $\mathbf{r}$  is in the planes perpendicular to the plane of  $\mathbf{R}$ . These two vectors are two-dimensional planar vectors; each of them can be described by two bi-lobal eigenvectors. If  $\mathbf{c}^{k_1}$ ,  $\mathbf{c}^{k_2}$ ,  $\mathbf{c}^{k_3}$ , and  $\mathbf{c}^{k_4}$  are for bi-lobal eigenvectors of the adjacency matrix  $\mathbf{A}$ , then using basic geometrical construction, the  $(x_i, y_i, z_i)$  topological coordinates of the  $i$ th atom on the torus are given by the relations (László et al. 2001; László and Rassat 2003)

$$x_i = S_1 c_i^{k_1} (1 + S_4 c_i^{k_4}), \quad (10.5)$$

$$y_i = S_2 c_i^{k_2} (1 + S_4 c_i^{k_4}), \quad (10.6)$$

$$z_i = S_3 c_i^{k_3}. \quad (10.7)$$

## 10.3.2 Algorithms: Based on Extremal Values

### 10.3.2.1 Spherical Clusters and Fullerenes

Hall described a  $k$ -dimensional quadratic placement algorithm for embedding a graph  $G(V, E)$  to the Euclidean space  $R^k$  (Hall 1970). The optimal embedding was defined by minimizing the following energy function:

$$E_H(\tau) = \sum_{i=1}^k \tau_i^T \mathbf{Q} \tau_i \quad (10.8)$$

with the constraints  $\|\tau_i\|^2 = \sum_{u=1}^n \tau(u)_i^2 = 1$ . This optimal embedding can be realized by the first  $k$  eigenvectors with nonzero eigenvalues of the Laplacian  $\mathbf{Q}$ . That is,  $\tau_i = \mathbf{c}^{i+1}$  for  $i = 1, \dots, k$ .

Pisanski and Shawe-Taylor (1993, 2000) defined the optimal embedding of the weighted graph  $G(V, E)$  by minimizing the energy function

$$E(\tau) = \sum_{(u,v) \in E} a_{uv} \|\tau(u) - \tau(v)\|^2 - \beta \sum_{(u,v) \notin E} \|\tau(u) - \tau(v)\|^2, \quad (10.9)$$

and it was subjected to the constraints

$$\begin{aligned} \|\tau_i\| &= 1, \quad \tau_i^T \mathbf{c}^1 = 0 \quad \text{for } i = 1, \dots, k, \\ \tau_i^T \tau_j &= 0 \quad \text{for } 1 \leq i < j \leq k \quad \beta \text{ is a positive constant.} \end{aligned}$$

It was proven in Pisanski and Shawe-Taylor (1993, 2000) that the optimal embedding for this problem is given by  $\tau_i = \mathbf{c}^{i+1}$  for  $i = 1, \dots, k$ , and the minimal value of  $E(\tau)$  is

$$\sum_{l=2}^{k+1} \lambda_l - \beta nk. \quad (10.10)$$

Here the corresponding Laplacian  $\mathbf{Q} = \mathbf{Q}(\mathbf{B})$  for the eigenvalues and eigenvectors was constructed from the matrix  $\mathbf{B}$  with the matrix elements  $b_{uv} = a_{uv} + \beta$  if  $(u, v) \in E$  and  $b_{uv} = 0$ , otherwise. It was proved also that in the case where the graph is not weighted, the optimal embedding does not depend on the parameter  $\beta$ .

Lovász and Schrijver (1999) defined a symmetric  $n \times n$  matrix  $\mathbf{M}$  for the three-connected planar graph  $G(V, E)$  with the following properties:

1.  $\mathbf{M}$  has exactly one negative eigenvalue, of multiplicity 1.
2. For all  $(u, v) \in E$ ,  $m_{uv} < 0$  and if  $u \neq v$  and  $(u, v) \notin E$ ,  $m_{uv} = 0$ .
3.  $\mathbf{M}$  has rank  $n - 3$ .



They have proved that if we have a matrix  $\mathbf{M}$  with the above-mentioned conditions, then the null space of  $\mathbf{M}$  (the eigenvectors  $\mathbf{c}^2$ ,  $\mathbf{c}^3$ , and  $\mathbf{c}^4$  of the eigenvalue  $\lambda = 0$ ) gives a proper embedding of  $G(V, E)$  in the sphere  $S^2$  as  $\tau_i = \mathbf{c}^{i+1}$  for  $i = 1, \dots, 3$  and  $\|\tau_i\|^2 = 1$ . Thus, the relation  $(x_u, y_u, z_u) = (\tau(u)_1, \tau(u)_2, \tau(u)_3)$  is valid for each vertex. It was also proved that this null space contains bi-lobal eigenvectors (van der Holst 1996). The matrix  $\mathbf{M}$  is often called Colin de Verdière matrix in the scientific literature.

### 10.3.2.2 Embedding of Any Molecular Arrangement

In the previous paragraph, we have seen that the applicability of three eigenvectors is restricted only to spherical structures and nanotubes. In Laszlo et al. (2011), we have shown that there exists a matrix  $\mathbf{W}$  which can reproduce practically exactly the  $(x_i, y_i, z_i)$  Descartes coordinates with the help of three eigenvectors. This matrix was obtained by minimizing the total energy

$$E(r) = E(r_{12}, r_{21}, \dots, r_{ij}, r_{ji} \dots) \quad (10.11)$$

of the system, and it was proved that

$$\mathbf{WX} = \mathbf{0}, \quad \mathbf{WY} = \mathbf{0}, \quad \mathbf{WZ} = \mathbf{0}. \quad (10.12)$$

The matrix elements of  $\mathbf{W}$  are calculated as

$$w_{ij} = -\frac{\partial E(r)}{r_{ij} \partial r_{ij}} - \frac{\partial E(r)}{r_{ji} \partial r_{ji}} \quad (10.13)$$

for the off-diagonal elements and as

$$w_{ii} = \sum_{j \neq i}^n \left( \frac{\partial E(r)}{r_{ij} \partial r_{ij}} + \frac{\partial E(r)}{r_{ji} \partial r_{ji}} \right) = -\sum_{j \neq i}^n w_{ij} \quad (10.14)$$

for the diagonal elements, and  $r_{ij}$  are the interatomic distances. We have found further that

$$\mathbf{WU} = \mathbf{0} \quad (10.15)$$

with  $u_i = \frac{1}{\sqrt{n}}$ .

Other details can be found in reference Laszlo et al. (2011).

If the center of mass of the molecule is in the origin and the molecule is directed in such a way that the eigenvectors of its tensor of inertia are showing to the directions of the  $x$ -,  $y$ -, and  $z$ -axis, then the vectors  $\mathbf{X}$ ,  $\mathbf{Y}$ ,  $\mathbf{Z}$ , and  $\mathbf{U}$  are orthogonal eigenvectors of the matrix  $\mathbf{W}$ . That is,

$$\mathbf{X} = S_x \mathbf{C}^x, \quad \mathbf{Y} = S_y \mathbf{C}^y, \quad \mathbf{Z} = S_z \mathbf{C}^z, \quad (10.16)$$

where  $\mathbf{C}^x$ ,  $\mathbf{C}^y$ ,  $\mathbf{C}^z$ , and  $\mathbf{U}$  are orthogonal and normalized eigenvectors of  $\mathbf{W}$  with zero eigenvalue and  $S_x$ ,  $S_y$ , and  $S_z$  are appropriate scaling factors.

The question arises that if we have any orthogonal and normalized eigenvectors  $\mathbf{A}^x$ ,  $\mathbf{A}^y$ ,  $\mathbf{A}^z$ , and  $\mathbf{U}$  of  $\mathbf{W}$  with zero eigenvalue, are there any appropriate scaling factors  $S_x$ ,  $S_y$ , and  $S_z$  for obtaining the Descartes coordinates with a relation

$$\mathbf{X} = S_x \mathbf{A}^x, \quad \mathbf{Y} = S_y \mathbf{A}^y, \quad \mathbf{Z} = S_z \mathbf{A}^z. \quad (10.17)$$

If the number of eigenvectors with zero eigenvalue is four, the answer is yes, but in Eq. (10.17) we obtain a rotation of the molecule as the vectors  $\mathbf{A}^x$ ,  $\mathbf{A}^y$ , and  $\mathbf{A}^z$  can be obtained as linear combination of the vectors  $\mathbf{C}^x$ ,  $\mathbf{C}^y$ , and  $\mathbf{C}^z$ . If the vectors  $\mathbf{C}^x$ ,  $\mathbf{C}^y$ , and  $\mathbf{C}^z$  are mixed with the vector  $\mathbf{U}$ , it means arbitrary translation and a rotation of the molecule. As the vector  $\mathbf{U}$  is known, it can be easily subtracted from the linear combinations in the case of mixings. If the degeneracy of the zero eigenvalue is higher than four, the Descartes coordinates of the atoms can be obtained with the help of a projection from a higher-dimensional space. In a similar way, the coordinates are constructed in a quasicrystal.

Usually the first-neighbor distances in a molecule do not determine the positions of the atoms, but the full structure can be described if we know the second-neighbor distances as well. From this follows that if the edges of a molecular graph  $G = (V, E)$  correspond to the first and second neighbors of a molecule, the matrix  $\mathbf{W}$  can be generated from a total energy  $E(r)$  which depends only on the first and second neighbors of the molecule. If the dimension of the null space of  $\mathbf{W}$  is four, then this null space contains three eigenvectors which give a proper embedding of  $G = (V, E)$  into  $R^3$ .

## 10.4 Study of the Matrix $\mathbf{W}$ in Harmonic Potential

### 10.4.1 Construction of Matrix $\mathbf{W}$ from Harmonic Potential

In our previous publication, we tested application of the matrix  $\mathbf{W}$  for several structures, as nanotube junctions, nanotori, and helical nanotubes (Laszlo et al. 2011). In that work, the interatomic interactions and the matrix  $\mathbf{W}$  were calculated with the help of the Brenner potential (Brenner 1990) and harmonic potential as well. From our point of view, the harmonic potential is simpler and more general than the Brenner one; as in the case of harmonic potential, there is no limitation for the number of first neighbors. In our preliminary calculations, we have found further that in some cases the multiplicity of the zero eigenvectors was greater than four. In the following, first, we calculate the matrix  $\mathbf{W}$  for harmonic potential and then apply it for several clusters taken out of simple cubic, face-centered cubic, body-centered cubic, and diamond structures.

We write the total energy of Eq. (10.11) in the form of

$$E(r) = E(r_{12}, r_{21}, \dots, r_{ij}, r_{ji}, \dots) = \sum_{i,j=1}^n \frac{1}{2} k_{ij} (r_{ij} - a_{ij})^2. \quad (10.18)$$

Here  $k_{ij} = k_{ji}$  are the spring constants and  $r_{ij} = a_{ij}$  are parameters. The summation goes for all the pairs  $(i, j)$  which are sufficient for determining the equilibrium positions of the atoms. From Eqs. (10.13) and (10.18) follows that

$$w_{ij} = -\frac{\partial E(r)}{r_{ij} \partial r_{ij}} - \frac{\partial E(r)}{r_{ji} \partial r_{ji}} = -2k_{ij} \left(1 - \frac{a_{ij}}{r_{ij}}\right). \quad (10.19)$$

As it is stated above in Eq. (10.19), the values  $r_{ij}$  minimize the total energy  $E(r)$  of Eq. (10.18). From this follows that the parameters  $a_{ij}$  must be different of the corresponding interatomic distance  $a_{ij}$ . In other cases  $\mathbf{W}$  is the zero matrix.

#### 10.4.2 *Descartes Coordinates for Cubic and Diamond Cluster Obtained from the Eigenvectors of Matrix W Based on Harmonic Potentials*

We have studied altogether 130 clusters of Tables 10.1, 10.2, 10.3 and 10.4. These clusters were cut out from simple cubic, basis-centered cubic, face-centered cubic, and diamond lattice systems. The spherical clusters had a maximal number of shells 20, and each of them contained an atom in the center of the cluster. These clusters contained all of the atoms inside the sphere given by the corresponding radius. The first-neighbor interatomic distance was 1.54 Å for each structure. The nonspherical structures were given by the number of unit cells  $n_x$ ,  $n_y$ , and  $n_z$  in the direction of the axes  $X$ ,  $Y$ , and  $Z$ . In the following, we shall call the clusters with the help of the number of atoms, number of shells, and the number of unit cells. Thus, the spherical cluster of 93 atoms and seven shells in Table 10.1a will be called cluster C93\_7. In the same way, the name of the cluster with number of atoms 336 and  $n_x$ ,  $n_y$ ,  $n_z$  unit cells 6, 7, and 8 will be C336\_6\_7\_8 in Table 10.1. The total energy of Eq. (10.18) was minimized with the help of the conjugate gradient method. In the graph  $G(V, E)$  of a cluster, the number of vertices equals to the number of atoms, and two vertices are connected if the corresponding atoms are first neighbors in the lattice. In Eqs. (10.18) and (10.19), we supposed that  $k_{ij} = 1$  and the unit of  $k_{ij}$  is the same as that of the matrix element  $w_{ij}$ . If we give values  $a_{ij}$  only for the first neighbors, most of the matrix elements  $w_{ij}$  will be zero because the solutions  $r_{ij} = a_{ij}$  can minimize the total energy.

Thus, in our first calculations, we used the value  $a_{ij} = a_1 = 1.54$  for the first neighbors and the value  $a_{ij} = a_2 = 2.7$  for the second neighbors. These parameters are not compatible with each other in any structure, and thus, the relation

**Table 10.1** Data obtained for clusters of simple cubic lattice

Number of		Radius of cluster (in Å)	Degeneracy of zero eigenvalue	Serial number of eigenvectors for drawing			
Atoms	Shells			$C^x$	$C^y$	$C^z$	
(a)							
7	1	1.54	4	3	4	5	
19	2	2.18	4	9	10	11	
27	3	2.67	4	13	14	15	
33	4	3.08	4	18	19	20	
57	5	3.44	4	34	35	36	
81	6	3.77	4	45	46	47	
93	7	4.36	4	59	60	61	
123	8	4.62	4	67	68	69	
147	9	4.87	4	93	94	95	
171	10	5.11	4	109	110	111	
179	11	5.34	4	110	111	112	
203	12	5.55	4	133	134	135	
251	13	5.76	4	166	167	168	
257	14	6.16	4	172	173	174	
305	15	6.35	4	188	189	190	
341	16	6.54	4	222	223	224	
365	17	6.72	4	241	242	243	
389	18	6.89	4	263	267	265	
437	19	7.06	4	298	299	300	
461	20	7.23	4	306	307	308	
Number of atoms	Number of unit cells			Degeneracy of zero eigenvalue	Serial number of eigenvectors for drawing		
	$n_x$	$n_y$	$n_z$		$C^x$	$C^y$	$C^z$
(b)							
8	2	2	2	4	2	3	4
27	3	3	3	4	13	14	15
64	4	4	4	4	29	30	31
125	5	5	5	4	74	75	76
216	6	6	6	4	123	124	125
343	7	7	7	4	202	213	204
512	8	8	8	4	313	314	315
394	7	7	8	4	232	233	234
448	7	8	8	4	269	270	272
336	6	7	8	4	198	199	201
288	6	6	8	4	166	168	169
200	5	5	8	4	115	117	118
128	4	4	8	4	66	67	69
72	3	3	8	4	38	40	41
32	2	2	8	4	7	9	10

The matrix  $\mathbf{W}$  included only first- and second-neighbor interactions. (a) Spherical clusters. (b) Nonspherical clusters

**Table 10.2** Data obtained for clusters of basis-centered cubic lattice

Number of		Radius of cluster (in Å)	Degeneracy of zero eigenvalue	Serial number of eigenvectors for drawing			
Atoms	Shells			$C^x$	$C^y$	$C^z$	
(a)							
9	1	1.54	4	6	7	8	
15	2	1.78	4	7	8	9	
27	3	2.52	4	18	19	20	
51	4	2.95	4	31	32	33	
59	5	3.08	4	41	42	43	
65	6	3.56	4	45	46	47	
89	7	3.88	4	63	64	65	
113	8	3.98	4	79	80	81	
137	9	4.36	4	102	103	104	
169	10	4.62	4	123	124	125	
181	11	5.03	4	132	133	134	
229	12	5.26	4	172	173	174	
259	13	5.34	4	196	197	198	
283	14	5.63	4	212	213	214	
307	15	5.83	4	231	232	233	
331	16	5.90	4	255	256	257	
339	17	6.16	4	259	260	261	
387	18	6.35	4	294	295	296	
411	19	6.41	4	313	314	315	
459	20	6.66	4	357	358	359	
Number of atoms	Number of unit cells			Degeneracy of zero eigenvalue	Serial number of eigenvectors for drawing		
	$n_x$	$n_y$	$n_z$		$C^x$	$C^y$	$C^z$
(b)							
16	2	2	2	4	9	10	11
54	3	3	3	4	41	42	43
128	4	4	4	4	99	100	101
250	5	5	5	4	195	197	198
432	6	6	6	4	343	345	346
686	7	7	7	4	548	549	550
672	6	7	8	4	537	539	540
576	6	6	8	4	459	461	462
400	5	5	8	4	318	319	320
256	4	4	8	4	201	202	204
144	3	3	8	4	109	111	112
64	2	2	8	4	43	45	46

The matrix  $\mathbf{W}$  included only first- and second-neighbor interactions. (a) Spherical clusters. (b) Nonspherical clusters

**Table 10.3** Data obtained for clusters of face-centered cubic lattice

Number of		Radius of cluster (in Å)	Degeneracy of zero eigenvalue	Serial number of eigenvectors for drawing			
Atoms	Shells			$C^x$	$C^y$	$C^z$	
(a)							
13	1	1.54	4	4	5	6	
19	2	2.18	4	6	7	8	
43	3	2.67	4	17	18	19	
55	4	3.08	4	23	24	25	
79	5	3.44	4	32	33	34	
87	6	3.77	4	40	41	42	
135	7	4.08	4	67	68	69	
141	8	4.36	4	73	74	75	
177	9	4.62	4	86	87	88	
201	10	4.87	4	86	87	88	
225	11	5.11	4	113	114	115	
249	12	5.34	4	132	133	134	
321	13	5.55	4	169	170	171	
369	14	5.97	4	194	195	196	
381	15	6.16	4	191	192	193	
429	16	6.35	4	222	223	224	
459	17	6.54	4	241	242	243	
531	18	6.71	4	285	286	287	
555	19	6.89	4	298	299	300	
603	20	7.06	4	326	327	328	
Number of atoms	Number of unit cells			Degeneracy of zero eigenvalue	Serial number of eigenvectors for drawing		
	$n_x$	$n_y$	$n_z$		$C^x$	$C^y$	$C^z$
(b)							
32	2	2	2	4	17	18	19
108	3	3	3	4	59	60	61
256	4	4	4	4	139	140	141
500	5	5	5	4	281	282	283
600	5	5	6	4	341	342	344
384	4	4	6	4	211	213	214
216	3	3	6	4	120	121	122
96	2	2	6	4	48	49	50
128	2	2	8	4	63	64	66
288	3	3	8	4	160	161	163
512	4	4	8	4	282	284	285
640	4	5	8	4	362	363	365

The matrix  $\mathbf{W}$  included only first- and second-neighbor interactions. (a) Spherical clusters. (b) Nonspherical clusters

**Table 10.4** Data obtained for clusters of diamond lattice

Number of		Radius of cluster	Degeneracy of zero eigenvalue	Serial number of eigenvectors for drawing			
Atoms	Shells			$C^x$	$C^y$	$C^z$	
(a)							
5	1	1.54	4	1	2	4	
17	2	2.52	12				
17*	2	2.52	4	9	10	11	
29	3	2.95	4	1	2	3	
35	4	3.56	4	1	2	3	
47	5	3.88	4	14	15	16	
71	6	4.36	4	7	8	9	
87	7	4.62	4	5	6	7	
99	8	5.03	4	17	18	19	
123	9	5.26	4	1	2	3	
147	10	5.63	4	2	3	4	
159	11	5.83	4	14	15	16	
167	12	6.16	4	9	10	11	
191	13	6.35	4	9	10	11	
239	14	6.66	4	36	37	38	
275	15	6.83	4	5	6	7	
281	16	7.11	4	2	3	4	
293	17	7.28	4	2	3	4	
329	18	7.55	4	7	8	9	
357	19	7.70	4	5	6	7	
381	20	7.96	4	6	7	8	
Number of atoms	Number of unit cells			Degeneracy of zero eigenvalue	Serial number of eigenvectors for drawing		
	$n_x$	$n_y$	$n_z$		$C^x$	$C^y$	$C^z$
(b)							
8	1	1	1	7			
8*	1	1	1	4	4	5	7
64	2	2	2	7			
64*	2	2	2	4	50	51	52
216	3	3	3	7			
216*	3	3	3	4	174	175	177
512	4	4	4	7			
512*	4	4	4	4	436	437	438
16	1	1	2	10			
16*	1	1	2	4	9	11	12
24	1	1	3	13			
24*	1	1	3	4	14	15	17
32	1	1	4	16			
32*	1	1	4	4	18	19	21
40	1	1	5	19			
40*	1	1	5	4	22	23	25

(continued)

**Table 10.4** (continued)

Number of atoms	Number of unit cells			Degeneracy of zero eigenvalue	Serial number of eigenvectors for drawing		
	$n_x$	$n_y$	$n_z$		$C^x$	$C^y$	$C^z$
160	2	2	5	7			
160*	2	2	5	4	128	129	131
360	3	3	5	7			
360*	3	3	5	4	301	302	303
768	4	4	6	7			
768*	4	4	6	4	662	663	665

The matrix  $\mathbf{W}$  included the first- and second-neighbor interactions, but in rows marked by (\*), the third-neighbor interactions are included too. (a) Spherical clusters. (b) Nonspherical clusters

$r_{ij} = a_{ij}$  does not minimize the total energy. This is why the first- and second-neighbor matrix element  $w_{ij}$  will be differences of zero. In Tables 10.1, 10.2, and 10.3, we can see that the degeneracy of the corresponding zero eigenvalues was four, and we could reconstruct the clusters from the three eigenvectors. It was surprising that the eigenvector  $u_i = (1/\sqrt{n})$  was always separated from the other eigenvectors of zero eigenvalue. This can be due to the numerical algorithm which we used for diagonalization. The other three eigenvectors of zero eigenvalue could mix with each other; thus, Eq. (10.16) produced the cluster with an affine transformation.

Table 10.4 shows that, for the spherical diamond structure C17.2, the degeneracy of the zero eigenvalue was 12 and, for the nonspherical diamond clusters, the degeneracy of zero eigenvalue was at least seven. Here we remark once more that in the total energy  $E(r)$  of Eq. (10.18), we took into account only the first- and second-neighbor interactions. Detailed analysis revealed that in the nonspherical diamond clusters, there were always surface atoms for which the condition  $r_{ij} = a_{ji}$  was fulfilled. If an atom with the vertex index  $kr_{kj} = a_{jk}$  for each neighbor, then there are only zero matrix elements in the row  $k$  and in the column  $k$  of matrix  $\mathbf{W}$ . Thus, such kind of atoms increases by one the number of degeneracy of the zero eigenvalue of  $\mathbf{W}$ . The case of the cluster C17.2 is a little bit different. The matrix  $\mathbf{W}$  determines not only the cluster C17.2 but each other clusters obtained by relative rotations of some parts of this cluster as well. During these rotations, the first- and second-neighbor distances are not changing, and these structures have the same matrix  $\mathbf{W}$ . This is why the degeneracy of the zero eigenvalue is higher than for at this cluster. Each of the above-mentioned extra degeneracy of zero eigenvalue can be suppressed by introducing the third-neighbor interactions as well with the parameter  $a_{ij} = a_3 = 3.5$ . Table 10.4 shows that using first-, second-, and third-neighbor interactions, the degeneracy of the zero eigenvalue was 4. Our calculations revealed as well that we do not need all of the third neighbors. We need only those which are sufficient to hinder the  $r_{ij} = a_{ji}$  solutions or the relative rotation of the cluster parts.



## 10.5 Conclusions

After revising the algorithms for generating eigenvectors in graph drawing, we studied the problems of constructing Descartes coordinates with the help of the matrix  $\mathbf{W}$ . Until now only this matrix can be used for resolving this problem if the atoms are in general position. That is, the atoms are not on a surface of spheres or tori or on that of some related similar structures. In this work we generated it using an energy minimalization algorithm with the help of a conjugate gradient method, and the total energy was calculated using harmonic potentials. The studied clusters were spherical and nonspherical clusters. With the help of the shape analysis (Graovac et al. 2008a, b), we have found that the final structure had coefficients only for the eigenvectors with zero eigenvalue of the matrix  $\mathbf{W}$ . Using these coefficients, we could reproduce the Descartes coordinates independent of the degeneracy of the zero eigenvalue. We have found further that the space of these zero eigenvectors does not have general meaning as the higher-dimensional space in the projection process in constructing quasicrystals. Using third-neighbor interactions, we obtained that the degeneracy was four at each cluster under study. The drawback of  $\mathbf{W}$  is that at present there is not a simple algorithm for its construction. There is a hope, however, that using appropriate approximations for the matrix elements of  $\mathbf{W}$ , a method can be found for constructing topological coordinates of complicated nonspherical structures as well. According to our present results, the harmonic potential looks to be a promising tool for resolving these problems.

**Acknowledgements** I. László thanks for the support of grants TAMOP-4.2.1/B-09/1/KONV-2010-0003 and TAMOP-4.2.1/B-09/1/KMR-2010-0002 and for the support obtained in the framework of bilateral agreement between the Croatian Academy of Science and Arts and the Hungarian Academy of Sciences. The research of T. Pisanski has been financed by ARRS project P1-0294 and within the EUROCORES Programme EuroGIGA (project GReGAS N1-0011) of the European Science Foundation.

## References

- Biyikoglu T, Hordijk W, Leydold J, Pisanski T, Stadler PF (2004) Graph Laplacians, nodal domains, and hyperplane arrangements. *Linear Algebra Appl* 390:155–174
- Biyikoglu T, Leydold J, Stadler PF (2007) Laplacian eigenvectors of graphs. Perron-Frobenius and Faber-Krahn type theorems, vol 1915, Lecture notes in mathematics. Springer, Berlin/Heidelberg
- Brenner DW (1990) Empirical potentials for hydrocarbons for use in simulating the chemical vapor deposition of diamond films. *Phys Rev B* 42:9458–9471
- Colin de Verdière Y (1998) Spectres de graphes, vol 4, Cours spécialisés. Société Mathématique de France, Paris
- Di Battista G, Eades P, Tamassia R, Tollis IG (1999) Graph drawing: algorithms for the visualization of graphs. Prentice Hall, Upper Saddle River
- Dresselhaus MS, Dresselhaus G, Eklund PC (1996) Science of fullerenes and carbon nanotubes: their properties and applications. Academic, New York/London

- Fowler PW, Manolopoulos DE (1995) An atlas of fullerenes. Clarendon, Oxford
- Fowler PW, Pisanski T, Shawe-Taylor JS (1995) Molecular graph eigenvectors for molecular coordinates. In: Tamassia R, Tollis EG (eds) Graph drawing, vol 894, Lecture notes in computer science. Springer, Berlin
- Godsil CD, Royle GF (2001) Algebraic graph theory. Springer, Heidelberg
- Graovac A, Plavšić D, Kaufman M, Pisanski T, Kirby EC (2000) Application of the adjacency matrix eigenvectors method to geometry determination of toroidal carbon molecules. *J Chem Phys* 113:1925–1931
- Graovac A, László I, Plavšić D, Pisanski T (2008a) Shape analysis of carbon nanotube junctions. *MATCH Commun Math Comput Chem* 60:917–926
- Graovac A, László I, Pisanski T, Plavšić D (2008b) Shape analysis of polyhex carbon nanotubes and nanotori. *Int J Chem Model* 1:355–362
- Hall KM (1970) An r-dimensional quadratic placement algorithm. *Manage Sci* 17:219–229
- Kaufmann M, Wagner D (eds) (2001) Drawing graphs. Methods and models, vol 2025, Lecture notes in computer science. Springer, Berlin
- Koren Y (2005) Drawing graphs by eigenvectors: theory and practice. *Comput Math Appl* 49:1867–1888
- László I (2004a) Topological coordinates for nanotubes. *Carbon* 42:983–986
- László I (2004b) The electronic structure of nanotubes and the topological arrangements of carbon atoms. In: Buzaneva E, Scharff P (eds) Frontiers of multifunctional integrated nanosystems, vol 152, NATO science series, II. Mathematics, physics and chemistry. Kluwer Academic, Dordrecht/Boston, p 11
- László I (2005) Topological coordinates for Schlegel diagrams of fullerenes and other planar graphs. In: Diudea MV (ed) Nanostructures: novel architecture. Nova Science Publishers, Inc., New York, pp 193–202
- László I (2008) Hexagonal and non-hexagonal carbon surfaces. In: Blank V, Kulnitskiy B (eds) Carbon nanotubes and related structures. Research Singpost, Trivandrum, Kerala, India, pp 121–146
- László I, Rassat A (2003) The geometric structure of deformed nanotubes and the topological coordinates. *J Chem Inf Comput Sci* 43:519–524
- László I, Rassat A, Fowler PW, Graovac A (2001) Topological coordinates for toroidal structures. *Chem Phys Lett* 342:369–374
- László I, Graovac A, Pisanski T, Plavšić D (2011) Graph drawing with eigenvectors. In: Putz MV (ed) Carbon bonding and structures: Advances in physics and chemistry. Springer, Dordrecht/Heidelberg/London/New York, pp 95–115
- Lovász L, Schrijver A (1999) On the null space of the Colin de Verdière matrix. *Annales de l'Institut Fourier (Grenoble)* 49:1017–1026
- Lovász L, Vesztergombi K (1999) Representation of graphs. In: Halász L, Lovász L, Simonovits M, Sós VT (eds) Paul Erdős and his mathematics, Bolyai society mathematical studies. Springer, New York
- Manolopoulos DE, Fowler PW (1992) Molecular graphs, point groups, and fullerenes. *J Chem Phys* 96:7603–7614
- Pisanski T, Shawe-Taylor JS (1993) Characterising graph drawing with eigenvectors. In: Technical report CSD-TR-93-20, Royal Holloway, University of London, Department of Computer Science, Egham, Surrey TW200EX, England
- Pisanski T, Shawe-Taylor JS (2000) Characterising graph drawing with eigenvectors. *J Chem Inf Comput Sci* 40:567–571
- Pisanski T, Zitnik A (2009) Representing graphs and maps. In: Beineke LW, Wilson RJ (eds) Topics in topological graph theory, vol 128, Encyclopedia of mathematics and its applications. Cambridge University Press, Cambridge, pp 151–180
- Pisanski T, Plestenjak B, Graovac A (1995) NiceGraph and its applications in chemistry. *Croat Chem Acta* 68:283–292
- Rassat A, László I, Fowler PW (2003) Topological rotational strengths as chirality descriptors for fullerenes. *Chem Eur J* 9:644–650

- Stone AJ (1981) New approach to bonding in transition-metal clusters and related compounds. *Inorg Chem* 20:563–571
- Trinajstić N (1992) *Chemical graph theory*. CRC Press, Boca Raton/Ann Arbor/London/Tokyo
- Tutte WT (1963) How to draw a graph. *Proc Lond Math Soc* 13:743–768
- van der Holst H (1996) *Topological and spectral graph characterizations*. PhD thesis, University of Amsterdam, Amsterdam

# Chapter 11

## Theoretical Analysis of the Reactivity of Carbon Nanotubes: Local Versus Topological Effects

Massimo Fusaro, Vincenzo Barone, Mauro Causa, Maddalena D'Amore, and Carmine Garzillo

**Abstract** In carbon materials the mobile  $\pi$  electrons are situated in topologically different circumstances at edge sites, and their  $\pi$  electronic states, essentially controlled by the network structure of  $sp^2$  carbon, may be significantly affected. In this work, we derived topological indications about the reactivity of carbon nanotubes and fullerenes with the hydroxyl radical ( $\text{OH}^*$ ), the most important oxidizing species in the troposphere. For each molecular structure, we computed the local softness, the Mulliken charges of the reacting carbons of  $(n,n)$  and  $(n,0)$  clusters, and their Huckel-type aromaticity rules, as an index to determine topologically independent sites and predicting a certain grade of reactivity of the nanotube and fullerenic carbon atoms. Using local softness, closely related to the energy gap, it was possible to separate the periodical nanotubes in three families according to their reactivity. A connection between the reactivity index  $\Delta E$  and the topology was established by means of the Fukui integrated function. It resulted that for  $(n,0)$  clusters, odd  $n$  implies aromaticity, whereas even  $n$ , non-aromaticity;  $(n,n)$  clusters are in any case non-aromatic. For a better understanding of some experimental results, we also discussed how edge effects can influence topological reactivity due to the increment of the number of benzene rings in some cluster arrangements.

---

M. Fusaro • M. Causa (✉) • M. D'Amore  
Department of Chemical Sciences, University "Federico II", Complesso Universitario  
di Monte Sant'Angelo, 80126 Naples, Italy  
e-mail: [maxitp@gmail.com](mailto:maxitp@gmail.com); [mauro.causa@unina.it](mailto:mauro.causa@unina.it); [mdamore@unina.it](mailto:mdamore@unina.it)

V. Barone  
Classe di Scienze, Scuola Normale Superiore, Piazza dei Cavalieri 7, 56126 Pisa, Italy  
e-mail: [vincenzo.barone@sns.it](mailto:vincenzo.barone@sns.it)

C. Garzillo  
Department of Preventive Medical Sciences, University "Federico II", Via S. Pansini 5,  
80131 Naples, Italy  
e-mail: [carmine.garzillo@unina.it](mailto:carmine.garzillo@unina.it)

## 11.1 Introduction

Fullerenes and nanotubes are very singular molecules: they are the object of a large number of experimental works (Tasis et al. 2006). The reasons of their importance are the following: (a) they may have interesting properties for applications and (b) their chemical nature and structure is quite well defined, with respect to all the sets of the carbonaceous materials like soot, coal, and polyarenes. One of the problems that synthetic chemistry must face is the solubilization of nanotubes and fullerenes (Arrais et al. 2004). The solubilization is obtained by the functionalization of these materials: by oxidation polar groups are attached to the graphenic surfaces. A necessary and relatively slow step of many oxidation processes of organic materials is the attachment of the stable hydroxyl radical to the  $\pi$  electronic system (Maranzana et al. 2005). This reaction step is always exoergic and does not have any energy barrier. On the other hand, following the minimum energy path (MEP), the free energy profile shows a maximum: therefore, the generalized transition state theory (Gonzalez-Lafont et al. 1998) can be applied here.

The most important oxidizing species in troposphere is the hydroxyl radical ( $\text{OH}^{\bullet}$ ). It is extremely reactive and it is able to oxidize most of the chemicals found in the troposphere. The hydroxyl radical is therefore known as the “detergent of the atmosphere.”

$\text{OH}^{\bullet}$  governs atmospheric chemistry during the day since its formation depends on radiation from the sun. The initial reaction involves the breakdown (photolysis) of ozone by solar radiation with wavelengths less than 310 nm. The oxygen atom (O) produced reacts with water to form  $\text{OH}^{\bullet}$ . This reaction mechanism is the reason why a small amount of ozone is essential in the troposphere. Other sources of  $\text{OH}^{\bullet}$  are the photolysis of nitrous acid ( $\text{HONO}$ ), hydrogen peroxide ( $\text{H}_2\text{O}_2$ ), or peroxy-methane ( $\text{CH}_3\text{OOH}$ ); the reaction of nitrogen monoxide ( $\text{NO}$ ) with the hydroperoxyl radical ( $^{\bullet}\text{HO}_2$ ); or the reaction of alkenes with ozone.

Only a few compounds in the troposphere do not react at all or react only very slowly with the hydroxyl radical. These include the chlorofluorocarbons (CFCs), nitrous oxide ( $\text{N}_2\text{O}$ ), and carbon dioxide ( $\text{CO}_2$ ). The rate of methane ( $\text{CH}_4$ ) oxidation by  $\text{OH}^{\bullet}$  is also very slow, between 100 and 1,000 times slower than other organic compounds. This is why methane concentrations in the atmosphere can reach around 1.7 ppm ( $1.7 \mu\text{mol mol}^{-1}$ ), a value significantly higher than the concentrations of other organic trace gas which are generally below 1 ppb ( $1 \text{ nmol mol}^{-1}$ ).

The focus of this chapter is the reaction



where S is a substrate that can be a nanotube, a fullerene, a polyaromatic molecule, or graphite;  $\text{SOH}^{\bullet}$  is the “intermediate” complex, a minimum on the potential energy surface.

## 11.2 Computational Methods

All the models were calculated within the density functional approximation; the molecular or crystalline orbitals have been expressed as a linear combination of atomic orbitals (LCAO) using a localized Gaussian basis set. We used a hybrid density functional B3LYP method (Becke 1996) with a split-valence basis set with d polarization function 6-31G(d) (Francl et al. 1982). This computational model is a reasonable compromise between accuracy and computational cost when applied to big molecules (Johnson et al. 1993): we expect that such a computational model gives reliable reaction energies when applied.

We used the Gaussian 03 program (Frisch et al. 2004) for molecular models and Crystal09 and Crystal98 programs (Dovesi et al. 2010) for periodical system. We studied  $(n,0)$  and  $(n,n)$ , zigzag and armchair dissection cuts, respectively; carbon nanotubes, both like cluster and periodical systems; and fullerenes and graphite crystal with 2D periodicity.

## 11.3 Carbon Nanotube Reactivity

As test of nanotube (S) of reactivity, we chose the reaction (11.1) with  $\text{OH}^\bullet$  radical, to produce the oxidrilated radical adduct ( $\text{SOH}^\bullet$ ).

The reaction energy  $\Delta E$  is the difference between the energy of the product  $\text{SOH}^\bullet$  and the energy of the reactants S and  $\text{OH}^\bullet$ .

$$\Delta E = E(\text{SOH}^\bullet) - E(\text{S}) - E(\text{OH}^\bullet)$$

$\Delta E$  is a negative number, do to the higher stability of the product respect to the reactants. Figure 11.1 shows a typical geometry of a radical adduct  $\text{SOH}^\bullet$ . The OH bond length is in the range 1.23–1.45 Å. The attack is “on top”: the carbon center bonded to  $\text{OH}^\bullet$  gets a pyramidal geometry because of a change from a  $sp^2$  tri-coordination to a partial  $sp^3$  tetra-coordination. Figure 11.2 shows the energy profile for the  $\text{OH}^\bullet$  attachment to a periodic nanotube (12,0), as a function of the carbon-oxygen d(C–O) distance. Each point is obtained via a constrained optimization, where all the internal coordinates are relaxed, but the “reaction” C–O distance is fixed to a desired value. The reaction profile does not show any activation barrier, as expected for a radical attachment to a  $\pi$  electronic system (Table 11.1).

In Fig. 11.3 we report the reaction energy  $\Delta E$  for the periodic nanotube models versus the  $1/n$  component of the rolling-up chiral vector  $(n,n)$  or  $(n,0)$ . This vector corresponds to the periodic boundary conditions and gives us the dispersion relations of the one-dimensional bands which link wavevector to energy (Saito et al. 1992). The nanotubes  $(3n,0)$  with zigzag dissection cuts are low-gap semiconductors (meV). The green ones  $(n,n)$  with armchair cuts are metallic, whereas light blue carbon nanotubes  $(n,0)$ , with  $n$  not multiple of 3, are semiconductors.

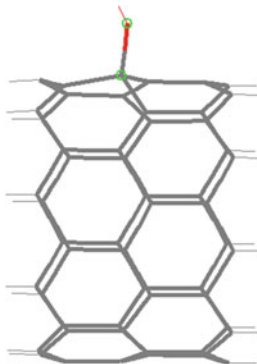


**Fig. 11.1** Molecular plot of the equilibrium geometry of the reaction product of the on-top attachment of OH radical on carbon nanotube. The on-top OH attachment to the nanotube is the only stable point of the potential energy surface (*PES*). The other possible geometry, the epoxy-like bridge, is a saddle point. The pyramidalization of the carbon coordination is evident in all cases: the (C–C(OH)–C) angle is in the range 110–120°

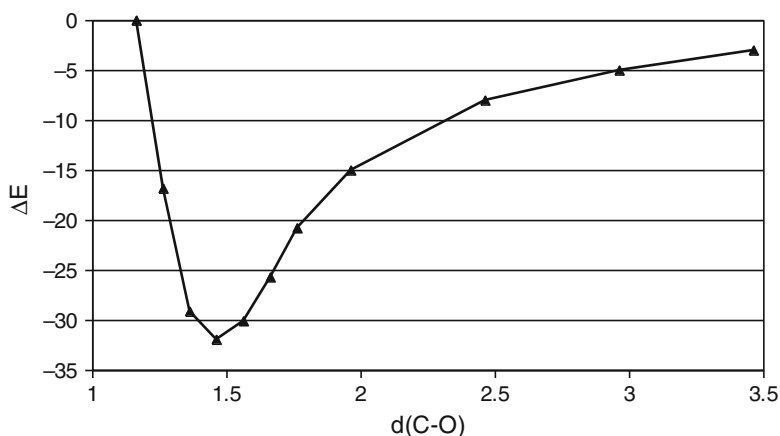


**Fig. 11.2** Reaction energy profile for the reaction of OH radical with the (12,0) periodic nanotube. Reaction energy  $\Delta E$  in kcal/mol, bond distance  $d(\text{C-O})$  in Angstrom. As expected for a radical addition to an unsaturated carbon system, there is no activation barrier; therefore, the reaction energy  $\Delta E$  can be assumed as an unambiguous index of reactivity

The fitting linear relation is  $-\Delta E = A + B/n$ , with a correlation coefficient of about 0.95; the number of carbon atoms per elementary cell is  $4n$ ,  $n$  being proportional to the nanotube radius. The graphene is the limit situation of a flat surface that corresponds to an infinite curvature radius:

$$\lim_{r \rightarrow \infty} (-\Delta E) = \lim_{n \rightarrow \infty} (-\Delta E) \cong \lim_{n \rightarrow \infty} A + \frac{B}{n} = A \quad (11.2)$$

**Table 11.1** Reaction energies  $\Delta E$  for the  $\text{OH}^*$  attachment to a variety of carbon nanotube substrates, either cluster or periodical

Periodic models			Molecular models		
Chiral vector	No. of struct. units	$-\Delta E$	Chiral vector	No. of struct. units	$-\Delta E$
(9,0)	1	37.0	(9,0)	2	72.3
(9,0)	2	36.0	(9,0)	3	59.8
(9,0)	3	29.4	(9,0)	4	58.3
(8,0)	1	49.9	(8,0)	2	43.9
(8,0)	2	36.3	(8,0)	3	28.9
(8,0)	3	28.0	(8,0)	4	28.9
(5,5)	1	49.9	(5,5)	2	43.9
(5,5)	2	36.3	(5,5)	3	28.9
(5,5)	3	28.0	(5,5)	4	28.9
(7,7)	1	44.8	(7,7)	2	16.6
			(7,7)	3	25.4
			(7,7)	4	18.9
(11,11)	1	27.8	(11,11)	2	10.7
			(11,11)	3	22.5
(13,0)	1	26.0	(13,0)	2	91.5
(19,0)	1	19.6	(19,0)	2	103.5
(15,15)	1	23.0	(15,15)	2	8.5
(18,0)	1	25.7	(18,0)	2	78.3
(12,0)	1	31.1	(12,0)	2	69.1
(26,0)	1	13.8	(26,0)	2	112.4
(24,0)	1	24.8	(24,0)	2	110.0
			(10,0)	2	71.8
			(6,6)	2	20.9
			(11,0)	2	80.9
			(14,0)	2	75.6
			(15,0)	2	90.4
			C60		36.6
			C20		87.0
			C30		62.5
			C36		6.0
			C50		38.3
Graphene	(3, 3)	15.2			

There is no way of finding a strict correlation between the reactivity  $\Delta E$  and some local geometrical feature, such as the diameter of the nanotube or the radius of curvature. The impossibility of rationalizing this table using only local geometry is the basis of our interest in the topology indexes

so that the reaction energy for a 2-dimension periodic planar system is about  $11 \pm 2$  kcal/mol; this is in good agreement with the value of  $-15.2$  kcal/mol obtained for a planar graphene by using a (3,3) super-cell for minimizing the lateral interaction among adsorbed OH. The large value of the correlation coefficient



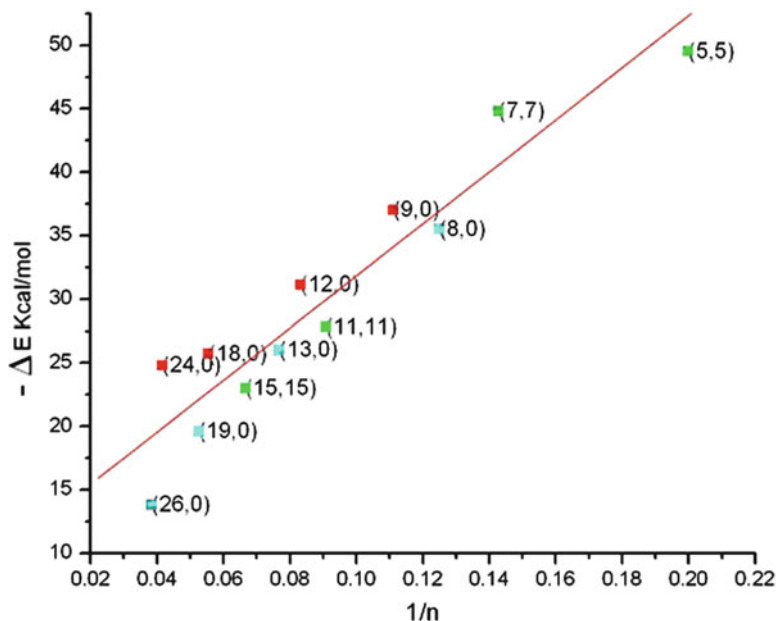


**Fig. 11.3** Plot of the reaction energy  $\Delta E$  for the periodic models versus the reciprocal of the chiral vector module that is proportional to the reciprocal of the curvature radius

**Table 11.2** Local softness for a selected set of periodic models of nanotubes

Chiral vector	Local softness (1/eV)
(9,0)	0.09
(8,0)	0.02
(5,5)	0.76
(7,7)	0.71

between the reactivity  $\Delta E$  and the nanotube curvature shows the importance of the local chemical factors in the reactivity: the smaller is the curvature radius, the more bent is the  $\pi$  bond between carbon atoms, the larger is the reaction energy  $-\Delta E$ , and the larger we consider the reactivity.

In the following, the considered set of the nanotubes will be divided in families that have a common algebraic structure of the chiral vector  $(n,m)$ : this quantity does not reflect a local feature of the bonds but represents a general topological feature of the model. Hence, we will use a topological analysis of the data reported in Table 11.2 and in Fig. 11.3 for a better understanding of the correlation between structure and reactivity. As a consequence, we also found a higher correlation coefficient between the reactivity and the radius, within each nanotube family.

## 11.4 Analysis of the Reactivity of the Periodic Models

### 11.4.1 Hardness–Softness Fukui Functions

It is known that (Paritosh et al. 2003) hardness–softness Fukui functions are powerful tools to predict the reactivity site of a molecule. These reactivity descriptors derive from DFT theory.

Global hardness and softness represent the global reactivity of a molecule, and Fukui's function defines the reactivity of an atom in a molecule, being a local property.

Fukui's function and local softness are suited to describe reactivity of different substrates, while Pearson's HSAB theory suggests that hard–hard and soft–soft acid–base interactions are favorite with respect to hard–soft interaction.

It is known that soft–soft interactions are favorite in the sites where Fukui's function has a maximal “frontier control,” and on the other hand, hard–hard interactions are favorite in the site where Fukui's function has a minimal “charge control.”

Fukui's function (Chandra and Nguyen 2002; Paritosh et al. 2003; Chermette 1999) is defined as a derivative of electronic density versus the electron number at a constant external potential (fixed nuclei):

$$f_i = \left( \frac{\partial n_i}{\partial N} \right)_{v(\underline{r})} \quad (11.3)$$

Global hardness (Chandra and Nguyen 2002; Paritosh et al. 2003) is defined as  $\frac{1}{2}$  of the second derivative of the energy versus the electron number at a constant external potential, that is, the derivative of the chemical potential versus the electron number:

$$\eta = \frac{1}{2} \left( \frac{\partial^2 E}{\partial N^2} \right)_{v(\underline{r})} = \frac{1}{2} \left( \frac{\partial \mu(\underline{r})}{\partial N} \right)_{v(\underline{r})} \quad (11.4)$$

The global softness is equivalent to

$$S = \frac{1}{2\eta} = \left( \frac{\partial N}{\partial \mu} \right)_{v(\underline{r})} \quad (11.5)$$

Similarly local softness is defined as

$$s(\underline{r}) = \left( \frac{\partial \rho(\underline{r})}{\partial \mu} \right)_{v(\underline{r})} = \left( \frac{\partial \rho(\underline{r})}{\partial N} \right)_{v(\underline{r})} \cdot \left( \frac{\partial N}{\partial \mu} \right)_{v(\underline{r})} = f(\underline{r}) \cdot S \quad (11.6)$$

In the case of periodic nanotubes, it is necessary to calculate the partial derivatives for an infinite system: in the following,  $E_c$  is the energy per unit cell, and  $N_c$  is the number of electrons per unit cell. If we want to compute the chemical potential for a periodic system, we have

$$\mu = \left( \frac{\partial E}{\partial N} \right)_{v(\underline{r})} = \lim_{n \rightarrow \infty} \left( \frac{\partial (n \cdot E_c)}{\partial (n \cdot N_c)} \right)_{v(\underline{r})} = \left( \frac{\partial (E_c)}{\partial (N_c)} \right)_{v(\underline{r})} \quad (11.7)$$

with  $n$  being the number of elementary cells.

So the chemical potential for a periodic system is equal to that one calculated in the elementary cell, or, better, the partial derivatives of the extensive quantities are equivalent to those calculated in the elementary cell. From now on, these results will be used omitting the  $c$  subscript.

As a further step, Fukui's condensed function was then calculated by integrating Fukui's function over the  $i$ th atomic volume (Kleiner and Eggert 2001):

$$\begin{aligned} f_i &= \iiint_{V_i} f(\underline{r}) d^3 \underline{r} = \iiint_{V_i} \left( \frac{\partial \rho(\underline{r})}{\partial N} \right)_{v(\underline{r})} d^3 \underline{r} \\ &= \left( \frac{\partial \iiint_{V_a} \rho(\underline{r}) d^3 \underline{r}}{\partial N} \right)_{v(\underline{r})} = \left( \frac{\partial n_i}{\partial N} \right)_{v(\underline{r})} \end{aligned} \quad (11.8)$$

The Fukui condensed function for the  $i$ th atom is equivalent to the derivative of the charge of the  $i$ th atom with respect to the total molecular charge.

### 11.4.2 Fukui's Function and Local Softness for "Symmetrical" Substrates

Fukui's condensed function for carbon nanotube substrates is obtained considering "extensively" the charge of the  $i$ th atom for the cells of the same atom periodically repeated.

If the elementary cell charge grows of a  $dN$  amount, all atom being equivalent for symmetry and  $4n$  being the atom number for the elementary cell in the  $(n, n)$  and  $(n, 0)$  carbon nanotubes, it follows

$$dn_i = \frac{dN}{4n} \quad (11.9)$$

from which

$$f_i = \left( \frac{\partial n_i}{\partial N} \right)_{v(\underline{r})} = \frac{1}{4n} \quad (11.10)$$

Considering the reaction of the periodic carbon nanotubes with  $\text{OH}^*$ , it follows that reactivity is proportional to the Fukui function, having a soft–soft interaction (easy polarizability, low charge density,  $B > 0$ ):

$$-\Delta E \approx A + \frac{B}{n} = -E_{\text{periodical-planar}} + k f_i = A + \frac{k}{4n} \quad (11.11)$$

$B < 0$  instead entailed a hard–hard interaction: low polarizability, high charge density.

Making a detailed analysis of the different families of nanotubes, using condensed local softness for the  $i$ th atom,

$$\begin{aligned} s_i &= \iiint_{V_i} s(\underline{r}) d^3 \underline{r} = \iiint_{V_i} f(\underline{r}) \cdot S d^3 \underline{r} \\ &= S \iiint_{V_i} f(\underline{r}) d^3 \underline{r} = S \cdot f_i \end{aligned} \quad (11.12)$$

In the case of periodic carbon nanotubes we have

$$s_i = S \cdot f_i = S \cdot \frac{1}{4n} \quad (11.13)$$

Global softness  $S$  is equal to

$$S = \frac{1}{2\eta} = \left( \frac{\partial N}{\partial \mu} \right)_{v(\underline{r})} = \frac{1}{\left( \frac{\partial^2 E}{\partial N^2} \right)_{v(\underline{r})}} \quad (11.14)$$

So it follows

$$s_i = \frac{1}{4n \cdot \left( \frac{\partial^2 E}{\partial N^2} \right)_{v(\underline{r})}} \quad (11.15)$$

We calculated the second derivative of the energy versus the electron number using the finite difference approximation— $f(x)$  can be developed in Taylor's series nearby to  $x$ :

$$\begin{aligned} f(x+h) &= f(x) + h \cdot f'(x) + \frac{h^2}{2} \cdot f''(x) + O(2) \\ f(x-h) &= f(x) - h \cdot f'(x) + \frac{h^2}{2} \cdot f''(x) + O(2) \end{aligned} \quad (11.16)$$

Adding the two equations, it results

$$f''(x) = \frac{f(x+h) + f(x-h) - 2f(x)}{h^2} + O(2) \quad (11.17)$$

Letting be  $h = 1$  the second derivative of the energy versus the electron number, we have

$$\begin{aligned} \left( \frac{\partial^2 E}{\partial N^2} \right)_{v(r)} &= E(N+1) + E(N-1) - 2E(N) + O(2) \\ &= (E(N+1) - E(N)) + (E(N-1) - E(N)) + O(2) \end{aligned} \quad (11.18)$$

In freezing MOs approximation, the ionization energy is  $I = E(N-1) - E(N)$  and the electron affinity is  $A = E(N) - E(N+1)$ . It follows

$$\left( \frac{\partial^2 E}{\partial N^2} \right)_{v(r)} = I - A + O(2) \quad (11.19)$$

According to Koopmans's theorem (Rioux 1999), ionization energy is simply the value of the HOMO orbital energy with the minus sign. In molecules with coupled spins (such as nanotube substrates), electron affinity is equal to minus LUMO energy. It follows

$$\left( \frac{\partial^2 E}{\partial N^2} \right)_{v(r)} = I - A + O(2) = E_{\text{LUMO}} - E_{\text{HOMO}} + O(2) = E_{\text{gap}} + O(2) \quad (11.20)$$

When substituting this result in the expression of local softness, we have

$$s_i = \frac{1}{4n \cdot \left( \frac{\partial^2 E}{\partial N^2} \right)_{v(r)}} \cong \frac{1}{4n \cdot E_{\text{gap}}} \quad (11.21)$$

On the right member of the last expression, we neglected terms of order superior to the second one ( $O(2)$ ).

Going from molecular to periodic system (nanotubes), MOs go into bands, and we use the gap for characterizing periodic nanotubes. If, for example, we consider the (9,0) nanotube cluster saturated at the borders with H atoms, we have a gap energy variation versus the number of sub-unities as shown in Table 11.3.

Hence, the local softness can be computed as

$$s_i \cong \frac{1}{4n \cdot E_{\text{gap}}} \quad (11.22)$$

**Table 11.3** HOMO-LUMO gap of the (9,0) nanotube cluster, varying the number of structure unit

No. of struct. units	Gap (eV)
2	0.60
3	0.41
4	0.30
5	0.30
Periodic	0.30

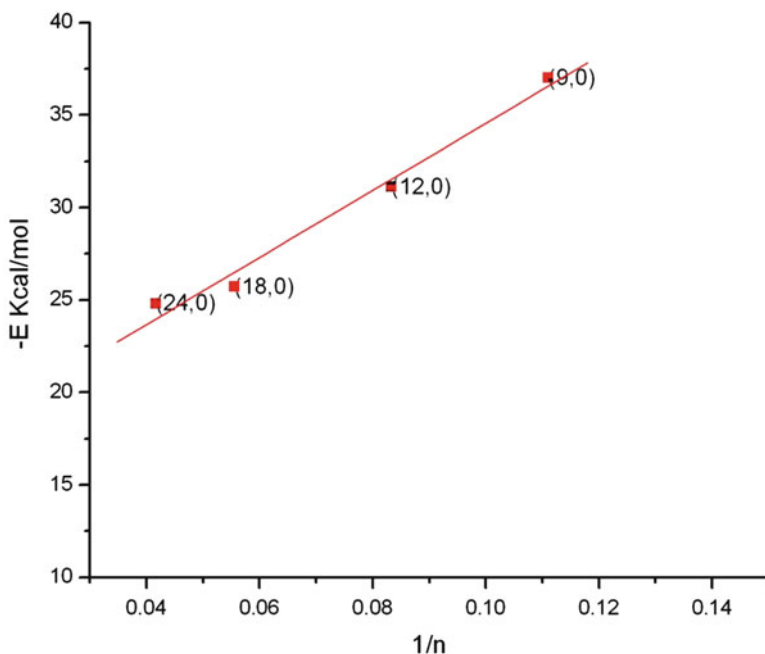


**Fig. 11.4** Reaction energy of  $\text{OH}^*$  with small-gap nanotubes  $(3n,0)$ . The correlation coefficient between the reactivity  $\Delta E$  and the radius is 0.97; we can also note that it is the same we found in Figs. 11.5 and 11.9

### 11.4.3 Reactivity of Periodic Nanotubes

By means of local softness, it is possible to classify the periodical nanotubes in three families, according to their reactivity:

Differently from the light blue family of  $(n,0)$  nanotubes ( $n$  is not a multiple of 3) which have higher gap (Kleiner and Eggert 2001; White and Mintmire 2005; Gülseren et al. 2002): 1.27 eV for (8,0) and local softness of 0.02 1/eV, the  $(3n,0)$  nanotubes (Fig. 11.4) are small-gap semiconductors (0.30 eV in (9,0) with a higher local softness of 0.09 1/eV). The electronic bands of these nanotubes are reported in Figs. 11.6 and 11.7.

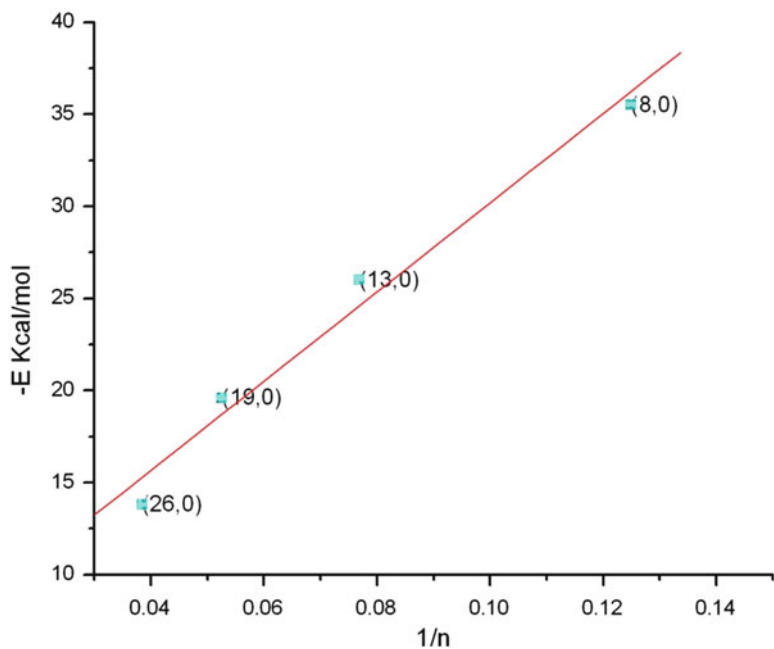


**Fig. 11.5** Reaction energy  $\Delta E$  for semiconductor nanotubes  $(n,0)$  versus the reciprocal of the nanotube radius

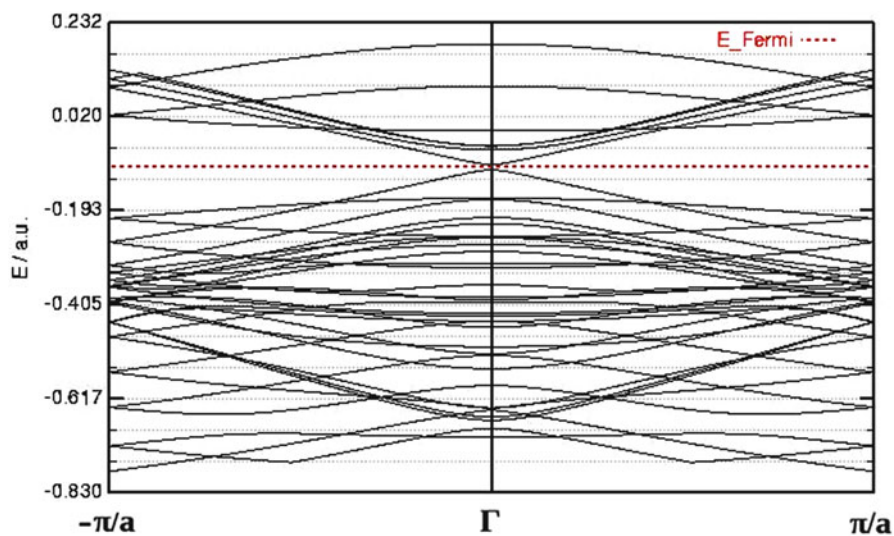


**Fig. 11.6** Electronic bands structure for a  $(9,0)$  nanotube, small-gap semiconductor (0.30 eV)

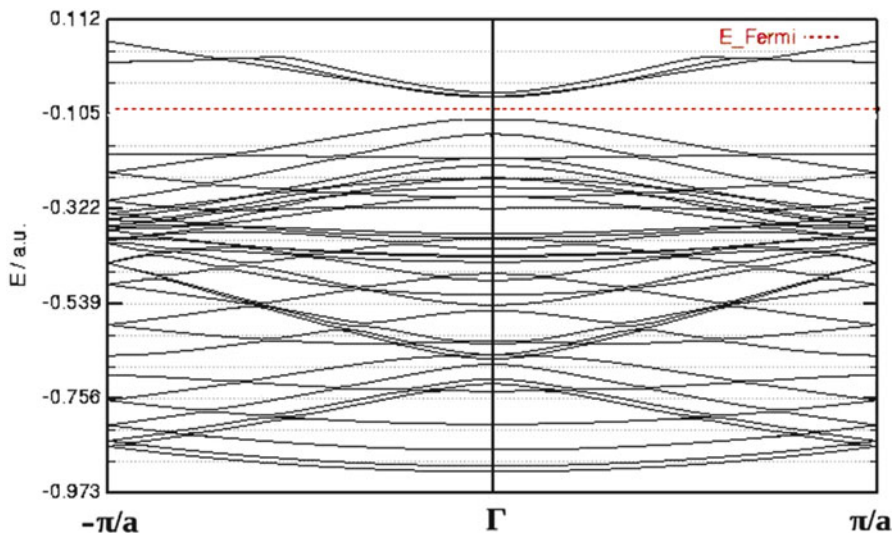


**Fig. 11.7** Electronic bands for a (8,0) nanotube, high-gap semiconductor (1.27 eV)

For both families we have a correlation of about 99 %; therefore, we can conclude that the gap separation criterion provides good results.

For the  $(3n,0)$  family, if the radius tends to infinity, the reaction energy becomes  $16.4 \pm 1.3$  kcal/mol that is in good agreement with P33 2D planar periodic graphene (15.2 kcal/mol). Noteworthy, graphenes are also small-gap systems.

#### 11.4.4 Local Softness of Metallic Nanotubes

The local softness formula used above does not match with the  $(n,n)$  metallic nanotubes (Chermette 1999) due to its diverging behavior, due to a zero gap. Because we cannot neglect the  $O(2)$  terms, it follows

$$s_i = \frac{1}{4n \cdot O(2)} \quad (11.23)$$

The literature gap (Chermette 1999; Kleiner and Eggert 2001; White and Mintmire 2005) is in agreement with our band calculation; for example, the  $(7,7)$  nanotube is metallic: the band structure calculated in this work and reported in Fig. 11.8 confirms this behavior.



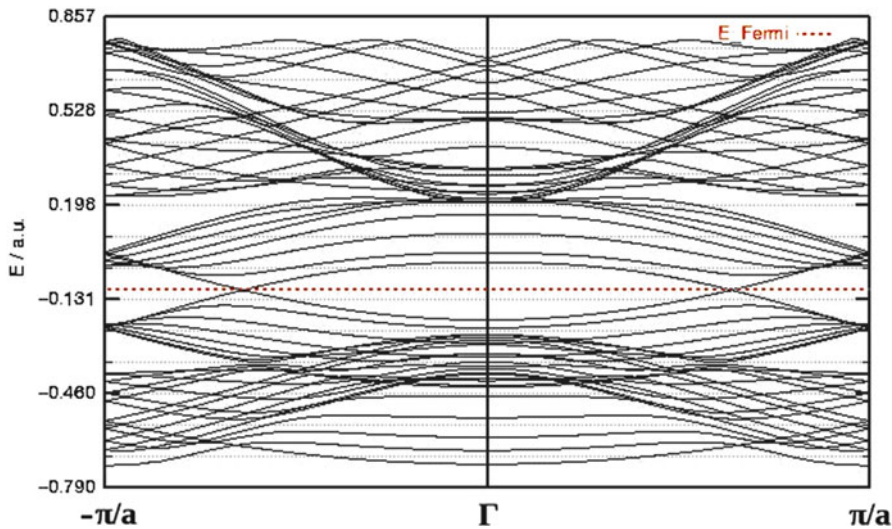


Fig. 11.8 Electronic bands structure for a (7,7) metallic carbon nanotube

We can calculate now the global softness for a zero-gap system (Chermette 1999). The number of electrons  $N$  can be expressed, at  $T = 0$  K and within the adiabatic approximation, as a functional of  $g(\varepsilon)$ , the density of states (DOS):

$$N = \int_0^{\varepsilon_F} g(\varepsilon) d\varepsilon \tag{11.24}$$

Then,

$$S = \left( \frac{\partial N}{\partial \mu} \right)_{v(\underline{r})} = \left( \frac{\partial N}{\partial \varepsilon_F} \right)_{v(\underline{r})} \tag{11.25}$$

It follows

$$S = \left( \frac{\partial \int_0^{\varepsilon_F} g(\varepsilon) d\varepsilon}{\partial \varepsilon_F} \right)_{v(\underline{r})} = g(\varepsilon_F) + \int_0^{\varepsilon_F} \frac{dg(\varepsilon)}{d\varepsilon_F} d\varepsilon \tag{11.25}$$

We can neglect the last term that cannot be omitted for small system (Chermette 1999); because nanotubes are periodic systems with a number of infinity of atoms, we obtain

$$S \cong g(\varepsilon_F) \tag{11.26}$$

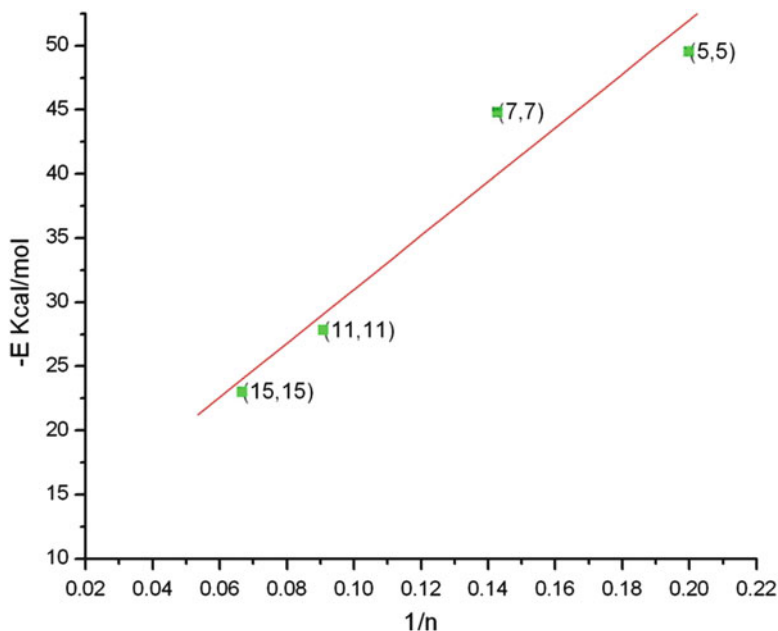


**Fig. 11.9** Plot of the reaction energy  $\Delta E$  versus the reciprocal of the nanotube radius for metallic nanotubes  $(n,n)$

We can calculate now the local softness, using the expression (11.10) for the local Fukui function:

$$s_i = S \cdot f_i = S \cdot \frac{1}{4n} \quad (11.27)$$

It follows

$$s_i \cong \frac{g(\varepsilon_F)}{4n} \cong \frac{1}{4n \cdot O(2)} \quad (11.28)$$

This expression of local softness holds true for  $(n,n)$  metallic nanotubes. We can write

$$g(\varepsilon_F) \cong \frac{1}{O(2)} \quad (11.29)$$

This term is more important than the  $1/E_{\text{gap}}$  term in the expression of local softness and will create a major distortion from the linear trend. The linear regression for a  $(n,n)$  family is shown in Fig. 11.9.

We find a good correlation (97 % ca), a little worst than the  $(n,0)$  case, and calculating the  $1/E_{\text{gap}}$ 's values for  $(9,0)$  and  $(8,0)$  (3.33 1/eV and 0.79 1/eV, respectively) and the  $g(E_f)$ 's (the DOS terms at the Fermi energy level) for  $(5,5)$  and  $(7,7)$  (15.29 1/eV and 19.99 1/eV, respectively), it follows that in the expression of local softness, the values for  $(n,n)$  have a higher weight when compared to the  $(n,0)$  ones whose values are shown in Table 11.2.

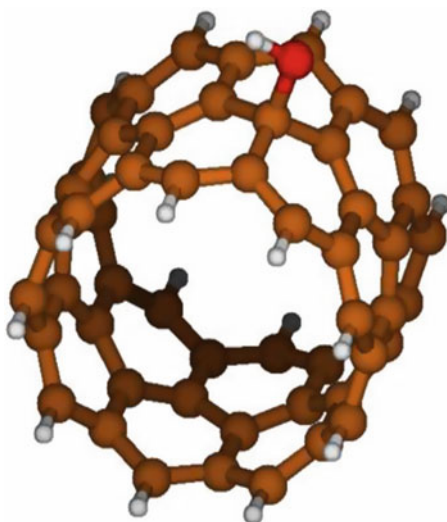
It should be noted that the variation of local softness between  $(5,5)$  and  $(7,7)$  is of the same entity as the one between  $(9,0)$  and  $(8,0)$  families.

## 11.5 Reactivity of Cluster Nanotubes

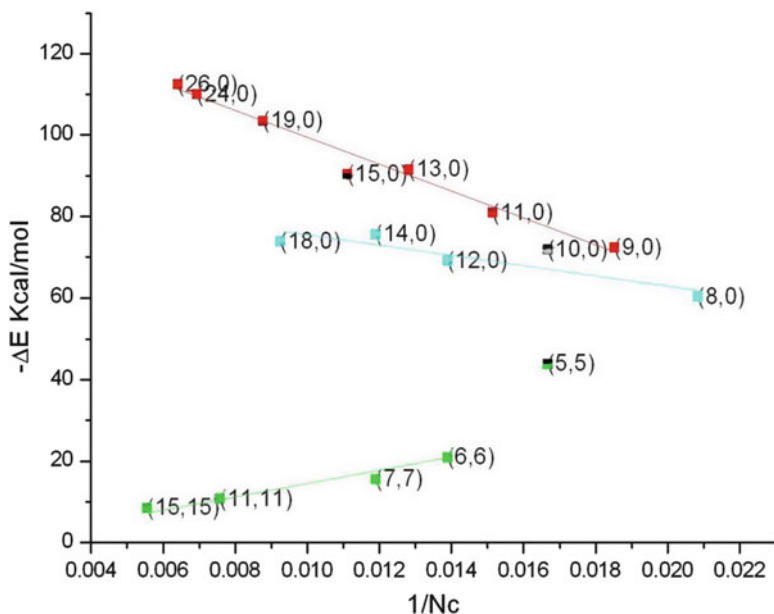
Figure 11.10 reports the structure of a  $(5,5)$  nanotube as a cluster of two sub-unities after reaction with  $\text{OH}^\bullet$ . The reaction energy of different clusters with  $\text{OH}^\bullet$  as a function of the  $1/N_c$  number ( $N_c$  is the number of carbon atoms constituting the cluster) is shown in Fig. 11.12. In the case of a symmetrical system,  $1/N_c$  is the Fukui function.

Figure 11.11 shows the reactivity ( $\Delta E$ ) versus the reciprocal of the number of carbon atoms  $N_c$ . Like periodic nanotubes the reactivities are grouped in three families. For the first two families  $(n,0)$  and  $(3n,0)$ , we get a linear fitting:  $-\Delta E = A + B/N_c$  with  $B < 0$  ( $N_c$  being the number of carbon atoms of the  $(n,m)$  cluster with formula,  $\text{C}_{6(n+m)}\text{H}_{2(n+m)}$ ); so there is an anti-correlation between the reaction energy and the Fukui function.

Also in the case of an armchair  $(n,n)$  cluster, a linear fitting with the Fukui function was found, and the trend is equivalent to that of periodic nanotubes with  $B > 0$ .

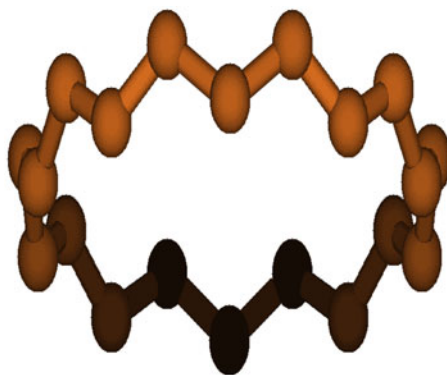


**Fig. 11.10** Molecular plot of the  $(5,5)$  nanotubes cluster composed of two structural units after reaction with  $\text{OH}^\bullet$



**Fig. 11.11** Plot of reaction energy  $\Delta E$  versus the reciprocal of the number of carbon atoms  $N_c$  for cluster models of nanotubes, all containing two structure units. Depending on chiral vector, the model clearly separates three families

**Fig. 11.12** Structural motive of the nanotube clusters



Comparing the geometry of  $(n,0)$  and  $(n,n)$  structures, we noticed that while the ratio  $C/H = 3$  is a constant value, the distance of the fourth nearest H atoms to the reacting carbon of the substrate varies, being 3.44, 3.44, 3.92, and 4.61 Å for  $(n,0)$  and 3.43, 3.90, 4.65, and 4.98 Å for  $(n,n)$ . In the  $(n,0)$  structures, hydrogen atoms are closer to carbon atoms than in the  $(n,n)$  cases.

Due to different electronegativity of C and H, we can predict that in the  $(n,0)$  clusters, the reacting carbon of the substrate is more negatively charged than in the  $(n,n)$  clusters, and in such a way, it results  $B > 0$ , both for periodical

**Table 11.4** Mulliken charges of the carbon atom subject to OH attachment in some nanotube cluster

Chiral vector	Mulliken charge
(5,5)	+0.003
(7,7)	+0.008
(8,0)	-0.008
(9,0)	-0.007

systems (no charge in the substrate for symmetry) and for  $(n,n)$  clusters. The Mulliken charges of the reacting carbons in  $(n,n)$  and  $(n,0)$  clusters are reported in Table 11.4.

### 11.5.1 Topological Analysis of Nanotube Clusters

The three families of nanotube clusters were analyzed from a topological point of view. Nanotube clusters are composed of two benzene belts, having three rings like the one shown in Fig. 11.12.

Every carbon in nanotube clusters has a  $sp^2$  tri-coordinated hybridization and one  $\pi$  delocalized electron, so that the number of delocalized electron is  $6n$  for  $(n,0)$  clusters and  $12n$  for  $(n,n)$  clusters. Applying the Hückel rule to a quasi-planar ring having  $2n$  electrons as in Fig. 11.12, it follows that for the  $(n,0)$  family,  $2n = 4k + 2$  ( $k = n/2 + 1/2$ ) and for the  $(n,n)$  family,  $4n = 4k + 2$  ( $k = n + 1/2$ ),  $k$  being a positive integer.

It results that for  $(n,0)$  clusters, an odd  $n$  means aromaticity, whereas an even  $n$  implies non-aromaticity; for each  $(n,n)$  clusters, we have non-aromaticity.

As shown in Fig. 11.12, the  $(n,0)$  family has  $4k + 2$   $\pi$  electrons (odd  $n$ ) with high reactivity in every “ring.” For a high value of  $n$ , the light blue family  $(n,0)$  with even  $n$  “tends” to the red  $(n,0)$  family with odd  $n$ . The  $(n,n)$  family, even  $n$ , and the  $(n,n)$  green one have  $4k$   $\pi$  electrons (not aromatic) and consequently are less reactive.

These considerations are also in agreement with the Aufbau sequence (Bellucci and Onorato 2005) of a carbon nanotube where  $4k$  electrons ( $k$  as integer) correspond to the filling of the shell, because of their atomic-like behavior where each shell is filled by four electrons with opposite spin.

The shell model of nanotubes whose electrons are subjected to harmonic forces implies the existence of magic numbers (Bellucci and Onorato 2005) of electrons  $N = 2, 6, 12, 20, k^*(k + 1)$ ,  $k$  integer. In our clusters of nanotubes for each ring (Fig. 11.12), we have a magic number if  $k^*(k + 1)/2 = n$  for  $(n,0)$  or  $k^*(k + 1)/4 = n$  for  $(n,n)$  clusters. Considering a single ring, the (10,0), (5,5), and (15,0) clusters correspond to magic numbers, and this explains the observed anomalies in Fig. 11.11 (half black quads).

**Table 11.5** Reactivity  $\Delta E$  for some cluster nanotube models

Chiral vector	No. of struct. units	$-\Delta E$
(9,0)	2	72.3
	3	59.8
	4	58.3
(8,0)	2	60.2
	3	58.9
	4	60.3
(5,5)	2	16.6
	3	25.4
	4	18.9

The edge effects decrease with the increase of the length of the cluster represented by the number of structural units

### 11.5.2 Edge Effects for Nanotube Clusters

In Table 11.5, we report the variations of the reaction energy  $\Delta E^*$ , due to the increment of the number of benzene rings for the (9,0), (8,0), and (5,5) clusters. We concluded that the edge effect can be considered a low entity phenomenon.

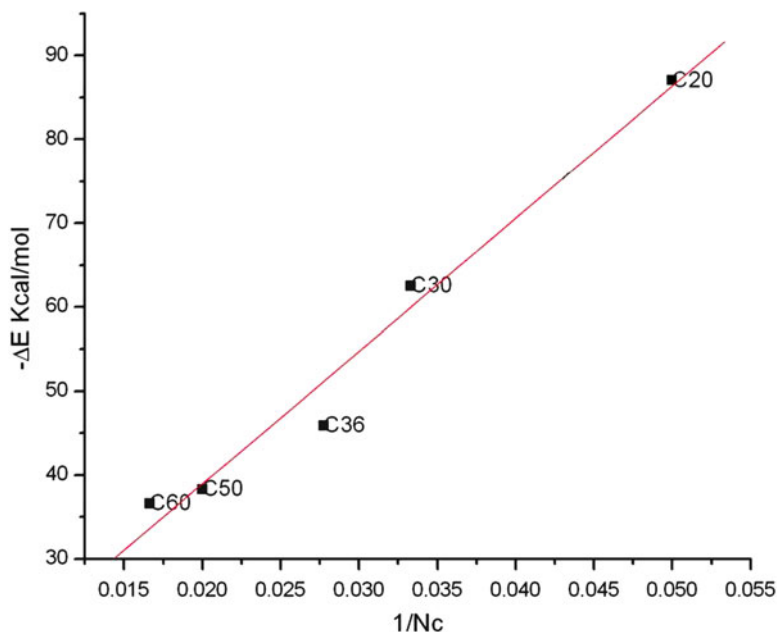
## 11.6 Reactivity of Fullerenes

Figure 11.13 reports the reactivity energies of fullerenes with  $\text{OH}^*$  as a function of the  $1/N_c$  values.

In these cases carbon atoms are quite equivalent, their charge being zero for symmetry, and from the fitting of the reaction energy  $-\Delta E = A + B/N_c$ , it results  $B > 0$ . The set of fullerenes considered in this study seems to belong to the same topological family.

## 11.7 Conclusions

The reaction of fullerenes and carbon nanotubes with hydroxyl radical ( $\text{OH}^*$ ) is the initial step of many oxidation mechanisms both in liquid and in gas phases. More in detail, such reaction is very important for the “large” chemical family of soot, due to the fact that the addition of the hydroxyl radical to the double bond is the recurring motive of the oxidation processes (may be photochemically or



**Fig. 11.13** Plot of the reactivity  $\Delta E$  versus the reciprocal of the total number of carbon atoms  $N_c$  for fullerenes

electrochemically driven) of these substances. Surprisingly the correlation between the nanotube structure and the reactivity toward OH cannot be established taking into account only local effects, such as the deformation of P carbon–carbon bond, due to the curvature of nanotube. The topology factors, represented by the numerical properties of the chiral vector  $(n,m)$ , have to be taken into account, as clearly shown by comparison of Fig. 11.3 with Figs. 11.4, 11.5, and 11.9. Further on we established a connection between the reactivity index  $\Delta E$  and the topology by means of the Fukui integrated function. In the case of periodic structures, it became possible to establish a link between the reactivity  $\Delta E$  and the electronic properties like the energy band gap, using the local softness index. In nanotube cluster models, the effects of the edge saturation on the reactivity have been rationalized.

## References

- Arrais A, Boccaleri E, Diana E (2004) Fullerenes Nanotubes Carbon Nanostruct 12:789–809  
 Becke AD (1996) J Chem Phys 104:1040–1046  
 Bellucci S, Onorato P (2005) Phys Rev B 71:1–8  
 Chandra AK, Nguyen MT (2002) Int J Mol Sci 3:310–315  
 Chermette HJ (1999) J Comput Chem 20:129–154

- Dovesi R, Saunders VR, Orlando R, Zicovich-Wilson CM, Pascale F, Civalleri B, Doll K, Bush IJ, D'Arco P, Lunell M (2010) Crystal 2009 user manual. Turin University, Turin. Saunders VR, Dovesi R, Roetti C, Causa M, Harrison NM, Orlando R, Zicovich-Wilson CM (1998) CRYSTAL98 user manual. Turin University, Turin
- Franci MM, Petro WJ, Hehre WJ, Binkley JS, Gordon MS, DeFrees DJ, Pople JAJ (1982) Chem Phys 77:3654
- Frisch MJ, Trucks GW, Schlegel HB, Scuseria GE, Robb MA, Cheeseman JR, Montgomery JA Jr, Vreven T, Kudin KN, Burant JC, Millam JM, Iyengar SS, Tomasi J, Barone V, Mennucci B, Cossi M, Scalmani G, Rega N, Petersson GA, Nakatsuji H, Hada M, Ehara M, Toyota K, Fukuda R, Hasegawa J, Ishida M, Nakajima T, Honda Y, Kitao O, Nakai H, Klene M, Li X, Knox JE, Hratchian HP, Cross JB, Bakken V, Adamo C, Jaramillo J, Gomperts R, Stratmann RE, Yazyev O, Austin AJ, Cammi R, Pomelli C, Ochterski JW, Ayala PY, Morokuma K, Voth GA, Salvador P, Dannenberg JJ, Zakrzewski VG, Dapprich S, Daniels AD, Strain MC, Farkas O, Malick DK, Rabuck AD, Raghavachari K, Foresman JB, Ortiz JV, Cui Q, Baboul AG, Clifford S, Cioslowski J, Stefanov BB, Liu G, Liashenko A, Piskorz P, Komaromi I, Martin RL, Fox DJ, Keith T, Al-Laham MA, Peng CY, Nanayakkara A, Challacombe M, Gill PMW, Johnson B, Chen W, Wong MW, Gonzalez C, Pople JA (2004) Gaussian 03, revision C.02. Gaussian, Inc., Wallingford
- Gonzalez-Lafont A, Villa J, Lluch JM, Bertran J, Steckler R, Truhlar DG (1998) J Phys Chem A 102:3420–3428
- Gülseren O, Yildirim T, Ciraci S (2002) Phys Rev B 65:153405–153410
- Johnson BG, Gill PMW, Pople JA (1993) J Chem Phys 98:5612–5626
- Kleiner A, Eggert S (2001) Phys Rev B 64:113402–113409
- Maranzana A, Serra G, Giordana A, Tonachini G, Barco G, Causa M (2005) J Phys Chem A 109:10929–10939
- Paritosh M, Kalyan KH, Ramesh C (2003) Phys Chem Commun 6:24–27
- Rioux F (1999) J Chem Educ 76:156–158
- Saito R, Fujita M, Dresselhaus G, Dresselhaus MS (1992) Phys Rev B 46:1804–1811
- Tasis D, Tagmatakis N, Bianco A, Prato M (2006) Chem Rev 105:1105–1122
- White BCT, Mintmire JW (2005) J Phys Chem B 109:52–57



# Chapter 12

## Computation of the Szeged Index of Some Nanotubes and Dendrimers

Ali Iranmanesh

**Abstract** Let  $e$  be an edge of a  $G$  connecting the vertices  $u$  and  $v$ . Define two sets  $N_1(e|G)$  and  $N_2(e|G)$  as  $N_1(e|G) = \{x \in V(G) | d(x, u) < d(x, v)\}$  and  $N_2(e|G) = \{x \in V(G) | d(x, v) < d(x, u)\}$ . The number of elements of  $N_1(e|G)$  and  $N_2(e|G)$  are denoted by  $n_1(e|G)$  and  $n_2(e|G)$ , respectively. The Szeged index of the graph  $G$  is defined as  $Sz(G) = \sum_{e \in E(G)} n_1(e|G) n_2(e|G)$ .

In this chapter, we compute the Szeged index of some types of dendrimers, for example, dendrimer nanostars, Styrylbenzene dendrimer, Triarylamine Dendrimer of Generation 1–3, and then we compute the Szeged index of some nanotubes, for example,  $TUC_4C_8(R)$  and  $TUC_4C_8(S)$  nanotubes, Armchair Polyhex nanotube, and  $HAC_5C_6C_7[k; p]$ ,  $VC_5C_7[p; q]$ , and  $HC_5C_7[p; q]$  nanotubes.

### 12.1 Introduction

Dendrimers are large and complex molecules with very well-defined chemical structures. From a polymer chemistry point of view, dendrimers are nearly perfect monodisperse (basically meaning of a consistent size and form) macromolecules with a regular and highly branched three-dimensional architecture. They consist of three major architectural components: core, branches, and end groups. Dendrimers are produced in an iterative sequence of reaction steps (Holister and Harper 2003). In 1985, the interest in this research field started to grow exponentially:

More than 1,000 articles have been published in 2002 concerning the various aspects of dendrimer chemistry. We can consider the figure of dendrimers as the shape of a molecular graph.

---

A. Iranmanesh (✉)

Department of Mathematics, Tarbiat Modares University, P.O. Box: 14115-137, Tehran, Iran  
e-mail: [iranmanesh@modares.ac.ir](mailto:iranmanesh@modares.ac.ir)

A graph  $G$  consists of a set of vertices  $V(G)$  and a set of edges  $E(G)$ . In chemical graphs, each vertex represented an atom of the molecule, and covalent bonds between atoms are represented by edges between the corresponding vertices. This shape derived from a chemical compound is often called its molecular graph, and can be a path, a tree, or in general a graph.

A topological index is a single number, derived following a certain rule, which can be used to characterize the molecule. Usage of topological indices in biology and chemistry began in 1947 when chemist Harold Wiener (1947) introduced Wiener index to demonstrate correlations between physicochemical properties of organic compounds and the index of their molecular graphs. Wiener originally defined his index ( $W$ ) on trees and studied its use for correlation of physicochemical properties of alkenes, alcohols, amines, and their analogous compounds. A number of successful QSAR studies have been made based in the Wiener index and its decomposition forms (Agrawal et al. 2000).

Another topological index was introduced by Gutman and called the Szeged index, abbreviated as Sz (Gutman 1994).

Let  $e$  be an edge of a graph  $G$  connecting the vertices  $u$  and  $v$ . Define two sets  $N_1(e|G)$  and  $N_2(e|G)$  as  $N_1(e|G) = \{x \in V(G) | d(u, x) < d(v, x)\}$  and  $N_2(e|G) = \{x \in V(G) | d(x, v) < d(x, u)\}$ . The number of elements of  $N_1(e|G)$  and  $N_2(e|G)$  are denoted by  $n_1(e|G)$  and  $n_2(e|G)$ , respectively. The Szeged index of the graph  $G$  is defined as  $Sz(G) = Sz = \sum_{e \in E(G)} n_1(e|G)n_2(e|G)$ . The Szeged index is a modification of Wiener index to cyclic molecules. The Szeged index was conceived by Gutman at the Attila Jozsef University in Szeged. This index received considerable attention. It has attractive mathematical characteristics (Diudea et al. 2004).

In this chapter, in Sect. 12.2, we compute the Szeged index of some types of dendrimers, for example, Naphthalene dendrimer, Styrylbenzene dendrimer, dendrimer nanostars, and then in Sect. 12.3, we compute the Szeged index of some nanotubes, for example,  $TUC_4C_8(R)$  and  $TUC_4C_8(S)$  nanotubes, Armchair Polyhex nanotube, and  $HAC_5C_6C_7[k; p]$ ,  $VC_5C_7[p; q]$ , and  $HC_5C_7[p; q]$  nanotubes.

## 12.2 Computation of Szeged Index of Some Type of Dendrimers

In this section, at first we compute the Szeged index of the first, second, third, and fourth type of dendrimer nanostars. All of the results in the first part of this section have been published in Iranmanesh and Gholami (2007, 2008).

In the second part, we compute the Szeged index of the Styrylbenzene dendrimers, Triarylamine Dendrimer of Generation 1–3, and a Naphthalene dendrimer. All of the results in the second part of this section have been published in Iranmanesh and Gholami (2009) and Iranmanesh et al. (2010).

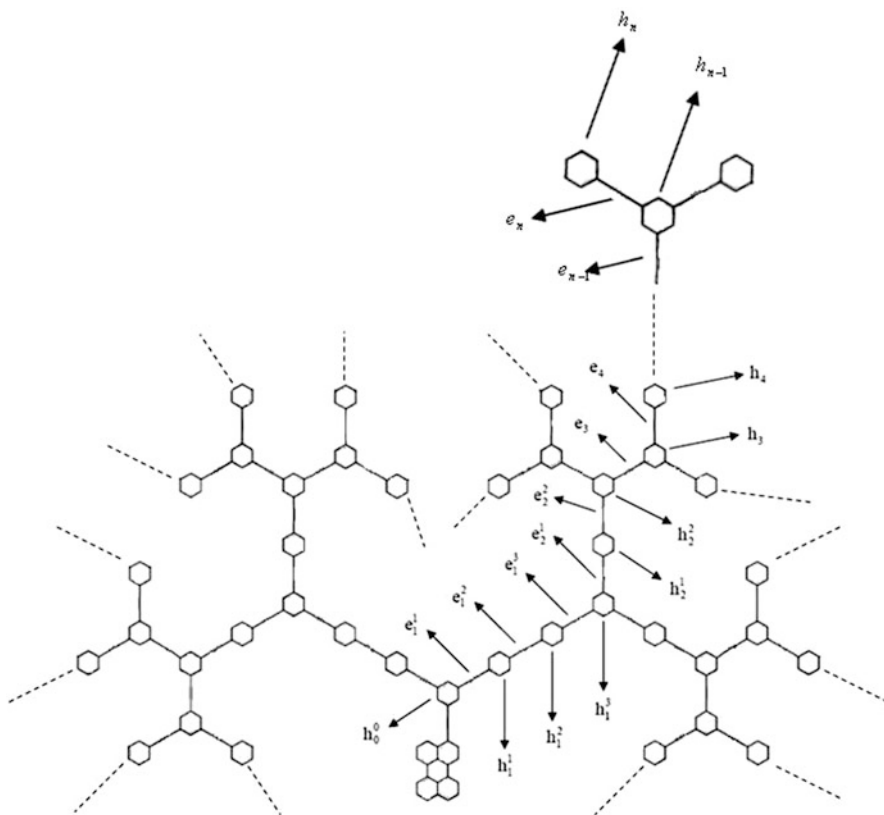


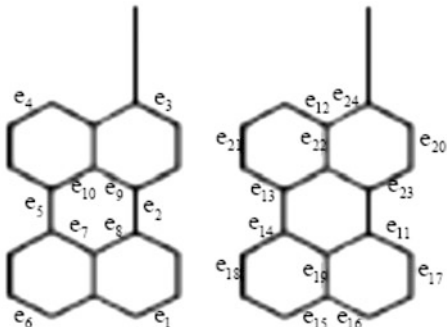
Fig. 12.1 First-type nanostar

### 12.2.1 Computing the Szeged Index of First-Type Nanostar

Figure 12.1 shows a first-type nanostar which has grown  $n$  stages.

In Fig. 12.1, we show the graph of this nanostar. In this figure we have 1 nucleus and a central hexagon denoted by  $h_0^0$ . In stages 1 and 2, we denoted the hexagons and edges by  $h_i^j$ , where  $1 \leq i \leq 2$ ,  $1 \leq j \leq 3$ , and in the other stages, we denoted the hexagons and edges by  $h_j$  and  $e_j$ . The growth of this nanostar from stage 3 is the same, and we have only two hexagons in each stage. Now, we start the computing of the Szeged index of this nanostar from stage  $n$ . Suppose that  $e$  is an edge of the hexagon  $h_n$ ; for all of the edges of  $h_n$ , we have  $n_1(e|G) = 3$ ; also the number of these hexagons is  $2^n$ . Suppose further that  $e$  is an edge of  $h_{n-1}$ ; for 4 of these edges we have  $n_1(e|G) = 1 \times 6 + 3$ , and for the other 2 edges we have  $n_1(e|G) = 2 \times 6 + 3$ ; also the number of these hexagons is  $2^{n-1}$ . Now assume

Fig. 12.2 Nucleus



that  $e$  is an edge of  $h_k$  so that  $3 \leq k \leq n$ ; in this case, for 4 of the edges we have  $n_1(e|G) = (2^{n-k} - 1) \times 6 + 3$ , and for the other 2 edges we have  $n_1(e|G) = 2 \times (2^{n-k} - 1) \times 6 + 3$ ; the number of these hexagons is  $2^k$ . If  $e$  is an edge of  $h_2^2$ , for 4 of the edges we have  $n_1(e|G) = (2^{n-2} - 1) \times 6 + 3$ , and for the other 2 edges we have  $n_1(e|G) = 2 \times (2^{n-2} - 1) \times 6 + 3$ ; the number of these hexagons is  $2^2$ . If  $e$  is an edge of  $h_2^1$ , for all 6 edges,  $n_1(e|G) = (2^{n-1} - 1) \times 6 + 3$ ; the number of these hexagons is  $2^2$ . If  $e$  is an edge of  $h_1^3$ , for 4 of the edges we have  $n_1(e|G) = 2^{n-1} \times 6 + 3$ , and for the other 2 edges we have  $n_1(e|G) = 2^n \times 6 + 3$ ; the number of these hexagons is 2. If  $e$  is an edge of  $h_1^2$ , for all 6 edges,  $n_1(e|G) = (2^n + 1) \times 6 + 3$ ; the number of these hexagons is 2. If  $e$  is an edge of  $h_1^1$ , for all 6 edges,  $n_1(e|G) = (2^n + 2) \times 6 + 3$ ; the number of these hexagons is 2. If  $e$  is an edge of  $h_0^0$ , for 4 of the edges we have  $n_1(e|G) = (2^n + 3) \times 6 + 3$ , and for the other 2 edges we have  $n_1(e|G) = 2 \times (2^n + 3) \times 6 + 3$ . Now assuming that  $e$  is the edge  $e_n$ , we have  $n_1(e_n|G) = 6$ , and the number of these edges is  $2^n$ . For the edge  $e_{n-1}$ , we have  $n_1(e_{n-1}|G) = (2 + 1) \times 6$ , and the number of these edges is  $2^{n-1}$ . For the edge  $e_k$ , in a way that  $3 \leq k \leq n$ , we have  $n_1(e_k|G) = (2^{n-k+1} - 1) \times 6$ ; the number of these edges is  $2^k$ . For the edge  $e_2^2$ , we have  $n_1(e_2^2|G) = (2^{n-1} - 1) \times 6$ . For the edge  $e_2^1$ , we have  $n_1(e_2^1|G) = 2^{n-1} \times 6$ ; the number of these edges is  $2^2$ . For the edge  $e_1^3$ , we have  $n_1(e_1^3|G) = (2^n + 1) \times 6$ . For the edge  $e_1^2$ , we have  $n_1(e_1^2|G) = (2^n + 2) \times 6$ . For the edge  $e_1^1$ , we have  $n_1(e_1^1|G) = (2^n + 3) \times 6$ ; the number of these edges in stage one is 2. For the edge between the nucleus and central hexagon ( $h_0^0$ ), we have  $n_1(e|G) = (2^{n+1} + 7) \times 6$ .

Now we obtain  $n_1(e|G)$  for the edges of the nucleus.

According to Fig. 12.2, we have  $n_1(e_i|G) = 10$  for  $i = 1, 2, 3, 4, 5, 6, 7, 8, 9, 10$ ; for  $i = 11, 12, 13, 14, 15, 16$ , we have  $n_1(e_i|G) = 3$ , for  $i = 17, 18, 19$ ,  $n_1(e_i|G) = 5$ , for  $i = 20, 21, 22$ ,  $n_1(e_i|G) = 15$ , and for  $i = 23, 24$ ,  $n_1(e_i|G) = 17$ .

The number of the vertices of this nanostar is equal to  $r = (2^{n+1} + 7) \times 6 + 20$ . But we know that  $n_2(e|G) = r - n_1(e|G)$  for any of edge  $e$ . Now the Szeged index of the above nanostar is obtained in the following way:

$$\begin{aligned}
 Sz(G_n) &= \sum_{k=3}^n \left[ 2^k \left( 4 \times \left( (2^{n-k} - 1) \times 6 + 3 \right) \left( r - (2^{n-k} - 1) \times 6 - 3 \right) \right. \right. \\
 &\quad \left. \left. + 2 \times \left( 2(2^{n-k} - 1) \times 6 + 3 \right) \left( r - 2(2^{n-k} - 1) \times 6 - 3 \right) \right) \right] \\
 &\quad + 2^2 \left[ 4 \times \left( (2^{n-2} - 1) \times 6 + 3 \right) \left( r - (2^{n-2} - 1) \times 6 - 3 \right) \right. \\
 &\quad \left. + 2 \left( 2(2^{n-2} - 1) \times 6 + 3 \right) \left( r - 2(2^{n-2} - 1) \times 6 - 3 \right) \right] \\
 &\quad 2^2 \left[ 6 \left( (2^{n-1} - 1) \times 6 + 3 \right) \left( r - (2^{n-1} - 1) \times 6 - 3 \right) \right] \\
 &\quad + 2 \left[ 4 \left( 2^{n-1} \times 6 + 3 \right) \left( r - 2^{n-1} \times 6 - 3 \right) \right. \\
 &\quad \left. + 2 \left( 2^n \times 6 + 3 \right) \left( r - 2^n \times 6 - 3 \right) \right] \\
 &\quad + 2 \left[ 6 \left( (2^n + 1) \times 6 + 3 \right) \left( r - (2^n + 1) \times 6 - 3 \right) \right] \\
 &\quad + 2 \left[ 6 \left( (2^n + 2) \times 6 + 3 \right) \left( r - (2^n + 2) \times 6 - 3 \right) \right] \\
 &\quad + 4 \left( (2^n + 3) \times 6 + 3 \right) \left( r - (2^n + 3) \times 6 - 3 \right) \\
 &\quad + 2 \left( (2(2^n + 3) \times 6 + 3) \left( r - 2(2^n + 3) \times 6 - 3 \right) \right) \\
 &\quad + \sum_{k=3}^n \left[ 2^k \left( (2^{n-k+1} - 1) \times 6 \left( r - (2^{n-k+1} - 1) \times 6 \right) \right) \right] \\
 &\quad + 2^2 \left[ (2^{n-1} - 1) \times 6 \left( r - (2^{n-1} - 1) \times 6 \right) \right] + 2^2 \left[ 2^{n-1} \times 6 \left( r - 2^{n-1} \times 6 \right) \right] \\
 &\quad + 2 \left[ (2^n + 1) \times 6 \left( r - (2^n + 1) \times 6 \right) \right] + 2 \left[ (2^n + 2) \times 6 \left( r - (2^n + 2) \times 6 \right) \right] \\
 &\quad + 2 \left[ (2^n + 3) \times 6 \left( r - (2^n + 3) \times 6 \right) \right] + (2^{n+1} + 7) \times 6 \left( r - (2^{n+1} + 7) \times 6 \right) \\
 &\quad 10 \times 10 \times (r - 10) + 6 \times 3 \times (r - 3) + 3 \times 5 \times (r - 5) \\
 &\quad + 3 \times 15 \times (r - 15) + 2 \times 17 \times (r - 17) \\
 &= 41788 + 16812 \times 2^n + 4440 \times 2^n \times n + 468 \times 4^n + 720 \times n \times 4^n
 \end{aligned}$$

**12.2.2 Computing the Szeged Index of Second-Type Nanostar**

The following figure shows a second-type nanostar which has grown  $n$  stages (Fig. 12.3).

Let  $h_i^i$  be the hexagon between hexagons  $h_i$  and  $h_{i-1}$ . Let  $e_i^j$  be the  $j$ th edge between two hexagons in the stage  $i$ ,  $1 \leq i \leq n$ ,  $1 \leq j \leq 2$ . In the first step we compute  $n_1(e|G)$  for  $h_i$ 's. For  $h_n$ , we have  $n_1(e|G) = 3$ , which is the same for all of its six edges; the number of these hexagons is  $2^n$ . If  $e$  is an edge of  $h_{n-1}$ , for 2 of the edges of the hexagon, we have  $n_1(e|G) = 2 \times 2 \times 6 + 3$ , and for the other 4

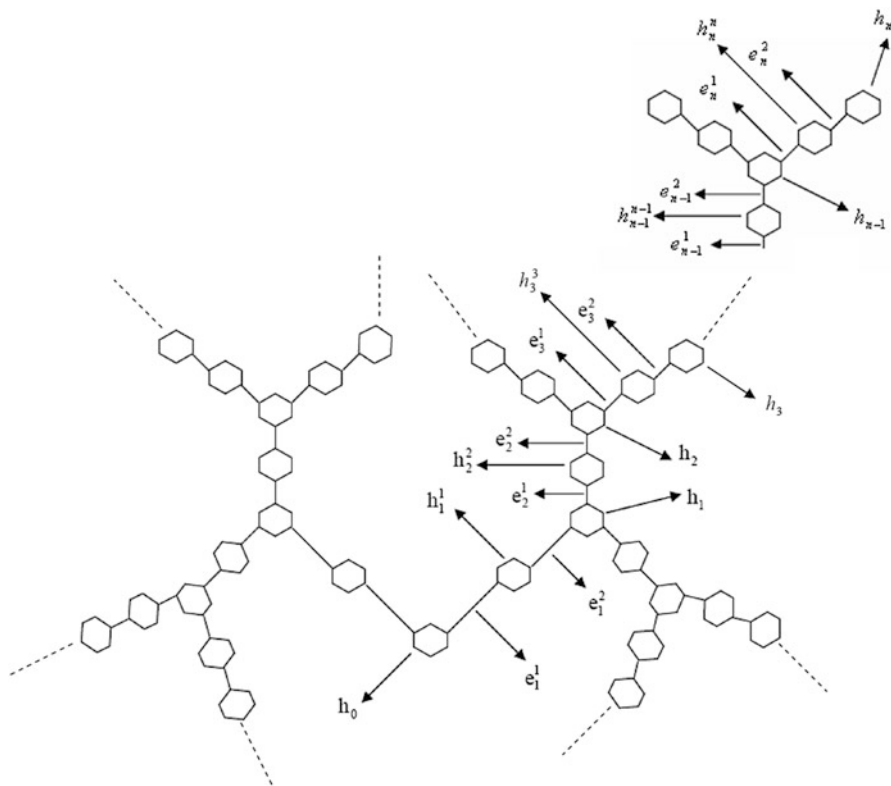


Fig. 12.3 Second-type nanostar

edges, we have  $n_1(e|G) = 2 \times 6 + 3$ ; the number of these hexagons is  $2^{n-1}$ . Now assume that  $e$  is an edge of  $h_{k-1}$ ,  $1 \leq k \leq n$ ; for 2 of the edges we have  $n_1(e|G) = 2 \times (2^{n-(k-1)} + 2^{n-k} + \dots + 2) \times 6 + 3 = 2 \times (2^{n-k+2} - 2) \times 6 + 3$  and for the other 4,  $n_1(e|G) = (2^{n-(k-1)} + 2^{n-k} + \dots + 2) \times 6 + 3 = (2^{n-k+2} - 2) \times 6 + 3$ ; the number of these hexagons is  $2^{(k-1)}$ . Now we compute  $n_1(e|G)$  for  $h_i^j$ 's. For all of six edges of  $h_n^n$ , we have  $n_1(e|G) = 9$ ; the number of these hexagons is  $2^n$ . If  $e$  is an edge of  $h_{n-1}^{n-1}$ , for all six edges,  $n_1(e|G) = (2^2 + 1) \times 6 + 3$ , the number of this hexagon is  $2^{n-1}$ . If  $e$  is an edge of  $h_k^k$ ,  $1 \leq k \leq n - 1$ , for all of the six edges,  $n_1(e|G) = (2^{n-k+1} + 2^{n-k} + \dots + 2^2 + 1) \times 6 + 3 = (2^{n-k+2} - 3) \times 6 + 3$ , the number of these hexagons is  $2^k$ . Now  $n_1(e|G)$  is computed for  $e_i^j$ . For the edge  $e_n^2$ ,  $n_1(e_n^2|G) = 1 \times 6$ . For the edge  $e_n^1$ ,  $n_1(e_n^1|G) = 2 \times 6$ ; the number of these edges is  $2^n$ . For the edge  $e_{n-1}^2$ ,  $n_1(e_{n-1}^2|G) = (2^2 + 1) \times 6$ . For the edge  $e_{n-1}^1$ ,  $n_1(e_{n-1}^1|G) = (2^2 + 2) \times 6$ ; the number of these edges is  $2^{n-1}$ . For the edge  $e_k^2$ , we have  $n_1(e_k^2|G) = (2^{n-k+2} - 3) \times 6$ , and  $n_1(e|G)$  for the edges  $e_i^1$  is as follows: for the edge  $e_k^1$ , we have  $n_1(e_k^1|G) = (2^{n-k+2} - 2) \times 6$ ; the number of

these edges is  $2^k$ . Therefore, we have computed  $n_1(e|G)$  for all of the edges of this nanostar. The number of the vertices of this nanostar is equal to  $r = (2^{n+2} - 3) \times 6$ . But we know that  $n_2(e|G) = r - n_1(e|G)$  for any of edge  $e$ . Now its Szeged index is obtained easily.

$$\begin{aligned}
 & Sz(G_n) \\
 &= \sum_{k=1}^n \left[ 2^{k-1} \times \left( 2 \times \left( 2 \times (2^{n-k+2} - 2) \times 6 + 3 \right) \left( r - 2 \times (2^{n-k+2} - 2) \times 6 - 3 \right) \right) \right. \\
 &\quad \left. + 4 \times \left( (2^{n-k+2} - 2) \times 6 + 3 \right) \left( r - (2^{n-k+2} - 2) \times 6 - 3 \right) \right] \\
 &\quad + \sum_{k=1}^{n-1} \left[ 2^k \left( 6 \times \left( (2^{n-k+2} - 3) \times 6 + 3 \right) \right) \left( r - (2^{n-k+2} - 3) \times 6 - 3 \right) \right] \\
 &\quad + 2^n (6 \times (9(r - 9) + 3(r - 3))) \\
 &\quad + \sum_{k=1}^n \left[ 2^k \left( (2^{n-k+2} - 3) \times 6 \right) \left( r - (2^{n-k+2} - 3) \times 6 \right) \right] \\
 &\quad + \sum_{k=1}^n \left[ 2^k \left( (2^{n-k+2} - 2) \times 6 \right) \left( r - (2^{n-k+2} - 2) \times 6 \right) \right] \\
 &= -882 + 6912 \times 4^n \times n - 15264 \times 4^n + 3456 \times 2^n \times n + 16200 \times 2^n
 \end{aligned}$$

### 12.2.3 Computing the Szeged Index of Three-Type Nanostar

Figure 12.4 shows a three-type nanostar which has grown  $n$  stages.

In Fig. 12.4, we show that the shape of this nanostar. In this figure we have 1 nucleus and a central hexagon denoted by  $h_0$ . We denoted the hexagons and edges by  $h_i$  and  $e_i$ . Now, we start the computing of the Szeged index of this nanostar from stage  $n$ . Suppose that  $e$  is an edge of the hexagon  $h_n$ ; for all of edges of  $h_n$ , we have  $n_1(e|G) = 3$ ; also the number of these hexagons is  $2^n$ . Suppose further that  $e$  is an edge of  $h_{n-1}$ ; for 4 of these edges we have  $n_1(e|G) = 1 \times 6 + 3 = 9$ , and for the other 2 edges we have  $n_1(e|G) = 2 \times 6 + 3 = 15$ ; also the number of these hexagons is  $2^{n-1}$ . Suppose that  $e$  is an edge of  $h_k$ ; for 4 of the edges we have  $n_1(e|G) = (2^{n-k} - 1) \times 6 + 3$ , and for the other 2 edges we have  $n_1(e|G) = 2 \times (2^{n-k} - 1) \times 6 + 3$ ; the number of these hexagons is  $2^k$ .

Now  $n_1(e|G)$  is computed for  $e_i$ . Suppose  $e$  is the edge  $e_n$ , we have  $n_1(e_n|G) = 1 \times 6 = 6$ ; the number of these edges is  $2^n$ . For the edge  $e_{n-1}$ , we have  $n_1(e_{n-1}|G) = (2 + 1) \times 6 = 18$ ; the number of these edges is  $2^{n-1}$ . For the edge  $e_k$ ,  $1 \leq k \leq n$ , we have  $n_1(e_k|G) = (2^{n-k+1} - 1) \times 6$ ; the number of these edges is  $2^k$ . For the edge between the nucleus and central hexagon ( $h_0$ ), we have  $n_1(e|G) = (2^{n+1} - 1) \times 6$ .

Now we obtain  $n_1(e|G)$  for the edges of the nucleus.

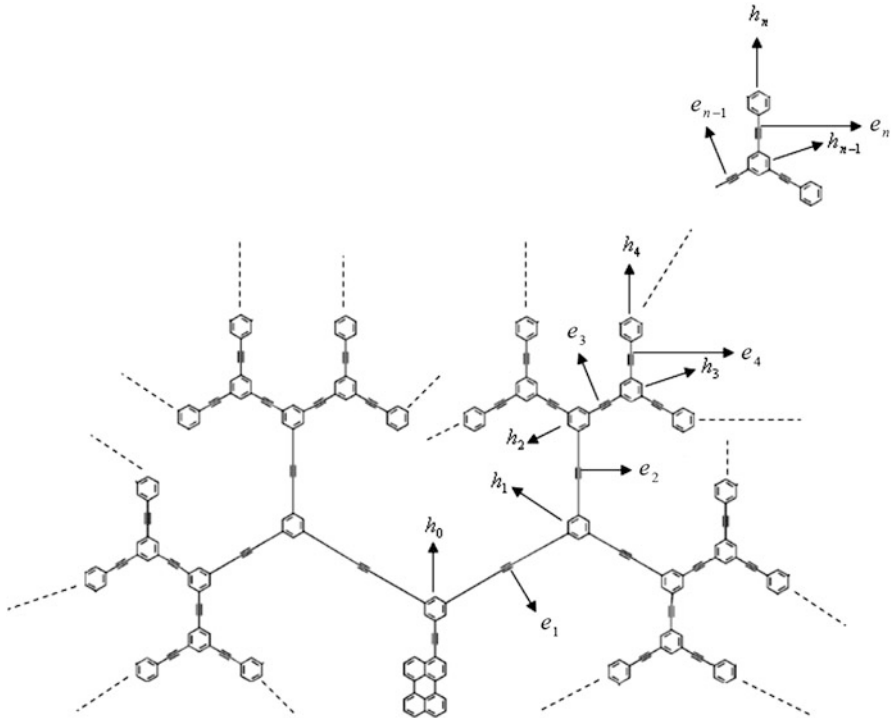


Fig. 12.4 Three-type nanostar

According to Fig. 12.2, we have computed  $n_1(e|G)$  for all of the edges of this nanostar. The number of the vertices of this nanostar is equal to  $r = (2^{n+1} - 1) \times 6 + 20$ . But we know that  $n_2(e|G) = r - n_1(e|G)$  for any edge  $e$ . Now the Szeged index of the above nanostar is obtained in the following way:

$$\begin{aligned}
 & Sz(G_n) \\
 &= \sum_{k=0}^n \left[ 2^k \left( \begin{array}{l} 2 \times ((2 \times (2^{n-k} - 1) \times 6 + 3) (r - 2 \times (2^{n-k} - 1) \times 6 - 3)) \\ + 4 \times ((2^{n-k} - 1) \times 6 + 3) (r - (2^{n-k} - 1) \times 6 - 3) \end{array} \right) \right] \\
 &+ \sum_{k=0}^n [2^k (((2^{n-k+1} - 1) \times 6) (r - (2^{n-k+1} - 1) \times 6))] \\
 &+ 10 \times 10 \times (r - 10) + 6 \times 3 \times (r - 3) + 3 \times 5 \times (r - 5) \\
 &+ 3 \times 15 \times (r - 15) + 2 \times 17 \times (r - 17) \\
 &= 3636 \times 2^n + 1324 + 720 \times n \times 4^n + 1560 \times n \times 2^n - 1296 \times 4^n
 \end{aligned}$$



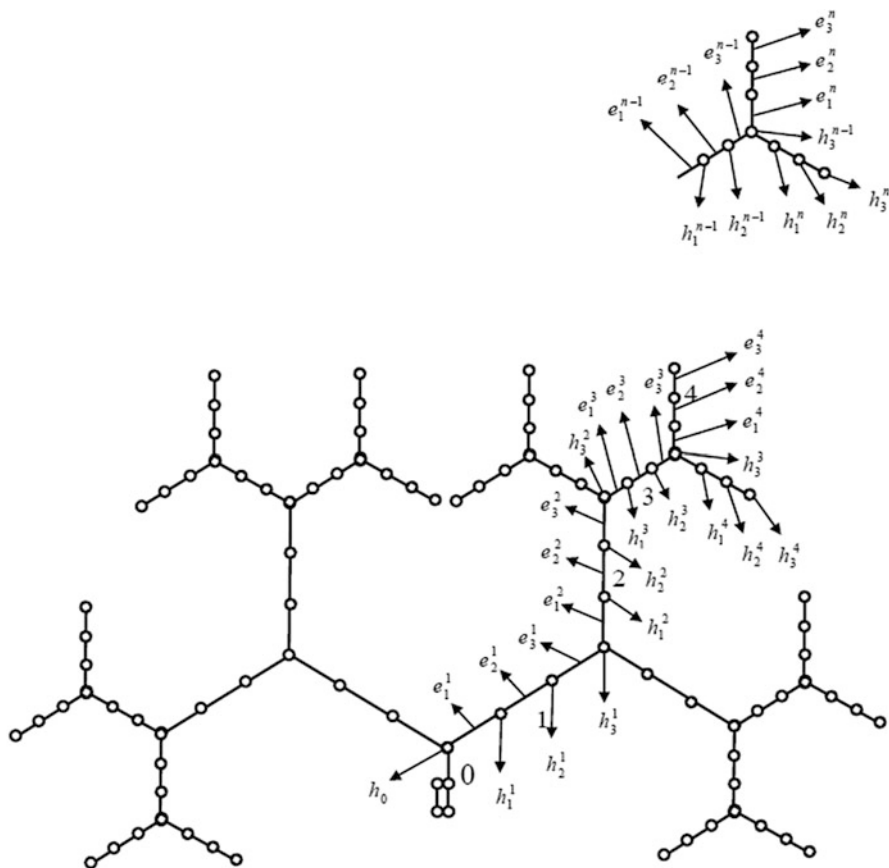


Fig. 12.5 Four-type nanostar

### 12.2.4 Computing the Szeged Index of Four-Type Nanostar

Figure 12.5 shows a four-type nanostar which has grown four stages.

In this figure, we have 1 nucleus and a central hexagon denoted by  $h_0$ . Let  $h_i^j$  be the  $i$ th hexagon in stage  $j$ ,  $1 \leq j \leq n$ ,  $1 \leq i \leq 3$ , and let  $e_i^j$  be the  $i$ th edge between two hexagons in stage  $j$ . Now, we start the computing of the Szeged index of this nanostar from stage  $n$ . Suppose that  $e$  is an edge of the hexagon  $h_3^n$ ; for all of edges of  $h_3^n$ , we have  $n_1(e|G) = 3$ ; for all of edges of  $h_2^n$ , we have  $n_1(e|G) = 6 + 3 = 9$ ; for all of edges of  $h_1^n$ , we have  $n_1(e|G) = 2 \times 6 + 3 = 15$ ; also the number of these hexagons is  $2^n$ . Suppose that  $e$  is an edge of the hexagon  $h_3^{n-1}$ ; for 4 of these edges we have  $n_1(e|G) = 3 \times 6 + 3 = 21$ , and for the other 2 edges we have  $n_1(e|G) = 2 \times 3 \times 6 + 3 = 39$ ; for all of edges of  $h_2^{n-1}$ , we have  $n_1(e|G) = 2 \times 3 \times 6 + 6 + 3 = 45$ ; for all of edges of  $h_1^{n-1}$ , we have

$n_1(e|G) = 2 \times 3 \times 6 + 2 \times 6 + 3 = 51$ ; also the number of these hexagons is  $2^{n-1}$ . We continue until to achieve stage 1. Suppose that  $e$  is an edge of the hexagon  $h_3^1$ ; for 4 of these edges we have

$$\begin{aligned} n_1(e|G) &= 3 \times (2^{n-2} + 2^{n-3} + \dots + 2 + 1) \times 6 + 3 \\ &= 3 \times (2^{n-1} - 1) \times 6 + 3, \end{aligned}$$

and for other 2 edges, we have

$$\begin{aligned} n_1(e|G) &= 3 \times (2^{n-1} + 2^{n-2} + \dots + 2) \times 6 + 3 \\ &= 3 \times (2^n - 2) \times 6 + 3; \end{aligned}$$

for all of edges of  $h_2^1$ , we have

$$\begin{aligned} n_1(e|G) &= 3 \times (2^{n-1} + 2^{n-2} + \dots + 2) \times 6 + 6 + 3 \\ &= 3 \times (2^n - 2) \times 6 + 9; \end{aligned}$$

for all of edges of  $h_1^1$ , we have

$$\begin{aligned} n_1(e|G) &= 3 \times (2^{n-1} + 2^{n-2} + \dots + 2) \times 6 + 2 \times 6 + 3 \\ &= 3 \times (2^n - 2) \times 6 + 15; \end{aligned}$$

also the number of these hexagons is 2. Suppose that  $e$  is an edge of the hexagon  $h_0$ ; for 4 of these edges we have

$$\begin{aligned} n_1(e|G) &= 3 \times (2^{n-1} + \dots + 2 + 1) \times 6 + 3 \\ &= 3 \times (2^n - 1) \times 6 + 3, \end{aligned}$$

and for the other 2 edges we have

$$\begin{aligned} n_1(e|G) &= 3 \times (2^n + 2^{n-1} + \dots + 2) \times 6 + 3 \\ &= 3 \times (2^{n+1} - 2) \times 6 + 3. \end{aligned}$$

Now  $n_1(e|G)$  is computed for  $e_j^i$ . Suppose  $e$  is the edge  $e_3^n$ , we have  $n_1(e_3^n|G) = 6 = a_1$ ; for the edge  $e_2^n$ , we have  $n_1(e_2^n|G) = a_1 + 6$ ; for the edge  $e_1^n$ , we have  $n_1(e_1^n|G) = a_1 + 12$ ; the number of these edges is  $2^n$ . Suppose  $e$  is the edge  $e_3^{n-1}$ , we have  $n_1(e_3^{n-1}|G) = 3 \times 2 \times 6 + 6 = 42 = a_2$ ; for the edge  $e_2^{n-1}$ , we have  $n_1(e_2^{n-1}|G) = a_2 + 6$ ; for the edge  $e_1^{n-1}$ , we have  $n_1(e_1^{n-1}|G) = a_2 + 12$ ; the number of these edges is  $2^{n-1}$ . We continue until to achieve stage 1. Suppose  $e$  is the edge  $e_3^1$ , we have

$$\begin{aligned} n_1(e_3^1|G) &= 3 \times (2^{n-1} + 2^{n-2} + \dots + 2) \times 6 + 6 \\ &= 3 \times (2^n - 2) \times 6 + 6 = a_n; \end{aligned}$$

for the edge  $e_2^1$ , we have  $n_1(e_2^1|G) = a_n + 6$ ; for the edge  $e_1^1$ , we have  $n_1(e_1^1|G) = a_n + 12$ ; the number of these edges is 2. Now assume that  $e$  is the edge between  $h_0$  and nucleus; we have  $n_1(e|G) = 3 \times (2^{n+1} - 2) \times 6 + 6$ . In this equation, we computed  $n_1(e|G)$  for edges of the nucleus.

Therefore, we have computed  $n_1(e|G)$  for all of the edges of this nanostar. The number of the vertices of this nanostar is equal to  $r = 18 \times (2^{n+1} - 2) + 26$ . But we know that  $n_2(e|G) = r - n_1(e|G)$  for any of edge  $e$ . Now its Szeged index is obtained easily.

$Sz(G_n)$

$$\begin{aligned} &= \sum_{i=1}^n 2^i \times \left[ \begin{aligned} &2 \times (3 \times (2^{n+1-i} - 2) \times 6 + 3) (r - (3 \times (2^{n+1-i} - 2) \times 6 + 3)) \\ &+ 4 (3 \times (2^{n-i} - 1) \times 6 + 3) (r - (3 \times (2^{n-i} - 1) \times 6 + 3)) \\ &+ 6 \times (3 \times (2^{n+1-i} - 2) \times 6 + 9) (r - (3 \times (2^{n+1-i} - 2) \times 6 + 9)) \\ &+ 6 \times (3 \times (2^{n+1-i} - 2) \times 6 + 15) (r - (3 \times (2^{n+1-i} - 2) \times 6 + 15)) \end{aligned} \right] \\ &+ 2 \times (3 \times (2^{n+1} - 2) \times 6 + 3) (r - (3 \times (2^{n+1} - 2) \times 6 + 3)) \\ &+ 4 \times (3 \times (2^n - 1) \times 6 + 3) (r - (3 \times (2^n - 1) \times 6 + 3)) \\ &\sum_{i=1}^n 2^i \times \left[ \begin{aligned} &(3 \times (2^{n+1-i} - 2) \times 6 + 6) (r - (3 \times (2^{n+1-i} - 2) \times 6 + 6)) \\ &+ (3 \times (2^{n+1-i} - 2) \times 6 + 12) (r - (3 \times (2^{n+1-i} - 2) \times 6 + 12)) \\ &+ (3 \times (2^{n+1-i} - 2) \times 6 + 18) (r - (3 \times (2^{n+1-i} - 2) \times 6 + 18)) \end{aligned} \right] \\ &+ (3 \times (2^{n+1} - 2) \times 6 + 6) (r - (3 \times (2^{n+1} - 2) \times 6 + 6)) \\ &+ 10 \times 10 \times (r - 10) + 6 \times 3 \times (r - 3) + 3 \times 5 \times (r - 5) \\ &+ 3 \times 15 \times (r - 15) + 2 \times 17 \times (r - 17) \\ &= 24,624 \times n \times 4^n + 25,992 \times n \times 2^n - 57,024 \times 4^n + 53,532 \times 2^n + 7,156 \end{aligned}$$

### 12.2.5 Computing the Szeged Index of Styrylbenzene Dendrimer

In this part, we bring all details of the computation of Styrylbenzene dendrimer, which have been published in Iranmanesh and Gholami (2009). Figure 12.6 shows a Styrylbenzene dendrimer which has grown  $n$  stages.

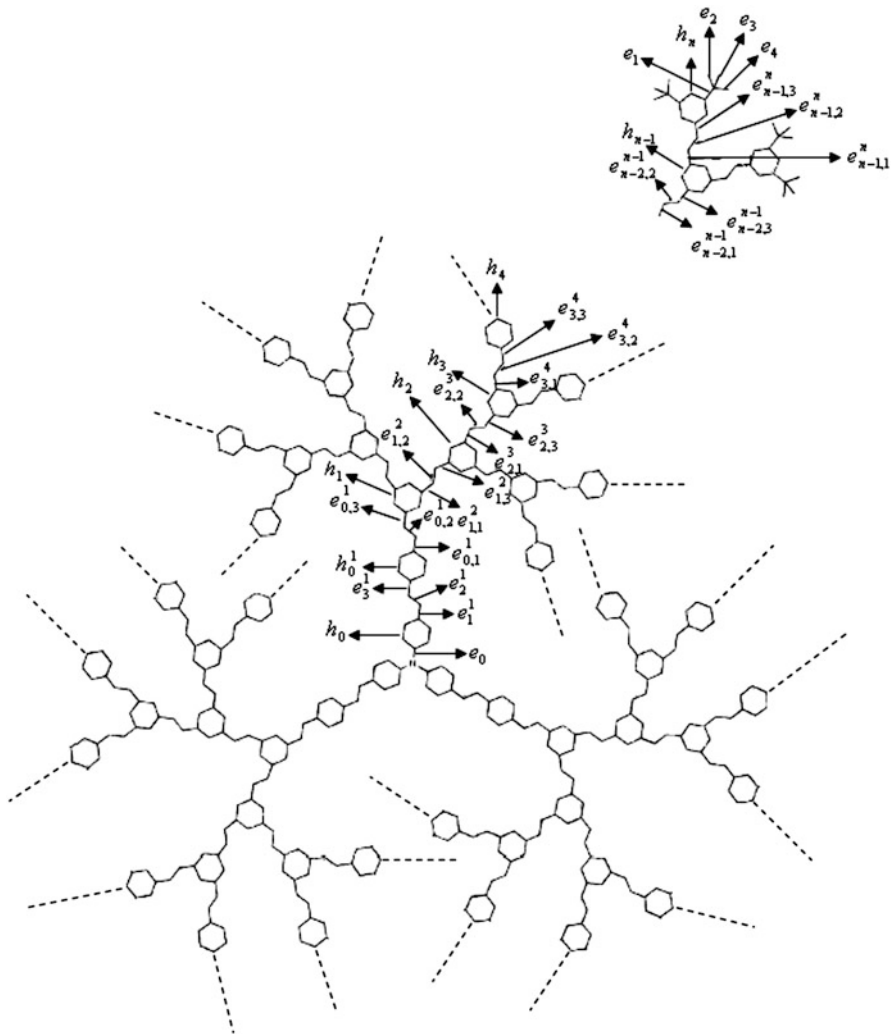


Fig. 12.6 Styrylbenzene Dendrimer

Let  $h_i$  be a hexagon which is in stage  $i$ . Since this dendrimer has grown in stage 1 in a different way from other stages, therefore  $h_0$  is central hexagon and  $h_0^1$  is the hexagon between  $h_0$  and  $h_1$ . And  $e_{i-1,j}^i$  be the  $j$ th edge between  $h_i$  and  $h_{i-1}$  such that  $1 \leq j \leq 3, 2 \leq i \leq n$ . Also, for the first stage the edges are denoted as shown in Fig. 12.6.

At first we compute  $n_1(e|G)$  for hexagons. Now assume that  $e$  is an edge of  $h_n$ ; for 4 of these edges we have  $n_1(e|G) = 3 + 4 = 7$ , and for the other 2 edges we have  $n_1(e|G) = 3 + 8 = 11$ ; also the number of these hexagons is  $3 \times 2^{n-1}$ . If  $e$  is an edge of  $h_{n-1}$ , for 4 of these edges we have  $n_1(e|G) = 1 \times 6 + 1 \times 2 + 1 \times 8 + 3 = 19$ ,

and for the other 2 edges we have  $n_1(e|G) = 2 \times 6 + 2 \times 2 + 2 \times 8 + 3 = 35$ ; also the number of these hexagons is  $3 \times 2^{n-2}$ . We continue until to achieve stage 1. Suppose that  $e$  is an edge of  $h_1$ ; for 4 of these edges we have

$$\begin{aligned} n_1(e|G) &= (2^{n-2} + 2^{n-3} + \dots + 1) \times 6 \\ &\quad + (2^{n-2} + 2^{n-3} + \dots + 1) \times 2 + 2^{n-2} \times 8 + 3 \\ &= (2^n - 1) \times 6 + (2^n - 1) \times 2 + 2^{n-2} \times 8 + 3, \end{aligned}$$

and for the other 2 edges we have

$$\begin{aligned} n_1(e|G) &= (2^{n-1} + 2^{n-2} + \dots + 2) \times 6 \\ &\quad + (2^{n-1} + 2^{n-2} + \dots + 2) \times 2 + 2^{n-1} \times 8 + 3 \\ &= (2^n - 2) \times 6 + (2^n - 2) \times 2 + 2^{n-1} \times 8 + 3; \end{aligned}$$

also the number of these hexagons is 3. If  $e$  is an edge of the hexagon  $h_0^1$ , for all of the edges of  $h_0^1$ , we have

$$\begin{aligned} n_1(e|G) &= (2^{n-1} + 2^{n-2} + \dots + 2 + 1) \times 6 \\ &\quad + (2^{n-1} + 2^{n-2} + \dots + 2 + 1) \times 2 + 2^{n-1} \times 8 + 3 \\ &= (2^n - 1) \times 6 + (2^n - 1) \times 2 + 2^{n-1} \times 8 + 3; \end{aligned}$$

also the number of these hexagons is 3. If  $e$  is an edge of the hexagon  $h_0$ , for all of edges of  $h_0$  we have

$$\begin{aligned} n_1(e|G) &= (2^{n-1} + 2^{n-2} + \dots + 2 + 2) \times 6 \\ &\quad + (2^{n-1} + 2^{n-2} + \dots + 2 + 2) \times 2 + 2^{n-1} \times 8 + 3 \\ &= 2^n \times 6 + 2^n \times 2 + 2^{n-1} \times 8 + 3; \end{aligned}$$

also the number of these hexagons is 3.

Now  $n_1(e|G)$  is computed for  $e_{i-1,j}^i$ . Suppose that  $e$  is the edge  $e_{n-1,3}^n$ , we have  $n_1(e|G) = 1 \times 6 + 1 \times 8 = 14$ ; for the edge  $e_{n-1,2}^n$ , we have  $n_1(e|G) = 15$ ; for the edge  $e_{n-1,1}^n$ , we have  $n_1(e|G) = 16$ ; the number of these edges is  $3 \times 2^{n-1}$ . We continue until to achieve stage 1. Suppose that  $e$  is the edge  $e_{0,3}^1$ , we have

$$\begin{aligned} n_1(e|G) &= (2^{n-1} + 2^{n-2} + \dots + 2 + 1) \times 6 \\ &\quad + 2^{n-1} \times 8 + (2^{n-1} + 2^{n-2} + \dots + 2) \times 2 \\ &= (2^n - 1) \times 6 + 2^{n-1} \times 8 + (2^n - 2) \times 2. \end{aligned}$$

Also

$$\begin{aligned} n_1(e|G) &= (2^{n-1} + 2^{n-2} + \dots + 2 + 1) \times 6 + 2^{n-1} \times 8 \\ &\quad + (2^{n-1} + 2^{n-2} + \dots + 2) \times 2 + 1 \\ &= (2^n - 1) \times 6 + 2^{n-1} \times 8 + (2^n - 2) \times 2 + 1 \end{aligned}$$

and

$$\begin{aligned} n_1(e|G) &= (2^{n-1} + 2^{n-2} + \dots + 2 + 1) \times 6 + 2^{n-1} \times 8 \\ &\quad + (2^{n-1} + 2^{n-2} + \dots + 2) \times 2 + 2 \\ &= (2^n - 1) \times 6 + 2^{n-1} \times 8 + (2^n - 2) \times 2 + 2; \end{aligned}$$

the number of these edges is 3. If  $e$  is the edge  $e_3^1$ , we have

$$\begin{aligned} n_1(e_3^1|G) &= (2^{n-1} + 2^{n-2} + \dots + 2 + 2) \times 6 + 2^{n-1} \times 8 \\ &\quad + (2^{n-1} + 2^{n-2} + \dots + 2 + 1) \times 2 \\ &= 2^n \times 6 + 2^{n-1} \times 8 + (2^n - 1) \times 2 = a; \end{aligned}$$

if  $e$  is the edge  $e_2^1$ , we have  $n_1(e_2^1|G) = a + 1$ ; if  $e$  is the edge  $e_1^1$ , we have  $n_1(e|G) = a + 2$ ; the number of these edges is 3. Suppose that  $e$  is the edge  $e_0$ , we have

$$\begin{aligned} n_1(e_0|G) &= (2^{n-1} + 2^{n-2} + \dots + 2 + 3) \times 6 + 2^{n-1} \times 8 \\ &\quad + (2^{n-1} + 2^{n-2} + \dots + 2 + 2) \times 2 \\ &= (2^n + 1) \times 6 + 2^{n-1} \times 8 + 2^n \times 2; \end{aligned}$$

the number of these edges is 3.

Suppose that  $e = e_1$  in Fig. 12.6, then  $n_1(e|G) = 4$ ; the number of these edges is  $3 \times 2^n$ . Now, let  $e$  be one of  $e_2, e_3$  or  $e_4$ , then  $n_1(e_2|G) = n_1(e_3|G) = n_1(e_4|G) = 1$ ; the number of these edges is  $3 \times 2^{n-1} \times 6$ . Now the Szeged index of this dendrimer when it grows  $n$  stages is computed:

$$\begin{aligned} Sz(G_n) &= \sum_{i=0}^{n-1} 3 \times 2^i \\ &\quad \times \left[ \begin{aligned} &2 \times \underbrace{((2^{n-i} - 2) \times 6 + (2^{n-i} - 2) \times 2 + 2^{n-1-i} \times 8 + 3)}_{a_1} \times (r - a_1) \\ &+ 4 \times \underbrace{((2^{n-1-i} - 1) \times 6 + (2^{n-1-i} - 1) \times 2 + 2^{n-2-i} \times 8 + 3)}_{a_2} \times (r - a_2) \end{aligned} \right] \end{aligned}$$

$$\begin{aligned}
 &+ 3 \times 6 \times \left[ \underbrace{((2^n - 1) \times 6 + (2^n - 1) \times 2 + 2^{n-1} \times 8 + 3)}_{a_3} \times (r - a_3) \right] \\
 &+ 3 \times 6 \times \left[ \underbrace{(2^n \times 6 + 2^n \times 2 + 2^{n-1} \times 8 + 3)}_{a_4} \times (r - a_4) \right] \\
 &+ \sum_{i=0}^{n-1} 3 \times 2^i \times \left[ \underbrace{((2^{n-i} - 1) \times 6 + 2^{n-1-i} \times 8 + (2^{n-i} - 2) \times 2)}_{a_5} \times (r - a_5) \right. \\
 &\quad \left. + (a_5 + 1) \times (r - a_5 - 1) + (a_5 + 2) \times (r - a_5 - 2) \right] \\
 &+ 3 \times \left[ \underbrace{(2^n \times 6 + 2^{n-1} \times 8 + (2^n - 1) \times 2)}_{a_6} \times (r - a_6) \right. \\
 &\quad \left. + (a_6 + 1) \times (r - a_6 - 1) + (a_6 + 2) \times (r - a_6 - 2) \right] \\
 &+ 3 \times \left[ \underbrace{((2^n + 1) \times 6 + 2^{n-1} \times 8 + 2^n \times 2)}_{a_7} \times (r - a_7) \right] \\
 &+ 3 \times 2^n \times 4 \times (r - 4) + 3 \times 2^{n-1} \times 6 \times (r - 1)
 \end{aligned}$$

Since  $r = 3 \times ((2^n + 1) \times 6 + 2^n \times 2 + 2^{n-1} \times 8) + 1 = 3 \times (12 \times 2^n + 6) + 1$  is the number of vertices of this graph, we have

$$Sz(G_n) = 17820 \times 2^n + 1512 \times 4^n + 9324 \times n \times 2^n + 9072 \times n \times 4^n + 4962$$

### 12.2.6 Computing the Szeged Index of Triarylamine Dendrimer of Generation 1–3

In this part, we bring all details of the computation of Szeged index of Triarylamine Dendrimer, which have been published in Iranmanesh and Gholami (2009). Figure 12.7 shows a Triarylamine Dendrimer of Generation 1–3 which has grown  $n$  stages.

Let  $h_i$  be a hexagon which is in stage  $i$ . Also, let  $e_{i-1,j}^i$  be the  $j$ th edge between  $h_i$  and  $h_{i-1}$  such that  $1 \leq j \leq 2$ ,  $1 \leq i \leq n$ . At first we compute  $n_1(e|G)$  for hexagons. Now assume that  $e$  is an edge of  $h_n$  for all 6 edges  $n_1(e|G) = 3 + 1 = 4$ ; the number of these hexagons is  $3 \times 2^n$ . If  $e$  is an edge of  $h_{n-1}$ , for all 6 edges  $n_1(e|G) = 2 \times 6 + 3 + 1 + 2 = 18$ ; the number of these hexagons is  $3 \times 2^{n-1}$ . We continue until to achieve stage 1. If  $e$  is an edge of the hexagon  $h_1$ , for all of the edges of  $h_1$ , we have

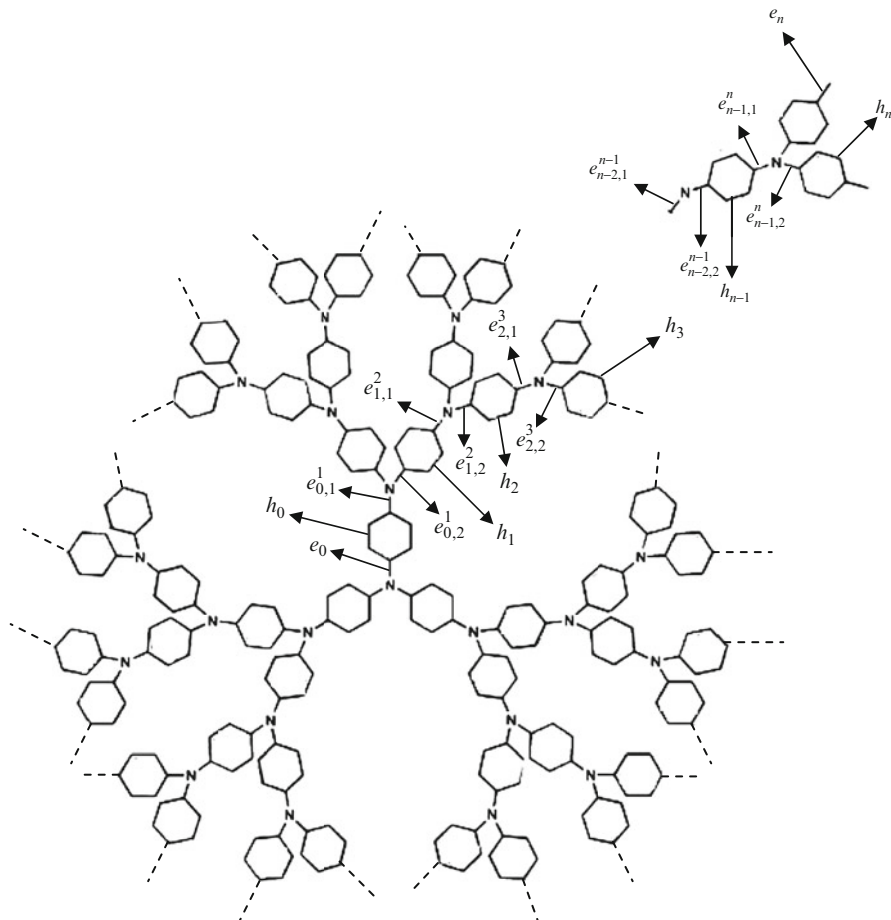


Fig. 12.7 Triarylamine Dendrimer of Generation 1– 3

$$\begin{aligned}
 n_1(e|G) &= (2^{n-1} + 2^{n-2} + \dots + 2) \times 6 + 3 + 1 + 2 + \dots + 2^{n-1} \\
 &= (2^n - 2) \times 6 + 3 + (2^n - 1).
 \end{aligned}$$

Also, the number of these hexagons is  $3 \times 2$ . If  $e$  is an edge of the hexagon  $h_0$ , for all of edges of  $h_0$ , we have

$$\begin{aligned}
 n_1(e|G) &= (2^n + 2^{n-1} + \dots + 2) \times 6 + 3 + 1 + 2 + \dots + 2^n \\
 &= (2^{n+1} - 2) \times 6 + 3 + (2^{n+1} - 1).
 \end{aligned}$$

Also, the number of these hexagons is 3. Suppose that  $e$  is the edge  $e_n$ , we have  $n_1(e|G) = 1$ ; the number of these edges is  $3 \times 2^n$ . Now  $n_1(e|G)$  is computed



for  $e_{i-1,j}^i$ . Suppose that  $e$  is the edge  $e_{n-1,2}^n$ , we have  $n_1(e|G) = 6 + 1 = 7$ ; the number of these edges is  $3 \times 2^n$ . If  $e$  is the edge  $e_{n-1,1}^n$ , we have  $n_1(e|G) = 2 \times 6 + 1 + 2 = 15$ ; the number of these edges is  $3 \times 2^{n-1}$ . We continue until to achieve stage 1. If  $e$  is the edge  $e_{0,2}^1$ , we have

$$\begin{aligned} n_1(e|G) &= (2^{n-1} + 2^{n-2} + \dots + 2 + 1) \times 6 + 1 + 2 + \dots + 2^{n-1} \\ &= (2^n - 1) \times 6 + (2^n - 1). \end{aligned}$$

The number of these edges is  $3 \times 2$ . If  $e$  is the edge  $e_{0,1}^1$ , we have

$$\begin{aligned} n_1(e|G) &= (2^n + 2^{n-1} + \dots + 2^2 + 2) \times 6 + 1 + 2 + \dots + 2^{n-1} + 2^n \\ &= (2^{n+1} - 2) \times 6 + (2^{n+1} - 1); \end{aligned}$$

the number of these edges is 3. Suppose that  $e$  is the edge  $e_0$ , we have

$$\begin{aligned} n_1(e|G) &= (2^n + 2^{n-1} + \dots + 2^2 + 2 + 1) \times 6 + 1 + 2 + \dots + 2^{n-1} + 2^n \\ &= (2^{n+1} - 1) \times 6 + (2^{n+1} - 1); \end{aligned}$$

the number of these edges is 3. Now the Szeged index of this dendrimer when it grows  $n$  stages is computed as follows:

$$\begin{aligned} Sz(G_n) &= \sum_{i=0}^n 3 \times 2^i \times \left[ \underbrace{6 \times ((2^{n+1-i} - 2) \times 6 + 3 + (2^{n+1-i} - 1))}_{a_1} \times (r - a_1) \right] \\ &+ \sum_{i=0}^n 3 \times 2^i \times \left[ \underbrace{((2^{n+1-i} - 1) \times 6 + (2^{n+1-i} - 1))}_{a_2} \times (r - a_2) \right] \\ &+ \sum_{i=1}^n 3 \times 2^{i-1} \times \left[ \underbrace{((2^{n+2-i} - 2) \times 6 + (2^{n+2-i} - 1))}_{a_3} \times (r - a_3) \right]. \end{aligned}$$

Since  $r = 21 \times (2^{n+1} - 1) + 1$  is the number of vertices of this graph, we have

$$Sz(G_n) = 14112 \times n \times 4^n - 15456 \times 4^n + 19476 \times 2^n - 2346.$$

Also, in Iranmanesh and Gholami (2010) we computed the Szeged index of Naphthalene dendrimer.

### 12.3 Computation of Szeged Index of Some Nanotubes

In this section, at first we compute the Szeged index of  $TUC_4C_8(R)$  nanotube and  $TUC_4C_8(S)$  nanotube. Then we compute the Szeged index of  $HAC_5C_7[r, p]$  nanotube,  $HAC_5C_6C_7[r, p]$  nanotube,  $HC_5C_7[r, p]$  nanotube, and Armchair Polyhex nanotube.

In the last part, we give an algorithm in the base of GAP program, which is faster than the direct implementation and enables us to compute the Szeged index of any graph.

#### 12.3.1 Computation of the Szeged Index of $TUC_4C_8(R)$ Nanotube

In this part, we compute the Szeged index of  $TUC_4C_8(R)$  nanotube.

We bring all details of the computation of the Szeged index of this nanotube, which have been published in Iranmanesh et al. (2007).

We denote the number of rhombs on the level 1 by  $p$  and the length of tube by  $q$ . Therefore, we have  $2q$  rows of oblique edges and  $q - 1$  rows of vertical edges in  $TUC_4C_8(R)$  nanotube. Throughout this part, our notation is standard. They are appearing in the same way as in Mansoori (2005) and Cameron (1994).

Let  $e$  be an arbitrary edge of nanotube.

For computing the Szeged index of  $T = TUC_4C_8(R)$ , we assume two cases:

*Case 1*  $p$  is even.

At first, we begin with an example.

*Example 12.3.1* Let  $e$  be a horizontal edge between  $u$  and  $v$  (see Fig. 12.8). All vertices lying among lines  $l_1$  and  $l_2$  in region  $R$  are closer to the vertex  $u$  than to  $v$ .

Since  $n_1(e|G) = 2pq$ , we have  $n_1(e|G) - n_2(e|G) = 2pq(4pq - 2pq) = 4p^2q^2$ .

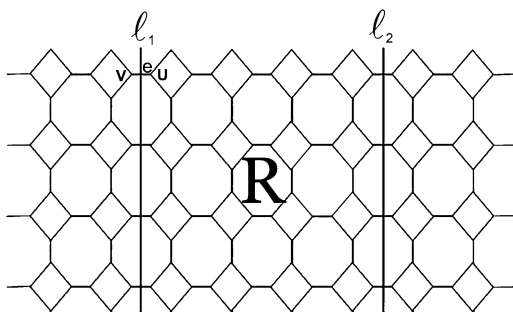


**Fig. 12.8**  $TUC_4C_8(R)$  nanotube for  $p = 8$  and  $q = 4$

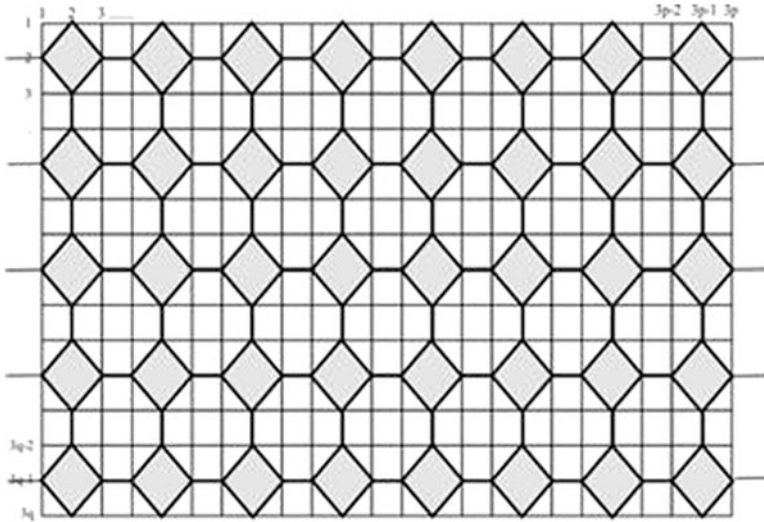


**Fig. 12.9**  $TUC_4C_8(R)$  nanotube with  $3p$  columns and  $3q$  rows of edges

**Lemma 12.3.2** *If  $e$  is a horizontal edge of  $T$ , then  $n_1(e|G) - n_2(e|G) = 4p^2q^2$ .*

*Proof* Suppose that  $e$  is a horizontal edge of  $T$ .  $2pq$  vertices of  $T$  are closer to one vertex of  $e$  than to the other. Thus,  $n_1(e|G) = 2pq$  and  $n_2(e|G) = (4pq - 2pq) = 2pq$ . So we have

$$n_1(e|G) - n_2(e|G) = 4p^2q^2. \tag{*}$$

A sample of horizontal edge is given in Example 12.3.1. By the symmetry of the  $TUC_4C_8(R)$  nanotube for every horizontal edge, the relation (\*) is hold. ■

**Lemma 12.3.3** *If  $e$  is a vertical edge in the  $k$ th row of vertical edges, then we have  $n_1(e|G) - n_2(e|G) = 16p^2[k(q - k)]$ .*

*Proof* Let us denote the vertices of  $TUC_4C_8(R)$  as described in Fig. 12.9.

If  $e = U_{ij}U_{i(j+1)}$  is a vertical edge, all vertices lying in rows of edges equal to or less than  $i$  are closer to  $U_{ij}$  than to  $U_{i(j+1)}$ , and all vertices lying in rows of edges equal to or greater than  $i + 1$  are closer to  $U_{i(j+1)}$  than to  $U_{ij}$ . Thus, if  $e$  is in the  $k$ th row of vertical edges, then  $n_1(e|G) - n_2(e|G) = 4pk(4pq - 4pk) = 16p^2[k(q - k)]$ . ■

Before the proof of next lemma, we give some examples.

**Example 12.3.4** Let  $e_i$  be a vertical edge between  $u_i$  and  $v_i$ ,  $1 \leq i \leq 4$ . All vertices lying among lines  $l$  and  $l_1$  are closer to vertex  $u_1$  than to  $v_1$  (Fig. 12.10). Thus,

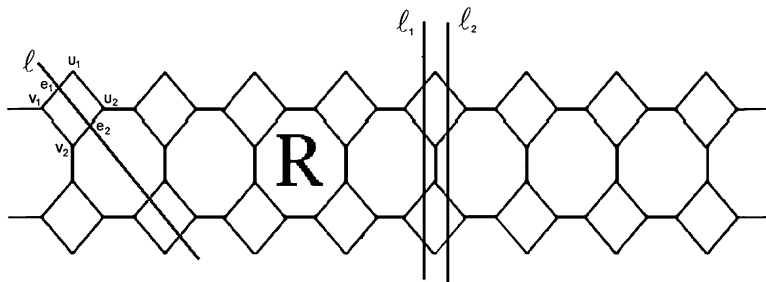


**Fig. 12.10** A nanotube with  $p = 8$  and  $q = 2$

$$n_1(e_1|G) n_2(e_1|G) = \left( \sum_{i=1}^q 2p - 4i + 3 \right) \left( 4pq - \sum_{i=1}^q 2p - 4i + 3 \right).$$

All vertices lying among lines  $l$  and  $l_2$  are closer to vertex  $u_2$  than to  $v_2$ . Thus,

$$n_1(e_2|G) n_2(e_2|G) = \left( \sum_{i=1}^q 2p - 4i + 5 \right) \left( 4pq - \sum_{i=1}^q 2p - 4i + 5 \right).$$

If we continue this method, then for  $e$  in the fourth row we have

$$n_1(e_4|G) n_2(e_4|G) = \left( \sum_{i=1}^q 2p - 4i + 9 \right) \left( 4pq - \sum_{i=1}^q 2p - 4i + 9 \right).$$

*Example 12.3.5* Let  $e_i$  be an edge between vertices  $u_i$  and  $v_i$ ,  $1 \leq i \leq 8$ .

All vertices lying among lines  $l_1$  and  $l_2$  in region  $R$  are closer to vertex  $u_1$  than to  $v_1$ . Thus,

$$n_1(e_1|G) n_2(e_1|G) = \left( \sum_{i=1}^{p/2} 2p - 4i + 3 \right) \left( 4pq - \sum_{i=1}^{p/2} 2p - 4i + 3 \right).$$

All vertices lying among lines  $l_3$  and  $l_4$  in region  $R$  are closer to vertex  $u_2$  than to  $v_2$ . Thus,

$$n_1(e_2|G) n_2(e_2|G) = \left( \sum_{i=1}^{p/2} (2p - 4i + 5) + 1/2 \times 2(2 - 1) \right)$$

$$\left( 4pq - \sum_{i=1}^{p/2} (2p - 4i + 5) - 1/2 \times 2(2 - 1) \right).$$

If we continue this method, then for  $e_8$  in the eighth row we have

$$n_1(e_8|G) \ n_2(e_8|G) = \left( \sum_{i=1}^{p/2} (2p - 4i + 17) + 1/2 \times 8(8 - 1) \right) \\ \left( 4pq - \sum_{i=1}^{p/2} (2p - 4i + 17) - 1/2 \times 8(8 - 1) \right).$$

*Example 12.3.6* In Fig. 12.11, all vertices lying among lines  $l'_1$  and  $l'_2$  in region  $R'$  are closer to vertex  $v_9$  than to  $u_9$ . Thus,

$$n_1(e_9|G) \ n_2(e_9|G) = \left( \sum_{i=1}^p (2p - 4i + 3) + 4p \text{int}((9 - p)/2) \right) \\ \left( 4pq - \sum_{i=1}^p (2p - 4i + 3) - 4p \text{int}((9 - p)/2) \right),$$

where  $\text{int}$  is the greatest integer function.

All vertices lying among lines  $l'_3$  and in region  $R'$  are closer to vertex  $v_{10}$  than to  $u_{10}$ . Thus,

$$n_1(e_{10}|G) \ n_2(e_{10}|G) = \left( \sum_{i=1}^p (2p - 4i + 1) + 4p \text{int}((10 - p)/2) \right) \\ \left( 4pq - \sum_{i=1}^p (2p - 4i + 1) - 4p \text{int}((10 - p)/2) \right).$$

**Lemma 12.3.7** *If  $e$  is an oblique edge in the  $k$ th row of oblique edges in nanotube  $T$ , then we have the following implications.*

1. If  $2q \leq p$ , then

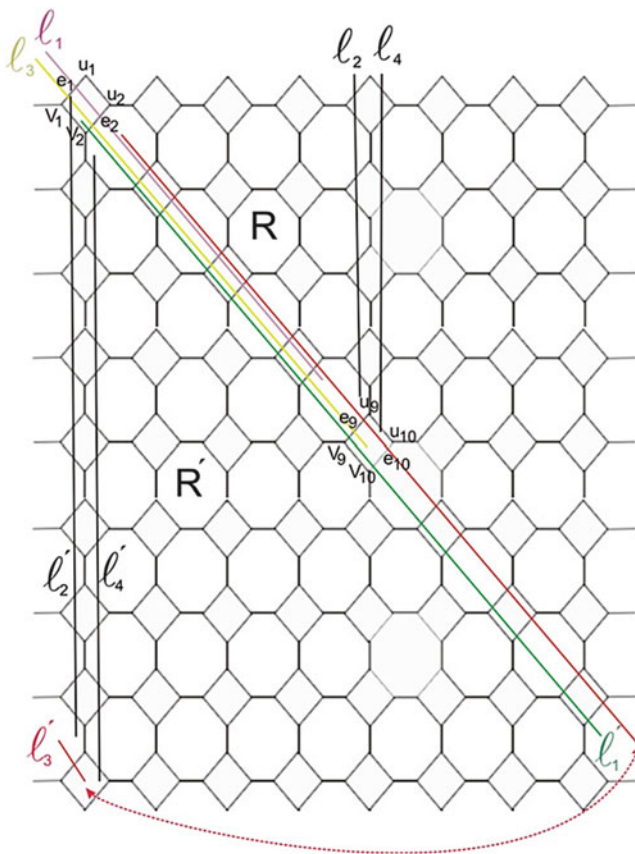


Fig. 12.11 A nanotube with  $p = 8$  and  $q = 9$

$$n_1(e|G) n_2(e|G) = \left( \sum_{i=1}^p (2p - 4i + 2k + 1) \right) \left( 4pq - \sum_{i=1}^p (2p - 4i + 2k + 1) \right).$$

2. If  $2q > p$ , then we have the following subcases:

(i) If  $2p - 1 \leq 2q$ , then

$$n_1(e|G) n_2(e|G) = \begin{cases} A(4pq - A) & 1 \leq k \leq p \\ B(4pq - B) & p + 1 \leq k \leq 2q - p \\ C(4pq - C) & 2q - p + 1 \leq k \leq 2q \end{cases},$$

where

$$A = \sum_{i=1}^{p/2} (2p - 4i + 2k + 1) + 1/2 \times k(k - 1)$$

$$B = \sum_{i=1}^p (4p - 4i + 2 - (-1)^k) + 4p \text{ int}((k - p)/2) \quad \text{and}$$

$$C = \sum_{i=1}^{p/2} (4p - 4i + 2(2q - k + 1) + 1) + 1/2(2q - k + 1)(2q - k).$$

(ii) If  $2p - 1 > 2q$ , then

$$n_1(e|G)n_2(e|G) = \begin{cases} D(4pq - D) & 1 \leq k \leq 2q - p + 1 \\ E(4pq - E) & 2q - p + 2 \leq k \leq p - 1, \\ F(4pq - F) & p \leq k \leq 2q \end{cases}$$

where

$$D = \sum_{i=1}^{p/2} (2p - 4i + 2k + 1) + 1/2 \times k(k - 1)$$

$$E = \sum_{i=1}^{p/2} (2p - 4i + 2k + 1) \quad \text{and}$$

$$F = \sum_{i=1}^{p/2} (4p - 4i + 2(2q - k + 1) + 1) + 1/2(2q - k + 1)(2q - k).$$

*Proof* Let  $2q \leq p$ . By the symmetry of  $TUC_4C_8(R)$  nanotube, it is sufficient that we compute  $n_1(e_i|G)n_2(e_i|G)$ ,  $1 \leq i \leq q$ . For this reason we use the method similar to Example 12.3.4. Therefore, the result holds.

Now suppose  $2q > p$  and  $2p - 1 \leq 2q$ . Let  $e$  be an oblique edge in the  $k$ th row,  $1 \leq k \leq p$ . For finding  $n_1(e_k|G)n_2(e_k|G)$ ,  $1 \leq k \leq p$ , we use the method similar to Example 12.3.5. Thus, we have

$$n_1(e_k|G)n_2(e_k|G) = \left( \sum_{i=1}^{p/2} (2p - 4i + 2k + 1) + 1/2 \times k(k - 1) \right) \times \left( 4pq - \sum_{i=1}^{p/2} (2p - 4i + 2k + 1) - 1/2 \times k(k - 1) \right).$$

Now let  $e$  be an oblique edge in the  $k$ th row,  $p + 1 \leq k \leq 2q - p$ . By using a method similar to Example 12.3.6, we can reach the result.

If  $e$  is an oblique edge in the  $k$ th row,  $2q - p + 1 \leq k \leq 2q$ , then by symmetry of  $TUC_4C_8(R)$  nanotube, the result is hold.

Now suppose  $2q > p$  and  $2p - 1 > 2q$ ; similar to the last case, we can obtain the desired result. ■

**Theorem 12.3.8** *If  $p$  is even, then the Szeged index of  $TUC_4C_8(R)$  is as follows:*

$$Sz(G) = \begin{cases} 68/3 \times p^3q^3 - 8/3 \times p^3q - 16/3 \times pq^5 + 4/3 \times pq^3 & 2q \leq p \\ 52/3 \times p^3q^3 - 4p^3q + p^4 - 13/15 \times p^6 + 8/3 \times p^5q - 2/15 \times p^2 & 2q > p \end{cases}$$

*Proof* At first, suppose A, B, and C are the sets of all horizontal, vertical, and oblique edges of T, respectively. Then, we have

$$Sz(G) = \sum_{e \in A} n_1(e|G)n_2(e|G) + \sum_{e \in B} n_1(e|G)n_2(e|G) + \sum_{e \in C} n_1(e|G)n_2(e|G). \tag{**}$$

The number of horizontal edges are  $pq$ . Thus, we have

$$\sum_{e \in A} n_1(e|G)n_2(e|G) = 4p^2q^2.pq = 4p^3q^3. \tag{1}$$

The number of vertical edges are  $p(q - 1)$ . So,

$$\begin{aligned} \sum_{e \in B} n_1(e|G)n_2(e|G) &= \sum_{i=1}^{q-1} p.16p^2i(i-1) \\ &= 16p^3 \sum_{i=1}^{q-1} i(i-1) = 8/3 \times p^3q(q^2 - 1). \end{aligned} \tag{2}$$

Now for  $2q \leq p$ , we have

$$\begin{aligned} &\sum_{e \in C} n_1(e|G)n_2(e|G) \\ &= 2p \left[ \sum_{k=1}^{2q} \left[ \sum_{i=1}^q (2p - 4i + 2k + 1)(4pq - 2p - 4i + 2k + 1) \right] \right] \\ &= 16p^3q^3 - 16/3 \times pq^5 + 4/3 \times pq^3. \end{aligned} \tag{3}$$



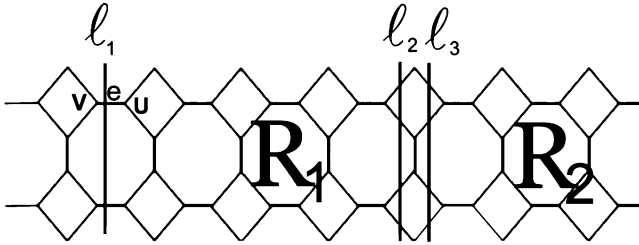


Fig. 12.12 A nanotube with  $p = 7$  and  $q = 2$

And for  $2q > p$ , we assume two cases:

1.  $2p - 1 \leq 2q$ . In this case, we represent the set of all oblique edges in the range  $1 \leq k \leq p$  and  $p + 1 \leq k \leq 2q - p$  with  $C_1$  and  $C_2$ , respectively. Thus, we have the following conclusion:

$$\begin{aligned}
 & \sum_{e \in C} n_1(e|G) n_2(e|G) \\
 &= 2 \sum_{e \in C_1} n_1(e|G) n_2(e|G) + \sum_{e \in C_2} n_1(e|G) n_2(e|G) \\
 &= 32/3 \times p^3 q^3 - 4/3 \times p^3 q + p^4 - 13/15 \times p^6 + 8/3 \times p^5 q - 2/15 \times p^2.
 \end{aligned} \tag{4}$$

2.  $2p - 1 > 2q$ . Similar to Case 1, we have

$$\begin{aligned}
 \sum_{e \in C} n_1(e|G) n_2(e|G) &= 32/3 \times p^3 q^3 - 4/3 \times p^3 q + p^4 - 13/15 \times p^6 \\
 &+ 8/3 \times p^5 q - 2/15 \times p^2.
 \end{aligned}$$

So if  $p$  is even, then by using (1), (2), (3), or (4) in (\*\*), we have

$$\text{Sz}(G) = \begin{cases} 68/3 \times p^3 q^3 - 8/3 \times p^3 q - 16/3 \times p q^5 + 4/3 \times p q^3 & 2q \leq p \\ 52/3 \times p^3 q^3 - 4p^3 q + p^4 - 13/15 \times p^6 + 8/3 \times p^5 q - 2/15 \times p^2 & 2q > p \end{cases} .$$

Case 2  $p$  is odd. At first, we begin with an example.

*Example 12.3.9* In Fig. 12.12, all vertices lying among lines  $l_1$  and  $l_2$  in region  $R_1$  are closer to the vertex  $u$  than to  $v$ , and all vertices lying among lines  $l_1$  and  $l_3$  in region  $R_2$  are closer to the vertex  $v$  than to  $u$ .

$$\text{So, } n_1(e|G) n_2(e|G) = q(2p - 1)q(2p - 1) = 4p^2 q^2 - 4p q^2 + q^2.$$

**Lemma 12.3.10** *If  $e$  is a horizontal edge, then  $n_1(e|G) n_2(e|G) = 4p^2q^2 - 4pq^2 + q^2$ .*

*Proof* By using a method similar to Example 12.3.9, the result is hold. ■

**Lemma 12.3.11** *If  $e$  is a vertical edge in the  $k$ throw of vertical edges, then we have  $n_1(e|G) n_2(e|G) = 16p^2[k(q-k)]$ .*

*Proof* The proof is similar to the proof of Lemma 12.3.3. ■

**Lemma 12.3.12** *If  $e$  is an oblique edge in the  $k$ throw of oblique edges, then we have the following implications:*

1. If  $2q \leq p$ , then

$$n_1(e|G) n_2(e|G) = \begin{cases} \left( \sum_{i=1}^q 2p - 4i + 2k + 1 \right) \left( 4pq - q - \sum_{i=1}^q 2p - 4i + 2k + 1 \right) & k \text{ is odd} \\ \left( \sum_{i=1}^q (2p - 4i + 2k + 1) - q \right) \left( 4pq - \sum_{i=1}^q 2p - 4i + 2k + 1 \right) & k \text{ is even} \end{cases}$$

2. If  $2q > p$ , then we have the following cases:

(i) If  $2p - 1 \leq 2q$ , then

$$n_1(e|G) n_2(e|G) = \begin{cases} \begin{cases} A(4pq - ((p+1)/2 + \text{int}(k-1)/2) - A) & k \text{ is odd } 1 \leq k \leq p \\ (A - ((p+1)/2 + \text{int}(k-1)/2))(4pq - A) & k \text{ is even } 1 \leq k \leq p \end{cases} \\ \begin{cases} B(4pq - p - B) & k \text{ is even } p+1 \leq k \leq 2q-p \\ C(4pq - p - C) & k \text{ is odd } p+1 \leq k \leq 2q-p \end{cases} \\ \begin{cases} D(4pq - ((p+1)/2 + \text{int}(2q-k+1)/2) - D) & k \text{ is even } 2q-p+1 \leq k \leq 2q \\ (D - ((p+1)/2 + \text{int}(2q-k+1)/2))(4pq - D) & k \text{ is odd } 2q-p+1 \leq k \leq 2q \end{cases} \end{cases}$$

(ii) If  $2p - 1 \geq 2q$ , then we have

$$n_1(e|G) n_2(e|G) = \begin{cases} \begin{cases} A(4pq - ((p+1)/2 + \text{int}(k-1)/2) - A) & k \text{ is odd } 1 \leq k \leq 2q-p+1 \\ (A - ((p+1)/2 + \text{int}(k-1)/2))(4pq - A) & k \text{ is even } 1 \leq k \leq 2q-p+1 \end{cases} \\ \begin{cases} E(4pq - q - E) & k \text{ is even } 2q-p+2 \leq k \leq p-1 \\ (E - q)(4pq - E) & k \text{ is odd } 2q-p+2 \leq k \leq p-1 \end{cases} \\ \begin{cases} D(4pq - ((p+1)/2 + \text{int}(2q-k+1)/2) - D) & k \text{ is even } p \leq k \leq 2q \\ (D - ((p+1)/2 + \text{int}(2q-k+1)/2))(4pq - D) & k \text{ is odd } p \leq k \leq 2q \end{cases} \end{cases}$$

where

$$\begin{aligned}
 A &= \sum_{i=1}^{(p+1)/2} (2p - 4i + 2k + 1) + (1/2 \times k^2 - 3/2 \times k + 1) \\
 B &= \sum_{i=1}^p (4i - 3) + 4p \operatorname{int}((2q - k - p + 1)/2) \\
 C &= \sum_{i=1}^p (4i - 2) + 4p \operatorname{int}((2q - k - p + 1)/2) \\
 D &= \sum_{i=1}^{(p+1)/2} (2p - 4i + 2(2q - k + 1) + 1) \\
 &\quad + \left(1/2 \times (2q - k + 1)^2 - 3/2 \times (2q - k + 1) + 1\right) \quad \text{and} \\
 E &= \sum_{i=1}^q (2p - 4i + 2k + 1).
 \end{aligned}$$

*Proof* The proof is similar to the proof of Lemma 12.3.7. ■

**Theorem 12.3.13** *If  $p$  is odd, then we have*

$Sz(G)$

$$= \begin{cases} 68/3 \times p^3q^3 - 12p^2q^3 - 8/3 \times p^3q + 19/3 \times pq^3 - 16/3 \times pq^5 & 2q \leq p \\ 52/3 \times p^3q^3 + 8/3 \times p^5q + p^4 + 2p^4q - 2p^2q - 1/30 \times p^6 - 15/4p^5 & \\ +199/24 \times p^4 + 57/8p^3 + 809/120 \times p^2 - 8p^3q^2 + 29/8 \times p - 4p^2q^3 + pq^3 & 2q > p \end{cases} .$$

*Proof* The proof is similar to Theorem 12.3.8. ■

### 12.3.2 Computation of the Szeged Index of $TUC_4C_8(S)$ Nanotube

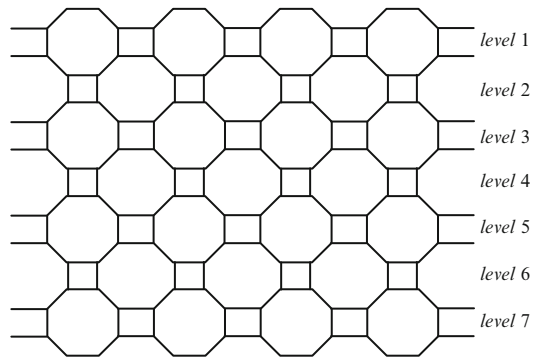
In this part, we bring some details of the computation of the Szeged index of  $TUC_4C_8(S)$  nanotube, which have been published in Iranmanesh and Pakravesh (2008).

According to Fig. 12.13, we denote the number of squares in one row by  $p$  and the number of levels by  $k$ . Throughout this part, our notation is standard. The notation  $[f]$  is the greatest integer function.

For computing the Szeged index of  $T = TUC_4C_8(S)$ , we assume two cases:

*Case 1*  $p$  is even.

**Fig. 12.13** Two-dimensional lattice of  $TUC_4C_8(S)$  nanotube,  $p = 4, k = 7$



In this case, we need to prove some lemmas which brings all of them without the detail of proof.

**Lemma 12.3.14** *If  $e$  is a horizontal edge of  $T$ , then*

$$n_1(e|G)n_2(e|G) = 4p^2(k + 1)^2.$$

**Lemma 12.3.15** *If  $e$  is a vertical edge in level  $m$ , then we have*

$$n_1(e|G)n_2(e|G) = 16p^2m(k - m + 1).$$

For simplicity, we define  $a = \lfloor \frac{m-1}{2} \rfloor$ ,  $b = \lfloor \frac{k-m+1}{2} \rfloor$ ,  $c = \lfloor \frac{m}{2} \rfloor$ ,  $d = \lfloor \frac{k-m}{2} \rfloor$ , and  $e = \lfloor \frac{k+1}{2} \rfloor$ .

**Lemma 12.3.16** *Suppose  $p$  is even. If  $e$  is an oblique edge in level  $m$ , then we have*

(i) *If  $m \leq p$  and  $k - m \leq p$ , then*

$$n_1(e|G) = 2p(k + 1) + 4m - 2 + (4m - 6)a - 4a^2 + (4m - 4k - 2)b + 4b^2. \tag{I}$$

(ii) *If  $m \leq p$  and  $k - m > p$ , then*

$$n_1(e|G) = 2p(m + 1/2) + 4m + p^2 - 2 + (4m - 6)a - 4a^2. \tag{II}$$

(iii) *If  $m > p$  and  $k - m \leq p$ , then*

$$n_1(e|G) = 2p(k + m) - p^2 - 7p + (4m - 4k - 2)b + 4b^2. \tag{III}$$

(iv) *If  $m > p$  and  $k - m > p$ , then*

$$n_1(e|G) = 4p(m - 2). \tag{IV}$$

**Theorem 12.3.17** *If  $p$  is even, then the Szeged index of  $TUC_4C_8(S)$  nanotube is given as follows:*

1.  $k$  is even.

(i) If  $k \leq p$ , then we have

$$\begin{aligned} Sz(T) &= p^3 (64/3k^3 + 64k^2 + 176/3k + 16) \\ &\quad - p (4k + 34/3k^3 + 6k^2 + 2/3k^5 + 2k^4). \end{aligned}$$

(ii) If  $p < k \leq 2p$ , then we have

$$\begin{aligned} Sz(T) &= p (2k^2 + 2k^3 - 2/15k^5 - 28/15k) + p^2 (4/3k^4 - 32/3k^3 + 28k^2 \\ &\quad + 8/3p^2k - 32/15) + p^3 (40/3k^3 + 120k^2 - 144k + 16/3) + \\ &\quad p^4 (32/3k^2 - 56k + 508/3) + p^5 (26/3 - 16/3k) + 4/5p^6. \end{aligned}$$

(iii) If  $k > 2p$ , then we have

$$\begin{aligned} Sz(T) &= p^3 (56/3k^3 + 56k^2 - 88k + 296/3) + p^4 (556/3 + 72k) \\ &\quad + p^5 (16/3k - 230/3) - 88/15p^2 - 52/15p^6. \end{aligned}$$

2.  $k$  is odd.

(i) If  $k \leq p$ , then we have

$$\begin{aligned} Sz(T) &= p^3 (64/3k^3 + 64k^2 + 176/3k + 16) \\ &\quad - p (34/3k^3 + 10k^2 + 2k^4 + 2/3k^5 - 4 - 4k). \end{aligned}$$

(ii) If  $p < k \leq 2p$ , then we have

$$\begin{aligned} Sz(T) &= p (2k^3 + 2k^2 - 28/15k - 2/15k^5 - 2) + p^2 (8/3k + 28k^2 - 32/3k^3 \\ &\quad + 4/3k^4 - 632/15) + p^3 (16/3 - 144k + 120k^2 + 40/3k^3) \\ &\quad + p^4 (508/3 - 56k + 32/3k^2) + p^5 (26/3 - 16/3k^3) + 4/5p^6. \end{aligned}$$

(iii) If  $k > 2p$ , then we have

$$\begin{aligned} Sz(T) &= p^3 (56/3k^3 + 56k^2 - 88k + 296/3) + p^4 (556/3 + 72k) \\ &\quad + p^5 (16/3k - 230/3) - 88/15p^2 - 52/15p^6. \end{aligned}$$

*Proof* At first, suppose A, B, and C are the sets of all horizontal, vertical, and oblique edges of  $T$ , respectively. Then, we have

$$Sz(T) = \sum_{e \in A} n_1(e|G)n_2(e|G) + \sum_{e \in B} n_1(e|G)n_2(e|G) + \sum_{e \in C} n_1(e|G)n_2(e|G). \tag{*}$$

The number of horizontal edges are  $2p(k + 1)$ . Thus, we have

$$\sum_{e \in A} n_1(e|G)n_2(e|G) = 4p^2(k + 1)^2 \cdot 2p(k + 1) = 8p^3(k + 1)^3.$$

The number of vertical edges are  $2pk$ . So,

$$\begin{aligned} \sum_{e \in B} n_1(e|G)n_2(e|G) &= \sum_{m=1}^k 2p \cdot 16p^2m(k - m + 1) = 32p^3 \sum_{m=1}^k m(k - m + 1) \\ &= p^3 (16/3k^3 + 16k^2 + 32/3k). \end{aligned}$$

Let  $k$  be even.

The number of oblique edges are  $2p(k + 1)$ . Now for  $k \leq p$ , we have

$$\begin{aligned} &\sum_{e \in C} n_1(e|G)n_2(e|G) \\ &= 2p \cdot \left\{ \sum_{m=1}^k \{(\text{I})(4p(k + 1) - (\text{I}))\} + (2p(k + 1)) \right. \\ &\quad \left. - (4k + 2)e + 4e^2 (4p(k + 1) - (2p(k + 1) - (4k + 2)e + 4e^2)) \right\} \\ &= 2p \cdot (p^2 (8k + 16k^2 + 8k^3) + p^3 (8k^2 + 16k + 8) - p (2k^4 + 4k^3 + 2k^2) \\ &\quad - 22/3k^3 - 4k^2 - 2/3k^5 - 4k). \end{aligned}$$

When  $p < k \leq 2p$ , we have

$$\begin{aligned} \sum_{e \in C} n_1(e|G)n_2(e|G) &= 2p \cdot \left\{ \sum_{m=1}^{k-p-1} \{(\text{II})(4p(k + 1) - (\text{II})) + \right. \\ &\quad \left. \sum_{m=k-p}^p (\text{I})(4p(k + 1) - (\text{I})) + \sum_{m=p+1}^k (\text{III})(4p(k + 1) - (\text{III})) \right\} \\ &\quad + (p + p^2) (4p(k + 1) - (p + p^2)) \end{aligned}$$

$$\begin{aligned}
 &= 2p \cdot (p (4/3k + 14k^2 - 16/3k^3 + 2/3k^4 - 16/15) \\
 &\quad + p^2 (40k^2 - 268/3k - 4/3) + p^3 (16/3k^2 - 28k + 254/3) \\
 &\quad + p^4 (13/3 - 8/3k) + 2/5p^5 - 14/15k - 1/15k^5 + k^3 + k^2).
 \end{aligned}$$

And if  $k > 2p$ , then we have

$$\begin{aligned}
 \sum_{e \in C} n_1(e|G)n_2(e|G) &= 2p \cdot \left\{ \sum_{m=1}^{k-p-1} \{(\text{II}) (4p(k+1) - (\text{II})) + \right. \\
 &\quad \left. \sum_{m=k-p}^p (\text{IV}) (4p(k+1) - (\text{IV})) + \sum_{m=p+1}^k (\text{III}) (4p(k+1) - (\text{III})) \right\} \\
 &\quad + (p + p^2) (4p(k+1) - (p + p^2)) \} \\
 &= 2p \cdot (p^2 (136/3 - 184/3k + 8k^2 + 8/3k^3) \\
 &\quad + p^3 (278/3 + 36k) + p^4 (8/3k - 115/3) - 44/15p - 26/15p^5).
 \end{aligned}$$

Suppose  $k$  is odd, in this case for  $k \leq p$  we have

$$\begin{aligned}
 \sum_{e \in C} n_1(e|G)n_2(e|G) &= 2p \cdot (p^2 (12k + 12k^2 + 4k^3 + 4) \\
 &\quad - 17/3k^3 - 5k^2 - 1/3k^5 + 2 + 2k - k^4)
 \end{aligned}$$

When  $p < k \leq 2p$ , we have

$$\begin{aligned}
 \sum_{e \in C} n_1(e|G)n_2(e|G) &= 2p \cdot (p (4/3k + 14k^2 - 16/3k^3 + 2/3k^4 - 16/15) \\
 &\quad + p^2 (40k^2 - 268/3k - 4/3) + p^3 (254/3 + 16/3k^2 - 28k) \\
 &\quad + p^4 (13/3 - 8/3k) - 14/15k + -1/15k^5 + k^3 + 2/5p^5 + k^2 - 1).
 \end{aligned}$$

And if  $k > 2p$ , then we have

$$\begin{aligned}
 \sum_{e \in C} n_1(e|G)n_2(e|G) &= 2p \cdot (p^2 (136/3 - 184/3k + 8k^2 + 8/3k^3) \\
 &\quad + p^3 (36k + 278/3) + p^4 (8/3k - 115/3) - 44/15p - 26/15p^5).
 \end{aligned}$$

So if  $p$  is even, then by using the above relations in (\*), the result is hold. ■

Case 2  $p$  is odd.

**Lemma 12.3.18** *If  $e$  is an oblique edge in level  $m$  ( $1 \leq m \leq k$ ), then we have*

(i) If  $m \leq p$  and  $k - m \leq p$ , then

$$\begin{aligned} n_1(e | G) &= 2p(k + 1) + 4m - 2k + (4m - 2)c - 4c^2 \\ &\quad + (2 - 4k + 4m)d + 4d^2. \end{aligned} \quad (1)$$

(ii) If  $m \leq p$  and  $k - m > p$ , then

$$n_1(e | G) = 2p(m + 1/2) + 2m + p^2 + (4m - 2)c - 4c^2. \quad (2)$$

(iii) If  $m > p$  and  $k - m \leq p$ , then

$$n_1(e | G) = 2p(k + m) - p^2 - 7p + 2m - 2k + (4m - 4k + 2)d + 4d^2. \quad (3)$$

(iv) If  $m > p$  and  $k - m > p$ , then

$$n_1(e | G) = 4p(m - 2). \quad (4)$$

**Theorem 12.3.19** *If  $p$  is odd, then the Szeged index of  $\text{TUC}_4\text{C}_8(S)$  nanotube is given as follows:*

1.  $k$  is even.

(i) If  $k \leq p$ , then we have

$$\begin{aligned} \text{Sz}(T) &= p^3 (64/3k^3 + 64k^2 + 176/3k + 16) \\ &\quad - p (4/3k + 2/3k^5 + 6k^3 + 10/3k^4 + 14/3k^2). \end{aligned}$$

(ii) If  $p < k \leq 2p$ , then we have

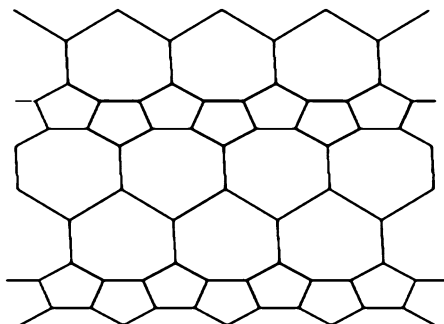
$$\begin{aligned} \text{Sz}(T) &= p (4/5k + 2/3k^2 - 2/3k^3 - 2/3k^4 - 2/15k^5) \\ &\quad + p^2 (32/3k + 4k^2 - 8k^3 + 4/3k^4 - 32/15) \\ &\quad + p^3 (40/3k^3 + 120k^2 - 80k) \\ &\quad + p^4 (32/3k^2 - 176/3k + 388/3) + p^5 (8 - 16/3k) + 4/5p^6. \end{aligned}$$

(iii) If  $k > 2p$ , then we have

$$\begin{aligned} \text{Sz}(T) &= p^3 (56/3k^3 + 56k^2 - 72k + 24) + p^4 (124 + 80k) \\ &\quad + p^5 (16/3k - 88) - 8/15p^2 - 52/15p^6. \end{aligned}$$



**Fig. 12.14**  $\text{HAC}_5\text{C}_7[8,4]$  nanotube



2.  $k$  is odd.

(i) If  $k \leq p$ , then we have

$$\begin{aligned} \text{Sz}(T) &= p^3 (64/3k^3 + 64k^2 + 176/3pk + 16) \\ &\quad - p (4/3k + 2/3k^5 + pk^3 + 10/3k^4 + 14/3k^2). \end{aligned}$$

(ii) If  $p < k \leq 2p$ , then we have

$$\begin{aligned} \text{Sz}(T) &= p (4/5k + 2/3k^2 - 2/3k^3 - 2/3k^4 - 2/15k^5) \\ &\quad + p^2 (32/3k + 4k^2 - 8k^3 + 4/3k^4 - 32/15) \\ &\quad + p^3 (40/3k^3 + 120k^2 - 80k) \\ &\quad + p^4 (388/3 - 176/3k + 32/3k^2) + p^5 (8 - 16/3k) + 4/5p^6. \end{aligned}$$

(iii) If  $k > 2p$ , then we have

$$\begin{aligned} \text{Sz}(T) &= p^3 (56/3k^3 + 56k^2 - 72k + 24) + p^4 (80k + 124) \\ &\quad + p^5 (16/3k - 88) - 8/15p^2 - 52/15p^6. \end{aligned}$$

*Proof* The proof is similar to the proof of Theorem 12.3.17. ■

### 12.3.3 Computation of the Szeged Index of $\text{HAC}_5\text{C}_7[r, p]$ Nanotubes

In this part, we compute the Szeged index of  $\text{HAC}_5\text{C}_7[r, p]$  nanotubes.

We bring all details of the computation of the Szeged index of this nanotube, which have been published in Iranmanesh and Khormali (2009) (Fig. 12.14).

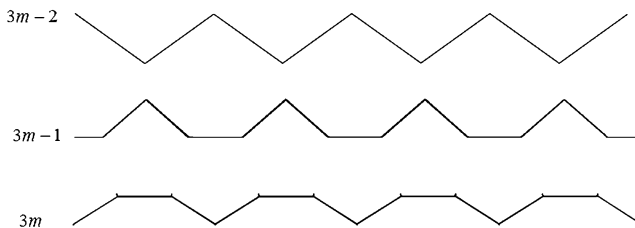


**Fig. 12.15** The  $m$ th period of  $HAC_5C_7[p,q]$  nanotube

We denote the number of heptagons in one row by  $p$  and the number of the periods by  $k$ , and each period consists of three rows as in Fig. 12.15, which shows the  $m$ th period,  $1 \leq m \leq k$ .

Let  $e$  be an edge in Fig. 12.14. Denote:

- $E_1 = \{e \in E(G) \mid e \text{ is an oblique edge between two heptagons}\}$
- $E_2 = \{e \in E(G) \mid e \text{ is a horizontal edge}\}$
- $E_3 = \{e \in E(G) \mid e \text{ is a vertical edge}\}$
- $E_4 = \{e \in E(G) \mid e \text{ is an oblique edge between heptagon and pentagon}\}$
- $E_5 = \{e \in E(G) \mid e \text{ is an oblique edge between two pentagons}\}.$

Also, we can define some subsets of  $E_i$ s as follows:

- $E_{2'} = \{e \in E_2 \mid e \text{ is an edge in } (3m - 1)\text{-th row}\}$
- $E_{2''} = \{e \in E_2 \mid e \text{ is an edge in } 3m\text{-th row}\}$  so that  $E_2 = E_{2'} \cup E_{2''}$ .
- $E_{3'} = \{e \in E_3 \mid e \text{ is an edge between } (3m - 1)\text{-th and } (3m - 2)\text{-th rows}\}$
- $E_{3''} = \{e \in E_3 \mid e \text{ is an edge between } 3m\text{-th and } (3(m + 1) - 2)\text{-th rows}\}$  so that  $E_3 = E_{3'} \cup E_{3''}$ .
- $E_{4'} = \{e \in E_4 \mid e \text{ is an edge in } (3m - 1)\text{-th row}\}$
- $E_{4''} = \{e \in E_4 \mid e \text{ is an edge in } 3m\text{-th row}\}$  so that  $E_4 = E_{4'} \cup E_{4''}$ .

And the number of vertices in each period of this nanotube is equal to  $8p$ .

For computing the Szeged index, we must discuss two cases:

*Case 1*  $p$  is even.

If  $p = 2$ , then

$$Sz = \frac{2560}{3}k^3 - 720k^2 + \frac{1118}{3}k + 2.$$

If  $p = 4$ , then

$$Sz = \begin{cases} \frac{9920}{3}k^3 + 6556k^2 + \frac{16240}{3}k & k \leq 2 \\ \frac{8192}{3}k^3 + 9312k^2 + \frac{113404}{3}k - 99912 & 2 < k \leq 4 \\ 6272k^3 - 7040k^2 + 26276k - 18,824 & k > 4 \end{cases} .$$

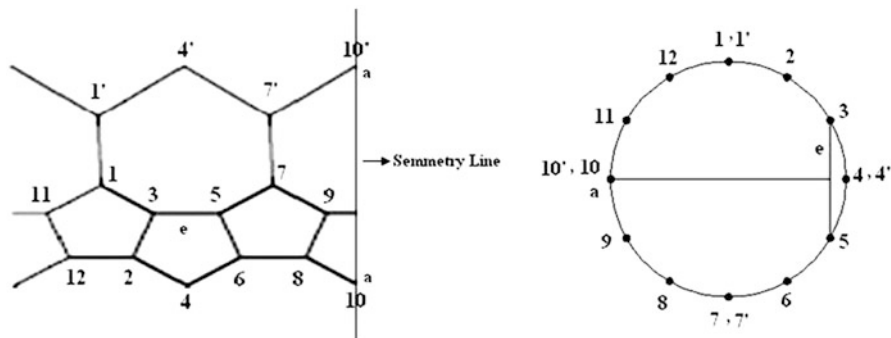


Fig. 12.16 The symmetry line for  $HAC_5C_7[4, 2]$

Now, let  $p \geq 6$ .

We can show all vertices in a period on a circle; let  $e$  be an arbitrary edge on this period.

This edge is connecting two points on the circle. Consider that a line perpendicular at the midpoint to this edge passed a vertex or an edge, say  $a$ , in the opposite side of the circle. A line through the point  $a$  and parallel to the height of nanotube is called a symmetry line of the nanotube.

For example, in Fig. 12.16, we show the symmetry line for  $HAC_5C_7[4, 2]$ :

(a)  $e \in E_1$ :

According to Fig. 12.17, the region  $R$  has the vertices that belong to  $N_1(e | G)$ , and the region  $R'$  has vertices that belong to  $N_2(e | G)$ . (The notations  $n_1(e | G)$  and  $n_2(e | G)$  are indicated with  $n_e(u)$  and  $n_e(v)$ , respectively.) Then,

$$n_e(u) = \begin{cases} 8km - 4k^2 - 9k + 4pk - 1, & m \leq \frac{p}{2}, k - m \leq \frac{p}{2} - 1 \\ 4pm - 9m + 4m^2 + p^2 - \frac{9}{2}p + 4, & m \leq \frac{p}{2}, k - m > \frac{p}{2} - 1 \\ 8km - \frac{9}{2}p - 6 - p^2 + 4pk + 4pm + 9m - 4k^2 - 4m^2 - 9k, & m > \frac{p}{2}, k - m \leq \frac{p}{2} - 1 \\ 8pm - 9p - 1, & m > \frac{p}{2}, k - m > \frac{p}{2} - 1 \end{cases}$$

$$n_e(v) = \begin{cases} -8km - 4k^2 + 4pk - 1, & m \leq \frac{p}{2}, k - m \leq \frac{p}{2} - 1 \\ 8pk - 4pm + 5m - 4m^2 - p^2 + \frac{5}{2}p - 2, & m \leq \frac{p}{2}, k - m > \frac{p}{2} - 1 \\ -8km + \frac{5}{2}p + p^2 + 4pm - 5m + 4k^2 + 4m^2 + 5k, & m > \frac{p}{2}, k - m \leq \frac{p}{2} - 1 \\ 8pk - 8pm + 5p - 1, & m > \frac{p}{2}, k - m > \frac{p}{2} - 1 \end{cases}$$

(b)  $e \in E_2$ :

According to Fig. 12.18, the region  $R$  has the vertices that belong to  $N_1(e | G)$ , and in this sub-case, we have  $n_e(u) = n_e(v)$ . Then,

**Fig. 12.17** The region  $R$  has the vertices that belong to  $N_1(e | G)$ , and the region  $R'$  has vertices that belong to  $N_2(e | G)$

$e \in E_1 :$

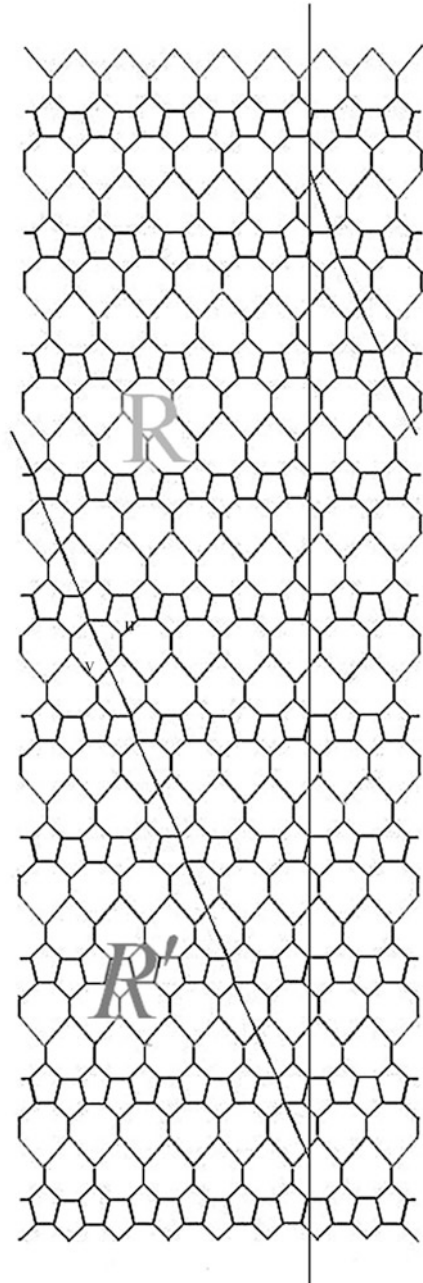
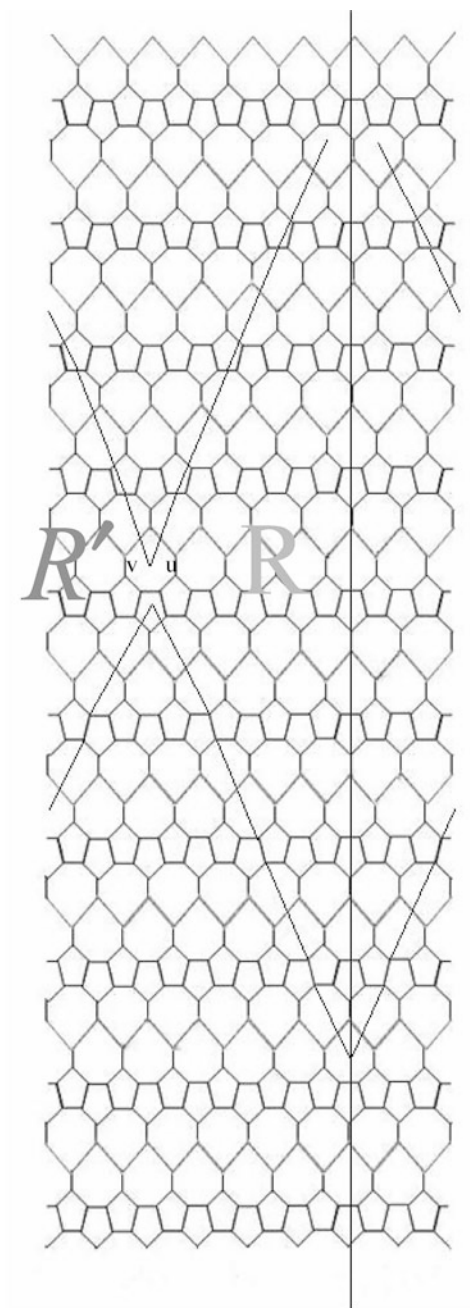


**Fig. 12.18** The region  $R$  has  
the vertices that belong to  
 $N_1(e|G)$   $e \in E_2$ :



(I)  $e \in E_{2'}$ :

$$n_e(u) = \begin{cases} 8km - 4k^2 - 7k + 4pk - 4 - 8m^2 + 12m, & m \leq \frac{p}{2}, k - m \leq \frac{p}{2} - 1 \\ 4pm + 5m - 4m^2 + p^2 - \frac{7}{2}p - 1, & m \leq \frac{p}{2}, k - m > \frac{p}{2} - 1 \\ 8km + \frac{5}{2}p - 4 + p^2 + 4pk - 4pm + & m > \frac{p}{2}, k - m \leq \frac{p}{2} - 1 \\ 7m - 4k^2 - 4m^2 - 7k, & m > \frac{p}{2}, k - m \leq \frac{p}{2} - 1 \\ 2p^2 - p - 1, & m > \frac{p}{2}, k - m > \frac{p}{2} - 1 \end{cases}.$$

(II)  $e \in E_{2''}$ :

$$n_e(u) = \begin{cases} 8km - 4k^2 - k + 4pk + 1 - 8m^2, & m \leq \frac{p}{2}, k - m \leq \frac{p}{2} - 1 \\ 4pm - m - 4m^2 + p^2 - \frac{1}{2}p - 2, & m \leq \frac{p}{2}, k - m > \frac{p}{2} - 1 \\ 8km - \frac{1}{2}p + 1 + p^2 + 4pk - 4pm + & m > \frac{p}{2}, k - m \leq \frac{p}{2} - 1 \\ m - 4k^2 - 4m^2 - k, & m > \frac{p}{2}, k - m > \frac{p}{2} - 1 \\ 2p^2 - p - 2, & m > \frac{p}{2}, k - m > \frac{p}{2} - 1 \end{cases}.$$

(c)  $e \in E_3$ :

According to Fig. 12.19, the region  $R$  has the vertices that belong to  $N_1(e | G)$ , and the region  $R'$  has vertices that belong to  $N_2(e | G)$ . Then,

(I)  $e \in E_{3'}$ :

$$n_e(u) = 8pm - 28$$

$$n_e(v) = 8p(k - m) + 14$$

(II)  $e \in E_{3''}$  (in this sub-case,  $m \neq k$ ):

$$n_e(u) = 8pm - 6p + 14$$

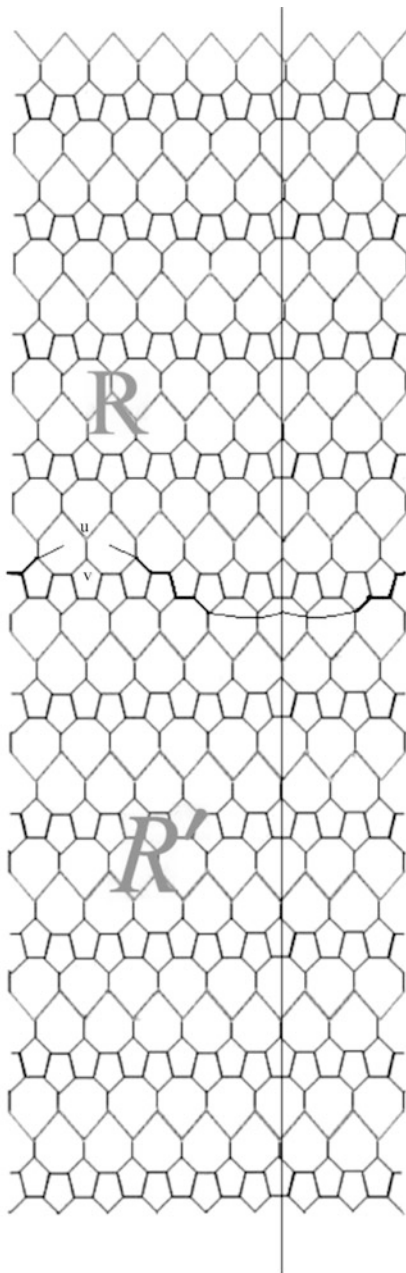
$$n_e(v) = 8(k - m) + 6p - 2$$

(d)  $e \in E_4$ :

According to Fig. 12.20, the region  $R$  has the vertices that belong to  $N_1(e | G)$ , and the region of  $R'$  has vertices that belong to  $N_2(e | G)$ . Then,

(I)  $e \in E_{4'}$ :

$$n_e(u) = \begin{cases} 4pm - m - \frac{p}{2} - 2 + 4m^2, & m \leq \frac{p}{2}, k - m \leq \frac{p}{2} - 1 \\ 4pm - m + 4m^2 - \frac{1}{2}p - 2, & m \leq \frac{p}{2}, k - m > \frac{p}{2} - 1 \\ 8pm + 1 - p^2 + 7p, & m > \frac{p}{2}, k - m \leq \frac{p}{2} - 1 \\ 8pm - p^2 + 7p + 1, & m > \frac{p}{2}, k - m > \frac{p}{2} - 1 \end{cases}.$$

$e \in E_3$ 


**Fig. 12.19** The region  $R$  has the vertices that belong to  $N_1(e | G)$  and the region  $R'$  has vertices that belong to  $N_2(e | G)$

$e \in E_4:$

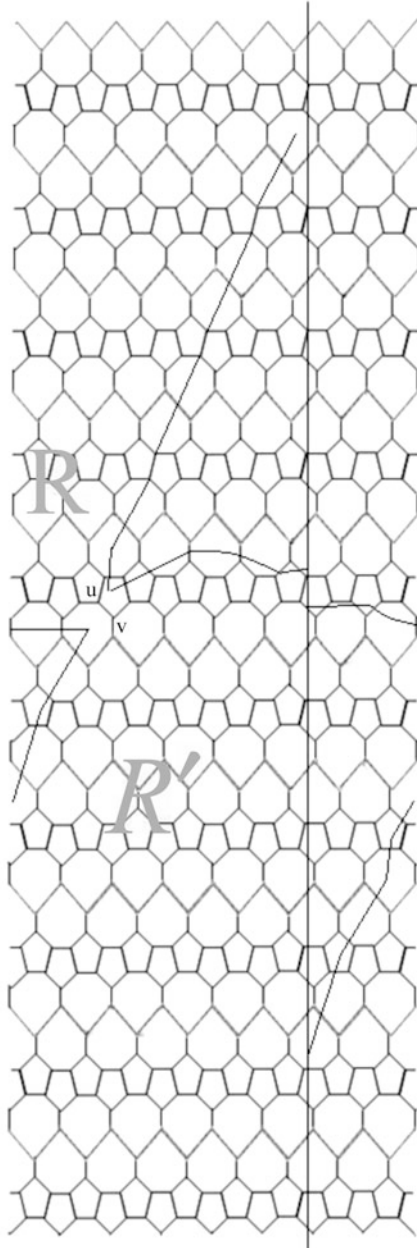


**Fig. 12.20** The region  $R$  has the vertices that belong to  $N_1(e | G)$  and the region  $R'$  has vertices that belong to  $N_2(e | G)$



$$n_e(v) = \begin{cases} k + 4k^2 - 8km + 4pk - 4pm - m + \frac{5p}{2} + 1 + 4m^2, & m \leq \frac{p}{2}, k - m \leq \frac{p}{2} - 1 \\ 8pk - p^2 + 3p + 4 - 8pm, & m \leq \frac{p}{2}, k - m > \frac{p}{2} - 1 \\ k + 4k^2 - 8mk + 4pk - 4pm - m + \frac{5p}{2} + 1 + 4m^2, & m > \frac{p}{2}, k - m \leq \frac{p}{2} - 1 \\ 8pm - p^2 + 3p + 4 - 8pm, & m > \frac{p}{2}, k - m > \frac{p}{2} - 1 \end{cases}.$$

(II)  $e \in E_{4'}$ :

$$n_e(u) = \begin{cases} 4pm - 13m - \frac{p}{2} + 11 + 4m^2, & m \leq \frac{p}{2}, k - m \leq \frac{p}{2} - 1 \\ 4pm - 13m + 4m^2 - \frac{1}{2}p + 11, & m \leq \frac{p}{2}, k - m > \frac{p}{2} - 1 \\ 8pm + 2 - p^2 + p, & m > \frac{p}{2}, k - m \leq \frac{p}{2} - 1 \\ 8pm - p^2 + p + 2, & m > \frac{p}{2}, k - m > \frac{p}{2} - 1 \end{cases}.$$

$$n_e(v) = \begin{cases} 9k + 4p(k - m) - 9m + \frac{p}{2} + 4(k - m)^2, & m \leq \frac{p}{2}, k - m \leq \frac{p}{2} - 1 \\ 8pk - p^2 + 7p - 6 - 8pm, & m \leq \frac{p}{2}, k - m > \frac{p}{2} - 1 \\ 9k + 4p(k - m) - 9m + \frac{p}{2} + 4(k - m)^2, & m > \frac{p}{2}, k - m \leq \frac{p}{2} - 1 \\ 8pm - p^2 + 7p - 6 - 8pm, & m > \frac{p}{2}, k - m > \frac{p}{2} - 1 \end{cases}.$$

(e)  $e \in E_5$ :

According to Fig. 12.21, the region R has vertices that belong to  $N_1(e | G)$ , and the region  $R'$  has vertices that belong to  $N_2(e | G)$ . Then,

$$n_e(u) = 8p(m - 1) + 5p - 9$$

$$n_e(v) = 8p(k - m) + 3p - 9.$$

For simplicity, we define:

In sub-case a:

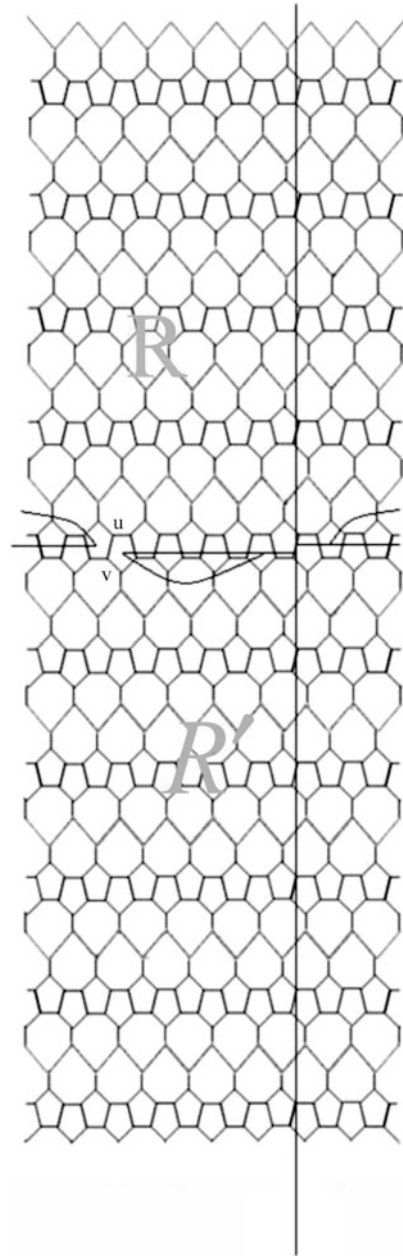
$$\begin{aligned} a_1 &= 8km - 4k^2 - 9k + 4pk - 1 \\ b_1 &= 4pm - 9m + 4m^2 + p^2 - \frac{9}{2}p + 4 \\ c_1 &= 8km - \frac{9}{2}p - 6 - p^2 + 4pk + 4pm + 9m - 4k^2 - 4m^2 - 9k \\ d_1 &= 8pm - 9p - 1 \\ a_2 &= -8km - 4k^2 + 5k + 4pk - 1 \\ b_2 &= 8pk - 4pm + 5m - 4m^2 - p^2 + \frac{5}{2}p - 2 \\ c_2 &= -8km + \frac{5}{2}p + p^2 + 4pk - 4pm - 5m + 4k^2 + 4m^2 + 5k \\ d_2 &= 8pk - 8pm + 5p - 1 \end{aligned}$$

In sub-case b:

$$\begin{aligned} a_3 &= 8km - 4k^2 - 7k + 4pk - 4 - 8m^2 + 12m \\ b_3 &= 4pm + 5m - 4m^2 + p^2 - \frac{7}{2}p - 1 \\ c_3 &= 8km + \frac{5}{2}p - 4 + p^2 + 4pk - 4pm + 7m - 4k^2 - 4m^2 - 7k \\ d_3 &= 2p^2 - p - 1 \end{aligned}$$

**Fig. 12.21** The region  $R$  has the vertices that belong to  $N_1(e | G)$  and the region  $R'$  has vertices that belong to  $N_2(e | G)$

$$e \in E_5$$



$$\begin{aligned}
 a_4 &= 8km - 4k^2 - k + 4pk + 1 - 8m^2 \\
 b_4 &= 4pm - m - 4m^2 + p^2 - \frac{1}{2}p - 2 \\
 c_4 &= 8km - \frac{1}{2}p + 1 + p^2 + 4pk - 4pm + m - 4k^2 - 4m^2 - k \\
 d_4 &= 2p^2 - p - 2
 \end{aligned}$$

In sub-case c:

$$\begin{aligned}
 z_1 &= 8pm - 28 \\
 t_1 &= 8p(k - m) + 14 \\
 z_2 &= 8pm - 6p + 14 \\
 t_2 &= 8(k - m) + 6p - 2
 \end{aligned}$$

In sub-case d:

$$\begin{aligned}
 a_5 &= 4pm - m - \frac{p}{2} - 2 + 4m^2 \\
 b_5 &= a_5 \\
 c_5 &= 8pm + 1 - p^2 + 7p \\
 d_5 &= c_5 \\
 a_6 &= k + 4k^2 - 8km + 4pk - 4pm - m + \frac{5p}{2} + 1 + 4m^2 \\
 b_6 &= 8pk - p^2 + 3p + 4 - 8pm \\
 c_6 &= a_6 \\
 d_6 &= b_6 \\
 a_7 &= 4pm - 13m - \frac{p}{2} + 11 + 4m^2 \\
 b_7 &= a_7 \\
 c_7 &= 8pm + 2 - p^2 + p \\
 d_7 &= c_7 \\
 a_8 &= 9k + 4p(k - m) - 9m + \frac{p}{2} + 4(k - m)^2 \\
 b_8 &= 8pk - p^2 + 7p - 6 - 8pm \\
 c_8 &= a_8 \\
 d_8 &= b_8
 \end{aligned}$$

In sub-case e:

$$\begin{aligned}
 z_3 &= 8p(m - 1) + 5p - 9 \\
 t_3 &= 8p(k - m) + 3p - 9
 \end{aligned}$$

Then:

$$\begin{aligned}
 s_1 &= 2pa_1a_2 + pa_3^2 + pa_4^2 + pz_1t_1 + 2pa_5a_6 + 2pa_7a_8 + 2pz_3t_3 \\
 s_2 &= 2pb_1b_2 + pb_3^2 + pb_4^2 + pz_1t_1 + 2pb_5b_6 + 2pb_7b_8 + 2pz_3t_3 \\
 s_3 &= 2pc_1c_2 + pc_3^2 + pc_4^2 + pz_1t_1 + 2pc_5c_6 + 2pc_7c_8 + 2pz_3t_3 \\
 s_4 &= 2pd_1d_2 + pd_3^2 + pd_4^2 + pz_1t_1 + 2pd_5d_6 + 2pd_7d_8 + 2pz_3t_3
 \end{aligned}$$

Then, we have for  $p \geq 6$ ,

$$Sz = \begin{cases} \sum_{m=1}^k s_1 + \sum_{m=1}^{k-1} pz_2t_2 & k \leq \frac{p}{2} \\ \sum_{m=1}^{\frac{p}{2}} s_2 + \sum_{m=\frac{p}{2}+1}^k s_3 + \sum_{m=1}^{\frac{p}{2}} pz_2t_2 + \sum_{m=\frac{p}{2}+1}^{k-1} pz_2t_2 & \frac{p}{2} < k \leq p \\ \sum_{m=1}^{\frac{p}{2}} s_2 + \sum_{m=\frac{p}{2}+1}^{k-\frac{p}{2}} s_4 + \sum_{m=k-\frac{p}{2}+1}^k s_3 + \sum_{m=1}^{\frac{p}{2}} pz_2t_2 + \sum_{m=\frac{p}{2}+1}^{k-\frac{p}{2}} pz_2t_2 + \sum_{m=k-\frac{p}{2}+1}^{k-1} pz_2t_2 & k > p \end{cases}$$

Case 2  $p$  is odd number.

If  $p = 1$ , then

$$Sz = \frac{320}{3}k^3 - 164k^2 + \frac{342}{3}k - 42.$$

If  $p = 3$ , then

$$Sz = 2880k^3 - 2952k^2 + 3180k - 822.$$

If  $p = 5$ , then

$$Sz = \begin{cases} \frac{24310}{3}k^3 + 13670k^2 + \frac{40985}{3}k + 240 & k \leq 2 \\ \frac{20000}{3}k^3 + 24400k^2 + \frac{13739084983828481}{206158430208}k - 190820 & 2 < k \leq 4 \\ \frac{44000}{3}k^3 - 24600k^2 + \frac{23552226261729281}{206158430208}k - 109220 & k > 4 \end{cases}$$

For  $p \geq 7$ , we can compute  $Sz$  as the same case of even. There are only some differences between odd and even numbers. For example, we must use  $[\frac{p}{2}]$  instead of  $\frac{p}{2}$ .

(a)  $e \in E_1$ :

$$n_e(u) = \begin{cases} 8km - 4k^2 - 9k + 4pk - 2 + m, & m \leq [\frac{p}{2}], k - m \leq [\frac{p}{2}] - 1 \\ 4pm - 8m + 4m^2 - 4[\frac{p}{2}]^2 + 4p[\frac{p}{2}] - [\frac{p}{2}] - 4p + 4, & m \leq [\frac{p}{2}], k - m > [\frac{p}{2}] - 1 \\ 8km - 4p - 6 + 4[\frac{p}{2}]^2 - 4p[\frac{p}{2}] + 4pk + 4pm + 9m - 4k^2 - 4m^2 - 9k, & m > [\frac{p}{2}], k - m \leq [\frac{p}{2}] - 1 \\ 8pm - 8p - [\frac{p}{2}], & m > [\frac{p}{2}], k - m > [\frac{p}{2}] - 1 \end{cases}$$

$$n_e(v) = \begin{cases} -8km + 4k^2 + 6k + 4pk - 1, & m \leq \left[\frac{p}{2}\right], k - m \leq \left[\frac{p}{2}\right] - 1 \\ 8pk - 4pm + 6m - 4m^2 + 4\left[\frac{p}{2}\right]^2 - 4p\left[\frac{p}{2}\right] - 2 \\ \quad \left[\frac{p}{2}\right] + 4p - 4, & m \leq \left[\frac{p}{2}\right], k - m > \left[\frac{p}{2}\right] - 1 \\ -3 + 4p\left[\frac{p}{2}\right] - 4\left[\frac{p}{2}\right]^2 - 2\left[\frac{p}{2}\right] + 4p(k - m + 1) \\ \quad - 2k + 2m + 4(k - m + 1)^2, & m > \left[\frac{p}{2}\right], k - m \leq \left[\frac{p}{2}\right] - 1 \\ 8pk - 8pm + 8p - 2 - 4\left[\frac{p}{2}\right], & m > \left[\frac{p}{2}\right], k - m > \left[\frac{p}{2}\right] - 1 \end{cases}$$

(b)  $e \in E_2$ :

In this sub-case  $n_e(u) = n_e(v)$ ,

(I)  $e \in E_{2'}$ :

$$n_e(u) = \begin{cases} 8km - 4k^2 - 7k + 4pk - 4 \\ \quad + 12m - 8m^2, & m \leq \left[\frac{p}{2}\right], k - m \leq \left[\frac{p}{2}\right] - 1 \\ 4pm + 5m + 4m^2 - 4\left[\frac{p}{2}\right]^2 \\ \quad + 4p\left[\frac{p}{2}\right] + \left[\frac{p}{2}\right] - 4p, & m \leq \left[\frac{p}{2}\right], k - m > \left[\frac{p}{2}\right] - 1 \\ 8km + 1 - 4\left[\frac{p}{2}\right]^2 + 4p\left[\frac{p}{2}\right] + 5\left[\frac{p}{2}\right] + 4pk \\ \quad - 4pm + 7m - 4k^2 - 4m^2 - 7k, & m > \left[\frac{p}{2}\right], k - m \leq \left[\frac{p}{2}\right] - 1 \\ 8p\left[\frac{p}{2}\right] - 4p + 6\left[\frac{p}{2}\right] - 8\left[\frac{p}{2}\right]^2 + 5, & m > \left[\frac{p}{2}\right], k - m > \left[\frac{p}{2}\right] - 1 \end{cases}$$

(II)  $e \in E_{2''}$ :

$$n_e(u) = \begin{cases} 8km - 4k^2 - k + 4pk + 1 - 8m^2, & m \leq \left[\frac{p}{2}\right], k - m \leq \left[\frac{p}{2}\right] - 1 \\ 4pm - m - 4m^2 - 4\left[\frac{p}{2}\right]^2 + 4p\left[\frac{p}{2}\right] \\ \quad - \left[\frac{p}{2}\right] + 1, & m \leq \left[\frac{p}{2}\right], k - m > \left[\frac{p}{2}\right] - 1 \\ 8km + 1 - 4\left[\frac{p}{2}\right]^2 + 4p\left[\frac{p}{2}\right] - \left[\frac{p}{2}\right] \\ \quad + 4pk - 4pm + m - 4k^2 - 4m^2 - k, & m > \left[\frac{p}{2}\right], k - m \leq \left[\frac{p}{2}\right] - 1 \\ 8p\left[\frac{p}{2}\right] - 2\left[\frac{p}{2}\right] - 8\left[\frac{p}{2}\right]^2 + 1, & m > \left[\frac{p}{2}\right], k - m > \left[\frac{p}{2}\right] - 1 \end{cases}$$

(c)  $e \in E_3$ :

(I)  $e \in E_{3'}$ :

$$n_e(u) = 8pm - 28$$

$$n_e(v) = 8p(k - m) + 14$$

(II)  $e \in E_{3''}$ :

$$n_e(u) = 8pm - 6p + 14$$

$$n_e(v) = 8(k - m) + 6p - 2$$

(d)  $e \in E_4$ :(I)  $e \in E_{4'}$ :

$$n_e(u) = \begin{cases} pm - \left[\frac{p}{2}\right] + 6m \left[\frac{p}{2}\right] + 7 - 7m + 4m^2, & m \leq \left[\frac{p}{2}\right], k - m \leq \left[\frac{p}{2}\right] - 1 \\ pm - 7m + 4m^2 + 6m \left[\frac{p}{2}\right] - \left[\frac{p}{2}\right] + 7, & m \leq \left[\frac{p}{2}\right], k - m > \left[\frac{p}{2}\right] - 1 \\ 8pm + 10\left[\frac{p}{2}\right]^2 - 7p \left[\frac{p}{2}\right] + 6\left[\frac{p}{2}\right] + p + 1, & m > \left[\frac{p}{2}\right], k - m \leq \left[\frac{p}{2}\right] - 1 \\ 8pm + p + 6\left[\frac{p}{2}\right] - 7p \left[\frac{p}{2}\right] + 10\left[\frac{p}{2}\right] + 1, & m > \left[\frac{p}{2}\right], k - m > \left[\frac{p}{2}\right] - 1 \end{cases}$$

$$n_e(v) = \begin{cases} -\left[\frac{p}{2}\right] + 6\left[\frac{p}{2}\right](k - m + 1) + p(k - m + 1) \\ \quad + 5m - 5k - p + 4(k - m + 1)^2, & m \leq \left[\frac{p}{2}\right], k - m \leq \left[\frac{p}{2}\right] - 1 \\ 8pk - 8pm + 10\left[\frac{p}{2}\right]^2 - 7p \left[\frac{p}{2}\right] - 5\left[\frac{p}{2}\right] \\ \quad + 7p + 9, & m \leq \left[\frac{p}{2}\right], k - m > \left[\frac{p}{2}\right] - 1 \\ 5m + 6\left[\frac{p}{2}\right](k - m + 1) - \left[\frac{p}{2}\right] \\ \quad + p(k - m + 1) + 4(k - m + 1)^2 - 5k - p, & m > \left[\frac{p}{2}\right], k - m \leq \left[\frac{p}{2}\right] - 1 \\ 8pk - 8pm + 10\left[\frac{p}{2}\right]^2 - 7p \left[\frac{p}{2}\right] - 5\left[\frac{p}{2}\right] \\ \quad + 7p + 9, & m > \left[\frac{p}{2}\right], k - m > \left[\frac{p}{2}\right] - 1 \end{cases}$$

(II)  $e \in E_{4''}$ :

$$n_e(u) = \begin{cases} pm - \left[\frac{p}{2}\right] + 6m \left[\frac{p}{2}\right] + 15 - 14m + 4m^2, & m \leq \left[\frac{p}{2}\right], k - m \leq \left[\frac{p}{2}\right] - 1 \\ pm - 14m + 4m^2 + 6m \left[\frac{p}{2}\right] - \left[\frac{p}{2}\right] + 15, & m \leq \left[\frac{p}{2}\right], k - m > \left[\frac{p}{2}\right] - 1 \\ 8pm + 10\left[\frac{p}{2}\right]^2 - 7p \left[\frac{p}{2}\right] - \left[\frac{p}{2}\right] + p, & m > \left[\frac{p}{2}\right], k - m \leq \left[\frac{p}{2}\right] - 1 \\ 8pm + p - \left[\frac{p}{2}\right] - 7p \left[\frac{p}{2}\right] + 10\left[\frac{p}{2}\right], & m > \left[\frac{p}{2}\right], k - m > \left[\frac{p}{2}\right] - 1 \end{cases}$$

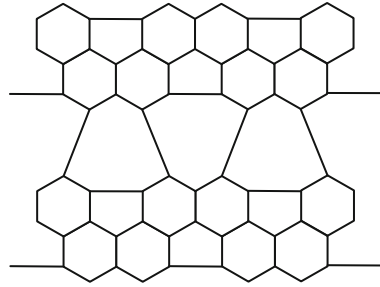
$$n_e(v) = \begin{cases} -\left[\frac{p}{2}\right] + 6\left[\frac{p}{2}\right](k - m + 1) + p(k - m + 1) \\ \quad - 1 + 4(k - m + 1)^2 - p, & m \leq \left[\frac{p}{2}\right], k - m \leq \left[\frac{p}{2}\right] - 1 \\ 8pk - 8pm + 10\left[\frac{p}{2}\right]^2 - 7p \left[\frac{p}{2}\right] - \left[\frac{p}{2}\right] + 7p - 4, & m \leq \left[\frac{p}{2}\right], k - m > \left[\frac{p}{2}\right] - 1 \\ 6\left[\frac{p}{2}\right](k - m + 1) - \left[\frac{p}{2}\right] + p(k - m + 1) \\ \quad + 4(k - m + 1)^2 - p - 1, & m > \left[\frac{p}{2}\right], k - m \leq \left[\frac{p}{2}\right] - 1 \\ 8pk - 8pm + 10\left[\frac{p}{2}\right]^2 - 7p \left[\frac{p}{2}\right] - \left[\frac{p}{2}\right] + 7p - 4, & m > \left[\frac{p}{2}\right], k - m > \left[\frac{p}{2}\right] - 1 \end{cases}$$

(e)  $e \in E_5$ :

$$n_e(u) = 8p(m - 1) + 5p - 9$$

$$n_e(v) = 8p(k - m) + 3p - 9$$

**Fig. 12.22**  $HAC_5C_6C_7[2, 2]$  nanotube,  $p = 2, k = 2$



Therefore, we obtain the Szeged index for odd number as follows:

$$Sz = \begin{cases} \sum_{m=1}^k s_1 + \sum_{m=1}^{k-1} pz_2t_2 & k \leq \lfloor \frac{p}{2} \rfloor \\ \sum_{m=1}^{\frac{p}{2}} s_2 + \sum_{m=\frac{p}{2}+1}^k s_3 + \sum_{m=1}^{\frac{p}{2}} pz_2t_2 + \sum_{m=\frac{p}{2}+1}^{k-1} pz_2t_2 & \lfloor \frac{p}{2} \rfloor < k \leq p \\ \sum_{m=1}^{\frac{p}{2}} s_2 + \sum_{m=\frac{p}{2}+1}^{k-\frac{p}{2}} s_4 + \sum_{m=k-\frac{p}{2}+1}^k s_3 + \sum_{m=1}^{\frac{p}{2}} pz_2t_2 + \sum_{m=\frac{p}{2}+1}^{k-\frac{p}{2}} pz_2t_2 \\ \quad + \sum_{m=k-\frac{p}{2}+1}^{k-1} pz_2t_2 & k > p \end{cases}$$

### 12.3.4 Computation of the Szeged Index of $HAC_5C_6C_7[r, p]$ Nanotube

In this part, we compute the Szeged index of  $HAC_5C_6C_7[r, p]$  nanotube.

We bring all details of the computation of the Szeged index of this nanotube, which have been published in Iranmanesh and Pakraves (2007).

In Fig. 12.22, an  $HAC_5C_6C_7[2, 2]$  lattice is illustrated.

We denote the number of pentagons in one row by  $p$  and the number of the periods by  $k$ , and each period consists of three rows as in Fig. 12.23, which shows the  $m$ th period,  $1 \leq m \leq k$ .

Let  $e$  be an edge in Fig. 12.22. Denote:

- $E_1 = \{e \in E(G) \mid e \text{ is a vertical edge between hexagon and pentagon}\}$
- $E_2 = \{e \in E(G) \mid e \text{ is an oblique edge between pentagon and hexagon}\}$
- $E_3 = \{e \in E(G) \mid e \text{ is an oblique edge between heptagon and hexagon}\}$
- $E_4 = \{e \in E(G) \mid e \text{ is an oblique edge between heptagon and hexagon adjacent with pentagon}\}$
- $E_5 = \{e \in E(G) \mid e \text{ is an oblique edge between two heptagons}\}$
- $E_6 = \{e \in E(G) \mid e \text{ is a horizontal edge}\}$

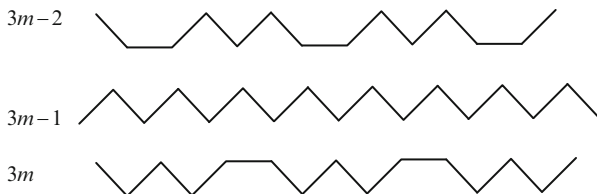


**Fig. 12.23** The  $m$ th period of  $HAC_5C_6C_7[r, p]$  nanotube

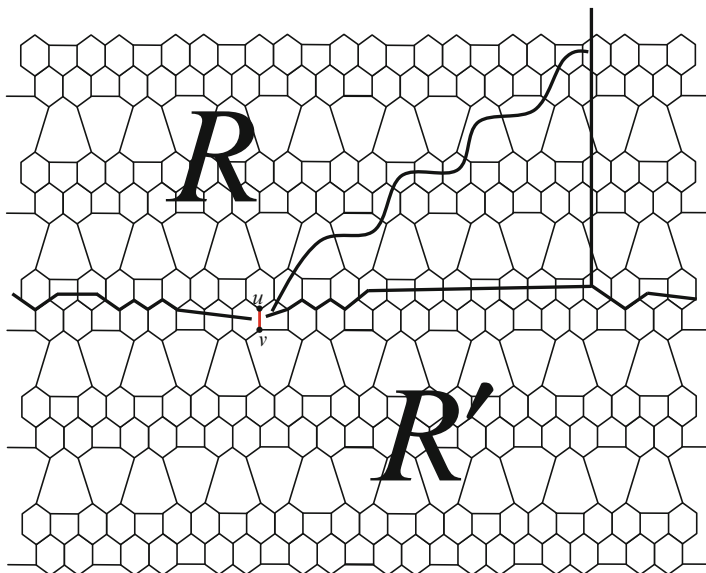


**Fig. 12.24**  $e = uv$  is an edge belonging to  $E_1$  in  $m = 3$  rd row

$E_7 = \{e \in E(G) \mid e \text{ is a vertical edge between two hexagons}\}$

$E_8 = \{e \in E(G) \mid e \text{ is an oblique edge between two hexagons}\}.$

And the number of vertices in each period of this nanotube is equal to  $16p$ . For computing the Szeged index, we must discuss two cases:

*Case 1*  $p$  is even.

Let  $e = uv$  be an edge denoted in Fig. 12.24.

- (a) If  $e \in E_1$ , then, according to Fig. 12.24, the region  $R$  has the vertices that belong to  $N_1(e|G)$ , and the region  $R'$  has vertices that belong to  $N_2(e|G)$  Then,



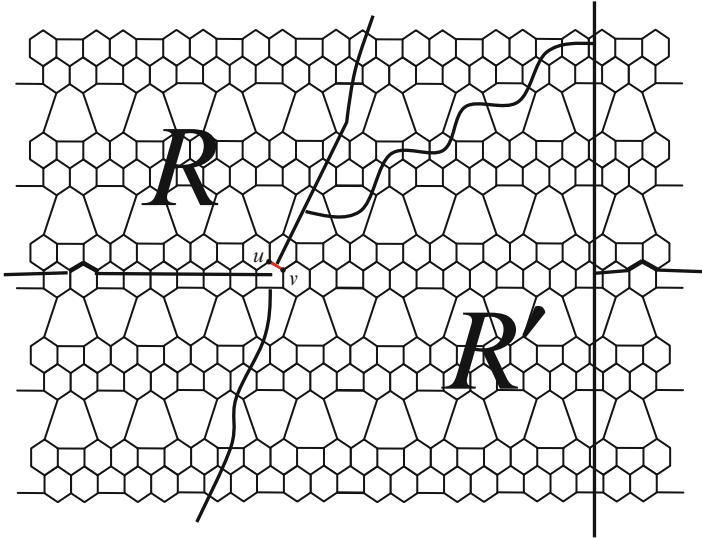


Fig. 12.25  $e = uv$  is an edge belonging to  $E_2$  in  $m = 3$ rd row

$$n_e(v) = 16p(k - m) + \frac{19}{2}p - 14.$$

If  $m \leq \left\lfloor \frac{5p-4}{20} \right\rfloor + 1$ , then

$$n_e(u) = 8pm - \frac{11}{2}p + 16m^2 - 19m + 11.$$

If  $m > \left\lfloor \frac{5p-4}{20} \right\rfloor + 1$ , then

$$\begin{aligned} n_e(u) = & p(16m - 11) + 25 + \left(7 + \frac{5}{2}p\right) \left\lfloor \frac{5p-4}{20} \right\rfloor + 5 \left\lfloor \frac{5p-4}{20} \right\rfloor^2 \\ & + \left(12 - \frac{21}{2}p\right) \left\lfloor \frac{5p-14}{20} \right\rfloor + 5 \left\lfloor \frac{5p-14}{20} \right\rfloor^2 \\ & + 16 \left\lfloor \frac{3p-10}{12} \right\rfloor + 6 \left\lfloor \frac{3p-10}{12} \right\rfloor^2. \end{aligned}$$

- (b) If  $e \in E_2$ , then, according to Fig. 12.25, the region  $R$  has the vertices that belong to  $N_1(e|G)$ , and the region  $R'$  has vertices that belong to  $N_2(e|G)$ . Then,

(i) If  $m \leq \left\lceil \frac{5p-2}{20} \right\rceil + 1$  and  $k - m \leq p$ , then

$$n_e(v) = k(8p + 5) + m(18 - 16m) - 9 \\ + (16(k - m) - 10) \left\lceil \frac{k - m}{2} \right\rceil - 16 \left\lceil \frac{k - m}{2} \right\rceil^2.$$

(ii) If  $m > \left\lceil \frac{5p-2}{20} \right\rceil + 1$  and  $k - m \leq p$ , then

$$n_e(v) = (8p + 5)(k - m) + \frac{27}{2}p - 16 + \left(\frac{5}{2}p - 6\right) \left\lceil \frac{5p - 2}{20} \right\rceil \\ - 5 \left\lceil \frac{5p - 2}{20} \right\rceil^2 + \left(\frac{5}{2}p - 11\right) \left\lceil \frac{5p - 12}{20} \right\rceil - 5 \left\lceil \frac{5p - 12}{20} \right\rceil^2 \\ + (3p - 14) \left\lceil \frac{3p - 8}{12} \right\rceil - 6 \left\lceil \frac{3p - 8}{12} \right\rceil^2 \\ + (16(k - m) - 10) \left\lceil \frac{k - m}{2} \right\rceil - 16 \left\lceil \frac{k - m}{2} \right\rceil^2.$$

(iii) If  $m \leq \left\lceil \frac{5p-2}{20} \right\rceil + 1$  and  $k - m > p$ , then

$$n_e(v) = 8p \left(2k - m - \frac{1}{2}p\right) - 16m^2 + 23m - 9.$$

(iv) If  $m > \left\lceil \frac{5p-2}{20} \right\rceil + 1$  and  $k - m > p$ , then

$$n_e(v) = 16p(k - m) - 4p^2 + \frac{27}{2}p - 16 + \left(\frac{5}{2}p - 6\right) \left\lceil \frac{5p - 2}{20} \right\rceil \\ - 5 \left\lceil \frac{5p - 2}{20} \right\rceil^2 + \left(\frac{5}{2}p - 11\right) \left\lceil \frac{5p - 12}{20} \right\rceil - 5 \left\lceil \frac{5p - 12}{20} \right\rceil^2 \\ + (3p - 14) \left\lceil \frac{3p - 8}{12} \right\rceil - 6 \left\lceil \frac{3p - 8}{12} \right\rceil^2.$$

And for  $n_e(u)$ , we have

(i) If  $m \leq p$ , then

$$n_e(u) = 4p(2m - 1) + 9m - 3 + (16m - 22) \left\lceil \frac{m - 1}{2} \right\rceil - 16 \left\lceil \frac{m - 1}{2} \right\rceil^2.$$

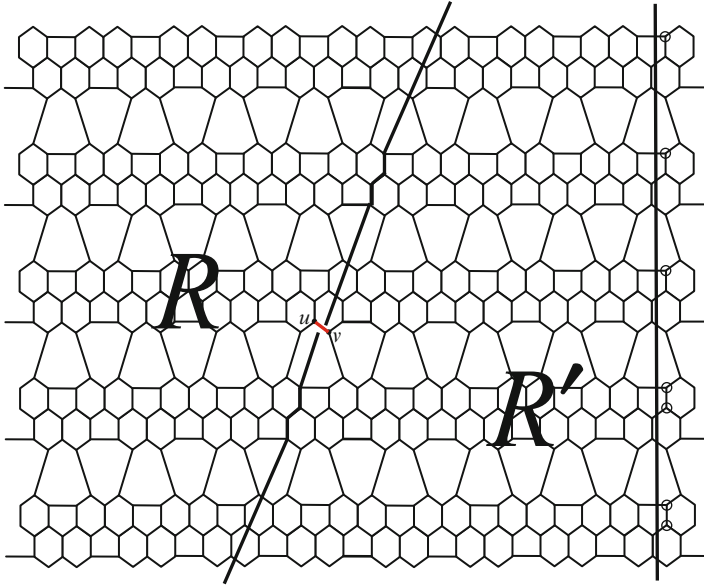


Fig. 12.26  $e = uv$  is an edge belonging to  $E_3$  in  $m = 3$ rd row

(ii) If  $m > p$ , then

$$n_e(u) = 4p(2m + p - 1) - 2m + 3.$$

(c) If  $e \in E_3$ , then,

according to Fig. 12.26, the region  $R$  has the vertices that belong to  $N_1(e|G)$ , and the region  $R'$  has vertices that belong to  $N_2(e|G)$ .

In Figs. 12.26, 12.27, and 12.28, the symbol  $\circ$  means that the vertex assigned with this symbol has the same distance from  $u$  and  $v$ . Then,

(i) If  $m \leq p$  and  $k - m \leq p$ , then

$$\begin{aligned} n_e(v) = & 8pk + 3k - 16m + 9 + (16(k - m) - 6) \left[ \frac{k - m}{2} \right] \\ & - 16 \left[ \frac{k - m}{2} \right]^2 + (26 - 16m) \left[ \frac{m - 1}{2} \right] + 16 \left[ \frac{m - 1}{2} \right]^2. \end{aligned}$$

(ii) If  $m > p$  and  $k - m \leq p$ , then

$$\begin{aligned} n_e(v) = & (8p + 3)(k - m) + 4p^2 - 1 \\ & + (16(k - m) - 6) \left[ \frac{k - m}{2} \right] - 16 \left[ \frac{k - m}{2} \right]^2. \end{aligned}$$

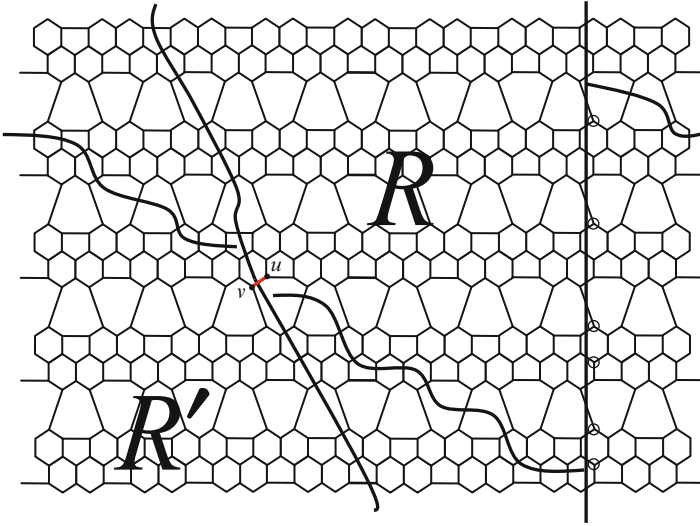


Fig. 12.27  $e = uv$  is an edge belonging to  $E_4$  in  $m = 3$  rd row

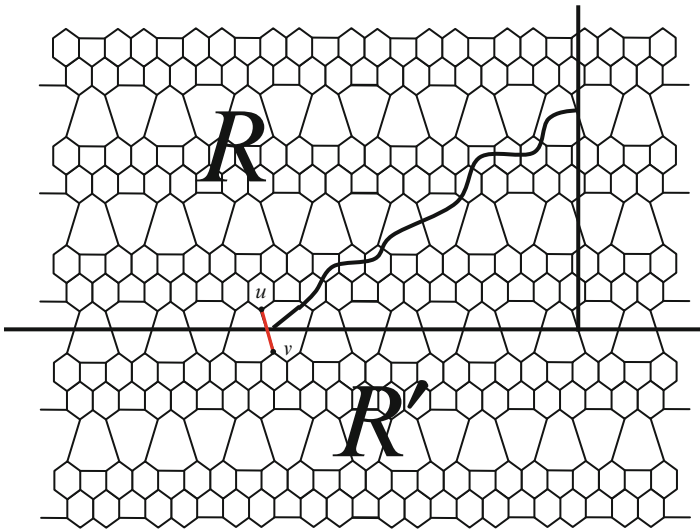


Fig. 12.28  $e = uv$  is an edge belonging to  $E_5$  in  $m = 3$  rd row

(iii) If  $m \leq p$  and  $k - m > p$ , then

$$\begin{aligned} n_e(v) &= 8p(2k - m) - 4p^2 + 9 - 13m \\ &\quad + (26 - 16m) \left[ \frac{m-1}{2} \right] + 16 \left[ \frac{m-1}{2} \right]^2. \end{aligned}$$

(iv) If  $m > p$  and  $k - m > p$ , then  $n_e(v) = 16p(k - m) - 1$ . And for  $n_e(u)$ , we have

(i) If  $m \leq p$  and  $k - m \leq p$ , then

$$\begin{aligned} n_e(u) &= 8pk - 6k + 18m - 11 + (6 - 16(k - m)) \left[ \frac{k-m}{2} \right] \\ &\quad + 16 \left[ \frac{k-m}{2} \right]^2 - 4 \left[ \frac{k-m+1}{2} \right] \\ &\quad + (16m - 30) \left[ \frac{m-1}{2} \right] - 16 \left[ \frac{m-1}{2} \right]^2. \end{aligned}$$

(ii) If  $m > p$  and  $k - m \leq p$ , then

$$\begin{aligned} n_e(u) &= 8p(k + m) + 6(m - k) - 4p^2 - 3p + 3 \\ &\quad + (6 - 16(k - m)) \left[ \frac{k-m}{2} \right] \\ &\quad - 4 \left[ \frac{k-m+1}{2} \right] + 16 \left[ \frac{k-m}{2} \right]^2. \end{aligned}$$

(iii) If  $m \leq p$  and  $k - m > p$ , then

$$\begin{aligned} n_e(u) &= 8pm + 4p^2 - 5p - 11 + 12m \\ &\quad + (16m - 30) \left[ \frac{m-1}{2} \right] - 16 \left[ \frac{m-1}{2} \right]^2. \end{aligned}$$

(iv) If  $m > p$  and  $k - m > p$ , then

$$n_e(u) = 16pm - 8p + 3.$$

(d) If  $e \in E_4$ , then,

according to Fig. 12.27, the region  $R$  has vertices that belong to  $N_1(e|G)$ , and the region  $R'$  has vertices that belong to  $N_2(e|G)$ . Then,

(i) If  $m \leq \left[ \frac{5p-10}{20} \right] + 1$  and  $k - m \leq p$ , then

$$n_e(v) = 8k(p+1) - 16m^2 + m - 1 \\ + (16(k-m) - 6) \left[ \frac{k-m}{2} \right] - 16 \left[ \frac{k-m}{2} \right]^2.$$

(ii) If  $m \leq \left[ \frac{5p-10}{20} \right] + 1$  and  $k-m > p$ , then

$$n_e(v) = 8p(2k-m) - 4p^2 + 5p + 9m - 16m^2 + 7.$$

(iii) If  $m > \left[ \frac{5p-10}{20} \right] + 1$  and  $k-m \leq p$ , then

$$n_e(v) = (8p+8)(k-m) + 8p - 8 + (16(k-m) - 6) \left[ \frac{k-m}{2} \right] \\ - 16 \left[ \frac{k-m}{2} \right]^2 + \left( \frac{5}{2}p - 11 \right) \left[ \frac{5p-10}{20} \right] - 5 \left[ \frac{5p-10}{20} \right]^2 \\ + \left( \frac{5}{2}p - 5 \right) \left[ \frac{5p}{20} \right] - 5 \left[ \frac{5p}{20} \right]^2 \\ + (3p-7) \left[ \frac{3p-1}{12} \right] - 6 \left[ \frac{3p-1}{12} \right]^2.$$

(iv) If  $m > \left[ \frac{5p-10}{20} \right] + 1$  and  $k-m > p$ , then

$$n_e(v) = 16p(k-m) + 5p - 4p^2 + \left( \frac{5}{2}p - 11 \right) \left[ \frac{5p-10}{20} \right] \\ - 5 \left[ \frac{5p-10}{20} \right]^2 + \left( \frac{5}{2}p - 5 \right) \left[ \frac{5p}{20} \right] - 5 \left[ \frac{5p}{20} \right]^2 \\ + (3p-7) \left[ \frac{3p-1}{12} \right] - 6 \left[ \frac{3p-1}{12} \right]^2.$$

For  $n_e(u)$ , we have

(i) If  $k-m \leq \left[ \frac{5p}{20} \right]$  and  $m \leq p$ , then

$$n_e(u) = 8k(p+4m-2k) - 16m^2 + 14m - 6k - 7 \\ + (16m-22) \left[ \frac{m-1}{2} \right] - 16 \left[ \frac{m-1}{2} \right]^2.$$

(ii) If  $m \leq p$  and  $k - m > \left\lceil \frac{5p}{20} \right\rceil$ , then

$$\begin{aligned} n_e(u) &= 8pm + 8m - 7 + (16m - 22) \left\lceil \frac{m-1}{2} \right\rceil - 16 \left\lceil \frac{m-1}{2} \right\rceil^2 \\ &\quad + \left(\frac{5}{2}p\right) \left\lceil \frac{5p+10}{20} \right\rceil - 5 \left\lceil \frac{5p+10}{20} \right\rceil^2 + \left(\frac{5}{2}p - 5\right) \left\lceil \frac{5p}{20} \right\rceil \\ &\quad - 5 \left\lceil \frac{5p}{20} \right\rceil^2 + (3p - 1) \left\lceil \frac{3p+5}{12} \right\rceil - 6 \left\lceil \frac{3p+5}{12} \right\rceil^2. \end{aligned}$$

(iii) If  $m > p$  and  $k - m \leq \left\lceil \frac{5p}{20} \right\rceil$ , then

$$n_e(u) = 8p(k + m) - 4p^2 - 3p + 6(m - k) - 16(m^2 + k^2) + 32km - 7.$$

(iv) If  $m > p$  and  $k - m > \left\lceil \frac{5p}{20} \right\rceil$ , then

$$\begin{aligned} n_e(u) &= 16pm - 3p - 4p^2 - 1 + \left(\frac{5}{2}p\right) \left\lceil \frac{5p+10}{20} \right\rceil - 5 \left\lceil \frac{5p+10}{20} \right\rceil^2 \\ &\quad + \left(\frac{5}{2}p - 5\right) \left\lceil \frac{5p}{20} \right\rceil - 5 \left\lceil \frac{5p}{20} \right\rceil^2 + (3p - 1) \left\lceil \frac{3p+5}{12} \right\rceil \\ &\quad - 6 \left\lceil \frac{3p+5}{12} \right\rceil^2. \end{aligned}$$

(e) If  $e \in E_5$ , then,

according to Fig. 12.28, the region  $R$  has vertices that belong to  $N_1(e|G)$ , and the region  $R'$  has vertices that belong to  $N_2(e|G)$ . Then,  $n_e(v) = 16p(k - m) - 1$ .

And for  $n_e(u)$ , we have

(i) If  $m \leq \left\lceil \frac{5p+4}{20} \right\rceil$ , then

$$n_e(u) = m(8p + 16m - 2).$$

(ii) If  $m > \left\lceil \frac{5p+4}{20} \right\rceil$ , then

$$\begin{aligned} n_e(u) &= 24pm - 11p + 6 + (3 - 5p) \left\lceil \frac{5p+4}{20} \right\rceil + 5 \left\lceil \frac{5p+4}{20} \right\rceil^2 \\ &\quad + (7 - 11p) \left\lceil \frac{5p-4}{20} \right\rceil + 5 \left\lceil \frac{5p-4}{20} \right\rceil^2 \\ &\quad + 10 \left\lceil \frac{3p-4}{12} \right\rceil + 6 \left\lceil \frac{3p-4}{12} \right\rceil^2. \end{aligned}$$

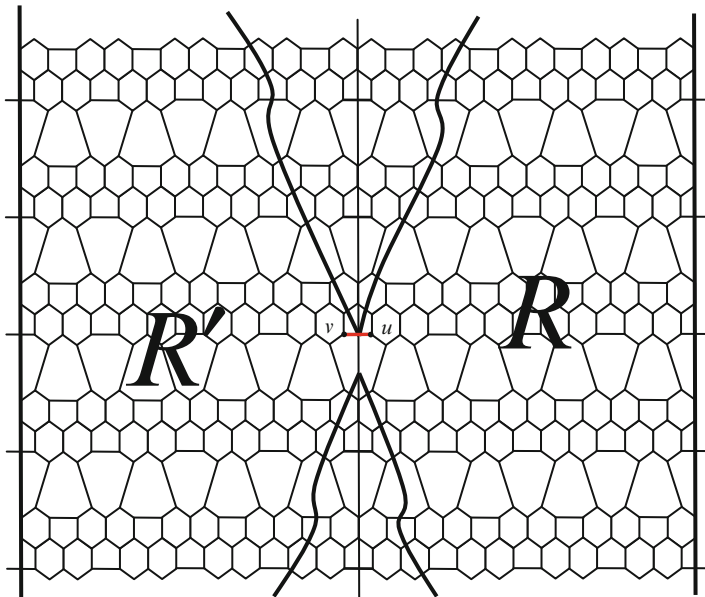


Fig. 12.29  $e = uv$  is an edge belonging to  $E_6$  in  $m = 3$  rd row

If  $e \in E_6$ , then,

according to Fig. 12.29, the region  $R$  has vertices that belong to  $N_1(e|G)$ , and the region  $R'$  has vertices that belong to  $N_2(e|G)$ . Then,

(f) (i) If  $m \leq p$  and  $k - m \leq p$ , then

$$n_e(v) = 8pk - 5k - 8m + 9 + (10 + 16(m - k)) \left[ \frac{k - m}{2} \right] + 16 \left[ \frac{k - m}{2} \right]^2 + (26 - 16m) \left[ \frac{m - 1}{2} \right] + 16 \left[ \frac{m - 1}{2} \right]^2.$$

(ii) If  $m > p$  and  $k - m \leq p$ , then

$$n_e(v) = (8p - 5)(k - m) + 4p^2 - 1 + (10 + 16(m - k)) \left[ \frac{k - m}{2} \right] + 16 \left[ \frac{k - m}{2} \right]^2.$$

(iii) If  $m \leq p$  and  $k - m > p$ , then

$$n_e(v) = 8pm + 4p^2 + 9 - 13m + (26 - 16m) \left[ \frac{m - 1}{2} \right] + 16 \left[ \frac{m - 1}{2} \right]^2.$$



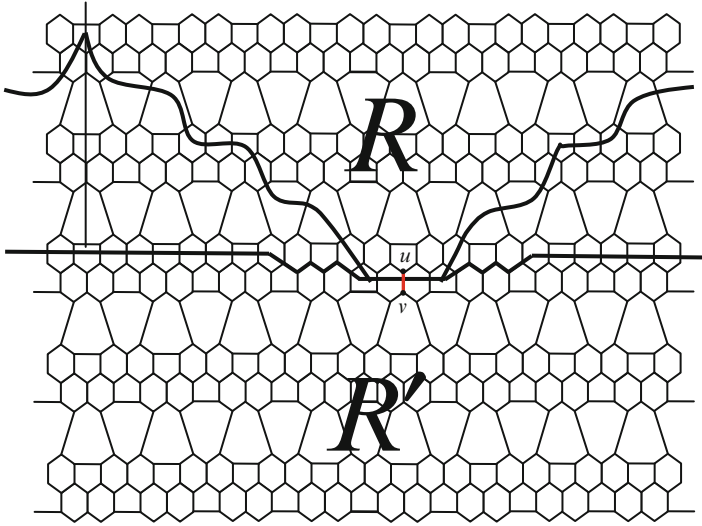


**Fig. 12.30**  $e = uv$  is an edge belonging to  $E_7$  in  $m = 3$  rd row

(iv) If  $m > p$  and  $k - m > p$ , then

$$n_e(v) = 8p^2 - 1.$$

And  $n_e(u) = n_e(v)$ .

(g) If  $e \in E_7$ , then,

according to Fig. 12.30, the region  $R$  has vertices that belong to  $N_1(e|G)$ , and the region  $R'$  has vertices that belong to  $N_2(e|G)$ . Then,

If  $p < 3$ , then

$$n_e(v) = 16p(k - m) + 5p - 1.$$

And if  $p \geq 3$ , then

$$n_e(v) = 16p(k - m) + 11p - 20.$$

For  $n_e(u)$ , we have

(i) If  $m \leq \left\lceil \frac{5p-8}{20} \right\rceil + 1$ , then

$$n_e(u) = 32m^2 - 28m + 10.$$

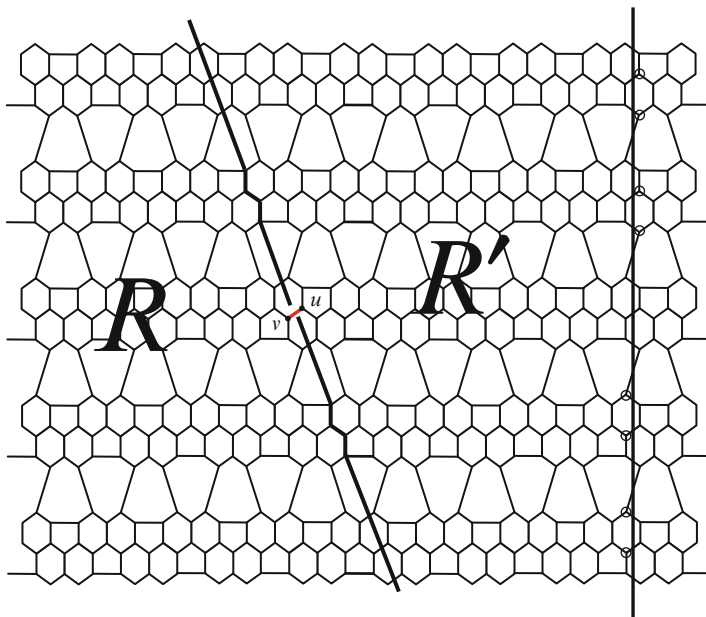


Fig. 12.31  $e = uv$  is an edge belonging to  $E_8$  in  $m = 3$ rd row

(ii) If  $m > \left\lceil \frac{5p-8}{20} \right\rceil + 1$ , then

$$\begin{aligned} n_e(u) &= 16p(m-1) + (18-5p) \left\lceil \frac{5p-8}{20} \right\rceil + 10 \left\lceil \frac{5p-8}{20} \right\rceil^2 \\ &\quad + (7-11p) \left\lceil \frac{5p+4}{20} \right\rceil + 10 \left\lceil \frac{5p+4}{20} \right\rceil^2 + 11 \left\lceil \frac{3p+1}{12} \right\rceil \\ &\quad + 12 \left\lceil \frac{3p+1}{12} \right\rceil^2. \end{aligned}$$

If  $e \in E_8$ , then,

according to Fig. 12.31, the region  $R$  has vertices that belong to  $N_1(e|G)$ , and the region  $R'$  has vertices that belong to  $N_2(e|G)$ . Then,

For  $n_e(v)$ , we have

(h) (i) If  $m \leq p$  and  $k-m \leq p$ , then

$$n_e(v) = 8pk + 6k - 18m + 11 + (16(k - m) - 6) \left[ \frac{k - m}{2} \right] \\ - 16 \left[ \frac{k - m}{2} \right]^2 + (26 - 16m) \left[ \frac{m - 1}{2} \right] + 16 \left[ \frac{m - 1}{2} \right]^2.$$

(ii) If  $m > p$  and  $k - m \leq p$ , then

$$n_e(v) = (8p + 6)(k - m) + 4p^2 + p + 1 \\ + (16(k - m) - 6) \left[ \frac{k - m}{2} \right] - 16 \left[ \frac{k - m}{2} \right]^2.$$

(iii) If  $m \leq p$  and  $k - m > p$ , then

$$n_e(v) = 8p(2k - m) - 4p^2 + 3p + 11 - 12m \\ + (26 - 16m) \left[ \frac{m - 1}{2} \right] + 16 \left[ \frac{m - 1}{2} \right]^2.$$

(iv) If  $m > p$  and  $k - m > p$ , then

$$n_e(v) = 16p(k - m) + 4p + 1.$$

And for  $n_e(u)$ , we have

(i) If  $m \leq p$  and  $k - m \leq p$ , then

$$n_e(u) = 8pk - 6k + 18m - 13 + (4 - 16(k - m)) \left[ \frac{k - m}{2} \right] \\ + 16 \left[ \frac{k - m}{2} \right]^2 - 6 \left[ \frac{k - m + 1}{2} \right] \\ + (16m - 32) \left[ \frac{m - 1}{2} \right] - 16 \left[ \frac{m - 1}{2} \right]^2.$$

(ii) If  $m > p$  and  $k - m \leq p$ , then

$$n_e(u) = 8p(k + m) - 4p^2 - 4p + 3 + 6(m - k) \\ + (4 - 16(k - m)) \left[ \frac{k - m}{2} \right] + 16 \left[ \frac{k - m}{2} \right]^2 - 6 \left[ \frac{k - m + 1}{2} \right].$$

(iii) If  $m \leq p$  and  $k - m > p$ , then

$$n_e(u) = 8pm + 4p^2 - 7p - 13 + 12m \\ + (16m - 32) \left[ \frac{m-1}{2} \right] - 16 \left[ \frac{m-1}{2} \right]^2.$$

(iv) If  $m > p$  and  $k - m > p$ , then

$$n_e(u) = 16pm - 11p + 3.$$

For simplicity, we define in sub-case a:

$$a_1 = 16p(k - m) + \frac{19}{2}p - 14.$$

$$a_2 = 8pm - \frac{11}{2}p + 16m^2 - 19m + 11.$$

$$a_3 = p(16m - 11) + 25 + \left( 7 + \frac{5}{2}p \right) \left[ \frac{5p-4}{20} \right] + 5 \left[ \frac{5p-4}{20} \right]^2 \\ + \left( 12 - \frac{21}{2}p \right) \left[ \frac{5p-14}{20} \right] + 5 \left[ \frac{5p-14}{20} \right]^2 + 16 \left[ \frac{3p-10}{12} \right] + 6 \left[ \frac{3p-10}{12} \right]^2.$$

In sub-case b:

$$b_0 = \left( \frac{5}{2}p - 6 \right) \left[ \frac{5p-2}{20} \right] - 5 \left[ \frac{5p-2}{20} \right]^2 + \left( \frac{5}{2}p - 11 \right) \left[ \frac{5p-12}{20} \right] \\ - 5 \left[ \frac{5p-12}{20} \right]^2 + (3p - 14) \left[ \frac{3p-8}{12} \right] - 6 \left[ \frac{3p-8}{12} \right]^2.$$

$$b'_0 = (16(k - m) - 10) \left[ \frac{k-m}{2} \right] - 16 \left[ \frac{k-m}{2} \right]^2.$$

$$b_1 = k(8p + 5) + m(18 - 16m) - 9 + b'_0.$$

$$b_2 = (8p + 5)(k - m) + \frac{27}{2}p - 16 + b_0 + b'_0.$$

$$b_3 = 8p(2k - m - \frac{1}{2}p) - 16m^2 + 23m - 9.$$

$$b_4 = 16p(k - m) - 4p^2 + \frac{27}{2}p - 16 + b_0.$$

$$b_5 = 4p(2m - 1) + 9m - 3 + (16m - 22) \left[ \frac{m-1}{2} \right] - 16 \left[ \frac{m-1}{2} \right]^2.$$

$$b_6 = 4p(2m + p - 1) - 2m + 3.$$

In sub-case c:

$$c_0 = (16(k - m) - 6) \left[ \frac{k-m}{2} \right] - 16 \left[ \frac{k-m}{2} \right]^2.$$

$$c'_0 = (26 - 16m) \left[ \frac{m-1}{2} \right] + 16 \left[ \frac{m-1}{2} \right]^2.$$

$$c_1 = 8pk + 3k - 16m + 9 + c_0 + c'_0.$$

$$c_2 = (8p + 3)(k - m) + 4p^2 - 1 + c_0.$$

$$c_3 = 8p(2k - m) - 4p^2 + 9 - 13m + c'_0.$$

$$c_4 = 16p(k - m) - 1.$$

$$c_5 = 8pk - 6k + 18m - 11 - c_0 - 4 \left[ \frac{k - m + 1}{2} \right] + (16m - 30) \left[ \frac{m - 1}{2} \right] - 16 \left[ \frac{m - 1}{2} \right]^2.$$

$$c_6 = 8p(k + m) + 6(m - k) - 4p^2 - 3p + 3 - c_0 - 4 \left[ \frac{k - m + 1}{2} \right].$$

$$c_7 = 8pm + 4p^2 - 5p - 11 + 12m + (16m - 30) \left[ \frac{m - 1}{2} \right] - 16 \left[ \frac{m - 1}{2} \right]^2.$$

$$c_8 = 16pm - 8p + 3.$$

In sub-case d:

$$d_0 = \left( \frac{5}{2}p - 11 \right) \left[ \frac{5p - 10}{20} \right] - 5 \left[ \frac{5p - 10}{20} \right]^2 + \left( \frac{5}{2}p - 5 \right) \left[ \frac{5p}{20} \right] - 5 \left[ \frac{5p}{20} \right]^2 + (3p - 7) \left[ \frac{3p - 1}{12} \right] - 6 \left[ \frac{3p - 1}{12} \right]^2.$$

$$d'_0 = \left( \frac{5}{2}p \right) \left[ \frac{5p + 10}{20} \right] - 5 \left[ \frac{5p + 10}{20} \right]^2 + \left( \frac{5}{2}p - 5 \right) \left[ \frac{5p}{20} \right] - 5 \left[ \frac{5p}{20} \right]^2 + (3p - 1) \left[ \frac{3p + 5}{12} \right] - 6 \left[ \frac{3p + 5}{12} \right]^2.$$

$$d_1 = 8k(p + 1) - 16m^2 + m - 1 + c_0.$$

$$d_2 = 8p(2k - m) - 4p^2 + 5p + 9m - 16m^2 + 7.$$

$$d_3 = (8p + 8)(k - m) + 8p - 8 + c_0 + d_0.$$

$$d_4 = 16p(k - m) + 5p - 4p^2 + d_0.$$

$$d_5 = 8k(p + 4m - 2k) - 16m^2 + 14m - 6k - 7 + (16m - 22) \left[ \frac{m - 1}{2} \right] - 16 \left[ \frac{m - 1}{2} \right]^2.$$

$$d_6 = 8pm + 8m - 7 + (16m - 22) \left[ \frac{m - 1}{2} \right] - 16 \left[ \frac{m - 1}{2} \right]^2 + d'_0.$$

$$d_7 = 8p(k + m) - 4p^2 - 3p + 6(m - k) - 16(m^2 + k^2) + 32km - 7.$$

$$d_8 = 16pm - 3p - 4p^2 - 1 + d'_0.$$

In sub-case e:

$$e_0 = (3 - 5p) \left[ \frac{5p + 4}{20} \right] + 5 \left[ \frac{5p + 4}{20} \right]^2 + (7 - 11p) \left[ \frac{5p - 4}{20} \right] + 5 \left[ \frac{5p - 4}{20} \right]^2 + 10 \left[ \frac{3p - 4}{12} \right] + 6 \left[ \frac{3p - 4}{12} \right]^2.$$

$$e_1 = 16p(k - m) - 1.$$

$$e_2 = m(8p + 16m - 2).$$

$$e_3 = 24pm - 11p + 6 + e_0.$$

In sub-case f:

$$f_0 = (10 + 16(m - k)) \left[ \frac{k - m}{2} \right] + 16 \left[ \frac{k - m}{2} \right]^2.$$

$$f_1 = 8pk - 5k - 8m + 9 + f_0 + c'_0.$$

$$f_2 = (8p - 5)(k - m) + 4p^2 - 1 + f_0.$$

$$f_3 = 8pm + 4p^2 + 9 - 13m + c'_0.$$

$$f_4 = 8p^2 - 1.$$

In sub-case g:

$$g_0 = (18 - 5p) \left[ \frac{5p - 8}{20} \right] + 10 \left[ \frac{5p - 8}{20} \right]^2 + (7 - 11p) \left[ \frac{5p + 4}{20} \right]$$

$$+ 10 \left[ \frac{5p + 4}{20} \right]^2 + 11 \left[ \frac{3p + 1}{12} \right] + 12 \left[ \frac{3p + 1}{12} \right]^2.$$

$$g_1 = 16p(k - m) + 11p - 20.$$

$$g_2 = 32m^2 - 28m + 10.$$

$$g_3 = 16p(m - 1) + g_0.$$

In sub-case h:

$$h_0 = (4 - 16(k - m)) \left[ \frac{k - m}{2} \right] + 16 \left[ \frac{k - m}{2} \right]^2 - 6 \left[ \frac{k - m + 1}{2} \right].$$

$$h'_0 = (16m - 32) \left[ \frac{m - 1}{2} \right] - 16 \left[ \frac{m - 1}{2} \right]^2.$$

$$h_1 = 8pk + 6k - 18m + 11 + c_0 + c'_0.$$

$$h_2 = (8p + 6)(k - m) + 4p^2 + p + 1 + c_0.$$

$$h_3 = 8p(2k - m) - 4p^2 + 3p + 11 - 12m + c'_0.$$

$$h_4 = 16p(k - m) + 4p + 1.$$

$$h_5 = 8pk - 6k + 18m - 13 + h_0 + h'_0.$$

$$h_6 = 8p(k + m) - 4p^2 - 4p + 3 + 6(m - k) + h_0.$$

$$h_7 = 8pm + 4p^2 - 7p - 13 + 12m + h'_0.$$

$$h_8 = 16pm - 11p + 3.$$

$$S_1 = 4p(a_1a_2 + b_1b_5 + c_1c_5 + d_1d_5) + 2p(f_1^2 + g_1g_2).$$

$$S_2 = 2p \left\{ \sum_{m=1}^{\left[ \frac{5p+4}{20} \right]} (e_1e_2) + \sum_{m=\left[ \frac{5p+4}{20} \right]+1}^{k-1} (e_1e_3) \right\}.$$

$$S_3 = 4p(b_1b_5 + c_1c_5) + 2p(h_1h_5 + f_1^2 + g_1g_2).$$

$$S_4 = 4p(b_2b_5 + c_1c_5 + d_3d_5) + 2p(h_1h_5 + f_1^2 + g_1g_3).$$

$$S_5 = 4p(b_3b_5 + c_3c_7 + d_2d_6) + 2p(h_3h_7 + f_3^2).$$

$$S_6 = 4p(b_2b_6 + c_2c_6 + d_3d_7) + 2p(h_2h_6 + f_2^2).$$

$$S_7 = 4p(b_2b_6 + c_2c_6 + d_3d_8).$$

$$S_8 = 2p \left\{ \sum_{m=1}^{\left\lceil \frac{5p-8}{20} \right\rceil + 1} (g_1g_2) + \sum_{m=\left\lfloor \frac{5p-8}{20} \right\rfloor + 2}^k (g_1g_3) \right\}.$$

$$S_9 = 4pc_3c_7 + 2p(h_3h_7 + f_3^2).$$

$$S_{10} = 4pc_2c_6 + 2p(h_2h_6 + f_2^2).$$

$$S_{11} = 4pc_1c_5 + 2p(h_1h_5 + f_1^2).$$

$$S_{12} = 4pc_4c_8 + 2p(h_4h_8 + f_4^2).$$

$$S_{13} = 4p \left\{ \sum_{m=\left\lfloor \frac{5p-2}{20} \right\rfloor + 2}^{k-p-1} (d_4d_6) + \sum_{m=1}^{\left\lceil \frac{5p-2}{20} \right\rceil + 1} (d_2d_6) + \sum_{m=p+1}^{k-\left\lfloor \frac{5p-2}{20} \right\rfloor - 1} (d_3d_8) + \sum_{m=k-\left\lfloor \frac{5p-2}{20} \right\rfloor}^k (d_3d_7) \right\}.$$

$$S_{14} = 4p \left\{ \sum_{m=\left\lfloor \frac{5p-2}{20} \right\rfloor + 2}^p (b_2b_5) + \sum_{m=k-p}^{\left\lceil \frac{5p-2}{20} \right\rceil + 1} (d_1d_6 + b_1b_5) + \sum_{m=\left\lfloor \frac{5p-2}{20} \right\rfloor + 2}^{k-\left\lfloor \frac{5p-2}{20} \right\rfloor - 1} (d_3d_6) + \sum_{m=k-\left\lfloor \frac{5p-2}{20} \right\rfloor}^p (d_3d_5) \right\}.$$

$$S_{15} = 4p \left\{ \sum_{m=\left\lfloor \frac{5p-2}{20} \right\rfloor + 2}^{k-\left\lfloor \frac{5p-2}{20} \right\rfloor - 1} (d_3d_8) + \sum_{m=k-\left\lfloor \frac{5p-2}{20} \right\rfloor}^k (d_3d_7) \right\}.$$

If  $p = 2$  and  $k > 4$ , then the Szeged index of  $\text{HAC}_5\text{C}_6\text{C}_7[r, p]$  nanotube is

$$Sz = 2048k^3 + 45080k^2 - 46136k - 57776.$$

The Szeged index of  $\text{HAC}_5\text{C}_6\text{C}_7[r, p]$  nanotube for  $p \geq 4$  is given as follows:

If  $k \leq \left\lceil \frac{5p+4}{20} \right\rceil$ , then

$$SZ = \sum_{m=1}^k S_1 + \sum_{m=1}^{k-1} 2pe_1e_2.$$

If  $\left\lceil \frac{5p+4}{20} \right\rceil < k \leq \left\lceil \frac{5p-2}{20} \right\rceil + 1$ , then

$$SZ = \sum_{m=1}^k (S_1) + S_2.$$

If  $\left\lceil \frac{5p-2}{20} \right\rceil + 1 < k \leq 2 \left( \left\lceil \frac{5p-2}{20} \right\rceil + 1 \right)$ , then

$$SZ = \sum_{m=1}^{\lfloor \frac{5p-2}{20} \rfloor + 1} S_3 + \sum_{m=\lfloor \frac{5p-2}{20} \rfloor + 2}^k S_4 + 4p \left\{ \sum_{m=1}^{k - \lfloor \frac{5p-2}{20} \rfloor - 1} (d_1 d_6) + \sum_{m=k - \lfloor \frac{5p-2}{20} \rfloor}^{\lfloor \frac{5p-2}{20} \rfloor + 1} (d_1 d_5) \right\} + S_2.$$

If  $2 \left( \lfloor \frac{5p-2}{20} \rfloor + 1 \right) < k \leq p$ , then

$$SZ = \sum_{m=1}^{\lfloor \frac{5p-2}{20} \rfloor + 1} (S_3 + 4pd_1 d_6) + \sum_{m=\lfloor \frac{5p-2}{20} \rfloor + 2}^k (S_4 - 4pd_3 d_5) + S_{15} + S_2.$$

If  $k = p + 1$ , then

$$SZ = \sum_{m=1}^{\lfloor \frac{5p-2}{20} \rfloor + 1} (S_3 + 4pd_1 d_6) + \sum_{m=\lfloor \frac{5p-2}{20} \rfloor + 2}^p (S_4 - 4pd_3 d_5 - 2pg_1 g_3) + \sum_{m=\lfloor \frac{5p-2}{20} \rfloor + 2}^{p+1} (2pg_1 g_3) + S_{15} + S_2 + S_7.$$

If  $p + 1 < k \leq p + \lfloor \frac{5p-2}{20} \rfloor + 1$ , then

$$SZ = \sum_{m=1}^{k-p-1} S_5 + \sum_{m=p+1}^k S_6 + \sum_{m=k-p}^p S_{11} + S_{14} + S_2 + S_8.$$

If  $p + \lfloor \frac{5p-2}{20} \rfloor + 1 < k \leq 2p$ , then

$$SZ = \sum_{m=1}^{k-p-1} S_9 + \sum_{m=p+1}^k S_{10} + \sum_{m=k-p}^p (S_{11} + d_3 d_6) + S_{13} + S_2 + S_8.$$

If  $k > 2p$ , then

$$SZ = \sum_{m=1}^p S_9 + \sum_{m=p+1}^{k-p-1} S_{12} + \sum_{m=k-p}^k (S_{10} - 2pf_2^2) + \sum_{m=k-p}^p (4pd_3 d_6 + 2pf_2^2) + S_2 + S_{13} + S_8.$$



Case 2  $p$  is odd.

(a) If  $e \in E_1$ , then

$$n_e(v) = 16p(k - m) + \frac{19}{2}p - \frac{25}{2}.$$

If  $m \leq \left\lceil \frac{5p-4}{20} \right\rceil + 1$ , then

$$n_e(u) = 8pm - \frac{11}{2}p + 16m^2 - 19m + \frac{23}{2}.$$

If  $m > \left\lceil \frac{5p-4}{20} \right\rceil + 1$ , then

$$\begin{aligned} n_e(u) &= p \left( 8m - \frac{11}{2} \right) + \frac{17}{2} + \left( \frac{15}{2} - \frac{5}{2}p \right) \left\lceil \frac{5p-5}{20} \right\rceil + 5 \left\lceil \frac{5p-5}{20} \right\rceil^2 \\ &\quad + \left( \frac{5}{2} - \frac{11}{2}p \right) \left\lceil \frac{5p+5}{20} \right\rceil + 5 \left\lceil \frac{5p+5}{20} \right\rceil^2 \\ &\quad + 4 \left\lceil \frac{3p+2}{12} \right\rceil + 6 \left\lceil \frac{3p+2}{12} \right\rceil^2. \end{aligned}$$

(b) If  $e \in E_2$ , then

(i) If  $m \leq \left\lceil \frac{5p-3}{20} \right\rceil + 1$  and  $k - m \leq p$ , then

$$\begin{aligned} n_e(v) &= k(8p + 5) + m(18 - 16m) - 9 \\ &\quad + (16(k - m) - 10) \left\lceil \frac{k - m}{2} \right\rceil - 16 \left\lceil \frac{k - m}{2} \right\rceil^2. \end{aligned}$$

(ii) If  $m > \left\lceil \frac{5p-3}{20} \right\rceil + 1$  and  $k - m \leq p$ , then

$$\begin{aligned} n_e(v) &= (8p + 5)(k - m) + 8p - 2 + \left( \frac{5}{2}p - \frac{13}{2} \right) \left\lceil \frac{5p-3}{20} \right\rceil \\ &\quad - 5 \left\lceil \frac{5p-3}{20} \right\rceil^2 + \left( \frac{5}{2}p - \frac{1}{2} \right) \left\lceil \frac{5p+9}{20} \right\rceil - 5 \left\lceil \frac{5p+9}{20} \right\rceil^2 \\ &\quad + (3p - 2) \left\lceil \frac{3p+4}{12} \right\rceil - 6 \left\lceil \frac{3p+4}{12} \right\rceil^2 \\ &\quad + (16(k - m) - 10) \left\lceil \frac{k - m}{2} \right\rceil - 16 \left\lceil \frac{k - m}{2} \right\rceil^2. \end{aligned}$$

(iii) If  $m \leq \left\lceil \frac{5p-2}{20} \right\rceil + 1$  and  $k - m > p$ , then

$$n_e(v) = 8p(2k - m - p + 1) - 16m^2 + 23m - 12.$$

(iv) If  $m > \left\lceil \frac{5p-2}{20} \right\rceil + 1$  and  $k - m > p$ , then

$$\begin{aligned} n_e(v) &= 16p(k - m) - 4p^2 + 8p - 1 + \left(\frac{5}{2}p - \frac{13}{2}\right) \left\lceil \frac{5p-3}{20} \right\rceil \\ &\quad - 5 \left\lceil \frac{5p-3}{20} \right\rceil^2 + \left(\frac{5}{2}p - \frac{1}{2}\right) \left\lceil \frac{5p+9}{20} \right\rceil \\ &\quad - 5 \left\lceil \frac{5p+9}{20} \right\rceil^2 + (3p-2) \left\lceil \frac{3p+4}{12} \right\rceil - 6 \left\lceil \frac{3p+4}{12} \right\rceil^2. \end{aligned}$$

And for  $n_e(u)$ , we have

(i) If  $m \leq p$ , then

$$n_e(u) = 4p(2m - 1) + 11m - 4 + (16m - 22) \left\lceil \frac{m-1}{2} \right\rceil - 16 \left\lceil \frac{m-1}{2} \right\rceil^2.$$

(ii) If  $m > p$ , then

$$n_e(u) = 4p(2m + p - 1) + 3.$$

(c) If  $e \in E_3$ , then

(i) If  $m \leq p$  and  $k - m \leq p$ , then

$$\begin{aligned} n_e(v) &= 8pk + 3k - 16m + 9 + (16(k - m) - 6) \left\lceil \frac{k-m}{2} \right\rceil \\ &\quad - 16 \left\lceil \frac{k-m}{2} \right\rceil^2 + (26 - 16m) \left\lceil \frac{m-1}{2} \right\rceil + 16 \left\lceil \frac{m-1}{2} \right\rceil^2. \end{aligned}$$

(ii) If  $m > p$  and  $k - m \leq p$ , then

$$\begin{aligned} n_e(v) &= (8p + 3)(k - m) + 4p^2 - 1 \\ &\quad + (16(k - m) - 6) \left\lceil \frac{k-m}{2} \right\rceil - 16 \left\lceil \frac{k-m}{2} \right\rceil^2. \end{aligned}$$

(iii) If  $m \leq p$  and  $k - m > p$ , then

$$n_e(v) = 8p(2k - m) - 4p^2 + 2 - 13m \\ + (26 - 16m) \left[ \frac{m-1}{2} \right] + 16 \left[ \frac{m-1}{2} \right]^2.$$

(iv) If  $m > p$  and  $k - m > p$ , then

$$n_e(v) = 16p(k - m) - 1.$$

And for  $n_e(u)$ , we have

(i) If  $m \leq p$  and  $k - m \leq p$ , then

$$n_e(u) = 8pk - 3k + 16m - 11 + (6 - 16(k - m)) \left[ \frac{k-m}{2} \right] \\ + 16 \left[ \frac{k-m}{2} \right]^2 - 4 \left[ \frac{k-m+1}{2} \right] + (16m - 30) \left[ \frac{m-1}{2} \right] \\ - 16 \left[ \frac{m-1}{2} \right]^2.$$

(ii) If  $m > p$  and  $k - m \leq p$ , then

$$n_e(u) = 8p(k + m) + 3(m - k) - 4p^2 - 2p + 1 \\ + (6 - 16(k - m)) \left[ \frac{k-m}{2} \right] - 4 \left[ \frac{k-m+1}{2} \right] + 16 \left[ \frac{k-m}{2} \right]^2.$$

(iii) If  $m \leq p$  and  $k - m > p$ , then

$$n_e(u) = 8pm + 4p^2 - 3p - 5 + 13m \\ + (16m - 30) \left[ \frac{m-1}{2} \right] - 16 \left[ \frac{m-1}{2} \right]^2.$$

(iv) If  $m > p$  and  $k - m > p$ , then

$$n_e(u) = 16pm - 5p.$$

(d) If  $e \in E_4$ , then

(i) If  $m \leq \left[ \frac{5p-11}{20} \right] + 1$  and  $k - m \leq p$ , then

$$n_e(v) = 8k(p + 1) - 16m^2 + 2m - 1 + (16(k - m) - 6) \left[ \frac{k-m}{2} \right] \\ - 16 \left[ \frac{k-m}{2} \right]^2.$$

(ii) If  $m \leq \left\lceil \frac{5p-11}{20} \right\rceil + 1$  and  $k - m > p$ , then

$$n_e(v) = 8p(2k - m) - 4p^2 + 5p + 10m - 16m^2 + 6.$$

(iii) If  $m > \left\lceil \frac{5p-11}{20} \right\rceil + 1$  and  $k - m \leq p$ , then

$$\begin{aligned} n_e(v) &= (8p + 8)(k - m) + 8p - 7 + (16(k - m) - 6) \left\lceil \frac{k - m}{2} \right\rceil \\ &\quad - 16 \left\lceil \frac{k - m}{2} \right\rceil^2 + \left( \frac{5}{2}p - \frac{21}{2} \right) \left\lceil \frac{5p - 11}{20} \right\rceil - 5 \left\lceil \frac{5p - 11}{20} \right\rceil^2 \\ &\quad + \left( \frac{5}{2}p - \frac{9}{2} \right) \left\lceil \frac{5p + 1}{20} \right\rceil - 5 \left\lceil \frac{5p + 1}{20} \right\rceil^2 \\ &\quad + (3p - 7) \left\lceil \frac{3p - 1}{12} \right\rceil - 6 \left\lceil \frac{3p - 1}{12} \right\rceil^2. \end{aligned}$$

(iv) If  $m > \left\lceil \frac{5p-10}{20} \right\rceil + 1$  and  $k - m > p$ , then

$$\begin{aligned} n_e(v) &= 8p(k - m) + 13p - 4p^2 - 8 + \left( \frac{5}{2}p - \frac{21}{2} \right) \left\lceil \frac{5p - 11}{20} \right\rceil \\ &\quad - 5 \left\lceil \frac{5p - 11}{20} \right\rceil^2 + \left( \frac{5}{2}p - \frac{9}{2} \right) \left\lceil \frac{5p + 1}{20} \right\rceil - 5 \left\lceil \frac{5p + 1}{20} \right\rceil^2 \\ &\quad + (3p - 7) \left\lceil \frac{3p - 1}{12} \right\rceil - 6 \left\lceil \frac{3p - 1}{12} \right\rceil^2. \end{aligned}$$

For  $n_e(u)$ , we have

(i) If  $k - m \leq \left\lceil \frac{5p-1}{20} \right\rceil$  and  $m \leq p$ , then

$$\begin{aligned} n_e(u) &= 8k(p + 4m - 2k) - 16m^2 + 14m - 6k - 7 \\ &\quad + (16m - 22) \left\lceil \frac{m - 1}{2} \right\rceil - 16 \left\lceil \frac{m - 1}{2} \right\rceil^2. \end{aligned}$$

(ii) If  $m \leq p$  and  $k - m > \left\lceil \frac{5p-1}{20} \right\rceil$ , then

$$\begin{aligned} n_e(u) &= 8pm + 8m - 7 + (16m - 22) \left\lceil \frac{m - 1}{2} \right\rceil - 16 \left\lceil \frac{m - 1}{2} \right\rceil^2 \\ &\quad + \left( \frac{5}{2}p - \frac{11}{2} \right) \left\lceil \frac{5p - 1}{20} \right\rceil - 5 \left\lceil \frac{5p - 1}{20} \right\rceil^2 \end{aligned}$$

$$\begin{aligned}
& + \left( \frac{5}{2}p + \frac{1}{2} \right) \left[ \frac{5p+11}{20} \right] \\
& - 5 \left[ \frac{5p+11}{20} \right]^2 + (3p-1) \left[ \frac{3p+5}{12} \right] - 6 \left[ \frac{3p+5}{12} \right]^2.
\end{aligned}$$

(iii) If  $m > p$  and  $k - m \leq \left[ \frac{5p-1}{20} \right]$ , then

$$n_e(u) = 8p(k+m) - 4p^2 - 3p + 6(m-k) - 16(m^2+k^2) + 32km.$$

(iv) If  $m > p$  and  $k - m > \left[ \frac{5p-1}{20} \right]$ , then

$$\begin{aligned}
n_e(u) &= 16pm - 3p - 4p^2 - 1 + \left( \frac{5}{2}p - \frac{11}{2} \right) \left[ \frac{5p-1}{20} \right] - 5 \left[ \frac{5p-1}{20} \right]^2 \\
& + \left( \frac{5}{2}p + \frac{1}{2} \right) \left[ \frac{5p+11}{20} \right] - 5 \left[ \frac{5p+11}{20} \right]^2 \\
& + (3p-1) \left[ \frac{3p+5}{12} \right] - 6 \left[ \frac{3p+5}{12} \right]^2.
\end{aligned}$$

(e) If  $e \in E_5$ , then  $n_e(v) = 16p(k-m)$ . And for  $n_e(u)$ , we have

(i) If  $m \leq \left[ \frac{5p+5}{20} \right]$ , then

$$n_e(u) = m(8p + 16m - 2).$$

(ii) If  $m > \left[ \frac{5p+5}{20} \right]$ , then

$$\begin{aligned}
n_e(u) &= 24pm - 11p + 6 + (3-5p) \left[ \frac{5p+5}{20} \right] + 5 \left[ \frac{5p+5}{20} \right]^2 \\
& + (7-11p) \left[ \frac{5p-5}{20} \right] + 5 \left[ \frac{5p-5}{20} \right]^2 \\
& + 10 \left[ \frac{3p-4}{12} \right] + 6 \left[ \frac{3p-4}{12} \right]^2.
\end{aligned}$$

(f) If  $e \in E_6$ , then

(i) If  $m \leq p$  and  $k - m \leq p$ , then

$$n_e(v) = 8pk - 5k - 8m + 9 + (10 + 16(m - k)) \left[ \frac{k - m}{2} \right] \\ + 16 \left[ \frac{k - m}{2} \right]^2 + (26 - 16m) \left[ \frac{m - 1}{2} \right] + 16 \left[ \frac{m - 1}{2} \right]^2.$$

(ii) If  $m > p$  and  $k - m \leq p$ , then

$$n_e(v) = (8p - 5)(k - m) + 4p^2 \\ + (10 + 16(m - k)) \left[ \frac{k - m}{2} \right] + 16 \left[ \frac{k - m}{2} \right]^2.$$

(iii) If  $m \leq p$  and  $k - m > p$ , then

$$n_e(v) = 8pm + 4p^2 + 8p - 13m + (26 - 16m) \left[ \frac{m - 1}{2} \right] + 16 \left[ \frac{m - 1}{2} \right]^2.$$

(iv) If  $m > p$  and  $k - m > p$ , then

$$n_e(v) = 8p^2 - 1.$$

And  $n_e(u) = n_e(v)$ .

(g) If  $e \in E_7$ , then

$$n_e(v) = 16p(k - m) + 11p - 20.$$

For  $n_e(u)$ , we have

(i) If  $m \leq \left[ \frac{5p-7}{20} \right] + 1$ , then

$$n_e(u) = 32m^2 - 28m + 10.$$

(ii) If  $m > \left[ \frac{5p-7}{20} \right] + 1$ , then

$$n_e(u) = 16p(m - 1) + 14 + (18 - 5p) \left[ \frac{5p - 7}{20} \right] + 10 \left[ \frac{5p - 7}{20} \right]^2 \\ + (7 - 11p) \left[ \frac{5p + 5}{20} \right] + 10 \left[ \frac{5p + 5}{20} \right]^2 + 11 \left[ \frac{3p + 1}{12} \right] \\ + 12 \left[ \frac{3p + 1}{12} \right]^2.$$

(h) If  $e \in E_8$ , then:

for  $n_e(v)$ , we have

(i) If  $m \leq p$  and  $k - m \leq p$ , then

$$\begin{aligned} n_e(v) = & 8pk + 5k - 15m + 9 + (16(k - m) - 4) \left[ \frac{k - m}{2} \right] \\ & - 16 \left[ \frac{k - m}{2} \right]^2 + (26 - 16m) \left[ \frac{m - 1}{2} \right] + 16 \left[ \frac{m - 1}{2} \right]^2. \end{aligned}$$

(ii) If  $m > p$  and  $k - m \leq p$ , then

$$\begin{aligned} n_e(v) = & (8p + 5)(k - m) + 4p^2 + 3p + 1 \\ & + (16(k - m) - 4) \left[ \frac{k - m}{2} \right] - 16 \left[ \frac{k - m}{2} \right]^2. \end{aligned}$$

(iii) If  $m \leq p$  and  $k - m > p$ , then

$$\begin{aligned} n_e(v) = & 8p(2k - m) - 4p^2 + 3p + 8 - 10m \\ & + (26 - 16m) \left[ \frac{m - 1}{2} \right] + 16 \left[ \frac{m - 1}{2} \right]^2. \end{aligned}$$

(iv) If  $m > p$  and  $k - m > p$ , then

$$n_e(v) = 16p(k - m) + 6p - 1.$$

and for  $n_e(u)$ , we have

(i) If  $m \leq p$  and  $k - m \leq p$ , then

$$\begin{aligned} n_e(u) = & 8pk - 5k + 13m - 11 + (4 - 16(k - m)) \left[ \frac{k - m}{2} \right] \\ & + 16 \left[ \frac{k - m}{2} \right]^2 - 4 \left[ \frac{k - m + 1}{2} \right] \\ & + (16m - 30) \left[ \frac{m - 1}{2} \right] - 16 \left[ \frac{m - 1}{2} \right]^2. \end{aligned}$$

(ii) If  $m > p$  and  $k - m \leq p$ , then

$$\begin{aligned} n_e(u) = & 8p(k + m) - 4p^2 - 7p - 1 + 5(m - k) \\ & + (4 - 16(k - m)) \left[ \frac{k - m}{2} \right] + 16 \left[ \frac{k - m}{2} \right]^2 - 4 \left[ \frac{k - m + 1}{2} \right]. \end{aligned}$$

(iii) If  $m \leq p$  and  $k - m > p$ , then

$$n_e(u) = 8pm + 4p^2 - 5p - 12 + 8m \\ + (16m - 30) \left[ \frac{m-1}{2} \right] - 16 \left[ \frac{m-1}{2} \right]^2.$$

(iv) If  $m > p$  and  $k - m > p$ , then

$$n_e(u) = 16pm - 12p - 1.$$

For simplicity, we define in sub-case a:

$$a'_1 = 16p(k - m) + \frac{19}{2}p - \frac{25}{2}. \\ a'_2 = 8pm - \frac{11}{2}p + 16m^2 - 19m + \frac{23}{2}. \\ a'_3 = p \left( 8m - \frac{11}{2} \right) + \frac{17}{2} + \left( \frac{15}{2} - \frac{5}{2}p \right) \left[ \frac{5p-5}{20} \right] + 5 \left[ \frac{5p-5}{20} \right]^2 \\ + \left( \frac{5}{2} - \frac{11}{2}p \right) \left[ \frac{5p+5}{20} \right] + 5 \left[ \frac{5p+5}{20} \right]^2 + 4 \left[ \frac{3p+2}{12} \right] + 6 \left[ \frac{3p+2}{12} \right]^2.$$

In sub-case b:

$$b''_0 = \left( \frac{5}{2}p - \frac{13}{2} \right) \left[ \frac{5p-3}{20} \right] - 5 \left[ \frac{5p-3}{20} \right]^2 + \left( \frac{5}{2}p - \frac{1}{2} \right) \left[ \frac{5p+9}{20} \right] \\ - 5 \left[ \frac{5p+9}{20} \right]^2 + (3p-2) \left[ \frac{3p+4}{12} \right] - 6 \left[ \frac{3p+4}{12} \right]^2. \\ b'_1 = k(8p+5) + m(18-16m) - 9 + b'_0. \\ b'_2 = (8p+5)(k-m) + 8p - 2 + b''_0 + b'_0. \\ b'_3 = 8p(2k-m-p+1) - 16m^2 + 23m - 12. \\ b'_4 = 16p(k-m) - 4p^2 + 8p - 1 + b''_0. \\ b'_5 = 4p(2m-1) + 11m - 4 + (16m-22) \left[ \frac{m-1}{2} \right] - 16 \left[ \frac{m-1}{2} \right]^2. \\ b'_6 = 4p(2m+p-1) + 3.$$

In sub-case c:

$$c'_1 = 8pk + 3k - 16m + 9 + c_0 + c'_0. \\ c'_2 = (8p+3)(k-m) + 4p^2 - 1 + c_0. \\ c'_3 = 8p(2k-m) - 4p^2 + 2 - 13m + c'_0. \\ c'_4 = 16p(k-m) - 1. \\ c'_5 = 8pk - 3k + 16m - 11 - c_0 - 4 \left[ \frac{k-m+1}{2} \right] + (16m-30) \left[ \frac{m-1}{2} \right] \\ - 16 \left[ \frac{m-1}{2} \right]^2.$$



$$c'_6 = 8p(k+m) + 3(m-k) - 4p^2 - 2p + 1 - c_0 - 4 \left[ \frac{k-m+1}{2} \right].$$

$$c'_7 = 8pm + 4p^2 - 3p - 5 + 13m + (16m-30) \left[ \frac{m-1}{2} \right] - 16 \left[ \frac{m-1}{2} \right]^2.$$

$$c'_8 = 16pm - 5p.$$

In sub-case d:

$$d''_0 = \left( \frac{5}{2}p - \frac{21}{2} \right) \left[ \frac{5p-11}{20} \right] - 5 \left[ \frac{5p-11}{20} \right]^2 + \left( \frac{5}{2}p - \frac{9}{2} \right) \left[ \frac{5p+1}{20} \right]$$

$$- 5 \left[ \frac{5p+1}{20} \right]^2 + (3p-7) \left[ \frac{3p-1}{12} \right] - 6 \left[ \frac{3p-1}{12} \right]^2.$$

$$d'''_0 = \left( \frac{5}{2}p - \frac{11}{2} \right) \left[ \frac{5p-1}{20} \right] - 5 \left[ \frac{5p-1}{20} \right]^2 + \left( \frac{5}{2}p + \frac{1}{2} \right) \left[ \frac{5p+11}{20} \right]$$

$$- 5 \left[ \frac{5p+11}{20} \right]^2 + (3p-1) \left[ \frac{3p+5}{12} \right] - 6 \left[ \frac{3p+5}{12} \right]^2.$$

$$d'_1 = 8k(p+1) - 16m^2 + 2m - 1 + c_0.$$

$$d'_2 = 8p(2k-m) - 4p^2 + 5p + 10m - 16m^2 + 6.$$

$$d'_3 = (8p+8)(k-m) + 8p - 7 + c_0 + d''_0.$$

$$d'_4 = 8p(k-m) + 13p - 4p^2 - 8 + d''_0.$$

$$d'_5 = 8k(p+4m-2k) - 16m^2 + 14m - 6k - 7 + (16m-22) \left[ \frac{m-1}{2} \right]$$

$$- 16 \left[ \frac{m-1}{2} \right]^2.$$

$$d'_6 = 8pm + 8m - 7 + (16m-22) \left[ \frac{m-1}{2} \right] - 16 \left[ \frac{m-1}{2} \right]^2 + d'''_0.$$

$$d'_7 = 8p(k+m) - 4p^2 - 3p + 6(m-k) - 16(m^2+k^2) + 32km.$$

$$d'_8 = 16pm - 3p - 4p^2 - 1 + d'''_0.$$

In sub-case e:

$$e'_1 = 16p(k-m).$$

$$e'_2 = m(8p+16m-2).$$

$$e'_3 = 24pm - 11p + 6 + (3-5p) \left[ \frac{5p+5}{20} \right] + 5 \left[ \frac{5p+5}{20} \right]^2$$

$$+ (7-11p) \left[ \frac{5p-5}{20} \right] + 5 \left[ \frac{5p-5}{20} \right]^2 + 10 \left[ \frac{3p-4}{12} \right] + 6 \left[ \frac{3p-4}{12} \right]^2.$$

In sub-case f:

$$f'_1 = 8pk - 5k - 8m + 9 + f_0 + c'_0.$$

$$f'_2 = (8p-5)(k-m) + 4p^2 + f_0.$$

$$f'_3 = 8pm + 4p^2 + 8p - 13m + c'_0.$$

$$f'_4 = 8p^2 - 1.$$

In sub-case g:

$$g'_1 = 16p(k - m) + 11p - 20.$$

$$g'_2 = 32m^2 - 28m + 10.$$

$$g'_3 = 16p(m - 1) + 14 + (18 - 5p) \left[ \frac{5p - 7}{20} \right] + 10 \left[ \frac{5p - 7}{20} \right]^2 \\ + (7 - 11p) \left[ \frac{5p + 5}{20} \right] + 10 \left[ \frac{5p + 5}{20} \right]^2 + 11 \left[ \frac{3p + 1}{12} \right] + 12 \left[ \frac{3p + 1}{12} \right]^2.$$

In sub-case h:

$$h''_0 = (16(k - m) - 4) \left[ \frac{k - m}{2} \right] - 16 \left[ \frac{k - m}{2} \right]^2.$$

$$h'''_0 = (16m - 30) \left[ \frac{m - 1}{2} \right] - 16 \left[ \frac{m - 1}{2} \right]^2.$$

$$h'_1 = 8pk + 5k - 15m + 9 + h''_0 + c'_0.$$

$$h'_2 = (8p + 5)(k - m) + 4p^2 + 3p + 1 + h''_0.$$

$$h'_3 = 8p(2k - m) - 4p^2 + 3p + 8 - 10m + c'_0.$$

$$h'_4 = 16p(k - m) + 6p - 1.$$

$$h'_5 = 8pk - 5k + 13m - 11 + h_0 + h'''_0.$$

$$h'_6 = 8p(k + m) - 4p^2 - 7p - 1 + 5(m - k) + h_0.$$

$$h'_7 = 8pm + 4p^2 - 5p - 12 + 8m + h'''_0.$$

$$h'_8 = 16pm - 12p - 1.$$

$$S'_1 = 4p(a'_1a'_2 + b'_1b'_5 + c'_1c'_5 + d'_1d'_5) + 2p(f_1'^2 + g'_1g'_2).$$

$$S'_2 = 2p \left\{ \sum_{m=1}^{\left[ \frac{5p+5}{20} \right]} (e'_1e'_2) + \sum_{m=\left[ \frac{5p+5}{20} \right]+1}^k (e'_1e'_3) \right\}.$$

$$S'_3 = 4p(b'_1b'_5 + c'_1c'_5) + 2p(h'_1h'_5 + f_1'^2 + g'_1g'_2).$$

$$S'_4 = 4p(b'_2b'_5 + c'_1c'_5 + d'_3d'_5) + 2p(h'_1h'_5 + f_1'^2 + g'_1g'_3).$$

$$S'_5 = 4p(b'_3b'_5 + c'_3c'_7 + d'_2d'_6) + 2p(h'_3h'_7 + f_3'^2).$$

$$S'_6 = 4p(b'_2b'_6 + c'_2c'_6 + d'_3d'_7) + 2p(h'_2h'_6 + f_2'^2).$$

$$S'_7 = 4p(b'_2b'_6 + c'_2c'_6 + d'_3d'_8).$$

$$S'_8 = 2p \left\{ \sum_{m=1}^{\left[ \frac{5p-7}{20} \right]+1} (g'_1g'_2) + \sum_{m=\left[ \frac{5p-7}{20} \right]+2}^k (g'_1g'_3) \right\}.$$

$$S'_9 = 4pc'_3c'_7 + 2p(h'_3h'_7 + f_3'^2).$$

$$S'_{10} = 4pc'_2c'_6 + 2p(h'_2h'_6 + f_2'^2).$$

$$S'_{11} = 4pc'_1c'_5 + 2p(h'_1h'_5 + f_1'^2).$$

$$S'_{12} = 4pc'_4c'_8 + 2p(h'_4h'_8 + f_4'^2).$$

$$S'_{13} = 4p \left\{ \sum_{m=\lceil \frac{5p-1}{20} \rceil + 2}^{k-p-1} (d'_4 d'_6) + \sum_{m=1}^{\lceil \frac{5p-1}{20} \rceil + 1} (d'_2 d'_6) + \sum_{m=p+1}^{k-\lceil \frac{5p-1}{20} \rceil - 1} (d'_3 d'_8) + \sum_{m=k-\lceil \frac{5p-1}{20} \rceil}^k (d'_3 d'_7) \right\}.$$

$$S'_{14} = 4p \left\{ \sum_{m=\lceil \frac{5p-1}{20} \rceil + 2}^p (b'_2 b'_5) + \sum_{m=k-p}^{\lceil \frac{5p-1}{20} \rceil + 1} (d'_1 d'_6 + b'_1 b'_5) + \sum_{m=\lceil \frac{5p-2}{20} \rceil + 2}^{k-\lceil \frac{5p-1}{20} \rceil - 1} (d'_3 d'_6) \right. \\ \left. + \sum_{m=k-\lceil \frac{5p-1}{20} \rceil}^p (d'_3 d'_5) \right\}.$$

$$S'_{15} = 4p \left\{ \sum_{m=\lceil \frac{5p-1}{20} \rceil + 2}^{k-\lceil \frac{5p-1}{20} \rceil - 1} (d'_3 d'_8) + \sum_{m=k-\lceil \frac{5p-1}{20} \rceil}^k (d'_3 d'_7) \right\}.$$

The Szeged index of  $\text{HAC}_5\text{C}_6\text{C}_7[r, p]$  nanotube is given as follows:

If  $k \leq \lceil \frac{5p+5}{20} \rceil$ , then

$$\text{SZ} = \sum_{m=1}^k S'_1 + \sum_{m=1}^{k-1} e'_1 e'_2.$$

If  $\lceil \frac{5p+5}{20} \rceil < k \leq \lceil \frac{5p-1}{20} \rceil + 1$ , then

$$\text{SZ} = \sum_{m=1}^k (S'_1) + S'_2.$$

If  $\lceil \frac{5p-1}{20} \rceil + 1 < k \leq 2 \left( \lceil \frac{5p-1}{20} \rceil + 1 \right)$ , then

$$\text{SZ} = \sum_{m=1}^{\lceil \frac{5p-1}{20} \rceil + 1} S'_3 + \sum_{m=\lceil \frac{5p-1}{20} \rceil + 2}^k \\ \times S'_4 + 4p \left\{ \sum_{m=1}^{k-\lceil \frac{5p-1}{20} \rceil - 1} (d'_1 d'_6) + \sum_{m=k-\lceil \frac{5p-1}{20} \rceil}^{\lceil \frac{5p-1}{20} \rceil + 1} (d'_1 d'_5) \right\} + S'_2.$$

If  $2 \left( \left\lceil \frac{5p-1}{20} \right\rceil + 1 \right) < k \leq p$ , then

$$SZ = \sum_{m=1}^{\left\lceil \frac{5p-1}{20} \right\rceil + 1} (S'_3 + 4pd'_1d'_6) + \sum_{m=\left\lceil \frac{5p-1}{20} \right\rceil + 2}^k (S'_4 - 4pd'_3d'_5) + S'_{15} + S'_2.$$

If  $k = p + 1$ , then

$$\begin{aligned} Sz &= \sum_{m=1}^{\left\lceil \frac{5p-1}{20} \right\rceil + 1} (S'_3 + 4pd'_1d'_6) + \sum_{m=\left\lceil \frac{5p-1}{20} \right\rceil + 2}^p (S'_4 - 4pd'_3d'_5 - 2pg'_1g'_3) \\ &+ \sum_{m=\left\lceil \frac{5p-1}{20} \right\rceil + 2}^{p+1} (2pg'_1g'_3) + S'_{15} + S'_2 + S'_7. \end{aligned}$$

If  $p + 1 < k \leq p + \left\lceil \frac{5p-1}{20} \right\rceil + 1$ , then

$$SZ = \sum_{m=1}^{k-p-1} S'_5 + \sum_{m=p+1}^k S'_6 + \sum_{m=k-p}^p S'_{11} + S'_{14} + S'_2 + S'_8.$$

If  $p + \left\lceil \frac{5p-1}{20} \right\rceil + 1 < k \leq 2p$ , then

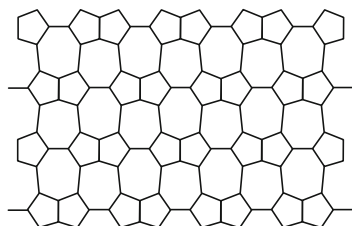
$$SZ = \sum_{m=1}^{k-p-1} S'_9 + \sum_{m=p+1}^k S'_{10} + \sum_{m=k-p}^p (S'_{11} + d'_3d'_6) + S'_{13} + S'_2 + S'_8.$$

If  $k > 2p$ , then

$$\begin{aligned} SZ &= \sum_{m=1}^p S'_9 + \sum_{m=p+1}^{k-p-1} S'_{12} + \sum_{m=k-p}^k (S'_{10} - 2pf_2'^2) \\ &+ \sum_{m=k-p}^p (4pd'_3d'_6 + 2pf_2'^2) + S'_2 + S'_{13} + S'_8. \end{aligned}$$

Therefore, the Szeged index of above nanotube is computed.

**Fig. 12.32**  $HC_5C_7[4, 8]$  nanotube,  $p = 8, k = 4$



### 12.3.5 Computation of the Szeged Index of $HC_5C_7[r, p]$ Nanotube

In this part, we compute the Szeged index of  $HC_5C_7[r, p]$  nanotube.

We bring all details of the computation of the Szeged index of this nanotube, which have been published in Iranmanesh et al. (2008b).

In  $HC_5C_7[r, p]$  nanotubes, we denote the number of pentagons in one row by  $p$  and number of the rows by  $k$ . In Fig. 12.32, an  $HC_5C_7[4, 8]$  lattice is illustrated.

Let  $e$  be an edge in Fig. 12.32. Denote:

- $E_1 = \{e \in E(G) \mid e \text{ is a oblique edge between heptagon and pentagon adjacent a vertical edge}\}$
- $E_2 = \{e \in E(G) \mid e \text{ is a oblique edge between heptagon and pentagon adjacent a horizontal edge}\}$
- $E_3 = \{e \in E(G) \mid e \text{ is an oblique edge between two heptagons}\}$
- $E_4 = \{e \in E(G) \mid e \text{ is an vertical edge between two pentagons}\}$
- $E_5 = \{e \in E(G) \mid e \text{ is a horizontal edge}\}.$

And the number of vertices in each period of this nanotube is equal to  $4p$ . For computing the Szeged index of above nanotube, we have the following cases:

- (e) If  $e \in E_1$ , then, according to Fig. 12.33, the region  $R$  has vertices that belong to  $N_1(e|G)$ , and the region  $R'$  has vertices that belong to  $N_2(e|G)$ . (The notations  $n_1(e|G)$  and  $n_2(e|G)$  are indicated with  $n_e(u)$  and  $n_e(v)$ , respectively.)

In Fig. 12.33, the vertex assigned by symbol  $*$  is closer to  $v$ , and the vertices assigned by symbol  $\circ$  have the same distance from  $u$  and  $v$ .

In this paper, for simplicity we define  $B = \lfloor \frac{m}{2} \rfloor$ ,  $C = \lceil \frac{m-1}{2} \rceil$ ,  $D = \lfloor \frac{k-m}{2} \rfloor$ ,  $E = \lfloor \frac{k-m+1}{2} \rfloor$ ,  $A(j) = \lfloor \frac{2p+j}{12} \rfloor$ ,  $A(j, i) = \lfloor \frac{A(j)+i}{2} \rfloor$ , where  $i, j = 0, \pm 1, \pm 2, \dots$

- (i) If  $m \leq \frac{p}{2}$ , then  $a_1 = n_e(u) = 2pk - 2m^2 + m - 1 - B - 2C + 2D$ .
- (ii) If  $m > \frac{p}{2}$ , then  $a_2 = n_e(u) = 2p(k - m) + \frac{1}{2}p^2 - p + 2D$ .

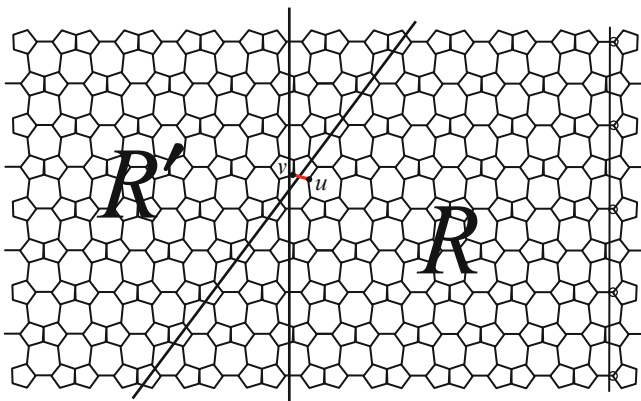
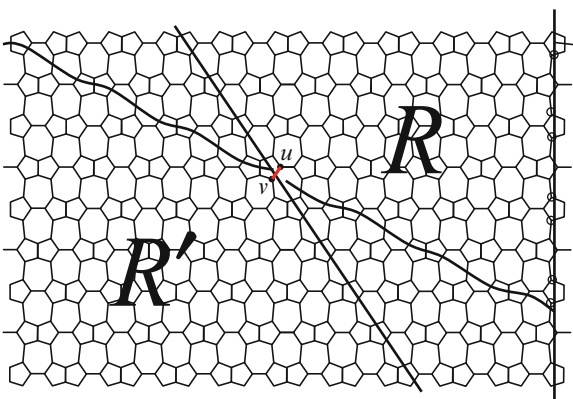


**Fig. 12.33**  $e = uv$  is an edge belonging to  $E_1$  in  $m = 4$  th row

**Fig. 12.34**  $e = uv$  is an edge belonging to  $E_2$  in  $m = 4$  th row



And for  $n_e(v)$ , we have

- (i) If  $k - m \leq \frac{p}{2}$ , then  $a_3 = n_e(v) = k(2p - 2k + 4m - 1) - 2m^2 + m - 1 - B - 2C$ .
  - (ii) If  $k - m > \frac{p}{2}$ , then  $a_4 = n_e(v) = 2pm + \frac{1}{2}p^2 + \frac{3}{2}p - 1 - B - 2C$ .
- (f) If  $e \in E_2$ , then, according to Fig. 12.34, the region  $R$  has vertices that belong to  $N_1(e|G)$ , and the region  $R'$  has vertices that belong to  $N_2(e|G)$ .

In Fig. 12.34, the vertices assigned by symbol  $\circ$  have the same distance from  $u$  and  $v$ . Then,

- (i) If  $m \leq A(-3)$  and  $k - m \leq A(3)$ , then

$$b_1 = n_e(u) = k(2p + 12m - 6k - 3) - 4m^2 + 2m - 1 - 2C - 2E.$$

(ii) If  $A(-3) < m \leq \frac{p}{2}$  and  $k - m \leq A(3)$ , then

$$b_2 = n_e(u) = k(2p + 12m - 6k - 3) - 4m^2 + 2m - 1 - A(-3) - 2E.$$

(iii) If  $m > \frac{p}{2}$  and  $k - m \leq A(3)$ , then

$$\begin{aligned} b_3 = n_e(u) &= k(2p + 12m - 6k - 4) + m(4 - 6m + 2p) \\ &\quad - \frac{3}{2}p^2 - \frac{1}{2}p - 1 - A(-3) - 2E. \end{aligned}$$

(iv) If  $m \leq A(-3)$  and  $k - m > A(3)$ , then

$$\begin{aligned} b_4 = n_e(u) &= m(2p + 2m - 1) - 1 - 2C + (2p - 3) \times A(3) \\ &\quad - 6(A(3))^2 - 2A(3, 1). \end{aligned}$$

(v) If  $A(-3) < m \leq \frac{p}{2}$  and  $k - m > A(3)$ , then

$$\begin{aligned} b_5 = n_e(u) &= m(2p + 2m - 1) - 1 + (2p - 3) \times A(3) \\ &\quad - 6(A(3))^2 - A(-3) - 2A(3, 1). \end{aligned}$$

(vi) If  $m > \frac{p}{2}$  and  $k - m > A(3)$ , then

$$\begin{aligned} b_6 = n_e(u) &= p \left( 2m + \frac{1}{2}p + 1 \right) + (2p - 3) \times A(3) \\ &\quad - 6(A(3))^2 - A(-3) - 2A(3, 1). \end{aligned}$$

And for  $n_e(v)$ , we have

(i) If  $m \leq A(-3)$  and  $k - m \leq \frac{p}{2}$ , then

$$b_7 = n_e(v) = k(2p - 4m + 2k + 1) - 4m^2 + 2m - 1.$$

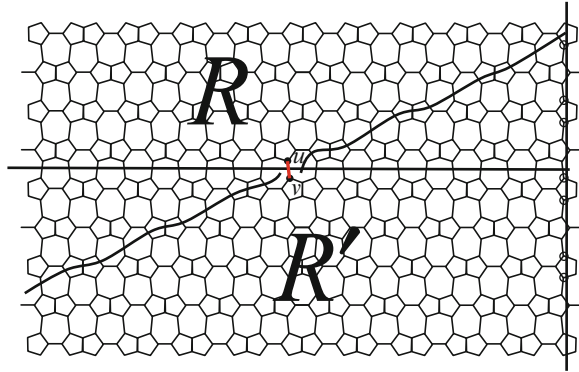
(ii) If  $m > A(-3)$  and  $k - m \leq \frac{p}{2}$ , then

$$\begin{aligned} b_8 = n_e(v) &= (2p + 1)(k - m) + k(2k - 4m) + 2m^2 + 2p - 4 \\ &\quad + (2p - 8) \times A(-3) - 6(A(-3))^2 - 2A(-3, 0). \end{aligned}$$

(iii) If  $m \leq A(-3)$  and  $k - m > \frac{p}{2}$ , then

$$b_9 = n_e(v) = 2p(2k - m) + 3m - 6m^2 - \frac{1}{2}p^2 + \frac{1}{2}p - 1.$$

**Fig. 12.35**  $e = uv$  is an edge belonging to  $E_3$  in  $m = 4$ th row



(iv) If  $m > A(-3)$  and  $k - m > \frac{p}{2}$ , then

$$b_{10} = n_e(v) = 4p(k - m) + \frac{5}{2}p - \frac{1}{2}p^2 - 4 + (2p - 8) \times A(-3) - 6(A(-3))^2 - 2A(-3, 0).$$

(g) If  $e \in E_3$ , then according to Fig. 12.35, the region  $R$  has vertices that belong to  $N_1(e|G)$ , and the region  $R'$  has vertices that belong to  $N_2(e|G)$ .

In Fig. 12.35, the vertices assigned by symbol  $*$  is closer to  $u$ , and the vertices assigned by symbol  $\circ$  have the same distance from  $u$  and  $v$ . Then,

(i) If  $m \leq A(-5)$ , then

$$c_1 = n_e(u) = m(2p + 6m - 1) - 1 + B.$$

(ii) If  $m > A(-5)$ , then

$$c_2 = n_e(u) = 4pm - 1 + 6(A(-5))^2 - (2p + 1) \times A(-5) + A(-5, 0).$$

And for  $n_e(v)$ , we have

(i) If  $k - m \leq A(-5)$ , then

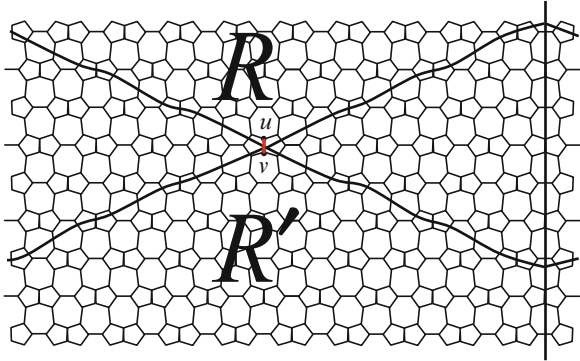
$$c_3 = n_e(v) = k(2p - 12m + 6k - 1) + m(6m - 2p + 1) - 1 - 2E.$$

(ii) If  $k - m > A(-5)$ , then

$$c_4 = n_e(v) = 4p(k - m) - 1 + 6(A(-5))^2 - (2p + 1) \times A(-5) - 2A(-5, 0).$$



**Fig. 12.36**  $e = uv$  is an edge belonging to  $E_4$  in  $m = 4$ th row



- (h) If  $e \in E_4$ , then, according to Fig. 12.36, the region  $R$  has vertices that belong to  $N_1(e|G)$ , and the region  $R'$  has vertices that belong to  $N_2(e|G)$ . Then,

- (i) If  $m \leq A(0) + 1$ , then

$$d_1 = n_e(u) = 12m(m - 1) + 2 - 3C.$$

- (ii) If  $m > A(0) + 1$ , then

$$d_2 = n_e(u) = 4pm - 4p + 2 + 12(A(0))^2 + (12 - 4p) \times A(0) - 3A(0, 0).$$

And for  $n_e(v)$ , we have

- (i) If  $k - m \leq A(0)$ , then

$$d_3 = n_e(v) = 12(k - m)(k - m + 1) + 2 - 3D.$$

- (ii) If  $k - m > A(0) + 1$ , then

$$d_4 = n_e(v) = 4p(k - m) + 2 + 12(A(0))^2 + (12 - 4p) \times A(0) - 3A(0, 0).$$

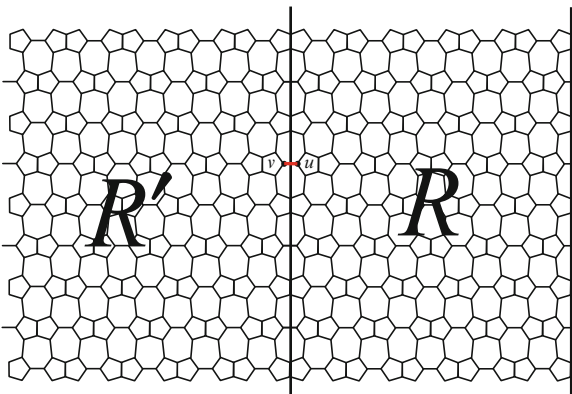
- (i) If  $e \in E_5$ , then according to Fig. 12.37, the region  $R$  has vertices that belong to  $N_1(e|G)$ , and the region  $R'$  has vertices that belong to  $N_2(e|G)$ . Then,

$$e_0 = n_e(u) = n_e(v) = 4pk - 1 - 2(E + B).$$

For simplicity, we define

$$S_0 = \sum_{m=1}^k \left\{ 2p(a_1a_2 + b_1b_7) + \frac{p}{2}(d_1d_3 + e_0^2) \right\}.$$

**Fig. 12.37**  $e = uv$  is an edge belonging to  $E_5$  in  $m = 4$ th row



$$\begin{aligned}
 S_1 &= p \left\{ \sum_{m=1}^{k-A(-5)-1} c_1 c_4 + \sum_{m=k-A(-5)}^{A(-5)} c_1 c_3 + \sum_{m=A(-5)+1}^{k-1} c_2 c_3 \right\}. \\
 S_2 &= p \left\{ \sum_{m=1}^{A(-5)} c_1 c_4 + \sum_{m=A(-5)+1}^{k-A(-5)-1} c_2 c_4 + \sum_{m=k-A(-5)}^{k-1} c_2 c_3 \right\}. \\
 S_3 &= 2p \left\{ \sum_{m=1}^{k-A(3)-1} b_4 b_7 + \sum_{m=k-A(3)}^{A(3)} b_1 b_7 + \sum_{m=A(3)+1}^k b_2 b_8 \right\}. \\
 S_4 &= 2p \left\{ \sum_{m=1}^{A(-3)} b_4 b_7 + \sum_{m=A(-3)+1}^{k-A(3)-1} b_5 b_8 + \sum_{m=k-A(3)}^k b_2 b_8 \right\}. \\
 S_5 &= 2p \left\{ \sum_{i=1}^{k-\frac{p}{2}-1} b_4 b_9 + \sum_{m=k-\frac{p}{2}}^{A(-3)} b_4 b_7 + \sum_{m=A(-3)+1}^{k-A(3)-1} b_5 b_8 + \sum_{m=k-A(3)}^{\frac{p}{2}} b_2 b_8 \right. \\
 &\quad \left. + \sum_{m=\frac{p}{2}+1}^k b_3 b_8 \right\}. \\
 S_6 &= 2p \left\{ \sum_{m=1}^{A(-3)} b_4 b_9 + \sum_{m=A(-3)+1}^{k-\frac{p}{2}-1} b_5 b_{10} + \sum_{m=k-\frac{p}{2}}^{\frac{p}{2}} b_5 b_8 + \sum_{m=\frac{p}{2}+1}^{k-A(3)-1} b_6 b_8 \right. \\
 &\quad \left. + \sum_{m=k-A(3)}^k b_3 b_8 \right\}. \\
 S_7 &= \frac{p}{2} \left\{ \sum_{m=1}^{k-A(0)-1} d_1 d_4 + \sum_{m=k-A(0)}^{A(0)} d_1 d_3 + \sum_{m=A(0)+1}^k d_2 d_3 \right\}. \\
 S_8 &= \frac{p}{2} \left\{ \sum_{m=1}^{A(0)} d_1 d_4 + \sum_{m=A(0)+1}^{k-A(0)-1} d_2 d_4 + \sum_{m=k-A(0)}^{k-1} d_2 d_3 \right\}.
 \end{aligned}$$

$$S_9 = \sum_{m=1}^k (2pa_1a_3 + \frac{p}{2}e_0^2).$$

$$S_{10} = 2p \left\{ \sum_{m=1}^{k-\frac{p}{2}-1} a_1a_4 + \sum_{m=k-\frac{p}{2}}^k a_1a_3 \right\}.$$

$$S_{11} = 2p \left( \sum_{m=1}^{\frac{p}{2}} a_1a_4 + \sum_{m=\frac{p}{2}+1}^{k-\frac{p}{2}-1} a_2a_4 + \sum_{m=k-\frac{p}{2}}^k a_2a_3 \right).$$

The Szeged index of  $HC_5C_7[r, p]$  nanotube is given as follows:

If  $k \leq A(-5)$ , then

$$SZ = S_0 + \sum_{m=1}^{k-1} pc_1c_3.$$

If  $A(-5) < k \leq A(-3)$ , then

$$SZ = S_1 + S_0.$$

If  $A(-3) < k \leq A(0) + 1$ , then

$$SZ = S_9 + S_3 + S_1 + \sum_{m=1}^k \frac{p}{2}d_1d_3.$$

If  $A(0) + 1 < k \leq 2A(-5)$ , then

$$SZ = S_9 + S_7 + S_1 + S_3.$$

If  $2A(-5) < k \leq A(3) + A(-3)$ , then

$$SZ = S_9 + S_7 + S_2 + S_3.$$

If  $A(3) + A(-3) < k \leq 2A(0) + 1$ , then

$$SZ = S_9 + S_7 + S_4 + S_2.$$

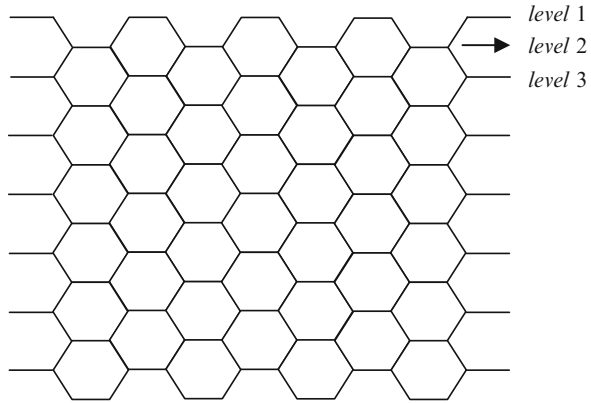
If  $2A(0) + 1 < k \leq \frac{p}{2}$ , then

$$SZ = S_9 + S_8 + S_2 + S_4.$$

If  $\frac{p}{2} < k \leq \frac{p}{2} + A(-3)$ , then

$$SZ = S_{10} + S_8 + S_2 + S_5 + \sum_{m=1}^k e_0^2.$$

**Fig. 12.38** Two-dimensional lattice of TUAC<sub>6</sub>[4, 14] nanotube,  $p = 4, k = 14$



If  $\frac{p}{2} + A(-3) < k \leq p$ , then

$$SZ = S_{10} + S_8 + S_2 + S_6 + \sum_{m=1}^k e_0^2.$$

If  $k > p$ , then

$$SZ = S_{11} + S_8 + S_2 + S_6 + \sum_{m=1}^k e_0^2.$$

Therefore, the Szeged index of above nanotube is computed.

### 12.3.6 Computation of the Szeged Index of Armchair Polyhex Nanotube

In this part, we compute the Szeged index of Armchair Polyhex nanotube. This nanotube is denoted by TUAC<sub>6</sub>[ $p, k$ ]. We bring all details of the computation of the Szeged index of this nanotube, which have been published in Mahmiani et al. (2008).

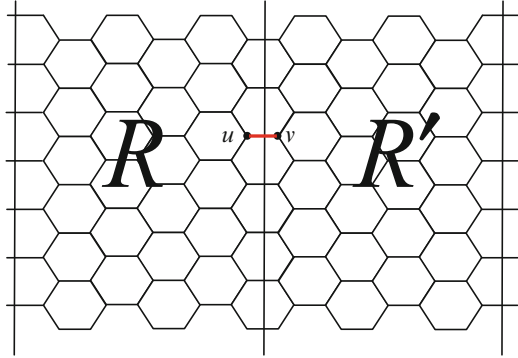
According to Fig. 12.38, we denote the number of horizontal lines in one row by  $p$ , and the number of levels by  $k$ .

Let  $e$  be an arbitrary edge of nanotube. For computing the Szeged index of  $T$ , we assume two cases:

*Case 1*  $p$  is even.

**Lemma 12.3.20** *If  $e$  is a horizontal edge of  $T$ , then  $n_1(e | G)n_2(e | G) = p^2k^2$ .*

**Fig. 12.39**  $e = uv$  is a horizontal edge in level  $m = 6$



*Proof* Suppose that  $e$  is a horizontal edge of  $T$ , for example,  $e = uv$  in Fig. 12.39. In this figure, the region  $R$  has vertices that belong to  $N_1(e|G)$ , and the region  $R'$  has vertices that belong to  $N_2(e|G)$ . So we have  $n_1(e|G) = n_2(e|G) = pk$ ; therefore,  $n_1(e|G)n_2(e|G) = p^2k^2$ . By the symmetry of  $TUAC_6[p, k]$  nanotube for every horizontal edge, the above relation is hold. ■

For simplicity, we define  $a = \lfloor \frac{k-m-1}{2} \rfloor$  and  $b = \lfloor \frac{m-1}{2} \rfloor$ .

**Lemma 12.3.21** *Suppose  $p$  is even. If  $e$  is an oblique edge in level  $m$ , then we have*

- (i) If  $m \leq p$  and  $k - m \leq p$ , then

$$n_1(e|G) = p(k + m - 1) + 2b(5 - 2m + 3b - p) + 2a(k - m - a - 2) + 2k - 6m + 2. \tag{I}$$

- (ii) If  $m \leq p$  and  $k - m > p$ , then

$$n_1(e|G) = p(2k - 1/2p - 1) + 2b(5 - p + 3b - 2m) - 4m + 4. \tag{II}$$

- (iii) If  $m > p$  and  $k - m \leq p$ , then

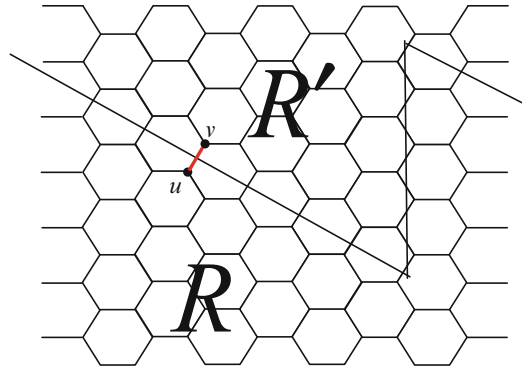
$$n_1(e|G) = p(k - m + 1/2p) + 2a(k - a - m - 2) + 2(k - m - 1). \tag{III}$$

- (iv) If  $m > p$  and  $k - m > p$ , then

$$n_1(e|G) = 2p(k - m) + 2. \tag{IV}$$

*Proof* Let  $e$  be an oblique edge of  $T$ , for example,  $e = uv$  in Fig. 12.40. In this figure, the region  $R$  has vertices that belong to  $N_1(e|G)$ , and the region  $R'$  has vertices that belong to  $N_2(e|G)$ .

**Fig. 12.40**  $e = uv$  is an oblique edge in level  $m = 6$



Number of vertices that are closer to  $u$  than to  $v$  are as follows: If  $m \leq p$  and  $k - m \leq p$ , then

$$\begin{aligned}
 n_1(e|G) &= p(k - m + 1) + \sum_{i=1}^a (4i) \\
 &\quad + \sum_{i=1}^b (2p - 4i) + (k - m - 2a - 1)(2a + 2) \\
 &\quad + (m - 2b - 1)(2p - 4b - 4) \\
 &= p(k + m - 1) + 2b(5 - 2m + 3b - p) + 2a(k - m - a - 2) \\
 &\quad + 2k - 6m + 2.
 \end{aligned}$$

If  $m \leq p$  and  $k - m \leq p$ , then

$$\begin{aligned}
 n_1(e|G) &= p(2k - 2m - p + 2) + \sum_{i=1}^{\frac{p-2}{2}} (4i) + \sum_{i=1}^b (2p - 4i) \\
 &\quad + (m - 2b - 1)(2p - 4b - 4) \\
 &= p(2k - 1/2p - 1) + 2b(5 - p + 3b - 2m) - 4m + 4.
 \end{aligned}$$

If  $m > p$  and  $k - m \leq p$ , then

$$\begin{aligned}
 n_1(e|G) &= p(k - m + 1) + \sum_{i=1}^a (4i) + \sum_{i=1}^{\frac{p-2}{2}} (2p - 4i) + (k - m - 2a - 1) \\
 &\quad (2a + 2) + 2 \\
 &= p(k - m + 1/2p) + 2a(k - a - m - 2) + 2(k - m - 1).
 \end{aligned}$$

And if  $m > p$  and  $k - m > p$ , then

$$n_1(e|G) = p(2k - 2m - p + 2) + \sum_{i=1}^{\frac{(p-2)}{2}} (4i) + \sum_{i=1}^{\frac{(p-2)}{2}} (2p - 4i) + 2 = 2p(k-m) + 2.$$

By the symmetry of  $TUAC_6[p, k]$  nanotube for every oblique edge, this relation is hold. ■

*Remark 12.3.22* According to Fig. 12.40, let  $e$  be an oblique edge in level  $m$ , then

$$n_2(e|G) = 2pk - n_1(e|G).$$

**Theorem 12.3.23** *If  $p$  is even, then the Szeged index of  $TUAC_6[p, k]$  nanotube is given as follows:*

1.  $k$  is even.

(i) If  $k \leq p$ , then we have

$$\begin{aligned} Sz(T) &= p^3(2k^3 - k^2 - k + 2) + p^2(k^2 - 2k) + p(-1/6k^5 + 1/3pk^4 \\ &\quad + 1/3k^3 - 1/3k^2 - 2/3k). \end{aligned}$$

(ii) If  $p < k \leq 2p$ , then we have

$$\begin{aligned} Sz(T) &= p^5(91/12 - 31/3k) + p^4(14/3k^2 - 22/3k - 10/3) \\ &\quad + p^3(2k^3 + 1/2k^2 + 4/3k - 4/3) \\ &\quad + p^2(11/3k^3 - 4k^2 - 2/3k^4 - 4/3k + 2/15) \\ &\quad + p(-1/30k^5 - 7/12k^4 + 7/3k^3 - 5/3k^2 - 4/5k) + 31/5p^6. \end{aligned}$$

(iii) If  $k > 2p$ , then we have

$$\begin{aligned} Sz(T) &= p(1/4k^4 - 1/5k^5 + 2/3k^3 - 22/15k) + p^2(+1/3k^4 \\ &\quad + 2/3k^3 + 2/3k^2 - 14/3k + 22/15) \\ &\quad + p^3(-2k^3 + 5/2k^2 - 8/3k + 8/3) + p^4(10k^2 - 6k - 2/3) \\ &\quad + p^5(91/12 - 31/3k) + 31/5p^6. \end{aligned}$$

2.  $k$  is odd.

(i) If  $k \leq p$ , then we have

$$\begin{aligned} Sz(T) &= p(-1/6k^5 + 1/3k^4 - 2/3k^3 - 4/3k^2 + 5/6k + 1) \\ &\quad + p^2(2k^2 - 2) + p^3(2k^3 - k^2 - k + 1). \end{aligned}$$

(ii) If  $p < k \leq 2p$ , then we have

$$\begin{aligned} \text{Sz}(T) = & p^3 (2k^3 + 1/2k^2 + 13/3k + 13/6) + p^4 (+14/3k^2 - 22/3k \\ & - 7/3) + p (-1/30k^5 - 1/12k^4 + 1/3k^3 + 5/6k^2 - 3/10k - 3/4) \\ & + p^2 (-2/3k^4 + 5/3k^3 - 13/3k + 17/15) + 91/12p^5 + 31/5p^6. \end{aligned}$$

(iii) If  $k > 2p$ , then we have

$$\begin{aligned} \text{Sz}(T) = & p^3 (-2k^3 + 5/2k^2 - 11/3k + 1/6) + p^4 (+10k^2 - 6k + 1/3) \\ & + 31/5p^6 + p (-1/5k^5 + 1/4k^4 - 1/3k^3 - 1/2k^2 + 8/15k + 1/4) \\ & + p^2 (1/3k^4 + 2/3k^3 + 5/3k^2 - 8/3k + 22/15) \\ & + p^5 (-31/3k + 91/12). \end{aligned}$$

Case 2  $p$  is odd.

**Lemma 12.3.24** *If  $e$  is an oblique edge in level  $m$ , then we have*

- (i) If  $m \leq p$  and  $k - m \leq p$ , then  $n_1(e|G) = p(k + m - 1) + 2b(5 - 2m + 3b - p) + 2a(k - m - a - 2) + 2k - 6m + 2$ .
- (ii) If  $m \leq p$  and  $k - m > p$ , then  $n_1(e|G) = p(2k - 1/2p - 1) + 2b(5 - p + 3b - 2m) + -4m + 7/2$ .
- (iii) If  $m > p$  and  $k - m \leq p$ , then  $n_1(e|G) = p(k + m - 1/2p) - 3/2 + 2a(k - m - a - 2) + 2(k - m)$ .
- (iv) If  $m > p$  and  $k - m > p$ , then  $n_1(e|G) = 2p(k - m)$ .

**Theorem 12.3.25** *If  $p$  is odd, then the Szeged index of  $\text{TUAC}_6[p, k]$  nanotube is given as follows:*

1.  $k$  is even.

(i) If  $k \leq p$ , then we have

$$\begin{aligned} \text{Sz}(T) = & p^3 (2k^3 - k^2 - k + 2) + p (-1/6k^5 + 1/3k^4 + 1/3k^3 - 1/3k^2 \\ & - 2/3k) + p^2 (k^2 - 2k). \end{aligned}$$

(ii) If  $p < k \leq 2p$ , then we have

$$\begin{aligned} \text{Sz}(T) = & p^3 (2k^3 + 1/2k^2 - 26/3k - 41/6) + p (-1/30k^5 - 7/12k^4 \\ & + 2/3k^3 + 11/6k^2 - 17/15k - 7/4) + p^2 (-2/3k^4 + 11/3k^3 \\ & + 2k^2 - 10/3k - 128/15) + p^4 (14/3k^2 - 22/3k + 4/3) \\ & + p^5 (91/12 - 31/3k) + 31/5p^6. \end{aligned}$$



(iii) If  $k > 2p$ , then we have

$$\begin{aligned} Sz(T) = & p^3 (-2k^3 + 5/2k^2 - 26/3k + 7/6) + p (-1/5k^5 + 1/4k^4 \\ & + 1/2k^2 - 4/5k + 1/4) + p^2 (1/3k^4 + 2/3k^3 + 8/3k^2 \\ & - 8/3k - 6/5) + p^4 (10k^2 - 6k + 4) \\ & + p^5 (91/12 - 31/3k) + 31/5p^6. \end{aligned}$$

2.  $k$  is odd.

(i) If  $k \leq p$ , then we have

$$\begin{aligned} Sz(T) = & p^3 (2k^3 - k^2 - k + 1) + p (-1/6k^5 + 1/3k^4 - 2/3k^3 - 4/3k^2 \\ & + 5/6k + 1) + 2p^2 (k^2 - 1). \end{aligned}$$

(ii) If  $p < k \leq 2p$ , then we have

$$\begin{aligned} Sz(T) = & p^3 (-2k^3 - 17/3k + 1/2k^2 - 10/3) + p (-1/30k^5 - 1/12k^4 \\ & - 4/3k^3 - 2/3k^2 + 41/30k) + p^2 (-2/3k^4 + 5/3k^3 + 3k^2 \\ & + 11/3k - 8/15) + p^4 (14/3k^2 - 22/3k + 7/3) \\ & + p^5 (91/12 - 31/3k) + 31/5p^6. \end{aligned}$$

(iii) If  $k > 2p$ , then we have

$$\begin{aligned} Sz(T) = & p^3 (-2k^3 + 5/2k^2 - 29/3k - 4/3) + p (-1/5k^5 + 1/4k^4 \\ & - k^3 + 1/5k) + p^2 (1/3k^4 + 2/3k^3 + 11/3k^2 - 2/3k - 1/5) \\ & + p^4 (10k^2 - 6k + 5) + p^5 (91/12 - 31/3k) + 31/5p^6. \end{aligned}$$

### ***12.3.7 Computation of the Szeged Index of Nanotubes by a Different Method***

In the previous parts, we computed the Szeged index of some nanotubes by a theoretical method. It takes a long time for computing the Szeged index of a graph theoretically, especially when the graph has many vertices. In this part, we give an algorithm in the base of GAP, which is faster than the direct implementation. We bring all details of this program published in Taherkhani et al. (2009) and Iranmanesh et al. (2008a).

We give an algorithm that enables us to compute the Szeged index of any graph. For this purpose, the following algorithm is presented:

1. We assign to any vertex one number.
2. We determine all of the adjacent vertices set of the vertex  $i, i \in V(G)$ , and this set is denoted by  $N(i)$ . The set of vertices that their distance to vertex  $i$  is equal to  $t(t \geq 0)$  is denoted by  $D_{i,t}$  and consider  $D_{i,0} = \{i\}$ . Let  $e = ij$  be an edge connecting the vertices  $i$  and  $j$ ; then we have the following result:

$$(a) \quad V = \bigcup_{f \geq 0} D_{i,f}, i \in V(G).$$

$$(b) \quad (D_{i,t} | D_{j,t}) \subseteq (D_{j,t-1} \cup D_{j,t+1}), t \geq 1.$$

$$(c) \quad (D_{i,t} \cap D_{j,t-1}) \subseteq N_2(e|G) \text{ and } D_{i,t} \cap D_{j,t+1} \subseteq N_1(e|G) t \geq 1.$$

$$(d) \quad (D_{i,1} \cup \{i\}) / (D_{j,1} \cup \{j\}) \subseteq N_1(e|G) \text{ and } (D_{j,1} \cup \{j\}) / (D_{i,1} \cup \{i\}) \subseteq N_2(e|G).$$

According to the above relations, by determining  $D_{i,t}, t \geq 1$ , we can obtain  $N_1(e|G)$  and  $N_2(e|G)$  for each edge  $e$ , and, therefore, the Szeged index of the graph  $G$  is computed. By continuing we obtain the  $D_{i,t}, t \geq 1$  for each vertex  $i$ .

3. The distance between vertex  $i$  and its adjacent vertices is equal to 1; therefore,  $D_{i,1} = N(i)$ . For each  $j \in D_{i,t}, t \geq 1$ , the distance between each vertex of set  $N(j) / (D_{i,t} \cup D_{i,t-1})$  and the vertex  $i$  is equal to  $t + 1$ ; thus, we have

$$D_{i,t+1} = \bigcup_{j \in D_{i,t}} (N(j) / (D_{i,t} \cup D_{i,t-1})), t \geq 1.$$

According to the above equation, we can obtain  $D_{i,t}, t \geq 2$  for each  $i \in V(G)$ .

4. In the start of the program, we set  $SZ$  equal to zero and  $T$  equal to an empty set. In the end of program, the value of  $SZ$  is equal to the Szeged index of the graph  $G$ . For each vertex  $i, 1 \leq i \leq n$ , and each vertex  $j$  in  $N(i)$ , we determine  $N_1(e|G)$  and  $N_2(e|G)$  for edge  $e = ij$ , then add the values of  $n_1(e|G).n_1(e|G)$  to  $SZ$ . Since the edge  $ji$  is equal to  $ij$ , we add the vertex  $i$  to  $T$  and continue this step for the vertex  $i + 1$  and for each vertex in  $N(i + 1) / T$ .

GAP stands for Groups, Algorithms, and Programming (Schonert et al. 1992). The name was chosen to reflect the aim of the system, which is group theoretical software for solving computational problems in group theory. The last years have seen a rapid spread of interest in the understanding, design, and even implementation of group theoretical algorithms. GAP software was constructed by GAP's team in Aachen. We encourage the reader to consult Dabirian and Iranmanesh (2005) and Trinajstic (1992) for background materials and computational techniques related to

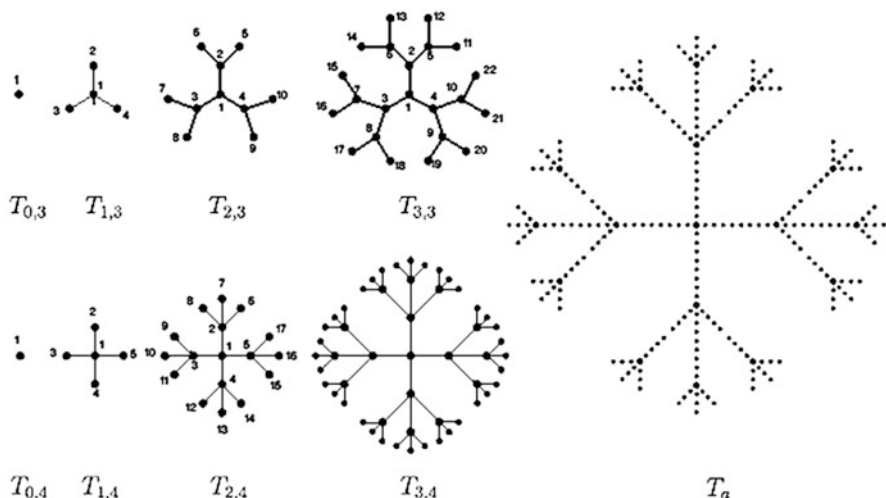


Fig. 12.41 Molecular graphs of dendrimers  $T_{k,d}$

applications of GAP in solving some problems in chemistry and biology. According to the above algorithm, we prepare a GAP program to compute the Szeged index of dendrimers  $T_{k,d}$ .

*Example 12.3.26* The Wiener index of tree dendrimers,  $T_{k,d}, k \geq 1, d \geq 3$ , is computed in Entringer et al. (1994) and Gutman et al. (1994). Since the Wiener and Szeged indices coincide on trees (Gutman 1994 and Karmarkar et al. 1997), the Szeged index of  $T_{k,d}$  is equal to its Wiener index (Fig. 12.41).

The following results are obtained in Entringer et al. (1994) and Gutman et al. (1994).

For every  $d \geq 3$ , the tree  $T_{k,d}$  has order

$$n(T_{k,d}) = 1 + \frac{d}{d-2} [(d-1)^k - 1]$$

and its Szeged index is equal to the Wiener index, that is,

$$\begin{aligned} Sz(T_{k,d}) = W(T_{k,d}) = & \frac{1}{(d-2)^3} [(d-1)^{2k} [kd^3 - 2(k+1)d^2 + d] \\ & + 2d^2(d-1)^k - d]. \end{aligned}$$

For computing of the Szeged index of  $T_{k,d}$  by the above program, at first we assign to any vertex one number; according to this numbering, the set of adjacent

vertices to each vertex,  $1 \leq i \leq n$ , is obtained by the following program (part 1). In fact, part 1 of the program is the presentation of the graph. We use part 2 for computing the Szeged index of the graph.

The following program computes the Szeged index of the  $T_{k,d}$  for arbitrary values of  $d$  and  $k$ .

```

d:=3; k:=3;#(For example)
n:=1+(d/(d-2))*((d-1)^k - 1);
N:=[];
K1:=[2..d+1];
N[1]:=K1;
for i in K1 do
  if k=1 then N[i]:=1];
  else
    N[i]:=[(d-1)*i+4-d..(d-1)*i+2];
    Add(N[i],1);fi;
od;
K2:=[d+2..1+(d/(d-2))*((d-1)^(k-1) - 1)];
for i in K2 do
  N[i]:=[(d-1)*i+4-d..(d-1)*i+2];
  Add(N[i],Int((i-4+d)/(d-1)));
od;
K3:=[2+(d/(d-2))*((d-1)^(k-1) - 1)..n];
for i in K3 do
  if k=1 then N[i]:=1];
  else
    N[i]:=[Int((i-4+d)/(d-1))]; fi;
od;
# (Part2)
D:=[];
for i in [1..n] do
  D[i]:=[];
  u:=[i];
  D[i][1]:=N[i];
  u:=Union(u,D[i][1]);
  s:=1;
  t:=1;
  while s<>0 do
    D[i][t+1]:=[];
    for j in D[i][t] do
      for m in Difference(N[j],u) do
        AddSet(D[i][t+1],m);
      od;
    od;
    u:=Union(u,D[i][t+1]);
    if D[i][t+1]=[] then

```

```

    s:=0;
    fi;
    t:=t+1;
    od;
od;
T:=[];
sz:=0;
pi:=0;
for i in [1..n-1] do
N1:=[];
  for j in Difference(N[i],T) do
N2:=[];
  N1[j]:=Union(Difference(N[i],Union([j],N[j])),[i]);
  N2[i]:=Union(Difference(N[j],Union([i],N[i])),[j]);
  for t in [2..Size(D[i])-1] do
    for x in Difference(D[i][t],Union(D[j][t],[j])) do
      if not x in D[j][t-1] then
        AddSet(N1[j],x);
      elif x in D[j][t-1] then
        AddSet(N2[i],x);
      fi;
    od;
  od;
  sz:=sz+Size(N1[j])*Size(N2[i]);
  od;
  Add(T,i);
od;
sz;# (The value of sz is equal to Szeged index of the graph)

```

Now, as an example, we compute the Szeged index of  $VC_5C_7[p,q]$  nanotube by GAP program.

A  $C_5C_7$  net is a trivalent decoration made by alternating  $C_5$  and  $C_7$ . It can cover either a cylinder or a torus nanotube (Fig. 12.42).

We denote the number of pentagons in the first row by  $p$ . In this nanotube, the first four rows of vertices and edges are repeated alternatively; we denote the number of this repetition by  $q$ . In each period, there are  $16p$  vertices and  $3p$  vertices which are joined to the end of the graph, and, hence, the number of vertices in this nanotube is equal to  $16pq + 3p$ .

We partition the vertices of the graph to the following sets:

$K_1$ : The vertices of the first row whose number is  $6p$ .

$K_2$ : The vertices of the first row in each period except the first one whose number is  $6p(q-1)$ .

$K_3$ : The vertices of the second row in each period whose number is  $2pq$ .

$K_4$ : The vertices of the third row in each period whose number is  $6pq$ .

$K_5$ : The vertices of the fourth row in each period whose number is  $2pq$ .

$K_6$ : The last vertices of the graph whose number is  $3p$ .

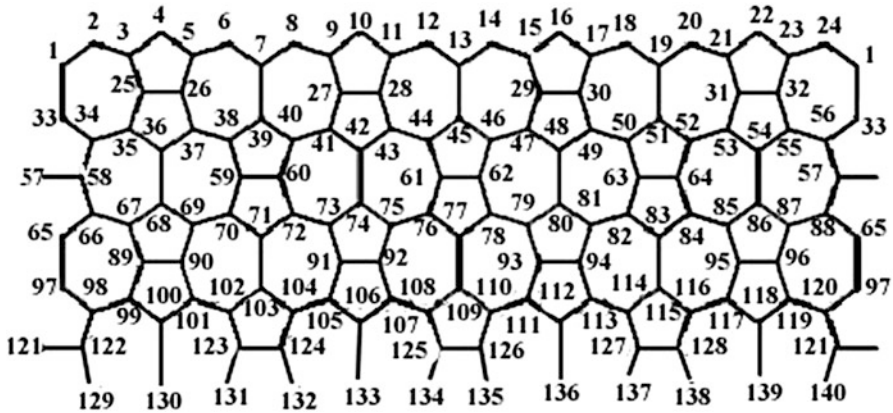


Fig. 12.42  $VC_5C_7 [4, 2]$  nanotube

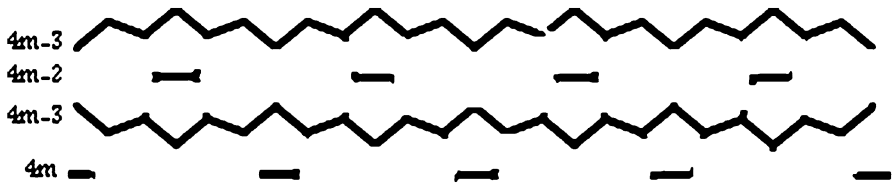


Fig. 12.43 The rows of  $m$ th period  $VC_5C_7 [p, q]$  nanotube

Figure 12.43 shows the rows of the  $m$ th period.

We write a program to obtain the adjacent vertices set to each vertex in the sets  $K_i, i = 1 \dots 6$ . We can obtain the adjacent vertices set to each vertex by joining these programs. In this program, the value of  $x$  is the assigned number of vertex  $i$  in that row.

The following program computes the Szeged index of  $VC_5C_7 [p, q]$  nanotube for arbitrary  $p$  and  $q$ .

```

p:=4; q:=2; # (for example)
n:=16*p*q+3*p;
N:=[];
K1:=[1..6*p];
V1:=[2..6*p-1];
for i in V1 do
  if i mod 6=1 then N[i]:=[i-1,i+1,i+8*p];
  elif i mod 6 in [0,2,4] then N[i]:=[i-1,i+1];
  elif i mod 6=3 then N[i]:=[i-1,i+1,(1/3)*(i-3)+6*p+1];
  elif i mod 6=5 then N[i]:=[i-1,i+1,(1/3)*(i-5)+6*p+2];fi;
N[1]:=[2,6*p,8*p+1];
N[6*p]:=[6*p-1,1];

```

```

od;
K:=[6*p+1..16*p*q];
K2:=Filtered(K,i->i mod (16*p) in [1..6*p]);
for i in K2 do
x:= i mod (16*p);
if x mod 6=1 then N[i]:=[i-1,i+1,i+8*p];
elif x mod 6=2 then N[i]:=[i-1,i+1,(1/3)*(x-2)+2+i-x-2*p];
elif x mod 6=3 then N[i]:=[i-1,i+1,(1/3)*(x-3)+1+i-x+6*p];
elif x mod 6=4 then N[i]:=[i-1,i+1,i-8*p];
elif x mod 6=5 then N[i]:=[i-1,i+1,(1/3)*(x-5)+2+i-x+6*p];
elif x mod 6=0 then N[i]:=[i-1,i+1,(1/3)*x+1+i-x-2*p];fi;
if x=1 then N[i]:=[i+1,i-1+6*p,i+8*p];fi;
if x=6*p then N[i]:=[i-1,i-6*p+1,i-8*p+1];fi;
od;
K3:=Filtered(K,i->i mod (16*p) in [6*p+1..8*p]);
for i in K3 do
x:=(i-6*p) mod (16*p);
if x mod 2=0 then N[i]:=[i-1,3*(x-2)+5+i-x-6*p,3*(x-2)+5+i-x+2*p];
else N[i]:=[i+1,2*x+i-6*p,2*x+i+2*p];fi;
od;
K4:=Filtered(K,i->i mod (16*p) in [8*p+1..14*p]);
for i in K4 do
x:=(i-8*p) mod (16*p);
if x mod 6=1 then N[i]:=[i-1,i+1,i-8*p];
elif x mod 6=2 then N[i]:=[i-1,i+1,(1/3)*(x-2)+2+i-x+6*p];
elif x mod 6=3 then N[i]:=[i-1,i+1,(1/3)*(x-3)+1+i-x-2*p];
elif x mod 6=4 then N[i]:=[i-1,i+1,i+8*p];
elif x mod 6=5 then N[i]:=[i-1,i+1,(1/3)*(x-5)+2+i-x-2*p];
elif x mod 6=0 then N[i]:=[i-1,i+1,(1/3)*x+1+i-x+6*p];fi;
if x=1 then N[i]:=[i-8*p,i+1,i+6*p-1];fi;
if x=6*p then N[i]:=[i-1,i-6*p+1,i+1];fi;
od;
K5:=Filtered(K,i->i mod (16*p) in Union([14*p+1..16*p-1],[0]));
for i in K5 do
x:=(i-14*p) mod (16*p);
if x mod 2=1 then N[i]:=[i+1,3*(x-1)+i-x-6*p,3*(x-1)+i-x+2*p];
else N[i]:=[i-1,3*(x-2)+2+i-x-6*p,3*(x-2)+2+i-x+2*p];fi;
if x=1 then N[i]:=[i+1,i-1,i-1+8*p];fi;
if x=2*p then N[i]:=[i-1,3*(x-2)+2+i-x-6*p,3*(x-2)+2+i-x+2*p];fi;
od;
K6:=[16*p*q+1..n];
for i in K6 do
x:=i mod (16*p);
if x mod 3=1 then y:=(2/3)*(x-1)+2+i-x-2*p;
elif x mod 3=2 then y:=i+x-8*p;

```

```

    elif x mod 3=0 then y:=(2/3)*(x- 3)+3+i-x-2*p;fi;
if x=3*p then y:=i- 5*p+1;fi;
N[i]:=[y];
N[y][3]:=i;
od;
D:=[];
for i in [1..n] do
  D[i]:=[];
  u:=[i];
  D[i][1]:=N[i];
  u:=Union(u,D[i][1]);
  s:=1;
  t:=1;
  while s<>0 do
    D[i][t+1]:=[];
    for j in D[i][t] do
      for m in Difference(N[j],u) do
        AddSet(D[i][t+1],m);
      od;
    od;
    u:=Union(u,D[i][t+1]);
    if D[i][t+1]=[] then
      s:=0;
    fi;
    t:=t+1;
  od;
od;
T:=[];
sz:=0;
for i in [1..n-1] do
  N1:=[];
  for j in Difference(N[i],T) do
  N2:=[];
  N1[j]:=Union(Difference(N[i],Union([j],N[j])),[i]);
  N2[i]:=Union(Difference(N[j],Union([i],N[i])),[j]);
  for t in [2..Size(D[i])-1] do
    for x in Difference(D[i][t],Union(D[j][t],[j])) do
      if not x in D[j][t-1] then
        AddSet(N1[j],x);
      elif x in D[j][t-1] then
        AddSet(N2[i],x);
      fi;
    od;
  od;
  sz:=sz+ Size(N1[j])*Size(N2[i]);

```



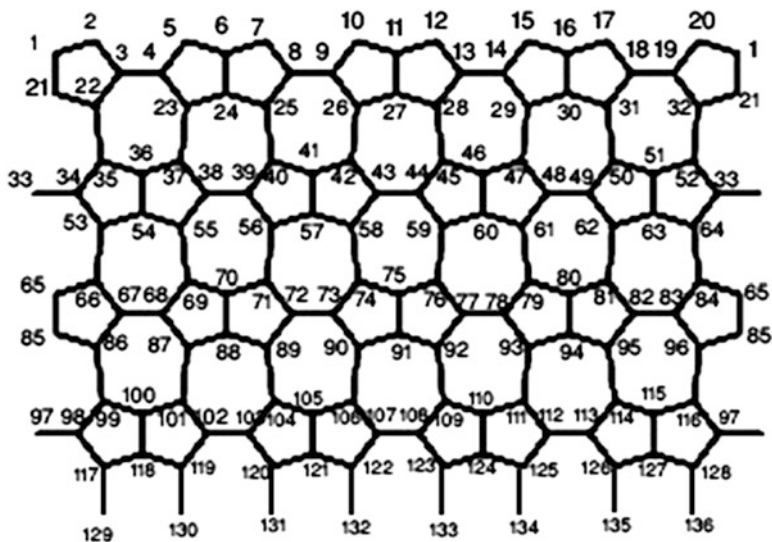


Fig. 12.44  $HC_5C_7 [4,2]$  nanotube

```

od;
Add(T,i);
od;
sz; # (The value of sz is equal to Szeged index of the graph)

```

Also, as another example, we compute the Szeged index of  $HC_5C_7 [p, q]$  nanotube similar to the previous section. We computed the Szeged index of this nanotube in Sect. 12.3.5 by a theoretical method. A  $HC_5C_7 [p, q]$  nanotube consists of heptagon, pentagon nets as below (Fig. 12.44).

We denote the number of heptagons in the first row by  $p$ . In this nanotube, the four first rows of vertices and edges are repeated alternatively; we denote the number of this repetition by  $q$ . In each period,  $16p$  vertices and  $2p$  vertices are joined to the end of the graph, and hence the number of vertices in this nanotube is equal to  $16pq + 2p$ .

The following program is the same as the last program. In this program, value of  $x$  is the number of vertex  $i$  in a row.

```

p:=6;q:=7;# (for example)
n:=16*p*q+2*p;
N:=[];
for i in [1..5*p] do
if i mod 5=1 then N[i]:=[i-1,i+1,(3/5)*(i-1)+1+5*p];
elif i mod 5 in [0,2] then N[i]:=[i-1,i+1];
elif i mod 5=3 then N[i]:=[i-1,i+1,(3/5)*(i-3)+2+5*p];
elif i mod 5=4 then N[i]:=[i-1,i+1,(3/5)*(i-4)+3+5*p];fi;
N[1]:=[2,5*p,5*p+1];

```

```

N[5*p]:=[1,5*p-1];
od;
K:=[5*p+1..16*p*q];
K1:=Filtered(K,i->i mod (16*p) in [1..5*p]);
for i in K1 do
x:=(i) mod (16*p);
if x mod 5=1 then N[i]:=[i-1,i+1,(3/5)*(x-1)+1+i-x+5*p];
elif x mod 5=2 then N[i]:=[i-1,i+1,(3/5)*(x-2)+1+i-x-3*p];
elif x mod 5=3 then N[i]:=[i-1,i+1,(3/5)*(x-3)+2+i-x+5*p];
elif x mod 5=4 then N[i]:=[i-1,i+1,(3/5)*(x-4)+3+i-x+5*p];
elif x mod 5=0 then N[i]:=[i-1,i+1,(3/5)*x+i-x-3*p];fi;
if x=1 then N[i]:=[i+1,i-1+5*p,i+(5*p)];fi;
if x=5*p then N[i]:=[i-1,i-5*p,i+1-5*p];fi;
od;
K2:=Filtered(K,i->i mod (16*p) in [5*p+1..8*p]);
for i in K2 do
x:=(i-5*p) mod (16*p);
if x mod 3=1 then N[i]:=[i-1,i+1,(5/3)*(x-1)+1+i-x-5*p];
elif x mod 3=2 then N[i]:=[i-1,(5/3)*(x-2)+3+i-x-5*p,(5/3)*(x-2)+3+i-
x+3*p];
elif x mod 3=0 then N[i]:=[i+1,(5/3)*x-1+i-x-5*p,(5/3)*x+i-x+3*p];fi;
if x=3*p then N[i]:=[i-3*p+1,(5/3)*x-1+i-x-5*p,(5/3)*x+i-x+3*p];fi;
if x=1 then N[i]:=[i-5*p,i+1,i-1+3*p];fi;
od;
K3:=Filtered(K,i->i mod (16*p) in [8*p+1..13*p]);
for i in K3 do
x:=(i-8*p) mod (16*p);
if x mod 5=1 then N[i]:=[i-1,i+1,(3/5)*(x-1)+i-x+5*p];
elif x mod 5=2 then N[i]:=[i-1,i+1,(3/5)*(x-2)+1+i-x+5*p];
elif x mod 5=3 then N[i]:=[i-1,i+1,(3/5)*(x-3)+2+i-x-3*p];
elif x mod 5=4 then N[i]:=[i-1,i+1,(3/5)*(x-4)+2+i-x+5*p];
elif x mod 5=0 then N[i]:=[i-1,i+1,(3/5)*x+i-x-3*p];fi;
if x=1 then N[i]:=[i+1,i-1+5*p,i-1+8*p];fi;
if x=5*p then N[i]:=[i-1,i-5*p,i+1-5*p];fi;
od;
K4:=Filtered(K,i->i mod (16*p) in Union([13*p+1..16*p-1],[0]));
for i in K4 do
x:=(i-13*p) mod (16*p);
if x mod 3=1 then N[i]:=[i+1,(5/3)*(x-1)+2+i-x-5*p,(5/3)*(x-1)+2+i-
x+3*p];
elif x mod 3=2 then N[i]:=[i-1,i+1,(5/3)*(x-2)+4+i-x-5*p];
elif x mod 3=0 then N[i]:=[i-1,(5/3)*x+1+i-x-5*p,(5/3)*x+i-x+3*p];fi;
if x=3*p then N[i]:=[i-1,i+1-8*p,(5/3)*x+i-x+3*p];fi;
od;
K5:=[16*p*q+1..n];

```

```

for i in K5 do
  x:=i mod(16*p);
  if x mod 2=0 then y:=(3/2)*x+i-x-3*p;
  else y:=(3/2)*(x-1)+1+i-x-3*p;fi;
  N[i]:=[y];
  N[y][3]:=i;
od;
D:=[];
for i in [1..n] do
  D[i]:=[];
  u:=[i];
  D[i][1]:=N[i];
  u:=Union(u,D[i][1]);
  s:=1;
  t:=1;
  while s<>0 do
    D[i][t+1]:=[];
    for j in D[i][t] do
      for m in Difference(N[j],u) do
        AddSet(D[i][t+1],m);
      od;
    od;
    u:=Union(u,D[i][t+1]);
    if D[i][t+1]=[] then
      s:=0;
    fi;
    t:=t+1;
  od;
od;
T:=[];
sz:=0;
for i in [1..n-1] do
  N1:=[];
  for j in Difference(N[i],T) do
  N2:=[];
  N1[j]:=Union(Difference(N[i],Union([j],N[j])),[i]);
  N2[i]:=Union(Difference(N[j],Union([i],N[i])),[j]);
  for t in [2..Size(D[i])-1] do
    for x in Difference(D[i][t],Union(D[j][t],[j])) do
      if not x in D[j][t-1] then
        AddSet(N1[j],x);
      elif x in D[j][t-1] then
        AddSet(N2[i],x);
      fi;
    od;
  od;

```

```

od;
sz:=sz+Size(N1[j])*Size(N2[i]);
od;
Add(T,i);
od;
sz;# (The value of sz is equal to Szeged index of the graph)

```

**Acknowledgments** This work was partially supported by Center of Excellence of Algebraic Hyperstructures and its Applications of Tarbiat Modares University (CEAHA).

## References

- Agrawal VK, Bano S, Mathur KC, Khadikar PV (2000) *Indian Acad Sci* 112:137
- Cameron P (1994) *Combinatorics: topics, techniques, algorithms*. Cambridge University Press, Cambridge
- Dabirian M, Iranmanesh A (2005) *MATCH Commun Math Comput Chem* 54:75
- Diudea MV, Stefu M, Parv B, John PE (2004) *Croat Chem Acad* 77:111
- Entringer RC, Meir AJ, Moon W, Székely LA (1994) *Australas J Combin* 10:211
- Gutman I (1994) *Graph Theory Notes N Y* 27:9
- Gutman I, Yeh YN, Lee SL, Chen JC (1994) *MATCH Commun Math Comput Chem* 30:103
- Holister CRV, Harper T (2003) *Cientifica* 6:1
- Iranmanesh A, Gholami N (2007) *Micro Nano Lett* 4:107
- Iranmanesh A, Gholami N (2008) *Croat Chemica Acta* 81:299
- Iranmanesh A, Gholami N (2009) *MATCH Commun Math Comput Chem* 62:371
- Iranmanesh A, Khormali O (2009) *J Appl Sci* 6:1670
- Iranmanesh A, Pakraveshteh Y (2007) *J Appl Sci* 7:3606
- Iranmanesh A, Pakraveshteh Y (2008) *Utilitas Mathematica* 75:89
- Iranmanesh A, Soleimani B, Ahmadi A (2007) *J Comput Theor NanoSci* 4:147
- Iranmanesh A, Alizadeh Y, Taherkhani B (2008a) *Int J Mol Sci* 9:131
- Iranmanesh A, Pakraveshteh Y, Mahmiani A (2008b) *Ars Comb* 87:193
- Iranmanesh A, Gholami N, Ahmadi A (2010) *Optoelectron Adv Mater Rapid Commun* 4:2190
- Karmarkar S, Joshi S, Das A, Khadikar PV (1997) *J Serb Chem Soc* 62:227
- Mahmiani A, Iranmanesh A, Pakraveshteh Y (2008) *Ars Comb* 89:309
- Mansoori GA (2005) *Principles of nanotechnology: molecular-based study of condensed matter in small systems*. World Scientific, Hackensack
- Schonert M et al (1992) *GAP, groups, algorithms and programming*. Lehrstuhl De fu Mathematik, RWTH, Aachen
- Taherkhani B, Alizadeh Y, Iranmanesh A (2009) *Asian J Chem* 21:3683
- Trinajstić N (1992) *Chemical group theory*. CRC Press, Boca Roton

# Chapter 13

## The Edge-Wiener Index and Its Computation for Some Nanostructures

Ali Iranmanesh

**Abstract** The first and the second edge versions of Wiener index, which were based on the distance between two edges in a connected graph  $G$ , were introduced by Iranmanesh et al. in (MATCH Commun Math Comput Chem 61:663, 2009).

In this chapter, at first we obtain the explicit relation between different versions of Wiener number and due to this relation, the edge-Wiener numbers of some graph have been computed. Then we find the first edge-Wiener index of the composition and sum of graphs. As an application of our results, we find the first and the second edge-Wiener indices of some nanostructures.

### 13.1 Introduction

Topological indices are numerical descriptors derived from the associate graphs of chemical compounds. Some indices based on the distances in graph are widely used in establishing relationships between the structure of molecules and their physico-chemical properties. Usage of topological indices in chemistry began in 1947 when the chemist Harold Wiener introduced Wiener index to demonstrate correlations between physicochemical properties of organic compounds and the index of their molecular graphs (Wiener 1947). Wiener originally defined his index ( $W$ ) on trees and studied its use for correlations of physicochemical properties of alkanes, alcohols, amines and analogous compounds (Khadikar and Karmarkar 2002). Starting from the middle of the 1970s, the Wiener index gained much popularity and, since then, new results related to it are constantly being reported. For a review, historical details and further bibliography on the chemical applications of the Wiener index see, Gutman et al. (1993, 1997) and Nikoli'c et al. (1995).

---

A. Iranmanesh (✉)

Department of Mathematics, Tarbiat Modares University, P.O. Box: 14115-137, Tehran, Iran  
e-mail: [iranmanesh@modares.ac.ir](mailto:iranmanesh@modares.ac.ir)

Let  $G$  be a connected graph. The vertex set and edge set of  $G$  denoted by  $V(G)$  and  $E(G)$ , respectively. The distance between the vertices  $u$  and  $v$ ,  $d(u, v)$ , in a graph is the number of edges in a shortest path connecting them. Two graph vertices are adjacent if they are joined by a graph edge. The degree of a vertex  $i \in V(G)$  is the number of vertices joining to  $i$  and denoted by  $\delta_i$ .

The Wiener index of  $G$  is

$$W(G) = W_v(G) = \sum_{\{x,y\} \subseteq V(G)} d(x, y) \tag{13.1}$$

The edge versions of Wiener index which were based on the distance between edges introduced by Iranmanesh et al. (2009). These versions have been introduced for a connected graph  $G$  as the first and second edge-Wiener, that is, the first edge-Wiener number was introduced as follows:

$$W_{e0}(G) = \sum_{\{e,f\} \subseteq E(G)} d_0(e, f) \tag{13.2}$$

where  $d_0(e, f) = \begin{cases} d_1(e, f) + 1 & e \neq f \\ 0 & e = f \end{cases}$  and  $d_1(e, f) = \min \{d(x, u), d(x, v), d(y, u), d(y, v)\}$  such that  $e = xy$  and  $f = uv$ . This version satisfies in  $W_{e0}(G) = W_v(L(G))$ .

The second edge-Wiener index was introduced as follows:

$$W_{e4}(G) = \sum_{\{e,f\} \subseteq E(G)} d_4(e, f) \tag{13.3}$$

where  $d_4(e, f) = \begin{cases} d_2(e, f) & e \neq f \\ 0 & e = f \end{cases}$  and  $d_2(e, f) = \max \{d(x, u), d(x, v), d(y, u), d(y, v)\}$  such that  $e = xy$  and  $f = uv$ .

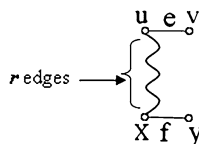
In this chapter, at first we obtain the explicit relation between different versions of Wiener number and due to this relation, the edge-Wiener numbers of some graph have been computed and then we compute the first and the second edge-Wiener indices of zigzag nanotube and  $TUC_4C_8(R)$  and  $TUC_4C_8(S)$  nanotubes.

In Sects. 13.3 and 13.4, we find the first edge-Wiener index of the composition and sum of graphs, respectively. As an application of our results, we find the first and the second edge-Wiener indices of  $C_4$ -nanotubes and  $C_4$ -nanotori.

### 13.2 Explicit Relation Between Vertex and Edge-Wiener Numbers

In this section, we restate some definitions and then we give an explicit relation between vertex and edge-Wiener indices. All of the results in the first part of this section have been published in Iranmanesh and Khormali (2011).

**Fig. 13.1** The edges of  $e$  and  $f$  are not adjacent



We recall the conditions of the distances.  $d$  is the distance on set  $X$  if it satisfies in the following conditions:

- (a)  $\forall u, v \in X; \quad d(u, v) \geq 0$
- (b)  $\forall u, v \in X; \quad u = v \Leftrightarrow d(u, v) = 0$
- (c)  $\forall u, v \in X; \quad d(u, v) = d(v, u)$
- (d)  $\forall u, v, w \in X; \quad d(u, v) + d(v, w) \geq d(u, w)$

At first, we restate the first edge-Wiener number according to the distances between vertices.

**Definition 13.2.1** Let  $e = uv, f = xy$  be the edges of connected graph  $G$ . Then, we define  $d'(e, f) = \frac{d(u,x)+d(u,y)+d(v,x)+d(v,y)}{4}$  and  $d''(e, f) = \begin{cases} \lceil d'(e, f) \rceil, & \{e, f\} \notin C \\ d'(e, f) + 1, & \{e, f\} \in C \end{cases}$ , where  $C = \{\{e, f\} \subseteq E(G) \mid \text{if } e = uv \text{ and } f = xy;$

$\{d(u, x) = d(u, y) = d(v, x) = d(v, y)\}$  and  $d_3(e, f) = \begin{cases} d''(e, f) & e \neq f \\ 0 & e = f \end{cases}$ .

Also,  $d'$  and  $d''$  do not satisfy the condition (b), hence, they are not a distance and are like distance.

**Claim**  $d_3 = d_0$ .

*Proof* We have to show for any  $e, f \in E(G), d_3(e, f) = d_0(e, f)$ .

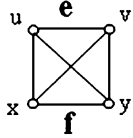
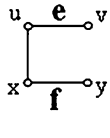
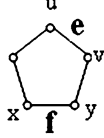
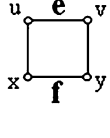
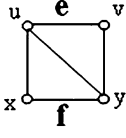
- (i) If  $e = f \in E(G)$ , then  $d_3(e, f) = d_0(e, f) = 0$ .
- (ii) If  $e, f \in E(G)$  are adjacent edges, then,

$$d_0(e, f) = d_1(e, f) + 1 = 0 + 1 = 1 \text{ and } d_3(e, f) = d_2(e, f) = \left\lceil \frac{1 + 1 + 2}{4} \right\rceil = 1. \text{ Therefore, } d_3(e, f) = d_0(e, f).$$

(iii) If  $e, f \in E(G)$  are not adjacent such as Fig. 13.1, then:

- 1. If  $\{e, f\} \notin C$ , then  $d_0(e, f) = d_1(e, f) + 1 = r + 1$  and  $d_3(e, f) = d''(e, f) = \left\lceil \frac{r+(r+1)+(r+1)+(r+2)}{4} \right\rceil = r + 1$ . Therefore,  $d_3(e, f) = d_0(e, f)$ .
- 2. If  $\{e, f\} \in C$ , then  $d_0(e, f) = d_1(e, f) + 1 = r + 1$  and  $d_3(e, f) = d''(e, f) = \frac{r+r+r+r}{4} + 1 = r + 1$ . Therefore,  $d_3(e, f) = d_0(e, f)$ . ■

**Table 13.1** Examples for sets which have been defined above

Set	$C$	$A_1$	$A_2$	$A_3$	$A_4$
Example					
$d'$	1	2	$\frac{7}{4}$	$\frac{6}{4}$	$\frac{5}{4}$
$d_3 = d_0$	2	2	2	2	2

**Corollary 13.2.2**

$$W_{e0}(G) = \sum_{\{e,f\} \subseteq E(G)} d_3(e, f).$$

*Proof* Since  $d_3 = d_0$ , we obtain the desired result. ■

Before stating the explicit relations, we define several sets due to the distance  $d_3$  as follow:

$$A_1 = \{\{e, f\} \subseteq E(G) \mid d_3(e, f) = d'(e, f)\},$$

$$A_2 = \left\{ \{e, f\} \subseteq E(G) \mid d_3(e, f) = d'(e, f) + \frac{1}{4} \right\},$$

$$A_3 = \left\{ \{e, f\} \subseteq E(G) \mid d_3(e, f) = d'(e, f) + \frac{2}{4} \right\},$$

$$A_4 = \left\{ \{e, f\} \subseteq E(G) \mid d_3(e, f) = d'(e, f) + \frac{3}{4} \right\}.$$

We denote all of the two element subsets of  $E(G)$  with  $S$  and therefore  $|S| = \binom{|E(G)|}{2}$ . Also, we have:  $S = A_1 \cup A_2 \cup A_3 \cup A_4 \cup C$  (Table 13.1).

Due to Definition 13.2.1 and Corollary 13.2.2, the relation between vertex and first edge versions of Wiener index has been defined.

**Theorem 13.2.3** *Suppose  $G$  is a graph with  $m$  edges and  $A_1, A_2, A_3, A_4$  and  $C$  are the sets which have been defined as above. Then, the first version of edge-Wiener number according to the distance between vertices of graph  $G$  is*



$$\begin{aligned}
W_{e0}(G) &= \frac{1}{8} \sum_{x \in V(G)} \sum_{y \in V(G)} \deg(x) \times \deg(y) \times d(x, y) - \frac{m}{4} + \\
&\quad \sum_{\{e, f\} \in A_3} \left(\frac{1}{2}\right) + \sum_{\{e, f\} \in A_2} \left(\frac{1}{4}\right) + \sum_{\{e, f\} \in A_4} \left(\frac{3}{4}\right) + |C|. \quad (13.4)
\end{aligned}$$

*Proof* By Definition 13.2.1 and Corollary 13.2.2, we have

$$\begin{aligned}
W_{e0}(G) &= \sum_{\{e, f\} \subseteq E(G)} d_3(e, f) \\
&= \sum_{\substack{\{e, f\} \subseteq E(G) \\ \text{if } e=uv, f=xy}} \left\lceil \frac{d(u, x) + d(u, y) + d(v, x) + d(v, y)}{4} \right\rceil \\
&= \sum_{\substack{\{e, f\} \in A_1 \\ \text{if } e=uv, f=xy}} \frac{d(u, x) + d(u, y) + d(v, x) + d(v, y)}{4} \\
&\quad + \sum_{\substack{\{e, f\} \in A_3 \\ \text{if } e=uv, f=xy}} \left( \frac{d(u, x) + d(u, y) + d(v, x) + d(v, y)}{4} + \frac{1}{2} \right) \\
&\quad + \sum_{\substack{\{e, f\} \in A_2 \\ \text{if } e=uv, f=xy}} \left( \frac{d(u, x) + d(u, y) + d(v, x) + d(v, y)}{4} + \frac{1}{4} \right) \\
&\quad + \sum_{\substack{\{e, f\} \in A_4 \\ \text{if } e=uv, f=xy}} \left( \frac{d(u, x) + d(u, y) + d(v, x) + d(v, y)}{4} + \frac{3}{4} \right) \\
&\quad + \sum_{\substack{\{e, f\} \in C \\ \text{if } e=uv, f=xy}} \left( \frac{d(u, x) + d(u, y) + d(v, x) + d(v, y)}{4} + 1 \right) \\
&= \sum_{\substack{\{e, f\} \subseteq E(G) \\ \text{if } e=uv, f=xy}} \frac{d(u, x) + d(u, y) + d(v, x) + d(v, y)}{4} \\
&\quad + \sum_{\{e, f\} \in A_3} \left(\frac{1}{2}\right) + \sum_{\{e, f\} \in A_2} \left(\frac{1}{4}\right) + \sum_{\{e, f\} \in A_4} \left(\frac{3}{4}\right) + |C|
\end{aligned}$$

For each pair of vertices  $u, x \in V(G)$  such that  $u \neq x$  which are not adjacent, the distance  $d(u, x)$  in like distance  $d'$  is repeated  $\deg(u) \times \deg(x)$  times. And if every pair of vertices  $u, x \in V(G)$ ,  $u \neq x$ , is adjacent, distance  $d(u, x)$  is repeated  $\deg(u) \times \deg(x) - 1$  times. Therefore,

$$W_{e0}(G) = \frac{1}{8} \sum_{x \in V(G)} \sum_{y \in V(G)} \text{deg}(x) \times \text{deg}(y) \times d(x, y) - \frac{m}{4} + \sum_{\{e, f\} \in A_3} \left(\frac{1}{2}\right) + \sum_{\{e, f\} \in A_2} \left(\frac{1}{4}\right) + \sum_{\{e, f\} \in A_4} \left(\frac{3}{4}\right) + |C|.$$

■

Now, because of the fact that the first edge-Wiener number has been written by distances between vertices, we repeat this trend for second edge version with definition of new distance.

**Definition 13.2.4** If  $e, f \in E(G)$ , we define

$$d'''(e, f) = \begin{cases} \lceil d'(e, f) \rceil & , \{e, f\} \notin A_1 \\ d'(e, f) + 1 & , \{e, f\} \in A_1 \end{cases} \text{ and } d_5(e, f) = \begin{cases} d'''(e, f) & e \neq f \\ 0 & e = f \end{cases}.$$

The mathematical quantity  $d'''$  is not distance because it does not satisfy the condition (b). Then, we say  $d'''$  is likedistance.

**Claim**  $d_5 = d_4$ .

*Proof* We have to show for any  $e, f \in E(G)$ ,  $d_5(e, f) = d_4(e, f)$ .

- (i) If  $e = f \in E(G)$ , then  $d_5(e, f) = d_4(e, f) = 0$ .
- (ii) If  $e, f \in E(G)$  are adjacent edges, then:  
 $d_4(e, f) = d_2(e, f) = 2$  and since  $\{e, f\} \in A_1$ ,  $d_5(e, f) = d_3(e, f) + 1 = \frac{1+1+2}{4} + 1 = 2$ . Therefore,  $d_5(e, f) = d_4(e, f)$ ..
- (iii) If  $e, f \in E(G)$  are not adjacent, then we have two sub-cases:

- 1. If  $\{e, f\} \in A_1$  such as Fig. 13.1, then  
 $d_4(e, f) = d_2(e, f) = r + 2$  and  $d_5(e, f) = d_3(e, f) + 1 = \frac{r+(r+1)+(r+1)+(r+2)}{4} + 1 = r + 2$ . Therefore,  $d_5(e, f) = d_4(e, f)$ .
- 2. If  $\{e, f\} \notin A_1$ , then  
 If  $d_4(e, f) = d_2(e, f) = r$ , then  $\max \{d(x, u), d(x, v), d(y, u), d(y, v)\}$  is  $r$  and  $r$  is repeated at least two times in  $d(u, x) + d(u, y) + d(v, x) + d(v, y)$  for  $d'$ . Hence,  
 $d(i, j)$ ,  $i = u, v$  and  $j = x, y$ , takes  $r$  or  $(r - 1)$ , then  $d_5(e, f) = d_3(e, f) = \left\lceil \frac{d(u,x)+d(u,y)+d(v,x)+d(v,y)}{4} \right\rceil = r$ . Therefore,  $d_5(e, f) = d_4(e, f)$ .

■

**Corollary 13.2.5**  $W_{e4}(G) = \sum_{\{e, f\} \subseteq E(G)} d_5(e, f)$ .

**Theorem 13.2.6** Suppose  $G$  is a graph with  $m$  edges and  $A_1, A_2, A_3, A_4$  and  $C$  are the sets which have been defined in Definition 13.2.1 and Corollary 13.2.2. Then, we can repeat the second version of edge-Wiener number according to the distance between vertices of graph  $G$  as follows:

$$\begin{aligned}
 W_{e4}(G) &= \frac{1}{8} \sum_{x \in V(G)} \sum_{y \in V(G)} \deg(x) \times \deg(y) \times d(x, y) - \frac{m}{4} + \\
 &\quad \sum_{\{e,f\} \in A_3} \left(\frac{1}{2}\right) + \sum_{\{e,f\} \in A_2} \left(\frac{1}{4}\right) + \sum_{\{e,f\} \in A_4} \left(\frac{3}{4}\right) + |A_1|. \tag{13.5}
 \end{aligned}$$

*Proof* Due to the definition of  $W_{e4}(G)$  and Definition 13.2.4 and Corollary 13.2.5, we have

$$\begin{aligned}
 W_{e4}(G) &= \sum_{\{e,f\} \subseteq E(G)} d_5(e, f) = \sum_{\{e,f\} \subseteq E(G)} d'''(e, f) = \\
 &\quad \sum_{\{e,f\} \subseteq E(G)} d'(e, f) + \sum_{\{e,f\} \in A_2} \frac{1}{4} + \sum_{\{e,f\} \in A_3} \frac{2}{4} + \sum_{\{e,f\} \in A_4} \frac{3}{4} + |A_1|.
 \end{aligned}$$

For each pair of vertices  $u$  and  $x$  such that  $u \neq x$  which is not adjacent, the distance  $d(u, x)$  in like-distance  $d'$  is repeated  $\deg(u) \times \deg(x)$  times. And if every pair of vertices  $u$  and  $x$ ,  $u \neq x$ , which is adjacent, distance  $d(u, x)$  is repeated  $\deg(u) \times \deg(x) - 1$  times. Therefore,

$$\begin{aligned}
 W_{e4}(G) &= \frac{1}{8} \sum_{x \in V(G)} \sum_{y \in V(G)} \deg(x) \times \deg(y) \times d(x, y) - \frac{m}{4} + \\
 &\quad \sum_{\{e,f\} \in A_2} \frac{1}{4} + \sum_{\{e,f\} \in A_3} \frac{2}{4} + \sum_{\{e,f\} \in A_4} \frac{3}{4} + |A_1|.
 \end{aligned}$$

■

**Corollary 13.2.7** *The explicit relation between edge versions of Wiener index is*

$$W_{e4}(G) = W_{e0}(G) + |A_1| - |C|. \tag{13.6}$$

*Proof* According to the relations 13.4 and 13.5, we can get above relation easily. ■

In the following table, we bring some examples for relation 13.6 (Table 13.2):

Now, we compute the first edge-Wiener number of cycles according to our relation as follows:

**Corollary 13.2.8** *The first edge-Wiener index and its vertex version are equal for cycles.*

**Table 13.2** Some examples due to relation 13.6

Graph ( $G$ )	$W_{e0}(G)$	$ A_1 $	$ C $	$W_{e4}(G)$
$P_n$	$\frac{1}{6}n(n-1)(n-2)$	$\binom{n-1}{2} = \frac{(n-1)(n-2)}{2}$	0	$\frac{1}{6}(n-1)(n-2)(n+3)$
$S_n$	$\frac{1}{2}(n-1)(n-2)$	$\binom{n-1}{2} = \frac{(n-1)(n-2)}{2}$	0	$(n-1)(n-2)$
$C_n, n$ is odd	$\frac{1}{8}n(n^2-1)$	$\binom{n}{2} - n = \frac{n(n-3)}{2}$	0	$\frac{1}{8}n(n^2+4n-13)$
$C_n, n$ is even	$\frac{1}{8}n^3$	$\binom{n}{2} - \frac{n}{2} = \frac{n(n-2)}{2}$	0	$\frac{1}{8}n(n^2+4n-8)$

*Proof* The relation 13.3 can be stated for cycles as follows:

$$\begin{aligned}
 W_{e0}(G) &= \frac{1}{2} \sum_{x \in V(G)} \sum_{y \in V(G)} d(x, y) - \frac{m}{4} + \begin{cases} \sum_{\substack{\{e,f\} \in A_3 \\ ife=uv, f=xy}} \left(\frac{1}{2}\right), & \text{if } n \text{ is even} \\ \sum_{\substack{\{e,f\} \in A_1 \\ ife=uv, f=xy}} \left(\frac{1}{4}\right), & \text{if } n \text{ is odd} \end{cases} \\
 &= \begin{cases} W_v(G) - \frac{m}{4} + \sum_{\substack{\{e,f\} \in A_3 \\ ife=uv, f=xy}} \left(\frac{1}{2}\right), & \text{if } n \text{ is even} \\ W_v(G) - \frac{m}{4} + \sum_{\substack{\{e,f\} \in A_1 \\ ife=uv, f=xy}} \left(\frac{1}{4}\right), & \text{if } n \text{ is odd} \end{cases}
 \end{aligned}$$

The numbers of elements of  $A_3$  in even cycles is  $\frac{m}{2}$  and in odd cycles is  $m$ . Then, the first edge-Wiener number is equal to its vertex version for cycles. ■

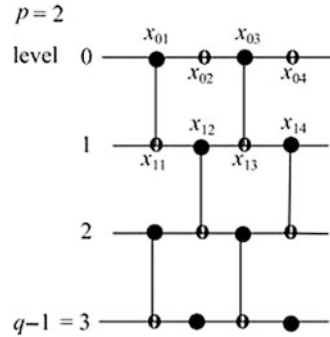
Now, we say the explicit relation of zigzag nanotube in pursue.

**Theorem 13.2.9** *The explicit relation between vertex Wiener number and the first edge-Wiener number for zigzag nanotubes which have been consisted of vertices with degrees 3 and 2 is*

$$\begin{aligned}
 W_{e0}(G) &= \frac{9}{4}W_v(G) + \frac{3}{8} \sum_{\substack{x \in V(G) \\ \deg(x)=2}} \sum_{\substack{y \in V(G) \\ \deg(y)=3}} d(x, y) \\
 &\quad - \frac{5}{8} \sum_{\substack{x \in V(G) \\ \deg(x)=2}} \sum_{\substack{y \in V(G) \\ \deg(y)=2}} d(x, y) - \frac{m}{4} + \sum_{\{e,f\} \in A_3} \frac{1}{2}. \tag{13.7}
 \end{aligned}$$

*Proof* We can get this result with replacing the degree of vertices in relation 13.4 and the fact that the sets  $A_2, A_4$  and  $C$  are empty. ■

**Fig. 13.2**  $(n, 0)$  zigzag polyhex SWNTs



The vertex version of Wiener number of zigzag nanotube is computed in John and Diudea (2004). They have focused on  $(n, 0)$  zigzag polyhex SWNTs which have  $p$  hexagons in a row and  $q$  hexagons in column. Because of their computation and relation (13.7), we state the first edge-Wiener number of zigzag nanotube such that  $p$  is even integer and  $q$  is odd integer.

They have colored the vertices with two colors white and black as shown in Fig. 13.2.

The white vertices in level 0 denote the vertices with degree 2 and the black vertices in last level denote the vertices with degree 2.

**Lemma 13.2.10** (John and Diudea 2004) *The sum of distances of one white vertex of level 0 to all vertices of level  $k$ , for  $k = 0, 1, \dots, q - 1$ , is given as:*

$$w_k = \sum_{r=1}^{2p} d(x_{02}, x_{kr}) = \sum_{r=1}^{2p} d(x_{04}, x_{kr}) = \begin{cases} (p+k)^2 + k & 0 \leq k < p \\ p(4k+1) & p \leq k \end{cases}.$$

**Lemma 13.2.11**  $\sum_{\substack{x \in V(G) \\ \text{deg}(x)=2}} \sum_{\substack{y \in V(G) \\ \text{deg}(y)=2}} d(x, y) =$

$$\begin{cases} 2p \left( 2 \sum_{i=1}^{\frac{p}{2}} 2i - p + 2 \sum_{i=1}^{\frac{q-1}{2}} (2q+1) + 2 \sum_{i=1}^{\frac{p}{2} - \frac{q-3}{2}} (2q+2i-1) \right), & q < p \\ 2p \left( 2 \sum_{i=1}^{\frac{p}{2}} 2i - p + 2 \sum_{i=1}^{\frac{p}{2}} (2q+1) \right), & p \leq q \end{cases}.$$

*Proof* Due to Fig. 13.2, we can get this result easily. ■

**Lemma 13.2.12**  $\sum_{\substack{x \in V(G) \\ \text{deg}(x)=2}} \sum_{\substack{y \in V(G) \\ \text{deg}(y)=3}} d(x, y)$  is equal to

$$2p \times \begin{cases} \sum_{k=1}^{q-1} w_k + 2 \sum_{i=1}^{\frac{p}{2}} (2i - 1) - 2 \sum_{i=1}^{\frac{q-1}{2}} (2q + 1) - 2 \sum_{i=1}^{\frac{p}{2} - \frac{q+1}{2}} (2q + i), & q < p \\ \sum_{k=1}^{q-1} w_k + 2 \sum_{i=1}^{\frac{p}{2}} (2i - 1) - 2 \sum_{i=1}^{\frac{p}{2}} (2q + 1), & p \leq q \end{cases} .$$

*Proof*  $\sum_{k=1}^{q-1} w_k$  is the sum of distances between  $x_{o2}$  and all of vertices in levels  $k = 1, \dots, q - 1$ . Then, we must reduce the distance between  $x_{o2}$  and vertices in last level with degree 2 and add the distances between vertex  $x_{o2}$  and vertices in level 0 with degree 3. Then, we can obtain the above relation. ■

**Theorem 13.2.13** (John and Diudea 2004) *The vertex-Wiener number of zigzag nanotube  $G$  which has  $p$  hexagons in a row and  $q$  hexagons in column such that  $p$  is even integer and  $q$  is odd integer is*

$$W_v(G) = \begin{cases} \frac{pq}{2} [6p^2q + (4p + q)(q^2 - 1)], & 0 < q \leq p \\ \frac{p^2}{2} [p^2(4q + p) + q(8q^2 - 6) + p], & p \leq q \end{cases} .$$

**Theorem 13.2.14** *The edge-Wiener number of zigzag nanotube  $G$  which has  $p$  hexagons in a row and  $q$  hexagons in column such that  $p$  is even integer and  $q$  is odd integer is*

$$W_{e0}(G) = \begin{cases} pq \left( \frac{9}{4}q^2p^2 + \frac{3}{4}q^2p - \frac{35}{8}p + \frac{3}{8}q^3 - \frac{11}{16}q + \frac{3}{4}p^2 + \frac{3}{4}pq + \frac{1}{4}q^2 - \frac{1}{4} \right) - \\ p \left( \frac{29}{16}p^2 - \frac{15}{4}p - \frac{55}{16} \right), & q < p \\ pq \left( \frac{3}{2}p^3 + 3pq^2 - \frac{27}{4}p + \frac{3}{2}pq + \frac{q}{2} + \frac{1}{4} \right) - p \left( \frac{3}{8}p^4 - \frac{1}{8}p^2 + \frac{11}{4}p \right), & p \leq q \end{cases}$$

*Proof* In molecular graph of zigzag nanotube, we have two types of edges. The first type is the oblique edges and the second type is vertical edges. The number of pair oblique edges which belongs to  $A_3$  is  $2p \binom{q+1}{2}$ , and the number of vertical edges which belongs to  $A_3$  is  $q \binom{p}{2}$ . Therefore, according to relation 13.7, Lemmas 13.3.4 and 13.3.5, Theorem 13.3.6, and the number of elements of  $A_1$ , the above relations are computed easily. ■

The explicit relation between first edge version and vertex version of Wiener number of nanotubes with vertex of degrees 3 and 2 has been declared in Theorem 13.2.9.

**Corollary 13.2.15** According to the relations 13.6 and 13.7, the explicit relation between vertex and the second edge-Wiener number for zigzag nanotubes which consists of vertices with degrees 3 and 2 is obtained directly:

$$\begin{aligned}
 W_{e4}(G) &= \frac{9}{4}W_v(G) + \frac{3}{8} \sum_{\substack{x \in V(G) \\ \deg(x)=2}} \sum_{y \in V(G)} d(x, y) \\
 &\quad - \sum_{\substack{x \in V(G) \\ \deg(x)=2}} \sum_{\substack{y \in V(G) \\ \deg(y)=2}} d(x, y) - \frac{m}{4} + \sum_{\{e,f\} \in A_3} \frac{1}{2} + |A_1|. \tag{13.8}
 \end{aligned}$$

**Theorem 13.2.16** The second edge-Wiener number of zigzag nanotube  $G$  which has  $p$  hexagons in a row and  $q$  hexagons in column such that  $p$  is even integer and  $q$  is odd integer is

$$\begin{aligned}
 &W_{e4}(G) \\
 &= \begin{cases} pq \left( \frac{9}{4}qp^2 + \frac{3}{4}q^2p - \frac{35}{8}p + \frac{3}{8}q^3 - \frac{11}{16}q + \frac{3}{4}p^2 + \frac{3}{4}pq + \frac{1}{4}q^2 - \frac{1}{4} \right) - \\ p \left( \frac{29}{16}p^2 - \frac{15}{4}p - \frac{55}{16} \right) + \binom{3pq + 2p}{2} - \frac{2pq^2 + qp^2 + pq}{2}, & q < p \\ \\ pq \left( \frac{3}{2}p^3 + 3pq^2 - \frac{27}{4}p + \frac{3}{2}pq + \frac{q}{2} + \frac{1}{4} \right) - p \left( \frac{3}{8}p^4 - \frac{1}{8}p^2 + \frac{11}{4}p \right) + \\ \binom{3pq + 2p}{2} - \frac{2pq^2 + qp^2 + pq}{2}, & p \leq q \end{cases}
 \end{aligned}$$

*Proof* The number of edges of zigzag nanotube with  $p$  hexagons in a row and  $q$  hexagons in column is  $3pq + 2p$ . In molecular graph of this nanotube, we have  $E(G) = A_1 \cup A_3$ , and  $|A_3| = \frac{2pq^2 + qp^2 + pq}{2}$ . Therefore, according to  $|A_1| = \binom{3pq + 2p}{2} - \frac{2pq^2 + qp^2 + pq}{2}$ ,  $W_{e4}(G)$  is computed easily by relation 13.6. ■

In this part, as the application of the above results, we compute the first edge-Wiener indices of  $TUC_4C_8(R)$  nanotube which has been published in Mahmiani, et al. (2010a).

**Corollary 13.2.17** Since there are not any odd cycles in  $TUC_4C_8(R)$  nanotube,  $A_2$  is empty. Hence for  $TUC_4C_8(R)$  nanotube, we have

$$\begin{aligned}
 W_{e0}(G) &= \frac{9}{4}W_v(G) + \frac{3}{8} \sum_{\substack{x \in V(G) \\ \deg(x)=2}} \sum_{y \in V(G)} d(x, y) \\
 &\quad - \sum_{\substack{x \in V(G) \\ \deg(x)=2}} \sum_{\substack{y \in V(G) \\ \deg(y)=2}} d(x, y) - \frac{m}{4} + \sum_{\{e,f\} \in A_3} \frac{1}{2} \tag{13.9}
 \end{aligned}$$

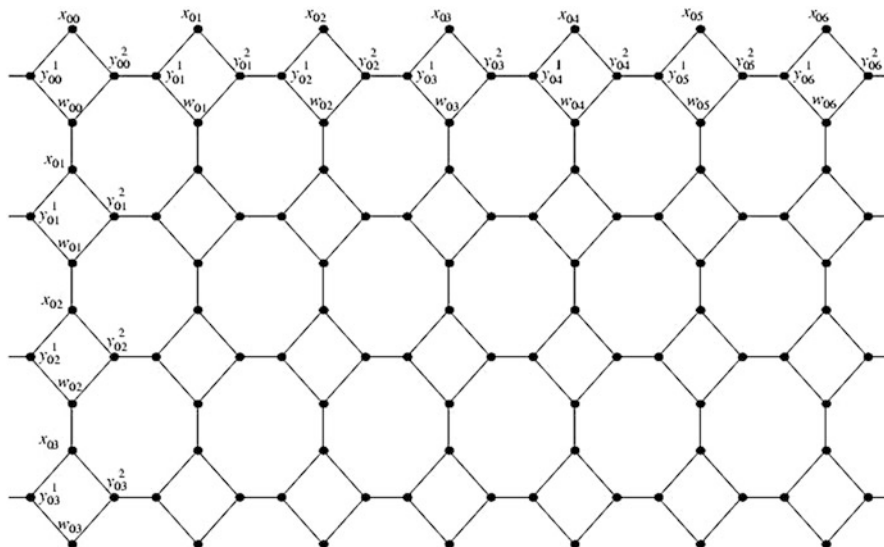


Fig. 13.3 A  $T(p,q)$  lattice with  $p = 7$  and  $q = 4$

Abbas Heydari and Bijan Taeri in (2007a) computed the vertex-Wiener index  $W_v(G)$  and  $\sum_{\substack{x \in V(G) \\ \deg(x)=2}} \sum_{y \in V(G)} d(x, y)$ .

We mention only the quantity of them in this part and omit details.

We denote  $TUC_4C_8(R)$  nanotube with  $T(p,q)$  where  $p$  is the number of squares in a row and  $q$  is the number of squares in a column. Also, we assumed  $P_1 = \left\lceil \frac{p+1}{2} \right\rceil$  and opted below coordinate label for vertices of  $T(p, q)$  as shown in Fig. 13.3.

**Lemma 13.2.18** (Heydari and Taeri 2007a)  $\sum_{\substack{x \in V(G) \\ \deg(x)=2}} \sum_{y \in V(G)} d(x, y) = 2pS_x(q - 1)$ ,

where

$$S_x(l) = \sum_{k=0}^l T_x(k) = \begin{cases} \frac{8}{3}l^3 + (2p + 8)l^2 + (3p^2 + 2p)l + \left(\frac{19}{3} + \frac{1 + (-1)^p}{2}\right)l + 3p^2 + 1 + \frac{1 + (-1)^p}{2}, & l < P_1 \\ 6pl^2 + \left(p^2 + 10p - \frac{1 - (-1)^p}{2}\right)l + \frac{1}{3}p^3 + p^2 + \frac{11}{3}p - + \frac{1 - (-1)^p}{2}, & l \geq P_1 \end{cases}$$



$$\text{and } T_x(k) = \begin{cases} 3p^2 + 4kp + 8k^2 + 8k - 1 + \\ 3 \frac{1 + (-1)^p}{2}, & 0 \leq k < P_1 \\ p^2 + 12kp + 4p - 1 + \\ \frac{1 + (-1)^p}{2}, & k \geq P_1 \end{cases}.$$

**Theorem 13.2.19** (Heydari and Taeri 2007a) *The Wiener index of  $T(p,q)$  is given by the following equation:*

$$W_v(p, q) = \begin{cases} \frac{pq}{3} \left( 8q^3 + 8pq^2 + \left( 18p^2 - 5 + 3 \frac{1+(-1)^p}{2} \right) q - 8p \right), & q < P_1 \\ \frac{p}{6} \left( -p^4 + 8qp^3 + \left( 12q^2 + 1 - \frac{1 - (-1)^p}{2} \right) p^2 \right) + \\ \frac{p^2}{6} (48q^3 - (14 + 3(1 + (-1)^p)) q) + \\ \left( 1 - \frac{1 + (-1)^p}{2} \right) \left( \frac{3}{2} - 12q^2 \right), & q \geq P_1 \end{cases}$$

**Lemma 13.2.20** *Summation*  $\sum_{\substack{x \in V(G) \\ \deg(x)=2}} \sum_{\substack{y \in V(G) \\ \deg(y)=2}} d(x, y)$  is equal to in  $T(p,q)$ :

If  $p$  is even:

$$\sum_{\substack{x \in V(G) \\ \deg(x)=2}} \sum_{\substack{y \in V(G) \\ \deg(y)=2}} d(x, y) = \begin{cases} 7q^2 - 7q + 4pq + p^2 - 2p + 1, & q < P_1 \\ 3pq + p^2 - 2p - 3q + 1, & q \geq P_1 \end{cases}$$

If  $p$  is odd:

$$\sum_{\substack{x \in V(G) \\ \deg(x)=2}} \sum_{\substack{y \in V(G) \\ \deg(y)=2}} d(x, y) = \begin{cases} 7q^2 + q + 4pq + p^2 - p - 2, & q < P_1 \\ 3pq + p^2 - p + 3q - 2, & q \geq P_1 \end{cases}$$

*Proof* There exist two types of vertices with degree 2. One of them is in the first row and another is in the last row (Fig. 13.3).

Since the situation of all vertices with degree 2 is the same, we can suppose a fix vertex  $x$  in first row. Then, we have for the first type

$$\sum_{\substack{y \in V(T(p,q)) \\ y \text{ is in the first row} \\ \deg(y)=2}} d(x, y) = \begin{cases} 2 \sum_{i=1}^{\frac{p}{2}} 3i - \frac{3p}{2}, & p \text{ is even} \\ 2 \sum_{i=1}^{\frac{p-1}{2}} 3i, & p \text{ is odd} \end{cases}$$

And we have for the second type:

(a)  $p$  is even:

$$\sum_{\substack{y \in V(T(p,q)) \\ y \text{ is in the last row} \\ \deg(y)=2}} d(x, y) = \begin{cases} 2 \sum_{i=0}^{q-1} (3q - 1 + i) + 2 \sum_{i=0}^{\frac{p}{2}-1} (4q - 1 + i) - (4q + \frac{p}{2} - 1), & q < P_1 \\ 2 \sum_{i=0}^{\frac{p}{2}-1} (3q - 1 + i) - (3q + \frac{p}{2} - 1), & q \geq P_1 \end{cases}$$

(b)  $p$  is odd:

$$\sum_{\substack{y \in V(T(p,q)) \\ y \text{ is in the last row} \\ \deg(y)=2}} d(x, y) = \begin{cases} 2 \sum_{i=0}^{q-1} (3q - 1 + i) + 2 \sum_{i=0}^{\frac{p+1}{2}-1} (4q - 1 + i), & q < P_1 \\ 2 \sum_{i=0}^{\frac{p+1}{2}-1} (3q - 1 + i), & q \geq P_1 \end{cases}$$

Therefore, we can obtain the desired results.

**Observation 13.2.21** The number of elements of  $A_1$  is equal to:  $(q - 1) \binom{p}{2} + p \binom{q}{2} + 2p \binom{2q}{2}$ .

By the above lemmas, Theorem 13.2.19, Observation 13.2.21 and the fact that the number of edges in  $T(p, q)$  are  $6pq - p$ , the following theorem can be proved:

**Theorem 13.2.22** The first version of edge-Wiener index of  $T(p, q)$  is equal to:

1. If  $p$  is even:

$$W_{e0}(T(p, q)) = \begin{cases} -\frac{39}{2}p + 2pq^3 + 6p^2q^4 + \frac{9}{8}pq^2(-1)^p + \frac{3}{8}pq(-1)^p + \frac{27}{2}p^3q^2 + 6pq^5 + \frac{81}{8}pq + \frac{15}{4}p^2 - \frac{115}{8}pq^2 - \frac{37}{4}p^2q + \frac{9}{4}p^3q - 2p^3 + \frac{3}{2}p^2q^2, & q < P_1 \\ -\frac{3}{2}p - \frac{27}{2}q^2 + \frac{3}{8}pq(-1)^p + \frac{9}{2}p^3q^2 + \frac{21}{8}pq + \frac{1}{2}p^2 + \frac{9}{8}p^2q(-1)^{p+1} + \frac{27}{16}(-1)^{p+1} + \frac{27}{16} - \frac{3}{8}p^5 + \frac{1}{4}p^4 + \frac{9}{4}pq^2 - \frac{85}{8}p^2q + \frac{3}{4}p^3q - \frac{29}{16}p^3 + \frac{3}{16}p^3(-1)^p + 18p^2q^3 + 27q^2(-1)^p + \frac{9}{2}p^2q^2, & q \geq P_1 \end{cases}$$

2. If  $p$  is odd:

$$W_{e_0}(T(p, q)) = \begin{cases} \begin{aligned} &-\frac{27}{2}p + 2pq^3 + 6p^2q^4 + \frac{9}{8}pq^2(-1)^p + \\ &\frac{3}{8}pq(-1)^p + \frac{27}{2}p^3q^2 + 6pq^5 - \\ &\frac{47}{8}pq + \frac{7}{4}p^2 - \frac{115}{8}pq^2 - \frac{37}{4}p^2q + \\ &\frac{9}{4}p^3q - 2p^3 + \frac{3}{2}p^2q^2, \end{aligned} & q < P_1 \\ \begin{aligned} &\frac{9}{2}p - \frac{27}{2}q^2 + \frac{3}{8}pq(-1)^p + \frac{9}{2}p^3q^2 - \\ &\frac{75}{8}pq + \frac{3}{2}p^2 + \frac{9}{8}p^2q(-1)^{p+1} + \\ &\frac{27}{16}(-1)^{p+1} + \frac{27}{16} - \frac{3}{8}p^5 + \frac{1}{4}p^4 + \\ &\frac{9}{4}pq^2 - \frac{85}{8}p^2q + \frac{3}{4}p^3q - \frac{29}{16}p^3 + \\ &\frac{3}{16}p^3(-1)^p + 18p^2q^3 + 27q^2(-1)^p + \\ &\frac{9}{2}p^2q^2, \end{aligned} & q \geq P_1 \end{cases} .$$

Now, we computed the first and the second edge-Wiener indices of  $TUC_4C_8(S)$  nanotube.

All of the following results have been published in Mahmiani, et al. (2010b).

Due to the fact that, there are no odd cycles in  $TUC_4C_8(S)$  nanotube,  $A_2$  is empty. Then, we have for  $TUC_4C_8(S)$  nanotube, the relation 13.9.

**Corollary 13.2.23** *According to the relations 13.6 and 13.7, the explicit relation between vertex and first edge-Wiener number for  $TUC_4C_8(S)$  nanotubes which consists of vertices with degrees 3 and 2 is*

$$W_{e_4}(G) = \frac{9}{4}W_v(G) + \frac{3}{8} \sum_{\substack{x \in V(G) \\ \deg(x)=2}} \sum_{y \in V(G)} d(x, y) - \sum_{\substack{x \in V(G) \\ \deg(x)=2}} \sum_{\substack{y \in V(G) \\ \deg(y)=2}} d(x, y) - \frac{m}{4} + \sum_{\{e, f\} \in A_3} \frac{1}{2} + |A_1|. \tag{13.10}$$

The explicit relation between edge versions of Wiener index is:

$$W_{e_4}(G) = W_{e_0}(G) + |A_1| - |C| \tag{13.11}$$

In  $TUC_4C_8(S)$  nanotube,  $p$  is the number of square in a row and  $q$  is the number of rows which is shown in Fig. 13.4.

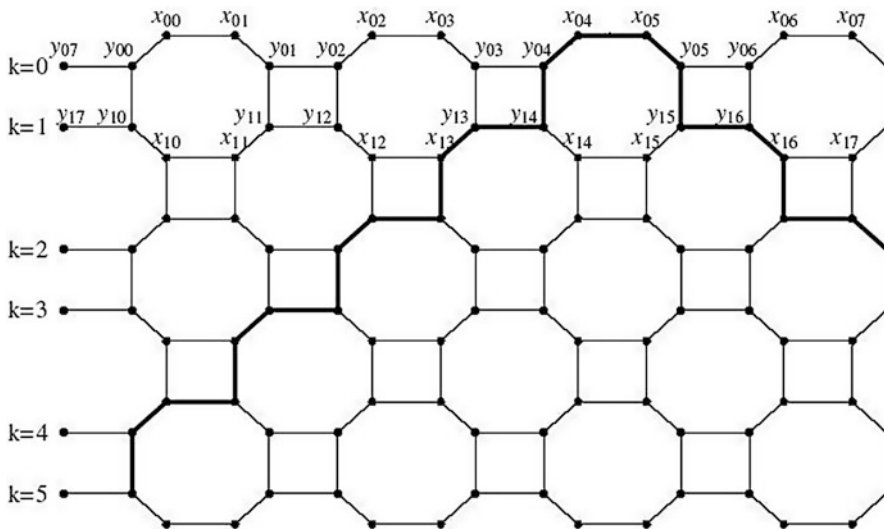


Fig. 13.4 A  $TUC_4C_8(S)$  lattice with  $p = 4$  and  $q = 6$

In Heydari and Taeri (2007b), some notations are defined as follows. For all  $0 \leq r < q$  and  $0 \leq t < 2p$ , let  $a_{rt} \in \{x_{rt}, y_{rt}\}$  and let  $d_{a_{rt}}(k)$  denote the sum of distances between  $a_{rt}$  and vertices on  $k$ -th row of the graph. By symmetry of the graph for all  $0 \leq t < 2p$ ,  $d_{x_{rt}}(k)$  equal. So we may compute this summation for  $x_{0p}$  in the 0th row of the graph, which is denoted by  $d_x(k)$ .

**Lemma 13.2.24** (Heydari and Taeri 2007b) *Let  $0 \leq k < q$ , then  $d_x(k) =$*

$$\begin{cases} 4p^2 + 4kp + 2(k^2 + k), & k \leq p \\ 2p^2 + 8kp + 2p, & k > p \end{cases}$$

Therefore, according to the Lemma 13.2.24, we can obtain  $\sum_{\substack{x \in V(G) \\ \deg(x)=2}} \sum_{y \in V(G)} d(x, y)$ .

**Lemma 13.2.25**

$$\sum_{\substack{x \in V(G) \\ \deg(x)=2}} \sum_{y \in V(G)} d(x, y) = \begin{cases} \frac{8}{3}pq(6p^2 + 3pq - 3p + q^2 - 1), & q \leq p \\ 8p^2q(p + 2q - 1), & q > p \end{cases}$$

*Proof* Due to the Lemma 13.2.24,  $d_{x_{0p}}(k)$  denotes the sum of distances between  $x_{0p}$  and vertices on  $k$ -th row of the graph. There are  $4p$  vertices such as  $x_{0p}$  in the first row. Therefore,

$$\sum_{\substack{x \in V(G) \\ \deg(x)=2}} \sum_{y \in V(G)} d(x, y) = 4p \sum_{k=0}^{q-1} d_x(k) = \begin{cases} \frac{8}{3}pq(6p^2 + 3pq - 3p + q^2 - 1), & q \leq p \\ 8p^2q(p + 2q - 1), & q > p \end{cases}$$

■

The vertex-Wiener index of  $TUC_4C_8(S)$  is computed in Heydari and Taeri (2007b). We state only the main result as a theorem as follows:

**Theorem 13.2.26** (Heydari and Taeri 2007b) *The Wiener index of  $TUC_4C_8(S) = G$  is given by the following equation:*

$$W_v(G) = \begin{cases} \frac{pq}{3}(2q^3 + 8pq(3p + q) - 2q - 8p), & q \leq p \\ \frac{p^2}{3}(-2p^3 + 8qp^2 + (12q^2 + 2)p + 16q^3 - 12q) +, & q > p \end{cases}$$

**Lemma 13.2.27** *Let  $TUC_4C_8(S) = G$ . Then,*

*If  $p$  is even:*

$$\sum_{\substack{x \in V(G) \\ \deg(x)=2}} \sum_{\substack{y \in V(G) \\ \deg(y)=2}} d(x, y) = \begin{cases} q^2 + 2q + 2pq + 4p^2 - p - 2 - 2 \left[ \frac{2p - 2q + 1}{4} \right], & q \leq p \\ 4pq + 3p^2 - 2p - 1, & q > p \end{cases}$$

*If  $p$  is odd:*

$$\sum_{\substack{x \in V(G) \\ \deg(x)=2}} \sum_{\substack{y \in V(G) \\ \deg(y)=2}} d(x, y) = \begin{cases} q^2 + q + 2pq + 2p^2 - 3p + 8 \left[ \frac{p}{2} \right] + 8 \left[ \frac{p}{2} \right]^2 - 2 \left[ \frac{2p - 2q + 1}{4} \right], & q \leq p \\ 4pq + p^2 - 2p + 8 \left[ \frac{p}{2} \right] + 8 \left[ \frac{p}{2} \right]^2, & q > p \end{cases}$$

*Proof* There exist two groups of vertices which have degree 2. One group is vertices in the first row and another is the vertices in the last row.

Due to the fact that the situation of all vertices with degree 2 is the same, we suppose the fix vertex  $x$  is in first row. Then, we have for the first group:

$$\sum_{\substack{y \in V(T(p,q)) \\ y \text{ is in first row} \\ \deg(y)=2}} d(x, y) = \begin{cases} \left( \sum_{k=0}^{\frac{p-2}{2}} (16k + 16) \right) - (4p + 1), & p \text{ is even} \\ \sum_{k=0}^{\lfloor \frac{p-2}{2} \rfloor} (16k + 16), & p \text{ is odd} \end{cases}$$

And we have for the second group:

(a)  $p$  is even:

$$\sum_{\substack{y \in V(T(p,q)) \\ y \text{ is in last row} \\ \deg(y)=2}} d(x, y) = \begin{cases} \sum_{i=2q}^{3q-1} (2i) + \sum_{i=3q-1}^{2p+q-1} (i) - 2 \left( \left\lfloor \frac{2p-2q-3}{4} \right\rfloor + 1 \right) - q, & q \leq p \\ \sum_{i=2q}^{2q+p-1} (2i) - p, & q > p \end{cases}$$

(b)  $p$  is odd:

$$\sum_{\substack{y \in V(T(p,q)) \\ y \text{ is in last row} \\ \deg(y)=2}} d(x, y) = \begin{cases} \sum_{i=2q}^{3q-1} (2i) + \sum_{i=3q-1}^{2p+q-1} (i) - 2 \left\lfloor \frac{2p-2q-4}{4} \right\rfloor - 2p - 2q - 3, & q \leq p \\ \sum_{i=2q}^{2q+p-1} (2i) - p, & q > p \end{cases}$$

Therefore, we can get results with the above summations. ■

**Observation 13.2.28** The number of elements of  $A_3$  is equal to:  $4p \binom{q}{2} + (q-1) \binom{2p}{2}$ .

Due to the fact that the number of edges in  $TUC_4C_8(S)$  is  $6pq - 2p$ , we state the first edge-Wiener index of  $TUC_4C_8(S)$ .

**Theorem 13.2.29** *The first version of edge-Wiener index of  $TUC_4C_8(S) = G$  is equal to:*

1. *If  $p$  is even:*

$$W_{e0}(T(p, q)) = \begin{cases} \frac{3}{2}pq^4 + 18p^3q^2 + 6p^2q^3 - \frac{pq^2}{2} - 8p^2q + 6p^3q + 3p^2q^2 - 6pq + pq^3 - \\ q^2 - 2q - 5p^2 + 2p + 2 + 2\left[\frac{2p - 2q + 1}{4}\right], & q \leq p \\ \frac{15}{2}p^5 + 6p^4q + \frac{3p^3}{2} + 12p^2q^3 - 11p^2q + 3p^3q + 6p^2q^2 - 7pq - 4p^2 + \\ 3p + pq^2 + 1, & q > p \end{cases}$$

2. *If  $p$  is odd:*

$$W_{e0}(T(p, q)) = \begin{cases} \frac{3}{2}pq^4 + 18p^3q^2 + 6p^2q^3 - \frac{pq^2}{2} - 8p^2q + 6p^3q + 3p^2q^2 - 6pq + pq^3 - \\ q^2 - q - 3p^2 + 2\left[\frac{2p - 2q + 1}{4}\right] - 8\left[\frac{p}{2}\right] - 8\left[\frac{p}{2}\right]^2, & q \leq p \\ \frac{15}{2}p^5 + 6p^4q + \frac{3p^3}{2} + 12p^2q^3 - 11p^2q + 3p^3q + 6p^2q^2 - 7pq - 2p^2 + \\ 3p + pq^2 - 8\left[\frac{p}{2}\right] - 8\left[\frac{p}{2}\right]^2, & q > p \end{cases}$$

*Proof* According to Lemmas 13.2.25 and 13.2.27, Theorem 13.2.26 and observation 13.2.28, we can conclude these results easily. ■

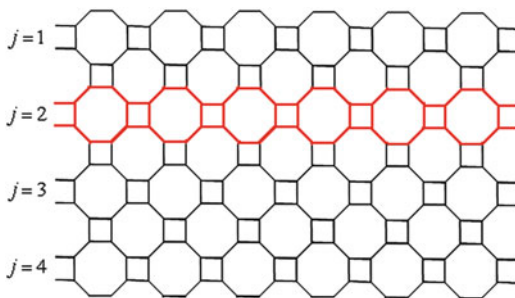
Now, In this part, we compute the second edge-Wiener index of  $TUC_4C_8(S)$ .

**Theorem 13.2.30** *The second version of edge-Wiener index of  $TUC_4C_8(S) = G$  where  $p$  is the number of squares in a row and  $q$  is the number of rows is equal to:*

1. *If  $p$  is even, then*

$$W_{e0}(T(p, q)) = \begin{cases} \frac{3}{2}pq^4 + 18p^3q^2 + 6p^2q^3 - \frac{pq^2}{2} - 22p^2q + 6p^3q + 21p^2q^2 - 6pq + pq^3 - \\ 2pq^2 - q^2 - 2q - p^2 + 2p + 2 + 2\left[\frac{2p - 2q + 1}{4}\right], & q \leq p \\ \frac{15}{2}p^5 + 6p^4q + \frac{3p^3}{2} + 12p^2q^3 - 25p^2q + 3p^3q + 24p^2q^2 - 7pq + \\ 3p - pq^2 + 1, & q > p \end{cases}$$

**Fig. 13.5**  $T(6, 4)$  nanotube with  $1 \leq j \leq 4$  periods



2. If  $p$  is odd, then

$$W_{e0}(T(p, q)) = \begin{cases} \frac{3}{2}pq^4 + 18p^3q^2 + 6p^2q^3 - \frac{pq^2}{2} - 22p^2q + 6p^3q + 21p^2q^2 - 6pq + pq^3 - \\ 2pq^2 - q^2 - q + p^2 + 2\left[\frac{2p-2q+1}{4}\right] - 8\left[\frac{p}{2}\right] - 8\left[\frac{p}{2}\right]^2, & q \leq p \\ \frac{15}{2}p^5 + 6p^4q + \frac{3p^3}{2} + 12p^2q^3 - 25p^2q + 3p^3q + 24p^2q^2 - 7pq + 2p^2 + \\ 3p - pq^2 - 8\left[\frac{p}{2}\right] - 8\left[\frac{p}{2}\right]^2, & q > p \end{cases}$$

*Proof* The number of edges of  $TUC_4C_8(S)$  nanotube with  $p$  squares in a row and  $q$  rows is  $6pq - 2p$ . In molecular graph of this nanotube, we have  $E(G) = A_1 \cup A_3$  and

$$|A_3| = 4p \binom{q}{2} + (q - 1) \binom{2p}{2}.$$

Therefore, according to reference Heydari and Taeri (2007a, b) and  $|A_1| = 18p^2q^2 - 14p^2q + 4p^2 - 2pq^2$ ,  $W_{e4}(G)$  is computed easily. ■

In the above, we computed the first edge-Wiener index of  $TUC_4C_8(S)$  nanotube by the result obtained in Iranmanesh and Khormali (2011). But, in Iranmanesh and Kafrani (2009), we computed this index with a different method. The base of this method is according to the definition of eight sets as follows:

Let  $T(p, q) = TUC_4C_8(S)$  where  $p$  is denoted the number of octagonal in rows and  $q$  is the number of octagons in columns. We consider  $j$  periods, where  $1 \leq j \leq q$ , for this nanotube that each period has an upper row and a lower row. For example in Fig. 13.5, we show  $T(6, 4)$  nanotube.



Suppose  $e \in E(G)$ . Set

$$A_u = \bigcup_{j=1}^q \{e \in E(G) \mid e \text{ is an edge over octagones in upper row of } j - \text{th period}\}$$

$$A_d = \bigcup_{j=1}^q \{e \in E(G) \mid e \text{ is an edge over squares in lower row of } j - \text{th period}\}$$

$$B_u = \bigcup_{j=1}^q \{e \in E(G) \mid e \text{ is an edge under octagones in upper row of } j - \text{th period}\}$$

$$B_d = \bigcup_{j=1}^q \{e \in E(G) \mid e \text{ is an edge under squares in lower row of } j - \text{th period}\}$$

$$C_u = \bigcup_{j=1}^q \{e \in E(G) \mid e \text{ is an oblique edge in upper row of } j - \text{th period}\}$$

$$C_d = \bigcup_{j=1}^q \{e \in E(G) \mid e \text{ is an oblique edge in lower row of } j - \text{th period}\}$$

$$D = \bigcup_{j=1}^q \{e \in E(G) \mid e \text{ is a vertical edge that located between upper and lower rows}\}$$

$$E = \bigcup_{j=1}^{q-1} \{e \in E(G) \mid e \text{ is vertical edge that located between } j - \text{th period and } j + 1 - \text{th period}\}$$

So we have

$$W_{e0}(G) = W_{e0}(A_u, G) + W_{e0}(A_d, G) + W_{e0}(B_u, G) + W_{e0}(B_d, G) + W_{e0}(C_u, G) + W_{e0}(C_d, G) + W_{e0}(D, G) + W_{e0}(E, G)$$

For compute the first edge index of  $TUC_4C_8(S)$  nanotube, we obtained this index in three cases:  $q < \lfloor \frac{p}{2} \rfloor + 1$ ,  $q = \lfloor \frac{p}{2} \rfloor + 1$ , and  $q > \lfloor \frac{p}{2} \rfloor + 1$  any by six theorems we could obtain the first edge-Wiener index of  $TUC_4C_8(S)$  nanotube.

### 13.3 Computation of the First Edge-Wiener Index of the Composition of Graphs

In this section, we find the first edge-Wiener index of the composition of graphs. All of the results in this section have been published in Azari et al. (2010).

We denote by  $[u, v]$  the edge connecting the vertices  $u, v$  of  $G$ , and the degree of a vertex  $u$  is the number of edges incident to  $u$  and denoted by  $\text{deg}(u|G)$ .

The Zagreb indices have been defined more than 30 years ago by Gutman and Trinajestic (1972):

**Definition 13.3.1** The first Zagreb index of  $G$  is defined as  $M_1(G) = \sum_{u \in V(G)} \text{deg}(u|G)^2$ .

Let us recall the definition of the composition of two graphs.

**Definition 13.3.2** Let  $G_1 = (V(G_1), E(G_1))$  and  $G_2 = (V(G_2), E(G_2))$  be two connected graphs. We denote the composition of  $G_1$  and  $G_2$  by  $G_1[G_2]$ , that is a graph with the vertex set  $V(G_1[G_2]) = V(G_1) \times V(G_2)$  and two vertices  $(u_1, u_2)$  and  $(v_1, v_2)$  of  $G_1[G_2]$  are adjacent if and only if:  $[u_1, v_1] \in E(G_1)$  and  $[u_2, v_2] \in E(G_2)$  or  $[u_1, v_1] \in E(G_1)$ .

By definition of the composition, the distance between every pair of distinct vertices  $u = (u_1, u_2)$  and  $v = (v_1, v_2)$  of  $G_1[G_2]$  is equal to

$$d(u, v|G_1[G_2]) = \begin{cases} d(u_1, v_1|G_1) & \text{if } u_1 \neq v_1 \\ 1 & \text{if } u_1 = v_1, [u_2, v_2] \in E(G_2) \\ 2 & \text{if } u_1 = v_1, v_2 \text{ is not adjacent to } u_2 \text{ in } G_2 \end{cases}$$

Consider the sets  $E_1$  and  $E_2$  as follows:

$$E_1 = \{[(u_1, u_2), (u_1, v_2)] \in E(G_1[G_2]) : u_1 \in V(G_1), [u_2, v_2] \in E(G_2)\}$$

$$E_2 = \{[(u_1, u_2), (v_1, v_2)] \in E(G_1[G_2]) : [u_1, v_1] \in E(G_1), u_2, v_2 \in V(G_2)\}$$

By definition of the composition,  $E_1 \cup E_2 = E(G_1[G_2])$  and obviously,  $E_1 \cap E_2 = \emptyset, |E_1| = |V(G_1)| |E(G_2)|$  and  $|E_2| = |V(G_2)|^2 |E(G_1)|$ .

Set

$$A = \{\{e, f\} \subseteq E(G_1[G_2]) : e \neq f, e, f \in E_1\}$$

$$B = \{\{e, f\} \subseteq E(G_1[G_2]) : e \neq f, e, f \in E_2\}$$

$$C = \{\{e, f\} \subseteq E(G_1[G_2]) : e \in E_1, f \in E_2\}$$

It is easy to see that each pair of the above sets is disjoint and the union of them is the set of all two element subsets of  $E(G_1[G_2])$ . Also we have  $|A| = \binom{|E_1|}{2} = \binom{|V(G_1)| |E(G_2)|}{2}, |B| = \binom{|E_2|}{2} = \binom{|V(G_2)|^2 |E(G_1)|}{2}, |C| = |E_1| |E_2| = |V(G_1)| |V(G_2)|^2 |E(G_1)| |E(G_2)|$

Consider four subsets  $A_1, A_2, A_3$  and  $A_4$  of the set  $A$  as follows:

$$A_1 = \{\{e, f\} \in A : e = [(u_1, u_2), (u_1, v_2)], f = [(u_1, u_2), (u_1, z_2)], u_1 \in V(G_1), \\ u_2, v_2, z_2 \in V(G_2)\}$$

$$A_2 = \{\{e, f\} \in A : e = [(u_1, u_2), (u_1, v_2)], f = [(u_1, z_2), (u_1, t_2)], u_1 \in V(G_1), \\ u_2, v_2, z_2, t_2 \in V(G_2), \text{ both } z_2 \text{ and } t_2 \text{ are adjacent neither to } u_2 \text{ nor to } v_2 \\ \text{ in } G_2\}$$

$$A_3 = \{\{e, f\} \in A : e = [(u_1, u_2), (u_1, v_2)], f = [(u_1, z_2), (u_1, t_2)], u_1 \in V(G_1), \\ u_2, v_2 \in V(G_2), z_2, t_2 \in V(G_2) - \{u_2, v_2\}\} - A_2$$

$$A_4 = \{\{e, f\} \in A : e = [(u_1, u_2), (u_1, v_2)], f = [(v_1, z_2), (v_1, t_2)], u_1, v_1 \in V(G_1), \\ v_1 \neq u_1, u_2, v_2, z_2, t_2 \in V(G_2)\}$$

It is clear that every pair of the above sets is disjoint and  $A = \bigcup_{i=1}^4 A_i$ .

In the next proposition, we characterize  $d_0(e, f | G_1 [G_2])$  for all  $\{e, f\} \in A$ .

**Proposition 13.3.3** *Let  $\{e, f\} \in A$ .*

- (i) *If  $\{e, f\} \in A_1$ , then  $d_0(e, f | G_1 [G_2]) = 1$*
- (ii) *If  $\{e, f\} \in A_2$ , then  $d_0(e, f | G_1 [G_2]) = 3$*
- (iii) *If  $\{e, f\} \in A_3$ , then  $d_0(e, f | G_1 [G_2]) = 2$*
- (iv) *If  $\{e, f\} \in A_4$ , then  $d_0(e, f | G_1 [G_2]) = 1 + d(u_1, v_1 | G_1)$ ,*

$$\text{where } e = [(u_1, u_2), (u_1, v_2)], f = [(v_1, z_2), (v_1, t_2)]$$

*Proof*

- (i) Let  $\{e, f\} \in A_1$  and  $e = [(u_1, u_2), (u_1, v_2)], f = [(u_1, u_2), (u_1, z_2)]$ . Due to the distance between two vertices in  $G_1 [G_2]$  and by definition of  $d_0(e, f)$ , we have

$$\begin{aligned} d_0(e, f | G_1 [G_2]) &= 1 + \min \{d((u_1, u_2), (u_1, u_2) | G_1 [G_2]), \\ &\quad d((u_1, u_2), (u_1, z_2) | G_1 [G_2]), \\ &\quad d((u_1, v_2), (u_1, u_2) | G_1 [G_2]), d((u_1, v_2), (u_1, z_2) | G_1 [G_2])\} \\ &= 1 + \min \{0, 1, 1, d(v_2, z_2 | G_2)\} = 1 + 0 = 1. \end{aligned}$$

- (ii) Let  $\{e, f\} \in A_2$  and  $e = [(u_1, u_2), (u_1, v_2)], f = [(u_1, z_2), (u_1, t_2)]$ . By definition of the set  $A_2$ ,  $z_2$  is adjacent neither to  $u_2$  nor to  $v_2$  in  $G_2$  and this is also true for  $t_2$ . Therefore,

$$\begin{aligned}
 d_0(e, f | G_1 [G_2]) &= 1 + \min \{d((u_1, u_2), (u_1, z_2) | G_1 [G_2]), \\
 &\quad d((u_1, u_2), (u_1, t_2) | G_1 [G_2]), \\
 &\quad d((u_1, v_2), (u_1, z_2) | G_1 [G_2]), d((u_1, v_2), (u_1, t_2) | G_1 [G_2])\} \\
 &= 1 + \min \{2, 2, 2, 2\} = 3.
 \end{aligned}$$

- (iii) Let  $\{e, f\} \in A_3$  and  $e = [(u_1, u_2), (u_1, v_2)]$ ,  $f = [(u_1, z_2), (u_1, t_2)]$ . By definition of the set  $A_3$ ,  $z_2 \notin \{u_2, v_2\}$ ,  $t_2 \notin \{u_2, v_2\}$ . On the other hand  $\{e, f\} \notin A_2$ , so at least one of the following situations occurs:

$$[u_2, z_2] \in E(G_2), [u_2, t_2] \in E(G_2), [v_2, z_2] \in E(G_2) \text{ or } [v_2, t_2] \in E(G_2).$$

This means that at least one of the distances  $d((u_1, u_2), (u_1, z_2) | G_1 [G_2])$ ,  $d((u_1, u_2), (u_1, t_2) | G_1 [G_2])$ ,  $d((u_1, v_2), (u_1, z_2) | G_1 [G_2])$  or  $d((u_1, v_2), (u_1, t_2) | G_1 [G_2])$  is equal to 1. Therefore,

$$\begin{aligned}
 d_0(e, f | G_1 [G_2]) &= 1 + \min \{d((u_1, u_2), (u_1, z_2) | G_1 [G_2]), \\
 &\quad d((u_1, u_2), (u_1, t_2) | G_1 [G_2]), \\
 &\quad d((u_1, v_2), (u_1, z_2) | G_1 [G_2]), d((u_1, v_2), (u_1, t_2) | G_1 [G_2])\} = 1 + 1 = 2.
 \end{aligned}$$

- (iv) Let  $\{e, f\} \in A_4$  and  $e = [(u_1, u_2), (u_1, v_2)]$ ,  $f = [(v_1, z_2), (v_1, t_2)]$ . Thus  $v_1 \neq u_1$  and

$$\begin{aligned}
 d_0(e, f | G_1 [G_2]) &= 1 + \min \{d((u_1, u_2), (v_1, z_2) | G_1 [G_2]), \\
 &\quad d((u_1, u_2), (v_1, t_2) | G_1 [G_2]), \\
 &\quad d((u_1, v_2), (v_1, z_2) | G_1 [G_2]), d((u_1, v_2), (v_1, t_2) | G_1 [G_2])\} = \\
 &= 1 + \min \{d(u_1, v_1 | G_1), d(u_1, v_1 | G_1), d(u_1, v_1 | G_1), \\
 &\quad d(u_1, v_1 | G_1)\} = 1 + d(u_1, v_1 | G_1),
 \end{aligned}$$

so the proof is completed. ■

In the following, we define five subsets  $B_1, B_2, B_3, B_4$  and  $B_5$  of the set  $B$ .

$$\begin{aligned}
 B_1 &= \{\{e, f\} \in B : e = [(u_1, u_2), (v_1, v_2)], f = [(u_1, u_2), (v_1, z_2)], \\
 &\quad u_1, v_1 \in V(G_1), u_2, v_2, z_2 \in V(G_2)\}
 \end{aligned}$$

$$\begin{aligned}
 B_2 &= \{\{e, f\} \in B : e = [(u_1, u_2), (v_1, v_2)], f = [(u_1, z_2), (v_1, t_2)], \\
 &\quad u_1, v_1 \in V(G_1), u_2, v_2, z_2, t_2 \in V(G_2), z_2 \neq u_2, t_2 \neq v_2\}
 \end{aligned}$$

$$\begin{aligned}
 B_3 &= \{\{e, f\} \in B : e = [(u_1, u_2), (v_1, v_2)], f = [(u_1, u_2), (z_1, z_2)], \\
 &\quad u_1, v_1, z_1 \in V(G_1), u_2, v_2, z_2 \in V(G_2), z_1 \neq v_1\}
 \end{aligned}$$

$$\begin{aligned}
 B_4 &= \{ \{e, f\} \in B : e = [(u_1, u_2), (v_1, v_2)], f = [(u_1, t_2), (z_1, z_2)], \\
 &\quad u_1, v_1, z_1 \in V(G_1), u_2, v_2, t_2, z_2 \in V(G_2), z_1 \neq v_1, t_2 \neq u_2 \} \\
 B_5 &= \{ \{e, f\} \in B : e = [(u_1, u_2), (v_1, v_2)], f = [(z_1, z_2), (t_1, t_2)], \\
 &\quad u_1, v_1 \in V(G_1), z_1, t_1 \in V(G_1) - \{u_1, v_1\}, u_2, v_2, z_2, t_2 \in V(G_2) \}
 \end{aligned}$$

It is clear that each pair of the above sets is disjoint and  $B = \bigcup_{i=1}^5 B_i$ .

The next proposition characterizes  $d_0(e, f | G_1 [G_2])$  for all  $\{e, f\} \in B$ .

**Proposition 13.3.4** *Let  $\{e, f\} \in B$ .*

- (i) *If  $\{e, f\} \in B_1$ , then  $d_0(e, f | G_1 [G_2]) = 1$*
- (ii) *If  $\{e, f\} \in B_2$ , then  $d_0(e, f | G_1 [G_2]) = 2$*
- (iii) *If  $\{e, f\} \in B_3$ , then  $d_0(e, f | G_1 [G_2]) = d_0([u_1, v_1], [u_1, z_1] | G_1)$ , where  $e = [(u_1, u_2), (v_1, v_2)], f = [(u_1, u_2), (z_1, z_2)]$*
- (iv) *If  $\{e, f\} \in B_4$ , then  $d_0(e, f | G_1 [G_2]) = d_0([u_1, v_1], [u_1, z_1] | G_1) + 1$ , where  $e = [(u_1, u_2), (v_1, v_2)], f = [(u_1, t_2), (z_1, z_2)]$*
- (v) *If  $\{e, f\} \in B_5$ , then  $d_0(e, f | G_1 [G_2]) = d_0([u_1, v_1], [z_1, t_1] | G_1)$ , where  $e = [(u_1, u_2), (v_1, v_2)], f = [(z_1, z_2), (t_1, t_2)]$*

*Proof*

- (i) Let  $\{e, f\} \in B_1$  and  $e = [(u_1, u_2), (v_1, v_2)], f = [(u_1, u_2), (v_1, z_2)]$ . Using the definition of  $d_0(e, f)$ , we have:

$$\begin{aligned}
 d_0(e, f | G_1 [G_2]) &= 1 + \min \{ d((u_1, u_2), (u_1, u_2) | G_1 [G_2]), \\
 &\quad d((u_1, u_2), (v_1, z_2) | G_1 [G_2]), \\
 &\quad d((v_1, v_2), (u_1, u_2) | G_1 [G_2]), d((v_1, v_2), (v_1, z_2) | G_1 [G_2]) \} \\
 &= 1 + \min \{ 0, 1, 1, d((v_1, v_2), (v_1, z_2) | G_1 [G_2]) \} = 1 + 0 = 1.
 \end{aligned}$$

- (ii) Let  $\{e, f\} \in B_2$  and  $e = [(u_1, u_2), (v_1, v_2)], f = [(u_1, z_2), (v_1, t_2)]$ . By definition of  $B_2$ ,  $z_2 \neq u_2, t_2 \neq v_2$ . So due to the distance between two vertices in  $G_1 [G_2]$ , the distances  $d((u_1, u_2), (u_1, z_2) | G_1 [G_2])$  and  $d((v_1, v_2), (v_1, t_2) | G_1 [G_2])$  are either 1 or 2. Therefore,

$$\begin{aligned}
 d_0(e, f | G_1 [G_2]) &= 1 + \min \{ d((u_1, u_2), (u_1, z_2) | G_1 [G_2]), \\
 &\quad d((u_1, u_2), (v_1, t_2) | G_1 [G_2]), \\
 &\quad d((v_1, v_2), (u_1, z_2) | G_1 [G_2]), d((v_1, v_2), (v_1, t_2) | G_1 [G_2]) \} = \\
 &= 1 + \min \{ d((u_1, u_2), (u_1, z_2) | G_1 [G_2]), 1, 1, d((v_1, v_2), (v_1, t_2) | G_1 [G_2]) \} \\
 &= 1 + 1 = 2.
 \end{aligned}$$

- (iii) Let  $\{e, f\} \in B_3$  and  $e = [(u_1, u_2), (v_1, v_2)]$ ,  $f = ((u_1, u_2), (z_1, z_2))$ . By definition of  $B_3$ ,  $z_1 \neq v_1$ . Hence,

$$\begin{aligned} d_0(e, f | G_1 [G_2]) &= 1 + \min \{d((u_1, u_2), (u_1, u_2) | G_1 [G_2]), \\ &\quad d((u_1, u_2), (z_1, z_2) | G_1 [G_2]), \\ &\quad d((v_1, v_2), (u_1, u_2) | G_1 [G_2]), d((v_1, v_2), (z_1, z_2) | G_1 [G_2])\} = \\ &1 + \min \{d(u_1, u_1 | G_1) d(u_1, z_1 | G_1), d(v_1, u_1 | G_1), d(v_1, z_1 | G_1)\} \\ &= d_0([u_1, v_1], [u_1, z_1] | G_1) \end{aligned}$$

- (iv) Let  $\{e, f\} \in B_4$  and  $e = [(u_1, u_2), (v_1, v_2)]$ ,  $f = [(u_1, t_2), (z_1, z_2)]$ . By definition of  $B_4$ ,  $z_1 \neq v_1$ , and  $t_2 \neq u_2$ . So  $d(v_1, z_1 | G_1) \geq 1$  and  $d((u_1, u_2), (u_1, t_2) | G_1 [G_2]) \geq 1$ . Therefore,

$$\begin{aligned} d_0(e, f | G_1 [G_2]) &= 1 + \min \{d((u_1, u_2), (u_1, t_2) | G_1 [G_2]), \\ &\quad d((u_1, u_2), (z_1, z_2) | G_1 [G_2]), \\ &\quad d((v_1, v_2), (u_1, t_2) | G_1 [G_2]), d((v_1, v_2), (z_1, z_2) | G_1 [G_2])\} = \\ &1 + \min \{d((u_1, u_2), (u_1, t_2) | G_1 [G_2]), 1, 1, d(v_1, z_1 | G_1)\} \\ &= 1 + 1 = d_0([u_1, v_1], [u_1, z_1] | G_1) + 1. \end{aligned}$$

- (v) Let  $\{e, f\} \in B_5$  and  $e = [(u_1, u_2), (v_1, v_2)]$ ,  $f = [(z_1, z_2), (t_1, t_2)]$ . By definition of  $B_5$ ,  $z_1 \neq u_1$ ,  $z_1 \neq v_1$ ,  $t_1 \neq u_1$ , and  $t_1 \neq v_1$ . So the edges  $[u_1, v_1]$  and  $[z_1, t_1]$  of  $G_1$  are distinct. Therefore,

$$\begin{aligned} d_0(e, f | G_1 [G_2]) &= 1 + \min \{d((u_1, u_2), (z_1, z_2) | G_1 [G_2]), \\ &\quad d((u_1, u_2), (t_1, t_2) | G_1 [G_2]), \\ &\quad d((v_1, v_2), (z_1, z_2) | G_1 [G_2]), d((v_1, v_2), (t_1, t_2) | G_1 [G_2])\} = \\ &1 + \min \{d(u_1, z_1 | G_1), d(u_1, t_1 | G_1), d(v_1, z_1 | G_1), d(v_1, t_1 | G_1)\} \\ &= d_0([u_1, v_1], [z_1, t_1] | G_1), \end{aligned}$$

and the proof is completed. ■

Now, we consider three subsets  $C_1$ ,  $C_2$  and  $C_3$  of the set  $C$  as follows:

$$\begin{aligned} C_1 &= \{\{e, f\} \in C : e = [(u_1, u_2), (u_1, v_2)], f = [(u_1, u_2), (z_1, z_2)], \\ &\quad u_1, z_1 \in V(G_1), u_2, v_2, z_2 \in V(G_2)\} \end{aligned}$$

$$C_2 = \{ \{e, f\} \in C : e = [(u_1, u_2), (u_1, v_2)], f = [(u_1, t_2), (z_1, z_2)], \\ u_1, z_1 \in V(G_1), u_2, v_2, t_2, z_2 \in V(G_2), t_2 \neq u_2, t_2 \neq v_2 \}$$

$$C_3 = \{ \{e, f\} \in C : e = [(u_1, u_2), (u_1, t_2)], f = [(v_1, v_2), (z_1, z_2)], \\ u_1, v_1, z_1 \in V(G_1), u_2, t_2, v_2, z_2 \in V(G_2), v_1 \neq u_1, z_1 \neq u_1 \}$$

Clearly, every pair of the above sets is disjoint and  $C = \bigcup_{i=1}^3 C_i$ .

In the following proposition, we find  $d_0(e, f | G_1 [G_2])$  for all  $\{e, f\} \in C$ .

**Proposition 13.3.5** *Let  $\{e, f\} \in C$ .*

- (i) *If  $\{e, f\} \in C_1$ , then  $d_0(e, f | G_1 [G_2]) = 1$*
- (ii) *If  $\{e, f\} \in C_2$ , then  $d_0(e, f | G_1 [G_2]) = 2$*
- (iii) *If  $\{e, f\} \in C_3$ , then  $d_0(e, f | G_1 [G_2]) = 1 + \min \{d(u_1, v_1 | G_1), d(u_1, z_1 | G_1)\}$ , where  $e = [(u_1, u_2), (u_1, t_2)], f = [(v_1, v_2), (z_1, z_2)]$*

*Proof*

- (i) Let  $\{e, f\} \in C_1$  and  $e = [(u_1, u_2), (u_1, v_2)], f = [(u_1, u_2), (z_1, z_2)]$ .  
By definition of  $d_0(e, f)$ , we have

$$d_0(e, f | G_1 [G_2]) = 1 + \min \{d((u_1, u_2), (u_1, u_2) | G_1 [G_2]), \\ d((u_1, u_2), (z_1, z_2) | G_1 [G_2]), \\ d((u_1, v_2), (u_1, u_2) | G_1 [G_2]), d((u_1, v_2), (z_1, z_2) | G_1 [G_2])\} \\ = 1 + \min \{0, 1, 1, 1\} = 1 + 0 = 1.$$

- (ii) Let  $\{e, f\} \in C_2$  and  $e = [(u_1, u_2), (u_1, v_2)], f = [(u_1, t_2), (z_1, z_2)]$ . By definition of  $C_2$ ,  $t_2 \neq u_2, t_2 \neq v_2$ . Thus, due to the distance between two vertices in  $G_1 [G_2]$ , the distances  $d((u_1, u_2), (u_1, t_2) | G_1 [G_2])$  and  $d((u_1, v_2), (u_1, t_2) | G_1 [G_2])$  are either 1 or 2. So

$$d_0(e, f | G_1 [G_2]) = 1 + \min \{d((u_1, u_2), (u_1, t_2) | G_1 [G_2]), \\ d((u_1, u_2), (z_1, z_2) | G_1 [G_2]), \\ d((u_1, v_2), (u_1, t_2) | G_1 [G_2]), d((u_1, v_2), (z_1, z_2) | G_1 [G_2])\} = \\ 1 + \min \{d((u_1, u_2), (u_1, t_2) | G_1 [G_2]), 1, d((u_1, v_2), (u_1, t_2) | G_1 [G_2]), 1\} \\ = 1 + 1 = 2.$$

- (iii) Let  $\{e, f\} \in C_3$  and  $e = [(u_1, u_2), (u_1, t_2)], f = [(v_1, v_2), (z_1, z_2)]$ . By definition of  $C_3$ ,  $v_1 \neq u_1, z_1 \neq u_1$ . Therefore,

$$\begin{aligned}
 d_0(e, f | G_1 [G_2]) &= 1 + \min \{d((u_1, u_2), (v_1, v_2) | G_1 [G_2]), \\
 &\quad d((u_1, u_2), (z_1, z_2) | G_1 [G_2]), \\
 &\quad d((u_1, t_2), (v_1, v_2) | G_1 [G_2]), d((u_1, t_2), (z_1, z_2) | G_1 [G_2])\} = \\
 &1 + \min \{d(u_1, v_1 | G_1), d(u_1, z_1 | G_1), d(u_1, v_1 | G_1), d(u_1, z_1 | G_1)\} = \\
 &1 + \min \{d(u_1, v_1 | G_1), d(u_1, z_1 | G_1)\},
 \end{aligned}$$

and the proof is completed. ■

**Definition 13.3.6** Let  $G = (V(G), E(G))$  be a graph.

- (i) Let  $u \in V(G)$ . Set  $\Delta_u = \{z \in V(G) : [z, u] \in E(G)\}$ . In fact,  $\Delta_u$  is the set of all vertices of  $G$ , which are adjacent to  $u$ . Suppose that  $\delta_u$  is the number of all vertices of  $G$ , which are adjacent to  $u$ . Clearly,  $\delta_u = |\Delta_u| = \text{deg } u | G$ .
- (ii) For each pair of distinct vertices  $u, v \in V(G)$ , let  $\delta_{(u,v)}$  be the number of all vertices of  $G$ , which are adjacent both to  $u$  and  $v$ . Obviously,  $\delta_{(u,v)} = |\Delta_u \cap \Delta_v|$ .
- (iii) Let  $u, v$ , and  $z$  be three vertices of  $G$ , which every pair of them is distinct. Assume that  $\delta_{(u,v,z)}$  denotes the number of all vertices of  $G$  which are adjacent to vertices  $u, v$  and  $z$ . It is easy to see that  $\delta_{(u,v,z)} = |\Delta_u \cap \Delta_v \cap \Delta_z|$ .
- (iv) Suppose that  $u, v$  and  $z$  be three vertices of graph  $G$ , which every pair of them is distinct. Denote by  $N_{(z,\tilde{u},\tilde{v})}$  the number of all vertices of  $G$ , which are adjacent to  $z$ , but neither to  $u$  nor to  $v$ . By the definition of  $N_{(z,\tilde{u},\tilde{v})}$ , we have

$$\begin{aligned}
 N_{(z,\tilde{u},\tilde{v})} &= |\Delta_z - (\Delta_u \cup \Delta_v)| = |\Delta_z| - |\Delta_z \cap (\Delta_u \cup \Delta_v)| \\
 &= |\Delta_z| - |(\Delta_z \cap \Delta_u) \cup (\Delta_z \cap \Delta_v)| = \\
 &|\Delta_z| - (|\Delta_z \cap \Delta_u| + |\Delta_z \cap \Delta_v| - |\Delta_z \cap \Delta_u \cap \Delta_v|) \\
 &= \delta_z - \delta_{(z,u)} - \delta_{(z,v)} + \delta_{(z,u,v)}.
 \end{aligned}$$

**Lemma 13.3.7**

$$\begin{aligned}
 \sum_{\{e,f\} \in A} d_0(e, f | G_1 [G_2]) &= |E(G_2)|^2 \left( \binom{|V(G_1)| + 1}{2} + W(G_1) \right) \\
 &\quad - \frac{1}{4} |V(G_1)| (2M_1(G_2) - N(G_2)),
 \end{aligned}$$

where,  $N(G_2) = \sum_{[u_2,v_2] \in E(G_2)} \sum_{z_2 \in V(G_2) - (\Delta_{u_2} \cup \Delta_{v_2})} N_{(z_2,\tilde{u}_2,\tilde{v}_2)}$ .

*Proof* At first, we need to find  $|A_2|$  and  $|A_2 \cup A_3|$ . It is easy to see that



$$|A_2| = \frac{1}{4} |V(G_1)| \sum_{[u_2, v_2] \in E(G_2)} \sum_{z_2 \in V(G_2) - (\Delta_{u_2} \cup \Delta_{v_2})} N_{(z_2, \tilde{u}_2, \tilde{v}_2)} = \frac{1}{4} |V(G_1)| N(G_2),$$

$$|A_2 \cup A_3| = \frac{1}{2} |V(G_1)| \sum_{[u_2, v_2] \in E(G_2)} (|E(G_2)| - (\delta_{u_2} + \delta_{v_2} - 1)) =$$

$$\frac{1}{2} |V(G_1)| \left( \sum_{[u_2, v_2] \in E(G_2)} |E(G_2)| - \sum_{[u_2, v_2] \in E(G_2)} (\delta_{u_2} + \delta_{v_2}) + \sum_{[u_2, v_2] \in E(G_2)} 1 \right) =$$

$$\frac{1}{2} |V(G_1)| (|E(G_2)|^2 + |E(G_2)| - M_1(G_2)),$$

Recall that, each pair of the sets  $A_i$  ( $1 \leq i \leq 4$ ) is disjoint and  $A = \bigcup_{i=1}^4 A_i$ , then by

Proposition 13.3.3, we have

$$\sum_{\{e, f\} \in A} d_0(e, f | G_1 [G_2]) = \sum_{i=1}^4 \sum_{\{e, f\} \in A_i} d_0(e, f | G_1 [G_2])$$

$$= |A_1| + 3|A_2| + 2|A_3| +$$

$$\sum \{1 + d(u_1, v_1 | G_1) : \{e, f\} \in A_4, e = [(u_1, u_2), (u_1, v_2)],$$

$$f = [(v_1, z_2), (v_1, t_2)]\} = |A_1| + 3|A_2| + 2|A_3| + |A_4| +$$

$$\sum \{d(u_1, v_1 | G_1) : \{e, f\} \in A_4, e = [(u_1, u_2), (u_1, v_2)], f = [(v_1, z_2), (v_1, t_2)]\} =$$

$$\sum_{i=1}^4 |A_i| + (|A_2| + |A_3|) + |A_2| + |E(G_2)|^2 \sum_{\{u_1, v_1\} \subseteq V(G_1)} d(u_1, v_1 | G_1) =$$

$$\left| \bigcup_{i=1}^4 A_i \right| + |A_2 \cup A_3| + |A_2| + |E(G_2)|^2 W(G_1) = |A| + |A_2 \cup A_3| + |A_2|$$

$$+ |E(G_2)|^2 W(G_1) =$$

$$\left( \frac{|V(G_1)| |E(G_2)|}{2} \right) + \frac{1}{2} |V(G_1)| (|E(G_2)|^2 + |E(G_2)| - M_1(G_2))$$

$$+ \frac{1}{4} |V(G_1)| N(G_2) + |E(G_2)|^2 W(G_1) =$$

$$\frac{1}{2} (|V(G_1)|^2 |E(G_2)|^2 - |V(G_1)| |E(G_2)| + |V(G_1)| |E(G_2)|^2$$

$$+ |V(G_1)| |E(G_2)|) -$$

$$\frac{1}{2} |V(G_1)| M_1(G_2) + \frac{1}{4} |V(G_1)| N(G_2) + |E(G_2)|^2 W(G_1) = |E(G_2)|^2 \left( \binom{|V(G_1)| + 1}{2} + W(G_1) \right) - \frac{1}{4} |V(G_1)| (2M_1(G_2) - N(G_2)).$$

■

**Lemma 13.3.8**  $\sum_{\{e,f\} \in B} d_0(e, f | G_1 [G_2]) = |V(G_2)|^2 \binom{|V(G_2)|}{2} M_1(G_1) + |V(G_2)|^4 W_{e_0}(G_1)$

*Proof* For the proof of this lemma, we need to obtain  $|B_1|$ ,  $|B_2|$ , and  $|B_4|$ . It is easy to see that:

$$|B_1| = 2 |E(G_1)| |V(G_2)| \binom{|V(G_2)|}{2}, \quad |B_2| = 2 |E(G_1)| \binom{|V(G_2)|}{2}^2, \\ |B_4| = |V(G_2)|^3 (|V(G_2)| - 1) \sum_{u_1 \in V(G_1)} \binom{\delta_{u_1}}{2} = |V(G_2)|^2 \binom{|V(G_2)|}{2} (M_1(G_1) - 2 |E(G_1)|).$$

Afterwards, we find  $\sum_{\{e,f\} \in B_3 \cup B_4 \cup B_5} d_0(e, f | G_1 [G_2])$ . By Proposition 13.3.3, we have

$$\sum_{\{e,f\} \in B_3} d_0(e, f | G_1 [G_2]) = \sum \{d_0([u_1, v_1], [u_1, z_1] | G_1) : \\ \{e, f\} \in B_3, e = [(u_1, u_2), (v_1, v_2)], f = [(u_1, u_2), (z_1, z_2)]\} = \\ |V(G_2)|^3 \sum_{u_1 \in V(G_1)} \sum_{\{[u_1, v_1], [u_1, z_1]\} \subseteq E(G_1)} d_0([u_1, v_1], [u_1, z_1] | G_1) \\ = \frac{1}{2} |V(G_2)|^3 \sum_{[u_1, v_1] \in E(G_1)} \sum_{\substack{z_1 \in \{u_1, v_1\}, \\ [z_1, t_1] \in E(G_1)}} d_0([u_1, v_1], [z_1, t_1] | G_1), \\ \sum_{\{e,f\} \in B_4} d_0(e, f | G_1 [G_2]) = \sum \{d_0([u_1, v_1], [u_1, z_1] | G_1) + 1 : \{e, f\} \in B_4, \\ e = [(u_1, u_2), (v_1, v_2)], f = [(u_1, t_2), (z_1, z_2)]\} = \\ (|V(G_2)|^4 - |V(G_2)|^3) \sum_{u_1 \in V(G_1)} \sum_{\{[u_1, v_1], [u_1, z_1]\} \subseteq E(G_1)} d_0([u_1, v_1], [u_1, z_1] | G_1) + |B_4| = \\ \frac{1}{2} (|V(G_2)|^4 - |V(G_2)|^3) \sum_{[u_1, v_1] \in E(G_1)} \sum_{\substack{z_1 \in \{u_1, v_1\}, \\ [z_1, t_1] \in E(G_1)}} d_0([u_1, v_1], [z_1, t_1] | G_1) + |B_4|,$$

$$\begin{aligned} \sum_{\{e,f\} \in B_5} d_0(e, f | G_1[G_2]) &= \sum \{d_0([u_1, v_1], [z_1, t_1] | G_1) : \\ &\{e, f\} \in B_5, e = [(u_1, u_2), (v_1, v_2)], f = [(z_1, z_2), (t_1, t_2)]\} = \\ &\frac{1}{2} |V(G_2)|^4 \sum_{[u_1, v_1] \in E(G_1)} \sum_{\substack{[z_1, t_1] \in E(G_1), \\ z_1, t_1 \notin \{u_1, v_1\}}} d_0([u_1, v_1], [z_1, t_1] | G_1). \end{aligned}$$

Based on the above computations and since each pair of  $B_i (1 \leq i \leq 5)$  is disjoint, we have

$$\begin{aligned} \sum_{\{e,f\} \in B_3 \cup B_4 \cup B_5} d_0(e, f | G_1[G_2]) &= \sum_{i=3}^5 \sum_{\{e,f\} \in B_i} d_0(e, f | G_1[G_2]) = \\ &\frac{1}{2} |V(G_2)|^3 \sum_{[u_1, v_1] \in E(G_1)} \sum_{\substack{z_1 \in \{u_1, v_1\}, \\ [z_1, t_1] \in E(G_1)}} d_0([u_1, v_1], [z_1, t_1] | G_1) + \\ &\frac{1}{2} (|V(G_2)|^4 - |V(G_2)|^3) \sum_{[u_1, v_1] \in E(G_1)} \sum_{\substack{z_1 \in \{u_1, v_1\}, \\ [z_1, t_1] \in E(G_1)}} d_0([u_1, v_1], [z_1, t_1] | G_1) + |B_4| + \\ &\frac{1}{2} |V(G_2)|^4 \sum_{[u_1, v_1] \in E(G_1)} \sum_{\substack{[z_1, t_1] \in E(G_1), \\ z_1, t_1 \notin \{u_1, v_1\}}} d_0([u_1, v_1], [z_1, t_1] | G_1) = \\ &\frac{1}{2} |V(G_2)|^4 \sum_{[u_1, v_1] \in E(G_1)} \sum_{\substack{z_1 \in \{u_1, v_1\}, \\ [z_1, t_1] \in E(G_1)}} d_0([u_1, v_1], [z_1, t_1] | G_1) + |B_4| + \\ &\frac{1}{2} |V(G_2)|^4 \sum_{[u_1, v_1] \in E(G_1)} \sum_{\substack{[z_1, t_1] \in E(G_1), \\ z_1, t_1 \notin \{u_1, v_1\}}} d_0([u_1, v_1], [z_1, t_1] | G_1) = \\ &|B_4| + \frac{1}{2} |V(G_2)|^4 (2W_{e_0}(G_1)) = |B_4| + |V(G_2)|^4 W_{e_0}(G_1). \end{aligned}$$

Now, since  $B = \bigcup_{i=1}^5 B_i$ , we have

$$\begin{aligned} \sum_{\{e,f\} \in B} d_0(e, f | G_1[G_2]) &= \sum_{\{e,f\} \in B_1} d_0(e, f | G_1[G_2]) + \\ &\sum_{\{e,f\} \in B_2} d_0(e, f | G_1[G_2]) + \sum_{\{e,f\} \in B_3 \cup B_4 \cup B_5} d_0(e, f | G_1[G_2]) = \end{aligned}$$

$$\begin{aligned}
 & |B_1| + 2|B_2| + |B_4| + |V(G_2)|^4 W_{e_0}(G_1) \\
 &= 2|E(G_1)| \binom{|V(G_2)|}{2} \left( |V(G_2)| + 2 \binom{|V(G_2)|}{2} - |V(G_2)|^2 \right) + \\
 & |V(G_2)|^2 \binom{|V(G_2)|}{2} M_1(G_1) + |V(G_2)|^4 W_{e_0}(G_1) \\
 &= |V(G_2)|^2 \binom{|V(G_2)|}{2} M_1(G_1) + |V(G_2)|^4 W_{e_0}(G_1).
 \end{aligned}$$

■

**Lemma 13.3.9**  $\sum_{\{e,f\} \in C} d_0(e, f | G_1 [G_2]) = |E(G_1)| |E(G_2)| |V(G_2)| (|V(G_1)| |V(G_2)| + 2|V(G_2)| - 4) + |E(G_2)| |V(G_2)|^2 \text{Min}(G_1)$   
 where,  $\text{Min}(G_1) = \sum_{u_1 \in V(G_1)} \sum_{[v_1, z_1] \in E(G_1)} \min \{d(u_1, v_1 | G_1), d(u_1, z_1 | G_1)\}$

*Proof* First, we find  $|C_2|$  and  $\sum_{\{e,f\} \in C_3} d_0(e, f | G_1 [G_2])$ . It is easy to see that

$$\begin{aligned}
 |C_2| &= |V(G_2)| (|V(G_2)| - 2) |E(G_2)| \\
 &\times \sum_{u_1 \in V(G_1)} \delta_{u_1} = 2|E(G_1)| |E(G_2)| |V(G_2)| (|V(G_2)| - 2),
 \end{aligned}$$

and by Proposition 13.3.5, we have

$$\begin{aligned}
 & \sum_{\{e,f\} \in C_3} d_0(e, f | G_1 [G_2]) \\
 &= \sum \{1 + \min \{d(u_1, v_1 | G_1), d(u_1, z_1 | G_1)\} : \\
 & \quad \times \{e, f\} \in C_3, e = [(u_1, u_2), (u_1, t_2)], f = [(v_1, v_2), (z_1, z_2)]\} \\
 &= |C_3| + |E(G_2)| |V(G_2)|^2 \sum_{\substack{u_1 \in V(G_1) \\ v_1 \neq z_1, z_1 \neq u_1}} \sum_{[v_1, z_1] \in E(G_1)} \min \{d(u_1, v_1 | G_1), d(u_1, z_1 | G_1)\} \\
 &= |C_3| + |E(G_2)| |V(G_2)|^2 \sum_{u_1 \in V(G_1)} \sum_{[v_1, z_1] \in E(G_1)} \min \{d(u_1, v_1 | G_1), d(u_1, z_1 | G_1)\} \\
 &= |C_3| + |E(G_2)| |V(G_2)|^2 \text{Min}(G_1).
 \end{aligned}$$

Since each pair of the sets  $C_i$  ( $1 \leq i \leq 3$ ) is disjoint and  $C = \bigcup_{i=1}^3 C_i$ , we have

$$\begin{aligned}
 \sum_{\{e,f\} \in C} d_0(e, f | G_1[G_2]) &= \sum_{\{e,f\} \in C_1 \cup C_2} d_0(e, f | G_1[G_2]) \\
 &+ \sum_{\{e,f\} \in C_3} d_0(e, f | G_1[G_2]) \\
 &= |C_1| + 2|C_2| + |C_3| + |E(G_2)| |V(G_2)|^2 \text{Min}(G_1) \\
 &= \sum_{i=1}^3 |C_i| + |C_2| + |E(G_2)| |V(G_2)|^2 \text{Min}(G_1) \\
 &= \left| \bigcup_{i=1}^3 C_i \right| + |C_2| + |E(G_2)| |V(G_2)|^2 \text{Min}(G_1) \\
 &= |C| + |C_2| + |E(G_2)| |V(G_2)|^2 \text{Min}(G_1) \\
 &= |V(G_1)| |V(G_2)|^2 |E(G_1)| |E(G_2)| \\
 &+ 2|E(G_1)| |E(G_2)| |V(G_2)| (|V(G_2)| - 2) \\
 &+ |E(G_2)| |V(G_2)|^2 \text{Min}(G_1) \\
 &= |E(G_1)| |E(G_2)| |V(G_2)| (|V(G_1)| |V(G_2)| + 2|V(G_2)| - 4) \\
 &+ |E(G_2)| |V(G_2)|^2 \text{Min}(G_1).
 \end{aligned}$$

■

Now, as the main purpose of this section, we express Theorem 13.3.10, which characterizes the first edge Wiener index of the composition of two graphs.

**Theorem 13.3.10** *Let  $G_1 = (V(G_1), E(G_1))$  and  $G_2 = (V(G_2), E(G_2))$  be two simple undirected connected finite graphs, then*

$$\begin{aligned}
 W_{e_0}(G_1[G_2]) &= |E(G_2)|^2 \binom{|V(G_1)| + 1}{2} \\
 &+ |E(G_1)| |E(G_2)| |V(G_2)| (|V(G_1)| |V(G_2)| + 2|V(G_2)| - 4) \\
 &+ |E(G_2)|^2 W(G_1) + |V(G_2)|^4 W_{e_0}(G_1) + |V(G_2)|^2 \binom{|V(G_2)|}{2} \\
 M_1(G_1) &+ |E(G_2)| |V(G_2)|^2 \text{Min}(G_1) - \frac{1}{4} |V(G_1)| (2M_1(G_2) - N(G_2)),
 \end{aligned}$$

where  $\text{Min}(G_1) = \sum_{u_1 \in V(G_1)} \sum_{[v_1, z_1] \in E(G_1)} \min\{d(u_1, v_1 | G_1), d(u_1, z_1 | G_1)\}$  and  $N(G_2) = \sum_{[u_2, v_2] \in E(G_2)} \sum_{z_2 \in V(G_2) - (\Delta_{u_2} \cup \Delta_{v_2})} N_{(z_2, \tilde{u}_2, \tilde{v}_2)}$ .

*Proof* Remember that each pair of the sets  $A$ ,  $B$ , and  $C$  is disjoint, and union of them is the set of all two element subsets of  $E(G_1 [G_2])$ . Now, using the definition of the first edge-Wiener index, we obtain that

$$W_{e_0}(G_1 [G_2]) = \sum_{\{e,f\} \subseteq E(G_1 [G_2])} d_0(e, f | G_1 [G_2]) = \sum_{\{e,f\} \in A} d_0(e, f | G_1 [G_2]) + \sum_{\{e,f\} \in B} d_0(e, f | G_1 [G_2]) + \sum_{\{e,f\} \in C} d_0(e, f | G_1 [G_2]).$$

Now, by the above lemmas, the proof is completed. ■

### 13.4 Computation of the Edge Wiener Indices of the Sum of Graphs

In this section, we find the edge-Wiener indices of the sum of graphs. Then as an application of our results, we find the edge-Wiener indices of graphene,  $C_4$  - nanotubes and  $C_4$  - nanotori. All of the results in this section have been published in Azari and Iranmanesh (2011).

At first, we give the definition of sum of two graphs.

**Definition 13.4.1** Let  $G_1 = (V(G_1), E(G_1))$  and  $G_2 = (V(G_2), E(G_2))$  be connected graphs. The sum of  $G_1$  and  $G_2$  is denoted by  $G_1 + G_2$ , that is, a graph with the vertex set  $V(G_1) \times V(G_2)$  and two vertices  $(u_1, u_2)$  and  $(v_1, v_2)$  of  $G_1 + G_2$  are adjacent if and only if  $[u_1 = v_1 \text{ and } [u_2, v_2] \in E(G_2)]$  or  $[u_2 = v_2 \text{ and } [u_1, v_1] \in E(G_1)]$ .

**Theorem 13.4.2** (Stevanovic 2001) *Let  $G_1 = (V(G_1), E(G_1))$  and  $G_2 = (V(G_2), E(G_2))$  be two connected graphs. The distance between two vertices  $(u_1, u_2)$  and  $(v_1, v_2)$  of  $G_1 + G_2$  is equal to  $d((u_1, u_2), (v_1, v_2) | G_1 + G_2) = d(u_1, v_1 | G_1) + d(u_2, v_2 | G_2)$ .*

In order to find the edge-Wiener indices of  $G_1 + G_2$ , first we define the sets  $A$  and  $B$  as follows:

$$A = \{[(u_1, u_2), (u_1, v_2)] \in E(G_1 + G_2) : u_1 \in V(G_1), [u_2, v_2] \in E(G_2)\}$$

$$B = \{[(u_1, u_2), (v_1, u_2)] \in E(G_1 + G_2) : u_2 \in V(G_2), [u_1, v_1] \in E(G_1)\}$$

It is easy to see that  $A \cup B = E(G_1 + G_2)$ ,  $A \cap B = \phi$ ,  $|A| = |V(G_1)| |E(G_2)|$  and

$$|B| = |E(G_1)| |V(G_2)|.$$

Set

$$A_1 = \{\{e, f\} \subseteq A : e \neq f, e = [(u_1, u_2), (u_1, v_2)], f = [(a_1, u_2), (a_1, v_2)], \\ u_1, a_1 \in V(G_1), u_2, v_2 \in V(G_2)\}$$

$$A_2 = \{\{e, f\} \subseteq A : e \neq f, e = [(u_1, u_2), (u_1, v_2)], f = [(a_1, a_2), (a_1, b_2)], \\ u_1, a_1 \in V(G_1), u_2, v_2, a_2, b_2 \in V(G_2), [u_2, v_2] \neq [a_2, b_2]\}$$

$$B_1 = \{\{e, f\} \subseteq B : e \neq f, e = [(u_1, u_2), (v_1, u_2)], f = [(u_1, a_2), (v_1, a_2)], \\ u_1, v_1 \in V(G_1), u_2, a_2 \in V(G_2)\}$$

$$B_2 = \{\{e, f\} \subseteq B : e \neq f, e = [(u_1, u_2), (v_1, u_2)], f = [(a_1, a_2), (b_1, a_2)], \\ u_2, a_2 \in V(G_2), u_1, v_1, a_1, b_1 \in V(G_1), [u_1, v_1] \neq [a_1, b_1]\}$$

Obviously,  $A_1 \cap A_2 = B_1 \cap B_2 = \phi$  and  $A_1 \cup A_2, B_1 \cup B_2$  are the sets of all two element subsets of  $A$  and  $B$ , respectively. Also,

$$|A_1| = \binom{|V(G_1)|}{2} |E(G_2)|, |B_1| = \binom{|V(G_2)|}{2} |E(G_1)|.$$

In the first proposition, we find  $d_0(e, f | G_1 + G_2)$  and  $d_4(e, f | G_1 + G_2)$  for all  $\{e, f\} \subseteq A$ .

**Proposition 13.4.3** *Let  $\{e, f\} \subseteq A$  and  $e \neq f$ .*

(i) *If  $\{e, f\} \in A_1$  and  $e = [(u_1, u_2), (u_1, v_2)], f = [(a_1, u_2), (a_1, v_2)]$ , then*

$$d_0(e, f | G_1 + G_2) = d_4(e, f | G_1 + G_2) = d(u_1, a_1 | G_1) + 1$$

(ii) *If  $\{e, f\} \in A_2$  and  $e = [(u_1, u_2), (u_1, v_2)], f = [(a_1, a_2), (a_1, b_2)]$ , then for  $i \in \{0, 4\}$ ,  $d_i(e, f | G_1 + G_2) = d_i([u_2, v_2], [a_2, b_2] | G_2) + d(u_1, a_1 | G_1)$*

*Proof*

(i) Let  $\{e, f\} \in A_1$  and  $e = [(u_1, u_2), (u_1, v_2)], f = [(a_1, u_2), (a_1, v_2)]$ . Using the definition of  $d_0(e, f)$ ,  $d_4(e, f)$  and the formula of the distance between two vertices of  $G_1 + G_2$ , we have

$$\begin{aligned} d_0(e, f | G_1 + G_2) &= 1 + \min \{d((u_1, u_2), (a_1, u_2) | G_1 + G_2), \\ &\quad \times d((u_1, u_2), (a_1, v_2) | G_1 + G_2) \\ &\quad d((u_1, v_2), (a_1, u_2) | G_1 + G_2), d((u_1, v_2), (a_1, v_2) | G_1 + G_2)\} \\ &= 1 + \min \{d(u_1, a_1 | G_1) + \\ &\quad d(u_2, u_2 | G_2), d(u_1, a_1 | G_1) + d(u_2, v_2 | G_2), d(u_1, a_1 | G_1) \\ &\quad + d(v_2, u_2 | G_2), d(u_1, a_1 | G_1) + \end{aligned}$$

$$\begin{aligned}
& d(v_2, v_2 | G_2) \} = 1 + \min \{d(u_2, u_2 | G_2), d(u_2, v_2 | G_2), d(v_2, u_2 | G_2), \\
& \quad \times d(v_2, v_2 | G_2)\} + \\
& d(u_1, a_1 | G_1) = 1 + \min \{0, 1, 1, 0\} + d(u_1, a_1 | G_1) = d(u_1, a_1 | G_1) + 1 \text{ and} \\
& d_4(e, f | G_1 + G_2) = \max \{d((u_1, u_2), (a_1, u_2) | G_1 + G_2), \\
& \quad \times d((u_1, u_2), (a_1, v_2) | G_1 + G_2), \\
& \quad d((u_1, v_2), (a_1, u_2) | G_1 + G_2), d((u_1, v_2), (a_1, v_2) | G_1 + G_2)\} \\
& \quad = \max \{d(u_1, a_1 | G_1) + \\
& \quad d(u_2, u_2 | G_2), d(u_1, a_1 | G_1) + d(u_2, v_2 | G_2), d(u_1, a_1 | G_1) \\
& \quad + d(v_2, u_2 | G_2), d(u_1, a_1 | G_1) + \\
& \quad d(v_1, v_2 | G_2)\} = \max \{d(u_2, u_2 | G_2), d(u_2, v_2 | G_2), d(v_2, u_2 | G_2) \\
& \quad \times d(v_2, v_2 | G_2)\} + \\
& d(u_1, a_1 | G_1) = \max \{0, 1, 1, 0\} + d(u_1, a_1 | G_1) = d(u_1, a_1 | G_1) + 1.
\end{aligned}$$

Therefore  $d_0(e, f | G_1 + G_2) = d_4(e, f | G_1 + G_2) = d(u_1, a_1 | G_1) + 1$  and the equality in part (i) of Proposition 13.2.1 holds.

- (ii) Let  $\{e, f\} \in A_2$  and  $e = [(u_1, u_2), (u_1, v_2)]$ ,  $f = [(a_1, a_2), (a_1, b_2)]$ . In this case  $[u_2, v_2] \neq [a_2, b_2]$  and we have

$$\begin{aligned}
& d_0(e, f | G_1 + G_2) = 1 + \min \{d((u_1, u_2), (a_1, a_2) | G_1 + G_2), \\
& \quad \times d((u_1, u_2), (a_1, b_2) | G_1 + G_2), \\
& \quad d((u_1, v_2), (a_1, a_2) | G_1 + G_2), d((u_1, v_2), (a_1, b_2) | G_1 + G_2)\} \\
& \quad \times = 1 + \min \{d(u_1, a_1 | G_1) + \\
& \quad d(u_2, a_2 | G_2), d(u_1, a_1 | G_1) + d(u_2, b_2 | G_2), d(u_1, a_1 | G_1) \\
& \quad + d(v_2, a_2 | G_2), d(u_1, a_1 | G_1) + \\
& \quad d(v_2, b_2 | G_2)\} = 1 + \min \{d(u_2, a_2 | G_2), d(u_2, b_2 | G_2), d(v_2, a_2 | G_2), \\
& \quad \times d(v_2, b_2 | G_2)\} + \\
& \quad d(u_1, a_1 | G_1) = d_0([u_2, v_2], [a_2, b_2] | G_2) + d(u_1, a_1 | G_1) \text{ and} \\
& d_4(e, f | G_1 + G_2) = \max \{d((u_1, u_2), (a_1, a_2) | G_1 + G_2), \\
& \quad \times d((u_1, u_2), (a_1, b_2) | G_1 + G_2), \\
& \quad d((u_1, v_2), (a_1, a_2) | G_1 + G_2), d((u_1, v_2), (a_1, b_2) | G_1 + G_2)\} \\
& \quad = \max \{d(u_1, a_1 | G_1) + d(v_2, b_2 | G_2)\} =
\end{aligned}$$



$$\begin{aligned}
& d(u_2, a_2 | G_2), d(u_1, a_1 | G_1) + d(u_2, b_2 | G_2), d(u_1, a_1 | G_1) \\
& + d(v_2, a_2 | G_2), d(u_1, a_1 | G_1) + \\
& \max\{d(u_2, a_2 | G_2), d(u_2, b_2 | G_2), d(v_2, a_2 | G_2), d(v_2, b_2 | G_2)\} \\
& + d(u_1, a_1 | G_1) = d_4([u_2, v_2], [a_2, b_2] | G_2) + d(u_1, a_1 | G_1).
\end{aligned}$$

Therefore, for  $i \in \{0, 4\}$ ,  $d_i(e, f | G_1 + G_2) = d_i([u_2, v_2], [a_2, b_2] | G_2) + d(u_1, a_1 | G_1)$ , which completes the proof.  $\blacksquare$

In the next proposition, we find  $d_0(e, f | G_1 + G_2)$  and  $d_4(e, f | G_1 + G_2)$  for all  $\{e, f\} \subseteq B$ .

**Proposition 13.4.4** Let  $\{e, f\} \subseteq B$  and  $e \neq f$ .

(i) If  $\{e, f\} \in B_1$  and  $e = [(u_1, u_2), (v_1, u_2)]$ ,  $f = [(u_1, a_2), (v_1, a_2)]$ , then

$$d_0(e, f | G_1 + G_2) = d_4(e, f | G_1 + G_2) = d(u_2, a_2 | G_2) + 1$$

(ii) If  $\{e, f\} \in B_2$  and  $e = [(u_1, u_2), (v_1, u_2)]$ ,  $f = [(a_1, a_2), (b_1, a_2)]$ , then for  $i \in \{0, 4\}$ ,

$$d_i(e, f | G_1 + G_2) = d_i([u_1, v_1], [a_1, b_1] | G_1) d(u_2, a_2 | G_2).$$

*Proof* The proof is similar to the proof of Proposition 13.4.3.  $\blacksquare$

In the next proposition, we find  $d_0(e, f | G_1 + G_2)$  and  $d_4(e, f | G_1 + G_2)$  for all  $e \in A$ ,  $f \in B$ .

**Proposition 13.4.5** Let  $e \in A$  and  $f \in B$ , such that  $e = [(u_1, u_2), (u_1, v_2)]$  and  $f = [(a_1, a_2), (b_1, a_2)]$ , then

$$(i) \quad d_0(e, f | G_1 + G_2) = 1 + \min\{d(u_1, a_1 | G_1), d(u_1, b_1 | G_1)\} + \min\{d(u_2, a_2 | G_2), d(v_2, a_2 | G_2)\}$$

$$(ii) \quad d_4(e, f | G_1 + G_2) = \max\{d(u_1, a_1 | G_1), d(u_1, b_1 | G_1)\} + \max\{d(u_2, a_2 | G_2), d(v_2, a_2 | G_2)\}$$

*Proof* Let  $e \in A$  and  $f \in B$ , such that  $e = [(u_1, u_2), (u_1, v_2)]$  and  $f = [(a_1, a_2), (b_1, a_2)]$ , then

$$(i) \quad d_0(e, f | G_1 + G_2) = 1 + \min\{d((u_1, u_2), (a_1, a_2) | G_1 + G_2), \\ \times d((u_1, u_2), (b_1, a_2) | G_1 + G_2), d((u_1, v_2), (a_1, a_2) | G_1 + G_2),$$

$$\begin{aligned}
 & d((u_1, v_2), (b_1, a_2) | G_1 + G_2) = 1 + \min \{d(u_1, a_1 | G_1) + d(u_2, a_2 | G_2), \\
 & \quad \times d(u_1, b_1 | G_1) + \\
 & d(u_2, a_2 | G_2), d(u_1, a_1 | G_1) + d(v_2, a_2 | G_2), d(u_1, b_1 | G_1) \\
 & \quad + d(v_2, a_2 | G_2)\} \\
 & = 1 + \min \{\min \{d(u_1, a_1 | G_1) + d(u_1, b_1 | G_1)\} + d(u_2, a_2 | G_2), \\
 & \min \{d(u_1, a_1 | G_1) + d(u_1, b_1 | G_1)\} + d(v_2, a_2 | G_2)\} \\
 & = 1 + \min \{d(u_1, a_1 | G_1), d(u_1, b_1 | G_1)\} + \\
 & \min \{d(u_2, a_2 | G_2), d(v_2, a_2 | G_2)\}
 \end{aligned}$$

and part (i) of Proposition 13.4.5, holds.

$$\begin{aligned}
 \text{(ii)} \quad & d_4(e, f | G_1 + G_2) = \max \{d((u_1, u_2), (a_1, a_2) | G_1 + G_2), \\
 & d((u_1, u_2), (b_1, a_2) | G_1 + G_2), d((u_1, v_2), (a_1, a_2) | G_1 + G_2), \\
 & d((u_1, v_2), (b_1, a_2) | G_1 + G_2)\} = \max \{d(u_1, a_1 | G_1) + d(u_1, a_2 | G_2), \\
 & d(u_1, b_1 | G_1) + d(u_2, a_2 | G_2), d(u_1, a_1 | G_1) \\
 & \quad + d(v_2, a_2 | G_2), d(u_1, b_1 | G_1) + d(v_2, a_2 | G_2)\} \\
 & = \max \{\max \{d(u_1, a_1 | G_1) + d(u_1, b_1 | G_1)\} + d(u_2, a_2 | G_2), \\
 & \quad \max \{d(u_1, a_1 | G_1) + d(u_1, b_1 | G_1)\} + d(v_2, a_2 | G_2)\} \\
 & = \max \{d(u_1, a_1 | G_1), d(u_1, b_1 | G_1)\} \\
 & \quad + \max \{d(u_2, a_2 | G_2), d(v_2, a_2 | G_2)\},
 \end{aligned}$$

so part (ii) of Proposition 13.4.5 holds. ■

Using Proposition 13.4.3, we conclude two following lemmas:

**Lemma 13.4.6** 
$$\sum_{\{e,f\} \in A_1} d_0(e, f | G_1 + G_2) = \sum_{\{e,f\} \in A_1} d_4(e, f | G_1 + G_2)$$

$$= |E(G_2)| W(G_1) + \binom{|V(G_1)|}{2} |E(G_2)|$$

*Proof* By part (i) of Proposition 13.4.3, we have

$$\begin{aligned}
 & \sum_{\{e,f\} \in A_1} d_0(e, f | G_1 + G_2) = \sum_{\{e,f\} \in A_1} d_4(e, f | G_1 + G_2) \\
 & = \sum \{d(u_1, a_1 | G_1) + 1 : \{e, f\} \in A_1, e = [(u_1, u_2), (u_1, v_2)], \\
 & \quad \times f = [(a_1, u_2), (a_1, v_2)]\} \\
 & = \sum \{d(u_1, a_1 | G_1) : \{e, f\} \in A_1, e = [(u_1, u_2), (u_1, v_2)], \\
 & \quad f = [(a_1, u_2), (a_1, v_2)]\} + |A_1|
 \end{aligned}$$

$$\begin{aligned}
 &= |E(G_2)| \sum_{\{u_1, a_1\} \subseteq V(G_1)} d(u_1, a_1 | G_1) + \binom{|V(G_1)|}{2} |E(G_2)| \\
 &= |E(G_2)| W(G_1) + \binom{|V(G_1)|}{2} |E(G_2)|.
 \end{aligned}$$

**Lemma 13.4.7** For  $i \in \{0, 4\}$ , we have:  $\sum_{\{e, f\} \in A_2} d_i(e, f | G_1 + G_2)$

$$= |V(G_1)|^2 W_{e_i}(G_2) + 2 \binom{|E(G_2)|}{2} W(G_1).$$

*Proof* By part (ii) of Proposition 13.4.3, for  $i \in \{0, 4\}$ , we have

$$\begin{aligned}
 &\sum_{\{e, f\} \in A_2} d_i(e, f | G_1 + G_2) \\
 &= \sum \{d_i([u_2, v_2], [a_2, b_2] | G_2) + d(u_1, a_1 | G_1) : \{e, f\} \in A_2, \\
 &\times e = [(u_1, u_2), (u_1, v_2)], f = [(a_1, a_2), (a_1, b_2)]\} \\
 &= \sum \{d_i([u_2, v_2], [a_2, b_2] | G_2) : \\
 &\{e, f\} \in A_2, e = [(u_1, u_2), (u_1, v_2)], f = [(a_1, a_2), (a_1, b_2)]\} \\
 &\quad + \sum \{d(u_1, a_1 | G_1) : \{e, f\} \in A_2, \\
 &e = [(u_1, u_2), (u_1, v_2)], f = [(a_1, a_2), (a_1, b_2)]\} = |V(G_1)|^2 \\
 &\quad \sum_{\{[u_2, v_2], [a_2, b_2]\} \subseteq E(G_2)} ([u_2, v_2], [a_2, b_2] | G_2) + \\
 &2 \binom{|E(G_2)|}{2} \sum_{\{u_1, a_1\} \subseteq V(G_1)} d(u_1, a_1 | G_1) = |V(G_1)|^2 W_{e_i}(G_2) \\
 &\quad + 2 \binom{|E(G_2)|}{2} W(G_1).
 \end{aligned}$$

By Lemmas 13.4.6 and 13.4.7, we have the following result:

**Corollary 13.4.8** For  $i \in \{0, 4\}$ , we have

$$\begin{aligned}
 &\sum_{\{e, f\} \subseteq A} d_i(e, f | G_1 + G_2) = |E(G_2)|^2 W(G_1) + |V(G_1)|^2 W_{e_i}(G_2) \\
 &\quad + \binom{|V(G_1)|}{2} |E(G_2)|
 \end{aligned}$$

*Proof* Since  $d_0$  and  $d_4$  are distances, so for every  $e \in E(G_1 + G_2)$ , we have  $d_0(e, e | G_1 + G_2) = d_4(e, e | G_1 + G_2) = 0$ . Now by Lemmas 13.4.6 and 4.7, for  $i \in \{0, 4\}$ , we have

$$\begin{aligned} \sum_{\{e,f\} \subseteq A} d_i(e, f | G_1 + G_2) &= \sum_{\{e,f\} \subseteq A, e \neq f} d_i(e, f | G_1 + G_2) \\ &= \sum_{\{e,f\} \in A_1} d_i(e, f | G_1 + G_2) + \sum_{\{e,f\} \in A_2} d_i(e, f | G_1 + G_2) = |E(G_2)| W(G_1) \\ &+ \left( \frac{|V(G_1)|}{2} \right) |E(G_2)| + |V(G_1)|^2 W_{e_i}(G_2) + 2 \left( \frac{|E(G_2)|}{2} \right) W(G_1) \\ &= |E(G_2)|^2 W(G_1) + |V(G_1)|^2 W_{e_i}(G_2) + \left( \frac{|V(G_1)|}{2} \right) |E(G_2)|. \end{aligned}$$

■

Using Proposition 13.4.4, we conclude two next lemmas.

**Lemma 13.4.9**

$$\begin{aligned} \sum_{\{e,f\} \in B_1} d_0(e, f | G_1 + G_2) &= \sum_{\{e,f\} \in B_1} d_4(e, f | G_1 + G_2) \\ &= |E(G_1)| W(G_2) + \left( \frac{|V(G_2)|}{2} \right) |E(G_1)| \end{aligned}$$

**Lemma 13.4.10** For  $i \in \{0, 4\}$ , we have  $\sum_{\{e,f\} \in B_2} d_i(e, f | G_1 + G_2)$

$$= |V(G_2)|^2 W_{e_i}(G_1) + 2 \left( \frac{|E(G_1)|}{2} \right) W(G_2)$$

Lemmas 13.4.9 and 13.4.10, indicate the following corollary:

**Corollary 13.4.11** For  $i \in \{0, 4\}$ , we have

$$\begin{aligned} \sum_{\{e,f\} \subseteq B} d_i(e, f | G_1 + G_2) &= |E(G_1)|^2 W(G_2) + |V(G_2)|^2 W_{e_i}(G_1) \\ &+ \left( \frac{|V(G_2)|}{2} \right) |E(G_1)| \end{aligned}$$

*Proof* Similar to the proof of Corollary 13.4.8, we can obtain the desired result. ■

Here, we introduce two topological indices of a graph  $G$  as follows:

$$\text{Min}(G) = \sum_{u \in V(G)} \sum_{[a,b] \in E(G)} \min \{d(u, a | G), d(u, b | G)\}$$

$$\text{Max}(G) = \sum_{u \in V(G)} \sum_{[a,b] \in E(G)} \max \{d(u, a | G), d(u, b | G)\}$$

Using Proposition 13.4.5, we have the following lemma:

**Lemma 13.4.12**

$$(i) \quad \sum_{e \in A, f \in B} d_0(e, f | G_1 + G_2) = |V(G_1)| |V(G_2)| |E(G_1)| |E(G_2)| \\ + |V(G_2)| |E(G_2)| \text{Min}(G_1) + |V(G_1)| |E(G_1)| \text{Min}(G_2),$$

$$(ii) \quad \sum_{e \in A, f \in B} d_4(e, f | G_1 + G_2) = |V(G_2)| |E(G_2)| \text{Max}(G_1) + |V(G_1)| \\ |E(G_1)| \text{Max}(G_2)$$

*Proof*

(i) By part (i) of Proposition 13.4.5, we have

$$\sum_{e \in A, f \in B} d_0(e, f | G_1 + G_2) = \sum \{1 + \min \{d(u_1, a_1 | G_1), d(u_1, b_1 | G_1)\}$$

$$+ \min \{d(u_2, a_2 | G_2),$$

$$d(v_2, a_2 | G_2)\} : e \in A, f \in B, e = [(u_1, u_2), (u_1, v_2)],$$

$$f = [(a_1, a_2), (b_1, a_2)]\} = |A| |B| + \sum \{\min \{d(u_2, a_2 | G_1), d(u_1, b_1 | G_1)\}$$

$$: e \in A, f \in B, e = [(u_1, u_2), (u_1, v_2)],$$

$$f = [(a_1, a_2), (b_1, a_2)]\} + \sum \{\min \{d(u_2, a_2 | G_2), d(v_2, a_2 | G_2)\} :$$

$$e \in A, f \in B,$$

$$e = [(u_1, u_2), (u_1, v_2)], f = [(a_1, a_2), (b_1, a_2)]\} = |V(G_1)| |V(G_2)|$$

$$|E(G_1)| |E(G_2)|$$

$$\begin{aligned}
 &+ |V(G_2)||E(G_2)| \sum_{u_1 \in V(G_1)} \sum_{[a_1, b_1] \in E(G_1)} \min \{d(u_1, a_1 | G_1), d(u_1, b_1 | G_1)\} \\
 &+ |V(G_1)||E(G_1)| \sum_{a_2 \in V(G_2)} \sum_{[u_2, v_2] \in E(G_2)} \min \{d(u_2, a_2 | G_2), d(v_2, a_2 | G_2)\} \\
 &= |V(G_1)||V(G_2)||E(G_1)||E(G_2)| + |V(G_2)||E(G_2)| \text{Min}(G_1) \\
 &+ |V(G_1)||E(G_1)| \text{Min}(G_2).
 \end{aligned}$$

(ii) By part (ii) of Proposition 13.4.5, we have

$$\begin{aligned}
 \sum_{e \in A, f \in B} d_4(e, f | G_1 + G_2) &= \sum \{ \max \{d(u_1, a_1 | G_1), d(u_1, b_1 | G_1)\} \\
 &+ \max \{d(u_2, a_2 | G_2), d(v_2, a_2 | G_2)\} : \\
 e \in A, f \in B, e &= [(u_1, u_2), (u_1, v_2)], f = [(a_1, a_2), (b_1, a_2)] \} \\
 &= \sum \{ \max \{d(u_1, a_1 | G_1), d(u_1, b_1 | G_1)\} : \\
 e \in A, f \in B, e &= [(u_1, u_2), (u_1, v_2)], \\
 f &= [(a_1, a_2), (b_1, a_2)] \} + \sum \{ \max \{d(u_2, a_2 | G_2), d(v_2, a_2 | G_2)\} : \\
 e \in A, f \in B, e &= [(u_1, u_2), (u_1, v_2)], \\
 f &= [(a_1, a_2), (b_1, a_2)] \} = |V(G_2)||E(G_2)| \\
 &\sum_{u_1 \in V(G_1)} \sum_{[a_1, b_1] \in E(G_1)} \max \{d(u_1, a_1 | G_1), d(u_1, b_1 | G_1)\} + \\
 |V(G_1)||E(G_1)| \sum_{a_2 \in V(G_2)} \sum_{[u_2, v_2] \in E(G_2)} \max \{d(u_2, a_2 | G_2), d(v_2, a_2 | G_2)\} \\
 &= |V(G_2)||E(G_2)| \text{Max}(G_1) + |V(G_1)||E(G_1)| \text{Max}(G_2).
 \end{aligned}$$

■

Finally, as the main purpose of this part, we express Theorem 13.4.13, which characterizes the edge Wiener indices of the sum of two graphs.

**Theorem 13.4.13** *Let  $G_1 = (V(G_1), E(G_1))$  and  $G_2 = (V(G_2), E(G_2))$  be two simple undirected connected finite graphs, then*

$$\begin{aligned}
 (i) \quad W_{e_0}(G_1 + G_2) &= |E(G_2)|^2 W(G_1) + |E(G_1)|^2 W(G_2) + |V(G_2)|^2 W_{e_0}(G_1) \\
 &+ |V(G_1)|^2 W_{e_0}(G_2) + \binom{|V(G_1)|}{2} |E(G_2)| + \binom{|V(G_2)|}{2} |E(G_1)| \\
 &+ |V(G_1)||V(G_2)||E(G_1)||E(G_2)| + |V(G_2)||E(G_2)| \text{Min}(G_1) \\
 &+ |V(G_1)||E(G_1)| \text{Min}(G_2)
 \end{aligned}$$

$$\begin{aligned}
 \text{(ii)} \quad W_{e_4}(G_1 + G_2) &= |E(G_2)|^2 W(G_1) + |E(G_1)|^2 W(G_2) + |V(G_2)|^2 W_{e_4}(G_1) \\
 &\quad + |V(G_1)|^2 W_{e_4}(G_2) + \binom{|V(G_1)|}{2} |E(G_2)| + \binom{|V(G_2)|}{2} |E(G_1)| \\
 &\quad + |V(G_2)| |E(G_2)| \text{Max}(G_1) + |V(G_1)| |E(G_1)| \text{Max}(G_2)
 \end{aligned}$$

*Proof* Since  $E(G_1 + G_2) = A \cup B$ ,  $A \cap B = \phi$ , for  $i \in \{0, 4\}$ , we have

$$\begin{aligned}
 W_{e_i}(G_1 + G_2) &= \sum_{\{e,f\} \subseteq E(G_1+G_2)} d_i(e, f | G_1 + G_2) = \sum_{\{e,f\} \subseteq A} d_i(e, f | G_1 + G_2) + \\
 &\quad \sum_{\{e,f\} \subseteq B} d_i(e, f | G_1 + G_2) + \sum_{e \in A, f \in B} d_i(e, f | G_1 + G_2).
 \end{aligned}$$

Now by Corollaries 13.4.8 and 13.4.11 and Lemma 13.4.12, the proof is clear. ■

**Corollary 13.4.14** For every two simple undirected connected finite graphs  $G_1 = (V(G_1), E(G_1))$  and  $G_2 = (V(G_2), E(G_2))$ , we have

$$\begin{aligned}
 W_{e_4}(G_1 + G_2) - W_{e_0}(G_1 + G_2) &= |V(G_2)|^2 (W_{e_4}(G_1) - W_{e_0}(G_1)) \\
 &\quad + |V(G_1)|^2 (W_{e_4}(G_2) - W_{e_0}(G_2)) + \\
 &\quad |V(G_2)| |E(G_2)| (\text{Max}(G_1) - \text{Min}(G_1)) + |V(G_1)| |E(G_1)| (\text{Max}(G_2) \\
 &\quad - \text{Min}(G_2)) - |V(G_1)| |V(G_2)| |E(G_1)| |E(G_2)|
 \end{aligned}$$

The Wiener index and edge-Wiener indices of these graphs have been computed previously (Iranmanesh et al. 2009; Sagan et al. 1996). So, we have the following tables (Tables 13.3 and 13.4):

Carbon nanotubes, carbon nanotori and graphene are three important types of carbon structures. See Figs. 13.6, 13.7 and 13.8, respectively. Carbon nanotubes (CNTs) are allotropes of carbon with molecular structures that are tubular in shape, having diameters on the order of a few nanometers and lengths that can be as much as several millimeters.

Nanotubes are categorized as single-walled (SWNTs) and multi-walled (MWNTs) nanotubes. If a nanotube is bent so that its ends meet, a nanotorus is produced. These types of carbon structures, form the strongest and stiffest materials yet discovered on Earth. Their novel properties make them potentially useful in many applications in materials science, nanotechnology, electronics, optics and architecture.

Graphene is a one-atom-thick planer sheet of carbon atoms that are densely packed in a two-dimensional (2D) honeycomb crystal lattice and is a basic building block for graphitic materials of all other dimensionalities. It can be wrapped up into 0D fullerenes, rolled into 1D nanotubes, or stacked into 3D graphite (Fig. 13.9). The term graphene was coined as a combination of graphite and the suffix -ene by Hannes-Peter Boehm, who described single-layer carbon foils in 1962.

**Table 13.3** Some topological indices of  $P_n$  and  $C_n$

Graph ( $G$ )	$P_n$	$C_n n$ is odd	$C_n n$ is even
$ V(G) $	$n$	$n$	$n$
$ E(G) $	$n - 1$	$n$	$n$
$W(G)$	$\binom{n+1}{3}$	$\frac{n}{8}(n^2 - 1)$	$\frac{n^3}{8}$
$W_{e_0}(G)$	$\binom{n}{3}$	$\frac{n}{8}(n^2 - 1)$	$\frac{n^3}{8}$
$W_{e_4}(G)$	$\binom{n-1}{2} \frac{n+3}{3}$	$\frac{n}{8}(n^2 + 4n - 13)$	$\frac{n}{8}(n^2 + 4n - 8)$

**Table 13.4** Some topological indices of  $S_n$ ,  $K_n$ , and  $K_{a,b}$

Graph ( $G$ )	$S_n$	$K_n$	$K_{a,b}$
$ V(G) $	$n$	$n$	$a + b$
$ E(G) $	$n - 1$	$\binom{n}{2}$	$ab$
$W(G)$	$(n - 1)^2$	$\binom{n}{2}$	$(a + b)^2 - ab$ $- a - b$
$W_{e_0}(G)$	$\binom{n-1}{2}$	$\binom{n}{2} \binom{n-1}{2}$	$\frac{ab}{2}(2ab - a - b)$
$W_{e_4}(G)$	$2 \binom{n-1}{2}$	$3 \binom{n+1}{4}$	$ab(ab - 1)$

**Fig. 13.6** A  $C_4$ -nanotori

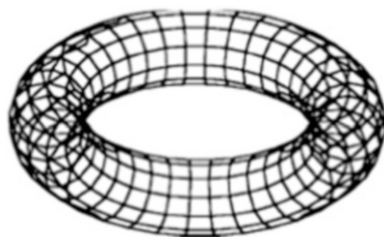


**Fig. 13.7** A  $C_4$ -nanotube

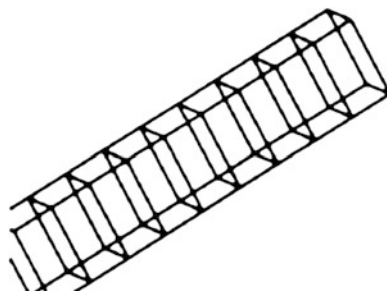




**Fig. 13.8** Graphene

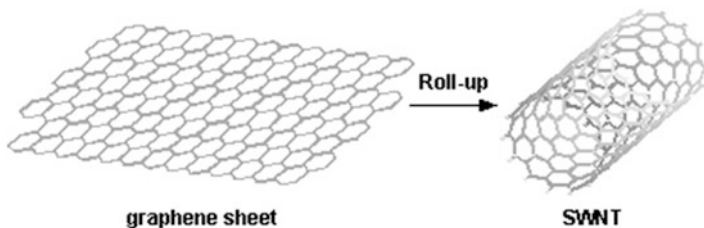
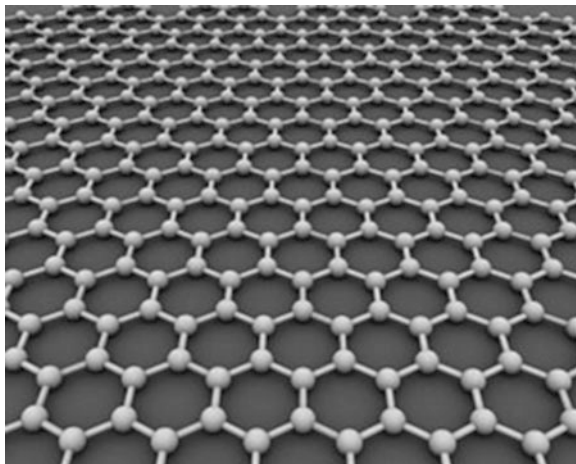


**Fig. 13.9** Graphene sheet can be rolled in to a single walled nanotube

According to the tables, Theorem 13.4.13 and Corollary 13.4.14, we can easily obtain the edge-Wiener indices of the sum of each pair of the above-mentioned graphs. Specially, we can obtain the edge-Wiener indices of graphene,  $C_4$ -nanotubes, and  $C_4$ -nanotori as  $P_n + P_m$ ,  $P_n + C_m$ , and  $C_n + C_m$ , respectively.

*Example 13.4.15* Suppose that  $G = P_n + P_m$ , where  $n$  and  $m$  are not necessarily equal. The edge Wiener indices of  $G$ , are as follows:

$$\begin{aligned}
 W_{e_0}(P_n + P_m) &= \frac{m^3}{6}(2n - 1)^2 + \frac{m^2}{6}(4n^3 - 12n^2 + 8n - 3) \\
 &\quad - \frac{m}{3}(2n^3 - 4n^2 + 2n - 1) + \frac{n}{6}(n^2 - 3n + 2), \\
 W_{e_4}(P_n + P_m) &= \frac{m^3}{6}(2n - 1)^2 + \frac{m^2}{6}(4n^3 - 7n + 3) - \frac{m}{6}(4n^3 + 7n^2 - 2n - 2) \\
 &\quad + \frac{n}{6}(n^2 + 3n + 2)
 \end{aligned}$$

*Example 13.4.16* Suppose that  $G = P_n + C_m$ , where  $n$  and  $m$  are not necessarily equal, then  $G = TUC_4[m, n]$  is a  $C_4$ -nanotube (John and Diudea 2004). The edge-Wiener indices of  $G$  are as follows:

*Case 1.* If  $m$  is odd, then

$$W_{e_0}(P_n + C_m) = \frac{m^3}{8}(2n-1)^2 + \frac{m^2}{6}(4n^3 - 6n^2 + 5n - 3) + \frac{m}{8}(4n^2 - 8n + 3)$$

$$W_{e_4}(P_n + C_m) = \frac{m^3}{8}(2n-1)^2 + \frac{m^2}{6}(4n^3 + 6n^2 - 10n + 3) - \frac{m}{8}(16n^2 - 3)$$

*Case 2.* If  $m$  is even, then

$$W_{e_0}(P_n + C_m) = \frac{m^3}{8}(2n-1)^2 + \frac{m^2}{6}(4n^3 - 6n^2 + 5n - 3) + \frac{m}{2}(n-1)^2$$

$$W_{e_4}(P_n + C_m) = \frac{m^3}{8}(2n-1)^2 + \frac{m^2}{6}(4n^3 + 6n^2 - 10n + 3) - \frac{m}{2}(n^2 + 2n - 1)$$

*Example 13.4.17* Suppose that  $G = C_n + C_m$ , where  $n$  and  $m$  are not necessarily equal, then  $G = TC_4[m, n]$  is a  $C_4$ -nanotorus (Diudea and John 2001). The first edge-Wiener index of  $G$  is equal to  $W_{e_0}(C_n + C_m) = \frac{m^3}{2}n^2 + \frac{m^2}{2}n(n^2 + 1) + \frac{m}{2}n(n-2)$

The second edge-Wiener index of  $G$  is as follows:

*Case 1.* If  $m$  and  $n$  are odd, then

$$W_{e_4}(C_n + C_m) = \frac{m^3}{2}n^2 + \frac{m^2}{2}n(n^2 + 4n - 4) - mn(2n + 1)$$

*Case 2.* If  $m$  and  $n$  are even, then

$$W_{e_4}(C_n + C_m) = \frac{m^3}{2}n^2 + \frac{m^2}{2}n(n^2 + 4n - 1) - \frac{m}{2}n(n + 2)$$

*Case 3.* If  $n$  is odd and  $m$  is even, then

$$W_{e_4}(C_n + C_m) = \frac{m^3}{2}n^2 + \frac{m^2}{2}n(n^2 + 4n - 4) - \frac{m}{2}n(n + 2)$$

**Acknowledgment** This work was partially supported by Center of Excellence of Algebraic Hyperstructures and its Applications of Tarbiat Modares University (CEAHA).

## References

- Azari M, Iranmanesh A (2011) *Ars Combinatoria* 100:113
- Azari M, Iranmanesh A, Tehranian A (2010) *Stud Univ Babes bolyai Chemia Liv* 4:183
- Diudea MV, John PE (2001) *MATCH Commun Math Comput Chem* 44:103
- Gutman I, Potgieter JH (1997) *J Serb Chem Soc* 62:185
- Gutman I, Trinajstić N (1972) *Chem Phys Lett* 17:535
- Gutman I, Yeh YN, Lee SL, Luo L (1993) *Indian J Chem* 32A:651
- Heydari A, Taeri B (2007a) *J Comput Theor NanoSci* 4:158
- Heydari A, Taeri B (2007b) *MATCH Commun Math Comput Chem* 57:665
- Iranmanesh A, Kafrani AS (2009) *MATCH Commun Math Comput Chem* 62:311
- Iranmanesh A, Khormali O (2011) *J Comput Theor NanoSci* 8:133
- Iranmanesh A, Gutman I, Khormali O, Mahmiani A (2009) *MATCH Commun Math Comput Chem* 61:663
- John PE, Diudea MV (2004) *Croat Chem Acta* 77:127
- Khadikar PV, Karmarkar S (2002) *Acta Chim Slov* 49:755
- Mahmiani A, Khormali O, Iranmanesh A (2010a) *Optoelectron Adv Mater Rapid Commun* 4:252
- Mahmiani A, Khormali O, Iranmanesh A, Ahmadi A (2010b) *Optoelectron Adv Mater Rapid Commun* 4:256
- Nikolić S, Trinajstić N, Mihalić Z (1995) *Croat Chem Acta* 68:105
- Sagan BE, Yen YN, Zhang P (1996) *Int J Quantum Chem* 60:959
- Stevanovic D (2001) *Discrete Math* 235:237
- Wiener H (1947) *J Am Chem Soc* 69:17

# Chapter 14

## Study of Fullerenes by Some New Topological Index

Ali Reza Ashrafi, Mohammad Ali Iranmanesh, and Zahra Yarahmadi

**Abstract** A molecular graph is a graph such that its vertices correspond to the atoms and the edges to the bonds of a given molecule. Fullerenes are molecules in the form of polyhedral closed cages made up entirely of  $n$  three-coordinate carbon atoms and having 12 pentagonal and  $(n/2-10)$  hexagonal faces, where  $n$  is equal or greater than 20. The molecular graph of a fullerene is called fullerene graph. In this chapter, the fullerene graphs under two new distance-based topological indices are investigated. Some open questions are also presented.

### 14.1 Introduction

Graph theory successfully provided the chemist with a variety of tools as *molecular graph* and *topological index*. *Molecular graphs* represent the constitution of molecules. They are generated using the following rule: vertices stand for atoms and edges for bonds. It is clear that the degree of each vertex in a molecular graph is

---

A.R. Ashrafi (✉)

Department of Mathematics, Faculty of Mathematics, Statistics and Computer Science,  
University of Kashan, Kashan 87317-51167, Islamic Republic of Iran  
e-mail: [ashrafi@kashanu.ac.ir](mailto:ashrafi@kashanu.ac.ir)

M.A. Iranmanesh

Department of Mathematics, Yazd University, Yazd 89175-741, Islamic Republic of Iran  
e-mail: [iranmanesh@yazduni.ac.ir](mailto:iranmanesh@yazduni.ac.ir)

Z. Yarahmadi

Department of Mathematics, Faculty of Science, Khorramabad Branch, Islamic Azad University,  
Khorramabad, Islamic Republic of Iran

at most four. A *topological index* is a numeric quantity for the molecular graph of a molecule. This number must be invariant under topological symmetry of molecules under consideration.

A *fullerene graph* is the molecular graph of a fullerene molecule. *Fullerenes* are molecules in the form of polyhedral closed cages made up entirely of  $n$  carbon atoms that are bonded in a nearly spherically symmetric configuration. The well-known fullerene, the  $C_{60}$  molecule, is a closed-cage carbon molecule with carbon atoms tiling the spherical or nearly spherical surface with a truncated icosahedral structure formed by 20 hexagonal and 12 pentagonal rings (Kroto et al. 1985, 1993). It is well known that  $C_{20}$  is the unique fullerene constructed fully from pentagons, and by Euler's theorem, there is no fullerene without pentagons.

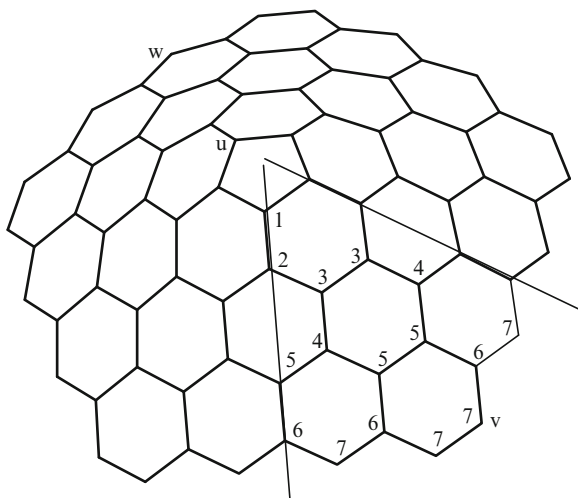
Suppose  $p$ ,  $h$ ,  $n$ , and  $m$  are the numbers of pentagons, hexagons, carbon atoms, and bonds between them, in a given fullerene  $F$ . Since each atom lies in exactly three faces and each edge lies in two faces, the number of atoms is  $n = (5p + 6h)/3$ , the number of edges is  $m = 3/2n = (5p + 6h)/2$ , and the number of faces is  $f = p + h$ . By Euler's formula  $n - m + f = 2$ , one can deduce that  $(5p + 6h)/3 - (5p + 6h)/2 + p + h = 2$ , and therefore,  $p = 12$ ,  $v = 2h + 20$ , and  $e = 3h + 30$ . This implies that such molecules made up entirely of  $n$  carbon atoms and having 12 pentagonal and  $(n/2 - 10)$  hexagonal faces, where  $n \neq 22$  is a natural number equal or greater than 20 (Fowler and Manolopoulos 1995; Kostant 1995).

Throughout this chapter all graphs considered are finite and simple. The notation we use is mostly standard and taken from standard graph theory textbooks such as Trinajstić (1992). The aim of this chapter is to investigate fullerene graphs under three new topological indices: *eccentric connectivity*, *bipartite edge frustration*, and *bipartite vertex frustration* which will be studied with details in Sects. 14.2 and 14.3.

## 14.2 Eccentric Connectivity Index of Fullerenes

Suppose  $u$  and  $v$  are vertices of a graph  $G$ . The *distance*  $d(u, v)$  is defined as the length of a shortest path connecting them. The *eccentricity*  $\varepsilon(u)$  is the largest distance between  $u$  and any other vertex  $x$  of  $G$ . The maximum eccentricity over all vertices of  $G$  is called the *diameter* of  $G$  and denoted by  $D(G)$ , and the minimum eccentricity among the vertices of  $G$  is called *radius* of  $G$  and denoted by  $R(G)$ . The set of vertices whose eccentricity is equal to the radius of  $G$  is called the *center* of  $G$ . It is well known that each tree has either one or two vertices in its center. The *eccentric connectivity index*  $\xi(G)$  of  $G$  is defined as  $\xi(G) = \sum_{u \in V(G)} \deg(u)\varepsilon(u)$  (Sharma et al. 1997). We encourage the reader to consult papers (Dureja and Madan 2007; Kumar et al. 2004; Sardana and Madan 2001; Gupta et al. 2002; Zhou and Du 2010) for more information on mathematical properties and chemical meaning of this topological index and (Ashrafi et al. 2011a, b; Saheli et al. 2010a, b; Ashrafi and Saheli 2010; Saheli and Ashrafi 2010a, b) for some applications in nanoscience.

**Fig. 14.1** The one-pentagonal carbon nanocone  $CNC_5[3]$



Since the molecular graph of a fullerene graph can be constructed from *nanocones*, we begin by computing eccentric connectivity index of this important class of nanostructures. *One-pentagonal carbon nanocones*, Fig. 14.1, was originally discovered by Ge and Sattler (1994). These are constructed from a graphene sheet by removing a  $60^\circ$  wedge, and joining the edges produces a cone with a single pentagonal defect at the apex.

To compute the eccentric connectivity index of one-pentagonal carbon nanocone  $C[n] = CNC_5[n]$  containing  $2n + 1$  layers, we have to compute the number vertices and edges of this graph. From Fig. 14.1, it is clear that

$$\begin{aligned}
 |V(C[n])| &= 5[1 + 1 + 2 + 2 + \dots + n + n + (n + 1)] = 5(n + 1)^2, \\
 |E(C[n])| &= 5[1 + 3 + 5 + \dots + (2n + 1)] + 1 + 2 + 3 + \dots + n \\
 &= 5\left[(n + 1)^2 + n(n + 1)/2\right] = \frac{5}{2}(n + 1)(3n + 2).
 \end{aligned}$$

We now assume that  $u$  is a vertex of the central pentagon of  $C[n]$ . Then from Fig. 14.1, one can see that there exists a vertex  $v$  of degree 2 such that  $d(u, v) = 2n + 2$  and so  $\varepsilon(u) = 2n + 2$ . On the other hand, there exists another vertex  $w$  of degree 2 such that  $d(u, w) = 2n$ . Therefore, the shortest path with maximum length is connecting two vertices of degree 2 in  $C[n]$ . This implies that  $D(G) = \text{Max}\{d(x, y) \mid \text{deg}(x) = \text{deg}(y) = 2\} = 4n + 2$  and  $R(G) = 2n + 2$ . Therefore, the eccentricities of vertices of  $C[n]$  are varied between  $2n + 2$  and  $4n + 2$ . From Fig. 14.1, we can see that if  $P$  is the central pentagon of  $C[n]$  and  $a$  and  $b$  are two vertices of  $C[n]$  such that  $d(a, P) = d(b, P)$ , then  $\varepsilon(a) = \varepsilon(b)$ , where  $d(x, P) = \text{Min}\{d(x, y) \mid y \in V(P)\}$ . Define

$$A_i = \{x \in C[n] \mid d(x, P) = i\}, \quad 1 \leq i \leq 2n + 1.$$

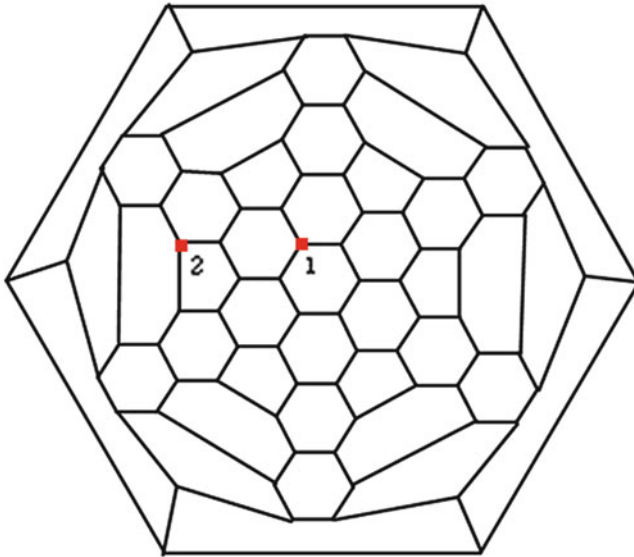


**Fig. 14.2** The molecular graph of the fullerene  $C_{12(2n+1)}$

From Fig. 14.1, it is clear that  $|A_i| = 5(1 + [(i - 1)/2])$ , where  $[x]$  denotes the greatest integer less than or equal to  $x$ . On the other hand, the eccentricity of vertices in each layer is constant, and the number of vertices in the layers  $2k$  and  $2k + 1$  is the same,  $1 \leq k \leq n$ . Thus, the summation of eccentricities in the layers  $2j$  and  $2j + 1$  is

$$\begin{aligned} t_j &= [2n + 2 + 2(j - 1)] + 2n + 2 + (2(j - 1) + 1)] \\ &= 4(n + j) + 1, \quad 1 \leq j \leq n. \end{aligned}$$

Therefore, we prove the following theorem:

**Theorem 14.2.1** *The radius, diameter, and eccentric connectivity index of  $C[n]$  can be computed by the following formulas:*

$$\begin{aligned} R(C[n]) &= 2n + 2, \quad D(C[n]) = 4n + 2, \\ \xi(C[n]) &= 5(10n^3 + 43/2n^2 + 31/2n + 4). \end{aligned}$$

We now define the eccentric connectivity polynomial (EC polynomial) of a graph  $G$  that is a useful polynomial for computing eccentric connectivity index. It is defined as  $ECP(G, x) = \sum_{a \in V(G)} \deg_G(a)x^{\varepsilon(a)}$ . Then the eccentric connectivity index is the first derivative of  $ECP(G, x)$  evaluated at  $x = 1$ . In what follows the eccentric connectivity polynomials of two infinite classes of fullerenes are computed. We encourage the interested readers to consult Ghorbani et al. (2009) for more details on our calculations. Consider the fullerene molecule  $C_{12n+2}$  depicted in Fig. 14.2. In Table 14.1, the EC polynomials of  $C_{12(2n+1)}$  fullerenes are computed for  $2 \leq n \leq 7$ .

**Table 14.1** Some exceptional cases of  $C_{12(2n+1)}$  fullerenes

Fullerenes	EC polynomials
$C_{60}$	$60x^9$
$C_{84}$	$84x^{11}$
$C_{108}$	$84x^{12} + 24x^{13}$
$C_{132}$	$60x^{12} + 24x^{13} + 24x^{14} + 24x^{15}$
$C_{156}$	$36x^{12} + 24x^{13} + 24x^{14} + 24x^{15} + 24x^{16} + 24x^{17}$
$C_{180}$	$12x^{12} + 24x^{13} + 24x^{14} + 24x^{15} + 24x^{16} + 24x^{17} + 24x^{18} + 24x^{19}$

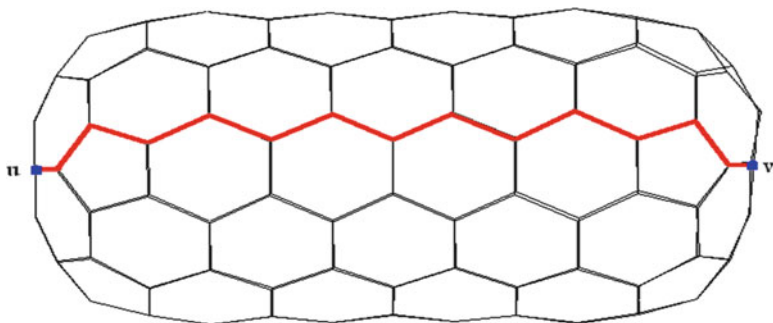


**Fig. 14.3** The value of  $\varepsilon(x)$  for vertices of central and outer hexagons

From Fig. 14.2, one can see that there are two types of vertices of fullerene graph  $C_{12(2n+1)}$ . These are the vertices of the central hexagon and other vertices of  $C_{12(2n+1)}$ . Obviously, we have the following:

Vertices	$\varepsilon(x)$	No.
The Type 1 vertices	$n + i \ (6 \leq i \leq n + 5)$	24
The Type 2 vertices	$n + 5$	12

Suppose  $n \geq 8$ . By using these calculations, Figs. 14.2 and 14.3, one can prove the following general formula for the EC polynomial of this class of fullerenes:

**Theorem 14.2.2** *The EC polynomial of  $C_{12(2n+1)}, n \geq 8$ , fullerenes are computed as*

$$ECP(C_{12(2n+1)}, x) = 12x^{n+5} + 24x^{n+6} \frac{x^n - 1}{x - 1}.$$

**Corollary 14.2.3** *The diameter of  $C_{12(2n+1)}$  fullerene,  $n \geq 2$  is  $2n + 5$ .*

In the end of this section, we consider another class of fullerene graphs with exactly  $12n + 4$  carbon atoms, Fig. 14.4. In Table 14.2, the EC polynomials of  $C_{12n+4}$  fullerenes are computed for each  $n, 2 \leq n \leq 7$ . For  $n \geq 8$  we will compute



**Fig. 14.4** The molecular graph of the fullerene  $C_{12n+4}$

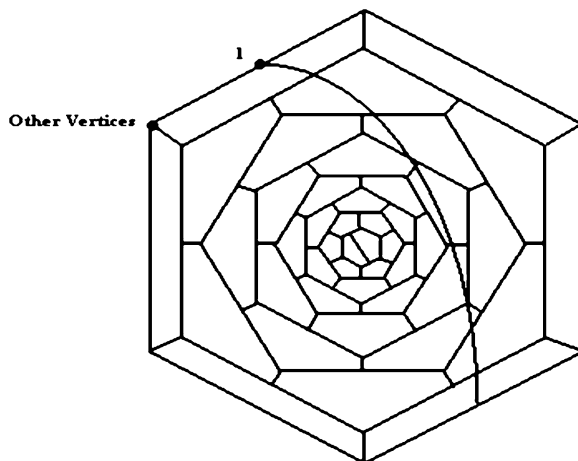


**Table 14.2** Some exceptional cases of  $C_{12n+4}$  fullerenes

Fullerenes	EC polynomials
$C_{28}$	$12x^5 + 16x^6$
$C_{40}$	$36x^7 + 4x^8$
$C_{52}$	$12x^7 + 32x^8 + 8x^9$
$C_{64}$	$24x^8 + 24x^9 + 12x^{10} + 4x^{11}$
$C_{76}$	$12x^8 + 24x^9 + 12x^{10} + 12x^{11} + 12x^{12} + 4x^{13}$
$C_{88}$	$24x^9 + 12x^{10} + 12x^{11} + 12x^{12} + 12x^{13} + 12x^{14} + 4x^{15}$

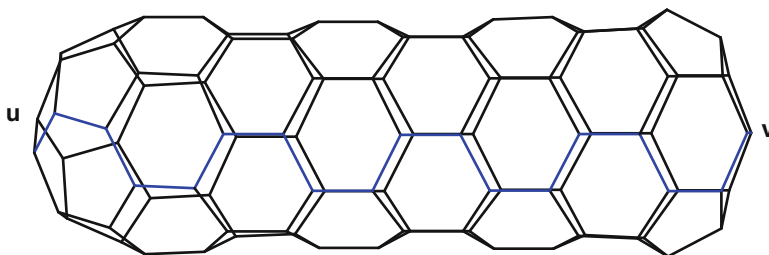


**Fig. 14.5** The value of  $\varepsilon(x)$  for vertices of central and outer polygons

a general formula for the EC polynomial of this class of fullerenes. In Table 14.2, the eccentric connectivity polynomial of six exceptional cases that  $2 \leq n \leq 7$  is computed.

From Figs. 14.4 and 14.5, one can see that there are two types of vertices for the fullerene graph  $C_{12n+4}$ . These are the vertices of the central pentagons and other vertices of  $C_{12n+4}$ . Obviously, we have the following:

Vertices	$\varepsilon(x)$	No.
The Type 1 vertices	$2n + 1$	4
Other vertices	$n + i (1 \leq i \leq n + 1)$	12

By using these calculations, we can prove the following theorem:

**Theorem 14.2.4** *The EC polynomial of the fullerene  $C_{12n+4}$  ( $n \geq 8$ ), fullerenes are computed as follows:*

$$\text{ECP}(C_{12n+4}, x) = 36x^{n+1} \frac{x^{n+1}-1}{x-1} + 12x^{2n+1}.$$

**Corollary 14.2.5** *The diameter of  $C_{12n+4}$  fullerenes,  $n \geq 4$ , is  $2n + 1$ .*

### 14.3 Edge and Vertex Frustration Indices of Fullerenes

A graph  $G$  with the vertex set  $V(G)$  is bipartite if  $V(G)$  can be partitioned into two subsets  $V_1$  and  $V_2$  such that all edges have one endpoint in  $V_1$  and the other in  $V_2$ . The smallest number of edges that have to be deleted from a graph to obtain a bipartite spanning subgraph is called the *bipartite edge frustration* of  $G$  and denoted by  $\varphi(G)$  (Došlić and Vukičević 2007). It is easy to see that  $\varphi(G)$  is a topological index and  $G$  is bipartite if and only if  $\varphi(G) = 0$ . It can be easily shown that  $\varphi(G) \leq |E(G)|/2$  and that the complete graph on  $n$  vertices has the maximum possible bipartite edge frustration among all graphs on  $n$  vertices. Hence, the bipartite edge frustration has properties that make it useful as a measure of non-bipartivity of a given graph. Instead of looking for large bipartite subgraphs of a given graph  $G$ , it is sometimes more convenient to look at the equivalent problem of finding a smallest set of edges that must be deleted from  $G$  in order to make the remaining graph bipartite. Borrowing from the terminology of the antiferromagnetic Ising model, the cardinality of any such set is then called the bipartite edge frustration of a graph.

This topological index has important applications in computing stability of fullerenes. Fajtlowicz and Larson (2003) claimed that the chemical stability of fullerenes is related to the minimum number of vertices/edges that need to be deleted to make fullerene graph bipartite. Schmalz et al. (1986) observed that the isolated pentagon fullerenes have the best stability. Because of this success, it is natural to study its vertex version. The *bipartite vertex frustration* of  $G$ ,  $\psi(G)$ , is defined as the minimum number of vertices that have to be deleted from  $G$  to obtain a bipartite subgraph  $H$  of  $G$  (Yarahmadi and Ashrafi 2011a). Obviously, if  $G$  is not bipartite, then  $H$  is not a spanning subgraph of  $G$  and so,  $H$  is not in general a large bipartite subgraph of  $G$ .

The quantity  $\varphi(G)$  is, in general, difficult to compute; it is NP-hard for general graphs. Hence, it makes sense to search for classes of graphs that allow its efficient computation. Some results in this direction are reported in Došlić and Vukičević

(2007) for fullerenes and other polyhedral graphs and in Ghohjavad and Ashrafi (2008) for some classes of nanotubes. For mathematical properties of this new topological index, we refer to Yarahmadi and Ashrafi (2011b), Yarahmadi et al. (2010), Yarahmadi and Ashrafi (2013) and Yarahmadi (2010).

For obtaining some results on the bipartite vertex frustration, it seems that it is possible to find an algorithm for constructing a large bipartite spanning subgraph from  $H$ . Suppose  $G$  is a graph. A subset  $A$  of  $V(G)$  such that  $G - A$  is bipartite is called a vertex bipartization for  $G$ . The vertex bipartization problem for the graph  $G$  is to find the minimum number of vertices whose removal makes the graph bipartite which is equivalent to the problem of computing  $\psi(G)$ .

It is clear that  $G$  is bipartite if and only if  $\varphi(G) = \psi(G) = 0$ . Since the quantity  $\psi(G)$  is, in general, difficult to compute, it makes sense to search for classes of fullerene graphs. Došlić and Vukičević (2007) proved the following theorem:

**Theorem 14.3.1** *Let  $G$  be a fullerene graph. Then  $\varphi(G) \geq 6$ . If  $G$  has IP, then  $\varphi(G) \geq 12$ .*

Given a graph  $G$ , a *matching*  $M$  in  $G$  is a set of pairwise nonadjacent edges; that is, no two edges share a common vertex. We say that a vertex is matched if it is incident to an edge in the matching. Otherwise, the vertex is unmatched.

*Example 14.3.2* Let  $K_n$ ,  $C_n$ , and  $W_n$  denote the complete cycle and wheel on  $n$  vertices. Then  $\psi(K_n) = n - 2$ . If  $n$  is even, then  $\psi(C_n) = 0$ , and  $\psi(C_n) = 1$ , otherwise. Finally, if  $n$  is even, then  $\psi(C_n) = 2$ , and  $\psi(C_n) = 1$ , otherwise.

It is an easy fact that if  $G$  is a graph with components  $G_1, G_2, \dots, G_n$ , then  $\psi(G)$  is the summation of  $\psi(G_i)$ 's,  $1 \leq i \leq n$ . The same property is satisfied by the edge frustration index. So, to compute the bipartite vertex or edge frustration index of graphs, it is enough to consider connected graphs and then apply above result. From now on all graphs are assumed to be connected.

Of particular interest are the fullerene graphs without adjacent pentagons. We call them *IP fullerenes*, where IP stands for "isolated pentagons." Fullerene graphs are not bipartite; hence, for all fullerene graphs  $G$ , we have  $\psi(G) > 0$ . Because in the boundary of every odd face at least one edge must be removed and at most two odd faces can be destroyed by a removal of one edge. In this section we compute the bipartite vertex frustration of  $C_{12(2n+1)}$ ,  $C_{12n+4}$ ,  $C_{24n}$ , and  $C_{12n+2}$ . The first two classes are depicted in Figs. 14.2 and 14.4, and the last two of them are depicted in Figs. 14.6 and 14.7.

Since fullerene graphs are not bipartite,  $\phi(G) > 0$ . Because in the boundary of every odd face at least one edge must be removed and at most two odd faces can be destroyed by a removal of one edge, we have the following lower bounds.

**Theorem 14.3.3** *Let  $G$  be a simple graph, then  $\psi(G) \leq \varphi(G)$  with equality if and only if there exists a matching  $M$  such that  $G - M$  is bipartite.*

We consider the fullerene graph  $C_{12n+4}$ . Every fullerene has 12 cycles of length 5 and then it is not bipartite. By removing specified edges in Fig. 14.7, one can see that the spanning bipartite subgraph of the fullerene graph  $C_{12n+4}$  remains. Then we

**Fig. 14.6** The molecular graph of fullerene  $C_{24n}$

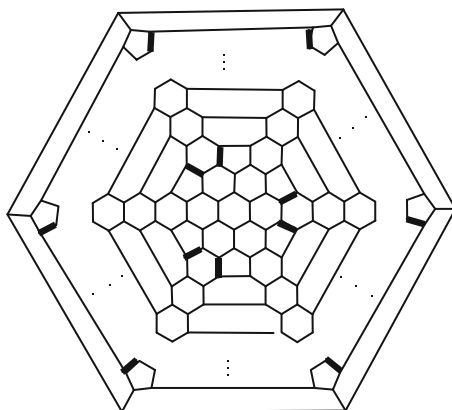
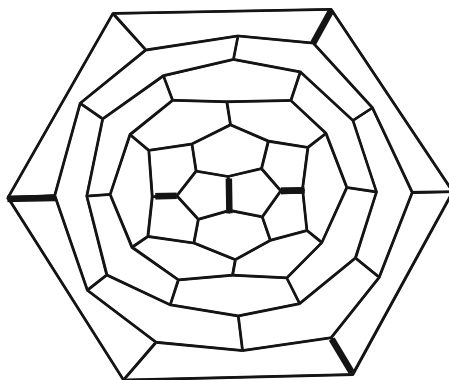


**Fig. 14.7** The molecular graph of fullerene  $C_{12n+2}$



can say that  $\varphi(C_{12+4}) \leq 6$ . Since the fullerene graph  $C_{12n+4}$  is not IP, by Theorem 14.3.1,  $\varphi(F_{12+4}) \geq 6$ . Hence, we prove the following theorem:

**Theorem 14.3.4**  $\varphi(C_{12+4}) = 6$  (Fig. 14.8).

Next we consider the molecular graph  $C_{12(2n+1)}$ . Suppose  $K$  is the subgraph of  $C_{12(2n+1)}$  obtained by deleting the specified edges in Fig. 14.9. It is easy to see that  $K$  is bipartite, so  $\varphi(C_{12(2n+1)}) \leq 6$ . The fullerene graph  $C_{12(2n+1)}$  is IP, and then by Theorem 14.3.1,  $\varphi(C_{12(2n+1)}) \geq 6$ . Therefore, we prove the following result:

**Theorem 14.3.5**  $\varphi(C_{12(2n+1)}) = 12$ .

Suppose  $C_{24n}$  and  $C_{12n+2}$  are fullerene graphs with exactly  $24n$  and  $12n + 2$  carbon atoms, respectively. These are depicted in Figs. 14.6 and 14.7. In what follows the edge frustration index of these classes of fullerenes is computed.

From Fig. 14.10, one can see that all of the pentagonal faces in this fullerene are isolated and so  $\varphi(C_{24n}) \geq 12$ . Moreover by removing 12 bold edges which are shown in Fig. 14.10, a spanning bipartite subgraph of  $C_{24n}$  is obtained. Then  $\varphi(C_{24n}) \leq 12$ , which proves that  $\varphi(C_{24n}) = 12$ . On the other hand, by removing specified edges in

**Fig. 14.8** The molecular graph of fullerene  $C_{12n+4}$

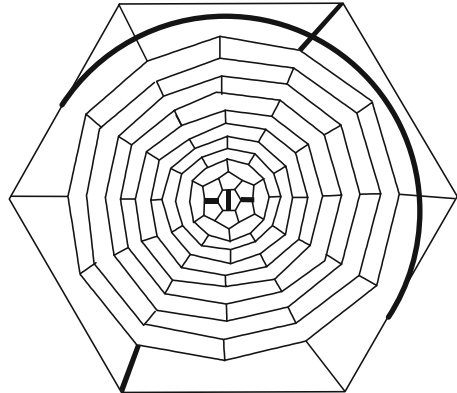


**Fig. 14.9** The molecular graph of fullerene  $C_{12(2n+1)}$

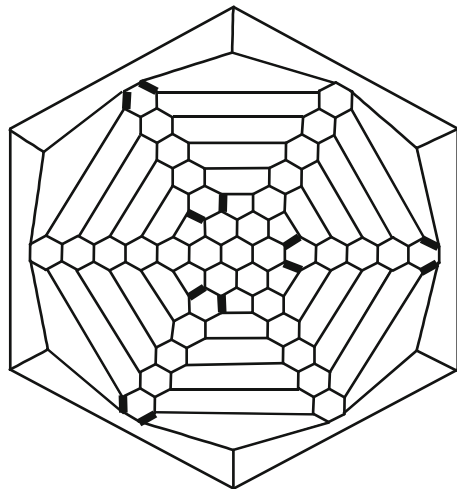


Fig. 14.11 from the fullerene  $C_{12n+2}$ , the remaining spanning subgraph is bipartite. Then we prove again that  $\varphi(C_{12n+2}) = 6$ . We record our calculations in the following theorem:

**Theorem 14.3.6**  $\varphi(C_{24n}) = 12$  and  $\varphi(C_{12n+2}) = 6$ .

We now calculate the bipartite vertex frustration of  $C_{12n+4}$ ,  $C_{12(2n+1)}$ ,  $C_{24n}$ , and  $C_{12n+2}$  fullerene graphs.

By Theorems 14.3.3 and 14.3.4, we conclude that  $\psi(C_{12n+4}) \leq \varphi(C_{12n+4}) = 6$ . The fullerene graph  $C_{12n+4}$  has two isomorphic subgraphs. For obtaining a bipartite subgraph of  $C_{12n+4}$ , we must obtain bipartite subgraphs of all subgraphs of  $C_{12n+4}$ . From Fig. 14.11, one can see that by removing vertices  $u$ ,  $v$ , and  $w$ , this subgraph of  $C_{12n+4}$  becomes bipartite. Since there are two isomorphic subgraphs, such as Fig. 14.11, for obtaining a bipartite subgraph of  $C_{12n+4}$ , we must delete at least six vertices. Hence,  $\psi(C_{12n+4}) \geq 6$ . So, we prove the following theorem:

**Fig. 14.10** The molecular graph of fullerene  $C_{24n}$

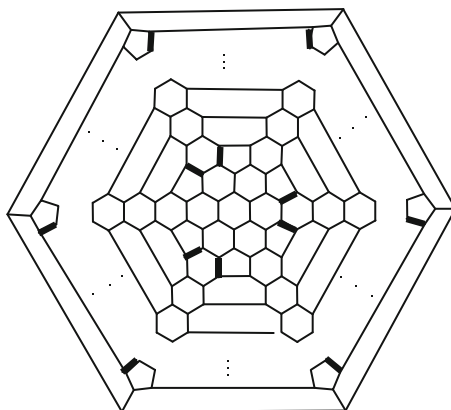
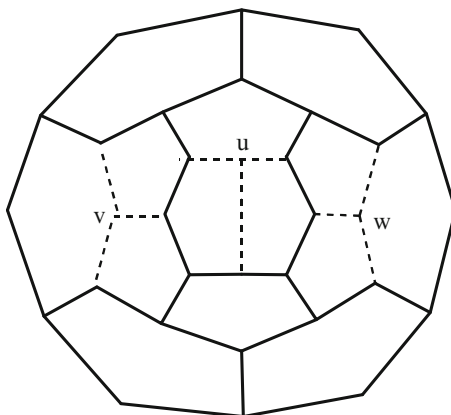


**Fig. 14.11** Deleted vertices of a subgraph of  $C_{12n+4}$



**Theorem 14.3.7**  $\psi(C_{12n+4}) = 6$ .

By Theorems 14.3.3 and 14.3.5, we conclude that  $\psi(C_{12(2n+1)}) \leq \varphi(C_{12(2n+1)}) = 12$ . The fullerene graph  $C_{12(2n+1)}$  has two isomorphic subgraphs which are shown in Fig. 14.12. For obtaining a bipartite subgraph of  $C_{12(2n+1)}$ , we must obtain bipartite subgraphs of all subgraphs of  $C_{12(2n+1)}$ . By Fig. 14.12, one can see that by removing vertices  $a, b, c, d, e,$  and  $f$ , this subgraph of  $C_{12(2n+1)}$  becomes bipartite. Since there are two isomorphic subgraph, we must delete at least 12 vertices to obtain a bipartite subgraph of  $C_{12(2n+1)}$ . Hence,  $\psi(C_{12(2n+1)}) \geq 12$ . We record our calculations in the following theorem:

**Theorem 14.3.8**  $\psi(C_{12(2n+1)}) = 12$ .

We now apply Theorems 14.3.3 and 14.3.6 to conclude that  $\psi(C_{24n}) \leq \varphi(C_{24n}) = 12$ . The fullerene graph  $C_{24n}$  has two isomorphic subgraphs which are shown in Fig. 14.13. For obtaining a bipartite subgraph of  $C_{24n}$ , we must obtain bipartite subgraphs of all subgraphs of  $C_{24n}$ . By Fig. 14.13, one can see that

**Fig. 14.12** Deleted vertices of a subgraph of  $C_{12(2n+1)}$

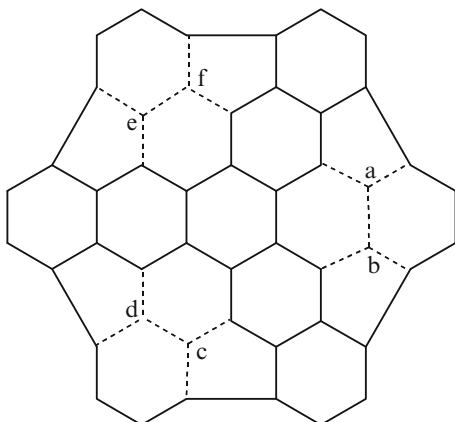
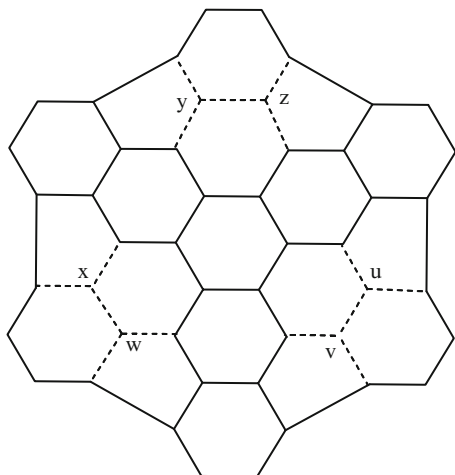


**Fig. 14.13** Deleted vertices of a subgraph of  $C_{24n}$



by removing vertices  $u, v, w, x, y,$  and  $z,$  this subgraph of  $C_{24n}$  becomes bipartite. Since there are two isomorphic subgraphs, such as Fig. 14.13, for obtaining a bipartite subgraph of  $C_{24n},$  we must delete at least 12 vertices. Hence,  $\psi(C_{24n}) \geq 12.$

Consider the fullerene class  $C_{12n+2}.$  Apply Theorem 14.3.3 to conclude that  $\psi(C_{12n+2}) \leq \varphi(C_{12n+2}).$  By Theorem 14.3.6  $\varphi(C_{12n+2}) = 6.$  Hence,  $\psi(C_{12n+2}) \leq 6.$  The fullerene graph  $C_{12n+2}$  has two subgraphs  $H$  and  $K$  which are shown in Fig. 14.14. To obtain a bipartite subgraph of  $C_{24n},$  we have to find bipartite subgraphs of all subgraphs of  $C_{12n+2}.$  By Fig. 14.14, one can see that by removing vertices  $u, v,$  and  $w,$  the subgraph  $K$  of  $C_{12n+2}$  becomes bipartite, and by similar way by removing vertices  $a, b,$  and  $c$  of subgraph  $H,$  a bipartite subgraph remains. Thus, we must delete at least six vertices to obtain a bipartite subgraph of  $C_{12n+2}.$  Hence,  $\psi(C_{12n+2}) \geq 6.$  Therefore, we have the following theorem:

**Theorem 14.3.9**  $\psi(C_{24n}) = 12$  and  $\psi(C_{12n+2}) = 6.$

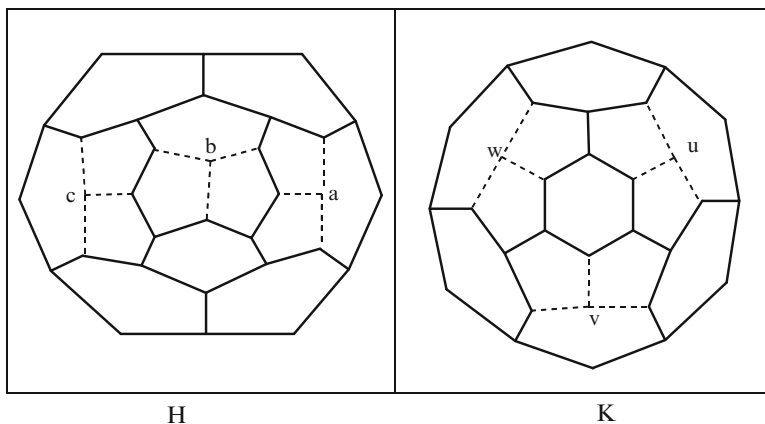


Fig. 14.14 Deleted vertices of two subgraphs of  $C_{12n+2}$

## References

- Ashrafi AR, Saheli M (2010) Optoelectron Adv Mater Rapid Commun 4:898  
 Ashrafi AR, Saheli M, Ghorbani M (2011a) J Comput Appl Math 235:4561  
 Ashrafi AR, Doslic T, Saheli M (2011b) MATCH Commun Math Comput Chem 65:221  
 Došlić T, Vukičević D (2007) Discrete Appl Math 155:1294  
 Dureja H, Madan AK (2007) Med Chem Res 16:331  
 Fajtlowicz S, Larson CE (2003) Chem Phys Lett 377:485  
 Fowler PW, Manolopoulos DE (1995) An atlas of fullerenes. Oxford University Press, Oxford  
 Ge M, Sattler K (1994) Chem Phys Lett 220:192  
 Ghojavand M, Ashrafi AR (2008) Dig J Nanomat Biosci 3:209  
 Ghorbani M, Ashrafi AR, Hemmasi M (2009) Optoelectron Adv Mater Rapid Commun 3:1306  
 Gupta S, Singh M, Madan AK (2002) J Math Anal Appl 266:259  
 Kostant B (1995) Not Am Math Soc 9:959  
 Kroto HW, Heath JR, O'Brien SC, Curl RF, Smalley RE (1985) Nature 318:162  
 Kroto HW, Fichier JE, Cox DE (1993) The fullerene. Pergamon Press, New York  
 Kumar V, Sardana S, Madan AK (2004) J Mol Model 10:399  
 Saheli M, Ashrafi AR (2010a) Maced J Chem Chem Eng 29:71  
 Saheli M, Ashrafi AR (2010b) J Comput Theor Nanosci 7:1900  
 Saheli M, Saati H, Ashrafi AR (2010a) Optoelectron Adv Mater Rapid Commun 4:896  
 Saheli M, Ashrafi AR, Diudea MV (2010b) Studia Univ Babes-Bolyai Chemia 55:233  
 Sardana S, Madan AK (2001) MATCH Commun Math Comput Chem 43:85  
 Schmalz TG, Seitz WA, Klein DJ, Hite GE (1986) Chem Phys Lett 130:203  
 Sharma V, Goswami R, Madan AK (1997) J Chem Inf Comput Sci 37:273  
 Trinajstić N (1992) Chemical graph theory. CRC Press, Boca Raton  
 Yarahmadi Z (2010) Appl Math Lett 23:1077  
 Yarahmadi Z, Ashrafi AR (2011a) Appl Math Lett 24:1774  
 Yarahmadi Z, Ashrafi AR (2011b) Comput Math Appl 62:319  
 Yarahmadi Z, Ashrafi AR (2013) Fullerene Nanotube Carbon Nanostruct 21:129  
 Yarahmadi Z, Došlić T, Ashrafi AR (2010) Discrete Appl Math 158:1551  
 Zhou B, Du Z (2010) MATCH Commun Math Comput Chem 63:181



# Chapter 15

## Topological Study of (3,6)– and (4,6)–Fullerenes

Ali Reza Ashrafi and Zeinab Mehranian

**Abstract** A (3,6)–fullerene is a cubic plane graph whose faces (including the outer face) have sizes 3 or 6. (4,6)–Fullerene graphs are defined analogously by interchanging triangles with quadrangles. (3,6)–Fullerenes have exactly four triangles and (4,6)–fullerenes have exactly 6 quadrangles. The (4,6)–fullerenes are also called boron fullerenes. In this chapter some infinite families of (3,6)– and (4,6)–fullerenes are presented. The modeling of these fullerenes by considering some topological indices is the main part of this chapter. Finally, some open questions are presented.

### 15.1 Introduction and Preliminaries

A *polytope*  $P$  is a tessellation of a given manifold  $M$ . If  $M$  has dimension  $n$ , then it is convenient to name  $P$  as  $n$ -polytope. A polygon is a 2-polytope and a polyhedron is a 3-polytope. Suppose  $P$  is a  $d$ -dimensional polytope. Then a *Schlegel diagram* of  $P$  is a projection of  $P$  into  $\mathbb{R}^{d-1}$ . The Schlegel diagrams are an important tool for studying combinatorial and topological properties of polytopes (Goodey 1977).

A *simple graph* is a graph without directed and multiple edges and without loops. If  $G$  is such a graph, then the vertex and edge sets of  $G$  are represented by  $V(G)$  and  $E(G)$ , respectively. Let  $M$  be a molecule. The molecular graph of  $M$  is a simple graph in which atoms of  $M$  are its vertices and two atoms are adjacent if there is a bond between them.

---

A.R. Ashrafi (✉)

Department of Pure Mathematics, Faculty of Mathematics, Statistics and Computer Science,  
University of Kashan, Kashan 87317-51167, Islamic Republic of Iran  
e-mail: [ashrafi@kashanu.ac.ir](mailto:ashrafi@kashanu.ac.ir)

Z. Mehranian

Department of Nanocomputing, Institute for Nanoscience and Nanotechnology,  
University of Kashan, Kashan 87317-51167, Islamic Republic of Iran

A  $(k,6)$ -fullerene is a cubic plane graph whose faces have sizes  $k$  and 6. The only values of  $k$  for which a  $(k,6)$ -fullerene exists are 3, 4, and 5. A  $(5,6)$ -fullerene is simply called a fullerene. They are molecules in the form of polyhedral closed cages made up entirely of  $n$  carbon atoms that are bonded in a nearly spherically symmetric configuration. The most important fullerene is buckyball. This is a molecule containing 60 carbon atoms, each of which is bonded to three adjacent carbon atoms in a sphere form that's about 1 nm in diameter (Kroto et al. 1985, 1993). The mathematical properties of ordinary fullerenes are studied in Fowler and Manolopoulos (1995) and Kostant (1995).

After successful history of fullerenes, it was natural to consider  $(3,6)$ - and  $(4,6)$ -fullerenes into account. The  $(3,6)$ -fullerenes have received recent attention from chemists due to their similarity to ordinary fullerenes (Yang and Zhang 2012; De Vos et al. 2009). The Euler's formula implies that an  $n$ -vertex  $(3,6)$ -fullerene has exactly four faces of size 3 and  $n/2 - 2$  hexagons. A  $(3,6)$ -fullerene is called *ITR* if its triangles have no common edge. Recently some chemists have been attracted to the  $(4,6)$ -fullerenes or boron fullerenes (Wang et al. 2010). If six quadrangles of these new types of fullerenes don't have common edge, then we will briefly name them *ISR fullerenes*.

In this chapter, we will describe the mathematical properties of some families of  $(3,6)$ - and  $(4,6)$ -fullerenes which are built from a given  $(3,6)$ - or  $(4,6)$ -fullerenes by adding edges in such a way that the resulting graph is cubic. Here, we will show how to construct bigger cages with similar structural characteristics to those found in the smaller one.

Throughout this chapter all graphs considered are simple. Our notation is standard and taken mainly from the standard graph theory textbooks such as (Trinajstić 1992). The aim of this chapter is to investigate  $(3,6)$ - and  $(4,6)$ -fullerenes under five topological indices, *eccentric connectivity*, *Szeged*, *revised Szeged*, *vertex PI*, and *Wiener index*, which will be studied with details in Sects. 15.2 and 15.3.

## 15.2 Basic Definitions

Suppose  $u$  and  $v$  are vertices of a graph  $G$ . The *distance*  $d(u, v)$  is defined as the length of a shortest path connecting them. The *eccentricity*  $\varepsilon(u)$  is the largest distance between  $u$  and any other vertex  $x$  of  $G$ . The maximum eccentricity over all vertices of  $G$  is called the **diameter** of  $G$  and denoted by  $D(G)$ , and the minimum eccentricity among the vertices of  $G$  is called *radius* of  $G$  and denoted by  $R(G)$ .

The *Wiener index* is the first distance-based topological index that introduced by chemist Harold Wiener (Wiener 1947). The Wiener defined his index as the sum of all distances between any two carbon atoms in the molecule, in terms of carbon-carbon bonds. The Wiener index is principally defined for trees. It was in 1972 that Hosoya (1971, 1988) described its calculation using the distance matrix and proposed the name "Wiener index."

The *eccentric connectivity index*  $\xi^c(G)$  of  $G$  is defined as  $\xi^c(G) = \sum_{u \in V(G)} \text{deg}(u) \varepsilon(u)$ , where for a given vertex  $u$  of  $V(G)$ , its eccentricity,  $\varepsilon(u)$ , is the largest distance between  $u$  and any other vertex  $v$  of  $G$  (Sharma et al. 1997). The maximum eccentricity over all vertices of  $G$  is called the diameter of  $G$  and denoted by  $D(G)$ . We encourage the reader to consult papers (Dureja and Madan 2007; Kumar et al. 2004; Sardana and Madan 2001; Gupta et al. 2002; Zhou and Du 2010) for more information on mathematical properties and chemical meaning of this topological index and (Ashrafi et al. 2011a, b; Saheli et al. 2010a, b; Ashrafi and Saheli 2010; Saheli and Ashrafi 2010a, b) for some applications in nanoscience.

The *Szeged index* is another distance-based topological index that was introduced by Ivan Gutman (1994). It is defined as  $Sz(G) = \sum_{e=uv} n_u(e) n_v(e)$ , where  $n_u(e)$  is the number of vertices closer to  $u$  than  $v$  and  $n_v(e)$  is defined analogously. We encourage the reader to consult paper for more information about Szeged index (Gutman and Dobrynin 1998).

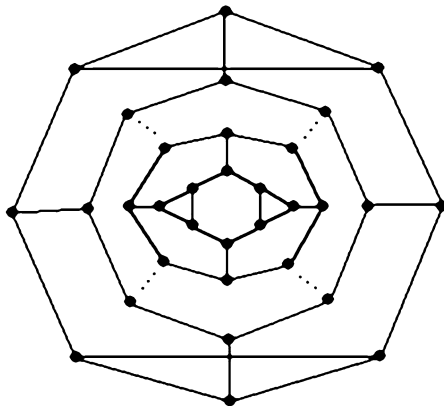
The *vertex PI index* is a recently proposed topological index defined as  $PI_v(G) = \sum_{e=uv} [n_u(e) + n_v(e)]$  (Khalifeh et al. 2008). This topological index was introduced in an attempt to obtain exact expression for the edge version of this index under Cartesian product of graphs. It is worth mentioning that there is an edge version of this topological index proposed by Padmakar Khadikar (2000). In Ashrafi and Loghman (2006a, b, c) this edge version is calculated for some classes of nanostructures.

A graph  $G$  is called *bipartite* if its vertex set can be partitioned into two subsets  $A$  and  $B$  such that each edge of  $G$  connects a vertex in  $A$  to a vertex in  $B$ . It is well known that a graph  $G$  is bipartite if and only if it does not have odd cycle. It is possible to characterize bipartite graphs by vertex PI index. A graph  $G$  is bipartite if and only if its vertex PI index is equal to  $|V(G)| \times |E(G)|$ . So, the vertex PI does not have good correlation with physicochemical properties of chemical compounds, when the molecular graph is bipartite.

The *revised Szeged index*  $Sz^*(G)$  of  $G$  is a molecular structure descriptor equal to the sum of products  $[n_u(e) + n_0(e)/2] \times [n_v(e) + n_0(e)/2]$  over all edges  $e = uv$  of the molecular graph  $G$ , where  $n_0(e)$  is the number of vertices equidistant from  $u$  and  $v$ . This topological index was introduced by Milan Randić (2002). Nowadays the scientists prefer the name revised Szeged index for this distance-based topological index. It is easy to prove that a graph  $G$  is bipartite if and only if the Szeged and revised Szeged indices of  $G$  are the same. The interested readers can consult papers (Pisanski and Randić 2010; Pisanski and Žerovnik 2009; Xing and Zhou 2011; Aouchiche and Hansen 2010) for mathematical properties and chemical meaning of this new topological index.

### 15.3 (3,6)-Fullerenes

The (3,6)-fullerenes that sometimes called (3,6)-cages have received recent attention from chemists due to their similarity to ordinary fullerenes. With the best of our knowledge, there is no classification of these cubic graphs. So, it is natural to

**Fig. 15.1**  $G[8n]$ ,  $n$  is even

construct more and more (3,6)–fullerenes to find such a classification. In this section seven infinite classes of (3,6)–fullerenes are constructed, and then the eccentric connectivity, Szeged, revised Szeged, vertex PI, and Wiener index of them are computed.

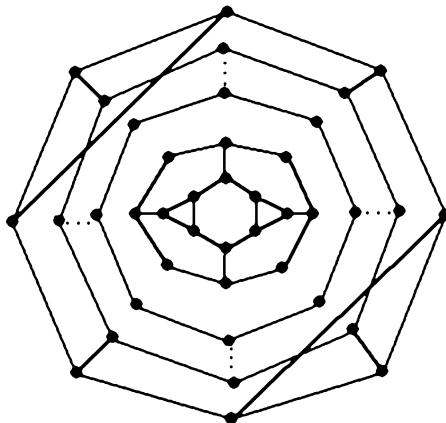
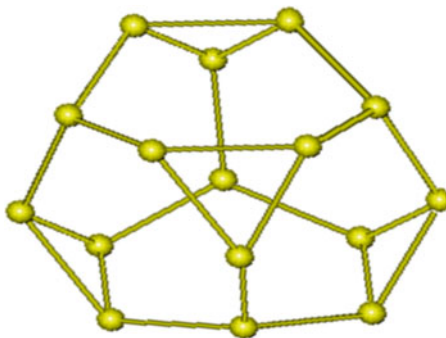
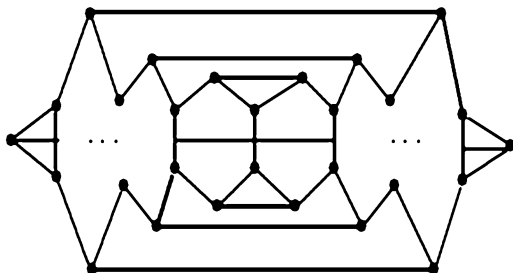
Suppose  $F$  is the molecular graph of an arbitrary  $n$ –vertex (3,6)– or (4,6)–fullerenes. The adjacency matrix of  $F$  is an  $n \times n$  matrix  $A = [a_{ij}]$  defined by  $a_{ij} = 1$ , if vertices  $i$  and  $j$  are connected by an edge and  $a_{ij} = 0$  otherwise. It is easy to prove the adjacency matrix will determine the fullerene graph up to isomorphism. An  $n \times n$  matrix  $A = [a_{ij}]$  is called *symmetric* if  $a_{j,i} = a_{i,j}$  and *centrosymmetric* when its entries satisfy  $a_{i,j} = a_{n-i+1}a_{n-j-1}$ , for  $1 \leq i, j \leq n$ . Recently it is proved that the adjacency matrix of some classes of fullerenes is centrosymmetric. This caused to find exact formula for the Wiener index of these fullerenes in general (Graovac et al. 2011).

The distance matrix  $D = [d_{ij}]$  of  $F$  is another  $n \times n$  matrix in which  $d_{ij}$  is the length of a minimal path connecting vertices  $i$  and  $j$ ,  $i \neq j$ , and zero otherwise. Clearly, the summation of all entries in distance matrix of a fullerene  $F$  is equal to  $2W(F)$ . To compute the Szeged, revised Szeged, vertex PI, eccentric connectivity, or Wiener indices of  $F$ , we first draw  $F$  by HyperChem (2002) and then apply TopoCluj software (Diudea et al. 2002) of Diudea and his team to compute the adjacency and distance matrices of this fullerene graph. Finally, we provide a GAP program (Schönert et al. 1995) to calculate these topological indices for  $F$ .

Our first class of (3,6)–fullerenes is depicted in Figs. 15.1, 15.2, and 15.3. These fullerenes have exactly  $8n$  vertices and their Schlegel diagrams show that they are ITR.

Our second class of (3,6)–fullerenes is again ITR with exactly  $8n + 4$  vertices depicted in Figs. 15.4 and 15.5.

The third class of (3,6)–fullerenes that is studied in this section is not ITR. The Schlegel diagram of an arbitrary member of this class is depicted in Fig. 15.6. The 3D perception of the first member  $I[16]$  of this class, Fig. 15.7, and the algorithm for construction of other members of the class from the first one shows that the elements of this class are different from the first two classes of (3,6)–fullerenes.

**Fig. 15.2**  $G[8n]$ ,  $n$  is odd**Fig. 15.3** The 3D perception of  $G[16]$ **Fig. 15.4** The Schlegel diagram of  $H[8n + 4]$ 

One of the pioneers of fullerene chemistry, P.W. Fowler, believed that a fullerene has to be 3-connected and so  $I[16]$  is not a fullerene. Notice that, we don't consider 3-connectivity in our definition for a fullerene.

Our fourth class of (3,6)-fullerenes is not ITR. The Schlegel diagram of an arbitrary element of this class, together with the 3D perception of the first,  $J[24]$ , is depicted in Figs. 15.8 and 15.9, respectively. It is not so difficult to prove that the members of this class are essentially different from the first three presented classes of (3,6)-fullerenes.

**Fig. 15.5** The 3D perception of  $H[20]$

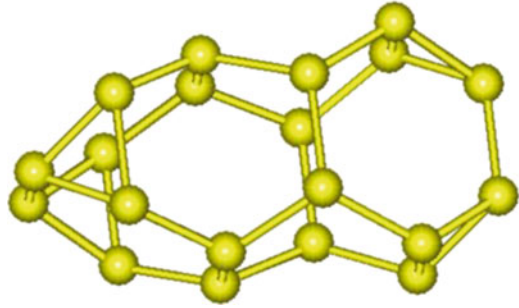


**Fig. 15.6** The Schlegel diagram of  $I[4n]$ ,  $n \geq 2$

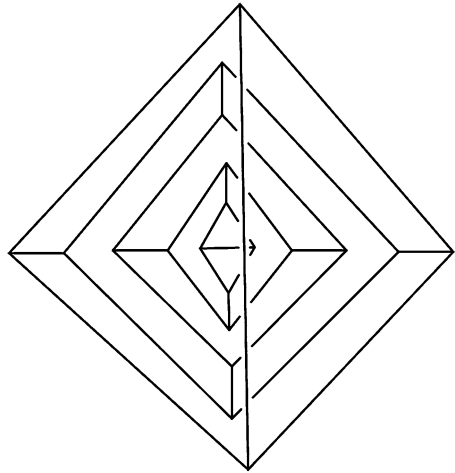
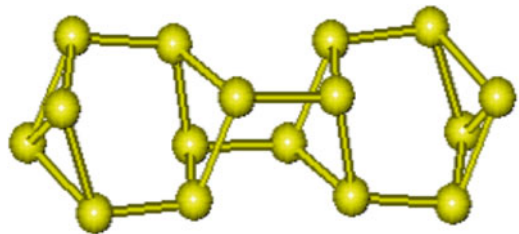


**Fig. 15.7** The 3D perception of  $I[16]$



The molecular graph of our fifth class of (3,6)–fullerenes is depicted in Fig. 15.10. These (3,6)–fullerenes have exactly  $16n - 32$  vertices and all of them are ITR. In Fig. 15.11, the 3D perception of the first member of this class is depicted.

The sixth class of (3,6)–fullerenes is again ITR which contains  $16n + 48$  vertices,  $n \geq 1$ . The Schlegel diagram and 3D perception of one member of this class are depicted in Figs. 15.12 and 15.13, respectively.

The seventh and our final class of (3,6)–fullerenes has exactly  $12n + 4$  vertices, and the molecular graph is ITR; see Figs. 15.14 and 15.15.

Since (3,6)–fullerenes are cubic, it is easy to see that the molecular graphs of  $G[8n]$ ,  $H[8n + 4]$ ,  $I[4n]$ ,  $J[24n]$ ,  $K[16n - 32]$ ,  $L[16n + 48]$ , and  $M[12n + 4]$  have exactly  $12n$ ,  $12n + 6$ ,  $6n$ ,  $36n$ ,  $24n - 48$ ,  $24n + 72$ , and  $18n + 6$  edges, respectively.

**Fig. 15.8** The Schlegel diagram of  $J[24n]$

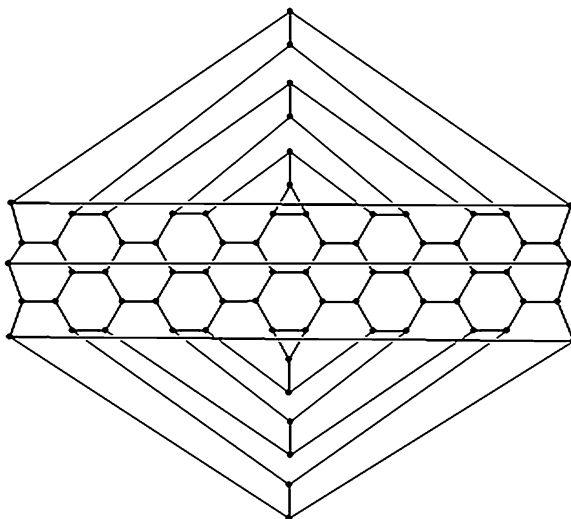


**Fig. 15.9** The 3D perception of  $J[24]$

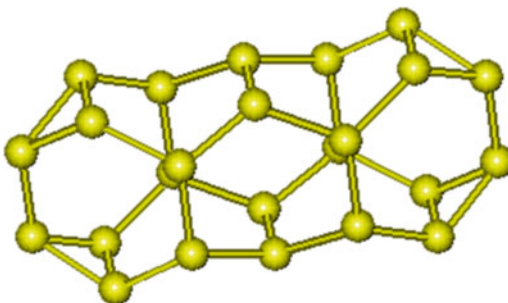
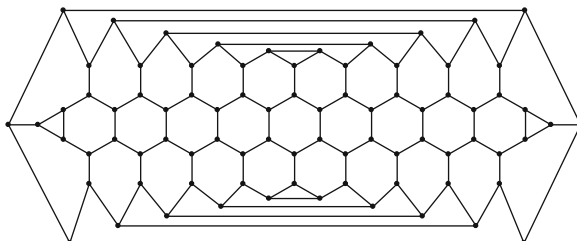


**Fig. 15.10** The Schlegel diagram of  $K[16n - 32]$ ,  $n \geq 5$



### 15.3.1 Wiener and Eccentric Connectivity Indices of (3,6)-Fullerenes

In this section the Wiener and eccentric connectivity indices of  $G[8n]$ ,  $H[8n + 4]$ ,  $I[4n]$ ,  $J[24n]$ ,  $K[16n - 32]$ ,  $L[16n + 48]$ , and  $M[12n + 4]$  are computed. By an easy calculation, one can see that  $W(G[16]) = 294$ ,  $\xi^c(G[16]) = 192$ ,  $\xi^c(G[24]) = 348$ ,

**Fig. 15.11** The 3D perception of  $K[48]$

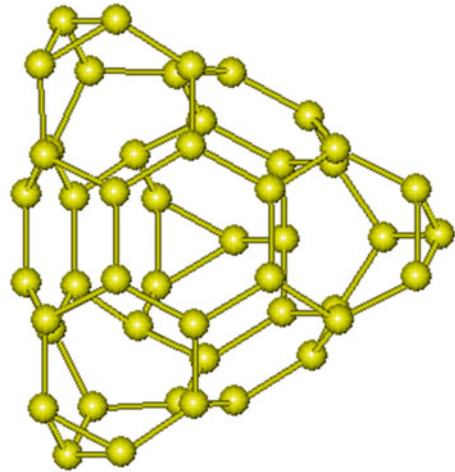
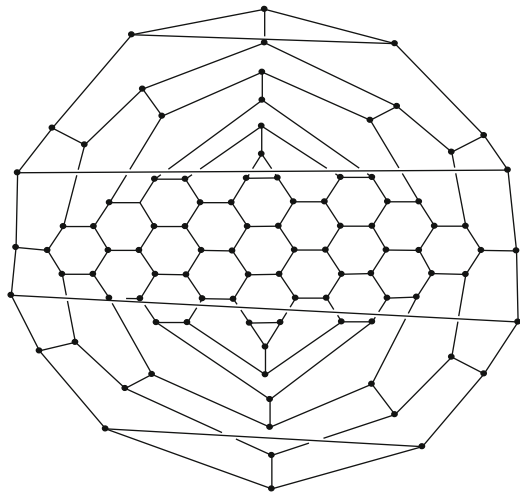


**Fig. 15.12** The Schlegel diagram of  $L[16n + 48]$ ,  $n \geq 1$



$\xi^c(G[32]) = 600$ ,  $\xi^c(G[40]) = 888$ , and  $\xi^c(G[48]) = 1,248$ . On the other hand, for  $n \geq 7$ , we can partition the vertex set of  $G[8n]$  into  $n$  parts, each of which contains eight vertices in such a way that the eccentricity of each vertex in the first part is  $n$ , the eccentricity of each vertex in the second part is  $n + 1, \dots$ , and the eccentricity of each vertex in the  $n$ th part is equal to  $2n - 1$ . In Fig. 15.16, the black vertices have the maximum eccentricity and red vertices have second maximum eccentricity in  $G[8n]$ ,  $n \geq 7$ .

Our calculations show the following:

**Result 15.1** For  $n \geq 3$ ,  $W(G[8n]) = (64/3)n^3 + (464/3)n - 206$ , and for  $n \geq 7$ ,  $\xi^c(G[8n]) = 36n^2 - 12n$ .



**Fig. 15.13** The 3D perception of  $L[64]$

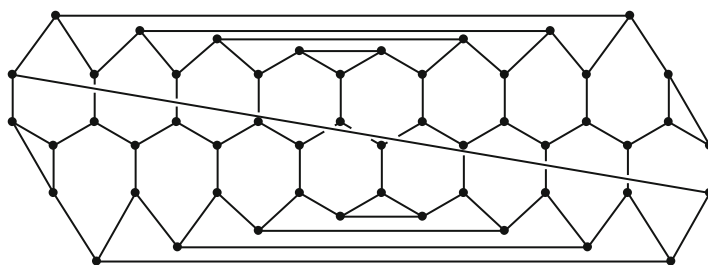
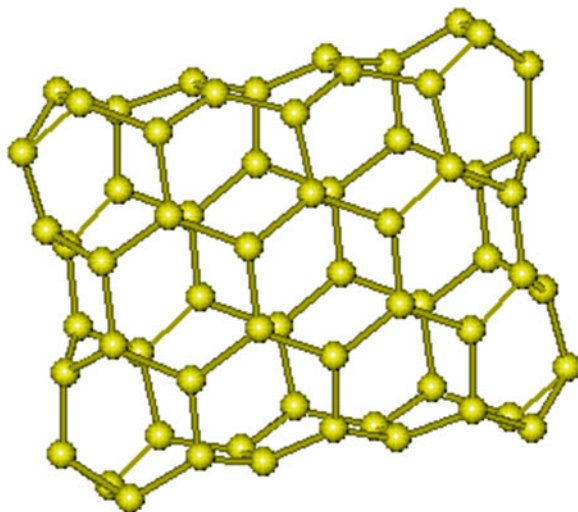


**Fig. 15.14** The Schlegel diagram of  $M[12n + 4]$ ,  $n \geq 1$

**Fig. 15.15** The 3D perception of  $M[40]$

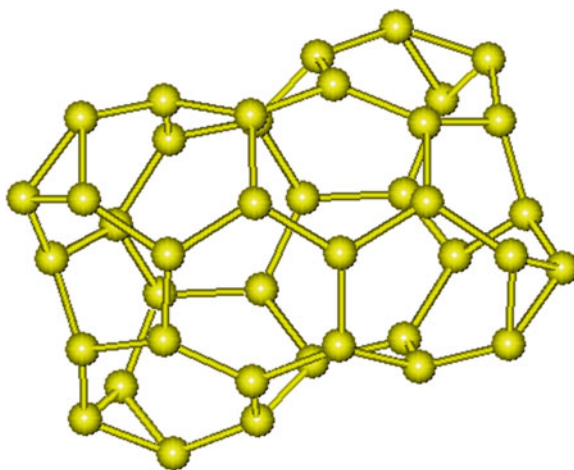


**Fig. 15.16** The maximum (black) and second maximum (red) eccentricities in  $G[n]$

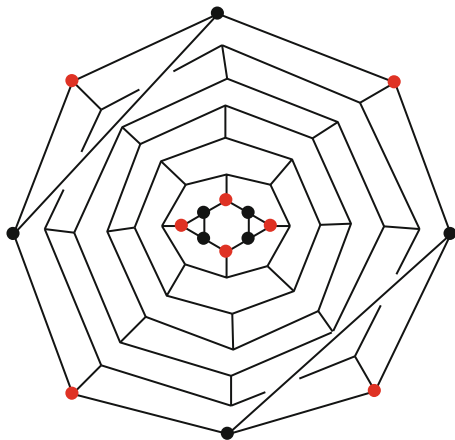
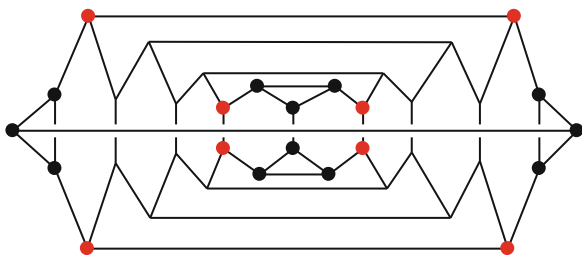


**Fig. 15.17** The maximum (black) and second maximum (red) eccentricities in  $H[8n + 4]$



We now consider the class  $H[8n + 4]$  of (3,6)-fullerenes. We can partition the set of vertices of  $H[8n + 4]$  into  $n - 1$  parts in which one of them has size 12 and any other parts having size eight. The eccentricity of the vertices of the first part is  $2n + 1$ , the second part is the set of vertices having eccentricity  $n + 2$ , the third part is the set of all vertices having eccentricity  $n + 3, \dots$ , and the  $n$ th part is the set of vertices having eccentricity  $2n$ . In Fig. 15.17, the black vertices have the maximum eccentricity and red vertices have the second maximum of eccentricity between vertices of  $H[8n + 4]$ . From these calculations, we have the following result:

**Result 15.2** For  $n \geq 1$ ,  $W(H[8n + 4]) = (64/3)n^3 + 64n^2 + (152/3)n + 2$  and  $\xi^c(H[8n + 4]) = 36n^2 + 60n + 12$ .

Consider the (3,6)-fullerene  $I[4n]$ . An easy calculation shows that  $\xi^c(I[8]) = 72$ . On the other hand, we can partition  $V(I[4n])$  into  $n$  parts, each of which having size four in such a way that the vertices of the first part have eccentricity  $n$ , the vertices of the second part have eccentricity  $n + 1, \dots$ , and the vertices of the  $n$ th part have eccentricity  $2n - 1$ . In Fig. 15.18, the black vertices have the maximum eccentricity and red vertices have the second maximum of eccentricity between vertices of  $I[4n]$ .

From the calculations given above, one can prove the following:

**Result 15.3** For  $n \geq 2$ ,  $W(I[4n]) = (16/3)n^3 + (20/3)n - 6$ , and for  $n \geq 3$ ,  $\xi^c(I[4n]) = 18n^2 - 6n$ .

**Fig. 15.18** The maximum (black) and second maximum (red) eccentricities in  $J[4n]$

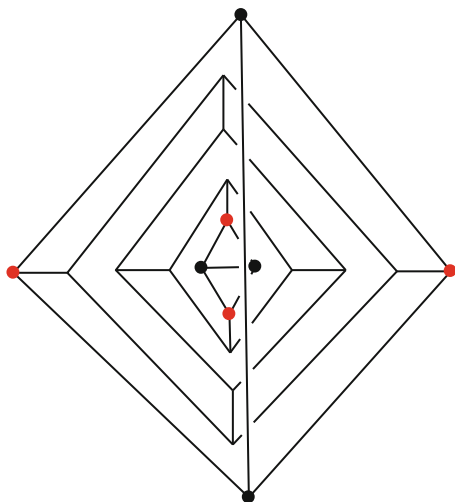
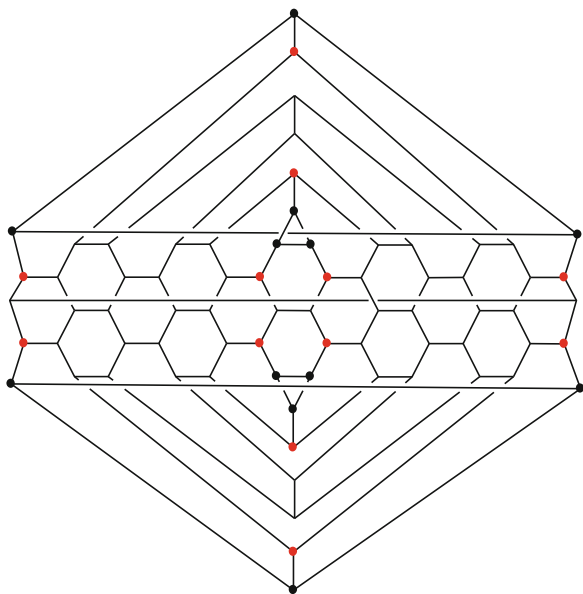


**Fig. 15.19** The maximum (black) and second maximum (red) eccentricities in  $J[24n]$



By an easy calculation, one can see that  $W(J[24]) = 864$ ,  $W(J[48]) = 4,824$ ,  $\xi^c(J[24]) = 396$ ,  $\xi^c(J[48]) = 1,140$ ,  $\xi^c(J[72]) = 2,064$ ,  $\xi^c(J[96]) = 3,420$ , and  $\xi^c(J[120]) = 5,256$ . On the other hand, for  $n \geq 6$ , we can partition the vertex set of  $J[24n]$  into  $2n$  parts, each of which contains four vertices in such a way that the eccentricity of each vertex in the first part is  $2n$ , the eccentricity of each vertex in the second part is  $2n + 1, \dots$ , and the eccentricity of each vertex in the  $2n$ th part is equal to  $4n - 1$ . In Fig. 15.19, the black vertices have the maximum eccentricity and red vertices have second maximum eccentricity in  $J[24n]$ ,  $n \geq 6$ .

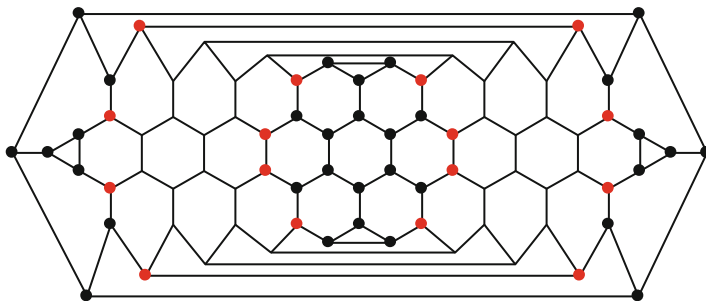


**Fig. 15.20** The maximum (black) and second maximum (red) eccentricities in  $K[16n - 32]$

The following result is a direct consequence of our calculations:

**Result 15.4** For  $n \geq 3$ ,  $W(J[24n]) = 384n^3 + 1,656n - 1,594$ , and for  $n \geq 6$ ,  $\xi^c(J[24n]) = 216n^2 - 36n$ .

We now consider the (3,6)-fullerene  $K[16n - 32]$ . An easy calculation shows that  $\xi^c(K[48]) = 1,008$  and  $\xi^c(K[64]) = 1,632$ . On the other hand, we can partition  $V(K[16n - 32])$  into  $n - 3$  parts such that one of them have size 32 and any other parts have size 16. Also, the vertices of the part of size 32 have eccentricity  $2n - 3$ , and vertices of other parts have eccentricities  $n + 1, n + 2, \dots, 2n - 4$ , respectively. In Fig. 15.20, the black vertices have the maximum eccentricity and red vertices have the second maximum of eccentricity between vertices of  $K[16n - 32]$ .

Our given calculations lead us to the following result:

**Result 15.5** For  $n \geq 5$ ,  $W(K[16n - 32]) = (256/3)n^3 - 256n^2 + (608/3)n - 492$ , and for  $n \geq 7$ ,  $\xi^c(K[16n - 32]) = 72n^2 - 168n$ .

By an easy calculation by our GAP program, we can see that  $W(L[64]) = 9,968$ ,  $W(L[80]) = 17,432$ ,  $W(L[96]) = 27,724$ ,  $\xi^c(L[64]) = 1,692$ ,  $\xi^c(L[80]) = 2,340$ ,  $\xi^c(L[96]) = 3,168$ ,  $\xi^c(L[112]) = 3,972$ ,  $\xi^c(L[128]) = 4,968$ ,  $\xi^c(L[144]) = 6,024$ ,  $\xi^c(16n-32L[160]) = 7,260$ ,  $\xi^c(L[176]) = 8,652$ ,  $\xi^c(L[192]) = 10,224$ ,  $\xi^c(L[208]) = 11,952$ ,  $\xi^c(L[224]) = 13,824$ ,  $\xi^c(L[240]) = 15,840$ ,  $\xi^c(L[256]) = 18,048$ , and  $\xi^c(L[272]) = 22,896$ .

On the other hand, for  $n \geq 15$ , we can partition the vertex set of  $L[16n + 48]$  into  $n + 3$  parts, each of which contains 16 vertices in such a way that the eccentricity of each vertex in the first part is  $n + 3$ , the eccentricity of each vertex in the second part is  $n + 4, \dots$ , and the eccentricity of each vertex in the  $(n + 3)$ th part is equal to  $2n + 5$ . In Fig. 15.21, the black vertices have the maximum eccentricity and red vertices have second maximum eccentricity in  $L[16n + 48]$ ,  $n \geq 15$ . These calculations suggest the following result:

**Result 15.6** For  $n \geq 4$ ,  $W(L[16n + 48]) = (256/3)n^3 + 768n^2 + (14,912/3)n + 5,340$ , and for  $n \geq 15$ ,  $\xi^c(L[16n + 48]) = 72n^2 + 408n + 576$ .

**Fig. 15.21** The maximum (black) and second maximum (red) eccentricities in  $L[16n + 48]$

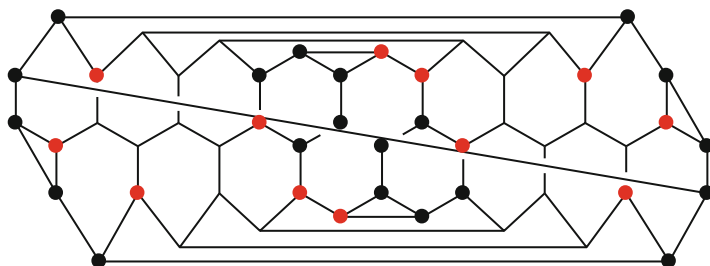
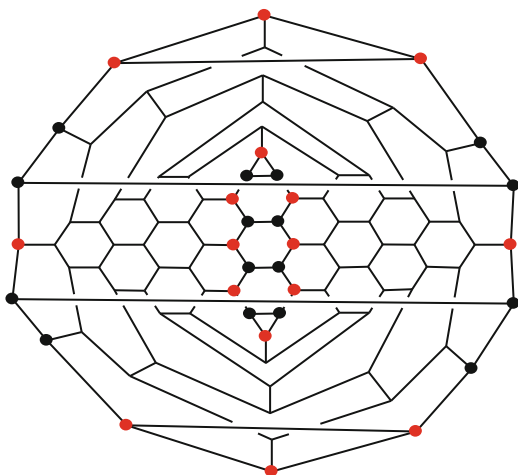


**Fig. 15.22** The maximum (black) and second maximum (red) eccentricities in  $M[12n + 4]$

In the end of this section, the Wiener and eccentric connectivity indices of (3,6)-fullerene  $M[12n + 4]$  is computed. Using our GAP program, we can see that  $W(M[16]) = 296$ ,  $\xi^c(M[16]) = 204$ ,  $\xi^c(M[28]) = 420$ ,  $\xi^c(M[40]) = 804$ , and  $\xi^c(M[52]) = 1,248$ . On the other hand, we can partition  $V(M[12n + 4])$  into  $n$  parts such that one of them has size eight, another of size 20, and any other parts have size 12 in such a way that the elements of these classes have the same eccentricity. The eccentricities of a representative of the first two classes are  $n + 2$  and  $2n + 1$ , respectively. On the other hand, the representatives of other parts have eccentricities  $n + 3$ ,  $n + 4$ ,  $\dots$ ,  $2n$ , respectively. In Fig. 15.22, the black vertices have the maximum eccentricity and red vertices have the second maximum of eccentricity between vertices of  $M[12n + 4]$ .

From these calculations, we have the following:

**Result 15.7** For  $n \geq 2$ ,  $W(M[12n + 4]) = 48n^3 + 144n^2 + 192n - 126$ , and for  $n \geq 5$ ,  $\xi^c(M[12n + 4]) = 54n^2 + 90n$ .

**Table 15.1** The values of  $n_u(e)$ ,  $n_v(e)$ , and  $n_0(e)$  for a given edge  $e = uv$  in  $G[8n]$

Edges	The values of $n_u(e)$ , $n_v(e)$ , and $n_0(e)$	No
1	$6, 6, 8n - 12$	4
2	$8n - 9, 8, 1$	4
3	$8n - 8, 8, 0$	4
4	$8n - 16, 10, 6$	8
5	$8n - 12, 10, 2$	8
6	$8n - 16, 16, 0$	8
7	$8n - 17, 15, 2$	8
8	$8n - 15, 14, 1$	8
9	$8n - 22, 21, 1$	16
10	$8n - 24 - 4i, 24 + 4i, 0; n = 6 + i, i = 0, 2, 4, \dots$	4
	$8n - 24 - 4i, 24 + 4i, 0; n = 6 + i, i = 1, 3, 5, \dots$	8
11	$8n - 24 - 4i, 24 + 4i, 0; n \geq 7 + i, i = 0, 2, 4, \dots$	8
	$8n - 24 - 4i, 24 + 4i, 0; n \geq 7 + i, i = 1, 3, 5, \dots$	16

### 15.3.2 Vertex PI, Szeged, and Revised Szeged Indices of (3,6)-Fullerenes

Consider the (3,6)-fullerene  $G[8n]$  depicted in Figs. 15.1 and 15.2. Apply our method described in the third paragraph of this section for some small numbers of  $n$ . Using our program we obtain four exceptional cases that  $n = 2, 3, 4$ , and  $5$ . Then an easy calculation shows that  $PI(G[16]) = 300$ ,  $Sz(G[16]) = 972$ ,  $Sz(G[24]) = 3,418$ ,  $Sz(G[32]) = 8,944$ ,  $Sz(G[40]) = 17,840$ ,  $Sz^*(G[16]) = 1,533$ ,  $Sz^*(G[24]) = 5,010$ ,  $Sz^*(G[32]) = 11,445$ ,  $Sz^*(G[40]) = 21,357$ .

From calculations given in Table 15.1 and Figs. 15.23 and 15.24, we have the following result:

**Result 15.8** For  $n \geq 6$ ,  $Sz^*(G[8n]) = 128n^3 + 64n^2 + 1648n - 4,519$ ,  $Sz(G[8n]) = 128n^3 + 1,216n - 4,280$ , and for  $n \geq 3$ ,  $PI_v(G[8n]) = 96n^2 - 32n - 60$ .

We now consider our second class  $H[8n + 4]$  of (3,6)-fullerenes. An easy calculation by our program shows that  $Sz(H[12]) = 34$  and  $Sz^*(H[12]) = 648$ .

By our calculations given in Table 15.2 and Figs. 15.25 and 15.26, we have the following result:

**Result 15.9** For  $n \geq 2$ ,  $Sz^*(H[8n + 4]) = (448/3)n^3 + 320n^2 + (656/3)n - 42$ ,  $Sz(H[8n + 4]) = (448/3)n^3 + 192n^2 + (188/3)n - 66$ , and for  $n \geq 1$ ,  $PI_v(H[8n + 4]) = 96n^2 + 56n + 4$ .

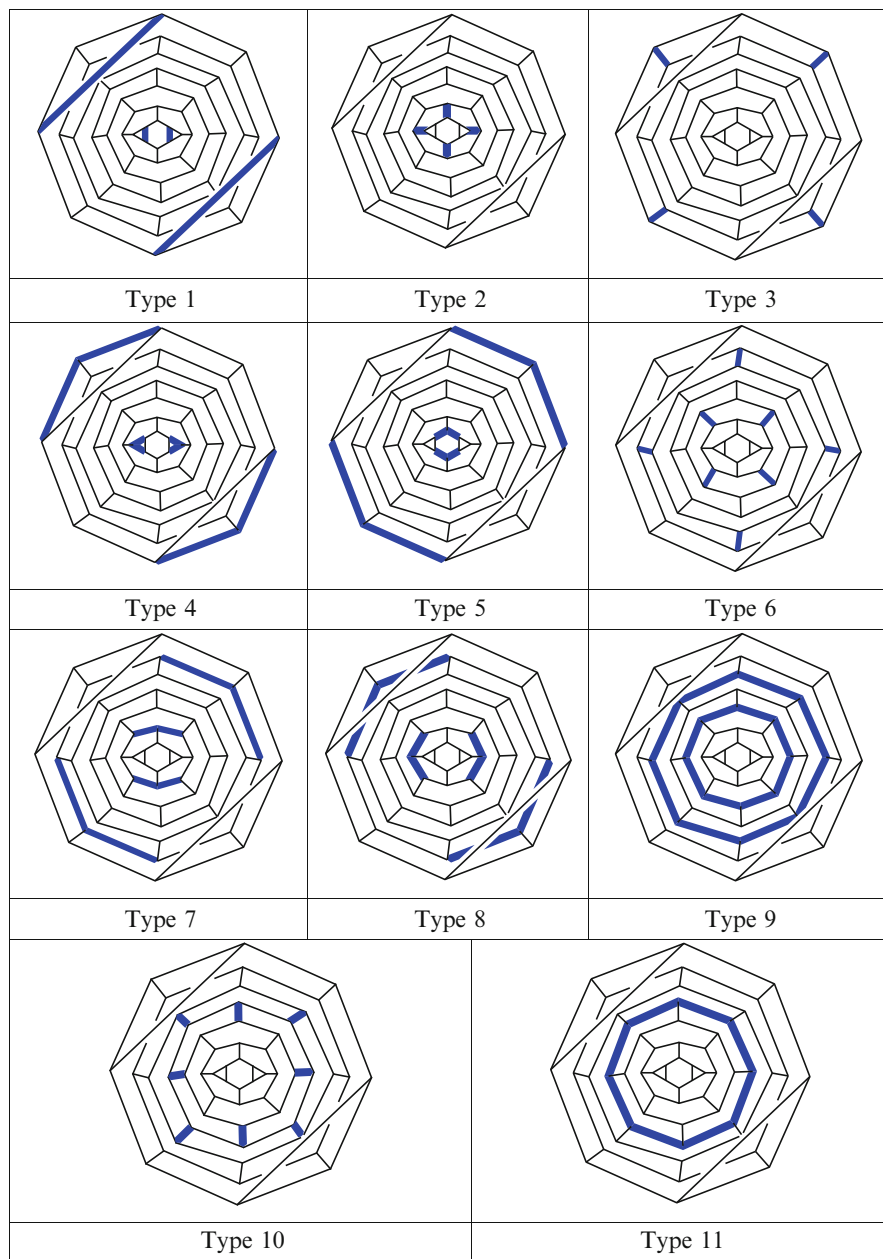


Fig. 15.23 The 11 types of edges in  $G[8n]$

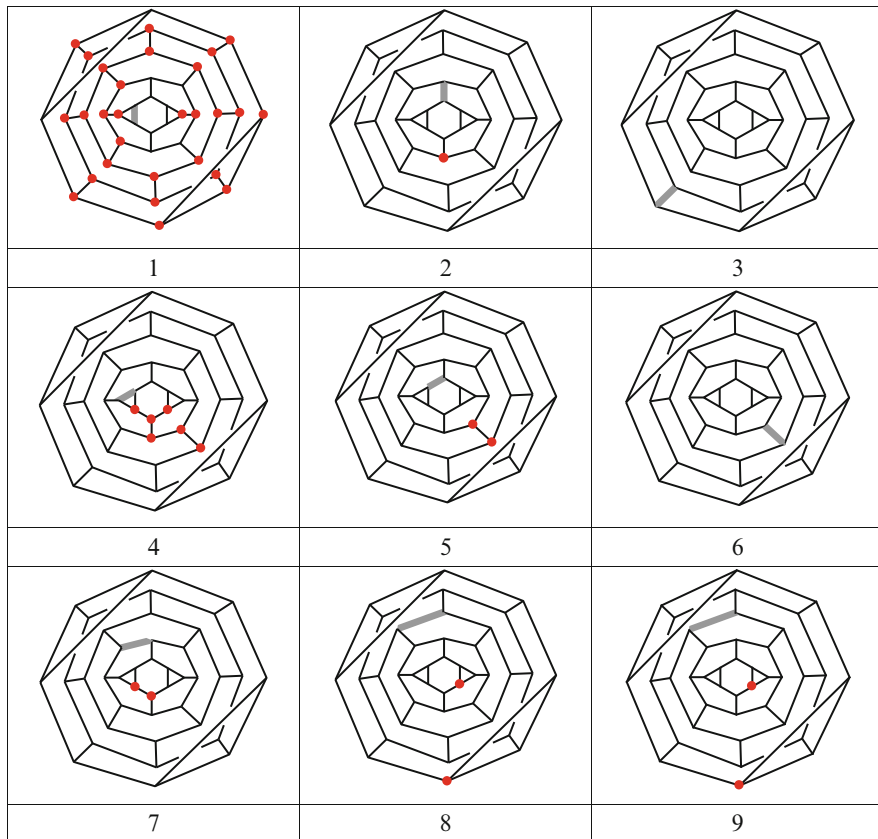


Fig. 15.24 The vertices equidistant from  $u$  to  $v$

Table 15.2 The values of  $n_u(e)$ ,  $n_v(e)$ , and  $n_0(e)$  for a given edge  $e = uv$  in  $H[8n + 4]$

Edges	The values of $n_u(e)$ , $n_v(e)$ , and $n_0(e)$	No
1	$4n, 4, 4n$	8
2	$4n, 4n, 4$	4
3	$8n - 3, 6, 1$	8
4	$4n + 2, 4n + 2, 0$	4
5	$4n + 1, 4n + 1, 2$	$4n - 2$
6	$8n - 6 - 4i, 10 + 4i, 0; n \geq 3 + i, i = 0, 1, 2, \dots$	8

### 15.4 (4,6)-Fullerenes

In this section two infinite families  $A[8n]$  and  $B[12n + 6]$  of (4,6)-fullerenes are constructed, Figs. 15.27, 15.28, 15.29, and 15.30. Since  $A[8n]$  and  $B[12n + 6]$  are bipartite,  $Sz(A[8n]) = Sz^*(A[8n])$ ,  $Sz(B[12n + 6]) = Sz^*(B[12n + 6])$ ,  $PI_v(A[8n]) =$



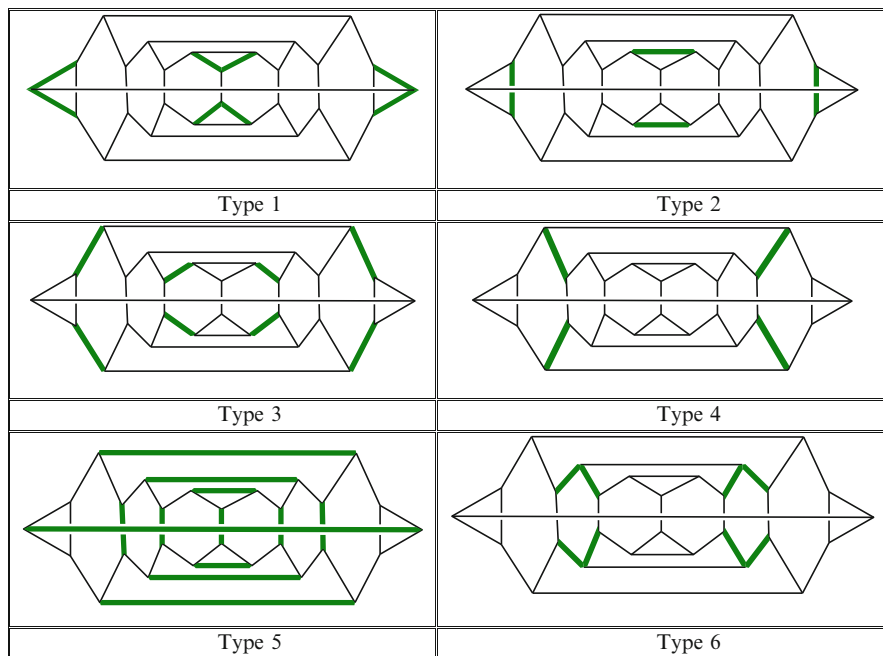


Fig. 15.25 The six types of edges in  $H[8n + 4]$

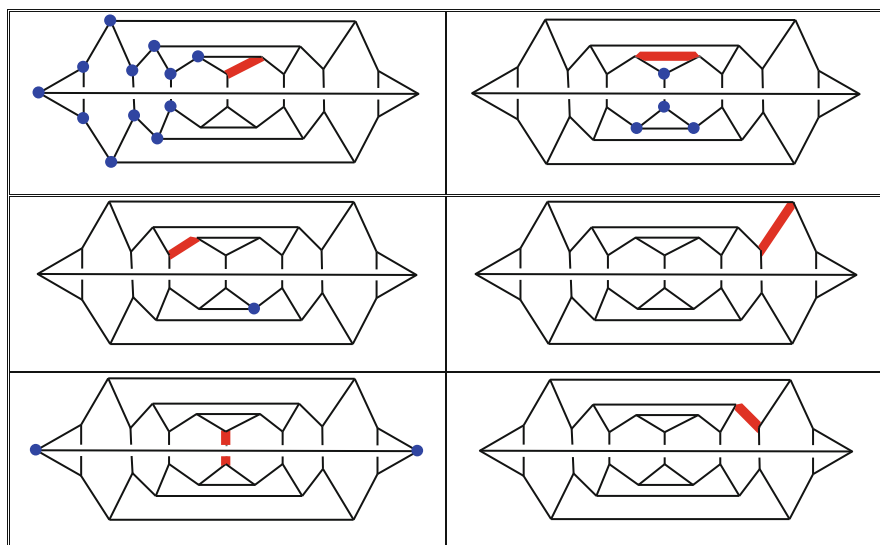
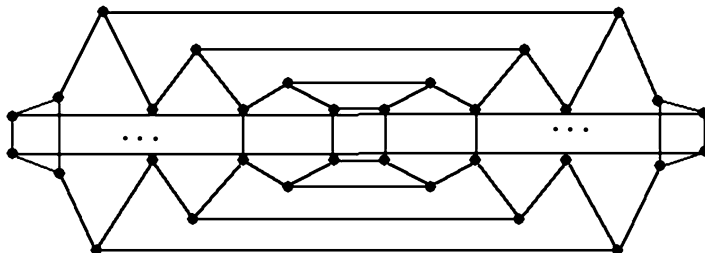
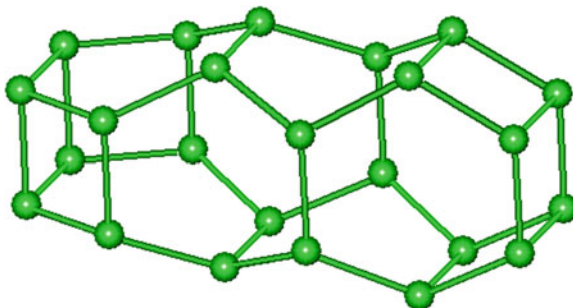


Fig. 15.26 The vertices equidistant from  $u$  to  $v$

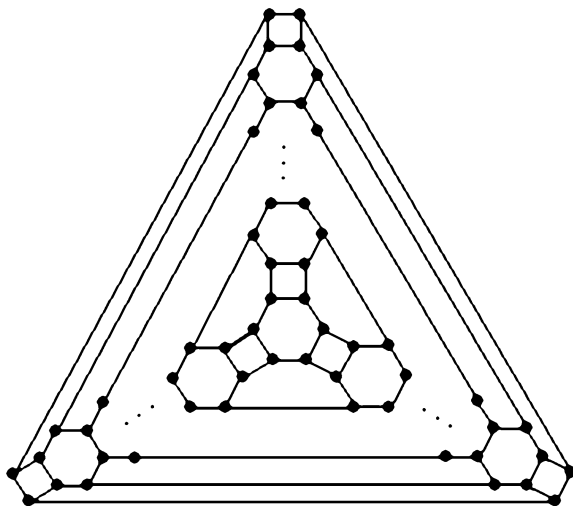


**Fig. 15.27** The Schlegel diagram of the (4,6)-fullerene  $A[8n]$ ,  $n \geq 2$

**Fig. 15.28** The 3D perception of  $A[24]$



**Fig. 15.29** The Schlegel diagram of the (4,6)-fullerene  $B[12n + 6]$ ,  $n \geq 2$



$8n \times 12n = 96n^2$ , and  $PI_v(B[12n + 6]) = (12n + 6) \times (18n + 9) = 216n^2 + 216n + 54$ . So, it is enough to compute the Wiener, eccentric connectivity, and Szeged indices of these families of fullerenes. We begin by computing these quantities for (4,6)-fullerene  $A[8n]$ .

**Fig. 15.30** The 3D perception of  $B[30]$

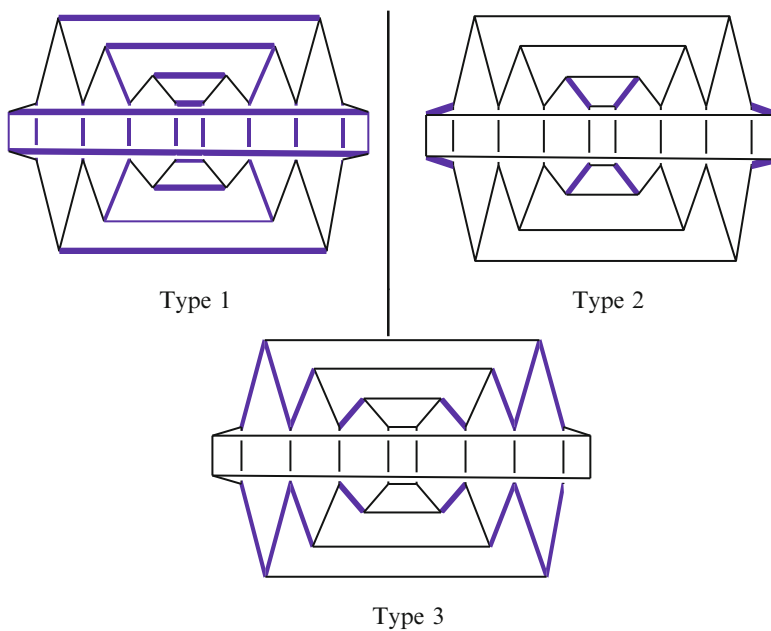
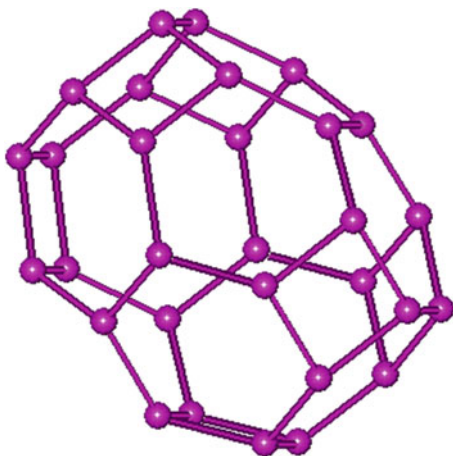


**Fig. 15.31** The three types of edges in  $A[8n]$

From Fig. 15.31, one can see that there are three types of edges in  $A[8n]$ . These together with quantities  $n_u$  and  $n_v$  are recorded in Table 15.3.

We can partition  $V(A[8n])$  into  $n$  parts such that each part has size eight in such a way that the elements of each part have the same eccentricity. Also, a representative of distinct parts has eccentricities  $n + 2, n + 3, \dots, 2n + 1$ , respectively. In Fig. 15.32, the black vertices have the maximum eccentricity and red vertices have the second maximum of eccentricity between vertices of  $A[8n]$ .

**Table 15.3** The values of  $n_u(e)$  and  $n_v(e)$  for a given edge  $e = uv$  in  $A[8n]$

Edges	The values of $n_u(e)$ and $n_v(e)$ in $A[8n]$	No
1	$4n, 4n$	$4n + 8$
2	$8n - 6, 6$	8
3	$8n - 4i + 4, 4i - 4, n \geq i, i = 3, 4, \dots$	8

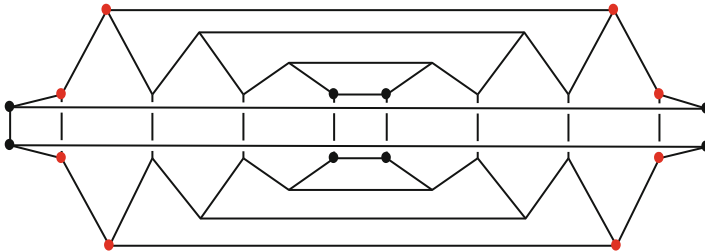
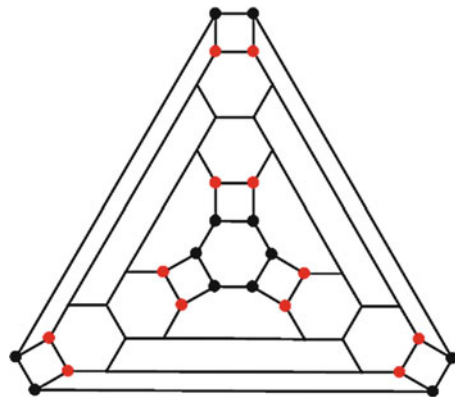


**Fig. 15.32** The maximum (black) and second maximum (red) eccentricities in  $A[8n]$

**Fig. 15.33** The maximum (black) and second maximum (red) eccentricities in  $B[12n + 6]$



By above calculations and our calculations given in Table 15.3, we have the following result:

**Result 15.10** For  $n \geq 2$ ,  $W(A[8n]) = (64/3)n^3 + 32n^2 + (32/3)n - 16$ ,  $Sz(A[8n]) = Sz^*(A[8n]) = (448/3)n^3 + 64n^2 + (320/3)n - 160$ , and  $\xi^c(A[8n]) = 36n^2 + 36n$ .

In the end of this section, we consider the (4,6)-fullerene graph  $B[12n + 6]$  into account. It is clear that  $\xi^c(B[30]) = 576$ . We partition again  $V(B[12n + 6])$ ,  $n \geq 3$ , into  $n + 1$  parts such that one of these parts has size six and any other parts have size 12. The vertices of each part have the same eccentricity, and a representative of the part of size six has eccentricity  $n + 3$ . The eccentricities of a representative of other parts are  $n + 4, n + 5, \dots, 2n + 3$ , respectively. In Fig. 15.32, the black vertices have the maximum eccentricity and red vertices have the second maximum of eccentricity between vertices of  $B[12n + 6]$  (Figs. 15.33 and 15.34).

From our discussion and calculations given in Table 15.4, one can prove the following result:

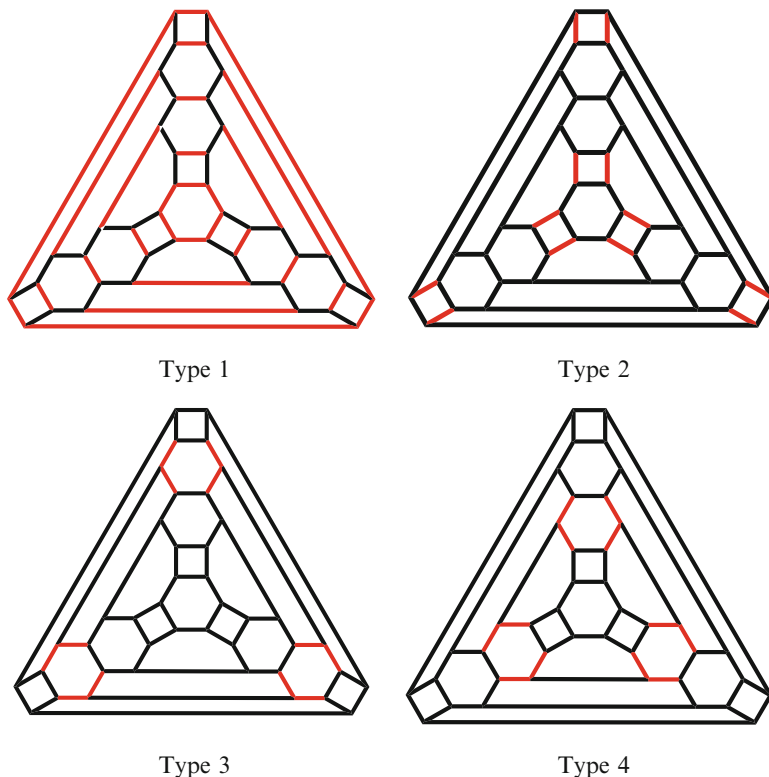


**Fig. 15.34** The four types of edges in  $B[12n + 6]$

**Table 15.4** The values of  $n_u(e)$  and  $n_v(e)$  for a given edge  $e = uv$  in  $B[12n + 6]$

Edges	The values of $nu(e)$ and $nv(e)$ in $B[12n + 6]$	No
1	$6n + 3, 6n + 3$	$6n + 9$
2	$12n - 6, 12$	12
3	$12n - 8, 14$	12
4	$12n - 6i + 6, 6i, n \geq i, i = 3, 4, \dots$	12

**Result 15.11** For  $n \geq 2, W(B[12n + 6]) = 48n^3 + 180n^2 + 228n - 45, Sz(B[12n + 6]) = Sz^*(B[12n + 6]) = 504n^3 + 972n^2 + 1,674n - 1,263,$  and for  $n \geq 3, \xi^c(B[12n + 6]) = 54n^2 + 144n + 54.$

### 15.5 Concluding Remarks

Since there are no classification of (3,6)- and (4,6)-fullerenes, it is natural to construct more and more of such molecular graphs. In this chapter, some constructions of these fullerene graphs are presented, and our calculations suggest the following conjectures:

*Conjecture 1:* The Wiener, Szeged, and revised Szeged indices of a  $(k,6)$ -fullerene with exactly  $n$  carbon atoms are a polynomial of degree 3.

*Conjecture 2:* The vertex PI and eccentric connectivity indices of a  $(k,6)$ -fullerene with exactly  $n$  carbon atoms are a polynomial of degree 2.

## Appendix 1 Some GAP Programs

Here, two GAP programs are presented which is useful for calculations presented in this chapter. The first program is for computing Wiener index and the second is for eccentric connectivity index. Notice that these GAP programs have to combine with calculations by TopoCluj described in the Sect. 15.1.

### A Gap Program for Computing Wiener Index of Fullerenes

```
f:=function(M)
local l,i,j,id,k,t,max,a,s,w,d,g;
l:=Length(M);id:=0;t:=[];s:=[];w:=0;d:=[];g:=0;
  for k in [1..l]do
    id:=1;
    for i in [1..l-1]do
      for j in [i+1..l] do
        if M[k][j]>M[k][id] then
          id:=j;
          fi;
        od;
      od;
      Add(t,M[k][id]);
    od;
  max:=t[1];
  for a in [2..Length(t)] do
    if t[a] > max then
      max:=t[a];
      fi;
    od;
  for a in [1..max] do
    for i in [2..l] do
      for j in [1..i-1] do
        if M[i][j]=a then
          g:=g+1;
          fi;
        od;
      od;
    od;
  Add(d,g);
  g:=0;
```

```

        od;
    for i in [2..l] do
        for j in [1..i-1] do
            w:=w+M[i][j];
        od;
    od;
    Print("Distans=",d,"\n");
    Print("Wiener index=",w,"\n");
    Print("*****","\n");
end;

```

### A Gap Program for Computing Eccentric Connectivity Index of Fullerenes

```

f:=function(M)
local l,i,j,k,t,id,ii,jj,s,a,iii,w,ww;
t:=[];l:=Length(M);id:=0;s:=0;a:=[];w:=0;ww:=0;
for k in [1..l]do
    id:=1;
    for i in [1..l-1]do
        for j in [i+1..l] do
            if M[k][j]>M[k][id] then
                id:=j;
            fi;
        od;
    od;
    Add(t,M[k][id]);
od;####centricity vertices of G
for ii in [1..l]do
    for jj in [1..l]do
        if M[ii][jj]=1 then
            s:=s+1;
        fi;
    od;
    Add(a,s);
    s:=0;
od;####degree vertices of G
for iii in [1..Length(t)] do
    w:=t[iii]*a[iii];
    ww:=ww+w;
    w:=0;
od;#####centricity connectivity index of G
Print("eccentricity=",t,"\n");
Print("degree=",a,"\n");
Print("eccentricity connectivity index=",ww,"\n");
Print("*****","\n");
end;

```

## References

- Aouchiche M, Hansen P (2010) *Eur J Combin* 31:1662
- Ashrafi AR, Loghman A (2006a) *MATCH Commun Math Comput Chem* 55:447
- Ashrafi AR, Loghman A (2006b) *J Comput Theor Nanosci* 3:378
- Ashrafi AR, Loghman A (2006c) *Ars Combin* 80:193
- Ashrafi AR, Saheli M (2010) *Optoelectron Adv Mater Rapid Commun* 4:898
- Ashrafi AR, Saheli M, Ghorbani M (2011a) *J Comput Appl Math* 235:4561
- Ashrafi AR, Doslic T, Saheli M (2011b) *MATCH Commun Math Comput Chem* 65:221
- DeVos M, Goddyn L, Mohar B, Šámal R (2009) *J Combin Theor Ser B* 99:358
- Diudea MV, Ursu O, CsL N (2002) *TOPOCLUJ*. Babes-Bolyai University, Cluj
- Dureja H, Madan AK (2007) *Med Chem Res* 16:331
- Fowler PW, Manolopoulos DE (1995) *An atlas of fullerenes*. Oxford University Press, Oxford
- Goodey PR (1977) *J Graph Theor* 1:181
- Graovac A, Ori O, Faghani M, Ashrafi AR (2011) *Iran J Math Chem* 2(1):99
- Gupta S, Singh M, Madan AK (2002) *J Math Anal Appl* 266:259
- Gutman I (1994) *Graph Theor Notes NY* 27:9
- Gutman I, Dobrynin AA (1998) *Graph Theor Notes NY* 34:37
- Hosoya H (1971) *Bull Chem Soc Jpn* 44:2332
- Hosoya H (1988) *Discrete Appl Math* 19:239
- HyperChem package (2002) Release 7.5 for windows. Hypercube Inc. Gainesville
- Khadikar PV (2000) *Nat Acad Sci Lett* 23:113
- Khalifeh MH, Yousefi-Azari H, Ashrafi AR (2008) *Discrete Appl Math* 156:1780
- Kostant B (1995) *Notices Am Math Soc* 9:959
- Kroto HW, Heath JR, O'Brien SC, Curl RF, Smalley RE (1985) *Nature* 318:162
- Kroto HW, Fichier JE, Cox DE (1993) *The fullerenes*. Pergamon Press, New York
- Kumar V, Sardana S, Madan AK (2004) *J Mol Model* 10:399
- Pisanski T, Randić M (2010) *Discrete Appl Math* 158:1936
- Pisanski T, Žerovnik J (2009) *Ars Math Contemp* 2:49
- Randić M (2002) *Acta Chim Slov* 49:483
- Saheli M, Ashrafi AR (2010a) *Maced J Chem Chem Eng* 29:71
- Saheli M, Ashrafi AR (2010b) *J Comput Theor Nanosci* 7:1900
- Saheli M, Saati H, Ashrafi AR (2010a) *Optoelectron Adv Mater Rapid Commun* 4:896
- Saheli M, Ashrafi AR, Diudea MV (2010b) *Studia Univ Babes Bolyai CHEMIA* 55:233
- Sardana S, Madan AK (2001) *MATCH Commun Math Comput Chem* 43:85
- Schönert M, Besche HU, Breuer T, Celler F, Eick B, Felsch V, Hulpke A, Mnich J, Nickel W, Pfeiffer G, Polis U, Theißen H, Niemeyer A (1995) *GAP, groups, Algorithms and Programming*. Lehrstuhl De für Mathematik, RWTH, Aachen
- Sharma V, Goswami R, Madan AK (1997) *J Chem Inf Comput Sci* 37:273
- Trinajstić N (1992) *Chemical graph theory*. CRC Press, Boca Raton
- Wang L, Zhao J, Li F, Chen Z (2010) *Chem Phys Lett* 501:16
- Wiener H (1947) *J Am Chem Soc* 69:17
- Xing R, Zhou B (2011) *Discrete Appl Math* 159:69
- Yang R, Zhang H (2012) *J Math Chem* 50:261
- Zhou B, Du Z (2010) *MATCH Commun Math Comput Chem* 63:181



# Chapter 16

## Enumeration of Hetero-molecules by Using Pólya Theorem

Modjtaba Ghorbani

**Abstract** A fullerene is any molecule composed entirely of carbon, in the form of a hollow sphere, ellipsoid, or tube. Spherical fullerenes are also called buckyballs and cylindrical ones are called carbon nanotubes or buckytubes. Fullerenes are similar in structure to graphite, which is composed of stacked graphene sheets of linked hexagonal rings; but they may also contain pentagonal rings. Enumeration of chemical compounds has been accomplished by various methods. The Pólya-Redfield theorem has been a standard method for combinatorial enumerations of graphs, polyhedra, chemical compounds, and so forth. Hetero-fullerenes are fullerene molecules in which one or more carbon atoms are replaced by heteroatoms such as boron or nitrogen. In this chapter, by using the Pólya's theorem, we compute the number of permutational isomers of some fullerene graphs.

### 16.1 Introduction

In this chapter, we introduce some notations which will be kept throughout. A graph is a collection of points and lines connecting them. The points and lines of a graph are also called vertices and edges, respectively. If  $e$  is an edge of  $\Gamma$ , connecting the vertices  $u$  and  $v$ , then we write  $e = uv$  and say “ $u$  and  $v$  are adjacent.” A connected graph is a graph such that there exists a path between all pairs of vertices. A molecular graph is a simple graph such that its vertices correspond to the atoms and the edges to the bonds. Note that hydrogen atoms are often omitted.

Group is a set of elements which satisfy the following properties (Trinajstić 1992):

---

M. Ghorbani (✉)

Department of Mathematics, Faculty of Science, Shahid Rajaei Teacher Training University, Tehran 16785-136, Islamic Republic of Iran  
e-mail: [mghorbani@srttu.edu](mailto:mghorbani@srttu.edu)

1. There is an identity element,  $e$ , so that  $a \cdot e = a$  for any  $a$  belonging to the group.
2. The product of two elements is also member of the group, that is, if  $a$  and  $b$  belong to the group, then  $a \cdot b$  will also be a member of the group. It means the group is closed under the given operation.
3. Every element has its inverse as the member of the group, that is, if  $a$  belongs to the group, then  $a^{-1}$  also belongs to the group. If  $a \cdot b = e$ , it means  $a$  is the inverse of  $b$  and vice versa.
4. Group members obey the associative law, that is,  $a(b \cdot c) = (a \cdot b)c$ .

The order of a group is defined as the number of elements present in the group. The elements of a group can be several things as you define them. It can be integers, vectors, matrices, symmetry operations (elements), etc. One has to define the operation which goes on in the group which can be several things like addition, multiplication, and symmetry operations. There are smaller groups present in the group. They obey all the rules of a group. Their order must divide the order of the group. That is, if you have a group of order seven, then you cannot have any subgroup except a subgroup of order 1 that contains identity only. Similarly, if you have a group of order 12, you should not waste your time in looking for a subgroup of order 5, 7, 8, 9, 10, and 11. Remember there is always a subgroup of order 1. An Abelian group is a group in which every element commutes with every other element, that is,  $a \cdot b = b \cdot a$  for every  $a$  and  $b$ . Cyclic group is a group which is generated by a single element called generator. In other words, if  $G$  be a cyclic group, then there is an element  $g$  in  $G$  where,  $G = \{g, g^2, \dots, g^n = 1\}$ . The order of this group is  $n$ .

A group can be divided into several classes, also called conjugacy classes. The importance of classes will be clear in our later studies. It is time consuming to find out all classes. Choose any element, and perform the so-called similarity transformation, that is, compute  $x^{-1}ax$ , where  $x$  and  $a$  belong to the group. For each  $a$ , perform this computation with  $x$  being all members of the group.

Symmetry plays a central role in the analysis of the structure, bonding, and spectroscopy of molecules. Chemists classify molecules according to their symmetry. The collection of symmetry elements present in a molecule forms a group, typically called a point group. Since all the symmetry elements (points, lines, and planes) will intersect at a single point, so we name it as point group. The symmetry properties of objects (and molecules) may be described in terms of the presence of certain symmetry elements and their associated symmetry operations. Symmetry elements are properties which are related to the structure of the molecule. They include mirror planes, axes of rotation, centers of inversion, and improper axes of rotation (an improper axis of rotation is a rotation followed by a reflection perpendicular to the rotational axis). Symmetry operations are actions which place the molecule in an orientation which appears to be identical to its initial orientation. Symmetry operations include rotation, reflection, inversion, rotation followed by reflection, and identity. The identity operation simply leaves the molecule where it is. All molecules have the identity operation. Certain physical properties of molecules are clearly linked to molecular symmetry. Molecules which are symmetrically bonded to the

same elements will not be polar, due to the canceling dipole moments. Likewise, chirality (left or right handedness) is clearly a symmetry property. Chirality can only be present in molecules which lack an improper axis or rotation. Molecules with a center of inversion or a mirror plane cannot be chiral. The symmetry properties of molecules are tabulated on character tables. A character table lists the symmetry elements of the point group, along with characters which are consistent with the different symmetry operations of the group. The table characterizes how various atomic properties (the symmetry of atomic orbitals, rotations about axes, etc.) are transformed by the symmetry operations of the group.

Character of a symmetry element will be defined as the sum of the diagonal elements in the matrix representing the element. Mathematically, it turns out that representations of a group can be expressed in terms of these characters.

Detecting symmetry of molecules is a well-studied problem with applications in a large number of areas. Randić (1974, 1976) and then Balasubramanian (1980) considered the Euclidean matrix of a chemical graph to find its symmetry. Here the Euclidean matrix of a molecular graph  $\Gamma$  is a matrix  $D(\Gamma) = [d_{ij}]$ , where for  $i \neq j$ ,  $d_{ij}$  is the Euclidean distance between the nuclei  $i$  and  $j$ . In this matrix  $d_{ii}$  can be taken as zero if all the nuclei are equivalent. Otherwise, one may introduce different weights for different nuclei.

Suppose  $\sigma$  is a permutation on  $n$  atoms of the molecule under consideration. Then the permutation matrix  $P_\sigma$  is defined as  $P_\sigma = [x_{ij}]$ , where  $x_{ij} = 1$  if  $i = \sigma(j)$  and 0 otherwise. It is easy to see that  $P_\sigma P_\tau = P_{\sigma\tau}$ , for any two permutations  $\sigma$  and  $\tau$  on  $n$  objects, and so, the set of all  $n \times n$  permutation matrices is a group isomorphic to the symmetric group  $S_n$  on  $n$  symbols. It is a well-known fact that a permutation  $\sigma$  of the vertices of a graph  $\Gamma$  belongs to its automorphism group if it satisfies  $P_\sigma' A P_\sigma = A$ , where  $A$  is the adjacency matrix of  $\Gamma$ . So, for computing the symmetry of a molecule, it is sufficient to solve the matrix equation  $P' E P = E$ , where  $E$  is the Euclidean matrix of the molecule under consideration and  $P$  varies on the set of all permutation matrices with the same dimension as  $E$ .

## 16.2 Main Results and Discussion

Groups are often used to describe symmetries of objects. This is formalized by the notion of a group action. Let  $G$  be a group and  $X$  a nonempty set. An action of  $G$  on  $X$  is denoted by  $G_X$  and  $X$  is called a  $G$ -set. It induces a group homomorphism  $\varphi$  from  $G$  into the symmetric group  $S_X$  on  $X$ , where  $\varphi(g)x = gx$  for all  $x \in X$ . The orbit of  $x$  will be denoted by  $Gx$  and defines as the set of all  $\varphi(g)x$ ,  $g \in G$ . The set of all  $G$ -orbits will be denoted by  $G \backslash X = \{Gx \mid x \in X\}$ . Suppose  $g$  is a permutation of  $n$  symbols with exactly  $\lambda_1$  orbits of size 1,  $\lambda_2$  orbits of size 2, ..., and  $\lambda_n$  orbits of size  $n$ . Then the cycle type of  $g$  is defined as  $1^{\lambda_1} 2^{\lambda_2} \dots, n^{\lambda_n}$ .

A mathematician, namely, Arthur Cayley, has been studying the combinatorial enumeration of rooted trees as models. Pólya's theorem has been widely applied to chemical combinatorics to enumerate objects. In this chapter we will show how

**Fig. 16.1** Two indistinguishable colorings

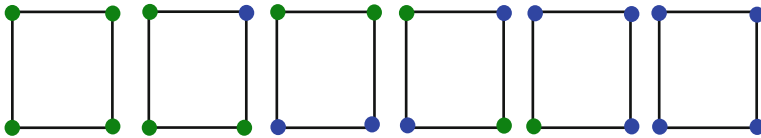
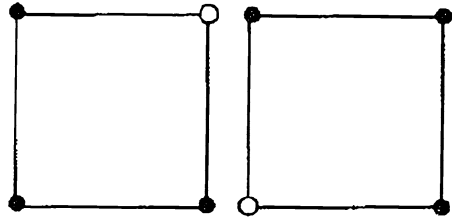


**Fig. 16.2** The six distinguishable colorings

Pólya theory can be used in counting objects, which is often the design basis for statistical tests. In other words, Pólya theory determines the number of distinct equivalence classes of objects. It can also give counts for specific types of patterns within equivalence classes.

*Example 16.1* As an example, let us consider the number of ways of assigning one of the colors red or white to each corner of a square. Since there are two colors and four corners, there are basically  $2^4 = 16$  possibilities. But when we take account of the symmetry of the square, we see that some of the possibilities are essentially the same. For example, the first coloring as in Fig. 16.1 is the same as the second one after rotation through  $180^\circ$ .

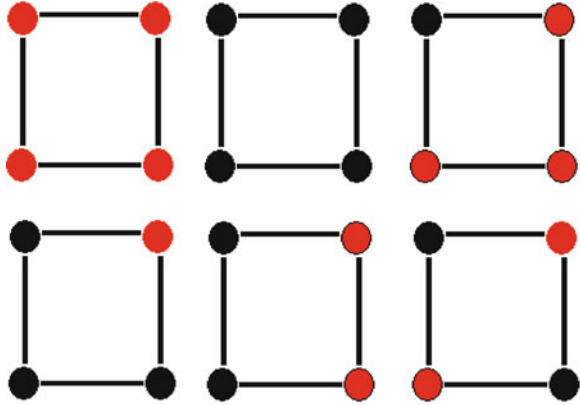
From above, we regard two colorings as being indistinguishable if one is transformed into the other by symmetry of the square. It is easy to find the distinguishable colorings (in this example) by trial and error: there are just six of them, as shown in the Fig. 16.2.

Now consider an  $n$  bead necklace. Let each corner of it be colored red or blue. How many different colorings are there? One could argue for  $2^n$ . For example, if  $n = 4$  and the corners are numbered 0,1,2,3 in clockwise order around the necklace, then there are only 6 ways of coloring the necklace RRRR, BBBB, RRRB, RBBB, RRBB, and RBRB; see Fig. 16.3.

### 16.2.1 Pólya's Theorem

We now introduce the notion of cycle index. Let  $G$  be a permutation group. The cycle index of  $G$  acting on  $X$  is the polynomial  $Z(G, X)$  over  $\mathcal{Q}$  in terms of indeterminates  $x_1, x_2, \dots, x_t$ ,  $t = |X|$ , defined by  $Z(G, X) =$

**Fig. 16.3** Distinguish colorings of four bead necklace



$(1/|G|) \sum_{p \in G} \prod_{i=1}^t x_i^{c_i(p)}$  in which  $(c_1(p), \dots, c_t(p))$  is the cycle type of the permutation  $p \in G$ . The generalized character cycle index is defined as  $P_G^\chi(x_1, x_2, \dots, x_t) = (1/|G|) \sum_{p \in G} \prod_{i=1}^t \chi(p) x_i^{c_i(p)}$ , where  $\chi(g)$  is the linear character of the irreducible representation of  $G$ . In this chapter, we use two special cases: one is the antisymmetric representation, that is,

$$\chi(g) = \begin{cases} 1 & \text{if } g \text{ is a proper rotation} \\ -1 & \text{if } g \text{ is an improper rotation} \end{cases}$$

and the other when  $\chi$  is 1 for all  $g$ . Since, all elements of a conjugacy class of a permutation group have the same cycle type, so the cycle index and the generalized character cycle index can be rephrased in the following way:

$$Z(G, x_1, \dots, x_t) = \frac{1}{|G|} \sum_{C \in \text{Conj}(G)} |C| \prod_{i=1}^t x_i^{c_i(g_C)}$$

$$P_G^\chi(x_1, \dots, x_t) = \frac{1}{|G|} \sum_{C \in \text{Conj}(G)} |C| \prod_{i=1}^t \chi(g_C) x_i^{c_i(g_C)}$$

Denote by  $C_{m,n}$  the set of all functions  $f: \{1, 2, \dots, m\} \rightarrow \{x_1, x_2, \dots, x_n\}$ . The action of  $p \in S_m$  induced on  $C_{m,n}$  is defined by  $\hat{p}(f) = f \circ p^{-1}, f \in C_{m,n}$ . Treating the colors  $x_1, x_2, \dots, x_n$  that comprise the range of  $f \in C_{m,n}$  as independent variables, the weight of  $f$  is  $W(f) = \prod_{i=1}^m f(i)$ . Evidently,  $W(f)$  is a monomial of (total) degree  $m$ . Suppose  $G$  is a permutation group of degree  $m$ ,  $\hat{G} = \{\hat{p} : p \in G\}$ ,  $\hat{p}$  is as defined above. Let  $p_1, p_2, \dots, p_t$  be representatives of the distinct orbits of  $\hat{G}$ . The weight of  $p_i$  is the common value of  $W(f), f \in p_i$ . The sum of the weights of the orbits is the pattern inventory  $W_G(x_1, x_2, \dots, x_n) = \sum_{i=1}^t W(p_i)$ .

**Theorem 16.2** (*Pólya's theorem* (Pólya and Read 1987)) *If  $G$  is a subgroup of  $S_m$ , the symmetry group on  $m$  symbols, then the pattern inventory for the orbits of  $C_{m,n}$  modula  $\hat{G}$  is*

$$W_G(x_1, x_2, \dots, x_n) = \frac{1}{|G|} \sum_{p \in G} M_1^{C_1(p)} M_2^{C_2(p)} \dots M_m^{C_m(p)},$$

where  $M_k = x_1^k + x_2^k + \dots + x_n^k$  is the  $k$ th power sum of the  $x$ 's.

**Theorem 16.3** (*Generalization of Pólya's theorem* (Zhang et al. 1998)) *Substituting  $M_i$  for  $x_i$  and in the generalized character cycle index,  $i = 1, 2, \dots, t$ , we get the chiral generating function  $\text{CGF} = P_G^\chi(M_1, \dots, M_k)$ .*

## 16.2.2 Fullerene Graphs

In the past years, nanostructures involving carbon have been the focus of an intense research activity which is driven to a large extent by the quest for new materials with specific applications. Fullerene is one of the main objects of nanostructures. A fullerene is any molecule composed entirely of carbon, in the form of a hollow sphere, ellipsoid, or tube. Spherical fullerenes are also called buckyballs and cylindrical ones are called carbon nanotubes or buckytubes. Fullerenes are similar in structure to graphite, which is composed of stacked graphene sheets of linked hexagonal rings; but they may also contain pentagonal rings. The fullerene era was started in 1985 with the discovery of a stable  $C_{60}$  cluster and its interpretation as a cage structure with the familiar shape of a soccer ball, by Kroto and his coauthors (Kroto et al. 1985, 1993). The well-known fullerene, the  $C_{60}$  molecule, is a closed-cage carbon molecule with three-coordinate carbon atoms tiling the spherical or nearly spherical surface with a truncated icosahedral structure formed by 20 hexagonal and 12 pentagonal rings. Let  $p$ ,  $h$ ,  $n$ , and  $m$  be the number of pentagons, hexagons, carbon atoms, and bonds between them, in a given fullerene  $F$ . Since each atom lies in exactly three faces and each edge lies in two faces, the number of atoms is  $n = (5p + 6h)/3$ , the number of edges is  $m = (5p + 6h)/2 = 3/2n$ , and the number of faces is  $f = p + h$ . By the Euler's formula  $n - m + f = 2$ , one can deduce that  $(5p + 6h)/3 - (5p + 6h)/2 + p + h = 2$ , and therefore,  $p = 12$ ,  $v = 2h + 20$ , and  $e = 3h + 30$ . This implies that such molecules made up entirely of  $n$  carbon atoms and are having 12 pentagonal and  $(n/2 - 10)$  hexagonal faces, where  $n \neq 22$  is a natural number equal or greater than 20; see Fig. 16.4. Hetero-fullerenes are fullerene molecules in which one or more carbon atoms are replaced by heteroatoms such as boron or nitrogen, whose formation is a kind of "on-ball" doping of the fullerene cage; see Fig. 16.5.

To enumerate all possibilities of the hetero-fullerene structures, we have to consider the rotation group of the fullerene and its whole automorphism group to

**Fig. 16.4** 3-D graph of fullerene  $C_{20}$

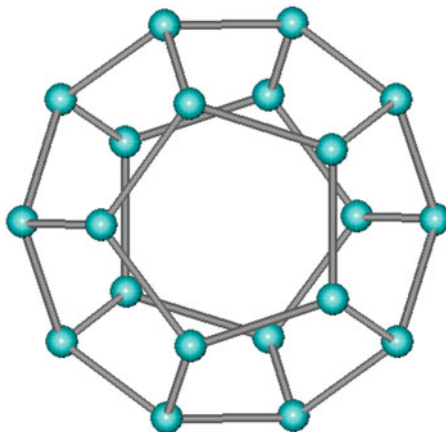
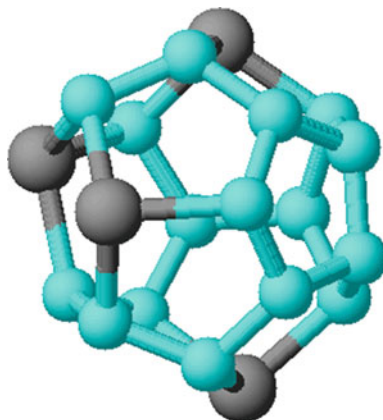


**Fig. 16.5** 3-D graph of hetero-fullerene  $C_{16}Br_4$



enumerate the number of chiral isomers. Friperinger (Friperinger 1996) computed the symmetry of some fullerenes and then applied SYMMETRICA to calculate the number of  $C_{60}H_kCl_{60-k}$  molecules, and Balasubramanian computed the number of  $C_{60}H_{36}$  isomers. (Zhang et al. 1998), for calculating the possibilities of different positional isomers, used the Pólya's counting theorem. He also applied the generalization of the Pólya's theorem to compute the number of chiral isomers.

Balasubramanian (1981, 1984, 1995a, b, 2004a, b) has done a lot of work on methods for isomer counting of hetero-fullerenes and of poly-substituted fullerenes, especially, using the generalized character cycle index. Mathematically the isomer counting of poly-substituted fullerene is essentially the same as that of hetero-fullerene. Shao and Jiang (1995) discussed hydrogenated  $C_{60}$ . Furthermore, (Zhang et al. 1998) also studied the fullerene cages. In Ghorbani et al. (2006a, b, 2009, 2011, 2012), Ashrafi and Ghorbani (2010) and Faghani and Ghorbani (2011), the number of permutational isomers of some classes of hetero-fullerenes is computed.

**Fig. 16.6** 2-D graph of zigzag nanotube  $T_z[6, p]$ , for  $p = 5$  and its Clar structures

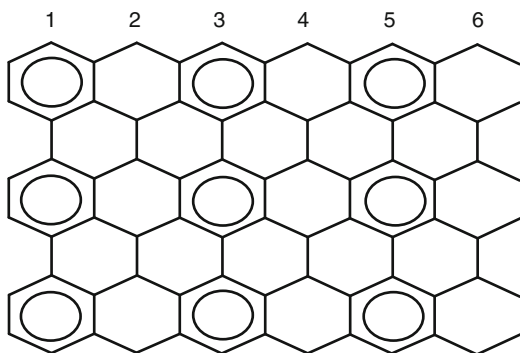
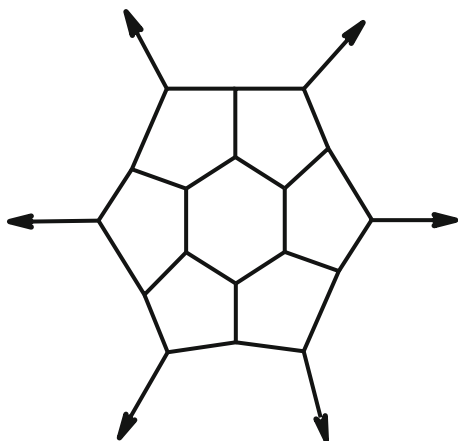


**Fig. 16.7** Caps  $B$



### 16.2.3 Construction of Infinite Classes of Fullerenes

In Ghorbani et al. (2011), a method is described to obtain a fullerene graph from a zigzag or armchair nanotubes. Here by continuing his method, we construct an infinite class of fullerenes. Denoted by  $T_z[q, p]$  means a zigzag nanotube with  $p$  rows and  $q$  columns of hexagons; see Fig. 16.6. Combining a nanotube  $T_z[6, p]$  with two copies of caps  $B$  (Fig. 16.7) as shown in Fig. 16.8, the resulted graph is a non-IPR fullerene, which has  $12p$  vertices and  $6p - 10$  hexagonal faces.

Now, combine a nanotube  $T_z[5, p]$  (Fig. 16.9) with two copies of caps  $C$  (Fig. 16.10) as shown in Fig. 16.11. The resulted graph is a non-IPR fullerene, which has  $10p$  vertices and  $5p - 10$  hexagonal faces.

Finally, we can construct a fullerene with  $12n + 30$  vertices (Fig. 16.12), by combining a  $T_z[6, p]$  nanotube and two caps  $E$  (see Fig. 16.13) added to its inside and its outside. In this chapter, we will construct some infinite classes of fullerene graphs and then compute the number of their chiral isomers.



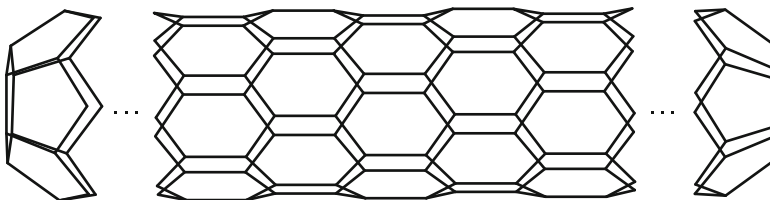


**Fig. 16.8** Fullerene  $C_{12p}$  constructed by combining two copies of caps  $B$  and the zigzag nanotube  $T_z[6, p]$

**Fig. 16.9** 2-D graph of zigzag nanotube  $T_z[6, p]$ , for  $p = 5$  and its Clar structures

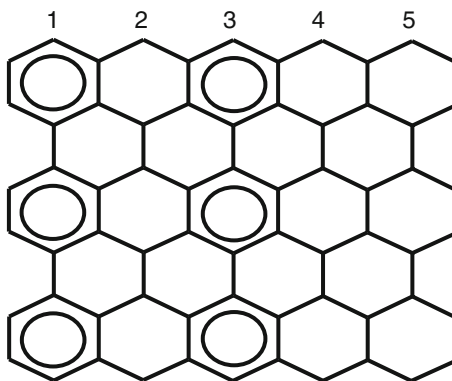


**Fig. 16.10** Caps  $C$

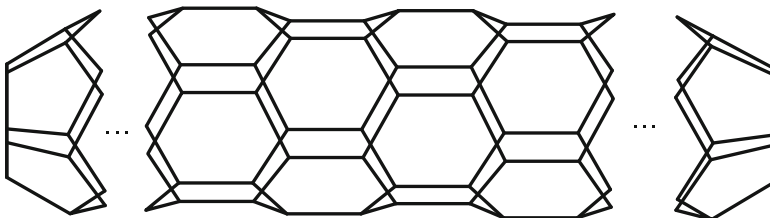
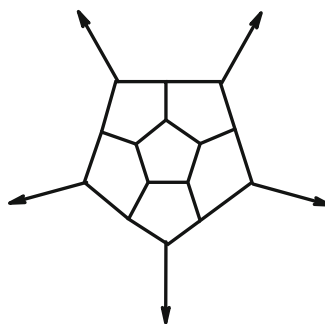


**Fig. 16.11** Fullerene  $C_{10p}$  constructed by combining two copies of caps  $C$  and the zigzag nanotube  $T_z[5, p]$

**Fig. 16.12** 2-D graph of fullerene  $C_{12n+30}$

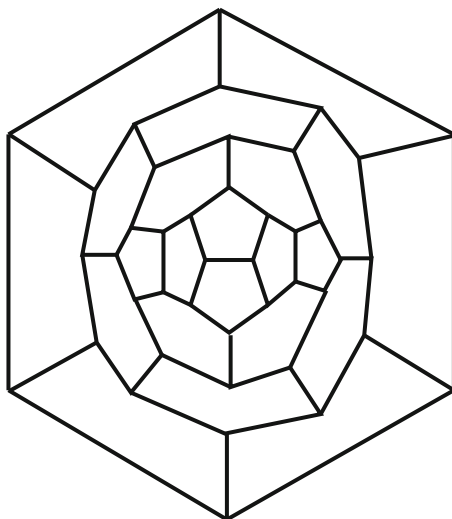
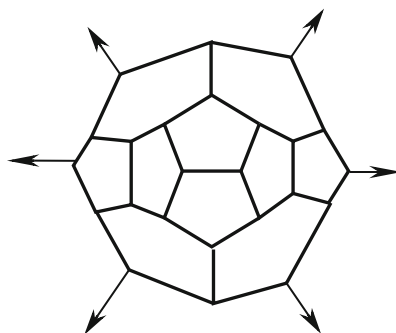


**Fig. 16.13** Caps  $E$



### 16.2.4 Leapfrog Fullerenes

A method (Fowler et al. 1986, 1987) has been described on how to construct a fullerene  $C_{3n}$  from a fullerene  $C_n$  having the same or even a bigger symmetry group as  $C_n$ . This method is called the Leapfrog principle. If one starts with a  $C_n$  cluster with icosahedral symmetry, all the new clusters will be of the same symmetry, since this is the biggest symmetry group in 3-dimensional space. In the first step, an extra vertex has to be put into the center of each face of  $C_n$ . Then, these new vertices have to be connected with all the vertices surrounding the corresponding face. Then, the dual polyhedron is again a fullerene having  $3n$  vertices, 12 pentagonal, and  $(3n/2) - 10$  hexagonal faces. From Fig. 16.14, it can be seen that  $Le(C_{20}) = C_{60}$ .

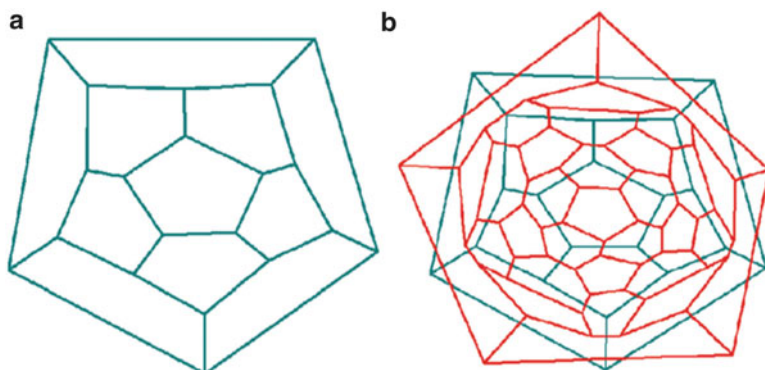


**Fig. 16.14** The fullerene  $C_{20}$  (a) and  $Le(C_{20})$  (b)

### 16.3 Enumeration of Nanostructures

Enumeration of chemical compounds has been accomplished by various methods. The Polya-Redfield theorem has been a standard method for combinatorial enumerations of graphs, polyhedra, chemical compounds, and so forth. Combinatorial enumerations have found a wide-ranging application in chemistry, since chemical structural formulas can be regarded as graphs or three-dimensional objects. The aim of this section is to enumerate the number of permutational isomers of hetero-fullerenes, see Appendix 16.B.

#### 16.3.1 Hetero-Fullerenes with Small Number of Vertices

To demonstrate our method, we should compute the number of permutational isomers of some well-known fullerenes. In this section, we enumerate hetero-fullerenes  $C_{n-k}B_k$  for  $n = 24, 80, 84,$  and  $150$ . Consider at first the molecular graph of the fullerene  $C_{24}$ , shown in Fig. 16.15. In Ghorbani et al. (2006b), the symmetry group of  $C_{24}$  is computed, and it is isomorphic with the group  $Z_2 \times S_4$ . So, we have the following theorem without proof:

#### Theorem 16.4

$$Z(C_{24}, X) = \frac{x_1^{24} + 16x_2^{12} + 8x_3^8 + 12x_4^6 + 8x_6^4 + 3x_1^8x_2^8}{48}.$$

Consider now the molecular graph of the fullerene  $C_{80}$ , Fig. 16.16. We have the following theorem:

**Fig. 16.15** 3-D graph of fullerene  $C_{24}$

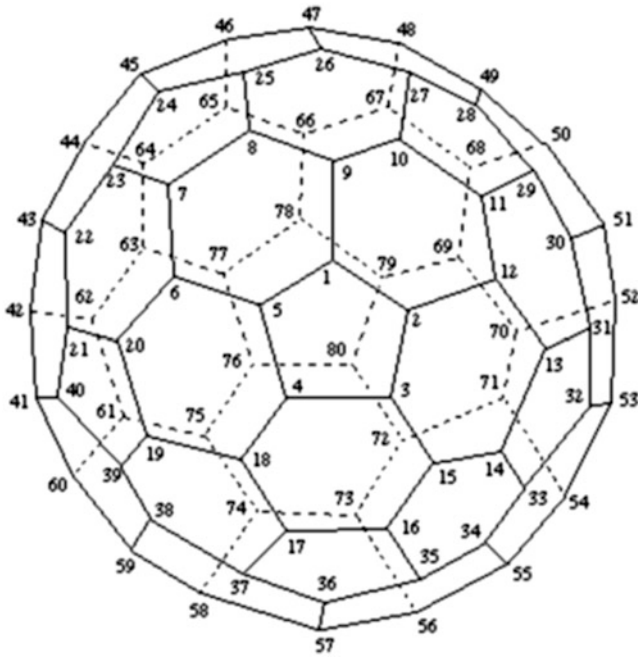
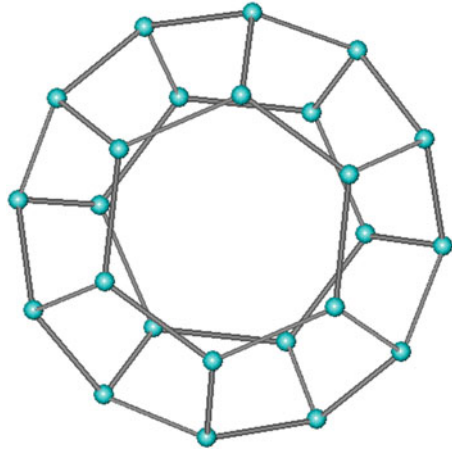


**Fig. 16.16** 3-D graph of fullerene  $C_{80}$

**Theorem 16.5**

$$Z(C_{80}, X) = \frac{x_1^{80} + 4x_5^{16} + 6x_2^{40} + 4x_{10}^8 + 5x_1^4x_2^{38}}{20}.$$

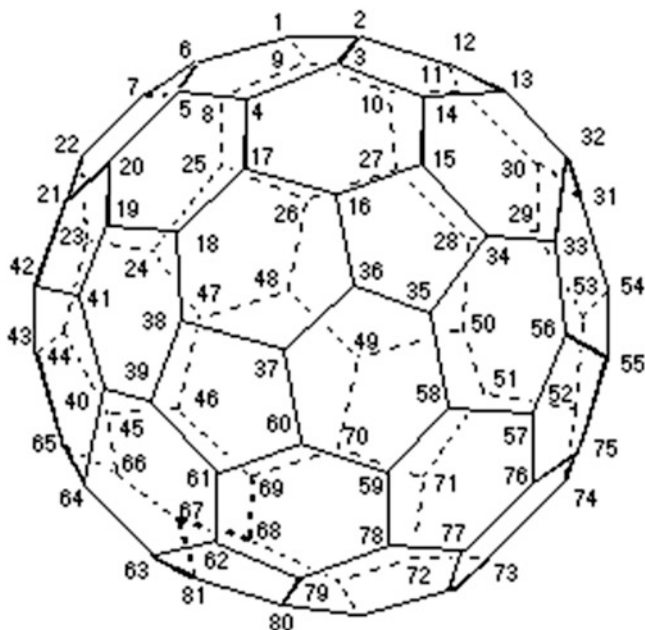


Fig. 16.17 2-D graph of fullerene  $C_{84}$

*Proof* By using concept of symmetry, one can see that the generators of fullerene graph  $C_{80}$  are as follows:

$X = (2,16)(4,14)(5,18)(6,17)(7,20)(8,19)(9,36)(10,35)(11,34)(12,33)(13,49)(15,51)(21,24)(22,23)(25,37)(26,52)(27,39)(28,50)(29,54)(30,53)(31,56)(32,55)(38,40)(41,42)(43,44)(45,60)(46,59)(47,58)(48,57)(62,67)(63,66)(65,77)(68,80)(69,73)(70,79)(71,78)(72,76)(74,75);$

$Y = (1,65)(2,66)(3,68)(4,67)(5,48)(6,45)(7,46)(8,47)(9,42)(10,43)(11,44)(12,41)(13,69)(14,70)(15,72)(16,71)(17,36)(18,33)(19,34)(20,35)(21,30)(22,31)(23,32)(24,29)(25,73)(26,74)(27,76)(28,75)(37,77)(38,78)(39,80)(40,79)(49,61)(50,62)(51,64)(52,63)(53,60)(54,57)(55,58)(56,59).$

By using GAP (The GAP Team 1995) program, one can see that  $X^2 = Y^2 = (XY)^{10} = 1$  and  $X^{-1}(XY)X = (XY)^{-1}$ , and so, this symmetry group is isomorphic with a dihedral group of order 20, namely,  $D_{20}$ . Now by using definition of the cycle index, the proof is completed, see Appendix 16.A.

In continuing consider the molecular graph of fullerene  $C_{84}$ , Fig. 16.17. We prove that the symmetry group of the  $C_{84}$  fullerene is isomorphic to the group  $S_4$ . To do this, suppose  $G$  is the symmetry group of this fullerene. Then  $G = \langle X, Y \rangle$ , where  $X$  and  $Y$  are the following permutations:

$X = (1, 2)(3, 4)(5, 8) (6,80) (7,81) (9,18) (10,19) (11,20) (12,78) (14,83) (15,82) (17,84)(21,54)(22,77)(23,55)(24,79)(25,76)(26,27)(28,59)(29,60)(30,57)(31,58)(32,66)(33,70)(34,72)(35,67)(36,64)(37,65)(38,74)(39,73)(40,75)(41,56)(42,51)(43,53)(44,52)(45,48) (46,49)(47,50)(61,71)(62,63)(68,69),$

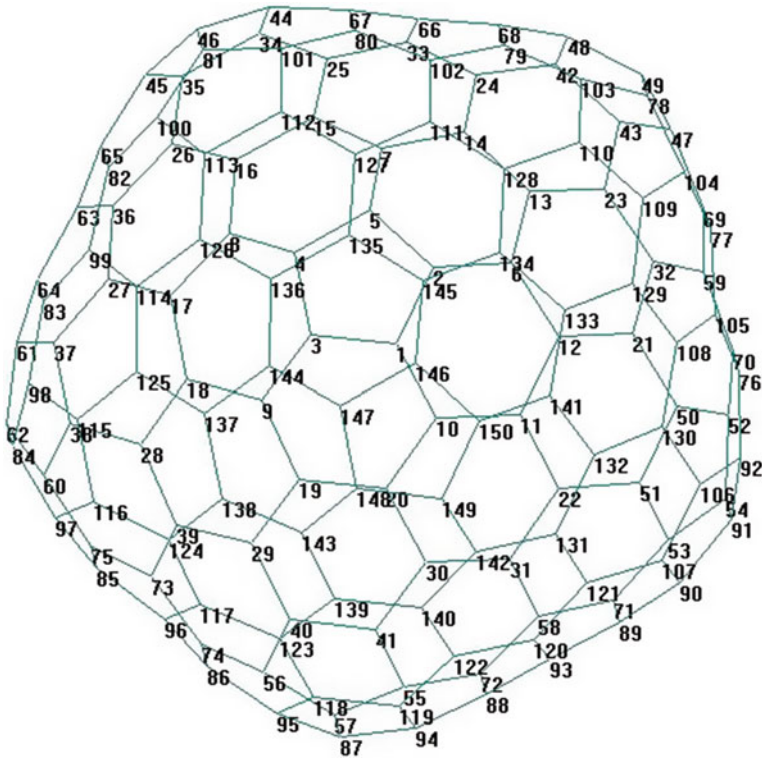


Fig. 16.18 3-D graph of fullerene  $C_{150}$

$Y = (1,76,31,69) (2,59,30,40) (3,79,28,68) (4,58,29,39) (5,51,35,17) (6,84,49,66) (7,83,48,65) (8,80,41,71) (9,77,42,61) (10,78,43,62) (11,81,44,63) (12,82,45,64) (13,55,27,33) (14,20,53,36) (15,19,52,37) (16,54,26,34) (18,56,32,38) (21,72,23,70) (22,74,46,67) (24,73,50,57) (25,75,47,60).$

By using GAP software one can see that this group is isomorphic with  $S_4$ . Thus, the cycle index of  $G$  is as follows:

**Theorem16. 6**

$$Z(C_{84}, X) = \frac{(x_1^{84} + 3x_2^{42} + 8x_3^{28} + 6x_4^{21} + 6x_1^2x_2^{41})}{24}.$$

*Proof* By means of group action, one can see that the number of conjugacy classes of symmetric group  $S_4$ , on the set of vertices of  $C_{84}$ , is 5. The cycle types of its elements are  $1^{84}, 2^{42}, 3^{28}, 4^{21}$ , and  $1^2 2^{41}$ , respectively. This completes the proof.

Now consider the molecular graph of the fullerene  $C_{150}$ , Fig. 16.18. In Ghorbani et al. (2006b), the symmetry group of  $C_{150}$  is computed, and it is isomorphic with dihedral group  $D_{20}$ . On the other hand, the 3-dimensional cycle index of  $C_{150}$  is computed, and so, we have

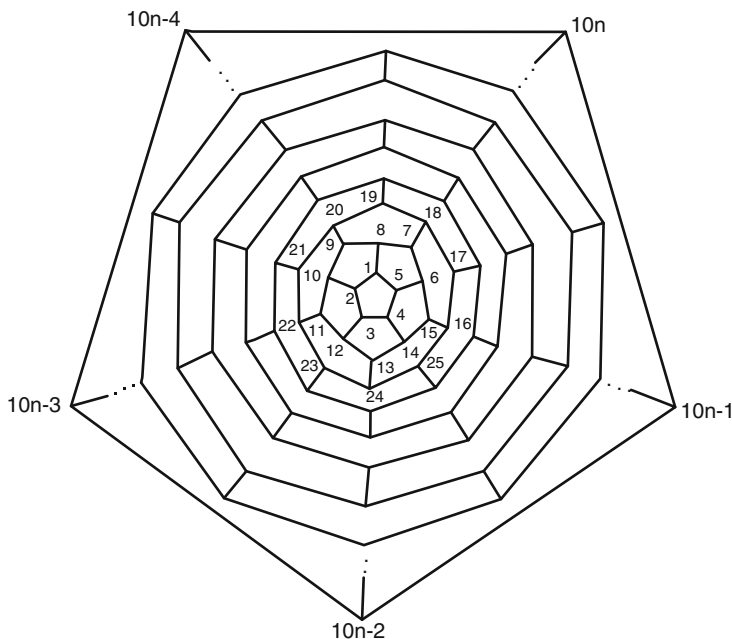


Fig. 16.19 The Schlegel diagram of  $C_{10n}$

**Theorem 16.7**

$$Z(C_{150}, X) = \frac{(x_1^{150} + 5x_2^{75} + 4x_5^{30} + 5x_1^8x_2^{71} + 4x_5^2x_{10}^{14} + x_1^{10}x_2^{70})}{20}$$

**16.3.2 Enumeration of Infinite Classes of Hetero-fullerenes**

In this section, we enumerate the number of infinite families of hetero-fullerenes, namely,  $C_{10n}$ ,  $C_{12n}$ ,  $C_{12n+6}$ ,  $C_{24n}$ , and  $C_{40n}$  fullerenes. Many properties of these classes of fullerenes are studied in Fowler et al. (1995, 2007), Ashrafi et al. (2008a, b, c, 2009), Ashrafi and Ghorbani (2010), Ghorbani (2011, 2012), Ghorbani and Naserpour (2011) and Ghorbani and Ashrafi (2012).

**16.3.2.1  $C_{10n}$  Fullerene**

This class of fullerenes has exactly  $10n$  carbon atoms ( $n \geq 2$ ). That’s why we denote this class of fullerenes by  $C_{10n}$ ; see Fig. 16.19. The first member of this class of fullerenes can be obtained by putting  $n = 2$ , for example,  $C_{20}$ . Our problem is reduced to the coloring of the corresponding fullerene graph with  $10n$  vertices. By

considering a labeling of its vertices as we did in Fig. 16.19, it is easy to see that the generators of this group are

$$\begin{aligned} \sigma &= (2, 5)(3, 4)(6, 10)(7, 9)(11, 15)(12, 14) \dots (10n - 4, 10n)(10n - 3, 10n - 1), \\ \tau &= (1, 10n - 4, 2, 10n - 3, 3, 10n - 2, 4, 10n - 1, 5, 10n) \dots \\ &\quad (7, 10n - 6, 9, 10n - 14, 11, 10n - 12, 13, 10n - 10, 15, 10n - 8), \end{aligned}$$

where  $\sigma$  fixes elements  $1, 8, 19, 30, \dots, 11i - 3, 11i + 2, \dots, 10n - 2, i = 1, 2, \dots, n - 1$  and  $\tau$  does not have fixed points.

Since  $\sigma^2 = \tau^{10} = \text{identity}$  and  $\sigma^{-1}\tau\sigma = \tau^{-1}$ , the symmetry group  $G$  of these fullerenes is isomorphic to the dihedral group of order 20. In the following table the cycle types of elements of  $G$  are computed:

Fullerene	Cycle type	#Permutations
$C_{10n}$	$1^{10n\#}$	1#
	$1^{2n}2^{4n\#}$	5#
	$5^{2n}$	4#
	$2^{5n}$	6#
	$10^n$	4

Thus, the cycle index of  $G$  is computed as

$$Z(G, X) = \frac{x_1^{10n} + 5x_1^{2n}x_2^{4n} + 4x_5^{2n} + 6x_2^{5n} + 4x_{10}^n}{20}.$$

### 16.3.2.2 $C_{12n}$ Fullerene

Now consider the graph of fullerene  $C_{12n}$  ( $n \geq 2$ ), Fig. 16.20. This class of fullerenes has exactly  $12n$  carbon atoms, and the first member of this class of fullerenes can be obtained by putting  $n = 2$ , for example,  $C_{24}$ . Again our problem is reduced to the coloring of the corresponding fullerene graph with  $12n$  vertices. By using the labeling of its vertices, similar to the last example, one can see that the generators of this group are as follows:

$$\begin{aligned} \sigma &= (1, 12n - 5)(2, 12n - 4)(3, 12n - 3) \dots (12n - 24, 12n - 18) \\ &\quad \times (12n - 22, 12n - 19)(12n - 21, 12n - 20), \\ \tau &= (1, 12n - 5, 2, 12n, 3, 12n - 1, 4, 12n - 2, 5, 12n - 3, 6, 12n - 4) \dots \\ &\quad \times (12n - 29, 12n - 25, 12n - 26, 12n - 18, 12n - 20, 12n - 19, 12n - 22, \\ &\quad \times 12n - 21, 12n - 24, 12n - 23, 12n - 28, 12n - 27). \end{aligned}$$

Since  $\sigma^2 = \tau^{10} = \text{identity}$  and  $\sigma^{-1}\tau\sigma = \tau^{-1}$ , the symmetry group  $G$  of these fullerenes is isomorphic to the dihedral group of order 24. In the following table, the cycle types of elements of  $G$  are computed:



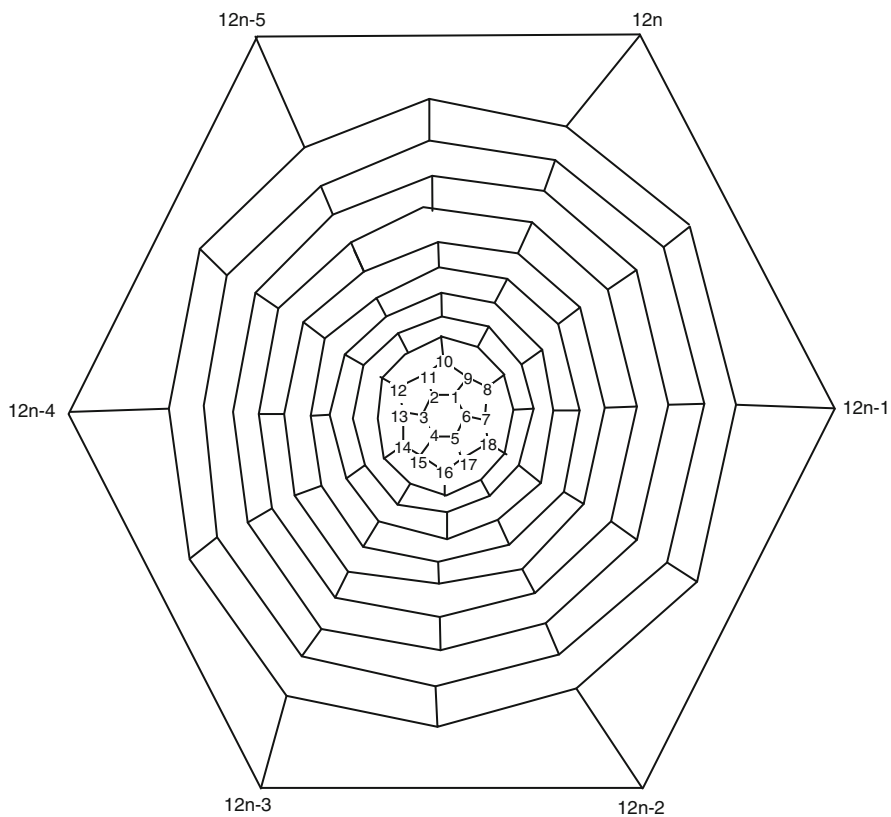


Fig. 16.20 The Schlegel diagram of  $C_{12n}$

Fullerene	Cycle type	#Permutations
$C_{12n}$	$1^{20n}$	1
	$1^{2n} 2^{9n}$	5
	$2^{10n}$	6
	$10^{2n}$	4
	$5^{4n}$	4

Thus, the cycle index of  $G$  is

$$Z(G, X) = \frac{x_1^{12n} + 6x_1^{2n}x_2^{5n} + 2x_6^{2n} + 2x_3^{4n} + 7x_2^{6n} + 4x_{12}^n + 2x_4^{3n}}{24}$$

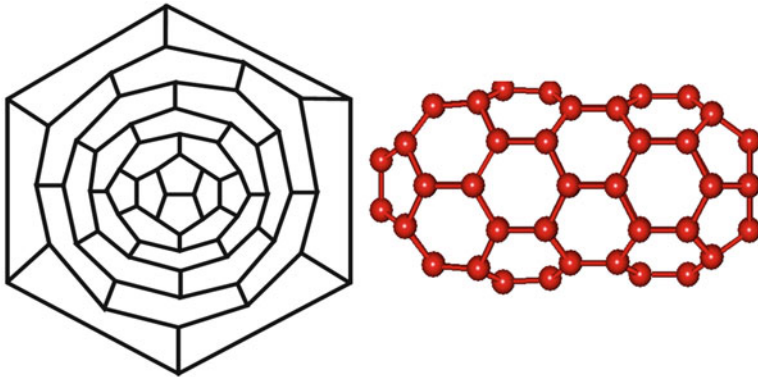


Fig. 16.21 2-D and 3-D graphs of fullerene  $C_{12n+6}$ , for  $n = 3$

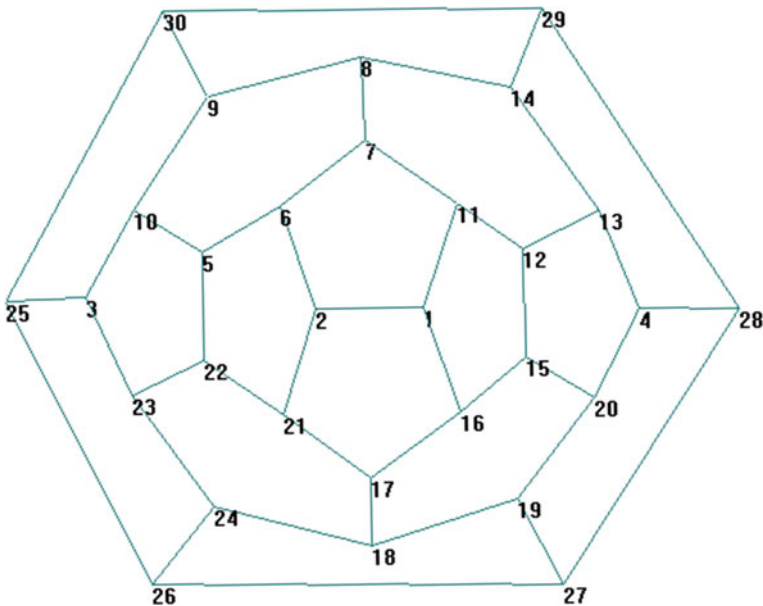


Fig. 16.22 Labeling of fullerene  $C_{30}$

### 16.3.2.3 $C_{12n+6}$ Fullerene

In this section consider a fullerene graph  $C_{12n+6}$  ( $n \geq 2$ ) with  $12n + 6$  carbon atoms, Fig. 16.21. As we know from the last discussions, our problem is reduced to the coloring of the corresponding fullerene graph with  $12n + 6$  vertices. Consider the labeling of the molecular graph  $C_{12n+6}$ , as depicted in Fig. 16.22. The generators of its symmetry group will be indicated by  $a$  and  $b$ , whereas  $a$  stands for a reflection. In the first step, we consider the labeling of vertices of the fullerene  $C_{30}$  (the first

member of this class) indicated in Fig. 16.12. The permutation representation of generators of symmetry group acting on the set of vertices is given by

$$a := (29, 30) (9, 14) (10, 13) (6, 11) (5, 12) (1, 2) (22, 15) (21, 16) (19, 24) (26, 27) \\ (20, 23) (3, 4) (25, 28) ;$$

$$b := (26, 30) (10, 23) (5, 22) (6, 21) (7, 17) (8, 18) (9, 24) (11, 16) (12, 15) (14, 19) \\ (13, 20) (27, 29) .$$

The generators satisfy in the following relations:

$$a^2 = b^2 = 1 \quad \text{and} \quad ab = ba.$$

This implies that the symmetry group of fullerene  $C_{30}$  is isomorphic with Abelian group  $Z_2 \times Z_2$ . So its cycle index is as follows:

$$Z(C_{30}, X) = \frac{x_1^{30} + x_1^6 x_2^{12} + x_1^4 x_2^{13} + 4x_2^{15}}{4}.$$

By using GAP [37], one can see that the symmetry group of  $C_{12n+6}$  fullerenes has two generators  $a, b$  of order 2, satisfying in the following relations:

$$a^2 = b^2 = 1 \quad \text{and} \quad ab = ba.$$

Further, this group is isomorphic to the Abelian group  $Z_2 \times Z_2$  of order 4, and the cycle types of elements of  $S$  are as in the following table:

Fullerene	Cycle type	#Permutations
$C_{12n+6}$	$1^{12n+6}\#$	1#
	$1^4 2^{6n+1}$	1
	$1^6 2^{6n}$	1
	$2^{6n+3}$	1

Thus, the cycle index of symmetry group is computed as

$$Z(G, S) = \frac{x_1^{12n+6} + x_1^4 x_2^{6n+1} + x_1^6 x_2^{6n} + x_2^{6n+3}}{4}.$$

### 16.3.2.4 $C_{24n}$ Fullerene

In this section we enumerate the number of hetero-fullerenes  $C_{24n}$  ( $n \geq 3$ ), Fig. 16.23. The first member of this family of fullerenes is  $C_{72}$ , obtained by putting  $n = 3$ . By considering the molecular graph of the fullerene  $C_{24n}$ , one can see that the generators of its symmetry group will be indicated by  $a$  and  $b$ , whereas  $a$  stands for a reflection. In the first step, consider the labeling of vertices of the fullerene

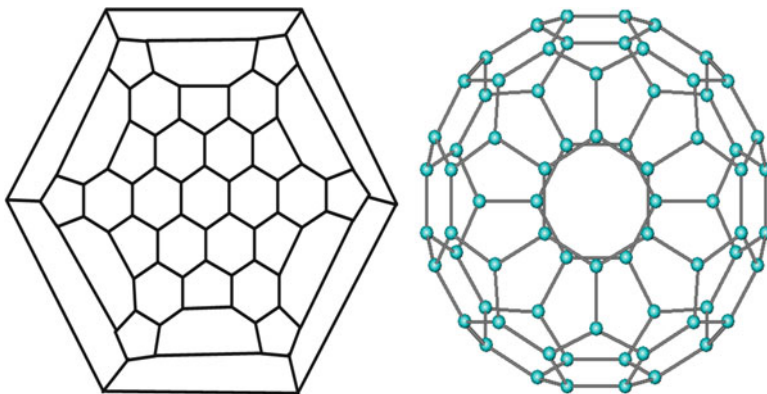
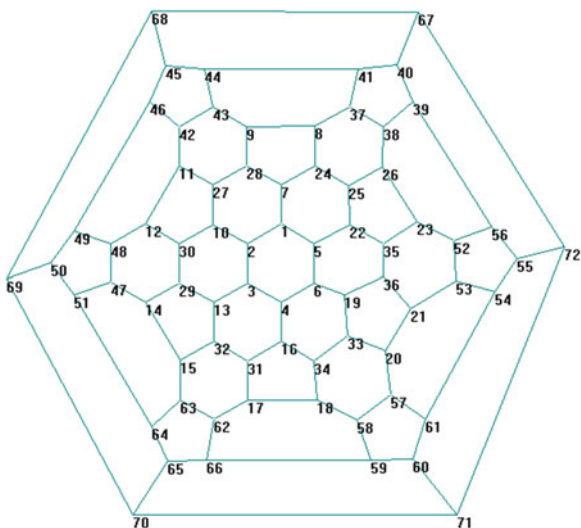


**Fig. 16.23** 2-D and 3-D graphs of fullerene  $C_{24n}$ , for  $n = 3$

**Fig. 16.24** Labeling of fullerene  $C_{72}$



$C_{72}$  as is indicated in Fig. 16.24, the permutation representation of generators of symmetry group  $S$  acting on the set of vertices is given by

$$a = (1,28,31,54,43,64,50,56,39,30,13,25)(2,24,10,44,51,70,59,65,49,37,16,21) \\ (3,9,32,52,60,69,68,66,48,27,19,17)(4,23,42,61,62,72,67,57,38,22,14,8)(5,34,41,63, \\ 53,71,58,47,20,26,7,18)(6,35,11,45,33,55,40,46,15,36,12,29);$$

$$b = (1,25)(2,18)(3,8)(4,17)(5,21)(6,29)(7,24)(9,14)(10,26)(11,36)(12,35)(13,28) \\ (15,45)(16,34)(19,23)(20,44)(22,32)(27,42)(30,31)(33,46)(37,41)(38,52)(39,54)(40, \\ 55)(43,56)(47,51)(48,61)(49,63)(50,64)(53,65)(57,60)(58,70)(59,71)(62,66)(67,69) \\ (68,72).$$

The generators satisfy in the following relations:

$$a^{12} = b^2 = 1 \text{ and } bab = a^{11} = a^{-1}.$$

This implies that the symmetry group of fullerene  $C_{72}$  is isomorphic with dihedral group  $D_{24}$ . However, by using GAP, one can see that the symmetry group of this family of fullerenes is isomorphic to the dihedral group  $D_{24}$  of order 24, and the cycle types of elements of  $S$  are as in the following table:

Fullerene	Cycle type	#Permutations
$C_{24n}$	$1^{24n\#}$	1#
	$1^4 2^{12n-2}$	6
	$2^{12n}$	7
	$3^{8n}$	2
	$4^{6n}$	2
	$6^{4n}$	2
	$12^{2n}$	4

Thus, the cycle index of symmetry group  $S$  is computed as

$$Z(G, S) = \frac{x_1^{24n} + 7x_2^{12n} + 6x_1^4 x_2^{12n-2} + 2x_3^{8n} + 2x_4^{6n} + 2x_6^{4n} + 4x_{12}^{2n}}{24}.$$

It is easy to see that the generators of the rotational group of fullerene  $C_{72}$  are

$$a = (1,2,3,4,5,6)*(7,10,13,16,19,22)*(29,31,33,35,25,27)*(30,32,34,36,26,28)*(8,11,14,17,20,23)*(62,57,52,47,42,37)*(63,58,53,48,43,38)*(12,15,18,21,24,9)*(66,61,56,51,46,41)*(65,60,55,50,45,40)*(64,59,54,49,44,39)*(69,70,71,72,67,68);$$

$$b = (68,69)*(47,53)*(40,65)*(39,66)*(62,38)*(41,64)*(37,63)*(9,8)*(29,28)*(23,12)*(27,30)*(10,22)*(11,24)*(44,61)*(2,6)*(5,3)*(25,32)*(20,15)*(42,58)*(46,59)*(45,60)*(67,70)*(13,19)*(36,33)*(21,14)*(52,48)*(17,18)*(34,35)*(57,43)*(49,56)*(50,55)*(51,54)*(72,71)*(26,31).$$

By using GAP, it is not difficult to see that  $a^6 = b^2 = 1$  and  $bab = a^5 = a^{-1}$ . Hence, this group is isomorphic with dihedral group  $D_{12}$ . In general, the cycle types of elements of rotational group  $R$  of  $C_{24n}$  are as in the following table:

Fullerene	Cycle type of rotational subgroup	#Permutations
$C_{24n}$	$1^{24n\#}$	1#
	$2^{12n-2}$	6
	$2^{12n}$	1
	$6^{4n}$	2
	$3^{8n}$	2

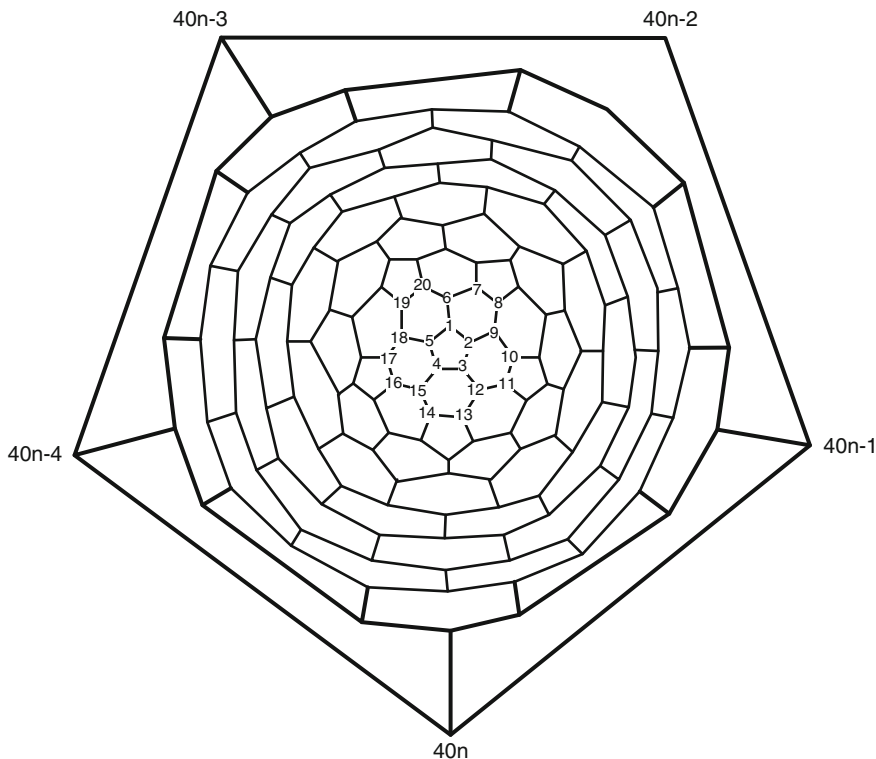


Fig. 16.25 The Schlegel diagram of  $C_{40n}$

This implies that the cycle index of rotational group  $R$  is as follows:

$$Z(G, R) = \frac{x_1^{24n} + x_2^{12n} + 6x_1^4 x_2^{12n-2} + 2x_3^{8n} + 2x_6^{4n}}{12}.$$

### 16.3.2.5 $C_{40n}$ Fullerene

In this section, we consider an infinite class  $C_{40n}$  ( $n \geq 2$ ) of fullerene molecules with  $40n$  carbon atoms as shown in Fig. 16.25. To compute the number of isomers of these fullerenes, we first compute a permutation representation for the symmetry group of these fullerenes. Consider the graph of fullerene  $C_{40n}$ . The generators of this group are

$$\begin{aligned} \sigma &= (2, 5)(3, 4)(7, 10) \dots (10n - 10, 10n - 7)(10n - 4, 10n - 2)(10n - 1, 10n), \\ \tau &= (1, 10n - 4, 3, 10n - 1, 5, 10n - 3, 2, 10n, 4, 10n - 2) \dots \\ &\quad \times (10n - 44, 10n - 36, 10n - 41, 10n - 38, 10n - 43, 10n - 39, \\ &\quad \times 10n - 40, 10n - 37, 10n - 42, 10n - 32). \end{aligned}$$

Since  $\sigma^2 = \tau^{10} = \text{identity}$  and  $\sigma^{-1}\tau\sigma = \tau^{-1}$ , the symmetry group  $G$  of these fullerenes is isomorphic to the dihedral group  $D_{20}$  of order 20. In the following table, the cycle types of elements of  $G$  are computed:

Fullerene	Cycle type	#Permutations
$C_{40n}$	$1^{40n}$	1
	$1^{4n}2^{18n}$	5
	$2^{20n}$	6
	$10^{4n}$	4
	$5^{8n}$	4

Thus, the cycle index of  $G$  is computed as

$$Z(G, X) = \frac{x_1^{40n} + 5x_1^{4n}x_2^{18n} + 6x_2^{20n} + 4x_{10}^{4n} + 4x_5^{8n}}{20}.$$

### 16.3.3 Fullerenes Constructed by Leapfrog Operation

Knowing the 3-dimensional cycle index of  $S(C_n)$  acting on the sets of vertices, edges, and faces, it is very easy to compute the cycle index for the induced action of  $S(C_n)$  on the set of vertices of  $C_{3n}$ . We just have to identify the vertices of  $C_n$  with the  $n$  new hexagonal faces of  $C_{3n}$ .

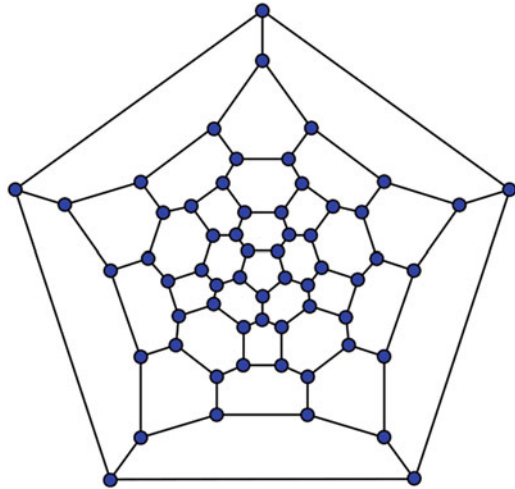
Here, we enumerate the number of hetero-fullerenes of two series of fullerenes constructed by Leapfrog, for example,  $C_{3^n \times 20}$  and two classes of  $C_{3^n \times 34}$  ( $n \geq 0$ ). From the above discussion our problem is reduced to the coloring of the corresponding fullerene graph with  $3^n \times m$  vertices ( $m \in \{20, 34\}$ ).

#### 16.3.3.1 $C_{3^n \times 20}$ Fullerene

Consider the molecular graph of the fullerene  $C_{3^n \times 20}$  as depicted in Fig. 16.26. The first member of this class is  $C_{20}$ , obtained by putting  $n = 0$ . It is well-known fact that the symmetry group of  $C_{20}$  is isomorphic to the non-Abelian group  $I_h = Z_2 \times A_5$  of order 120. So, according to the Leapfrog principle, the symmetry group  $G$  of these fullerenes is again isomorphic to the group  $I_h$ , and the cycle types of elements of  $G$  are as follows:

Fullerene	Cycle type	#Permutations
$C_{3^n \times 20}$	$1^{3^n \times 20}$	1
	$2^{3^n \times 10}$	16
	$1^{3^n-1 \times 4} 2^{3^n-1 \times 28}$	15
	$3^{3^n-1 \times 20}$	20
	$5^{3^n \times 4}$	24
	$6^{3^n-1 \times 10}$	20
	$10^{3^n \times 2}$	24

**Fig. 16.26** The Schlegel diagram of  $C_{3^n \times 20}$ , for  $n = 2$



This implies that the cycle index of  $G$  can be computed as

$$Z(G, X) = \left( x_1^{20 \times 3^n} + 20(x_3^{20 \times 3^{n-1}} + x_6^{10 \times 3^{n-1}}) + 24 \left( x_5^{4 \times 3^n} + x_{10}^{2 \times 3^n} \right) + 15x_1^{4 \times 3^{n-1}} x_2^{28 \times 3^{n-1}} + 16x_2^{10 \times 3^n} \right).$$

But from the cycle indices, one can compute the number of possible positional isomers, the number of chiral isomers, and the number of orbits under the whole point group  $I_h$ . For the number of orbits under the whole point group  $I_h$ , we simply note that  $Z_{I_h} - P_{I_h}^X = P_{I_h}^1$ . We use from this relation and then we obtain the number of  $C_{72-k}B_k$  molecules for both symmetry group and rotational group.

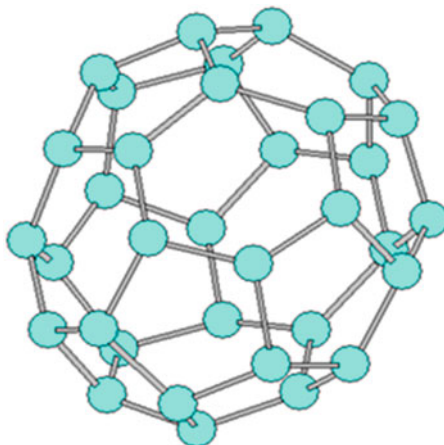
### 16.3.3.2 $C_{3^n \times 34}$ Fullerene

In this section, we compute the number of permutational isomers of a class of fullerenes with  $3^n \times 34$  vertices ( $n = 0, 1, \dots$ ); see Fig. 16.27. The symmetry group of the first member of this class of fullerenes, namely,  $C_{34}$ , is isomorphic with the non-Abelian group  $S_3$  of order 6. From Leapfrog principle, the symmetry group  $G$  of  $C_{3^n \times 34}$  fullerene is isomorphic to  $S_3$ , and so, the cycle types of elements of  $G$  are as in the following table:

Fullerene	Cycle type	# Permutations
$C_{3^n \times 34}$	$1^{3^n \times 34}$	1
	$1^{6n} 2^{17 \times 3^n - 3n}$	3
	$3^{3^{n-1} \times 34}$	2



**Fig. 16.27** 3-D graph of fullerene  $C_{3^n \times 34}$ ,  $n = 1$



Hence, the cycle index of  $G$  is computed as [25]

$$Z(G, X) = \frac{x_1^{34 \times 3^n} + 3x_1^{6n}x_2^{17 \times 3^n - 3n} + 2x_3^{34 \times 3^{n-1}}}{6}.$$

### 16.3.3.3 $F_{3^n \times 34}$ Fullerene

Finally, we enumerate the number of hetero-fullerenes in a new series of fullerenes constructed by Leapfrog. This class of fullerenes has again  $3^n \times 34$  vertices, and we denote this class of fullerenes by  $F_{3^n \times 34}$ ; see Figs. 16.28 and 16.29. Similar to the last discussion, our problem is reduced to the coloring of the corresponding fullerene graph with  $3^n \times 34$  vertices. The symmetry group of this fullerene is isomorphic with cyclic group of order 2, namely,  $Z_2$ . From Leapfrog principle, one can see that the symmetry group  $G$  of these fullerenes is isomorphic to the group  $Z_2$  of order 2, and the cycle types of elements of  $G$  are as in the following table:

Fullerene	Cycle type#	Cycle type#	#Permutations
	$n$ is even	$n$ is odd	
$F_{3^n \times 34}$	$1^{34 \times 3^n \#}$	$1^{34 \times 3^n \#}$	1
	$1^{6 \times 3^{n/2}} 2^{34 \times 3^n - 6 \times 3^{n/2}}$	$1^{4 \times 3^{(n-1)/2}} 2^{34 \times 3^n - 4 \times 3^{(n-1)/2}}$	1

This implies that the cycle index of  $G$  is computed as

$$Z(G, X) = \begin{cases} \frac{1}{2} \left( x_1^{34 \times 3^n} + x_1^{6 \times 3^{n/2}} x_2^{17 \times 3^n - 3 \times 3^{n/2}} \right) & 2|n \\ \frac{1}{2} \left( x_1^{34 \times 3^n} + x_1^{4 \times 3^{(n-1)/2}} x_2^{17 \times 3^n - 2 \times 3^{(n-1)/2}} \right) & 2 \nmid n \end{cases}.$$

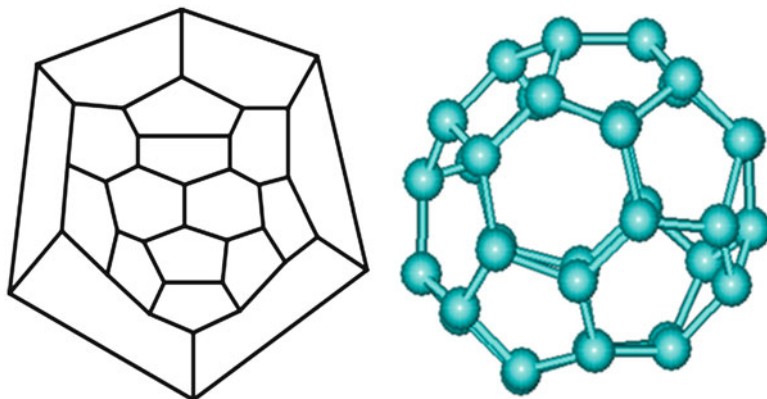


**Fig. 16.28** 2-D and 3-D graphs of fullerene  $C_{3^n \times 34}$ ,  $n = 1$

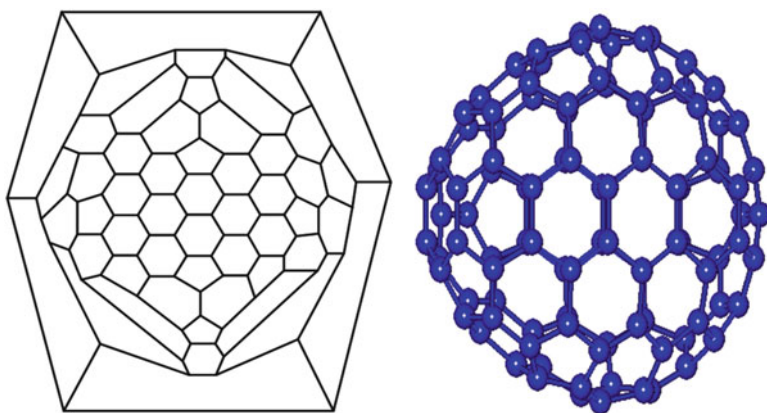


**Fig. 16.29** 2-D and 3-D graphs of fullerene  $C_{3^n \times 34}$ ,  $n = 2$

We can also apply our GAP program to compute the number of hetero-fullerenes  $F_{3^n \times 34-k} B_k$ .

## 16.4 Other Structures

Carbon exists in several forms in nature. One is the so-called nanotube which was discovered for the first time in 1991. Unlike carbon nanotubes, carbon nanohorns can be made simply without the use of a catalyst [38, 39]. The tips of these short nanotubes are capped with pentagonal faces; see Fig. 16.30a. Let  $p$ ,  $h$ ,  $n$ ,

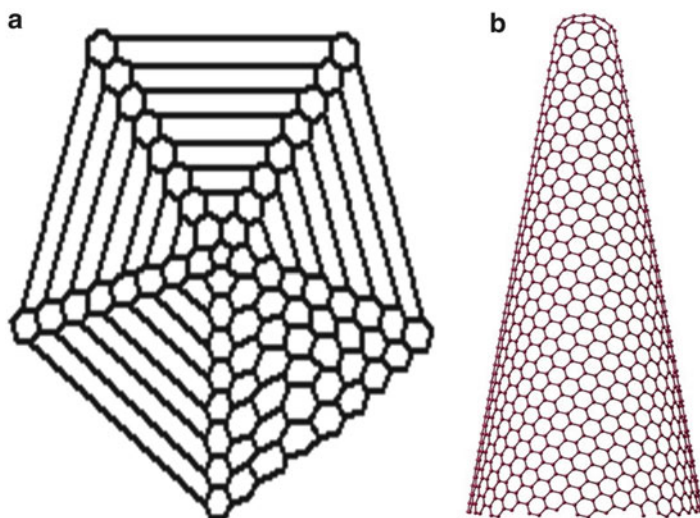


**Fig. 16.30** 2-D and 3-D graphs of nanohorn  $H$

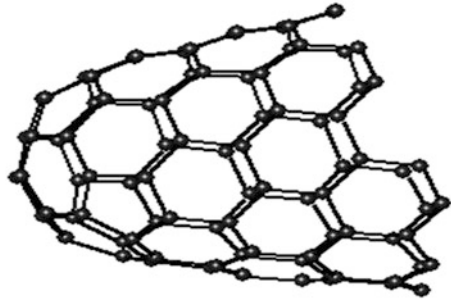
and  $m$  be the number of pentagons, hexagons, carbon atoms, and bonds between them, in a given nanohorn  $H$ . Then one can see that  $n = r^2 + 22r + 41$ ,  $m = \frac{3r^2 + 65r + 112}{2}$  ( $r = 0, 1, \dots$ ), and the number of faces is  $f = p + h$ . By the Euler's formula  $n - m + f = 2$ , one can deduce that  $p = 5$  and  $h = \frac{r^2 + 21r + 40}{2}$ ,  $r = 1, 2, \dots$ . From the above discussion our problem is reduced to the coloring of the corresponding nanohorn graph with  $n = r^2 + 22r + 41$  vertices. Consider the molecular graph of the nanohorn  $H$ ; see Fig. 16.30 for the case of  $r = 8$ . By using GAP software, one can see that the symmetry group  $H$  of these fullerenes is isomorphic to the group  $C_2$  of order 2. Thus, the cycle index of  $H$  is computed as

$$Z(H, X) = \frac{\left( x_1^{r^2 + 22r + 41} + x_1^{1+r} x_2^{\frac{(r^2 + 21r + 40)}{2}} \right)}{2}.$$

But from the cycle indices, one can compute the number of possible positional isomers and the number of chiral isomers under the symmetry group  $C_2$ .

In what follows we prepare a GAP program to compute the number of possible positional isomers for  $H$ . We mention here that our computations of symmetry properties and cycle indices of molecules were carried out with the use of GAP. In Table 16.14 (Appendix 16.B), we apply this program to compute the number of possible positional isomers for the case of  $r = 4$ , Fig. 16.31.

**Fig. 16.31** Nanohorn H for the case of  $r = 4$



## 16.5 USCI Table

The concept of the table of marks of a finite group was introduced by one of the pioneers of finite groups, William Burnside, in the second edition of his classical book (Burnside 1897). This table describes a characterization of the permutation representations of a group  $G$  by certain numbers of fixed points and in some detail the partially ordered set of all conjugacy classes of subgroups of  $G$ .

Shinsaku Fujita in some of his leading papers introduced the term markaracter to discuss marks for permutation representations and characters for linear representations in a common basis. To explain, we assume that  $G$  is a finite group and  $M$  is the mark table of  $G$ . By considering the rows and columns of  $M(G)$  corresponding to cyclic subgroups of  $G$ , a new table  $MC(G)$  is obtained. Fujita named this table as markaracter table of  $G$  (Fujita 1988a, b, c, d, e, 1999a, b, c, 2000, 2001; El-Basil 2002; Ashrafi and Ghorbani 2008). So, it is a modification of the classical notion of mark table. A dominant markaracter for a cyclic subgroup is defined as a row vector appearing in the resulting markaracter table.

A permutation representation (PR) of a finite group  $G$  is produced when the group  $G$  acts on a finite set  $X = \{x_1, x_2, \dots, x_k\}$ . The PR( $P_G$ ) is a set of permutations ( $P_g$ ) on  $X$ , each of which is associated with an element  $g \in G$ . Let  $H$  be a subgroup of  $G$ . The set of cosets of  $H$  in  $G$  provides a partition of  $G$ , that is,  $G = Hg_1 + Hg_2 + \dots + Hg_m$ , where  $g_1 = I$  (identity) and  $g_i \in G$ . Consider the set of cosets  $\{Hg_1, Hg_2, \dots, Hg_m\}$ . For any  $g \in G$ , the set of permutations of degree  $m$ ,

$$(G/H)_g = \begin{pmatrix} Hg_1 & Hg_2 & \dots & Hg_m \\ Hg_1g & Hg_2g & \dots & Hg_mg \end{pmatrix},$$

constructs a permutation representation of  $G$ , which is called a coset representation (CR) of  $G$  by  $H$  and notified as  $G/H$ . The degree of  $G/H$  is  $m = |G|/|H|$ , where  $|G|$  is the number of elements in  $G$ . Obviously, the coset representation  $G/H$  is transitive and, in other words, has one orbit.

The Burnside's theorem states that any permutation representation  $P_G$  of a finite group  $G$  acting on  $X$  can be reduced into transitive CRs in accord with equation

$P_G = \sum_{i=1}^s \alpha_i G/G_i$ , wherein the multiplicity  $\alpha_i$  is a nonnegative integer, where  $\alpha_i$  is obtained by solving

$$\mu_j = \sum_{i=1}^s \alpha_i M_{ij} \quad (1 \leq j \leq s) \tag{16.1}$$

where  $\mu_j$  is the number of fixed points of  $G_j$  in  $P_G$ , mark of  $G_j$ , and the symbol  $M_{ij}$  denotes the mark of  $G_j$  in  $G/G_i$ . Following Burnside, the matrix  $M(G) = [M_{ij}]$  is called the table of mark or mark table of  $G$ . If we restrict such elements within those of  $G_j \leq G$ , we have a permutation representation of the subgroup  $G_j$ . We call this permutation representation a subduced representation of  $G/G_i$  by  $G_j$  and designate this by the symbol  $G/G_i \downarrow G_j$ . According to  $P_G = \sum_{i=1}^s \alpha_i G/G_i$ , we arrive at a definition of the subduced representation,  $G/G_i \downarrow G_j = \{\pi_g | g \in G_j\}$ . Since this permutation representation is transitive in general, it can be reduced to a sum of CRs of the group  $G_j$ . Then the subduced representation (Fujita 2001) is represented by

$$G/G_i \downarrow G_j = \sum_{k=1}^{v_j} \beta_k^{(ij)} G/G_k^{(j)}, \quad 1 \leq i, j \leq s,$$

where the  $\beta_k^{(ij)}$  multiplicity is obtained by solving  $\mu_l^{(j)} = \sum_{k=1}^{v_j} \beta_k^{(ij)} m_{kl}^{(j)}$   $1 \leq l \leq v_j$  and  $\mu_l^{(j)}$  is the mark of  $G_l^{(j)}$  in  $G/G_i \downarrow G_j$ . A unit-subduced cycle index (USCI) is defined by

$$Z(G(/G_i) \downarrow G_j; s_d) = Z(G/G_i \downarrow G_j; s_d) = \prod_{k=1}^{v_j} s_{d_{jk}} \beta_k^{(ij)},$$

for each  $G/G_i \downarrow G_j$ , where the subscript  $d_{jk}$  is expressed by  $d_{jk} = |G_j| / |G_k^{(j)}|$ .

### 16.5.1 Markaracter Table

In this section we obtain some results about markaracter table. We also use of these results in the next section to compute the markaracter table of symmetry group of icosahedral fullerenes. Suppose the set of fixed points of the subgroup  $U$  in the action of  $G$  on  $X$  is  $\text{Fix}_X(U) = \{x \in X : x.u = x; \forall u \in U\}$ . Then the  $ij$ th entry of mark table of  $G$  is as follows:

$$M_{ij}(G) = |\text{Fix}_{G/G_j}(G_i)|.$$

Let also  $U$  and  $V$  be subgroups of  $G$  and  $v_G(V, U) = |\{U^g : g \in G, U^g \leq V\}|$ ; thus, we have

**Lemma 16.8 (Pfeiffer 1997)**

$$|\text{Fix}_{G/V}(U)| = [G : V] v_G(V, U) / v_G(G, U).$$

**Theorem 16.9** *Let  $G$  be a finite group and  $G_1, G_2, \dots, G_s$  be all nonconjugated subgroups of  $G$  in which  $|G_1| \leq |G_2| \leq \dots \leq |G_s|$ . Then the matrix  $M(G)$  is a lower triangular matrix and for all  $1 \leq i, j \leq s, M_{ij} | M_{1j}$ .*

*Proof* For the first claim use definition of markaracter table and for the second part use Lemma 16.8.

**Lemma 16.10** *Let  $G$  be a finite group and  $G_i \leq G$  be a subgroup. Then*

$$M_{ii} = (N_G(G_i) : G_i).$$

*Proof* By using definition of mark table, we have

$$\begin{aligned} M_{ii} &= |\{gG_i : \forall x \in G_i, x.gG_i = gG_i\}| \\ &= |\{gG_i : \forall x \in G_i, g^{-1}xgG_i = G_i\}| \\ &= |\{gG_i : \forall x \in G_i, x \in gG_i g^{-1}\}| \\ &= |\{gG_i : G_i = gG_i g^{-1}\}|. \end{aligned}$$

**Corollary 16.11** *If  $G_j$  be a normal subgroup of  $G$  ( $1 \leq j \leq s$ ), then*

$$M_{ij} = \begin{cases} |G|/|G_j| & G_i \subseteq G_j \\ 0 & \text{otherwise} \end{cases}.$$

*Proof* Similar to proof of Lemma 16.10, it is easy to see that  $M_{ij} = |\{gG_j : G_i \subseteq g^{-1}G_jg\}|$ . Since  $G_j$  is normal, then  $g^{-1}G_jg = G_j$ . This completes the proof.

**Theorem 16.12** *Table of marks of a non-Abelian group of order  $pq$  ( $p > q$ ), where  $p$  and  $q$  are prime numbers, is as follows:*

Mark table	$G_1$	$G_2$	$G_3$	$G_4$
$G/G_1$	$pq$	0	0	0
$G/G_2$	$p$	1	0	0
$G/G_3$	$q$	0	$q$	0
$G/G_4$	1	1	1	1

*Proof* It is easy to see that all nonconjugated subgroups of  $G$  are  $G_1 = ()$ ,  $G_2 = Q$ ,  $G_3 = P$ , and  $G_4 = G$ , in which  $|Q| = q$  and  $|P| = p$ . By Sylow theorem, one can see that  $P \triangleleft G$ . So, by using Lemma 16.10, we have  $M_{12} = p$ ,  $M_{22} = 1$ , and  $M_{32} = M_{42} = 0$ . On the other hand,  $Q \not\triangleleft G$ , because  $G$  is non-Abelian; hence,  $M_{23} = M_{43} = 0$  and  $M_{13} = M_{33} = 0$ .

**Fig. 16.32** The skeleton of naphthalene

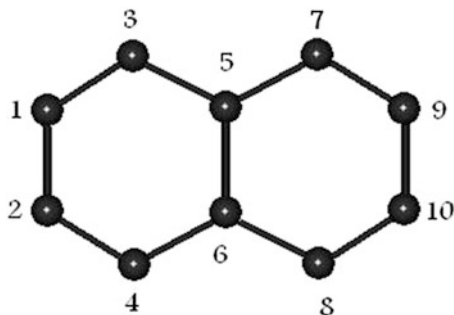


**Table 16.1** Mark table of the point group  $Z_2 \times Z_2$

Mark table	$G_1$	$G_2$	$G_3$	$G_4$	$G_5$
$G/(G_1)$	4	0	0	0	0
$G/(G_2)$	2	2	0	0	0
$G/(G_3)$	2	0	2	0	0
$G/(G_4)$	2	0	0	2	0
$G/(G_5)$	1	1	1	1	1

**Table 16.2** Markaracter table of the point group  $Z_2 \times Z_2$

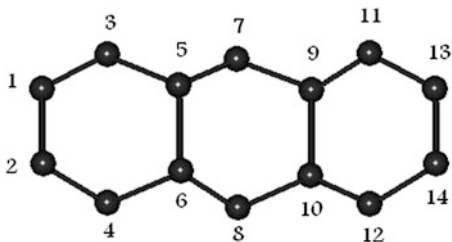
Mark table	$G_1$	$G_2$	$G_3$	$G_4$
$G/(G_1)$	4	0	0	0
$G/(G_2)$	2	2	0	0
$G/(G_3)$	2	0	2	0
$G/(G_4)$	2	0	0	2

### 16.5.2 Benzenoid Chains

Consider the skeleton of naphthalene, Fig. 16.32. Generators of its symmetry group are  $\lambda$  and  $\omega$ , where  $\lambda = (1, 9)(2, 10)(3, 7)(4, 8)$  and  $\omega = (1, 2)(3, 4)(5, 6)(7, 8)(9, 10)$ . The subgroups of  $G$  are  $G_1 = \langle () \rangle$ ,  $G_2 = \langle \lambda \rangle$ ,  $G_3 = \langle \omega \rangle$ ,  $G_4 = \langle \lambda\omega \rangle$ , and  $G_5 = G$ . This group is isomorphic with  $Z_2 \times Z_2$ , where  $Z_2$  is a group of order 2. Since every group of order 4 is Abelian and then  $Z_2 \times Z_2$ , by using Corollary 16.11, for any subgroup  $G_i$  of  $Z_2 \times Z_2$ ,  $M_{ij} = 0$  or  $|Z_2 \times Z_2|/|G_i|$ . But for pure subgroup  $H$  of  $Z_2 \times Z_2$ ,  $|H| = 2$ . This implies that the entries of mark table are 1, 2, and 4. By Theorem 16.9,  $M_{11} = 4$  and  $M_{i1} = 0$  for  $2 \leq i \leq 4$ . Also  $M_{4j} = 1$  for  $1 \leq j \leq 4$ . Since all subgroups in Abelian group are normal, by using Lemma 16.10, we have  $M_{12} = M_{22} = 2$  and  $M_{32} = M_{42} = 0$ . Using again Lemma 16.10, it is easy to see that  $M_{13} = M_{33} = 2$  and  $M_{23} = M_{43} = 0$ . In Tables 16.1 and 16.2, the mark table and markaracter table of this group are computed. On the other hand, the number of  $(\mu_j)$  of fixed points is obtained by a geometrical examination of Eq. (16.1):

$$(10, 2, 0, 0, 0) = (\alpha_{G_1}, \alpha_{G_2}, \alpha_{G_3}, \alpha_{G_4}, \alpha_{G_5}) \times \begin{pmatrix} 4 & 0 & 0 & 0 & 0 \\ 2 & 2 & 0 & 0 & 0 \\ 2 & 0 & 2 & 0 & 0 \\ 2 & 0 & 0 & 2 & 0 \\ 1 & 1 & 1 & 1 & 1 \end{pmatrix}.$$

**Fig. 16.33** The skeleton of anthracene



So,  $\alpha_{G_5} = \alpha_{G_4} = \alpha_{G_3} = 0$ ,  $\alpha_{G_1} = 2, \alpha_{G_2} = 1$ , and  $P_G = 2G (/G_1) + G (/G_2)$ . This implies that sub-orbits of  $X$  are

$$X_{11} = \{1, 2, 9, 10\}, X_{21} = \{5, 6\}, X_{12} = \{3, 4, 7, 8\}.$$

With a similar discussion, the generators of the point group of anthracene skeleton (Fig. 16.33) are  $\delta$  and  $\gamma$ , where

$$\begin{aligned} \gamma &= (1, 13)(2, 14)(3, 11)(4, 12)(5, 9)(6, 10), \\ \eta &= (1, 2)(3, 4)(5, 6)(7, 8)(9, 10)(11, 12)(13, 14). \end{aligned}$$

The subgroups of  $G$  are  $G_1 = \langle () \rangle$ ,  $G_2 = \langle \gamma \rangle$ ,  $G_3 = \langle \eta \rangle$ ,  $G_4 = \langle \gamma\eta \rangle$ , and  $G_5 = G$ . Also, the mark table and markaracter table of this group are the same of naphthalene. The number of  $(\mu_j)$  of fixed points is

$$(10, 2, 0, 0, 0) = (\alpha_{G_1}, \alpha_{G_2}, \alpha_{G_3}, \alpha_{G_4}, \alpha_{G_5}) \times \begin{pmatrix} 4 & 0 & 0 & 0 & 0 \\ 2 & 2 & 0 & 0 & 0 \\ 2 & 0 & 2 & 0 & 0 \\ 2 & 0 & 0 & 2 & 0 \\ 1 & 1 & 1 & 1 & 1 \end{pmatrix}.$$

Hence,  $\alpha_{G_5} = \alpha_{G_4} = \alpha_{G_3} = 0$ ,  $\alpha_{G_2} = 1$ ,  $\alpha_{G_1} = 2$ , and then by the similar way, one can see that  $P_G = 2G (/G_1) + G (/G_2)$ . Thus, the sub-orbits of  $X$  are  $X_{11} = \{1, 2, 13, 14\}$ ,  $X_{21} = \{7, 8\}$ ,  $X_{22} = \{5, 6, 9, 10\}$ , and  $X_{12} = \{3, 4, 11, 12\}$ .

In generally, consider the graph of benzenoid chain with exactly  $n$  hexagons, Fig. 16.34. Its point group is isomorphic with group  $Z_2 \times Z_2$  generated by  $\alpha$  and  $\beta$  where

$$\begin{aligned} \alpha &= (1, 3)(2, 4) \cdots (4n - 4, 4n - 2)(4n - 3, 4n - 1), \\ \beta &= (1, 2)(3, 4) \cdots (4n - 1, 4n)(4n + 1, 4n + 2). \end{aligned}$$

This implies the mark table and markaracter table of a benzenoid chain with exactly  $n$  hexagons are similar to anthracene and naphthalene; see Ghorbani et al. (2012) for more details.



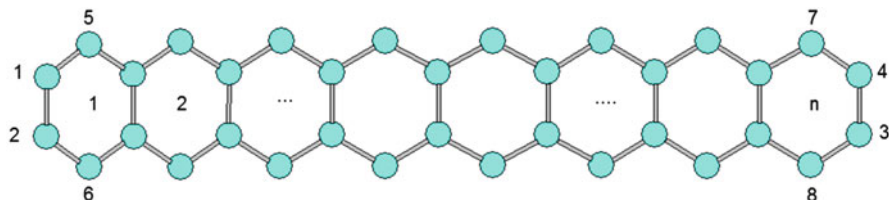
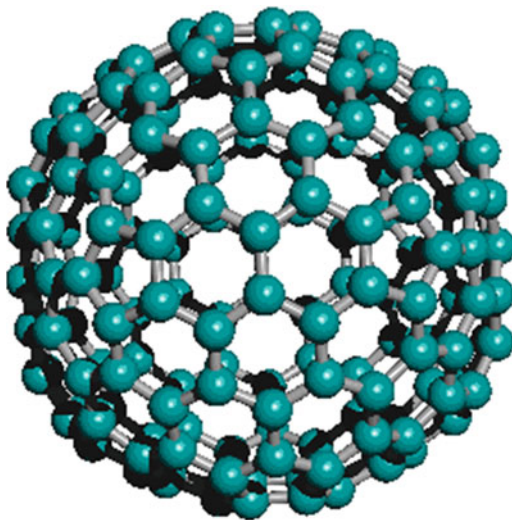


**Fig. 16.34** The skeleton of a benzenoid chain with  $n$  hexagons

**Fig. 16.35** The fullerene  $C_{3^n \times 20}$  for  $n = 2$



Now is the time to compute the markaracter table and then *USCI* table of fullerenes in a series of fullerenes constructed by Leapfrog. From the above discussion, the problem is reduced to compute the markaracter table and *USCI* table of the corresponding fullerene graph with 20 vertices. Consider the molecular graph of the fullerene  $C_{3^n \times 20}$ , Fig. 16.35. From the Leapfrog principle, it can be seen that the symmetry group  $G$  of these fullerenes is isomorphic to the group  $I_h = Z_2 \times A_5$  of order 120, where  $A_5$  is an alternating group on five symbols. Consider the fullerene graph  $C_{20}$ , depicted in Fig. 16.36, with symmetry group  $Z_2 \times A_5$ . By using computer algebra system GAP, one can see that this group has exactly 22 conjugacy classes of subgroups and the generators of its symmetry group

```
gap > List(ConjugacyClassesSubgroups(G), x -> Elements(x)); z := Length(aa);
```

Hence, this group has eight nonconjugated cyclic subgroups as follows:

$$G_1 = \langle () \rangle,$$

$$G_2 = \langle (1,9)(2,16)(3,10)(4,13)(5,17)(6,14)(7,15)(8,18)(11,20)(12,19) \rangle,$$

$$G_3 = \langle (1,3)(2,18)(4,15)(5,17)(6,14)(7,13)(8,16)(9,10)(11,19)(12,20) \rangle,$$

$$G_4 = \langle (2,4)(5,6)(7,8)(11,19)(12,20)(13,16)(14,17)(15,18) \rangle,$$

**Fig. 16.36** The fullerene  $C_{20}$

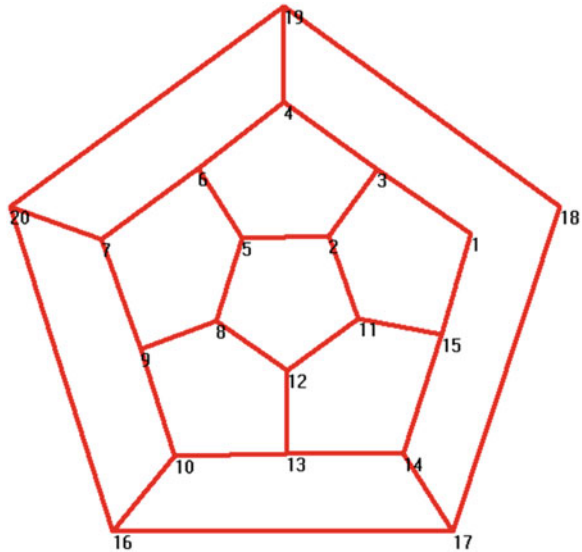


**Table 16.3** Mark table of the symmetry group  $Z_2 \times A_5$

Markaracter table	$G_1$	$G_2$	$G_3$	$G_4$	$G_5$	$G_6$	$G_7$	$G_8$
$G/G_1$	120	0	0	0	0	0	0	0
$G/G_2$	60	60	0	0	0	0	0	0
$G/G_3$	60	0	4	0	0	0	0	0
$G/G_4$	60	0	0	4	0	0	0	0
$G/G_5$	40	0	0	0	4	0	0	0
$G/G_6$	24	0	0	0	0	4	0	0
$G/G_7$	20	20	0	0	2	0	2	0
$G/G_8$	12	12	0	0	0	2	0	2

$$G_5 = \langle (2,14,19)(3,15,18)(4,11,17)(5,13,20)(6,12,16)(7,8,10) \rangle,$$

$$G_6 = \langle (1,2,8,10,17)(3,5,9,16,18)(4,6,7,20,19)(11,12,13,14,15) \rangle,$$

$$G_7 = \langle (2,14,19)(3,15,18)(4,11,17)(5,13,20)(6,12,16)(7,8,10), (1,9)(2,16)(3,10)(4,13)(5,17)(6,14)(7,15)(8,18)(11,20)(12,19) \rangle,$$

$$G_8 = \langle (1,2,8,10,17)(3,5,9,16,18)(4,6,7,20,19)(11,12,13,14,15), (1,9)(2,16)(3,10)(4,13)(5,17)(6,14)(7,15)(8,18)(11,20)(12,19) \rangle$$

By considering the rows and columns of  $M(Z_2 \times A_5)$  corresponding to cyclic subgroups of  $Z_2 \times A_5$ , the markaracter table is obtained as follows (Table 16.3).

According to Fujita's theorem for computing the *USCI* table of group  $G = Z_2 \times A_5$ , it is enough to compute the inverse of markaracter table of every subgroup  $H$ , and then  $M(G)M^{-1}(H)$  results the corresponded column of *USCI* table. For example, if  $H = G_2$ , then the mark table and its inverse are as follows (Table 16.4):

**Table 16.4** Mark table and its inverse of group  $Z_2$

$M(G)$	$G_1$	$G_2$		$M^{-1}(G)$	$G_1$	$G_2$
$G/G_1$	2	0	$\Rightarrow$	$G/G_1$	1/2	0
$G/G_2$	1	1		$G/G_2$	-1/2	1

So, the entries of the second column of *USCI* table are as follows:

$$\begin{pmatrix} 120 & 0 \\ 60 & 60 \\ 60 & 0 \\ 60 & 0 \\ 40 & 0 \\ 30 & 0 \\ 30 & 0 \\ 30 & 30 \\ 24 & 0 \\ 20 & 0 \\ 20 & 0 \\ 20 & 20 \\ 15 & 15 \\ 12 & 0 \\ 12 & 0 \\ 12 & 12 \\ 10 & 0 \\ 10 & 10 \\ 6 & 6 \\ 5 & 5 \\ 2 & 0 \\ 1 & 1 \end{pmatrix} \times \begin{pmatrix} 1/2 & 0 \\ -1/2 & 1 \end{pmatrix} = \begin{pmatrix} S_2 & S_1 \\ 60 & 0 \\ 0 & 60 \\ 30 & 0 \\ 30 & 0 \\ 20 & 0 \\ 15 & 0 \\ 15 & 0 \\ 0 & 30 \\ 12 & 0 \\ 10 & 0 \\ 10 & 0 \\ 0 & 20 \\ 0 & 15 \\ 6 & 0 \\ 6 & 0 \\ 0 & 12 \\ 5 & 0 \\ 0 & 10 \\ 0 & 6 \\ 0 & 5 \\ 1 & 0 \\ 0 & 1 \end{pmatrix} \Rightarrow \text{USCI}(G)_j \begin{pmatrix} S_2^{60} \\ S_1^{60} \\ S_2^{30} \\ S_2^{30} \\ S_2^{20} \\ S_2^{15} \\ S_2^{15} \\ S_1^{30} \\ S_2^{12} \\ S_2^{10} \\ S_2^{10} \\ S_1^{20} \\ S_1^{15} \\ S_2^6 \\ S_2^6 \\ S_1^{12} \\ S_2^5 \\ S_1^{10} \\ S_1^6 \\ S_1^5 \\ S_2 \\ S_1 \end{pmatrix}$$

It should be noted that we use from GAP software to compute the mark table of the group  $G = Z_2 \times A_5$  by the following function:

```
gap> Display(TableOfMarks(DirectProduct(CyclicGroup(2),AlternatingGroup(5)))).
```

By a similar method, one can compute the whole of *USCI* table. This table is reported in the Appendix 16.C.

## Appendices

### Appendix 16.A: GAP Programs

This software was constructed by the GAP team in Aachen. GAP is a system for computational discrete algebra, with particular emphasis on computational group theory. GAP provides a programming language, a library of thousands of functions implementing algebraic algorithms written in the GAP language as well as large data libraries of algebraic objects. GAP is used in research and teaching for studying groups and their representations, rings, vector spaces, algebras, combinatorial structures, and more; see The GAP Team (1995).

#### A GAP Program for Enumerating the Hetero-fullerenes

```

h:=function (f,g)
  local t,i,tt;
    Print("Coefficients of f are:", "\n");
    t:=CoefficientsofLaurentPolynomial(f);
    for i in t[1] do
      Print(i, "\n");
    od;
    Print("Coefficients of g are:", "\n");
    tt:=CoefficientsofLaurentPolynomial(g);
  for i in tt[1] do
    Print(i, "\n");
  od;
  return();
end;

```

#### A Gap Program for Counting the Number of Nanohorn $H$

```

f:=function (n)
  locals,i,f,x,t;
    x:=Indeterminate(Rationals, "x");
    f:=((1+x)^(89)+(1+x)^5*(1+x^2)^(42))/2;
    t:= CoefficientsOfLaurentPolynomial(f);
  Print("*****", "\n");
  Print("\n");
  Print("Number of Molecules for Symmetry Group =", "\n");
  for i in t[1] do
    Print(i, "\n");
  od;
  Print("*****", "\n");
  return;end;

```

**Appendix 16.B: Number of Permutational Isomers****Table 16.5** The number of  $C_{20-k}B_k$  molecules

$k, 20 - k$	Number of $C_{20-k}B_k$ molecules for symmetry group
0,20	1
1,19	1
2,18	12
3,17	51
4,16	265
5,15	931
6,14	2972
7,13	7365
8,12	15730
9,11	27582
10,10	41544

**Table 16.6** Number of  $C_{24-k}B_k$  molecules

$k, 24 - k$	Number of $C_{24-k}B_k$ molecules for symmetry group	Number of $C_{24-k}B_k$ molecules for rotational group
0,24	1	1
1,23	2	2
2,22	19	30
3,21	96	170
4,20	489	924
5,19	1826	3542
6,18	5775	11350
7,17	14586	28842
8,16	31034	61578
9,15	54814	108968
10,14	82358	163900
11,13	104468	208012
12,12	113434	225898

**Table 16.7** Number of  $C_{30-k}B_k$  molecules

$k, 30 - k$	Number of $C_{30-k}B_k$ molecules for symmetry group	Number of $C_{30-k}B_k$ molecules for rotational group
0,30	1	1
1,29	3	3
2,28	51	33
3,27	406	226
4,26	2793	1467
5,25	14253	7287
6,24	59605	30173
7,23	203580	102468
8,22	585975	294255
9,21	1430715	717299
10,20	3006009	1506051
11,19	5462730	2735358
12,18	8651825	4331275
13,17	11975985	5994081
14,16	14545485	7279821
15,15	15511760	7762876

**Table 16.8** Number of  $C_{34-k}B_k$  molecules

$k, 34 - k$	Number of $C_{34-k}B_k$ molecules for symmetry group
0,34	1
1,33	6
2,32	102
3,31	1001
4,30	7801
5,29	46376
6,28	224509
7,27	896621
8,26	3027224
9,25	8741931
10,24	21857839
11,23	47682960
12,22	91398638
13,21	154664070
14,20	232005664
15,19	309328074
16,18	367339214
17,17	388934370

**Table 16.9** The number of  $C_{60-k}B_k$  molecules

$k, 60-k$	Number of $C_{60-k}B_k$ molecules for rotational group	Number of $C_{60-k}B_k$ molecules for symmetry group	Number of orbits under whole point group $I_h$
0,60	1	1	0
1,59	1	1	0
2,58	23	37	14
3,57	303	577	274
4,56	4190	8236	4046
5,55	45718	91030	45312
6,54	418470	835476	417006
7,53	3220218	6436782	3216564
8,52	21330558	42650532	21319974
9,51	123204921	246386091	123181170
10,50	628330629	1256602779	628272150
11,49	2855893755	5711668755	2855775000
12,48	11661527055	23322797475	11661270420
13,47	43057432740	86114390460	43056957720
14,46	144549869700	289098819780	144548950080
15,45	443284859624	886568158468	443283298844
16,44	1246738569480	2493474394140	1246735824660
17,43	3226849468425	6453694644705	3226845176280
18,42	7708584971055	15417163018725	7708578047670
19,41	17040023323785	34080036632565	17040013308780
20,40	34932048763560	69864082608210	34932033844650
21,39	66537224405790	133074428781570	66537204375780
22,38	117952355252550	235904682814710	117952327562160
23,37	194877787472550	389755540347810	194877522875260
24,36	300436595453640	600873146368170	300436550914530
25,35	432628675734195	865257299572455	432628623838260
26,34	582384767014701	1164769471671687	582384704656986
27,33	733373386161407	1466746704458899	733373318297492
28,32	864332935668892	1728665795116244	864332859447352
29,31	953746664302456	1907493251046152	953746586743696
30,30	985538239868528	1971076398255692	985538158387164

**Table 16.10** The number of  $C_{72-k}B_k$  molecules

$k, 72 - k$	Number of $C_{72-k}B_k$ molecules for rotational group	Number of $C_{72-k}B_k$ molecules for symmetry group
0,72	1	1
1,71	4	8
2,70	127	236
3,69	2522	5044
4,68	43243	86168
5,67	583576	1167152
6,66	6514407	13025244
7,65	61386116	122772232
8,64	498746918	997464358
9,63	3546427742	7092855484
10,62	22342414424	44684640352
11,61	125928884480	251857768960
12,60	640138180164	1280275386294
13,59	2954479373440	5908958746880
14,58	12451019242744	24902034311648
15,57	48143925115958	96287850231916
16,56	171512731027768	343025446924856
17,55	564983065793776	1129966131587552
18,54	1726337142727692	3452674238383744
19,53	4906431753373920	9812863506747840
20,52	13002044149467636	26004088171840416
21,51	32195537606713866	64391075213427732
22,50	74635109937400116	149270219574397584
23,49	162250238419042800	324500476838085600
24,48	331260903551195565	662521806476549181
25,47	636020933801574048	1272041867603148096
26,46	1149730149855983496	2299460298556572192
27,45	1958799512979179380	3917599025958358760
28,44	3148070646470848632	6296141291043543360
29,43	4776383047609873920	9552766095219747840
30,42	6846149035990297176	13692298069196643072
31, 41	9275427723456099744	18550855446912199488
32, 40	11884141772331102516	23768283541008261684
33, 39	14405020327110683172	28810040654221366344
34,38	16523405671536565290	33046811338774382280
35,37	17939697583328247888	35879395166656495776
36,36	18438022518784399786	36876045033031223812



**Table 16.11** The number of  $C_{80-k}B_k$  molecules

$k, 80 - k$	Number of $C_{80-k}B_k$ molecules for symmetry group
0,80	1
1,79	5
2,78	181
3,77	4147
4,76	79546
5,75	1202745
6,74	15031147
7,73	158844959
8,72	1449435558
9,71	11595097111
10,70	82325041251
11,69	523884428977
12,68	3012334769066
13,67	15756817617163
14,66	75407624568509
15,65	331793506218077
16,64	1347911111443259
17,63	5074488744913588
18,62	17760710591159316
19,61	57956002543262252
20,60	176765807739834016
21,59	505045163808913156
22,58	1354439302981356268
23,57	3415542587404475164
24,56	8111913645381087112
25,55	18170686559985988028
26,54	38437990801023264444
27,53	76875981591517458868
28,52	145515250872462217832
29,51	260923898098627253308
30,50	443570626773816168644
31,49	715436494770338700580
32,48	1095512132628624165470
33,47	1593472192879288312630
34,46	2202740972528516942390
35,45	2895030992423701444170
36,44	3618788740556990692460
37,43	4303424448183910977070
38,42	4869664507190697241610
39,41	5244254084621907482050
40,40	5375360436777969680320

**Table 16.12** The number of  $C_{84-k}B_k$  molecules

$k, 84 - k$	Number of $C_{84-k}B_k$ molecules for symmetry group
0,84	1
1,83	4
2,82	161
3,81	4000
4,80	80724
5,79	1286744
6,78	16941162
7,77	188728904
8,76	1816506426
9,75	15339084436
10,74	115043064318
11,73	773924297744
12,72	4708039172851
13,71	26075285193864
14,70	132238945055628
15,69	617115040987920
16,68	2661308609905260
17,67	10645234310343900
18,66	39623927700233625
19,65	137641011605240660
20,64	447333287699520054
21,63	1363301447106388504
22,62	3903999598530800496
23,61	10523825001987843104
24,60	26748055213518461739
25,59	64195332506438811392
26,58	145674023765218737768
27,57	312929384372799539932
28,56	637034818189367985288
29,55	1230136200620880101792
30,54	2255249701142983248018
31,53	3928499479377611057376
32,52	6506577262729079657604
33,51	10252788413950491335316
34,50	15379182620943916403538
35,49	21970260887002103927160
36,48	29903966207337904208345
37,47	38794334539178147226960
38,46	47982466403762890020840
39,45	56594703963337371170880
40,44	63669041958809577715404
41,43	68327752345967341397280
42,42	69954603592363988835420

**Table 16.13** The number of  $C_{150-k}B_k$  molecules

$k, 150 - k$	Number of $C_{150-k}B_k$ molecules for symmetry group
0,150	1
1,149	10
2,148	608
3,147	27762
4,146	1015132
5,145	29587626
6,144	714908767
7,143	14705679304
8,142	262861756418
9,141	4147359263564
10,140	58477733568550
11,139	744261878846444
12,138	8621033058155532
13,137	91515579793041740
14,136	895545312914462338
15,135	8119610820294861024
16,134	68509216265755052423
17,133	540013822200718017274
18,132	3990102130481989637532
19,131	27720709537206337672482
20,130	181570647467256032286270
21,129	1124008770030069888944122
22,128	6590778696986152507958223
23,127	36679116226676561530421568
24,126	194093656699453439146865712
25,125	978232029765102584306831360
26,124	4703038604639712304854528992
27,123	21599140258344705503374136608
28,122	94881937563441939987580122208
29,121	399158495956546227316507706912
30,120	1609939267024733028272418627950
31,119	6232022969127988937630220494912
32,118	23175335416444696549270781265772
33,117	82869381186074941227257032574344
34,116	285168164669728433394496223305568
35,115	945128774333956983333854159548184
36,114	3019161362455695793849475118633168
37,113	9302280954593224550068789712330120
38,112	27662045996553535806719975891990092
39,111	79439721836256307048558318405485664
40,110	220445228095611251123048465578384610
41,109	591438416841883842130309387714175824
42,108	1534923510375365207042049180063976208
43,107	3855156723733475398082512651736762064
44,106	9375040214533678803733124039197920912
45,105	22083428060901554502735720945545628656

(continued)

**Table 16.13** (continued)

$k, 150 - k$	Number of $C_{150-k}B_k$ molecules for symmetry group
46,104	50407824921623113527709622686290336312
47,103	111540718975506463949387235122286925152
48,102	239347792801607620535970453784351147068
49,101	498234180933958720246386671215627247400
50,100	1006433045486596614856890256732735499706
51,99	1973398128405091401582018701627687530440
52,98	3757046436771231706787858155503142213536
53,97	6946991524595862401059693903626311024424
54,96	12478855146033308386976398312593227196124
55,95	21781274436712683729716490061393340262312
56,94	36950376276566159898459691595847481631824
57,93	60935708245565246147909753636832722794208
58,92	97707256324785653305903584594286513690016
59,91	152357077658987798374692146630075734026208
60,90	231074901116131494201332210976565629621470
61,89	340930181974620237345396728498808495051488
62,88	489399777350664534253556972312070143515984
63,87	683606038204102841495979056024525881046720
64,86	929276958183702300158285743952520137280386
65,85	1229504898519975350977406221073619443220268
66,84	1583453278396937952016116475798783021139936
67,83	1985225005751384895063598575468858890976508
68,82	2423142286431837445445179468870345772615144
69,81	2879676340397256094585598969401799560569164
70,80	3332196908173967766592027941721540605994000
71,79	3754588065548132694750220759988813194524464
72,78	4119617460809756706740212819065590964482316
73,77	4401783040317274289392463027500946909902536
74,76	4580233704113920544368502750626698489294984
75,75	4641303486835439484959145718568923895458472

**Table 16.14** The number of  $H_{89-k}B_k$  molecules

$k, 89 - k$	Number of $H_{89-k}B_k$ molecules for symmetry group
0,89	1
1,88	47
2,87	1984
3,86	56892
4,85	1221456
5,84	20756184
6,83	290563644
7,82	3445167312
8,81	35312741949
9,80	317813975539

(continued)

**Table 16.14** (continued)

$k, 89 - k$	Number of $H_{89-k}B_k$ molecules for symmetry group
10,79	2542510116752
11,78	18259840795912
12,77	118688954831096
13,76	703003784422072
14,75	3816306205549832
15,74	19081530912625424
16,73	88252080242700895
17,72	378964814703449873
18,71	1515859257963982160
19,70	5664526699240696204
20,69	19825843444588399064
21,68	65142057027473837360
22,67	201348176258905833868
23,66	586535991698093381120
24,65	1612973977150092969259
25,64	4193732340560438311493
26,63	10323033453643439331136
27,62	24087078058438832974432
28,61	53335672843599223614176
29,60	112188829084695301825888
30,59	224377658169237491264096
31,58	427041349418676753435712
32,57	774012445821111101559914
33,56	1336930588236176461627382
34,55	2202003321800426034874816
35,54	3460290934257434856293432
36,53	5190436401385740907480896
37,52	7434949439822385325514640
38,51	10174141338703878921425976
39,50	13304646365996955576915552
40,49	16630807957495803542747490
41,48	19875843656519036615151870
42,47	22715249893164345209272800
43,46	24828296394853866796169520
44,45	25956855321892585506612240

### Appendix 16.C

USCI table of the point group  $Z_2 \times A_5$

$\downarrow G_{11}$	$\downarrow G_{10}$	$\downarrow G_9$	$\downarrow G_8$	$\downarrow G_7$	$\downarrow G_6$	$\downarrow G_5$	$\downarrow G_4$	$\downarrow G_3$	$\downarrow G_2$	$\downarrow G_1$	USCI table
$S_6^{20}$	$S_6^{20}$	$S_5^{24}$	$S_4^{30}$	$S_4^{30}$	$S_4^{30}$	$S_2^{40}$	$S_2^{60}$	$S_2^{60}$	$S_2^{60}$	$S_1^{120}$	G/G <sub>1</sub>
$S_6^{10}$	$S_6^{10}$	$S_5^{12}$	$S_2^{30}$	$S_4^{15}$	$S_4^{15}$	$S_3^{20}$	$S_2^{30}$	$S_1^{60}$	$S_1^{60}$	$S_1^{60}$	G/G <sub>2</sub>
$S_6^{10}$	$S_6^8 S_3^4$	$S_5^{12}$	$S_4^{14} S_2^2$	$S_4^{13} S_3^4$	$S_4^{15}$	$S_3^{20}$	$S_2^{30}$	$S_2^{28} S_1^4$	$S_2^{30}$	$S_1^{60}$	G/G <sub>3</sub>
$S_6^8 S_3^4$	$S_6^{10}$	$S_5^{12}$	$S_4^{14} S_2^2$	$S_4^{14} S_2^2$	$S_4^{12} S_2^6$	$S_3^{20}$	$S_2^{28} S_1^4$	$S_2^{30}$	$S_2^{30}$	$S_1^{60}$	G/G <sub>4</sub>
$S_6^6 S_2^2$	$S_6^6 S_2^2$	$S_5^8$	$S_4^{10}$	$S_4^{10}$	$S_4^{10}$	$S_3^{12} S_1^4$	$S_2^{20}$	$S_2^{20}$	$S_2^{20}$	$S_1^{40}$	G/G <sub>5</sub>
$S_6^2 S_3^6$	$S_6^5$	$S_5^6$	$S_4^6 S_2^3$	$S_4^6 S_2^3$	$S_4^6 S_1^6$	$S_3^{10}$	$S_2^{12} S_1^6$	$S_2^{15}$	$S_2^{15}$	$S_1^{30}$	G/G <sub>6</sub>
$S_6^4 S_3^2$	$S_6^3 S_3^4$	$S_5^6$	$S_4^6 S_2^3$	$S_4^6 S_2^4$	$S_4^6 S_2^3$	$S_3^{10}$	$S_2^{14} S_1^2$	$S_2^{13} S_1^4$	$S_2^{15}$	$S_1^{30}$	G/G <sub>7</sub>
$S_6^4 S_3^2$	$S_6^4 S_3^2$	$S_5^6$	$S_2^{14} S_1^2$	$S_4^6 S_2^3$	$S_4^6 S_2^3$	$S_3^{10}$	$S_2^{14} S_1^2$	$S_2^{14} S_1^2$	$S_1^{30}$	$S_1^{30}$	G/G <sub>8</sub>
$S_6^4$	$S_6^4$	$S_5^4 S_1^4$	$S_4^6$	$S_4^6$	$S_4^6$	$S_3^8$	$S_2^{12}$	$S_2^{12}$	$S_2^{12}$	$S_1^{24}$	G/G <sub>9</sub>
$S_6^3 S_2$	$S_6^2 S_3^2 S_1^2$	$S_5^4$	$S_4^4 S_2^2$	$S_4^3 S_3^4$	$S_4^5$	$S_3^6 S_1^2$	$S_2^{10}$	$S_2^8 S_1^4$	$S_2^{10}$	$S_1^{20}$	G/G <sub>10</sub>
$S_6^2 S_3^2 S_1^2$	$S_6^3 S_2$	$S_5^4$	$S_4^4 S_2^2$	$S_4^4 S_2^2$	$S_4^2 S_2^6$	$S_3^6 S_1^2$	$S_2^8 S_1^4$	$S_2^{10}$	$S_2^{10}$	$S_1^{20}$	G/G <sub>11</sub>
$S_6^3 S_2$	$S_6^3 S_2$	$S_5^4$	$S_2^{10}$	$S_4^5$	$S_4^5$	$S_3^6 S_1^2$	$S_2^{10}$	$S_2^{10}$	$S_2^{10}$	$S_1^{20}$	G/G <sub>12</sub>
$S_6^3 S_3$	$S_6^3 S_3$	$S_5^3$	$S_2^6 S_1^3$	$S_4^3 S_1^3$	$S_4^3 S_1^3$	$S_3^5$	$S_2^6 S_1^3$	$S_2^6 S_1^3$	$S_1^{15}$	$S_1^{15}$	G/G <sub>13</sub>
$S_3^4$	$S_6^2$	$S_5^2 S_1^2$	$S_4^2 S_2^2$	$S_4^2 S_2^2$	$S_2^6$	$S_3^4$	$S_2^4 S_1^4$	$S_2^6$	$S_2^6$	$S_1^{12}$	G/G <sub>14</sub>
$S_6^2$	$S_3^4$	$S_5^2 S_1^2$	$S_4^2 S_2^2$	$S_4^2 S_2^2$	$S_4^3$	$S_3^4$	$S_2^4 S_1^4$	$S_2^4 S_1^4$	$S_2^6$	$S_1^{12}$	G/G <sub>15</sub>
$S_6^2$	$S_6^2$	$S_5^2 S_1^2$	$S_3^6$	$S_4^3$	$S_4^3$	$S_3^4$	$S_2^6$	$S_2^4 S_1^4$	$S_2^6$	$S_1^{12}$	G/G <sub>16</sub>
$S_3^2 S_2^2$	$S_6^2 S_2^2$	$S_5^2$	$S_4^2 S_2$	$S_4^2 S_2$	$S_4^2 S_1^2$	$S_3^2 S_1^4$	$S_2^4 S_1^2$	$S_2^6$	$S_1^{12}$	$S_1^{12}$	G/G <sub>17</sub>
$S_6^5 S_3 S_1$	$S_6^5 S_3 S_1$	$S_5^2$	$S_2^4 S_1^2$	$S_4 S_2^3$	$S_4 S_2^3$	$S_3^2 S_1^4$	$S_2^4 S_1^2$	$S_2^4 S_1^2$	$S_2^5$	$S_1^{10}$	G/G <sub>18</sub>
$S_3^2$	$S_3^2$	$S_5 S_1$	$S_2^2 S_1^2$	$S_2^3$	$S_2^3$	$S_3^2$	$S_2^2 S_1^2$	$S_2^2 S_1^2$	$S_1^6$	$S_1^6$	G/G <sub>19</sub>
$S_3 S_2$	$S_3 S_2$	$S_5$	$S_2^2 S_1$	$S_4 S_1$	$S_4 S_1$	$S_3 S_1^2$	$S_2^2 S_1$	$S_2^2 S_1$	$S_1^5$	$S_1^5$	G/G <sub>20</sub>
$S_1^2$	$S_2$	$S_1^2$	$S_2$	$S_2$	$S_1^2$	$S_1^2$	$S_1^2$	$S_2$	$S_2$	$S_1^2$	G/G <sub>21</sub>
$S_1$	$S_1$	$S_1$	$S_1$	$S_1$	$S_1$	$S_1$	$S_1$	$S_1$	$S_1$	$S_1$	G/G <sub>22</sub>

$\downarrow G_{22}$	$\downarrow G_{21}$	$\downarrow G_{20}$	$\downarrow G_{19}$	$\downarrow G_{18}$	$\downarrow G_{17}$	$\downarrow G_{16}$	$\downarrow G_{15}$	$\downarrow G_{14}$	$\downarrow G_{13}$	$\downarrow G_{12}$	USCI table
S <sub>120</sub>	S <sub>60</sub> <sup>2</sup>	S <sub>24</sub> <sup>5</sup>	S <sub>12</sub> <sup>10</sup>	S <sub>12</sub> <sup>10</sup>	S <sub>12</sub> <sup>10</sup>	S <sub>10</sub> <sup>12</sup>	S <sub>10</sub> <sup>12</sup>	S <sub>10</sub> <sup>12</sup>	S <sub>8</sub> <sup>15</sup>	S <sub>6</sub> <sup>20</sup>	G/G <sub>1</sub>
S <sub>60</sub>	S <sub>60</sub>	S <sub>12</sub> <sup>5</sup>	S <sub>6</sub> <sup>10</sup>	S <sub>6</sub> <sup>10</sup>	S <sub>12</sub> <sup>5</sup>	S <sub>5</sub> <sup>12</sup>	S <sub>10</sub> <sup>6</sup>	S <sub>10</sub> <sup>6</sup>	S <sub>4</sub> <sup>15</sup>	S <sub>3</sub> <sup>20</sup>	G/G <sub>2</sub>
S <sub>24</sub>	S <sub>60</sub>	S <sub>24</sub> <sup>2</sup> S <sub>6</sub>	S <sub>12</sub> <sup>4</sup> S <sub>6</sub> <sup>2</sup>	S <sub>12</sub> <sup>4</sup> S <sub>6</sub> <sup>2</sup>	S <sub>12</sub> <sup>5</sup>	S <sub>10</sub> <sup>6</sup>	S <sub>10</sub> <sup>4</sup> S <sub>5</sub> <sup>4</sup>	S <sub>10</sub> <sup>6</sup>	S <sub>6</sub> <sup>8</sup> S <sub>4</sub> <sup>3</sup>	S <sub>6</sub> <sup>10</sup>	G/G <sub>3</sub>
S <sub>20</sub>	S <sub>12</sub> <sup>2</sup>	S <sub>24</sub> <sup>2</sup> S <sub>8</sub>	S <sub>12</sub> <sup>4</sup> S <sub>6</sub> <sup>2</sup>	S <sub>12</sub> <sup>4</sup> S <sub>6</sub> <sup>2</sup>	S <sub>12</sub> <sup>4</sup> S <sub>4</sub> <sup>2</sup>	S <sub>10</sub> <sup>6</sup>	S <sub>10</sub> <sup>6</sup>	S <sub>10</sub> <sup>4</sup> S <sub>5</sub> <sup>4</sup>	S <sub>8</sub> <sup>6</sup> S <sub>4</sub> <sup>3</sup>	S <sub>6</sub> <sup>10</sup>	G/G <sub>4</sub>
S <sub>12</sub>	S <sub>10</sub> <sup>2</sup>	S <sub>24</sub> S <sub>4</sub> <sup>2</sup>	S <sub>12</sub> <sup>3</sup> S <sub>4</sub>	S <sub>12</sub> <sup>3</sup> S <sub>4</sub>	S <sub>12</sub> <sup>2</sup> S <sub>3</sub> <sup>4</sup>	S <sub>10</sub> <sup>4</sup>	S <sub>10</sub> <sup>4</sup>	S <sub>10</sub> <sup>4</sup>	S <sub>8</sub> <sup>5</sup>	S <sub>6</sub> <sup>6</sup> S <sub>2</sub> <sup>2</sup>	G/G <sub>5</sub>
S <sub>12</sub>	S <sub>6</sub> <sup>2</sup>	S <sub>24</sub> S <sub>4</sub>	S <sub>12</sub> S <sub>6</sub> <sup>3</sup>	S <sub>12</sub> S <sub>6</sub> <sup>3</sup>	S <sub>12</sub> <sup>2</sup> S <sub>2</sub> <sup>2</sup>	S <sub>10</sub> <sup>3</sup>	S <sub>10</sub> <sup>3</sup>	S <sub>5</sub> <sup>6</sup>	S <sub>8</sub> <sup>3</sup> S <sub>2</sub> <sup>3</sup>	S <sub>6</sub> <sup>5</sup>	G/G <sub>6</sub>
S <sub>10</sub>	S <sub>12</sub>	S <sub>24</sub> S <sub>3</sub>	S <sub>12</sub> S <sub>6</sub> S <sub>6</sub> <sup>2</sup>	S <sub>12</sub> S <sub>6</sub> S <sub>6</sub> <sup>2</sup>	S <sub>12</sub> <sup>2</sup> S <sub>4</sub>	S <sub>10</sub> <sup>3</sup>	S <sub>10</sub> S <sub>5</sub> <sup>4</sup>	S <sub>10</sub> <sup>2</sup> S <sub>2</sub> <sup>2</sup>	S <sub>8</sub> <sup>3</sup> S <sub>2</sub> <sup>4</sup>	S <sub>6</sub> <sup>5</sup>	G/G <sub>7</sub>
S <sub>10</sub>	S <sub>12</sub>	S <sub>12</sub> <sup>2</sup> S <sub>4</sub>	S <sub>6</sub> <sup>4</sup> S <sub>3</sub> <sup>2</sup>	S <sub>6</sub> <sup>4</sup> S <sub>3</sub> <sup>2</sup>	S <sub>12</sub> <sup>2</sup> S <sub>4</sub>	S <sub>5</sub> <sup>6</sup>	S <sub>10</sub> <sup>2</sup> S <sub>5</sub> <sup>2</sup>	S <sub>10</sub> <sup>2</sup> S <sub>5</sub> <sup>2</sup>	S <sub>4</sub> <sup>6</sup> S <sub>2</sub> <sup>3</sup>	S <sub>3</sub> <sup>10</sup>	G/G <sub>8</sub>
S <sub>10</sub>	S <sub>5</sub> <sup>2</sup>	S <sub>24</sub>	S <sub>12</sub> <sup>2</sup>	S <sub>12</sub> <sup>2</sup>	S <sub>12</sub> <sup>2</sup>	S <sub>10</sub> <sup>2</sup> S <sub>2</sub> <sup>2</sup>	S <sub>10</sub> <sup>2</sup> S <sub>2</sub> <sup>2</sup>	S <sub>10</sub> <sup>2</sup> S <sub>5</sub> <sup>2</sup>	S <sub>8</sub> <sup>3</sup>	S <sub>6</sub> <sup>4</sup>	G/G <sub>9</sub>
S <sub>8</sub>	S <sub>10</sub>	S <sub>6</sub> S <sub>4</sub>	S <sub>12</sub> S <sub>6</sub> S <sub>2</sub>	S <sub>12</sub> S <sub>6</sub> S <sub>2</sub>	S <sub>12</sub> S <sub>3</sub> <sup>2</sup>	S <sub>10</sub> <sup>2</sup>	S <sub>5</sub> <sup>4</sup>	S <sub>10</sub> <sup>2</sup>	S <sub>8</sub> S <sub>4</sub> <sup>3</sup>	S <sub>6</sub> <sup>3</sup> S <sub>2</sub>	G/G <sub>10</sub>
S <sub>6</sub>	S <sub>4</sub> <sup>2</sup>	S <sub>8</sub> S <sub>4</sub>	S <sub>12</sub> S <sub>6</sub> S <sub>2</sub>	S <sub>12</sub> S <sub>6</sub> S <sub>2</sub>	S <sub>4</sub> <sup>2</sup> S <sub>3</sub> <sup>2</sup>	S <sub>10</sub> <sup>2</sup>	S <sub>10</sub> <sup>2</sup>	S <sub>5</sub> <sup>4</sup>	S <sub>8</sub> S <sub>4</sub> <sup>3</sup>	S <sub>6</sub> <sup>3</sup> S <sub>2</sub>	G/G <sub>11</sub>
S <sub>6</sub>	S <sub>10</sub>	S <sub>12</sub> S <sub>2</sub> <sup>2</sup>	S <sub>6</sub> <sup>3</sup> S <sub>2</sub>	S <sub>6</sub> <sup>3</sup> S <sub>2</sub>	S <sub>12</sub> S <sub>3</sub> <sup>2</sup>	S <sub>5</sub> <sup>4</sup>	S <sub>10</sub> <sup>2</sup>	S <sub>10</sub> <sup>2</sup>	S <sub>4</sub> <sup>5</sup>	S <sub>3</sub> <sup>6</sup> S <sub>1</sub> <sup>2</sup>	G/G <sub>12</sub>
S <sub>6</sub>	S <sub>6</sub>	S <sub>12</sub> S <sub>2</sub>	S <sub>6</sub> S <sub>3</sub> <sup>3</sup>	S <sub>6</sub> S <sub>3</sub> <sup>3</sup>	S <sub>12</sub> S <sub>2</sub>	S <sub>5</sub> <sup>3</sup>	S <sub>5</sub> <sup>3</sup>	S <sub>5</sub> <sup>3</sup>	S <sub>4</sub> <sup>5</sup>	S <sub>3</sub> <sup>5</sup>	G/G <sub>13</sub>
S <sub>5</sub>	S <sub>3</sub> <sup>2</sup>	S <sub>8</sub>	S <sub>6</sub> <sup>2</sup>	S <sub>6</sub> <sup>2</sup>	S <sub>4</sub> <sup>2</sup>	S <sub>10</sub> S <sub>2</sub>	S <sub>10</sub> S <sub>2</sub>	S <sub>3</sub> <sup>2</sup> S <sub>1</sub> <sup>2</sup>	S <sub>4</sub> <sup>3</sup>	S <sub>6</sub> <sup>2</sup>	G/G <sub>14</sub>
S <sub>4</sub>	S <sub>5</sub>	S <sub>6</sub>	S <sub>6</sub> <sup>2</sup>	S <sub>6</sub> <sup>2</sup>	S <sub>12</sub>	S <sub>10</sub> S <sub>2</sub>	S <sub>5</sub> <sup>2</sup> S <sub>1</sub> <sup>2</sup>	S <sub>10</sub> S <sub>2</sub>	S <sub>4</sub> <sup>3</sup>	S <sub>6</sub> <sup>2</sup>	G/G <sub>15</sub>
S <sub>4</sub>	S <sub>5</sub>	S <sub>12</sub>	S <sub>6</sub> <sup>2</sup>	S <sub>6</sub> <sup>2</sup>	S <sub>12</sub>	S <sub>5</sub> <sup>2</sup> S <sub>1</sub> <sup>2</sup>	S <sub>10</sub> S <sub>2</sub>	S <sub>10</sub> S <sub>2</sub>	S <sub>4</sub> <sup>3</sup>	S <sub>3</sub> <sup>4</sup>	G/G <sub>16</sub>
S <sub>4</sub>	S <sub>2</sub> <sup>2</sup>	S <sub>4</sub> S <sub>2</sub>	S <sub>6</sub> S <sub>4</sub>	S <sub>6</sub> S <sub>4</sub>	S <sub>3</sub> <sup>2</sup> S <sub>1</sub> <sup>2</sup>	S <sub>10</sub>	S <sub>10</sub>	S <sub>5</sub> <sup>2</sup>	S <sub>8</sub> S <sub>2</sub>	S <sub>6</sub> S <sub>2</sub> <sup>2</sup>	G/G <sub>17</sub>
S <sub>3</sub>	S <sub>4</sub> S <sub>2</sub>	S <sub>4</sub> S <sub>2</sub>	S <sub>6</sub> S <sub>3</sub> S <sub>1</sub>	S <sub>6</sub> S <sub>3</sub> S <sub>1</sub>	S <sub>4</sub> S <sub>3</sub>	S <sub>5</sub> <sup>2</sup>	S <sub>5</sub> <sup>2</sup>	S <sub>5</sub> <sup>2</sup>	S <sub>4</sub> S <sub>2</sub> <sup>3</sup>	S <sub>3</sub> <sup>3</sup> S <sub>1</sub>	G/G <sub>18</sub>
S <sub>2</sub>	S <sub>3</sub>	S <sub>4</sub>	S <sub>2</sub> <sup>2</sup>	S <sub>3</sub> <sup>2</sup>	S <sub>4</sub>	S <sub>5</sub> S <sub>1</sub>	S <sub>5</sub> S <sub>1</sub>	S <sub>5</sub> S <sub>1</sub>	S <sub>2</sub> <sup>3</sup>	S <sub>3</sub> <sup>2</sup>	G/G <sub>19</sub>
S <sub>2</sub>	S <sub>2</sub>	S <sub>2</sub> S <sub>1</sub>	S <sub>3</sub> S <sub>2</sub>	S <sub>3</sub> S <sub>2</sub>	S <sub>3</sub> S <sub>1</sub>	S <sub>5</sub>	S <sub>5</sub>	S <sub>5</sub>	S <sub>4</sub> S <sub>1</sub>	S <sub>3</sub> S <sub>1</sub> <sup>2</sup>	G/G <sub>20</sub>
S <sub>2</sub>	S <sub>1</sub> <sup>2</sup>	S <sub>2</sub>	S <sub>2</sub>	S <sub>2</sub>	S <sub>1</sub> <sup>2</sup>	S <sub>2</sub>	S <sub>2</sub>	S <sub>1</sub> <sup>2</sup>	S <sub>2</sub>	S <sub>2</sub>	G/G <sub>21</sub>
S <sub>1</sub>	S <sub>1</sub>	S <sub>1</sub>	S <sub>1</sub>	S <sub>1</sub>	S <sub>1</sub>	S <sub>1</sub>	S <sub>1</sub>	S <sub>1</sub>	S <sub>1</sub>	S <sub>1</sub>	G/G <sub>22</sub>

## References

- Ashrafi AR, Ghorbani M (2008) A note on markaracter tables of finite groups. *MATCH Commun Math Comput Chem* 59:595–603
- Ashrafi AR, Ghorbani M (2010) Enumeration of a class of IPR hetero-fullerenes. *J Serb Chem Soc* 75:361–368
- Ashrafi AR, Jalali M, Ghorbani M, Diudea MV (2008a) Computing PI and omega polynomials of an infinite family of fullerenes. *MATCH Commun Math Comput Chem* 60(3):905–916
- Ashrafi AR, Ghorbani M, Jalali M (2008b) Detour matrix and detour index of some nanotubes. *Dig J Nanomater Bios* 3:245–250
- Ashrafi AR, Ghorbani M, Jalali M (2008c) The vertex PI and Szeged indices of an infinite family of fullerenes. *J Theor Comput Chem* 7:221–231
- Ashrafi AR, Ghorbani M, Jalali M (2009) Study of IPR fullerenes by counting polynomials. *J Theor Comput Chem* 8:451–457
- Balasubramanian K (1980) The symmetry groups of non-rigid molecules as generalized wreath products and their representations. *J Chem Phys* 72:665–677
- Balasubramanian K (1981) Generating functions for the nuclear spin statistics of nonrigid molecules. *J Chem Phys* 75:4572–4585
- Balasubramanian K (1984) Recent applications of group theory to chemical physics in conceptual quantum chemistry models and applications. *Croat Chim Acta* 57:1465–1492
- Balasubramanian K (1995a) Combinatorics and spectroscopy in chemical group theory techniques and applications. Gordon & Breach Publications, Amsterdam
- Balasubramanian K (1995b) Graph theoretical perception of molecular symmetry. *Chem Phys Lett* 232:415–423
- Balasubramanian K (2004a) Non rigid group theory tunneling splittings and nuclear spin statistics of water pentamer. *J Phys Chem* 108:5527–5536
- Balasubramanian K (2004b) Nuclear spin statistics of extended aromatic C<sub>48</sub>N<sub>12</sub> azafullerene. *Chem Phys Lett* 391:69–74
- Burnside W (1897) *Theory of groups of finite order*. The University Press, Cambridge
- El-Basil S (2002) Prolegomenon on theory and applications of tables of marks. *MATCH Commun Math Comput Chem* 46:7–23
- Faghani M, Ghorbani M (2011) The number of permutational isomers of CL-20 molecule. *MATCH Commun Math Comput Chem* 65:21–26
- Fowler PW (1986) How unusual is C<sub>60</sub>? Magic numbers for carbon clusters. *Chem Phys Lett* 131:444–450
- Fowler PW, Manolopoulos DE (1995) *An atlas of fullerenes*. Clarendon, Oxford, Reprinted: Dover, New York, NY (2006)
- Fowler PW, Steer JI (1987) The leapfrog principle – a rule for electron counts of carbon clusters. *J Chem Soc Chem Commun* 18:1403–1405
- Fowler PW, Horspool D, Myrvold W (2007) Vertex spirals in fullerenes and their implications for nomenclature of fullerene derivatives. *Chem A Eur J* 13:2208–2217
- Friepertinger H (1996) The cycle index of the symmetry group of the fullerene C<sub>60</sub>. *MATCH Commun Math Comput Chem* 33:121–138
- Fujita S (1988a) Markaracter tables and Q-conjugacy character tables for cyclic groups an application to combinatorial enumeration. *Bull Chem Soc Jpn* 71:1587–1596
- Fujita S (1988b) Maturity of finite groups an application to combinatorial enumeration of isomers. *Bull Chem Soc Jpn* 71:2071–2080
- Fujita S (1988c) Inherent automorphism and Q-conjugacy character tables of finite groups, an application to combinatorial enumeration of isomers. *Bull Chem Soc Jpn* 71:2309–2321
- Fujita S (1988d) Direct subduction of Q-conjugacy representations to give characteristic monomials for combinatorial enumeration. *Theor Chem Acc* 99:404–410
- Fujita S (1988e) Subduction of Q-conjugacy representations and characteristic monomials for combinatorial enumeration. *Theor Chem Acc* 99:224–230



- Fujita S (1999a) Systematic enumeration of ferrocene derivatives by unit-subduced-cycle-index method and characteristic-monomial method. *Bull Chem Soc Jpn* 72:2409–2416
- Fujita S (1999b) A simple method for enumeration of non-rigid isomers an application of characteristic monomials. *Bull Chem Soc Jpn* 72:2403–2407
- Fujita S (1999c) Möbius function and characteristic monomials for combinatorial enumeration. *Theor Chem Acc* 101:409–420
- Fujita S (2000) Characteristic monomials with chirality fittingness for combinatorial enumeration of isomers with chiral and achiral ligands. *J Chem Inf Comput Sci* 4:1101–1112
- Fujita S (2001) The unit-subduced-cycle-index methods and the characteristic-monomial method their relationship as group-theoretical tools for chemical combinatorics. *J Math Chem* 30(3):249–270
- Ghorbani M (2011) Computing the vertex PI and Szeged polynomials of fullerene graphs  $C_{12n+4}$ . *MATCH Commun Math Comput Chem* 65:183–192
- Ghorbani M (2012) Enumeration of heterofullerenes: a survey. *MATCH Commun Math Comput Chem* 68(2):381–414
- Ghorbani M, Ashrafi AR (2006a) Counting the number of hetero fullerenes. *J Comput Theor Nanosci* 3:803–810
- Ghorbani M, Ashrafi AR (2006b) The cycle index of the symmetry group of fullerenes  $C_{24}$  and  $C_{150}$ . *Asian J Chem* 19:1109–1114
- Ghorbani M, Ashrafi AR (2012) Computing USCI table of an infinite family of fullerenes. *Comput Theor Nanosci* 9(5):681–687
- Ghorbani M, Jalali M (2009) The vertex PI, Szeged and omega polynomials of carbon nanocones  $CNC_4[n]$ . *MATCH Commun Math Comput Chem* 62:352–363
- Ghorbani M, Naserpour E (2011) The clar number of fullerene  $C_{24n}$  and carbon nanocone  $CNC_4[n]$ . *Iran J Math Chem* 2(1):53–59
- Kroto HW, Heath JR, O'Brien SC, Curl RF, Smalley RE (1985)  $C_{60}$ : buckminsterfullerene. *Nature* 318:162–163
- Kroto HW, Fichner JE, Cox DE (1993) *The fullerene*. Pergamon Press, New York
- Pfeiffer G (1997) The subgroups of  $M_{24}$  or how to compute a table of marks. *Exp Math* 6:247–270
- Pólya G, Read RC (1987) *Combinatorial enumeration of groups and chemical compounds*. Springer, New York
- Randić M (1974) On the recognition of identical graphs representing molecular topology. *J Chem Phys* 60:3920–3928
- Randić M (1976) On discerning symmetry properties of graphs. *Chem Phys Lett* 42:283–287
- Shao Y, Jiang Y (1995) Symmetry of hydrogenated  $C_{60}$ . *Chem Phys Lett* 242:191
- SYMMETRICA, A program system devoted to representation theory, invariant theory and combinatorics of finite symmetric groups and related classes of groups, Copyright by "Lehrstuhl II für Mathematik, Universität Bayreuth, 95440 Bayreuth". Distributed via anonymous ftp 132.180.16.20 in dist/SYM.tar.Z
- The GAP Team (1995) *GAP groups algorithms and programming*. RWTH, Aachen
- Trinajstić N (1992) *Chemical graph theory*. CRC Press, Boca Raton
- Zhang F, Li R, Lin G (1998) The enumeration of heterofullerenes. *J Mol Struct* 453:1–6

# Index

## A

- Adjacency matrix (AM)  
defined, 109  
D-type schwarzite (C<sub>38</sub>)<sub>2</sub> element, 110, 111  
global topological indices, 112  
(C<sub>34</sub>)<sub>2</sub> isomers, 110, 112  
isomers, D-type schwarzite (C<sub>32</sub>)<sub>2</sub>, (C<sub>34</sub>)<sub>2</sub>,  
(C<sub>36</sub>)<sub>2</sub> element, 109, 110  
(C<sub>28</sub>)<sub>2</sub> isomer with hexagonal necks, 110,  
111  
topological coordinates, 109  
Ajami, D., 229  
AM. *See* Adjacency matrix (AM)  
André, J.M., 206  
Armchair polyhex nanotubes  
horizontal edge of *T*, 406–407  
oblique edge in level *m*, 407–410  
Szeged index, TUAC<sub>6</sub>[*p*, *k*] nanotube,  
409–411  
Ashrafi, A.R., 477–478, 487, 515, 523  
Ayme, J.-F., 230  
Azari, M., 444, 457

## B

- Balasubramanian, K., 511  
Banhart, F., 44  
Bao, W., 32  
Benzenoid chains  
anthracene skeleton, 540  
benzenoid chain skeleton, 540–541  
C<sub>3n×20</sub> for n = 2, 541  
Fujita's theorem, 542  
mark table, 542–543  
point group, Z<sub>2</sub> × Z<sub>2</sub>, 539  
Bilayer and multilayer AGNRs  
α and β alignments, 218, 219

- band structure, PPP-RHF method,  
218, 219  
optical properties, 219  
Biyikoglu, T., 287  
Bonchev, D., 233  
Buehler, M.J., 2  
Bühl, M., 113  
Burke, K., 126  
Burnside's theorem, 536–537

## C

- Cameron, P., 340  
Carbon-based nanostructures  
chemical properties, 99  
creation, structural defects, 92  
1-D CNTs and 2-D graphene layers, 78  
dislocation, CNTs, 81  
divacancy defects, 84–86  
electron/ion irradiated carbon  
nanostructures, 80  
foreign atoms, 80  
HR-TEM and STM instruments, 80  
impurity adatom, 90–91  
issue, chemical doping, 81  
low-dimensional samples, 79  
macroscopic crystalline materials, 80  
massive graphene body, 79  
metallic/semiconducting, 78  
monovacancy defects, 82–84  
reconstruction, defects (*see* Defects  
reconstruction)  
silicon-based devices, 78  
*sp*<sup>2</sup>-hybridized carbon atoms, 79  
STEM, 82  
structural defects, 81  
structures, different allotropes, 78, 79

- Carbon-based nanostructures (*cont.*)  
 substitutional doping (*see* Substitutional doping)  
 SW defect (*see* Stone–Wales (SW) defects)  
 vacancy cluster, 86–88  
 XRD studies, 81
- Carbon nanobuds (CNBs)  
 C<sub>60</sub>-CNT  
 DFT, 150  
 fullerene-functionalized SWNTs, 149  
 energetic parameters and reaction barrier  
 atomic chemical susceptibility  
 distribution over tube 1, 156, 157  
 chemical contribution to coupling energy, 156  
 deformation energy, 156  
 of equilibrium, 155  
 photodimerization and/or oligomerization, C<sub>60</sub> molecules, 158  
 profile, barrier of [C<sub>60</sub> + (4, 4)], 156, 157  
 topochemistry of reactions, 159
- Cataldo, F., 270
- C<sub>60</sub> + C<sub>60</sub> Dyad  
 ACS *N<sub>DA</sub>*, 141  
 atomic chemical susceptibility, fullerenes, 141, 142  
 Coulomb's interaction, 144  
 electronic characteristics, 141, 143  
 fragment composition, HOMO and LUMO, 141  
 IMI potential, type 1 and branches, 140, 141  
 photoexcitation, van der Waals C<sub>60</sub> pair, 144  
 photostimulated charge transfer, 143  
 starting composition and equilibrium structure, 141, 142  
 thermal and high pressure technologies, 143
- (C<sub>60</sub>)<sub>2</sub> dimer  
 barrier profile, decomposition, 144–145  
 components, 145  
 covalent coupling, 146  
 description, 144  
 energy–distance dependence, 146  
 intermolecular C–C bonds, 144
- Chandross, M., 202
- Chemical hardness. *See* Electronegativity
- Chemical reactivity  
 basal atoms, 175  
 SWCNTs, 175
- Chernozatonskii, L.A., 119, 175
- Choi, H., 90
- Cluster nanotubes  
 carbon atom subject, 318  
 edge effects, 319  
 electronegativity, 317  
 molecular plot, 316  
 structural motive, 317  
 topological analysis, 318–319
- C<sub>60</sub> molecules. *See* Single-layer graphene (SLG)
- C<sub>4</sub>-nanotori, 424, 457, 466–468
- C<sub>4</sub>-nanotubes, 424, 466–469
- CNBs. *See* Carbon nanobuds (CNBs)
- C<sub>60</sub> oligomers  
 chemical and physical experiments, 148  
 chemical reactivity, *ca* atoms, 147  
 description, 146  
 $E_{gap} = I_A - \epsilon_B$ , 146  
 empirical reality, 148  
 linear orthorhombic crystalline modification, 149  
 stepwise, dimer to tetramer, 146, 147  
 tetramer compositions, 147–148  
 topochemical reactions, 149
- “Colored” molecular topology  
 CFD, 279–283  
 electronegativity and chemical hardness reactivity indices, 265–268  
 environmental protection, 278  
 molecular graph nodes, 278  
 PAH, 272–277  
 quantum chemistry, 277  
 ranking method, 278  
 semiempirical quantum computation, 264  
 Timisoara–Parma rule, 268–269  
 topological invariants, molecular graphs, 269–271
- Compact finite differences (CFD)  
 global dependence, 279  
 ionization energy and electronic affinity, 281  
 Pearson nucleophilic–electrophilic reactivity gap, 282  
 SLR, 280  
 spectral molecular analytical forms, electronegativity, 282  
 stabilized/optimized molecular structure, 283
- COMPASS. *See* Condensed-phase optimized molecular potentials for atomistic simulation studies (COMPASS)
- Zagreb indices, 444

- Condensed-phase optimized molecular potentials for atomistic simulation studies (COMPASS), 3, 19
- Co substitutionals ( $\text{Co}_{\text{sub}}$ ), graphene  
classical Heisenberg model, 66  
Lieb's theorem, bipartite lattices, 66  
PAR solutions, 68  
relative stability, 65  
single  $\pi$ -vacancies (*see* Single  $\pi$ -vacancies)  
spin couplings, 65–66  
spin densities, configurations, 66, 67
- Covalent functionalization, magnetic coupling  
Co substitutionals, 71–72  
description, 68  
FM and AFM spin solutions, 68  
isosurface, magnetization density, 70, 71  
spin polarization texture, 70  
t-DOS, 68–70  
variation, total energy, 70, 72
- ( $\text{C}_{38}$ )<sub>2</sub>, planar schwarzites, 126–128
- Crystal-like networks  
D-type surface, polybenzenes, 248, 252  
energetic data, 248, 251  
polybenzenes, P-type surface, 248, 251  
P-type surface, 248, 250
- Cycle index, 512, 515
- D**
- Dabirian, M., 412
- Defects reconstruction  
band structure, (7,7) and (12,0) SWNT, 93, 95  
Brillouin zone, CNTs, 93  
2-D graphene material, 95  
different geometric reconstruction, graphene edges, 96, 97  
GNR-based nanodevices, 95  
intramolecular junctions, SWNTs, 93  
SW defects, 96  
vacancy configurations, structural models, 93, 94  
zigzag GNR, 95
- Dendrimers  
coronene and sumanene motifs, 248, 249  
first-type nanostar, 325–327  
four-type nanostar, 331–333  
hyper-branched structure, 244  
mathematical progression, 244  
peptide, 244  
polyamidoamine, 244  
polybenzene dendrimer, 248, 250  
second-type nanostar, 327–329  
spanned cages, 247  
styrylbenzene dendrimer, 333–337  
three-type nanostar, 329–331  
triarylamine dendrimer of generation 1–3, 337–339  
types, 324
- Density functional theory (DFT), 265
- Descartes coordinates  
basis-centered cubic lattice, clusters, 292, 294  
clusters, face-centered cubic lattice, 292, 295  
conjugate gradient method, 292  
data, simple cubic lattice, 292, 293  
diamond lattice, data, 292, 296–297
- DFT. *See* Density functional theory (DFT)
- Distance  
explicit relations,  $d_3$ , 426  
 $a_n$  and vertices, 438  
vertices, 424, 425  
 $x_{o2}$  and vertices, 432  
 $x_{op}$  and vertices, 438
- Diudea, M.V., 244, 254, 255, 431
- Divacancy defects  
ball-and-stick models, SWNT, 84, 85  
5–8–5 defect, CNTs, 84  
description, 84  
migration in graphene, 85, 86  
SW-type transformations, 85
- Djoković, D.Ž., 257
- D'Mello, M., 269
- Došlić, T., 477–478
- Drawing. *See* Graph drawing
- E**
- EA. *See* Electro-absorption (EA)
- Eccentric connectivity index, 270
- Edge-Wiener index  
chemical applications, 423  
definition, 423  
explicit relation, 424–444  
first, 444–457  
graph vertices, 424  
sum of graphs, 457–469  
topological indices, 423, 497
- Eigenvectors  
algorithms, graph (*see* Graph drawing)  
conjugate gradient method, 298  
definitions, 286–287  
harmonic potential (*see* Harmonic potential)  
physical and chemical properties, 286

- Electro-absorption (EA)  
 $\pi$ -conjugated polymers, 219–220  
 and linear, 220  
 optical probe to probe, 220
- Electronegativity  
 aromatic compounds, 268  
 CFD, 266  
 conceptual reformulation, 265  
 DFT, 265  
 SLR, 266, 267
- Embedding in 3D and higher dimensional spaces  
 construction, quasicrystals, 298  
 molecular arrangement, 290–291
- Entringer, R.C., 413
- Ernzerhof, M., 126
- Estrada, E., 230
- Explicit relation, vertex and edge-Wiener numbers  
 conditions, 425  
 definition, 424  
 number of cycles, 429–430  
 $TUC_4C_8(R)$  nanotube, 433–437  
 $TUC_4C_8(S)$  nanotube, 437–444  
 vertices of graph  $G$ , 428–429  
 $(n, 0)$  zigzag polyhex SWNTs, 431–433
- F**
- Faghani, M., 515
- Fajtlowicz, S., 277
- Finite systems, PPP model  
 description, 206  
 optical absorption spectrum, graphene nanodisks, 209–211  
 optical properties, fullerene  $C_{60}$ , 206–209
- First edge Wiener index, composition of graphs, 444–457
- Fowler, P.W., 287, 486, 523
- Fujita's theorem, 542
- Fukui functions and local softness  
 electron number, 309  
 elementary cell, 308  
 energy variation vs. sub-unities, 310–311  
 ionization energy, 310  
 periodic carbon nanotubes, 309
- Fullerene  $C_{60}$   
 approximate  $\pi$ -electron system, 206  
 Coulomb parameters, 209  
 HOMO and LUMO, 207  
 lowest triplet excited state, 206  
 MRSDCI calculation, 208  
 nearest-neighbor hoppings, 207  
 optical absorption experiments, 208  
 optical absorption spectra, 207, 208  
 SCI level, 207  
 Soccer ball structure, 206, 207  
 wave function, 208–209
- Fullerene  $C_{60}$  + CNTs composites  
 CNBs  
 $C_{60}$ -CNT, 149–150  
 energetic parameters and reaction barrier, 155–159  
 UBS HF, computational synthesis (*see* Unrestricted broken symmetry Hartree-Fock (UBS HF) approach)
- Fullerene  $C_{60}$  + graphene composites  
 $C_{60}$  + NGr nanobuds, 159–160  
 GNBs (*see* Graphene nanobuds (GNBs))
- Fullerene + fullerene composites  
 $C_{60}$  +  $C_{60}$  Dyad, 141–144  
 $C_{60}$  oligomers, 146–149  
 $(C_{60})_2$  dimer, 144–146
- Fullerenes  
 bipartite, 487  
 eccentric connectivity index, 487  
 (3,6)-fullerenes (*see* (3,6)-Fullerenes)  
 (4,6)-fullerenes (*see* (4,6)-Fullerenes)  
 molecular graph, 485–486  
 polytope, 485  
 Szeged index, 487  
 vertex PI index, 487  
 Wiener index, 486
- (3,6)-Fullerenes  
 adjacency matrix, 488  
 arbitrary element, 489  
 bipartite, 487  
 description, 487–488  
 eccentric connectivity index, 487  
 $G[8n]$ , perception, 492  
 $J[24n]$ , 3D perception, 489, 491  
 $L[16n + 48]$ , 492  
 $M[40]$ , 488, 493  
 $M[12n + 4]$ , 488, 493  
 $8n + 4$  vertices, 488, 490  
 polytope, 485  
 revised Szeged index, 487  
 Wiener and eccentric connectivity indices (*see* Wiener and eccentric connectivity indices, (3,6)-fullerenes)  
 Wiener index, 486
- (4,6)-Fullerenes  
 $A[24]$ , 500, 502  
 $B[30]$ , 500, 503  
 bipartite, 487

- $B[12n + 6]$ , 500, 502, 505  
 eccentric connectivity index, 487  
 edges,  $A[8n]$ , 500–503  
 polytope, 485  
 revised Szeged index, 487  
 Wiener index, 486
- G**
- Gaito, S., 127  
 Gan, Y., 43  
 GAP programs  
   algorithm, 412–413  
   computation, 411  
   eccentric connectivity index, fullerenes, 507  
   hetero-fullerenes, 544  
   nanohorn, 544  
   number of vertices, 419–422  
   tree dendrimers, Wiener index, 413–415  
    $VC_5C_7 [p, q]$  nanotube, 416–419  
   vertices of graph, 415  
   Wiener index, fullerenes, 506–507  
 Gasyana, Z., 208  
 Ge, M., 473  
 Ghojavand, M., 477–478  
 Gholami, N., 324, 333, 337, 339  
 Ghorbani, M., 474, 515, 522, 523  
 GNBs. *See* Graphene nanobuds (GNBs)  
 GNRs. *See* Graphene nanoribbons (GNRs)  
 GNRs vs. SWNTs  
   adhesion intensity calculation, 14–15  
   bending rigidity, 6  
   binding, vdW, 4  
   carbon shell, 3  
   concentration distribution profiles, 9  
   corrugations and ripples, 4  
   cylindrical structure, 10  
   dangling  $\sigma$ -orbitals, 9  
   defects, chemical modifications, 17  
   dependence, diameter and chirality, 13–14  
   description, 6  
   1D interaction, 3  
   displacement, carbon rings, 9  
   effect of gap, helix-forming process, 16  
   helically inserting into, 4, 5  
   helically wrapping onto, 4, 5  
   helicity, 6  
   heterogeneous nucleation, silicon, 11  
   honeycomb lattice,  $sp^2$  hybridization, 2  
   interactions, 10, 11  
   materials, 2  
   MD simulation, 3–4  
   “molecular straws”, 3  
   nanoscale vehicle, 16–17  
   NGNRs, 9–10  
   noncovalent “wrapping”, polymer chains, 2–3  
   norepinephrine molecules, 17, 18  
   offset face-to-face  $\pi$ – $\pi$  stacking interaction, 7–8  
   potential energy, vdW interaction energy ( $E_{vdW}$ ), 7, 8  
   ribbon length variations and instantaneous velocities  $V_t$ , 12  
   rigid  $MoS_2$  inorganic nanoribbon, 10–11  
   saturation interaction energies per unit area, 15  
   self-assembled, 6  
   sidewalls and wrinkles, 4  
   spirogyra cell in chloroplast ribbon, 6  
   stacked structures, 8  
   vdW interaction, 7  
   worm-like chain conformation, 7  
 Godsil, C.D., 287  
 Graovac, A., 236, 288  
 Graph drawing  
   algorithms, analogy  
     nanotori, 288  
     spherical clusters and fullerenes, 287–288  
   extremal values, analogy  
     embedding, molecular arrangement, 290–291  
     spherical clusters and fullerenes, 289–290  
 Graphene + CNTs composites  
   ACS distribution, 175  
   cutting-blade CNT + NGr, 177–178  
   description, 173–174  
   donors and acceptors, electrons, 174  
   DWCNTs and SWCNTs, 177  
   equilibrium structures, 179  
   equilibrium structures, CNT + NGr, 175, 176  
   “hammer” and “cutting-blade” structures, 176  
   intermolecular C–C bonds, 177  
   investigations, 179–180  
    $sp^2$ - $sp^3$  transformation, 176  
   structure, contact zones, 174  
 Graphene nanobuds (GNBs)  
   chemically bound products, 162  
   “chemical portraits”, 162

- Graphene nanobuds (GNBs) (*cont.*)  
energetic parameters and single-reaction barrier  
 $[C_{60} + (9, 8)]$ , GNB decomposition, 169, 170  
components, total coupling energy, 168–169  
topochemistry, 170  
equilibrium structures and chemical portraits, 160–161  
hydrogen-terminated edges (*see* Hydrogen-terminated edges, GNBs)  
non-terminated edges (*see* Non-terminated edges, GNBs)  
odd electrons, 160
- Graphene nanodisks  
HOMO to LUMO orbitals, 210  
linear optical absorption spectra, 209, 211  
optical properties, 209  
quasi-1D GNRs and 0D, 209  
regular-shaped, 209  
structures, 209, 210  
triangular, 210
- Graphene nanoribbons (GNRs)  
and aminothiols-modified GNS, 32  
band structure  
AGNR-8, general GNR and ZGNR-8, 213  
armchair and zigzag, 211–212  
quasi 1D structures, 211  
spin density distribution, ZGNR-8, 214  
unit cell, eight dimer lines across the width, 212–213
- Fe NWs, 29  
gated  
device applications, spintronics field, 214  
DFT-based calculations, 216  
energy variation band gaps with electric field, 215–216  
half-metallic nature, ZGNRs, 215  
variation, band gaps of AGNRs, 216  
ZGNR-12, 214, 215  
optical properties  
AGNR-8, PPP-RHF method, 217  
determination, electronic structure, 216  
ZGNR-6 and bilayer-ZGNR-6, 217–218  
*vs.* SWNTs (*see* GNRs *vs.* SWNTs)
- Graphene nanosheets (GNSs)  
in biochemical and medical realms, 2  
C60 molecule, SLG (*see* Single-layer graphene (SLG))  
description, 1  
Fe NWs (*see* Iron (Fe) nanowires (NWs))  
GNRs *vs.* SWNTs (*see* GNRs *vs.* SWNTs)  
isolation, planar, 2  
two-dimensional, 1–2
- Graph invariants  
chemical structures, 232  
cyclacenes stability, 234  
cyclacene zigzag belts,  $N$  atoms and  $B$  bonds, 233, 234  
graphenic nanocone growth, 232  
Möbius-cyclacenes, 234, 235  
topological efficiency index, 231  
Wiener-weights (WW), 231
- Graphite ribbon, 229  
Guo, Z.L., 230, 235, 236  
Gutman, I., 324, 413, 423, 444, 487
- H**
- HAC<sub>5</sub>C<sub>6</sub>C<sub>7</sub>[ $k, p$ ], 324  
HAC<sub>5</sub>C<sub>6</sub>C<sub>7</sub>[ $r, p$ ] nanotube  
 $e \in E_1$ , 370–371, 387  
 $e \in E_2$ , 371–373, 387–388  
 $e \in E_3$ , 373–375, 388–389  
 $e \in E_4$ , 375–377, 389–391  
 $e \in E_5$ , 377–378, 391  
 $e \in E_6$ , 378–379, 392  
 $e \in E_7$ , 379–380, 392  
 $e \in E_8$ , 380–382, 393  
 $m$ th period, 369, 370  
[2,2] nanotube,  $p = 2, k = 2, 369$   
sub-case a, 382, 394  
sub-case b, 382, 394  
sub-case c, 382–383, 394–395  
sub-case d, 383, 395  
sub-case e, 383–384, 395  
sub-case f, 384, 395  
sub-case g, 384, 396  
sub-case h, 384–385, 396–397  
Szeged index, 385–386, 397–398
- HAC<sub>5</sub>C<sub>7</sub>[ $r, p$ ] nanotube  
 $e \in E_1$ , 357, 366–367  
 $e \in E_2$ , 357–360, 367  
 $e \in E_3$ , 360, 367  
 $e \in E_4$ , 360–363, 368  
 $e \in E_5$ , 363, 368  
 $m$ th period, 356  
 $p = 1, 366$   
 $p = 2, 356$   
 $p = 3, 366$   
 $p = 4, 356$   
 $p = 5, 366$   
 $p \geq 6, 357$   
 $p \geq 7, 366$   
sub-case a, 363

- sub-case b, 363–365
  - sub-case c, 365
  - sub-case d, 365
  - sub-case e, 365–366
  - subsets,  $E_i$ s, 356
  - Szeged index, 355, 369
  - Haddon, R.C., 171
  - Hardness–softness Fukui function, 307–308
  - Harigaya, K., 235
  - Harmonic potential
    - descartes coordinates, cubic and diamond cluster (*see* Descartes coordinates)
    - matrix construction, 291–292
  - Hartree-Fock equations
    - finite systems, 203–204
    - periodic systems, 204–206
    - RHF and UHF, 203
  - $HC_5C_7[r, p]$  nanotube
    - $e \in E_1$ , 399–400
    - $e \in E_2$ , 400–402
    - $e \in E_3$ , 402
    - $e \in E_4$ , 403
    - $e \in E_5$ , 403–405
    - $HC_5C_7[4, 8]$  nanotube,  $p = 8$ ,  $k = 4,399$
    - Szeged index, 405–406
  - Heilbronner, E., 230
  - Hetero-fullerenes
    - caps  $B$  and  $C$ , 516–517
    - carbon nanotubes, 534
    - $C_{16}B_{14}$ , 3-D graph, 514, 515
    - $C_{20}$ , 3-D graph, 514–515
    - $C_{12n+30}$ , 516, 518
    - conjugacy classes, 510
    - graph, 509
    - graphite, 514
    - infinite classes, 516
    - nanohorn, 535–536
    - permutation matrix, 511
    - Pólya's theorem (*see* Pólya's theorem)
    - poly-substituted fullerene, 515
    - symmetry group, 509–510
    - symmetry operations, 510–511
    - USCI table (*see* Unit-subduced cycle index (USCI))
    - zigzag nanotube, 516
  - Heydari, A., 434, 438, 439, 442
  - High-resolution transmission electron microscopy (HRTEM)
    - Au and Pt atoms, 43
    - combined with XRD studies, 81
    - and STM, 80
  - Hirsch, A., 113
  - Hoffmann, R., 138, 140
  - HRTEM. *See* High-resolution transmission electron microscopy (HRTEM)
  - Hydrogenation, graphenes
    - atomic and molecular adsorption, 184
    - description, 180
    - energetic characteristics, nanographene, 185–189
    - equilibrium structures, 182, 183
    - external factors, 180
    - final products, (5,5) nanographene, 181, 182
    - fixed membrane/unrestricted motion, carbon atoms, 180
    - fullerene  $C_{60}$  and graphene, 189–191
    - hydrogen atom attachment, 184
    - sequential adsorption pattern and cyclohexanoid conformers, 185
  - Hydrogen-terminated edges, GNBS
    - $[C_{60} + (9, 8)]$ , 168, 169
    - $[C_{60} + (5, 5)]$ ,  $C_{60}$  fullerene to zigzag and armchair, 166, 167
    - coupling energies, 167
    - IMI potential, type 3, 168
- ## I
- IMI. *See* Intermolecular interaction (IMI)
  - Infinite 1D periodic systems
    - bilayer AGNRs, 218–219
    - EA, zigzag GNRs (*see* Electro-absorption (EA))
    - GNRs (*see* Graphene nanoribbons (GNRs))
    - SWCNTs (*see* Single-walled carbon nanotubes (SWCNTs))
  - Intermolecular interaction (IMI)
    - in  $C_{60}$  pair, 141
    - donor-acceptor (DA) interaction, 139
    - equilibrium positions,  $R^{00}$  and  $R^{+-}$ , 146
    - $sp^2$  nanocarbons and monatomic species, 138
    - topochemical reactions, 140
  - Iranmanesh, A., 269, 324, 333, 337, 339, 340, 349, 355, 369, 399, 411, 412, 424, 442, 457
  - Iron (Fe) nanowires (NWs)
    - aminothiol molecule, GNS and GNR, 31–32
    - at angle of  $\varphi = 60^\circ$ , axis, 30–31
    - concentration profiles, X and Y direction, 23
    - description, 17
    - diameters and atomic size, 17
    - different chirality GNSs wrapping onto, 27, 28



- Iron (Fe) nanowires (NWs) (*cont.*)  
 and GNS layers, contact area, 22–23  
 helical rolling of one and two GNRs, 28–30  
 interaction energies, 30, 31  
 interaction energy calculation, 21–22  
 magnetic core-shell nanostructures, 18–19  
 MD simulation, 19  
 offset face-to-face  $\pi$ – $\pi$  stacking  
   interaction, 25  
 position effect, 28, 29  
 potential energy  $E_P$  and vdW energy  $E_{vdW}$   
   vs. time, 24  
 saturation interaction energies, 27–28  
 “scroll-forming” stage, 25  
 self-scrolling of GNSs, different lengths  
   onto, 27  
 spontaneous self-scrolling, GNS, 20–21  
 stability and properties, GNS, 18  
 structural transition, 23–24  
 thermodynamic model, 25–27
- J**  
 Jiang, Y., 515  
 John, P.E., 431
- K**  
 Kamien, R.D., 11  
 Kan, E.J., 216  
 Khadikar, P.V., 487  
 Khormali, O., 355, 424, 442  
 Klavžar, S., 257  
 Koopmans, T., 282  
 Kostant, B., 486  
 Krasheninnikov, A., 45
- L**  
 Larson, C.E., 477  
 László, L., 209  
 LDOS. *See* Local density of states (LDOS)  
 Leach, S., 209  
 Leapfrog fullerenes  
    $C_{20}$  and  $Le(C_{20})$ , 518–519  
   principle, 518  
 Lenosky, T., 245  
 Lieb, E.H., 54, 64, 66, 73  
 Local density of states (LDOS), 83  
 Loghman, A., 487  
 Lovász, L., 289
- M**  
 Mackay, A.L., 245  
 Magnetic coupling  
    $Co_{sub}$  impurities (*see* Co substitutionals  
     ( $Co_{sub}$ ), graphene)  
   covalent functionalization, 68–72  
   covalently chemisorbed molecules, 64  
   mechanical deformations, 63  
    $\pi$ -vacancy, 63–64  
 Mahmiani, A., 406, 433, 437  
 Mahmiani, O., 433  
 Manolopoulos, D.E., 486  
 Manolopoulos, D.E., 287  
 Mansoori, G.A., 340  
 Markaracter table  
   definition, 538  
   naphthalene, 539  
   non-Abelian group, 538  
 Mataga, N., 201  
 Mazumdar, S., 202, 222  
 MD. *See* Molecular dynamics (MD) simulation  
 Mekenyan, O., 233  
 Mermin, N.D., 20  
 Merrifield, R.E., 137  
 Metallic nanotubes  
   electronic bands structure, 313–314  
   local softness, 315  
   zero-gap system, 314  
 Meyer, J.C., 34  
 Milan Randić, M., 487  
 Möbius, A.F., 228  
 Möbius-nanoribbon topological invariants  
   aromatic hydrocarbons, 229  
   atomic eccentricities, 237  
   belt-shaped carbon allotropes, 230  
   closed graphenic zigzag nanoribbons, 235,  
     236  
   cyclacene zigzag belts, 230, 231  
   distance-based topological invariants, 238  
   electronic and magnetic properties, 230  
   graphenic nanoribbons, 236  
   graph invariants, 231–235  
   mechanical engineering, 229  
   physical properties, 229  
   Wiener index, 239  
 Möbius strip  
   chiral structure, 228  
   defined, 228  
   robust metallic surface, 230  
   theoretical pathway, 229  
   zigzag edge configuration, 230

## Molecular dynamics (MD) simulation

- Fe NWs, 19
- GNRs vs. SWNTs, 3–4
- SLG, 33

## Molecular graphs

- $C_{12n+4}$ , 474
- $C_{24n}$ , 481
- definition, 324
- dendrimers  $T_{k,d}$ , 413
- fullerene graph, 472
- physicochemical properties, 324
- topological index, 472
- topological invariants
  - carbon  $sp^2$  networks, 270
  - crystallographic materials, 271
  - efficiency index, 270
  - Wiener index, 269
  - Wiener-reactive matrices, 271

Monkhorst, H.J., 127

## Monovacancy defects

- description, 82
- electrons/ions irradiation, 84
- hexagonal lattices, 83
- LDOS, 83
- single vacancy (5-1DB), 83, 84

MRSDCI. *See* Multi-reference SDCI

(MRSDCI) method

Multi-reference SDCI (MRSDCI) method,  
203, 208

Multi-walled nanotubes (MWNTs), 466

Muñoz, E., 35

MWNTs. *See* Multi-walled nanotubes  
(MWNTs)

## N

Nagy, C.L., 255

## Nanostructures

- $C_{24}$ , 3-D graph, 519–520
- $C_{80}$ , 3-D graph, 519, 520
- $C_{84}$ , 3-D graph, 519, 521
- $C_{72}$  fullerene, 528–529
- $C_{3n \times 20}$ , 531–532
- $C_{3n \times 34}$ , 532–533
- $C_{12n+6}$ , 525–256
- $C_{40n}$ , 530–531
- $C_{10n}$  fullerene, 523–524
- $C_{12n}$  fullerene, 524–525
- $C_{24n}$  fullerene, 527–528
- cycle index, 525–526
- and eigenvectors, matrices (*see*  
Eigenvectors)
- hetero-fullerenes, vertices, 519
- Polya-Redfield theorem, 519

## Nanotubes

- armchair polyhex nanotube, 406–411
  - carbon, reactivity, 303
  - computational methods, 303
  - electronic bands structure, 312
  - fullerenes and, 302
  - GAP program (*see* GAP programs)
  - graphene, 304
  - $HAC_5C_6C_7[r, p]$  nanotube (*see*  
 $HAC_5C_6C_7[r, p]$  nanotube)
  - $HAC_5C_7[r, p]$  nanotube (*see*  $HAC_5C_7[r, p]$   
nanotube)
  - hardness–softness Fukui functions,  
307–308
  - $HC_5C_7[r, p]$  nanotube, 399–406
  - hydroxyl radical, 302
  - metallic (*see* Metallic nanotubes)
  - periodic models, 306
  - pyramidalization, 303, 304
  - reaction energies, 303, 305
  - reactivity fullerenes, 319
  - semiconductor, 312
  - $TUC_4C_8(R)$  nanotube (*see*  $TUC_4C_8(R)$   
nanotubes)
  - $TUC_4C_8(S)$  nanotube (*see*  $TUC_4C_8(S)$   
nanotubes)
  - zigzag dissection cuts, 303
- Naserpour, E., 523
- Near-edge x-ray absorption fine structure  
(NEXAFS) spectra, 106
- Negatively curved carbon surfaces
- ab initio calculation and topological  
arguments, 109
  - AM (*see* Adjacency matrix (AM))
  - growth mechanisms and spectroscopic  
characterization, 106
  - planar schwarzites (*see* Planar schwarzites)
  - P-type and D-type schwarzites, 108
  - Raman and NEXAFS spectra, 106
  - SCBD experiments, 108
  - spongy carbon, 107
  - TEM, random carbon schwarzites, 106,  
107
  - topological electronic states, 112–113
  - topological phonon structure, 114–118
  - triply periodic minimal surfaces, 107
  - Wiener index (*see* Wiener index)
- NEXAFS. *See* Near-edge x-ray absorption fine  
structure (NEXAFS) spectra
- Ni-doped graphene with uniaxial strains
- DOS around  $E_F$ , 56
  - DOS,  $Ni_{sub}$  defect, 57, 58
  - energy position, shifts, 58
  - evolution, 57

- Ni-doped graphene with uniaxial strains (*cont.*)  
 exchange splittings,  $3d_{xz}$  and  $3d_{yz}$  levels, 58  
 experimental setup, magnetic properties, 59, 60  
 external magnetic field, 60  
 magnetoelastic devices, 59  
 spin densities,  $Ni_{sub}$  defects, 59  
 spin moment, strain along  $(n, n)$  and  $(n, 0)$ , 56, 57  
 STM, 59–60  
 strain-tunable spin device, 56
- Nikolić, S., 423
- Nishimoto, K., 201
- Ni substitutionals ( $Ni_{sub}$ ), CNTs  
 armchair tubes, 61  
 band structure, 62  
 description, 61  
 $d_{xz}$ - and  $d_{yz}$ -like levels, 63  
 $d_{yz}$  contribution, 62  
 effect of curvature, 63, 64  
 Ni-doped SWCNTs, 62  
 relaxed geometry and isosurface, 61  
 spin polarization, 61–62  
 unreconstructed carbon vacancy, 63
- Non-terminated edges, GNBS  
 ACS distribution, 163–165  
 $C_{60}$  fullerene to zigzag and armchair edge atoms, 163  
 description, 162  
 energetic characteristics, equilibrium, 162, 164  
 multiple  $[(C_{60})_6 + (5,5)]$ , 163–164, 166
- NWs. *See* Iron (Fe) nanowires (NWs)
- O**
- Ohno, K., 201, 202
- Omega polynomial, polybenzenes  
 Cluj-Ilmenau (CI) index, 257  
 linear periodic BMTA $20-k$  network, 259, 260  
 orbit analysis, 256  
 polybenzene networks, net parameters, 257–259
- Ori, O., 269
- P**
- Pack, J.D., 127
- PAHs. *See* Poly-aromatic hydrocarbons (PAHs)
- Pakraves, Y., 349, 369
- Parabolic reactivity, 273
- Pariser–Parr–Pople (PPP) model Hamiltonian-based approach  
 $\pi$ -conjugated molecules, 198  
 core and  $\sigma$  electrons, 201  
 Dirac points, 198  
 disadvantages, 199  
 e–e interactions, 199  
 effect,  $\sigma$ -electrons, 199  
 electronic structure and optical properties, 200  
 finite and infinite  $\pi$ -electron systems, 200  
 finite systems (*see* Finite systems, PPP model)
- Fortran 90 computer program, 200
- GNRs, 198
- Hartree-Fock equations (*see* Hartree-Fock equations)
- HF MOs, 202
- infinite 1D periodic systems (*see* Infinite 1D periodic systems)
- long-range Coulomb interactions, 199
- Mataga–Nishimoto parametrization, 201
- on-site and long-range Coulomb interactions, 201
- PDPAs, 202
- planar hydrocarbons, 201
- SDCI and MRSDCI, 202–203
- static dielectric polarizabilities, finite systems, 202
- synthesis, graphene, 198
- Pariser, R., 199
- Parr, R.G., 199, 201
- Perdew, J.P., 126
- Permutational isomers  
 $C_{20-k}B_k$  molecules, 545  
 $C_{24-k}B_k$  molecules, 545  
 $C_{30-k}B_k$  molecules, 546  
 $C_{34-k}B_k$  molecules, 546  
 $C_{60-k}B_k$  molecules, 547  
 $C_{72-k}B_k$  molecules, 548  
 $C_{80-k}B_k$  molecules, 549  
 $C_{84-k}B_k$  molecules, 550  
 $C_{150-k}B_k$  molecules, 551–552  
 $H_{89-k}B_k$  molecules, 553  
 point group  $Z_2 \times A_5$ , 554–555
- Permutation representation (PR), 536
- Pisanski T, 287
- Planar schwarzites  
 $(C_{38})_2$ , 126–128  
 $(C_{18})_2$  and  $(C_{26})_2$ , 121, 122  
 formation, Y-shaped nanojunctions, 118, 119

- plumber art, connecting elbow-shaped nanotubes, 118, 119
  - smallest G-type planar schwarzite (C<sub>14</sub>)<sub>2</sub>, 120, 121
  - transformation, graphene bilayer into planar schwarzite (C<sub>38</sub>)<sub>2</sub>, 119, 120
  - vibrational characterization, perfect and defective configurations, 122
  - DOS, 122
  - functionalized *sp*<sup>2</sup> carbon samples, 126
  - zero wavevector, (C<sub>14</sub>)<sub>2</sub>, 122, 123
  - zero wavevector, (C<sub>18</sub>)<sub>2</sub>, 122, 124
  - zero wavevector, (C<sub>26</sub>)<sub>2</sub>, 122, 125
  - vibrational spectrum, 121
  - welding of nanotubes, 119, 120
  - Poly-aromatic hydrocarbons (PAHs)
    - chemical hardness values, 273
    - chemical reactivity information, 276
    - colored algorithm, 272
    - electronegativity values, 272, 273
    - electro-topological coloring algorithm, 272
    - octanol–water partition coefficients, 274
    - perylene structure, 272
    - structural–experimental values, 274, 275
    - topological descriptors, 273
  - Pólya’s theorem
    - cycle index, 512–513
    - generalization, 514
  - Polybenzenes
    - D-type surface, 248, 252
    - Omega polynomial (*see* Omega polynomial, polybenzenes)
    - P-type surface, 248, 251
  - Pople, J.A., 199
  - Popova, N.A., 182
  - PR. *See* Permutation representation (PR)
  - Putz, M.V., 266
- Q**
- Quasicrystal nanostructures
    - Euler formula calculation, multi-tori BMTX, 256
    - Gaussian curvature, 255
    - multi-tori, 252
    - multi-torus BMTA20, 254
    - orbit analysis, 256
    - pentagonal hyper-rings BMTXCy5, 253
- R**
- Randić, M., 511
  - Reactive empirical bond order (REBO), 33
  - REBO. *See* Reactive empirical bond order (REBO)
  - Romo-Herrera, J.M., 119
  - Royle, G.F., 287
- S**
- Saremi, S., 66
  - Sattler, K., 473
  - Scanning transmission electron microscope (STEM), 82
  - Scanning tunneling microscope (STM)
    - C<sub>0sub</sub>, 66, 67
    - Fermi energy, 59
    - with spin-STM, 60
    - π-vacancies, 66
  - SCBD. *See* Supersonic cluster beam deposition (SCBD)
  - Schmalz, T.G., 477
  - Schrijver, A., 289
  - Schwarz, H.A., 108
  - SDCI. *See* Singles-doubles-CI (SDCI) method
  - Second edge Wiener index, 424, 433, 437, 441, 469
  - Sedlar, J., 233
  - Shao, Y., 515
  - Shawe-Taylor, J.S., 289
  - Shaymardanova, L.K., 155, 164, 171, 173
  - Sheka, E.F., 143, 155, 164, 171, 173, 175, 180, 182
  - Simmons, H.E., 137
  - Simón-Manso Y, 230
  - Single-layer graphene (SLG)
    - features, ripples, 37
    - graphene ripples, stroked by energetic C60 molecule, 33
    - impact, C60 molecule, 32
    - MD simulation, 33
    - onset and propagation, 34
    - propagation, diffraction and interference, impacting ripples, 36, 37
    - ripples, 32
    - thermal equilibrium, 34–35
    - transverse bending vibrations, 35
    - water waves, throwing a pebble to static water pond, 33
    - Z direction displacements, 35–36

- Single  $\pi$ -vacancies  
 $\text{Co}_{\text{sub}}$  impurity, 53  
 covalent functionalization, 54  
 isosurface, spin density, 52–54  
 majority and minority spins,  $\text{Co}_{\text{sub}}$  defect, 52–54  
 spin-unpolarized band structure,  $D_{3h}$  carbon vacancy, 52–54
- Singles-doubles-CI (SDCI) method, 202–203
- Single-walled carbon nanotubes (SWCNTs)  
 carbon layer, 55  
 chemical reactivity, 175  
 description, 221  
 electronic structure, 96  
 functionalization, 70  
 vs. GNRs (*see* GNRs vs. SWNTs)  
 optical absorption spectrum, 221, 222  
 PPP-RHF method, band structure, 221  
 structure, 220, 221
- Single-walled nanotubes (SWNTs)  
 and MWNTs, 466  
 ( $n, 0$ ) zigzag polyhex, 431
- SLG. *See* Single-layer graphene (SLG)
- SLR. *See* Spectral-like resolution (SLR)
- Snir, Y., 11
- Son, Y.W., 90
- Spadoni, S., 119
- Spagnolatti, I., 127
- Spanning fullerenes  
 Archimedean, 243  
 coronene-and sumanene-preserving opening, 246, 247  
 crystal-like networks, 248–252  
 dendrimers (*see* Dendrimers)  
 energetics, hypothetical nano-junctions, 247, 248  
 junctions, map operations, 246  
 multi-tori, 245  
 omega polynomial, polybenzenes, 257–259  
 periodic nanostructures, 244  
 Platonic, 243  
 quasicrystals, 245  
 Sumanene motif, octahedral nano-junction, 246, 247
- Spectral-like resolution (SLR), 266, 267
- Spin-moment formation  
 antibonding regime, 48  
 bonding and nonbonding regimes, 48  
 Co substitutionals, 53  
 $D_{3h}$  carbon vacancy, 50, 51  
 electron–electron and metal–carbon interactions, 49  
 electronic structure near  $E_F$ , 50, 51  
 entities, 49–50
- GGA+U method, 49  
 “hybridization” model, 49  
 Jahn–Teller distortion, 53  
 localized defect levels, 52  
 Mulliken population analysis, 49  
 Sc impurities, 53  
 substitutional transition and noble metals, 47–48
- $sp^2$  Nanocarbons  
 [2 + 2] cycloadditions and topochemistry, 170–173  
 description, 138  
 fullerene  $\text{C}_{60}$  + CNTs composites (*see* Fullerene  $\text{C}_{60}$  + CNTs composites)  
 fullerene  $\text{C}_{60}$  + graphene composites (*see* Fullerene  $\text{C}_{60}$  + graphene composites)  
 fullerene + fullerene composites (*see* Fullerene + fullerene composites)  
 graphene + CNTs composites (*see* Graphene + CNTs composites)  
 hydrogenation, graphene (*see* Hydrogenation, graphenes)  
 IMI investigation, 138  
 odd electrons and donor-acceptor ability, 139–140  
 topochemical reactions, 138  
 topology and deformation, graphene, 189, 191, 192  
 topology, chemistry, 137
- Spontaneous self-scrolling, GNS  
 determination, speed, 20  
 Mermin–Wagner theorem, 20  
 metallic NWs, 21  
 onto Fe NWs, 20  
 structural transition, 2D to 3D phase, 20–21
- Stefu, M., 244
- STEM. *See* Scanning transmission electron microscope (STEM)
- STM. *See* Scanning tunneling microscope (STM)
- Stone–Wales (SW) defects  
 description, 82  
 electron and ion bombardment, 82  
 formation and characterization, 82, 83
- Strains, graphene magnetism  
 description, 55  
 Ni-doped graphene with uniaxial strain, 56–61
- $\text{Ni}_{\text{sub}}$   
 CNTs, 61–63  
 dopants, 55
- Structural defects, carbon nanostructures  
 covalently bonded adsorbates, 43

- Dirac-like wave equation, 42
- graphene magnetism, strains (*see* Strains, graphene magnetism)
- magnetic coupling, impurities (*see* Magnetic coupling)
- magnetic properties, point defects, 42
- substitutional transition-metal impurities (*see* Substitutional transition-metal impurities, graphenes)
- substitutional transition metals, 42–43
- Styrylbenzene dendrimer
- compute  $n_1(e|G)$ , 334–337
  - grown  $n$  stages, 333–334
- Substitutional doping
- atomic structure after asymmetric SW defects, 98–99
  - boron and nitrogen dopants, 88–89
  - conductance, SWNTs, 90
  - description, 88
  - description, nitrogen and two-probe system, 97, 98
  - DFT calculations, 97
  - electronic band modification, 96–97
  - of heteroatom, 96
  - model, nitrogen substitutional in (8,0) carbon nanotube, 89
  - nanodevices and foster innovative applications, 99
  - quasi bond states, 90
  - Raman spectroscopy, 89
  - sensing properties, 1-D CNT and 2-D graphene materials, 90
  - structural defects, 99
- Substitutional transition-metal impurities, graphenes
- bond lengths, 47
  - carbon–metal bond length, 47
  - Co<sub>sub</sub>, single  $\pi$ -vacancies (*see* Single  $\pi$ -vacancies)
  - diffusion barriers, 43
  - 3d shell and Mn transition, 47
  - DWCNT, 44
  - HRTEM, 43
  - spin-moment formation (*see* Spin-moment formation)
  - structural parameters and binding energies, 45–46
  - structural parameters, noble metals and Zn, 46, 47
  - SWCNTs, 44
  - typical geometry, transition and noble, 44, 45
  - unusual magnetic interactions, 44
- Sum of graphs, edge Wiener indices
- carbon nanotubes, 466
  - C<sub>4</sub>-nanotori, 466, 467
  - C<sub>4</sub>-nanotube, 466, 467
  - $G_1 = (V(G_1), E(G_1))$  and  $G_2 = (V(G_2), E(G_2))$ , 457–462
  - $G = C_n + C_m$ , 469
  - $G = P_n + C_m$ , 469
  - $G = P_n + P_m$ , 468
  - graphene, 466, 468
  - for  $i \in$ , 462–466
  - SWNTs, 466
  - topological indices, 466, 467
  - undirected connected finite graphs, 466
- Supersonic cluster beam deposition (SCBD)
- periodic schwarzites, 112
  - spongy carbon, 108
- SW. *See* Stone–Wales (SW) defects
- SWCNTs. *See* Single-walled carbon nanotubes (SWCNTs)
- SWNTs. *See* Single-walled nanotubes (SWNTs)
- Symmetry group
- cycle index, 529
  - fullerene, 533
  - generators, 539
- Szeged index
- architectural components, 323
  - dendrimers (*see* Dendrimers)
  - graph  $G$ , 324
  - nanotubes (*see* Nanotubes)
  - physicochemical properties, 324
  - topological index, 324
- T**
- Taeri, B., 434, 438, 439
- Taherkhani, B., 411
- t-DOS. *See* Total spin-polarized density of states (t-DOS)
- Terrones, H., 119, 245
- Timisoara–Parma topo-reactivity method
- CFD, 268
  - topological-reactivity energy, 268
  - topo-reactive indices, 269
- Topological efficiency index., 233
- Topological indices
- edge version, 487
  - edge Wiener indices
  - $P_n$  and  $C_n$ , 466, 467
  - $S_n$ ,  $K_n$  and  $K_{a,b}$ , 466, 467
  - mathematical properties and chemical meaning, 472

- Topological indices (*cont.*)  
 molecular graph, 471  
 properties and chemical meaning, 487  
 Szeged index, 487  
 vertex PI index, 487  
 Wiener index, 486
- Topological phonon structure  
 AM, P-type element/D-type schwarzite unit cell, 114  
 angular frequencies, 114  
 description, 114  
 eigenvalue equation, 114  
 force constants  $f_\alpha$ , 114  
 fullerenes and schwarzites, 115–117  
 spectrum vs. genus, 117–118  
 topological dynamics and phonons, 114
- Total spin-polarized density of states (t-DOS), 68, 69
- Triarylamine dendrimer of generation 1–3, 337–339
- Trinajstić, N., 412
- Trinajstić, N., 472
- $TUC_4C_8(R)$  nanotubes  
 horizontal edge, 340–341, 348  
 oblique edge, 343–346, 348–349  
 odd cycles, 433–434  
 Szeged index, 340, 346–347  
 vertical edge, 341–342, 348  
 vertices, 342–343  
 vertices lying among lines, 343, 347  
 vertices of  $T(p, q)$ , 434
- $TUC_4C_8(S)$  nanotubes  
 edge-Wiener index, 441–444  
 horizontal edge, 350  
 lattice with  $p = 4$  and  $q = 6$ , 437, 438  
*Let*  $TUC_4C_8(S) = G$ , 439–440  
 oblique edge, 350, 354  
 odd cycles, 437  
 Szeged index, 349, 351–355  
 two-dimensional lattice, 349, 350  
 vertex and first edge-Wiener number, 437–438  
 vertex-Wiener index, 439  
 vertical edge, 350
- U**
- UBS HF. *See* Unrestricted broken symmetry Hartree-Fock (UBS HF) approach
- Udvardi, L., 209
- Ugeda, M.M., 59–60
- Unit-subduced cycle index (USCI)  
 Burnside's theorem, 536–537  
 markaracter table (*see* Markaracter table)  
 PR, 536
- Unrestricted broken symmetry Hartree-Fock (UBS HF) approach  
 atomic chemical susceptibility  $N_{DA}$  over atoms, 150, 151  
 description, 150  
 equilibrium structures,  $[C_{60} + (4, 4)]$  CNBs, 152, 154–155  
 equilibrium structures, SWCNTs and hydrogen-terminated, 150, 151  
 evolution, atomic chemical susceptibility distribution, 150, 153  
 starting and structures, carbon nanobuds, 150, 152
- USCI. *See* Unit-subduced cycle index (USCI)
- Ushiro, M., 44
- V**
- Vacancy cluster  
 anomalous conductance, zigzag nanotubes, 88  
 atomic reconstruction, 86  
 corresponding electronic band structures, 87, 88  
 dangling bonds, 86  
 energetic irradiation impact, 86  
 Fermi levels, 87–88  
 structures, defective (7,7) SWNT, 86, 87
- $VC_5C_7[p, q]$  and  $HC_5C_7[p, q]$  nanotubes, 324, 415–419
- Vertex and edge-Wiener numbers  
 $TUC_4C_8(R)$  nanotube, 433–437  
 $TUC_4C_8(S)$  nanotube, 437–444
- Vukičević, D., 270, 477–478
- W**
- Wakabayashi, K., 235
- Wang, X.-B., 143
- Weaver, J.H., 143
- Wiener and eccentric connectivity indices, (3,6)-fullerenes  
 edges,  $G[8n]$ , 498, 499  
 $H[8n + 4]$ , 491, 494  
 $I[4n]$ , 494, 495  
 $J[24n]$ , 494, 496  
 $K[16n-32]$ , 496

- Wiener and eccentric connectivity indices,  
(3,6)-fullerenes (*cont.*)  
 $L[16n + 48]$ , 496, 497  
 $M[12n + 4]$ , 497  
vertex, 491, 492
- Wiener, H., 128, 324, 423
- Wiener index. *See also* Edge-Wiener index  
chemical reactivity principles, 133  
chemical structures, 239  
colored forms, 264  
conjugation force, 130  
conjugation force  $F_{k,m0}$ , 131  
correlations, 324  
cyclacenes, 236  
defined, topological distance, 130  
description, 128  
electronegativity and chemical hardness,  
271  
inverse-range vector  $\alpha_{k,m}$ , 130  
linear correlation, 274  
Möbius-type periodicity, 239  
modification, 324  
molecular graphs, 269  
order 1 for site 0, 131–132  
PAH, 278  
and Szeged index, 413  
topological efficiency index  $\rho$ , 133  
total conjugation potential energy, 132  
tree dendrimers, 413  
wavefunctions,  $\pi$  electronic band,  
129
- Winkler, P.M., 257
- Woodward, R.B., 138, 140
- Wu, X., 159
- X**
- Xing, S.K., 232
- Y**
- Yakobson, B.I., 4  
Yakubo, K., 229  
Yarahmadi, Z., 477–478
- Z**
- Zakharchenko, K.V., 117
- Zeng, X.C., 159
- Zhao, H., 222
- Zigzag GNRs. *See* Electro-absorption (EA)
- Zig-zag nanotubes  
nanotubeG, 432  
TUC<sub>4</sub>C<sub>8</sub>(R) and TUC<sub>4</sub>C<sub>8</sub>(S) nanotubes,  
424  
vertex and first edge-Wiener number,  
430–431  
vertex and second edge-Wiener number,  
433  
vertex and the second edge-Wiener number,  
433  
( $n, 0$ ) zigzag polyhex SWNTs, 431  
( $n,0$ ) zigzag polyhex SWNTs, 431
- Zitnik, A., 287